NATO Advanced
Research Workshop



META'10

2nd International Conference on Metamaterials, Photonic crystals and Plasmonics

22-25 February, 2010, Cairo - Egypt

ISBN: 978-2-9545460-6-3
ISSN: 2429-1390

Edited by

Saïd Zouhdi | University Paris-Sud, France

January 18th, 2010

meta10.lgep.supelec.fr

META'10 Organizers

META'10 General Chair

S. Zouhdi, University of Paris Sud, France

META'10 General co-Chair

Hadia Elhennawy, Ain Shams University, Egypt

Organizing Committee

A. Safwat, Ain Shams University, Egypt
T. M. Abuelfadl, Cairo University, Egypt
I. El-Kady, Sandia National Laboratories, USA
I. A. Eshrah, Cairo University, Egypt
L. Santandrea, CNRS, France

International Advisory Committee

A. Boardman, UK
I. El-Kady, USA
N. Engheta, USA
M. Fink, France
S. He, Sweden
M. Inoue, Japan
T. Itoh, USA
Y. Kivshar, Australia
Y.-H. Lee, Korea
L.-W. Li, Singapore
R. Marques, Spain
O. E. Martinez, Argentina
G. Milton, USA
S. Noda, Japan
M. Notomi, Japan
Y. Rahmat-Samii, USA
V. Shalaev, USA
Ari Sihvola, Finland
M. Stockman, USA
S. Tretyakov, Finland
D. P. Tsai, Taiwan
Y. Vardaxoglou, UK
A. Vinogradov, Russia
M. Wegener, Germany
X. Zhang, USA
N. Zheludev, UK
R. W. Ziolkowski, USA

Technical Program Committee

T. M. Abuelfadl, Egypt
M. Ahachad, Morocco
T. Akalin, France
X. Begaud, France
Y. Bernard, France
F. Capolino, USA
R. Dkiouak, Morocco
N. El Minyawi, Egypt
A. El Sherbeni, USA
V. Fouad Hanna, France
J. Garcia de Abajo, Spain
S. Hrabar, Croatia
R.-B. Hwang, Taiwan
M. M. Ibrahim, Egypt
N. P Johnson, UK
D. Khalil, Egypt
P. Lalanne, France
S. Maier, UK
F. Martin, Spain
A. Nicolet, France
D. Pawlak, Poland
A. Priou, France
S. Prosvirnin, Ukraine
C.-W. Qiu, Singapore
A. Razek, France
A. Safwat, Egypt
A. Schuchinsky, UK
C. Sibilia, Italy
C. Simovsky, Finland
T. Szoplik, Poland
S. Tedjini, France
A. Zaghloul, USA
A. B. Yakovlev, USA

Special Session Organizers

T. Akalin, France
X. Begaud, France
A. Chipouline, Germany
I. El-Kady, USA
S. He, Sweden
S. Maier, UK
F. Martin, Spain
A. Vinogradov, Russia

Supporters & Sponsors

NATO Science for Peace & Security, Belgium
Office of Naval Research Global, UK
US Army International Technology Center, UK
European Office of Aerospace Research & Development, UK
GDR Ondes, France
SUPELEC, France
Optical Soceity of America, USA
IOP Publishing, UK
EPL, UK
European Optical Society, Germany
IEEE-APS, USA
IEEE-MTT, USA
URSI, Belgium
CST Middle East
Ain Shams University, Egypt
VI METAMORPHOSE, Belgium
ASTF, UAE

Contents

Progress on CRLH Metamaterials Based on Dielectric Resonators 13
T. Ueda and T. Itoh

Tunable Transmission and Enhanced Emission in Ordered Metallic Nanostructures Having Varying Channel Shape 20
Yalin Lu

Multilayer based interferential-plasmonic structure: metal cluster 3D grating combined with dielectric mirror 56
V. Janicki, J. Sancho-Parramon and H. Zorc

Multiband Small Zeroth-Order Metamaterial Antenna 60
Nabil. Dakhli, Fethi Choubani and Jacques. David

Dual Mode Composite Right-Left handed Unit Cells 64
Amr M. E. Safwat

The Motifs of Crystals and their Nano-aggregates 69
X. M. Lu, X. D. Shi, Y. G. Bi, Z. X. Chi, T. Min, L. L.Zhu, S. F. Xiao, and L. J. Zhong

Investigation of magneto-dielectric thin films as substrate for high impedance surfaces 73
F. Grange, C. Delaveaud, and K. Mahdjoubi

Reducing backscattering cross section of an electrically large sphere with metamaterial coating 77
M. Haghparast and M. S. Abrishamian

Sub-wavelength transmission resonances in multilayer partially-reflecting surfaces 80
C. S. R. Kaipa, A. B. Yakovlev, F. Medina, and F. Mesa

Parametric studies on modified split ring resonator (MSRR) and capacitance loaded strip (CLS) for left handed metamaterial 85
H. A. Majid, and M. K. A. Rahim

Plasmonic Crystal Waveguides 89
Slobodan M.Vuković, Zoran Jakšić, Ilya V. Shadrivov and Yuri S. Kivshar

Performance improvement of inverted L antenna with metamaterials 93
A. H. Amin Beidokhti, P. Rezaei
Thin-film sensing using circular split-ring resonators at mm-wave frequencies..... 97
A. Elhawil, J. Stiens, C. D. Tandt, W. Ranson, R. Vounckx

Finite element modeling of an acoustic cloak for three dimensional flexible
shells with structural excitation 100
M. Ramadan, W. Akl, T. Elnady, A. Elsabbagh

A novel subwavelength plasmon polariton optical filter based on tilted
coupled structures..... 106
L. O. Diniz, F. D. Nunes, E. Marega, Jr. and B.-H. V. Borges

Direct experimental optical characterization of metamaterials..... 111
E. Pshenay-Severin, F. Setzpfandt, C. Helgert, U. Hübner, C. Menzel, C. Rockstuhl,
A. Tünnerman, F. Lederer, and T. Pertsch

Photoconductivity studies on amorphous and crystalline TiO2 films
doped with gold nanoparticles..... 116
G. Valverde-Aguilar, J. A. García-Macedo, Víctor Renteria-Tapia, Manuel Aguilar-Franco

Optical Multistability in 1D Photonic Crystals with Nonlinear
Thue-Morse Structure..... 122
E. Lotfi, K. Jamshidi-Ghaleh, F. Moslemi and H. Masalehdan

Imaging of surface plasmon polariton interference using phase-sensitive
Photon Scanning Tunneling Microscope 127
J. Jose, F. B. Segerink, J. P. Korterik, J. L. Herek, and H. L. Offerhaus

Calculation of Surface Impedance for High Impedance Surface 132
Y. Zhu, and S. Zouhdi

Tunable effective permittivity of composites based on ferromagnetic
microwires with high magneto-impedance effect..... 138
M. Ipatov, G.R. Aranda, V.Zhukova, L. V. Panina, J. González, and A. Zhukov

Application of the McCutchen theorem to image-forming metamaterial slabs 145
Carlos J. Zapata-Rodriguez and Juan J. Miret

Subwavelength nondiffractting beams in multilayered media 150
C. J. Zapata-Rodríguez, and J. J. Miret

Optical absorption and SHG in PMMA and SiO2-matrices doped
with DO3 as function of poling time..... 155
J. García-Macedo, A, A. Franco, G. Valverde-Aguilar, and L. Romero

Using EBG Ground Plane for Improving Radiation in Low Profile Dipole Antenna 161
M. Rezaei Abkenar, P. Rezaei, and R. Narimani

Bandwidth evaluation of dispersive transformation electromagnetics based devices 166
C. Argyropoulos, E. Kallos, and Y. Hao

Phase Change Associated with Resonant Surface Plasmon Polariton-Assisted Transmission in Nanohole Arrays 171
T. Yang and H. P. Ho

Optical and structural properties of Au-Ag islands films for plasmonic applications 177
J. Sancho-Parramon, *V. Janicki, M. Lončarić, H. Zorc, P. Dubček and S. Bernstorff*

Optical devices based on materials with negative refraction 181
V. S. Gorelik and V. V. Shchavlev

Composite Right/Left-Handed Circular Meta-Waveguide 187
Tamer M. Abuelfadl

Dyadic Green's Function of a PEMC Cylinder 192
M. Rasouli Disfani, K. Vafi, and M. S. Abrishamian

Some left handed structures for microwave devices 197
I. A. Mocanu, T. Petrescu, N. Militaru, G. Lojewski and M. G. Banciu

Investigation of backward-wave propagation on LHM Split Ring Resonators 202
H. Talleb, Z.Djeffal, D. Lautru and V. Fouad Hanna

Numerical analysis of 2D tunable HIS on GaAs support 207
L. Matekovits, M. Heimlich, and K. Esselle

Resonances and dipole moments in dielectric, magnetic, and magnetodielectric cylinders – an overview 212
A. Dirksen, S. Arslanagic, and O. Breinbjerg

Anomalous reflection in metallic structures with subwavelength grooves: a circuit theory model 217
F. Medina, F. Mesa, and D. M. Skigin

Analytical methods for AMC and EBG characterisations 221
M. Grelier, F. Linot A. C. Lepage, X. Begaud, J.M. LeMener and M. Soiron

Single-layer metal nanolenses with tight foci in far-field 225
Piotr Wróbel, Tomasz J. Antosiewicz, Jacek Pniewski, Tomasz Szoplik

Planar Wide-Band 2-D Isotropic Negative Refractive Index Metamaterial 231
N. Amiri, K. Forooraghi, and Z. Atlasbaf

Excitation of Linear and Nonlinear Cavity Modes upon Interaction of
Femtosecond Pulses with Arrays of Metallic Nanowires 233
C. G. Biris and N. C. Panoiu

Hybrid biosignal-based filters for metamaterials spectral analysis 238
I. Sliesoraitytert, E. E. Fedorot, R Dubakienel, and V. Sliesoraitiene

Fabrication and characterization of membranes for extraordinary
optical transmission 242
G. Zacco, T. Ongarello, D. Garoli, P. Zilio, M.Massari, H. Kang, M.Tormen and F. Romanato

Microwave Metamaterials With Ferromagnetic Microwires..... 248
L. V. Panina, M. Ipatov, V. Zhukova, J. Gonzalez2 and A. Zhukov

Design and Characterization of a Tunable DNG Metamaterial Superstrate
for Small Beam Steering Antennas..... 255
H. Griguer, M. Drissi, E. Marzolf, H. Lalj and F. Riouch

Multipole approach in electrodynamycs of metamaterials..... 260
A. Chipouline, J. Petschulat, A. Tuennermann, T. Pertsh

Scattering by a nihility elliptic cylinder 266
A.-K. Hamid and M. I. Hussein

TM Scattering by a Perfect Electromagnetic Conducting Strip 270
A.-K. Hamid and M. I. Hussein

Sensitivity enhancement in optical waveguide sensors using metamaterials 274
Sofyan A. Taya and Mohammed M. Shabat

Electromagnetic response of a slit diffraction grating embedded in a dielectric
slab via an equivalent circuit model 280
R. Rodriguez-Berral, F. Mesa, and F. Medina

Analysis of a Transmission Line Periodically Loaded with
Position-Modulated Loads 284
E. S. Sakr and I. A. Eshrah

Characteristics of multilayer slab waveguide structure with a double negativity material 288
M. M. Shabat, S. A. Taya, and M. M. Abadla

Optical Memory Made of Photonic Crystal Working over the C-Band of ITU..... 299
A. Wirth Lima Jr. and A. S. B. Sombra

Zero-Reflection Metal Slabs: A Mechanism of Light Tunneling in Metamaterials..... 303
Guiqiang Du, Haitao Jiang , Zhanshan Wang and Hong Chena

Phonon considerations in the reduction of thermal conductivity in phononic crystals 308
P. E. Hopkins, L. M. Phinney, P. T. Rakich, R. H. Olsson III, and I. El-Kady

Acoustic wave propagation in fluid metamaterial with solid inclusions 317
I. V. Lisenkov, R. S. Popov and S. A. Nikitov

Band Gap Engineering in Simultaneous Phononic and Photonic Crystal Slabs 322
B. Djafari Rouhani, Y. Pennec, E.H. El Boudouti, J.O. Vasseur, Y. El Hassouani, C. Li, A.Akjouj and D. Bria

Acoustic meta-materials in MEMS bar resonators 328
X. Rottenberg, R. Jansen, Y. Zhang, A. Coosemans, G. Delcour, K. Herdewyn, J. Vanpaemel, C. Van Hoof and H.A.C. Tilmans

Optical Properties of HTcSc-Dielectric Photonic Crystals 333
Arafa H. Aly

Design and fabrication of subwavelength nanogratings based light-emitting diodes..... 338
Liang Zhang, Jinghua Teng, Soo Jin Chua, Eugene. A. Fitzgerald

Influence of the Group-velocity on the Pulse Propagation in 1D Silicon Photonic Crystal Waveguides..... 344
N. C. Panoiu and J. F. McMillan and C. W. Wong

Gold Film-Terminated 3-Dimensional Photonic Crystals 349
B. Ding, M. E. Pemble, A. V. Korovin, U. Peschel, S. G. Romanov

Rectangular Patch Antennas over Electromagnetic Band Gap Structure 354
Nihal F. F. Areed

Palladium sub-wavelength hole arrays for hydrogen sensing 358
E. Maeda, S. Mikuriya, M. Shuzo, I. Yamada, and J.-J. Delaunay

Performance Improvement of Patch-Antenna by Beam Focusing Using Left-Handed Metamaterial Perfect Lens Composed of Complementary Split Ring Resonators 362
E. K. I. Hamad, and A. A. A. Abdel-Raheem

Near-field Subsurface Detection using Metamaterial Inspired Probes 367
Zhao Ren, Muhammed S. Boybay, and Omar M. Ramahi

Manipulation of near field by means of arrays of wires 371
P.A. Belov, G. Palikaras, Y. Zhao, R. Dubrovka, and C.R. Simovski

All-dielectric Metamaterials for Patch Antenna Gain Enhancement 376
R.Alaee and K.Moussakhani

Analytical Theory of Effective Global Cloaking Processes: designing the Spherical EM Cloaking Nano-Element 380
T. Sengor

Disorder in optical metamaterials made of silver nanospirals 384
G. Guida, B. Gallas, R. Abdeddaim, A. Priou, J. Rivory, K. Robbie

Control of near-field radiative heat transfer via surface phonon-polariton coupling in thin films 390
M. Francoeur, M. P. Mengüç, and R. Vaillon

The optical characteristics of planar bi-layered metallic prisms 394
K. Yamaguchi, M. Fujii, T. Inoue, M. Haraguchi, T. Okamoto and M. Fukui

Investigation of coupling length in a semi-cylindrical surface plasmonic coupler 398
Pouya Dastmalchi, Nosrat Granpayeh, and Majid Rasouli Disfani

Plasmonic Dicke effect 403
T. V. Shahbazyan, V. N. Pustovit

Low loss surface polaritons and quantum memory in meta-materials 408
Ali A. Kamli, Sergey A. Moiseev , and Barry C Sanders

Investigated New Embedded Shapes of Electromagnetic Bandgap Structures and Via Effect for Improved Microstrip Patch Antenna Performance 410
D. N. Elsheakh, H. A. Elsadek, E. A. Abdallah, M. F. Iskander, and H. Elhenawy

Dual-band microwave duplexer based on metamaterial concepts 414
Adolfo Velez, Gerard Siso, Miguel Duran-Sindreu, jordi Bonache, Ferran Martin

Design of waveguides with Left-handed materials 420
Mondher Labidi, Jamel Belhad Tahar, Fethi Choubani

Automated Design and Sensitivity of CRLH Balanced Structures using Co-Design Approach 424
R. Siragusa, E. Perret, H. V. Hoang, P. Lemaître-Auger, S. Tedjini, and C. Caloz

Compact cavity resonators using high impedance surfaces 429
D. Dancila, X. Rottenberg, N. Focant, H.A.C. Tilmans, W. De Raedt and I. Huynen

Extraction of Capacitive Profiles with a Planar Metamaterial Sensor 434
M. Puentes, M. Schüßler, C. Damm, and R. Jakoby

Planar Superstrate for Dual-frequency RHCP-LHCP Array 439
E. Ugarte-Muñoz, F. J. Herraiz-Martínez, J. Montero-de-Paz, L.E. García-Muñoz and D. Segovia-Vargas

Effects of anisotropic disorder in an optical metamaterial 445
C. Helgert, C. Rockstuhl, C. Etrich, E.-B. Kley, A. Tünnerman, F. Lederer, and T. Pertsch

Theoretical and experimental investigations of easy made fishnet metamaterials at microwave frequencies 450
Riad Yahiaoui, Valérie Vignéras, and Patrick Mounaix

Crystallographic-oriented metal nanowires on semiconductor surface: technology and modeling 454
N. L. Dmitruk, T. R. Barlas, A. M. Dmytruk, A. V. Korovin, and V. R. Romanyuk

Nth Order Rose Curve as a Generic Candidate for RF Artificial Magnetic Material 459
A. Kabiri and O. M. Ramahi

A new model of dispersion for metals leading to a more accurate modeling of plasmonic structures using the FDTD method 463
A. Vial, T. Laroche, and M. Dridi

Effective Parameters of Metamaterial Substrate: Analytical and Semi-Analytical Methods 468
W. Abdouni, A. C. Tarot, A. Sharaiha

Rigorous surface polarizability models for oblique incidence on metamaterial mono-layers 473
A. I. Dimitriadis, D. L. Sounas, N. V. Kantartzis, and T. D. Tsiboukis

Frequency-dependent homogenization of split-ring arrays 478
M. H. Belyamoun, A. Bossavit and S. Zouhdi

Novel magnetic properties of metamaterials LH devices 483
M. A. Abdalla, and Z. Hu

Broadband filters based on OSRR and OCSRR balanced composite right/left handed transmission lines 488
Miguel Durán-Sindreu, Adolfo Vélez, Jordi Bonache and Ferran Martín

Increasing the bandwidth of coaxial apertures arrays in radar frequencies 494
S. Nosal, P. Soudais, and J.-J. Greffet

Wideband FSS for Electromagnetic Architecture in buildings 499
B. Sanz-Izquierdo, J.-B. Robertson, E. A. Parker and J.C. Batchelor

Wideband QAMC reflector's antenna for low profile applications 505
M. Grelier, M. Jousset, S. Mallégol, A. C. Lepage, X. Begaud and J.M. LeMener

Eigenmode and Array-Scanning Approaches for the Analysis of Wideband Metamaterials 510
N. A. Ozdemir, X. Radu, R.Mateos and C. Craeye

Substrateless micrometric metal mesh for mid-infrared plasmonic sensors 516
F. Mattioli, M. Ortolani, S. Lupi, O. Limaj and R. Leoni

Comparison of the Sensitivity of Plasmonic Peaks in Hole and Slit Arrays with the Surrounding Media 522
J. W. Menezes, L. F. Avila, E. S. Braga and L. Cescato

Electromagnetic waves refraction on the interface of transparent with absorptive right or left-handed media 526
N. L. Dmitruk, and A. V. Korovin

Nonlinear-optical metamirror 531
A. K. Popov, S. A. Myslivets

Enhanced broadband optical transmission in metallized woodpiles 536
R. Malureanu, A. Alabastri, W. Cheng, R. Kiyan, B. Chichkov, A. Andryieuski and A. Lavrinenko

Omega-shaped Stereometamaterials 541
R.Alaee, and K.Moussakhani

Thin-film polarizer made of heterogeneous medium with uniformly oriented silver nanoparticles 545
S. G. Moiseev

Effects of Acoustic Band Gap on Stimulated Brillouin Scattering in Microstructured Optical Fiber 550
Xinzhi Sheng, Di Wu, Jian Wang, Yin Wang, and Chenying Bao
Active coated nano-particles: impact of plasmonic material choice 552
S. Arslanagic, and R. W. Ziolkowski

New surface plasmon polariton photodetectors based on diffraction gratings with anticorrelated relief 557
S. V. Mamykin, M. L. Dmitruk, M. V. Sosnova, A. V. Korovin and V. I. Mynko

Tuning the Polarization States of Optical Spots at the Nanoscale on the Poincaré Sphere using a Plasmonic Nanoantenna 561
E. Ogut and K. Sendur

Photorealistic depictions of spherical gradient-index Metamaterials based objects 566
A. J. Danner

Threshold-free Cerenkov radiation in metallic metamaterials 571
Jin-Kyu So, Jong-Hyo Won, Seung-Ho Bak, Kyu-Ha Jang, D. S. Kim, Gun-Sik Park and F. J. Garcia-Vidal

Monolithic excitation and manipulation of surface plasmon polaritons on a vertical cavity surface emitting laser 574
J.-M. Lamy, J. Justice, G. Lévêque and B. Corbett

Tunable THz metamaterials based on an array of paraelectric SrTiO3 rods 578
R. Yahiaoui, H. Němec, P. Kužel, F. Kadlec, C. Kadlec and P. Mounaix

Localized Radiative Energy Transfer from a Plasmonic Bow-Tie Nanoantenna to a Magnetic Thin Film Stack 582
K. Sendur, A. Kosar, and M. P. Menguc

Analytical Formulation of the Radiation Field of Printed Antennas in the Presence of Artificial Magnetic Superstrates 587
Hussein Attia, Leila Yousefi, Omar Siddiqui and Omar M. Ramahi

Progress on CRLH Metamaterials Based on Dielectric Resonators

T. Ueda[1] **and T. Itoh**[2]
[1] Kyoto Institute of Technology, Japan
[2] University of California, Los Angeles, USA
ueda@kit.ac.jp, itoh@ee.ucla.edu

Abstract- Combination of magnetically-resonant dielectric resonators and TE cut-off waveguide structures provides unbalanced or balanced composite right/left handed transmission lines. This idea has been expanded into 1-D, 2-D, and 3-D composite structures, and can be applied to potential microwave and millimeter wave circuits and antennas in the same manner as conventional composite right/left handed transmission lines.

1. INTRODUCTION

In this paper, composite right/left handed (CRLH) metamaterial structures based on dielectric resonators are discussed. Basic idea of the metamaterial structures based on dielectric resonators is simple in that magnetic resonators, such as well-known split ring resonators, are replaced by magnetically-resonant mode of nonmetallic dielectric resonators inserted in TE cut-off waveguides with negative effective permittivity [1]. The use of dielectric resonators can reduce the insertion loss, compared to the metal-based resonators. However, the insertion or distribution of dielectric resonators into the artificial structures inevitably suffers from the increase in material loss due to the anti-resonance. Still, only the spatial distribution of dielectric resonators with their simple configuration without the help of wire connection for the networks, results in easy construction of higher-dimensional negative-permeability structures or CRLH metamaterial structures, in contrast to the cases where series capacitive elements are inserted into 3-D printed-circuit-type network structures. This dielectric resonator-based CRLH metamaterial structure can also be designed to be in balanced case [2] where no band gap between left-handed and right-handed modes appears, and where electromagnetic waves propagation along the composite structures have zero phase constants and nonzero group velocity. This balanced condition provides uniform field distribution with nonzero transmitted power flow along the transmission line, which leads to zeroth order resonators with resonant frequency independent of their whole size [3], resonant-type beam forming antenna, continuously backfire-to-endfire beam steering leaky wave antenna [2].

2. BASIC CONCEPT, 1-D CRLH STRUCTURE, AND EQUIVALENT CIRCUIT MODEL [2]

The geometry of a typical 1-D dielectric-resonator-based CRLH metamaterial structure is illustrated in Fig. 1. It is composed of a 1-D array of disc-type dielectric resonators inserted in a parallel plates or rectangular waveguide with open windows on the top wall, bottom wall, or both as an aperture to the air. In addition, a host medium is inserted in the waveguide to mechanically hold dielectric resonators. The polarization of the propagated waves is in the plane of the

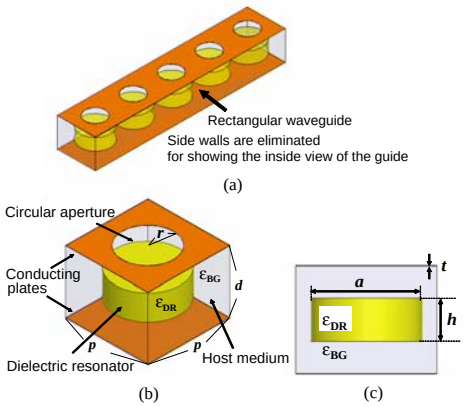


Fig. 1. Geometry of the 1-D dielectric-resonator-based CRLH metamatrial structure (After [2] © 2008 IEEE).

parallel plates. In order to explain the physical mechanism of wave propagation along the structure, the schematic of an equivalent circuit model for the unit cell is shown in Fig. 2. The field profiles in the vicinity of the dielectric disc under the fundamental $TE_{01\delta}$ resonance are similar to those of a magnetic dipole placed along the symmetric axis. As a result, the collective and macroscopic behavior of dielectric resonators under the magnetic resonance provides positive or negative effective permeability to the incident waves with the magnetic field component along the dipole. In the equivalent circuit model in Fig. 2, the resonant frequency of the $TE_{01\delta}$ resonant mode is expressed in terms of a closed loop of LC elements by $f_r = \omega_r / 2\pi = 1/2\pi\sqrt{L_r C_r}$. The effective permeability of the total structure is determined by a magnetic mutual coupling L_m of the incident wave propagating along the TE cut-off waveguide with the magnetically-resonant dielectric discs. Then the effective permeability shows anti-resonant characteristics, and negative permeability frequency region appears from f_r to $f_S = \omega_S / 2\pi = f_r / \sqrt{1-k^2}$, where k is a coupling coefficient between the dielectric resonator and TE cut-off waveguide. On the other hand, the effective permittivity can be changed by altering the configuration parameters of the TE cut-off parallel plate waveguide, such as the design of the distance of plates and the aperture size of the conducting mesh. The cut-off frequency, f_c, may be affected by insertion of the high dielectric constant discs, and is expressed in terms of the shunt branches by $f_C = \omega_C / 2\pi = 1/2\pi\sqrt{L_C C_C}$. By appropriately adjusting the frequency at zero effective permeability f_S and the frequency at zero effective permittivity f_C, we can design the balanced CRLH metamaterial structure. When a structure has open boundaries, radiation loss must be taken into account. The simulated effective permittivity and permeability for a balanced case of lossless CRLH transmission line are plotted in Fig. 3. They are extracted from the scattering parameters [2]. It is found from Fig. 3 that the imaginary part of effective permeability is almost zero and the effect of radiation loss appears in the imaginary part of epsilon. Therefore, the radiation loss leads to insertion of resistive elements into the shunt branch in the equivalent circuit model for the unit cell.

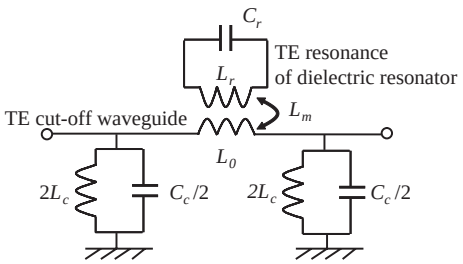


Fig. 2. Equivalent circuit model of the 1-D CRLH metamatrial structure (After [2] © 2008 IEEE).

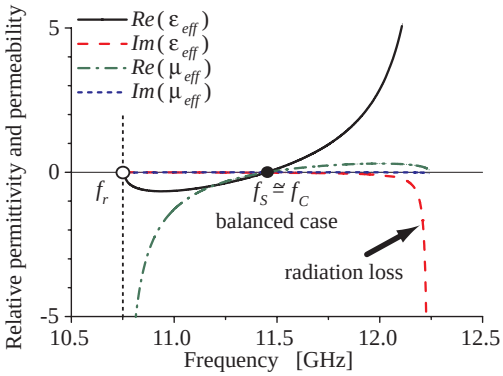


Fig. 3. Example of simulated effective permittivity and permeability estimated from S-parameters.

3. LEAKY WAVE ANTENNA APPLICATION [2]

Frequency-scanned backfire-to-endfire leaky wave antennas can be implemented by using the balanced dielectric-resonator-based CRLH transmission lines in the same manner as printed circuit-type CRLH transmission lines. The geometry of the designed leaky wave antenna operating at X band is shown in Fig. 4. The beam angle θ is taken from the broadside to the

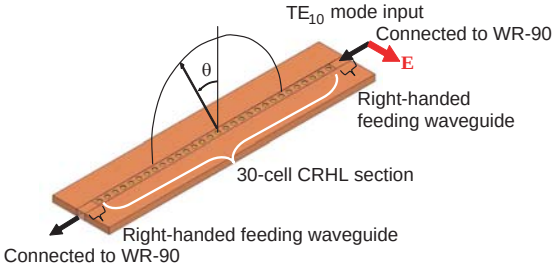
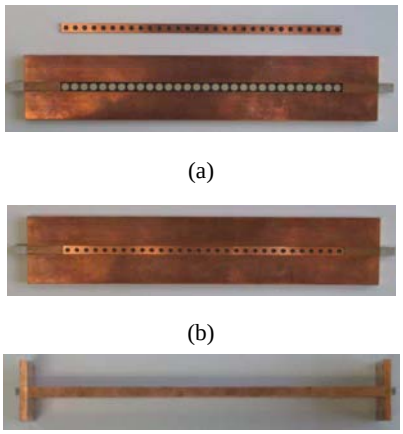


Fig. 4. Schematic of the 1-D DR-based CRLH transmission line for leaky wave radiation measurement (After [2] © 2008 IEEE).

forward direction, and the simulated radiation angles at 11.0 GHz, 11.5 GHz, and 12.0 GHz are -46 deg., 4 deg., and 52 deg., respectively. The corresponding antenna gains are 9.6 dBi, 10.5 dBi, and 11.2 dBi, respectively. The simulated directivity at 11.5 GHz is 19.7, which corresponds to the aperture efficiency of 84.3 %. The simulated maximum gain of 11.5 dBi is achieved at f = 11.9 GHz with the angle of θ = 38 degrees in the forward direction. The broadside radiation was obtained at f = 11.45 GHz. Thus, the backfire–to-endfire wide angle beam steering with the operational frequency was numerically confirmed with the gain of about 10 dBi. The leaky wave radiation from the fabricated CRLH transmission line shown in Fig. 5 was measured. In Fig. 6, the measured radiation patterns are shown at f = 10.9 GHz, 11.3 GHz and 12.0 GHz. The beam angles θ at these frequencies are -43 deg., 0 deg., and 64 deg., respectively. The corresponding antenna gains are 6.1 dBi, 7.4 dBi, and 6.6 dBi, respectively. The measured maximum gain of 8.7 dBi was achieved at f = 11.9 GHz with the angle of θ = 48 deg in the forward direction. In the numerical simulation, radiation for cross-polarization is negligible since the cross-polarized modes along the waveguide are in the cut-off region. From further simulation, it was confirmed that the measured gain for cross-polarization in the H-plane was -25dB less than that for the co-polarization. It should be mentioned that the proposed antenna provides continuous backfire-to-endfire radiation, and that the beam steering angle of 100 degrees has been achieved with steady gain of about 10 dBi.



(a) (b) (c)

Fig. 5. Photograph of the fabricated 30-cell CRLH transmission line fed by right-handed waveguides. (a) Uncovered CRLH section. (b) Top view. (c) Side view (After [2] © 2008 IEEE).

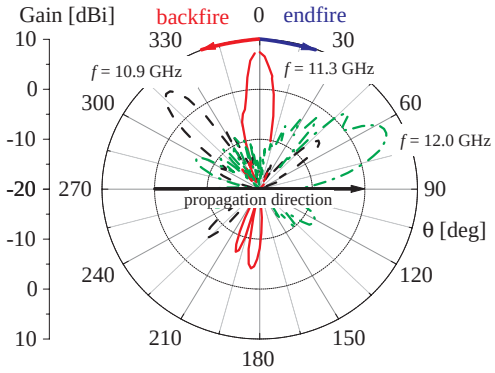
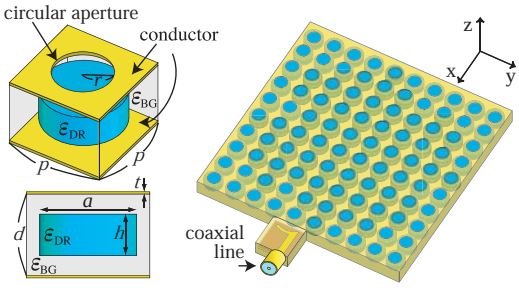


Fig. 6. Measured radiation pattern of the 30-cell CRLH transmission lines (After [2] © 2008 IEEE).

4. 2-D CRLH STRUCTURES AND APPLICATION TO ZEROTH ORDER RESONATORS [3]

It is straightforward to extend the concept of the CRLH transmission lines based on dielectric resonators into the 2-D structures, if the axes of dielectric disc are set normal to the parallel plates and the polarization of the incident waves is in the parallel plates [1]. The 2-D CRLH metamaterial structure can be applied to zeroth order resonators [3]. It is well-known that the resonant frequency of the zeroth order resonators does not depend on the whole size of the resonators but on electromagnetic characteristics of the unit cell. In addition, they can provide the uniform field distribution of the phase and magnitude along the structure. To date, the zeroth order resonance is investigated for miniaturization of antenna, gain



(a) (b)

Fig. 7. Geometry of the 2-D zeroth order resonator (After [3] © 2008 IEEE).

enhancement of the antenna, and microwave power dividers. The electrically large scale antenna based on the zeroth-order resonators have been proposed and have numerically shown the gain enhancement for the 1-D CRLH transmission lines [4]. In what follows, we consider the 2-D large-scale zeroth-order resonator, as illustrated in Fig. 7. It is composed of a 2-D array of disc-type dielectric resonators inserted in the parallel-plate waveguide with open windows on the top wall as an aperture to the air. The side walls are covered with conductor. The conducting side walls correspond to the conditions where both terminals are shorted in the equivalent circuit model. The balanced CRLH metamaterial structure is designed by adjusting the frequencies at zero effective permittivity and zero permeability. In general, resonant condition of transmission line resonators with length of l, and with both terminals shorted or open is provided by $\beta l = m\pi$, where the quantity m is an integer. In terms of the number of the unit cells in the transmission line, n, the condition is rewritten by $\beta p / \pi = m/n$. The zeroth-order resonance occurs when the $m = 0$, i.e. the phase constant $\beta = 0$. As found from the above condition, the resonant frequency for $m \neq 0$ varies with the change in the total size of the transmission line, while the zeroth-order resonant frequency does not. In Fig. 8, the simulated radiation patterns are shown as a function of the resonator's size. The E-plane is determined by the feeding methods and now in the y-z plane. The half-power beam widths for 3×3 cells, 5×5 cells, and 9×9 cells in the x-z plane are 68 deg, 52 deg, and 38 deg, respectively. The corresponding gains are 6.86 dBi, 6.60 dBi, and 8.3 dBi. Thus, the antenna directivity and gain are enhanced by increasing the number of the unit cells. The zeroth-order resonance of the designed 2-D dielectric-based CRLH metamaterial structures is confirmed by the numerical simulations. The configuration parameters for the fabricated circuits are almost the same as those in the numerical simulation, except for the aperture size. The radius of the aperture was carefully adjusted so that fabricated CRLH structures almost satisfy the balanced condition in the measurement. For large-scale and unbalanced CRLH structures with significant band gaps between LH and RH bands, the radiation from this type of zeroth-order resonance could not be achieved. The radius of

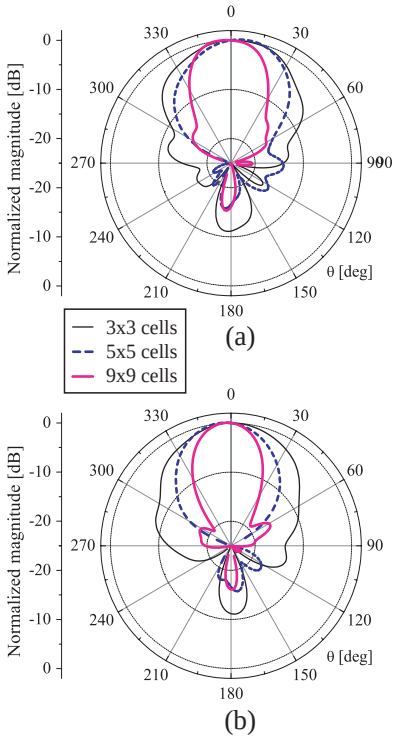


Fig. 8. Simulated radiation pattern as a function of number of cells (After [3] © 2008 IEEE). (a) In the H (x-z) plane. (b) In the E (y-z) plane.

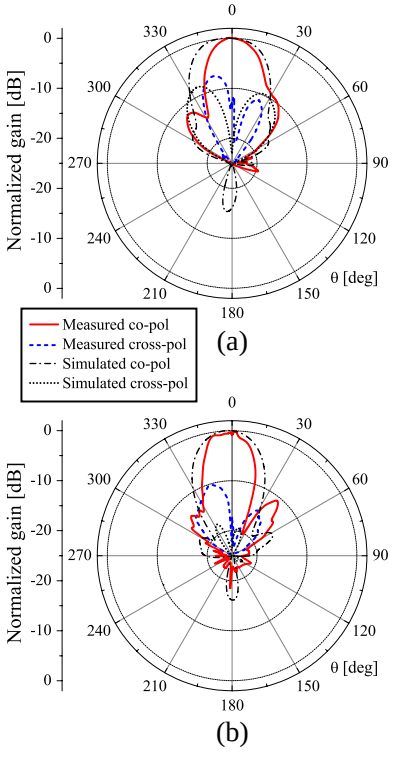


Fig. 9. Measured radiation pattern for 9×9 cells (After [3] © 2008 IEEE). (a) In the H-plane. (b) In the E-plane.

the aperture was set to r = 1.6 mm. A line probe was used as a transformer from an input coaxial cable to the designed resonators. The probe was fed with a microstrip line, aligned in the transverse direction, and was magnetically coupled to the dielectric resonators. The impedance matching was made by adjusting the position of the ground edge of the microstrip line. In Fig. 9, the measured radiation patterns are shown along with the numerical results for 9×9 cells. The measured half-power beam width is 26 deg, while the corresponding simulated value is 38 deg. The measured patterns in both E- and H-planes are in good agreement with the simulation results. The measured gain was 6.57 dBi for 9×9 cells, whereas the simulated gain was 8.3 dBi. Thus, it is experimentally confirmed that the directivity and gain are enhanced with the increase in size of the 2-D zeroth order resonators.

3. ANISOTROPIC 3-D CRLH STRUCTURES [6]

In what follows, one example of realization of 3-D CRLH metamaterial structures is shown, based on the concept of the combination of magnetically-resonant dielectric resonators with TE cut-off waveguide structures. Recently, we proposed multilayered volumetric CRLH metamaterial structures which were composed of a conducting mesh plate and a dielectric layer including dielectric resonators, as shown in Fig. 10 [5]. However, even the stacked structures supported CRLH transmission only for the 2-D propagation direction in the plane parallel to the layers, but not in the normal direction. In order to achieve new configuration realizing 3-D CRLH transmission, we need to take into account the dependence of polarizations and propagation directions of the incident waves on the propagation characteristics. As easily predicted from the geometry in Fig. 10, wave propagation in the stacked structure has essentially anisotropic characteristics. In the previous work, it was shown that the almost isotropic characteristics can be achieved in some frequency region when the polarization and the direction of the propagation are restricted to be in the 2-D regions parallel to the mesh plate. Therefore, in order to achieve less anisotropic characteristics for the 3-D CRLH metamaterial structures, there exist

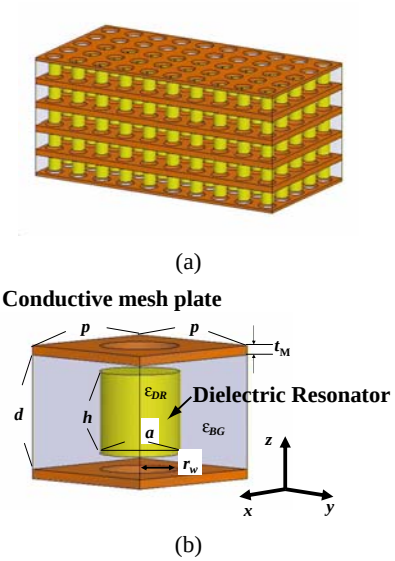


Fig. 10. Geometry of the proposed 3-D composite right/left handed metamaterial structure (After [5] © 2008 IEEE). (a) Perspective view. (b) Geometry of the unit cell.

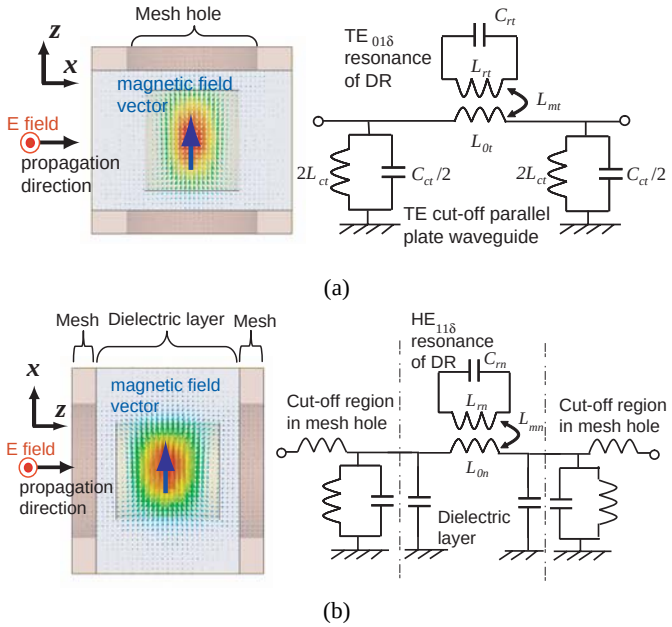


Fig. 11. Equivalent circuit models of the unit cell in the proposed CRLHTL for two different propagation directions (After [6] © 2008 IEEE). (a) In-plane propagation. (b) Propagation normal to the stacked layers.

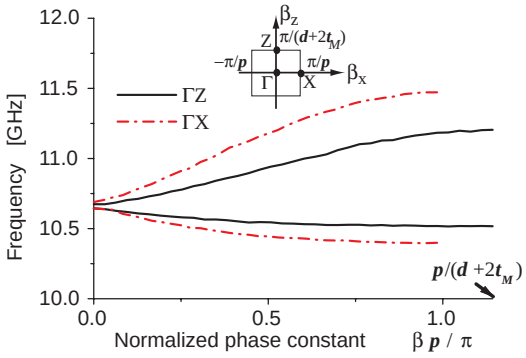
following two cases to be solved, (1) the difference of refractive indices for the in-plane propagations with the different polarizations parallel and normal to the mesh plates, (2) the anisotropy between propagation directions parallel and normal to the mesh plates. Here, we treat the latter case, that is, we attempt to make the anisotropy as small as possible for the propagation directions parallel and normal to the mesh plates, but the polarizations of the electric fields are limited to be in the mesh plates [6].

A. In-plane propagation

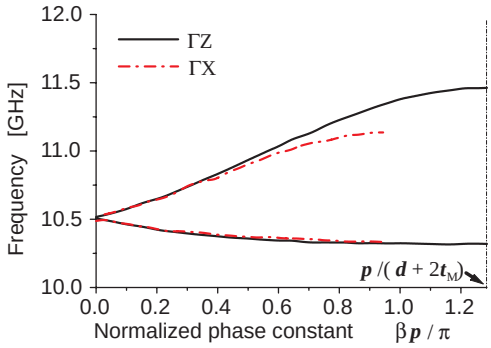
For the wave propagation parallel to the mesh plates, the fundamental mechanism is quite the same as that for the previous work in Ref. [4]. The equivalent circuit model is shown on the right hand side of Fig. 11(a). The effective permeability of the structure is governed by $TE_{01\delta}$ resonance of the dielectric disc. The typical magnetic field profile at the frequency near the resonance is shown on the left hand side of Fig. 11(a). The frequency regions with negative and positive permeability can be controlled by the density of the dielectric resonators. On the other hand, the effective permittivity can be changed by appropriately adjusting the configuration parameters of the TE cut-off parallel plate waveguide, such as the design of the distance of plates and the aperture size of the conducting mesh, which can lead to the design of the balanced CRLH structures.

B. Propagation normal to stacked layers

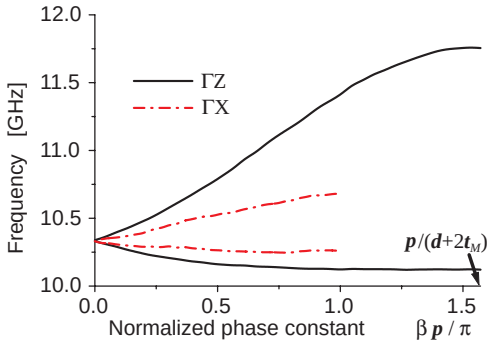
For the wave propagation normal to the stacked layers, the $HE_{11\delta}$ resonant mode of the dielectric disc is employed for the design of the positive and negative effective permeability, as shown in Fig. 11(b). In order for the above-mentioned $TE_{01\delta}$ and $HE_{11\delta}$ modes of the DR to be degenerate at the same operational frequency, the height and the diameter of the DR are set to be about the same. On the other hand, when designing the effective permittivity of the structure, the unit cell can be separated into two sections; a dielectric layer section including DRs, and conducting mesh plate sections. The effective permittivity of the former section is always positive, whereas the propagation through the aperture hole is under the cut off region. Therefore, the net shunt admittance in the equivalent circuit model for the unit cell provides the positive and negative permittivity of the structure. By adjusting configuration parameters in order for both the frequencies at zero permittivity and zero permeability to coincide with each other, balanced CRLH structures for the propagation normal to the stacked layers can be designed.



(a)



(b)



(c)

Fig. 12. Dispersion diagram for the balanced CRLHTL for two different propagation directions with d = 6 mm, t_M = 0.5 mm (After [6] © 2008 IEEE). (a) For p = 8 mm, r_w = 2.1 mm. (b) For p = 9 mm, r_w = 2.6 mm. (c) For p = 11 mm, r_w = 3.15 mm.

C. Challenge for less anisotropic characteristics

In this subsection, we will show some examples of dispersion diagrams that are numerically obtained for the proposed structure. The configuration parameters used in the simulation are as follows; the diameter, height and dielectric constant of DRs are a = 4.24 mm, h = 4.3 mm, and ε_{DR} = 38, respectively. The dielectric constant of the host medium in the dielectric layers is 2.2. In Fig. 12, dispersion diagrams for the distance between mesh plates d = 6 mm, the thickness of the mesh plates t_M = 0.5 mm are shown as a function of the period p. It is found from Fig. 12 that balanced CRLH structure can be constructed not only for the parallel propagation directions, but also for the normal direction. In addition, the CRLH band for ΓZ becomes narrower with a smaller size of the period. On the other hand, the CRLH band for the propagation parallel to the mesh plates becomes larger with a smaller period. For the present case, the propagation characteristics for both the normal and parallel propagation directions are about the same in the small phase-constant region for p = 9 mm, as shown in Fig. 12(b). In this case, almost isotropic characteristics are achieved. Only when focusing on these dispersion diagrams, the result in Fig. 12(b) seems isotropic around Γ point. However, it is found still significantly anisotropic, from the impedance point of view. From the further numerical simulation, it is found that the ratio of conducting mesh's thickness to the dielectric layer should get larger in order to decrease the anisotropy of the impedance.

6. CONCLUSIONS

The CRLH metamaterial structures based on dielectric resonators have been discussed. This idea was expanded into 1-D, 2-D, and 3-D composite structures, and was shown to be applicable to potential microwave and millimeter wave circuits and antennas in the same manner as conventional CRLH transmission lines.

REFERENCES

1. T. Ueda, A. Lai, T. Itoh, "Demonstration of negative refraction in a cut-off parallel-plate waveguide loaded with two-dimensional lattice of dielectric resonators," *IEEE Trans. Microw. Theory Tech*., Vol. 55, No. 6, pp. 1280-1287, June 2007.
2. T. Ueda, N. Michishita, M. Akiyama, T. Itoh, "Dielectric-resonator-based composite right/left handed transmission lines and their application to leaky wave antenna," *IEEE Trans. Microw. Theory Tech.*, Vol. 56, No. 10, pp. 2259-2269, Oct. 2008.
3. T. Yoshida, T. Ueda, M. Akiyama, T. Itoh, "Radiation characteristics of zeroth-order resonators composed of 2-D dielectric-based composite right/left handed metamaterial structures," *in Proc. of the 39th European Microw. Conf.*, Sept. 2009, pp. 205-208.
4. C. Caloz, T. Itoh, and A. Rennings, "CRLH metamaterial leaky-wave and resonant antennas," *IEEE Antennas and Propagation Magazine*, vol. 50, no. 5, pp. 25-39, Oct. 2008.
5. T. Ueda, N. Michishita, A. Lai, M. Akiyama, T. Itoh, "2.5-D stacked composite right/left handed metamaterial structures using dielectric resonators and parallel mesh plates," *in IEEE MTT-S Int. Microw. Symp. Dig.* , June 2008, pp. 335-338.
6. T. Ueda, N. Michishita, M. Akiyama, T. Itoh, "Anisotropic 3-D right/left handed metamaterial structures composed of stacked layers using dielectric resonators and mesh plates," *in IEEE MTT-S Int. Microw. Symp. Dig.*, June 2009, pp. 59-62.

Tunable Transmission and Enhanced Emission in Ordered Metallic Nanostructures Having Varying Channel Shape

Yalin Lu

Laser Optics Research Center, the Physics Department, US Air Force Academy, CO 80840

Abstract

Extraordinary transmission spectra for one-dimensional (1D) gratings and two-dimensional (2D) metallic hole arrays change with the hole channel shape. In this paper, a converging-diverging channel (CDC) design was introduced. The transmission spectra corresponding to CDC-embedded nanostructures of 1D grating, circular and rectangular holes (2D hole arrays) are analyzed using three-dimensional (3D) finite element method. Tuning of optical transmission by changing the CDC structure has been investigated. In addition, a cavity composed of a CDC metallic grating and a 1D photonic crystal (PhC) can lead to an enhanced emission. Large coherence length of the emission can be achieved by exploiting coherent properties of surface waves in grating and PhC.

Email: *yalin.lu@usafa.edu*

1. Introduction

It was thought that transmission through a subwavelength aperture will be low according to the standard aperture theory by Bethe [1], which states that transmission through a subwavelength circular hole ($r << \lambda$) in an infinitely thin perfectly conducting metal sheet would scale uniformly with the ratio of r to λ to the power of four. But, an extraordinary transmission (EOT) of several orders of magnitude more than Bethe's prediction has been reported in arrays with subwavelength holes [2]. Observation of EOT has sparked renewed interests in studying transmission in metallic gratings [2] and hole arrays, to explain the underlying physics for EOT. Apparently, transmission between gratings and hole arrays will be fundamentally different. In a grating there is always a propagating mode inside the channel, whereas in a hole all modes are evanescent when the hole diameter is smaller than half the wavelength, and thus, there is a cutoff for the transmission [3]. Nevertheless, it is believed in general that EOT is mainly due to surface plasmon polariton (SPP) modes trapped at the interface between metal and surrounding dielectric layer. However, not all agree on the same SPP mechanism for the observed EOT [4,5]. According to several other studies the enhanced transmission can be divided into three steps: coupling of light to SPPs on the incident surface, transmission through holes to the other surface and then re-emission from there [6]. It was also reported that for metallic gratings there are two transmission resonances: coupled surface SPP modes, and cavity modes located inside the slits [7].

Manipulation of optical transmission has several structural variables, such as hole shape, periodicity, film thickness, and so on. In previous work, different hole shapes like elliptical [8], rectangular [9], C-shaped [10, 11], X-shaped [12], coaxial [13] have been studied. However, effect of the hole channel's shape on transmission has not received considerable attention. The hole's size/shape along with the hole channel's shape are supposed to be significant to the transmission

because that holes are expected to mediate SPP coupling between the two surfaces. Indeed, changing both hole's and channel's shape is an additional mean of not only tuning the transmission, but also making the device polarization-distinctive. This will be attractive to many potential photonic applications including infrared optics, imaging, security, etc.

In a thermal source light generation at the microscopic level is a spontaneous emission of photon when an emitter thermally excited relaxes to a lower state. Unlike a laser which produces highly coherent light, thermal light is a broad isotropic spectrum. In fact, thermal light is coherent in the near field [14-16]. This near field coherence is due to the surface wave role. Hence a grating on the surface can couple these waves to propagating waves, which will extend the coherence into the far field. Thus by modifying the surface profile, the near field coherence can be extended to far field in a particular direction at a given wavelength. This has been observed first on a doped silicon grating [17]. Similarly, a peak in the thermal emission by gratings on ZnSe [18], gold [19], and SiC [20] was also observed. For these gratings, it was noted that the excited surface waves could couple to the emitted radiation only for *p*-polarization [21].

In this study the CDC subwavelength gratings and hole arrays were studied. The CDC shape would still allow similar EOT effect, but, would give an extra degree of freedom in geometric variable to tune and to optimize the transmission. When a 1D CDC grating was used with a 1D PhC as a cavity, the enhanced emission, which will be similar to a 'laser', can be realized. In this design surface waves that could be present on both metallic gratings and PhCs would become useful.

2. The CDC design and simulation

The converging-diverging channel (CDC) design is shown in Fig. 1 (a), in which the CDC throat is located right at the center of the channel. Here *a* is the channel aperture, *g* the throat gap, *t*

the thickness, and θ the converging angle. Fig. 1 (a) describes a CDC grating having a period of d along x-axis. The grating's normal is along z-axis and its dimension along y-axis is assumed to be infinite. A p-polarized electromagnetic (EM) wave incident to the grating with an angle of α is also shown. A rectangular hole array is shown in Fig. 1 (c), in which the CDC is applied along both x- and y-axis in each hole channel. The hole has an aperture of a and b along the two directions. Both converging angle (θ) and period (d) along the two directions are kept the same. Similarly, a circular aperture CDC hole array is shown in Fig. 1 (d). The metals to be considered for such structures are aluminum (Al), silver (Ag) and gold (Au). Their dielectric function can be referenced from [22, 23]. For frequency range around 100 THz, dielectric constant of Ag can be described by the Drude model $\varepsilon = \varepsilon_\infty - \omega_p^2 / (\omega^2 + i\gamma\omega)$, where $\varepsilon_\infty = -175.0$, $\omega_p = 1.1 \times 10^{16}$ s^{-1}, and $\gamma = 10.51 \times 10^{13}$ s^{-1} [24]. The EM fields were assumed to be time-harmonic and the resulting governing equations for the steady-state distribution was solved using commercial 2D (for gratings) and 3D (for arrays) finite element software (COMSOL 3.3) [25]. The computational domain considered is a single unit cell surrounded either by periodic boundary conditions or by perfectly matching layers (PML) [26].

3. The CDC grating

Figure 2 shows CDC gratings' zero-order transmittance at normal incidence as a function of wavelength when using different channel configurations. Fig. 2 (a) discusses results from an Au grating. Two well-separated transmission peaks for straight channel grating can be identified as SPP & waveguide coupled resonance (~ 3.9 μm) and cavity resonance (~ 7.4 μm) [7]. Two peaks for the converging-only channel grating are at almost the same position as those from straight channel. However, their transmittance is much lower. For the CDC grating, the two transmittance peaks are approaching to each other as g decreases. This leads to an enhanced transmission in a very narrow

wavelength band. The CDC grating with g = 5 nm has a remarkable narrow-band transmission. Similar behaviors are observed for silver gratings (Fig. 2b). Shifting of the transmission resonance band with g can be seen in Fig. 3, where transmittance of an Al CDC grating, as functions of wavelength in the UV-visible range and g, is shown. Full width at half maximum (FWHM) of the transmission peak shrinks with reduction in g, and the peak's magnitude as well.

4. The CDC rectangular hole array

According to the rectangular CDC array design shown in Fig. 1 (c), the array is periodic along both x and y directions, and the periodicity along the two directions are the same. Fig. 4 shows transmission spectra for Ag rectangular hole arrays having different *a/b* ratios. In all cases, hole area ($a \times b$), periodicity (d = 22 μm), converging angle ($\theta = 60^o$) and metal thickness (t = 2 μm) were kept the same. Their responses are very polarization-distinctive. By decreasing the *a/b* ratio, an increase in FWHM and a red-shift will occur. At frequencies below the cutoff ω_c (the frequency at which the transmission reaches half maximum of the peak), the transmission rapidly drops to below 0.1. All above results indicate a potential to use such rectangular CDC structures with different *a/b* ratios as filters for low frequencies.

Figure 5 shows the transmission for Ag rectangular hole arrays with different θ while keeping the same hole area, *a/b* ratio (16 μm/12 μm) and film thickness (2 μm). The results show a high-selectivity over incident polarization as well. The transmission for an E-field perpendicular to the long side has a strong peak for each θ in the selected wavelength range, while there is no peak for the case of an E-field parallel to the long side. Both peak position and FWHM can be tuned by changing θ. The peak position blue-shifts nearly linearly as decreasing θ. Moreover, since the g varies as θ changes, magnitude of the transmission peak and FWHM increase as θ decreases.

Interestingly, change of the magnitude with respect to θ is nearly linear. For frequencies beyond the cut off frequency ω_c, the transmissions drop rapidly.

Figure 6 shows the transmission with different metal thicknesses (*t*) while keeping the same hole area, *a*/*b* ratio (16 μm/12 μm) and converging angle (60°). Both solid and dashed lines are for different incident polarizations, and the transmission is highly polarization-selective. Similarly, strong peaks are only for the cases of E-field perpendicular to the long side. As *t* increases, one of the peaks stays almost at the same location (~21.8 μm), yet the location of the other peak blue-shifts. This behavior may be due to the excitation of two types of EM modes: coupled SPP and waveguide resonance. Those nearly fixed peaks are excited by coupled SPPs whose locations are not sensitive to film thickness, whereas the other peaks are caused by the waveguide resonance.

From t = 2.0 to 2.5 μm, transmission peaks caused by waveguide resonance blue-shift and their magnitude and FWHM decrease as well. Contrarily, magnitudes of the peaks related to SPP increase as *t* increases. One possible reason is that as the waveguide resonance peak blue-shifts, interaction between them becomes stronger. When t = 2.5μm, the interaction is so strong that the location of the SPP peak slightly red-shifts. For the case of t = 3.0 μm, however, only the SPP peak is left and it is relatively small (<0.5). This shows that without the contribution of the waveguide resonance, the SPP peak magnitude will decrease with increasing *t*.

5. The CDC circular hole array

The CDC circular hole arrays to be considered is made of Ag and have a fixed period (d = 19.0 μm) and thickness (t = 2.0 μm). Fig. 7 (a) and (b) show the transmission for arrays having straight channel with different apertures, and different CDC shapes when the aperture '*a*' is fixed at 10 μm. In straight channel arrays, transmission peaks become sharper when the aperture decreases.

A blue-shift also occurs with decreasing the aperture. Comparing to those straight channel arrays, CDC transmittance becomes narrower along with a further blue-shift. The blue-shift is larger when *g* gets smaller. The transmission after the peak decays faster for smaller *g*. Also, the peak magnitude does not change with the CDC shape, which supports the expected EOT.

Figure 8 (a) shows the transmittance at λ = 20 μm for two different aperture sizes with a varying *g*. For *a* = 10 μm the straight channel array (when *g* = 10 μm) has the highest transmission. It decreases exponentially with decreasing *g* and reaches zero asymptotically. For *a* = 12 μm the transmission for straight channel (when *g* = 12 μm) is not the highest. Instead the CDC with *g* = ~9.75 μm has an almost perfect transmittance. Hence, it can be seen that when a = 12 μm the transmittance increases as *g* reduces until it reaches a maximum and then further decreases exponentially with decreasing *g*. This suggests that the CDC shape with a particular *g* aids a mediation of SPP mode coupling between the incident and the transmitted surfaces. Similar behavior was observed previously in gold metallic gratings having the CDC shape [27].

Figure 8 (b) shows the transmittance for varying *t* at two different wavelengths. For straight channel with *t* = 2 μm the transmittance is maximal at λ = 19.825 μm (Fig 7(a)). At this wavelength the transmittance through the straight channel array does not vary much with *t*. In CDC the transmittance is maximum with *t* = 2 μm at λ = 19.25 μm (Fig. 7(b)). At this wavelength the transmittance increases as *t* increases until it reaches a maximum for *t* ~1.9 μm and then decreases with a further increase in thickness. A small dip near the peak is due to a slight mismatching in the waveguide resonance condition. Above results indicate that CDC arrays are more sensitive to *t* when comparing to straight channel arrays.

Figure 9 (a)-(d) show the transmittance of different arrays with respect to wavelength and aperture size *a* or throat size *g*, when *t* is fixed. Fig. 9 (a) shows the transmittance for straight

channel arrays or $\theta = 0^o$. It can be seen that at large aperture the transmittance is high at large wavelengths and decreases very slowly as the wavelength reduces. When the aperture is small the transmittance is high at lower wavelengths and it decrease very sharply as the wavelength increases. Also, it can be noted from Fig. 9 (a) that location of the transmittance peak changes linearly as the *a* or *g* decreases. In addition, FWHM of the transmittance peaks is large when the aperture is big and it becomes very narrow as the aperture reduces. Similar transmittance variation (Fig. 9 (b)) is observed for the CDC arrays having $\theta = 50^o$. But, this time transmission suffers a cut-off aperture size where there is no transmittance below a particular aperture size. Furthermore the location of the transmittance peak with respect to *a* or *g* is not exactly linear. When θ in CDC arrays increases to 65° (Fig. 9 (c)) and 72° (Fig. 9(d)), the cut-off aperture for zero transmittance increases.

6. The enhanced emission

A cavity is composed by a 1D CDC grating and a 1D PhC. The 1D PhC considered is made of lossless dielectrics (SiO_2 and InSb) with refractive indices given by [22] $n_{SiO_2} = 1.46$ and $n_{InSb} = 3.95$. A freely available MIT photonic band (MPB) package was used for calculating the photonic band structure (PBS) of the PhC. The first or lower band-gap in the PBS is between the normalized frequency range from 0.136 to 0.217. So, a PhC having a 100 nm unit cell thickness would have a first band-gap between 460 nm to 735 nm.

According to Kirchhoff's law, the directional spectral emissivity ($\varepsilon_{\lambda,\theta}$) can be determined by using $1-\rho_{\lambda,\theta}-\tau_{\lambda,\theta}$ [28], where the directional spectral reflectance, ($\rho_{\lambda,\theta}$) and the directional spectral transmittance, ($\tau_{\lambda,\theta}$) are evaluated by using a plane monochromatic wave incident from the air at an angle of incidence 'θ' as shown in Fig. 1 (b). It is plausible to use Maxwell's equation when the absolute lower limit of the length of macroscopic domain is 10 nm [29]. Therefore, it is assumed

that the results obtained here for gap of 5 nm will be rational. The transmission for metallic lamellar gratings with Transverse Electric (TE) polarization suffers a cut-off wavelength [30]. Hence, we have analyzed the gratings with only TM polarization (magnetic field parallel to the gratings).

Figure 10 (a) and (b) show normal emittance spectrum with *p*-polarization for the CDC grating with a 5 nm gap and 1D PhC with various cavity lengths. In Fig. 10 (a), the 50 nm cavity has one smaller emissive peak at the low wavelength end. When the cavity increases to 100 nm, the peak increases in magnitude and its position moves to the high wavelength end (a red shift). When the cavity increases to 200 nm, the only emissivity peak in the entire wavelength range of interest further red-shifts and has a magnitude almost close to unity. The 300 nm cavity has the major peak further red-shifted. A new peak appears in the low wavelength end and the major peak becomes a few narrow peaks. This indicates an onset of higher-order resonance inside the cavity. Similar high-order resonance behavior can be observed when further increases the cavity length to 690 nm (Fig. 10 (b)). Furthermore, FWHM of those emissive peaks for 100 nm and 200 nm cavities are around 4 nm. For the 300 nm cavity FWHM is around 5 nm. According to the Wiener-Khinchin theorem width of emission peak is inversely proportional to the coherence time [31]. This would then suggest that the cavity length is a good degree of freedom for achieving a tunable monochromatic thermal emitter for any desired wavelength with large temporal coherence.

Fig. 11 (a), (b) and (c) show the electric field intensity distribution normalized to the incident along a line through the center of the CDC throat and into the 1D PhC for different cavity lengths. The intensity variation seems to be like a first harmonic standing wave inside the cavity. The magnitude of the electric field intensity variation in the cavity increases with the cavity length, suggesting that the increase in emissive peak magnitude is due to the increase in the cavity resonance strength. When the cavity length increases to a certain range, there would be an onset of

higher order resonances at lower wavelengths. Also, in 1D PhC the electric field intensity decays within a smaller number of units for larger cavity lengths.

7. Conclusion

In conclusion, we have shown that CDC metallic gratings and hole arrays have enhanced transmission, and their transmission properties can be further optimized or tuned by varying the CDC design. Also, a thermal emitter with a cavity surrounded by a CDC metallic grating and 1D PhC has very sharp spectral emission peak. This is mainly due to the strong resonances in the cavity supported by the CDC grating and 1D PhC. Thus the emitter is tunable to various wavelengths with the choice of right materials along with the parameters of the grating, cavity length and 1D PhC. Such CDC subwavelength arrayed devices can be very important for many applications such as optical communications, biological sensing, optoelectronics, etc.

Acknowledgement

The authors acknowledge the support from the United States Air Force of Scientific Research (AFOSR) and United States Air Force Research Laboratories (AFRL).

References:

[1]. H. A. Bethe, "Theory of Diffraction by Small Holes", Physical Review, 66, 163-182 (1944).
[2]. T. W. Ebbesen, H. J. Lezec, H. F. Ghaemi, T. Thio, P. A. Wolff, "Extraordinary optical transmission through sub-wavelength hole arrays", Nature, 391, 667-669 (1998).
[3]. F. J. Garcia-Vidal, L. Martin-Moreno, "Transmission and focusing of light in one-dimensional periodically nanostructured metals", Physical Review B, 66, - (2002).
[4]. H. J. Lezec, T. Thio, "Diffracted evanescent wave model for enhanced and suppressed optical transmission through subwavelength hole arrays", Optics Express, 12, 3629-3651 (2004).
[5]. Q. Cao, P. Lalanne, "Negative role of surface plasmons in the transmission of metallic gratings with very narrow slits", Physical Review Letters, 88, - (2002).
[6]. C. Genet, T. W. Ebbesen, "Light in tiny holes", Nature, 445, 39-46 (2007).
[7]. J. A. Porto, F. J. Garcia-Vidal, J. B. Pendry, "Transmission resonances on metallic gratings with very narrow slits", Physical Review Letters, 83, 2845-2848 (1999).
[8]. R. Gordon, A. G. Brolo, A. McKinnon, A. Rajora, B. Leathem, and K. L. Kavanagh, "Strong Polarization in the Optical Transmission through Elliptical Nanohole Arrays," Phys. Rev. Lett. 92, 037401 (2004).
[9]. K. J. Klein Koerkamp, S. Enoch, F. B. Segerink, N. F. van Hulst, and L. Kuipers, "Strong Influence of Hole Shape on Extraordinary Transmission through Periodic Arrays of Subwavelength Holes," Phys. Rev. Lett. 92, 183901 (2004).
[10]. J. A. Matteo, D. P. Fromm, Y. Yue, P. J. Schuck, W. E. Moerner, and L. Hesselink, "Spectral analysis of strongly enhanced visible light transmission through single C-shaped nanoapertures," Appl. Phys. Lett. 85, 648 (2004).
[11]. X. L. Shi, L. Hesselink, and R. L. Thornton, "Ultrahigh light transmission through a C-shaped nanoaperture," Opt. Lett. 28, 1320 (2003).
[12]. Y. H. Ye, D. Y. Jeong, and Q. M. Zhang, "Fabrication of strain tunable infrared frequency selective surfaces on electrostrictive poly(vinylidene fluoride–trifluoroethylene) copolymer films using a stencil mask method," Appl. Phys. Lett. 85, 654 (2004).
[13]. W. Fan, S. Zhang, B. Minhas, K. J. Malloy, and S. R. J. Brueck, "Enhanced Infrared Transmission through Subwavelength Coaxial Metallic Arrays," Phys. Rev. Lett. 94, 033902 (2005).
[14]. R. Carminati, J. J. Greffet, "Near-field effects in spatial coherence of thermal sources", Physical Review Letters, 82, 1660-1663 (1999).
[15]. C. Henkel, K. Joulain, R. Carminati, J. J. Greffet, "Spatial coherence of thermal near fields", Optics Communications, 186, 57-67 (2000).
[16]. A. V. Shchegrov, K. Joulain, R. Carminati, J. J. Greffet, "Near-field spectral effects due to electromagnetic surface excitations", Physical Review Letters, 85, 1548-1551 (2000).
[17]. P. J. Hesketh, J. N. Zemel, B. Gebhart, "Organ Pipe Radiant Modes of Periodic Micromachined Silicon Surfaces", Nature, 324, 549-551 (1986).
[18]. E. A. Vinogradov, G. N. Zhizhin, A. G. Malshukov, V. I. Yudson, "Thermostimulated Polariton Emission of Zinc Selenide Films on Metal-Substrate", Solid State Communications, 23, 915-921 (1977).
[19]. M. Kreiter, J. Oster, R. Sambles, S. Herminghaus, S. Mittler-Neher, W. Knoll, "Thermally induced emission of light from a metallic diffraction grating, mediated by surface plasmons", Optics Communications, 168, 117-122 (1999).

[20]. J. J. Greffet, R. Carminati, K. Joulain, J. P. Mulet, S. P. Mainguy, Y. Chen, "Coherent emission of light by thermal sources", Nature, 416, 61-64 (2002).
[21]. P. Ben-Abdallah, "Thermal antenna behavior for thin-film structures", Journal of the Optical Society of America a-Optics Image Science and Vision, 21, 1368-1371 (2004).
[22]. E. D. Palik, Ed., Handbook of optical constants of solids (Academic Press, Orlando, 1985).
[23]. D. R. Lide, handbook of chemistry and physics (CRC Press, Cleveland, Ohio, 1992), vol. 58th ed. (1977-1978).
[24]. E. D. Palik, Handbook of Optical Constants of Solids (Academic, 1985).
[25]. COMSOL 3.2a Reference Manual, version 3.2 ed. (Comsol AB, 2005).
[26]. A. Lavrinenko, P. I. Borel, L. H. Frandsen, M. Thorhauge, A. Harpoth, M. Kristensen, T. Niemi, H. M. H. Chong, "Comprehensive FDTD modelling of photonic crystal waveguide components", Optics Express, 12, 234-248 (2004).
[27]. A. Battula, and S. C. Chen, “Extraordinary transmission in a narrow energy band for metallic gratings with converging-diverging channels,” Appl. Phys. Lett. 89, 131113 (2006).
[28]. J. J. Greffet, M. Nieto-Vesperinas, "Field theory for generalized bidirectional reflectivity: derivation of Helmholtz's reciprocity principle and Kirchhoff's law", Journal of the Optical Society of America a-Optics Image Science and Vision, 15, 2735-2744 (1998).
[29]. J. D. Jackson, Classical electrodynamics (Wiley, New York, ed. 3rd, 1999).
[30]. Y. Xie, A. R. Zakharian, J. V. Moloney, M. Mansuripur, "Transmission of light through slit apertures in metallic films", Optics Express, 12, 6106-6121 (2004).
[31]. J. LeGall, M. Olivier, J. J. Greffet, "Experimental and theoretical study of reflection and coherent thermal emission by a SiC grating supporting a surface-phonon polariton", Physical Review B, 55, 10105-10114 (1997).

Figure Captions:

Figure 1: Schematic view of converging-diverging channel (CDC) design (a), lamellar metallic CDC grating (b), metallic CDC rectangular hole array (c), and metallic CDC circular hole array (d).

Figure 2: Zero-order transmittance for a normal incident plane wave on gratings in vacuum with different channel configurations (straight, converging-only, and CDC channels). (a) d = 3.5 μm, a = 0.5 μm and t = 3.0 μm in gold film. (b) d = 650 nm, a = 300 nm and t = 500 nm in silver film.

Figure 3: Transmittance in vacuum as a function of wavelength and *g* for an Al CDC grating having d = 315 nm, a = 125 nm and t = 100 nm.

Figure 4: Transmittance in Ag rectangular hole arrays with a same hole area, a converging angle θ= 60° and different *a/b* ratios as (a) a=16μm, b=12μm ,(b) a=18μm, b=10.7μm and (c) a=20μm, b=9.6μm. The solid and dashed lines represent the transmissions for different polarizations.

Figure 5: Transmission in Ag rectangular hole arrays having different converging angles. The hole area, film thickness and aspect ratio (16μm×12μm) remain the same in all cases.

Figure 6: Transmission in Ag rectangular hole arrays having different thicknesses. The hole area, converging angle (60°) and aspect ratio remain the same in all cases. The solid and dashed lines represent the transmissions for different polarizations.

Figure 7: (a): Transmission in a Ag hole array with a straight channel shape having period d = 19 μm, thickness t = 2 μm and different aperture sizes a; (b): In CDC Ag hole array having period d = 19 μm, thickness t = 2 μm, aperture a = 10 μm and different gaps at the throat g.

Figure 8: (a): Transmittance at wavelength λ = 20 μm for CDC Ag hole array having period d = 19 μm, thickness t = 2 μm, different a and g. (b): Transmittance variation with respect to the film thickness at different wavelengths λ for Ag hole arrays having d = 19 μm, a = 10 μm for straight channel and CDC with g = 7.61 μm.

Figure 9: Transmittance in Ag hole array with d = 19 μm, t = 2 μm for varying a and hole channel shapes as (a) straight, (b) CDC shape with angle $\theta = 50^o$, (c) $\theta = 65^o$, and (d) $\theta = 72^o$.

Figure 10: Normal *p*-polarization emittance for Ag CDC grating having parameters a = 250 nm, t = 100 nm, g = 5 nm and a photonic crystal having the parameters a = 100 nm; $d_1 = d_2$ = 50 nm with cavity length: (a) L = 50 nm, 100 nm, 200 nm, 300 nm, and 320 nm; and (b) L = 350 nm, 400 nm, 500 nm, 600 nm, and 690 nm.

Figure 11: Electric field intensity distribution normalized to the incident along the line passing through the center of the CDC grating throat and into the photonic crystal with cavity length: (a) L = 100 nm, 200 nm, and 300 nm; (b) L = 350 nm, 400 nm, 500 nm, and 600 nm; and (c) L = 600 nm and 690 nm.

Figure 1 (a)

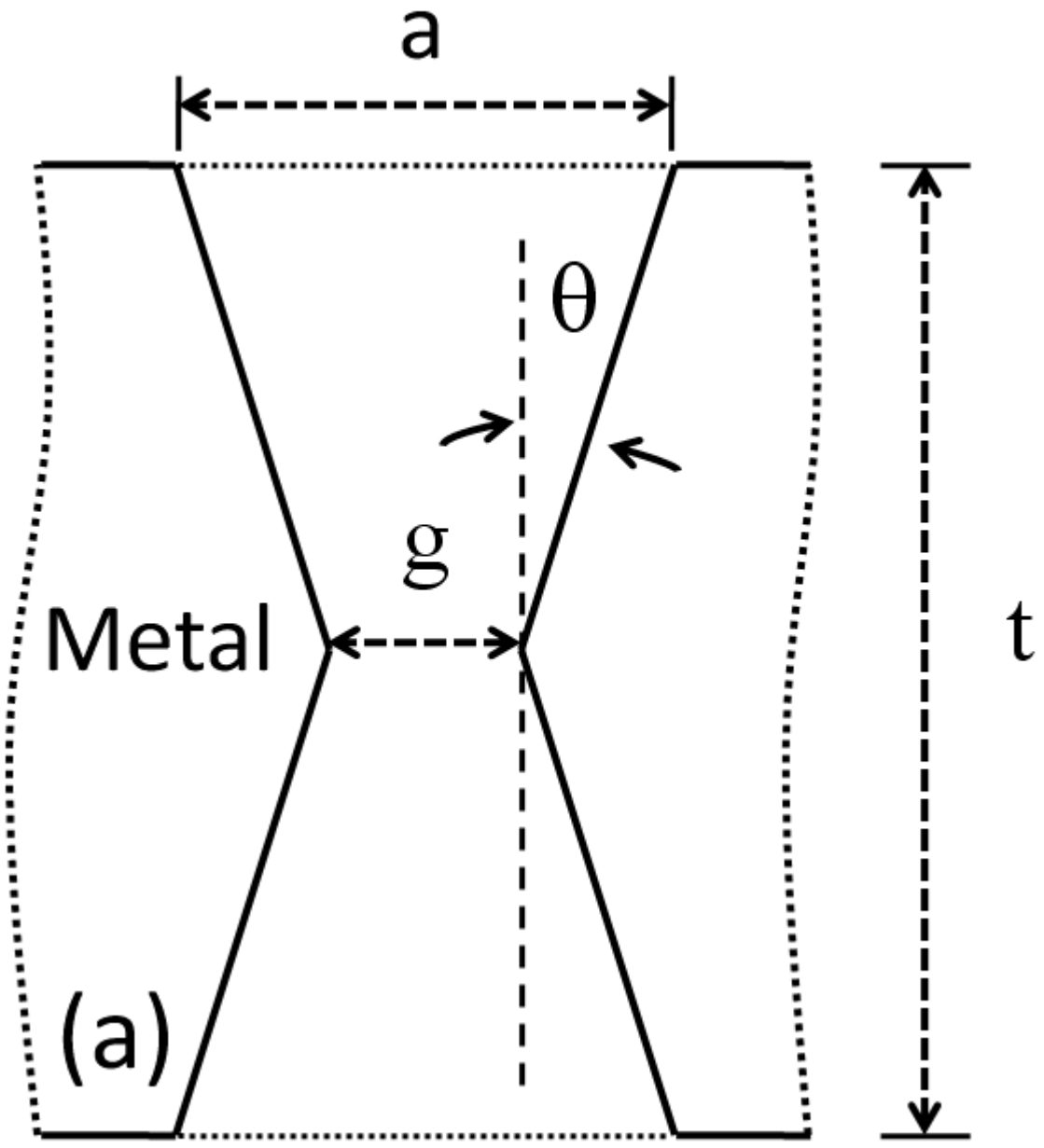


Figure 1 (b)

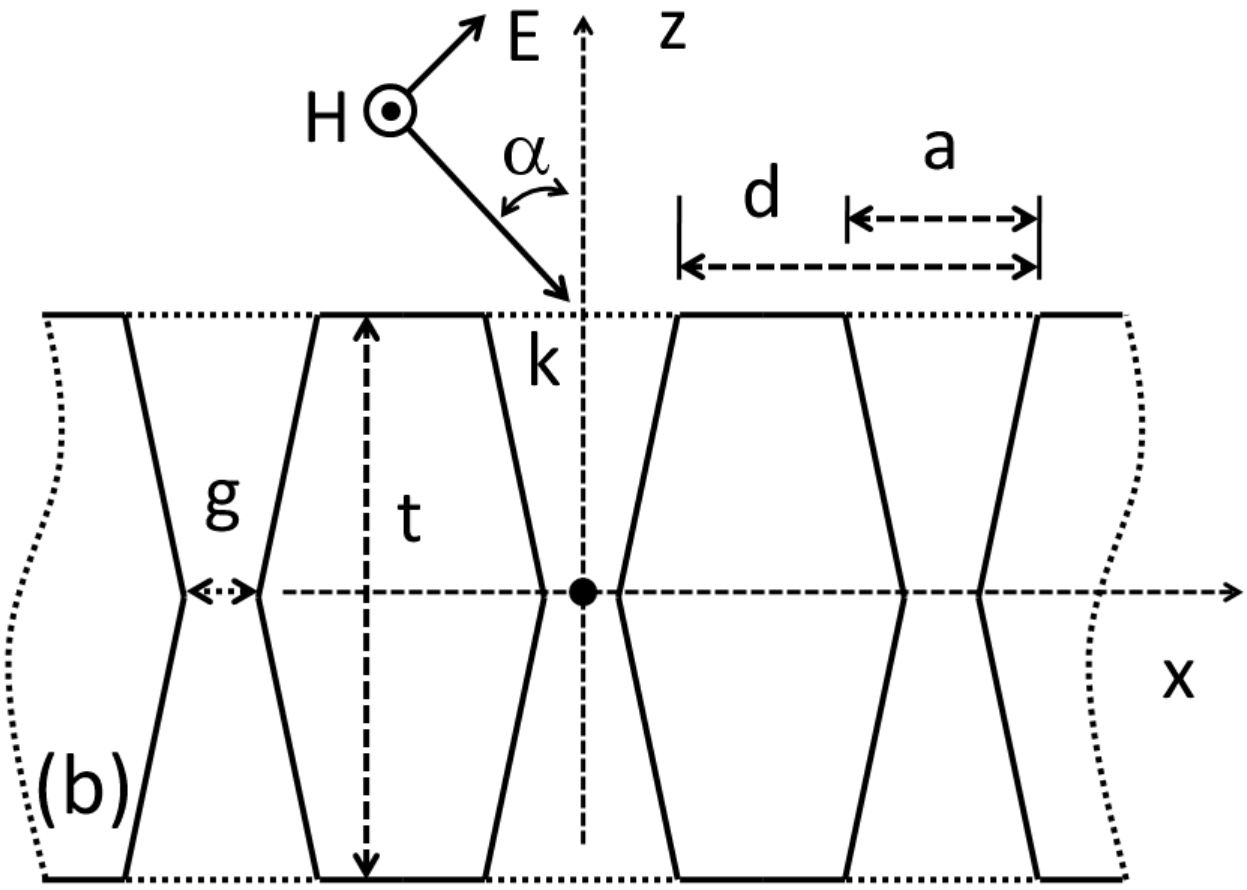


Figure 1 (c)

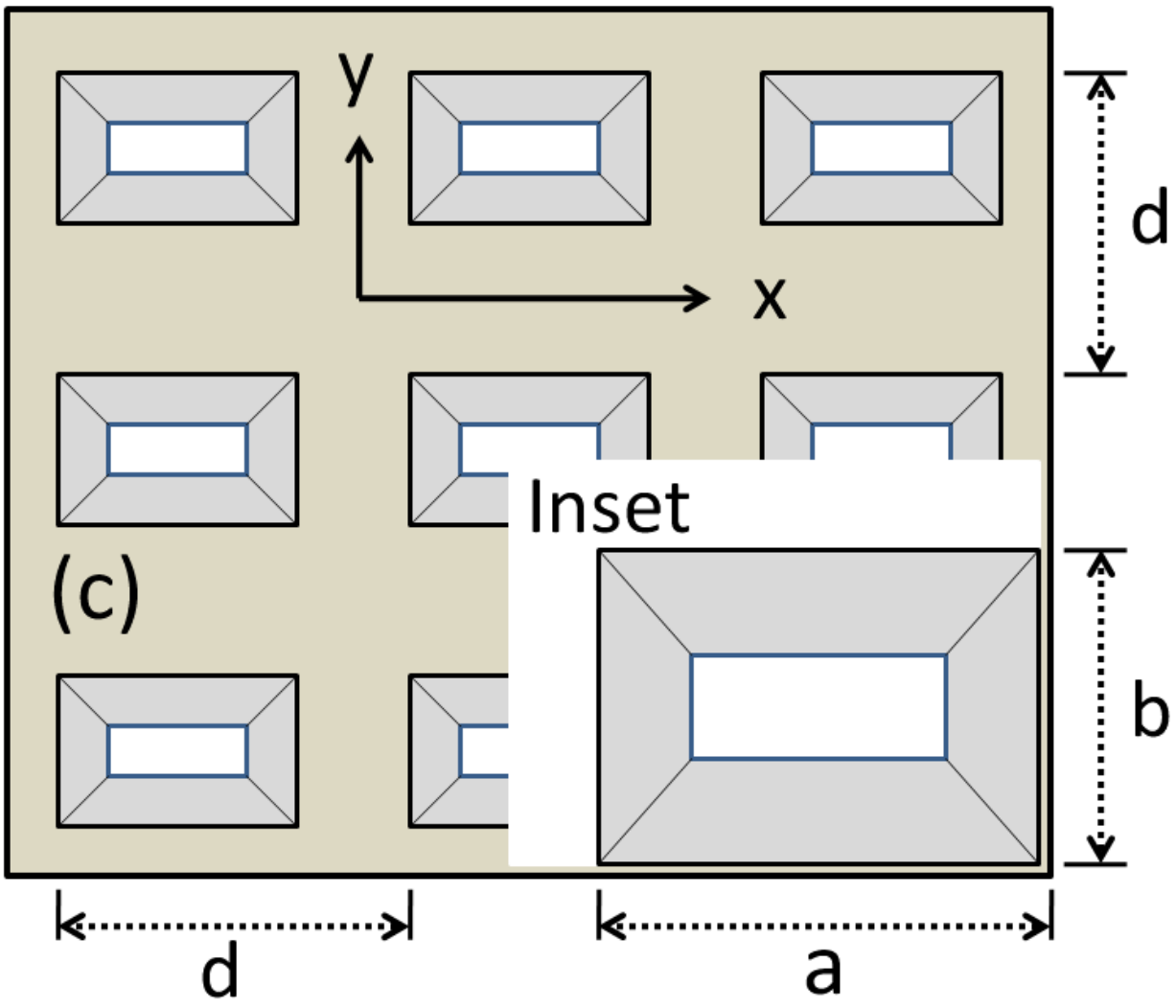


Figure 1 (d)

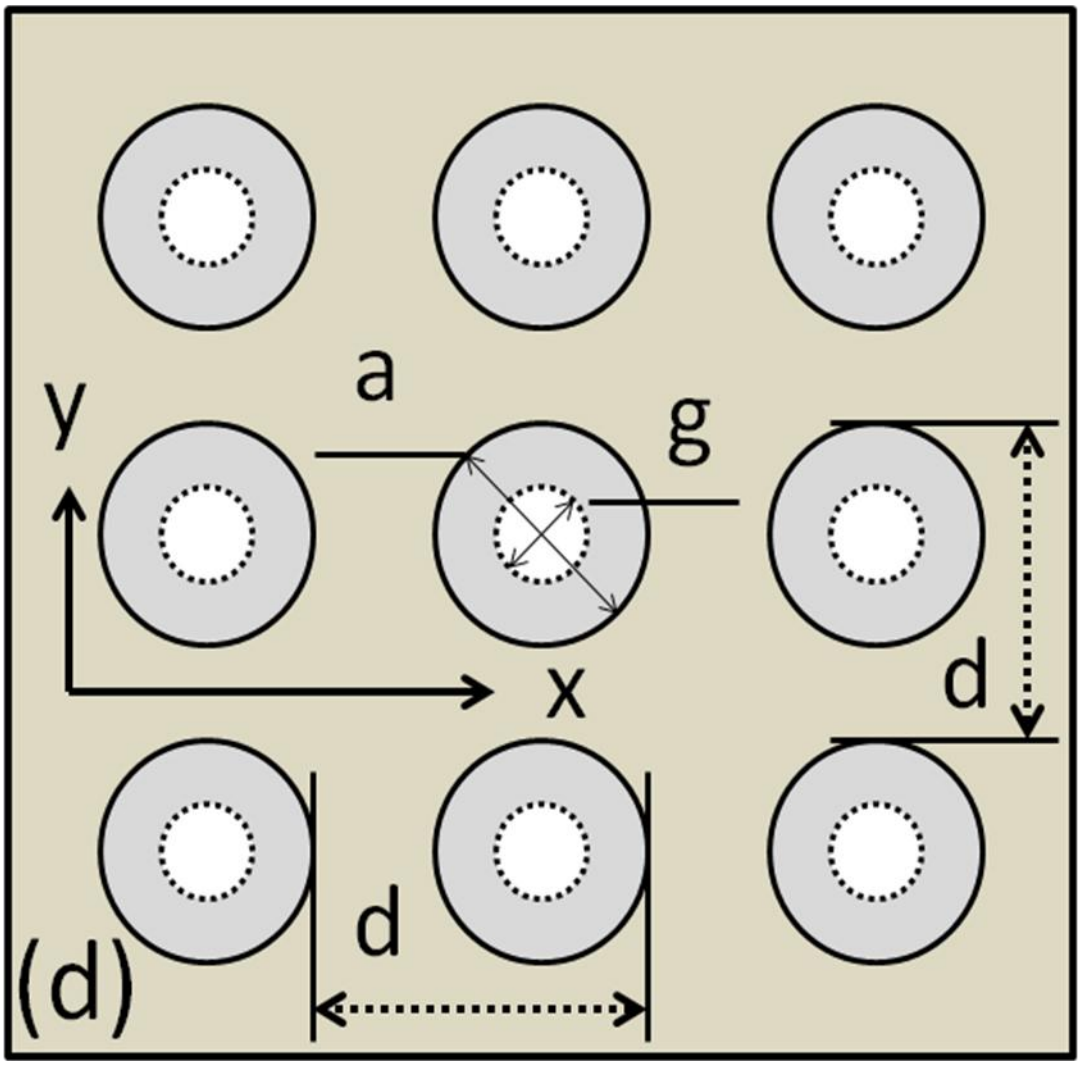


Figure 2 (a)

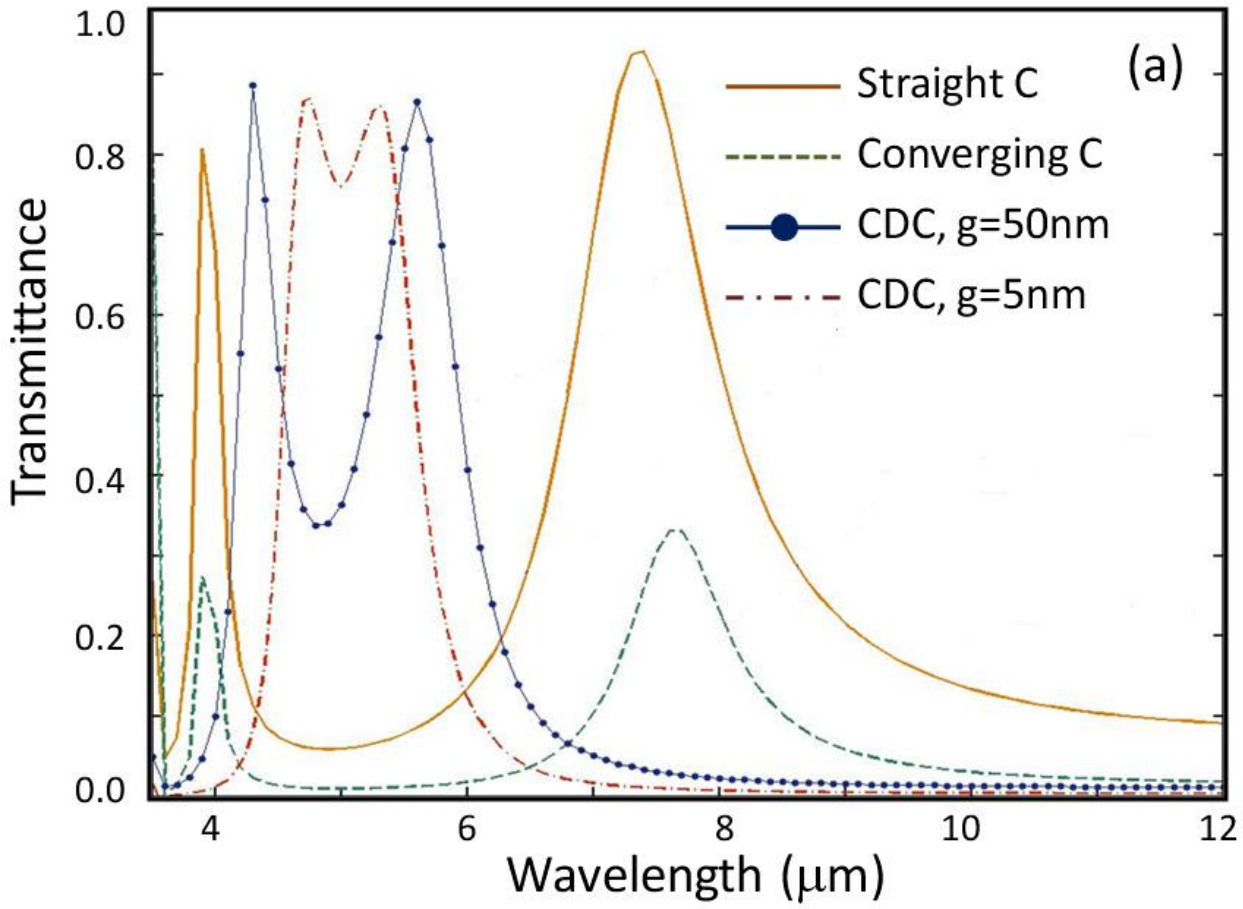

(a)
Straight C
Converging C
CDC, g=50nm
CDC, g=5nm
Transmittance
Wavelength (μm)
1.0
0.8
0.6
0.4
0.2
0.0
4
6
8
10
12

Figure 2 (b)

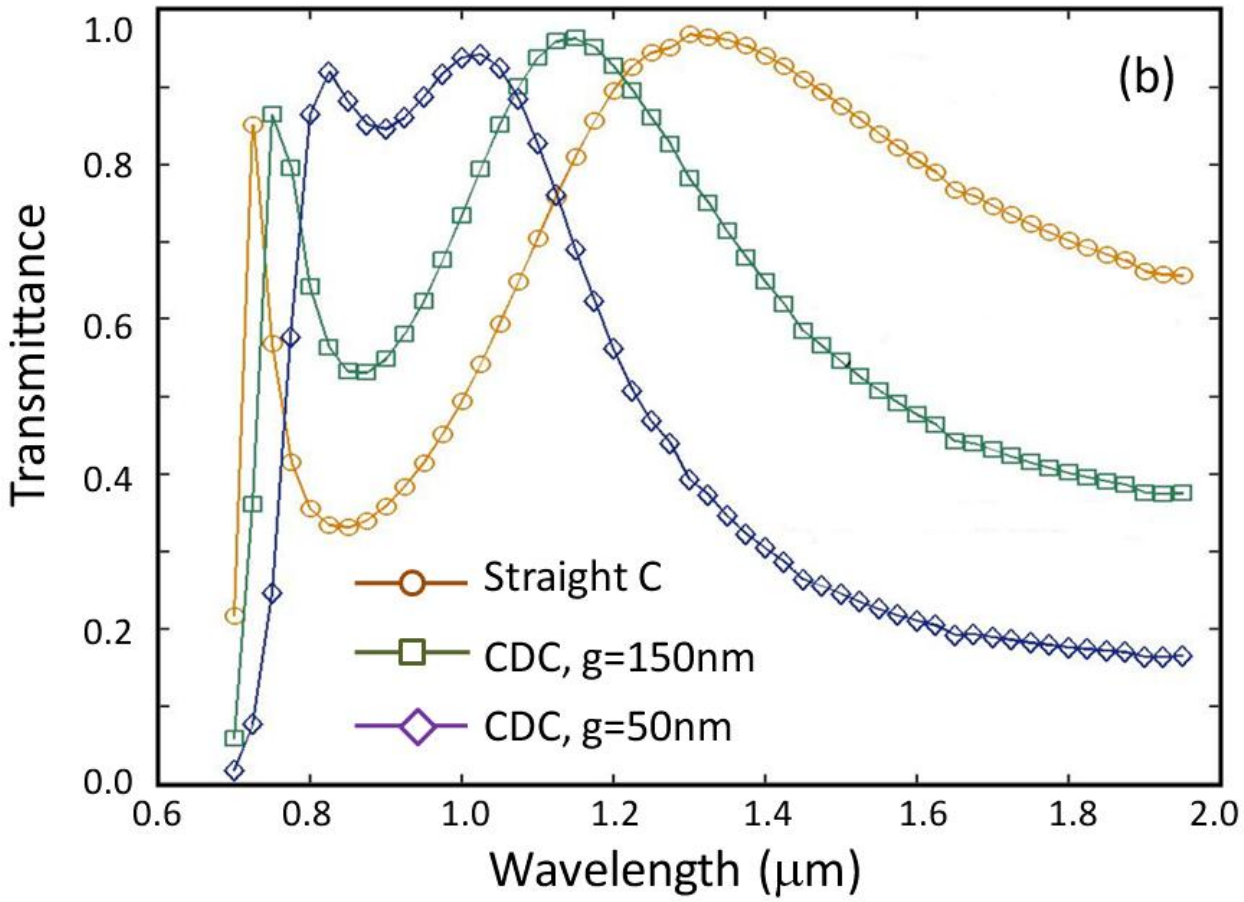

(b)
Transmittance
Wavelength (μm)
Straight C
CDC, g=150nm
CDC, g=50nm
0.0
0.2
0.4
0.6
0.8
1.0
0.6
0.8
1.0
1.2
1.4
1.6
1.8
2.0

Figure 3

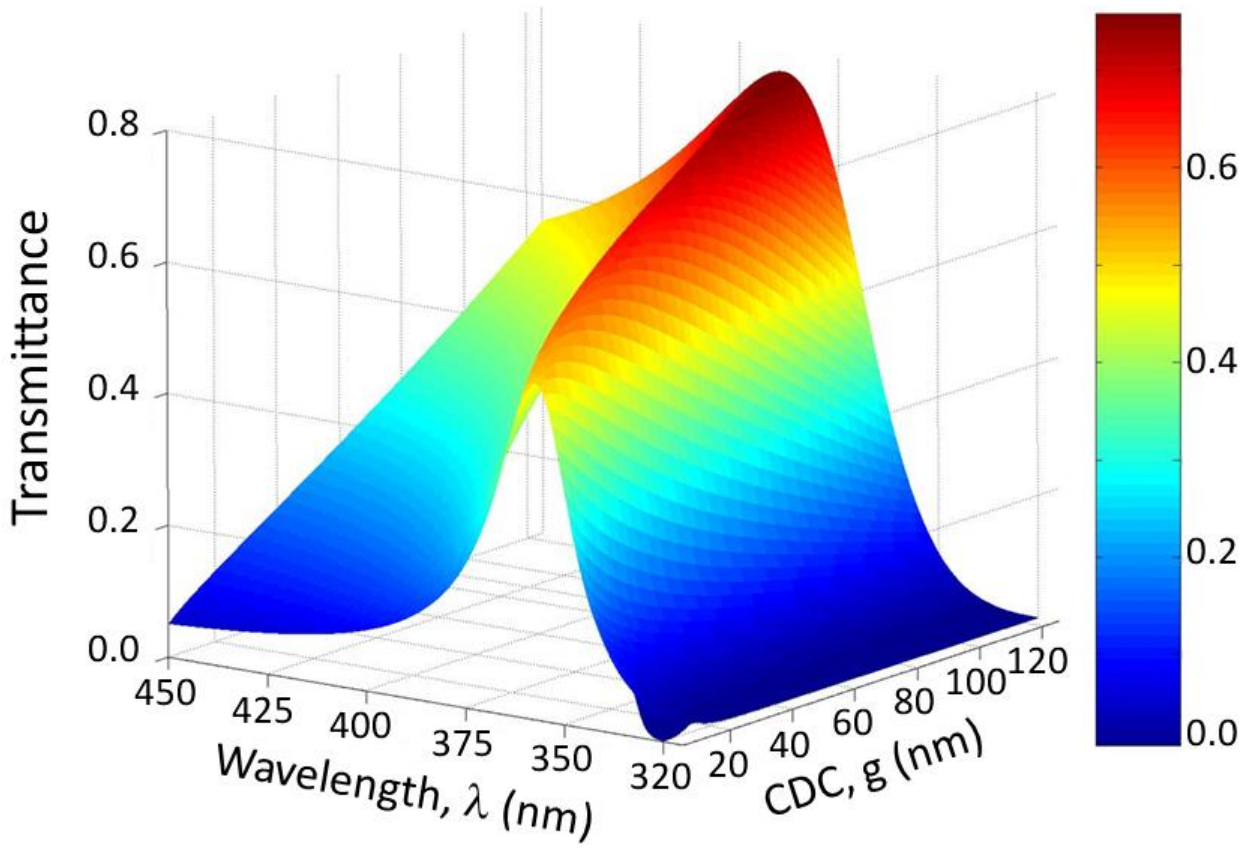

Transmittance
0.8
0.6
0.4
0.2
0.0
450
425
400
375
350
320
Wavelength, λ (nm)
20
40
60
80
100
120
CDC, g (nm)
0.6
0.4
0.2
0.0

Figure 4

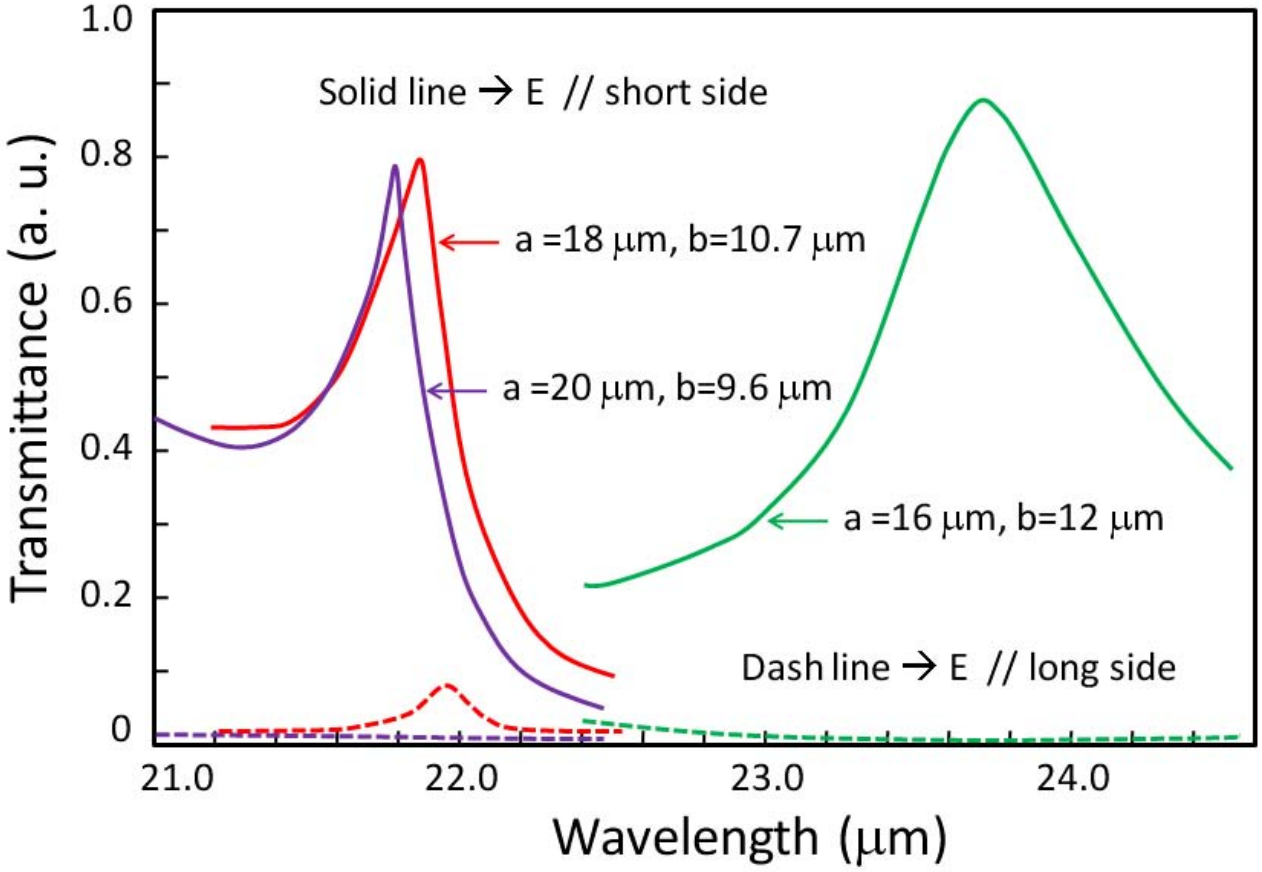

1.0
0.8
0.6
0.4
0.2
0
Transmittance (a. u.)
Solid line → E // short side
a =18 μm, b=10.7 μm
a =20 μm, b=9.6 μm
a =16 μm, b=12 μm
Dash line → E // long side
21.0
22.0
23.0
24.0
Wavelength (μm)

Figure 5

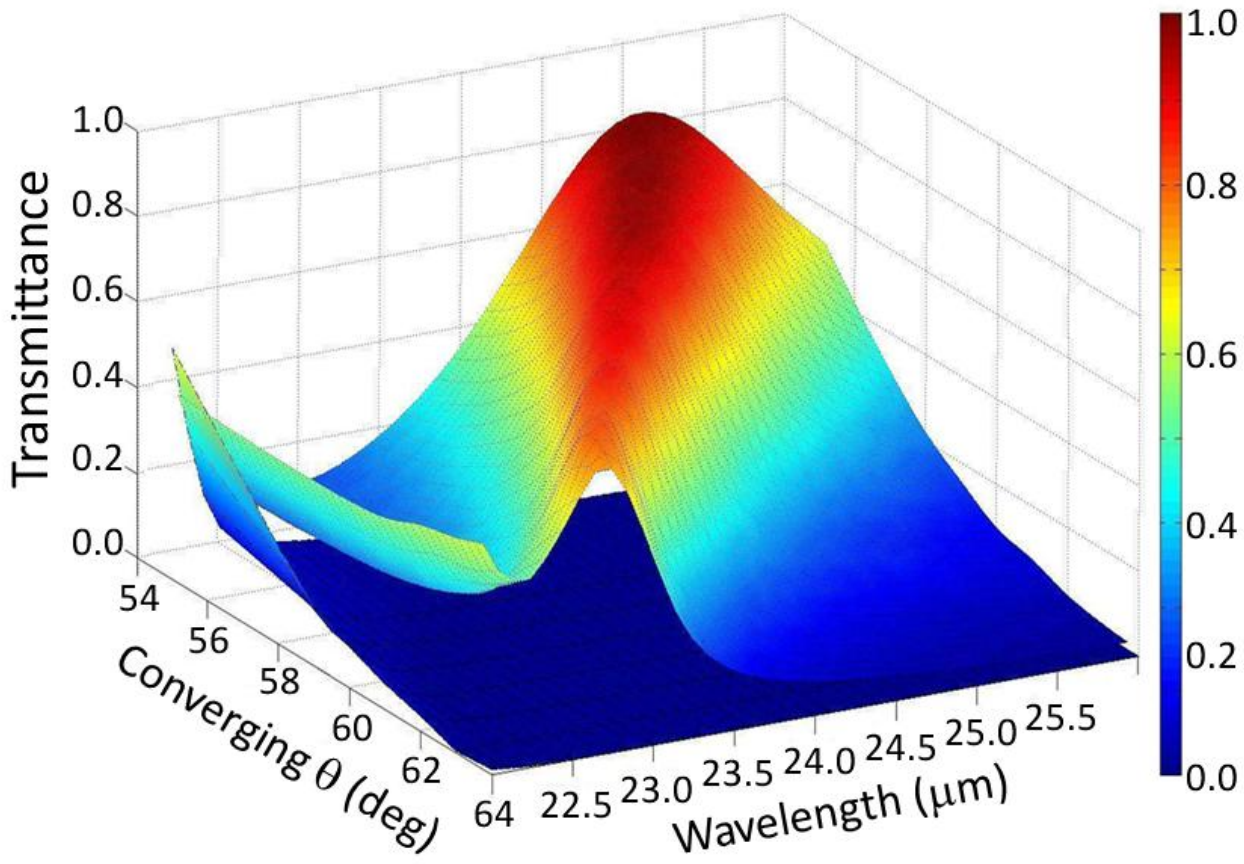

Transmittance
1.0
0.8
0.6
0.4
0.2
0.0
54
56
58
60
62
64
Converging θ (deg)
22.5
23.0
23.5
24.0
24.5
25.0
25.5
Wavelength (μm)
1.0
0.8
0.6
0.4
0.2
0.0

Figure 6

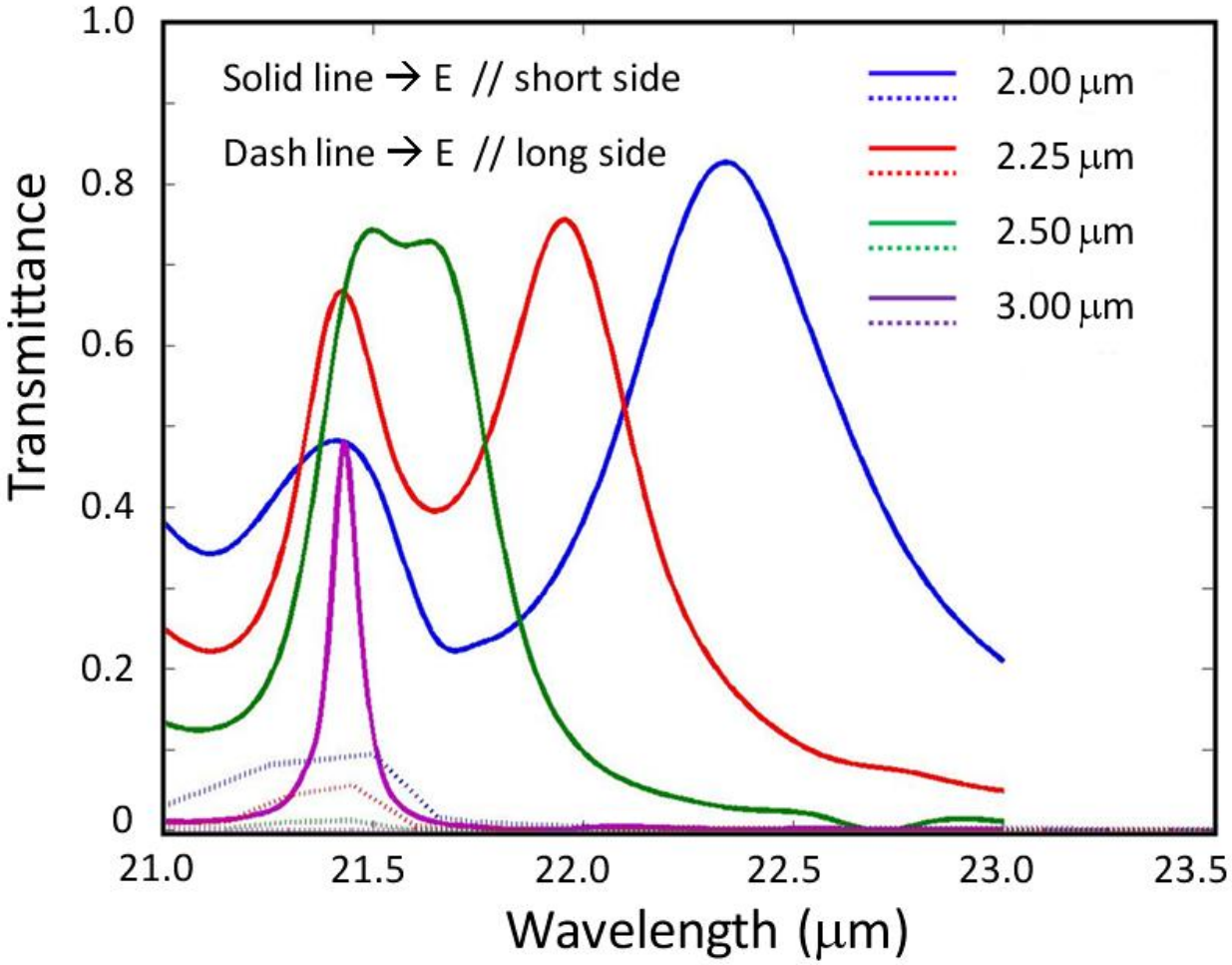

Solid line → E // short side
Dash line → E // long side
2.00 μm
2.25 μm
2.50 μm
3.00 μm
Transmittance
1.0
0.8
0.6
0.4
0.2
0
21.0
21.5
22.0
22.5
23.0
23.5
Wavelength (μm)

Figure 7 (a)

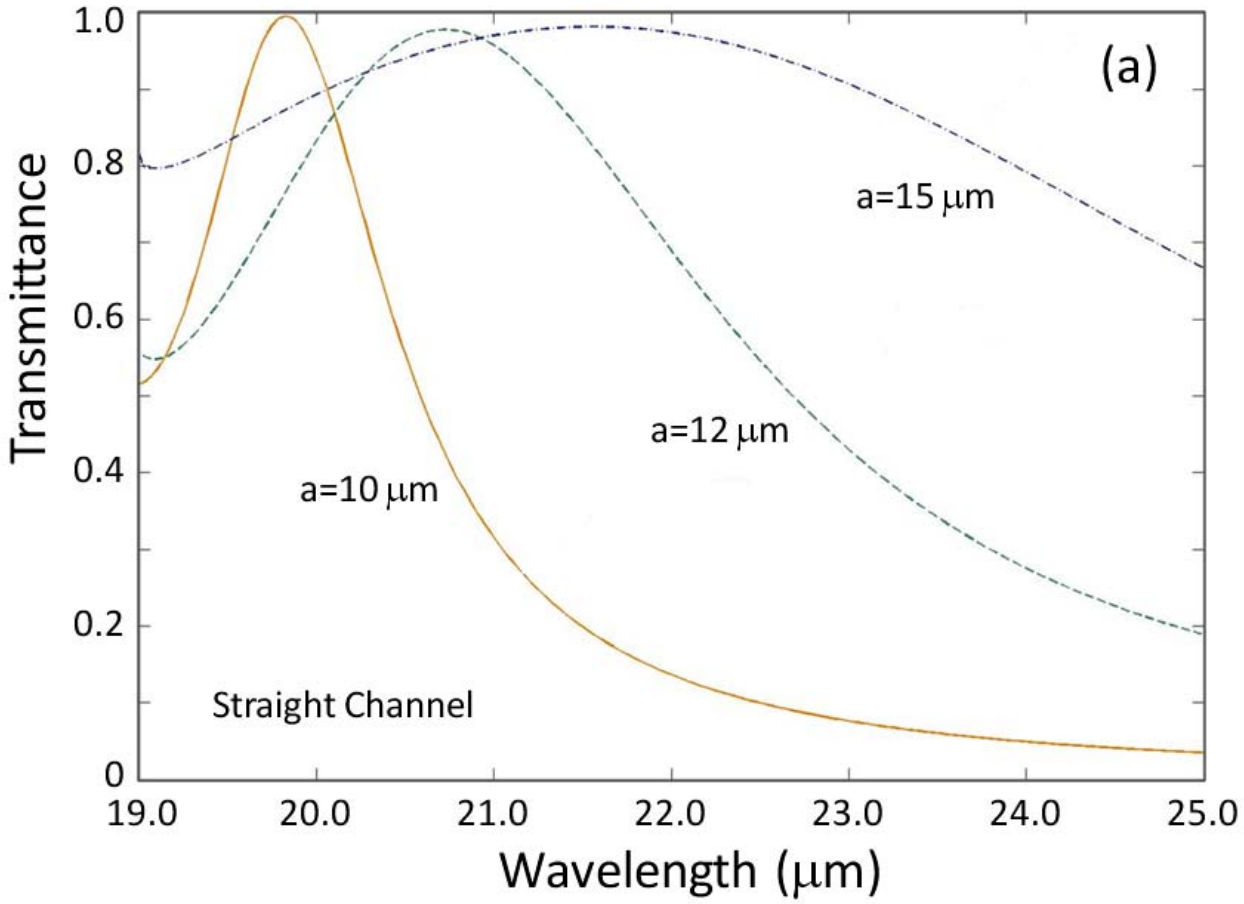

(a)
Transmittance
Wavelength (μm)
a=15 μm
a=12 μm
a=10 μm
Straight Channel
1.0
0.8
0.6
0.4
0.2
0
19.0
20.0
21.0
22.0
23.0
24.0
25.0

Figure 7 (b)

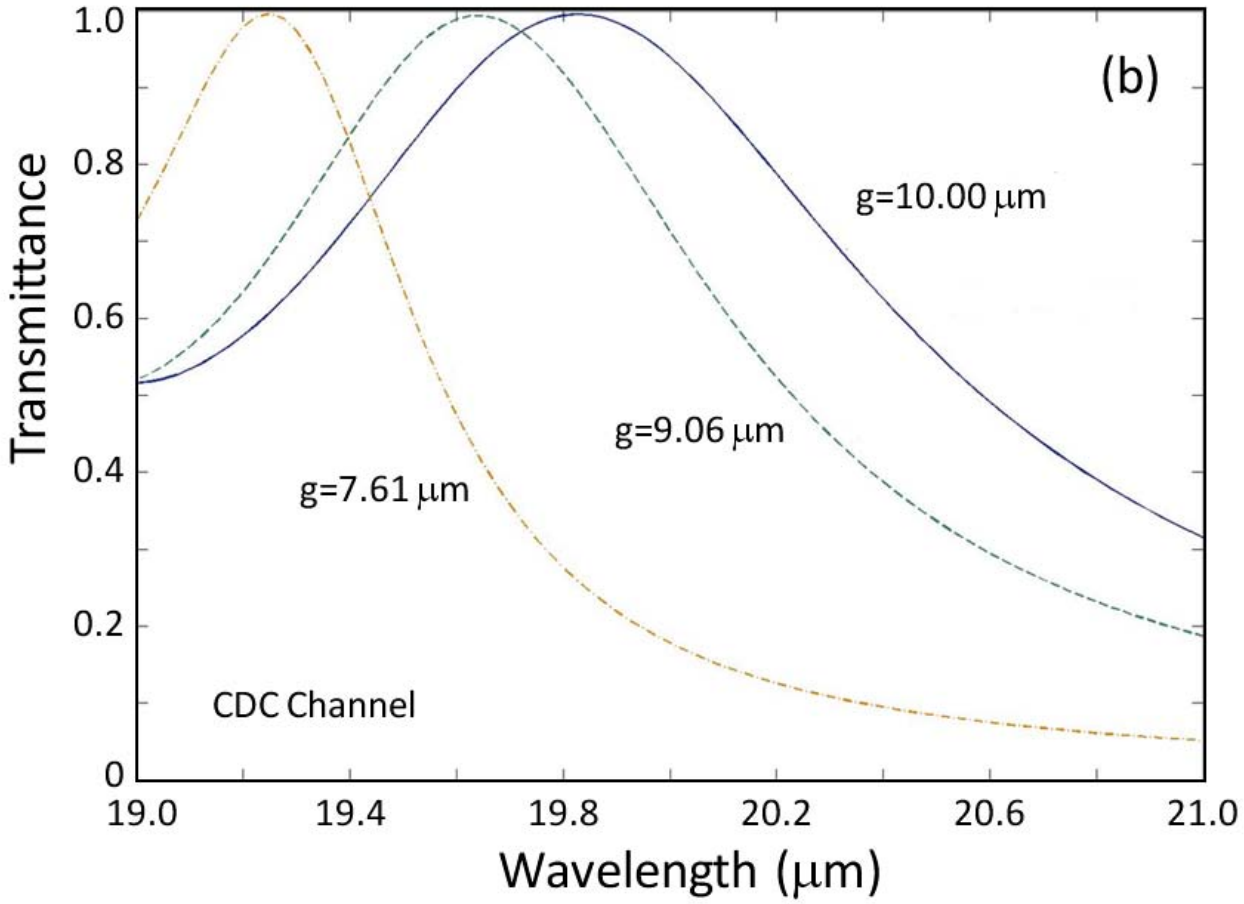

(b)
Transmittance
1.0
0.8
0.6
0.4
0.2
0
19.0
19.4
19.8
20.2
20.6
21.0
Wavelength (μm)
g=10.00 μm
g=9.06 μm
g=7.61 μm
CDC Channel

Figure 8 (a)

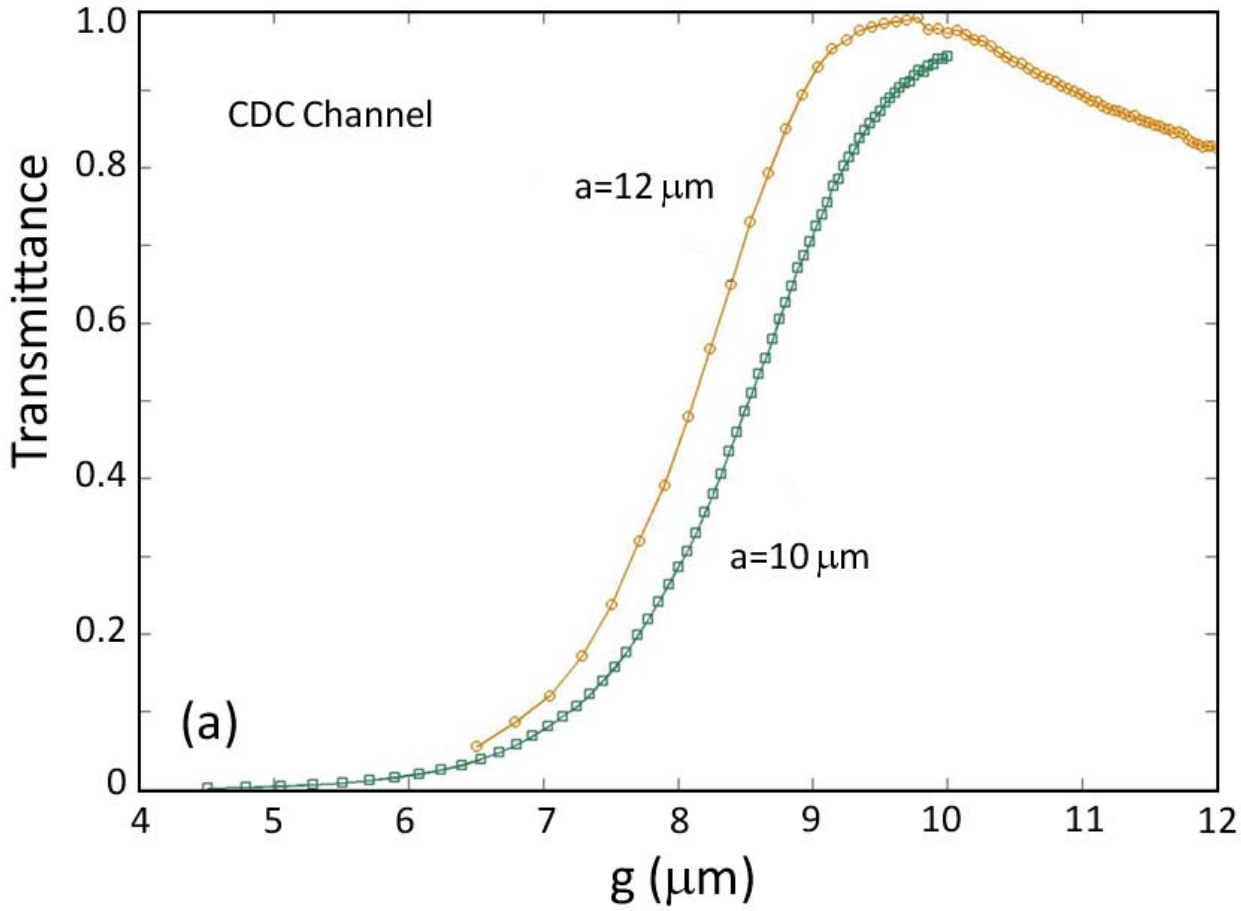

CDC Channel
a=12 μm
a=10 μm
(a)
Transmittance
g (μm)
1.0
0.8
0.6
0.4
0.2
0
4
5
6
7
8
9
10
11
12

Figure 8 (b)

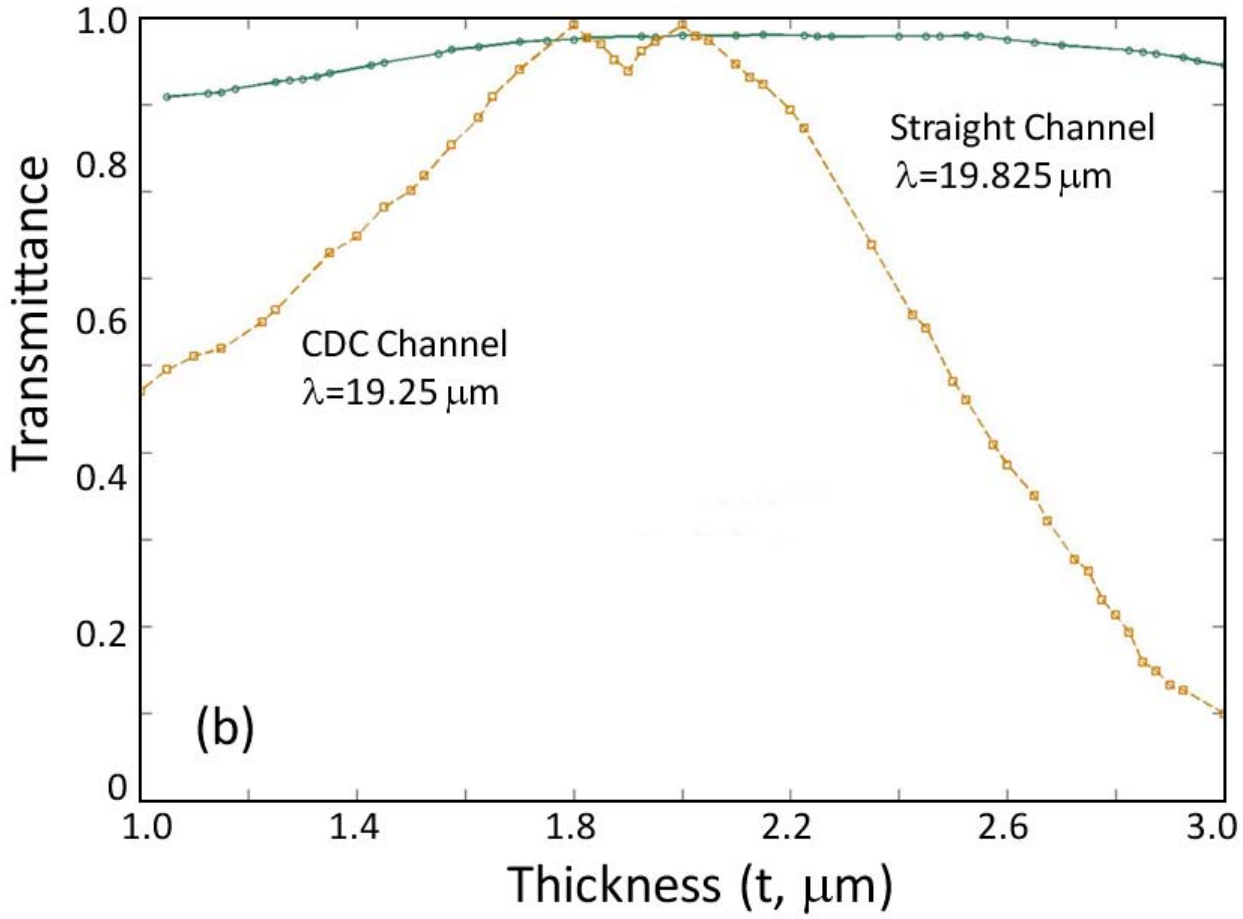

1.0
0.8
0.6
0.4
0.2
0
Transmittance
Straight Channel
λ=19.825 μm
CDC Channel
λ=19.25 μm
(b)
1.0
1.4
1.8
2.2
2.6
3.0
Thickness (t, μm)

Figure 9 (a)

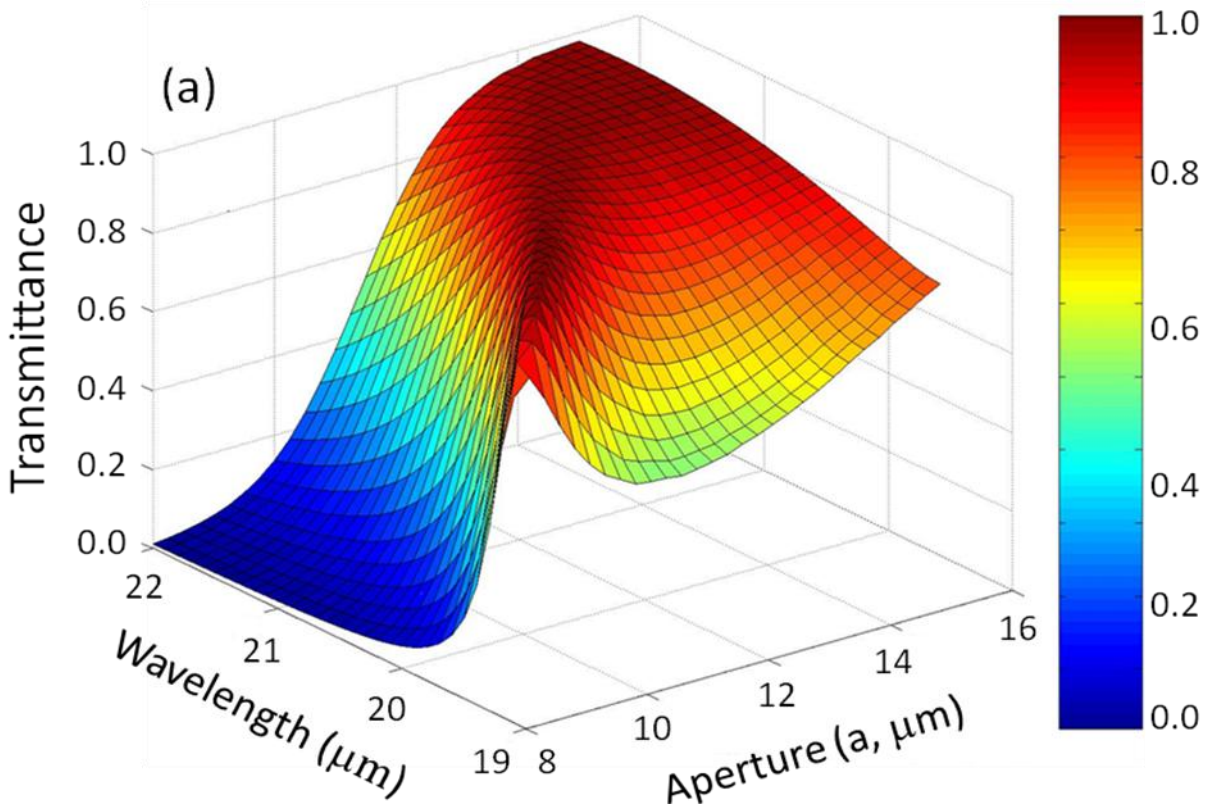

(a)
Transmittance
1.0
0.8
0.6
0.4
0.2
0.0
22
21
20
19
Wavelength (μm)
8
10
12
14
16
Aperture (a, μm)
1.0
0.8
0.6
0.4
0.2
0.0

Figure 9 (b)

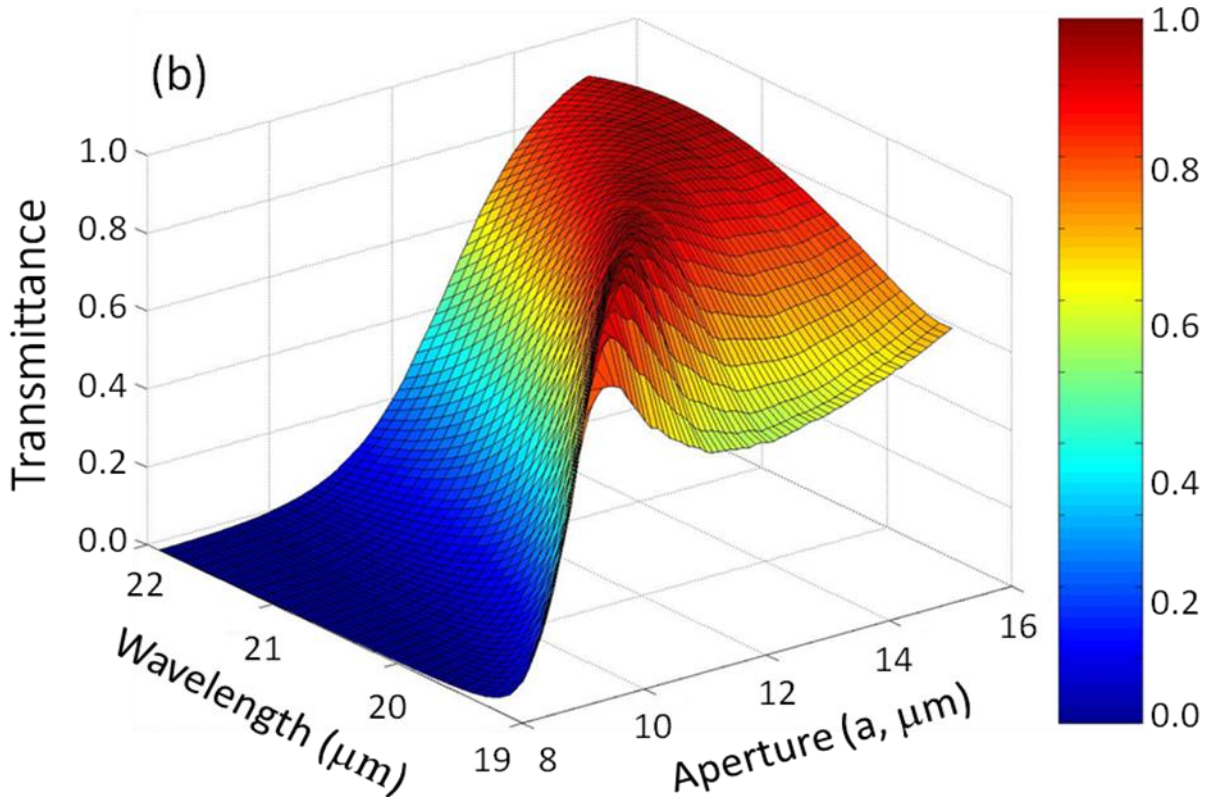

(b)
Transmittance
1.0
0.8
0.6
0.4
0.2
0.0
22
21
20
19
Wavelength (μm)
8
10
12
14
16
Aperture (a, μm)
1.0
0.8
0.6
0.4
0.2
0.0

Figure 9 (c)

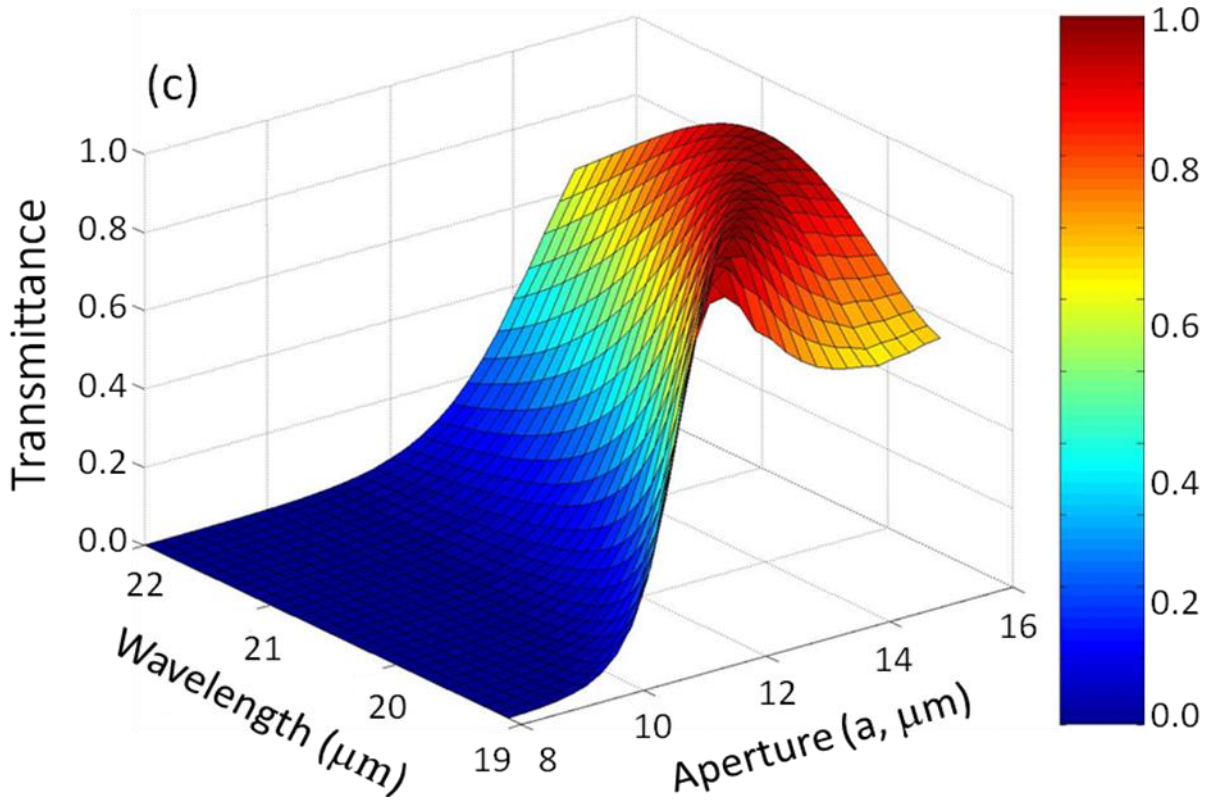

(c)
Transmittance
1.0
0.8
0.6
0.4
0.2
0.0
22
21
20
19
Wavelength (μm)
8
10
12
14
16
Aperture (a, μm)
1.0
0.8
0.6
0.4
0.2
0.0

Figure 9 (d)

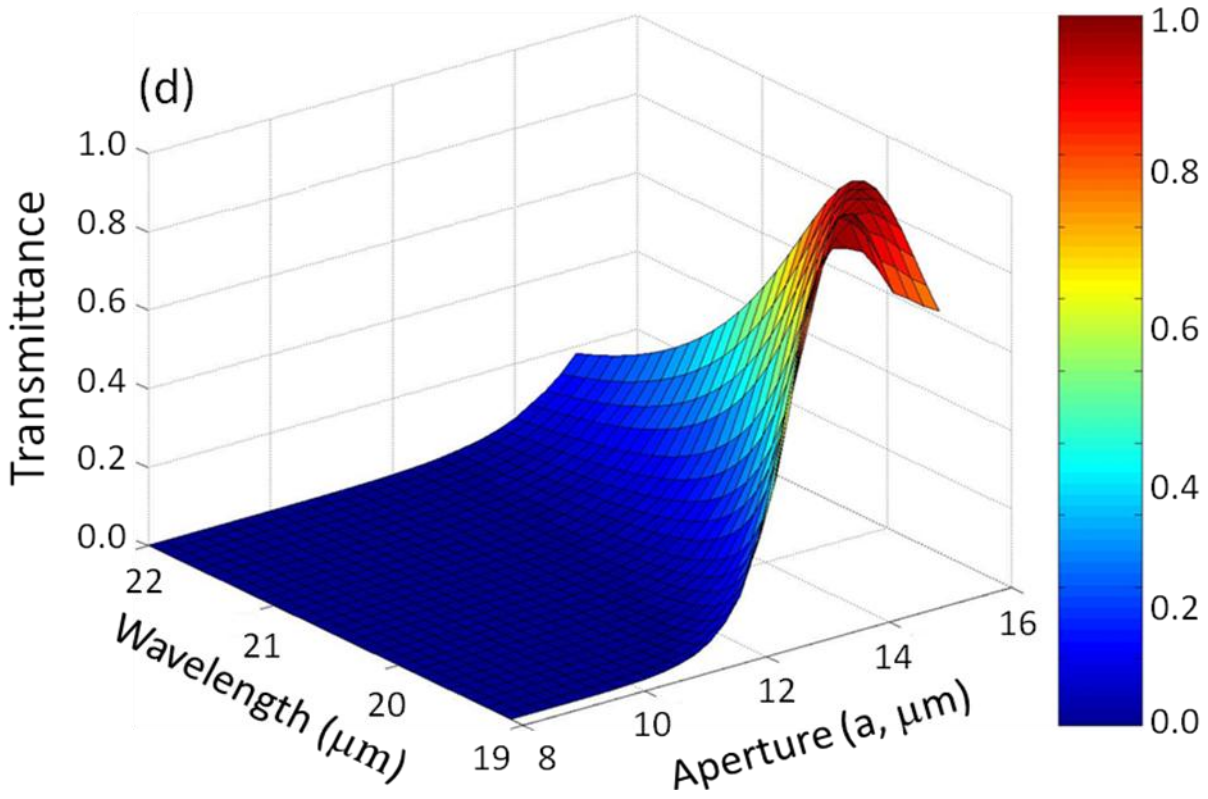

(d)
Transmittance
1.0
0.8
0.6
0.4
0.2
0.0
22
21
20
19
Wavelength (μm)
8
10
12
14
16
Aperture (a, μm)
1.0
0.8
0.6
0.4
0.2
0.0

Figure 10 (a)

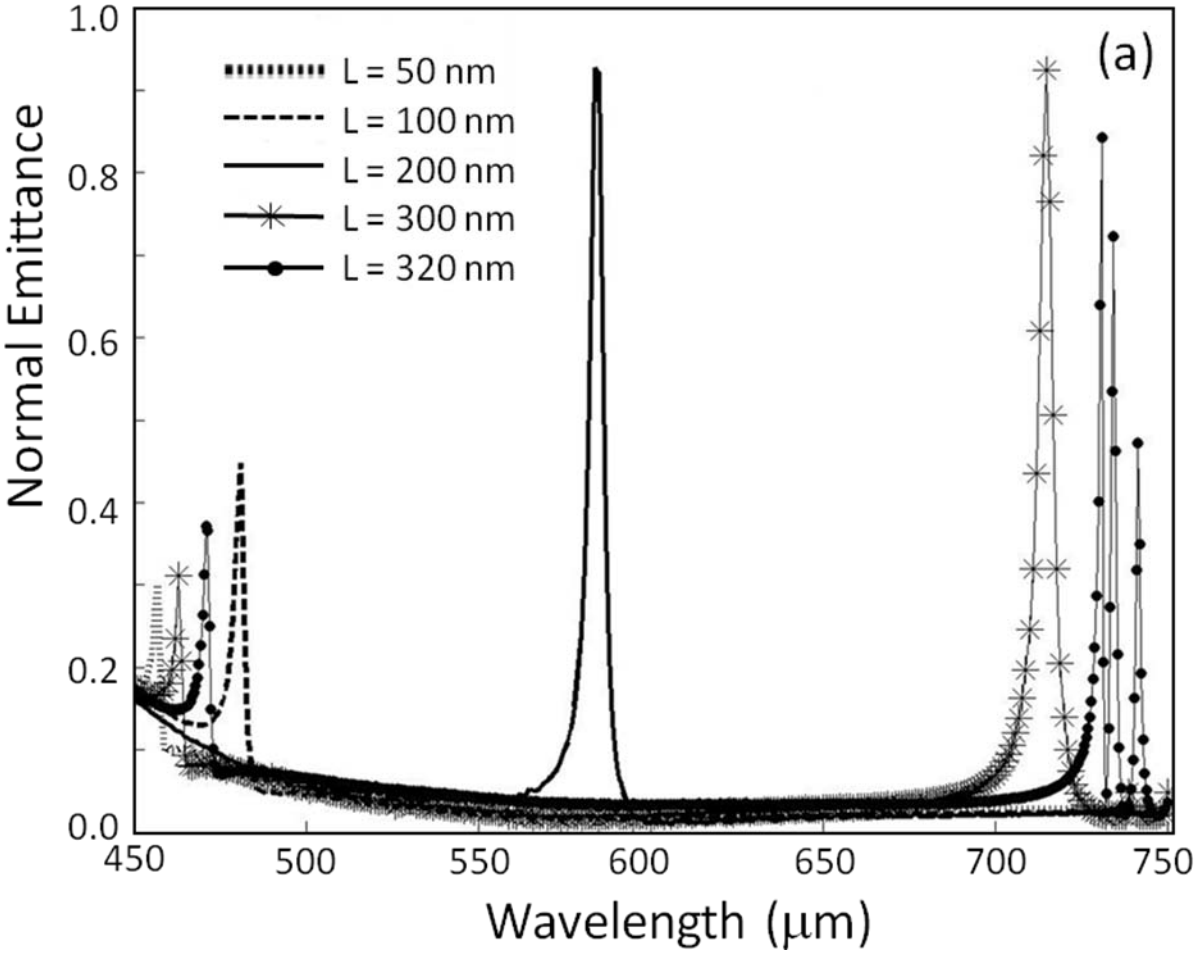

(a)
L = 50 nm
L = 100 nm
L = 200 nm
L = 300 nm
L = 320 nm
Normal Emittance
1.0
0.8
0.6
0.4
0.2
0.0
450
500
550
600
650
700
750
Wavelength (μm)

Figure 10 (b)

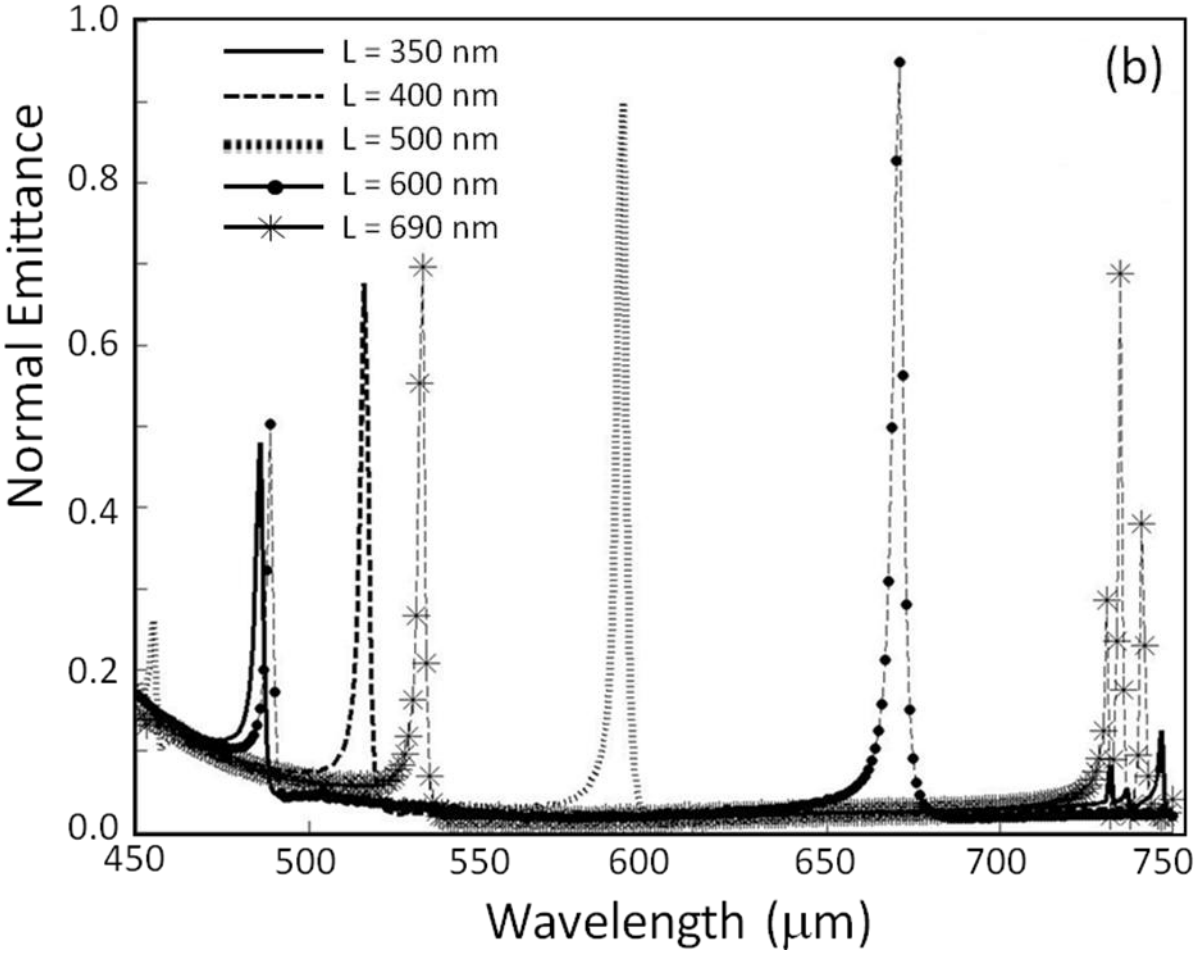

(b)
L = 350 nm
L = 400 nm
L = 500 nm
L = 600 nm
L = 690 nm
Normal Emittance
1.0
0.8
0.6
0.4
0.2
0.0
450
500
550
600
650
700
750
Wavelength (μm)

Figure 11 (a)

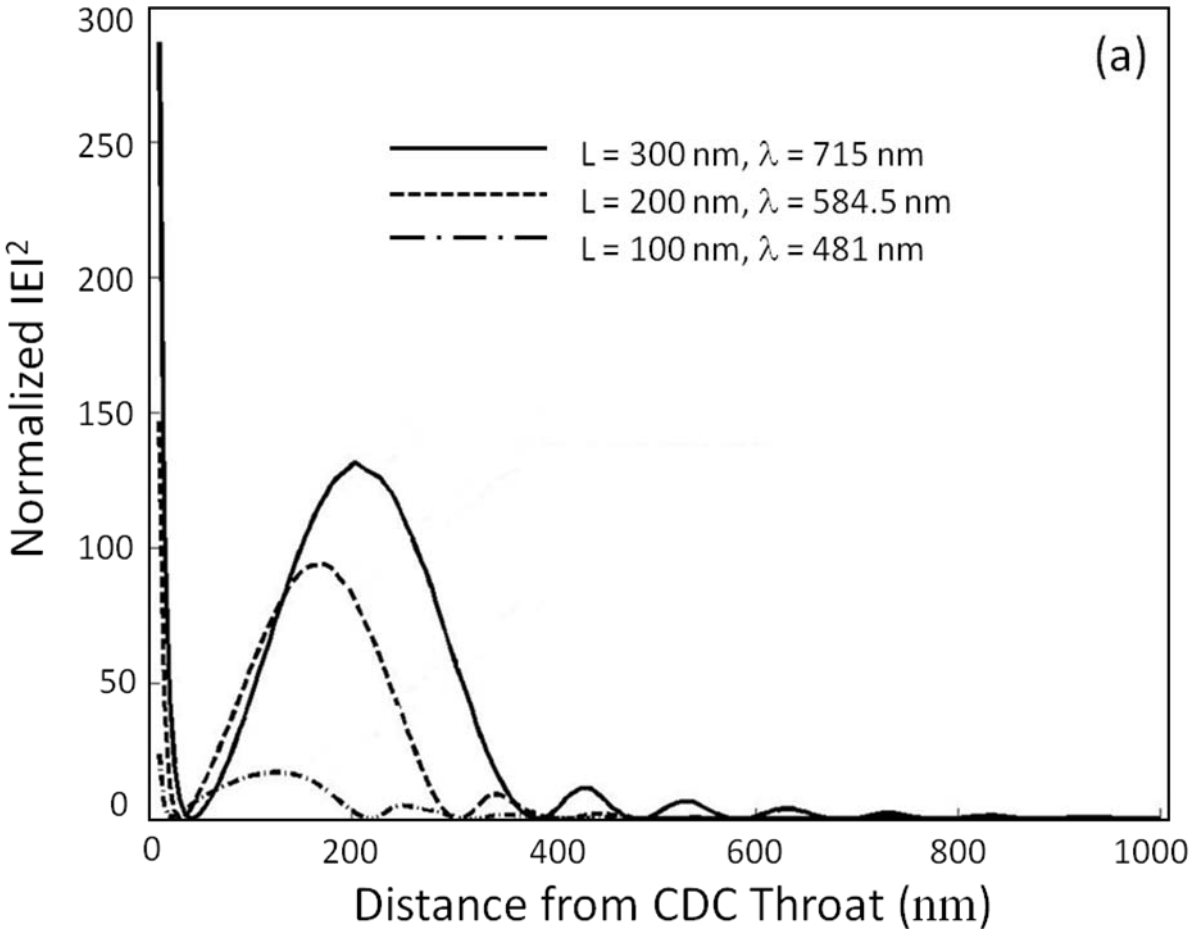

(a)
L = 300 nm, λ = 715 nm
L = 200 nm, λ = 584.5 nm
L = 100 nm, λ = 481 nm
Normalized IEI²
Distance from CDC Throat (nm)
0
50
100
150
200
250
300
0
200
400
600
800
1000

Figure 11 (b)

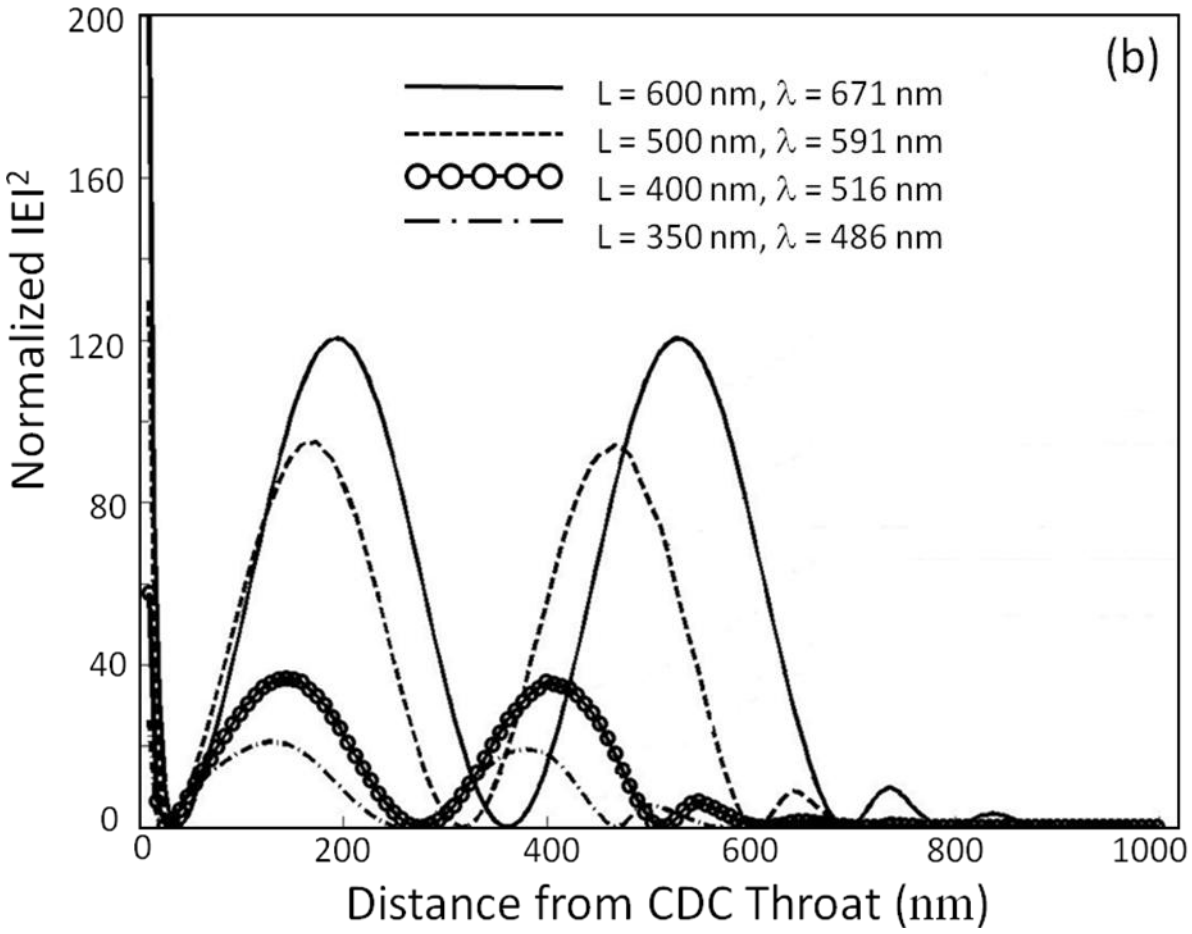
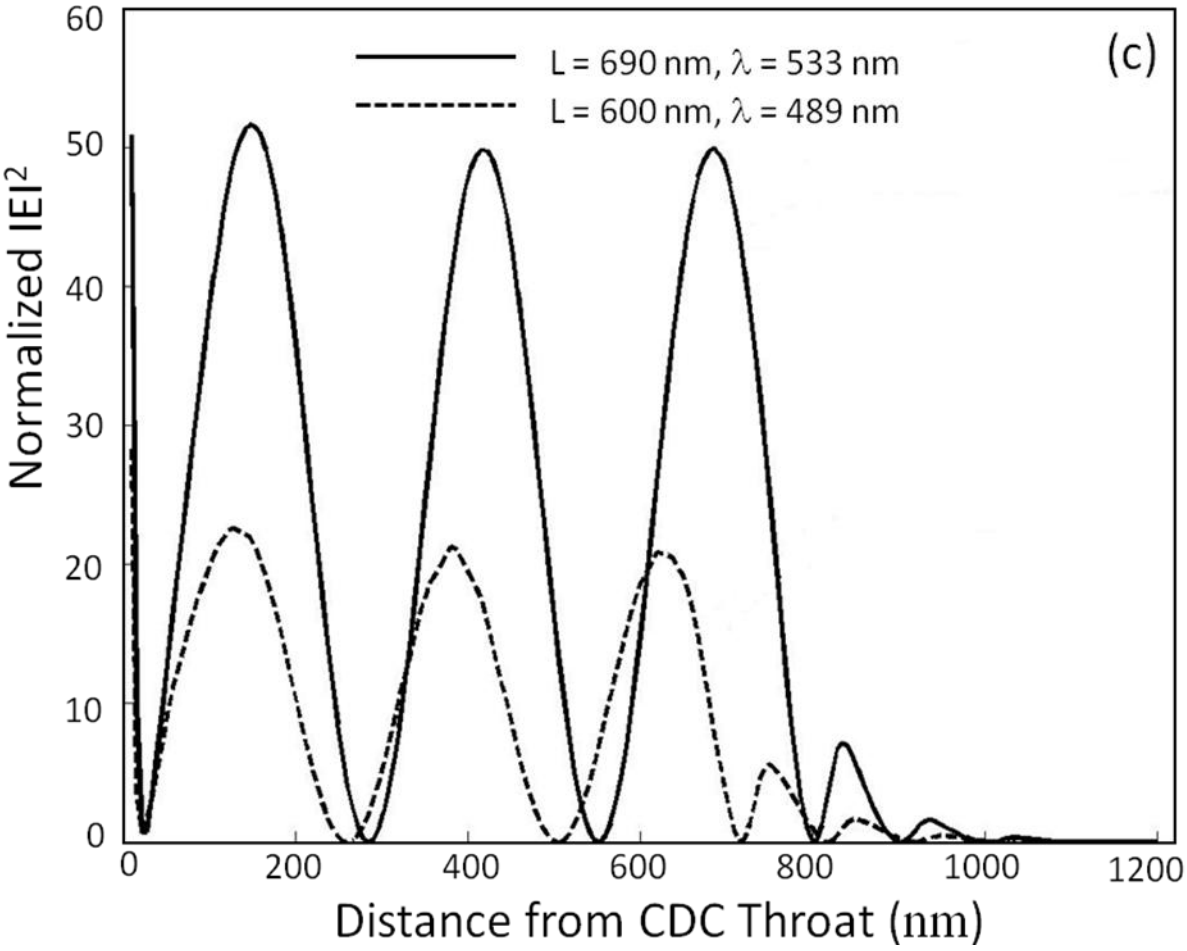

(b)
L = 600 nm, λ = 671 nm
L = 500 nm, λ = 591 nm
L = 400 nm, λ = 516 nm
L = 350 nm, λ = 486 nm
Normalized IEI²
200
160
120
80
40
0
0
200
400
600
800
1000
Distance from CDC Throat (nm)

Figure 11 (c)


(c)
L = 690 nm, λ = 533 nm
L = 600 nm, λ = 489 nm
Normalized IEI²
Distance from CDC Throat (nm)
0
10
20
30
40
50
60
0
200
400
600
800
1000
1200

Multilayer based interferential-plasmonic structure: metal cluster 3D grating combined with dielectric mirror

V. Janicki[1*], J. Sancho-Parramon[1] and H. Zorc[1]
[1]Ruđer Bošković Institute, Bijenička c. 54, 10000 Zagreb, Croatia
[*]corresponding author: janicki@irb.hr

Abstract- A three dimensional (3D) photonic microstructure consisting of metal clusters embedded in dielectric matrix is coated with a dielectric mirror. The produced photonic structure shows optical behaviour that combines the interferential effects of the multilayer stack and the surface plasmon resonance of metal clusters. Due to its feasibility and the possibility to widely modify the optical properties of the resulting interferential-plasmonic structure, this approach represents a promising method for the production of novel optical components.

1. INTRODUCTION

Metal clusters attract lot of interest due to the effect of surface plasmon resonance of free electrons, showing a strong absorption at specific wavelengths that depend on the particle size, shape and spatial distribution[1]. They are used in selective absorbers, optical polarizers and data storage[2-4], or in chemical and biological sensing and surface enhanced spectroscopy[5,6]. Metal clusters in dielectric matrix or present on the surface of a substrate can be structured by electric field assisted dissolution (EFAD)[7]. Simultaneous application of electric field and increased temperature induces dissolution of metal clusters. Using patterned electrodes EFAD can be applied locally, giving mirrored pattern on the sample containing metal clusters. Due to the possibility of structuring, the application can be extended to the production of devices ranging from plasmonic waveguides[8] to gratings[9].

We have fabricated 3D microstructure by EFAD of metal clusters embedded in multilayer stacks[10,11]. The optical behaviour of the structure is additionally tailored by the interferential effects: the stack is further coated with a dielectric mirror. The obtained structure shows the tailored optical behaviour of the resulting 3D structure and the interference phenomenon that takes place within the multilayer stack.

2. EXPERIMENTAL

A multilayer structure of metal clusters embedded in dielectric matrix was prepared by electron beam evaporation of Ag and SiO_2 at N-BK7 glass substrates of 1 mm thickness. The structure of the coating was glass/$(Ag/SiO_2)^{10}$, with layer mass thickness 7 nm (Ag) and 20 nm (SiO_2). Deposition rates were 2-3 Å/s for Ag and 10Å/s for SiO_2. There was no pre-heating of the substrates. Ag film deposited in this conditions remains in the shape of metal clusters with no significant percolation among the clusters. The SiO_2 layers of the given thickness cover the metal nanoclusters completely, so the resulting coating has a real multilayer structure[11,12].

The prepared samples were mounted between electrodes and exposed to EFAD for 2 hours at 250 ^oC and 1000 V. One part of the anode was a diffracting grating, the other part was made as uniform contact and a part of the sample has not been in contact with the anode[10].

Upon the treatment, the sample has been returned to the deposition chamber and a dielectric TiO_2/SiO_2 quarter wave $H(LH)^3$ mirror centered at 450 nm has been deposited.

The measurements of optical performances of different parts of the samples were done by Perkin Elmer

Lambda 25 spectrophotometer and Woollam VWASE ellipsometer. Reflectance and transmittance measurements were performed in the range 350-1100 nm, each 1 nm, and ellipsometric measurements of ψ and Δ in the range 0.57-4.35 eV, each 0.02 eV at 45°, 60° and 75° incidence angle. In addition to this, diffraction patterns of generated structures were measured with ellipsometer working in scatterometry mode. The incidence beam was coming to the uncoated side of the sample. Transmittance and reflectance in the range 300-1100 nm, each 25 nm, at the scattering angles 0-10° and 20-30°, respectively, by 0.2°.

3. RESULTS AND DISCUSSION

Optical performance of as deposited (AD) samples is dominated by surface plasmon resonance of metal clusters, showing maximum of absorption in the range 350-480 nm (Figure 1.). It is possible to distinguish three different parts of the sample after the treatment. Zone A is the transparent part where metal clusters are dissolved due to EFAD. The spectrum shows interferential fringes that can be related to the refractive index difference of SiO_2 layers and voids remaining after dissolution of layers containing metal clusters (Figure 1.). The significant absorption (A) in the visible and UV part can also be related to the voids, i.e. representing losses due to scattering of the light at voids. Zone B was not in the contact with the anode during the treatment, so it was exposed to the increased temperature only. The optical spectra show no significant difference corresponding to the AD sample (Figure 1.). The absorption peak is somewhat narrower and more intense after annealing that can be related to the thermally induced changes in shape and/or size of nanoclusters[10].

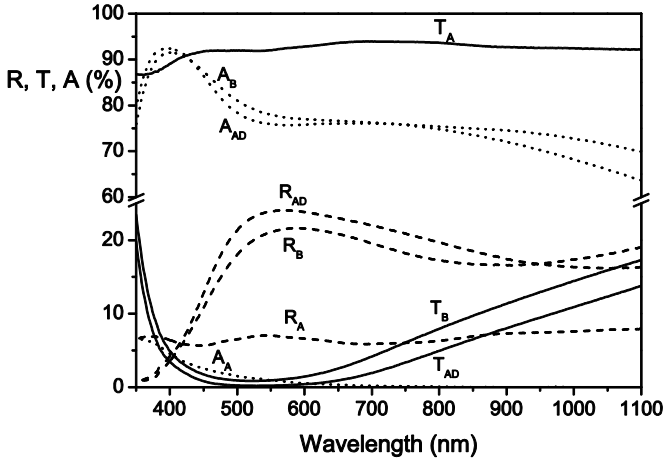


Figure 1. Reflectance (dashes), transmittance (full line) and absorption (dots) of the AD sample and zones of the sample where metal nanoclusters were dissolved (A) and where they were annealed only (B). The measurements were taken at 0° angle of incidence.

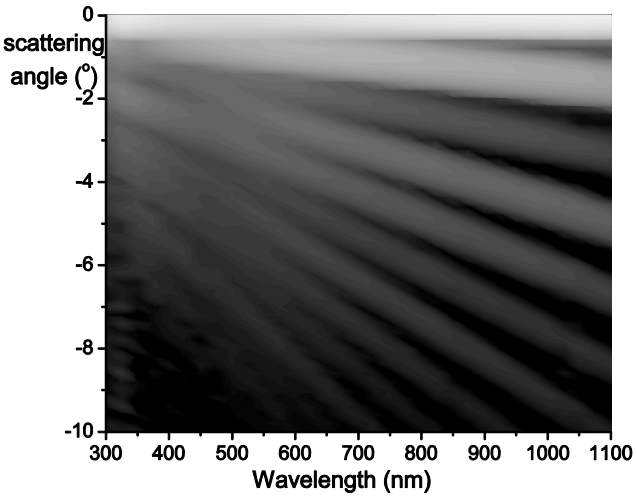


Figure 2. Diffraction transmittance pattern in logarithmic scale of zone C (diffraction grating) of the treated sample, in respect to the wavelength and scattering angle. It is possible to see different diffraction orders and their intensities. The incidence beam comes from the uncoated side of the sample.

Zone C is the one with the EFAD imprinted structure of diffraction grating from the anode. This planar structure consisting of stripes with dissolved and non-dissolved metal clusters is repeated throughout the coating forming in this way a 3D structure. The diffraction pattern is presented in Figure 2. showing the efficiency of the grating in transmittance in respect to the wavelength and scattering angle. The efficiency is higher for the wavelengths

where T_B is lower (500-600 nm).

The dielectric mirror has been deposited onto the treated sample and a bare glass substrate. Optical measurements of zones A, B and C were performed. Optical performance of the final structure is presented in Figure 3. and Figure 4.

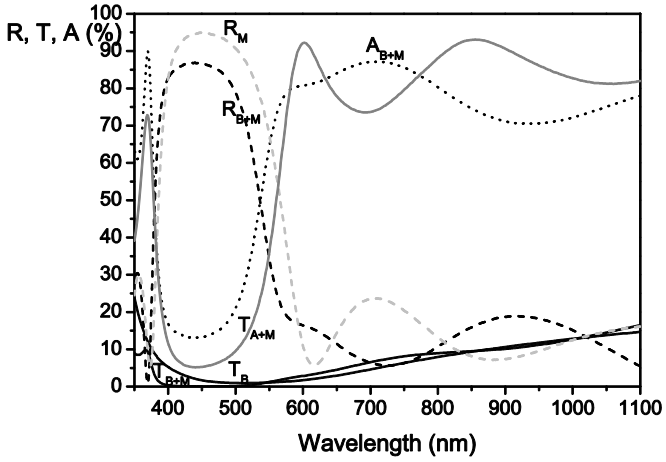


Figure 3. Reflectance (dashes), transmittance (full line) and absorption (dots) of the mirror (R_M), sample before deposition of mirror (T_B) and zones A and B after deposition of mirror. The measurements were taken at 0° angle of incidence.

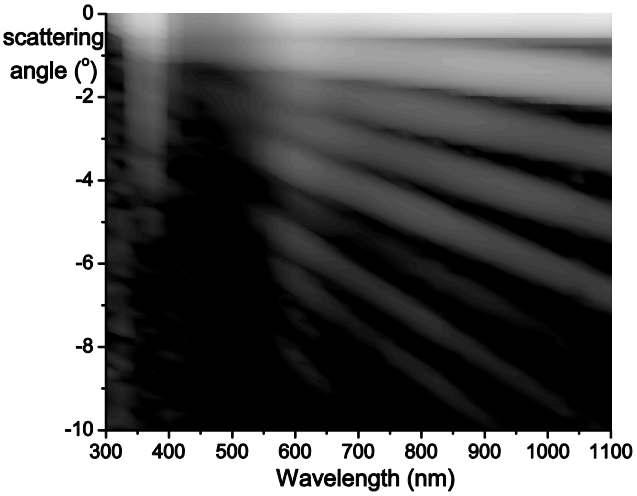


Figure 4. Diffraction transmittance pattern in logarithmic scale of zone C (diffraction grating) of the sample with mirror, in respect to the wavelength and scattering angle. It is possible to see the reduced efficiency of the grating in the range 390-540 nm. The incidence beam comes from the uncoated side of the sample.

Reflectance and transmittance of zone A, same as reflectance of zone B, are dominated by the performance of the mirror itself, that reflectance (R_M) is shown for comparison as well. In the case of incidence light coming to the coated side, high proportion of the intensity is reflected, so less intensity is absorbed in the comparison to the sample without the mirror. Therefore, the absorption of the zone B (A_B) is following opposite trend than reflectance R_{B+M}. In the range below 400 nm absorption of TiO_2 contributes as well. The resulting transmittance (T_{B+M}) is finally lower than the one for the sample without the mirror. It is also possible to see that T_A and T_B, that correspond to the transmittance of the lines and space between them in the diffraction grating, both have low values between 390 and 540 nm. This reduces the performance of the grating that is clearly seen in Figure 4. Additional diffraction orders maxima are present due to the interference effects.

4. CONCLUSIONS

3D microstructure has been obtained by EFAD of metal clusters embedded in multilayer stacks. The parts of the stack containing metal clusters i.e. where electric field dissolution was not performed show absorption due to surface plasmon resonance, while the rest of the stack is transparent. The stack is further coated with a dielectric mirror. Thus, in addition to the SPR-based metallodielectric properties, the optical behaviour of the structure is refined by the interferential effects. The obtained structure shows the tailored optical behaviour of the resulting 3D structure and the interference phenomenon that takes place within the multilayer stack.

From a technological point of view these 3D structures can be fabricated easily, as their production requires the combination of well established thin film deposition processes and the EFAD technique. Multilayer thin film stacks enable the design of a wide variety of components with different optical performances: antireflective coatings, band-pass filters, mirrors, polarisers etc. The production of these interferential-plasmonic structures could be done at low cost and easily implemented in mass-production processes, as it requires well-established thin film deposition technology and inexpensive EFAD technique.

ACKNOWLEDGEMENT

The authors would like to thank to Mr. Zdravko Dundović for preparing the original diffraction grating.

REFERENCES

1. Kreibig, U. and M. Vollmer, *Optical Properties of Metal Clusters*, Springer Series in Material Science, Springer, Berlin, 1995.
2. Kachan, S., O. Stenzel and A. Ponyavina, "High-absorbing gradient multilayer coatings with silver nanoparticles", *Appl. Phys. B: Lasers Opt*., Vol. 84, 281-287 , 2006.
3. Gotschy, W., K. Vonmetz, A. Leitner and F. R. Aussenegg, "Optical dichroism of lithographically designed silver nanoparticle films", *Opt. Lett*., Vol. 21, 1099-1101 , 1996.
4. Yih, J.-N., W.-C. Hsu, S.-Y. Tsai and S.-J. Chen, "Enhanced readout signal of superresolution near-field structure disks by control of the size and distribution of metal nanoclusters", *Appl. Opt*., Vol. 44, 3001-3005, 2005.
5. Lahav, M., A. Vaskevich and I. Rubinstein, "Biological Sensing Using Transmission Surface Plasmon Resonance Spectroscopy", *Langmuir*, Vol. 20, 7365-7367 , 2004.
6. Sockalingum, G. D., A. Beljebbar, H. Morjani, J. F. Angiboust and M. Manfait, "Characterization of island films as surface-enhanced Raman spectroscopy substrates for detecting low antitumor drug concentrations at single cell level", *Biospectroscopy*, Vol. 4, S71-S78, 1998.
7. Podlipensky, A., A. Abdolvand, G. Seifer, H. Graener, O. Deparios and P.G. Kazansky, "Dissolution of Silver Nanoparticles in Glass through an Intense DC Electric Field", *J. Phys. Chem. B*, Vol. 108, 17699-17702, 2004.
8. Krenn, J. R., "Nanoparticle waveguides: Watching energy transfer", *Nat. Mater*., Vol. 2, 210-211 , 2003.
9. Wedge, S. and W. L. Barnes, "Surface plasmon-polariton mediated light emission through thin metal films", *Opt. Express*, Vol. 12, 3673-3685, 2006.
10. Sancho-Parramon J., V. Janicki, J. Arbiol, H. Zorc and F. Peiro, "Electric field assisted dissolution of metal clusters in metal island films for photonic heterostructures", *Appl. Phys. Lett*., Vol. 92**,** 163108-1-163108-3, 2008.
11. Janicki V., J. Sancho-Parramon, F.Peiró and J. Arbiol, "Three-dimensional photonic microstructures produced by electric field assisted dissolution of metal nanoclusters in multilayer stacks", *Appl.Phys. B*, Vol. 98, 93-98, 2010.
12. Lončarić, M., J. Sancho-Parramon, M. Pavlović, H. Zorc, P. Dubček, A. Turković, S. Bernstorff, G. Jakopic, and A. Haase, "Optical and structural characterization of silver islands films on glass substrates", *Vacuum*, Vol. 84, 188–192, 2010.

Multiband Small Zeroth-Order Metamaterial Antenna

Nabil. Dakhli[1*], Fethi. Choubani[1], and Jacques. David[2]

[1]Research Unit of Telecommunication Systems (6Tel) at Sup'COM, Tunisia

[2]ENSEEIHT, France

[*]nabil.dakhli@supcom.rnu.tn

Abstract- A novel resonant metamaterial antenna based on the Composite Right/Left-Handed (CRLH) transmission line (TL) model is presented. The proposed small antenna is designed to operate simultaneously over multiple wireless services (UMTS-WLAN-WIMAX).

1. INTRODUCTION

Metamaterials represent a new breakthrough in electromagnetic engineering. In response to an increasing demand for compactness and multifunction wireless antennas, the unique electromagnetic properties of metamaterials are exploited. Some of them, such as negative permittivity and permeability, infinite wavelength propagation at specific non-zero frequency are shown by artificial transmission line (TL) metamaterials structures, mainly called the CRLH (Composite Right/Left Handed) structures. Various applications using the infinite wavelength were reported, for instance power divider, zeroth-order resonator (ZOR), and ZOR antenna. Novel planar antennas are realized, with reduced size in comparison with equivalent conventional antennas. This reduction is due to resonant property at the infinite wavelength. A general model for a CRLH TL unit-cell consists of a series capacitance, a series inductance, a shunt capacitance, and a shunt inductance. The shunt admittance of a CRLH TL unit-cell determines the infinite wavelength frequency or the zeroth-order mode. By modifying either shunt capacitance and/or shunt inductance circuit parameters, the infinite wavelength frequency and the physical size of the antenna can be modified.

In this paper, we propose a small resonant antenna based on CRLH TL, implemented by periodic arrangement of mushroom structures, where gaps are working as series capacitances, vias and half wavelength meander stubs are working as shunt inductances, separated from the ground by air layer. This antenna gives rise to a monopolar radiation pattern at zeroth-order mode at 3.5 GHz (WIMAX), a first negative order mode and second negative order mode at 2.4 GHz (WLAN), 2.03 GHz(UMTS) respectively. The two latter modes are dipolar ones. Thus, the antenna operates over multiple wireless systems (Tri-Band antenna).

2. THEORY OF CRLH TRANSMISSION LINE

The equivalent electric model of a lossless CRLH unit cell $(\mathrm{R} = 0 \text{ et } \mathrm{G} = 0)$ is given by Figure.1a. The physical length of the unit cell is $p < \frac{\lambda}{4}$, so that the CRLH network can be considered as an homogenous transmission line.

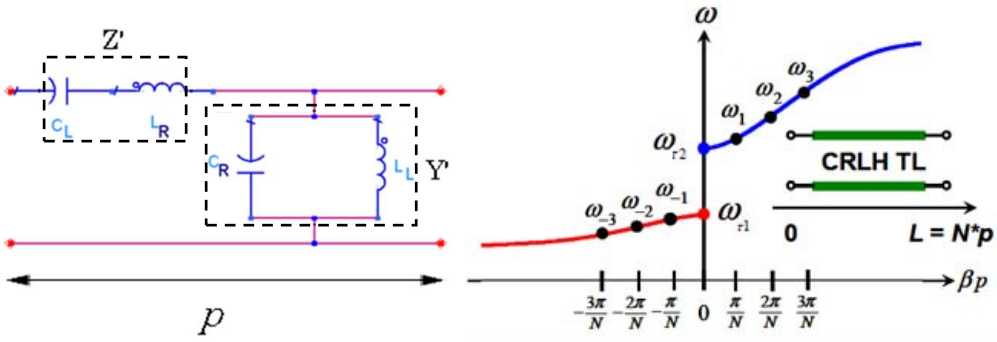


Figure 1. (a) Electric model of CRLH unit cell, (b) Dispersion diagram

By applying Bloch-Floquet theory to the proposed unit cell, we obtain the dispersion relation [1-3]

$$\cos\beta p = 1 - \frac{1}{2}\left\{\frac{\omega^2}{\omega_R^2} + \frac{\omega_L^2}{\omega^2} - \left(\frac{1}{\omega_{sh}^2} + \frac{1}{\omega_{se}^2}\right)\omega_L^2\right\} \quad (1)$$

Where $\omega_R = \frac{1}{\sqrt{L_R C_R}}$, $\omega_L = \frac{1}{\sqrt{L_L C_L}}$, $\omega_{se} = \frac{1}{\sqrt{L_R C_L}}$ and $\omega_{sh} = \frac{1}{\sqrt{L_L C_R}}$

For an open-ended CRLH transmission line, the resonant condition of $\beta_m L = m\pi$ must be satisfied, where $m = (0, \pm1, \pm2, \pm3, \ldots, \pm(N-1))$ is the resonance mode and $L = N \times p$ the total physical length of the transmission line; therefore the equation (1) is rewritten

$$\frac{m\pi}{N} = \cos^{-1}\left\{1 - \frac{1}{2}\left\{\frac{\omega^2}{\omega_R^2} + \frac{\omega_L^2}{\omega^2} - \left(\frac{1}{\omega_{sh}^2} + \frac{1}{\omega_{se}^2}\right)\omega_L^2\right\}\right\} \quad (2)$$

As a consequence, $2N-1$ Eigen-frequencies in both LH and RH regions would be expected as shown in Figure.1b. In the case where $m = 0$ (zeroth-order resonance mode), an infinite guided wavelength is supported. It is observed from Figure.1b that this condition is satisfied by the couple of Eigen-frequencies $\{\omega_{\tau 1} = \min(\omega_{sh}, \omega_{se}) \le \omega \le \omega_{\tau 2} = \max(\omega_{sh}, \omega_{se})\}$.

The exact determination of the Eigen-frequencies ω_{se} and ω_{sh} can be solved by studying the input impedance of a CRLH open-ended transmission line [3]

$$Z_{in} = -jZ_0 \cot\beta L \underset{\beta\to 0}{=} -jZ_0 \frac{1}{\beta L} = -j\sqrt{\frac{Z'}{Y'}}\left(\frac{1}{-j\sqrt{Z'Y'}}\right)\frac{1}{L} = \frac{1}{Y'L} = \frac{1}{YN} \quad (3)$$

Where $Y' = \frac{j(\omega C_R - \frac{1}{\omega L_L})}{p} = \frac{Y}{p}$

Because Z_{in} is expressed as the impedance of the shunt anti-resonant tank circuit, the zeroth-order resonance frequency of the whole structure is given by $\omega_{\tau 1} = \omega_0 = \omega_{sh}$, this frequency depends only on L_L/C_R parameters and not on the physical length as in pure right-handed TL, as a result, the number N of CRLH unit cells can be set arbitrarily. The other Eigen-frequency $\omega_{\tau 2} = \omega_{+1}$ corresponds to the first order positive resonant mode.

3. ZOR ANTENNA DESIGN

The substrate choice has a great impact on the antenna performance. The increase in relative effective permittivity ε_{reff}, results in decrease in gain G, efficiency η, and bandwidth (BW), this is attributed to the growth of different losses. Another cause which explains the reduction of gain and efficiency is the radiation resistance decrease due to the miniaturization of ZOR antenna, the conductivity loss fraction is important relative to other types of losses incorporated in the input impedance of the antenna. G and η reduction will be more severe for the non fundamental resonant modes $(m \neq 0)$ [3].

In the limit of fabrication and measurement tolerances, the FR4 Epoxy substrate with dielectric constant $\varepsilon_r = 4.4$ and thickness $h_d = 1.52$ mm was used as candidate for the ZOR

antenna design, nevertheless, it was mentioned in literature [4] that such an antenna has a poor performance, due to great dielectric loss $\tan\delta = 0.02$ and weak efficiency which does not exceed 50%.To overcome this problem, an air layer was added between the substrate and the ground, as a consequence, the relative effective permittivity decreased. In order to explain the addition of air, it is of interest to study the radiation quality factor of the antenna

$$Q_r = \frac{\omega_0 W_T}{P_{rad}} \propto \frac{1}{V} \quad (4)$$

With ω_0 the zeorth-order frequency, W_T the total stored energy, P_{rad} the radiated energy and V the antenna volume.

To antenna volume V increase corresponds ε_{reff} and Q_r decrease, and therefore radiation efficiency rises $\eta_r = \frac{Q}{Q_r}$.

In purpose to realize the antenna, three periodically arranged unit cells based on mushroom structure were used, each unit consists of a metal plate with dimensions $3 \times 3\ mm^2$ shorted by via to the ground plane, the via radius is $0.2\ mm$, between any pair of cells a gap separation has been fixed to $0.2\ mm$ .Two open ended meander stubs are attached from each side, in order to tune up L_L and consequently ω_{sh}.The stub consists of four turns, each of length $3\ mm$,width and spacing are equal to $0.1\ mm$ .The substrate and the ground plane are separated by an air layer of thickness $6.2\ mm$ and have the following dimensions $20 \times 20 \times 1.52\ mm^3$, $60 \times 60\ mm^2$, respectively.

The antenna has $\frac{\lambda_0}{12} \times \frac{\lambda_0}{8} \times \frac{\lambda_0}{28}$ as volume, it can be classified as small antenna. For the excitation, a coaxial cable was used with inner and outer radii fixed to $0.4\ mm$ and $0.9\ mm$ respectively. The antenna is shown in Figure.2.

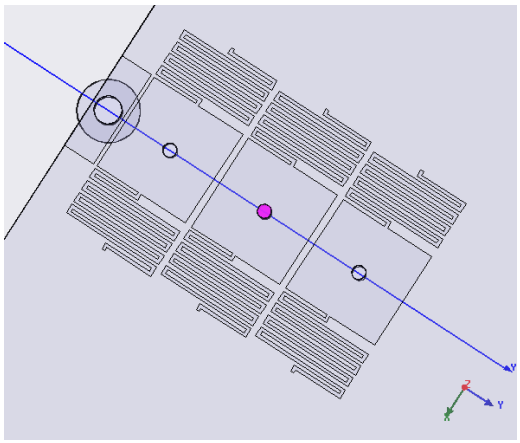
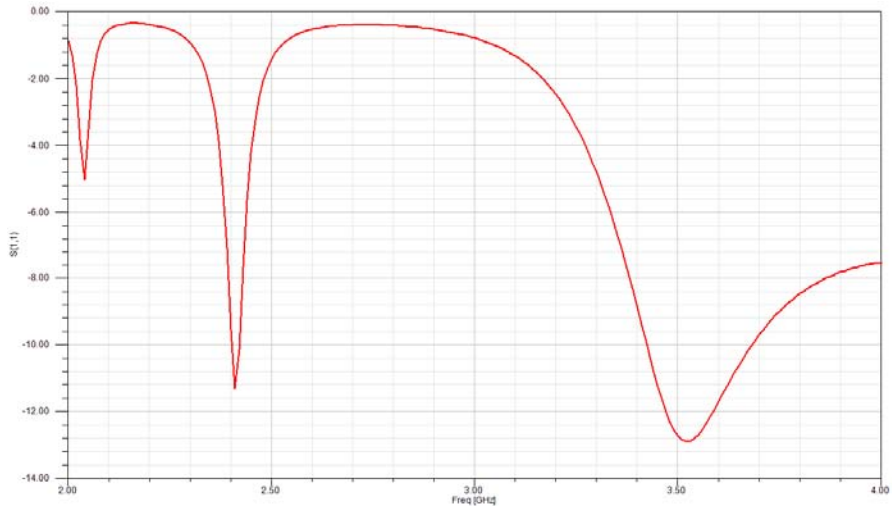


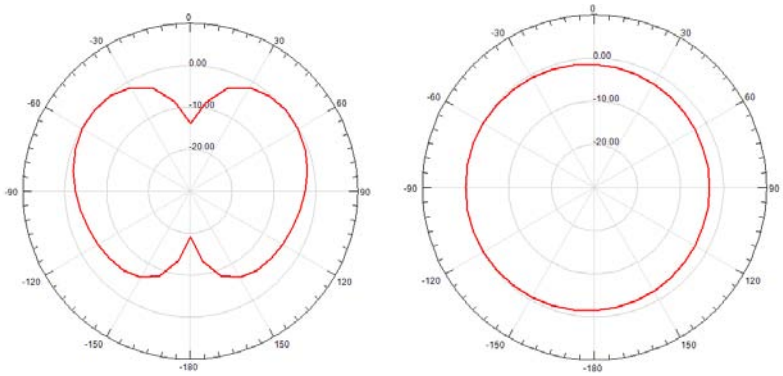
Figure 2. ZOR antenna layout

A full-wave electromagnetic simulation was carried using Ansoft HFSS gives the S-parameters, displayed in Figure.3a. The first and second order negative resonant modes correspond to $f_{-1} = 2.41\ GHz$ (WLAN) and $f_{-2} = 2.04\ GHz$ (UMTS) respectively. The zeorth-order resonance mode is located at $f_0 = 3.52\ GHz$ (WIMAX) with corresponding return loss coefficient $S_{11} = -12.89\ dB$. The radiation efficiency was enhanced to approximately 93 % at this frequency, but it drops quickly for the other modes due to a high rise of conductivity loss. The gain of value 2.37 dBi is acceptable at f_0 but it becomes negative for the non fundamental resonant modes, which deteriorates the antenna function.

The radiation patterns at *E(x-z)* and *H(x-y)* planes are shown in Figure.3b and Figure.3c, respectively, reveal the expected monopolar radiation pattern at f_0.



(a)



(b) (c)

Figure. 3. (a) Return loss S_{11}, Radiation patterns (b) *E(x-z)* and (c) *H(x-y) planes*

4. CONCLUSION

A multiband small zeroth-order antenna has been presented and demonstrated to exhibit higher gain and radiation efficiency at the fundamental resonant mode than other CRLH antennas. Generation of a vertical uniform electric field by the antenna is confirmed at 3.52 GHz.

REFERENCIES

1. A. Lai, C. Caloz and T. Itoh, "Composite Right/Left-Handed Transmission Line Metamaterials," IEEE Microwave Magazine, Vol. 5,No. 3,pp. 34-50, September 2004.

2. A. Lai, K. Leong and T. Itoh, "Infinite Wavelength Resonant Antennas With Monopolar Radiation Pattern Based on Periodic Structures," IEEE Trans. Antenna Propag.,Vol. 55,No. 3,pp. 868-875,March 2007.

3. C. Caloz and T. Itoh, "Electromagnetic Metamaterials: Transmission Line Theory and Microwave Applications " . John Wiley & Sons, Press, 2006.

4. D. Vrba and M. Polivka, "Radiation Efficiency Improvement of Zeroth-Order Resonator Antenna," RADIOENGINEERING, Vol. 18,No. 1,April 2009.

Dual Mode Composite Right-Left handed Unit Cells

Amr M. E. Safwat
Electronics and Communication Eng. Dept., Faculty of Engineering, Ain Shams University,
1 El-Sarayat St., Abbassia, 11517, Cairo, Egypt
asafwat@ieee.org

Abstract- This paper presents a new category of composite right-left-handed (CL-CRLH) unit cells. The new cells rely on complementary stubs, e.g. open and short circuited stubs in planar transmission lines or dual modes in coupled lines. They have geometrical circuit model, do not rely on commercial off-the-shelf components, and do not require vias. Theoretical expectations have been confirmed by EM simulations and measurements.

1. INTRODUCTION

CRLH transmission lines have paved the way for the realization of compact microwave devices, and for the implementation of novel applications [1-4]. Some designs of the unit cell are persuaded by the first implementation of metamaterial [5], where split ring resonator (SRR) were used, while others rely on patterned or commercial off-the-shelf (COTS) lumped-components.

This paper revisits some conventional microwave structures, short/open stubs and coupled-lines. It shows the application of these structures as CRLH unit cells. The proposed cells have geometrical circuit model, and are not limited to specific values as in COTS components.

2. COMPLEMENTARY STUBS CRLH UNIT CELL

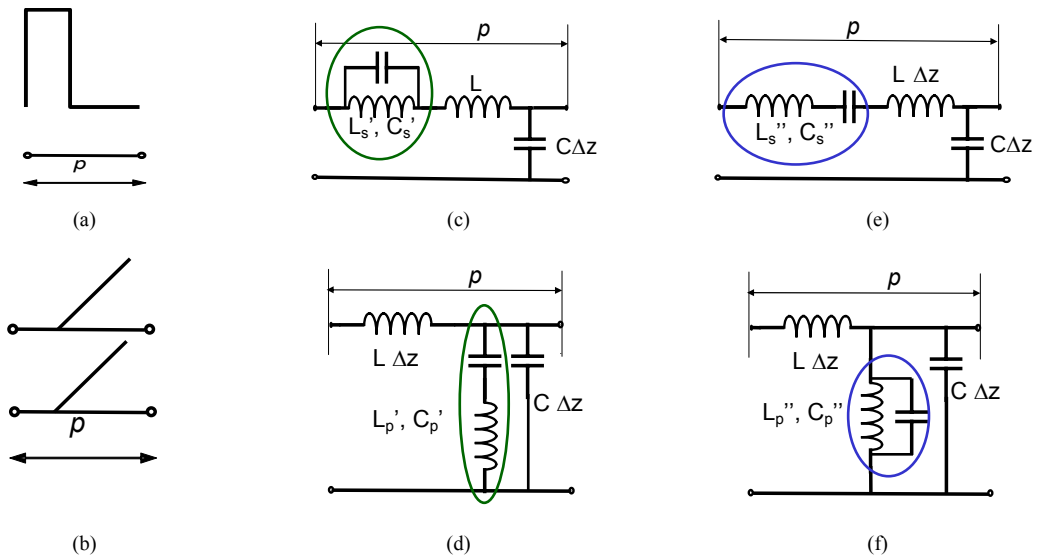
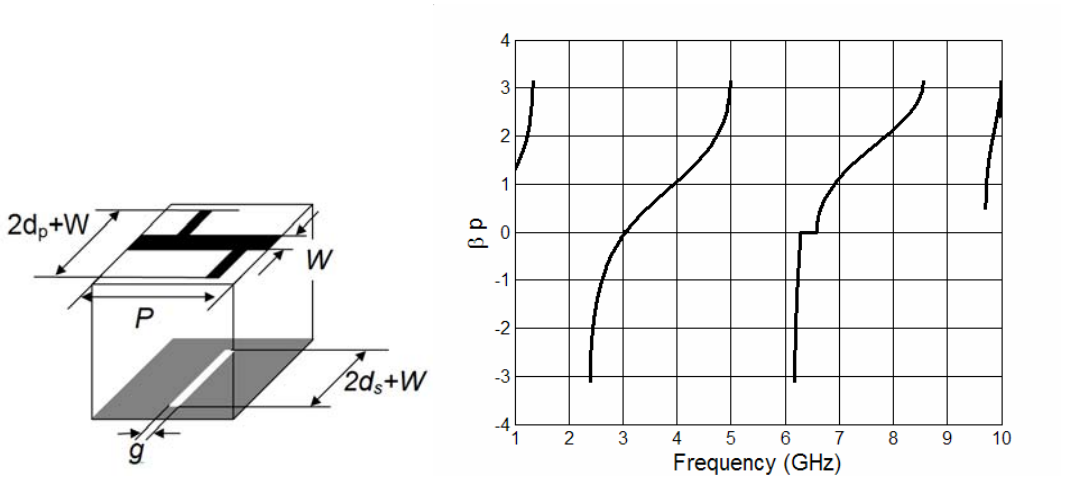


Fig. 1 a) Series stub, b) Parallel stub, c) and d) equivalent circuit model of the series and parallel stubs at λ/4, e) and f) equivalent circuit model of the series and parallel stubs at λ/2.

Series-short and shunt-open circuited stubs, shown in Fig. 1 (a) and (b) respectively, are basic components in RF circuits. At λ/4, their equivalent circuit models are a shunt resonant and a series resonant circuit respectively, Fig. 1 (c) and (d), and at λ/2 their equivalent circuit models are a series resonant and a shunt resonant circuit respectively, Fig. 1 (e) and (f). Combining these two simple structures, results in a CRLH unit cell. If the dispersion relation of the short and open –circuited stubs are identical the transition frequencies for both stubs will be the same and consequently a balanced CRLH TL will be achieved at λ/2.



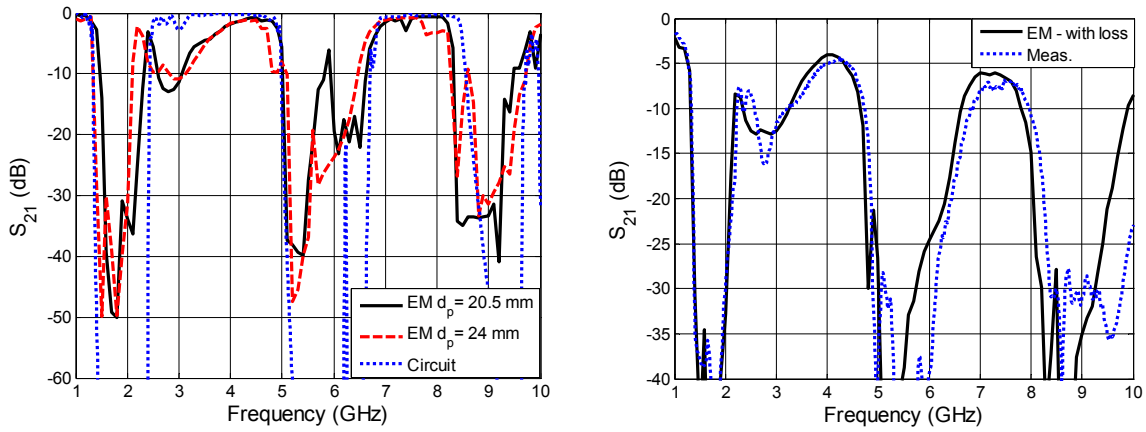
(a) (b)

Fig. 2 a)Series and parallel stubs CRLH unit cell, b) dispersion relation, substrate height h = 1.6 mm, dielectric constant ε_r = 4.4, p = 6.5 mm, d_s = 25 mm, g = 0.5 mm, w_p = 0.5 mm, and W = 2.8 mm, and d_p = 20.5 mm.

Fig. 2(a) shows the microstrip implementation of the proposed unit cell, where the slot in the ground behaves as a series short-circuited stub [6]. The length of the parallel stub was tailored to achieve the balance condition at the second transition frequency, f = 3 GHz. The optimum length was found to be d_p = 20.5 mm. The corresponding dispersion relation is shown in Fig. 2(b). The second left-handed band appears at 6 GHz, however, the balance condition at this frequency could not be achieved. This is mainly due to the difference in dispersion relations of the series and shunt stubs.

The performance of seven cascaded cells was simulated using both EM, HFSS [7], and circuit simulations. A comparison between the circuit model and EM simulations when d_p equals 20.5 mm is shown in Fig. 3(a). Transmission bands alternating between right and left -handed appear at the output. However, both EM and circuit simulations results show imbalance between left and right –handed bands. The length of the parallel stubs was optimized in the EM simulations to reduce the imbalance at the lower frequency, the optimum value was found to be 24 mm. The results, which are also depicted on Fig. 3(a), show that there is a slight increase in S_{21} for the first left-handed band, however the imbalance could not be eliminated. The optimized structure was fabricated on FR4 (h = 1.6 mm, ε_r = 4.4, tan δ = 0.02). Fig. 3(b) shows the measurement and EM simulation results. Good agreement is achieved between simulation and measurement results.

Although the use of complementary stubs eliminate the need of vias as in CRLH traditional designs, however, the physical separation between the stubs and the different dispersion characteristics degrade the performance of the cell and prevent the balance condition. Moreover, and as expected, radiation near the balance frequency reduces the transmission coefficient significantly.



(a) (b)

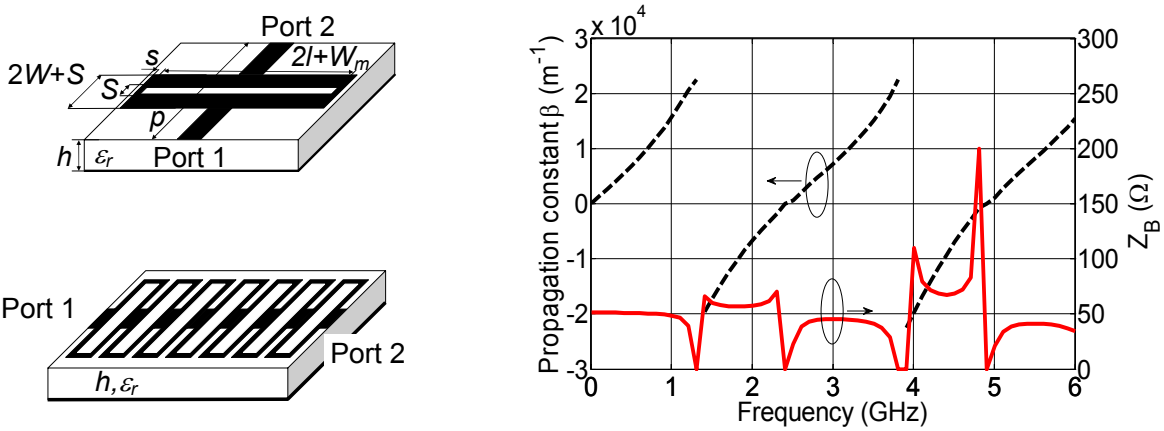
Fig. 3 Transmission coefficient of a transmission line that consists of 7series/parallel stubs unit cells.

3. DUAL MODE CRLH UNIT CELL

Combining physically the two stubs and having identical dispersion relation will definitely improve the performance. This sounds unrealistic unless we make use of orthogonal modes as in dual mode filters. Fig. 4(a) shows the layout of the coupled line, CL, CRLH unit cell, which was recently proposed in [8]. It consists of two microstrip coupled lines (*W, l, S*) inserted symmetrically at the center of a host transmission line (W_m, L_m). The two ends of the CL are connected together. Hence, the differential and common modes generated in the coupled lines see short and open circuited stubs respectively creating the two complementary stubs. The substrate has a smaller dielectric constant to ensure almost equal dispersion relations of the two modes at low frequency. Fortunately, this geometrical circuit model allows the tuning of the components dimensions to achieve two goals: minimum imbalance between the LH and RH bands, and the optimum matching over the largest bandwidth.

Fig. 4(b) shows the dispersion characteristics and Bloch impedance of the proposed unit cell, the balance frequency, $\omega_{0,2}$, equals 2.4 GHz. Very narrow stop bands appear at the transition frequencies, a large LH band, 1 GHz, appears between $\omega_{0,1}$ and $\omega_{0,2}$, and the Bloch impedance equals approximately 50 Ω up to 4 GHz.

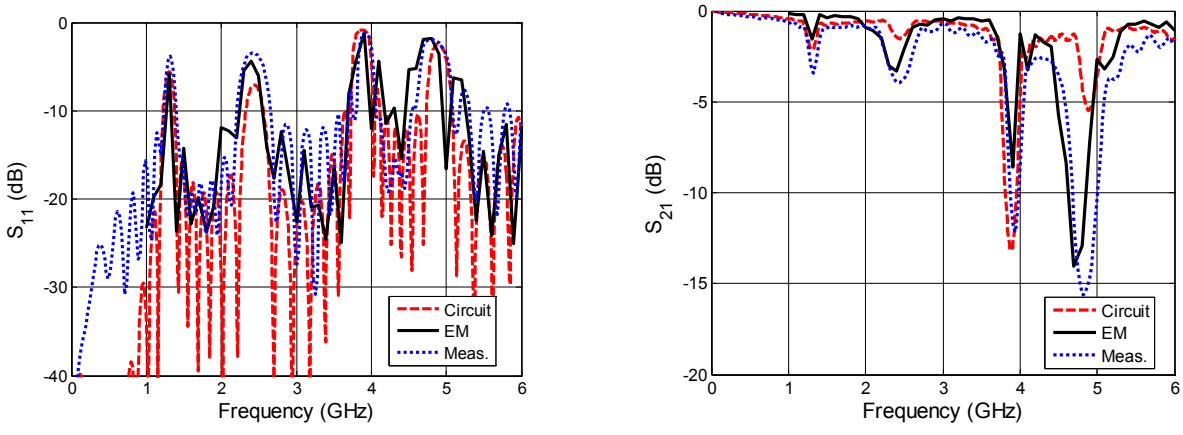
Seven unit cells were cascaded on RT/Duroid 5870 (h = 1.6 mm, ε_r = 2.33, tanδ = 0.002, and copper metallization) to form the proposed CRLH TL. Circuit simulations, depicted on Fig. 5 (a) and (b), show that transitions within -2 dB insertion loss were achieved at 1.2 GHz, $\omega_{0,1}$, and 2.4 GHz, $\omega_{0,2}$, and matching was achieved over the entire bandwidth. However, at higher transition frequencies, S_{21} drops to less than -10 dB, while S_{11} increases significantly. These results were confirmed by simulating the device using EM commercial software. EM simulation time was significantly high, and hence the number of simulated points was reduced. EM simulation results, S_{11} and S_{21}, are also plotted on Fig. 5 (a) and (b). Good agreement between circuit and EM simulations was achieved. However, deviation between EM and circuit simulations increases after 4 GHz, the second LH band is narrower than the expected value and the total loss is larger.



(a) (b)

Fig. 4 a) Schematic of the coupled line unit cell and seven cells, b) the dispersion relation, S = 0.5 mm, l = 40 mm, h = 1.6 mm, ε_r = 2.33, p = 8 mm, W_m = 3.9 mm and W = 1 mm.

The device was fabricated and characterized. Measurement results are also shown in Fig. 5 (a) and (b). A very good agreement between measurements, EM and circuit simulations was achieved up to 4 GHz. After 4 GHz, the circuit model is able to predict the transition frequencies only while the expected values of the insertion and return losses are not accurate. On the other hand, the agreement between the measurements and EM results extends over the entire bandwidth. The difference between the circuit model from one side, and the measurements and EM simulations from the other side, lies in the radiation losses, which cannot be described precisely in circuit simulators. This design reduces significantly the size of the unit cell and widens the LH band width, however small stopbands are still present. All pass band (insertion loss is negligible at the balance frequencies) CRLH unit cell is achievable if the dispersion characteristics of both modes are identical. This condition can be achieved in stripline technology.



(a) (b)

Fig. 5 S-parameters of a transmission line that consists of 7 coupled line unit cells.

4. CONCLUSION

A new family of CRLH unit cells, which is based on complementary stubs and dual modes in coupled lines was proposed. The new topologies have geometrical circuit model, which facilitates significantly the design since it does not depend on EM simulations, don't need via, and are not limited to specific values as in COTS components.

ACKNOWLEDGMENT

The author would like to thank the Science and Technology Development Fund (STDF), Egypt for supporting this work.

REFERENCES

1. Caloz, C., and T Itoh, *Electromagnetic Metamaterials: Transmission Line Theory and Microwave Applications*, John Wiley & Sons, New York, 2006.
2. Engheta, N., and R. W. Ziolkowski, *Metamaterials: Physics and Engineering Explorations*, Wiley-IEEE Press, New York, 2006.
3. Eleftheriades, G., and K. Balmain, *Negative-Refraction Metamaterials: Fundamental Principles and Applications*, John Wiley & Sons, New York, 2005.
4. Marques R., F. Martin and M. Sorolla M., *Metamaterials with negative parameters*, John Wiley and Sons, New York, 2007.
5. Shelby, R. A., D.R. Smith and S. Schultz, "Experimental verification of a negative index of refraction," *Science*, Vol. 292, 77–79, 2001.
6. Safwat, A. M. E., S. Tretyakov and A. Raisanen, "High impedance wire," *IEEE Antennas and Wireless Propagation Letters*, Vol. 6, 631 – 634, 2007.
7. HFSS, *High Frequency Structures Simulator*, Ansoft Corporation, Pittsburgh, PA, 2008.
8. Safwat, A. M. E. "Microstrip coupled line composite right/left-handed unit cell," *IEEE Microw. Wireless Compon. Lett.,* Vol. 34, No. 7, 1064–1076, 2009.

The Motifs of Crystals and their Nano-aggregates

X. M. Lu*, X. D. Shi, Y. G. Bi, Z. X. Chi, T. Min, L. L.Zhu, S. F. Xiao, and L. J. Zhong
Department of Chemistry, Capital Normal University, 100048, Beijing, Chian
lu-xiaoming@126.com

Abstract- Metal-organic-hybrid bulk chain-like, block**,** tubular**,** and plate crystals have been synthesized by wet chemical method. Single crystal X-ray diffraction and TEM reveal that all the nano-structures are associated with their crystal motifs, which provide a successful and effective access to assemble controlled specific nano-structures from bulk crystal of which their motifs are fine-desired.

1. INTRODUCTION

Nanostructures have been successfully synthesized due to their potential application in materials and medicines [1,,2]. How to assemble controlled nano-architectures has aroused extensive attention[3-8]. Mo/W-based nano-structures are of special interest due to the key role of Mo/W in modern optics, magnetism, catalysis, and medical science. At present, various methods, such as catalytic vapor-liquid-solid growth [9], direct solid-solid and gas-solid reaction [10], and template-based design techniques [11], have been applied to assemble these architectures. However, the well-controlled nano-structures are still hard to obtain especially the repeatability. Here we report a series of crystals and nano-spices which are constituted by molybdenum-organic-hybrids $\{[NH_3CH_2CH(NH_2)CH_3](C_6H_4O_2)[\mu_2\text{-}OC_6H_4O](Mo^{VI}\text{-}O\text{-}Na\text{-}O)[NH_2CH_2CH(NH_2)CH_3]\}_n$ (**1**) , $[NH_3CH_2CH(NH_2)CH_3]_2[Mo^{VI}(O_2)(O_2C_6H_4)]$ (**2**) , and $(NH_3CH_2CH_2NH_2)_3[Mo^{V}(O_2)(O_2C_6H_4)]$ (**3**), separately, and study the relationship between the motif of the bulk crystals and nano-structures.

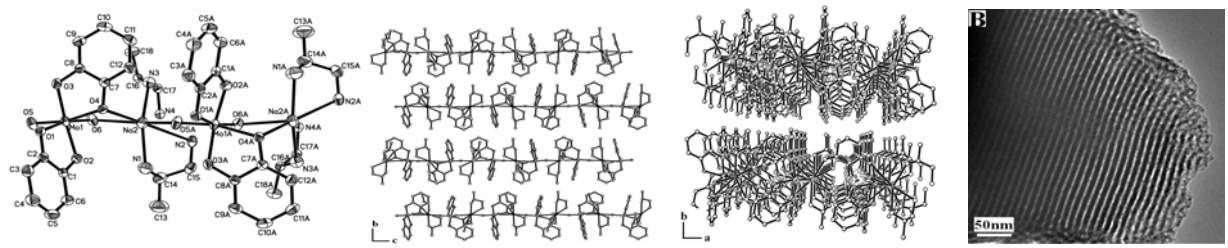
2. CRSTALS AND THEIR NANO-STRUCTURES

Single crystal X-ray analysis reveals that complex **1** crystallized in an orthorhombic system with P_{bca} space group. The complex $\{[NH_3CH_2CH(NH_2)CH_3](C_6H_4O_2$（$\mu_2\text{-}OC_6H_4O](Mo\text{-}O\text{-}Na\text{-}O)[NH_2CH_2CH(NH_2)CH_3]\}_n$ (**1**) displays an infinite coordinated one-dimensional structure. The structure of the repeating unit of complex **1** $[NH_3CH_2CH(NH_2)CH_3](C_6H_4O_2)[\mu_2\text{-}OC_6H_4O](Mo\text{-}O\text{-}Na\text{-}O)[NH_2CH_2CH(NH_2)CH_3]$ (Fig.1A) exhibits the coordination environment of metal Mo and Na atoms. The most striking structural feature of the complex is its infinite one-dimensional structure linked by Mo-O-Na-O unit along *c* axis (Fig. 1B), and the chains align parallel along *a* axis assemble a chains array which linked through hydrogen bond in *ac* plane forming lamella, and the lamellas pile into multi-layered architecture through Van der vaals force along *b* axis (Fig.1C). It is also worthy to note that, similar to graphite, the multi-layer architecture is possible to slip into thin-lamella.

After bulk crystal **1** was grounded into fine powder **1,** the powder **1** was put into ether forming a mixture, and the mixture was sonicated at 40 kHz room temperature for 1h, nano-wire which parallel-aligned into wire-array was observed under TEM (Figure.1D). The parallel alignment of the nano-wire is similar to the chains array in figure 1B and 1C., and magnified image displays the nano-wire with diameter about 2 nm, length over thousands nm, and distance about 2 m between adjacent nano-wires.

The forming mechanism of the nano-wire is that when ultrasonic wave passes through a liquid medium, a large number of micro-bubbles form, grow, and collapse in a very short time, which is called ultrasonic cavitation[12]. The cavitation can generate local temperatures as high as 5000K and local pressures as high as 500atm, with

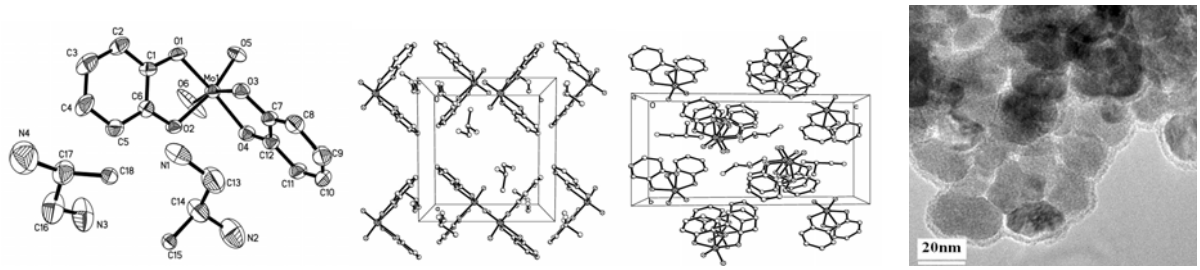
heating and cooling rates greater than 109K/s[13]. When the mixture containing ether and the well-ground powder **1** are treated by ultrasonic technique, the weak Van der vaals force between adjacent lamellas along *b* axis are destroyed and the multi-layer architecture slip into nano-lamellas which is assembled by parallel aligned nano-wires along *a* axis in *ac* plan. It is obvious that the nano-wire observed under TEM is the morphology of the infinite one-dimensional complex **1** and the nano-wire array is the parallel-alignment of complex **1**.



A **B** **C** **D**

Figure 1. Structure of complex **1** (A), their packing along *c* (B), *a* axis (C), nano-wire array (D,scale bar 50nm).

Crystal **2** with block morphology was formed after the reactant $Na_2MoO_4{\cdot}2H_2O$ in reaction **1** is replaced by $[(CH_2CH_2CH_2CH_2)_4N]_4Mo_8O_{24}$. X-ray crystal structural analysis reveals that crystal **2** was crystallized by complex $[NH_3CH_2CH(NH_2)CH_3]_2[Mo(O_2)(O_2C_6H_4)]$ (**2**) in monoclinic with space group P21/n, a=10.964(1)Å, b=10.43(9)Å, c=18.985(5)Å, β＝96.399(5)°, and Z = 4. The Mo center coordinates with two catecholato ligands, displaying a cis-dioxo fashion with chiral pseudo-octahedral $[MO_6]$ coordination geometry (Figure 2A), and the chiral anions $[Mo^{(VI)}O_2(OC_6H_4O)_2]^{2-}$ exhibited two types of enantiomers (lambda / delta configuration). In contrast to the infinite one-dimensional complex **1**, the pair of enantiomers of $[Mo^{(VI)}O_2(OC_6H_4O)_2]^{2-}$ as discrete particle repeat along three-dimensions and linked through $[NH_3CH_2CH(NH_2)CH_3]^+$ by hydrogen bonds (Figure 2B and 2C). Since hydrogen bonds are unstable and $[NH_3CH_2CH\ (NH_2)CH_3]^+$ cations are volatile under ultrasonication with 5000K temperature, 500atm pressure, and heating and cooling rates greater than 109K/s[11], so it is inferred that the parts of hydrogen bonds were destroyed, $NH_2CH_2CH(NH_2)CH_3$ molecules were volatized, and parts of $[Mo^{(VI)}O_2(OC_6H_4O)_2]^{2-}$ anions were protonated into $[Mo^{(VI)}(OH)_2(OC_6H_4O)_2]$, so that parts of the linkage of the framework in crystal lattice were broken and the powder **2** were dispersed into discrete nano-particles.



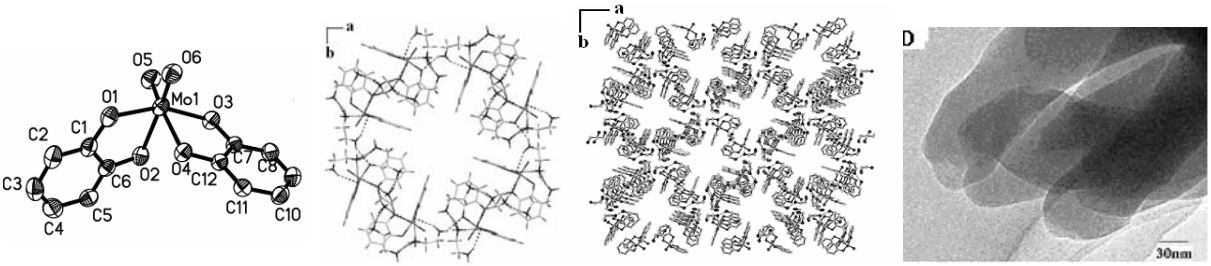
A **B** **C** **D**

Figure 2. Structure of complex 2 (A), their packing along *c* (B), *a* axis (C), nano-spheres (D, scale bar 20 nm)

As expected, when the bulk block crystal **2** was ground into powder **2**, put into ether, and treated by sonication, the nano-spheres with diameter between 30 nm to 50 nm were observed under TEM (Figure 2D). It is shown

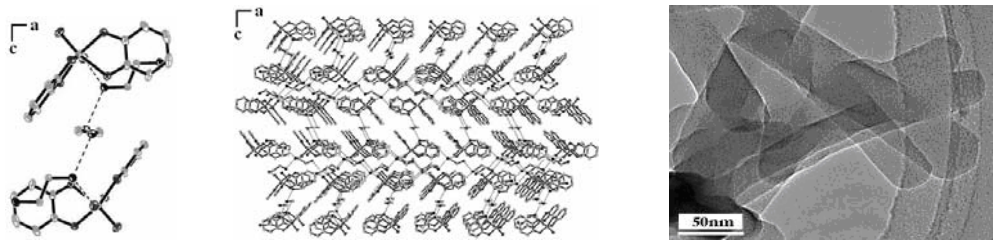
further that the cavitation environment caused by ultrasonic wave can break weak interaction among molecules, and disperse the crystal powders into nano-aggregates which associate with the motif in crystal lattice. It is also worthy to note that the nano-particle assembled by the discrete complex **2** is different totally from the nano-wire assembled by the infinite one-dimensional complex **1**.

To confirm the conclusion obtained above further, $(NH_3CH_2CH_2NH_2)^+$ instead of $[NH_3CH_2CH(NH_2)CH_3]^+$ was used and bulk tubular crystal **3α** and bulk plate crystal **3β,** both of them consisted in complex $(NH_3CH_2CH_2NH_2)_3[Mo^V(O_2)(O_2C_6H_4)]$ (**3**), were obtained under different temperature. X-ray crystal structural analysis reveals that the crystal **3α** crystallized in tetragonal system, space group P4(2)/n, a=25.214(8), c=7.484(4)Å, and Z=8 under 5 ℃. The chiral $[Mo^{(V)}O_2(OC_6H_4O)_2]^{3-}$ (Figure 3A) also have two types of enantiomers (lambda / delta configuration), and four pairs of enantiomers form a tubular structure (Figure 3B), and the tubule as motif assemble multi-tubular framework linked by $(NH_3CH_2CH_2NH_2)^+$ cations (3D). Similar to crystal **2**, hydrogen bonds are not stable and $(NH_3CH_2CH_2NH_2)^+$ are is to volatized under sonication, so it is also inferred that the multi-tubular framework could be break into motif eg nano-tubules. As expected, when the bulk single crystal **3a** was ground, put into ether, and treated by sonication, the nano-tubules with internal diameter about 50 nm were observed under TEM (Figure 3D). The nano-tubular morphology is also similar to the tubular motif of crystal **3a**.



A **B** **C** **D**

Figure 3. Structure of **3** (A), packing in *ab* plan in crystal **3a** (B and C), nano-tubules (D, scale bar 30 nm).



A B C

Figure 4. The packing of complex **3** in *ac* plan (A and B) in crystal **3β**, and nano-ribbons split from crystal **3β**.

Crystal **3β**, which is the allomorphism of crystal **3a,** with macro-lamella morphology crystallized above 10 ℃ in monoclinic, space group P21/c, a=7.1254(2)Å, b=30.7496(9)Å, c=9.7857(3)Å, β＝102.411(2)°, and Z=4. The difference between crystal **3β** and **3α** is the packing of the complex **3** in crystal lattice. In crystal **3β**, the motif of the crystal **3β** is bi-molecular-layered structure constituted by enantiomeres of chiral $[Mo^{(V)}O_2(OC_6H_4O)_2]^{3-}$ anions, and the motif form multi-bi-molecular-layered architecture linked by $(NH_3CH_2CH_2NH_2)^+$ cations along *c* axis (Figure 4 A and B). It is also inferred that the multi-lamellar framework could be slip into motif eg nano-lamella and the lamellas break into nano-ribbon further. As expected, when the bulk single crystal 3β was

ground, put into ether, and treated by sonication, the nano-ribbon with width about 30 nm and length hundreds nm was observed under TEM (Figure 4C).

3. CONCLUSIONS

Controlled nano-structures can be prepared from bulk crystal by grounding and ultrasonication. The dimension and morphology of the nano-structures are associated with the motifs in crystal lattice. The adding of the small organic molecules which are volatile and easy to form hydrogen bonds is an effective access to obtain controlled nano-structures under mild environment.

4. ACKNOWLEDGEMENT

We acknowledge the financial support of Chinese National Natural Science Foundation (20871085) and Beijing Natural Science Foundation (2092009).

5.REFERENCES

1 Alivisatos A. P., “Semiconductor Clusters, Nanocrystals, and Quantum Dots,” Science, Vol. 271, No.5251, 933–937, 1996.

2 Yakobson B. I. and R. E. Smalley, “Fullerene nanotubes: C1,000000 and beyond,” Am. Sci. Vol.85, No.4, 324–337, 1997.

3 Braun P. V., P. Osener and S. I. Stupp, “Semiconducting superlattices templated by molecular assemblies,” Nature. Vol.380, No.6572, 325–328. 1996.

4 Kiely.C. J., J. Fink, M. Brust, D. Bethell and D. J. Schiffrin, “Spontaneous ordering of bimodal ensembles of nanoscopic gold clusters” Nature, Vol.396, 444-446,1998.

5 Penn.R. L. and J. F. Banfield, “Imperfect Oriented Attachment: Dislocation Generation in Defect-Free Nanocrystals” Science, Vol.281, No.5379，969-971,1998.

6 Cui.Y and C. M. Lieber, “Functional nanoscale electronic devices assembled using silicon nanowire building blocks,” Science, Vol.291, No.5505, 851–853,2001

7 Puntes. V. F., K. M. Krishnan and A. P. Alivisatos, “Colloidal Nanocrystal Shape and Size Control: The Case of Cobalt”, Science, Vol.291, 2115-2117,2001.

8 Tang. Z.Y., N. A. Kotov and M.Giersig, “Spontaneous organization of single CdTe nanoparticles into luminescent nanowires”, Science, Vol.297, No.5579,237-240,2002.

9 Gao.P. X., Y. Ding and Z. L. Wang, “Crystallographic Orientation-Aligned ZnO Nanorods Grown by a Tin Catalyst”, Nano Lett., Vol.3, No.9,1315-1320,2003.

10 Lao J. Y., J. Y. Huang, D. Z. Wang and Z. F. Ren, “ ZnO Nanobridges and Nanonails, ” Nano Lett. Vol. 3, No. 2, 235–238. 2003,

11 Li J., C. Papadopoulos and J.M.Xu, anoelectronics: “Growing Y-junction carbon nanotubes,” Nature , Vol. 402, 253–254, 1999.

12 Tang E.S.K., M. Huang, and L.Y. Lim, “Ultrasonication of chitosan and chitosan nanoparticles , ” Inter. J. Pharm, Vol. 265, No. 2, 103–114 , 2003.

13 Lu X.F., H. Mao, D.M. Chao, et al., “Ultrasonic synthesis of polyaniline nanotubes containing Fe_3O_4 nanoparticles,” J. Solid State Chem. Vol.179, No. 6572, 2609–2615, 2006.

Investigation of magneto-dielectric thin films as substrate for high impedance surfaces

F. Grange[1], **C. Delaveaud**[1], **and K. Mahdjoubi**[2]

[1]CEA-LETI, France
[2]IETR, Rennes
francois.grange@cea.fr

Abstract—

In the present paper we study the effect of magneto-dielectric laminated thin films on the characteristics of high impedance surface. Analytical and numerical modelings are compared by using the AEMT method and a full-wave simulation tool respectively.

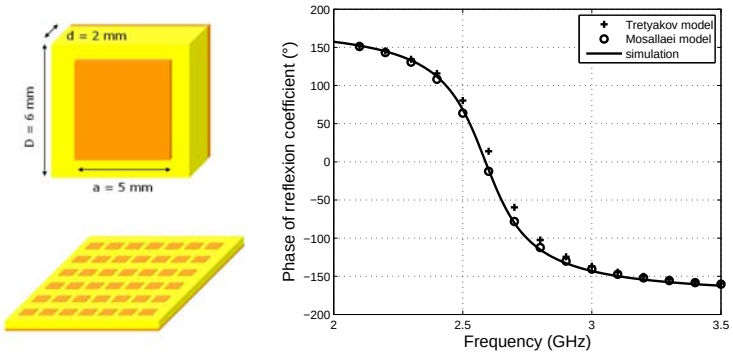
1. INTRODUCTION

This paper relates to high impedance surfaces and in particular, to Artificial Magnetic Conductor (AMC) or Reactive Impedance Surface (RIS) loaded with magnetic materials. In the past few years, an increasing interest was born for ground planes showing high impedance surface properties. Recently, new artificial high impedance surfaces have been introduced by [1]. Usually AMC and RIS consist of an array of conductive patches printed on metal-backed dielectric substrate with a periodicity smaller than the free space wavelength. This distinguishes AMC from Frequency Selective Surface (FSS). Unlike the Sievenpiper's mushroom structure [2], this new surface does not contain any via or DC contact. Perfect Magnetic Conductors (PMC) consist in a surface exhibiting a reflexion coefficient of $\Gamma = 1$. Thus, image currents are not phase reversed but in-phase with the original current. Consequently, low profile antennas can be imagined by using AMCs (i.e. a practically realisable PMC) allowing to place radiating element close to the reflector. High impedance surfaces have been used in various antenna applications [3] despite such reflectors suffer from a lack of bandwidth [4]. Besides, recent technological advances in microelectronics allowed the emerging of new multilayered materials performed by thin film deposition [5]. These heterostructures constitutes an original solution for high permeability materials suitable for microwave regime. By using a combination of ultrahigh magnetization and ultrahigh exchange-biased FeCo multilayers with dielectrics, this material exhibits a particularly interesting electromagnetic behavior for radiofrequency applications. This article aims to analytically investigate the impact of such layers on reflexion coefficient phase. Authors of [6] used the Anisotropic Effective Medium Theory (AEMT) to determine radioelectric parameters of magneto-dielectric stacked layers. We developped an original model, based on a simple analytical formula for the surface impedance [7], to predict their impact. Indeed, our model take into account conductivity of magnetic layers by including the magnetization relaxation mechanism due to Eddy currents [8].

2. ARTIFICIAL MAGNETIC CONDUCTOR MODELING

In order to characterize the electromagnetic behavior of AMC, theoretical investigations have been widely driven by many authors: 1) Sievenpiper stated that reflection properties of the mushroom structure can be partly described by an equivalent LC resonator [2]; 2) several authors used the transmission line model for the characterization; 3) Mosallaei and Sarabandi proposed a method for designing a reactive impedance surface with a prescribed surface impedance property; 4) Tretyakov developped a simple analytical model based on a description of their electromagnetic properties, in terms of grid impedance [9]. Indeed, by applying the Babinet principle on planar strip grids located at a dielectric interface, one can derive the grid impedance for the complementary structure, e.g. an array of patches. In this section, we present two different types of models for reflexion coefficient computing of AMC in case of normal-incidence plane-wave excitation. Concerning the model developped by Mosallaei, the effective length of the square patch has to be chosen slightly shorter than its physical length because of the finite size edge effects [6]. Thus, by properly choosing the effective length, the model fits very well the Finite Element method (HFSS). In addition same

authors have shown an independant incidence angle of the surface response, in consequence we do not consider, in this article, any oblique incidence and arbitrary polarization plane wave.



(a) (b)

Figure 1: (a) Unit cell, (b) Modeled and simulated phase of the reflexion coefficient, (c) AMC

In spite of a better agreement with Mosallaei model, our choice for the magneto-dielectric thin films impact evaluation went to the Tretyakov model due to very good agreement without any approximation on physical or geometrical properties.

3. RADIO ELECTRIC PARAMETERS MODELING OF MULTILAYER THIN FILMS

In order to characterize the interaction between electromagnetic waves and a complex finite or infinite medium periodically laminated, one can use an analytical method based on the AEMT [6]. This recursive method can be applied to multilayer thin films stacks. However, this model is only valid for the incident wave direction of propagation and polarization, shown in Fig. 2, leading to a particular fields configuration . It is important to ensure that the pattern leads to the right fields configuration inside the patch cavity when illuminating by a plane wave. Zhang [1] investigated the field distribution of a patch array surface excitated by a z-polarised normal TEM incident wave. His conclusion has shown a very similar field distribution on both single patch antenna and periodic patches arrays.

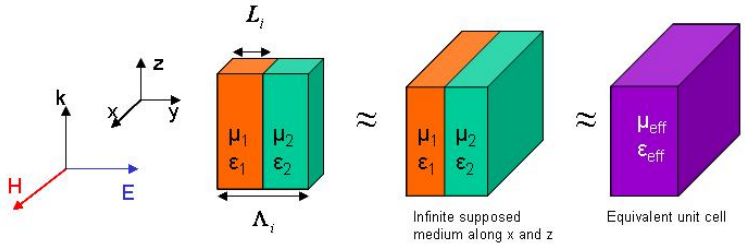


Figure 2: Anisotropic effective material model for the 1-D periodic magneto-dielectric.

Originally, AEMT method was limited to non dispersive and non conductive materials. In previous work [10], we strived to take into account the highly conductive magnetic layers property, by integrating the contribution of Eddy currents in the calculation of permeability on the one hand and through the expression of complex permittivity on the other hand.

$$\frac{1}{\epsilon_{eff}} = \frac{1}{\epsilon_1}\frac{L_i}{\Lambda_i} + \frac{1}{\epsilon_2}\left(1 - \frac{L_i}{\Lambda_i}\right) \tag{1}$$

$$\mu_{eff} = \mu_1\frac{L_i}{\Lambda_i} + \mu_2\left(1 - \frac{L_i}{\Lambda_i}\right) \tag{2}$$

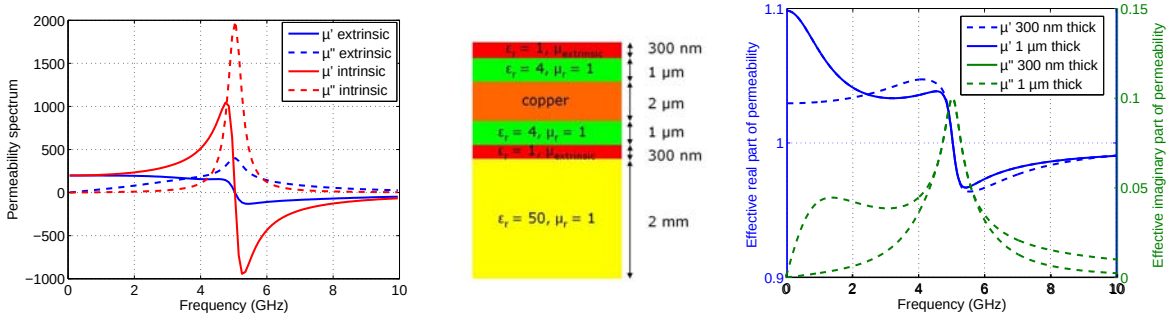
Authors of [6] used the AEMT to determine radioelectric parameters of magneto-dielectric stacked layers. We developped an original model, based on a simple analytical formula for the surface

impedance [7], to predict their impact. Indeed, our model takes into account conductivity of magnetic layers by including the magnetization relaxation mechanism due to Eddy currents [8] in the AEMT model.

$$\mu_{extrinsic} = \mu_1 = \mu_{LLG}\left[\frac{2\delta}{(1+j)e}\tanh\frac{(1+j)e}{2\delta}\right] \tag{3}$$

$$\mu_{intrinsic} = \mu_{LLG} = 1 + \frac{\gamma 4\pi M_S\left(\gamma H + \gamma 4\pi M_S + j\omega\alpha\right)}{\left(\gamma H + j\omega\alpha\right)\left(\gamma 4\pi M_S + j\omega\alpha\right) - \omega^2} \tag{4}$$

where δ skin depth, α damping factor, Ms saturation magnetization, γ gyroscopic factor, H_eff effective magnetic field and e the magnetic layer thickness. Figure 3 (a) and (c) illustrate the magnetization relaxation mechanism due to Eddy currents. We can observe a permeability fall both on extrinsic and effective permeability when using a 1 μm thick magnetic and conductive layer.



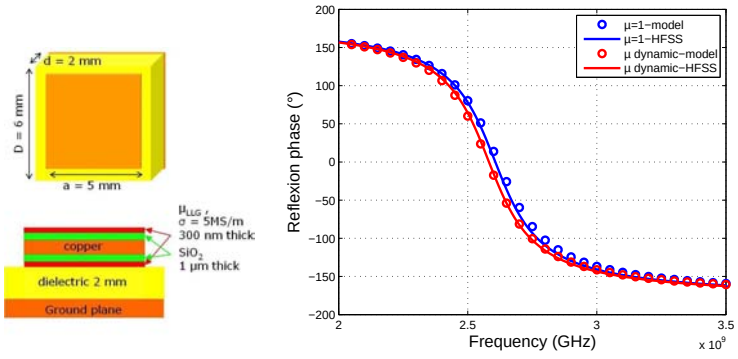
(a) (b) (c)

Figure 3: (a) Permeability spectrum, (b) Magneto-dielectric multilayer stack, (c) Effective permeability spectrum

In this section we put the emphasis on the critical role of magnetic layers conductivity.

4. MAGNETO-DIELECTRIC THIN FILMS IMPACT

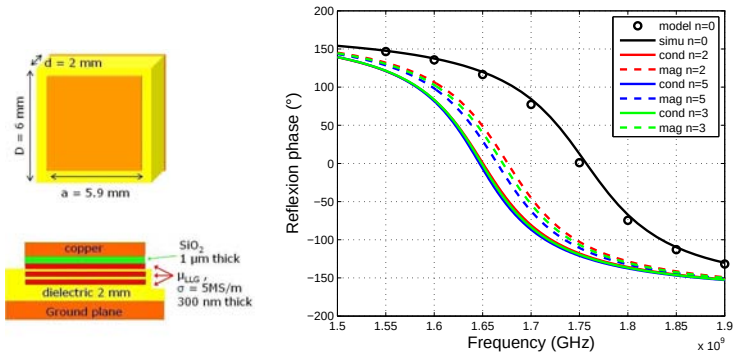
Our contribution consists in combining the Tretyakov model and the model from [10] developped in section 3 . Instead of using $\mu_r = 1$ we introduced the complex permeability expression (2) inside the equivalent surface impedance expression.



(a) (b)

Figure 4: (a) Example of influence of μ on the reflexion phase diagram, (b) Top view and cut plane of magneto-dielectric stack unit cell of HIS patch array,

As shown in Fig.4(b), we obtain a good agreement between analytical and simulated results. Main results concern a frequency downshift in spite of using two magnetic layers only 300 nm thick each. Figure 5 present the reflexion phase diagram for a multilayer stack cell configuration.



(a) (b)

Figure 5: (a) Top view and cut plane of magneto-dielectric stack unit cell of HIS patch array, (b) Example of influence of μ on the reflexion phase diagram

One can note that a miniaturization is achieved even if $\mu_r = 1$, as shown by dotted lines. As hypothese to explain that we can say that strong capacitive coupling opers between closed layers.

5. CONCLUSION

The loading of AMC with such laminated magneto-dielectric conductive thin films leads to a 6% pattern miniaturization. Both analytical and numerical results illustrate the influence of a single magnetic layer whereas a complex heterostructure can not yet be modeled. Future work will explain in detail this particular behavior.

REFERENCES

1. Y. Zhang, J. von Hagen, M. Younis, C. Fischer, and W. Wiesbeck, "Planar artificial magnetic conductors and patch antennas," *IEEE Transactions on Antennas and Propagation*, vol. 51, no. 10, pp. 2704–2712, Oct. 2003.
2. D. Sievenpiper, L. Zhang, R. Broas, N. Alexopolous, and E. Yablonovitch, "High-impedance electromagnetic surfaces with a forbidden frequency band," *Microwave Theory and Techniques, IEEE Transactions on*, vol. 47, no. 11, pp. 2059–2074, Nov 1999.
3. A. Foroozesh and L. Shafai, "Application of combined electric- and magnetic-conductor ground planes for antenna performance enhancement," *Electrical and Computer Engineering, Canadian Journal of*, vol. 33, no. 2, pp. 87–98, Spring 2008.
4. ——, "Application of the artificial magnetic conductor ground plane for enhancement of antenna input impedance bandwidth," in *Antennas and Propagation Society International Symposium, 2009. APSURSI '09. IEEE*, June 2009, pp. 1–4.
5. B. Viala, G. Visentin, and P. Gaud, "Af-biased cofe multilayer films with fmr frequency at 5 ghz and beyond," *IEEE Transactions on Magnetics*, vol. 40, no. 4, pp. 1996–1998, July 2004.
6. H. Mosallaei and K. Sarabandi, "Engineered meta-substrate for antenna miniaturization," *Ann Arbor*, vol. 1001, pp. 48 109–2122, 2004.
7. O. Luukkonen, C. Simovski, G. Granet, G. Goussetis, D. Lioubtchenko, A. Raisanen, and S. Tretyakov, "Simple and accurate analytical model of planar grids and high-impedance surfaces comprising metal strips or patches," *IEEE Transactions on Antennas and Propagation*, vol. 56, no. 6, pp. 1624–1632, June 2008.
8. A. Berthault, E. Durbin, and J. Russat, "Perméabilité intrinsèque et extrinsèque de couches minces ferromagnétiques et de multicouches ferromagnétique-isolant en fonction de la fréquence : comparaison expérience - modèle," *JOURNAL DE PHYSIQUE IV*, vol. 2, pp. C3–229, 1992.
9. S. Tretyakov and C. Simovski, "Dynamic model of artificial reactive impedance surfaces," *Journal of Electromagnetic Waves and Applications*, vol. 17, pp. 131–145, 2003.
10. F. Grange, L. Fourneaud, E. Benevent, C. Delaveaud, and K. Mahdjoubi, "Modélisation de paramètres radioélectriques effectifs: application aux couches minces magnéto-diélectriques," in *16èmes Journées Nationales Microondes*, 2009.

Reducing backscattering cross section of an electrically large sphere with metamaterial coating

Maysam.Haghparast[1*] **and M.S.Abrishamian**[1**]

[1]Department of electrical Engineering, K.N.Toosi University of Technology, Tehran, Iran

[*]maysam.haghparast@gmail.com

[**]msabrish@eetd.kntu.ac.ir

Abstract- In this paper, we showed that homogeneous metamaterial coatings with relative permeability and permittivity less than one can reduce backscattering cross section of an electrically large sphere. Since monostatic radar cross section (RCS) is based on backscatter waves, such a coated sphere can not be detected. We also considered the effect of loss in coating and proved that even with a lossy coating, transparency in front of monostatic radar is achievable.

1. INTRODUCTION

Invisibility was a highly attentioned subject during last decades. After introducing the concept of metamaterials, many researches have been conducted in the field of achieving invisibility by metametrials. Different methods and simulations have been investigated in this subject. A concept in cloaking subject, introduced in [2], is an object-dependent cloak. In this method, cloak with $\varepsilon_r < 1$ and $\mu_r < 1$ is designed so that the cloak-object pair's scattering become zero. As was shown in [2], hiding objects is doable only for small objects compared to wavelength. When the object become larger, the ability of this method is affected and a complete transparency is not possible. For large spheres, it is impossible to decrease total scattering cross section. We will show that it is possible to reduce the backscattering cross section of an electrically large object by this method. Monostatic RCS is based on backscattered wave and using this method, make it possible to hide a large sphere in front of a monostatic radar. We will show that, it is possible to reduce the backscattering cross section of large objects, although, because of non-zero total scattering cross section, a bistatic radar is capable of detecting this kind of coated objects.

2. Basic Theory

Consider a dielectric sphere with permittivity ε, permeability μ and radius R_1, coated by a spherical concentric shell with permittivity ε_c, permeability μ_c and outer radius of R_2. This sphere-coating structure is located in free space with constitutive parameters ε_0 and μ_0. All of permeability and permittivity values can be complex, which allows us to model dispersive medias. The structure is depicted in figure 1. Adding coating to main sphere, increase the overall dimension of our structure, and generally speaking, larger objects have larger scattering and backscattering cross sections. Now the question is this, is it possible to add a specific coating to a sphere and make an extreme decrease in overall scattering cross section? As proved in [2], it is possible by metamaterial coatings. According to figure 1, consider a plane wave, traveling toward the sphere-coating pair. The time dependence of wave is $e^{j\omega t}$ and λ is free space wavelength.

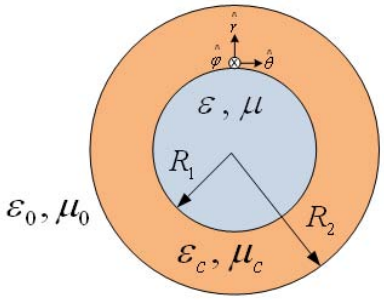


Figure1: Cross section of the main sphere and its coating

Using Mie expansion theory [3], we can express scattered field in a summation of harmonics of c_n^{TM} and c_n^{TE}, in which n is an integer. As mention in[2], these terms are:

$$c_n^{TM} = -\frac{U_n^{TM}}{U_n^{TM} + jV_n^{TM}} \tag{1}$$

$$c_n^{TE} = -\frac{U_n^{TE}}{U_n^{TE} + jV_n^{TE}} \tag{2}$$

U_n^{TM} and V_n^{TM} are obtained from the below determinants [2]:

$$U_n^{TM} = \begin{vmatrix} j_n(kR_1) & j_n(k_cR_1) & y_n(k_cR_1) & 0 \\ [(kR_1)j_n(kR_1)]'/\varepsilon & [(k_cR_1)j_n(k_cR_1)]'/\varepsilon_c & [(k_cR_1)y_n(k_cR_1)]'/\varepsilon_c & 0 \\ 0 & j_n(k_cR_2) & y_n(k_cR_2) & j_n(k_0R_2) \\ 0 & [(k_cR_2)j_n(k_cR_2)]'/\varepsilon_c & [(k_cR_2)y_n(k_cR_2)]'/\varepsilon_c & [(k_0R_2)j_n(k_0R_2)]'/\varepsilon_0 \end{vmatrix} \tag{3}$$

$$V_n^{TM} = \begin{vmatrix} j_n(kR_1) & j_n(k_cR_1) & y_n(k_cR_1) & 0 \\ [(kR_1)j_n(kR_1)]'/\varepsilon & [(k_cR_1)j_n(k_cR_1)]'/\varepsilon_c & [(k_cR_1)y_n(k_cR_1)]'/\varepsilon_c & 0 \\ 0 & j_n(k_cR_2) & y_n(k_cR_2) & y_n(k_0R_2) \\ 0 & [(k_cR_2)j_n(k_cR_2)]'/\varepsilon_c & [(k_cR_2)y_n(k_cR_2)]'/\varepsilon_c & [(k_0R_2)y_n(k_0R_2)]'/\varepsilon_0 \end{vmatrix} \tag{4}$$

For TE mode, U and V will be calculated using duality, replacing ε with μ in the above determinants. In addition, k is the wave number of different mediums, i.e:

$$k_0 = \omega\sqrt{\mu_0\varepsilon_0}\ , k = \omega\sqrt{\mu\varepsilon}\ \text{ and }\ k_c = \omega\sqrt{\mu_c\varepsilon_c} \tag{5}$$

j_n and y_n are the spherical Bessel function of first and second kind and prime($[\,.\,]'$) denotes differentiation with respect to the argument of relevant spherical Bessel function.

After calculating these coefficients, total scattering and backscattering cross section can be calculated respectively:

$$Q_s = \frac{2\pi}{|k_0|^2}\sum_{n=1}^{\infty}(2n+1)\left(\left|c_n^{TE}\right|^2 + \left|c_n^{TM}\right|^2\right) \tag{6}$$

$$\sigma = \pi\left|\frac{1}{k_0}\sum_{n=1}^{\infty}(-1)^n(2n+1)(c_n^{TE} - c_n^{TM})\right|^2 \tag{7}$$

Analyzing c_n^{TM} and c_n^{TE}, will show us that as n increases, these coefficients decrease and after a specific n, called Nmax, the terms will be negligible. So after determining Nmax, we replace it in upper limit of summation. As the structure become larger, Nmax will increase. Here, we should determine the value of Nmax. Nmax is directly proportional to dimension of the structure. As a rule of thumb we can consider $\mathrm{Nmax} = k_0 R_2$ [1]. As we anticipated before, this proposed value of Nmax shows that bigger structure will have larger value of Nmax. In addition, when the object is small ($R_2 \ll 1$), $\mathrm{Nmax} = 1$, which means that only first term should be calculated.

3. Backscatter wave reduction for large objects

Total scattering cross section (we will abbreviate it as $\mathrm{Q_s}$) could not be omitted completely, when the coated sphere is not small(compared to wavelength), but in the term of backscattering cross section(we will abbreviate it $as\ \sigma$), it is possible to be omitted completely even for large spheres. For large sphere $\mathrm{Q_s}$ and σ is independent and σ could be zero, whilst $\mathrm{Q_s}$ is not. Here we focus on metamaterial application as a coating to omit σ for large sphere and start our investigation with a sphere with relatively large size. We consider a sphere which is larger than wavelength. Consider a sphere with $R_1 = 7\lambda_0$, $\varepsilon = 10\varepsilon_0$ and $\mu = \mu_0$ coated with a $\varepsilon_c = 0.001\varepsilon_0$ and $\mu_c = 0.01\mu_0$ shell. Using such coating with specified constitutive parameters, as mention above, make it possible to have a zero minimum in $R_2 = 1.34\, R_1$ for σ, but not for $\mathrm{Q_s}$. Thus a monostatic can not detect this sphere-coating structure. The normalized plot of σ can be seen in figure (3-a).

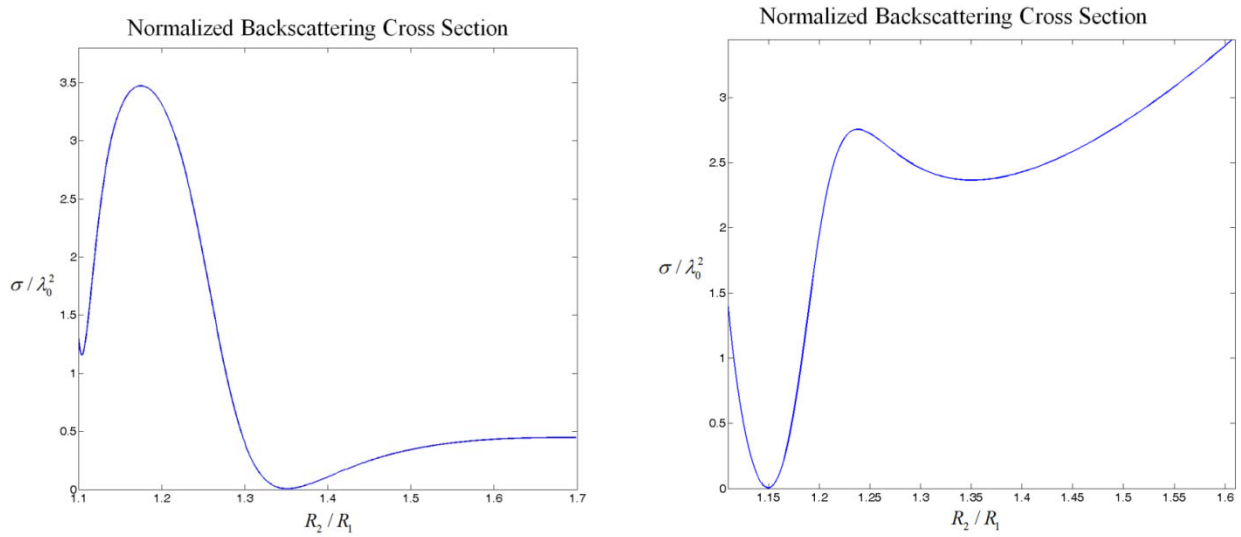


Figure 2: (a) Normalized σ for sphere with $\mathrm{R_1} = 7\lambda_0$, $\varepsilon = 10\varepsilon_0$ and $\mu = \mu_0$ coated with $\varepsilon_c = 0.001\varepsilon_0$, $\mu_c = 0.01\mu_0$
(b) Normalized σ for sphere with $\mathrm{R_1} = 10\lambda_0$, $\varepsilon = 10\varepsilon_0$ and $\mu = \mu_0$ coated with $\varepsilon_c = 0.01\varepsilon_0$, $\mu_c = 0.01\mu_0$

Next example which we consider is larger and much larger than wavelength i.e $\mathrm{R_1} = 10\lambda_0$, $\varepsilon = 10\varepsilon_0$ and $\mu = \mu_0$ coated with $\varepsilon_c = 0.01\varepsilon_0$ and $\mu_c = 0.01\mu_0$. Here we can say that the dimension of investigated sphere is much larger than wavelength and there is no doubt that $\mathrm{Q_s}$ is much larger than zero for any value of $\mathrm{R_2}$ while our defined coating make the σ zero when $\mathrm{R_2} = 1.15\ \mathrm{R_1}$. The nomalized σ is plotted in figure (3-b).

4. Effect of loss

In previous section, we assumed that both main sphere and coating are lossless. Now we consider the effect of

loss. This consideration is important because: first, loss in the term of conductivity is present in many materials in nature and second, we are using metamaterials as coating and so far loss is an inherent property of implemented metamaterials. Here we consider last example of previous section and compare the ideal coating with two coatings with same constitutive parameters plus adding loss in term of loss tangent. In figure 4, we plotted normalized σ for last structure with 3 different coatings, $\varepsilon_c = 0.01\varepsilon_0$,$\varepsilon_c = 0.01\varepsilon_0(1 + j0.05)$ and $\varepsilon_c = 0.01\varepsilon_0(1 + j0.1)$ while $\mu_c = 0.01\mu_0$ in 3 case. It can be seen from figure 4 when the effect of loss is not dominant (i.e less than 10%), coating's performance is not affected so much and transparency is available. It should be noticed that the optimum value of R_2 shifts downward, when loss increases.

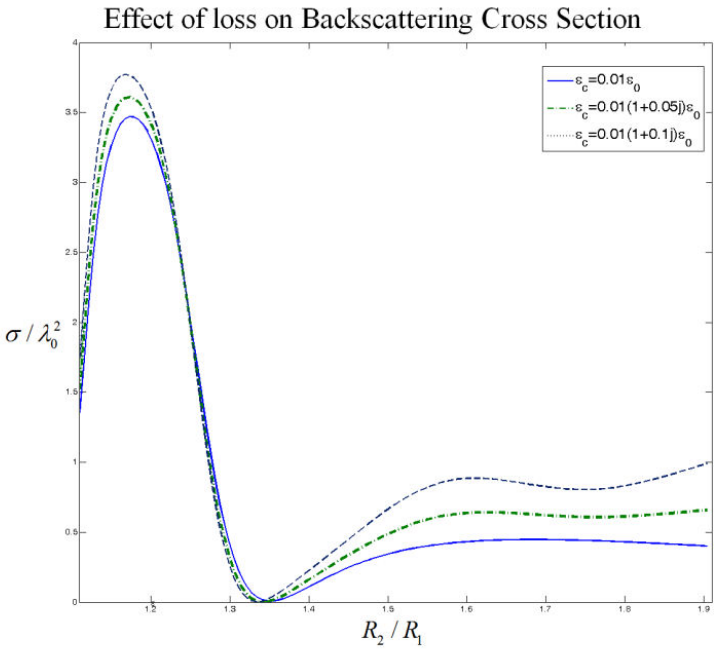


Figure 3: Normalized σ for a sphere with three different value of ε_c, one lossless coating and two lossy coatings

5. CONCLUSION

We investigated a hiding method for large spheres with homogenous isotropic coating with $0 \leq \varepsilon_r < 1$ and $0 \leq \mu_r < 1$ in front of a monostatic radar and showed that with this method, it is possible to make a drastic omit in backscattered fields, while it is impossible to reduce total scattering cross section for large spheres. We confirmed our claim by different examples. At last we showed that effect of adding loss to coating in negligible until it is limited to a reasonable value.

REFRENCES

1. A.Alù and N.Engheta, "*Polarizabilities and effective parameters for collections of spherical nano-particles formed by pairs of concentric double-negative (DNG), single-negative(SNG), and/or double-positive(DPS) metamaterial layers*," *Journal of Applied Physics*, Vol. 97, 094310 (12 pages), May 1, 2005.
2. A.Alù and N.Engheta, "*Achieving transparency with plasmonic and metamaterial coatings,*" *Physical Review E*, Vol. 72, 016623 (9 pages), July 26, 2005.
3. J.A.Stratton," *Electromagnetic Theory* ," McGraw - Hill, 1941.
4. J.B.Pendry, D.Shurig, and D.R.Smith, "*Controlling electromagnetic fields*," Science, Vol. 312, pp. 1780-1782, 2006.

Sub-wavelength transmission resonances in multilayer partially-reflecting surfaces

C. S. R. Kaipa[1], A. B. Yakovlev[1*], F. Medina[2], and F. Mesa[3]

[1]Department of Electrical Engineering, University of Mississippi, University, MS 38677, USA

[2]Department of Electronics and Electromagnetism, Faculty of Physics, University of Seville, 41012, Seville, Spain

[3]Department of Applied Physics I, ETS de Ingeniería Informática, University of Seville, 41012, Seville, Spain

yakovlev@olemiss.edu

Abstract- The microwave transmission through stacked perforated metal layers (2-D metal meshes) is modeled using simple circuit-like models. The most relevant parameters of the circuit are accurately determined, taking into account the effect of losses. The model is tested by proper comparison with previously obtained numerical and experimental results. The physical mechanisms of transmission resonances are clearly explained in terms of the behavior of a finite number of strongly coupled Fabry-Pérot resonators, whereas the approximate positions of the first and last transmission peaks in the pass-band are obtained from the analysis of infinitely-periodic coupled resonators.

1. INTRODUCTION

The electromagnetic propagation through multilayer metal-dielectric stacks in the visible region has been reported in [1], showing a series of bands of high transmissivity. The transmission through such stacks is several orders of magnitude more than that for a single layer. This is because the electromagnetic waves inside metals at optical frequencies exist in the form of evanescent waves, which provide the necessary coupling mechanism between successive dielectric layers (in the sense of Fabry-Pérot (FP) resonators), separated by one metal film. An equivalent study at microwave frequencies is impractical because the metals are characterized by their high conductivities. However, in [2] and [3] physical systems that exhibit the observed behavior of stacked metal-dielectric layers at optical frequencies, in the microwave regime have been recently reported. In these structures the metal films used in optical experiments are substituted by perforated metal layers (fishnet grids) acting as partially-reflecting surfaces (PRS). Our first goal here is to show how a circuit model, whose parameters can be analytically obtained, accounts for the experimental and numerical results reported in [2]. Moreover, apart from avoiding lengthy and cumbersome computations, circuit modeling provides additional physical insight and a methodology to design devices based on the physical phenomena described by the model. In addition, the same circuit approach is used to extract some general features of the transmission frequency bands based on the analysis of infinitely-periodic structures.

2. STACKED GRIDS

An example of a multilayer fishnet-type PRS analyzed in this paper is shown in Fig. 1(a). This is the same structure reported in [2] with the numerical and experimental results, which is formed by printing five copper fishnet grids on low-loss dielectric substrates and stacking them to produce an electrically thick block, whose transmission characteristics at microwave frequencies are the subject of the study. The copper meshes are of thickness t = 18 μm separated by low-loss dielectrics of thickness h = 6.35 mm. The measured relative permittivity of the dielectric material is $\varepsilon_r \approx 3$ $(2.96 \le \varepsilon_r \le 3.07)$ and its loss factor is $0.001 \le \tan\delta \le 0.0014$. The

unit cell of the fishnet grid is with period D = 5 mm and strip width w = 0.15 mm. When a y-polarized uniform transverse electromagnetic plane wave normally impinges on the structure, the fields are identical for each of the unit cell of the 2-D periodic system. Taking into consideration the symmetry of the unit cell and the polarization of the impinging electric field, a single cell such as the one shown in Fig. 1(b) has to be employed in the analysis. We have a number of uniform sections corresponding to the parallel-plate waveguide filled with the air and dielectric material separated by diaphragm discontinuities.

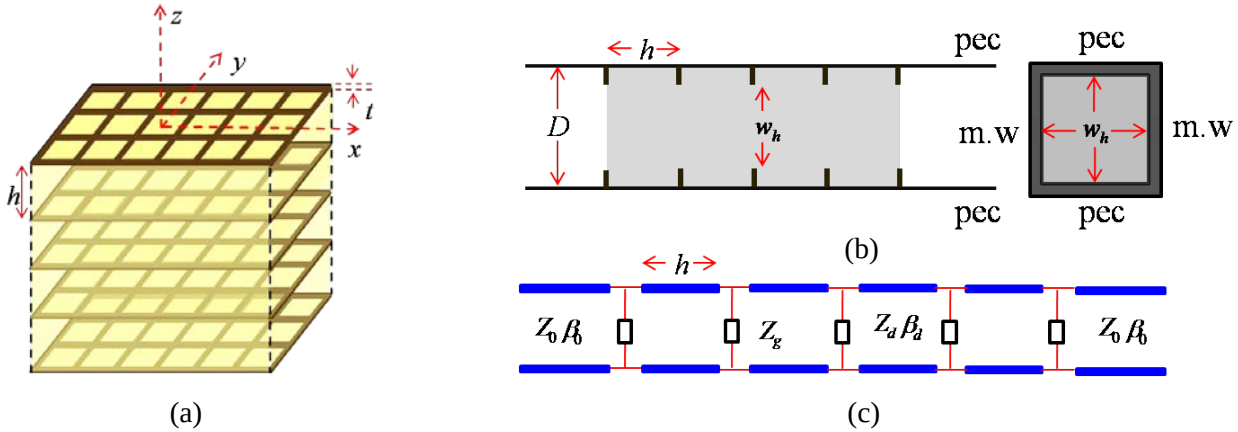


Fig. 1: (a) Five-layered fishnet-type PRS separated by dielectric slabs similar to the one used in [2]. (b) Transverse unit cell of the 2-D periodic structure corresponding to the analysis of normal incidence of a y-polarized uniform plane wave on the multilayer fishnet structure. Here, "pec" stands for a perfect electric conductor and "m.w" stands for a magnetic wall. (c) Equivalent circuit for the electrically small unit cell.

This is a typical waveguide problem with discontinuities, commonly considered in microwave engineering practices [4]. Since for the frequencies of interest a single transverse electromagnetic (TEM) mode propagates along the uniform waveguide sections, the circuit model describing the physical system in Fig. 1(b) is the one depicted in Fig. 1(c). This model is valid provided the attenuation factor of the first higher-order mode generated at the discontinuities is large enough to ensure that the interaction between successive discontinuities through higher-order modes is neglected. For the transmission line in Fig. 1(c) the propagation constants and characteristic impedances for both the air-filled and dielectric regions are known in the closed form [4]:

$$\beta_0 = \frac{\omega}{c}, \quad \beta_d = \beta_0\sqrt{\varepsilon_r\left(1 - j\tan\delta\right)} \tag{1}$$

$$Z_0 = \sqrt{\frac{\mu_0}{\varepsilon_0}}, \quad Z_d = \frac{Z_0}{\sqrt{\varepsilon_r\left(1 - j\tan\delta\right)}} \tag{2}$$

where c is the speed of light.

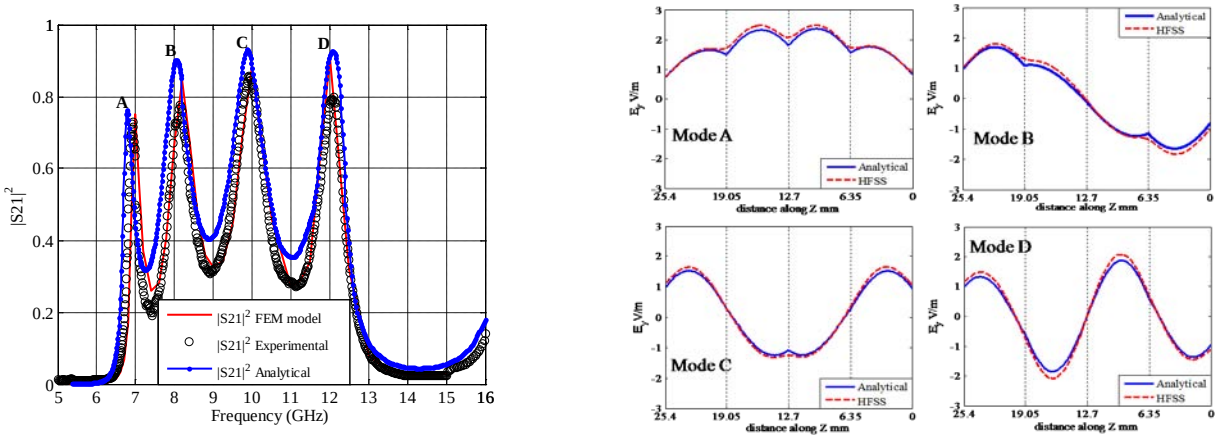
For the reactive loads Z_g in Fig. 1(c), there are no closed-form expressions available in engineering practice. However, for electrically small dimensions and period, accurate estimations based on dynamic solutions for some periodic structures are available in the literature. Following [5], the analytical expression for the inductive grid impedance can be obtained as follows:

$$Z_g = j\omega L_g, \quad L_g = \frac{\eta_0 D}{2\pi c}\ln\left[\csc\left(\frac{\pi w}{2D}\right)\right] \tag{3}$$

where ω is the angular frequency and η_0 is the free-space impedance. Ohmic losses can be taken into account by using the surface resistance of the metal, since the skin effect penetration depth, δ_s, is much smaller than the thickness of the metal strips. This resistance, series connected with the inductance in (3), is given by $R_g = D/\sigma\delta_s w$. Since the expressions for Z_g is not exact, the accuracy of the model has to be verified by experimental and/or numerical results.

3. RESULTS AND DISCUSSION

The results of the circuit model are compared with the numerical and experimental results reported in [2]. Fig. 2(a) demonstrates the transmissivity of the five-layered fishnet-type PRS with the experimental, numerical, and analytical results. There is a perfect agreement between the results, where our analytical model clearly predicts the bands, consisting of four transmission peaks (pass-band) followed by a deep rejection band (stop-band). The essential fact is that we have four FP cavities strongly coupled through the square holes of each grid, i.e., four transmission line sections separated by predominantly reactive impedances. The circuit model and HFSS results (used in [2]) of the field distributions (corresponding to transmission peaks) are demonstrated in Fig. 2(b), showing a good agreement. It can be observed how the field values near and over each of the three internal grids are meaningfully different for each of the considered resonance frequencies.

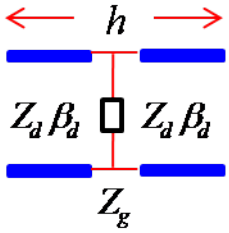


(a) (b)

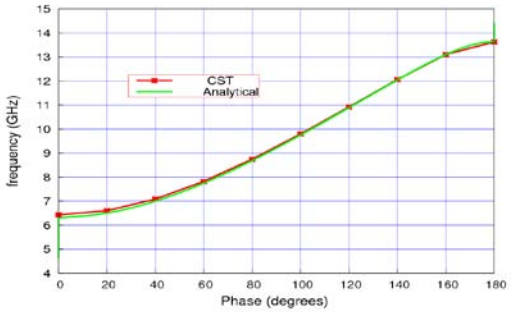
Fig. 2: (a) Sub-wavelength power transmission resonances of the five-layered fishnet-type PRS: comparison of analytical, experimental, and numerical (HFSS) results. Here, A, B, C, and D correspond to the transmission peaks in the increasing order. (b) Electric-field distribution corresponding to the transmission peaks in five-layered fishnet-type PRS: comparison of analytical and numerical (HFSS) results.

It should be noted that, in particular, the behavior of field distribution of the first and the last resonance peaks for any number of slabs has the same qualitative behavior shown for modes A and D. We can say that the phase shift from cell to cell (along the *z*-direction) is close to zero for the first mode and close to π for the last mode (with intermediate values for the other modes). It is observed that, when the number of identical layers is increased, the number of peaks also increases (indeed, there are as many peaks as slabs), and all the peaks lie within a characteristic frequency band whose limits are given by the electrical parameters and dimensions of the grid. However, with the increase in the number of layers, the resonance peaks corresponding to the first and last modes approach to the limiting values of 6.38 GHz and 13.65 GHz, respectively. In the limiting case of an

infinite number of unit cells, instead of resonances we should have a continuous transmission band, out of which the transmission is not possible. This kind of periodic structures can be analyzed using the microwave methods [6], and the dispersion equation of the infinite periodic structure can be easily obtained. The unit cell of the infinite periodic structure and the Brillouin diagram obtained by solving the dispersion equation for the first transmission band are shown in Fig. 3.



(a)



(b)

Fig. 3: (a) Unit cell of an infinite periodic structure under study. (b) Brillouin diagram for the first transmission band of the infinite periodic structure, showing an excellent agreement of circuit model and full-wave (CST) results.

5. CONCLUSION

The analysis of multilayer stacked grids (acting as PRS) separated by dielectric slabs can be analytically carried out with negligible computational effort making use of the simple circuit model. The main characteristics of the transmission bands (frequencies of the lower and upper resonances) are directly related to the behavior of infinite 1-D periodic structures. The transmission bands and band-gaps are accurately determined using the circuit model concepts and methods of microwave engineering.

ACKNOWLEDGEMENT

The authors are thankful to C. A. M. Butler, A. P. Hibbins, and J. R. Sambles of the Electromagnetic Materials group at the University of Exeter, UK, for providing numerical and experimental data.

REFERENCES

1. M. Scalora, M. J. Bloemer, A. S. Pethel, J. P. Dowling, C. M. Bowden, and A. S. Manka, "Transparent, metallo-dielectric, one-dimensional, photonic band-gap structures ," *J. Appl. Phys.*, Vol. 83, pp. 2377–2383, 1998.
2. C. A. M. Butler, J. Parsons, J. R. Sambles, A. P. Hibbins, and P. A. Hobson, "Microwave transmissivity of a metamaterial-dielectric stack," *Appl. Phys. Lett*, Vol. 95, 174101, 2009.
3. A. B. Yakovlev, C. S. R. Kaipa, Y. R. Padooru, F. Medina, and F. Mesa, "Dynamic and circuit theory models for the analysis of sub-wavelength transmission through patterned screens," in *3rd International Congress on Advanced Electromagnetic Materials in Microwaves and Optics*, London, UK, 30 Aug. – 4 Sept., 2009, pp. 671-673.
4. R. E. Collin, *Field Theory of Guided Waves*, IEEE Press, 1971.
5. O. Luukkonen, C. Simovski, G. Granet, G. Goussetis, D. Liobtchenko, A. V. Raisanen, and S. A. Tretyakov, "Simple and accurate analytical model of planar grids and high-impedance surfaces comprising metal strips or patches," *IEEE Trans. Antennas Propagat.*, Vol. 56, No. 6, pp. 1624-1632, 2008.
6. D. M. Pozar, *Microwave Engineering*, 3rd Edition, John Wiley & Sons, 2004.

PARAMETRIC STUDIES ON MODIFIED SPLIT RING RESONATOR (MSRR) AND CAPACITANCE LOADED STRIP (CLS) FOR LEFT HANDED METAMATERIAL

H. A. Majid[1], **and M. K. A. Rahim**[1]
[1]Faculty of Electrical Engineering, Universiti Teknologi Malaysia, 81310 Skudai, Johor, Malaysia
Huda_set@yahoo.com, mkamal@fke.utm.my

Abstract- This paper describes and analyzes a new structure of left-handed metamaterial (LHM) based on parametric studies. The combination of the modified square rectangular split ring (MSRR) and the capacitance loaded strip (CLS) was used to obtain LHM structure. The simulation and analysis was done using CST software. The parametric of the LHM structure was studied to see the effect of the frequency and the range of negative permeability (-μ) and the (-ε). The changes in the dimension of MSSR and CLS effect the S_{11} and S_{21} of the LHM structure. Whereby effect the value of permeability and the permittivity. The value of permeability and the permittivity was extracted from the reflection and transmission coefficient data. The studies proved that the LHM structure can be designed in the frequency range of interest.

1.0 INTRODUCTION

Left-Handed Metamaterial (LHM) is a material that exhibit negative permittivity and permeability in a certain frequency range [1]. This phenomenon can be characterized by the negative refraction index and backward wave. The backward wave propagation has been verified in [2] and the negative refraction has been proven in [3]. Many have proposed and published new structures that produce negative permittivity and permeability [4]. In this paper, the parametric study on LHM has been done to analyze the effect of resonant frequency and the value of ε_r and μ_r. The dimension of the LHM unit cell is shown in Figure 1.0. It consists of one MSRR between two pairs of CLSs in planar form. MSRR exhibits negative value of permeability while CLS exhibits negative value of permittivity. The width of gaps and lines, W_2 and G_1 is 0.5 mm, the gap between two CLSs is G_3 = 1mm, the width of CLS, W_1 = 1 mm and the inner SRR is L_3 = 7.1 mm. The height of the CLS inclusions, L_1 = 15.1 mm, the length of the full capacitance strips is L_4 = 13.1 mm, and the length of the half strips is L_5 = 6.55 mm. The length of the outer MSRR, L_2 and the gap between SRR and CLS, G_2 are varied. The dielectric constant of the substrate is 4.7 with a thickness of 1.6 mm and a tangential loss of 0.019.

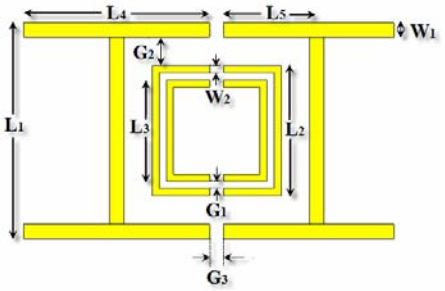


Figure 1.0: The dimension of the LHM structure

2.0 BOUNDARY CONDITION FOR THE SIMULATION SETUP

The simulation of LHM has been done using Computer Simulation Technology (CST) software. Perfect magnetic conductor (PMC) boundary condition is set on the front and back faces of the block in z-axis and perfect electric conductor (PEC) boundary condition is set on the top and bottom of the block in the y-axis. The E-field of the incident wave is polarized along y-axis while the H-field of the incident wave is polarized along z-axis and the wave propagate in x direction. Figure 2.0 illustrates the simulated structure.

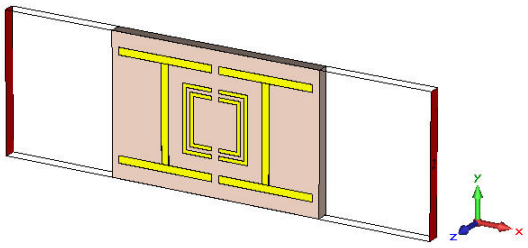


Figure 2.0: Boundary condition for simulation setup

Through this configuration, the S-Parameters (S_{11} and S_{21}) data are collected and exported to MathCAD for the calculation of the LHM region using the modified NRW Approach [5]. Two parameters of the unit cell (L_2 and G_2) are varied in order to study the influence in the determination of the resonant frequency and the value of ε_r and μ_r.

3.0 PARAMETRIC STUDIES & ANALYSIS OF THE DEPENDENCE BETWEEN RESONANT FREQUENCY & PARAMETERS OF LHM UNIT

3.1 Varying the Gap between the MSRR and the CLS, (G_2)

In this case, the gap between the MSRR and the CLS, G_2 is varied to observe the effect of the resonant frequency, permittivity and permeability. The dimension of the MSRR is fixed as an initial structure shown in Figure 1.0. The results are plotted and shown in Figure 3.0 and Table 3.0.

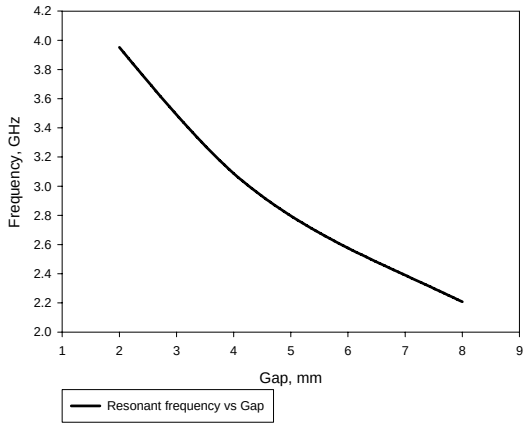


Figure 3.0: Correlation between gap, G_2 and resonant frequency

Table 3.0: Correlation between frequency range of negative permittivity, ε_r and negative permeability, μ_r with gap, G_2

Gap (G_2)	Frequency range of negative permittivity & permeability (GHz)
2mm	4.0 - 4.224
4mm	3.104 - 3.264
6mm	2.592 - 2.736
8mm	2.224 - 2.336

Table 3.1: Correlation between gap, G_2 and length, L_1

Gap (G_2)	CLS inclusion length (L_1)
2 mm	15.1 mm
4 mm	19.1 mm
6 mm	23.1 mm
8 mm	27.1 mm

Table 3.2: Correlation between gap, G_2 and length, L_4

Gap (G_2)	CLS strip length (L_4)
2 mm	13.1 mm
4 mm	17.1 mm
6 mm	21.1 mm
8 mm	25.1 mm

Referring to Figure 3.0, the resonant frequency is shifted by varying the gap, G_2. When the gap, G_2 increase, the resonant frequency becomes lower while the range of negative ε_r and negative μ_r is shifted to the lower region as shown in Table 3.0. Note that, by varying the gap between the SRR and CLS, G_2 the CLS inclusion, L_1 and CLS length, L_4 also varies. Table 3.1 shows the correlation between the gap, G_2 and CLS inclusion, L_1. Meanwhile, Table 3.2 shows the correlation between the gap, G_2 and the CLS length, L_4.

3.2 Varying the Length of outer MSRR, (L_2)

In this simulation, the length of the outer MSRR, L_2 is varied to observe the effect of resonant frequency, permittivity and permeability. As the L_2 varied, other parameters such L_1, L_3 and L_4 are altered as those parameters are related to L_2.

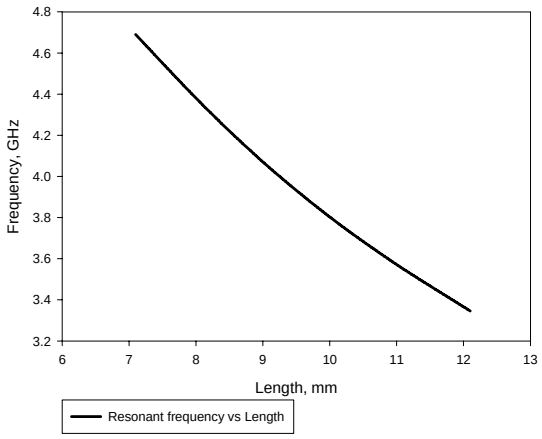


Figure 3.1: Correlation between length, L_2 and resonant frequency

Table 3.3: Correlation between frequency range of negative permittivity, ε_r and negative permeability, μ_r with length, L_2

MSRR outer length (L_2)	Frequency range of negative permittivity & permeability (GHz)
7.1 mm	4.762 - 4.936
8.1 mm	4.426 - 4.552
9.1 mm	4.084 - 4.264
10.1 mm	3.808 - 4.036
11.1 mm	3.568 - 3.808
12.1 mm	3.358 - 3.736

Figure 3.1 shows the correlation between L_2 and the resonant frequency. As the length of the outer MSRR increase, the resonant frequency goes to the lower region. Consequently, the range of negative ε_r and μ_r also goes to the lower frequency region as the value of L_2 increases as shown in Table 3.3. As a result on varying the value of L_2, other parameters are also altered. Table 3.4 shows the correlation between the MSRR outer length, L_2 with the MSRR inner length, L_3. Table 3.5 shows the correlation between MSRR outer length, L_2 with the CLS inclusion length, L_1. While, Table 3.6 shows the relationship between the MSRR outer length, L_2 with the CLS strip length, L_4. As can be seen from these three tables, the value of L_3, L_1 and L_4 increases as the MSRR outer length, L_2 increase. This shows that increasing the size of the structure will make the resonant frequency and the

range of negative ε_r and μ_r shift to the lower region.

Table 3.4: Correlation between length, L_2 and L_3

MSRR outer length (L_2)	MSRR inner length (L_3)
7.1 mm	5.1 mm
8.1 mm	6.1 mm
9.1 mm	7.1 mm
10.1 mm	8.1 mm
11.1 mm	9.1 mm
12.1 mm	10.1 mm

Table 3.5: Correlation between length, L_2 and L_1

MSRR outer length (L_2)	CLS inclusion length (L_1)
7.1 mm	13.1 mm
8.1 mm	14.1 mm
9.1 mm	15.1 mm
10.1 mm	16.1 mm
11.1 mm	17.1 mm
12.1 mm	18.1 mm

Table 3.6: Correlation between length, L_2 and L_4

MSRR outer length (L_2)	CLS strip length (L_4)
7.1 mm	11.1 mm
8.1 mm	12.1 mm
9.1 mm	13.1 mm
10.1 mm	14.1 mm
11.1 mm	15.1 mm
12.1 mm	16.1 mm

4.0 CONCLUSIONS

From observation, there are parameters that have strong influence to the resonant. In conclusion, the parameters of G_2 and L_2 have strong influence in the resonant frequency and the frequency range of the negative value of ε_r and μ_r. The parameters of G_2 and L_2 plays important roles as they denotes the C and L values that determine the operating frequencies of the structures. If a large change in the resonant frequency needed, those three parameters should be varied accordingly. Further works are needed to observe other parameters of LHM of their influence toward the resonant frequency, permittivity and permeability. It is predicted that other parameters would also produce similar results as G_2 and L_2.

ACKNOWLEDGEMENT

The authors wish to thank the Ministry of High Education (MOHE) for supporting the research work, Research Management Centre (RMC) and Radio Communication Engineering Department (RACeD), Universiti Teknologi Malaysia (UTM) for the support of the paper in META 2010.

REFERENCES

1. Christophe Caloz and Tatsuo Itoh, Electromagnetic Metamaterials Transmission Line Theory and Microwave Applications, John Wiley & Sons, Inc. 2006.
2. Jorge Carbonell, Luis J. Rogla, Vicente E. Boria, Didier Lippens, Design and Experimental Verification of Backward-Wave Propagation in Periodic Waveguide Structures, *IEEE Transactions on Microwave Theory and Techniques*. Vol. 54, No. 4, 4 April 2006.
3. A. Aydin, G. Kaan and O Ekmel, "Two-Dimensional Left-handed Metamterial with a Negative Refractive Index", *Journal of Physics.* Conference Series 36, 2006.
4. B.-I. Wu, W. Wang, J. Pacheco, X. Chen, T. Grzegorczyk and J. A. Kong, A Study of Using Metamaterials as Antenna Substrate to Enhance Gain, *Progress In Electromagnetics Research*, PIER 51, 295-328, 2005.
5. Richard W. Ziolkowski, Design, Fabrication, and Testing of Double Negative Metamaterials, *IEEE Transactions on Antennas and Wireless Propagation,* Vol. 51, No. 7, 2003.

Plasmonic Crystal Waveguides

Slobodan M.Vuković[1], Zoran Jakšić[2], Ilya V. Shadrivov[3] and Yuri S. Kivshar[3]
[1] Institute of Physics, University of Belgrade, 11080 Zemun, Serbia
[2] Institute of Chemistry, Technology and Metallurgy, University of Belgrade, Serbia
[3] Nonlinear Physics Centre, Research School of Physics and Engineering,
The Australian National University, Canberra, Australia
svukovic@ ipb.ac.rs

Abstract- We study the properties of electromagnetic waves propagating along the waveguides with a periodic core created by alternating metal and dielectric layers, the so-called quasi-one-dimensional plasmonic crystal waveguides. Such waveguides can be symmetric or asymmetric depending on the cladding or substrate material properties, as well as on the termination of the periodic structure. We analyze the dispersion characteristics as well as the profiles of the guided modes for several types of the waveguide structures.

1. INTRODUCTION

The increasing development of nanofabrication technologies enabled a qualitatively new step in the exploitation of plasmonic properties of metal-dielectric nanocomposites for new ultra-compact photonic devices. In order to overcome the diffraction limit that prevents confinement and manipulation of light on the scales smaller than a half of the wavelength, various promising designs have been proposed such as hyperlenses [1, 2], hypergratings [3], and planar lenses based on nanoscale slit arrays in metallic films [4, 5]. A possible path toward guiding below diffraction limit is to use the anisotropic metamaterials, such as subwavelength plasmonic crystals (SPC), which ensure ultra-compact dimensions and optical operating frequencies and at the same time enable proper waveguiding through efficient elimination of parasitic conversion of surface plasmon polaritons into free-space modes [6]. A general SPC may have any of various 1D, 2D or 3D geometries, similar to those of photonic crystal guides, and may contain various metal inclusions, e.g. different nanoparticles, nanorods or ultrathin slabs.

In fact, SPC represents a periodic nanostructured (super)lattice with alternating metal and dielectric parts. Optical properties of such a planar structure are strongly anisotropic, and similar to uniaxial crystal that supports various types of surface and guided modes [7], and creates plasmonic bandgaps. The relative dielectric permittivity of its metal parts should be below zero in the operating frequency range.

Potential application fields for devices based on SPC guides are enormously wide and include among others optical telecommunications, sensors (where plasmonics is already widely applied for chemical/biological sensing), energy harvesting, biomedicine, etc. Maybe the most important envisioned role of plasmon-based subwavelength structures and devices is to serve as a link between electronics and photonics [8, 9] enabling a continuation of Moore's law in micro/nanoelectronics at optical frequencies.

The easiest SPC geometry to fabricate is a 1D planar multilayer with alternating metal-dielectric strata having a nanometric thickness (the so-called quasi-one-dimensional SPC). This is the simplest and the oldest plasmonic crystal structure, yet it offers a wealth of effects. Depending on the geometry and the dimensions, as well as on the type of terminating strata, such multilayer guides may be symmetric, antisymmetric or asymmetric [10, 11].

In this paper we study, both theoretically and numerically, propagation of electromagnetic waves along the

planar waveguides with anisotropic plasmonic crystal core designed with symmetric or asymmetric metal or dielectric claddings. The plasmonic crystal core with binary metal-dielectric unit cell is placed inside the waveguide with the main optical axis either along or normal to the core-cladding interfaces. We obtain the conditions for the existence of TM- and TE-polarized modes, which may appear both above and below the light line.

2. FORMULATION OF THE PROBLEM

We consider an electromagnetic wave propagation through a planar SPC waveguide as shown in Fig. 1; $\vec{k}$ denotes the wave vector and $\vec{q}$ is the Bloch vector. The unit cell is binary, consisting of a metal and a dielectric layer with a total thickness *L*. Each stratum is described by its relative dielectric permittivity, metal with a Drude-type $\varepsilon_m(\omega)$ and dielectric with a dispersionless ε_d, and thickness d_m and d_d, respectively. The multilayer is sandwiched between thick claddings. In this paper we assume that the cladding material is identical to one of the unit cell constituents. A generalization to other cladding materials is straightforward. The structure represents a waveguide with an SPC core supporting propagation of both in-plane waves (along the wave vector $\vec{k}$ in the x-y plane) and perpendicular ones (along the Bloch vector $\vec{q}$ in z-direction).

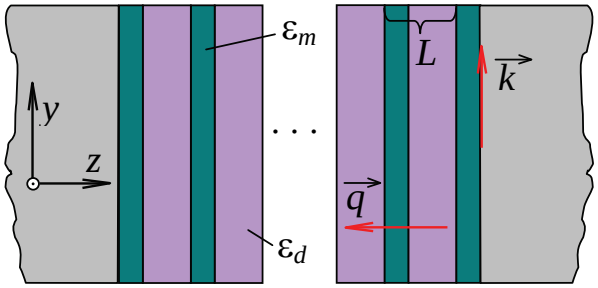


Fig. 1. Geometry of a planar multilayer subwavelength plasmonic crystal. Outer gray areas denote cladding which is identical to either metal or dielectric part of the unit cell.

For a multilayer with an infinite number of strata Floquet-Bloch dispersion relating frequency ω with $\vec{k}$ and $\vec{q}$ is valid: $\cos(qL)=\cos(k_m d_m)\cos(k_d d_d)-(1+\alpha_{s,p}^2)\sin(k_m d_m)\sin(k_d d_d)/2\alpha_{s,p}^2$. Here $\alpha_s = k_d/k_m$, $\alpha_p = k_d\varepsilon_m/k_m\varepsilon_d$ for s and p polarization, respectively and $k_{m,d}=(\varepsilon_{m,d}-k^2)^{1/2}$. All spatial dimensions are normalized to c/ω and wave numbers to ω/c; c is the speed of light in vacuum. In the uniaxial crystal approximation which implies layers with subwavelength thickness $k_m d_m << 1, k_d d_d << 1$ Floquet-Bloch dispersion relation, derived without any limitations regarding the value of *qL*, can be written as [7]

$$(1/\varepsilon_s)\sin^2(qL/2)+(1/\varepsilon_{s,p})k^2(L/2)^2=(L/2)^2, \qquad (1)$$

where $\varepsilon_s=(1-\delta)\varepsilon_d+\delta\varepsilon_m$, $\varepsilon_p=\varepsilon_m\varepsilon_d[\delta\varepsilon_d+(1-\delta)\varepsilon_m]$ and the fill factor is defined as $\delta = d_m/L$.

In the case of a finite superlattice consisting of *N* unit cells using the transfer matrix method [12] we obtain the dispersion relation valid for symmetric waveguides with the cladding made of one of the core constituents

$$(1/2)(T_{11}-T_{22})(\sin NqL)(\sin qL)+\cos NqL=0 \qquad (2)$$

where T_{11} and T_{22} are the diagonal elements of the transfer matrix [12].

3. RESULTS

Upon elimination of the Bloch vector from (2) by replacing it directly from Floquet-Bloch dispersion rather than from (1) we calculated frequency ω versus the wave number *k*. It should be stressed here that the elimination of the in-plane wave vector can be also done in analog manner, using (1), thus obtaining frequency versus the Bloch wave number *q*. In Figs. 2 and 3 we show normalized frequency ω/ω_p versus normalized in-plane wave vector k/k_p, where ω_p is the plasma frequency, and $k_p=c/\omega_p$. Fig. 2 shows the dependence for a metallic waveguide with a planar SPC core incorporating 7 dielectric layers, $\varepsilon_d=1$. It can be seen that there is one TE-band within the light cone and two bands for TM-polarized radiation in the frequency range where $\varepsilon_m<0$. There are exactly 7 solutions located within each of the p-bands. The upper curve of the lower band and the lowest curve of the upper band cross band edges and enter into the gap. These two, represented by red lines, coalesce later on and coincide with the standard surface plasmon dispersion curve (black curve).

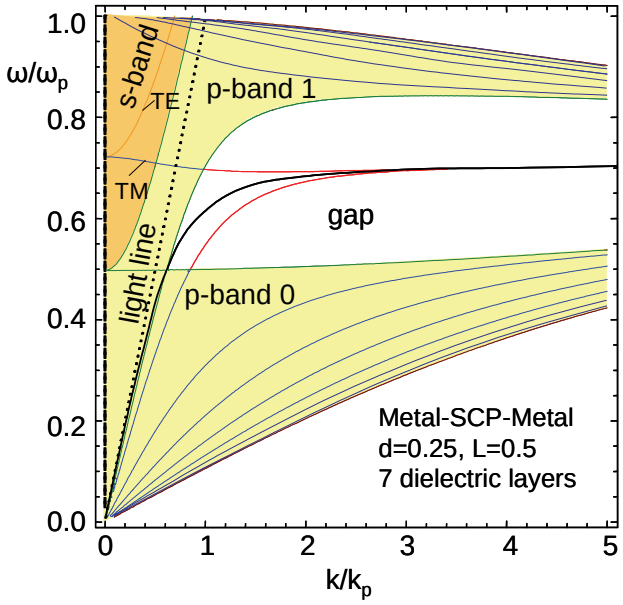


Fig. 2. Dispersion of guided modes for *N*=7, Drude metal on both sides of the multilayer SPC guide.

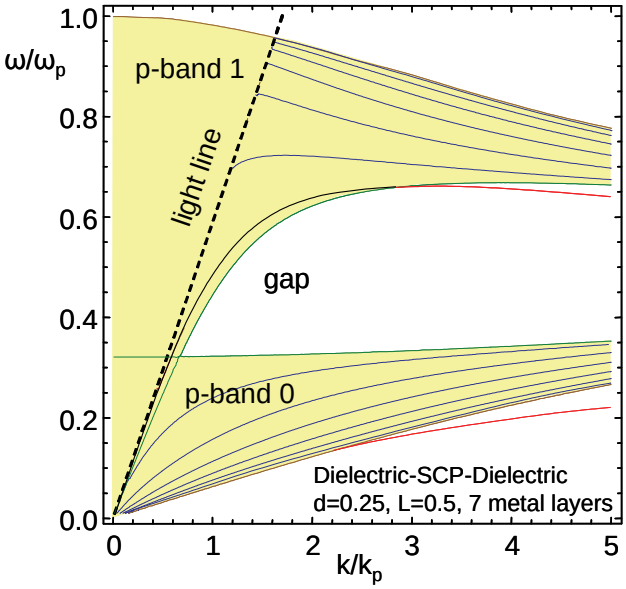


Fig. 3. Dispersion of guided modes for *N*=3, dielectric ε=10 on both sides of the multilayer SPC guide.

The bottom curve of the upper p-band starting from the light cone crosses the light line and enters the gap, all the while possessing a negative group velocity. It means that this backward wave can be directly excited by the propagating modes from the outside.

Only a single TE line can be seen in Fig 2, shown within the light cone, with the origin at the same point as the lowest curve of the upper p-band. Other 6 curves are not shown, since they are very close to $\omega/\omega_p=1$. All 7 branches in the s-band are forward waves, and the same is true for the lower p-band.

Fig. 3 shows the dispersion for a waveguide with a planar SPC core incorporating 7 metal layers and with a dielectric cladding $\varepsilon_d=2.89$ (silica). In this configuration TE modes are not supported. There are two TM bands, each with 7 branches. The lowest branches from each band cross the band edge and enter the gap.

4. CONCLUSIONS

We calculated the dispersion properties of planar multilayer SPC structures to assess their applicability for plasmonic waveguides. The anisotropic nature of these structures offers a wealth of effects, among those being the appearance of modes with negative group velocity (left-handed) for some TM modes, as well as those with zero group velocity. These are dependent on the size and structure of the unit cell, as well as on the degree of core anisotropy. The choice of the cladding for the SPC waveguides enables in some situations direct coupling of plasmons with the propagating modes.

ACKNOWLEDGEMENT

This work was partially funded by the Serbian Ministry of Science and Technology within the projects TR-11027 and OI-141031.

REFERENCES

1. Liu, Z., Lee, H., Xiong, Y., Sun, C., and Zhang, X., "Far-field optical hyperlens magnifying sub-diffraction-limited objects," *Science,* vol. 315, no. 5819, pp. 1686, 2007.
2. Xiong, Y., Liu, Z., and Zhang, X., "Projecting deep-subwavelength patterns from diffraction-limited masks using metal-dielectric multilayers," *Appl. Phys. Lett.,* vol. 93, no. 11, 2008.
3. Thongrattanasiri, S., and Podolskiy, V. A., "Hypergratings: Nanophotonics in planar anisotropic metamaterials," *Opt. Lett.,* vol. 34, no. 7, pp. 890-892, 2009.
4. Catrysse, P. B., Veronis, G., Shin, H., Shen, J. T., and Fan, S., "Guided modes supported by plasmonic films with a periodic arrangement of subwavelength slits," *Appl. Phys. Lett.,* vol. 88, no. 3, pp. 1-3, 2006.
5. Verslegers, L., Catrysse, P. B., Yu, Z., White, J. S., Barnard, E. S., Brongersma, M. L., and Fan, S., "Planar lenses based on nanoscale slit arrays in a metallic film," *Nano Lett.,* vol. 9, no. 1, pp. 235-238, 2009.
6. Elser, J., and Podolskiy, V. A., "Scattering-free plasmonic optics with anisotropic metamaterials," *Phys. Rev. Lett.,* vol. 100, no. 6, 2008.
7. Vukovic, S. M., Shadrivov, I. V., and Kivshar, Y. S., "Surface Bloch waves in metamaterial and metal-dielectric superlattices," *Appl. Phys. Lett.,* vol. 95, no. 4, 2009.
8. Ozbay, E., "Plasmonics: Merging Photonics and Electronics at Nanoscale Dimensions," *Science,* vol. 311, no. 5758, pp. 189-193, 2006.
9. Alù, A., and Engheta, N., "All optical metamaterial circuit board at the nanoscale," *Phys. Rev. Lett.,* vol. 103, no. 14, pp. 143902:1-4, 2009.
10. Jakšić, Z., Maksimović, M., and Sarajlić, M., "Silver-silica transparent metal structures as bandpass filters for the ultraviolet range," *J. Opt. A-Pure Appl. Opt.,* vol. 7, no. 1, pp. 51-55, 2005.
11. Feng, S., Elson, J., and Overfelt, P., "Optical properties of multilayer metal-dielectric nanofilms with all-evanescent modes," *Opt. Express,* vol. 13, no. 11, pp. 4113-4124, 2005.
12. Yeh, P., Yariv, A., and Hong, C.-S., "Electromagnetic propagation in periodic stratified media. I. General theory," *J. Opt. Soc. Am.,* vol. 67, no. 4, pp. 423-438, 1977.

Performance improvement of inverted L antenna with metamaterials

A. H. Amin Beidokhti , P. Rezaei

Semnan University, Electrical Engineering and Computer Faculty, Iran

ah_amin_b@yahoo.com, P_rezaei@itrc.ac.ir

Abstract- In this paper, a method for improving characterizations of antennas, especially in order to increase their gain and band width, is presented. This method is using metamaterial in electromagnetic perfomances. At first, an initial Inverted L Antenna (ILA) is designed and its radiation properties is took into consideration. Then by adding ground plane and metamaterial, changes in antenna's band width, radiation beam and gain is observed. The purpose of these designs and simulations is getting to the desirable effects of metamaterials on ILA radiation beam. NEC software, that its performance is based on numerical moment method, is used for simulating ILA, ground plane and metamaterial.

1. INTRODUCTION

The Inverted L Antenna (ILA) has the most similar performances to Infinite Length Antenna. Length of this antenna is designed in a way that can be equal to several full periods of wave signal or less than a signal wave length. ILA is often in AM receivers. The intensity of received signal increases as the length of ILA becomes longer. As its length becomes closer to half of signal wave length, received signal intensifies. So, in long and medium wave bands,length of ILA is a fraction of signal wave length. On the other side, length of such antenna could be equal to several full cycles of short wave band signals.

A method for improving characterizations of antennas, especially in order to increase their gain and band width, is using metamaterial. Metamaterials can make desirable effects on Electromagnetical and Optical performances [1].

Metamaterial is made by using some small wires or several metal rings and similar things. In these structures, ε, μ are negative, therefore their refraction index is negagative, too. This negative refraction index leads to a extraordinary capability to bend electromagnetic waves in a direction different from materials with positive refraction index [2, 3].

In customary ILA, length of antenna is equal to several signal wave length. Thus, some parts of signal's energy get to the end of antenna. If this terminal of antenna be as a open circuit, there will be a discontinuity in signal's way. Therefore the wave which is going to the end of antenna is reflected after contacting to this discontinuity and returns to signal's source. The reflected signal produces electromagnetic fields in contradiction with source signal and eliminates some parts of antenna's signal. Thus antenna's gain decreases.

Connecting the end of antenna to a resistance equal to antenna's characteristic impedance is a way to increase efficiency. In this way, the whole energy of signal is transferred to the end of antenna and is absorbed by its terminal resistance. Therefore a reflected wave, which leads to eliminate antenna wave signal, is not produced.

The antenna efficiency decreases, as its length becomes shorter. Even a small wire could be used as a transmitter or receiver antenna. Hence, if a small wire connects to antenna, it affects the intensity of transmitting or receiving signal. Of course, in this case the efficiency would be low but because of high sensibility of modern receivers, it is possible to receive the signals.

2. Simulation of ILA by using NEC software

In order to observe the performance of ILA and to improve its radiation properties, at first, an initial ILA is designed and its radiation properties is took into consideration. Then by adding ground plane, changes in antenna's band width, radiation beam and gain is observed. Finally, metamaterial is put under ILA and over the ground plane and its effects in improving performance of ILA is observed [4, 5].

2. 1. Design and simulation of initial ILA

An ILA with lengths of 28 and 19 cm and a radius of 1 cm is considered. As below figures show, this initial ILA has unsuitable radiation properties.

The studied frequency in this ILA is 300 MHz. The results from 280 to 320 MHz is shown below:

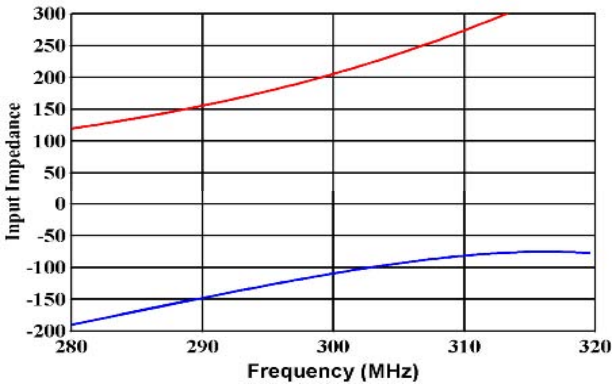


Fig. 1. Input impedance versus frequency for initial ILA

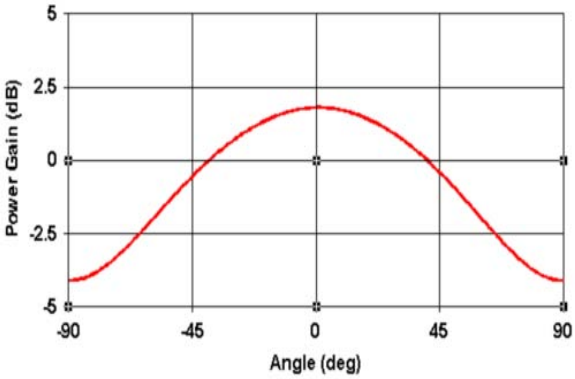


Fig. 3. Power gain versus frequency for initial ILA

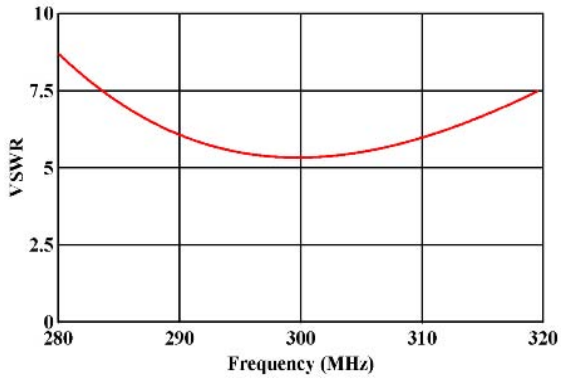


Fig. 2. VSWR versus frequency for initial ILA

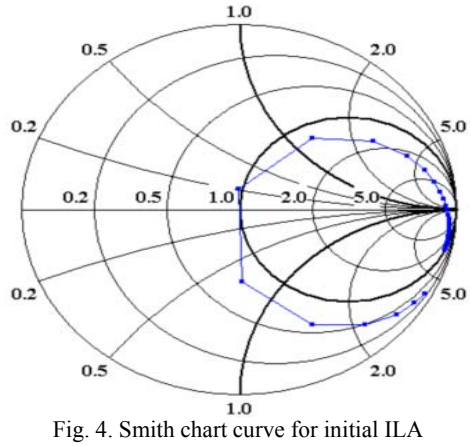


Fig. 4. Smith chart curve for initial ILA

Considering to above result, it is concluded that initial ILA has unsuitable radiation properties, its band width is zero, the radiation gain is 2 dB and the input impedance is not appropriate.
In the next step, it is tried to improve initial ILA properties by using ground plane under ILA.

2. 2. Simulation of ILA on the ground plane

In this step, ground plane is put under ILA.
As Fig. 5 shows, for achieving the highest band width, distance between antenna and ground plane is limited to 70 - 100 mm.
In this paper, the distance between ILA and ground plane is set 74 mm. The results from 280 to 320 MHz is observed in below figures.

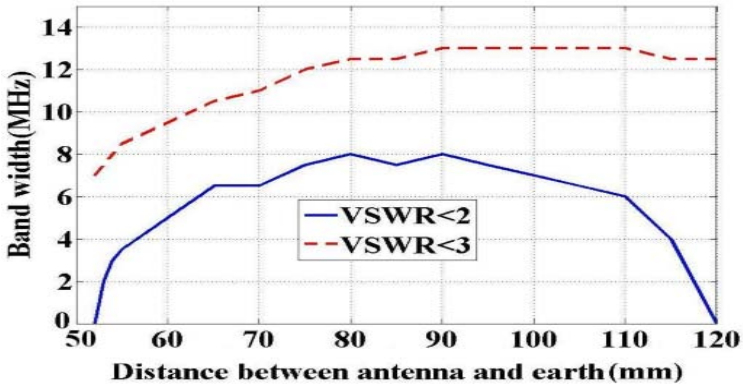


Fig. 5. Band width versus distance between ILA and ground

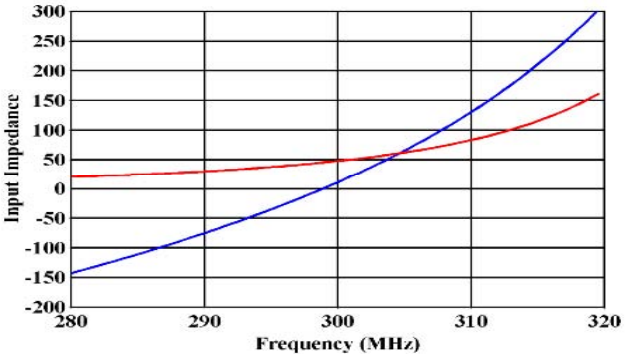


Fig. 6. Input impedance versus frequency for ILA on the ground plane

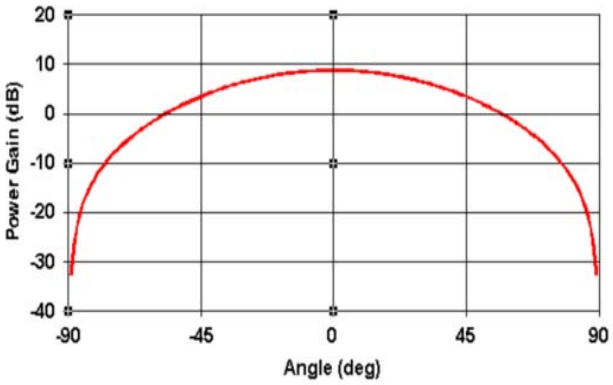


Fig. 8. Power gain versus frequency for ILA on the ground plane

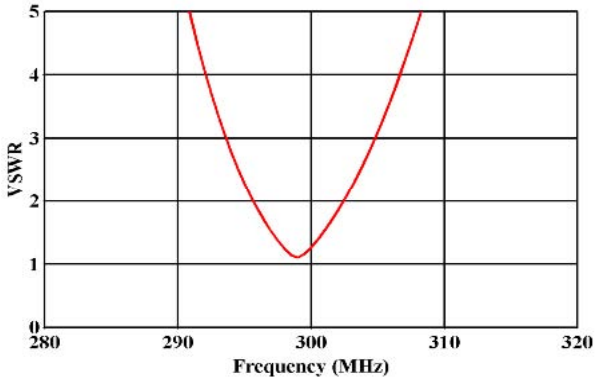
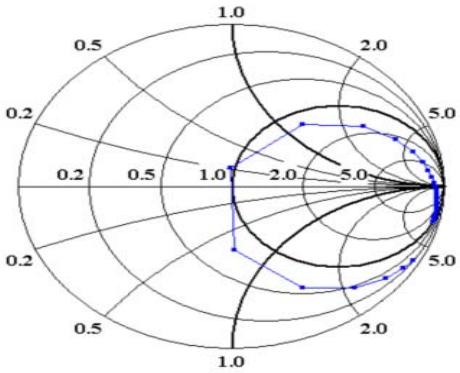


Fig. 7. VSWR versus frequency for ILA on the ground plan


Fig. 9. Smith chart curve for ILA on the ground plane

Regarding to above figures, it is obtained that by putting ground plane in a suitable situation under ILA, radiation gain, VSWR and band width are significantly improved. VSWR amount in 300 MHz improves from 5.3 to 1.2, impedance band width becomes 7 MHz and radiation gain is 8.7 dB.
In the next step, it is tried to improve the radiation gain and impedance band width again by putting metamaterial under ILA.

2. 3. Design and simulation of ILA by using ground plane and ILA

Metamaterial ,that consists of two orthogonal arrays of wires, is put under the antenna. Each of arrays consists of 10 thin wires that length of each of wires is 30 cm and the radius is 1 mm. The space between wires is 5 cm. Distance between metamaterial and ground plane is 5 mm. So distance between metamaterial and ILA becomes 6.9 cm. The results from 280 to 320 MHz is shown in below figures:

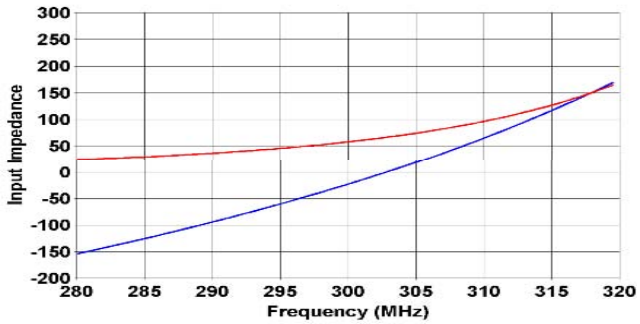


Fig. 10. Input impedance versus frequency for ILA on the ground plane and metamaterial

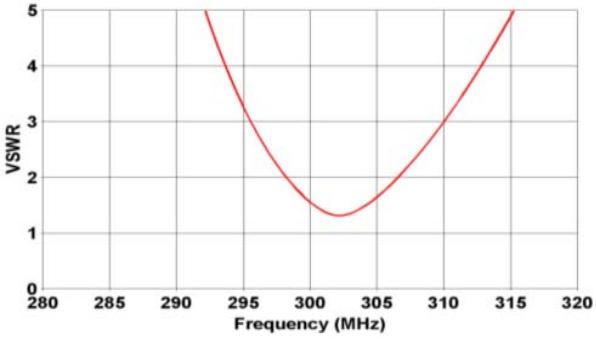


Fig. 11. VSWR versus frequency for ILA on the ground plane and metamaterial

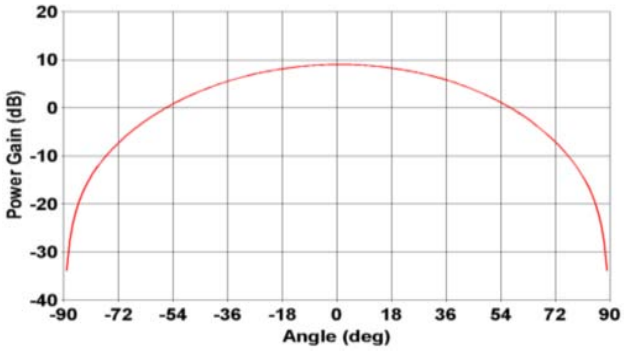


Fig. 12. Power gain versus frequency for ILA on the ground plane and metamaterial

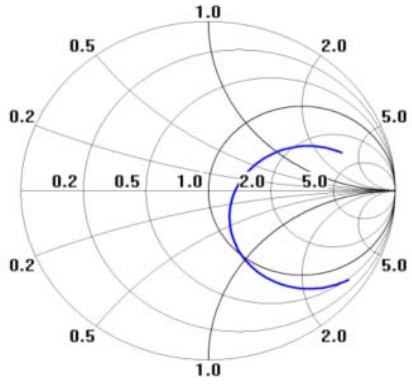


Fig. 13. Smith chart curve for ILA on the ground plane and metamaterial

Considering to above results, it is obtained that by using metamaterial, impedance band width improves to 9 MHz and radiation gain becomes 9 dB. So, the effects of using metamateril for improving ILA radiation properties is observed.

3. CONCLUSIONS

Regarding to low impedance band width of initial ILA, metamaterial is used for improving its radiation properties. Fig. 1 and Table 1 show that by putting ground plane under ILA, radiation gain, VSWR and band width are significantly improved. Metamaterial ,that consists of two orthogonal arrays of wires, is put under the antenna.

Fig. 14 and Table 1 show that by using metamaterial, ILA band width increases 28.5% and also its radiation gain improves.

Table 1. Comparison between the results of various simulated structures

Gain (dB)	Band Width (MHz)	Antenna structure
2	0	Primary ILA
8.7	7	ILA on the ground plane
9	9	ILA on the ground plane and metamaterial

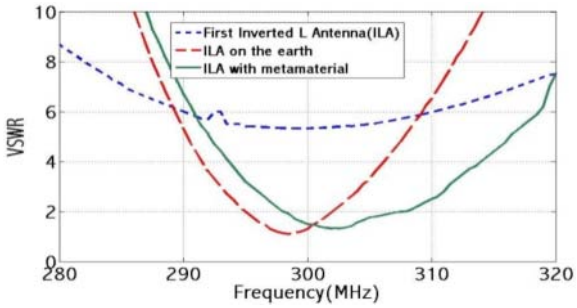


Fig. 14. VSWR versus frequency for various structures

Several other metamaterials with different structures is also examined but the results are not suitable. The research on other metamaterial structures for improving the results is in review.

ACKNOWLEDGEMENT

This work was supported by the Semnan University.

REFERENCES

1. Feurer and Thomas, "A tutorial on metamaterials and THz thechnology", institute of applied physics, 2007.
2. Ramakrishna, S. Anantha, Grzegorczyk and Tomasz M," Physics and applications of negative refractive index materials" , Spie press, Washington USA, Bellingham, 2009.
3. K Sarychev, Andrey, M Shalaev and Vladimir, "Electrodynamics of metamaterials", world scientific, 2007.
4. M.Hosseini , "Design of a non-uniform high impedance surface for a low profile antenna", j. of Electromagn. Waves and Appl, Vol. 20, No. 11, 1455–1465, 2006.
5. V.Wang, G.Pacheco, X.Chen, J.A.Kong, "A study of using metamaterial as antenna substrate to enhance gain", Massachusetts Institute of Technology, MIT, 2005.

Thin-film sensing using circular split-ring resonators at mm-wave frequencies

A. Elhawil, J. Stiens, C. D. Tandt, W. Ranson, R. Vounckx

Department of Electronics and Informatics (ETRO), Laboratory for micro- and photonelectronics (LAMI), Vrije Universiteit Brussels (VUB), Pleinlaan 2, B-1050 Brussels, Belgium
Aelhawil@etro.vub.ac.be

Abstract— In this paper, we investigate a thin-film sensing approach using split ring resonators. The sensitivity based on tuned magnetic resonance has been demonstrated using three methods: by depositing the film in the gap, under the rings as an intermediate layer and on the rings as an overlayer. The numerical simulations and experimental results are presented. In addition, the advantages and the limitations of each approach are discussed. Moreover, the sensitivity of the circular rings are compared with that of the square rings.

1. INTRODUCTION

In recent years, thin-film sensing using metamaterials has been of great interest to scientists. This mainly due to the wide range of applications that require detecting and characterising the chemical, biological and dielectric properties of minute amount of sample substances. High sensitivity sensors are typically based on resonant structures whose frequency response is shifted by the dielectric loading [1]. To date, various structures of metamaterials and frequency selective surfaces have been developed and introduced as thin film sensors. For example, double split ring resonators [2], asymmetric single split ring resonators [1] - [5]. In fact, split ring resonators are presented to have a high sensitivity. In this paper we investigate the resonant behaviour of a circular split-ring resonator (SRR) after inducing a material on the structure. We present different approaches of sensing: by depositing the material in the gap or either on or under the rings. The practical advantages and limitations of each method are illustrated. The sensing properties have been investigated using quasi-optical technique at mm-wave frequency range.

2. MEASUREMENT AND SIMULATIONS

In this work, circular split rings are fabricated using the positive photolithography. The SRRs are designed to resonate in the frequency range of 70-170 GHz. The geometric parameters are listed in the caption of Fig. 1. Furthermore, in this study, the measurements are carried out using the free-space AB 8-350-2 millimetre vector network analyser [6]. A detailed description of the setup can be found elsewhere [7]. On the other hand, the simulations are performed using the commercial software CST MICROWAVE STUDIO. The propagation direction of the incident EM field is perpendicular to the SRR plane, with the electric field parallel to the gap as shown in Fig. 1.

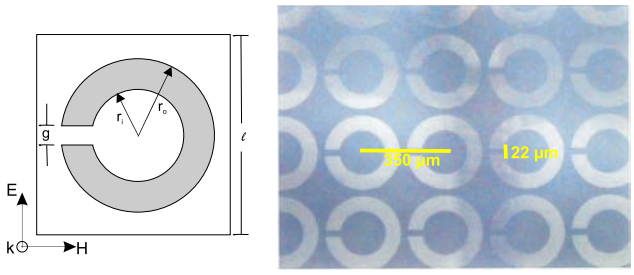


Figure 1: Geometrical dimensions and Photograph of SRR array l=350 μm, r_o=140 μm, r_i=78, μm, g=22 μm and Aluminium thickness is 0.7 μm.

2.1. Film deposited under the rings

In the first experiment, Epson SU-8 photoresist of 1.4 and 1.7 μm thick are deposited under the rings as intermediate layers. Figs. 2a and b show the measured and simulated spectra, respectively. In the simulation the dielectric property of the photoresist is considered to be 1.725 and tan δ equals to 0.02 [9]. Although the low-resistivity silicon substrate provides a quite weak resonance (-13 dB), but a significant shift in the resonant frequency is observed. It is 9.45 GHz for 1.4 μm and 9.48 GHz for 1.7 μm SU-8 photoresist.

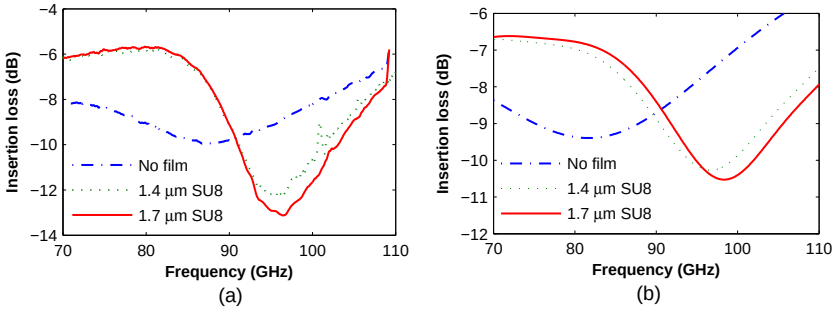


Figure 2: a) Measured and b) simulated transmission of SRR with and without SU-8 deposited under rings

2.2. Film deposited in the gap

In general, split ring resonators can be viewed as a LC-oscillator circuit. The magnetic resonance is excited by the electric field when it is parallel to the gaps. The electric field concentration has a maximum effect in the gap area. In fact, the capacitance due to the gap C_g forms about 65-70 % of the total capacitance of the ring [8]. Therefore, placing a material in this area changes C_g and as a consequence shifts the resonant frequency. In our previous publication [8] we proposed an analytical equivalent model of SRR structure. It has been shown that the shift in the resonant frequency is inversely proportional to the total capacitance C. Moreover, this capacitance is directly proportional to the permittivity of the substrate. It is also obvious that, the shift of f_0 is directly proportional to both the width of the ring w and the change in the permittivity of the material in the gap with respect to air.

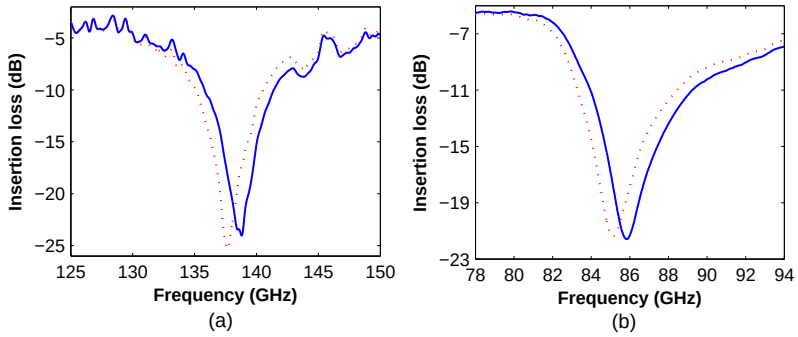


Figure 3: Measured transmission of SRR without (solid) and with AZ6612 in the gap (dotted) a) Quartz substrate, b) Silicon substrate

To verify that experimentally, two distinct substrates are used: high resistivity silicon with its high permittivity value, and quartz substrate with its fairly low dielectric constant and also very low loss factor. AZ6612 photo-resist is deposited in the gap with a thickness equals to the ring's thickness. The measured insertion loss of both samples are presented in Fig. 3. It can be seen that quartz substrate gives higher shift (about 1.16 GHz) than the high resistivity silicon (0.71 GHz). We could not simulate the SRR with filled gap, because there is no available information about the dielectric properties of AZ6612 photoresist at mm-wave frequency range.

2.3. Film deposited on the top of the rings

Alternatively, the thin film can be spun on the rings. This approach is more practical than the previous ones, because it offers several advantages: first the fabrication process is much easier than depositing the film under the rings. Second, only U.V photoresist materials can be deposited in the gap or under the rings. This limitation is due to the development process using the solvent in the photolithography processing. In contrast, the spin coating method is applicable to sense a wider range of materials including liquids.

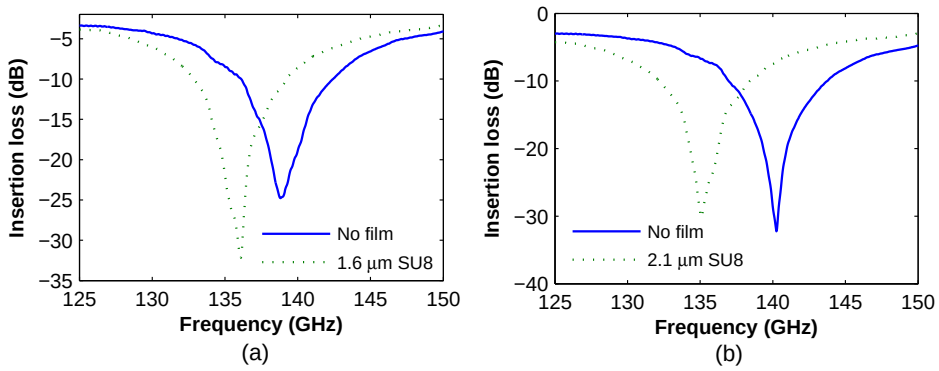


Figure 4: Measured frequency shift of SRR composed of quartz substrate and a) 1.6 μm thick b) 2.1 μm thick SU-8 photoresist overlayer

In order to check the sensitivity of our design, we fabricated two different SRR arrays. The quartz substrate of both arrays is coated with Epson SU-8 photoresist. Both arrays have same geometric parameters (l=360 μm, r_o=144 μm, r_i=84 μm), the only difference is the gap width. The first array has 22 μm gap width and coated with 1.6 μm thick SU-8 photoresist while the second array, which has 24 μm gap width, is covered with 2.1 μm thick SU-8 photoresist. The measured insertion losses of both arrays are depicted in Fig. 4. As it can be observed, there are significant shifts in the resonant frequencies of both samples. They are about 3.73 GHz and 5.18 GHz respectively. In average the design provides about 2.3 GHz shift for each 1 μm thick of SU-8. Knowing that the shift is proportional to the permittivity of the overlayer, this shows the high sensitivity of our design.

Alternatively, high silicon substrate gives lower shift than quartz substrate, as in the case of depositing the film in gap. The shift was about 0.95 GHz for 1.8 μm SU-8 and only 0.62 GHz for 1.4 μm SU-8 overlayer. The measured insertion loss of both arrays are depicted in Fig. 5.

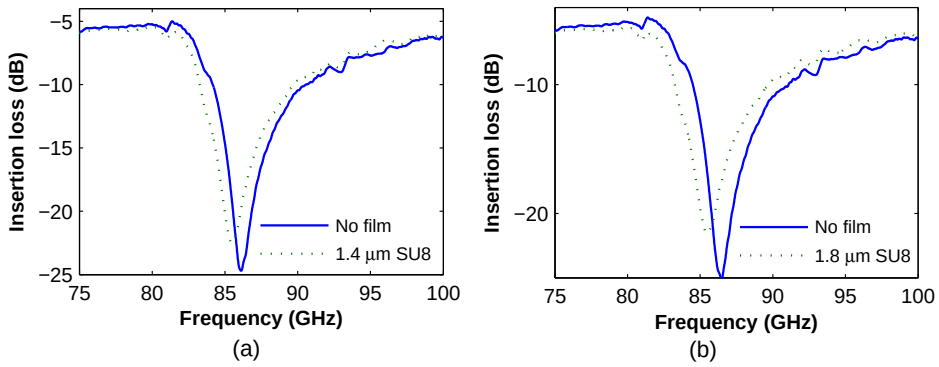


Figure 5: Measured frequency shift of SRR composed of high resistivity silicon substrate and a) 1.4 μm thick b) 1.8 μm thick SU-8 photoresist overlayer

3. CIRCULAR AND SQUARE SRR

The last part of this paper concerns comparing the sensitivity of the circular rings with square rings. We simulated the resonant frequency as function of the substance thickness when its deposited under

rings. The considered square SRR cell has the same area as the circular rings described above. By increasing the thickness of the photoresist SU-8, the shift of the resonant frequency of both designs are saturated as shown in Fig. 6a. This result agree with that obtained using double square SRR [2] and asymmetric SRR [3]. The interesting thing is that, the saturation of circular rings occurs at 55 μm whereas it is at only 25 μm for the square rings.

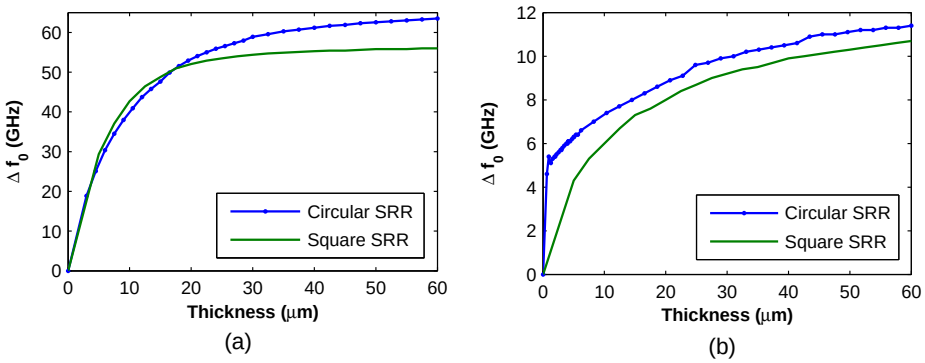


Figure 6: Simulated shift of the resonant frequency in function of the thickness of a) film in gap b) overlayer for square and circular rings.

Furthermore, Fig. 6b depicts the shift of the resonant frequency of square and circular ring with SU-8 photoresist deposited as an overlayer. The sensitivity of circular rings is quite high comparing with that of the square rings especially at small thicknesses.

4. CONCLUSION

In summary, we demonstrate the sensing feature of circular split ring resonators at mm-wave frequencies. The quasi-optical measurements show that it is easily to detect thin films of 0.7 μm thick of a dielectric substance deposited in the gap, and a 1.4 μm thick deposited as an intermediate layer. In the last case the sensitive was high, a shift of more than 9 GHz is measured. In addition, about 4 GHz shift in the resonant frequency have been observed for a film of 1.6 μm thick spun on the rings. Although, the sensitivity feature of the circular and square rings are mostly equivalent, but the circular rings can sense double thickness than the square rings before the resonant shift is saturated.

Acknowledgement

This work was partially funded by Libyan Ministry of Higher Education and the Flemish Institute for the encouragement of innovation in science and technology (IWT-SBO 231.011114).

REFERENCES

1. C. Debus and P. H. Bolivar,"Frequency selective surfaces for high sensitivity terahertz sensing, *Appl. Phys. Lett.* ,Vol. 93, 184102, 2007.
2. J. F. O'Hora, R. Singh, I. Brener, E. Smirnova, J. Han, a. J. Taylor and W. Zhang ,"Thin-film sensing with planar terahertz metamaterials: sensitivity and limitations," *Opt. Express* , Vol. 16, No. 3, 2008.
3. B. Lahiri, A. Z. Khokhar, R. M. D. La Rue, S. G. McMeekin and N. P. Johnson ,"Asymmetric split ring resonators for optical sensing of organic materials," *Opt. Express*,Vol. 17,No. 2, 2009
4. A. Ibraheem, I . AlNaib, C. Jansen and M. Koch, " Thin-film sensing with planar asymmetric metamaterial resonators," *Appl. Phys. Lett.*, Vol. 93,083507, 2008
5. L. Si, Y. Yuan, H. Sun, and X. Lv, "Characterization and Application of Planar Terahertz Narrow Bandpass Filter with Metamaterial Resonators," *Proc. of the 2008 International Workshop on Metamaterials*, 2008.
6. "AB millimetre," http://www.abmillimetre.com.
7. A. Elhawil, G. Koers, L. Zhang, J. Stiens and R. Vounckx," Reliable Method for Material Characterisation using a Quasi-Optical Free-Space Measurement in the W-Band ," *IET Science Measurement & Technology* , Vol. 3,No. 1, 2009.
8. A. Elhawil, J. Stiens, C. De Tandt, W. Ranson and R. Vounckx ,"Equivalent Circuit Model of Single Circular Open-ring Resonators," *IEEE J. Quantum Electron.*, (Accepted for publication).
9. C. E. Collins, R. E. Miles, R. D. Pollard, D. P. Steenson, J. W. Digby, G. M. Parkhurst, J. M. Chamberlain, N. J. Cronin, S. R. Davies and J. W. Bowen " Millimetre Wave Measurements of the Complex Dielectric Constant of an Advanced Thick Film Photoresist," *J. Electronics Materials* , Vol. 27,No. 6, 1998.

Finite element modeling of an acoustic cloak for three dimensional flexible shells with structural excitation

M. Ramadan[1], **W. Akl**[1*], **T. Elnady**[1], **A. Elsabbagh**[1]
[1]Sound and Vibration Lab, Faculty of Engineering, Ain Shams University, Egypt
*corresponding author: wakl@svlab-asu.com

Abstract- A finite element model for three dimensional acoustic cloaks in both cylindrical and spherical coordinates is presented. The model is developed through time-harmonic analysis to study pressure and velocity field distributions as well as the cloak's performance. The model developed accounts for the fluid-structure interaction of thin fluid-loaded shells. A plane strain model is used for the thin shell. Mechanical harmonic excitation is applied to the fluid loaded shell to investigate the effect of mechanical oscillation of the shell on the performance of the acoustic cloak. In developing this model, a deeper insight into the acoustic cloak phenomena presented by Cummer and Shurig in 2007 is presented. Different nonlinear coordinate transformations are presented to study their effect on the acoustic cloak performance.

1. INTRODUCTION

Cloaking and media transformation studies have attracted tremendous attention in recent years. Pendry and Leanhardt [1] were the first to present the transformation-based solutions to the Maxwell's equations rendering various objects electromagnetically invisible. Consequently, two dimensional acoustic cloaking was developed based on the analogy between the Maxwell's equation and the two dimensional acoustic wave equation [2, 3] as a result of the invariance of the acoustic wave equation to coordinate transformation, where two- and three dimensional cloaks have been investigated [4]. However ideal acoustic cloaks are far from being realizable as they both require unrealistic values of the density and density-Bulk's Modulus distribution far from any feasible physical existence.

In an attempt to alleviate the physical constraints of the acoustic cloak and heading towards physical realization, Cheng et al. [5, 6] proposed material distribution of the acoustic cloak domain to be structured in concentric alternating layered fashion with homogeneous isotropic material properties based on the effective medium theory which eliminated the infinite mass constraint at inner boundary of the cloak domain. Their model was applied to two- as well as three dimensional acoustic cloaks, where they have illustrated the convergence to the ideal cloak with increasing number of isotropic layers.

In all these attempts for modeling acoustic cloaks, rigid objects were only considered, which is not true for most structures. In this study a finite element model has been developed to investigate the effect of cloaking dynamic flexible structures coupled to the fluid domain. Although the mechanical oscillations of the flexible structure are assumed to be small enough not to deteriorate the cloak physical domain, its fluid-structure interaction characteristics would result in acoustic pressure waves emitted to the fluid domain as a result of structural excitation. The quality of the cloak performance for different structural excitation levels is quantified and two- and three dimensional flexible structures are studied.

2. MODELING OF ACOUSTIC CLOAKS FOR 3D FLEXIBLE STRUCTURES

To achieve 3D acoustic cloaking, the pressure field within a cylindrical or spherical region $(0 < r < b)$ is mapped to an annular domain $(a < r^{'} < b)$, where r and r' are the radial coordinates in the original and the transformed systems respectively, a is the cloak's inner radius and b is the cloak's outer radius. Based on the form invariance of the acoustic wave equation, Helmholtz acoustic equation is defined as:

$$\nabla'.(\rho'^{-1}\nabla' p') + \omega^2 k'^{-1} p' = 0, \tag{1}$$

where the material properties ρ' and k' are given by:

$$\frac{\rho^{'}}{\rho_o} = \begin{bmatrix} \frac{Q_1}{Q_2 Q_3} & 0 & 0 \\ 0 & \frac{Q_2}{Q_1 Q_3} & 0 \\ 0 & 0 & \frac{Q_3}{Q_1 Q_2} \end{bmatrix} \qquad \frac{k^{'}}{k_o} = \frac{1}{Q_1 Q_2 Q_3} \tag{2}$$

In equation (2) Q_i is defined as the ratio of infinitesimal lengths in the transformed and the untransformed coordinates while ρ_o and k_o are the mass density and bulk modulus of the base medium.

Linear vs. nonlinear domain transformation:

The cloak domain is formed using a nonlinear transformation $r^{'} = a + (b-a)(r/b)^n$, $\theta' = \theta$, $z' = z$, where n, an arbitrary transformation exponent that depends on cloak's geometry and excitation frequency, is used to control the bending of the acoustic wave inside the cloak. For $n = 1$, the material properties for cylindrical and spherical cloaks respectively are:

$$\frac{\rho_r}{\rho_o} = \frac{r'}{r^{'} - a} \qquad \frac{\rho_\theta}{\rho_o} = \frac{r^{'} - a}{r'} \qquad \frac{\rho_z}{\rho_o} = \frac{k}{k_o} = \left(\frac{b-a}{b}\right)^2 \frac{r'}{r^{'} - a} \tag{3}$$

$$\frac{\rho_r}{\rho_o} = \left(\frac{b-a}{b}\right)\left(\frac{r'}{r^{'} - a}\right)^2 \qquad \frac{\rho_\theta}{\rho_o} = \frac{\rho_\varphi}{\rho_o} = \frac{b-a}{b} \qquad \frac{k}{k_o} = \left(\frac{b-a}{b}\right)^3 \left(\frac{r'}{r^{'} - a}\right)^2 \tag{4}$$

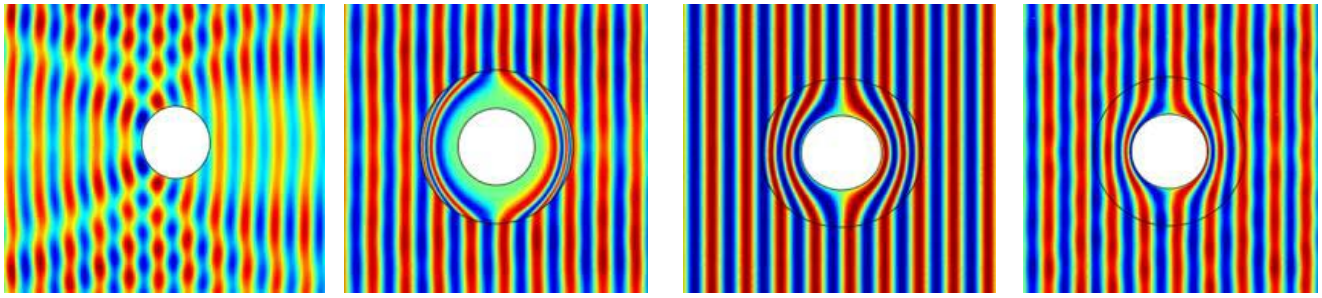
Nonlinear transformation is used to avoid the severe deterioration of the cloak performance at specific domain resonance frequencies when using linear transformation [2] as illustrated in figures (1.a, .b), which represents an "ideal" cloak subject to external pressure wave of 1500 Hz.



(a) (b)

Figure (1): Acoustic pressure field plot of the ideal cloak: (a) linear (n=1), (b) nonlinear (n=0.3)

Different values for nonlinear transformation exponent were tested for cylindrical objects immersed in air domain with external pressure excitation of 2000 Hz applied. Results are as illustrated in figure (2).



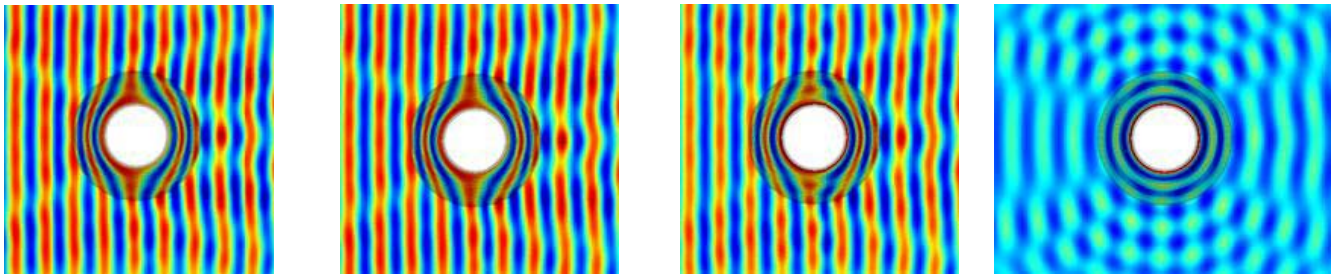
(a) (b) (c) (d)

Figure (2): Full wave acoustic pressure field corresponding to a cylinder: (a) uncloaked, (b) cloaked with n=0.3, (c) cloaked with n=1 and (d) cloak with n=1.7.

A finite element model based on the approximation approach adopted by Cheng et al. [5, 6] is implemented here to eliminate the infinite density constraint in ideal cloaks that would have blocked any structural excitations from affecting the fluid domain.

Cylindrical Cloaks

A finite element model for a cylindrical cloak with an inner radius $a = 0.2m$, an outer radius $b = 2a$ for rigid and flexible steel shells of thickness $t = 0.01m$ inside (3m×2m) water domain using COMSOL Multi-Physics has been developed. The fluid domain is excited with an acoustic pressure wave with amplitude $P_0 = 1Pa$ from one side at 8000 Hz. Perfectly Matched Layers are applied to all sides of the computational domain to prevent any reflections from the boundaries. Rigid as well as flexible shells are presented in figure (3.a, .b, .c, .d), in order to study the effect of shell structural oscillations on the cloak quality. Upon structurally exciting the shell with harmonic force, additional source of acoustic pressure excitation is introduced into the fluid domain, due to fluid-structure coupling. A normal harmonic point force is applied to the cylindrical shell with the same frequency as that of the external domain acoustic excitation. The shell is modeled using plane strain model and appropriate boundary conditions are implemented to ensure proper pressure-displacement coupling across the fluid-structure interface boundary. Hence, both acoustic and structural equations are solved simultaneously. The effect of the force magnitude on the cloak performance is illustrated, where it is shown that the relative amplitude of the external domain pressure and that due to the shell mechanical excitation define the cloak quality.



(a) (b) (c) (d)

Figure (3): Cloak quality for: (a) rigid shell, (b) flexible shell, F=0.1N, (c) flexible shell, F=1N and (d) flexible shell, F=10N.

To quantify the performance of the cloak due to the shell oscillation, the scattering behavior outside the cloak $(r > b)$ is analyzed using the acoustic scattering theory [7-9] to calculate the angular distribution of the scattered acoustic wave $f(\theta)$ which can be evaluated by the far-field scattering:

$$f(\theta) = |\sum_{n=0}^{\infty}(-i)^{n+1}A_n P_n(cos\theta)|^2 \tag{5}$$

where, P_n is the nth degree Legendre polynomial, A_n are constants determined by boundary conditions. In figure (4), the calculated normalized scattering patterns for all azimuth angles for different harmonic force cases compared with the case without structural excitation are presented. A primary beam in the forward direction is always present and is almost quiescent in other directions; however this beam becomes dramatically larger upon increasing the shell excitation force, where backward scattering becomes also significant in the case of the F=10 N.

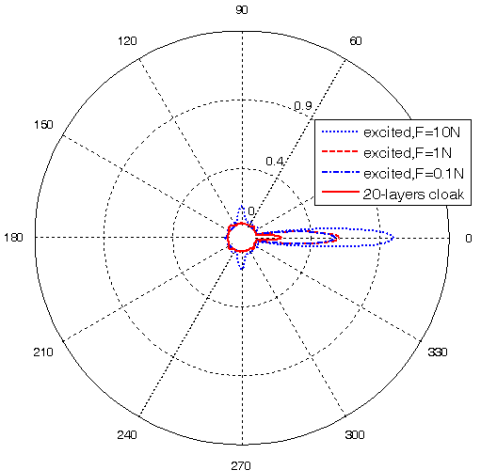
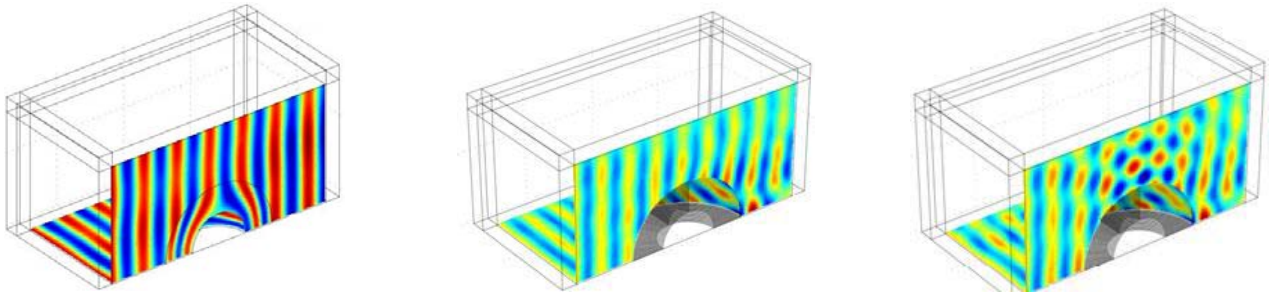


Figure (4): Scattering pattern for all azimuth angles for different force cases.

Spherical Cloaks

Acoustic cloaking of spherical objects is also presented. A spherical shell with radius a is immersed in a uniform fluid domain. A cloak with an inner radius a, and an outer radius b is considered. Following the same procedure, and by applying coordinate transformation, the spherical region $(0 < r < b)$ is mapped to the spherical annular region $(a < r' < b)$. The analytical form of the density tensor with the proper coordinate transformation (for rigid objects) and the approximate isotropic layered cloaks (for flexible objects) are both implemented in the finite element model to investigate the cloaking effect as a function of the external excitation mechanical force. In this model, a spherical annular cloak with inner radius $a = 0.2\,m$ and outer radius $b = 2a$ is developed. The domain is excited with an incident pressure wave of amplitude $P_o = 1\,\text{Pa}$. Utilizing, the double symmetry of the problem, only a quarter of the computational domain is solved, and symmetry boundary conditions are applied at the symmetry planes. Figure (5) illustrates the cloak phenomenon of spherical objects subject to different mechanical force cases. Again the cloak performance is significantly dependent on the relative pressure amplitudes of the domain pressure wave and that due to the spherical shell mechanical excitation.



(a) (b) (c)

Figure (5): Cloak quality for: (a) rigid shell, (b) flexible shell, F=0.1N, (c) flexible shell, F=1N.

3. CONCLUSIONS

Finite element models for both cylindrical and spherical acoustic cloaks have been implemented using both ideal transformations and approximations of the cloak domains. The structural objects have been modeled as flexible structures with mechanical excitations introducing secondary acoustic pressure source to the fluid domain. In the current analysis the secondary pressure source is due to structure-fluid interaction, which has been modeled. Although the excitation force was externally introduced, the same effect would have been appeared if the structure itself would have been excited by the domain pressure field, where it would act as an additional sound source. The cloak performance is proven to be sensitive to the relative pressure amplitude of the external domain to that due to the fluid-structure interaction. Further investigations of the effect of the shell deformation on the cloak performance should be conducted and means of adaptive cloak to counterbalance the external structural disturbances should be studied.

REFERENCES

1. Pendry, J. B. and Leanhardt "Controlling electromagnetic fields", *Science* 312-1780, 2006.
2. Cummer, S. A. and Schurig, D.,"One path to acoustic cloaking", *New Journal of Physics,* 9, 45, 2007.
3. Norris, A. N., "Acoustic cloaking theory", *Proceedings of the Royal Society* A 464, 2411-2434, 2008.
4. Chen, H. and Chan, T., "Acoustic cloaking in three dimensions using acoustic metamaterials", *Applied Physics Letters, American institute of Physics,* 91, 183518, 2007.
5. Cheng, Y., Yang, F., Xu, J. Y. and Liu X. J., "A multilayer structured acoustic cloak with homogeneous isotropic materials", *Applied Physics Letters* , 92, 151913 , 2008.
6. Cheng, Y. and Liu X. J., "Three dimensional multilayered acoustic cloak with homogeneous isotropic materials", *Applied Physics A,* 94, 25-30, 2009.
7. Torrent, D. and Sanchez-Dehesa, J., "Acoustic cloaking in two dimensions: a feasible approach", *New Journal of Physics,* 10, 063015, 2008.
8. Cai, L. W. and Sanchez-Dehesa, J., "Analysis of Cummer-Schurig acoustic cloaking", *New Journal of Physics,* 9, 450, 2007.
9. Cummer, S. A., Popa, B., Schurig, D., Smith, D. R., Pendry, J. B., Rahm, M. and Starr, A. "Scattering theory derivation of a 3D acoustic cloaking shell", *Physical Review Letters,* 100, 024301, 2008.

A novel subwavelength plasmon polariton optical filter based on tilted coupled structures

L. O. Diniz[1], **F. D. Nunes**[2], **E. Marega, Jr**[3]**. and B.-H. V. Borges**[1]
[1]University of São Paulo, Electrical Engineering Dept., São Carlos, SP, Brazil
[2]Federal University of Pernambuco, Electrical Engineering Dept., Recife, PE, Brazil
[3]University of São Paulo, Physics Institute, São Carlos, SP, Brazil
benhur@sc.usp.br

Abstract- This work proposes a completely new approach for the design of resonant structures aiming at wavelength filtering applications. The structure consists of a subwavelength metal-insulator-metal (MIM) waveguide presenting tilted coupled structures transversely arranged in the midpoint between the input and output ports. The cavity-like response of this device has shown that this concept can be particularly attractive for optical filter design for telecom applications. The extra degree of freedom provided by the tilting of the cavity has proved to be not only very effective on improving the quality factor of these structures, but also as an elegant way of extending the range of applications for tuning multiple wavelengths.

1. INTRODUCTION

The rapid development of the field of plasmonics observed in the past few years has paved the way for the development of a myriad of devices capable of guiding electromagnetic waves at subwavelength scale. This remarkable field has been particularly important for telecom and sensing applications since it allows further miniaturization of already classical devices, such as wavelength selective waveguides [1]-[3], wave splitters [4]-[5], and (bio)sensors [6]-[7]. The possibility of propagating electromagnetic energy in such a small scale is provided by the interaction between free electrons in the metal and photons (giving rise to surface plasmon polaritons, or SPP, due to its hybrid nature [8]), and therefore trapping the electromagnetic wave on the surface of the metal. The electromagnetic distribution of SPP modes decreases exponentially in the direction perpendicular to the metal surface, resulting in subwavelength confinement of the propagating mode. The ability to confine electromagnetic energy near the vicinity of the metal-dielectric interface leads to an extraordinarily sensitive characteristic that opens the possibility of manipulating light just by working with the geometry of these structures.

SPP structures can be as simple as a combination of metal-insulator-metal (MIM), or an insulator-metal-insulator (IMI), which greatly simplifies the fabrication process. A MIM-based configuration is of particular interest here as it provides superior field confinement when compared to its IMI counterpart. Even though higher field confinement implies higher propagation losses, MIM structures have been successfully employed in resonant structures for wavelength filtering applications (which is the focus of this work). Many approaches have been suggested for this purpose, such as teeth-shaped structures [9]-[10], and gap based filters [11]-[12]. A key aspect of any wavelength filter device is to be able to provide high wavelength selectivity, which means high quality factor Q ($Q = \lambda_0/\Delta\lambda$, where λ_0 is the peak wavelength and $\Delta\lambda$ is the half width of the peak). However, losses significantly limit the quality factor of MIM-based plasmonic structures to only a few tens, therefore sacrificing selectivity. Examples of MIM-based cavities can be found in [11]-[12]. In [11], the quality factor Q is as high as 50, while in [12] it is less than 25. Other configurations, such as plasmonic ring/disk resonators have also been suggested

for wavelength selection purposes, resulting in a quality factor Q=30 [13].

In this contest, the present work explores a completely new approach for the design of resonant structures, which is based on tilted transverse cavities, aiming at wavelength filtering applications. The extra degree of freedom provided by the tilting of the cavity has proved to be not only very effective on improving the quality factor of these structures, but also as an elegant way of extending the range of applications for tuning multiple wavelengths.

2. MATHEMATICAL MODELING

The top view of the proposed structure is schematically shown in Fig. 1(a). An important aspect of the present approach is the possibility of tilting the cavity (while preserving all other geometrical parameters), as shown with dashed lines in this figure. As will be described later on in this paper, the tilting of the cavity helps improving the quality factor of this device. The simplified mathematical model that physically describes the resonance condition of this resonant-like cavity is based on the scattering matrix theory, also adopted in the design of tooth shaped waveguide filters [10]. Even thought the present approach is substantially different from Lin and Huang's [10], we have found that the resonant condition of the present structure can be closely described by their model. Therefore, and with the help of Fig. 1(b), one can easily obtain the transmittance from Port 1 to Port 2 as follows,

$$\begin{pmatrix} E_1^{out} \\ E_2^{out} \\ E_3^{out} \\ E_4^{out} \end{pmatrix} = S \begin{pmatrix} E_1^{in} \\ E_2^{in} \\ E_3^{in} \\ E_4^{in} \end{pmatrix}, \qquad \text{with } S = \begin{pmatrix} r_1 & t_1 & s_3 & s_3 \\ t_1 & r_1 & s_3 & s_3 \\ s_1 & s_1 & r_3 & r_3 \\ s_1 & s_1 & r_3 & r_3 \end{pmatrix}.$$

In the above equations, r_i, t_i, and s_i (i=1,2,3,4) are, respectively, the reflection, transmission, and splitting coefficients of the incident wave from Port i. $E_i^{in,out}$ refers to the incident/output field at the specified port. Expanding the above system as in [10] one obtains

$E_2^{out} = t_1 E_1^{in} + S_3 E_3^{in} + S_3 E_4^{in}$, where $E_{3,4}^{out} = \frac{S_1 E_1^{in}}{1-r_3 e^{i\theta(\lambda)}} e^{i\theta(\lambda)}$, and $E_2^{out} = t_1 E_1^{in} + \frac{2S_1 S_3 E_1^{in}}{1-r_3 \cdot e^{i\theta(\lambda)}} e^{i\theta(\lambda)}$.

The phase delay $\theta(\lambda)$ is given by $\theta(\lambda) = (4\pi/\lambda)\, n_{eff}\, h + \Delta\varphi(\lambda)$, where $n_{eff} = \beta/k_0$ (β is the propagation constant, and $k_0 = 2\pi/\lambda_0$), and $\Delta\varphi(\lambda)$ is a phase shift at the air/silver interface. Finally, the transmittance from Port 1 to 2, can be obtained as

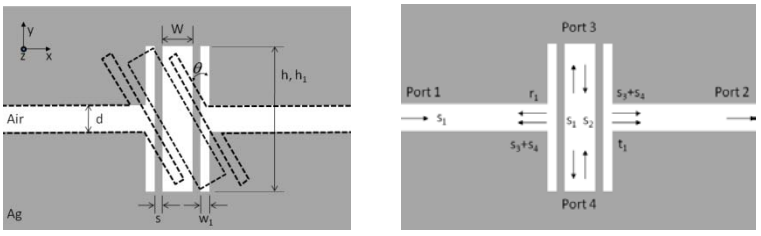
$$T = \left|\frac{E_2^{out}}{E_1^{in}}\right|^2 = \left|t_1 + \frac{2S_1 S_3}{1-r_3 e^{i\theta(\lambda)}} e^{i\theta(\lambda)}\right|^2 \tag{1}$$

From (1) one can obtain the wavelength for maximum transmission, which is given by

$$\lambda_m = \frac{4 n_{eff}\, h}{(2m+1)+\frac{\Delta\varphi}{\pi}} \tag{2}$$

As in [10], the modal dependence of the central cavity on the width W is expressed in terms of the effective

index n_{eff}. As will be discussed in the next section, the width W_1 influences only weakly the position of the through wavelength (and also *Q*).



(a) (b)

Figure 1: (a) Geometry of the filter; *h* and h_1 are the heights of the central cavity and lateral arms, respectively. They will assume different values throughout the paper. (b) Scattering Matrix Formalism for a four-port structure.

3. NUMERICAL RESULTS

The metal used in the simulations is silver, whose permittivity is defined here via polynomial fitting of the experimental data from Johnson and Christy [14]. It is well known that the performance of resonant structures is strongly influenced by the choice of the material model. The lossy Drude model adopted in [11], for example, agrees very well with the experimental data from [14] at high angular frequencies (above 3.5×10^{15} rad/s), but not that much at the frequency range adopted in the present work (which is about the same as in [11]). Therefore, in order to make a fair comparison in terms of the quality factor, we have simulated both cases using the same material model, i.e., with the polynomial fitting from [14]. All simulations discussed in this section where carried out with *COMSOL Multiphysics* for TM polarized waves [15]. The waveguide width *d* is kept constant in all simulations (*d* = 150 nm). The structure is designed to operate at 1000 nm. The cavity height, *h*, was obtained from (2) assuming *m* = 3, without loss of generality. The cavity parameters (*s, h, h1, W, W1* and *θ*) will be individually analyzed next.

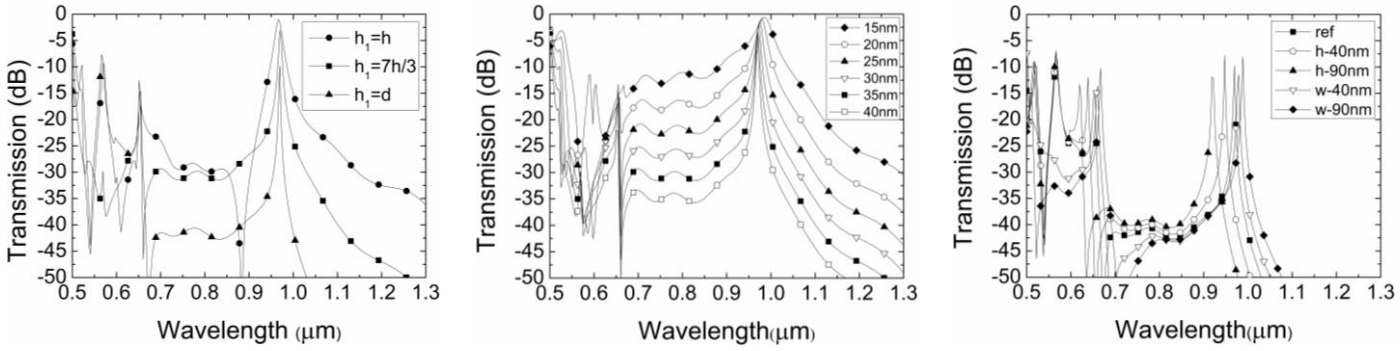
First of all, lets investigate the influence of the lateral arms of the structure on its frequency response. The results are shown in Fig. 2(a) for three different arm heights, i.e., $h_1=h$ (circles), $h_1=7h/3$ (squares), and $h_1=d$ (triangles). Observe that the lateral arms play an important role in improving the *Q* of the cavity, at the expense of a somewhat higher insertion loss. Next, we have investigated the influence of the metallic gap *s* on the frequency response, which is shown in Fig. 2(b). The metallic gap act as a mirror for the central cavity. A thicker *s* provides a better reflectivity at the expense of a lower transmittance to port 2. It can be clearly seen in this figure that the cavity *Q* improves dramatically as *s* increases. An interesting aspect regarding this structure is that both lateral arms also help to improve the energy coupling into the central cavity. This is particularly true if compared to the $h_1=d$ case (when there is no lateral arm). The insertion loss in this case increases by several dB at the center wavelength owed to the reduced coupling efficiency to the central cavity.

The influence of the central cavity parameters *h* (height) and *W* (width) are now shown in Fig. 2(c). The solid square symbols refer to the reference structure (*W* = 240 nm, *s* = 35 nm, W_1 = 50 nm, h_1 = 7h/3 nm, and θ = 0°). The idea is to observe how these parameters influence the operating condition of the cavity. The results show that the performance is more significantly affected by variations on the cavity height, *h*. This is expected since variations on the cavity width *W* causes minor changes in the modal effective index, n_{eff}. The cavity height, by its turn, does not influences n_{eff}, but strongly influences the position of the through wavelength (see also equation (2)).

Finally, we can now choose an appropriate set of parameters based on the previous analysis and investigate the

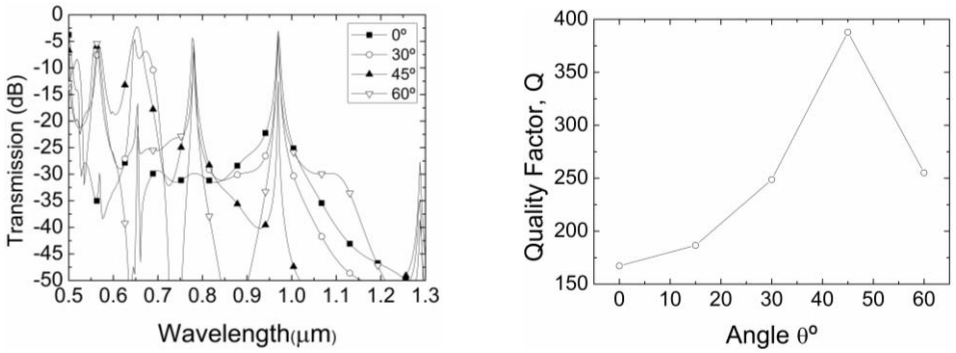
role of the tilting angle on the frequency response of the structure. The pertinent parameters are W = 240 nm, s = 35 nm, h = 1730 nm. We have set the wavelength range from 500 nm to 1300 nm. The results are shown in Fig. 3(a), with the peak wavelength occurring at 980 nm. Observe how the structure becomes more selective (better Q) as the tilting angle increases. Again, all other geometrical parameters (h, W, W_1, h_1 and the horizontal separation (gap) s) are kept the same as in the original (θ = 0°) structure. The better Q values observed for wider angles is due to the improved reflectivity (due to oblique incidence). Yet, at the same time the insertion loss observed in these cases are not as high as those observed in Fig. 3(b), which indicates that the tilting of the cavity can indeed be a more efficient approach both in terms of Q and insertion loss. The influence of the tilting angle on Q is shown in Fig. 3(b). Observe that a quality factor as high as 388 can be obtained for θ = 45°. As far as the authors are aware of, this value is far superior than other resonator-like structures based on slot waveguides reported so far. An interesting behavior is the appearance of other frequencies as the angle further increases, as can be observed around 800 nm. This unexpected behavior can be useful for multiple wavelength selection for telecom applications.

It is worth mentioning at this point that the Q-factor of the proposed structure would be considerably higher than it actually is if simulated with the Drude model from [11], for example. A complete study taking into account the influence of different material models on the performance of resonant structures will be submitted elsewhere.



(a) (b) (c)

Figure 2: Frequency response in terms of: (a) height of the coupling arm, (b) gap s, (c) W and h of the central cavity.



(a) (b)

Figure 3: (a) Frequency response with the tilting angle θ as a parameter. (b) Q-factor as a function of θ.

4. CONCLUSIONS

We have proposed a novel design for SPP-based structures aiming at wavelength filtering applications. The structure consisted of a subwavelength MIM waveguide with a transverse tilted coupled cavity. The present approach was able

to provide a quality factor *Q* as high as 388, for a cavity tilting angle of 45°. We have also shown that the extra degree of freedom provided by the tilting of the cavity not only improved the quality factor of the structure, but also allowed for extending the range of applications by tuning multiple wavelengths.

ACKNOWLEDGEMENT

This work has been carried out in the National Institute for Optics and Photonics (INOF) which has the financial support from FAPESP and CNPq.

REFERENCES

1. Volkov, V. S., S. I. Bozhevolnyi, E. Devaux, J.-Y. Laluet, and W. Ebbesen, "Wavelength selective nanophotonics components utilizing channel plasmon polaritons," *Nano Lett.*, vol. 7, no. 4, 880-884, 2007.
2. T. Holmgaard, S. I. Bozhevolnyi, L. Markey, and A. Dereux, "Dielectric-loaded surface plasmon-polariton waveguides at telecommunication wavelengths: Excitation and characterization," *Appl. Phys. Lett.*, vol. 92, 011124, 2008.
3. Holmgaard, T., Z. Chen, S. I. Bozhevolnyi, L. Markey and A. Dereux, "Dielectric-loaded plasmonic waveguide-ring resonators," *Opt. Express*, vol. 17, no. 4, 2968-2975, 2009.
4. Bozhevolnyi, S. I, V. S. Volkov, E.Devaux, J.-Y. Laluet and T. W. Ebbesen, "Channel plasmon subwavelength waveguide components including interferometers and ring resonators," *Nature*, vol. 440, 508-511, 2006.
5. Yamazaki, T., J. Yamauchi, and H. Nakano, "A Branch-Type TE/TM Wave Splitter Using a Light-Guiding Metal Line," *J. Lightwave Technol*., vol. 25, no. 3, 922-928, 2007.
6. Homola, J, "Present and future of surface plasmon resonance biosensors," *Anal. Bioanal* Chem, vol. 377, 528-539, 2003.
7. Nesterov, M. L., A. V. Kats, and S. K. Turitsyn, "Extremely short-length surface plasmon resonance devices," *Opt. Express*, vol. 16, 20227-20240, 2008.
8. Barnes, W. L., A. Dereux and T. W. Ebbesen, "Surface plasmon subwavelength optics," *Nature*, vol. 424, 824-830, 2003.
9. Tao, J., X.G. Huang, X. Lin, Q. Zhang, and X. Jin, "A narrow-band subwavelength plasmonic waveguide filter with asymmetric multiple-teeth-shaped structure," *Opt. Express*, Vol. 17, No. 16, 13989–13994, 2009.
10. Lin, X.-S. and X.-G. Huang, "Tooth-shaped plasmonic waveguide filters with nanometeric sizes," *Opt. Lett.*, vol. 33, no. 23, 2008.
11. Noual A., Pennec Y., Akjouj A., Djafari-Rouhani B. and Dobrzynski L., "Nanoscale plasmon waveguide including cavity resonator", *J. Phys. Condens. Matter*, vol. 21, 2009.
12. Q. Zhang, X.-G. Huang, X.S. Lin, J. Tao, and X.-P. Jin, "A subwavelength coupler-type MIM optical filter," *Opt. Express*, vol. 17, no. 9, 7549-7554, 2009.
13. S. Xiao, L. Liu, and M. Qiu, "Resonator channel drop filters in a plasmon-polaritons metal," *Opt. Express*, vol. 14, no. 7, 2932-2937, 2006.
14. Johnson, P. B. and R. W. Christy, "Optical constants of the noble metals," *Phys. Rev. B*, vol. 6, no. 12, 4370-4379, 1972.
15. COMSOL Multiphysics, www.comsol.com.

Direct experimental optical characterization of metamaterials.

E. Pshenay-Severin[1], F. Setzpfandt[1], C. Helgert[1], U. Hübner[2], C. Menzel[3], C. Rockstuhl[3], A. Tünnermann[1], F. Lederer[3], and T. Pertsch[1]

[1]Institute of Applied Physics, Friedrich-Schiller-Universität, Germany
[2]Institute of Photonic Technologies, Germany
[3]Institute of Condensed Matter Theory and Solid State Optics, Friedrich-Schiller-Universität, Germany
katja.severin@uni-jena.de

Abstract— We present a method to determine the complex reflection and transmission coefficients of metamaterials by purely experimental means in the optical domain. In order to define effective constants of the metamaterial without resorting to simulations, we employ a white-light interferometer for phase and a spectrometer for amplitude measurements. The method is applied for two referential metamaterial geometries: the fishnet and the double-element structure. Problematic aspects of the phase measurements as well as the accuracy of the method are discussed.

1. INTRODUCTION

Thus far, nearly all methods developed for the characterization of optical material properties address only the dielectric properties, since natural materials do not exhibit magnetism in the optical domain. This restriction was lifted with the availability of metamaterials [1].

Nowadays metamaterials (MMs) in most cases have periodically arranged nanostructured unit cells which may be termed meta-atoms. To integrate a metamaterial into a functional device it is essential to know how it affects light propagation. In order to describe light propagation in an arbitrary medium it suffices to solve the respective eigenvalue problem resulting in eigenfunctions (modes) which have to obey a dispersion relation relating the wave vector components to the frequency $\omega = \omega(k_x, k_y, k_z)$. Of course, this dispersion relation will be governed by the intrinsic material dispersion and, most notably, by the meta-atom shape. It has been shown that in most cases the periodic optical metamaterial, although spatially dispersive, may be described as an effective homogeneous medium [2]. If the dispersive properties are dominated by the lowest order Bloch mode, it can be replaced by the eigenmode of a homogeneous medium, i.e. a plane wave. For a given frequency the medium can then be characterized by an effective wave vector, which constitutes an *effective wave parameter*. It is even possible to introduce an effective refractive index ($n_{\mathrm{eff}}(\omega) = k(\omega)/k_0$ with $k_0 = \omega/c$) as usually done in the metamaterial literature, if the dispersion relation is a sphere or if one is only concerned with a definite transverse wave vector component (angle of incidence). The effective index can be retrieved from the complex transmission $t(\omega)$) and the reflection ($r(\omega)$) coefficients [3]:

$$k = k_0 n_{\mathrm{eff}} = \frac{1}{d}\left[\arccos\left(\frac{k_{\mathrm{s}}(1-r^2)+k_{\mathrm{c}}t^2}{t(k_{\mathrm{s}}(1-r)+k_{\mathrm{c}}(1+r))}+2m\pi\right)\right]. \quad (1)$$

Here, d is the thickness of the MM layer, k_{s} and k_{c} are the wave numbers in the substrate and cladding, respectively. Because $t(\omega)$ and $r(\omega)$ are complex, information on their amplitude and their phase are required to be known. The necessity of phase measurements for the comprehensive experimental characterization of MMs has been already discussed in literature [4, 5]. However, there are only a few works addressing direct measurements of the MMs effective optical parameters [5, 6, 7]. Though these experiments successfully demonstrated the negative refractive index of MMs, they can be hardly used as a routine technique.

In the experiments described in this contribution we implement a white-light Fourier-transform spectral interferometer [8] for broad band (1.1 μm - 1.7 μm) phase measurements to determine the effective refractive index of MMs at normal incidence by purely experimental means.

2. PHASE MEASUREMENTS: BACKGROUND

The measurements of the complex transfer function of MM samples were performed by white-light Fourier-transform spectral interferometry [8]. In this type of spectral interferometry experiments

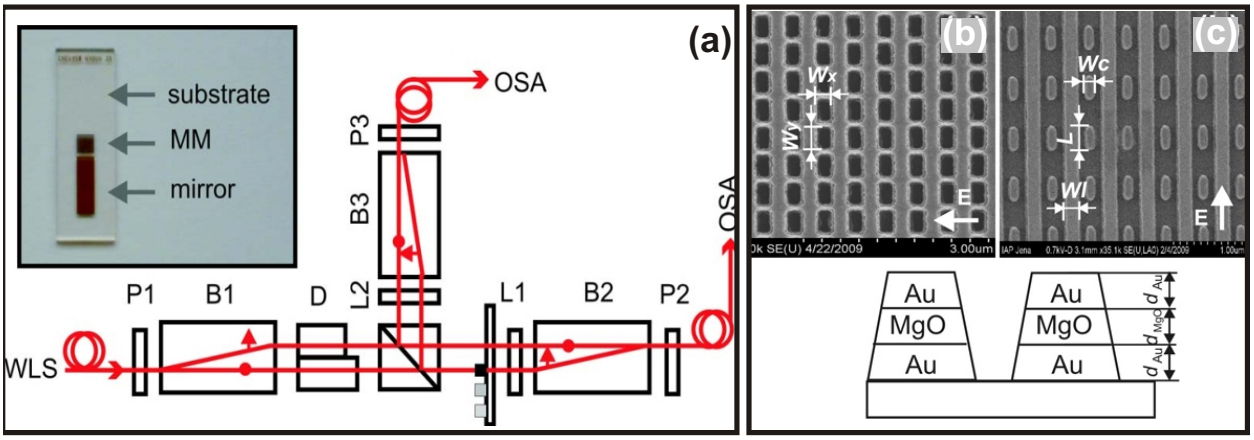


Figure 1: (a) Interferometric setup. P1,P2,P3 - polarizers. B1,B2,B3 - beam displacers, L1,L2 - half-wave plates, D - delay element. The insert shows the configuration of the experimental chip. (b),(c)Investigated structures.(a) is the SEM image of the fishnet structure, (b) is the the SEM image of the double-element structure.

a time delay (τ) between two beams is introduced in an interferometer with two arms of different geometrical length. Interference of the reference ($E_{\mathrm{ref}}(\omega)$) and the sample arm ($E_{\mathrm{sam}}(\omega)$) fields gives rise to a measured optical signal in the frequency domain that is

$$\begin{aligned} I(\omega) &= |E_{\mathrm{sam}}(\omega)+E_{\mathrm{ref}}(\omega)|^2 = |E_{\mathrm{sam}}(\omega)|^2+|E_{\mathrm{ref}}(\omega)|^2+ \\ &\quad +2\,|E_{\mathrm{sam}}(\omega)|\,|E_{\mathrm{ref}}(\omega)|\cos(i(\phi_{\mathrm{sam}}(\omega)+\phi_{\mathrm{MM}}(\omega)+\omega\tau-\phi_{\mathrm{ref}}(\omega))). \end{aligned} \quad (2)$$

Here $\phi_{\mathrm{ref}}(\omega)$ is the phase delay in the reference arm that is induced due to the dispersive optical elements. The phase delay in the sample arm can be separated into three terms. The term $\phi_{\mathrm{sam}}(\omega)$ is the phase delay due to the dispersive optical elements placed in the sample arm, the term $\phi_{\mathrm{MM}}(\omega)$ is the phase delay in the MM sample (which is to be retrieved), and the term $\omega\tau$ corresponds to the geometrical length difference between the two arms. Extraction of the interference term can be easily achieved in the time domain. The signal in the time domain $S(t)$ obtained by Fourier transformation of $I(\omega)$ is

$$\begin{aligned} S(t) &= FT\,[I(\omega)] = E_{\mathrm{sam}}(t)\otimes E^*_{\mathrm{sam}}(-t)+E_{\mathrm{ref}}(t)\otimes E^*_{\mathrm{ref}}(-t)+ \\ &\quad +E_{\mathrm{sam}}(t+\tau)\otimes E^*_{\mathrm{ref}}(t)+E^*_{\mathrm{sam}}(t-\tau)\otimes E_{\mathrm{ref}}(t). \end{aligned} \quad (3)$$

In Eq. (3) the first two terms are the autocorrelation functions of the individual fields, centered at $t=0$. The third and the fourth terms are the correlation functions of two fields centered at $t=\tau$ and $t=-\tau$, respectively. If the time delay τ is sufficiently large, the correlation term does not overlap with the autocorrelation terms and can be extracted by applying a finite time window.

Applying the inverse Fourier transform to the interference pattern after filtering gives the sought-after interference term in the frequency domain. However a reference measurement is required for extraction of $\phi_{\mathrm{MM}}(\omega)$ from $\Delta\phi=\phi_{\mathrm{sam}}(\omega)+\phi_{\mathrm{MM}}(\omega)-\phi_{\mathrm{ref}}(\omega)$. For the reference measurement the MM sample is replaced by a known material, for instance air in the case of the transmission measurement or a mirror in the case of the reflection measurement. If $\phi_{\mathrm{ref.sam.}}$ is the phase delay due to the known reference object, the phase difference measured and retrieved in the reference measurement is $\Delta\phi_{\mathrm{ref}}=\phi_{\mathrm{sam}}(\omega)+\phi_{\mathrm{ref.sam.}}(\omega)-\phi_{\mathrm{ref}}(\omega)$. If the dispersion and thickness of the reference sample are known, the $\phi_{\mathrm{MM}}(\omega)$ can be defined as $\phi_{\mathrm{MM}}(\omega)=\Delta\phi-\Delta\phi_{\mathrm{ref.sam.}}+\phi_{\mathrm{ref.sam.}}(\omega)$.

The retrieved phase has an ambiguity of 2π and additionally *a priori* information about the sample under consideration is required in order to remove the ambiguity. For MMs, where the thickness d is in the order of only a few hundreds of nanometers, the measured phase ϕ_{MM} can be safely assumed to lie between $-\pi<\phi_{\mathrm{MM}}<\pi$. For the retrieval of the effective constants as outlined in Eq. 1 this implies that we assume that $m=0$. However, for thicker MMs made of a larger number of functional layers, $m\neq 0$ has to be considered. In this case, the choice of an appropriate value of m has to be based on an effective refractive index measured in the low frequency limit, where the magnetic properties disappear.

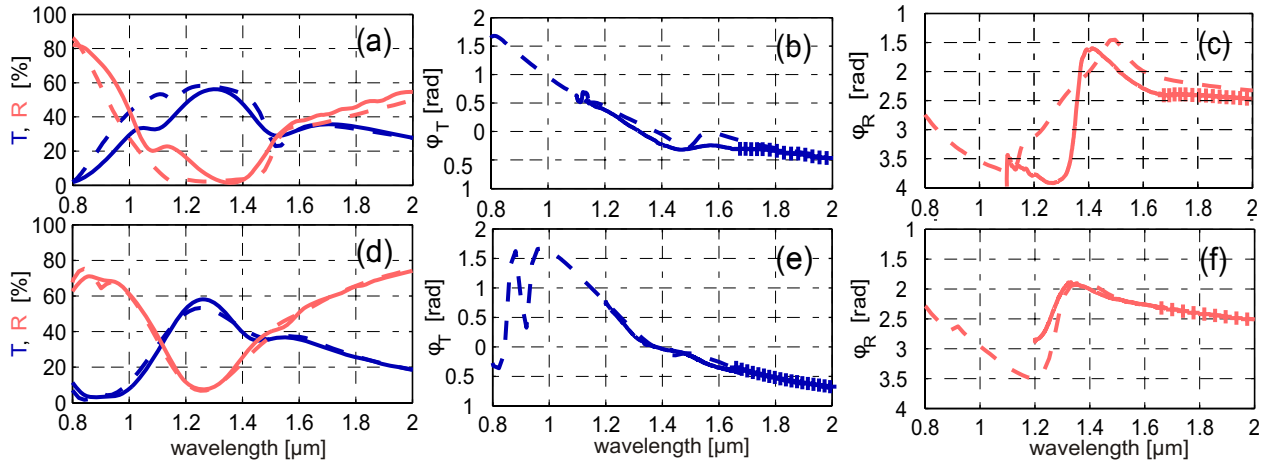


Figure 2: (a),(b),(c) are results for the fishnet structure. (d),(e),(f) are results for the double-element structure. Solid lines correspond to measured data, dotted lines to simulated data. (a),(d) Blue lines are transmittances; red lines are reflectances. (c),(e) Phase of the transmitted amplitude: solid line is the normalized measured phase, dotted is the simulated data, crossed line is the phase from the amplitude measurements. (d),(f) Phase of the reflected amplitude: solid line is the normalized measured phase, dotted is the simulated data, crossed line is the phase from the amplitude measurements.

3. EXPERIMENT AND RESULTS

The interferometric setup for the phase measurements is shown in Fig. 1(a). The interferometer represents a Jamin-Lebedeff scheme modified for simultaneous measurements in transmission and reflection, and was also used in [5].

The interferometric measurements were performed with the supercontinuum light source SuperK Versa from KOHERAS (spectral bandwidth 0.4 μm - 1.7 μm). The constant path difference (τ) between the arms of the interferometer was introduced by a delay element (D). It consists of two BK7 glass blocks of the length of 22 mm and 20 mm, respectively.

Two metamaterial samples were investigated: the first is a fishnet structure [9] (Fig. 1(b)) and the second is a double-element structure comprising a cut-wire pair and a continuous wire element [10] (Fig. 1(c)). The structures were fabricated by a standard electron-beam lithography technology combined with a lift-off process. The parameters of the fishnet structure with the period of 500 nm were d_{Au}=20 nm, d_{MgO}=40 nm, W_x=180 nm, and W_y=380 nm. The parameters of the double-element structure with the period of 550 nm had d_{Au}=40 nm, d_{MgO}=30 nm, L=270 nm, W_{c}=140 nm, W_{l}=150 nm. All structures were fabricated on a 1 mm SiO_2 substrate. These structures have been primarily studied for identifying spectral domains exhibiting a negative refraction. The test sample arrangement is shown in Fig. 1(a). The MM sample (2×2 mm^2) is situated in the middle of the chip. The field above is the pure substrate serving as a reference for the transmission measurements. The field below is a non-structured multi-layer system corresponding to that of the MM sample and is used as the reference for the reflection measurements. The phase delay $\phi^R_{\mathrm{ref.mirror}}$ occurring upon reflection at the non-structured multi-layer system was calculated with great accuracy using standard multilayer matrix routines.

Spectroscopic measurements of the transmittance and reflectance were performed under normal incidence with the spectrometer Perkin Elmer Lambda 950 in the wavelength range from 0.4 μm to 2.5 μm. Phases were measured in the wavelength region from 1.1 μm to 1.7 μm where the negative refractive index is expected. Here we demonstrate results for the polarization (Fig. 1(b),(c)) that allows the excitation of the anti-symmetric resonance at $\approx$1.5 μm for both structures. Relevant resonances for the opposite polarization occur in a spectral domain not accessible by the current experimental setup.

Simulations of the fabricated structures were performed by the FMM [11]. In the simulations the refractive index of MgO was assumed to be 1.72. We assumed a dispersive permittivity for gold as documented in the literature [12].

The measured and simulated transmittance and reflectance as well as the phase of the transmitted and reflected fields are presented in Fig. 2(a),(b),(c) for the fishnet structure and in Fig. 2(d),(e),(f) for the double-element structure. Since the coincidence of the simulated and measured transmit-

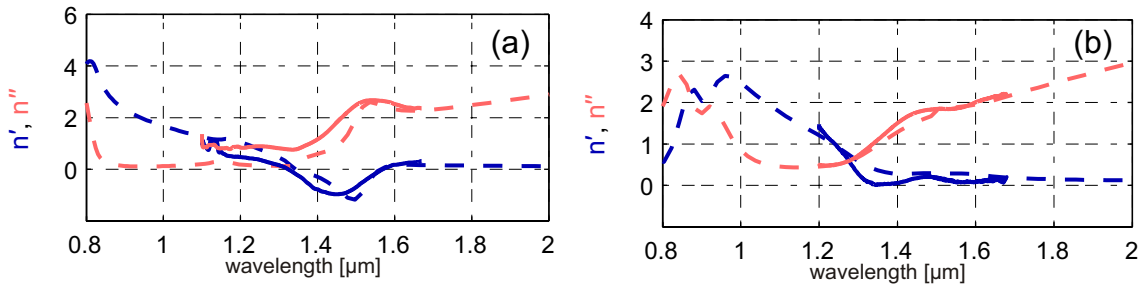


Figure 3: Effective refractive index of the fishnet structure (a) and the double-element structure (b). Real parts n' are represented with blue lines, imaginary parts n'' with red lines. Solid lines correspond to measured data, dashed lines to simulated data.

tance and reflectance for the fishnet structure (Fig. 2(a)) is not perfect, some quantitative deviations of the phases are expected, though their qualitative behavior is similar. In the spectral region where an anti-symmetric resonance is expected (fishnet structure at about 1.45 μm, double-element structure at about 1.38 μm) the phase in transmission has a dip corresponding to a decreasing refractive index. The phase jump of π in the reflection corresponds to vanishing reflection, due to impedance matching between the MM and air.

It turned out that an additional uncertainty in the measured phase between the sample and the reference arm is most detrimental to the accuracy of the phase measurements. This is introduced by the shift of the sample and due to variations in the thickness of the substrate. Therefore, a correction for this offset was mandatory. To do so we take advantage of the fact that magnetic properties well off the resonance disappear. In this spectral region the refractive index can be defined using the standard techniques from a measured transmittance ($|t|^2$) and reflectance ($|r|^2$) [13]. With this index the expected absolute phase can be retrieved and compared with the measured values. The obtained difference is used for final data adjustment.

These reference measurements were performed in the long wavelength region, where the anti-symmetric (magnetic) resonance does not appear. The resonance bandwidth can be estimated from the absorption measurements. It implies that for wavelengths larger than 1.6 μm both MMs can be described by an effective refractive index $n_{\text{eff}} = \sqrt{\epsilon_{\text{eff}}}$ where ϵ_{eff} follows from a simple effective medium approach. In Fig. 2(b),(c) and Fig. 2(e),(f) the crossed curves depict the transmission and the reflection phases obtained from the transmittance and reflectance measurements. By using Eq. 1 the dispersion relation (or the effective refractive index) of the MM structures can be determined. Results for the fishnet and the double-element structure are shown in Fig. 3(a) and Fig. 3(b) respectively. These results agree with values documented in literature. It should be stressed again, that, in contrast to the previously reported results, they were exlusively obtained from experimental data only.

The accuracy of the refractive index ($n = n' + in''$) measurements can be estimated following the definition of the root mean square error (σ) of indirectly measured quantities. The root mean squared errors of the measured quantities are: $\sigma_{|t|} = 0.01$, $\sigma_{|r|} = 0.01$, $\sigma_{\arg t} = 0.02$, and $\sigma_{\arg r} = 0.02$. These values represent maximum observable ones in the region of the wavelength of interest (1.1 μm-1.7 μm).

The partial derivatives for the fishnet structure obtained from the simulations are shown in Fig. 4. The real parts of the respective derivatives are depicted by blue lines, and the imaginary parts by the red ones. It is seen that in the region where the negative refraction is expected the real part of the refractive index depends mostly on the phases of the transmission and reflection coefficients. The dependence on the absolute values of t and r is weak. On the contrary, the imaginary part of the refractive index depends more on the absolute values of t and r than on their phases. This makes the standard retrieval procedure questionable, which is based on the amplitude measurements only. This issue, namely the necessity of phase measurements for the correct refractive index retrieval was discussed in [5]. Taking the accuracy of the transmittance and reflectance measurements and the experimental values for the derivatives we obtain $\sigma_{n'} = 0.04$ and $\sigma_{n''} = 0.07$ for the fishnet structures at $\lambda = 1.45$ μm and $\sigma_{n'} = 0.03$ and $\sigma_{n''} = 0.04$ for the double element structures at $\lambda = 1.38$ μm.

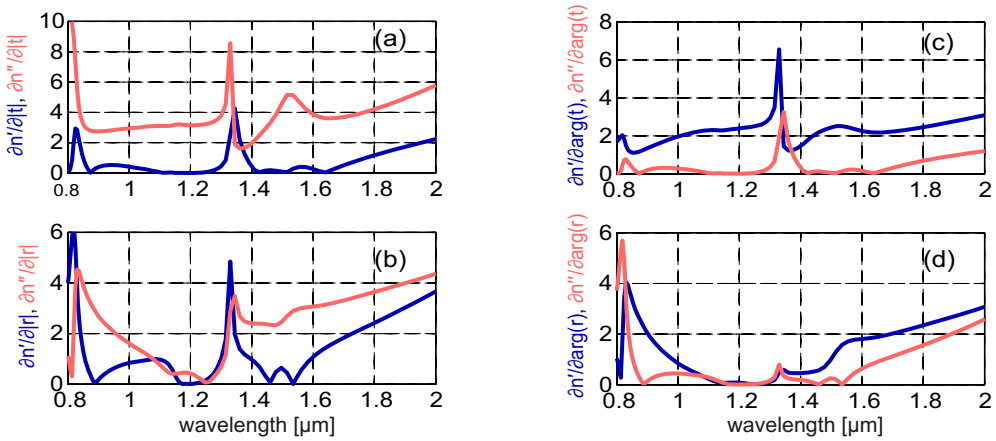


Figure 4: partial derivatives of n with respect to $|t|$ (a), $|r|$ (b), $\arg t$ (c), and $\arg r$ (d). Real part n' is represented by blue lines, imaginary part n'' by red lines.

4. CONCLUSION

We have presented an experimental method for the determination of the dispersion relation in optical metamaterials for normal incidence. We implemented the white-light Fourier-transform spectral interferometry [8] for broad band (1.1 μm - 1.7 μm) phase measurements in transmission and reflection. The experimental setup for the phase measurements was a Jamin-Lebedeff interferometer modified for measurements in the transmission and in the reflection under normal incidence. For the transmittance and the reflectance measurements we used a PerkinElmer Lambda 950 spectrometer. The effective refractive indices of the investigated MMs have been calculated by using a standard retrieval algorithm [6] using measured complex transmission and reflection coefficients. For both structures investigated this technique provides an accuracy of about 4% with respect to both the real and imaginary part of the the refractive index .

The method was applied to a fishnet and a double-element MM. The measured refractive index was $n = -0.97 \pm 0.04 + i(1.76 \pm 0.07)$ at $\lambda = 1.45$ μm for the fishnet structure, and $n = 0.16 \pm 0.03 + i(0.24 \pm 0.04)$ at the $\lambda = 1.38$ μm for the double element structure.

ACKNOWLEDGMENT

The authors gratefully acknowledge financial support from the German Federal Ministry of Education and Research (Metamat) and the State of Thuringia (Proexzellenz Mema).

REFERENCES

1. J. B. Pendry, Phys. Rev. Lett. **85**, 3966 (2000).
2. C. Rockstuhl, T. Paul, F. Lederer, T. Pertsch, T. Zentgraf, T. P. Meyrath, and H. Giessen, Phys. Rev. B **77**, 035126 (2008).
3. C. Menzel, C. Rockstuhl, T. Paul, F. Lederer, and T. Pertsch, Physical Review B (Condensed Matter and Materials Physics) **77**, 195328 (2008).
4. W. J. Padilla, D. R. Smith, and D. N. Basov, J. Opt. Soc. Am. B **23**, 404 (2006).
5. V. Drachev, W. Cai, U. Chettiar, H. Yuan, A. Sarychev, A. Kildishev, G. Klimeck, and V. Shalaev, Laser Phys. Lett. **3**, 49 (2006).
6. S. Zhang, W. Fan, N. C. Panoiu, K. J. Malloy, R. M. Osgood, and S. R. J. Brueck, Phys. Rev. Lett. **95**, 137404 (2005).
7. G. Dolling, C. Enkrich, M. Wegener, C. M. Soukoulis, and S. Linden, Science **312**, 892 (2006).
8. L. Lepetit, G. Chériaux, and M. Joffre, J. Opt. Soc. Am. B **12**, 2467 (1995).
9. G. Dolling, C. Enkrich, M. Wegener, C. M. Soukoulis, and S. Linden, Opt. Lett. **31**, 1800 (2006).
10. E. Pshenay-Severin, U. Hübner, C. Menzel, C. Helgert, A. Chipouline, C. Rockstuhl, A. Tünnermann, F. Lederer, and T. Pertsch, Opt. Lett. **34**, 1678 (2009).
11. L. Li, J. Opt. Soc. Am. A **14**, 2758 (1997).
12. P. B. Johnson and R. W. Christy, Phys. Rev. B **6**, 4370 (1972).
13. J. M. del Pozo and L. Díaz, Appl. Opt. **31**, 4474 (1992).

Photoconductivity studies on amorphous and crystalline TiO_2 films doped with gold nanoparticles

G. Valverde-Aguilar[1], J. A. García-Macedo [1], Víctor Renteria-Tapia[1], Manuel Aguilar-Franco[2]

[1] Departamento de Estado Sólido. Instituto de Física, Universidad Nacional Autónoma de México. México D.F. C.P. 04510.

[2]Departamento de Física Química. Instituto de Física, Universidad Nacional Autónoma de México. México D. F. C. P. 04510

Phone: (5255) 56225103, Fax: (5255) 56225011, 56161535

E–mail: valverde@fisica.unam.mx

Abstract- In this work, amorphous and crystalline TiO_2 films were synthesized by the sol–gel process at room temperature. The TiO_2 films were doped with gold nanoparticles. The films were spin-coated on glass wafers. The samples were annealed at at 100°C for 30 minutes and sintered at 520°C for 2 h. All films were characterized using X-ray diffraction, transmission electronic microscopy and UV-Vis absorption spectroscopy. Two crystalline phases, anatase and rutile, were formed in the matrix TiO_2 and TiO_2/Au. An absorption peak was located at 570 nm (amorphous) and 645 nm (anatase). Photoconductivity studies were performed on these films. The experimental data were fitted with straight lines at darkness and under illumination at 515 nm and 645 nm. This indicates an ohmic behavior. Crystalline TiO_2/Au films are more photoconductive than the amorphous ones.

1. INTRODUCTION

Titanium dioxide (TiO_2) is a non-toxic material. TiO_2 thin films exhibit high stability in aqueous solutions and no photocorrosion under band gap illumination. Due to its wide-ranging chemical and physical properties (electrical conductivity, photosensitivity, and aqueous environments) TiO_2 has a large variety of potential applications. These films are already widely used in the study of the photocatalysis and photoelectrocatalysis of organic pollutants [1, 2]. TiO_2 is the subject of intensive research, especially with regard to its end uses in solar cells, chemical sensors, photoelectrochemical cells and electronic devices [3, 4]. By applying small bias, recombination of generated electron–hole pairs is retarded. As a wide band gap semiconductor, TiO_2 shows a diverse heterogeneity of crystalline phases, whereby it is possible to find it in anatase, rutile or brookite form [5].

In the present work, we described the synthesis, characterization and photoconductivity behaviour of amorphous and crystalline TiO_2 films doped with gold nanoparticles (NP's). The films were produced by the sol–gel process at room temperature. The obtained films were studied by X-ray diffraction (XRD), optical absorption (OA) and transmission electron microscopy (TEM). Photoconductivity studies were performed on these films to determine their transport mechanisms. Gans theory including a variable refractive index was used to fit the experimental absorption spectrum and these results are discussed.

2. EXPERIMENTAL

Preparation of TiO_2 solution. All reagents were Aldrich grade. The precursor solutions for TiO_2 films were prepared by the following method. Tetrabutyl orthotitanate and diethanolamine ($NH(C_2H_4OH)_2$) which prevent the precipitation of oxides and stabilize the solutions were dissolved in ethanol. After stirring vigorously 2h at room temperature, a mixed solution of deionized water and ethanol was added dropwise slowly to the above solution with a pipette under stirring. Finally, Tetraethyleneglycol (TEG) was added to the above solution. This solution was stirred vigorously to obtain a uniform sol. The resultant alkoxide solution was kept standing at room temperature to perform hydrolysis reaction for 2h, resulting in the TiO_2 sol.

Preparation of Au stock solution. 0.03 M of Hydrogen Tetrachloroaurate(III) hydrate ($HAuCl_4 \cdot aq$) was dissolved in a mixture of deionized water and ethanol. It was stirred for 5 minutes.

The Au stock solution was added to 20 ml of TiO_2 solution. This final solution was stirred for 17 hours at room temperature to obtain a purple colour. The final chemical composition of all reagents was $Ti(OC_4H_9)_4$: $NH(C_2H_4OH)_2$: C_2H_5OH : DI H_2O : TEG: nitric acid: $HAuCl_4$ = 1:1: 14.1:1:1.028:0.136:0.024. The TiO_2/Au solution has a pH = 6.0. The TiO_2 films were deposited by the spin-coating technique. The precursor solution was placed on the glass wafers (2.5 x 2.5 cm^2) using a dropper and spun at a rate of 3000 rpm for 20 s. After coating, the film was dried at 100 °C for 30 min in a muffle oven in order to remove organic components and sintered at 520 °C for 2 h in a muffle oven to produce the crystallization.

UV-vis absorption spectra were obtained on a Thermo Spectronic Genesys 2 spectrophotometer with an accuracy of ±1 nm over the wavelength range of 300-900 nm. The structure of the final films was characterized by XRD patterns. These patterns were recorded on a Bruker AXS D8 Advance diffractometer using Ni-filtered CuKα radiation. A step-scanning mode with a step of 0.02° in the range from 1.5 to 60° in 2θ and an integration time of 2 s was used. IR spectra were obtained from a KBr pellet using a Bruker Tensor 27 FT-IR spectrometer. Pellets were made from a finely ground mixture of the sample and KBr at a ratio of KBr:sample = 1:0.019. The thickness of the films was measured using a SEM microscopy Model STEREOSCAN at 20 kV. For photoconductivity studies [6] silver electrodes were painted on the sample. It was maintained in a 10^{-5} Torr vacuum cryostat at room temperature in order to avoid humidity. For photocurrent measurements, the films were illuminated with light from an Oriel Xe lamp passed through a 0.25m Spex monochromator. Currents were measured with a 642 Keithley electrometer connected in series with the voltage power supply. The applied electrostatic field E was parallel to the film. Light intensity was measured at the sample position with a Spectra Physics 404 power meter.

3. RESULTS AND DISCUSSION

3.1 X-ray diffraction patterns. The XRD patterns of the amorphous and crystalline TiO_2 films with gold NP's are presented in Figure 1. From amorphous film, its spectrum reveals the presence of gold NP's by the diffraction peaks located at 2θ = 38.24, 44.39, 64.62 and 77.60 which can be indexed as (111), (200), (220) and (311) respectively. The position of the diffraction peaks is in good agreement with those given in ASTM data card (#04-0784). The crystalline film sintered at 520 °C for 2 h exhibits very good crystallization that corresponds to anatase and rutile phases. The anatase phase was identified by the diffraction peaks located at 2θ = 25.33, 47.97, 54.00, 55.16 and 62.71 which can be indexed as (101), (200), (105), (211) and (204) respectively. The rutile phase was identified by the diffraction peaks located at 2θ = 27.47, 36.14 and 41.32 which can be indexed as (110), (101) and (111) respectively. The position of the diffraction peaks in the film is in good agreement with those given in ASTM data card (#21-1272) for anatase and ASTM data card (#21-1276) for rutile. The presence of gold NP's was detected by the same diffraction peaks identified in the amorphous film.

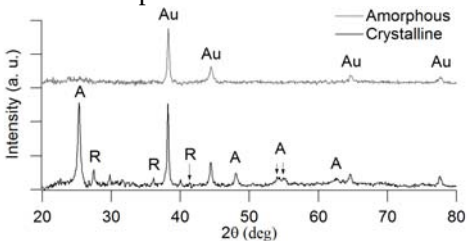


Fig. 1. XRD pattern at high angle of the amorphous and crystalline TiO_2 films with gold NP's.

The average crystalline size (D) was calculated from Scherrer´s formula [7] by using the diffraction peak (101) for anatase phase and the peak (110) for rutile phase with $\lambda=1.54056 \times 10^{-10}$ m. The percentage

of anatase, rutile and gold phases was calculated by means of a Rietveld refinement. These calculations are shown in Table 1.

Table 1. Summary of nanoscopic characteristics of amorphous and crystalline TiO_2/Au films.

Phase	B	Radian	D (nm)	Crystal phase (wt%)
Anatase (101)	0.44°	0.00768	18.5	59.7 ± 4
Rutile (110)	0.31°	0.00543	26.3	37.4 ± 3
Au	-	-	-	2.9 ± 4

3.2 Optical absorption. Figure 2 shows the OA spectra of the amorphous and crystalline TiO_2/Au films taken at room temperature in the range of 300-900 nm. The spectrum of the crystalline film shows an absorption band A located at 402 (3.08 eV) corresponding to the TiO_2 matrix, and a second band B located 651 nm (1.93 eV) corresponding to the surface plasmon resonance (SPR) of the gold NP's. The spectrum from amorphous film shows a peak C at 568 nm (2.68 eV) which is the SPR band due to spherical Au nanoparticles [8].

To clarify the XRD and optical absorption experimental results, the formation mechanism of Au nanoparticles is discussed below. It is known that the photolysis of $HAuCl_4$ to the Au atom, Au^0, is a multiphoton event [9], and it proceeds by irradiation. Therefore, for amorphous TiO_2/Au film, the Au nucleation was slow and random because the $HAuCl_4$ ions were reduced by daylight (containing a little UV light) and this mostly happened after the gelation. The nuclei were thus distributed randomly within the TiO_2 skeleton and consequently led to the growth of the Au particles that were inhomogeneous, and their size distribution very wide.

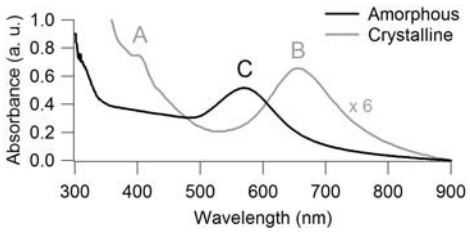


Fig. 2. OA spectra of the amorphous (black solid line) and crystalline (grey solid line) TiO_2/Au.

Literature [6, 10] reports an absorption peak for surface plasmon resonance (SPR) of gold nanoparticles around 500-550 nm. A red-shift in the maximum in absorbance towards larger wavelength (from 568 to 651 nm) with respect to the amorphous TiO_2 film is evident as well as a broadening of the peak absorption width compared to the amorphous film. The dependence of this shift on the embedding medium indicates the high sensitivity of surface plasmon band to cluster-matrix interface properties. This fact is originated due to the increase in the diameter of Au nanoparticles and an increment of the refractive index of TiO_2 matrix with increasing the heat-treatment temperature [11]. It is well known that the refractive index of TiO_2 films is related to the crystal phase (anatase or rutile), the crystalline size and the densities of the films [12]. For these reasons, the OA spectrum (Fig. 2) of the crystalline film was fitted very well using Gans theory [13] with a local refractive index $n_{local} = 2.6$ (Figure 3). This index has a value close to the refractive index reported for the anatase phase ($n_{anatase} = 2.54$) [14]. This is consistent with the result of XRD which indicates that the anatase phase has the highest proportion (59.7 wt%). While the rutile phase ($n_{rutile} = 2.75$) also contributes to obtain this high refractive index in a minor proportion (37.4 wt%).

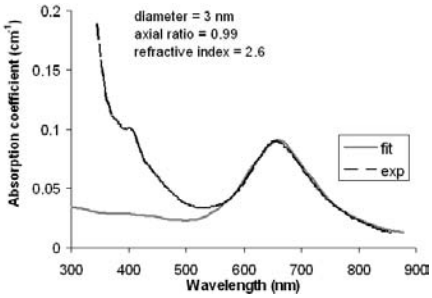


Fig. 3. OA spectrum (black dotted line) of the crystalline TiO_2/Au film. The calculated optical absorption spectrum (grey solid line) was obtained by Gans theory.

3.3 HRTEM measurements. Figure 4 shows the HRTEM images of the crystalline TiO_2/Au film. Figure 4 (a) shows gold NP's which were identified as brilliant particles. Figure 4 (b) shows the reflection (101) which corresponds to the anatase phase; and the reflection (111) corresponds to the gold nanoparticle identified as Au_3O_2. The inset shows the diffraction patterns showing these reflections. From HRTEM studies taking into account a population of gold NP's, the corresponding size-distribution histograms were obtained. The distributions from the major axis A and minor length axis B and their respective standard deviations are A = 9.8 ± 7.8 nm and B = 6.6 ± 3.9 nm, respectively.

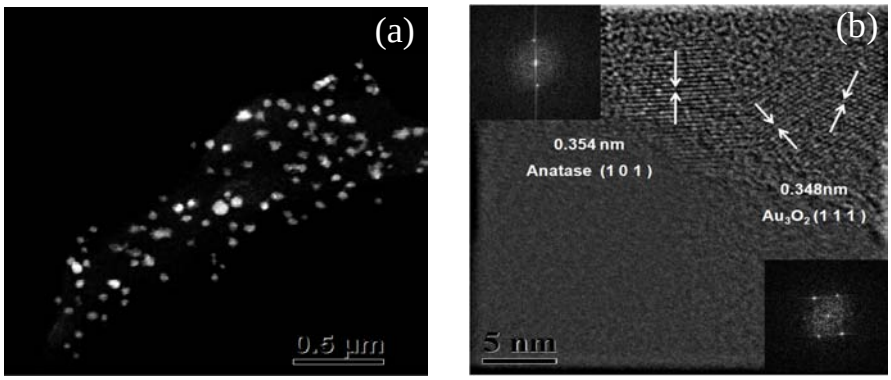


Fig. 4. (a) HRTEM image of the crystalline TiO_2/Au film exhibits several gold NP's. (b) The reflections correspond to anatase nanocrystals and gold nanoparticles were identified with white arrows.

3.4 Photoconductivity studies. Usually [6] Ohm's law under light illumination is given by

$$\vec{J} = \vec{J}_{ph} + (\sigma_d + \sigma_{ph})\vec{E} \tag{1}$$

where $\vec{J}_{ph}$ is the photovoltaic current density and σ_{ph} is the photoconductivity. When the current densities are assumed to be parallel to the electric field $\vec{E}$ Eq. (1) becomes into the next one:

$$J = \frac{e\phi l_0 \alpha I}{h\nu} + \left(\sigma_d + \frac{e\phi\mu\tau\alpha I}{h\nu}\right)E \tag{2}$$

with ϕ as the quantum efficiency of charge carrier photogeneration, l_0 as the charge carrier mean free path, α as the sample absorption coefficient, I as the light intensity at the frequency ν of illumination, h as the Planck´s constant and τ as the charge carriers mean lifetime. The first term is the photovoltaic transport effect, the second one is the dark conductivity $\sigma_d = en_0\mu$ (n_0 is the carrier density that produces dark conductivity and μ is the charge mobility), and the third one is the photoconductivity itself.

Eq (2) can be written as:

$$J = A_1 E + J_0 \quad (3)$$

From the absorption spectrum of crystalline film (Fig. 2), the illumination wavelength for photoconductivity studies were chosen: 645 nm that corresponds to the maximum absorption band and 515 nm were there is no absorption. Photoconductivity results of amorphous and crystalline TiO_2 films with gold NP's are shown in Figure 5. Current density as function of electric applied field on the film was plotted. The experimental data were fitted by least-squares with straight lines at darkness and under illumination. This indicates an ohmic behaviour. The linear fits are shown in Table 2.

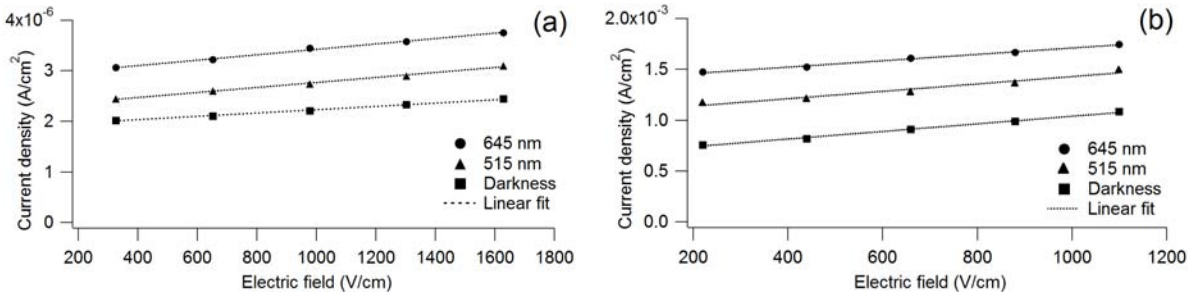


Fig. 5. Plots of current density vs. electric field spectra for (a) amorphous and (b) crystalline TiO_2/Au films. Linear fits correspond to the dotted lines.

For both kinds of TiO_2/Au films, when the illumination wavelength decreases the J_0 value decreases. For crystalline film, when the illumination wavelength decreases, the slope A_1 increases. It indicates a strong photoconductive behavior in these films.

Table 2. Linear fittings of amorphous and crystalline TiO_2 films.

λ (nm)	TiO_2/Au film	A_1	J_0
645	Crystalline	3.14×10^{-7}	1.40×10^{-3}
	Amorphous	5.36×10^{-10}	2.89×10^{-6}
515	Crystalline	3.64×10^{-7}	1.07×10^{-3}
	Amorphous	4.97×10^{-10}	2.27×10^{-6}
Darkness	Crystalline	3.73×10^{-7}	6.66×10^{-4}
	Amorphous	3.32×10^{-10}	1.89×10^{-6}

4. CONCLUSIONS

High optical quality crystalline TiO_2 films with gold NP's were obtained by sol-gel process. XRD measurements reveal the presence of the anatase and rutile phases, which were produced after sintering treatment of 520 °C for 2 h. The anatase phase has a bigger proportion (59.75 wt%) than the rutile phase (37.4 wt%). The optical absorption spectrum was very well fitted using Gans theory considering a local refractive index $n_{local} = 2.6$. This index is related to refractive index from crystal phases, anatase and rutile, taking into account that the anatase is the major phase. The experimental data J vs E were fitted by straight lines corresponding to an ohmic behaviour. Crystalline TiO_2/Au films exhibit a strong photoconductive effect. Anatase phase leads a better conduction of the carriers than the amorphous phase.

ACKNOWLEDGMENTS

The authors acknowledge the financial supports of CONACYT 79781, NSF-CONACYT, PUNTA, ICYTDF and PAPIIT 116506-3. GVA is grateful for PUNTA fellowship. The authors are thankful to M. in Sci. Manuel Aguilar-Franco (XRD), Luis Rendón (HRTEM), Roberto Hernández-Reyes (SEM) and Diego Quiterio (preparation of the samples for SEM studies) for technical assistance.

REFERENCES

1. Suarez, R., P. K. Nair and P. V. Kamat, "Photoelectrochemical Behavior of Bi_2S_3 Nanoclusters and Nanostructured –Thin Films", *Langmuir*, 14, 12, 3236-3241, 1998.
2. Shaogui, Y., Q. Xie, L. Xinyong, L. Yazi, C. Shuo and C. Guohua, "Preparation, characterization and photoelectrocatalytic properties of nanocrystalline Fe_2O_3/TiO_2, ZnO/TiO_2, and $Fe_2O_3/ZnO/TiO_2$ composite film electrodes towards pentachlorophenol degradation", *Phys. Chem. Chem. Phys.*, 6, 3, 659-664, 2004.
3. Graziani Garcia, C., N-Y. Murakami Iha, R. Argazzi and C.-A. Bignozzi, "4-Phenylpyridine as ancillary ligand in ruthenium (II) polypyridyl complexes for sensitization of n-type TiO_2 electrodes", *J. Photochem. Photobiol. A: Chem.*, 115, 3, 239-242, 1998.
4. Dueñas, S., H. Castán, H. García, E. San Andrés, M. Toledano-Luque, I. Mártil, G. González-Díaz, K. Kukli, T. Uustare and J. Aarik, "A comparative study of the electrical properties of TiO_2 films grown by high-pressure reactive sputtering and atomic layer deposition", *Semicond. Sci. Technol.*, 20, 10, 1044-1051, 2005.
5. Hu, L., T. Yoko, H. Kosuka and S. Sakka, "Effects of solvent on properties of sol-gel derived TiO_2 coating films", *Thin Solid Films*, 219, 1-2, 18-23, 1992.
6. García M., J., G. Valverde, D. Cruz, A. Franco, J.I. Zink and P. Minoofar, "Structure and PPV concentration effect on the Photoconductivity response from mesostructured silica films", *J. of Phys. Chem. B*, 107, 10, 2249-2252, 2003.
7. Wilson, G. J., A. S. Matijasevich, D. R. G. Mitchell, J. C. Schulz and G. D. Will, "Modification of TiO_2 for Enhanced Surface Properties: Finite Ostwald Ripening by a Microwave Hydrothermal Process", *Langmuir*, Vol. 22, No. 5, 2016-2027, 2006.
8. Manera, M. G., J. Spadavecchia, D. Busoc, C. de Julián Fernández, G. Mattei, A. Martucci, P. Mulvaney, J. Pérez-Juste, R. Rella, L.Vasanelli and P. Mazzoldi, "Optical gas sensing of TiO_2 and TiO_2/Au nanocomposite thin films", *Sensors and Act. B*, 132, 1, 107-115, 2008.
9. Shen, W., F. G. Liu, J. Qiu, and B. Yao, "The photoinduced formation of gold nanoparticles in a mesoporous titania gel monolith", *Nanotechnology*, 20, 10, 105605, 2009.
10. Yu, J., L. Yue, S. Liu, B. Huang and X. Zhang, "Hydrothermal preparation and photocatalytic activity of mesoporous Au–TiO_2 nanocomposite microspheres", *J. Colloid and Interf. Sci.*, 334, 1, 58–64, 2009.
11. Ito, A., H. Masumoto and T. Goto, "Optical Properties of Au Nanoparticle Dispersed TiO_2 Films Prepared by Laser Ablation", *Materials Transactions*, 44, 8, 1599-1603, 2003.
12. Brinker, C. J., G. C. Frye, A. J. Hurd and C. S. Ashley, "Fundamentals of sol-gel dip coating", *Thin Solid Films*, 201, 1, 97-108, 1991.
13. Rentería, V. M. and J. García–Macedo, "Influence of the local dielectric constant on modeling the optical absorption of silver nanoparticles in silica gels", *Colloids and Surfaces A: Physicochem. & Eng. Aspects*, 278, 1-3, 1-9, 2006.
14. Wang, Z., U. Helmersson and P.-O. Käll, "Optical properties of anatase TiO_2 thin films prepared by aqueous sol–gel process at low temperature", *Thin Solid Films*, 405, 50–54, 2002.

Optical Multistability in 1D Photonic Crystals with Nonlinear Thue-Morse Structure

E. Lotfi [a,b], K. Jamshidi-Ghaleh [c,d] F. Moslemi [a], and H. Masalehdan [d, e] *

[a] Faculty of Bonab Engineering and Technology, Bonab, Iran

[b] Rice University, 6100 Main street, Houston, TX 77005, USA

[c] Department of Physics, Azarbaijan University of Tarbiat Moallem, Tabriz, Iran

[d] Department of Physics Engineering (Optics-Laser), Islamic Azad University, Bonab Branch, Iran.

[e] Smithsonian Institute, Washington, D.C. 20013-7012, USA

[*]corresponding author: H.Masalehdan@Gmail.com

Abstract- A 1D photonic crystal structure contains 16 layers, 8 common dielectric layers and 8 layers with nonlinear medium, with an arrangement similar to 5th generation, Thue-Morse multilayer is presented. The properties of photonics band-gap, field distribution and optical multistability are investigated. On the band gap, 5 resonant modes is observed. On the behaviour of output intensity versus input intensity around resonant frequencies, the multistability response observed. When the frequency of incident field is close to the resonant frequency, the threshold intensity of multistability is decreased.

1. INTRODUCTION

Photonic crystals are arrays of materials with different optical characteristics which have been considered as one of the major research topics due to their electromagnetic applications and unique properties [1-3]. Different structures of the photonic crystals have already been considered as the periodic and quasi-periodic arrays. Different kinds of materials are used in designing of the photonic crystals such as the typical linear and nonlinear dielectric materials [1-4], metals [5], metamaterials (materials with negative refractive index) [6], superconductors [7], dispersive media [8], materials with gradient refractive index [9] etc. Photonic crystals show unique features based on various structural arrangements, materials used on the structure and the number of underlying structural layers. One of the newly introduced structures in photonic crystals with quasi-periodic arrays is Thue-Morse structures [10]. It has different successive generations in different arrangements and various number of layers (For instance, the 2nd generation appears as AB, the 3rd generation as ABBA, the 4th generation as ABBABAAB and the 5th generation appears as ABBABAABBAABABBA in which A and B are typical dielectric materials).

In this work, we propose a new photonic crystal structure multilayer similar to the 5th generation Thue-Morse multilayer (5GTM) structure in layer's arrangement but different in the aspect that all B layers are replaced with a nonlinear medium. Fig.1 shows a schematic view of the proposed photonic crystal structure. One of the major characteristics exhibited by photonic crystals containing a nonlinear medium is the ability of displaying optically bistability and multistability [11] i.e. for a single input intensity there exist two or more output intensities. Bistabile optical devices have been applied in many optoelectronic applications such as photo-memories,

photo-diodes, photo-switches and so on. Achieving a low intensity threshold of bistability of multistability is a major objective for researchers nowadays. We will show that the introduced photonic crystal not only presents a bistable operating feature but also a multistable property around and near the resonance-mode frequencies appearing in the energy gap.

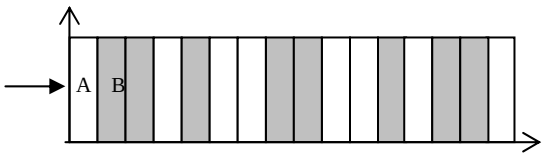


Fig. 1. Schematic of the 5GTM multilayer. Here A and B are typical linear dielectric and nonlinear media respectively.

2. THORETICAL MODEL

In Fig.1, we consider an electromagnetic wave at TE polarization normally incident on the photonic crystal structure. If we assume the z-axis to be the propagation direction (normal to layers surface) and enforce the boundary conditions dominant over the fields in the layers interface, the characteristic transmission matrix for the linear and nonlinear media would be as the following:

$$\mathrm{M}_A = \begin{pmatrix} \cos(k_A d_A) & \dfrac{-i}{q_A}\sin(k_A d_A) \\ -iq_A \sin(k_A d_A) & \cos(k_A d_A) \end{pmatrix} \tag{1}$$

$$\mathrm{M}_B = \frac{k_0}{k_+ + k_-}\begin{pmatrix} (k_-/k_0)\exp(-ik_+ d_B)+(k_+/k_0)\exp(ik_- d_B) & \exp(-ik_+ d_B)-\exp(ik_- d_B) \\ (k_- k_+/k_0^{\,2})[\exp(-ik_+ d_B)-\exp(ik_- d_B)] & (k_+/k_0)\exp(-ik_+ d_B)+(k_-/k_0)\exp(ik_- d_B) \end{pmatrix} \tag{2}$$

where $k_A = (\omega/c)\sqrt{\varepsilon_A}\sqrt{\mu_A}$, $\mathrm{q_A} = \sqrt{\varepsilon_A}/\sqrt{\mu_A}$ and $\mathrm{k_+}$, $\mathrm{k_-}$ are propagating constants of the forward and the backward propagation waves defined as:

$$\mathrm{k_\pm} = \mathrm{k_0}\sqrt{\varepsilon_B}\sqrt{\mu_B}\sqrt{1+\chi^{(3)}(|\xi_\pm|^2 + 2|\xi_\mp|^2)} \tag{3}$$

in which $\mathrm{k_0} = \omega/\mathrm{c}$ and $\chi^{(3)}$ is the third-order nonlinearity coefficient and $\xi_\pm$ is the range of the forward and the backward propagating waves. The overall transfer matrix for the 5GTM multilayer structure in question is obtained from the Eqs. (1) and (2):

$$M = M_A (M_B)^2 M_A M_B (M_A)^2 (M_B)^2 (M_A)^2 M_B M_A (M_B)^2 M_A. \tag{4}$$

Hence, after having computed the entries transfer metrics elements, m_{ij}, the related transmission coefficient from the photonic crystal structure is given by:

$$T = \left| \frac{2n_0}{(m_{11} + m_{12}n_0)n_0 + (m_{21} + m_{22}n_0)} \right|^2 \quad (5)$$

where, n_0 is the refractive index of air. For the transmission intensity of U_t, the incident intensity is given by $U_{in} = U_t / T$.

3. NUMARICAL CALCULATIONS

In numerical computations, the layer A is chosen as a dielectric medium with the dielectric constant of $\varepsilon_A = 5.29$ and B is a nonlinear medium with $\varepsilon = \varepsilon_B + \chi^{(3)} |E(z)|^2$, in which ε_B is the linear dielectric constant of the medium calculated to be 1.71 and $\chi^{(3)}$ is the 3rd order nonlinear susceptibility. The optical thickness of the both layers, are $\lambda/4$, i.e. $\sqrt{\varepsilon_A \mu_A} d_A = \sqrt{\varepsilon_B \mu_B} d_B = \lambda/4$ where λ is the wavelength of the incident field in vacuum and is supposed to be 7.8422 μm .Both of the A and B layers are assumed to be non-magnetic; $\mu_A = \mu_B = 1$. Transmission spectrum of the proposed structure is presented in the Fig.2 (curve 1, red color). To compare the transmission spectrum of the corresponding periodic structure of type the $(AB)^8$ with the same number of layers is also presented by the Curve 2 (blue color). It can be seen that there are fundamental differences in the band gap region of the proposed structure compared to the periodic one. First, the gap region is widened and the second one is the appearance of the several sharp peaks so-called resonate modes. These resonate peaks are placed from the left to the right at 29.15 THz, 35.68 THz, 38.25 THz, 40.83 THz and 47.36 THz frequencies respectively. The frequency of the incident wave is chosen the same as the central resonant mode frequency (38.25 THz).

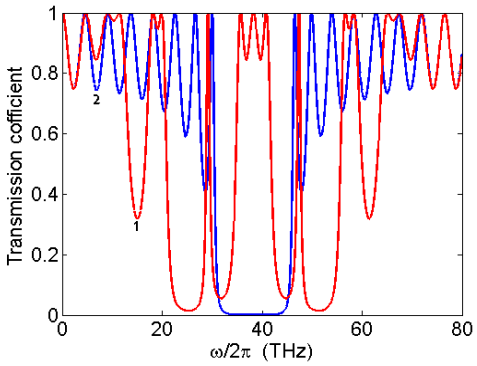


Fig. 2. Shows the linear transmission of the 5GTM (red) and the corresponding periodic structure $(AB)^8$ (blue) with the same number of layers.

The dynamic displacement of the band-gap edge and strong field localization at the defect modes [12] are two physical mechanisms that appear at the peaks. In order to determine how these resonate modes are created, the distribution of the field strength over distance in layers direction is carried out using the transmission matrix.

This distribution is graphically shown in Fig.3 for two resonating frequencies of 38.25 THz and 47.36 THz.

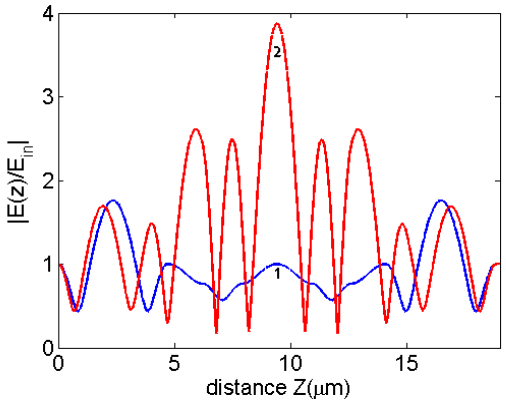
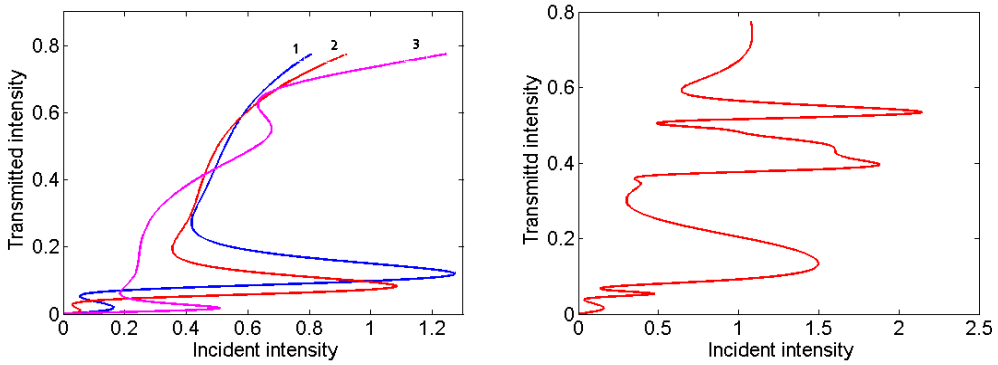


Fig. 3. The distribution of the electric field intensity inside the 5GTM structure on two the resonating frequency of 38.25 THz (curve 1, blue color) and 47.36 9 THz (curve 2, red color)

Fig.4 shows the behavior of the transmission intensity versus the incident intensity from the 5GTM structure on three frequencies close to the resonant mode frequency of 47.36 THz, labeled by curve 1; 45 THz, curve 2; 45.8 THz and curve 3; 48.88 THz. On all of the three frequencies, the bistability behavior is observable. For frequency closer to the incident field frequency, curve 3, lower threshold intensity for the optical bistability is achievable.



A **B**

Fig. 4.A. The behavior of transmission intensity versus incident intensity at three different frequencies of, 45 THz, 45.8 THz and 48.88 THz close to the 47.36 THz. **Fig. 4.B.** Shows the behavior of transmission intensity over incident intensity in the frequency at the 45.8 THz and optical thickness of $\lambda/2$.

The Fig.4.B shows the behavior of the output intensity versus of the incident intensity for the case that the optical thickness of nonlinear layers (B) is the half of the wavelength, $\lambda/2$. It can be seen that the number of multistablities increase while the threshold intensity decreases compared to the former state (Fig.4 curve 2)

4. CONCLUSIONS

The characteristics of the energy gap, field distribution, and optical bistability and multistability of photonic crystals with a similar structure to the 5GTM multilayer consisting of 8 nonlinear layers are studied in this work. In the band gap region of this structure, 5 resonating modes are observed. The behavior of the optical multistability is seen in the nearby the resonance frequency. At those frequencies, the threshold intensity of the optical multistability is decreased and also by increasing the thickness of the nonlinear media, the number of the multistabilities decreases while the intensity threshold decreases.

REFERENCES

1. Wang, F.Y., G. X. Li, H. L. Tam, K. W. Cheah and S. N. Zhu, "Single longitudinal mode and optical bistability Tm,Ho:YLF lasers at room temperature," .*Appl. Phys. Lett*. 92 211109-211111, 2008

2. Hou P., Y. Chen, J. Shi, Q. Kong, L. Ge, and Q. Wang, "Transmission property for a one-dimensional photonic crystal containing a subwavelength layer and a nonlinear layer," *Appl. Phy. A*, 91, 41-46, 2008

3. Hou P., Y. Chen, X. Chen, J. Shi, and Q. Wang, "Anomalous bistable shift for a one-dimensional photonic crystal doped with a subwavelength layer and a nonlinear layer," *Phy. Rev. A*, 75, 045802, 2008

4. Mandal, B. and A. R. Chowdhury, "Spatial soliton scattering in a quasi phase matched quadratic media in presence of cubic nonlinearity," *J. of Electromagn. Waves and Appl.*, Vol. 21, No. 1, 123–135, 2007

5. Jian Z., Pearce J. and Mittleman D.M, "Two-dimensional photonic crystal slabs in parallel-plate metal waveguides studied with terahertz time-domain spectroscopy," *Semicond. Sci. Technol.* 20 No 7, 300-306 July 2005

6. Li, J. L. Zhou, C.T. Chan and P. Sheng, "Photonic Band Gap from a Stack of Positive and Negative Index Materials," *Phys. Rev. Lett.* 90, 083901, 2003

7. Chien, J. W. and J. Y. Tzong , "Anomalous Microwave Transmission in a Superconducting Periodic Multilayer Structure" *PIERS ONLINE*, Vol. 4, No. 8, 801-805, 2008

8. Lyubchanskii, I. L., Dadoenkova, N. N., Zabolotin, A. E., Lee, Y. P. and Rasing, Th. "A one-dimensional photonic crystal with a superconducting defect layer," J. Opt. A: Pure Appl. Opt. 11 114014, 2009

9. Monsouriu J. A., R. A. Depine and E. J. Silvestre, "Non-Bragg band gaps in 1D metamaterial aperiodic multilayers," *Europ. Optic. Soci*. 2, 07002-1-5, 2007

10. Xu, G. T. Pan, T. Zang and G. San, "Optical multistability in nonlinear negative index Fibonacci multilayers," Phys. Lett. A. 372 , 4958-4961, 2008

11. Lavrinenko, A.V. S. V. Zhukovsky, K. S. Sandomirskii and S. V. Gaponenko, "Propagation of classical waves in non-periodic media: Scaling properties of an optical Cantor filter", *Phys. Rev. E* 65 pp. 036621/1-8, 2002

Imaging of surface plasmon polariton interference using phase-sensitive Photon Scanning Tunneling Microscope

J. Jose*, **F. B. Segerink**, **J. P. Korterik**, **J. L. Herek**, **and H. L. Offerhaus**

Optical Sciences group, Mesa$^+$ Institute for Nanotechnology,
University of Twente, 7500 AE, Enschede, The Netherlands
*j.jose@tnw.utwente.nl

Abstract— We report the surface plasmon polariton interference, generated via a 'buried' gold grating, and imaged using a phase-sensitive Photon Scanning Tunneling Microscope (PSTM). The phase resolved PSTM measurement unravels the complex surface plasmon polariton interference fields at the gold-air interface.

1. INTRODUCTION

One prominent development in the field of optical microscopy date back to 1989, when Reddick *et al* [1] developed a new form of scanning optical microscope called Photon Scanning Tunneling Microscope (PSTM). The operating principle of PSTM is based on the generation of evanescent waves by total internal reflection of a light beam followed by its frustration using a sharpened optical fiber probe. Observed first in 1957 [2], Surface Plasmon Polaritons (SPPs) excited at a metal-dielectric interface were found to inherit many properties of the evanescent waves, except that the fields associated with the SPPs decays exponentially into both sides of the metal-dielectric interface. SPPs are charge density waves that can be optically excited on the metal - dielectric interface when the in-plane wave vector component of the incident photon (k_x) matches the SPP wave vector (k_{sp}) [3]. Excitation of multiple SPP modes by patterning the metal surface have found a range of applications like surface plasmon interference nanolithography [4], photonic band gap materials [5], sensing devices [6]. However, there has not been an attempt made to separate the different SPP modes excited on a patterned metal surface.

A conventional PSTM measurement [7, 8] on a patterned metal surface yields only the intensity of the optical field. In order to separate multiple SPP modes, one should measure both amplitude and phase of the optical field on the metal surface. In this work, we use a heterodyne interferometric (or phase-sensitive) PSTM [9, 10, 11, 12, 13] to measure the complex SPP interference, generated on a gold-air interface by simultaneously driving two SPP modes on the interface: one using prism coupling and another using grating coupling [3]. The interference between the two SPP modes, having same energy and propagating in different in-plane directions, manifests as a beating pattern formed along the direction of k_x. The two SPP modes are separated by filtering the desired wave vectors in the 2D Fourier Transform image of the total optical field [11].

The paper is organized as follows. Section 2 explains the different steps involved in the fabrication of a gold buried grating. In Sec. 3, we explain the phase matching condition for the simultaneous excitation of two SPPs and the experimental procedure to acquire the phase-sensitive PSTM images of the SPP interference. The PSTM images showing the interference of two SPPs along with discussions and conclusion are presented in Sec. 4 and Sec. 5 respectively.

2. FABRICATION OF BURIED GRATING

In a Kretchmann-Raether (KR) configuration [14] of SPP excitation, a periodic corrugation of the metal-air interface scatters the SPPs at that interface into radiation. The scattering can be minimized by turning the grating upside down to form a 'buried grating'. The glass-metal interface is corrugated leaving a flat metal layer on top to support SPPs [15]. The steps to fabricate a buried gold grating are illustrated in Fig. 1. A 0.5 duty cycle linear grating, with period of 1.65 μm and depth of 50 nm, is milled into a 0.15 mm thick glass cover slip using a Focused Ion Beam (FIB) (Fig. 1(b)). A thin layer of gold-palladium mixture is deposited on the cover slip prior to the milling action to eliminate charging effects(not shown). The grooves are subsequently filled with gold again using the FIB together with a gold gas injection system (Fig. 1(c)). A 50 nm thick gold layer is deposited on top of the grating using electron beam evaporation technique (Fig. 1(d)). A drift of the FIB and an inaccurate dwell time for the deposition of gold causes a FIB positioning error and hence an over/under filling of the grooves.

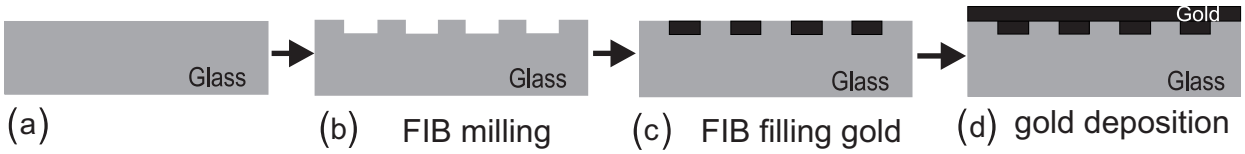


Figure 1: Schematic illustrating fabrication of a gold buried grating.

3. EXPERIMENTAL PROCEDURE

The buried gold grating is placed on a glass (BK7) hemispherical prism with index matching oil in between. The hemispherical prism is mounted on a convenient rotating stage providing an azimuthal rotation angle ranging from 0° to 90°, in steps of 0.5°. A fiber collimator, mounted on a goniometric stage for angles ranging from 42° to 50.8° illuminates the sample from the prism side [13]. A polarizer ensures an input beam polarized in a direction perpendicular (p) to the plane of incidence. Figure 2(a) shows the reciprocal space representation of the phase matching condition

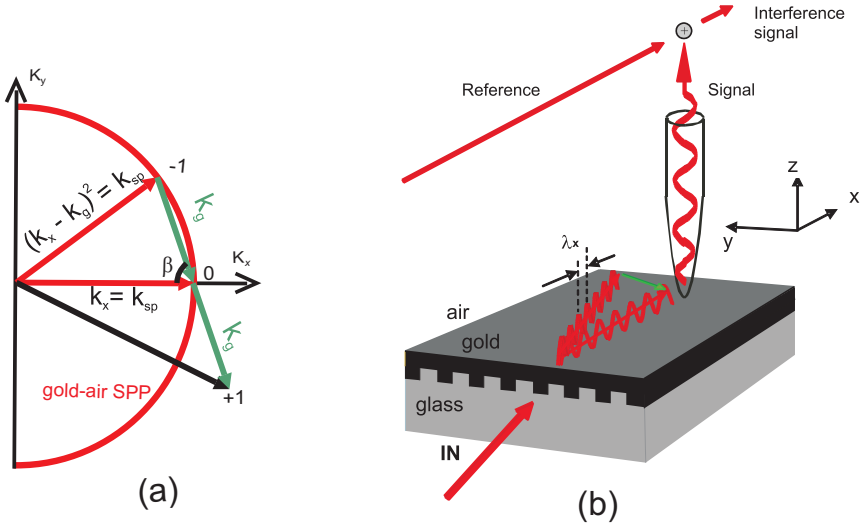


Figure 2: (a) Reciprocal space representation of the theoretical phase matching condition to excite two SPP modes by the in-plane rotation of k_g, (b) Schematic illustration of a heterodyne interferometric PSTM

to excite two SPPs at the gold-air interface. The incident light couples to SPPs when $k_x = k_{sp}$. The grating wave vector (k_g) is rotated in-plane by an angle β such that the -1st evanescent diffracted order couple to SPPs. The evanescent waves associated with the 0th or the -1st diffracted order cannot couple to SPPs at the periodic glass-gold interface due to the higher momentum of SPPs at that interface [3]. Hence the coupling between the SPPs through the gold film is not relevant in this particular study.

The principle of the phase-sensitive PSTM imaging of two SPP modes is shown in figure 2(b). The laser light (657.3 nm vacuum wavelength) is split into two branches: one forms the reference branch of the interferometer and the other forms the signal branch that illuminates the sample. The optical frequency in the reference branch is shifted by 100 KHz using two acousto optic modulators. A metal-coated optical fiber probe raster scans the gold surface. The photon-tunneling signal, picked up by the fiber probe, combines with the signal in the reference branch in a 2 x 2 fiber coupler (heterodyne mixing). The interference signal from the two outputs of the fiber coupler is 180° out of phase with each other. A balanced detection scheme [16] is used to cancel the noise in the reference signal and enhance the intensity of the difference signal. The signal is measured using a photodiode and a dual-phase Lock-in-Amplifier(LIA) to extract the amplitude and the phase of the optical field. The PSTM is operated in constant distance mode using tuning fork shear-force feedback [17]. Thus topographical information and complex optical field on the gold surface are simultaneously retrieved.

4. MEASUREMENTS AND DISCUSSION

A phase-sensitive PSTM measurement on the buried gold grating is presented in figure 3. The topography of the grating shows a residual modulation of 34.5 ± 3.9 nm on the surface due to an over-filling of the grating grooves. A comparison between the topography and the optical amplitude

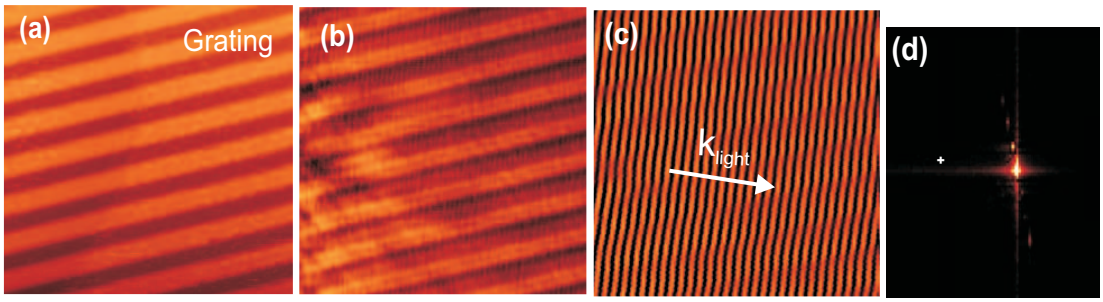


Figure 3: PSTM measurement of a gold buried grating for a scan range of $13.3 \times 18.5 \mu m^2$. (a) The measured topography with dark regions correspond to valleys and brighter regions to peaks, (b) the measured optical amplitude on the gold surface, (c) the measured optical amplitude times cosine of the phase, (d) Intensity of the 2D fourier transform of the total optical field with an area of $4.6 \times 6.4 \mu m^2$. The white cross indicates the zero-frequency point in the fourier image.

images shows that the optical amplitude is minimum where the topography shows a maximum and vice versa. The former behaviour can be attributed to an over-filling of the grooves, mentioned in Sec. 2, which leads to an under-coupling of the prism-coupled SPPs. The minimum in the topography image corresponds to the optimum thickness (50 nm) to excite prism-coupled SPPs [3] and hence we see a maximum in the optical amplitude. In the real part of the total optical field, shown in Fig. 3(c), we can see a plane wave whose wave vector lies in the plane of incidence. In order to separate the different plane waves present in the optical field image, a Fast Fourier Transform (FFT) of the total optical field is taken. A zoom-in region of the intensity of the 2D FFT of the total optical field is shown in Fig. 3(d). There is an intense spot in the image which corresponds to the 0th order evanescent wave. The intensity spots corresponding to the evanescent diffracted orders are seen on either side of the 0th order spot. The 0th, -1st and the $+1^{st}$ diffracted

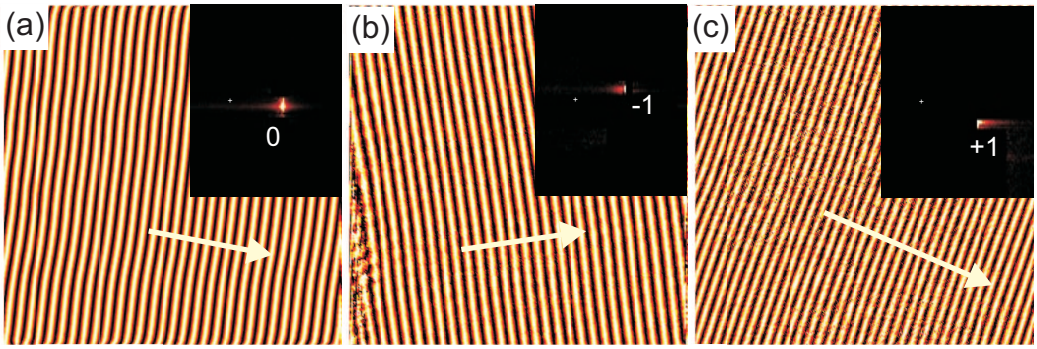


Figure 4: Two-dimensional Fourier analysis of the optical field excited using a gold buried grating for a scan range of $13.3 \times 18.5 \mu m^2$. The wavelength component of the SPP mode coupled by the (a) 0th order evanescent wave, (b) -1st evanescent diffracted order. (c) The wavelength component of the $+1^{st}$ diffracted order having a higher spatial frequency. The cosine of the optical phase is shown. Insets shows the 2D FFT of the different orders filtered from Fig. 3(d) with an area of $4.6 \times 6.4 \mu m^2$. The white cross indicates the zero-frequency point in the fourier image.

orders are filtered from the 2D FFT image shown in Fig. 3(d) and shown separately in Fig. 4(a-c). Investigating those components by Fourier back transformation gives three plane waves which propagate under different angles. The angle between the plane waves shown in Fig. 4 (a) and (b) is 19.3°. That means the two SPP modes, coupled individually by the prism and the buried grating,

are at an angle of 19.3° with respect to each other. The $+1^{st}$ evanescent diffracted order has a shorter wavelength, as expected from the phase matching diagram shown in Fig. 2(a).

5. CONCLUSION

In conclusion, the complex SPP interference generated at a gold-air interface using a gold buried grating has been measured with sub-wavelength resolution using a phase-sensitive PSTM. Fourier analysis untangles the interfering fields and reveals the excitation of two SPP modes propagating under different angles. We believe that the capability of a phase-sensitive PSTM to separate the SPP modes will find application in the optical characterization of other plasmonic (nano)structures with sub-wavelength resolution.

ACKNOWLEDGMENT

The authors thank professor Kobus Kuipers for his valuable comments. This work is supported by NanoNed, a nanotechnology program of the Dutch Ministry of Economic Affairs.

REFERENCES

1. Reddick, R. C., R. J. Warmack and T. L. Ferrell, "New form of scanning optical microscopy," *Phys. Rev. B*, Vol. 39, No. 1, 767–770, 1989.
2. Ritchie, R. H., "Plasma losses by fast electrons in thin films," *Phys. Rev.*, Vol. 1, No. 5, 874–881, 1957.
3. Raether, H., *Surface Plasmons on Smooth and Rough Surfaces and on Grating*, Springer, Berlin, 1988.
4. Liu, Z. W., Q. H. Wei, and X. Zhang, "Surface plasmon interference nanolithography," *Nano Lett.*, Vol. 5, No. 5, 957–961, 2005.
5. Kitson, S. C., W. L. Barnes, and J. R. Sambles, "Full photonic band gap for surface modes in the visible," *Phys. Rev. Lett.*, Vol. 77, No. 13, 2670–2673, 1996.
6. Romanato, F., K. H. Lee, H. K. Kang, G. Ruffato, and C. C. Wong, "Sensitivity enhancement in grating coupled surface plasmon resonance by azimuthal control," *Opt. Exp.*, Vol. 17, No. 14, 12145–12154, 2009.
7. Dawson, P., F. Defornel, and J. P. Goudonnet, "Imaging of surface-plasmon propagation and edge interaction using a photon scanning tunneling microscope," *Phys. Rev. Lett.*, Vol. 72, No. 18, 2927–2930, 1994.
8. Weeber, J. C., J. R. Krenn, A. Dereux, B. Lamprecht, Y. Lacroute, and J. P. Goudonnet, "Near-field observation of surface plasmon polariton propagation on thin metal stripes," *Phys. Rev. B*, Vol. 6404, No. 4, 2001.
9. Balistreri, M. L. M., J. P. Korterik, L. Kuipers, and N. F. van Hulst, "Local observations of phase singularities in optical fields in waveguide structures," *Phys. Rev. Lett.*, Vol. 85, No. 2, 294–297, 2000.
10. Nesci, A., R. Dandliker, M. Salt, and H. P. Herzig, "Measuring amplitude and phase distribution of fields generated by gratings with sub-wavelength resolution," *Opt. Comm.*, Vol. 205, No. 4-6, 229–238, 2002.
11. Fluck, E., M. Hammer, A. M. Otter, J. P. Korterik, L. Kuipers, and N. F. van Hulst, "Amplitude and phase evolution of optical fields inside periodic photonic structures," *J. Lightwave Technol.*, Vol. 21, No. 5, 1384–1393, 2003.
12. Offerhaus, H. L., B. van den Bergen, M. Escalante, F. B. Segerink, J. P. Korterik, and N. F. van Hulst, "Creating focused plasmons by noncollinear phasematching on functional gratings," *Nano Lett.*, Vol. 5, No. 11, 2144–2148, 2005.
13. Jose, J., F. B. Segerink, J. P. Korterik, and H. L. Offerhaus, "Near-field observation of spatial phase shifts associated with Goos-Hanschen and Surface Plasmon Resonance effects," *Opt. Exp.*, Vol. 16, No. 3, 1958–1964, 2008.
14. Kretschmann, E, and H. Raether, "Radiative deacy of nonradiative surface plasmons excited by light," *Z.Naturforsch.A*, Vol. 23, 2135–2136, 1968.
15. Schroter. U., and D. Heitmann, "Grating couplers for surface plasmons excited on thin metal films in the Kretschmann-Raether configuration," *Phys. Rev. B*, Vol. 60, No. 7 4992–4999, 1999.
16. Stierlin, R., R. Battig, P. D. Henchoz, and H. P. Weber, "Excess-noise suppression in a fiberoptic balanced heterodyne-detection system," *Opt. Quan. Electr.*, Vol. 18, No. 6, 445–454, 1986.

17. Ruiter, A. G. T., J. A. Veerman, K. O. vanderWerf, and N. F. vanHulst, "Dynamic behavior of tuning fork shear-force feedback," *Appl. Phys. Lett.*, Vol. 71, No. 1, 28–30, 1997.

Calculation of Surface Impedance for High Impedance Surface

Y. Zhu[1], **and S. Zouhdi**[1]

[1]Laboratoire de Genie Electronique de Paris, France
yu.zhu@supelec.fr

Abstract— Different analytical and numerical methods of calculating the surface impedance of a high impedance surface (HIS) structure have been studied and compared, but most of them limit to the symmetric planar structures. In this article, two new approaches of estimating the surface impedance are proposed and are applied to more general HIS structures (including an asymmetric planar structure). These new numerical methods based on 'the three dimensional finite element method (FEM) using edge element'.

1. INTRODUCTION

The HIS has always been a good candidate for improving low-profile antennas' performance [1, 2]. Within a certain frequency band, it can enhance the gain of antennas while simultaneously suppressing surface waves. As a benefit from these two properties, a better coupling to the surrounding circuits and more desirable antenna's radiation patterns can be achieved [3].

A large number of structures are proposed and investigated, within which the mushroom structure is the classical HIS design, originally introduced in [2]. It is composed of an FSS layer on the top and a grounded substrate, with embedded vertical metal vias.

The effective model [2] and the transmission-line model [6] are introduced and studied by resolving the analytical equations, which helps us to find appropriate design criteria. However, in face of these complicated structures and conditions, analytical methods are limited and rather pale. Thus many numerical methods have been proposed [8], such as the finite-difference time domain method (FDTD). In this work, the 'three dimensional finite element analysis using edge elements' [9, 10] is chosen as our numerical method.

This paper is organized as follows: In section II, we present the existing analytical solutions for calculating the surface impedance of two HIS symmetric structures. In section III, we propose our numerical model of calculating the surface impedance value by a home-made code and validate by comparing the analytical and numerical results. In section IV, we extend the method to asymmetric structure, following with some results and discussion. In the last section, a short conclusion is given and ended by a glimpse on potential applications.

2. ANALYTICAL MODEL FOR SYMMETRIC HIS STRUCTURE

In this section, a quick introduction to several analytical models is given and we concentrate on the calculation of the surface impedance which is one of the essential parameters to characterize the HIS' performances.

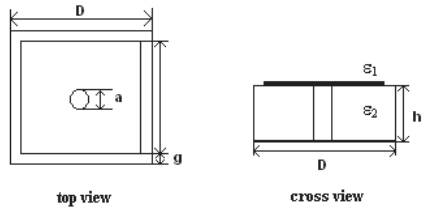


Figure 1: Geometry of one unit cell (the mushroom structure) figure

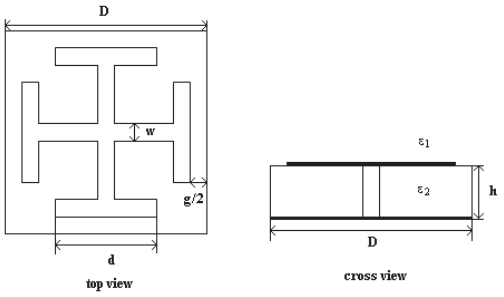


Figure 2: Geometry of one unit cell (the Jesusalem-cross structure) with D = 2.4mm, g = 0.15 mm, d = 1.8 mm, w = 0.4 mm, h = 1.6mm)

2.1. LC equivalent circuit for Mushroom Structure

The mushroom structure is studied first because of its simplicity. Since the period of the unit cell is largely smaller than the wavelength at the operating frequency, the mushroom structure is described as a parallel LC equivalent circuit by using an effective medium model in [2]. The frequency-dependent impedance of this parallel resonant LC circuit is given by:

$$Z_s(\omega) = \frac{j\omega L}{1-\omega^2 LC}. \tag{1}$$

Here, the capacitance L results from the gap between the neighboring patches and the inductance C results from the current flowing around a path through the vias and the bottom plate.

2.2. Transmission-line equivalent circuit for Mushroom Structure

In [7], analytical models of this mushroom structure are differently interpreted by the static (quasi-TEM) wave theory and the equivalent transmission-line approach is applied. The surface impedance is not uniform with respect to different incidence angles of the wave, so the TE and TM-polarization of the incident wave are considered. With the consideration of these two cases, Z_d is given by [5]:

$$Z_d^{TE} = \frac{j\eta_0}{\sqrt{\epsilon_r - \sin^2\theta}} \tan(k_{zd}h),\ Z_d^{TM} = \frac{j\eta_0}{\sqrt{\epsilon_r}} \tan(k_{zd}h), \tag{2}$$

The FSS grid impedance Z_g is considered in two different cases too by using the Babinet principle [5].

$$Z_g^{TE} = \frac{1}{\sqrt{j\omega C_g \cos^2\theta}},\ Z_g^{TM} = \frac{1}{j\omega C_g}, \tag{3}$$

2.3. Transmission-line equivalent circuit for Jerusalem-cross Structure

To get a more stable resonance, the self-resonant grid structure has been proposed instead of the grid of square patches and thin metal strips. The surface impedance Z_s will be less influenced by the incidence angle in the TM-case and a more uniform parameter can be achieved for a broad spectrum of TM spatial harmonics radiated by an antenna. That's why we are interested in this type of structure.

Considering as an approximate transmission-line model again, the surface impedance of JC structure is also solved by equation 2. The impedance for the dielectric layer Z_d is considered as the same case obtained from the mushroom structure's case. For the grid impedance Z_g, a unit cell of JC structure is treated as a LC resonant circuit composed of an effective capacitance and an inductance. With the consideration of TE and TM polarization, the formulas given by [5] are:

$$Z_g^{TE} = j\omega L_g^{JC} + \frac{1}{j\omega C_g^{JC}},\ Z_g^{TM} = cos^2\theta(j\omega L_g^{JC} + \frac{1}{j\omega C_g^{JC}}), \tag{4}$$

3. NUMERICAL MODEL FOR SYMMETRIC HIS STRUCTURES

3.1. The introduction of the numerical method

Since HIS structure is spatially periodic, our numerical model concerns a single unit cell of HIS structure. When the dimension of one unit cell is relatively small compared to the wavelength in the dielectric medium, the tangential component of electric field in the grid surface average on the grid period is proportional to the average current induced in the grid. This average current is equal to the jump of the tangential component of the average magnetic field across this grid surface [5]. With these definitions, the grid impedance Z_g is denoted by:

$$Z_g = \frac{< E_{t+} >}{< H_{t+} > - < H_{t-} >} \tag{5}$$

When we calculate the surface impedance Z_s, two different schemes are considered. One is half numerically computed and another is totally numerically computed. A general illustration is shown in Fig. 3. The difference between the HIS planar surface and the observation surface is denoted δh.

In scheme 1, we concentrate on the numerical by computed value of the grid impedance Z_g. First, the average numerical results of tangential electric and magnetic field are calculated on two surfaces near the HIS planar structure with a distance of δh on two sides. Then Z_g is calculated

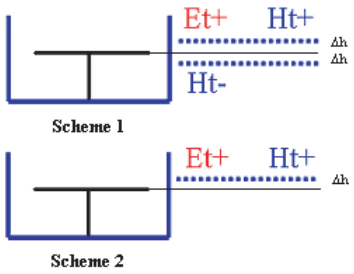


Figure 3: Two schemes of calculating surface impedance by numerical methods

by equation 8 with the average values obtained from the upper and the lower surface. Last, we get the surface impedance Z_s by a parallel combination of the grid impedance Z_g and the dielectric impedance Z_d. Here, Z_d keeps the analytical values defined in the last section. With this scheme, the surface impedance Z_s is given by:

$$Z_s = \frac{Z_{g(numerical)} \cdot Z_{d(analytical)}}{Z_{g(numerical)} + Z_{d(analytical)}}. \tag{6}$$

In scheme 2, we concentrate on the macro numerical results of the surface impedance. Only the average tangential electric field and magnetic fields on the plane above the HIS structure are calculated. It is assumed that all the electromagnetic information beneath the chosen surface has already been included on the surface. In this case, the numerical surface impedance is defined as:

$$Z_s = \frac{< E_{t+} >_{numerical}}{< H_{t+} >_{numerical}}. \tag{7}$$

3.2. Comparison of the surface impedance given by the analytical methods and numerical methods

We calculate the surface impedance through the analytical methods mentioned in the last section and the numerical methods with two different schemas illustrated in this section. Here, some comparisons are made among these methods. In order to have a comparable result, we choose the same period of one unit cell for both the mushroom structure and the Jerusalem structure.

Since all the structures here are symmetric for two orthogonal planar directions: x-axis and y-axis, the excitation is simplified to a normal incident electrical field with only x-component. Another orientation can be achieved by an only y-component E-field. Different boundary conditions are selected by considering the feature of periodicity and the orientation of the excitation. The substrate between the planar HIS structure and the ground is considered as a non-lossy dielectric media, thus the real part of Z_s is predicted to be zero and more attention is paid on the reactance.

In Fig. 4, we compared the surface impedance value calculated by two analytical methods and by our numerical methods with two different schemas. The maximum values are founded between 12.8 GHz to 14.4GHz, which means the resonant frequency has a difference around 2GHz among these methods.

The effective frequency band is another important criteria to judge the HIS structure's performance, but there is no common rule to define this range. Referring to [2], the useful frequency band is defined by the phase of the reflection coefficient, which is between $-90\,^\circ$ and $90\,^\circ$. The resonant frequency is expected at the point phase $= 0\,^\circ$ and the reflection coefficient is defined as $(Z_s - Z_0)/(Z_s + Z_0)$, where Z_0 is the free space impedance.

Fig. 5 showed the phase curves for the mushroom structure. For a further comparison, the result got from the commercial software Microwave Studio CST [11] is added too. The mushroom structure's dimension comes from [1]. Compared with the measurement values in this article, our numerical method with scheme 2 is more effective. As to the scheme 1, it appears less effective at high frequency, this is mainly caused by its half analytical calculations. For the transmission model, the result is less effective too, owing to the fact that the distributed capacitabce and inductances depend on frequency.

With the same period, but a Jerusalem planar structure, a similar resulat is obtained and a higher resonant frequency is achieved. In these cases, the excitation is a TE mode field with

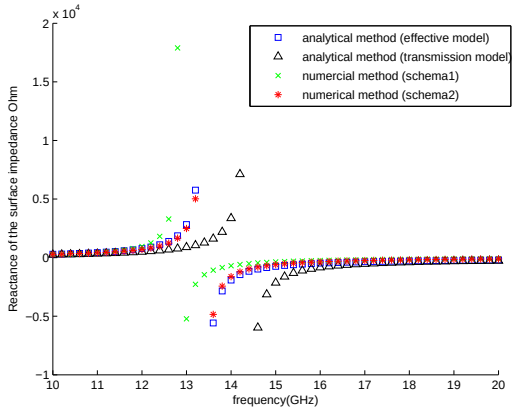


Figure 4: Comparison between analytical method and numerical method for surface impedance (Mushroom structure

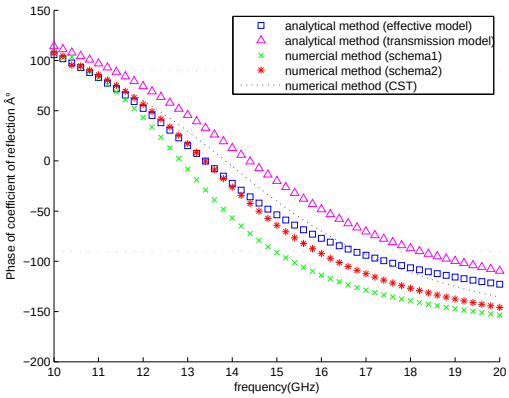


Figure 5: Comparison between analytical method and numerical method for phase of coefficient of reflection (Mushroom structure)

normal incidence, so no electric field will cross the via. This means that the influence of the via's presence is not so evident. Our model detected that the resonant frequency has a shift to lower frequency while adding the via into the structure. All these calculated results showed that this numerical method is valid.

4. THEORY OF CALCULATING SURFACE IMPEDANCE FOR ASYMMETRIC HIS STRUCTURE

4.1. Surface impedance matrix through the extension of 1D result

The planar HIS structure is located in the x−y plane, and the impedance of this surface can be generally expressed in a 2×2 matrix form as:

$$Z_s|_{(x-y)plane} = \begin{bmatrix} Z_{xx} & Z_{xy} \\ Z_{yx} & Z_{yy} \end{bmatrix} \tag{8}$$

Both the Mushroom structure and the Jerusalem structure are symmetrical planar HIS structures, with respect to the diagonal of the planar structure. Owing to these symmetries, the matrix of surface impedance can be simplified as:

$$Z_s|_{(x-y)plane} = \begin{bmatrix} Z_s & 0 \\ 0 & Z_s \end{bmatrix} \tag{9}$$

4.2. Introduction of calculating 2D surface impedance matrix for asymmetric structure

In section II and III, all the methods for calculating surface impedance offer us a one-dimensional value of Z_s. A two-dimensional surface impedance matrix is obtained by an extension of this 1D result, indicated in equation 9. But for an asymmetrical HIS structure, the equation 9 is no more available. Here, we introduce a new method for calculating a general impedance matrix without the limit of planar structure's geometry.

In our case, the problem of calculating the surface impedance for a HIS structure becomes the problem of resolving an approximate boundary condition. In Fig. 6, we adress the model of our problem, which resemble a waveguide. Inside a cubic box, delimiting domain D, an alternative electromagnetic field at angular frequency ω is created by the imposition of a uniform tangential field E on the top surface, denoted S_g. The whole boundary of domain D is denoted by ∂D. Considering the structure's periodicity and the excitation, two opposite perfect electric wall and two perfect magnetic wall are lined up at side walls. The HIS structure is beneath the surface $z = h$ and its planar structure is contained in the x−y plane. At the same time, a ground condition is applied to the bottom surface.

We cut our domain into two regions by the surface defined by $z = h$. The region below surface S is called interior system D_i and the region above is called exterior system D_e. The interior system with all its complexity is considered as a black box and it will be characterised by its input-output characteristic: the impedance boundary relation. Our goal is to obtain the relation between the

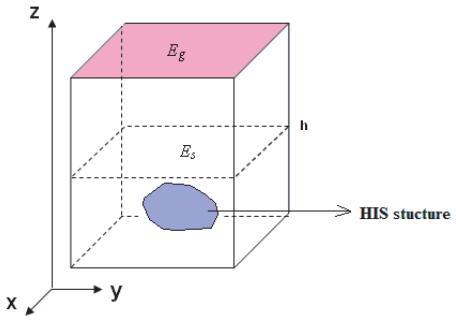


Figure 6: Model for sloving general HIS structure

averages $< H_s >$ and $< E_s >$ of the tangential magnetic and electric fields on S, which is expressed as:

$$n\times < H_s > +Y < E_s >= 0. \tag{10}$$

Here, mathematically, Y is a linear map between two-dimensional complex vectors, and physically, the admittance of the surface. The expected surface impedance matrix $Z_{2\times 2}$ can easily be obtained by inverting it.

Since the surface S is on the x−y plane, thus the tangential electric field E_s on this surface can be represented by its two non-zero components E_{sx} and E_{sy}, both complex numbers, same with H_s. Y is a 2×2 matrix, having four unknown values and only one excitation case is not enough to obtain it. Let us consider two different excitation vectors E_1 and E_2, to which will correspond the fields E_1, H_1 and E_2, H_2 in D. Four equations are obtained as follows:

$$\int_D (i\omega\epsilon E_i \cdot E_j + i\omega\mu H_i \cdot H_j) = -\int_s (Y \cdot E_{is}) \cdot E_{js}, (i, j = 1, 2) \tag{11}$$

Now, these four equations suffice to obtain the four entries of Y. This method of calculating surface impedance can be physically understood as the flux traveling through the surface.

Meanwhile, another procedure which consists in directly computing Y from the tangential electric and magnetic fields on the surface is proposed here. In the previous method, we have to know the field not only on the surface S but also in the whole interior domain. Now, the present method get the matrix Y merely from the tangential value obtained on surface S

With two different excitations, we calculate the x-component or y-component of the tangential fields on the surface, like E_{1sx} , H_{2sy}. Then we get the matrix Y by resolving the following equation.

$$\begin{bmatrix} -H_{1sy} & -H_{2sy} \\ H_{1sx} & H_{1sx} \end{bmatrix} = -Y \begin{bmatrix} E_{1sx} & E_{2sx} \\ E_{1sy} & E_{2sy} \end{bmatrix} \tag{12}$$

4.3. Results

We began our tests from the same symmetrical structure as before. The resulting impedance matrices are shown in Fig. 8 and Fig. 9. Theoretically, for the symmetric structure, $Z_{11} = Z_{22}$ and $Z_{12} = Z_{21} = 0$. Numerically, we get $Z_{11} \approx Z_{22}$ and $Z_{12} \approx Z_{21}$, except very near the resonant frequency. Z_{12} and Z_{21} are not zero, but are much smaller than the values of Z_{11} or Z_{22} (most of them are less than 5 per cent). These numerical errors are acceptable.

Compared with the result from 1D calculation, the 2D results reveal a lower resonant frequency: A difference of 2GHz for Mushroom stucture and 1GHz for Jerusalem Structure. In general, the numerical results are in accordance with the thereotical prediction and the proposed models are valid.

The case with a lossy substrate is also tested. We take example of Jerusalem structure and assume that the lossy substrate's relative permittivity $= 2.2 - j0.001$. In Fig. 9, compared with the ideal substrate's case, the admittance of Zs is no more zero, and the resonant frequency is a little bit higher.

A more complex F-like structure is chosen and tested. In order to have an isotropic HIS planar surface, each cell of HIS contains four F-like structures, shown in Fig. 10. To have an infinite network, we selected electric walls and magnetic walls as the boundary condition around the unit

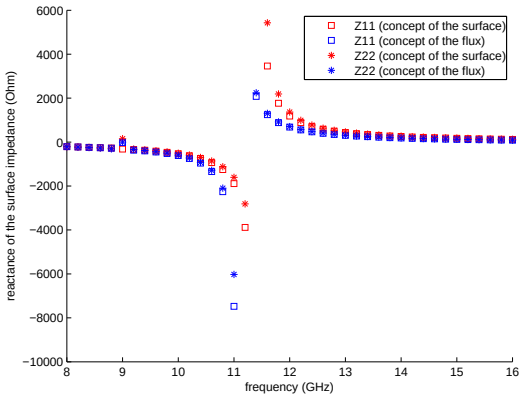


Figure 7: Surface impedance calculated by 2D method (Mushroom structure)

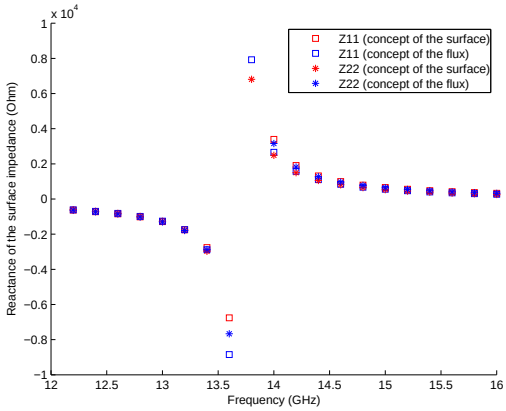


Figure 8: Surface impedance calculated by 2D method (Jerusalem structure)

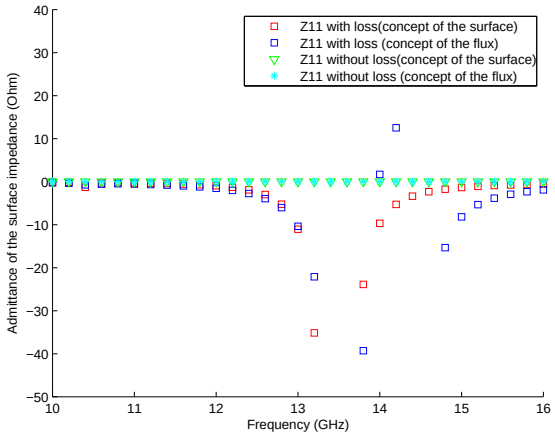


Figure 9: Comparison of surface impedance between ideal and lossy case)

HIS cell. Geometrically, this will be a little different to the direct extension of periods in [4]. However, these two networks can be considered the same, except for extremely high frequency.

In [4], with this F-like structure, two bandgaps are measured below 10GHz. One is around 3.5GHz, the other is around 6.7GHz. With our proposed method, two resonant frequencies are also found at around 4 GHz and 6.5 GHz,seen in Fig. 11. This small frequency shift can be caused by the absence of the microstrip antenna in our simulation and the small difference of our network's geometry.

4.4. Discussion

As shown above, both proposed methods are effective and of comparable accuracy. It is difficult to tell which method is better. However, both of them have limitations which we discuss now.

The unit cell of HIS structure is always considered as far smaller than the effective wavelengh λ. Precisely speaking, it satisfies the condition $\lambda/D > 10$ (D is the spatial period). Under this condition, the fluctation of tangential electric field is negligible on the HIS planar surface, thus we assume that the tangential electric field on the surface is uniform. Theoretically, with the increase of operating frequency, our numerical model will be less and less valid.

The accuracy can be also influenced by the height of the observation surface. The excitation on the top of our study domain is homogeneous, but the farther away from the excitation, the less uniform the E field on the chosen surface will be. However, the increasing height means more computing time.

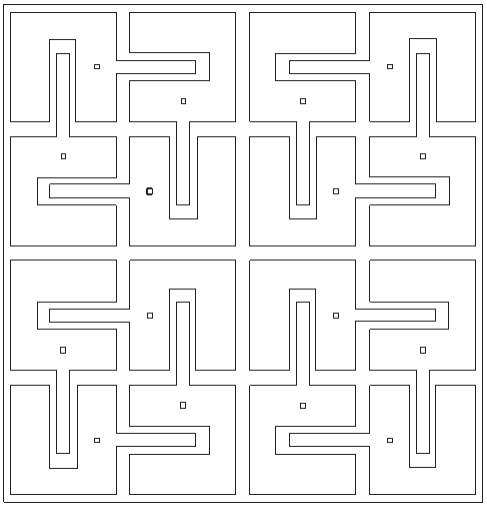


Figure 10: Planar geometry of a F-like structure network

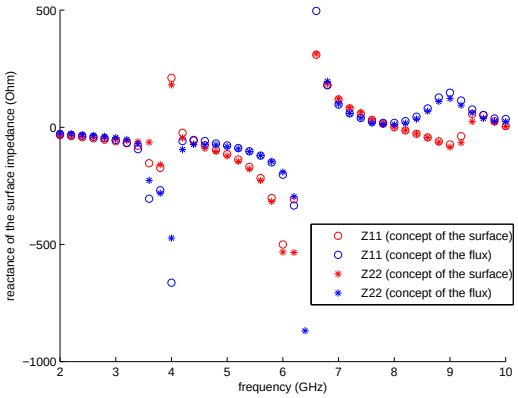


Figure 11: Reactance of surface impedance (F-like structure)

5. CONCLUSION

Two new approaches of calculating the surface impedance for HIS structure have been proposed, which are not limited to symmetric planar structure. These methods have been validated by the comparison with different analytical and numerical results. The limit of the model is also discussed and we expect this numerical model to be a useful tool of featuring HIS structure's performance and give out some numerical estimations for antenna design.

ACKNOWLEDGMENT

The authors would like to thank Prof. A. Bossavit for fruitful discussions on the fourth section of this article.

REFERENCES

1. D. Sievenpier, L. Zhang, R.F.J. Broas, N.G. Alexopoulos, and E. Yablonovitch,"High-Impedance Electromagnetic Surfaces with a Forbidden Frequency Band," *IEEE Trans. Microw. Theory Tech.*, Vol. 47, No. 11, 2059–2074, 1999.
2. D.F. Sievenpiper, *High Impedance electromagnetic surfaces*, Ph.D. dissertation, Electrical Engineering Department, University of California, Los Angeles, 1999.
3. L. Yousefi, B.Mohajer-Iravani, and O.M. Ramahi, "Enhanced Bandwidth Artificial Magnetic Ground Plane for Low-profile Antennas", *IEEE Antennas Wireless Propag. Lett.*, Vol. 6, No. 11, 289–292, 2007.
4. Y. Li, M.Y. Fan, F. L. Chen, J.Z. She, and Z.H. Feng, "A Novel Compact Electromagnetic-Bandgap (EBG) Structure and Its applications for Microwave Circuits, *IEEE Trans. Microw. Theory Tech.*, Vol. 53, No. 1, 183–190, 2005
5. C.R. Simovski, P. de Maagt, I. V. Melchakova, "High-Impedance Surface Having Stable Resonance With Respect to Polarization and Incidence Angle, *IEEE Trans. Antennas Propagat.*, Vol. 53, No. 3, 908–914, 2005.
6. M. Rahman and M. A. Stuchly, "Transmission line periodic circuit representation of planar microwave photonic bandgap structures, *Microwave Optical Tech. Lett.*, Vol. 30, No. 1, 15–19, 2001.
7. S. A. Tretyakov, *Analytical Modeling in Applied electromagnetics*, Boston, MA: Artech House, 2003.
8. D. B. Davidson, *Computational Electromagnetics for RF and Microwave Engineering*, Cambridge University Press, Cambridge, UK, 2005.
9. J. Jin, *The finite element method in electromagnetics*, John Wiley& Sons, Inc., New York, 2002.
10. A.Bossavit, *Computational Electromagnetism*, Acdamic Press, USA, 1998.
11. CST MICROWAVE STUDIO (CST MWS) 2009, www.cst.com.

Tunable effective permittivity of composites based on ferromagnetic microwires with high magneto-impedance effect

M. Ipatov[1*], G.R. Aranda[1], V.Zhukova[1], L. V. Panina[2], J. González[1], and A. Zhukov[1]

[1]Dpto. de Física de Materiales, Fac. Químicas, Universidad del Pais Vasco San Sebastián 20009, Spain

[2]School of Computing, Communications and Electronics, University of Plymouth, Plymouth, PL4 8AA, United Kingdom

[*]corresponding author: mihail.ipatov@ehu.es

Abstract- The effect of the external magnetic field on the dispersion of the effective permittivity in a single array of parallel CoFe-based amorphous wires is demonstrated by measuring the transmission/reflection spectra in free space in the frequency band of 0.9-17 GHz. The magnetic field is applied along the wires sensitively changing their magnetization and high frequency impedance. Based on the measurements of magneto-impedance in a single wire and S-parameters of composites in free space, we show the correlation between magneto-impedance and the field dependence of the effective permittivity.

1. INTRODUCTION

The response of a homogeneous material to electromagnetic radiation is described by two macroscopic parameters: dielectric permittivity ε and magnetic permeability μ. Artificially structured materials often referred to as metamaterials, can be characterized by certain averaged ε_{ef} and μ_{ef} that takes values not readily found in natural materials. In particular, composites containing periodically arranged array of continuous parallel metallic wires may demonstrate a strong dispersion of the effective permittivity ε_{ef} in the microwave range which is of a plasmonic type and takes negative real part below the plasma frequency [1-4]. These composites have attracted much interest as a constitute part of a metamaterial with simultaneously negative ε_{ef} and μ_{ef} [5,6]. Whilst the practical realisation of fascinating properties of such materials (superimaging, invisibility) is still doubtful, they can be useful to realize tunable and self-sensing materials with electromagnetic properties dependent on structural scaling, external stimuli or internal state of the material. For example, a material with self-monitoring properties could be able to evidence invisible structural damages, defects, excessive loadings, local stress and temperature distribution, thus considerable facilitating the *in-situ* health monitoring of large scale objects such as infrastructure (bridges, buildings, etc.).

The adjustability of the material's effective permittivity has been realised in composites with embedded ferromagnetic wires having large and sensitive magneto-impedance (MI) effect at GHz frequencies [7-11] by applying the external stimuli such as magnetic field or stress which affect the wire's magnetic structure. Strong frequency dispersion of the effective permittivity in wire composites is very sensitive to the losses which depend on the wire impedances. Changing the magnetic structure in the wires by magnetic, mechanical or thermal stimuli, it is possible to vary their high frequency impedance by more than twice [12]. If the impedance is increased, this will result in broader permittivity spectra with reduced values and improved wave propagation. The opposite case of impedance reduction will enhance band stop properties.

In this work, we investigated a magnetic field tunability of microwave response from a single layer of continuous magnetic wires as depicted in Fig. 1. CoFe glass-coated amorphous microwires with nearly-zero

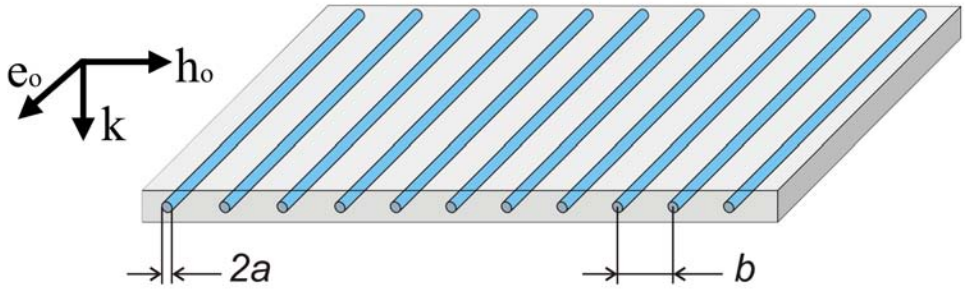


Figure 1. Composite structure based on array of long continuous wires.

magnetostriction constant showing large MI effect up to GHz range are used. We demonstrated that the application of a magnetic field to the whole composite strongly affects the permittivity spectra due to increased losses. A similar strong field effect on the permittivity spectra was found previously in resonant short cut wire composites [8-10]. The modelling results are in a good agreement with the experimental spectra deduced from S-parameter measurements in the free space.

2. THEORY

Artificial light weight dielectrics consisting of lattices of conducting elements have been known for decades [1] as materials the refractive index of which could be tailored in a wide range being greater or less than unity. A wire media (or rodded media [2]) was also considered demonstrating that their electric dispersive properties imitate those of plasma. Accordingly, the basic physics behind these systems was considered in terms of beam shaping effects. Recently, a lot of work has been devoted to various artificial dielectrics, and in particular, to wire media, exploiting the property of the negative permittivity below the plasma frequency:

$$\varepsilon_{ef} = 1 - \frac{\omega_p^2}{\omega^2(1+i\gamma)}, \qquad (1)$$

where ω_p is the plasma frequency depending on the wire radius *a* and spacing between the wires *b*; γ is some relaxation parameter. There are a number of methods of deducing Eq.(1) in which typically the wires are considered perfectly conductive and the relaxation is introduced from qualitative estimations. Various methods give numerically similar values for ω_p. Thus, a local field approach developed in [13] yields:

$$\omega_p = \frac{2\pi c^2}{b^2(\ln(b/2\pi a) + 0.5275)}, \qquad (2)$$

where *c* is the velocity of light. In this work we consider the wire medium as highly dispersive and lossy system to realize tunable dielectric response. In this way, a rigorous calculation of the relaxation parameter becomes essential. We also will have to take account of magnetic properties of wires. This is realized by imposing the impedance boundary conditions at the wire surface and averaging the electric field to deduce ε_{ef}. The parameter γ depends on the wire surface impedance ς_{zz} which combines electric and magnetic properties:

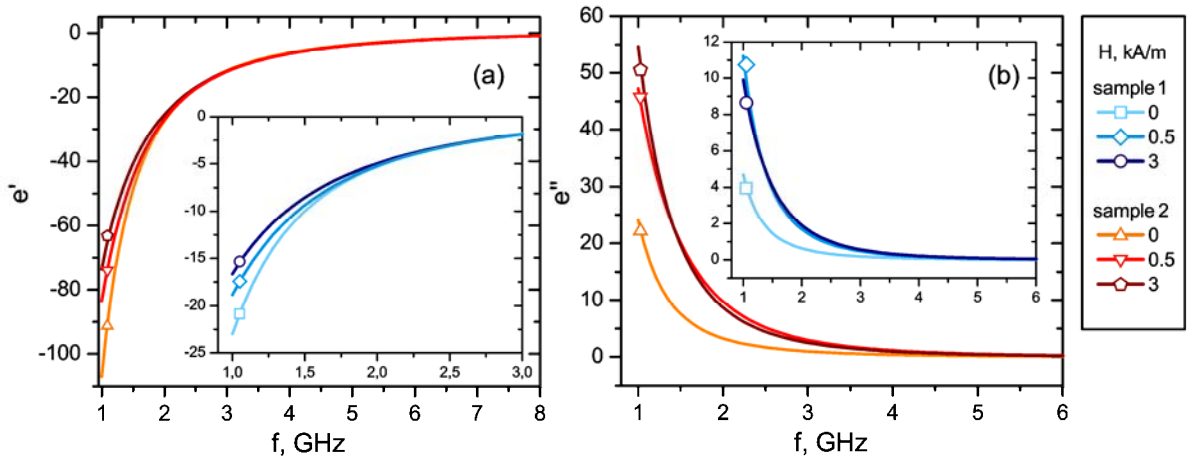


Figure 2. Effective permittivity spectra for the polarisation with electric field along the wires calculated from (1)-(3) in composites with different spacing *b*: 10 mm (sample 1) and 5 mm (sample 2) with the applied magnetic field H as a parameter. Modelling is performed for wires with a circumferential anisotropy (anisotropy field H_k=500A/m). The other parameters are: resistivity 130 μΩcm, saturation magnetisation 0.05T, wire radius a =36 μm. The field effect is seen below the plasma frequency when the relaxation is relatively large.

$$\gamma = \frac{c\varsigma_{zz}}{2\pi f a \ln(b/a)} \qquad (3)$$

For magnetic wires with circular magnetic anisotropy, this parameter may change greatly when an external magnetic field is applied as a result of the MI effect. Then, the permittivity spectra will depend on the external magnetic field as demonstrated in Figure 2.

The magnetic state in amorphous ferromagnetic microwires of Co-based composition with nearly zero magnetostriction is very sensitive to the external magnetic field applied along the wires. This field opposes the circular anisotropy field bringing the wire magnetisation along the axis. This magnetic state corresponds to high ac permeability of wires induced by the wire currents and high surface impedance (MI effect). Increasing the wire impedance affects the permittivity dispersion: the relaxation parameter increases and the magnitude of the real part decreases. As the wire impedance depends on the dc magnetisation it is expected that any physical effects (mechanical stress, temperature) that results in change in the magnetic structure (whilst the ac permeability remains high) will affect the dispersion of the effective permittivity.

3. EXPERIMENT

The microwave properties of wire composites were investigated by free space method requiring large samples. $Co_{66}Fe_{3.5}B_{16}Si_{11}Cr_{3.5}$ (magnetostriction constant $\lambda_s \approx -3\cdot10^{-7}$) glass coated amorphous wires with radius *a* of 36 μm and glass coating thickness of 5 μm were glued in paper to form wire-lattices of 60x60 cm^2 with separation b of 10 mm and 5 mm, as shown in Figure 1. The S-parameters were measured in the frequency range of 0.9-17 GHz in the presence of external magnetic field ranging up to 3000 A/m applied along the wires. The magnetic field was generated by means of a plane coil [10] with turns perpendicular to the electrical field in the incident wave. The effective permittivity spectra were deduced from S-parameters with the help of Reflection-

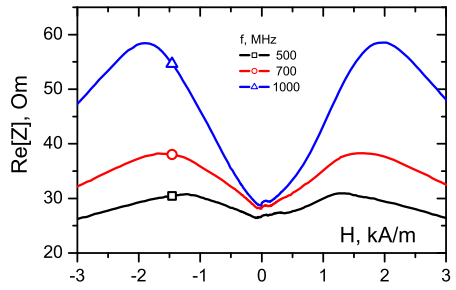


Figure 3. Wire impedance vs. field for different frequencies.

Transmission Epsilon Fast Model. The effective thickness of the samples was taken equal to the wire spacing *b*. The magnetic and impedance properties of wires were defined from measurements of the dc magnetisation loops and MI in the frequency range up to 3.5 GHz.

4. DISCUSSION

As it was demonstrated above, the dispersion of the effective permittivity ε_{ef} depends on the wire surface impedance. Therefore, large and sensitive MI in the wires is essential for developing tunable dielectrics. The results on dc magnetisation loops (not shown here) have confirmed that the wires possess a circumferential anisotropy with the effective anisotropy field of about 500A/m. Figure 3 shows the impedance vs. magnetic field plots in 6 mm long sample. The MI dependences have two symmetrical peaks typical of a circumferential anisotropy.

Figure 4 shows the permittivity dispersion deduced from S-parameter measurements for the two samples with the applied magnetic field *H* as a parameter. The effective thickness for the permittivity calculation was taken equal to the lattice period (10 mm and 5 mm, accordingly) although the real composites thickness is much smaller

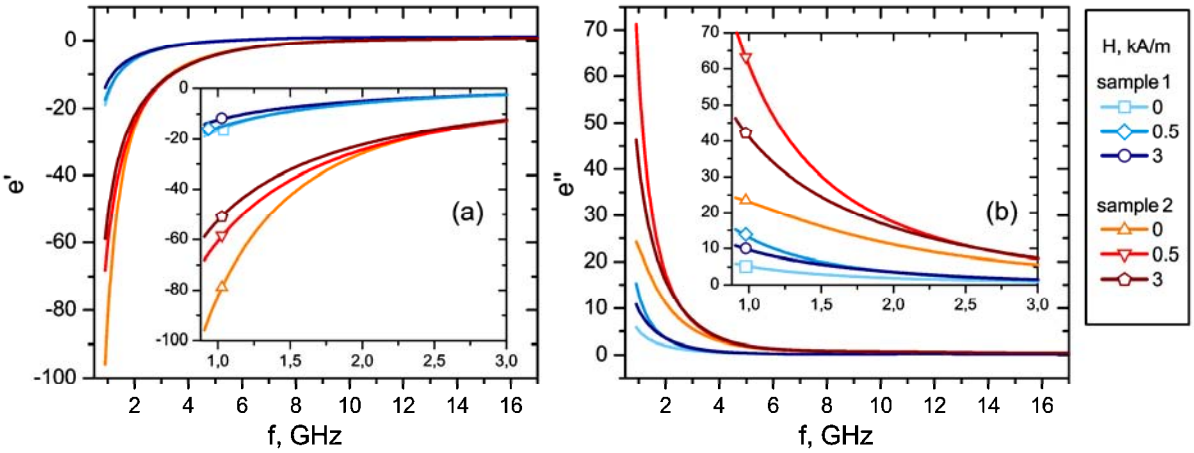


Figure 4. Real (a) and imaginary (b) parts of ε_{ef} deduced from S-parameter measurements with applied magnetic field H as a parameter.

and is defined by the host matrix thickness. The relevance of this approach to the effective thickness of even 1-layer wire lattices was experimentally and numerically proven [14]. The real part of ε_{ef} has a negative value below the plasma frequency which is equal to 5.04 GHz 10.8 GHz for samples with lattice period of 10 mm and 5 mm , accordingly. For higher frequency sample (b= 5 mm) the real part changes from -90 at zero field to -55 for H=3 kA/m at a frequency of 1 GHz. This behaviour agrees well with the theoretical results shown in Fig. 2. Using analogy with plasma, the application of external magnetic field suppresses low-frequency plasmons decreasing the magnitude of the real part of the permittivity while its imaginary part increases with the field due to the increase in the wire impedance. Both the dispersion and filed effect is stronger for the 5 mm sample comparing to those for 10 mm sample since the plasma frequency is higher and magnetic field effect is stronger at lower frequencies. In the frequency region below 2 GHz the maximum of the imaginary part is observed when the applied magnetic field is about 500 A/m that is equal to the anisotropy field.

CONCLUSION

Here we report novel results on the magnetic field effect on the dielectric response in composites with array of parallel magnetic wires with two different lattice constant of 5 and 10 mm. We studied the composite permittivity in the frequency region of 0.9-17 GHz utilising free-space measurement method and analysis in terms of the effective permittivity depending on the wire surface impedance. Both the real and imaginary parts of ε_{ef} show strong variations with increasing the field owing to the field dependence of the wire impedance which controls the losses in the dielectric response. Long-wire composites have a plasmonic type dispersion of ε_{ef} with negative values of its real part below the plasma frequency which is about 5 GHz for wire spacing of about 10 mm and 10.8 GHz for 5 mm array with wire diameter being of 72 microns. The presence of the external magnetic field suppresses “low-frequency plasmons” increasing the value of the real part of the permittivity. Thus, the investigated composites with ferromagnetic microwires exhibited a strong dependence of the effective permittivity on the external magnetic field that makes them suitable for large scale applications as tuneable microwave materials.

REFERENCES

1. Brown J., “Artificial dielectrics,” *Prog. Dielectr*. Vol. 2, 193–225, 1960.
2. Rotman W., “Plasma simulation by artificial dielectrics and parallel-plate media,” *IRE Trans. Antennas Propag*. Vol. 10, 82–95, 1962.
3. Pendry J. B., A. J. Holden, W. J. Stewart, and I. Youngs, “Extremely Low Frequency Plasmons in Metallic Mesostructures,” *Phys. Rev. Lett*. Vol. 76, 4773, 1996.
4. Sarychev A.K., V.M. Shalaev, “Electromagnetic field fluctuations and optical nonlinearities in metal-dielectric composites,” *Physics Reports* Vol. 335, 275, 2000.
5. Pendry J. B., “Negative Refraction Makes a Perfect Lens,” *Phys. Rev. Lett*. Vol. 85, 3966–3969, 2000.
6. Smith D. R., W. J. Padilla, D. C. Vier, S. C. Nemat-Nasser, and S. Schultz, “Composite Medium with Simultaneously Negative Permeability and Permittivity,” *Phys. Rev. Lett*. Vol. 84, 4184–4187, 2000.
7. Reynet O., A.-L. Adent, S. Deprot, O. Acher, M. Latrach, “Effect of the magnetic properties of the inclusions on the high-frequency dielectric response of diluted composites,” *Phys. Rev. B* Vol. 66, 94412, 2002.
8. Makhnovskiy D. P., L. V. Panina, “Field dependent permittivity of composite materials containing ferromagnetic wires,” *J. Appl. Phys*. Vol. 93 4120, 2003.

9. Makhnovskiy D.P., L. V. Panina, C. Garcia, A. P. Zhukov, and J. Gonzalez, “Experimental demonstration of tunable scattering spectra at microwave frequencies in composite media containing CoFeCrSiB glass-coated amorphous ferromagnetic wires and comparison with theory,” *Phys. Rev. B* Vol. 74064205-1–064205-11, 2006.
10. Panina L. V., S. I. Sandacci, and D. P. Makhnovskiy, “Stress effect on magnetoimpedance in amorphous wires at gigahertz frequencies and application to stress-tunable microwave composite materials,” *J. Appl. Phys*. Vol. 97, 013701, 2005.
11. Peng H.X., F.X. Qin, M.H. Phan, Jie Tang, L.V. Panina, M. Ipatov, V. Zhukova, A. Zhukov, J. Gonzalez, J. “Co-based magnetic microwire and field-tunable multifunctional macro-composites,” *Non-Crystalline Solids* Vol. 355 1380–1386, 2009.
12. Sandacci, D. Makhnovskiy, L. Panina, and V. Larin, “Stress-Dependent Magnetoimpedance in Co-Based Amorphous Wires With Induced Axial Anisotropy for Tunable Microwave Composites,” *IEEE Tran. Magn*. Vol. 41, No. 10, 3553-3555, 2005.
13. Belov P., S. Tretyakov, and A. Viitanen, “Dispersion and Reflection Properties of Artificial Media Formed By Regular Lattices of Ideally Conducting Wires,” *J. Electromagn. Waves Appl.* Vol. 16, 1153-1170, 2002.
14. Smith D. R., S. Schultz , P. Markos, C. M. Soukoulis, “Determination of Effective Permittivity and Permeability of Metamaterials from Refection and Transmission Coefficient,” *Phys. Rev. B*, Vol. 65, 195104-1–195104-5, 2002.

Application of the McCutchen theorem to image-forming metamaterial slabs

Carlos J. Zapata-Rodríguez[1] and Juan J. Miret[2]

[1]Departamento de Óptica, Universidad de Valencia, Dr. Moliner 50, 46100 Burjassot, Spain.
[2]Departamento de Óptica, Universidad de Alicante, P.O. Box 99, Alicante, Spain.
carlos.zapata@uv.es

Abstract— A nonsingular, polarization-dependent, 3D impulse response is derived to determine unambiguously the amplitude distribution in the image volume of a negative-refractive-index layered lens. The generalized amplitude transfer function is introduced to gain a deep insight into the resolution power of the optical element. In the near-field regime, fine details containing some depth information may be transmitted through the lens. Metamaterials with moderate absorption are appropriate for subwavelength resolution keeping limited degree of depth discrimination.

1. INTRODUCTION

The possibility of recovering sub-wavelength details of an object is a subject of growing interest leading to a profusion of superresolving image-forming techniques. In 2000 Pendry [1] showed that a thin slab of a medium with negative refractive index (NRI) is capable of generating a exact replica of a plane object, thus being coined as a perfect lens. For the homogeneous part of the field, a phase reversal is accomplished within the NRI medium that compensates the phase gathered by the wave when travelling away from the source. On the other hand, the evanescent components of the wavefield carrying those sub-wavelength features are amplified in the metamaterial layer in order to regain their amplitudes at the image plane. To do it, coupled surface plasmons are excited at the input and output interfaces of the NRI-material slab. Unfortunately, absorption inherent in NRI media restrains a perfect lens from ideal reconstruction of the object.

To derive the resolution limit of the system, the amplitude transfer function (ATF) has been preferably examined since it provides straight the cutoff frequency beyond which one cannot find any spectral component in the reconstructed image. Thus separating the s-polarized and p-polarized components of the field, the image-forming metamaterial layer behaves as a linear and shift-invariant system having a scalar transfer function [2]. As a consequence, the response of the imaging slab for each polarization may be developed by means of the point spread function (PSF), resulting from the Fourier transform of the corresponding ATF.

In a complementary analysis it may be adopted the Rayleigh criterion of resolution for which two point sources are just resolved when the first diffraction minimum of the image of one object point coincides with the maximum of the adjacent source. Thus the PSF may be referred to a resolution gauge for our optical element since the full width of its central peak may be used to measure the limit of resolution. Moreover, in optical microscopy we generally have point sources placed at different distances from the layered lens leading to different limits of resolution along a direction either parallel or perpendicular to the surfaces. Specifically the transverse resolution has been studied in detail but little is said about axial resolution of these metamaterial image formers [3].

In this paper we introduce the generalized ATF, identifying a closed-surface sheet for the far field and a hyperboloid sheet for the evanescent wave component. From the geometry of the generalized ATF we interpret the PSF pattern in the image volume. Moreover this allows us to provide some relevant aspects on the depth-discrimination capabilities of the perfect lens.

2. IMAGE FORMATION WITH NRI SLABS

Let us consider a thin metamaterial slab with its front face (input plane) at $z = 0$ and the output plane at $z = d$ thus d denoting the layer width. This optical element depicted in Fig. 1(a) will generate an image in the semi-space $z \geq d$ from a given plane object laying on $z = -z_0$ ($z_0 \geq 0$). For simplicity we assume that both object and image media are the vacuum. To have a high-fidelity reproduction at the image plane, the negative index of refraction n_2 of the metamaterial

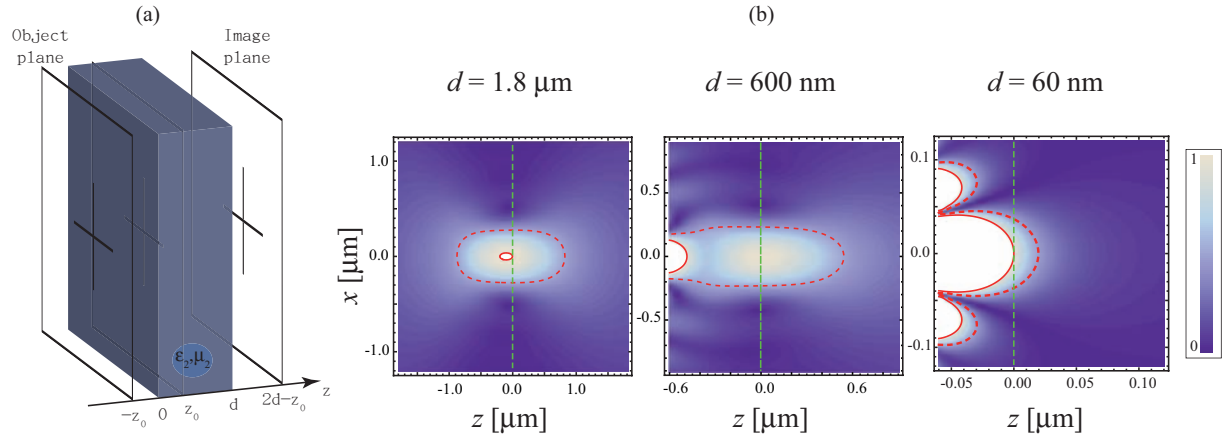


Figure 1: (a) Schematic geometry of the planar-layer-based perfect lens. (b) Absolute value of the PSF $|h_3|$ in $z \geq -d$ at $\lambda_0 = 600$ nm for absorbing slabs of $\delta = 0.1$ and different widths d. The plot is normalized to unity at $\vec{r} = 0$, and contour lines for values 1 (solid line) and 1/2 (dotted line) are drawn in red. The image plane is now shifted to $z = 0$ (vertical green line).

should coincide in magnitude with that of the object (and image) medium ($n_1 = 1$). Material losses prevent from this ideal situation and we therefore assume a realistic, simple model, in which permittivity and permeability are of the form $\epsilon_2 = \mu_2 = -1 + i\delta$. Under these circumstances perfect imaging cannot be achieved since $n_2 = -1 + i\delta$. However a good replica may be found at the plane $z = 2d - z_0$ if $\delta \ll 1$. Moreover, the condition $0 \leq z_0 \leq d$ leads to real images in $d \leq z \leq 2d$.

In order to determine the wave fields in the image plane, it is customary to separate the s-polarized waves ($E_z = 0$) from the p-polarized waves ($H_z = 0$) constituting the electromagnetic field emitted by the source. Nieto-Vesperinas [2] showed that the *perfect* lens is a linear and 3D shift invariant (3D LSI) system. For s-polarized waves, the transverse electric (TE) field emerging from the NRI slab satisfies

$$\vec{E}_{out}(\vec{R}, z) = \iint \vec{E}_{in}(\vec{R}_0, -z_0) h_3(\vec{R} - \vec{R}_0, z - 2d + z_0) d^2\vec{R}_0, \tag{1}$$

where $\vec{E}_{in}(\vec{R}_0, -z_0)$ is the TE wave field at the object plane travelling in direction to the input plane. We recognize the 3D function

$$h_3(\vec{R}, z) = (2\pi)^{-2} \iint T(\vec{k}_\perp) \exp\left(i\vec{k}_\perp \vec{R}\right) \exp\left(i\beta_1 z\right) d^2\vec{k}_\perp, \tag{2}$$

as the PSF of the optical system. In Eq. (2), the layer transmittance

$$T(\vec{k}_\perp) = \frac{t_{12} t_{21} \exp\left[i\left(\beta_1 + \beta_2\right) d\right]}{1 - r_{21}^2 \exp\left(2i\beta_2 d\right)}, \tag{3}$$

follows the Airy formula [5] except for a linear phase factor. If $k_0 = 2\pi/\lambda_0$ denotes the wavenumber in vacuum, the propagation constant reads

$$\beta_j = \sigma_j \sqrt{k_0^2 \epsilon_j \mu_j - \vec{k}_\perp \cdot \vec{k}_\perp}, \text{ for } j = \{1, 2\}. \tag{4}$$

Note that $\sigma_1 = 1$ for the vacuum and $\sigma_2 = -1$ for the NRI material. Also

$$t_{jk} = \frac{\mu_k \beta_j - \mu_j \beta_k}{\mu_k \beta_j + \mu_j \beta_k} \tag{5}$$

is the transmittance factor for s-polarized waves at a single interface, and $r_{jk} = 1 - t_{jk}$.

For p-polarized waves it is convenient to derive first the transverse magnetic (TM) field $\vec{H}_{out}(\vec{R}, z \geq d)$ from that TM field at the object plane $\vec{H}_{in}(\vec{R}_0, -z_0)$. This yields a convolution similar to (1), where its PSF may be written again into the plane-wave representation (2) by means of the layer

transmittance (3). It is well known that the substitutions $\epsilon_j \leftrightarrow \mu_j$ switches the Airy formula for TM waves and TE waves, respectively [5]. In our case, however, both material parameters are set equal providing an unique PSF.

Disregarding material losses ($\delta = 0$) we have $T = 1$ yielding $h_3(\vec{R}, 0) = \delta_2(\vec{R})$. In this limiting case [1], the presence of the 2D Dirac delta function δ_2 leads to a perfect image

$$\vec{E}_{out}(\vec{R}, 2d - z_0) = \vec{E}_{in}(\vec{R}_0, -z_0). \tag{6}$$

However $h_3(\vec{R}, z)$ would exhibit a singular behaviour in $z < 0$ [2]. Thus absorption δ acts as a regularizing parameter that provides a Wiener-like filter T.

The amplitude of the 3D PSF $|h_3|$ is depicted in Fig. 1(b) for NRI slabs of different widths d. Since T is radially symmetric, the PSF varies upon the axial coordinate z and the modulus of the transverse vector, R. In the numerical simulation we set a wavelength $\lambda_0 = 600$ nm in vacuum, and losses $\delta = 0.1$ for the metamaterial. Shifting the image plane at $z = 0$, the exit surface of the layered lens would be found at $z = z_0 - d$. Bearing in mind that $z_0 \geq 0$, the meaningful part of the PSF lies within the range $z \geq -d$ as considered in the graphical representation. The 3D amplitude distribution of the PSF for a subwavelength width d shows a distinct behavior in comparison with those impulse responses for $d \gg \lambda_0$. For instance, the FWHM of the PSF at the image plane $\Delta_\perp = 73.5$ nm is clearly subwavelength at $d = 60$ nm; in fact $\Delta_\perp$ would vanish if d were identically zero. Moreover, the amplitude reaches a maximum value at the center point $R = 0$ on the output plane. On the contrary, $\Delta_\perp = 552$ nm comes near the wavelength at $d = 1.8$ μm. Here the maximum amplitude is found approaching the image plane far from the output plane, existing a small longitudinal shift of 104 nm. Furthermore one may determine a FWHM along the z-axis, and in our case we found $\Delta_z = 1.70$ μm.

3. THE GENERALIZED ATF

A convenient interpretation of these results is derived by writing explicitly the far-field term and the evanescent-wave term of the PSF given in Eq. (2). Within the spectral domain $\vec{k}_\perp \cdot \vec{k}_\perp = k_\perp^2 \leq k_0^2$, β_1 yields a real value leading to waves that carry energy to the far field $z \to \infty$. If $k_\perp > k_0$, however, β_1 is purely imaginary so that this part of the wave field contributes exclusively to the near field $z \gtrsim z_0 - d$. The 3D PSF is then written as $h_3 = h_N + h_F$ where the far-field term,

$$h_F(\vec{R}, z) = \frac{-ik_0}{2\pi} \iint a(\vec{s}) \exp\left(ik_0 \vec{s}\vec{r}\right) d\Omega, \tag{7}$$

is evaluated from Eq. (2) within the far-field spectral domain, $0 \leq \theta \leq \pi/2$, being $d\Omega = \sin\theta d\theta d\phi$ the element of solid angle in spherical coordinates. In Eq. (7), the point of observation $\vec{r} = \vec{R} + z\hat{z}$ and the 3D unitary vector $\vec{s} = \vec{s}_\perp + s_z\hat{z}$ is deduced from the dispersion equation $k_0\vec{s} = \vec{k}_\perp + \beta_1\hat{z}$. Finally, the angular spectrum

$$a\left(\vec{s}\right) = \frac{i}{\lambda_0} T\left(\vec{s}\right) s_z, \tag{8}$$

where $s_z = \cos\theta$. Since $k_\perp = k_0 \sin\theta$, the transmittance T depends exclusively upon the azimuthal coordinate θ, and so does a.

To gain a deep insight into the PSF term h_F, let us consider the limiting case $\delta \to 0$. In this case $T = 1$ and the transverse distribution of the PSF is an Airy disk,

$$h_F(\vec{R}, 0) = \frac{J_1\left(k_0 R\right)}{\lambda_0 R}, \tag{9}$$

where J_1 is a Bessel function of the first kind. Along the axis $R = 0$ the PSF may be expressed analytically as

$$h_F(0, z) = \frac{\left(1 - ik_0 z\right) \exp\left(ik_0 z\right) - 1}{2\pi z^2}. \tag{10}$$

We remark that $|h_F|$ is maximum at the origin, whose central lobe has FWHMs $\Delta_\perp = 0.705\ \lambda_0$ and $\Delta_z = 1.55\ \lambda_0$. At $\lambda_0 = 600$ nm we have $\Delta_\perp = 423$ nm and $\Delta_z = 929$ nm. These numbers are roughly in agreement with the numerical simulation performed in Fig. 1(b) at $d = 1.8$ μm revealing that h_F is the dominant part of the PSF. This is also true for higher values of d. Otherwise the

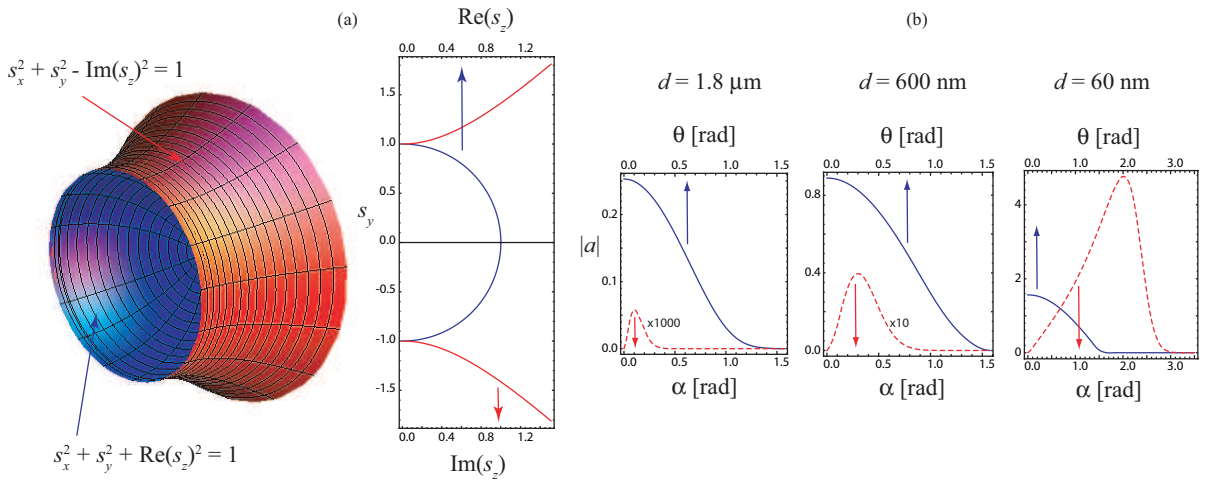


Figure 2: Spherical and hyperboloidal sheets constituting the generalized ATF are shown in (a) in 3D and on the meridional plane $s_x = 0$. In (b) we represent the angular spectrum $|a|$ (in blue) and the near-field term of the ATF (in red) for the numerical simulation of Fig. 1(b)

near-field component becomes of significance (see sub-figure at $d = 600$ nm), even taking the control of the amplitude distribution in the image volume for slabs of a subwavelength width.

We point out that h_F represents a focused wave with focus at the origin $\vec{r} = 0$ and, as a consequence, it may follow the standard mathematical treatment of apertured spherical beams. In the limiting case $\delta = 0$ it yields an aberration-free focal wave since $a(\vec{s})$ is a real function excepting a constant complex factor [6]; otherwise monochromatic aberrations arise [2]. From Eq. (7) we infer that h_F may be written in terms of a 3D Fourier transform of the function $a(\vec{s})$, which has extent in three dimensions and is wrapped around the unit semisphere $\vec{s} \cdot \vec{s} = 1$ and $s_z \geq 0$ [see Fig. 2(a)]. In the McCutchen's original paper [4], the function a is coined as the *generalized aperture* describing the patch of solid angle occupied by the Huygenian source at the aperture plane of the converging wave. In our case, however, the transmission is determined by the function T rather than absorption on an opaque screen. Therefore $a(\vec{s})$ is simply recalled as the generalized ATF of the perfect lens.

The near-field wave h_N might be expressed in the form of Eq. (7) if the angular coordinate θ is represented in the complex plane. Setting $\theta = \pi/2 - i\alpha$ and running α from 0 to ∞ allows us to consider the normalized wave vector $\vec{s}$ with real transverse component of modulus $s_\perp = \cosh\alpha > 1$ and purely-imaginary axial component $s_z = i \sinh\alpha$. The dispersion equation is conveniently rewritten as $s_\perp^2 - (s_z'')^2 = 1$, where $s_z = s_z' + i s_z''$, representing a unit hyperboloid shown in Fig. 2(a). It is immediate that the angular spectrum $a(\vec{s})$ wrapped around such a surface constitutes the second sheet of the generalized ATF associated with evanescent components of the wave field.

Previously we mentioned that h_3 is singular in a lossless metamaterial lens, caused by the near-field term h_N. In this case, the unbounded function $a(\vec{s})$ modulates the ATF over the hyperboloidal sheet having infinite extent. However the PSF is bandlimited when $\delta \neq 0$ [7]. As shown in Fig. 2(b), the modulus $|a|$ is maximum at $\theta = 0$ for the far-field term, approaching $\lambda_0^{-1} \exp(-k_0 \delta d)$, and it decreases to zero at $\theta = \pi/2$. Within the near-field regime, $|a|$ grows exponentially at increasing values of α, however attaining a local maximum $|a|_{\max}$ before it decreases for $\alpha \to \infty$. For $d = 60$ nm, the maximum $|a|_{\max} = 4.77\ \mu\text{m}^{-1}$ at $\alpha_{\max} = 2.02$ rad, which corresponds to a normalized spatial frequency $s_\perp = 3.82$ (and $s_z = i3.69$). On the far-field sheet the generalized ATF remains comparatively low since $|a| \leq 1.57\ \mu\text{m}^{-1}$ [$= |a(\theta = 0)|$]. The effective area of the hyperboloidal surface where $a(\vec{s})$ takes significant values also surpasses in several units that from the unit semisphere. On the other hand, for $d = 1.8\ \mu$m, $|a|_{\max} = 5.76\ 10^{-5}\ \mu\text{m}^{-1}$ at $\alpha_{\max} = 0.104$ rad, associated with a unit vector of $s_\perp = 1.005$ (and $s_z = i0.104$). This is several orders of magnitude lower than the maximum $|a| = 0.253\ \mu\text{m}^{-1}$ given at $\theta = 0$. Expectedly the effective area of $a(\vec{s})$ on the hyperboloid is here a fraction of that from the semisphere.

We conclude that the generalized ATF provides geometrical and analytical arguments in order to derive critically whether h_N represents the dominant contribution to the PSF. This is of relevance since subwavelength resolution is achieved exclusively in such a case.

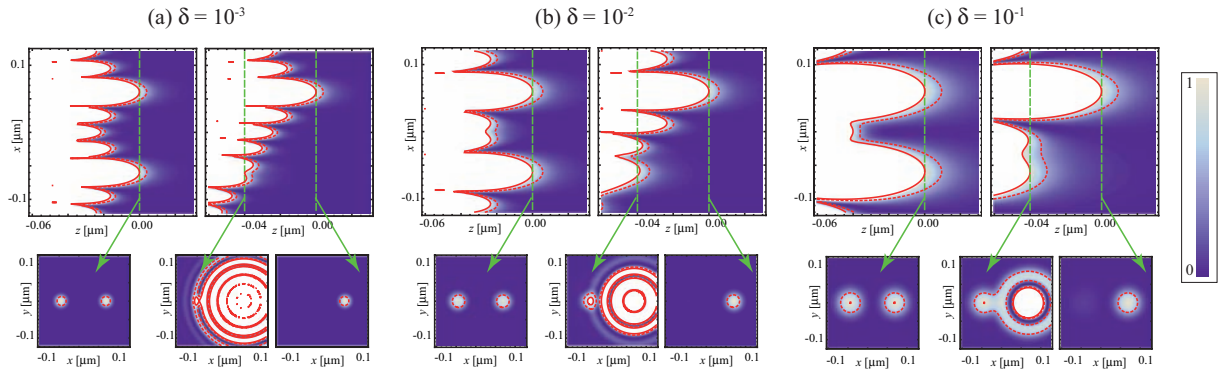


Figure 3: Energy density in the image volume of two point sources centered at $x = \pm 60$ nm provided under different conditions of absorption and depth.

Superresolving layered lenses made of metamaterials with moderate absorption are limited by a subwavelength width. For microscopy applications, an extended object should be confined in the vicinities of the NRI slab in order to give rise to real images. Moreover, the decay of the wave field from the output plane of the lens leads to inability for producing 3D focusing of energy in spots smaller than λ_0 [3]. However, a quasi-planar object with grooves and small surface defects contains some depth information that might be transmitted through the lens. As illustration we show in Fig. 3 the contour plot of energy density in the image space which is produced by two equienergetic point sources. An incoherent superposition is assumed to get rid of interference phenomena. Both points are separated 120 nm along the transverse direction. We analyze the case one of these objects O_1 stays closer to the lens than O_2, and therefore its image O_1' remains in a plane (here $z = 0$) further from the lens back face. In this plane the presence of the second image O_2' is imperceptible in virtue of the evanescent nature of its wave field. Moving to the image plane $z = -40$ nm of O_2' it is clearly detected, however, superposed to the strong back tail produced by O_1'. For the lower-absorbing layer ($\delta = 10^{-3}$) the higher superresolving power along the transverse direction is achieved. Nevertheless its back tail at $z < 0$ spreads much faster hindering the observation of O_2'.

4. CONCLUSION

In direct analogy with conventional image-forming systems we show that when a NRI planar lens produces an image of a point source the 3D diffraction pattern which results is the 3D Fourier transform of a function that here we called the generalized ATF. This feasible application of the McCutchen analysis [4] relies on the relation between the angular spectrum of the PSF and the lens transmittance in the spatial-frequency domain. Particularly, subwavelength resolution is mostly determined by the modulation of the generalized ATF on the hyperboloidal sheet. In connection with this result we have understood that increasing transverse resolution within the near-field regime may be produced at the cost of loss in depth discrimination.

This research was funded by Ministerio de Ciencia e Innovación (MICIIN) under the project TEC2009-11635.

REFERENCES

1. Pendry, J. B., "Negative refraction makes a perfect lens," *Phys. Rev. Lett.*, Vol. 85, No. 18, 3966–3969, 2000.
2. Nieto-Vesperinas, M., "Problem of image superresolution with a negative-refractive-index slab," *J. Opt. Soc. Am. A*, Vol. 21, No. 4, 491–498, 2004.
3. Marques, R., M. J. Freire and J. D. Baena, "Theory of three-dimensional subdiffraction imaging," *Appl. Phys. Lett.*, Vol. 89, No. 21, 211113, 2006.
4. McCutchen, C. W., "Generalized aperture and the three-dimensional diffraction image," *J. Opt. Soc. Am.*, Vol. 54, No. 2, 240–242, 1964.
5. Yeh, P., *Optical Waves in Layered Media*, Wiley, New York, 1988.
6. Collet, E. and E. Wolf, "Symmetry properties of focused fields," *Opt. Lett.* , Vol. 5, No. 6, 264–266, 1980.
7. Smith, D. R., D. Schurig, M. Rosenbluth and S. Schultz, "Limitations on subdiffraction imaging with a negative refractive index slab," *Appl. Phys. Lett.*, Vol. 82, No. 10, 1506–1508, 2003.

Subwavelength nondiffractting beams in multilayered media

C. J. Zapata-Rodríguez[1*], and J. J. Miret[2]

[1] Departamento de Óptica, Universidad de Valencia, Spain

[2]Departamento de Óptica, Farmacología y Anatomía, Universidad de Alicante, Spain

[*]corresponding author: carlos.zapata@uv.es

Abstract- We present a family of p-polarized optical beams that are highly localized around its optical axis and are sustained in a layered medium. This medium is comprised of a stack of thin films made of a material exhibiting negative permittivity, regularly placed in a dielectric host. We exploit the excitation of surface plasmon polaritons leading to enhanced localization near the optical axis. Also we perform an appropriate correction of the 2D wavefront in the vicinity of the beam axis for a perfect phase matching showing an optimal concentration of light.

1. INTRODUCTION

Tightly confinement of light has been motive of interest in the scientific community during decades. In this context we include the Bessel beams [1], a family of optical wavefields with the ability of suppressing the spreading effect associated with diffraction thus being transversally localized around its axial *focus.* They are interpreted as a suitable superposition of plane waves all having a wavevector that projected onto the optical beam axis (OBA) gives the characteristic propagation constant β. This sort of solutions may be found also in stratified media if the vector normal to the interfaces lies along the OBA leading to normal incidence of the beam. However, they cannot be supported with out-of-plane excitation [2].

On other hand, assuming the medium is periodic, the elements of any wave superposition are necessarily Bloch modes. Provided the projection β of the pseudomoment along a direction perpendicular to the periodicity of the medium coincides for all Bloch components we can construct a localized diffraction-free beam if, additionally, a phase matching condition is satisfied [3].

In this work we identify some 1D layered structures that can sustain nondiffracting wavefields propagated along the OBA with transversal beamsizes clearly surpassing the diffraction limit. This subwavelength effect is due to two different mechanisms, the existence of photonic bandgaps and the formation of surface resonances in the metal-dielectric interfaces. The excitation of such surface plasmons polaritons (SPPs) are attained at comparatively high values of β, however leading to a subwavelength beam size.

2. DIFRACTION-FREE BEAMS IN 1D LAYERED MEDIA

Let us consider a monochromatic nondiffracting beam propagating in a 1D lossless periodic structure consisting of alternating layers of negative- and positive-permittivity materials as shown in Fig. 1(a). The y axis is set such that it is perpendicular to the separating surfaces. The period is $L = d_d + d_m$ where d_d and d_m are the thicknesses of the dielectric and *metallic* layers. We also assume that beam propagation is directed along the z axis, so that we may cast the electromagnetic fields as

$$\mathbf{E}(x,y,z,t) = \mathbf{e}(x,y)\exp(i\beta z - i\omega t)$$
$$\mathbf{H}(x,y,z,t) = \mathbf{h}(x,y)\exp(i\beta z - i\omega t) \quad (1)$$

being ω the frequency of the monochromatic radiation. The homogeneity of the wave field in the coordinate z is explicitly parametrized in terms of the propagation constant β. We consider TM waves, where **H** is in the plane XZ and, therefore $\mathbf{h}_y$ vanishes.

The Maxwell's equations provide some relations between the transverse fields **e** and **h**. The electric field **e** may be derived from **h** by means of the equation $\nabla \times \mathbf{H} = -i\omega\,\varepsilon_0\,\varepsilon\,\mathbf{E}$, where $\varepsilon(y)$ is the relative dielectric constant of the foliar structure, and relation between the magnetic components can be obtained from the equation $\nabla\cdot(\mu_0\,\mathbf{H}) = 0$. Thus h_x is the scalar wave field from which we may describe the nondiffracting beam unambiguously.

According to the Bloch theorem the modes in a multilayer periodic medium are Bloch waves, that for our stratified medium are of the form,

$$h_K(y)\exp(iKy)\exp(i\boldsymbol{k}_{//}\mathbf{R}) \quad (2)$$

where $h_K(y+L) = h_K(y)$ is a periodic function, $\boldsymbol{k}_{//} = (k_x, \beta)$ is the wave vector onto a plane parallel to the interfaces, $\mathbf{R} = (x, z)$, and K is the Block wave number. The function $h_K(y)$ may be written as

$$h_K(y) = \begin{cases} a_m(K)\exp[i(k_{ym}-K)y] + b_m(K)\exp[-i(k_{ym}+K)y] & 0 \le y < d_m \\ a_d(K)\exp[i(k_{yd}-K)y] + b_d(K)\exp[-i(k_{yd}+K)y] & d_m \le y < L \end{cases} \quad (3)$$

the amplitudes a_α and b_α are constants where α = m refers to the medium of negative dielectric constant (NDC), and α = d stands for the dielectric, and $k_{y\alpha} = \sqrt{(\omega/c)^2\varepsilon_\alpha - |\boldsymbol{k}_{//}|^2}$. The relationship between a_α and b_α can be found by enforcing the boundary conditions and its values by normalization. Therefore, using a matrix method [4] we may obtain in a rather simple way the dispersion equation

$$\cos(KL) = \cos[k_{yd}\,d_d]\cos[k_{ym}\,d_m] - \frac{(k_{ym}^2\,\varepsilon_d^2 + k_{yd}^2\,\varepsilon_m^2)}{2\,k_{yd}\,k_{ym}\,\varepsilon_d\,\varepsilon_m}\sin[k_{yd}\,d_d]\sin[k_{ym}\,d_m] \quad (4)$$

The existence of the Bloch modes requires that $-1 \le \cos(KL) \le 1$, i.e. K is real. In Fig. 1(b) we plot the real-valued K solutions of equation (4) for the multilayer medium we have selected. It is composed of thin metallic films of width d_m = 50 nm embedded in a dielectric medium of $\varepsilon_d = 2.25$. The period is L = 450 nm, and we consider a conductor that at a frequency ω = 3.4 fs^{-1} (wavelength λ_0 = 550 nm in vacuum) has $\varepsilon_m \approx -15$ (similar to its value for silver but neglecting losses). There are three allowed bands (Im(K) = 0). Interestingly two of those bands appear for values $|\boldsymbol{k}_{//}| > \sqrt{\varepsilon_d}(\omega/c)$ (red line in Fig. 1(b)), range where the wavefields are of evanescent nature in the layers. These propagating Bloch modes are a consequence of resonant tunneling of the evanescent waves and possess features of both surface plasmon and Bloch waves.

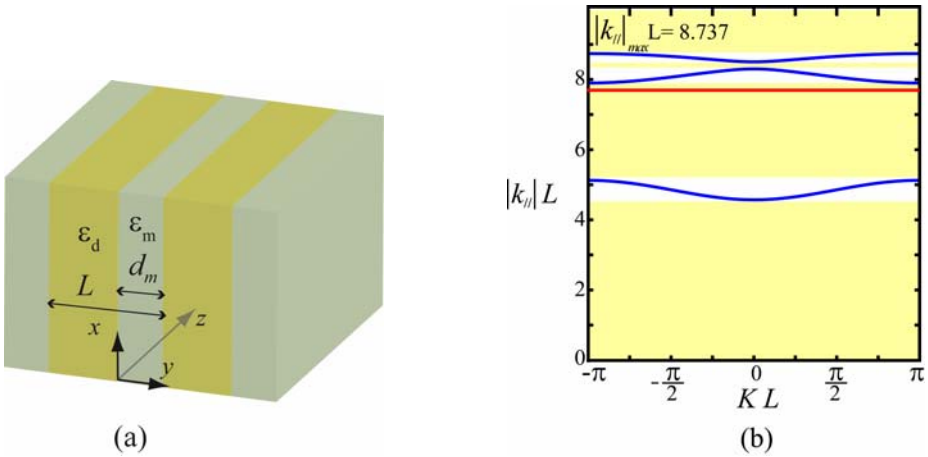


Figure 1: (a) Schematic geometry of the planar nanolayer-based medium. (b) Dispersion relation for the periodic media chosen ($\omega = 3.4 \times 10^{15}$ rad/s). The regions in yellow denote the bandgaps. The red line marks the boundary between the homogeneous-wave regime and evanescent-wave regime in the dielectric.

Returning to our principal objective, we obtain a diffraction-free beam as an adequate superposition of Bloch modes. In particular, the propagating wavefield H_x is constructed as

$$H_x(x,y,z) = \exp(i\beta z) h_x(x,y) = \exp(i\beta z) \sum_K \int_{-\infty}^{\infty} w_K \, h_K(y) \exp(iKy) \exp(ik_x x) \, dk_x \qquad (5)$$

where w_K is simply the weight for the different Bloch modes in the superposition. Keeping in mind that we only consider propagating Bloch modes we set $w_k = 0$ if Im(K)≠ 0.

We point out that given the propagation constant β, not only the pseudomoment K but also the spatial frequency k_x is bandlimited. Accordingly, we can generate different nondifractive waves superposing the Bloch modes belonging to one band or to different bands. In Fig. 2(a) and 2(b) we map different contours of isofrequency β in the k_xK plane for the first and second allowed bands respectively.

3. FOCUS GENERATION AND RESULTS

Only superposing Bloch modes in the form proposed in Eq. (5) is not enough to generate a localized beam. We need to establish some favorable conditions for the formation of a focus along the z axis. An advantageous point is the normalization of the periodic function h_K, so we chose $h_K(0) = 1$. In this way using (x, y) = (0, 0) in Eq. (5) we obtain the wavefield amplitude $h_x = \sum_K \int_{-\infty}^{\infty} w_K \, dk_x$ at the origin as a summation of the amplitudes w_K corresponding to different Bloch modes. This may be interpreted as an interference of Bloch-type individuals. If the phase of their amplitudes is manipulated in order to have the same value leading to in-phase waves, the oscillatory superposition yields the highest intensity achievable. Moreover, under general conditions it cannot be found a point other than the origin from the xy plane where such a phase matching holds. As a consequence, a strong localization of the nondiffracting beam is expected to occur around the origin, such a point unquestionably constituting a focus. Finally we chose $w_K = 1 \Big/ \sqrt{|\mathbf{k}_{//}|^2 - (k_x^2 + \beta^2)}$, a form approaching the spectral strength that can be experimental attained, between others, using an opaque screen with a centered extremely-thin transparent annulus placed at the front focal plane of a perfect lens [5].

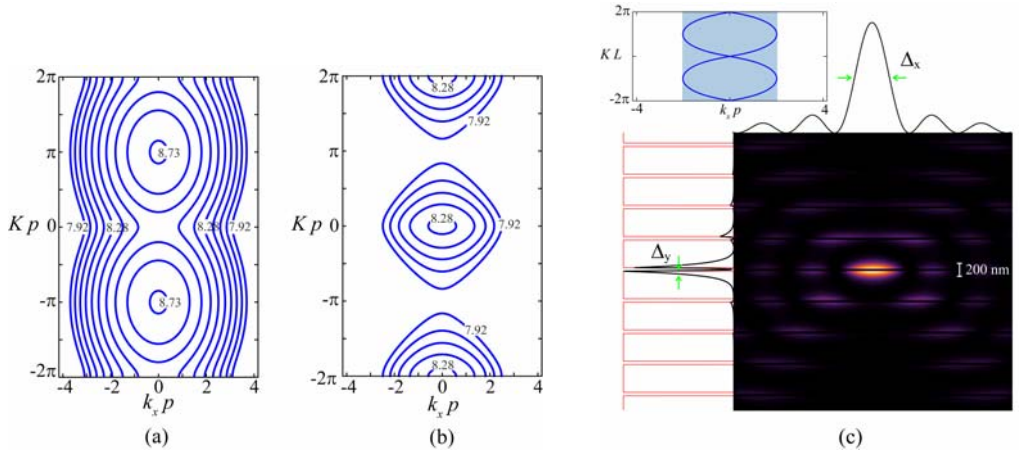


Figure 2: (a) y (b) Isofrequency curves at different propagation constants β in the first and second sheet of the dispersion curve respectively. (c) Transverse intensity $|h_x|^2(x, y)$ corresponding to a localized diffraction-free beam of normalized propagation constant $\beta L = 8.503$. Intensity distributions along the coordinate axes are shown at the top and left sides. Inset: Isofrequency curve where shaded region corresponds to the excited spatial bandwidth.

To illustrate the focus generation along the z-axis, we perform different numerical simulations for various propagation constants. In Fig 2(b) we show the field intensity $|h_x|^2$ for a nondiffracting beam of propagation constant corresponding to the lower limit of the first band ($\beta L = 8.503$). The isofrequency curve is also depicted, where excited frequencies are shaded in grey. The FWHM of the intensity peak along the x-axis is $\Delta_x = 505$ nm, which is above the wavelength in the dielectric medium ($\lambda_d = 367$ nm). However, the behavior along the ordinate is significantly different. The wavefield is high localizated in the interfaces of the slabs, leading to fast decays when moving away from the surfaces and thus forming wedge-like shapes. Although the highest peak is attained at $y = 0$, a large one also arises at the other side of the NDC film, $y = d_m$. Ignoring this sidelobe, the FWHM of the figure is Δ_y =61.58 nm, well below λ_d. In the previous example we have used only the first allowed band. Now fixing the value of β as the corresponding to the lower limit of the second band ($\beta L = 7.899$) we may excite every allowed spatial frequency in the evanescent-wave regime of the two highest bands. In this case (Fig. 3(a)) the FWHM along the x axis is $\Delta_x = 277$ nm, lower than λ_d and, more importantly, the high sidelobe appearing previously in the y axis seems to be wiped out completely. This effect may be explained considering that Bloch components from the first band and those from the second band are roughly out of phase at $y = d_m$ so that they interfere destructively in Eq. (5). Additionally, the FWHM is $\Delta_y = 54$ nm.

In the simulations given above we have shown that beamsizes along the x-axis are larger than the diffraction limit $\lambda_d/2$ attained by quasi-stationary Bessel beams propagating in the medium of dielectric constant ε_d, whereas Δ_y is clearly a subwavelength width. Control over the wave pattern and thus over its FWHM in the x direction is exercised by the spectrum of spatial frequencies k_x: the higher bandwidth the lower Δ_x. In our last illustration we select β coinciding with the lower limit of $k_{//}$ for the third band. We can see the results in Fig. 3(b). A narrow peak on the focus is produced exhibiting a width $\Delta_x = 132$ nm. Also strong sidelobes arise in the vicinity of focus. The presence of two bandgaps explains these effects. The field distribution in the y-axis demonstrates a subwavelength focus of FWHM $\Delta_y = 44$ nm. Sidelobes on the interfaces are accompanied by other peaks in the middle of the dielectric slabs. This is not surprising since Bloch components of the third band contributing in the expansion (5) have such a behavior.

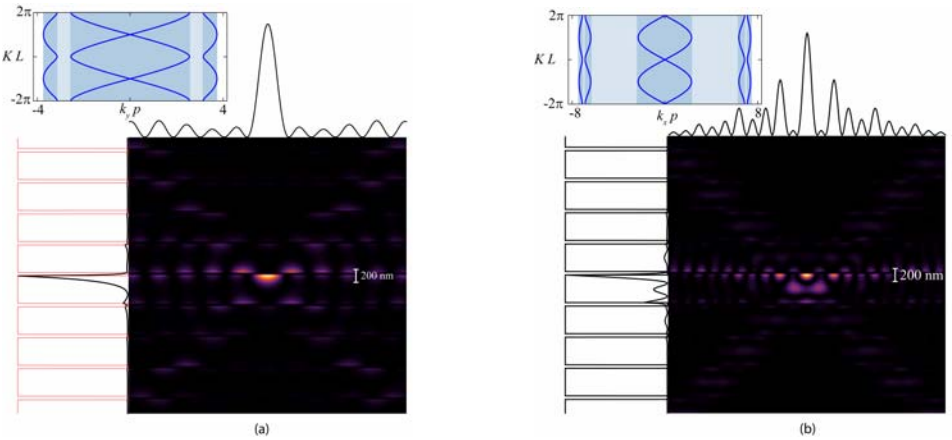


Figure 3: Transverse intensity $|h_x|^2(x, y)$ for diffraction-free beams of normalized propagation constant (a) $\beta L = 7.899$, and (b) $\beta L = 4.571$. In this last case all three bands of allowed frequencies are excited.

4. CONCLUSIONS

We have demonstrated that diffraction-free beams propagating in structured media composed of alternating layers of positive and negative ε may reach beamsizes surpassing the diffraction limit. In the layered system, two different mechanisms lead to the superresolving effect. A bandpass filtering due to the existence of gaps in the spatial spectrum of k_x modifies the response of the system transversally providing a narrow peak along the x-axis with moderate gain ($\Delta_x < \lambda_d/2$) and high sidelobes (secondary foci). In the direction of the periodicity, however, superresolution is carried out by the formation of surface resonances leading to fast decays out of the interfaces. In our numerical simulations, Δ_y can be as low as a third of $\lambda_d/2$. Additionally, dephase of Bloch constituents belonging to different bands contributes to the growth control of secondary foci in nearby surfaces.

ACKNOWLEDGEMENT

This research was funded by Ministerio de Ciencia e Innovación (MICIIN) under the project TEC2009-11635.

REFERENCES

1. Hernández-Figueroa, H. E., M. Zamboni-Rached and E. Recami, *Localized Waves*, John Wiley & Sons, New Jersey, 2008.
2. Longhi, S., D. Janner and P. Laporta, "Propagating pulsed Bessel beams in periodic media," *J. Opt. B*, Vol. 6, No. 11, 477-481, 2004.
3. Miret, J. J. and C. J. Zapata-Rodríguez, "Diffraction-free beams with elliptic Bessel envelope in periodic media," *J. Opt. Soc. Am. B*, Vol. 25, No. 1, 1–6, 2008.
4. Pochi, Y., *Optical waves in layered media*, Wiley-Interscience, New Jersey, 2005.
5. Indebetouw, G., "Nondiffracting optical fields: some remarks on their analysis and synthesis," *J. Opt. Soc. Am. A* Vol 6, No. 1, 150–152, 1989.

Optical absorption and SHG in PMMA and SiO_2-matrices doped with DO3 as function of poling time

J. García-Macedo[1]A, A. Franco[1], G. Valverde-Aguilar[1], and L. Romero[2]

[1]Departamento de Estado Sólido, Instituto de Física, Universidad Nacional Autónoma de México, México, D.F. 04510, México

A conrresponding author

e-mail: gamaj@fisica.unam.mx

Fax number: +52 (55) 5622 5011, Telephone number: +52 (55) 5622 5103

Abstract- The orientation of non-linear dyes embedded in different matrices plays an important role on the optical properties of films. The order parameter is related with the dyes orientation through the optical absorption (OA). The answer of the dye to a corona poling treatment depends of the molecule-molecule and molecule-matrix interactions. Amorphous and nanostructured films of PMMA and SiO_2 doped with the organic dye Disperse Orange 3 (DO3) were prepared. Sodium Dodecyl Sulfate (SDS) was used as template to perform a large-order lamellar nanostructure, detected by X-ray diffraction (XRD). The films were characterized by scanning electronic microscopy (SEM). OA and second harmonic generation (SHG) intensity measurements were carried out at several corona poling times. SHG measurements were registered at 60, 80, 100 and 120ºC. The experimental results are shown in plots of order parameter and SHG intensity against corona poling time. We fitted the OA and the SHG results as function of the corona poling time with a model developed by us, employing only one fitting parameter related to the matrix-chromophore interactions. The lamellar structure provides largest order parameter values. The most intense SHG signal was obtained in the SiO_2:DO3 films with lamellar phase.

1. INTRODUCTION

In the last years a lot of attention has been put on the development of materials with well controlled nanostructures, due to their remarkable enhanced properties with respect to those materials without that ordered structure at the nanometric scale. Several kinds of properties in the materials have been improved by means of the incorporation of nanoparticles or nanostructures. In particular, the development of materials with very specific optical properties has experienced an important evolution due to the incorporation of nanoparticles in well organized nanostructures induced in the materials [1]. Metamaterials, photonic crystals and plasmonics are very important areas of the scientific research involved in the development of materials with new and interesting linear and non-linear optical features. Clear examples of materials whose optical properties are governed by their order at the nano-level scale are the nanostructured films doped with push-pull molecules. The collective orientation of the push-pull molecules inside the films changes the linear and non-linear optical responses of the films. One of the most striking optical properties of these films is observed when their chromophores are arranged in a non-centrosymmetrical distribution. When that happens, the films exhibit second-order non-linear optical properties detectable by second harmonic generation (SHG) measurements. A non-centrosymmetric

distribution of the orientation of the push-pull chromophores in a film can be attained by applying an intense external electric field across the film, like the well know case of the corona technique [2]. The orientation of the chromophores by corona poling is affected by local matrix-chromophore and chromophore-chromophore electrostatic interactions. The presence of nanostructures in the materials, in which the chromophores are embedded, helps to overcome some chromophores orientation difficulties related to the electrostatic interactions mentioned above. It means that the intensity of SHG, the speed of the chromophore orientation and the others parameters are expected to be controlled by means of the modification of the local environment around each one of the chromophores. That happens when the material is nanostructurated.

In this work the materials were nanostructurated by means of the incorporation of an ionic surfactant during the film matrix formation step. The presence of nanostructures in the films was confirmed by X-ray diffraction (XRD) measurements. The effect of the nanostructures in the chromophores orientation was monitored by UV-vis optical absorption and SHG intensity measurements as function of corona poling time at several temperatures on amorphous and nanostructured films. The fitting of the experimental results by means of our model [3] helps to quantify the effects of the nanostructures on the materials SHG signal intensity, speed of the chomophores orientation and stability of the non-centrosymmetric molecular arrangement.

2. EXPERIMENTAL DETAILS

2.1 Synthesis of the materials. All the materials under study were doped with the push-pull chromophore 4-amino-4-nitrobenzene, better known as Disperse Orange 3 (DO3), which has a big permanent dipole moment equal to 2.47×10^{-29} C m. Four kinds of different materials were studied in this work. These materials can be classified in two main groups: amorphous and nanostructured. The aim of the paper is to detect the main effects of the nanostructures in the optical responses of the materials. Besides, the matrices of the films had two different compositions, one of them was polymethylmethacrylate (PMMA) and the other one was SiO_2. The first one typically has weaker bonds than the second one, i.e., the chromophore orientation is easier in the first one at low temperatures. The PMMA films were made by mixing 80% in weight of tetrahydrofuran (THF) and 20% in weight of PMMA and DO3. From the total of PMMA and DO3, 95% in weight is PMMA and 5% in weight is DO3. The SiO_2 films were made by sol-gel technique, mixing tetraethylortosilicate (TEOS), ethanol (EtOH), deionized water and DO3 in the next molar ratios: TEOS : DO3 : EtOH : H_2O = 1 : 0.015 : 4 : 10.

An ionic surfactant Sodium Dodecyl Sulfate (SDS) was added to the solutions in order to nanostructurate the films. The ratio of SDS is 5% in weight with respect to the total solution. The total solution was filtered and the deposition of the films was carried out by dip-coating at an extraction rate of 5 cm/min.

2.2 Corona poling technique. The orientation of the chromophores was done using the well documented corona poling technique. Our system basically consists on a silver needle positioned at 5 centimeters from a copper plate. The silver needle is orthogonal to the plate and both of them serve as electrodes. The sample is hold by the copper plate and there is a voltage between the electrodes equal to 6 kilovolts. The copper plate works as a heater too, and has a hole just under the sample where the light can pass through. The corona poling setup is described in detail elsewhere.

2.3 Second harmonic generation. The second harmonic generation was measured in situ by transmittance using a YAG:Nd laser at 1064 nm as the fundamental beam of light. This fundamental beam is collected and focused onto the sample by a convergent lens. Another lens, set after the corona poling system, collects all the light coming from the sample and sends it to a photomultiplier. The light passes through a color filter which blocks the fundamental beam and allows the transmission of the generated beam at 532 nm. In a previous work this

set-up is completely described.

3. RESULTS AND DISCUSSION

XRD patterns confirmed the existence of nanostructures in the films with SDS, as well as the kind of the geometrical arrangement of the nanostructures (Figure 1). In both cases, PMMA and SiO_2, the long-range order corresponds to a lamellar geometrical arrangement. The average distances between nanostructures were 3.85 nm for the samples with PMMA and 3.80 nm for the samples with SiO_2.

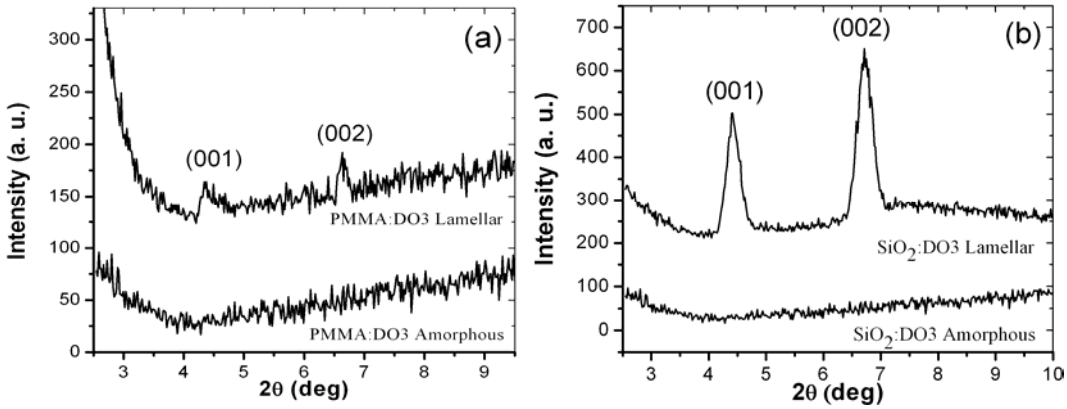


Figure 1. XRD patterns obtained for (a) PMMA:DO3 and (b) SiO_2:DO3 amorphous and nanostructured films.

The films thicknesses were determined by means of a statistical analysis based on SEM images obtained from the samples as shown in Figure 2. It was found the films were very homogeneous and the corresponding average thicknesses were 9.63 μm for the PMMA:DO3 amorphous film, 5.64 μm for the PMMA:DO3 nanostructured film, 2.75 μm for the SiO_2:DO3 amorphous film and 3.38 μm for the SiO_2:DO3 nanostructured film.

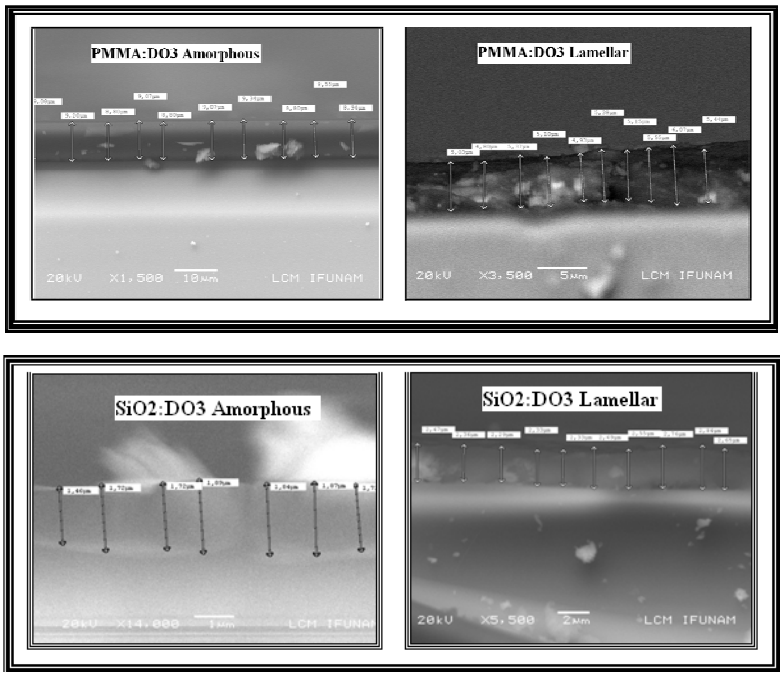


Figure 2. SEM images obtained for amorphous and nanostructured films (a) PMMA:DO3 (top) and (b) SiO_2:DO3 (bottom).

The UV-vis spectra of the samples shows that the maximum absorption is centered at 440 nm for all the samples, with or without SDS, as shown in Figure 3. It means there are not optical properties due directly to the surfactants. After corona poling the height of the maximum in the spectra decreases. The order parameter ρ relates de UV-vis spectra to the efficiency in the orientation of the chromophores through equation 1 [3, 4],

$$\rho = 1 - \frac{A_{\perp}}{A} \tag{1}$$

where $A_{\perp}$ is the film absorbance at 440 nm after poling and A is the corresponding absorbance before poling. It is remarkable that the nanostructured films exhibit larger order parameter.

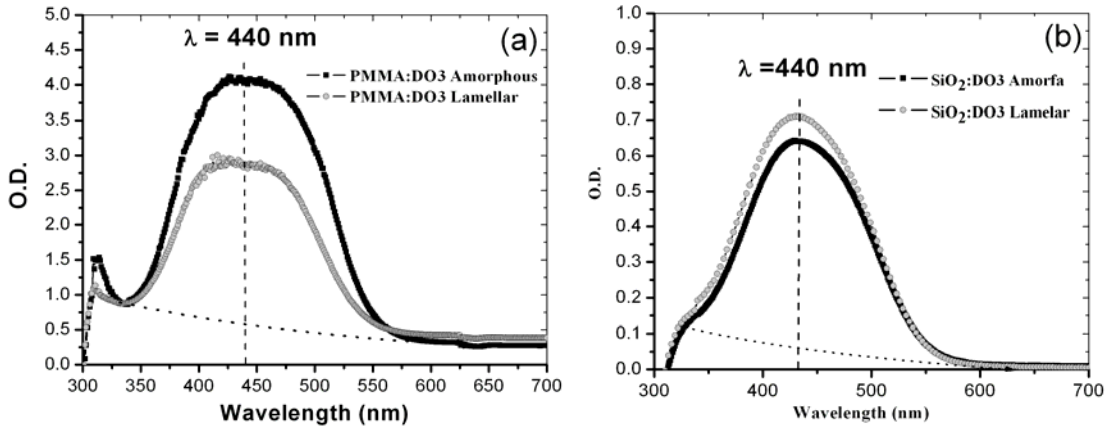


Figure 3. UV-vis absorption spectra obtained for (a) PMMA:DO3 and (b) SiO_2:DO3 amorphous and nanostructured films before corona poling. The ratio between the maximum spectrum height before and after corona poling determines the order parameter, i.e., it shows how easy the orientation of the chromophores is. It was found that the largest order parameter corresponds to the lamellar nanostructures.

The SHG intensity signal dynamics is plotted as function of the corona poling time at several temperatures, as shown in Figure 4. The SHG *vs.* corona poling time spectra was fitted with a model developed by us, employing only one fitting parameter related to the matrix-chromophore interactions. The theoretical fit corresponds to the solid black line. These plots show a growth in the signal until a maximum plateau. The maximum value is directly related to the number of chromophores oriented non-centrosymmetrically, the largest value was obtained for the SiO_2:DO3 nanostructured films. The speed of the orientation of the chromophores can be represented by a matrix-chromophore interactions parameter γ, as larger this parameter is slower the orientation is, too. The lowest value of this parameter was attained for the SiO_2:DO3 nanostructured films. It means that the stability also is poor in these samples, in the sense that if the matrix-chromophore interactions are small then the chromophores easily lost their orientation.

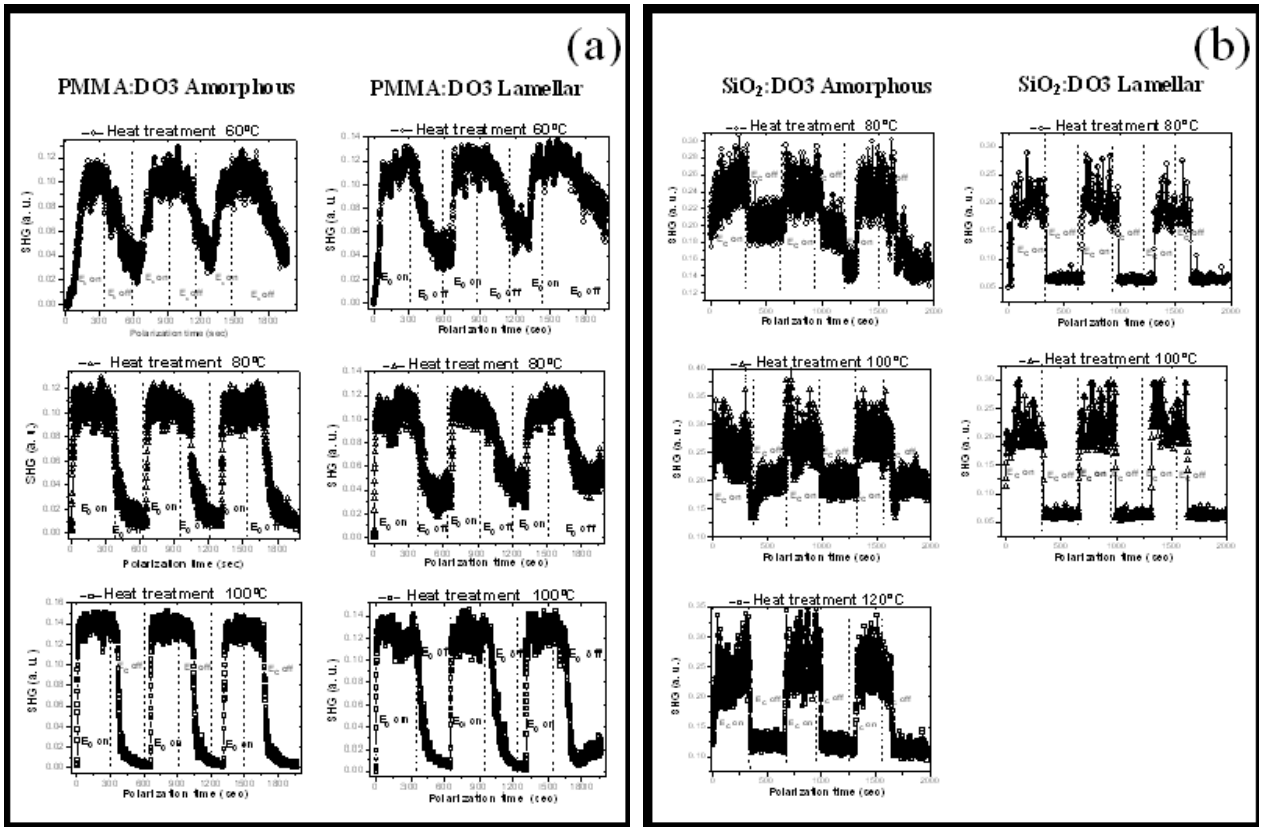


Figure 4. Plots of SHG intensity vs. Corona poling time for (a) PMMA:DO3 and (b) SiO_2:DO3 amorphous and nanostructured films at several temperatures.

4. CONCLUSIONS

XRD patterns show a better long-range order of the SiO_2 matrix than the PMMA one. The samples do not degrade with the experimental studies, as can be deduced from the cyclic measurements. The lamellar nanostructures give place to the largest order parameter values. The most intense SHG signal was obtained in the sample of SiO_2 with lamellar nanostructure. The orientation and disorientation of the DO3 molecules was faster in the samples of SiO_2 with lamellar nanostructure. It means that the nanostructures are a good option for modifying the dynamics of the chromophores orientation, which would allow increasing the efficiency of the SHG signal, the stability of the system and the speed for reaching the maximum SHG intensity.

ACKNOWLEDGEMENTS

The authors acknowledge the financial supports of CONACyT 79781, CONACyT 89584, NSF-CONACyT, PUNTA, ICyTDF and PAPIIT 116506-3. GVA is grateful for PUNTA postdoctoral fellowship. The authors are thankful to M. in Sc. Manuel Aguilar-Franco (XRD), Diego Quintero (preparation of the samples for SEM studies) and Roberto Hernández-Reyes (SEM) for technical assistance.

REFERENCES

1. Franco A., J. A. García-Macedo, I. G. Marino and P. P. Lottici, “Photoinduced birefringence in nanostructured SiO_2:DR1 Sol-Gel films”, *J. of Nanosc. & Nanotechn.*, 8, 12, 6576–6583, 2008.

2. Franco A., G. Valverde-Aguilar, J. García-Macedo, "Optical absorption and second harmonic generation in SiO_2:DR1 sol-gel films as function of poling time", in *Proceedings of SPIE*, San Diego, USA, 2006, 633116-1 to 633116-12.
3. Franco A., G. Valverde-Aguilar, J. García-Macedo, M. Canva, F. Chaput and Y. Levy, "Modeling of the Second harmonic generation in SiO_2 sol-gel films doped with nanoscopic DR1 molecules as function of the poling time", *Opt. Mater.*, 29, 1, 6-11, 2006.
4. Franco A., G. Valverde-Aguilar and J. García-Macedo, "Orientational dynamics of DR1 molecules in sol-gel films", *Opt. Mater.*, 29, 7, 814-820, 2007.

Using EBG Ground Plane for Improving Radiation in Low Profile Dipole Antenna

M. Rezaei Abkenar[1], **P. Rezaei**[1], **and R. Narimani**[2]
[1]Faculty of Electrical and Computer Engineering, Semnan University, Iran
[2]K. N. Toosi University of Technology, Iran
m_rezaie@semnan.ac.ir

Abstract- This paper investigates performance of a low profile dipole antenna embedded on a mushroom-like Electromagnetic Band-Gap ground plane. We utilize the in-phase reflection feature and surface wave band gap of EBG to improve radiation of antenna. Simulation results represent the low profile dipole antenna radiates efficiently, with a good return loss and radiation pattern.

1. INTRODUCTION

In recent years, electromagnetic band-gap (EBG) structures have attracted increasing interests because of their desirable electromagnetic properties that cannot be observed in natural materials. EBG structures are defined as artificial periodic (or sometimes non-periodic) objects that prevent/assist the propagation of electromagnetic waves in a specified band of frequency for all incident angles and all polarization states. Another important property of EBG structures is the phase response to the plane wave illumination, where the reflection phase changes from 180º to -180º as the frequency increases [1].

According to these properties a wide range of applications have been reported, such as TEM waveguides, microwave filters and low profile antennas [2-4].

In this paper we have utilized a mushroom-like EBG ground plane to improve the radiation efficiency of a dipole antenna near ground plane. We place a dipole antenna horizontally over a mushroom-like EBG ground plane. To study the effect of the EBG structure, performance of antenna have been studied and compared with perfect electric conductor (PEC) ground plane.

2. Mushroom-like EBG Structure

Mushroom-like EBG structures exhibit unique electromagnetic properties characteristic, such as frequency band gap and in-phase reflection, that have led to a wide range of electromagnetic device applications. One important application of EBG structures is that one can replace a conventional perfect electric conductor (PEC) ground plane with an EBG ground plane for a low profile wire antenna design. For this design, the operational frequency band of an EBG structure is defined as the frequency region within which a low profile wire antenna radiates efficiently, namely, having a good return loss and radiation patterns. The operational frequency band is the overlap of the input-match frequency band and the surface-wave frequency band gap [5].

The basic mushroom-like EBG structure is shown in fig.1. It consists of a flat metal sheet covered with an array of metal protrusions on a dielectric substrate which are connected to the lower conducting surface by metal plated vias [6]. The parameters of the EBG structure are labeled as patch width w, gap width g, substrate thickness h, dielectric constant ε_r, and vias radius r. When the periodicity (w + g) is small compared to the operating wavelength, the operation mechanism of this EBG structure can be explained using an effective medium model with equivalent lumped LC elements, as explain in [7].

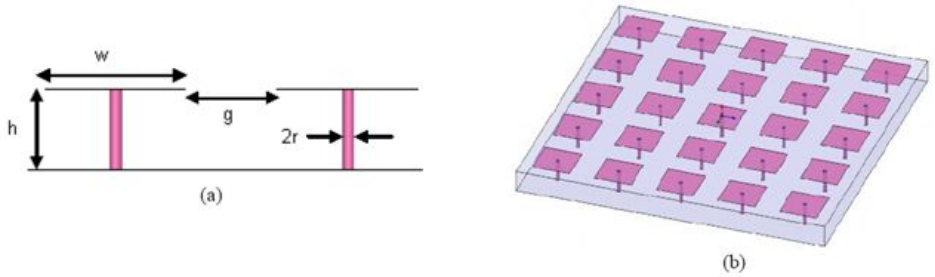


Fig.1 : Mushroom-like EBG structure a)unit cell b)3D view.

In this paper center frequency is set at 12GHz in order to design EBG ground plane, so parameters of EBG structure are:

w=0.12λ (3mm), g=0.02λ (0.5mm), h=0.04λ (1mm) and r=0.005λ (0.125mm). A dielectric layer with $\varepsilon_r = 2.33$ is used as substrate.

Ansoft HFSS v10 and CST Microwave Studio 2008, have been applied to simulate and analyze the structure.

2.1. Phase Reflection Diagram

An important property of EBG structure is phase reflection. The reflection phase is determined as the phase of reflected electric field at the reflecting surface. In these structures reflection phase varies with frequency from -180º to 180º. So in a specific frequency band they can be used as proper ground planes.

By modeling a unit cell with periodic boundary condition on side walls and running a parametric sweep using an incident wave excitation at different frequencies the reflection phase can be calculated from field results in HFSS [8].

It has been shown that, desired band of antenna radiation over an EBG ground plane, is close to the frequency region where the EBG surface shows a reflection phase in the range 90º±45º [5]. The 90º±45º criterion is consistent with the PEC, PMC, and EBG comparison. The PEC has a 180º reflection phase and the dipole antenna suffers from the reverse image current. The PMC surface has 0º reflection phase and the dipole antenna does not match well due to the strong mutual coupling. When the EBG ground plane exhibits a reflection phase in the middle, a good return loss is obtained for the dipole antenna. For our structure this frequency region is 11.7GHz-16.7GHz and it has been shown in fig.2.

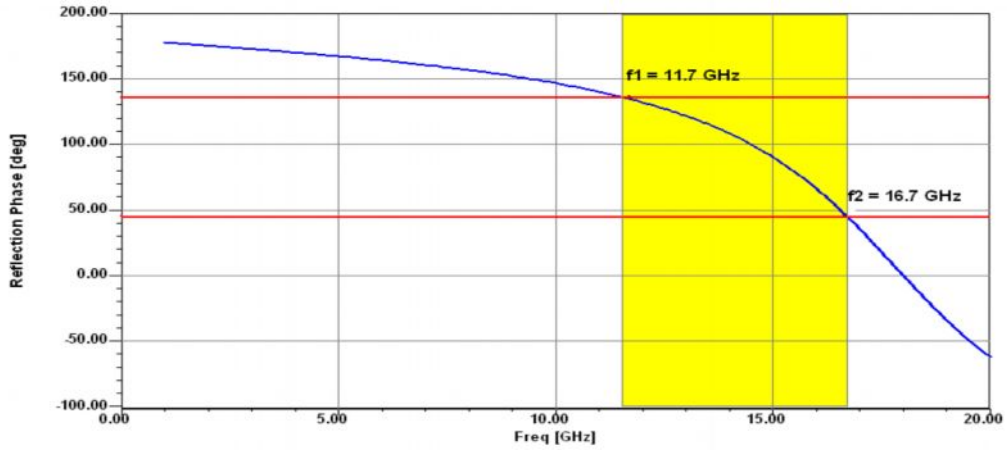


Fig.2 : Reflection phase of EBG structure.

3. Low profile dipole antenna with EBG ground plane

In wireless communications, it is desirable for antennas to have a low profile configuration. In such a design, the overall height of the antenna structure is usually less than one tenth of the operating wavelength and a fundamental challenge is the coupling effect of ground plane [1].

When a PEC surface is used as the ground plane, an electric current is vertical to that plane, the image current has the same direction and reinforces the radiation from the original current. Thus, this antenna has good radiation efficiency, but suffers from relative large antenna height due to the vertical placement of the current. To realize a low profile configuration, wire antenna should be positioned horizontally close to the ground plane. However, the problem is the poor radiation efficiency because of 180 º reflection phases in PEC. In contrast, the EBG surface is capable of providing a constructive image current within a certain frequency band, resulting in good radiation efficiency.

We place a dipole horizontally over the mushroom-like EBG ground plane with $\lambda \times \lambda$ size. The radius of the dipole is set to 0.125mm and the height of the dipole is set to 0.5mm, so the overall height of antenna is 0.06λ.

In order to obtain a resonant condition for a half-wave dipole, the physical length must be somewhat shorter than a free space half-wavelength [9]. So, to find optimum length of dipole, it has been changed from 0.4λ to 0.5λ and each time return loss of the antenna was obtained. It has been shown in fig.3 that the best return loss is achieved by dipole with length of 0.44λ.

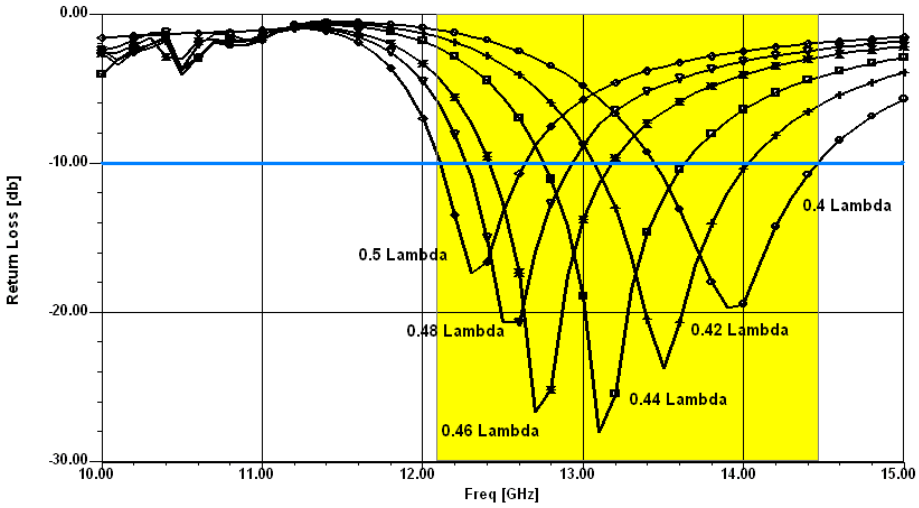


Fig.3 : Return loss of dipole antenna with its length varying from 0.4λ to 0.5λ.

For this range of length, the dipole shows a return loss better than -10dB from 12.1GHz to 14.5GHz. Thus, the input-match frequency band is from 12.1 to 14.5 GHz.

3.1. Simulation Results

As is shown in Fig.4, resonant frequency of antenna with EBG ground plane is 13.1GHz and in this frequency return loss is -28dB, but when PEC surface is used, the dipole has a return loss of -2.85dB at 12.55GHz.This is because of 180º reflection phase and reverse image current of PEC surface.

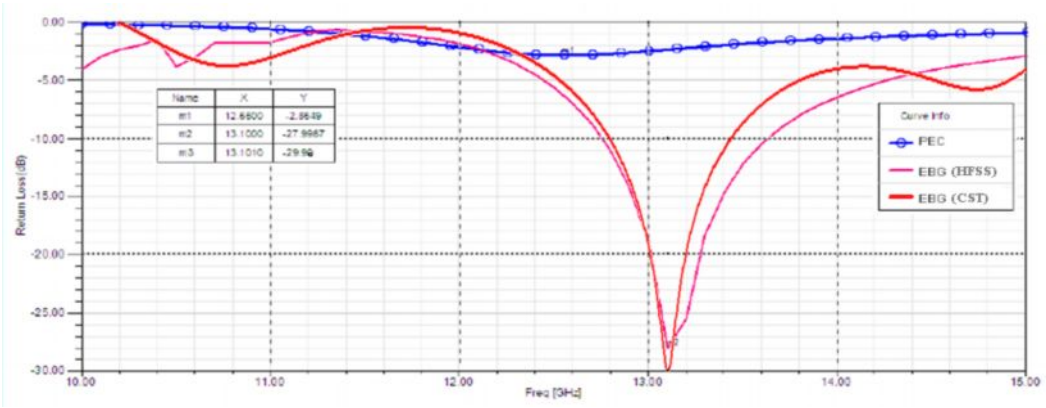


Fig.4: Comparison of return loss of antenna with EBG and PEC.

In fig.5 radiation pattern of dipole antenna over EBG and PEC ground plane at their resonant frequencies can be observed. Since the frequency is in band gap region, EBG structure shows high impedance, prevents surface-wave propagation in ground plane and leads to less wasted power in back lobes. In opposite, we have radiation increase at desired direction. This increase reaches to 10dB in some direction. As you can see in fig.6, front to back ratio of radiation pattern of antenna increase from 8.98dB with PEC plane to 13.47dB with EBG.
Fig.6 shows surface current density at resonant frequency. In EBG structure, surface current reduced because of its frequency band gap.

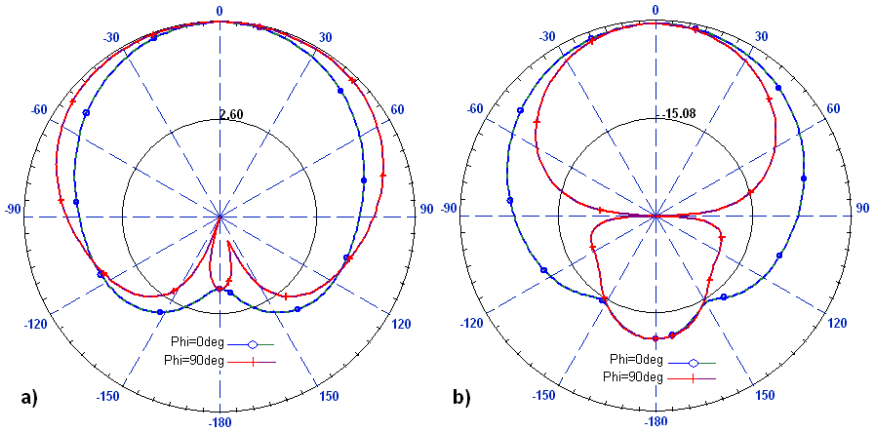


Fig.5: Radiation pattern of antenna (E-plane and H-plane) over, a) EBG ground plane, b) PEC ground plane.

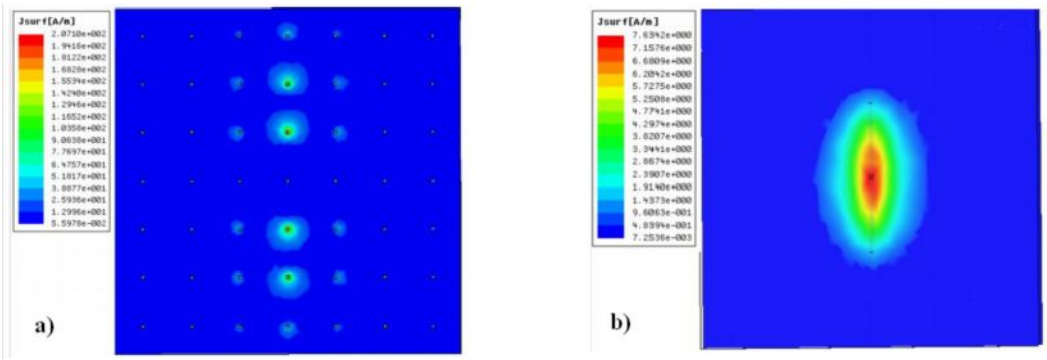


Fig.6: Surface current density a) EBG, b) PEC.

4. CONCLUSIONS

In this paper we discussed about mushroom-like EBG structures as a ground plane for low profile antenna. It is revealed that the frequency region where the EBG surface has a reflection phase in the range $90^{o}\pm45^{o}$ is very close to the input-match frequency band. For this designed antenna with EBG ground plan, input-match frequency band is near 6%.

Simulation results show that using EBG structure as ground plane improve antenna radiation patterns in comparison with PEC plane, because of surface-wave frequency band gap and reflection phase of EBG surface. EBG structure causes 25dB reduction in return loss of antenna, improvement of far field radiation near 10dB in some directions and 4.49dB increase in front to back ratio of radiation pattern.

ACKNOWLEDGEMENT

This work was supported by Faculty of Electrical and Computer Engineering, Semnan University.

REFERENCES

1. Yang.F and Y.Rahmat-Samii. "*Electromagnetic Band Gap Structures in Antenna Engineering*," Cambridge University Press, 2008.
2. Yang.F and Y. Rahmat-Samii, "Wire antenna on an EBG ground plane vs. patch antenna: A comparative study on low profile antennas," *URSI Electromagnetic Theory Symposium*, Ottawa, Canada, July 26–28, 2007.
3. Li.Z and Y. Rahmat-Samii, "PBG, PMC and PEC surface for antenna applications: A comparative study," *2000 IEEE APS Dig*., pp. 674–7, July 2000.
4. Akhoondzadeh-Asl.L , P. S. Hall, J. Nourinia, and Ch. Ghobadi, "Influence of Angular Stability of EBG Structures on Low Profile Dipole Antenna Performance," *IEEE Int. Workshop on Antenna Technology Small Antennas and Novel Metamaterials*, pp. 253–6, March 2006.
5. Yang.F and Y. Rahmat-Samii, "Reflection phase characterizations of the EBG ground plane for low profile wire antenna applications," *IEEE Trans. Antennas Propagat.*, Vol. 51, No. 10, 2691–703, 2003.
6. Sievenpiper.D, L. Zhang, R. F. J. Broas, N. G. Alexpolus, and E.Yablonovitch , "High-impedance electromagnetic surfaces with a forbidden frequency band," IEEE *Trns. Microwave Theory Tech*, Vol.47, 2059-74, 1999.
7. Sievenpiper.D, "High-Impedance Electromagnetic Surfaces," Ph.D. dissertation at University of California, Los Angeles, 1999.
8. Remski, R., "Analysis of photonic band gap surfaces using ansoft HFSS," *Microwave Journal*, September 2000.
9. Stutzman.W.L and G. A. Thiele, " *Antenna Theory and Design*," John-Wiley, 1991.

Bandwidth evaluation of dispersive transformation electromagnetics based devices

C. Argyropoulos[1], **E. Kallos**[1], **and Y. Hao**[1]

[1]Queen Mary, University of London, London, UK
christos.a@elec.qmul.ac.uk

Abstract— In this paper the transient responses of some devices which are based on transformation electromagnetics are studied, such as invisible cloaks and concentrators, by using the Finite-Difference Time-Domain (FDTD) numerical technique. In particular, effects of the inherent losses as well as the coating size of the ideal cylindrical cloak on its bandwidth and cloaking performance are examined. In addition, it is demonstrated that the performance of transformation electromagnetics based devices is affected by the material parameters in the design, although they may behave nicely under monochromatic plane wave illuminations. The obtained results are of interest for the future practical implementation of these structures.

1. INTRODUCTION

Transformation electromagnetics [1, 2] enables the design of exotic devices for the manipulation of electromagnetic waves in ways that are not occurring naturally. The most prominent application so far has been the cloak of invisibility [1], a structure that can be constructed using dispersive metamaterials [3]. Other design examples include the rotation coating [4], which rotates the apparent position of an object placed inside it, and the ideal concentrator [5], which enhances the amplitude of external fields in a small region of space. So far, however, such devices have been mostly studied under single frequency plane wave illumination [6], which effectively ignores their inherently dispersive nature. For example, the investigation of the cloaking bandwidth has been very limited in the literature to mostly analytical treatments [7, 8].

In this paper, we examine the transient responses of transformation-based devices. The goal is to demonstrate their bandwidth performance and better understand the physics involved in their frequency response. This is achieved using the robust and efficient dispersive radially-dependent FDTD numerical technique [9]. This numerical modeling method is advantageous compared to the Finite Element Method (FEM) used in previous works [10], since the transient response and the operational bandwidth of a device can be easily computed. Dispersive FDTD also self-consistently includes the frequency-dependent effects of the electric and magnetic components that arise in resonance-based metamaterial structures.

Initially, FDTD simulations are carried out to obtain the bandwidth of various lossy cylindrical cloaks, which is found to be strongly dependent on the loss characteristics of the materials. Next, the bandwidth of an ideal cloak is quantified as a function of the thickness of materials coating the object. Finally, we demonstrate that devices with more extreme material parameters exhibit reduced bandwidth. This is shown through comparing the transient responses of the ideal cylindrical cloak [10], the rotation coating [4] and the ideal concentrator [5]. Although we only present results from a few example devices here, we expect that these results are generally applicable to other devices based on metamaterials and transformation electromagnetics.

2. BANDWIDTH OF LOSSY IDEAL CYLINDRICAL CLOAKS

In this section we investigate the bandwidth of the ideal cloak under the effect of losses. For the two-dimensional (2-D) FDTD simulations presented here, a perfect electric conductor (PEC) cylinder (the object to be cloaked) is surrounded by an ideal cylindrical cloak. Without loss of generality, a TM plane wave is incident and only three field components are non-zero: E_x, E_y and H_z. The ideal cloak is characterized by three radially-dependent parameters given in cylindrical coordinates: $\varepsilon_r, \varepsilon_\phi$ and μ_z. The computational domain of the infinite (towards the z-direction) ideal cloak can be seen in Fig. 1(a). The FDTD cell size, throughout the modeling, is chosen $\Delta x = \Delta y = \lambda/150$, where λ is the wavelength of the excitation signal in free space. The domain size is 850×850 cells, or approximately $5.66\lambda \times 5.66\lambda$. The temporal discretization is chosen according to the Courant

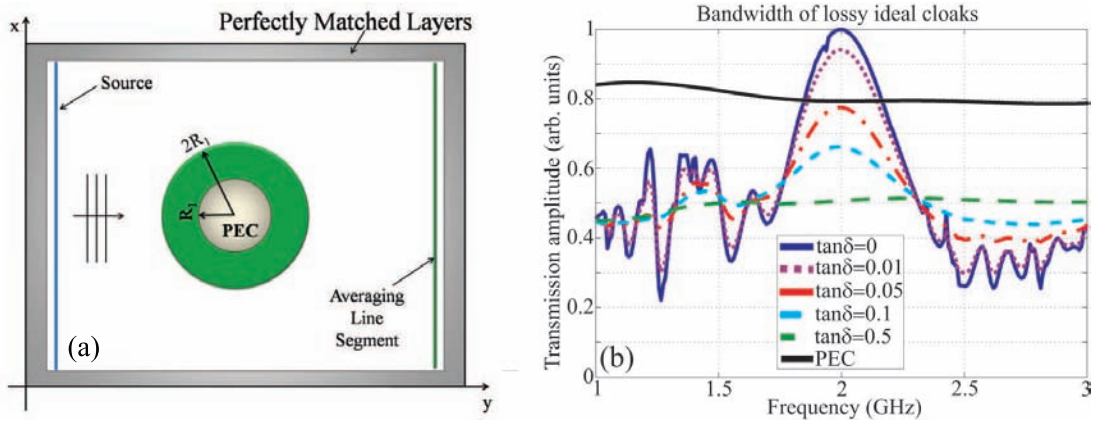


Figure 1: (a) FDTD computational domain of the ideal cylindrical cloak. Time-dependent temporally finite signals are excited on the source line shown on the left hand side, and recorded on the line segment shown on the right hand side after averaging over the segment's length. (b) Comparison of bandwidth performance of lossy ideal cloaks as a function of the material loss tangent. The performance of a bare PEC cylinder and the lossless cloak are also shown.

stability condition [11] and the time step is given by $\Delta t = \Delta x/\sqrt{2}c$, where c is the speed of light in free space. Throughout the paper the devices are designed to have an operating frequency of $f = 2$ GHz, where the free space wavelength is $\lambda \simeq 15$ cm.

The electromagnetic parameters of the ideal cloaking structure, in cylindrical coordinates, are given by [10]:

$$\varepsilon_r(r) = \frac{r - R_1}{r}, \quad \varepsilon_\phi(r) = \frac{r}{r - R_1}, \quad \mu_z(r) = \left(\frac{R_2}{R_2 - R_1}\right)^2 \frac{r - R_1}{r} \tag{1}$$

where R_1 is the inner radius, R_2 the outer radius and r an arbitrary radius inside the cloaking structure. When the parameters have dispersive values, they are mapped using the Drude dispersion model: $\hat{\varepsilon}(\omega) = 1 - \frac{\omega_p^2}{\omega^2 - j\omega\gamma}$, where ω_p is the plasma frequency and γ is the collision frequency characterizing the losses of the dispersive material. The frequency-dependent material parameters, denoted with a hat ($\hat{}$), are the ones implemented in the FDTD algorithm. These should be clearly distinguished from the design parameters of the device (Eq. (1)), which are valid at a single frequency only. Furthermore, the parameters can have non-dispersive values, and in that case they are simulated with a conventional dielectric/magnetic model: $\hat{\varepsilon}(\omega) = \varepsilon + \frac{\sigma}{j\omega}$, where ε is the radially-dependent parameter and σ is the electric or magnetic conductivity. A detailed description of the radially-dependent dispersive FDTD algorithm employed to model the ideal cloak can be found in [6, 9].

In the case of Drude model mapping of the material parameters, a lossy parameter can be presented in an alternative way: $\hat{\varepsilon} = \varepsilon(1 - j\tan\delta)$, where the parameter ε is dependent upon the radius of the device and $\tan\delta$ is the loss tangent of the lossy material. If the previous formula is substituted in the Drude model and $\tan\delta$ is assumed constant, the radially-dependent plasma and collision frequencies are obtained: $\omega_p(r) = \sqrt{(1-\varepsilon)\omega^2 + \varepsilon\omega\gamma\tan\delta}$, $\gamma(r) = \frac{\varepsilon\omega\tan\delta}{(1-\varepsilon)}$. Similarly, the conductivity of the conventional dielectric/magnetic model is given by (using ε as an example): $\sigma(r) = \varepsilon\omega\tan\delta$, which is again function of the radially-dependent parameter ε.

The lossy ideal cylindrical cloak is simulated with the proposed FDTD technique. The device is excited with a plane wave pulse centered at 2 GHz confined in a broadband Gaussian envelope with a Full Width at Half Maximum (FWHM) bandwidth of 1 GHz. The dimensions of the cloaking structure are $R_1 = \frac{2\lambda}{3}$ and $R_2 = \frac{4\lambda}{3}$ in terms of the free space wavelength. The Total-Field Scattered-Field (TF-SF) technique [11] is used for the FDTD computational domain throughout this paper in order to excite the plane waves. The magnetic field values H_z are spatially averaged along a parallel to the x-axis line segment, approximately equal to the length of the domain, as shown in Fig. 1(a). The transmitted Fourier spectrum is then retrieved from the time-dependence of the averaged field signals, which is next divided by the spectrum of the input pulse, yielding the transmission amplitude as a function of the frequency.

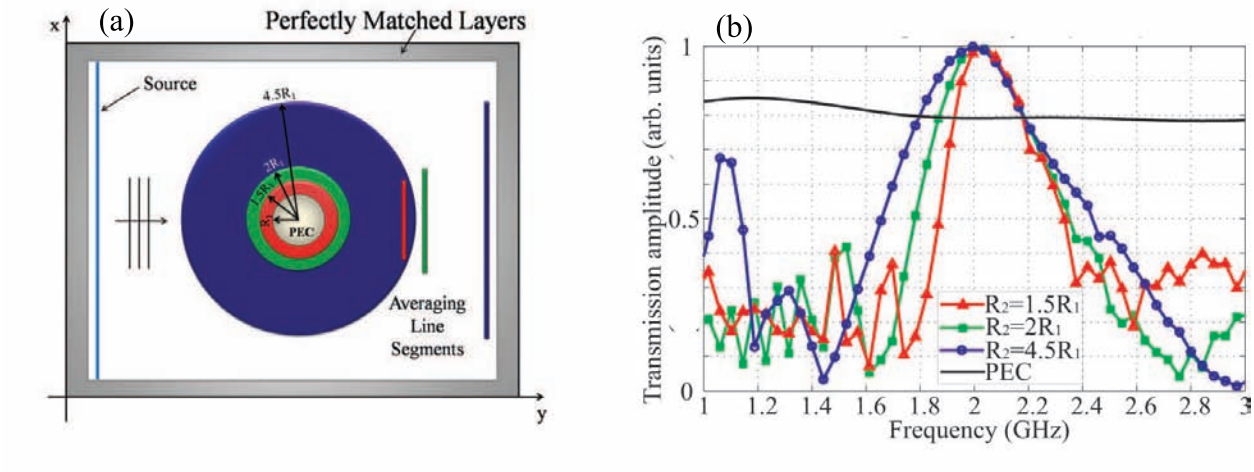


Figure 2: (a) FDTD computational domain of the ideal cylindrical cloak. Time-dependent temporally finite signals are excited on the source line shown on the left hand side, and recorded on the line segments shown on the right hand side after averaging over the segment's length. For each of the three cloaks shown, the fields are averaged over a different line segment, with a length equal to each cloak's diameter. (b) Comparison of bandwidth performance of lossless ideal cloaks with different thicknesses. The frequency response of the broadband source pulse onto a bare PEC cylinder is also shown.

The cloaking bandwidth for five different values of the loss tangent ($\tan\delta$) can be seen in Fig. 1(b). The case of the lossless cloak is also included in this graph, which is shown to peak at 1 at the operating frequency of 2 GHz: this confirms the operation of the ideal cloak at its design frequency as the signal amplitude is fully restored. The scattering amplitude of the bare PEC cylinder is also included in the graph, with an amplitude around 0.8 and relatively independent from frequency. Thus, the bandwidth of the ideal lossless cloak, defined through the range of frequencies where the transmitted field amplitude is higher than the field amplitude transmitted without a cloak, is estimated to be approximately 11.5%.

It is observed that the transmission amplitudes for cloaks that have increasingly higher loss tangents are dropping rapidly. This occurs over the whole frequency range for all the lossy cloaks. The cloaking effect ceases to exist when the losses are higher than $\tan\delta \geq 0.05$, which is actually a typical loss value for metamaterial structures close to the resonance [12]. Thus, a practical cloak will require very low loss factors in order to provide any useful type of cloaking. It is worth noticing that such inherent losses will impose qualitatively similar performance constraints on the majority of transformation-based structures. Finally, the results indicate that the cloak can work as a good absorber for loss values of $\tan\delta \geq 0.05$, as was explored in our previous work [13].

3. BANDWIDTH OF IDEAL CYLINDRICAL CLOAKS WITH VARYING THICKNESSES

In this section, we are interested in the dependence of the bandwidth on the size of the ideal cloak. In principle, the thickness of the cloaking coating can be arbitrary, since the parameters R_1 and R_2 in Eq. (1) can be freely chosen as long as $R_2 > R_1$. For any given pair of R_1 and R_2, the cloak will operate perfectly under plane wave illumination that matches the device's operating frequency (which is determined by the resonant frequency of the device's metamaterial elements), as long as the material parameters satisfy Eq. (1). However, thinner cloaks with $R_2 \simeq R_1$ require more extreme material parameters in order to operate, because the denominators of ε_ϕ and μ_z in Eq. (1) are becoming arbitrarily small as $R_2 \to R_1$. Similarly, thicker cloaks with $R_2 \gg R_1$ require more relaxed values for these parameters. These differences, effectively undetected by a perfect plane wave, are expected to materialize when the ideal cloak interacts with more broadband pulses: thinner cloaks should operate over narrower bandwidths.

Similarly to the method outlined in the previous section, the transmitted field amplitude is recorded, when a 1 GHz-wide Gaussian pulse centered at 2 GHz impinges on a bare metallic object with radius $R_1 = \frac{2\lambda}{3}$. Three different FDTD scenarios are investigated, where the object is coated with an ideal lossless cylindrical cloak that extends up to the outer radius R_2, which can take the values $1.5R_1$, $2.0R_1$, or $4.5R_1$. The computational domain is the same as before and the three

modeling scenarios are depicted in Fig. 2(a). The magnetic field values H_z are recorded at a tunable area, which scales with the size of the cloaks, as it is graphically depicted in Fig. 2(a). In order to make fair comparisons between the transmitted spectra for the different-sized cloaks, the fields for each device are averaged along a different line segment, as shown in Fig. 2(a). In all cases the averaging line segment is positioned 1.5λ away from the outer cloaking shell, while the segment's length is equal to the diameter of each device.

The transmission amplitudes of cloaks with three different sizes are reported in Fig. 2(b). It is indeed verified that thicker cloaks have less extreme material parameters and thus wider bandwidths. The thicker cloak with $R_2 = 4.5R_1$ has a bandwidth equal to 13.2%, broader than the thinner cloaks with thicknesses $R_2 = 2R_1$ and $R_2 = 1.5R_1$, which have bandwidths equal to 12.1% and 9.8%, respectively. From a physics perspective, thicker cloaks allow the wavefronts to bend less inside the cloaking coating, thus requiring more moderate values of material parameters. On the other hand, the cloak is becoming less attractive in terms of application and less practical in the design as its size is increased. Ultimately, a higher number of discrete concentric layers of metamaterial structures might be required to construct the device, thus leading to imperfections in the cloaking operation.

Note that a secondary smaller peak appears in the transmission spectra of the thick cloak ($R_2 = 4.5R_1$) close to the frequency of 1.1 GHz. This peak is attributed energy accumulation due to the interference pattern of the transmitted field at the monitoring point. It does not imply a cloaking effect since it depends on the distance between the device and the averaging line segment.

Finally, it should be noted that if the arguments presented in this section are reversed and dimensions of the object is know in prior, then by monitoring the transmission of broadband pulses one could detect not only the presence of an ideal cloak in the direction of propagation of the pulse, but also determine its exact size through monitoring the off-frequency field amplitude.

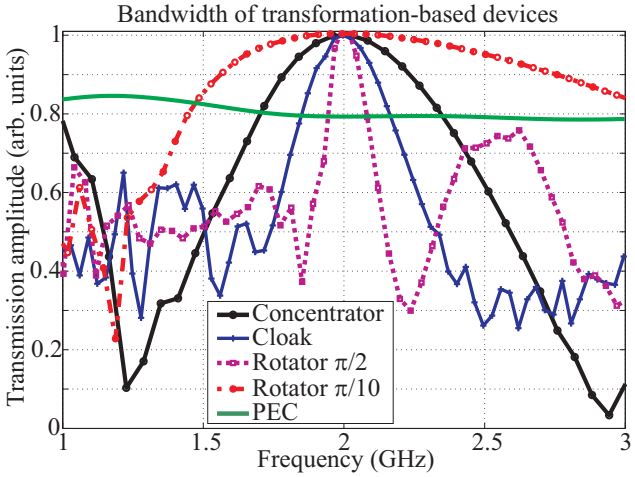


Figure 3: Comparison of the bandwidth performance of different transformation-based devices. The bare PEC cylinder performance is also included.

4. BANDWIDTH COMPARISONS OF TRANSFORMATION-BASED DEVICES

In this section, the bandwidth performance of different transformation-based cylindrical devices is compared. Specifically, the cylindrical ideal cloak [10], the rotation coating [4] and the ideal concentrator [5] are modeled with the radially-dependent FDTD technique. Two different rotation coatings are modeled: one that rotates the fields inside the core by an angle of $\pi/2$ and one that rotates the fields by $\pi/10$. All the devices are lossless.

Cylinders of different materials are placed inside the inner core of these devices. The core of the ideal cloak is a PEC cylinder, as discussed previously. The rotation coatings have a free space core to achieve unperturbed propagation of the electromagnetic radiation. Finally, inside the concentrator a magnetic material is placed with permeability $\mu_z = \left(\frac{R_2}{R_1}\right)^2$ in order to comply with its proposed design material values given in [5] for the given polarization examined here.

The computational domain is the same with the one in section 2, as shown in Fig. 1(a). The dimensions of the inner core and outer shell for all the devices are chosen to be the same, equal to

$R_1 = \frac{2\lambda}{3}$ and $R_2 = \frac{4\lambda}{3}$, for better comparison of their performance. The transmission amplitude for an incident broadband pulse is calculated in the same way as in section 2 for each device independently and the results are shown in Fig. 3.

By comparing the bandwidths of the various devices, we observe that the rotator with the large rotation angle has the narrowest bandwidth, followed by the ideal cloak. The two most broadband devices are the concentrator and the rotator with the small rotation angle. These differences are attributed to the material parameters where more dispersive values are required. For example, the rotator with the large rotation angle imposes larger bending onto the incoming electromagnetic wavefronts, thus requiring more extreme material parameters. Moreover, for the cases of the concentrator and the rotators, these devices allow wave propagation through their inner cores, and, hence, require less bending of the electromagnetic waves in comparison to the ideal cloaks. Note that the ideal concentrator can also be regarded as an ideal, more broadband, cloak, where the fields can penetrate its core, similar to the plasmonic cloaking devices proposed in [14].

5. CONCLUSION

The transient responses of transformation-based devices are numerically studied with a robust radially-dependent dispersive FDTD technique. The operational bandwidths of an ideal concentrator and a rotation coating is presented, leading to a better understanding of these metamaterial devices. Moreover, the inherent losses of the resonating metamaterial structures are exploited, and are found to cause distortions in the frequency response of the ideal cloaking structure. Hence, metamaterials with minimum loss factor have to be constructed, prior to the practical implementation of transformation-based devices. Finally, it is shown that thicker cloaks have wider bandwidths because they require more moderate anisotropic material parameters.

REFERENCES

1. J. B. Pendry, D. Schurig, and D. R. Smith, "Controlling electromagnetic fields," *Science*, vol. 312, pp. 1780-1782, 2006.
2. U. Leonhardt, Optical conformal mapping," *Science*, vol. 312, pp. 1777-1780, 2006.
3. D. Schurig *et al*, "Metamaterial electromagnetic cloak at microwave frequencies," *Science*, vol. 314, 977–980, 2006.
4. H. Chen and C. T. Chan, "Transformation media that rotate electromagnetic fields," *Appl. Phys. Lett.*, vol. 90, 241105, 2007.
5. M. Rahm *et al*, "Design of Electromagnetic Cloaks and Concentrators Using Form-Invariant Coordinate Transformations of Maxwells Equations," *Phot. and Nanostr. Fund. and Appl.*, vol. 6, 87-95, 2008.
6. Y. Zhao, C. Argyropoulos, and Y. Hao, "Full-wave finite-difference time-domain simulation of electromagnetic cloaking structures," *Opt. Express*, vol. 16, No. 9, 6717-6730, 2008.
7. B. Zhang *et al*, "Rainbow and Blueshift Effect of a Dispersive Spherical Invisibility Cloak Impinged On by a Nonmonochromatic Plane Wave," *Phys. Rev. Lett.*, vol. 101, 063902, 2008.
8. B. Ivsic, Z. Sipus, and S. Hrabar, "Analysis of Uniaxial Multilayer Cylinders Used for Invisible Cloak Realization," *IEEE Trans. Ant. and Propag.*, vol. 57, No. 5, 1521-1527, 2009.
9. C. Argyropoulos, Y. Zhao, and Y. Hao, "A Radially-Dependent Dispersive Finite-Difference Time-Domain Method for the Evaluation of Electromagnetic Cloaks," *IEEE Trans. Ant. and Propag.*, vol. 57, No. 5, 1432–1441, 2009.
10. S.A. Cummer *et al*, "Full-wave simulations of electromagnetic cloaking structures," *Phys. Rev. E*, vol. 74, 036621, 2006.
11. A. Taflove, *Computational Electrodynamics: The Finite Difference Time Domain Method*, Norwood, MA: Artech House, 1995.
12. V. Podolskiy and E. Narimanov, "Near-sighted superlens," *Opt. Lett.*, vol. 30, 75, 2005.
13. C. Argyropoulos *et al*, "Manipulating the loss in electromagnetic cloaks for perfect wave absorption," *Opt. Express*, vol. 17, No. 10, 8467–8475, 2009.
14. A. Alù and N. Engheta, "Cloaking a Sensor," *Phys. Rev. Lett.*, vol. 102, 233901, 2009.

Phase Change Associated with Resonant Surface Plasmon Polariton-Assisted Transmission in Nanohole Arrays

T. Yang and H. P. Ho

Department of Electronic Engineering, the Chinese University of Hong Kong, Hong Kong
Correspondence e-mail: hpho@ee.cuhk.edu.hk

***Abstract* – We report FDTA simulation results demonstrating that the optical phase change of surface plasmon polariton-assisted transmission through nanohole arrays in a gold film undergoes a sharp change under resonant conditions. The phenomenon can be explained by various resonant modes between the nanoholes. We further explore the possibility of using this effect for phase-sensitive surface plasmon resonance biosensing applications.**

***Index Terms* – extraordinary optical transmission, surface plasmon resonance, phase interrogation.**

I. INTRODUCTION

Surface plasmon resonance (SPR) sensors are widely used in biomedical and biochemical research for the characterization and quantification of binding events [1-3]. One important reason that SPR sensors have become a powerful analytical tool is their capability for real-time measurement with high detection sensitivity. They also have the ability to quantitatively detect interactions between biomolecules. Traditional SPR devices generally operate in total-internal reflection mode using the Kretschmann configuration [1]. These devices for extracting information from SPR are primarily concerned with analyzing the reflected light within the resonant reflectance dip. Recently, research attention in SPR sensing has shifted to measuring the SPR phase shift [4], because the resonant phase behavior exhibits a steep jump, which leads to potential in achieving extremely high sensitivity. In contrast, Kretschmann configuration requires special incidence angle to realize high sensitivity and the probe area also is quite large.

In this paper, we report simulation analysis of the change associated with will plasmon polariton-assisted transmission and demonstrate that a periodic square array of sub-wavelength holes on gold films can be utilized as a SPR phase sensor. SPR-based phase sensors that operate in transmission geometry can be established for ultrathin gold island films and nanoparticles immobilized on glass. Phase detection is used instead of intensity detection in order to realize even high sensitivity. This novel sensor operates in transmission mode, allowing for a simpler collinear optical arrangement and providing a smaller probing area than the typical Kretschmann configuration.

II. PRINCIPLE OF THE PHASE SENSOR

As schematically shown in Fig. 1, the extraordinary optical transmission effect may be separated into two contributions. The first one corresponds to the direct transmission of incoming field through the holes, i.e. the Bethe-type diffraction regime and the transmission coefficient presented by T_{Bethe}. This component is wavelength dependent and proportional to an identity matrix. The second contribution, with the transmission coefficient described by T_{Plasmon}, corresponds to the resonant part of the transmission matrix and is related to the

plamonic effect. In the present case, T_{Plasmon} is the main item that provides the phase change in our device. This resonant transmission process may be described by a four-step process. (i) The incident plane wave is converted into a surface wave at a given point scatterer. Normally the scatterer is the edge of the nanohole array. (ii) The surface wave propagates on the surface of the hole array and builds up several constructive interference modes according to the propagation distance. (iii) The surface wave is coupled into one of the holes and goes back and forth several times inside, thus resulting in some constructive interference effect. (iv) The surface waves within the hole array also produce constructive interference between them, and some energy will re-emit from the system as a plane wave. This four-step process indicates that when the effective refractive index of the dielectric on the surface of the metal experiences some change, the resonance parameters will also shift accordingly, thus leading to a sharp change in the phase of the radiation that drives the resonance. Therefore maximum change of the phase should occur near the resonant region, while the resonance parameters are dependent on the choice of hole periodicity, shape and size of the holes and thickness of the metal.

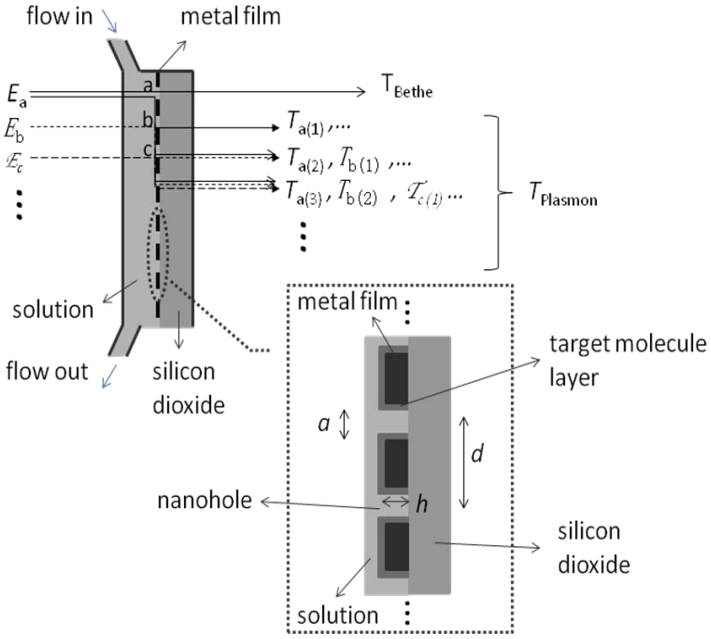


Fig. 1. Cross-section of nanohole structure

The above structure is a multi-resonance system. Even the resonance in the steps (ii) and (iii) is not prominent due to the change of effective refractive index of the dielectric, the constructive interference condition in step (iv) is always satisfied. The detailed explanation is as follows. Assuming there is an incident light E_a scattered at hole *a*, after passing through a distance of one hole period (*d*) and one hole depth (*h*), the generated surface plasmon at last re-emit as $T_{a(1)}$ from the adjacent hole b. The same process occurs for E_b , which is scattered at hole *b* and re-emit as $T_{b(1)}$ from the adjacent hole *c* or *a*. The same process is for $T_{c(1)}$, $T_{d(1)}$ and so on. Because $T_{a(1)}$, $T_{b(1)}$, $T_{c(1)}$,⋯ have the same phase, they form constructive interference. The surface plasmon generated at hole a can also re-emit from hole *c* as $T_{a(2)}$ after passing through two hole period (2*d*) and one hole depth (*h*). The same process is for $T_{b(2)}$, which comes from hole *b* and re-emit at hole *d*. Therefore, $T_{a(2)}$, $T_{b(2)}$,⋯ also have the same phase, they form constructive interference too. From the above analysis, we conclude that the surface plasmon passing through m_0 hole periods with a distance m_0 * *d* and going back and forth n_0 times inside *a* hole with a distance ($2n_0$-1) * *h* will always result in constructive interference and form a plane wave, so the electric field of the generated plane wave in the far-field can be expressed as:

$$
\begin{aligned}
Ee^{i\phi} = E_0\{&T_{11}e^{i[\omega t-(k_1 d+k_2 h)+\phi_0]} + T_{21}e^{i[\omega t-(2k_1 d+k_2 h)+\phi_0]} + T_{31}e^{i[\omega t-(3k_1 d+k_2 h)+\phi_0]} + \cdots \\
&+ T_{12}e^{i[\omega t-(k_1 d+3k_2 h)+\phi_0]} + T_{22}e^{i[\omega t-(2k_1 d+3k_2 h)+\phi_0]} + T_{32}e^{i[\omega t-(3k_1 d+3k_2 h)+\phi_0]} + \cdots \\
&+ T_{13}e^{i[\omega t-(k_1 d+5k_2 h)+\phi_0]} + T_{23}e^{i[\omega t-(2k_1 d+5k_2 h)+\phi_0]} + T_{33}e^{i[\omega t-(3k_1 d+5k_2 h)+\phi_0]} + \cdots \\
&+ \cdots\}
\end{aligned}
$$

where E_0 and E are the amplitude of the incident plane wave and the transmitted plane wave respectively. ϕ is the phase of the transmission light in the far field. ω is the angle frequency of the incident light. T_{m0n0} is the amplitude transmission coefficient of corresponding mode. ϕ_0 is the phase item that includes the initial phase of the source, the phase change from source to the front surface of the device and the phase change from the device to the point in the far field. k_1 and k_2 is the propagation constants of the surface plasmon on the front surface of the metal film and in the hole respectively. We can just approximately calculate the k_1 and k_2 by assuming metal and aqueous medium are infinite, i.e.

$$
k_1 \approx k_2 \approx \mathrm{Re}[\frac{\omega}{c}(\frac{\varepsilon_{metal}\varepsilon_{eff}}{\varepsilon_{metal}+\varepsilon_{eff}})^{1/2}]
$$

where $\varepsilon_{\mathrm{metal}}$ is the permittivity of the metal, and $\varepsilon_{\mathrm{eff}}$ is the effective permittivity of the dielectric containing receptors, target molecules and water. Therefore, if we neglect high mode due to their week amplitudes, the far-field equation can be simplified as

$$
Ee^{i\phi} \approx E_0 T_{11} e^{i\{\omega t-\mathrm{Re}[\frac{\omega(d+h)}{c}(\frac{\varepsilon_{metal}\varepsilon_{eff}}{\varepsilon_{metal}+\varepsilon_{eff}})^{1/2}]+\phi_0\}}
$$

Therefore if the effective refractive index of the dielectric $\varepsilon_{\mathrm{eff}}$ is changed, the phase of the transmitted light will also shift accordingly.

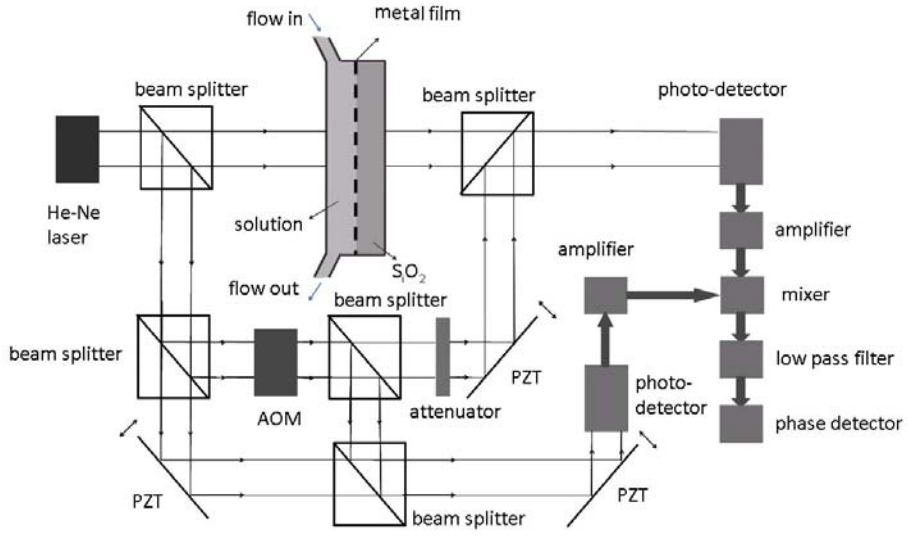


Fig. 2. Proposed optical setup for SPR phase shift measurement

Fig. 2 shows a proposed phase interrogation scheme based on a heterodyne interferometric system, which offers the benefits of detecting time-varying signals only and high noise rejection capability upon using long integration time. A typical heterodyne interferometer uses an acousto-optic modulator to impose a frequency shift in the input laser beam. When

the frequency-shifted reference beam interferes with the signal beam, the phase of the beat frequency, which may be readily measured by the lockin technique, will provide the phase reading introduced by the sensor device. In other words, when the device is used as a biosensor and target receptor molecules in the sample solution are immobilized on the nanohole sensor surface that has been functionalized by the conjugate ligands, the resultant refractive index change will shift the optical phase of the plasmon polariton-assisted transmission accordingly. The heterodyne interferometer will then process the optical beams and produce the required phase reading as desired.

III. Simulation Results and Discussion

FDTD Solutions (Lumerical Solutions, Inc) with minimum 2 nm mesh size is used to study the device structure proposed in Fig. 1. We have performed a series of simulation experiments by varying the hole size and array periodicity in order to find the optimized device parameter. It was found the optimal dimensions of nanohole structure are: 100nm for hole width, 427.6nm for hole period and 109nm for hole depth, with the holes being square ones. While, a number of plots have been generated in the optimization process, we report the important one for showing the resonant nature of the system. For this point, Fig. 3 shows the variation of phase change versus hole periodicity in silver and gold films.

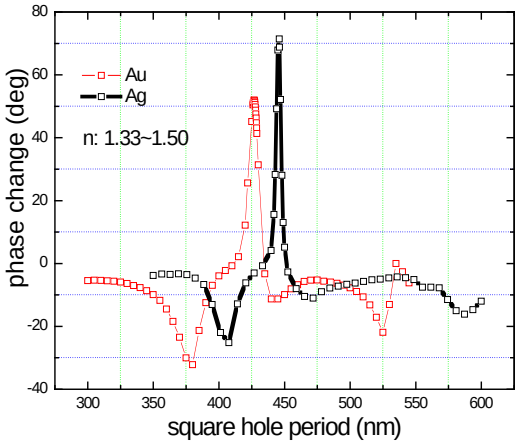


Fig. 3. Variation of phase change versus square hole periodicity.

In Fig. 4 we also show the intensity distribution of electromagnetic field intensity in the near-field using the optimal parameters for nanoholes in gold films. The intensity is shown on a logarithmic scale and the source power propagates in the direction of –Z.

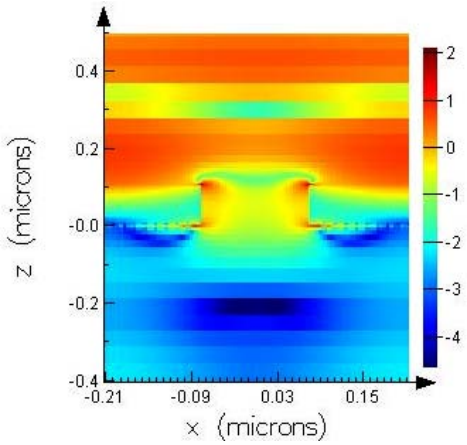


Fig. 4. Logarithmic intensity distribution in near-field

If the device is used as a bisensor, i.e. when bio-molecules are immobilized on to nanohole surface, the effective refractive index of the surface layer will increase, the phase of the transmitted light will shift. Simulation results shown in Fig. 5 confirms that this will take place the device is capable of being used as transmission based biosensor.

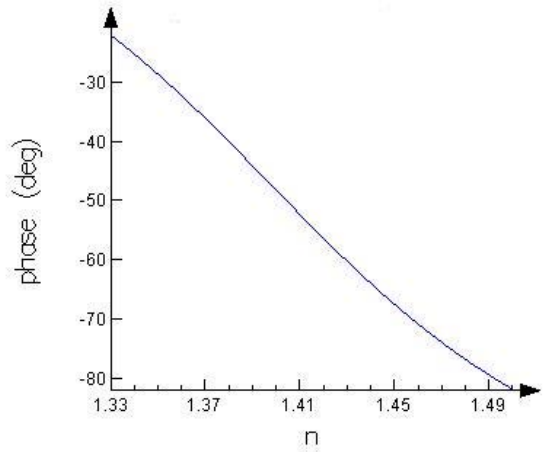


Fig. 5 Relation between effective refractive index of sensor layer and phase of transmitted light

Simulation result shows that when the refractive index changes from 1.33 to 1.50, the phase has changed by 59° as shown in Fig. 5. For a signal power W_s of 2.5μW (Assuming that the power of the incoming beam is 0.25mW and the transmission coefficients are 1%, although simulation results indicate that the transmission coefficients are 1.7509% and 1.3233% for silver and gold respectively.) and a bandwidth Δf of 1Hz, we find δx_N=0.0213pm. Therefore, the detection resolution is 1.93×10^{-6} degree. The predicted sensitivity limit of an optimal gold device and an optimal silver device are 6.33×10^{-9} RIU and 4.37×10^{-9} RIU respectively [5].

It is clear from Fig.5 that the arrays of sub-wavelength holes on gold act as a highly sensitive sensor to the detection of molecular adsorption. Similarly to other SPR configurations, the good sensitivity to surface binding is the result of the tightly confined SP mode [4]. It is precisely this SP mode that allows for the enhanced transmission resonance in the arrays of nanoholes. The measured sensitivity of these arrays to refractive index variation is comparable to those calculated for a grating-based SPR sensor. The absolute sensitivity is, however, smaller than that obtained by fixed-angle SPR using the Kretschmann configuration. The advantage of using the nanohole array is that it provides a smaller sensing probe (given by the surface area of the array). Consequently, the analytical response is generated by a smaller absolute number of molecules and leads to better spatial resolution than typical SPR devices. The transmission geometry is also advantageous for device implementation because it allows for easy optical alignment.

IV. CONCLUSION

In summary, we have performed FDTD analysis on the phase change associated with plasmon polariton-assisted transmission in nanohole arrays and its application SP-based phase sensors for the adsorption of biomolecules. The monolayer sensitivity of this substrate is comparable to other SP systems. The array of sub-wavelength holes investigated here are only a few micrometers in length, and the detection was made in transmission mode. These features render this substrate ideal for miniaturization and integration as detection systems in microfluidics architectures and lab-on-chip devices.

ACKNOWLEDGEMENT

The authors wish to acknowledge the funding support from the Hong Kong Research Grants Council under CERG project # 411907.

REFERENCES

[1] E. C. Nice, B. Catimel, Instrumental biosensors: new perspectives for the analysis of biomolecular interactions, BioEssays, vol. 21. pp. 339 – 352, 1999.

[2] T. Vo-Dinh, B. M. Cullum, Biosensors and. biochips, advances in biological and medical. diagnostics, Fresenius, J. Anal. Chem., vol.366, pp540-551, 2000.

[3] A. G. Brolo, R. Gordon et al, Surface plasmon sensor based on the enhanced light transmission through arrays of nanoholes in gold films, Langmuir, vol. 20, pp. 4813-4815, 2004.

[4] S. Y. Wu, H. P. Ho et al, Highly sensitive differential phase-sensitive surface plasmon resonance biosensor based on the Mach-Zehnder configuration, Opt. Lett., vol. 29, pp.2378-2380, 2004.

[5] T. Yang and H.P. Ho, Computational investigation of nanohole array based SPR sensing using phase shift, Optics Express, vol. 17, pp11205-11216 ,2009

Optical and structural properties of Au-Ag islands films for plasmonic applications

J. Sancho-Parramon[1*], V. Janicki[1], M. Lončarić[1], H. Zorc[1], P. Dubček[1] and S. Bernstorff[2]
[1] Ruđer Bošković Institute, Bijenička 54, 10000 Zagreb, Croatia
[2]Sincrotrone Trieste, SS 14 km 163.5, 34012 Basovizza (Trieste), Italy
*e-mail: jsancho@irb.hr

Abstract- Bimetallic islands films consisting of composite Au-Ag nanoparticles are deposited on glass substrates by electron beam evaporation. Broad tuning of the surface plasmon resonance (SPR) characteristics can be achieved by controlling film composition, deposition temperature and post-deposition thermal annealing. Optical and structural characterization of the samples enables to establish the link between the SPR and the morphological and compositional characteristics of nanoparticles.

1. INTRODUCTION

Gold and silver are the most widely used metals for nanoparticle-based plasmonic applications, such as chemical and biological sensing, luminescence enhancement or photovoltaic efficiency increase. Tuning of the SPR is usually achieved by controlling the size, shape and spatial arrangement of nanoparticles. Further tuning of the SPR over a wide energy range can be obtained using Au-Ag bimetallic nanoparticles, either as core-shell or as alloyed structure[1]. A simple way to obtain Au-Ag nanoparticle systems is deposition of metals islands films. These films can be considered as two-dimensional ensembles of metal clusters and are one of the most easy-to-prepare cases of nanostructured matter, as they can be obtained during the first stage of evaporation process. Recently, metal islands films have been used as building blocks for photonic and plasmonic structures[2]. Typical growth of metal islands films results into broad distribution of size and shape of particles that can be partially controlled by the deposition conditions and post-deposition treatments.

In the present work we study the optical properties of Au-Ag metal islands films deposited on glass substrates by electron beam evaporation. The influence of composition, deposition temperature and post-deposition annealing treatment is analyzed using spectrophotometry and spectroscopic ellipsometry for optical characterization, while the structural properties of the islands are determined using grazing-incidence small-angle x-ray scattering (GISAXS). The results illustrate the strong correlation between optical and structural properties of the islands and evidence the possibility to widely tailor the SPR of these systems.

2. EXPERIMENTAL

Metal islands films consisting of Au-Ag particles were deposited on 1 mm thick BK7 glass substrates by electron beam evaporation in a Varian 3117 deposition chamber. The Au-Ag films were deposited by the subsequent deposition of few nanometers of Ag and of Au. Due to the poor wetting of metals on glass substrate, the films follow an island-like growth mechanism (Volmer-Weber growth) rather than forming a compact film[3]. Films with different Ag/Au composition were deposited with the following mass thickness (in nanometers): 2/6, 4/4 and 6/2. Films were deposited on substrates at room temperature (T_d = 25 °C) and pre-heated at T_d = 220 °C.

After deposition, samples were annealed 20 minutes at 350°C in air in a Lindberg/Blue M furnace.

The surface plasmon resonance was characterized with photometric measurements (reflectance and transmittance at near-normal incidence) with a Perkin Elmer Lambda 25 spectrophometer in the range 300 nm – 1100 nm. Ellipsometric measurements were performed at different angles of incidence (45°, 55°, 65°) in the range 300 nm – 2200 nm with a J. A. Woollam V-VASE spectroscopic ellipsometer. Fitting of the ellipsometric data allows determining the effective optical constants and thickness of the islands film. A multiple oscillator approach was used to represent the dispersion of the optical constants of the films. GISAXS measurements were carried out at the Austrian SAXS beam line at the Synchrotron ELETTRA in Trieste (Italy), using 8 keV X-ray photon energy (λ = 0.154 nm). The GISAXS intensity curves are obtained from the scattering pattern recorded by a two-dimensional charge-coupled device (CCD) sensitive detector. A motorized Al beam stop was positioned perpendicularly to the sample surface to reduce the transmitted and specularly reflected beams. The samples were mounted on a stepper-motor-controlled tilting stage with a step resolution of 0.001^{o} and measured at the chosen grazing angles.

3. RESULTS AND DISCUSSION

For all the samples, spectrophotometric measurements show strong optical extinction in the visible spectral range that can be associated to the surface plasmon resonance of islands (Figure 1). Additional absorption was observed in the UV spectral range that can be associated to the electronic interband transition of Au and Ag. As deposited samples show a broad SPR that, in general, becomes narrower and blue-shifted upon thermal annealing (Table 1). This change is more evident for the islands films deposited at room temperature.

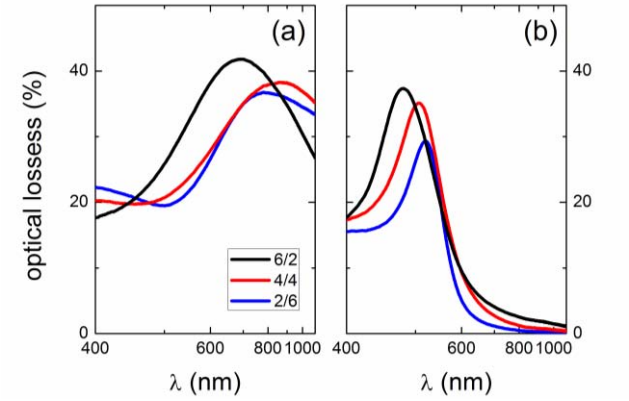


Figure 1. Optical losses of metal islands films deposited at room temperature with Ag/Au ratios 6/2 (black line) 4/4 (red line) and 2/6 (blue line): as deposited (a) and after thermal annealing (b).

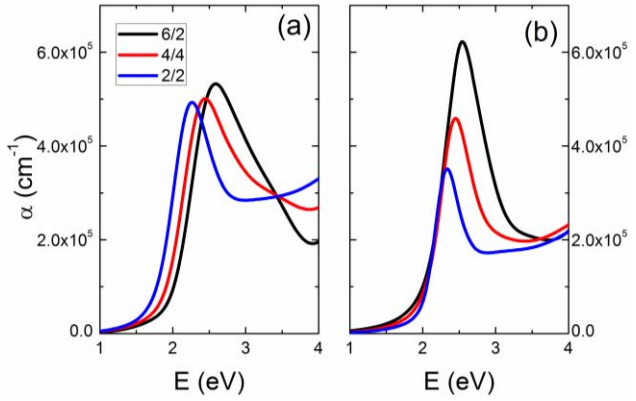


Figure 2. Effective absorption coefficient obtained from ellipsometric measurements for the films deposited at 220 °C with Ag/Au ratios 6/2 (black line) 4/4 (red line) and 2/6 (blue line): as deposited (a) and after thermal annealing (b).

The effective optical constants of the islands films extracted from spectroscopic ellipsometry agree with the results from spectrophotometry (Figure 2). In order to fit the ellipsometric data, two oscillators are required to model the SPR for the as-deposited samples while only one oscillator is necessary for the annealed samples. This double-peak structure of the SPR for the as deposited samples has been previously associated to a core-shell structure (one peak associated to the core material and the other to the shell material)[4,5]. Upon annealing, alloying of the particles takes place, leading to a single-peak SPR[6,7].

GISAXS scattering patterns reveal that the film is composed of nanometric clusters distributed at the sample surface, as shown by the presence of two lobes of scattered light symmetric with respect to the incidence angle. For the annealed samples the intensity of the scattered light is more concentrated at smaller angles, suggesting that the particle size increases upon annealing. An estimation of the particle size can be done in terms of the so-called Guinier approximation, that gives the particle radius in the direction perpendicular (R_V) and parallel (R_H) to the sample surface from analysis of 1D intensity distributions in the two characteristic directions parallel and perpendicular to sample surface (Table 1)[8]. In addition, the average interparticle distance (D) can be estimated from the position of the maximum of scattered light[8]. As observed previously in metal islands films[9], samples deposited at room temperature show a more elliptical shape and smaller size than those deposited at hot substrates. Upon annealing, particle size and interparticle interaction increases, indicating the particle growth.

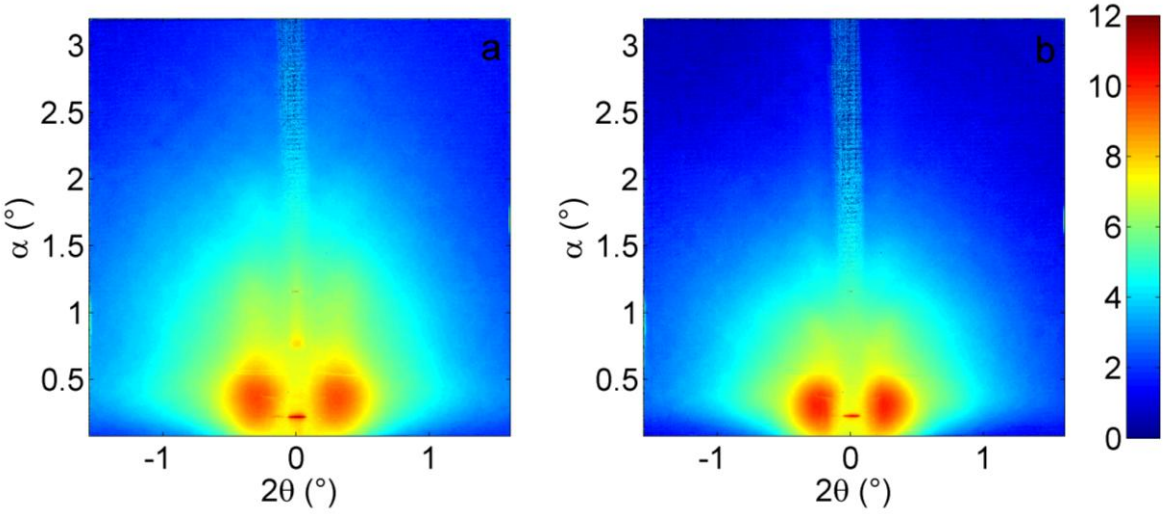


Figure 3: GISAXS intensity patterns (logarithmic scale) for the Ag/Au film deposited at 220 °C with composition 2/6: as deposited (a) and after annealing (b). α and 2θ are the scattering angles in the direction perpendicular and parallel to the islands film, respectively.

The results show a strong interplay between the islands composition and shape and the observed optical properties. Thus, while the SPR of the films deposited at hot substrates is red-shifted with higher Au content, this trend is not observed for the films deposited at room temperature. In this case, the SPR peak appears to be more correlated with the degree of sphereicity of the islands than with the Au content. Indeed, islands films deposited at cold substrates have a small aspect ratio (R_V/R_H) that strongly affects the SPR[9].

Upon thermal annealing, SPR red-shift with higher Au content is observed for films deposited at both, room temperature and hot substrates. In this case, the SPR is well defined as a single and narrow peak that indicates the particle alloying. For single-material islands films, increase of annealing induces increase of particle sphereicity and consequent blue-shift of the SPR[9]. In several of the samples studied here, the islands become more elliptical after annealing. This shape change can compensate the blue-shift due to alloying and even result in a red-shift of the SPR respect of the as deposited films, as observed for the films with higher Ag content deposited at hot substrates. Since Ag islands grow more spherically than Au, alloying of Ag-Au islands may result in a more elliptical shape than the original core-shell particle, especially if the Ag core is close to spherical, as expected for the samples deposited at hot substrates.

Td	Treatment	Ag/Au	R_V (nm)	R_H (nm)	D (nm)	t (nm)	SPR max (nm)
25 °C	As deposited	2/6	4.1	6.5	21.3	7.1	781
		4/4	3.4	6.9	21.4	7.8	860
		6/2	4.2	7.7	22.8	7.9	683
	Annealed	2/6	10.5	17.5	53.3	16.1	519
		4/4	11.6	15.2	45.6	14.2	506
		6/2	9.1	15.5	45.3	11.5	477
220 °C	As deposited	2/6	6.9	10.9	29.1	10.4	568
		4/4	8.3	11.8	29.7	11.6	522
		6/2	9.3	10.7	29.1	13.1	494
	Annealed	2/6	9.9	13.3	36.6	13.1	537
		4/4	10.2	15.1	41.3	12.0	523
		6/2	9.4	14.5	39.1	11.8	504

Table 1: Summary of results from GISAXS analysis (vertical radius R_V, horizontal radius R_H and interparticle distance *D*) ellipsometry (thickness *t*) and photometric measurements (*SPR* wavelength) for the studied samples.

4. CONCLUSIONS

The optical and structural properties of bimetallic Ag/Au islands films obtained by electron beam evaporation have been determined. A strong interplay between the SPR properties and the islands shape and composition is observed. As required for many plasmonic applications, the SPR of these systems can be widely tuned depending on the deposition conditions and post-deposition annealing treatments.

REFERENCES

1. F. Hubenthal, N. Borg and F. Träger "Optical properties and ultrafast electron dynamics in gold-silver alloy and core-shell nanoparticles", *Appl. Phys. B*, Vol. 93, 39–45, 2008.
2. V. Janicki, J. Sancho-Parramon, F. Peiró and J. Arbiol "Three-dimensional photonic microstructures produced by electric field assisted dissolution of metal nanoclusters in multilayer stacks", *Appl. Phys. B*, Vol. 98, 93–98, 2010.
3. N. Kaiser "Review of the fundamentals of thin film growth" *App. Optics*, Vol. 41, No. 16, 3053–3060, 2002.
4. M. Moskovits, I. Srnova-Sloufova and B. Vlckova "Bimetallic Ag-Au nanoparticles: Extracting meaningful optical constants from the surface-plasmon extinction spectrum" *J. Chem. Phys.* Vol. 116, No. 23, 10435–10446, 2002.
5. W. Benten, N. Nilius, N. Ernst and H. –J. Freund "Photon emission spectroscopy of single oxide-supported Ag-Au alloy clusters" *Phys. Rev. B*, Vol. 72, 045403, 2005.
6. K. Baba, T. Okuno and M. Miyagi "Silver-gold compound metal island films prepared by using a two-step evaporation method" *Appl. Phys. Lett.*, Vol. 62, No. 5, 437–439, 1992.
7. K. Baba, Y. Ohkuma, T. Yonezawa and M. Miyagi "Silver-based compound metal island films for write-once optical data-storage media" *Appl. Optics*, Vol. 40, No. 16, 2796–2804, 2001.
8. M. Lončarić, et. al. "Optical and structural characterization of silver islands films on glass substrates", *Vacuum*, Vol. 84, 188-192, 2009.
9. R. R. Singer, A. Leitner, F. R. Aussenegg "Structure analysis and models for optical constants of discontinuous metallic silver films" *J. Opt. Soc. Am. B* Vol. 12, No. 2, 220–228, 1995.

Optical devices based on materials with negative refraction.

V. S. Gorelik[1] and V. V. Shchavlev[2]
[1] P.N. Lebedev Physical Institute of the Russian Academy of Sciences, Moscow, Russia.
[2] P.N. Lebedev Physical Institute of the Russian Academy of Sciences and Moscow Institute of Physics and Technology, Moscow, Russia.
[1]gorelik@sci.lebedev.ru
[2]vova_mipt@mail.ru

Abstract
The current paper presents an overview of the physics of the negative refraction. It derives Abbe invariant for media with positive and negative refractive index. It also develops a formula to calculate the distance to the image and a formula for the magnification given by the various superlenses. We introduce a schematic diagram of "superfocuser", "supermicroscope" and "superspectrograph" - devices based on materials with negative refraction. We also evaluate the magnification given by superlenses installed in the superfocuser and supermicroscope and calculate linear dispersion of the superspectrograph.

1. INTRODUCTION

The history of negative refraction goes a long way back. In 1944, L.I. Mandelstam in his lecture spoke about negative refraction occurring at the plane boundary between two media, one of which may be subject to waves with negative group velocity [1]. Still earlier, in 1904 Lamb wrote about the negative group velocity for acoustic waves [2]. In 1967, UFN published an article by V.G. Veselago, that proved that the substances with simultaneously negative permittivity and permeability possess a negative refractive index [3]. Over a long period of time it was impossible to observe the negative refraction of waves at the interface. In 2000, David Smith along with his colleagues from the University of California created a material with a negative refractive index, and conducted an experiment that confirmed negative refraction at microwave wavelengths [4].

2. PHYSICS OF NEGATIVE REFRACTION

We are now going to focus on the physics of the phenomenon of negative refraction. In fact, the negative refraction of waves at the interfaces occurs as a consequence of negative group velocity in one of the adjacent media. The article by V.M. Agranovich and Yu.N. Gartstein gives the following proof of this assertion [5].

A plane sinusoidal wave incident at angle φ to the plane section y = 0 is given by the equation:

$$E = e^{i\{\omega t - k(x\sin\varphi + y\cos\varphi)\}} \tag{1}$$

Reflected and refracted waves are described by the equations:

$$\begin{aligned} E &= e^{i\{\omega t - k(x\sin\varphi' - y\cos\varphi')\}} \\ E &= e^{i\{\omega t - k'(x\sin\psi + y\cos\psi)\}} \end{aligned} \tag{2}$$

The laws of reflection and refraction arise from the boundary conditions on the plane y = 0:

$$\begin{aligned} \sin\varphi &= \sin\varphi' \\ k\sin\varphi &= k'\sin\psi \end{aligned} \tag{3}$$

The last equality is satisfied at angles $\psi > 0$ and $\psi < 0$. If the wave refracts at angle $\psi < 0$, the phase velocity is directed opposite to the group velocity. Algebraic value of wave vector for incident and refractive waves are $k = n\frac{\omega}{c}$ and $k' = n'\frac{\omega}{c}$ correspondingly. Accordingly Snell's law takes the shape:

$$n \sin \varphi = n' \sin \psi \tag{4}$$

From (4) we can conclude, that if $\psi < 0$, refraction index n' should be negative. The refraction of waves at angles $\psi > 0$ and $\psi < 0$ is illustrated in Figure 1.

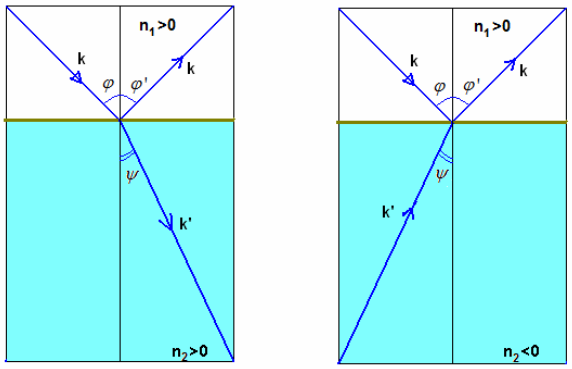


Fig.1. Reflection and refraction at the interface of two media with positive and negative refractive index.

3. ABBE INVARIANT

Let us derive Abbe invariant under the refraction of light on the spherical surface of the medium with a positive and a negative refractive index [6]. Suppose that we have two media, separated by a spherical surface S, whose centre O lies on the line LL'. A point source is located in point L, and the image is created in point L '.

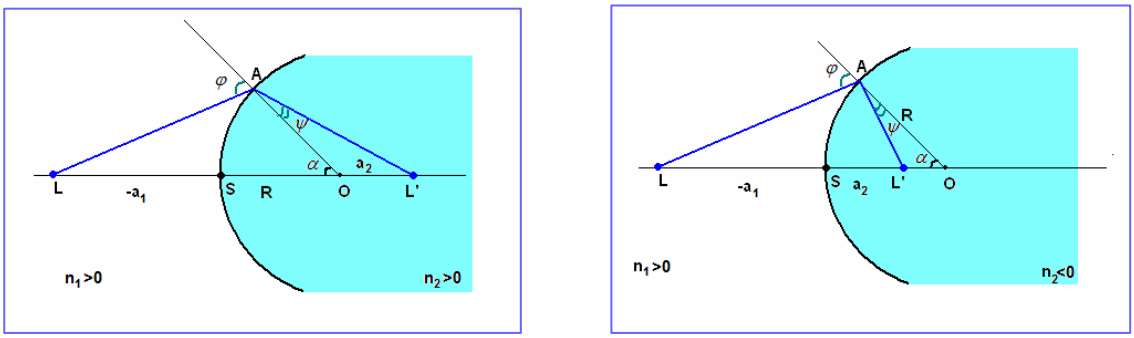


Fig.2. Refraction of waves on the spherical surface of the medium with positive and negative refraction.

Figure 2 shows the variation of the beam (LAL'). Let us consider a paraxial beam, therefore $LA \simeq LS$, $L'A \simeq L'S$. From $\triangle ALO$ and $\triangle AL'O$, according to the law of sines, we get the following relations for the parties:

$$\begin{aligned} &\triangle ALO: \frac{LO}{LA} = \frac{\sin(180-\varphi)}{\sin\alpha} = \frac{\sin\varphi}{\sin\alpha} \\ &\triangle AL'O: \frac{AL'}{OL'} = \frac{\sin\alpha}{\sin\psi} \end{aligned} \tag{5}$$

It follows that:

$$\begin{aligned} &\frac{LO}{LA}\frac{AL'}{OL'} = \frac{\sin\varphi}{\sin\psi} = \frac{n_2}{n_1} \quad (\text{if } n_2>0) \\ &\frac{LO}{LA}\frac{AL'}{OL'} = \frac{\sin\varphi}{\sin\psi} = \frac{(-n_2)}{n_1} \quad (\text{if } n_2<0) \end{aligned} \tag{6}$$

The minus comes from the fact that ψ here is the absolute value of the angle. We are going to measure all the segments along the axis from point S, considering the segments, laid off from S to the right to be positive, and the ones laid off to the left to be negative. Let R be the radius of the spherical surface, $(-a_1), a_2$ - the distance from O to L and L '. Then

$$\begin{aligned} AL &= SL = (-a_1) \\ AL' &= SL' = a_2 \\ LO &= R - a_1 \\ OL' &= a_2 - R \text{ (if } n_2 > 0) \\ OL' &= R - a_2 \text{ (if } n_2 < 0) \end{aligned} \tag{7}$$

Substituting the expressions for the distances from (7) in (6), we get

$$\frac{R - a_1}{(-a_1)} \frac{a_2}{a_2 - R} = \frac{n_2}{n_1} \tag{8}$$

In that manner we deduce Abbe invariant:

$$Q = n_1\left(\frac{1}{a_1} - \frac{1}{R}\right) = n_2\left(\frac{1}{a_2} - \frac{1}{R}\right) = const \tag{9}$$

Note that in the case of a flat interface $(R = \infty)$ Abbe invariant takes the simplified form:

$$Q = \frac{n_1}{a_1} = \frac{n_2}{a_2} = const \tag{10}$$

Abbe invariant presupposes, in particular, that the distance to the image is equal to:

$$a_2 = \frac{n_2 a_1 R}{a_1(n_2 - n_1) + n_1 R} \tag{11}$$

In the case of a flat interface (11) is equal to the following relation:

$$a_2 = \frac{n_2}{n_1} a_1 \tag{12}$$

4. MAGNIFICATIONS OF SUPERLENS

The formula for the magnification of superlens can be derived in the following way. Let us consider a superlens with a flat and concave surface (Fig. 3).

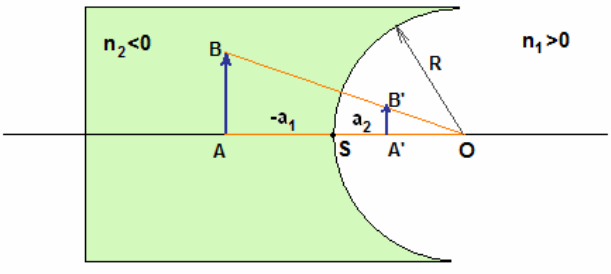


Fig.3. Magnification of an image given by a superlens.

The image AB is converted into the image A'B'. The triangles ΔABO and $\Delta A'B'O$ are similar and, therefore $\frac{A'B'}{AB} = \frac{A'O}{AO}$, in our notation $AO = R - a_1$, $A'O = R - a_2$. The distance is measured from point S with regard to signs, and the superlens magnification can be calculated by the formula:

$$V = \frac{A'B'}{AB} = \frac{R - a_2}{R - a_1} \tag{13}$$

In addition, in the paraxial optics, the magnification can be calculated by the formula:

$$V = \frac{a_2}{a_1}\frac{n_1}{n_2} \tag{14}$$

5. OPTICAL DEVICES BASED ON MATERIALS WITH NEGATIVE REFRACTION

A number of various optical devices can be constructed using materials with negative refraction. Below are schematic diagrams of some of them.

5.1. SUPERLENS

A superlens performs the same function as the normal lens - allows you to obtain an image of an object. It is worth mentioning that the magnification given by a plane-parallel superlens is equal to unity. Below is the relevant calculation.

$$V = V_1 V_2 = (\frac{a_2}{a_1}\frac{n_1}{n_2})(\frac{n_2}{n_1}\frac{a'_1}{a'_2}) = 1 \tag{15}$$

Here we used relations (10) and (14). A schematic diagram of the superlens is shown at Figure 4.

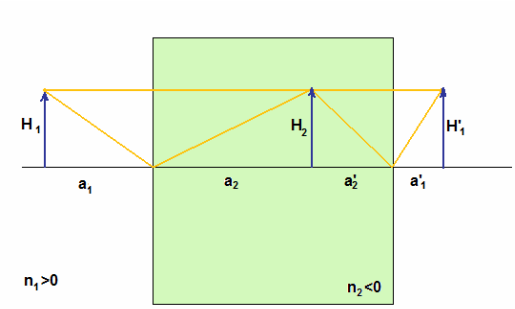


Fig.4. The image given by a plane-parallel superlens.

5.2. SUPERFOCUSER

A superfocuser provides a reduced image of the object. A schematic diagram of the setup is shown in Figure 5.

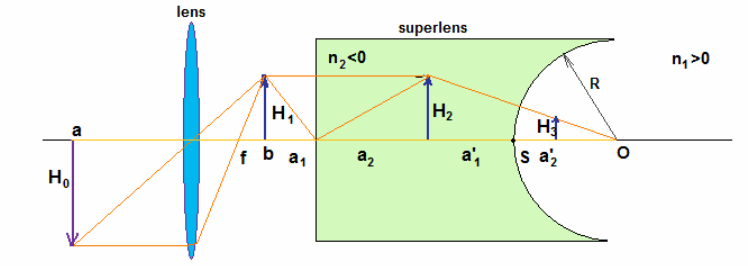


Fig. 5. The scheme of a superfocuser.

From Fig. 5, we deduce that $R > 0,\ \ a'_1 < 0,\ 0 < a'_2 < R$. Therefore

$$V = \frac{R - a'_2}{R - a'_1} < 1 \tag{16}$$

Thus, the magnification given by a superlens set on a superfocuser is, as expected, less than unity.

5.3. SUPERMICROSCOPE

A supermicroscope is designed to produce magnified images of small objects. A schematic diagram of the device is shown in Figure 6.

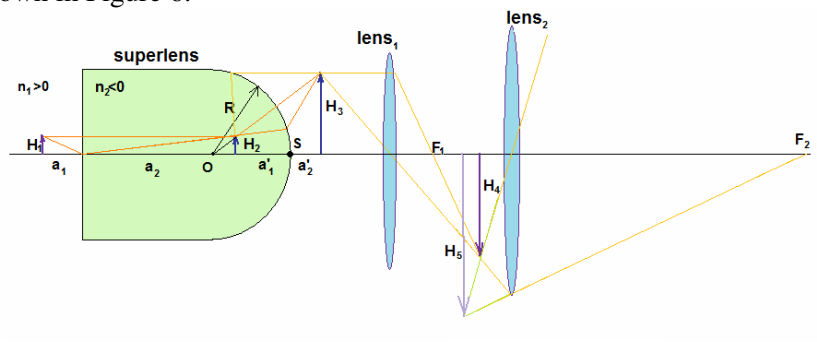


Fig. 6. The scheme of a supermicroscope.

The difference between a conventional microscope and a supermicroscope is in the presence of a superlens, which can magnify the object under study, the dimensions of which are smaller than the wavelength of radiation used to study the object. From Fig.6, we deduce that $R<0$, $a'_1<0<R$, $a'_2>0$. We conclude that a superlens installed in the supermicroscope, gives the magnification

$$V=\frac{R-a'_2}{R-a'_1}>1 \tag{17}$$

The closer is the image of the object to the center on a spherical surface, the greater is the magnification.

5.4. SUPERSPECTROGRAPH

A superspectrograph is used to register the emission spectrum. A schematic diagram of the setup is shown in Figure 7.

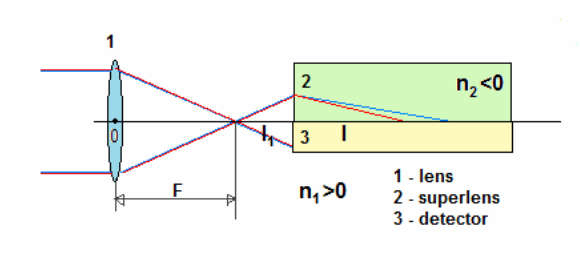


Fig. 7. The scheme of a superspectrograph.

The advantages of this superspectrograph are its small size and simplicity of design. The calculation of rhe superspectrograph dispersion using the electron theory of dispersion leads to the following acceptable result:

$$\frac{d\lambda}{dl}=\left[\frac{dl}{d\lambda}\right]^{-1}=\left[\frac{Ne^2}{m\varepsilon_0}\frac{(-1)}{(2\pi c)^2}\frac{\lambda_o^{\,4}\lambda}{(\lambda^2-\lambda_0^{\,2})^2}\frac{1}{n_2}\frac{l_1}{n_1}\right]^{-1}=190,5\frac{A}{мм} \tag{18}$$

Here:

$n=-1,46,\ \ l_0=0.2(m),\ \ \lambda_0=200(nm),\ \ \lambda=486(nm),\ \ \varepsilon_0=8.85\cdot10^{-12}\left(\frac{F}{m}\right),\ \ e=1.6\cdot10^{-19}(\mathrm{C}),$

$m=9.1\cdot10^{-31}(kg)$

4. CONCLUSIONS

In this term paper we disclosed the physics of negative refraction, obtained Abbe invariant for the media with positive and negative refraction, calculated the magnification of the superlenses and the linear dispersion of the superspectrograph.

In conclusion, we note that the devices based on media with negative refraction have certain advantages over conventional optical devices, the advance in this area capable of bringing about improvements in people's lives. That is why today this field of science is rapidly developing - scientists from different countries are trying to create a medium with negative refraction in the optical range.

REFERENCES

1. Mandelshtam L.I. "Lectures on optics, the theory of relativity and quantum mechanics" (Moscow: Nauka, 1972).
2. Lamb H. *Proc. London Math. Soc.,* **1**, 473, 1904.
3. Veselago V.G. "The electrodynamics of substances with simultaneously negative values of ε and μ". *Phys. Usp.,* **10,** 509-514, 1968.
4. Pendry J. B. and D. R. Smith "The Quest for the Superlens", *Scientific American,* №7, 60-68, 2006.
5. Agranovich V.M. and Y.N. Gartstein "Spatial dispersion and negative refraction of light" *Phys. Usp.,* **49,** 1029-1044, 2006.
6. Landsberg G.S. "Optics", pp. 280-281, (Moscow: Nauka, 1976)

Composite Right/Left-Handed Circular Meta-Waveguide

Tamer M. Abuelfadl

Electronics and Electrical Communications Dept., Faculty of Engineering, Cairo University, Egypt.
telfadl@ieee.org

Abstract— A new realization of cylindrical meta-waveguide is proposed. The guide is a metallic cylinder loaded azimuthally with conducting rods short-circuited to the outer cylinder. It can be simplified to a planar periodically cascaded coupled-lines. However, the actual circuit is described in cylindrical coordinates as screw or helically periodic structure. The dispersion relation was obtained from the circuit model and from the actual structure using EM simulation, with a good agreement between both. An 8-cell structure was simulated to show the overall guide transmission characteristic. The major advantage of this new guide is that it does not contain any dielectrics, which makes it favorable in applications involving electron beams such as Backward Wave Oscillator BWO, Gyrotron BWO, and Cherenkov backward wave detector.

1. INTRODUCTION

Left-Handed LH transmission lines and waveguides are the 1D version of metamaterial [1], where the guided wave has opposite phase and group velocities. So, they are also named backward wave transmission lines. They are usually realized on conventional Right-Handed RH lines using series capacitors and shunt inductors [2]. Hence, they exhibit RH characteristic on a portion of their operating frequency and a LH characteristic on another portion, and so they are named Composite Right/Left-Handed CRLH transmission lines [1]. They can be realized using lumped or semi-distributed elements [3]. Coupled lines have been also employed to achieve the CRLH transmission lines [4, 5, 6]. The LH waveguide version has been realized using dielectric filled corrugations in rectangular waveguide and named mataguide or meta-waveguide [7].

In this paper, a CRLH circular meta-waveguide that have the first (dominant) mode propagating as a backward wave or LH, is realized by periodically loading a circular waveguide with coupled lines. The loading is done by azimuthally placement of conducting rods close to the circular guide surface. These rods act as coupled lines and the outer conducting cylinder as ground.

This paper is organized as follows: section 2 presents the equivalent circuit of the short-circuited ideal coupled lines, and their dispersion relation. In section 3 the actual metaguide which is a circular waveguide loaded with coupled conducting rods is described, and the screw or helical periodicity of the structure is demonstrated. The dispersions relations and the transmission characteristics are discussed in section 4. The main conclusions are presented in section 5.

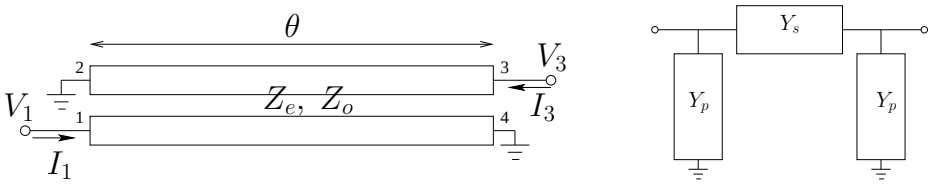
2. COMPOSITE RIGHT/LEFT-HANDED TRANSMISSION LINES USING COUPLED LINES

The proposed CRLH line is a periodic structure. The unit cell for for such structure shown in Fig. 1(a) can be obtained from the simple coupled line by terminating two ports (port 1 and 4 in Fig. 1(a)) with short circuit. The resulting 2-port admittance matrix written in terms of the 4-port network Y-parameters [8],

$$\begin{bmatrix} I_1 \\ I_3 \end{bmatrix} = \begin{bmatrix} Y_{11} & Y_{13} \\ Y_{31} & Y_{33} \end{bmatrix} \begin{bmatrix} V_1 \\ V_3 \end{bmatrix}, \tag{1}$$

where $Y_{11} = Y_{33} = -j\,(Y_o + Y_e)\cot\theta/2$, $Y_{13} = Y_{31} = -j\,(Y_o - Y_e)\csc\theta/2$, and $\theta = kL$ is the electrical length of the coupled lines of physical length L. The considered coupled line has no dielectric filling, hence its propagation factor $k = \omega/c$, where c is the speed of light in vacuum. The parameters Y_o and Y_e, are the odd and even admittance, respectively. The proposed unit cell can be modeled by the Π network shown in Fig. 1(b). In this equivalent circuit the series Y_s and parallel Y_p are given in terms of the elements of the admittance matrix Eq. (1) by [9],

$$Y_p = Y_{11} + Y_{13} = -j\,(Y_e + Y_o)\,\frac{\cos\theta + \cos\theta_c}{2\sin\theta}, \qquad Y_s = -Y_{13} = j\,(Y_e + Y_o)\,\frac{\cos\theta_c}{2\sin\theta}, \tag{2}$$



(a) Ideal Coupled Lines. (b) Equivalent Circuit

Figure 1: (a) Schematic of ideal coupled lines, and (b) Equivalent circuit when port 3 and 4 are short circuited.

where $\cos\theta_c = (Y_o - Y_e)/(Y_o + Y_e)$. The electrical length θ is directly proportional to the operating frequency, so it can be considered as the normalized frequency. In the first range of $\theta < \pi - \theta_c$, the series admittance Y_s in Eq. (2) is pure capacitive while the parallel admittance Y_p is pure inductive, making the cell acts as a left handed one.

For a unit cell with period d, the dispersion relations and the Bloch impedance can be written as [1, 10],

$$\cos\beta d = 1 + \frac{Y_p}{Y_s} = -\frac{\cos\theta}{\cos\theta_c}, \qquad Z_B = \frac{1}{\sqrt{Y_p\left(Y_p + 2Y_s\right)}} = \frac{2\left|\sin\theta\right|}{\left(Y_o - Y_e\right)\sqrt{1 - \cos^2\theta/\cos^2\theta_c}}. \tag{3}$$

Both the propagation factor β and the Bloch impedance Z_B, in Eq. (3), are real in the first frequency range $\theta_c < \theta < \pi - \theta_c$, as previously mentioned the periodic line will be left-handed in this range of frequency. The solid curve in Fig. 3(b) shows this dispersion relation between the normalized frequency θ and the propagation factor represented in βd, which is the phase shift per cell in the periodically infinite line.

One problem with this realization in its planar configuration is that the cell periodicity is directly related to the electrical length of the coupled lines ($d = L = \theta/k$, where θ can not exceed π). So, in order to operate at small frequencies very long lines have to be employed. A solution to this problem is to circularly bend the structure, such that the periodicity of the structure becomes the spacing between the line, where the periodicity now will be accompanied with a rotation by a certain angle, and the structure is called screw or helically periodic.

3. CIRCULAR WAVEGUIDE LOADED WITH ROD COUPLED LINES

In principle, the coupled lines geometry can be taken of arbitrary cross section, depending on the required admittances Y_e and Y_o, and the application. As an example, circular rod coupled lines, Fig. 2(a), are considered in this paper, however other types can be treated in a similar fashion. The planar circular rod coupled lines, Fig. 2(a), are bent to form a cylinder as shown in Figs. 2(b), and 2(c), where the ground plan becomes the outer cylinder of the bent structure and the coupled rods are short circuited with small rods connecting between the bent lines and the outer cylinder, which at the same time act as mechanical supports for them.

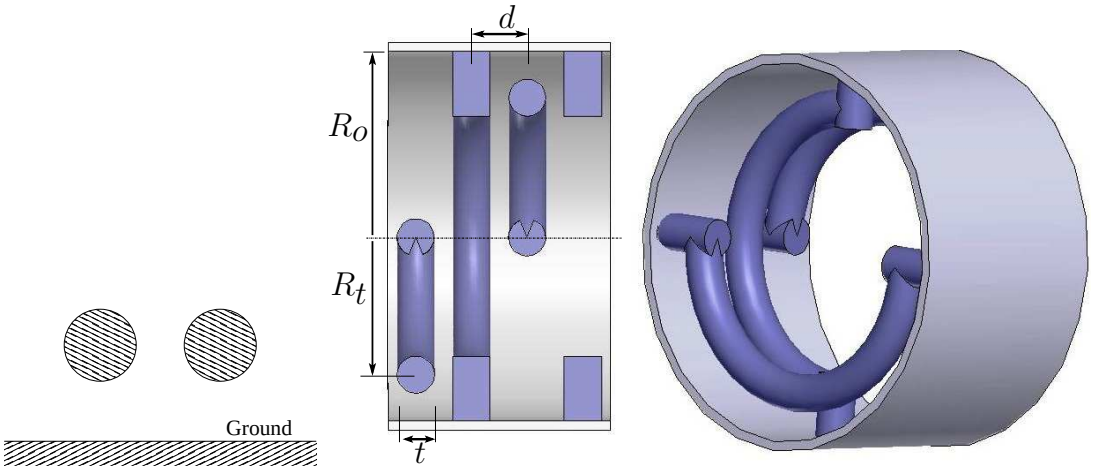
After bending the structure it became no longer planar but a three dimensional screw or helically periodic structure. As an example Fig. 2 shows that the structure is periodic when we make a simultaneous rotation of 90° and a translation of distance d, respectively, around and along the z-axis. In general, for a screw or helically periodic structure the periodicity is achieved with simultaneous rotation of angle ϕ_0 around the z-axis along the ϕ direction and translation with distance d along the z-axis. Hence, in cylindrical coordinates (ρ, ϕ, z) the Floquet theory applied with these simultaneous shift and translation is expressed as [11],

$$\Psi\left(\rho, \phi + \phi_0, z + d\right) = e^{-j\beta d}\Psi\left(\rho, \phi, z\right), \tag{4}$$

where the Ψ function stands for any of the field components. It can be shown, using Eq. (4) and the cylindrical fields expansion in Reference [12], that the fields can be written as,

$$\Psi(\rho, \phi, z) = e^{-i\beta z}\sum_{n,m} a_{n,m} J_n\left(k_{c_{n,m}}\rho\right) e^{jn(\phi - z\phi_0/d)} e^{-i2m\pi z/d}, \tag{5}$$

where $k_{c_{n,m}} = \sqrt{k^2 - \left(\beta + n\phi_0/d + 2m\pi/d\right)^2}$. In principle, the angle ϕ_0 can have any real value and the structure is still screw or helically periodic. However, in order to have periodicity along



(a) Planar Rode Coupled Lines. (b) Cross Section. (c) 3D View.

Figure 2: (a) Cross section of planar coupled circular rodes, (b) Cross section of cylindrical waveguide loaded with rode coupled lines, and (c) 3D view of subfigure (b).

z, the angle ϕ_0 must be representable as $\phi_0 = 2\pi p/q$, where $p < q$ and both p and q are integers satisfying, $\gcd(p, q) = 1$. For this case structure will be periodic along z, with "macro-period" qd.

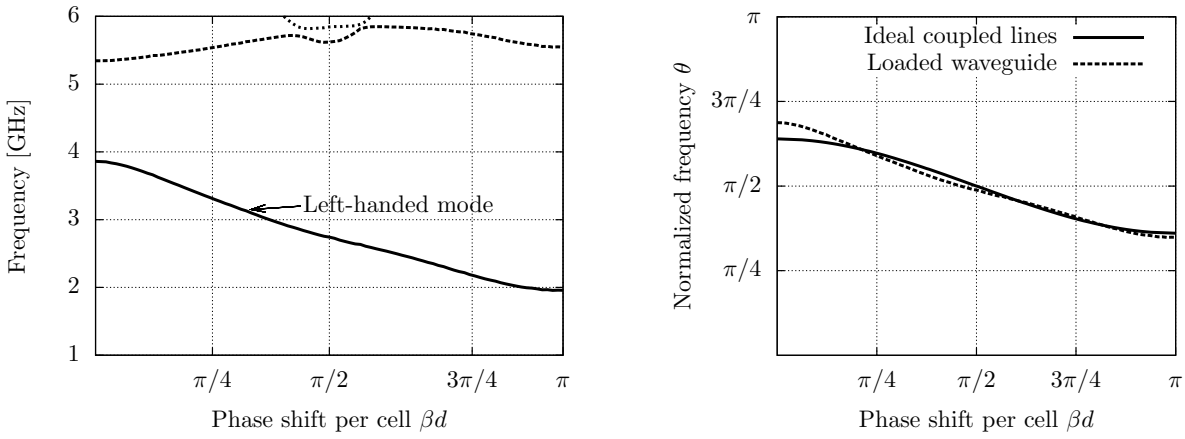
The coefficients $a_{n,m}$ in Eq. (5), at least in principle, can be obtained through applying the boundary conditions on all the cell boundaries, however it is not easy for complicated geometry like ours. Although the expansion Eq. (5) is not that helpful by itself in solving the screw periodic structure fields and in obtaining the mode dispersion ($\omega - \beta$ relation), it demonstrates the screw symmetry of the structure fields and it can be used together with other methods of solution such as FEM to extract the different spatial harmonics amplitudes $a_{m,n}$ which are important in studying possible application devices such as Backward Wave Oscillators (BWO) and Gyrotron BWO [11].

4. RESULTS AND DISCUSSION

In this section we present the dispersion characteristics for the proposed coupled line loaded cylindrical waveguide, both from the circuit analysis discussed in section 2 and from the screw periodic guide described in section 3, where in the latter case the electromagnetic problem is solved using the FEM HFSS code. The dispersion is obtained from the analysis of one unit cell of the guide, however the multi-cell guide composed from 8-cells is also solved numerically to see how the overall structure will behave. The unit cell used, see Fig. 2 , is composed of a hosting conducting cylinder with radius $R_o = 2$ cm, loaded with rod coupled lines that form quarter of a torus. The torus radius is $R_t = 1.5$ cm, the rod diameter is $t = 4$ mm and the cell period is $d = 6$ mm.

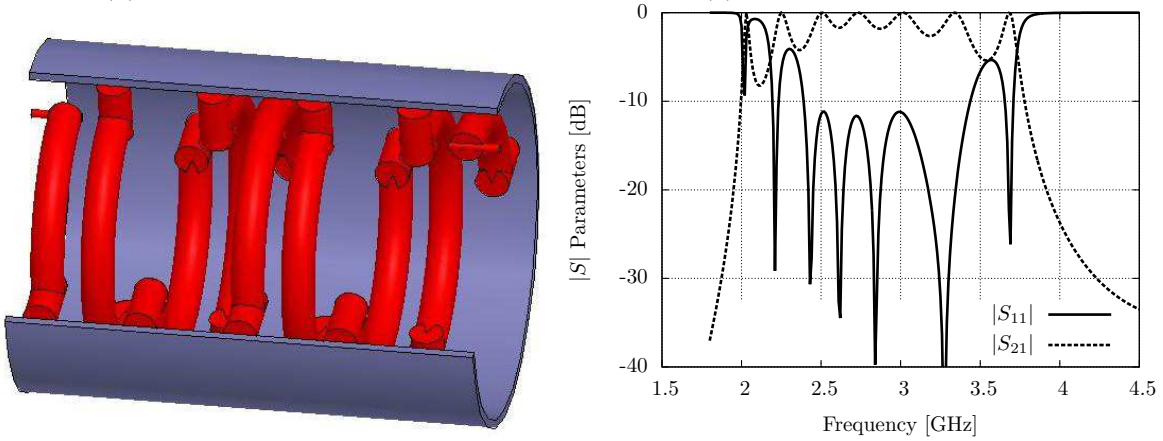
4.1. Dispersion Characteristic

In order to get the dispersion characteristic from the planar circuit, the coupled line parameters Y_o and Y_e need to be calculated. The cross section of the planar coupled lines considered in this calculations is shown in Fig. 2(a). The rods diameters taken is $t = 4$ mm, the spacing is $d = 6$ mm, and the rods hight from the ground plane is $R_o - R_t = 5$ mm. In order to calculate Y_e and Y_o we solved the 2D electrostatic problem in the cross section using FEM (Maxwell 2D SV). The resulting admittances are $Y_e = 7.8\,\mathrm{m}\mho$ and $Y_o = 19.27\,\mathrm{m}\mho$. The dispersion relation for planar periodic structure formed from those coupled lines is the solid curve shown in Fig. 3(b), where $\theta = \omega L/c$ is the normalized frequency, and L is the coupled line length. The dispersion of cylindrical waveguide loaded with the coupled-lines can be calculated from the electromagnetic fields. The structure unit cell resonance frequencies are calculated subject to the Floquet boundary conditions, discussed in section 3, when applied between the the two ends of the cell. The βd phase shift relates the fields at one end of the unit cell with the ϕ_0 rotated points at the other end. In the example considered in this paper the rotation angle $\phi_0 = 90°$ and the phase βd is varied between 0 and π to scan the first Brillouin zone. The FEM code HFSS was used to solve this eigenvalue problem. The resulting dispersion curves shown in Fig. 3(a), reveals that the first propagation mode is a backward or left-handed mode. This left-handed mode frequency range is below the cutoff frequency of the first mode (TE_{11}) of the empty guide which is 4.395 GHz. Operation below the cut-off frequency was also adopted before in designing left-handed rectangular guide [7].



(a) Dispersion Curves. (b) Normalized Dispersion for First Mode.

Figure 3: (a) Dispersion curves of the meta-guide obtained using FEM, where the dotted lines are for higher modes, and (b) Normalized dispersion of LH mode of subfigure (a) compared to that obtained from circuit.



(a) 8-Cells Backward Wave Waveguide (inside view). (b) $|S|$ Parameters.

Figure 4: (a) 3D inside view of 8-cells meta-guide, and (b) $|S|$ parameters obtained by FEM.

Comparison between the dispersion relation obtained from circuit and from the cylinder loaded coupled lines, required normalizing the calculated frequency from the EM dispersion to $\theta = \omega L_{eff}/c$. In Fig. 2 the coupled line lengths fills quarter of the circumference, with a length $L_{eff} = \pi R_e/2$, where the effective radius R_e satisfies $R_t < R_e < R_o$ (for our structure R_e=1.7 cm is taken). The normalized dispersion curve for the cylinder loaded coupled line structure formed is shown in Fig. 3(b) to have good agreement with that obtained from the planar circuit.

4.2. Deployment of the Meta-waveguide

The performance of the proposed cylindrical waveguide loaded with coupled lines is investigated by studying the transmission through an 8-cell composed guide. The guide termination ports could be mounted on the side cylindrical surface, or fixed on the end flat faces of the tube. In the proposed structure in Fig. 4(a), the end flat faces act as transmission line ports with inner conductor diameter chosen such that port impedance match the structure Bloch impedance at phase $\pi/2$. Such a choice of the way of coupling the ports is not unique, it depends on the application involved and the range of frequency of interest to work at. Fig 4(b) shows a transmission along the guide in the frequency range 2-3.7 GHz, which is the same left-handed frequency range shown in Fig. 3(a).

Among the possible applications of this meta-guide is its use in Backward Wave Oscillator (BWO), Gyrotron BWO and accelerator applications [13]. In these applications the use of all metallic structure is favorable as it does not block any portion of the electron beam, like in waveguides filled with metamaterial [13, 14]. Even with a clear beam path the absence of dielectric is favorable in these applications, where dielectrics beside being not easy to integrate with metals, they deteriorate the vacuum level inside these tubes. Of course for such applications the coupled

lines has to be tailored to provide enough axial field for interaction with the electron beam. Another candidate application is in charged particle detection through reverse Cherenkov radiation [15].

5. CONCLUSION

We presented a new type of left handed waveguide (metaguide), which is a cylindrical waveguide loaded with short circuited coupled lines. The proposed guide has the characteristic of supporting a backward wave at frequencies below the empty guide cut-off. The guide is considered as a bent version of the planar periodically cascaded short-circuited coupled lines. Hence, it can be analyzed using the symmetric coupled line circuit theory, which enables the design of the operating Floquet frequency band and the Bloch impedance for the matching purpose of the periodic structure.

Although, the circuit modeling was a simple 1D Floquet analysis, our actual guide is a screw (helically) periodic structure. Using the screw periodic Floquet condition, dispersion relation using electromagnetic simulation was calculated and compared to that obtained with simple circuit coupled-lines model, where good agreement between both models was observed.

The introduced metaguide has the advantage of not containing any dielectrics, which makes it very suitable for vacuum tube applications. Backward Wave Oscillator (BWO), Gyrotron BWO and Cherenkov backward radiation detectors are among the possible applications for this guide.

ACKNOWLEDGMENT

Special thanks go to A. Safwat at Ain Shams University for providing access to the HFSS code.

REFERENCES

1. C. Caloz and T. Itoh, *Electromagnetic Metamaterials: Transmission Line Theory and Microwave Applications*. John Wiley and Sons, 2006.
2. A. Lai, T. Itoh, and C. Caloz, "Composite right/left-handed transmission line metamaterials," *Microwave Magazine, IEEE*, vol. 5, no. 3, pp. 34–50, 2004.
3. C. Caloz and T. Itoh, "Transmission line approach of Left-Handed (LH) materials and microstrip implementation of an artificial LH transmission line," *IEEE Transactions on Antennas and Propagation*, vol. 52, no. 5, pp. 1159–1166, 2004.
4. A. F. Abdelaziz, T. M. Abuelfadl, and O. L. Elsayed, "Realization of composite right/left-handed transmission line using coupled lines," *PIER*, vol. 92, pp. 299–315, 2009.
5. ——, "Realization of composite right/left-handed transmission line using broadside coupled coplanar waveguides," in *2009 IEEE International Symposium on Antennas and Propagation*, Charleston, SC, Jun 2009.
6. A. M. E. Safwat, "Microstrip coupled line composite Right/Left-Handed unit cell," *IEEE Microwave and Wireless Components Letters*, vol. 19, no. 7, pp. 434–436, 2009.
7. I. Eshrah, A. Kishk, A. Yakovlev, and A. Glisson, "Evanescent rectangular waveguide with corrugated walls: a composite right/left-handed metaguide," in *Microwave Symposium Digest, 2005 IEEE MTT-S International*, 2005, p. 4 pp.
8. E. Jones, "Coupled-Strip-Transmission-Line filters and directional couplers," *Microwave Theory and Techniques, IRE Transactions on*, vol. 4, no. 2, pp. 75–81, 1956.
9. D. M.Pozar, *Microwave Engineering*, 3rd ed. Wiley India Pvt. Ltd., 2007.
10. R. Marques, F. Martin, and M. Sorolla, *Metamaterials with negative parameter*. Wiley, 2008.
11. W. N. Cain and R. W. Grow, "Floquet's theorem in three dimensions and its application to the dispersion characteristics of circular waveguides with screw periodicity for use with gyrotron backward-wave oscillators," *International Journal of Infrared and Millimeter Waves*, vol. 10, no. 10, pp. 1289–1310, Oct. 1989.
12. R. F. Harrington, *Time-Harmonic Electromagnetic Fields*, 2nd ed. Wiley-IEEE Press, 2001.
13. S. Antipov, L. K. Spentzouris, M. Conde, W. Gai, W. Liu, R. Konecny, J. G. Power, and Z. Yusof, "Metamaterial-loaded waveguides for accelerator applications," in *2007 IEEE Particle Accelerator Conference (PAC)*, Albuquerque, NM, 2007, pp. 2906–2908.
14. S. Antipov, W. Liu, W. Gai, J. G. Power, L. Spentzouris, C. B. Schroeder, W. Leemans, and E. Esarey, "Observation of wakefield generation in Left-Handed band of Metamaterial-Loaded waveguide," in *AIP Conference Proceedings*, Santa Cruz (California), 2009, pp. 556–560.
15. D. Shchegolkov, A. Azad, J. O'Hara, and E. Smirnova, "A proposed measurement of the reverse cherenkov radiation effect in a metamaterial-loaded circular waveguide," in *Infrared, Millimeter and Terahertz Waves, 2008. IRMMW-THz 2008. 33rd International Conference on*, 2008, pp. 1–2.

Dyadic Green's Function of a PEMC Cylinder

M. Rasouli Disfani, K. Vafi, and M. S. Abrishamian

Department of Electrical Engineering, K. N. Toosi University of Technology, Iran
m.rasouli@ee.kntu.ac.ir

Abstract— The dyadic Green's function of a PEMC cylinder is derived with the aid of the principle of scattering superposition and Ohm-Rayleigh method. The PEMC boundary conditions are presented in dyadic form and it shows that how the impedance parameter of PEMC and cross-polarized fields appear in the Green's function. The asymptotic expansions of the dyadic function is calculated in order to attain a closed form for the electrical field.

1. INTRODUCTION

Dyadic Green's Functions (DGFs) as a valuable tool in studying various electromagnetic phenomena such as scattering and radiation have been extensively applied in solving source-free and source incorporated electromagnetic boundary value problems [1]. The closed form, compact formulation and solution of some electromagnetic problems offered by DGFs have been of interest. Hence, dyadic Green's functions of different canonical geometries such as infinite cylinder and spheres, perfectly conducting or dielectric, have been investigated in detail [1, 2].

By introducing perfect electromagnetic conductors (PEMC) [3] and suggesting possibilities for the generalization of a PEMC boundary by Lindell [4], a considerable numbers of investigations have been recently performed on the electromagnetic scattering analysis for geometries with PEMC [5]-[12]. Moreover, theory of PEMC allows occurring cross-polarized fields in the scattered waves [3]. This manifestly non-reciprocal property that has been demonstrated for simple geometries such as the planar, spherical, and cylindrical ones, does not exist in the standard Mie theory [3, 5, 7, 8].

Knowledge of dyadic Green's function of geometries with PEMC boundary conditions, makes it possible to investigate accurately various electromagnetic properties, such as scattered fields from the arbitrary current source and cross-polarization effects for linear polarizations, TE and TM, due to PEMC boundary conditions.

In this paper, a rigorous formulation of dyadic Green's function for the problem of scattering from a infinite PEMC cylinder with arbitrary radius a is presented by employing the principle of scattering superposition as well as the well-known Ohm-Rayleigh method [1]. In addition, the second vector-dyadic Green's theorem [1] for the PEMC cylinder is applied to obtain the scattered field from the current arbitrary source. Also, co-polarized and cross-polarized coefficients of the scattered wave for TE and TM polarizations have been discussed in detail.

2. FORMULATION OF THE PROBLEM

Perfect electromagnetic conductor (PEMC) is a non-reciprocal generalization of both perfect electric conductor (PEC) and perfect magnetic conductor (PMC) [3]. Possibilities for the realization of a PEMC boundary has been suggested in [4] in terms of a layer of certain non-reciprocal materials resting on a PEC plane. Parameters of a bi-isotropic medium can be chosen so that the interface of the layer acts as a PEMC boundary. The surface of perfectly electric conductors and perfectly magnetic conductors have to satisfy the following boundary conditions:

$$\hat{\mathbf{n}} \times \mathbf{E} = 0 \quad \hat{\mathbf{n}} \cdot \mathbf{B} = 0 \qquad (PEC) \tag{1}$$

$$\hat{\mathbf{n}} \times \mathbf{H} = 0 \quad \hat{\mathbf{n}} \cdot \mathbf{D} = 0 \qquad (PMC) \tag{2}$$

where $\hat{\mathbf{n}}$ denotes the unit vector normal to the boundary surface. Due to continuity of tangential components of **E** and **H** fields as well as of the normal components of **D** and **B**, the boundary conditions at the

surface of a PEMC are [3]:

$$\hat{\mathbf{n}} \times (\mathbf{H} + M\mathbf{E}) = 0 \tag{3}$$

$$\hat{\mathbf{n}} \cdot (\mathbf{D} - M\mathbf{B}) = 0 \tag{4}$$

where M denotes the admittance of the PEMC boundary. For $M = 0$, the PMC case is retrieved, while the limit $M \to \pm\infty$ corresponds to the PEC case. The most noticeable difference is the non-reciprocity of the PEMC boundary when M has finite nonzero value. In this case, the scattered fields from a PEMC has cross polarization term that does not occur in the standard scattering theory [3]-[12].

If a harmonic source $\exp(-i\omega t)$ time dependence is assumed, the source incorporated wave equation for the electric field has to satisfy the Helmholtz equation [1]:

$$\nabla \times \nabla \times \mathbf{E} - k_0^2 \mathbf{E} = i\omega\mu_0 \mathbf{J}(\overline{\mathbf{R}'}) \tag{5}$$

According to the duality and the superposition of electromagnetic fields, only the electric type of dyadic Green's function due to an electric current source needs to be solved in order to avoid unnecessary repetition. The magnetic type of dyadic Green's function can be easily obtained according to duality principle. By applying second vector-dyadic Green's theorem, the general formulation for the electric field E, excited by an electric current source J, can be given by

$$\mathbf{E}(\overline{R}) = i\omega\mu_0 \int_V \mathbf{J}(\overline{\mathbf{R}}) \cdot \overline{\overline{\mathbf{G}}}_{e_1}(\overline{\mathbf{R}}, \overline{\mathbf{R}'}) dV \tag{6}$$

where V denotes the volume occupied by the excitation source and $\overline{\mathbf{R}}$ and $\overline{\mathbf{R}'}$ are the position vectors to observation and source points, respectively. In addition, the electric dyadic Green's function,$\overline{\overline{\mathbf{G}}}_{e_1}$, to be determined, has to satisfy the Helmholtz equation:

$$\nabla \times \nabla \times \overline{\overline{\mathbf{G}}}_{e_1} - k_0^2 \overline{\overline{\mathbf{G}}}_{e_1} = \overline{\overline{\mathbf{I}}} \delta(\overline{\mathbf{R}} - \overline{\mathbf{R}}') \tag{7}$$

In (7), $\overline{\overline{\mathbf{I}}}$ and δ denote the identity dyadic and Dirac delta functions. PEMC boundary conditions (3) and (4) at the circular cylindrical interface $r = a$, can be expressed in terms of the electric and magnetic dyadic Green's functions as [1, 3]:

$$\hat{\mathbf{r}} \times (\overline{\overline{\mathbf{G}}}_{m_2} + i\omega\mu_0 M \overline{\overline{\mathbf{G}}}_{e_1}) = 0 \tag{8}$$

$$\hat{\mathbf{r}} \cdot (\overline{\overline{\mathbf{G}}}_{m_2} - \frac{i\omega\mu_0}{M\eta_0^2} \overline{\overline{\mathbf{G}}}_{e_1}) = 0 \quad \eta_0 = \sqrt{\frac{\mu_0}{\varepsilon_0}} \tag{9}$$

By substituting $\overline{\overline{\mathbf{G}}}_{m_2} = \nabla \times \overline{\overline{\mathbf{G}}}_{e_1}$, (8) and (9) can be expressed only in term of the electric type of dyadic green's function at $r = a$:

$$\mathbf{r} \times (\nabla \times \overline{\overline{\mathbf{G}}}_{e_1} + i\omega\mu_0 M \overline{\overline{\mathbf{G}}}_{e_1}) = 0 \tag{10}$$

$$\mathbf{r} \cdot (\nabla \times \overline{\overline{\mathbf{G}}}_{e_1} - \frac{i\omega\mu_0}{M\eta_0^2} \overline{\overline{\mathbf{G}}}_{e_1}) = 0 \tag{11}$$

3. DYADIC GREEN'S FUNCTION

The knowledge of the free space dyadic Green's function of the electric type allows the calculation of the dyadic Green's function for an infinite PEMC cylinder by the method of scattering superposition.

The free space dyadic Green's function of the electric type satisfies (7) and may be solved by making use of the Ohm-Rayleigh method with the result, in a circular-cylindrical coordinate system, given by the famous Tai's book [1] in the form of

$$\overline{\overline{\mathbf{G}}}_{\substack{e\\o}\ \eta}(\overline{\mathbf{R}} - \overline{\mathbf{R}'}) = -\frac{1}{k_0^2}\hat{\mathbf{r}}\hat{\mathbf{r}}\delta_0(\overline{\mathbf{R}} - \overline{\mathbf{R}'}) + \frac{i}{8\pi}\int_{-\infty}^{+\infty} dh \sum_n \frac{2-\delta_0}{\eta^2} \tag{12}$$

$$\left\{ \begin{array}{l} \mathbf{M}_{\substack{e\\o}\ \eta}(h)\mathbf{M}'^{(1)}_{\substack{e\\o}\ \eta}(-h) + \mathbf{N}_{\substack{e\\o}\ \eta}(h)\mathbf{N}'^{(1)}_{\substack{e\\o}\ \eta}(-h) \\ \mathbf{M}^{(1)}_{\substack{e\\o}\ \eta}(h)\mathbf{M}'_{\substack{e\\o}\ \eta}(-h) + \mathbf{N}^{(1)}_{\substack{e\\o}\ \eta}(h)\mathbf{N}'_{\substack{e\\o}\ \eta}(-h) \end{array} \right\}, r \begin{array}{c} < \\ > \end{array} r'$$

where $\eta = \sqrt{k_0^2 - h^2}$. The functions $\mathbf{M}_\eta(h)$ describe the electric field of TE_{nm} mode in a cylindrical waveguide and the functions $\mathbf{N}_\eta(h)$ for the TM_{nm} mode. Also, in (12) terms with prime are coefficients of linear polarizations, TE_{nm} and TM_{nm} [1].

According the principle of scattering superposition, the dyadic Green's function for the PEMC cylinder is therefore given by

$$\overline{\overline{\mathbf{G}}}_{e_1}(\overline{\mathbf{R}}, \overline{\mathbf{R}}') = \overline{\overline{\mathbf{G}}}_{eo}(\overline{\mathbf{R}}, \overline{\mathbf{R}}') + \overline{\overline{\mathbf{G}}}_{es}(\overline{\mathbf{R}}, \overline{\mathbf{R}}') \tag{13}$$

where $\overline{\overline{\mathbf{G}}}_{es}(\overline{\mathbf{R}}, \overline{\mathbf{R}}')$ must have the form

$$\overline{\overline{\mathbf{G}}}_{es}(\overline{\mathbf{R}} - \overline{\mathbf{R}}') = -\frac{1}{k_0^2}\mathbf{rr}\delta_0(\overline{\mathbf{R}} - \overline{\mathbf{R}}') + \frac{i}{8\pi}\int_{-\infty}^{+\infty} dh \sum_n \frac{2-\delta_0}{\eta^2} \left\{ A_\eta \mathbf{M}_\eta^{(1)} + B_\eta \mathbf{N}_\eta^{(1)} \right\} \tag{14}$$

To determine the unknown coefficients A_η and B_η in the scattered wave, the PEMC boundary conditions (10) and (11) have to be satisfied at $r = a$. In the case of ordinary scattering problems, coefficient A_η and B_η are independently determined for TE and TM polarizations respectively. But, here, owing to the mixing of electric and magnetic types of dyadic Green's functions in (10) and (11), A_η and B_η, are not determined in terms of just the exciting field polarization. Therefore, the scattered field for a certain exciting polarization, for example TE, has the cross polarization term, TM, in addition to the exciting field polarization, TE [3, 7, 8]. In other words, A_η consists of two terms, co-polarized (TE) components and cross-polarized (TM) components while B_η consists of co-polarized (TM) components as well as cross-polarized (TE) components.

The tangential field components have to satisfy (10) at the cylinder surface

$$\begin{aligned} &\nabla \times \left(\mathbf{M}_\eta(h)\mathbf{M}_\eta^{'(1)}(-h) + \mathbf{N}_\eta(h)\mathbf{N}_\eta^{'(1)}(-h) + A_\eta \mathbf{M}_\eta^{(1)}(h) + B_\eta \mathbf{N}_\eta^{(1)}(h) \right) \\ &+ i\omega\mu_0 \left(\mathbf{M}_\eta(h)\mathbf{M}_\eta^{'(1)}(-h) + \mathbf{N}_\eta(h)\mathbf{N}_\eta^{'(1)}(-h) + A_\eta \mathbf{M}_\eta^{(1)}(h) + B_\eta \mathbf{N}_\eta^{(1)}(h) \right) = 0 \end{aligned} \tag{15}$$

By applying the condition (15) to the z and ϕ components of vector eigenfunction M and N and substituting

$$\nabla \times \mathbf{N}_\eta(h) = k_0 \mathbf{M}_\eta(h) \tag{16}$$

$$\nabla \times \mathbf{M}_\eta(h) = k_0 \mathbf{N}_\eta(h) \tag{17}$$

we obtain the following system of linear equations:

$$H_n(\alpha)A_\eta + iM\eta_0 H_n(\alpha)B_\eta = -J_n(\alpha)\mathbf{M}_\eta^{'(1)}(-h) - iM\eta_0 J_n(\alpha)\mathbf{N}_\eta^{'(1)}(-h) \tag{18}$$

$$H_n'(\alpha)A_\eta + \frac{1}{iM\eta_0}H_n'(\alpha)B_\eta = -J_n'(\alpha)\mathbf{M}_\eta^{'(1)}(-h) - \frac{1}{iM\eta_0}J_n'(\alpha)\mathbf{N}_\eta^{'(1)}(-h) \tag{19}$$

where $\alpha = \eta_0 a$ is the cylinder size parameter. The above set yields unknown coefficients in terms of amplitudes of linearly polarized incidents fields TE and TM, i.e. $\mathbf{M}_\eta^{'(1)}$ and $\mathbf{N}_\eta^{'(1)}$, respectively.

$$A_\eta = A^{TE}\mathbf{M}_\eta^{'(1)} + A^{TM}\mathbf{N}_\eta^{'(1)} = A_\eta^{TE} + A_\eta^{TM} \tag{20}$$

$$B_\eta = B^{TE}\mathbf{M}_\eta^{'(1)} + B^{TM}\mathbf{N}_\eta^{'(1)} = B_\eta^{TE} + B_\eta^{TM} \tag{21}$$

where

$$A_\eta^{TE} = -\frac{M^2\eta_0^2 H_n(\alpha)J_n'(\alpha) + J_n(\alpha)H_n'(\alpha)}{(1+M^2\eta_0^2)H_n(\alpha)H_n'(\alpha)}\mathbf{M}_\eta^{'(1)} \tag{22}$$

$$A_\eta^{TM} = \frac{2M\eta_0}{\pi\alpha\left(1+M^2\eta_0^2\right)H_n(\alpha)H_n'(\alpha)}\mathbf{N}_\eta^{'(1)} \tag{23}$$

$$B_\eta^{TE} = \frac{-2M\eta_0}{\pi\alpha\left(1+M^2\eta_0^2\right)H_n(\alpha)H_n'(\alpha)}\mathbf{M}_\eta^{'(1)} \tag{24}$$

$$B_\eta^{TM} = -\frac{M^2\eta_0^2 J_n(\alpha)H_n'(\alpha)+H_n(\alpha)J_n'(\alpha)}{(1+M^2\eta_0^2)H_n(\alpha)H_n'(\alpha)}\mathbf{N}_\eta^{'(1)} \tag{25}$$

In above equations, (22) and (25) are the co-polarized coefficients, whereas (23) and (24) show the cross-polarized coefficients for exciting TE and TM polarizations,respectively. In PEC case, when $M \to \infty$, we obtain scattering co-polarized coefficients $A_\eta^{TE} = -\frac{J_n'(\alpha)}{H_n'(\alpha)}\mathbf{M}_\eta^{'(1)}$ and $B_\eta^{TM} = -\frac{J_n(\alpha)}{H_n(\alpha)}\mathbf{N}_\eta^{'(1)}$ which are as same as scattering coefficients form a PEC cylinder given by [1]. Also, as we expect, cross-polarization terms become zero due to PEC boundary conditions. In PMC case, as we expect, the dual results of PEC case, i.e. $A_\eta^{TE} = -\frac{J_n(\alpha)}{H_n(\alpha)}\mathbf{M}_\eta^{'(1)}$ and $B_\eta^{TM} = -\frac{J_n'(\alpha)}{H_n'(\alpha)}\mathbf{N}_\eta^{'(1)}$, are obtained and cross-polarized terms vanish.

By substituting (20)-(25) into (14) and making use of (6), the electric field for an arbitrary current source can be calculated.

4. ASYMPTOTIC EXPRESSION

To find the far-zone field of a radiating source in the presence of a perfectly electromagnetic cylinder or the far-zone field of an aperture antenna on the surface of the cylinder, asymptotic expression for $\overline{\overline{\mathbf{G}}}_{e_1}$ should be found by the method of saddle-point integration. Assuming ηr is large compared to unity, the Hankel function in $\mathbf{M}_\eta^{(1)}$ and $\mathbf{N}_\eta^{(1)}$ can be expressed by asymptotic expression [1]; that is

$$H_n^{(1)}(\eta r) \simeq \left(\frac{2}{\pi\eta r}\right)^2 (-i)^{n+\frac{1}{2}} e^{i\eta r} \tag{26}$$

The function $\mathbf{M}_\eta^{(1)}$ and $\mathbf{N}_\eta^{(1)}$, therefore, become

$$\mathbf{M}_{\substack{e\\o}\ \eta}(h) \simeq (-i)^{n+\frac{3}{2}}\eta\left(\frac{2}{\pi\eta r}\right)^2 e^{i\eta r+hz}\ \begin{matrix}\cos\\ \sin\end{matrix}\ n\phi\hat{\phi} \tag{27}$$

$$\mathbf{N}_{\substack{e\\o}\ \eta}(h) \simeq (-i)^{n+\frac{1}{2}}\frac{\eta}{k_0}\left(\frac{2}{\pi\eta r}\right)^2 e^{i\eta r+hz}\ \begin{matrix}\cos\\ \sin\end{matrix}\ n\phi(-h\hat{r}+\eta\hat{z}) \tag{28}$$

The approximate expression for $\overline{\overline{\mathbf{G}}}_{e_1}$, using (12) and (14) with the functions $\mathbf{M}_\eta^{(1)}$ and $\mathbf{N}_\eta^{(1)}$ replaced by above equations, can be written as

$$\overline{\overline{\mathbf{G}}}_{e_1}(\overline{\mathbf{R}},\overline{\mathbf{R}}') = \frac{i}{4\pi}\int_{-\infty}^{+\infty} dh \sum_n \frac{2-\delta_0}{\eta}\frac{1}{(2\pi\eta r)^{\frac{1}{2}}}(-i)^{n+\frac{1}{2}}e^{i\eta r+hz}$$
$$\cdot\left\{-i\ \begin{matrix}\cos\\ \sin\end{matrix}\ n\phi\hat{\phi}'\left[\mathbf{M}_\eta'(-h)+A_\eta\right]+\frac{1}{k}\ \begin{matrix}\cos\\ \sin\end{matrix}\ n\phi(-h\hat{r}+\eta\hat{z})\left[\mathbf{N}_\eta'(-h)+B_\eta\right]\right\} \tag{29}$$

where terms of the order equal to and greater than $(\eta r)^{-\frac{3}{2}}$ have been neglected. By changing the cylindrical variables in spherical variable

$$\begin{aligned}\eta &= k\sin(\beta); h = k\cos(\beta)\\ r &= R\sin(\theta); z = R\cos(\theta)\end{aligned} \tag{30}$$

and calculating the integral regarding to method discussed in [1], $\overline{\overline{\mathbf{G}}}_{e_1}$ can be expressed as

$$\overline{\overline{\mathbf{G}}}_{e_1}(\overline{\mathbf{R}},\overline{\mathbf{R}}') = \frac{e^{ikR}}{4\pi kR\sin(\theta)}\sum_n (2-\delta_0)(-i)^{n+1}\ \begin{matrix}\cos\\ \sin\end{matrix}\ n\phi \tag{31}$$
$$\cdot\{\hat{\phi}\left[\mathbf{M}_s'(-k\cos\theta)+A^{TE}\mathbf{M}_s^{'(1)}(-k\cos\theta)+A^{TM}\mathbf{N}_s^{'(1)}(-k\cos\theta)\right]$$
$$-i\hat{\theta}\left[\mathbf{N}_s'(-k\cos\theta)+B^{TE}\mathbf{M}_s^{'(1)}(-k\cos\theta)+B^{TM}\mathbf{N}_s^{'(1)}(-k\cos\theta)\right]\}$$

where $s = k \sin\theta$, corresponding to the values of η evaluated at $\beta = \theta$. As discussed in [1], the singularity at $\theta = 0$, in practice, does not exist because θ never goes to zero due to finite radius cylinder.

As far as the actual field concerned, it is of course necessary to use (6). It should be mentioned that the cross-polarized terms show their effects by the coefficient A^{TM} and B^{TE}.

5. CONCLUSION

A rigorous formulation of dyadic green's function for scattering of a PEMC cylinder is derived .Mixed boundary condition of PEMC is represented in dyadic form and the results are verified by special cases of $M = 0$ (PMC) and $M = \pm\infty$ (PEC). Also, asymptotic expansions of Hankel functions are taken into account to attain a closed form for electrical field in far-field zone.

ACKNOWLEDGMENT

Authors would like to thank Iran Telecommunication Research Center for the financial support of this research.

REFERENCES

1. Tai, C. T, *Dyadic Greens Functions in Electromagnetic Theory*, 2nd ed. Piscataway, NY, IEEE Press, 1994.
2. Xiang, Z. and Y. Lu, "Electromagnetic dyadic Green's functions in cylidrically multilayered media," *IEEE Trans. Microwave Theory Tech.*, Vol. 44, No. 4, 614–621, 1996.
3. Lindell, I. V. and A. H. Sihvola, "Perfect electromagnetic conductor," *J. Electromagn. Waves Appl.*, Vol. 19, No. 7, 861-869, 2005.
4. Lindell, I. V. and A. H. Sihvola, "Realization ofthe PEMC boundary," *IEEE Trans. Antennas Propag.*, Vol. 53, No. 9, 3012-3018, Sep. 2005.
5. Lindell, I. V. and A. H. Sihvola, "Transformation method for problems involving perfect electromagnetic conductor (PEMC) structures," *IEEE Trans. Antennas Propag.*, Vol. 53, No. 9, 3005-3011, Sep. 2005.
6. Lindell, I. V. and A. H. Sihvola, "Losses in PEMC boundary," *IEEE Trans. Antennas Propag.*, Vol. 54, No. 9, 2553-2558, Sep. 2006.
7. Ruppin, R., "Scattering of electromagnetic radiation by a perfect electromagnetic conductor sphere," *J. Electromagn. Waves Appl.*, Vol. 20, No. 12, 1569-1576, 2006.
8. Ruppin, R., "Scattering of electromagnetic radiation by a perfect electromagnetic conductor cylinder," *J. Electromagn. Waves Appl.*, Vol. 20, No. 13, 1853-1860, 2006.
9. Ahmed, S. and Q. A. Naqvi, "Electromagnetic scattering from a perfect electromagnetic conductor cylinder buried in a dielectric half space," *Progress In Electromagnetics Research*, PIER 78, 2538, 2008.
10. Ahmed, S. and Q. A. Naqvi, " Electromagnetic scattering from parallel perfect electromagnetic from parallel perfect electromagnetic conductor cylinder of circular cross-section using an itterative procedure, "Perfect electromagnetic conductor," *J. Electromagn. Waves Appl.*, Vol. 22, 987-1003, 2008.
11. Hussain, A., Q. A. Naqvi, and M. Abbas, " Fractional duality and perfect electromagnetic concuctor (PEMC)," *Progress In Electromagnetics Research*, PIER 71, 85-94, 2007
12. Fiaz, M. A., A. Aziz, A. Ghaffar, and Q. A. Naqvi, " High-frequency expression for the field in the caustic region of a PEMC Greogerian system using Maslov's method," *Progress In Electromagnetics Research*, PIER 81, 135-148, 2008

Some left handed structures for microwave devices

I.A. Mocanu[1], T. Petrescu[1], N. Militaru[1], G. Lojewski[1], and M. G. Banciu[2]

[1]Telecommunications Department, Electronics, Telecommunications and Information Technology Faculty, University POLITEHNICA of Bucharest, 1-3, Bd. Iuliu Maniu, 061071, Bucharest 6, Romania

[2]National Institute of Materials Physics, Magurele, Jud. Ilfov, Romania

mihai.iulia83@yahoo.com

Abstract- Investigations on microwave devices obtained by modeling left handed periodic microstrip structures are presented in this paper. The structures are analyzed in a broadband range (1-10 GHz) and the magnitude and phase of the S parameters reveal new properties, different from conventional microstrip devices. A new asymmetric coupler is proposed and analyzed.

1. INTRODUCTION

Metamaterials are a new class of artificial composite structures, which exhibit special electromagnetic properties [1, 2] and include periodically, ordered inhomogeneities usually smaller than a tenth of the wavelength.

The electromagnetic propagation phenomena in one direction through an effectively homogeneous material can be essentially modeled by a one-dimensional transmission-line. However, in practice, such a pure left-handed (PLH) transmission line is impossible to manufacture, so that a more practical model is the composite right- / left- handed (CRLH) model of line [3]. A microstrip CRLH line may be obtained by chaining several unit cells. In this work, each unit cell contains a six-digit inter-digital capacitor and a shunt stub inductor. Each stub inductor is terminated in a via-hole short circuit. The CRLH lines were investigated in microstrip technology on a 1.524 mm thick substrate with 3.02 dielectric constant and 0.0013 dielectric loss tangent.

Due to the fact that the transmission lines use nonresonant reactive elements, the devices created with them are characterized by low loss and broad bandwidth.

2. SYMETRIC CRLH COUPLERS

When CRLH cells are positioned in a symmetrical way on each side of a symmetry plane, an edge-coupling will appear.

First, couplers with 7-cell CRLH lines were investigated using specialized software [4, 5]. The ports were designated as in Figure 1. A very interesting coupling phenomenon occurs in the stop-band: the magnitude of the S_{31} is very close to 0 dB. In fact, such a strong coupling is achieved for CRLH lines with relative large number of cells.

Since the coupling signal is directed to port 3 and not to port 4, the coupler can be designated as a backward wave coupler. This coupling effect is very different from what is happening in conventional edge-coupled lines couplers: an edge-coupler with conventional microstrip lines can achieve a maximum coupling factor about 10 dB, while the CRLH device in Figure 2 can exhibit very strong coupling, up to 0 dB.

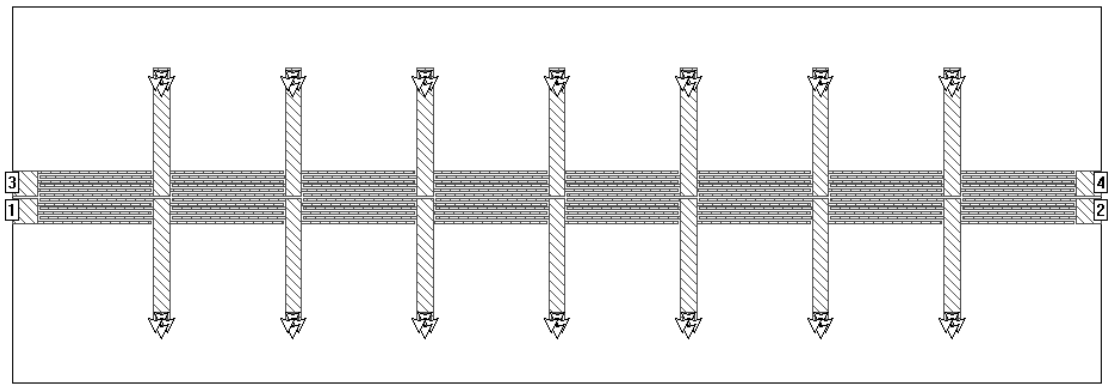


Figure 1. Symmetric CRLH coupler with 7 cells.

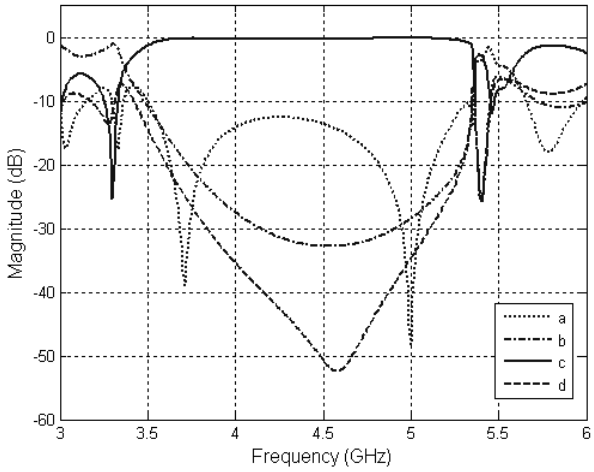


Figure 2. Scattering parameters for the symmetric coupler in Figure 1; a) $|S_{11}|$, b) $|S_{21}|$, c) $|S_{31}|$, d) $|S_{41}|$.

We have also analyzed the scattering parameters for a symmetric coupler similar to the one presented in Figure 1, but with unit cells two times smaller, respectively two times larger. The results are presented in Figure 3 and Figure 4.

One can see that modifying the dimensions of the cells leads to a translation in frequency: if the dimensions are reduced, then the coupling effect appears at higher frequencies, meanwhile, if the dimensions are increased, then the coupling effect appears at lower frequencies. Another aspect is that better behavior in frequency is obtained when the homogeneous condition is respected, rather then when it is closer to the limit.

A very good directivity better than 20 dB, is obtained in a working band between 3.6 and 5.4 GHz for the initial example, meanwhile for the other two cases it was obtained in a working band between 7.19 and 9.11 GHz, respectively between 1.9 and 2.7 GHz.

While strong coupling (0 dB) requires CRLH lines of at least 7 cells, lower coupling levels can be achieved even with a reduced number of cells. The main advantage of this choice is that a more compact device can be achieved. The response of a three-cell 3 dB coupler is presented in Figure 5.

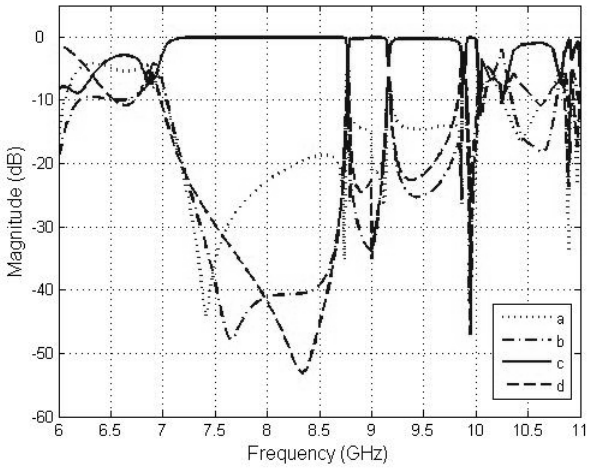


Figure 3. Scattering parameters for the symmetric coupler with unit cells two times smaller; a) $|S_{11}|$, b) $|S_{21}|$, c) $|S_{31}|$, d) $|S_{41}|$.

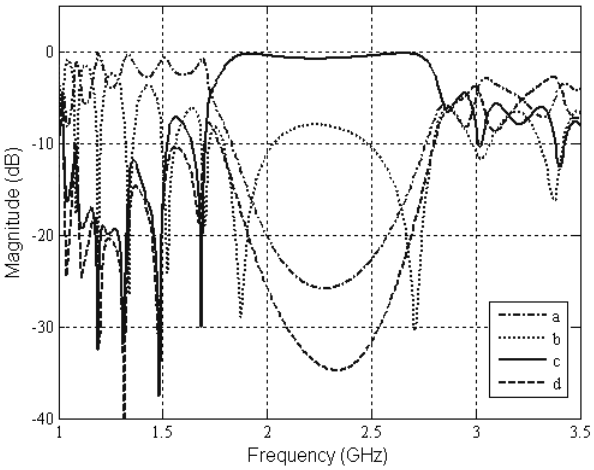


Figure 4. Scattering parameters for the symmetric coupler with unit cells two times larger; a) $|S_{11}|$, b) $|S_{21}|$, c) $|S_{31}|$, d) $|S_{41}|$.

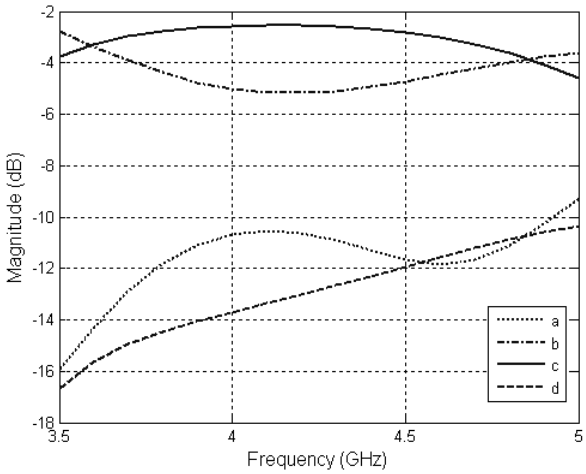


Figure 5. Scattering parameters for a 3-cell symmetric coupler; a) $|S_{11}|$, b) $|S_{21}|$, c) $|S_{31}|$, d) $|S_{41}|$.

2. ASYMETRIC CRLH COUPLER

Having in mind the performances that we have obtained in the cases of symmetric couplers with different sizes of unit cells, we propose a new asymmetric coupler as in Figure 6. This coupler is formed of two CRLH transmission lines: the first one is similar to the ones presented in Figure 1, meanwhile the second one is made of cells two times smaller than the original ones in Figure 1.

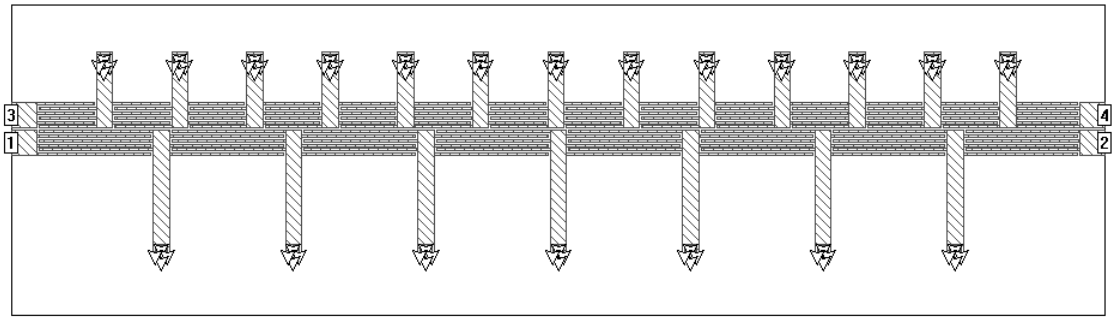


Figure 6. Asymmetric coupler with different sizes of unit cells

In this case, we have obtained a backward wave coupler with strong coupling for dual frequency bands, as one can see in Figure 7. [4, 5] The directivity reaches 41dB in the first band and in the second one reaches about 56dB, so the device can be used for two frequency bands with very high directivity, as one can see in Figure 8.

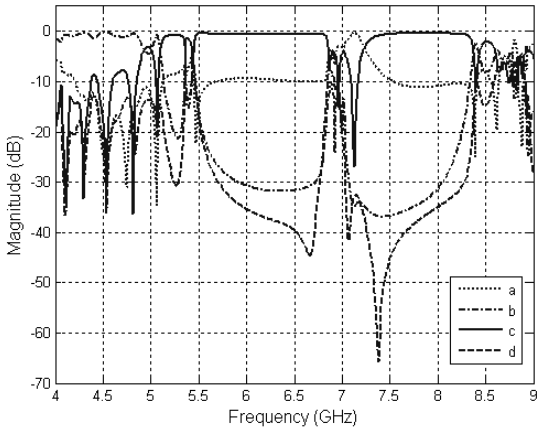


Figure 7. Scattering parameters for an asymmetric coupler with different sizes of unit cells; a) $|S_{11}|$, b) $|S_{21}|$, c) $|S_{31}|$, d) $|S_{41}|$.

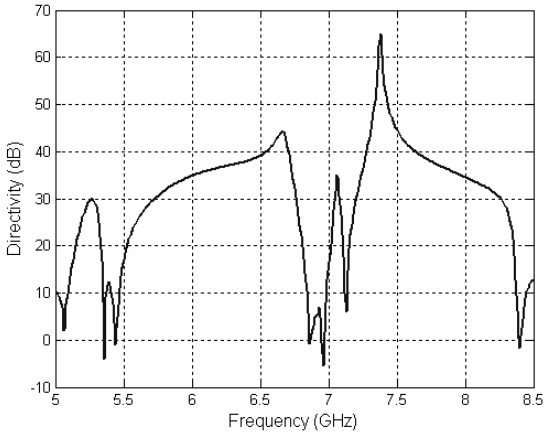


Figure 8. Directivity for an asymmetric coupler with different sizes of unit cells.

3. CONCLUSIONS

The performances of the new devices, modeled using left handed periodic unit cells, show that they can be used for DC blocking in order to isolate the bias voltages applied to various circuits as well as to block DC and low-frequency voltages while allowing the RF signal to pass through with minimal loss.

REFERENCES

1. Engheta N. and R.W. Ziolkowski, *Metamaterials – Physics and Engineering Explorations*, Wiley-IEEE Press, New York, 2006.
2. Eleftheriades, G.V. and K.G. Balmain, *Negative Refraction Metamaterials: Fundamental Principles and Application*, Wiley-IEEE Press, 2005.
3. Caloz, C. and H. V. Nguyen, "Novel broadband conventional- and dual-composite right/left-handed (C/D-CRLH) metamaterials", *Appl. Phys. A 87*, pp. 309-316, 2007.
4. ***, Advanced Design System 2008, Agilent Technologies, Santa Clara, May 2008.
5. ***, 'em User's Manual', Sonnet Software Inc., New-York – Sonnet Professional release 10.52.

Investigation of backward-wave propagation on LHM Split Ring Resonators

H. Talleb , Z.Djeffal, D.Lautru and V.Fouad Hanna
UPMC Univ Paris 06, EA 2385, L2E, F-75005, Paris, France
hakeim.talleb@upmc.fr, zineddine.djeffal@upmc.fr

Abstract-
Full-wave electromagnetic rigorous simulations of a structure composed of split ring resonators (SRRs) have demonstrated backward-wave propagation along the structure of elliptically polarized eigenwaves. This result confirms that an increase of magnetoelectric gyrotropic activities inside a bianistropic chiral medium can lead to a left-handed material (LHM) as predicted by the recently chiral medium works.

1. INTRODUCTION

Metamaterials attract many researchers in electromagnetic engineering domains as they exhibit counterintuitive phenomenon such as negative refraction and backward-wave propagation. So far, there have been very few successfully realized engineering applications making use of materials that can exhibit backward-wave propagation phenomenon. Most of them are utilizing planar microwave circuits [1]. Investigation on an edge of a prism structure composed of split ring resonators (SRRs) and metallic wires had demonstrated the presence of negative refraction through the structure, which does not mean necessarily the presence of a backward-wave propagation phenomenon since a negative refraction can be produced without having negative index materials using the ultra-refraction principle [2]. Moreover, experimental data the electromagnetic interactions between both, SSR_S and metallic wires arrays, cause dramatic ohmic and magnetic losses [3]. Recently, some rigorous works [4,5,6] have proved that chiral medium can lead to negative refraction index since the backward-wave could be propagated. But, in these last works both permeability and permittivity have to be quite small at working frequencies. However, the backward-wave phenomenon can be realized without these restrictive conditions using gyrotropic (bianisotropic or anisotropic) chiral medium since the magnetoelectric effects reduce the refractive index [4]. In this paper, it will be demonstrated that a dense split ring resonators (SRRs) array can be considered as gyrotropic bianistropic due to pseudo-chiral ferrite medium effects and magnetoelectric ones. Hence it is shown that a classical extraction method of relative effective medium parameters can be used to predict a negative eigenmode in a specific frequency band. The full-wave simulations have confirmed the backward-wave propagation phenomenon in the studied frequency band while showing the importance of magnetoelectric coupling activities.

2. PROPAGATION IN GYROTROPIC CHIRAL MEDIUM

The response of the bianisotropic medium to an electromagnetic field can be characterized by the following standard relations (the time-harmonic field dependence $e^{-j\omega t}$ is assumed but always suppressed) [7]:

$$\boldsymbol{D} = \bar{\bar{\epsilon}}\boldsymbol{E} + \overline{\overline{a_1}}\,\boldsymbol{H} \tag{1}$$

$$\boldsymbol{B} = \overline{\overline{a_2}}\,\boldsymbol{E} + \bar{\bar{\mu}}\boldsymbol{H} \tag{2}$$

where $\boldsymbol{D}$ is the electric displacement vector, $\boldsymbol{E}$ the electric field vector, $\boldsymbol{B}$ the magnetic induction field, **H** the

magnetic field intensity $\overline{\overline{a_1}}$ and $\overline{\overline{a_2}}$ denote two coupling dyadic parameters expressing magnetoelectric effects and $\bar{\bar{\epsilon}}$ and $\bar{\bar{\mu}}$ are constitutive tensors. In gyrotropic chiral media G-media (called also nonreciprocal media) the electromagnetic field is the sum of two elliptically or circularly polarized eigenwaves. The phenomenon of rotation of a linearly polarized field vector, when passing through a gyrotropic media is due to either Faraday effect (nonreciprocal effects) or an optical activity (reciprocal effect) or a combination of both effects to create a Faraday chiral medium (FCM) [8,9,10]. Usually, the conditions (1) and (2) for a G-media can be rewritten using Tellegen's relations or Post's relation [5] but here we considered only Tellegen's relations which are more explicit to describe a G-medium [4,6]:

$$\overline{\overline{a_1}} = (\chi + i\kappa)\sqrt{\mu_0\epsilon_0} \tag{3}$$

$$\overline{\overline{a_2}} = (\chi - i\kappa)\sqrt{\mu_0\epsilon_0} \tag{4}$$

where χ and κ denote the nonreciprocity and chirality parameters, respectively.

The asymmetrical constitutive tensors $\bar{\bar{\epsilon}}$ and $\bar{\bar{\mu}}$ can be expressed as:

$$\bar{\bar{q}} = \begin{bmatrix} q_1 & jq_2 & 0 \\ -jq_2 & q_1 & 0 \\ 0 & 0 & q_3 \end{bmatrix} \tag{5}$$

$$(\bar{\bar{q}} = \bar{\bar{\epsilon}}\ or\ \bar{\bar{\mu}}\ )$$

where ϵ_2 and μ_2 denote the electric and magnetic gyrotropic parameters, respectively. They are the contributions of the electric and magnetic Faraday effects.

The refractive index and The corresponding wavenumbers for the backward-wave propagation is then given by following relations [6] :

$$n_1 = \boldsymbol{c_0}\left[\sqrt{(\epsilon_1 + \epsilon_2)(\mu_1 + \mu_2) - \chi^2} - \kappa\right] \tag{7}$$

$$n_2 = \boldsymbol{c_0}\left[\sqrt{(\epsilon_1 - \epsilon_2)(\mu_1 - \mu_2) - \chi^2} + \kappa\right] \tag{8}$$

$$k_1 = \omega\frac{n_1}{c}\ ,\ k_2 = \omega\frac{n_2}{c} \tag{9}$$

We can see that by amplifying gyrotropic parameters or nonreciprocity and chirality parameters the refraction index can attain negative values. Each parameter (more specificaly gyrotropic parameters) plays an essential role in achieving backward-waves propagation and making refraction index negative.

3. BIANISTROPIC STRUCTURE CHARACTERIZATION

Here, we return to the dense copper SSRs structure studied in [11] represented in Fig 1 and for which the dimensions of a unit cell are given. The lattice periods along, x,y, and z axes are 9.3 mm, 9 mm, and 6.5 mm, respectively. We restrict our study on plane wave propagation along the y axis where the electric field and magnetic field have been polarized along the z axis and the y axis, respectively. Each SSR particle can then be considered as a pseudo-Ω chiral cell since this arrangement is asymmetric and exhibit an opposite mirror image with respect to the case of a symmetry plane. If we take the optical axis as the system axis, the system can then be considered as uniaxial.

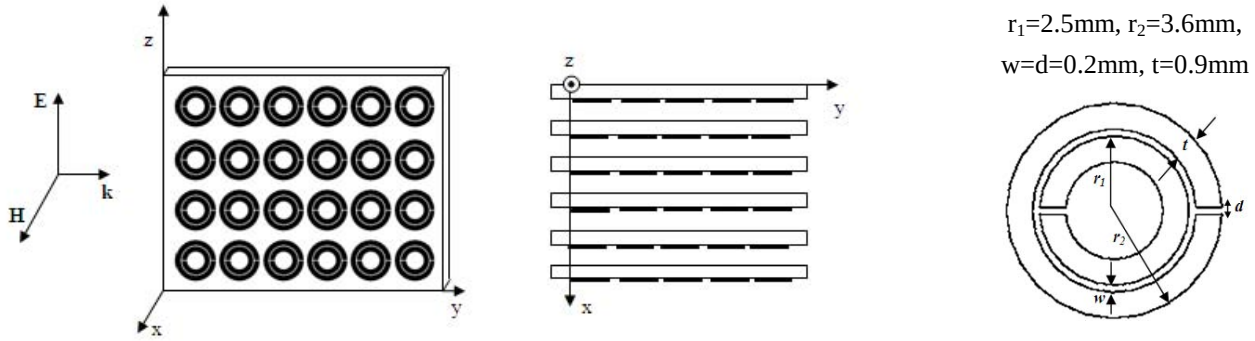


Figure 1: Dense copper SSRs structure employed in [11]

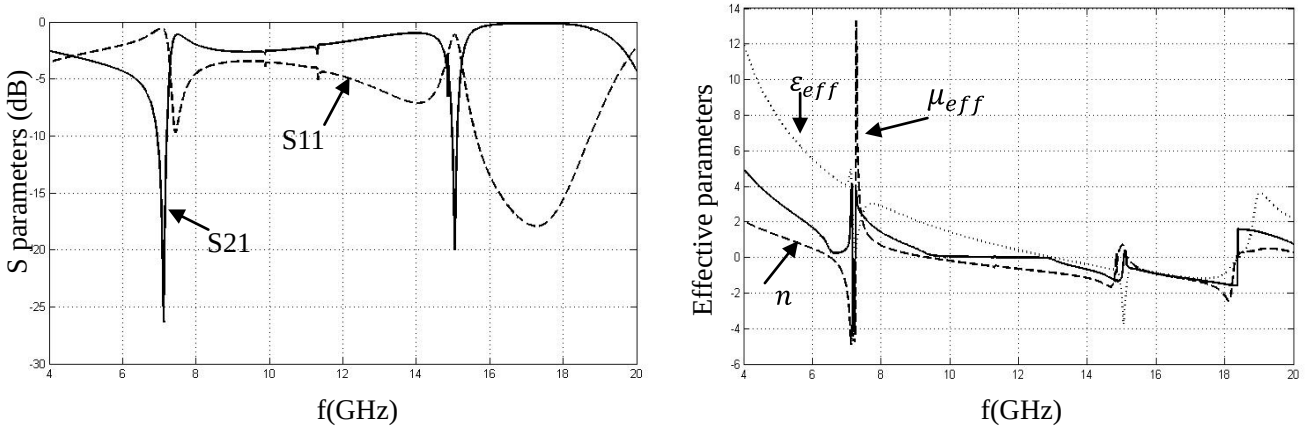
The frequency dependent constitutive relative effective parameters of a unit cell can be extracted from the values of S parameters determined from simulations or measurements using the robust method proposed in [12]. The principal relations for the refractive index *n* and wave impedance *Z* are given by following relations:

$$n = \frac{j}{k_o} ln\left(\frac{S_{21}}{1-S_{11}\frac{z-1}{z+1}}\right) \quad , Z = \pm\sqrt{\frac{(1+S_{11})^2-S_{21}{}^2}{(1-S_{11})^2-S_{21}{}^2}} \qquad (9)$$

where S_{21}, S_{11} denote the transmission and reflection parameters, j the complex number and k_o the wavenumber of the incident wave in free space.

The effective relative permittivity and permeability are then directly calculated from the relations $\varepsilon_{eff} = n/z$, $\mu_{eff} = n.z$. The requirement $\varepsilon'' \geq 0$ and $\mu'' \geq 0$ lead to $|n'z''| \leq n''z'$. Fig 2(a) and Fig 2(b) show the simulated S parameters using an FSS unit cell method (periodic boundary conditions) calculated by CST Microwave Studio software and the effective parameters that have been extracted employing the robust method. Considering our structure as a gyrotropic structure, the relative effective permittivity and permeability are parameters that depend on gyrotropic nonreciprocity and chirality parameters.

From Fig 2(a) and Fig 2(b), one can observe a classical first resonance frequency at 7GHz where the relative effective permeability obeys Lorentz model and where the relative effective permittivity resonance variation reveals the bianisotroipic effect due magnetoelectric coupling.



(a) S parameters simulated using FSS unit cell method

(b) Variation of relative effective parameters as a function of frequency

Figure 2: The frequency dependence of S parameters and relative effective parameters

However, the second resonance frequency at 15GHz reveals a frequency band where the permittivity obeys Lorentz model reversion and involves a reversion of the phase velocity (Fig.4) which leads to negative effective medium. Fig 3 shows a focus on this frequency band where one can notice that the negative index is localized in the band15 GHz-18.5GHz.

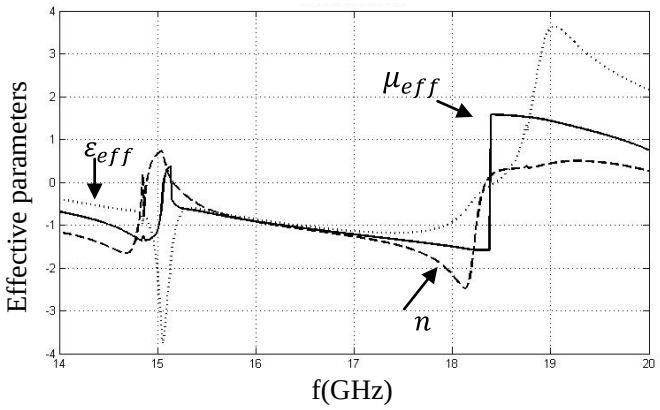


Figure 3: Focus on negative refraction index frequency band

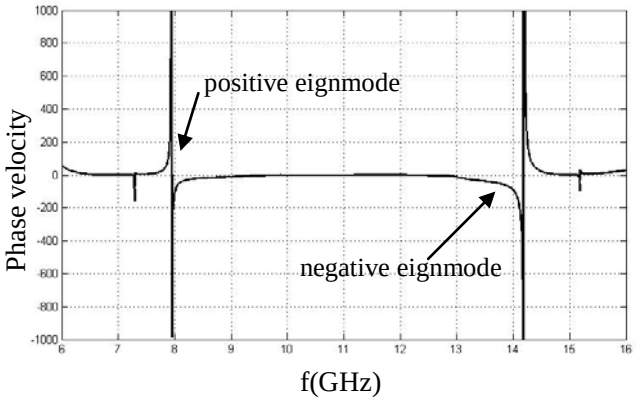


Figure 4: Variation of phase velocities as a fonction of frequency

The phase velocity showing a negative eignmode behavior in Fig 4 is in concordance with results given in [4] and [8] which indicate that for a gyrotropic media, the longitudinally propagating eigenwaves involve four wave numbers roots corresponding to eigenmodes but only two roots involve a backward-waves propagation. Indeed, one root corresponds to an eigenwave which is parallel to the direction of energy transportation while the other root orresponds to the opposite eigenwave which exhibits backward-wave propagation. Both eigenwaves are right-circularly polarized.

4. ELECTROMAGNETIC SIMULATION INTERPRETATION

Rigorous electromagnetic simulations have been performed using the full-wave 3D software CST Microwave Studio. Careful observation of numerical results s in the working frequency range 8-16GHz show that the distribution of electric fields inside the structure is the sum of two elliptically polarized electric fields (right and left handed) along the z axis. This confirms our choice of considering the structure as a potential G-medium. As predicted from the negative eignmode and index frequency behaviors, the backward-wave phenomenon has appeared at 15GHz, but it is strongly emphasized at 16GHz. To better understand the causality of this phenomenon, magnetic field plot contours inside the structure in the working frequency range have been performed. We found that the negative eignmode leads to a meandered continuum circulation of the magnetic field along the z axis. So, the electromagnetic oupling begins with important values involving a Faraday effect and expanded in the whole structure. In fact, each SSR cell behaves as a peuso-chiralferrite. The backward-wave phenomenon propagation is due to a combination of principal effects, namely the optical activity of a chiral medium and the Faraday effect. These results provide lots of potential opportunities of investigation in electromagnetic and optic domains. To illustrate an important example, a negative lens illumined by a plane wave at 15GHz is represented in Fig 6 for which the focalized point is visible.

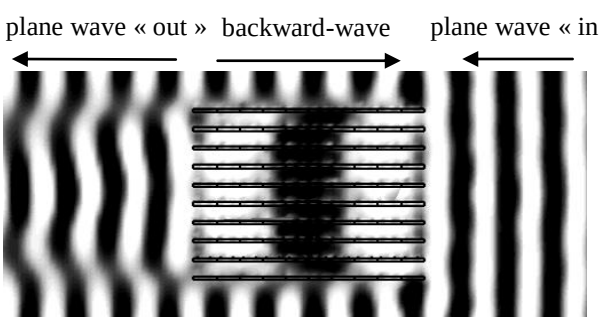


Figure 5: Backward-wave phenomenon – top view

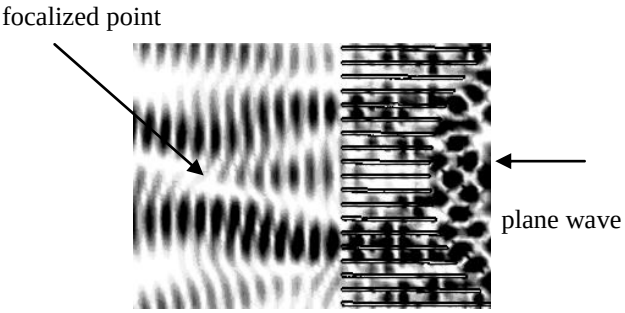


Figure 6: Negative lens illumined by a plane wave

5. CONCLUSION

A G-chiral medium has been proposed composed of dense copper SSRs. An analysis using an extraction method of constitutive effective parameters has predicted the frequency band where the refraction index can attain negative values involving a backward-wave propagation phenomenon. Electromagnetic simulation results have enabled to show the strong contribution of the Faraday effect on the optic activity of a chiral media.

REFERENCES

1. S. Hrabar, F. M. "Backward-wave meta-materials-a brief review, "*17'lnternational Conference on Applied Electromagnetics and Communications"*, 1 - 3 October 2003. Dubrovnik. Croatia.
2. J, Pendry, and al., "Negative refraction without negative index in metallic photonic crystals," *Opt Express*, Vol. 11, No. 7, 746–754, 2003.
3. C.R. Simovski, B. Sauviac, "Role of wave interaction of wire and split-ring resonantors for the losses in a left-handed composite, *Phys. Review E70, 046607, 2004*.
4. C.W. Qiu, H.Y Yao, L.W Li; S. Zouhdi, T.S. Yeo, "Routes to left-handed materials by magnetoelectric couplings", *Phys. Review B75, 245214, 2007*.
5. C.W. Qiu, H.Y Yao, L.W Li; S. Zouhdi, T.S. Yeo, "Backward waves in magnetoelectrically chiral media: Propagtion, impedance, and negative refraction, *Phys. Review B75, 155120, 2007*.
6. C.W. Qiu, H.Y Yao, S. Zouhdi, L.W Li;, M.S Leong,"On the constitutive relations of G-chiral media and the possibility to realize negative-index media, *Micro. Opt. Tech. Lett, Vol. 48, No.12, December 2006*.
7. H. Taouk, "Optical wave propagation in active media: gyrotropic-gyrochiral media, *J.Opt.Soc.Am. Vol.14, No.8, August 1997.*
8. N. Engheta, D.L. Jaggard, M.W. Kowarz, "Electromagnetic Waves in Faraday Chiral Media", *IEEE Trans. Antennas Propag. Vol. 40, April 1992.*
9. W.S. Weiglholfer, A. Lakhtakia, B. Michel, "On the constitutive parameters of a chiroferrite composite medium", *Micro. Opt. Tech. Lett, Vol. 18, No.5, August 1998*.
10. T. G. Mackay and A. A. Lakhtakia, "Negative reflection in a Faraday chiral medium", *Micro. Opt. Tech. Lett, Vol. 50, No.5, May 2008.*
11. E.Ozbay, K.Aydin, E.Cubukcu, and M.Bayindir, "Transmission and Reflection properties of Composite Double Negative Metamaterials in Free Space, *IEEE Trans. Antennas Propag. Vol. 51, October 2003*.
12. X. Chen and al.," Robust method to retrieve the constitutive effective parameters of metamaterials", Phys. Review E70,2004.

Numerical analysis of 2D tunable HIS on GaAs support

L. Matekovits[1,2*], M. Heimlich[2], and K. Esselle[2]

[1] Dipartimento di Elettronica, Politecnico di Torino, C.so Duca degli Abruzzi, 24, 10129 Torino, Italy

[2] Electronic Engineering, Macquarie University, Sydney, NSW 2109, Australia

ladislau.matekovits@polito.it, ladislau.matekovits@mq.edu.au

Abstract- Numerical analysis of the dispersion characteristics of a 2D tunable periodic structure in microsptrip technology is presented. The high relative dielectric constant gallium-arsenide (GaAs) substrate hosts the embedded active FET switches, allowing dynamic changes in the propagation conditions of the electromagnetic wave. The position, aperture of band-gaps and hence the value of the effective dielectric constant can be controlled. These effects will be monitored through the change of the scattering parameters for different number of repetition of the unit cell in the transverse direction.

1. INTRODUCTION

Real-time responses to dynamically changing external excitations are a challenging issue in many fields of science. Antenna engineering is no exception, and a large interest in the configurable antenna best demonstrates this. Reconfigurability can be achieved in any number of ways either by changing geometry or by advanced electronic control. As contrary to the geometrical variation, the latter offers the possibility of faster adaptation and larger dynamics.

On the other hand, periodic structures present interesting features, and have become more prevalent in the modern antenna systems. Application extends from reducing coupling between antennas sharing the same ground plane, cloaking, leaky wave antennas and many other challenging issues, that cannot be achieved without efficiently exploit the characteristics of these engineered structures.

In this context a tunable, planar, periodic microstrip structure has been recently introduced by the same authors [1]. Starting with a periodic structure, the usual responses of such arrangements like existence of band-gaps, frequency dependent phase- and group velocities, etc. are expected to be present. As predictable, inserting externally controllable switches inside the structure with the aim of changing the propagation of the electromagnetic wave in its inside, the resulting device allows altering the aforementioned characteristics, namely adaptivity. After verifying the proof of concept in [1], the study aiming to the characterization of a much more realistic building, including manufacturing constrains, has been presented in [2]. The application example of controlling of the radiation of a 1D leaky wave antenna is quite encouraging.

Based on the aforementioned promising 1D results, here we are going to extend the analysis to a 2D case. The preliminary results reported in the following refer to an idealized case, since we are interested in the general behavior of the response without entering in technological details. As a first step of the presentation, we are going to describe the geometry, and discuss some aspects related to this extension. Numerical results concerning the number of the unit cell in the transverse direction with respect to the initial 1D case for achieving convergence of the solution are presented. It takes into account a global response of the system, and allows further investigation to be carried out, with a quite reduce extension of the geometry. The importance of this study is straightforward, taking into account the sometimes prohibitive computational effort in terms of both CPU time and memory requirement, even in the case when advanced numerical techniques like fast multiple

method (FMM) [3], Synthetic function eXpansion (SFX) [4], characteristic basis function (CBF) [5], etc. are employed.

2. DESCRIPTION OF THE GEOMETRY

The geometry we are considering here, and reported in Fig.1, consists in a transversely repeated single periodically loaded microstrip line, where the loads are represented by patches which can be grounded at their two ends. Unit cells with a given number of patches are described by the on- and off- states of the switches, coded as “1” for the short-circuited patch, and “0” for the open, floating case. The three patch unit cells in Fig. 1 are in 011 state for the 1D case and in the 010 state for the 2D case. In the latter case, the transverse dimension D_v of the unit cell has also been defined.

As discussed in [1], the effect of the connection of the patch to the ground corresponds to a changing in the reactive load locally seen by the microstrip line, with consequent variation of the phase velocity of the propagating wave. The periodicity of the on- and off- states of the switches for the cascaded unit cells along the longitudinal direction assures the characteristics offered by periodic structures. In this study, we will consider no variation of the switches along the transverse direction.

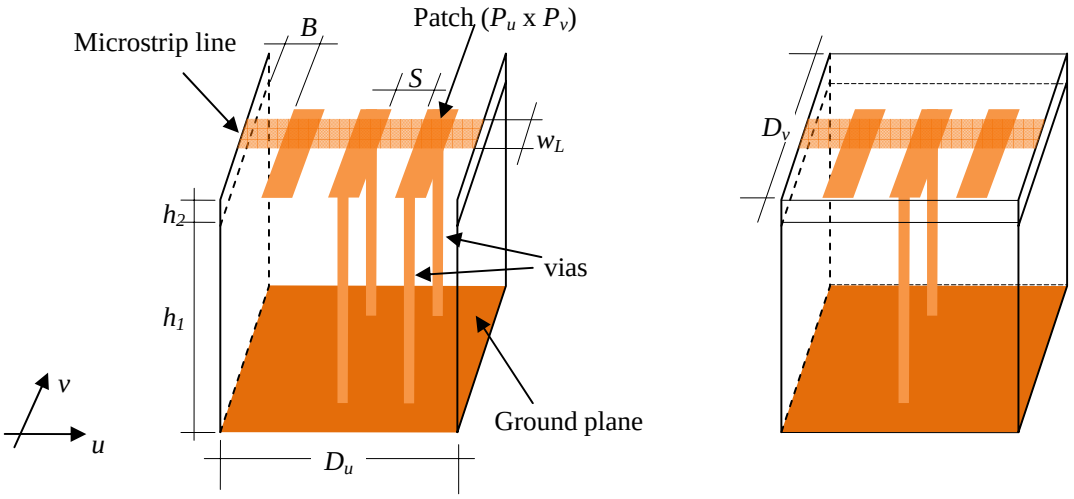


Figure 1. Idealized geometries: 1D (left) 011 state: 2D (right) 010 state.

Higher the variation of the load reactance, more pronounced the effect will be. The main factors influencing the variations of the equivalent reactive loads are attributed to the dimension of the patches, to the change in the dielectric constant (both in the case of multilayer configuration with layers with different dielectric constants or of the same value) and to the ratio between the thicknesses of the initial and final ground plane represented by the grounded patches. As discussed in [1], the effects are not independent each from the other and the grounding can deeply change the propagation mechanism. Due to the presence of the continuous line, the fundamental propagation mode supported by the geometry is TEM with zero cut-off frequency. Increasing frequency, the grounded patches act as loops, and the geometry is similar to a helix-like slow wave configuration. A transition zone in the response has also been observed.

3. COMPARISON BETWEEN 1D AND 2D CASES

The extension from 1D to 2D case implicates many differences. The main effect of the repetition of the microstrip line and patches in the transverse direction manifests in changing of the longitudinal phase velocity of the single line. As observed and analyzed in [6], the effective value of the resulting dielectric constant increases, due to the increases in the coupling between adjacent cells. Quantification of this effect can be done considering the structure as a multiconductor configuration, but the presence of the periodic loads and of the large frequency band requires equivalent circuit models not always available. A numerical approach can be employed as we will do here. On the other hand the structure being periodic in two directions, the full characterization requires the computation of the dispersion diagram on the contour of the irreducible Brillouin zone that becomes a triangle for the rectangular geometry we are considering.

The propagation in the transverse direction is different with respect to those in the longitudinal direction due to the discontinuity of the structure in the former case, since no electric continuity is present. While the microstrip line guaranties the propagation of the TEM mode in the longitudinal case, for low frequencies approaching zero, no propagation in the transverse direction is present. The dispersion diagram starts at a higher frequency. As a consequence, at low frequencies, where stop-band in the transverse direction is present, the electromagnetic field will not goes in that direction as for the 1D case, but will reflect from both sides of the unit cell. The high Q resonator will strongly affect the frequency behavior of the structure.

Further issues that must be consider for the 2D extension is represented by the large number of the switches. Solutions for reducing their number can be devised, but consequently the flexibility of the electromagnetic response of the device will also reduce. Technological issues tackling the control of the large number of switches represent another challenging issue. Grouping of unit cells for reducing the complexity of the control scheme has been proposed in the literature [7] for other kind of reconfigurable geometry.

3. NUMERICAL RESULTS

As concerning the numerical simulation, we have considered a dielectric support usually employed in the MMIC technology. In the particular, the GaAs substrate has a thickness of h_{sub}=100 μm, and characterized by $\varepsilon_{r,sub}$=12.9. The patches positioned on the top of this layer are covered by a superstrate with h_{super}=2 μm and $\varepsilon_{r,sub}$=6.8. This corresponds to a relatively low-loss GaAs dielectric substrates typically used in IC processing. Note the huge ratio between h_{sub} and h_{super} and the difference in the dielectric constant.

The microstrip lines run on the top of the stackup. The patches of dimension P_x=60 μm and P_y=160 μm are spaced by S=40 μm (edge-to-edge). The vertical pins have square section of 10 μm.

In all case we have considered a 9 x 24 array of patches. The periodic behavior in the longitudinal direction is assured by the 24 unit cell, while the same effect on the reference line positioned on the central row of patches is monitored by changing the number of lines parallel to them. The case of N=2 (parasitic) lines per part is shown in the Fig. 2; in this case, two rows of patches per part remains uncovered by any microstrip line. The reference line has been fed while the other lines have been let in open configuration. Commercial numerical code [8] has been used for the modeling, and the scattering parameters have been computed. The results for N=2, 3, and 4 are summarized in Fig. 3. Increasing N, converge of the solution can be observed. Moreover, the existing stop-band disappears, because of the reflection of the field from the neighbor cells.

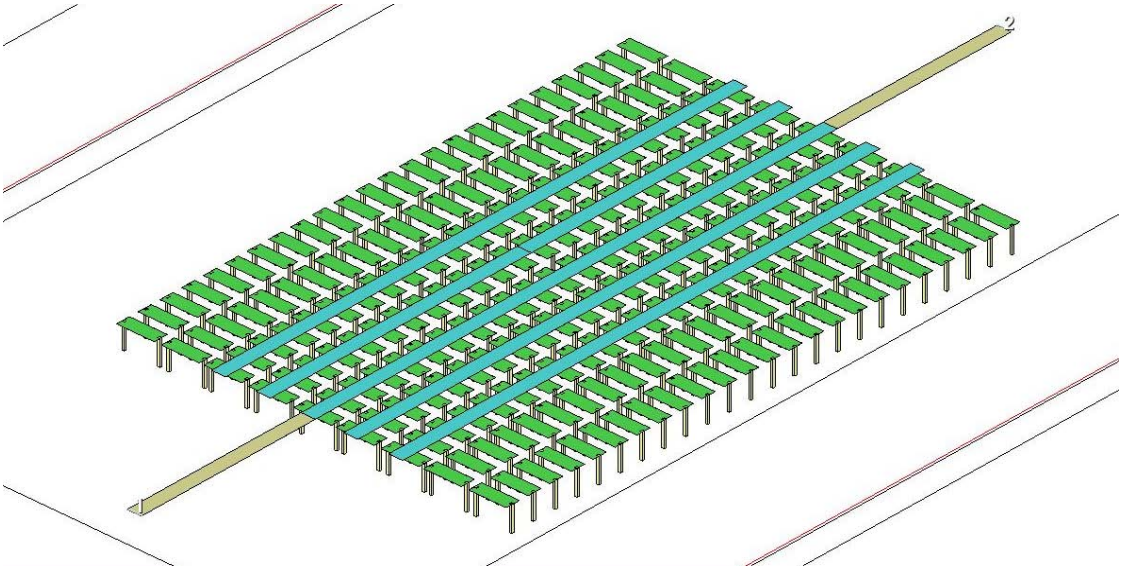


Figure 2. CAD model of the considered configuration.

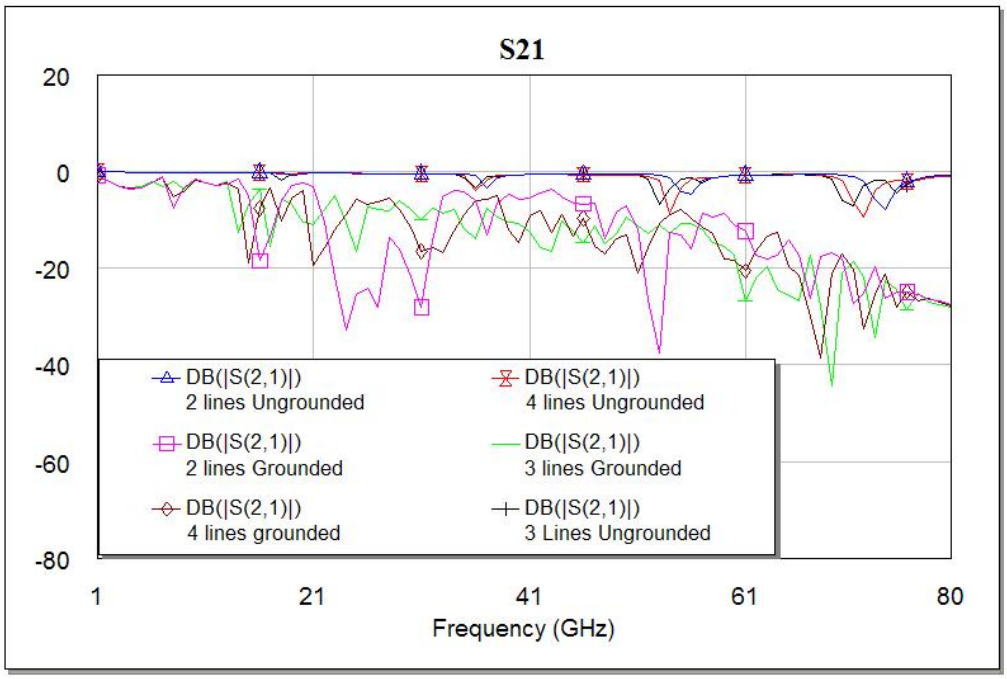


Figure 3. Comparison between the transmission coefficients S21 of the device with a reference line and N=2, 3, and 4 parasitic lines per part.

4. CONCLUSIONS

The geometry proposed here allows extending the periodic arrangement to a quasi-periodic one, with local changes in the responses of the unit cell. Numerical analysis with commercial code [8] demonstrates the feasibility of such configuration, widening the degrees of freedom one has to reach the desired reconfigurability goals in the design.

Adequately designed, the structure reported here can be successfully employed in different application, like delay lines, steerable leaky-wave antennas, holographic antennas, adaptive radio frequency elements, etc.

ACKNOWLEDGEMENT

This research was supported by a Marie Curie International Outgoing Fellowship within the 7th European Community Framework Programme.

REFERENCES

1. Matekovits, L., Heimlich, M. and Esselle K., "Tunable periodic microstrip structure on GaAs wafer," Progress in Electromagnetic Research, *PIER*, Vol. 97, page 1-10, 2009.
2. Matekovits, L., Heimlich, M. and Esselle K., "Metamaterial-Based Millimeter-Wave Switchable Leaky Wave Antenna for On-Chip Implementation in GaAs Technology," submitted to IET Microwaves, Antennas and Propagation, Special issue on: Microwave Metamaterials: Application to Devices, Circuits and Antennas.
3. Zhao, J. S., Chew, W. C. "Three-dimensional multilevel fast multipole algorithm from static to electrodynamic," Microw. Opt. Technol. Lett., Vol. 26, No. 1, 43–48, 2000.
4. Matekovits, L., Laza, V. A., Vecchi G., "Analysis of large complex structures with the synthetic-functions approach," IEEE Trans. Antennas and Propag., Vol. 55, No. 9, 2509–2521, Sept. 2007.
5. Prakash, V. V. S., Mittra R., "Characteristic basis function method: A new technique for fast solution of integral equations," Microw. Opt. Technol. Lett., 95–100, Jan. 2003.
6. L. Matekovits, G. Vietti Colomè, M. Orefice, "Controlling the Bandlimits of TE-Surface Wave Propagation Along a Modulated Microstrip-Line-Based High Impedance Surface," IEEE Trans. Antennas and Propagat., Vol. 56, No. 8, August, 2008, pp. 2555–2562.
7. J.S. Colburn, A. Lai, D.F. Sievenpiper, A. Bekaryan, B.H. Fong, J.J. Ottusch, P. Tulythan, "Adaptive artificial impedance surface conformal antennas," in Digest of the 2009 IEEE International Symposium on Antennas and Propagation, North Charleston, SC, USA, June 2009, 1–4.
8. http://web.awrcorp.com/

Resonances and dipole moments in dielectric, magnetic, and magnetodielectric cylinders – an overview

A. Dirksen, S. Arslanagic*, and O. Breinbjerg

Department of Electrical Engineering, Electromagnetic Systems,

Technical University of Denmark, Build. 348, Ørsteds Plads, DK-2800 Kgs. Lyngby, Denmark

*corresponding author: sar@elektro.dtu.dk

Abstract – An eigenfunction solution to the problem of plane wave scattering by dielectric, magnetic, or magnetodielectric cylinders, is used for a detailed investigation of their resonances. An overview of the resonances with electric and magnetic dipole moments, needed in *e.g.*, the synthesis of metamaterials, is given with an emphasis on their strength, bandwidth, and isolation.

1. Introduction

Among a large variety of metamaterial (MTM) realizations, see *e.g.*, [1] and the works referenced therein, special attention has recently been devoted to designs based on cylindrical or spherical inclusions of dielectric or magnetodielectric materials [2]-[4]. One main feature of these designs, as compared to previous arrangements of conducting wires and split ring resonators [1], is their potential of providing low-loss and isotropic MTMs. The basics of the novel MTM realizations rest upon the excitation of electric and magnetic dipole moments in the dielectric or magnetodielectric inclusions, which, when arranged appropriately, give the possibility of achieving *e.g.*, negative effective permittivity and permeability. In consequence hereof, there is an increased interest in a detailed understanding of the underlying physics of these resonances. The present work provides a detailed overview of the resonances providing electric and magnetic dipole moments in dielectric, magnetic, and magnetodielectric cylinders illuminated by a uniform plane wave. Using the exact analytical solution, the resonant properties are illustrated for a variety of cylinders having altering electrical and geometrical parameters. In particular, the strength, bandwidth, and isolation of the resonances, these being crucial parameters in MTM designs, are discussed. Moreover, analytical expressions are derived for electric and magnetic dipoles in all cylinders, thus providing additional insight in the potential of such inclusions for MTM design.

2. Configuration and theory

The cross-sectional view of the investigated configuration is shown in Figure 1. It consists of an infinite circular cylinder illuminated by a plane wave and immersed into free-space with the permittivity ε_0, permeability μ_0, and the wave number $\beta_0 = \omega\sqrt{\varepsilon_0\mu_0}$, $= 2\pi/\lambda_0$ with λ_0 being the free-space wavelength of operation. The cylinder has a radius a and is made of a simple and lossy material with the permittivity $\varepsilon_c = \varepsilon_0\varepsilon_r = \varepsilon_0(\varepsilon_r' - j\varepsilon_r'')$, permeability $\mu_c = \mu_0\mu_r = \mu_0(\mu_r' - j\mu_r'')$, and wave number $\beta = \omega\sqrt{\varepsilon_c\mu_c}$, with $\mathrm{Im}\{\beta\} \le 0$. A cylindrical coordinate system (ρ, ϕ, z), and the associated Cartesian coordinate system (x, y, z) are introduced such that the z-axis coincides with the axis of the cylinder, and the wave is incident on the cylinder along the positive x-direction. Two polarizations of the incident wave are considered, *cf.* Figure 1: transverse electric (TE^z) and transverse magnetic (TM^z). The exact solution to

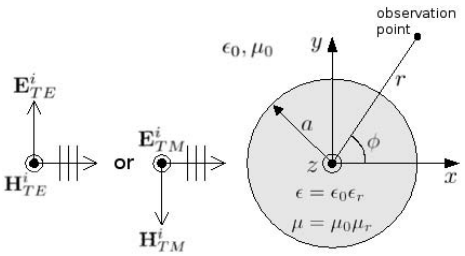


Figure 1. The configuration.

these problems is based on the eigenfunction expansion technique and is rather straightforward to obtain, see *e.g.*, [5]. For the TE^z polarization, let $\boldsymbol{H}_{TE}^i$ denote the known magnetic field incident on the cylinder, $\boldsymbol{H}_{TE}^s$ denotes the magnetic field scattered by the cylinder, and $\boldsymbol{H}_{TE}^t$ denotes the total magnetic field inside the cylinder; moreover, let $\boldsymbol{E}_{TE}^i$, $\boldsymbol{E}_{TE}^s$, and $\boldsymbol{E}_{TE}^t$ denote the corresponding electric fields. The unknown fields outside ($\boldsymbol{H}_{TE}^s$, $\boldsymbol{E}_{TE}^s$) and inside ($\boldsymbol{H}_{TE}^t$, $\boldsymbol{E}_{TE}^t$) the cylinder are expanded in cylindrical wave functions with the unknown expansion coefficients a_n and b_n, respectively, where n is the mode number (*i.e.*, $n=0$ is the monopole mode, $n=1$ is the dipole mode, etc.). For the TM^z polarization, let $\boldsymbol{E}_{TE}^i$ denote the electric field incident onto the cylinder, $\boldsymbol{E}_{TE}^s$ denotes the electric field scattered by the cylinder, and $\boldsymbol{E}_{TE}^t$ denotes the total electric field inside the cylinder; moreover, let $\boldsymbol{H}_{TE}^i$, $\boldsymbol{H}_{TE}^s$, and $\boldsymbol{H}_{TE}^t$ denote the corresponding magnetic fields. The unknown fields outside ($\boldsymbol{E}_{TE}^s$, $\boldsymbol{H}_{TE}^s$) and inside ($\boldsymbol{E}_{TE}^t$, $\boldsymbol{H}_{TE}^t$) the cylinder are expanded in cylindrical wave functions with the unknown expansion coefficients d_n and e_n, respectively. All expansion coefficients are determined by use of the boundary conditions at the cylinder surface, and the problems have thus been solved.

With this solution, the different electric and magnetic dipole moments can be calculated. For a dielectric cylinder, the electric and magnetic dipole moments are given by

$$\boldsymbol{p}_d = \frac{1}{j\omega}\int_V \boldsymbol{J}_p(\boldsymbol{r}')dv', \qquad \text{and} \qquad \boldsymbol{m}_d = \frac{1}{2}\int_V \boldsymbol{r}'\times\boldsymbol{J}_p(\boldsymbol{r}')dv', \tag{1}$$

respectively, where $\boldsymbol{J}_p = j\omega(\varepsilon_c-\varepsilon_0)\boldsymbol{E}_{TE,TM}^t$ is the polarization current inside the cylinder, and dv' denotes a differential volume element with the position vector $\boldsymbol{r}'$. For a magnetic cylinder the electric and magnetic dipole moments are given by

$$\boldsymbol{p}_m = -\frac{\varepsilon_0}{2}\int_V \boldsymbol{r}'\times\boldsymbol{J}_m(\boldsymbol{r}')dv', \qquad \text{and} \qquad \boldsymbol{m}_m = \frac{1}{j\omega\mu_0}\int_V \boldsymbol{J}_m(\boldsymbol{r}')dv', \tag{2}$$

where $\boldsymbol{J}_m = j\omega(\mu_c-\mu_0)\boldsymbol{H}_{TE,TM}^t$ is the magnetization current inside the cylinder. In a magneto- dielectric cylinder, both electric and magnetic polarization currents exist, and the total electric and magnetic dipole moments are $\boldsymbol{p}_{md} = \boldsymbol{p}_d + \boldsymbol{p}_m$ and $\boldsymbol{m}_{md} = \boldsymbol{m}_d + \boldsymbol{m}_m$, respectively. Recalling that an electric line current is equivalent to a magnetic loop current, and that an electric loop current is equivalent to a magnetic line current, it follows that an electric dipole moment can be created by an electric line current or a magnetic loop current and that a magnetic dipole moment can be created by an electric loop current or a magnetic line current. Furthermore, by recalling that the fields inside the cylinder are represented as multipole expansions, it follows that the necessary line and loop currents, and thus the respective moments, can be created by exploiting the terms $n=0$ and $n=1$; these modes are thus of relevance in the design of artificial materials such as MTMs.

3. Numerical results: resonant properties of expansion coefficients, fields and dipole moments

The expansion coefficients a_n and b_n, as well as d_n and e_n, depend on $\beta_0 a$, ε_r, and μ_r. For specific values of these parameters, the coefficients become resonant, *i.e.*, their magnitude attains large values. Figures 2(a)-(b) and (c)-(d) show the magnitudes of (a_0, b_0) and (a_1, b_1), respectively, as a function of $\sqrt{\varepsilon_r}$ and $\beta_0 a$ for a lossless dielectric cylinder in case of TE^z polarization (other cases are not included here but will be shown at the presentation). The maxima of the coefficients are seen to follow specific resonance curves and the corresponding resonances are designated as the TE_{nl}^d resonances, where for each n, $l=0$ corresponds to the leftmost curve, $l=1$ corresponds to the second leftmost curve, etc. Thus, Figures 2(a)-(b) show the TE_{0l}^d resonances, and Figures 2(c)-(d) show the TE_{1l}^d resonances.

When felt necessary, the designations $\mathrm{TE}_{nl}^{d}(a_n)$ and $\mathrm{TE}_{nl}^{d}(b_n)$ are used to refer to a specific coefficient. Following a resonance curve, *e.g.*, the TE_{01}^{d} resonance, it is found that, of course, a higher ε_r results in a smaller $\beta_0 a$ (implying a smaller radius a at a given frequency) and a noticeable narrowing of the resonances. Moreover, the TE_{1l}^{d} resonances are pushed toward higher $\beta_0 a$ values. By duality, Figures 2(a)-(b) and (c)-(d) also show the magnitudes of (d_0, e_0) and (d_1, e_1), respectively, as a function of $\sqrt{\mu_r}$ and $\beta_0 a$ for a lossless magnetic cylinder with TM^z polarization – these are the TM_{nl}^{m} resonances and are identified in terms of the symbols in the parentheses included in all subfigures of Figure 2.

Figures 2(e)-(f) and (g)-(h) show, respectively, the magnitudes of (a_0, b_0) and (a_1, b_1) as a function of $\beta_0 a$ for specific values of $\sqrt{\varepsilon_r}$ for a lossless dielectric cylinder under the TE^z polarization. This corresponds to horizontal cuts in Figures 2(a)-(d) but with a reduced range of $\beta_0 a$. The width of the resonances for the $n=0$ mode is found to be broader than for the $n=1$ mode, and it differs considerably for different resonances for a given value of $\sqrt{\varepsilon_r}$. In addition, the higher the value of $\sqrt{\varepsilon_r}$ the narrower is the width, and the higher is the amplitude of the b_0 and b_1 coefficients. As will be shown in the presentation, the inclusion of moderate losses has the effect of lowering the amplitude of the resonances, and shifts slightly their position in frequency, and broadens their width.

With the aim of exploiting resonances for MTM realizations, it is important that the $n=0$ and $n=1$ modes are sufficiently dominant, *i.e.*, their expansion coefficients should be large as compared to others. Figure 2(i) shows the isolation of the $n=0$ mode in terms of the quantity $|a_1/a_0|$ for the $\mathrm{TE}_{01}^{d}(a_0)$ resonance, and $|b_1/b_0|$ for the $\mathrm{TE}_{01}^{d}(b_0)$ resonance as a function of $(\varepsilon_r')^{1/2}$, while the isolation of the TE_{1l}^{d} resonances ($n=1$ mode) is shown in Figure 2(j) in terms of $|a_1/a_0|$ and $|a_2/a_0|$, evaluated at the $\mathrm{TE}_{11}^{d}(a_1)$, and $|b_1/b_0|$ and $|b_2/b_0|$ for the $\mathrm{TE}_{11}^{d}(b_1)$ resonance. In Figures 2(i)-(j), a curve with a given color appears twice; the upper (lower) curve corresponds to the lossless (lossy) case for which $\varepsilon_r''/\varepsilon_r' = 0$ ($\varepsilon_r''/\varepsilon_r' = 0.05$). In the lossless cases, larger $(\varepsilon_r')^{1/2}$ results in a more isolated mode, whereas the isolation is worsened as the loss is included. As an example, it is seen in Figure 2(i) that for *e.g.*, $(\varepsilon_r')^{1/2} = 5$ and zero loss, the exterior (interior) coefficient a_1 (b_1) is about 18% (6%) of a_0 (b_0), whereas for $(\varepsilon_r')^{1/2} = 25$ it is only about 0.8% (0.06%) of a_0 (b_0). It is interesting to remark that the isolation of the $n=1$ mode in the lossy case is in fact worsened as $(\varepsilon_r')^{1/2}$ increases. In general, the isolation properties for a given $(\varepsilon_r')^{1/2}$ are better for $n=0$ than for the $n=1$ mode; the former mode also has a wider width of the resonances. Thus, a trade-off between the width and isolation of the resonances exists since an increase of $(\varepsilon_r')^{1/2}$ lowers the width while increasing the isolation for lossless cylinders.

The above results are next confirmed with a number of field illustrations. Figure 2(k) shows, for a resonance frequency of 300 MHz, the magnitude (color) and the direction at the time $t=0$ (arrows) of the total electric field for a dielectric cylinder $(\varepsilon_r = 625)$ at the $\mathrm{TE}_{01}^{d}(b_0)$ resonance. The circulating electric field creates a polarization current loop which, *cf.*, the discussion in Section 2 yields a magnetic dipole with the moment $\boldsymbol{m}_{TEd}$ which is calculated analytically by use of (1) (closed form expressions of all dipole moments will be included in the presentation). The magnitude and phase of $\boldsymbol{m}_{TEd}$ are shown in Figure 3(a) (the vertical left axis). By duality, Figure 2(k) also shows the quantity $-(\mu_0/\varepsilon_0)\boldsymbol{H}_{TM}^{t}$ for a magnetic cylinder $(\mu_r = 625)$ at the $\mathrm{TM}_{01}^{m}(e_0)$ resonance, with the result corresponding to a circulating magnetization current, and thus to an electric dipole with the moment $\boldsymbol{p}_{TMm}$; its magnitude and phase, as calculated by (2), are shown in Figure 3(a) (the vertical left axis). For the $n=1$ mode, the magnitude and the direction (for $t=0$) of the total electric field at the $\mathrm{TE}_{11}^{d}(b_1)$ resonance, and of $-(\mu_0/\varepsilon_0)\boldsymbol{H}_{TM}^{t}$ at the $\mathrm{TM}_{11}^{m}(e_1)$ resonance, are shown in Figure 3(b); these lead to an electric, $\boldsymbol{p}_{TEd}$, and magnetic, $\boldsymbol{m}_{TMm}$, dipole moment, respectively, and their magnitude and phase are depicted on the left and right vertical axes of Figure 3(b), respectively.

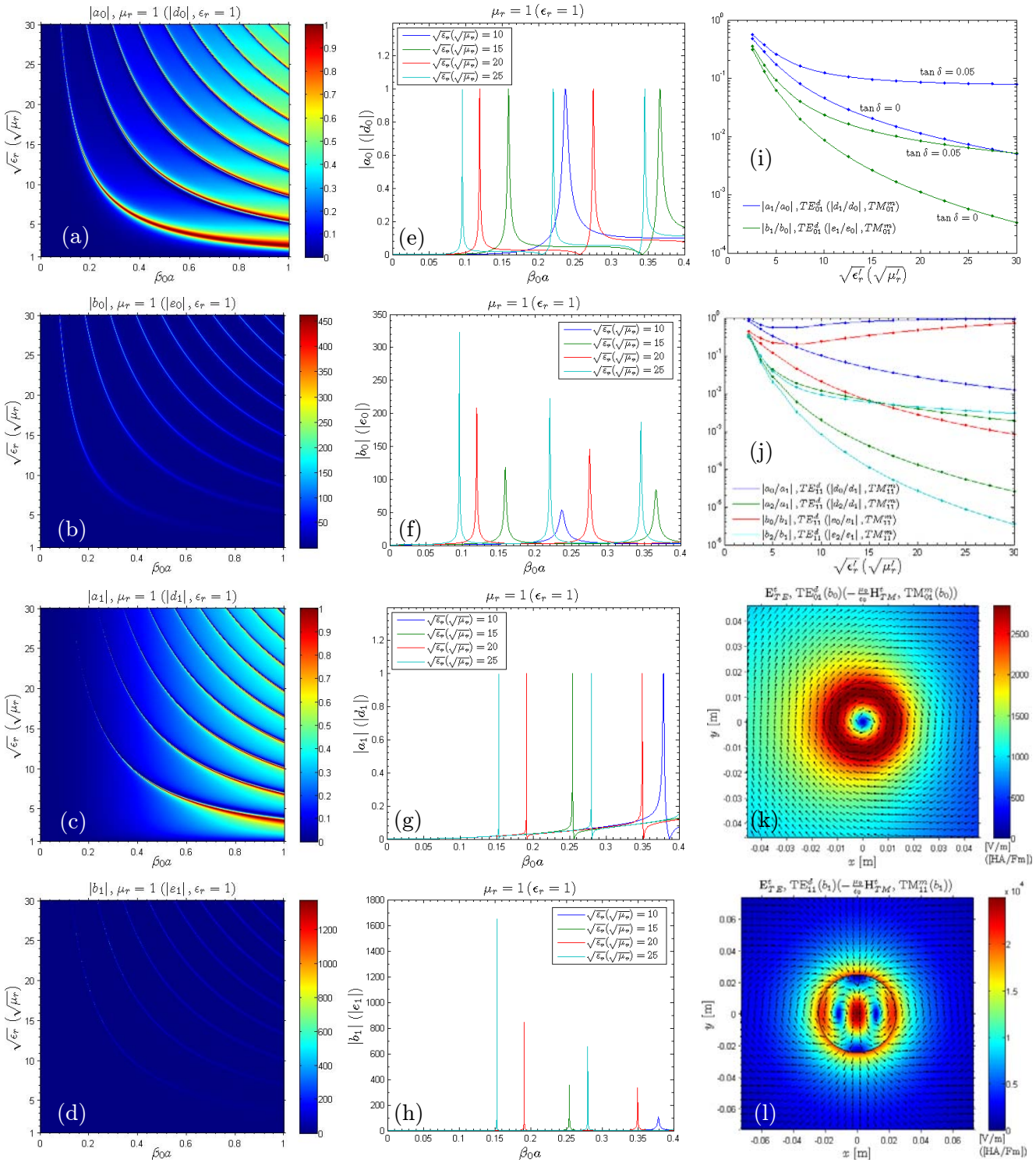
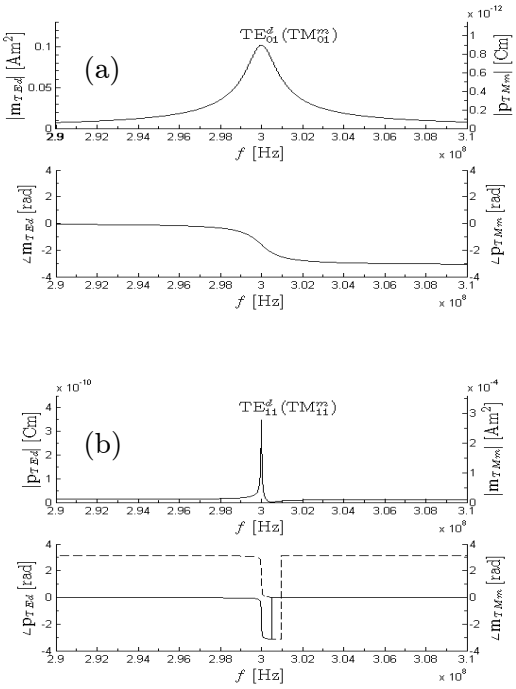


Figure 2: The shown results apply for a dielectric (magnetic) cylinder with the TE^{z} (TM^{z}) polarization, with those for the magnetic cylinder indicated by the symbols in the parentheses included in the respective figures. (a)-(d): the magnitude of the expansion coefficients as a function of $\sqrt{\varepsilon_r}$ ($\sqrt{\mu_r}$) and $\beta_0 a$. (e)-(h): magnitude of the expansion coefficients as a function of $\beta_0 a$ for specific values of $\sqrt{\varepsilon_r}$ ($\sqrt{\mu_r}$). (i)-(j): isolation properties of the $n=0$ and $n=1$ modes. (k)-(l): the magnitude and the direction of the total fields at the $\mathrm{TE}_{01}^{d}(b_0)$ and $\mathrm{TE}_{11}^{d}(b_1)$ resonances inside and outside the cylinders for the $n=0$ and $n=1$ modes. See the main text for further explanations.

Figure 3: Magnitude and phase of (a) $\boldsymbol{m}_{TEd}$ (left vertical axis) and $\boldsymbol{p}_{TMm}$ (right vertical axis), and of (b) $\boldsymbol{p}_{TEd}$ (left vertical axis) and $\boldsymbol{m}_{TMm}$ (right vertical axis). See the main text for further explanations.



In Figure 3, the magnitude of the dipole moments peaks at the resonance frequency across which a phase shift of π also occurs (additional phase shifts in Figure 3(b) at a frequency right to the resonance frequency are in order due to the zero magnitudes of the two dipole moments at this particular frequency). Since, as will be shown in the presentation, all the electric (magnetic) dipole moments are parallel to the incident electric (magnetic) field of which the amplitude is assumed real, the latter implies a change in the sign, and thus the direction, of dipole moments at the resonance frequency, thus rendering such cylinders applicable as inclusions in a MTM design.

4. Summary and conclusions

An overview of electric and magnetic dipole resonances was given for dielectric and magnetic cylinders with an emphasis on their strength, bandwidth, and isolation. In general, a higher material parameter was found to lead to larger amplitude of the resonances, while narrowing the bandwidth, but improving their isolation which turn to be better for the monopole than for the dipole mode. Although the numerical results were devoted to specific cylinders and specific polarizations, the present manuscript provides, as will be shown in the presentation, a means of devising dielectric, magnetic, and/or magnetodielectric cylinders capable of exciting the dipole moments, of which a complete characterization, in terms of the strength, bandwidth, and isolation of the resonances, can be made for both polarizations.

Acknowledgements

This work is supported by the Danish Research Council for Technology and Production Sciences within the TopAnt project.

REFERENCES

1. Engheta N., and R. W. Ziolkowski, *Metamaterials: physics and engineering applications*, John Wiley & Sons, New York, 2006.
2. Holloway C., Kuester E., Baker-Jarvis J., and P. Kabos, "A double negative (dng) composite medium composed of magnetodielectric spherical particle embedded in a matrix," *IEEE Trans. Antennas Propagat.*, Vol. 51, 2596-2603, 2003.
3. Vendik I., Vendik O., and M. Odit, "Isotropic artificial media with simultaneously negative permittivity and permeability," *Microwave Opt. Techn. Lett.,* Vol. 48, 2553-2556, 2006.
4. Peng L., Ran L., Chen H., Zhang H., Kong J. A., and T. M. Grzegorczyk, "Experimental observation of left-handed behavior in an array of standard dielectric resonators," *Phys. Rev. Lett. B.*, Vol. 98, 157-403, 2007.
5. C. A. Balanis, Advanced Engineering Electromagnetics, John Wiley & Sons, 1989.

Anomalous reflection in metallic structures with subwavelength grooves: a circuit theory model

F. Medina[1], **F. Mesa**[2], **and D. M. Skigin**[3]

[1]Dept. Electrónica y Electomagnetismo, University of Seville, 41012-Seville, Spain
[2]Dept. Física Aplicada 1, University of Seville, 41012-Seville, Spain
[3]Grupo de Electromagnetismo Aplicado, FCEN, University of Buenos Aires, Buenos Aires, Argentina
medina@us.es

Abstract— An equivalent-circuit approach is proposed to explain the behavior of metallic dual-period structures with several grooves per period. The Fabry-Pérot resonances and reflection peaks that appear in these structures are well accounted for by the proposed equivalent-circuit model. This equivalent circuit is based on well established concepts of waveguide and circuit theory and it provides a simple and accurate description of the phenomenon which is also appropriate for educational purposes as well as for the design of potential devices based on the behavior of the structures under study.

1. INTRODUCTION

Metallic surfaces with sub-wavelength slits present interesting optical/electromagnetic properties. In recent years, compound transmission diffraction gratings have been shown to exhibit phase resonances in the transmission spectrum. These phase resonances significantly modify the electromagnetic response, as it has been theoretically reported in [1] and experimentally demonstrated in [2, 3]. These exotic transmission phenomena can easily be explained in terms of equivalent networks involving lumped elements and transmission lines [4]. However, before analyzing compound transmission gratings, the reflection properties of metallic surfaces with periodically distributed grooves had been studied. Some interesting properties of the reflection spectrum of this kind of structured surfaces can be found in [5] or [6, 7]. The goal of this paper is to extend the concepts and methods used in [4] to the modeling of these reflective structured surfaces. The extension is not trivial because transmission gratings operate in the non-diffraction regime (the unit cell is smaller than the operation wavelength) whereas the interesting features of reflection gratings appear above the onset of the first higher-order grating lobe.

Our modeling is based on the existance of a simple equivalent circuit, whose parameters are calculated. Curves of reflected intensity as a function of the wavelength are explained to the light of the behavior of this equivalent circuit. The results obtained with this simplified model completely capture the details of the reflection spectrum computed by means of a rigorous modal method. The concepts reported in this paper provide a relatively simple explanation of an apparently complex physical phenomenon. However, the most important benefit of the reported theory, from an engineering point of view, is that it provides a convenient methodology to analyze structures and/or to conceive new devices based on the studied physical phenomenon. The design tasks can be considerably simplified since the effect of each of the elements of the equivalent circuit model on the reflected response is qualitatively known *a priori*.

2. COMPOUND DIFFRACTION GRATINGS: STATEMENT OF THE PROBLEM

An schematic view of a compound reflection grating having three identical slits per period ($N = 3$) is shown in Fig. 1. The structure is assumed to be infinitely long along the z–direction. Although only three slits are considered here for the sake of simplicity, an arbitrary number of slits per period could be accommodated too. Due to the periodic nature of the geometry and the excitation (the impinging wave is a normally incident TEM wave with the electric field linearly polarized along the x-direction), attention is focused on the analysis of the unit cell that is drawn in the figure. For wavelengths larger than the period of the structure, $\lambda > d$ (non diffracting regime), all the impinging power is specularly reflected along the normal direction. The magnitude of the specular reflection coefficient is then 1 (lossless case). For $\lambda < d$, at least the first order grating lobe appears

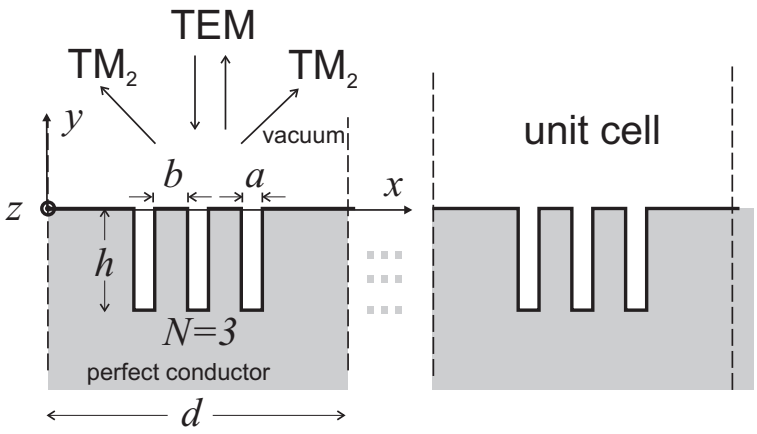


Figure 1: Example of compound diffraction grating with three ($N = 3$) grooves per period. The unit cell is the structure within dashed lines. Dashed lines are electric wall for normal incidence of a TEM wave with an x-polarized electric field.

above the horizon. Thus, part of the impinging power is scattered into that grating lobe and specular reflection is reduced (*i.e.*, the specular reflection coefficient, defined as the ratio between the specularly reflected power and incident power, is less than 1). This reflection coefficient exhibits a frequency dependent behavior that can be explained in terms of the periodicity and groove depth. For instance, for frequencies where $d \approx n\lambda$, reflection peaks are expected. These reflection peaks, which appear for grooves of any depth h (even for very shallow grooves), can be explained in terms of the excitation of surface plasmon polaritons. Clearly, when $h \approx n\lambda/2$, internal resonances of the cavities formed by the grooves play an important role. Strong specular reflection peaks can be observed in connection with such resonances. All those phenomena have been studied in depth in the past [8] for the case of simple gratings (a single groove per period). However, in this paper, we are interested on a different kind of resonance that appears in infinite gratings with a finite number of grooves per period (compound gratings) [5, 6]. In these structures, sharp peaks of the specular reflection coefficient appear in the frequency region between two successive Rayleigh anomalies. These peaks are found at frequencies for which $h \lessapprox \lambda/4$, and are attributed to phase resonances associated with the presence of three or more slits per period [5, 6]. However, it can easily be inferred that this phenomenon is closely related to the sharp transmission dips that have been observed in the transmission coefficient of compound transmission gratings [1] (several slits per period). For transmission gratings it has been shown that a simple equivalent circuit explains the main features of the observed transmission spectra [4]. The purpose of this contribution is to show that a simple equivalent circuit is also available for the modeling of reflection gratings. This will be explained in the forthcoming section.

3. EQUIVALENT CIRCUIT FOR COMPOUND GRATINGS

As has been stated above, the diffraction problem in Fig. 1 can be reduced to the analysis of a single unit cell. Following the reasonings in [4], it is not difficult to understand that, for normal incidence, the problem under consideration reduces to the analysis of the parallel-plate waveguide problem shown in Fig. 2(a). A parallel-plate waveguide of arbitrary width, with characteristic admittance Y_0, is terminated by the three grooves depicted in that figure (an arbitrary number of grooves could have been considered). Each groove is again considered as a parallel-plate transmission line having a meaningfully higher characteristic admittance (for the specific geometry in Fig. 2(b), $Y_1 = Y_2/2 \gg Y_0$). It must be noticed that two transmission lines are used to model the three grooves system because of the existence of the symmetry plane BB' (see [4] for further explanations). The specularly reflected beam is represented by the TEM reflected mode, while the TM_2 mode would account for the first diffraction order field. In contrast with the analysis reported in [4], we are interested on the frequency range where both, TEM and TM_2 modes operate above cutoff, while all the other TM modes scattered by the termination are below cutoff.

From the point of view of the impinging TEM mode, the equivalent circuit representing the situation is given in Fig. 2(b). This is very similar to the circuit reported in [4] for the so-called "odd excitation". However, an important difference should be taken into account: the TM_2 mode

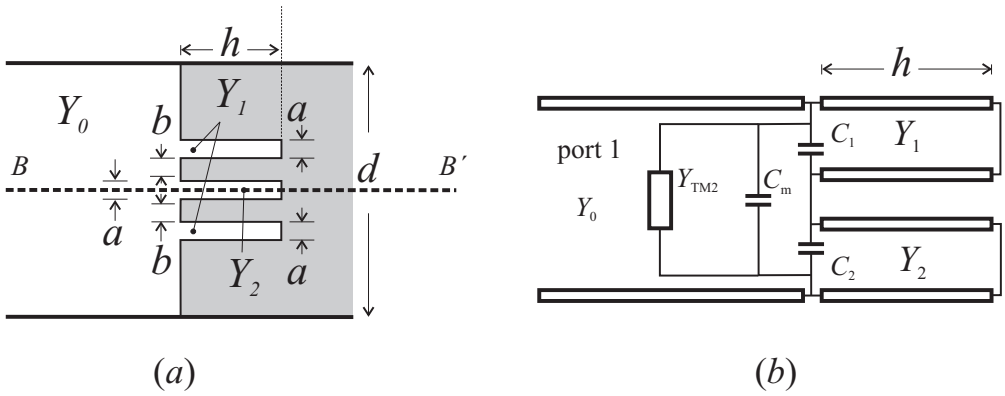


Figure 2: (a) Unit cell for the analysis of normal incidence on the periodic grating in Fig. 1. (b) Equivalent circuit for the range of frequencies comprised between the onsets of first and second grating lobes.

is above cutoff, in such a way that its characteristic admittance, Y_{TM2} is real (otherwise, total reflection should be expected for any frequency). The effect of higher-order TM modes operating below cutoff can be accounted for through the π–capacitance network shown in Fig. 2(b). As it has been explained in [4] and [9], the capacitances of the model are singular at the onset frequencies of grating lobes (TM modes in our formalism), thus giving place to total reflection for the TEM mode (the TEM mode represents specular reflection). If the groove depth is $h = n\lambda/2$, conventional circuit theory tell us that a short circuit is seen by the TEM transmission line, in such a way that total specular reflection should be expected for frequencies satisfying the above condition. This is in perfect agreement with observations coming from experimental or numerical results. But what is more interesting in the context of this paper is the explanation of the extremely sharp peaks that can be observed in the specular transmission coefficient at some frequencies for which the electrical depth of the grooves is smaller than $\lambda/4$. Following the discussion in [4] for transmission gratings, we can realize that the equivalent electrical lengths of the two transmission lines appearing in Fig. 2(b) are not identical because $C_2 \neq 2C_1$ while $Y_2 = 2Y_1$. Due to this fact, at certain frequency between the frequencies f_1 and f_2 that make the equivalent length of each of those lines equal to $\lambda/4$, the impedance of the transmission lines together with the capacitance network becomes zero (short circuit). This is a very narrow band condition (impedances reach very high values at f_1 and f_2, which are commonly very close to each other). For the three grooves per period situation, this model predicts the existence of a single peak of this nature. This peak corresponds to a phase resonance in the frame of the theory reported in [5]. Note that this explanation also predicts the absence of this kind of peaks when the number of grooves per period is 1 or 2 (in perfect agreement with the results reported in [5]). If the number of grooves per period is 3 or 4, two transmission lines are involved in the modeling of grooves, in such a way that a single peak is expected. If 5 or 6 grooves per period are present, the model in Fig. 2(b) would require the addition of a third transmission line for groove modeling. It is evident that three transmission lines would yield the short circuit condition at two frequencies, thus giving place to two sharp peaks. This rule can be extended to any number of grooves per period in such a way that the results reported in [5] or [6] are accurately accounted for by the simple circuit model proposed in this contribution.

4. CONCLUSION

Circuit models that have been recently proposed to explain extraordinary transmission phenomena in 1D compound gratings of slits and 2D diffraction grids have been adapted here to the analysis of compound reflection gratings made of periodic distributions of groups of grooves in a perfect conductor surface. The model provides simple understanding of the qualitative aspects of the specular reflection response of the grating. Since the number of unknown parameters of the circuit model is small, the parameters could be easily computed from simulated results for a few frequency values. The circuit model with the obtained parameters can be used to generate the wideband response of the grating.

ACKNOWLEDGMENT

F. Medina and F. Mesa acknowledge funding from Spanish Ministerio de Ciencia e Innovación (Project no. TEC2007-65376 and Project Consolider Ingenio 2010, "Engineering Metamaterials", CSD2008-00066). D. C. Skigin acknowledges financial support from Consejo Nacional de Investigaciones Científicas y Técnicas (under Grant PIP 5700), Universidad de Buenos Aires (under UBA Grants X283 and X208), and Agencia Nacional de Promoción Científica y Tecnológica (ANPCYT-BID Grant 802/OC-AR03-14099).

REFERENCES

1. Skigin, D. C. and Depine, R. A., "Transmission resonances in compound metallic gratings with subwavelength slits," *Phys. Rev. Lett.*, Vol. 95, 217402, 2005.
2. Hibbins, A. P., Hooper, I. R. Lockyear, M. J. and Sambles, J. R., "Microwave transmission of a compound metal grating," *Phys. Rev. Lett.*, Vol. 96, 257 402, 2006.
3. Navarro-Cía, M., Skigin, D. C., Beruete, M. and Sorolla, M., "Experimental demonstration of phase resonances in metallic compound gratings with subwavelength slits in the millimeter wave regime," *App. Phys. Lett.*, Vol. 94, 091 107, 2009.
4. Medina, F., Mesa, F. and Skigin, D. C., "Extraordinary transmission through arrays of slits: a circuit theory model," *IEEE Trans. on Microwave Theory Tech.*, Vol. 58, No. 1, in press, 2010.
5. Skigin, D. C., Veremey, V. V. and Mittra, R., "Superdirective radiation from finite gratings of rectangular grooves," *IEEE Trans. on Antennas Propagat.*, Vol. 47, No. 2, 376–383, 1999.
6. Fantino, A. N., Grosz, S. I. and Skigin, D. C, "Resonant effects in periodic gratings comprising a finite number of grooves in each period," *Phys. Rev. E*, Vol. 64, 056619, 2001.
7. Grosz, S. I., Skigin, D. C and Fantino, A. N., "Resonant effects in compound diffraction gratings: influence of the geometrical parameters of the surface," *Phys. Rev. E*, Vol. 65, 056619, 2002.
8. López-Rios, T., Mendoza, D., García-Vidal, F. J., Sánchez-Dehesa, J. and Pannetier, B., "Surface shape resonances in lamellar metallic gratings," *Phys. Rev. Lett.*, Vol. 81, No. 3, 665, 1998.
9. Medina, F., Mesa, F. and Marqués, R., "Extraordinary transmission through arrays of electrically small holes from a circuit theory perspective," *IEEE Trans. Microwave Theory Tech.*, Vol. 56, No. 12, 3108, 2008.

Analytical methods for AMC and EBG characterisations

M. Grelier[1,2*], F. Linot[1,3], A. C. Lepage[1], X. Begaud[1], J.M. LeMener[2] and M. Soiron[3]

[1]Institut TELECOM, TELECOM ParisTech - LTCI CNRS UMR 5141,
46 rue Barrault 75634 Paris Cedex 13, France

[2]Thales Systèmes Aéroportés, 10 avenue de la 1ere DFL 29238 Brest Cedex 3, France

[3]Thales Systèmes Aéroportés, 78852 Elancourt Cedex, France

[*]corresponding author: grelier@ieee.org

Abstract- AMC and EBG behaviours are respectively characterized by reflection phase method and dispersion diagram. A fast and simple analytical model based on transmission line theory is proposed for each analysis. The validity of these analytical methods is verified by a comparison between circuit representations, measurements and numerical results.

1. INTRODUCTION

In the past few decades, artificial materials have received considerable attention for their applications in microwave and sub-millimeter wave frequencies [1]. They possess two unique features that can control the propagation of electromagnetic waves [2]. The first one provides a behaviour of artificial magnetic conductor (AMC) allowing incident plane waves to be reflected with a near zero phase shift. The second one exhibits an electromagnetic band-gap (EBG) characteristic which stops surface wave propagation in all directions.

Several analysis methods have been developed to characterise these surfaces. Among them, analytical methods are the fastest to design these structures. In this work, we present two analytical models to identify either AMC or EBG properties. Experimental and numerical results are investigated to demonstrate the validity of these methods.

Fig. 1 displays the studied structure. It consists of a planar array of square metal patches without vias printed on a metal backed substrate. The parameters of the structure are the following: the length of each square patch w, the gap between the adjacent patches g, the period P=w+g, the thickness of the substrate h and its relative dielectric constant ε_r.

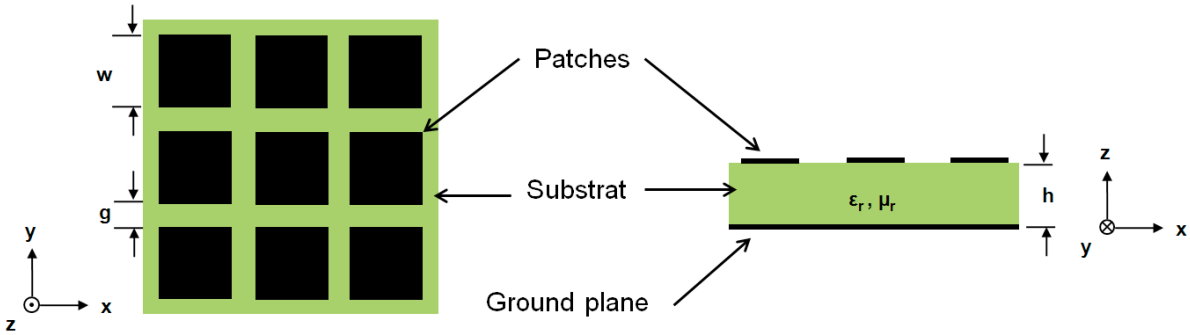


Fig. 1: Top view and side view of the studied structure

2. ANALYTICAL MODELS

An AMC is commonly characterized by its phase reflection diagram. It represents the phase of the reflected electric field which is normalized to the phase of the incident electric field at the reflecting surface [3]. According to [4], the input surface impedance Zs of an AMC can be modelled through a transmission line when

the wave propagation is assumed to be along the z-direction (Fig. 2a). Zs is considered as a parallel connection of a capacitance C, due to the planar grid of metallic patches response, and an inductance L due to the metal-backed dielectric slab response:

$$Z_s^{TE/TM} = \left(Z_C^{TE/TM}\right)^{-1} + \left(Z_L^{TE/TM}\right)^{-1} \quad (1)$$

The resonance frequency of the artificial material conductor can be adjusted by altering L or C: $\omega=(LC)^{-1/2}$. The formulas of the capacitance and inductance for each polarization of the incident field, are issued from [5]:

$$Z_c^{-1\,TM} = j\omega\frac{P}{\pi}\varepsilon_0(1+\varepsilon_r)\log\left(\csc\left(\frac{\pi g}{2P}\right)\right) \quad (2)$$

$$Z_c^{-1\,TE} = j\omega\frac{P}{\pi}\varepsilon_0(1+\varepsilon_r)\log\left(\csc\left(\frac{\pi g}{2P}\right)\right)\cdot\left(1-\frac{k_0^2}{k_{eff}^2}\sin^2\theta\right) \quad (3)$$

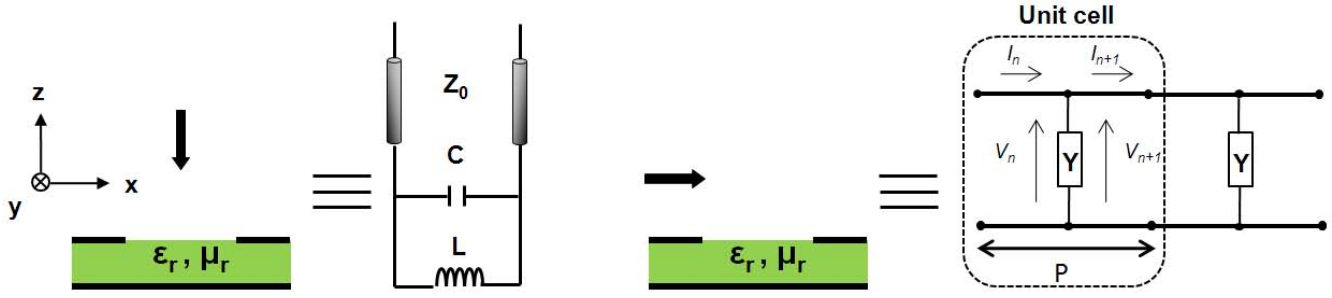
$$Z_L^{TE/TM} = j\omega\mu_0\frac{\tan(\beta h)}{\beta}\left(\overline{\overline{I_t}}-\frac{k_t k_t}{k^2}\right) \quad (4)$$

Where $\beta=\sqrt{k^2-k_t^2}$ is the normal component of the wave vector in the substrate with k the wave vector in the substrate and k_t the tangential wave vector component imposed by the incident wave. $k_{eff}=k_0\sqrt{\varepsilon_{eff}}$ is the wave vector in the effective host medium, ε_0 and μ_0 are respectively the permittivity and permeability of free space, $\overline{\overline{I_t}}$ is the dyadic unit and θ is the incident angle. To improve the accuracy of the expression of ε_{eff}, the closed expression given by Schneider has been used [6].

$$\varepsilon_{eff} = \frac{\varepsilon_r+1}{2}+\frac{\varepsilon_r-1}{2}\cdot\left(1+10\cdot\frac{h}{w}\right)^{-1/2} \quad (5)$$

The above expressions are valid for $k_{eff}.P \ll 2\pi$ and $g \ll P$. The phase reflection diagram is plotted from the the reflection coefficients Γ^{TE} and Γ^{TM} of the two incident wave's polarizations following the below expressions:

$$\Gamma^{TE} = \frac{Z_s{}^{TE}\cos\theta - Z_0}{Z_s{}^{TE}\cos\theta + Z_0} \quad \text{and} \quad \Gamma^{TM} = \frac{Z_s{}^{TM} - Z_0\cos\theta}{Z_s{}^{TM} + Z_0\cos\theta} \quad \text{with } Z_0=\sqrt{\mu_0/\varepsilon_0} \quad (6)$$



(a) (b)

Fig. 2: (a) Equivalent model for the AMC case, (b) Equivalent model for the EBG case

The EBG feature analysis is obtained by plotting the dispersion diagram. If we consider the propagation along the *x* axis direction, the structure can be modelled as a transmission line periodically loaded by a microstrip gap displayed in Fig. 2b [7].

The voltage V_n and current I_n are related on each side of the *n*th unit cell using the ABCD matrix:

$$\begin{bmatrix} V_n \\ I_n \end{bmatrix} = \begin{bmatrix} A & B \\ C & D \end{bmatrix} \begin{bmatrix} V_{n+1} \\ I_{n+1} \end{bmatrix} \quad (7)$$

The matrix parameters represent a cascade of a transmission line section of length P/2, a shunt load, and another transmission line section of length P/2. The ABCD matrix can be expressed as:

$$\begin{bmatrix} A & B \\ C & D \end{bmatrix} = \begin{bmatrix} \cos\frac{\theta_l}{2} & j\,Z_c \sin\frac{\theta_l}{2} \\ j\,Y_c \sin\frac{\theta_l}{2} & \cos\frac{\theta_l}{2} \end{bmatrix} \begin{bmatrix} 1 & 0 \\ Y & 1 \end{bmatrix} \begin{bmatrix} \cos\frac{\theta_l}{2} & j\,Z_c \sin\frac{\theta_l}{2} \\ j\,Y_c \sin\frac{\theta_l}{2} & \cos\frac{\theta_l}{2} \end{bmatrix} \text{ with } Y = jC\omega \quad (8)$$

Where $Z_c=1/Y_c$ is the characteristic impedance of a transmission line section in the absence of reactive elements and θ_l the electrical length.

Since the structure is infinite, the voltage and the current at the *n*th terminal only differ from the voltage and current at the *n*+1 terminal only by the propagation factor $e^{-\gamma P}$:

$$\begin{bmatrix} V_{n+1} \\ I_{n+1} \end{bmatrix} = \begin{bmatrix} V_n \\ I_n \end{bmatrix} e^{-\gamma P} \quad (9)$$

Where $\gamma=\alpha+j\beta$ is the propagation constant for the periodic structure. By developing equations (7), (8) and (9), the constant of propagation γ can be obtained as:

$$\gamma = \frac{1}{P} cosh^{-1}\left(\frac{A+D}{2}\right) = \alpha + j\beta \quad (10)$$

The stopband of the structure is defined when $\alpha \neq 0$ and $\beta = 0, \pi$.

3. EXPERIMENTAL RESULTS

A waveguide simulator is used to measure the phase reflection of the AMC. It is an oversized rectangular waveguide: the walls of the waveguide act as pairs of electric and magnetic walls which make the enclosed structure an infinity periodic environment. Waveguide simulators are generally used to characterize antenna arrays but they can also be useful to estimate the reflection coefficient of artificial material. Advantages and limitations of this method are described in [8]. The simulator uses TE_{10} excitation where the plane waves associated to this mode have an incidence angle θ defined by [9]:

$$\theta = \sin^{-1}\left(\frac{\lambda_0}{2a}\right) \quad (11)$$

Where a is the largest side of the waveguide and λ_0 is the wavelength in free space. The cross section of the waveguide must be commensurate to the periodicity of the structure. The dimensions of the waveguide simulator are a x b = 48mm x 8mm. The characterized structure is composed of 12 x 2 cells and is positioned at the end of the waveguide. The 48mm cross-section of the guide corresponds to $\theta=21.3°$ at f=8.6GHz. This structure is simulated using CST MWS to compare numerical results to the analytical and experimental ones (see Fig. 3). The dimensions of the studied structure are: P=4mm, g=0.4mm, h=1mm and $\varepsilon_r=10.2$. The experimental results agree with the analytical and numerical ones, showing that the proposed analytical model is accurate to design an AMC.

The method of suspended microstrip line is applied to analyze the band-gap characteristic of a structure with a finite number of cells [10]. A drop of the transmission coefficient S_{12} highlights the EBG behaviour. In [2], authors show that an EBG band-gap can be obtained with a periodicity close to $\lambda_m/2$ where $\lambda_m= \lambda_0/(\varepsilon_{eff})^{1/2}$. So, we consider an array of 7 x 7 cells whose dimensions are P=8.3mm, g=1mm, h=0.762mm and $\varepsilon_r=2.2$.

The curve obtained from the analytical method represents the normalised phase constant β_n, corresponding to the phase constant β multiplied by P and divided by π. This product ranges from 0 to 1 and also reveals a stopband between 11.8GHz and 13.3GHz. By considering a $|S_{21}|$ criterion below -10dB, a distinctive stopband appears from 11.6GHz to 13.6GHz which is close to the analytical one given by the dispersion diagram as show Fig. 3.

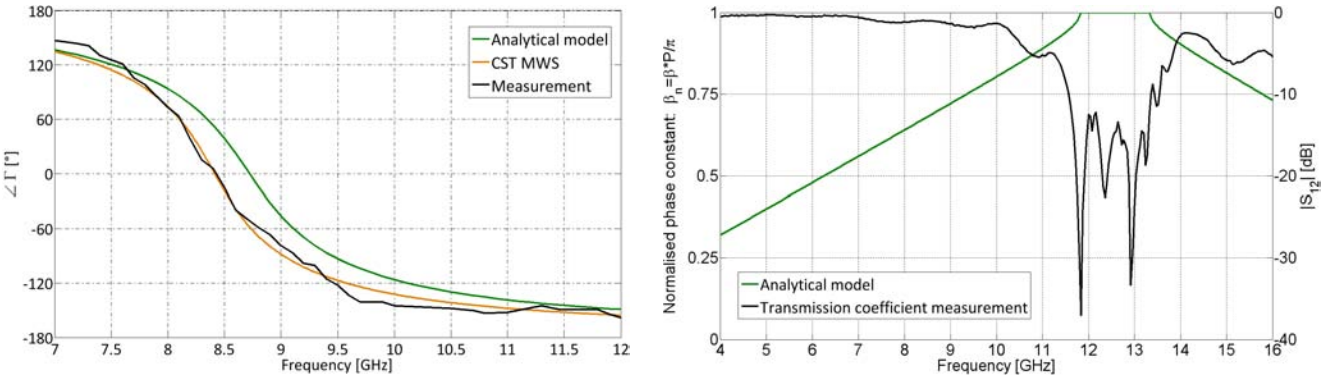


Fig. 3: Comparison of analytical model and measurement: AMC case (on the left) and EBG case (on the right)

4. CONCLUSIONS

In this communication two analytical methods based on transmission line theory are investigated to characterise AMC and EBG features. The validity of these models has been verified by experimental procedures thanks to a waveguide simulator and the suspended microstrip line method. These models yield accurate and fast methods to design such surfaces.

REFERENCES

1. De Maagt, P., R. Gonzalo and Y. Vardaxoglou, "Review of Electromagnetic Bandgap Technology and Applications," *The Radio Science Bulletin*, Vol. 309, 11–25, 2004.
2. Gousettis, G., A.P. Fresedis and J.Y.C. Vardaxoglou, "Tailoring the AMC and EBG characteristics of periodic metallic arrays printed on grounded dielectric substrate," *IEEE Trans. on Antennas and Propagation*, Vol. 54, No. 1, 82–89, 2006.
3. Yang, F. and Y. Rahmat-Samii, "*Reflection phase characterizations of the EBG ground plane for low profile wire antenna applications,*" IEEE Trans. on Antennas and Propagation., Vol. 51, No. 10, 2691-2703, 2003.
4. Tretyakov, S.A., *Analytical Modeling in Applied Electromagnetics*, Norwood, MA: Artech House, 2003.
5. Luukkonen, O. , C. Simovski, G. Granet, G. Goussetis, D. Lioubtchenko, A.V. Räisänen and S.A. Tretyakov, "*Simple and accurate analytical model of planar grids and high impedance surfaces comprising metal strips or patches,*" IEEE Trans. on Antennas and Propagation, Vol. 56, No. 6, 1624-1632, 2008.
6. Schneider, M.V., "*Microstrip lines for microwave integrated circuits,*" Bell System Technical Journal, Vol. 48, 1421-1444, 1969.
7. Pozar, D.M., *Microwave Engineering*, 2nd edition, John Wiley & Sons, 422-425, 1998.
8. Pearson, R.A., B. Phillips, K.G. Mitchell and M. Patel, *"Application of waveguide simulators to FSS and wideband radome design,"* Digest Inst. Elect. Eng. Colloq. on Advances in Electromagnetic Screens, Radomes and Materials, London, U.K., 7/1-7/6, 1996.
9. Mailloux, R.J., "*Phased Array Antenna Handbook*", Artech House, 1994
10. Fan, M.Y., R. Hu, Q. Hao, X.X. Zhang and Z.H. Feng, "New method for 2D-EBG structures," *J. Infrared Millim. Waves,* Vol. 22, No. 2, 127-131, 2003.

Single-layer metal nanolenses with tight foci in far-field

Piotr Wróbel[1], Tomasz J. Antosiewicz[2], Jacek Pniewski[1], Tomasz Szoplik[1]
[1]Faculty of Physics, University of Warsaw, Pasteura 7, 02-093 Warszawa, Poland
[2]Interdisciplinary Centre for Mathematical and Computational Modelling, University of Warsaw, Pawińskiego 5A, 02-106 Warsaw, Poland
Corresponding author: piotr.wrobel@igf.fuw.edu.pl

Abstract— In simulations we analyse performance of plasmonic nanolenses made of a single metal layer. We consider the nanolenses in two configurations. In the first, the nanolens is a free standing silver layer with no hole on the optical axis and double-sided concentric corrugations. In the second, the nanolens has a set of slits instead of grooves. This necessitates integrating the annular metal elements with a dielectric matrix. We examine the following parameters of the nanolenses: film thickness, diameter of an on-axis stop, and lattice constant of slits or double-sided concentric grooves, as well as depth and width of grooves. Due to radially polarized illumination lenses have foci of full widths at half maxima (FWHMs) better than half a wavelength, though foci formed by propagating waves do not decrease beyond the diffraction limit. Due to proper geometry of slits or double sided grooves lenses have focal lengths of the order of a few wavelengths. Transmission of light through lenses with double sided narrow grooves reaches 30% while through ones with slits exceeds 80%.

1. INTRODUCTION

The idea of imaging by means of nanoscale plasmonic devices goes far beyond possibilities of refractive or diffractive microlenses and lenslet arrays made of optically transparent media. Nanoscale devices for imaging comprise several nanotools such as flat or corrugated thin metal films [1] and metal-dielectric multilayers [e.g. 2] as well as optical probes for scanning near-field optical microscopes (SNOM) [1,3]. The probes are of various kinds: pure metal, metalised dielectric with aperture or spectrally tunable apertureless dielectric-metal-dielectric [4]. Wide interest in plasmonic lenses has started a decade ago, when transverse resolution considerably better than the Abbe resolution limit was predicted [5] and experimentally proven [6,7]. A lot of research was devoted to generation of surface plasmon-polariton (SPP) waves on circular and elliptical gratings milled in thin Ag layers and to focusing of plasmons on lens surfaces [8-11]. In a recent paper by Chen *et al*. [12], a plasmonic lens made of concentric silver rings with on-axis stop and illuminated with radially polarized light is experimentally proven to concentrate evanescent fields into a narrow needle. The needle results from propagation of generated plasmons toward the lens axis and their constructive interference, what results in strong enhancement of polaritons over the on-axis stop.

Previous work on optical properties of single layer lenses with grooves or slits was focused on such properties, as transmission mechanism through a continuous layer [13], role of concentric grooves flanking an aperture [14] and slit widths on transmission [15]. Diameters of focal spots in the far-field depend on the use of linearly [16,17] or radially polarized [12,18] illumination.

In this paper we deal with plasmonic nanolenses in the form of a single metal layer either grooved and continuous [19] or with slits. We analyse focusing properties of such lenses in the far-field rather than their abilities to confine the SPP wave. As a consequence, we do not achieve superresolution, what is possible in the near-field due to contribution of evanescent fields.

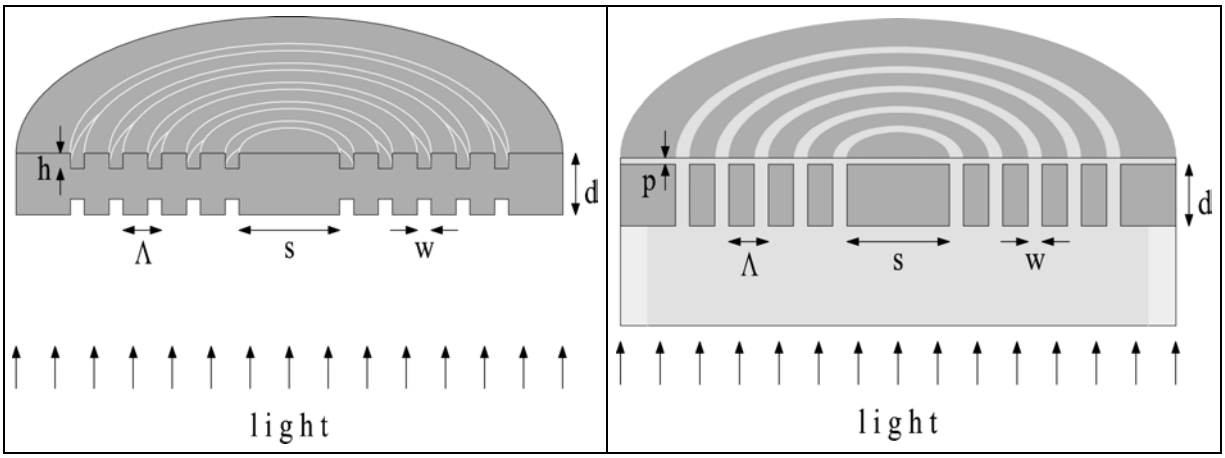


Figure 1. Schemes of a free-standing single Ag layer nanolens with double sided concentric grooves (left) and nanolens made of concentric silver rings and integrated with a silica fiber and cladding. Thickness of Ag layers is *d*, diameter of an on-axis stop is *s*, groove or slit lattice constant is Λ and groove or slit width is *w*. In a lens with grooves they are *h* deep, and in a lens with slits a dielectric cladding is *p* thick.

2. NANOLENSES AND SIMULATION TOOL

Figure 1 show schematic views of the two considered nanolenses. The left side shows a lens in the form of a free standing silver nanolayer with concentric corrugations on both surfaces and no hole at the optical axis [19]. On the right, a lens is composed of annular Ag rings and an on-axis stop which are integrated with an optical fiber and dielectric antioxidation cladding. A silver film of thickness *d* is deposited onto a flat end of a multimode silica fiber of core diameter $2r = 10$ μm with permittivity values $\varepsilon_c = 2.12$ and $\varepsilon_l = 2.11$ of core and cladding respectively. Periodic slits of width *w* and lattice constant Λ are filled with the same dielectric as that of the fiber core. Transmission of light through the lenses of both types is conditioned by efficient photon-plasmon and plasmon-photon coupling, where momentum matching is assured due to the groove/slit periodicity $\Lambda - w = 2\lambda_{SPP}$, where λ_{SPP} is the SPP wavelength. The grating coupling method makes use of the reciprocal vector of the grating $k_g = 2\pi/\Lambda$, which shifts the wavevector of impinging light to the value of the wavevector of the SPP wave k_{SPP}

$$k_{SPP} = k_0 n \sin\varphi + q k_g , \tag{1}$$

where k_0 is the wavevector in free space, φ is the angle of incidence, *n* is the refractive index of air (left side lens) or glass (right), and *q* is an integer.

Photon-plasmon momentum matching is efficient on the whole perimeters of grooves or slits due to radially polarized illumination with Laguerre-Gauss (LG) intensity profile [18,19]. The axis of symmetry of grooves and slits coincides with the optical axis of the incident LG beam with pure radial polarization and radial beam profile of electric field

$$E_r(r) = \left(\frac{r}{R}\right)\exp\left(-\frac{r^2}{2R^2}\right), \tag{2}$$

where *R* is a radius of maximum intensity. Matching the beam diameter with that of grooved or perforated areas maximizes efficient use of light energy, that is efficient photon-plasmon coupling on outer edges of grooves or slits. Each point of these edges on the backside of the lenses radiates spherical waves, which contribute to the focus.

Simulations are performed in cylindrical coordinates with the finite difference time domain (FDTD) method using freeware package Meep [20] and in-house body-of-revolution FDTD code [4,19]. Silver is modeled using Drude dispersion $\varepsilon(\omega) = \varepsilon_\infty - \omega_p^2 / [\omega(\omega + i\Gamma)]$ with the following parameters $\varepsilon_\infty = 3.70$, $\omega_p = 13673$ THz and $\Gamma =$ 27.35 THz [4,19,21]. We use a Cartesian grid of spatial discretization 2 nm. Transmission properties are analyzed for the following ranges of lens parameters: silver layer thickness *d* from 80 to 500 nm, slit width *w* from 20 to 400 nm, lattice constant Λ from 400 to 800 nm, and groove depth *h* from 10 to 40 nm. Other parameters are kept constant: the dielectric cladding thickness $p = 10$ nm, the fiber core radius $r = 5$ μm, and, dependent on *r*, the radius of maximum beam intensity $R = 1.7$ μm.

3. TRANSMISSION OF NANOLENSES

Figure 2 shows intensity distributions of plasmons generated on the backside of a grooved lens, shown with a solid line with squares, and the Fourier Transform (FT) of the structure geometry of exactly the same lens, shown with a dashed line, as a function of the plasmon and structure spatial frequency. According to Eq. 1, the frequency matching condition is, in our case of $\varphi = 0$, entirely dependent on the values of k_g provided by the profile of the lenses. Thus, relative intensities of generated SPP waves with spatial frequencies $k_{SPP}/2\pi$ are dependent on k_g and are the higher the greater is k_g intensity in FT of the lens profile. We theoretically predict, that incident light in the wavelength range λ of 400 to 800 nm couples most efficiently to SPP waves for $1/\lambda_{SPP} = 1.86\times10^6$ m^{-1} (what corresponds to $\lambda_0 \approx 560$ nm in free space) and $1/\lambda_{SPP} = 2.11\times10^6$ m^{-1} ($\lambda_0 \approx 500$ nm) and with smaller efficiency for spatial frequencies greater than 2.3×10^6 m^{-1}. This is confirmed by an analysis of SPP wave intensity on the backside of the lens, where we observe maxima at $1/\lambda_{SPP} = 1.75\times10^6$ m^{-1} ($\lambda_0 \approx 570$ nm) and $1/\lambda_{SPP} = 1.86\times10^6$ m^{-1} ($\lambda_0 \approx 500$ nm)

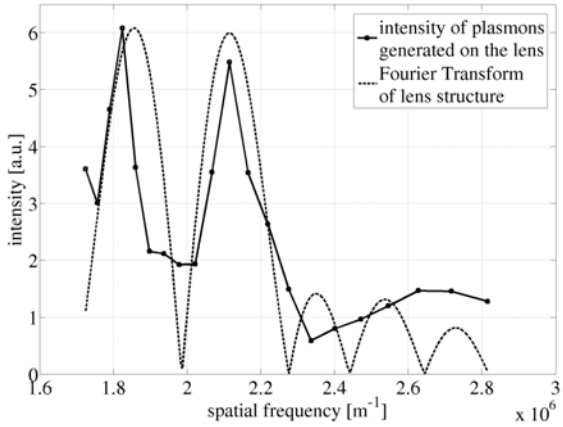


Figure 2. Intensity (in arbitrary units) of plasmons generated on the backside of a grooved lens (solid line with squares) and the FT of the structure of the same lens (dashed line) as a function of the plasmon and structure spatial frequency.

Once photons are coupled to plasmons on the input sides of the lenses different mechanisms govern transition of electron oscillations to the output sides, depending on whether grooves or slits are present. In the lens with double sided grooves transmission of light results from resonant tunneling via strongly localized surface plasmons in a manner recognized in an early paper of Tan *et al.* [22]. This coupling of plasmons from grooves on the incident surface to ones in grooves on the back surface is shown in Fig. 3a. Transmission through this

nanolens, based on resonant tunnelling, reaches 30%. In the case of a lens with slits, increased transmission results from coupling light directly to waveguided modes in the slits. It can be further enhanced by properly tuning the thickness of the metal film to exploit Fabry-Perot resonances of guided SPP modes in narrow channels [23,24], as seen in Fig. 3b. Transmission of light through the second nanolens, dependent on waveguided modes, approaches 80%.

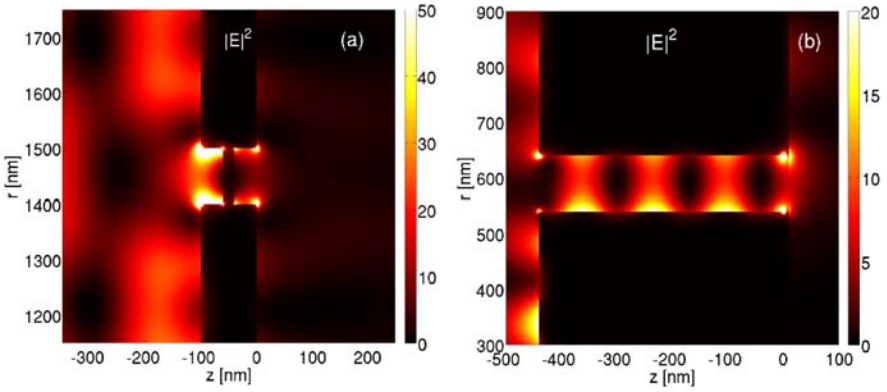


Figure 3. Electric energy density distributions in (a) grooves for wavelength $\lambda = 400$ nm and in (b) slits for $\lambda = 500$ nm. (a) Localized plasmons in grooves on the incident side couple via resonant tunneling to plasmons on the other side of metal links. (b) In slits energy is transported by waveguided SPP modes, which show Fabry-Perot resonances.

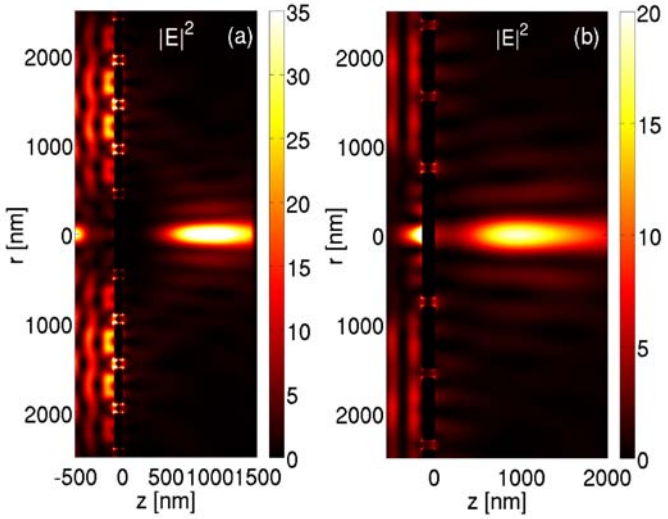


Figure 4. Electric energy density in the vicinity of simulated nanolenses (a) with grooves for wavelength $\lambda = 400$ nm and (b) with slits for $\lambda = 700$ nm.

4. FAR-FIELD FOCUSING PROPERTIES

A nanolens with double-sided grooves focuses propagating waves in the far-field as was shown in [19]. Here, we show that a similar process without contribution of evanescent fields is realized by means of a lens composed of multiple concentric annular rings with an on-axis stop. Both lenses are illuminated with radially polarized light and generate plasmons uniformly distributed along circumferences of grooves or slits. Deviations from axial symmetry of SPPs may only arise from fabrication inaccuracies [21]. Plasmons on the lenses backsides scatter at concentric edges. The fields originating at grooves or slits on the backside are of radiative nature and propagate

into the far-field, where they contribute to focusing in such a way, that the radial electric field component interferes destructively at the axis and its energy flows into the longitudinal component. Because this constructive interference takes place in the far-field, where evanescent components will have decayed, the transversal dimensions of the focal spots are limited by diffraction. In both cases the mechanism of focus formation is similar to that in classical refractive optics, though very different from that in diffractive optical elements. Foci formed by these lenses have FWHMs slightly bigger than 0.4λ and their focal lengths depend on the wavelength of incident light and range from one to a few λ. Both nanolenses focus LG beams as tightly as classical high-NA refractive optical systems. Figure 4 shows electric energy densities in focal regions of both lenses. A characteristic separation of foci from the metal surface can be seen, what is very different from plasmonic needles observed in other works [9,12].

5. CONCLUSIONS

A free standing 3D silver nanolens with concentric double-sided grooves and no hole on the optical axis is illuminated with a radially polarized visible range Laguerre-Gauss beam. The second nanolens is composed of annular Ag rings and an on-axis stop which are integrated with an optical fiber and a dielectric antioxidation cladding. Both lenses focus light in the far-field into spots of FWHM conforming to the diffraction limit. Their focal lengths depend on wavelength and range from one to a few λ. In both cases foci are formed in a similar way. Behind the lenses radial components of transmitted electric field scatter on backside edges of grooves or slits, propagate and interfere destructively on the axis. The longitudinal component of transmitted electric field, in turn, interferes constructively. Transmission through the continuous nanolens with grooves is based on resonant tunnelling and for resonant frequencies reaches 30%. Transmission of light through the nanolens composed of rings embedded in a dielectric matrix results from coupling light to waveguided modes in the slits and reaches 80%. Both nanolenses concentrate radially polarized LG illumination as tightly as classical high-NA refractive optical systems. The proposed nanolenses may be employed for nanolithography [25] and endoscopy.

ACKNOWLEDGEMENT

This work has been supported by the Polish Ministry of Science and Higher Education under the project N N507 445534 and the National Centre for R&D under the project N R15 0018 06. The authors are partners in COST Actions MP 0702 and MP 0803. Numerical computations were performed in the Interdisciplinary Centre for Mathematical and Computational Modelling (ICM), University of Warsaw, grant number G33-7.

REFERENCES

1. Kawata, S., Y. Inouye and P. Verma, "Plasmonics for near-field nano-imaging and superlensing," *Nature Photonics*, Vol. 3, 388–394, 2009.
2. Kotynski, R. and T. Stefaniuk, "Comparison of imaging with sub-wavelength resolution in the canalization and resonant tunnelling regimes," *J. Opt. A: Pure Appl. Opt*., Vol. 11, 015001, 2009.
3. Novotny, L. and B. Hecht, *Priciples of Nano-Optics*, Cambridge University Press, Cambridge, 2007.
4. Antosiewicz, T.J., P. Wróbel and T. Szoplik, "Nanofocusing of radially polarized light with dielectric-metal-dielectric probe," *Opt. Express*, Vol. 17, 9191–9196, 2009.
5. Pendry, J.B., "Negative refraction makes a perfect lens," *Phys. Rev. Lett*., Vol. 85, 3966–3969, 2000.
6. Melville, D.O.S., R.J. Blaikie and C.R. Wolf, "Submicron imaging with a planar silver lens," *Appl. Phys. Lett*., Vol. 84, 4403–4405, 2004.

7. Fang, N., H. Lee, C. Sun and X. Zhang, "Sub-diffractionlimited optical imaging with a silver superlens," *Science*, Vol. 308, 534–537, 2005.
8. Liu, Z., J.M. Steele, W. Srituravanich, Y. Pikus, C. Sun and X. Zhang, "Focusing Surface Plasmons with a Plasmonic Lens," *Nano Lett*., Vol. 5, 1726–1729, 2005.
9. Steele, J.M., Z. Liu, Y. Wang and X. Zhang, "Resonant and non-resonant generation and focusing of surface plasmons with circular gratings," *Opt. Express*, Vol. 14, 5664–5670, 2006.
10. Chang, C.-K., D.-Z. Lin, C.-S. Yeh, C.-K. Lee, Y.-C. Chang, M.-W. Lin, J.-T. Yeh and J.-M. Liu, "Experimental analysis of surface plasmon behavior in metallic circular slits," *Appl. Phys. Lett.*, Vol. 90, 061113, 2007.
11. Srituravanich, W., L. Pan, Y. Wang, C. Sun, D.B. Bogy and X. Zhang, "Flying plasmonic lens in the near field for high-speed nanolithography," *Nature Nanotechnology*, Vol. 3, No. 12, 733–737, 2008.
12. Chen Weibin, D.C. Abeysinghe, R.L. Nelson and Qiwen Zhan, "Plasmonic lens made of multiple concentric metallic rings under radially polarized illumination," *Nano Lett*., Vol. 9, No. 12, 4320–4325, 2009.
13. Bonod, N., S. Enoch, L. Li, E. Popov and M. Neviere, "Resonant optical transmission through thin metallic films with and without holes," *Opt. Express*, Vol. 11, 482–490, 2003.
14. Baida, F.I., D. Van Labeke and B. Guizal, "Enhanced Confined Light Transmission by Single Subwavelength Apertures in Metallic Films," *Appl. Opt*., Vol. 42, 6811–6815, 2003.
15. Shi Haofei, Changtao Wang, Chunlei Du, Xiangang Luo, Xiaochun Dong and Hongtao Gao, "Beam manipulating by metallic nano-slits with variant widths," *Opt. Express*, Vol. 13, 6815–6820, 2005.
16. Lin, D.-Z., C.-H. Chen, C.-K. Chang, T.-D. Cheng, C.-S. Yeh and C.-K. Lee, "Subwavelength nondiffraction beam generated by a plasmonic lens," *Appl. Phys. Lett*., Vol. 92, 233106, 2008.
17. Wang, J., J. Zhang, X. Wu, H. Luo and Q. Gong, "Subwavelength-resolved bidirectional imaging between two and three dimensions using a surface plasmon launching lens," *Appl. Phys. Lett*., Vol. 94, 081116, 2009.
18. Q. Zhan, "Cylindrical vector beams: from mathematical concepts to applications," *Adv. Opt. Photon*., Vol. 1, No. 1, 1–57, 2009.
19. Wróbel, P., J. Pniewski, T.J. Antosiewicz and T. Szoplik, "Focusing radially polarized light by concentrically corrugated silver film without a hole," *Phys. Rev. Lett.*, Vol. 102, 183902, 2009.
20. Farjadpour, A., D. Roundy, A. Rodriguez, M. Ibanescu, P. Bermel, J.D. Joannopoulos, S.G. Johnson, and G. Burr, "Improving accuracy by subpixel smoothing in FDTD," *Opt. Lett*., Vol. 31, 2972–2974, 2006.
21. Antosiewicz T.J. and T. Szoplik, "Description of near– and far–field light emitted from a metal–coated tapered fiber tip," *Opt. Express*, Vol. 15, 7845–7852, 2007.
22. Tan, W.C., T.W. Preist and R. J. Sambles, "Resonant tunneling of light through thin metal films via strongly localized surface plasmons," *Phys. Rev. B*, Vol. 62, No. 16, 11134–11138, 2000.
23. Porto, J.A., F.J. Garcia-Vidal and J.B. Pendry, "Transmission resonances on metallic gratings with very narrow slits," *Phys. Rev. Lett*., Vol. 83, 2845–2848, 1999.
24. Astilean, S., Ph. Lalanne and M. Palamaru, "Light transmission through metallic channels much smaller than the wavelength," *Opt. Commun*., Vol. 175, 265–273, 2000.
25. Wang, Y., W. Srituravanich, C. Sun and X. Zhang, "Plasmonic Nearfield Scanning Probe with High Transmission," *Nano Lett*., Vol. 8, 3041–3045, 2008.

Planar Wide-Band 2-D Isotropic Negative Refractive Index Metamaterial

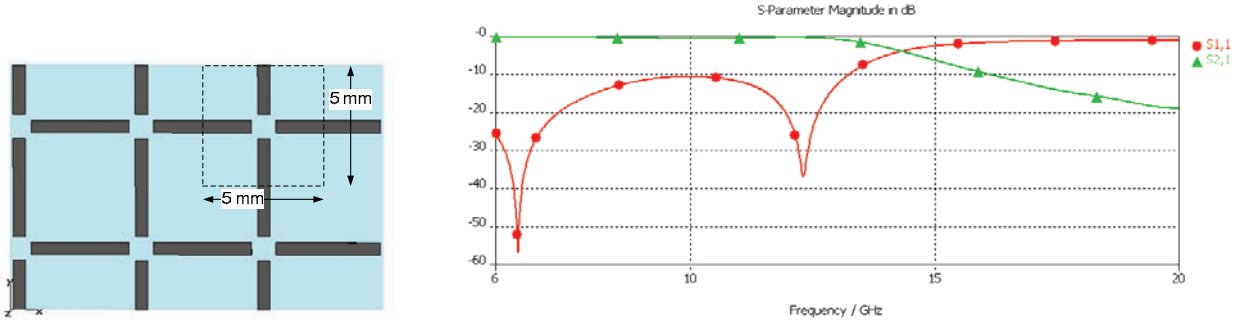
N. Amiri[1*], K. Forooraghi[1], and Z. Atlasbaf[1]

[1]Computer and Electrical Engineering Department, Tarbiat Modares University, Iran

[*]n_amiri@modares.ac.ir

Abstract- In this paper a novel left-handed metamaterial composed of only conducting strips is proposed. This symmetrical 2-D isotropic structure shows a controllable super-wide and very low-loss DNG band. The negative refraction index and other constitutive parameters are obtained by simulation and parameter retrieval algorithm and exhibit good impedance matching to free space.

The proposed Metamaterial is composed of periodic array of perpendicular strips, which is shown in Figure 1(a). All dimensions and substrate characteristics are displayed in the caption under Figure 1. Figure 1(b) shows the S-parameters obtained by simulating the structure in the commercial Software, CST Microwave Studio. Owing to the unit cell symmetry, such a metamaterial is responsive to any linearly polarized incident wave.



(a) (b)

Figure 1: (a) A layer of the proposed metamaterial; unit cell dimension is 5mm×5mm×2.762mm (as outlined by the square dashed line). The Thickness of the substrate is 0.762 mm with $\varepsilon_r = 3.5$ and $\tan\delta = 0.0018$. All the strips width is 0.5mm, while the gap width is 1mm, (b) Transmission and reflection coefficients versus frequency.

Figure 2 shows the real and imaginary parts of effective permittivity, permeability and refractive index, which shows more than 5.75GHz DNG pass band, with negligible loss.

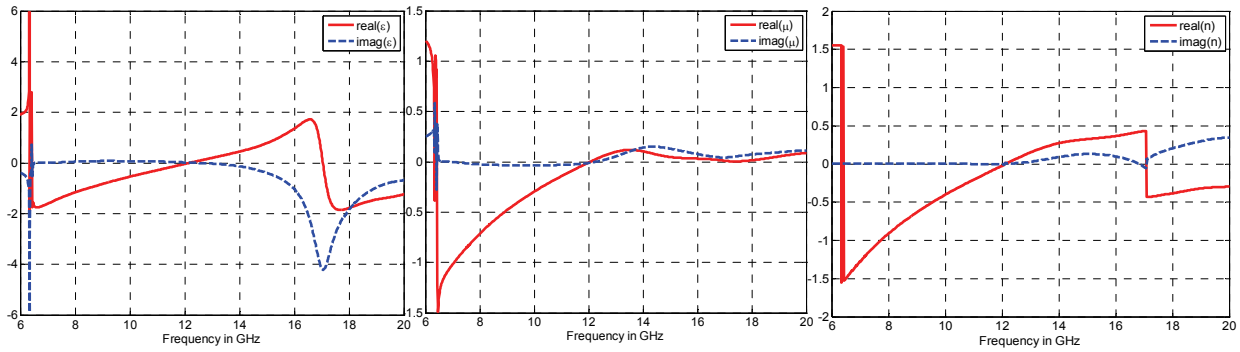


Figure 2: (a) Permittivity, (b) permeability and (c) index of refraction

REFERENCES

1. R. Marques, F. Medinaand, and R. Rafi-El-Idrissi, “Role of Bi-anisotropy in Negative Permeability and Left Handed Metamaterials,” *Phys. Rev. B.*, vol. 65, paper 144441, 2002.
2. S. Enoch, G. Tayeb, P. Sabouroux, N. Guerin and P. Vicent, “A Metamaterial for Directive Emission,” *Phys. Rev. Lett. 89*, 213902-1-213902-4, 2002
3. Z. Sheng, and V. V. Varadan, “Tuning the Effective Properties of Metamaterials by Changing the Substrate Properties,” *J. Appl. Phys.*, vol. 101, paper 014909, 2007.
4. X. Chen, T. M. Grzegorczyk, B. I. Wu, J. Pacheco, Jr. and J. A. Kong, “Robust method to retieve the constitutive effective parameters of metamaterials,” *Phys. Rev. E.*, vol. 70, paper 016608, 2004.

Excitation of Linear and Nonlinear Cavity Modes upon Interaction of Femtosecond Pulses with Arrays of Metallic Nanowires

C. G. Biris and N. C. Panoiu
Photonics Group, Department of Electronic and Electrical Engineering, University College London, Torrington Place, London WC1E 7JE, United Kingdom

Abstract— We investigate linear and nonlinear effects induced by the scattering of femtosecond optical pulses by two-dimensional distributions of metallic cylinders. In particular, by employing a numerical method based on the multiple scattering matrix algorithm, we demonstrate that, at both the fundamental frequency and the second-harmonic, such arrays of metallic nanowires support localized (cavity) surface plasmon-polariton modes with characteristic life-time ranging from a few femtoseconds to more than a hundred of femtoseconds.

1. INTRODUCTION

During the recent years we have witnessed a rapidly increasing research interest in an emerging class of electromagnetic materials, the so-called metamaterials. These developments have been made possible, in part, by significant advances in nanofabrication techniques, which now allows one to control at nanoscale the geometrical and material structure of nanomaterials. One prevalent idea that has emerged as a result of these technological developments is that, by carefully engineering the primary unit cell of a metamaterial, the effective optical properties of the material can be controlled and tuned as well. Specifically, unlike naturally occuring materials, for which the range of possible intrinsic configurations of the fundamental building blocks is rather limited and difficult to modify, a broad variety of artificial metamaterials with a wide spectrum of physical properties can be fabricated by simply tuning the geometry and material structure of the primary unit cell of the metamaterial. This approach has lead to the design and experimental demonstration of metamaterials with new and remarkable functionalities. In particular, magnetically active materials at terahertz and optical frequencies [1], materials with negative index of refraction [2, 3], and materials with low index of refraction [4, 5] have recently been demonstrated.

Subwavelength patterning of a metamaterial not only increases the potential for tailoring its linear physical properties but, equally important, could lead to a significant enhancement of nonlinear optical interactions [6]. In this connection, of particular importance are metamaterials based on metallic nanoparticles, as in this case the nonlinear optical interactions are further enhanced by the excitation of localized or propagating surface plasmon-polariton (SPP) modes. One immediate consequence of the resonant excitation of SPPs is that strong nonlinear optical effects can be achieved at a moderate optical power. Practical applications based on this effect include surface-enhanced Ramman scattering [7], enhanced second-harmonic generation (SHG) at metal/dielectric interfaces [8, 9], and subwavelength, optically active, guiding nanostructures [10].

In a recent theoretical study we have investigated the generation of the second-harmonic (SH) upon the scattering of monochromatic plane waves by distributions of metallic cylinders [11], the main conclusion of our study being that the optical response of the system of metallic cylinders is strongly influenced by the excitation of SPPs. In this paper we extend our analysis to the important case of the nonlinear optical interaction between ultrashort (femtosecond) optical pulses and arrays of metallic cylinders. The paper is organized as follows. In Sec. 2 we introduce the physical model and the mathematical formalism used in our analysis. Then, in Sec. 3, the main results of our study are presented and discussed. Finally, the main conclusions are summarized in Sec. 4.

2. THEORETICAL APPROACH

Our analysis of the scattering of femtosecond optical pulses by arrays of metallic cylinders relies on numerical simulations based on the multiple scattering method (MSM) [11, 12]. In our formalism the optical losses at the fundamental frequency (FF) are due to losses in the metallic cylinders

only, and therefore the energy transfer from the SH to the FF is neglected. Taking into account the reduced conversion efficiency of the SHG interaction, this undepleted pump approximation provides a reliable description of the temporal dynamics of the nonlinear scattering process. To this end, the time dependence of the electromagnetic field is determined in two steps. In a first phase, the incident pulse is Fourier transformed in the frequency domain and for each spectral component the field at both the FF and SH is determined by using the formalism introduced in [11]. Then, in the second stage, these spectra are Fourier transformed back in the time domain, and as such one obtains the complete temporal evolution of the fields at the FF and SH. Importantly, the numerical method developed in [11] allows for both the surface and bulk contributions to the nonlinear polarization to be taken into account. These two second-order nonlinear polarizations represent the sources of the optical field at the SH.

The nonlinear polarization that generates the field at the SH can be decomposed in a dipole-allowed surface component, whose support is the interface between the metallic cylinders and the background medium, and a bulk component, which is generated by the electric quadrupoles and magnetic dipoles inside the metal [13]. The surface polarization, $\mathbf{P}_s(\mathbf{r};2\omega)$, can be expressed as

$$\mathbf{P}_s(\mathbf{r};2\omega) = \epsilon_0 \hat{\chi}_s^{(2)} : \mathbf{E}(\mathbf{r};\omega)\mathbf{E}(\mathbf{r};\omega)\delta(\mathbf{r}-\mathbf{r}_s), \tag{1}$$

where $\hat{\chi}_s^{(2)}$ and $\mathbf{E}(\mathbf{r};\omega)$, are the surface second-order susceptibility tensor and the electric field at the FF, respectively. Furthermore, the bulk polarization, $\mathbf{P}_b(\mathbf{r};2\omega)$, is given by

$$\mathbf{P}_b(\mathbf{r};2\omega) = \alpha[\mathbf{E}(\omega)\cdot\nabla]\mathbf{E}(\omega) + \beta\mathbf{E}(\omega)[\nabla\cdot\mathbf{E}(\omega)] + \gamma\nabla[\mathbf{E}(\omega)\cdot\mathbf{E}(\omega)], \tag{2}$$

where α, β, and γ are material dependent parameters. In our numerical simulations we have considered arrays of Ag cylinders embedded in vacuum, the electric permittivity of the metallic cylinders being described by the Drude model

$$\epsilon(\omega) = \epsilon_0\left[1 - \frac{\omega_p^2}{\omega(\omega+i\nu)}\right]. \tag{3}$$

In this relation, ω_p and ν are the plasma and damping frequency, respectively. As specific values for these parameters we have chosen $\omega_p = 1.35\times10^{16}$ rad/s and $\nu = 2.73\times10^{13}$ s^{-1} [14]. In the case of nonlinear surface polarization tensor, we have used the values for Ag: $\hat{\chi}^{(2)}_{s,\perp\perp\perp} = 2.79\times10^{-18}$ m^2/V, $\hat{\chi}^{(2)}_{s,\|\|\perp} = \hat{\chi}^{(2)}_{s,\|\perp\|} = 3.98\times10^{-20}$ m^2/V, and $\hat{\chi}^{(2)}_{s,\perp\|\|} = 0$ [15]. It should be noted that due to the symmetry properties of the surface nonlinear susceptibility tensor, the SH is generated only if the incident field is TE polarized, namely, if the electric field of the incident plane wave is perpendicular onto the cylinders. Since in our previous work [11] we have demonstrated that the contribution of the surface nonlinear polarization is much larger than that of the bulk polarization, we will neglect in what follows the contribution of the latter component. Furthermore, for the values of the bulk polarization coefficients, we have employed the free electron model [16],

$$\alpha = 0, \quad \beta = \epsilon_0\frac{e}{2m_0\omega^2}, \quad \gamma = \frac{\beta}{4}[1-\epsilon_r(\omega)], \tag{4}$$

where m_0 is the mass of the electron and $\epsilon_r = \epsilon/\epsilon_0$ is the relative electric permittivity of the metal.

3. RESULTS AND DISCUSSION

As scattering geometries we consider two sets of metallic cylinders with radius $R = 1000$ nm, arranged so as to form a (plasmonic) cavity. Incident onto the set of cylinders is an optical pulse with a temporal full-width at half-maximum of 150 fs. This pulse can resonantly excite SPP modes on the surface of the cylinders, at both the FF and the SH. However, since these modes are tightly confined at the surface of the cylinders they are characterized by large optical losses, and consequently have a very short lifetime. In this work we demonstrate that a different type of SPP modes can be excited, namely, cavity SPP modes whose field is chiefly concentrated in the plasmonic cavity formed by the metallic cylinders. Since these SPP modes are trapped in the plasmonic cavity they are characterized by a large lifetime and, in addition, the scattering cross-section of the system does not have a spectral peak at the corresponding frequency. As expected, however, the absorption cross-section does have a spectral peak at the frequency of the cavity mode.

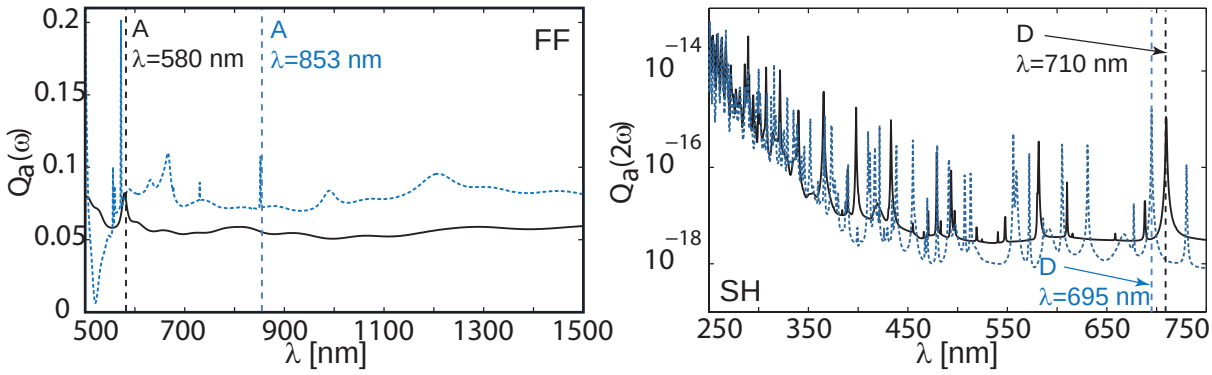


Figure 1: The absorption cross-sections spectra corresponding to a set of 4 (solid) and 6 (dashed) cylinders forming a plasmonic cavity. The radius of the cylinders is $R = 1000$ nm and the separation distance is $d = 100$ nm. Left and right panels correspond to the FF and SH, respectively.

Figure 1 shows the absorption cross-section spectra corresponding to the plasmonic cavities formed by a distribution of 4 and 6 metallic cylinders. Although there are some similarities between the two cases, Fig. 1 also illustrates some important differences. Thus, in both cases the absorption cross-section spectra present a series of peaks, at both the FF and the SH. The wavelength separation between the spectral peaks decreases with the wavelength, which is explained by the fact that at smaller wavelengths the incident field can penetrate more easily inside the plasmonic cavity. As expected, the hexagonal arrangement of metallic cylinders shows a higher absorption in almost the entire spectral domain considered, when compared to the square cavity, which is due to a larger area of contact between the electric field and the set of metallic cylinders. In addition, the more complex geometrical arrangement leads to a larger number of peaks in the absorption spectra corresponding to the hexagonal distribution of cylinders as compared to the square one. Furthermore, in both cases, towards the red side of the spectrum the absorption cross-section at the SH presents a series of strong resonances, which, as we will show, are not induced by a resonant enhancement of the field at the FF. More specifically, these SPP cavity modes are not excited directly by the incident optical pulse, but by the surface nonlinear polarization. Importantly, these cavity modes are observed for both distributions of metallic cylinders. A deeper insight into the physical properties of these SPP cavity modes can be gained by investigating their temporal dynamics, namely, their characteristic lifetime.

Figure 2 and Fig. 3 summarize our results pertaining to the field distribution of the SPP cavity modes associated to the square and hexagonal distributions of cylinders, respectively, as well as the temporal dynamics of these modes. Thus, as can be seen in panels A and B in Fig. 2 and Fig. 3, the resonances at lower wavelengths, in the spectra at the FF, correspond to the existence of "hot spots" in the spatial distribution of the electric field, which are excited in the vicinity of the metallic cylinders. As a consequence, this effect leads to a strong optical absorption. The temporal evolution of the field shows that these resonances have a very short lifetime, which is similar to that of SPPs excited on a single metallic cylinder. The corresponding lifetime, τ_r, can be determined by simply calculating the decay rate at large time of the intensity of the field,

$$|\mathbf{E}(t)| \sim |\mathbf{E}(t_0)| \exp\left(-\frac{t}{\tau_r}\right). \tag{5}$$

In the spectral region of longer wavelengths this physical picture changes significantly. The FF field still penetrates inside the cavity, but a large portion of it is scattered into the far field as radiation. The electric field at the SH, however, is almost entirely contained inside the plasmonic cavity and, in the case of the hexagonal cavity, most of it is concentrated away from the metallic interfaces. This spatial distribution of the electric field is directly related to the temporal characteristics of the scattering process. Thus, whereas the field at the FF shows an ultra-fast decay, the SPP cavity mode at the SH, in the case of the hexagonal cavity, has a lifetime as large as 120 fs. This behavior can be understood as follows. At large wavelengths the plasmonic cavity does not support cavity modes at the FF, and therefore the incident field is mostly scattered by the metallic cylinders. In turn, at the SH, such cavity modes do exist and are excited by the nonlinear surface

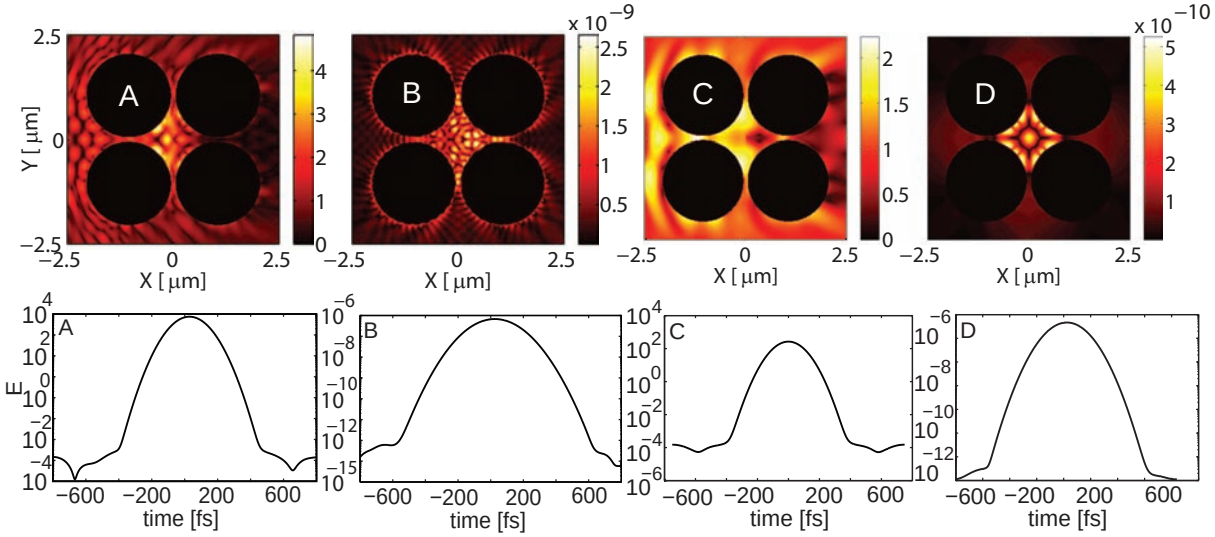


Figure 2: Top panels show the spatial profile of the amplitude of the electric field for the wavelength $\lambda = 580$ nm (A and B correspond to the FF and SH, respectively) and $\lambda = 1420$ nm (C and D correspond to the FF and SH, respectively). Bottom panels show field intensity *vs* time at a point near the center of the plasmonic cavity formed by the cylinders.

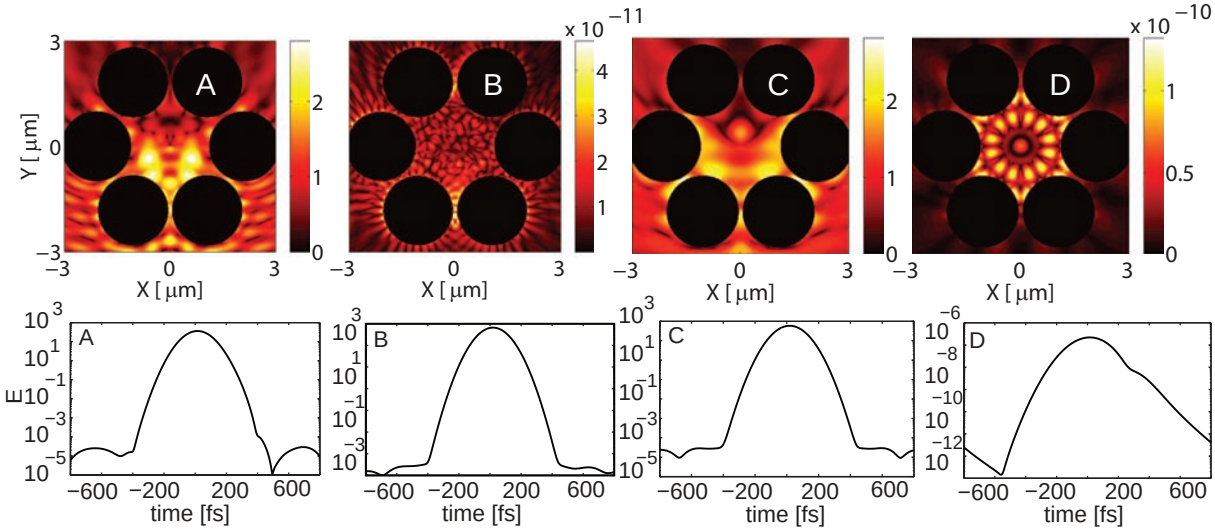


Figure 3: The same as in Fig. 2, but for a hexagonal arrangement of cylinders. The operating wavelengths are $\lambda = 853$ nm and $\lambda = 1391$ nm (A and B correspond to the FF and SH, respectively), (C and D correspond to the FF and SH, respectively).

polarization. Furthermore, the field profile at the SH, and consequently the corresponding lifetime of the mode, is determined by the shape of the plasmonic cavity. More specifically, whereas in the case of the square cavity the field is chiefly concentrated at the surface of the cylinders, in the case of the hexagonal cavity most of the field does not interact with the cylinders. As a result, the lifetime of the SPP mode of the hexagonal cavity is much larger than the lifetime of the mode excited in the square cavity. Thus, we can conclude that the shape of the actual structure has a strong influence on the physical properties of the SPP modes excited inside the plasmonic cavity.

4. CONCLUSION

We have employed the MSM formalism, a powerful and versatile numerical method, to study the temporal dynamics of SPP modes excited inside plasmonic cavities formed by metallic nanowires. As particular cases of such plasmonic cavities we have considered a set of metallic cylinders arranged

in a square and hexagonal necklace. The results of our study have shown that the nonlinear interaction between femtosecond optical pulses and the distribution of metallic cylinders can lead to the excitation at the SH of SPP cavity modes with lifetime of more than a hundred of femtoseconds. These results can advance our theoretical understanding of the physical properties of nonlinear plasmon resonances in metallic metamaterials, and spur future experimental investigations of these phenomenae.

ACKNOWLEDGMENT

The authors acknowledge the use of the UCL Legion High Performance Computing Facility, and associated support services, in the completion of this work. This work was supported by the UK Engineering and Physical Sciences Research Council (EPSRC), grant no. EP/G030502/1.

REFERENCES

1. Pendry, J. B., Holden, A. J., Robbins, D. J. and Stewart, W. J., "Magnetism from Conductors, and Enhanced Non-Linear Phenomena" *IEEE Trans. Microw. Theory Tech.*, Vol. 47, 2075, 1999.
2. Shelby, R. A., Smith, D. R. and Schultz, S., "Experimental Verification of a Negative Index of Refraction," *Science*, Vol. 292, No. 5514, 77–79, 2001.
3. Zhang, S., Fan, W., Panoiu, N. C., Malloy, K. J., Osgood, R. M. and Brueck, S. R. J., "Experimental Demonstration of Near-Infrared Negative-Index Metamaterials," *Phys. Rev. Lett.*, Vol. 95, No. 13, 137404–137408, 2005.
4. Panoiu, N. C., Osgood, R. M., Zhang, S. and Brueck, S. R. J., "Zero-$\bar{n}$ bandgap in photonic crystal superlattices," *J. Opt. Soc. Am. B* , Vol. 23, No. 3, 506–513, 2006.
5. Kocaman, S., R. Chatterjee, N. C. Panoiu, J. F. McMillan, M. B. Yu, R. M. Osgood, D. L. Kwong, and C. W. Wong, "Observation of Zeroth-Order Band Gaps in Negative-Refraction Photonic Crystal Superlattices at Near-Infrared Frequencies," *Phys. Rev. Lett.*, Vol. 102, 203905, 2009.
6. Soljacic, M. and Joannopoulos, J. D., "Enhancement of nonlinear effects using photonic crystals," *Nature Mat.*, Vol. 3, No. 4, 211-220, 2004.
7. Kneipp, K., Wang, Y., Kneipp, H., Perelman, L. T., Itzkan, I., Dasari, R. R. and Feld, M. S., "Single Molecule Detection Using Surface-Enhanced Raman Scattering (SERS)," *Phys. Rev. Lett.*, Vol. 78, No. 9, 1667–1670, 1997.
8. van Nieuwstadt, J. A. H., M. Sandtke, R. H. Harmsen, F. B. Segerink, J. C. Prangsma, S. Enoch, and L. Kuipers, "Strong Modification of the Nonlinear Optical Response of Metallic Subwavelength Hole Arrays," *Phys. Rev. Lett.*, Vol. 97, 146102, 2006.
9. Cao, L., N. C. Panoiu, R. D. R. Bhat, and R. M. Osgood, "Surface second-harmonic generation from scattering of surface plasmon polaritons from radially symmetric nanostructures," *Phys. Rev. B*, Vol. 79, 235416, 2009.
10. Panoiu, N. C. and Osgood, R. M., "Subwavelength nonlinear plasmonic nanowire," *Nano Lett.*, Vol. 4, No. 12, 2427–2430, 2004.
11. Biris, C. G. and Panoiu, N. C., "Second Harmonic Generation in Metamaterials based on Centrosymmetric Nanowires," *Phys. Rev. B.*, (submitted).
12. Centeno, E. and Felbacq, D., "Second-harmonic emission in two-dimensional photonic crystals," *J. Opt. Soc. Am. B*, Vol. 23, No. 10, 2257–2264, 2006.
13. Heinz, T. F., "Second-order nonlinear optical effects at surfaces and interfaces" in *Nonlinear Surface Electromagnetic Phenomena,* edited by H. E. Ponath and G. I. Stegeman, Elsevier, Amsterdam, 1991.
14. Ordal, M. A., Bell, R. J.,Alexander, R. W., Long, L. L. and Querry, M. R., "Optical properties of fourteen metals in the infrared and far infrared: Al, Co, Cu, Au, Fe, Pb, Mo, Ni, Pd, Pt, Ag, Ti, V, and W.," *Appl. Opt.*, Vol. 24, No. 24, 4493–4499, 1985.
15. Krause, D., Teplin, C. W. and Rogers, C. T., "Optical surface second harmonic measurements of isotropic thin-film metals: Gold, silver, copper, aluminum, and tantalum," *J. Appl. Phys.*, Vol. 96, No. 7, 3636–3634, 2004.
16. Valencia, C. I., Mendez, R. E. and Mendoza, B. S., "Second-harmonic generation in the scattering of light by an infinite cylinder," *J. Opt. Soc. Am. B*, Vol. 21, No. 1, 36–44, 2004.

Hybrid biosignal-based filters for metamaterials spectral analysis

I. Sliesoraityte[1*], E. E. Fedorov[2], R. Dubakiene[1], and V. Sliesoraitiene[3]
[1]Interfaculty Drug Synthesis and Research, Vilnius University, Lithuania
[2]Dedicated Computer System Department, Donetsk Academy of Automobile Transport, Ukraine
[3]Department of biomechanics, Vilnius Gediminas Technical University, Lithuania
[*]corresponding author: sliesoraityte@yahoo.com

Abstract- In this report we will review our recent results on experimental development of hybrid biosignal-based filters used for metamaterials spectral analysis. We have simulated the signal spectrum and computed significant features. It is shown that hybrid biosignal-based filters may be effective in reducing the scattering from acoustic objects and might be applied for signals connected to various frequency bands and in different data domains spectral analysis.

1. INTRODUCTION

Any obtained signal comprises noise waves, which are connected with both the object of interest and hardware properties. Noisy signal proved to be more difficult to analyze, likewise signal comparison to the standard is challenging. Existing methods for signal denoising, when processing the signals received by means of metamaterials requires preliminary noise training, filter sequencing input, smoothing a spectrum [1, 2]. Analogue filters might be applied at the first stage of processing of a signal for the extraction of a range of frequencies associated with particular object [2, 3]. Although, the lack of filters designed for metamaterials, confirms that to date the analysis of a signal is intended only for extraction of certain band of a spectrum of a signal rather than full signal analysis. The presented biosignal-based method allows selecting the significant features of a metamaterials transformed signal, and makes a decision on a significance of maxima of a signal.

2. HYBRID BIOSIGNAL-BASED METHOD

The offered method is based on a biosignal based routine, which suppresses insignificant features and extracts significant in the absence of the aprioristic information on the signal form. The significant features are maxima which exceeds adaptive threshold ε for metamaterials. The biosignal-based filters allows selecting the significant features of metamaterials transformed signal, and makes a decision on a significance of maxima by comparing maximum of a signal to the one before the transformation. The average distance δ_1 between maxima in the source and received signal was determined. It was assumed that, if δ_1 is significant, the signal form has changed adversely - fluctuations in a signal are strongly displaced:

$$\delta_1 = \frac{1}{CountMaxDest} \sum_{j=1}^{CountMaxDest} \min_{i \in 1, CountMaxSource} | PosMaxSource_i - PosMaxDest_j |. \quad (1)$$

The distance δ_2 between number of frequencies in last significant maximum in a spectrum and quantity of maxima in the received signal was assessed. It was assumed that, if δ_2 is significant, the received signal has deteriorated, as became less periodic:

$$\delta_2 = | PosMax_{CountMax} - CountMaxDest | . \quad (2)$$

Hybrid biosignal-based filters assume the parametric identification, which utilizes significant maximum of a signal spectrum:

$$x_{\mathrm{mod}}(n) = A_0 + \sum_{i=1}^{CountMax} A_i \sin(\varphi_i + \omega_i n), \quad n \in \overline{0, N-1}. \quad (3)$$

Where A_0- displacement, A_i- amplitude, φ_i- phase, ω_i- frequency, I - quantity of significant maxima.

3. SIGNAL FILTRATION ON A BASIS OF METAMATERIALS SPECTRAL ANALYSIS

Filtration of a signal derived from metamaterials spectral analysis was carried out, which allowed suppression the noise component of a signal and allocation of significant maxima of a signal spectrum (fig. 1).

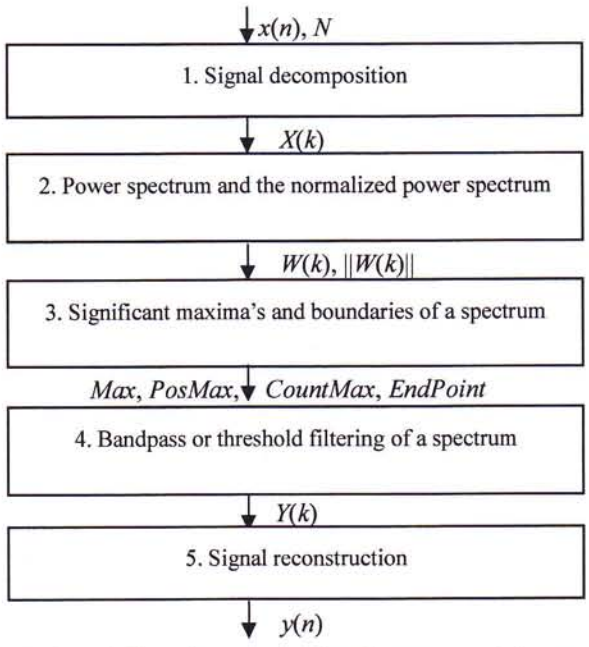


Figure 1. Signal filtration on a basis of metamaterials spectral analysis.

Signal decomposition was followed using direct discrete Fourier transform [4-6]. A power spectrum and the normalized power spectrum were calculated.

Adaptive threshold ε for allocation of significant maxima were defined:

$$\| W(k) \| = \frac{| X(k) |^2}{\sum_{k=0}^{N/2-1} | X(k) |^2}, \quad k \in \overline{0, N/2-1} \tag{4}$$

It was assumed that significant maxima's of power spectrum exceed adaptive threshold ε. Threshold ε depends on the value of the maximum maxima (global maxima) in normalized power spectrum, i.e. if this value is significant ε is greater, if this value is small ε is lesser. Threshold ε cannot exceed the maximum maxima. Thus, we select only those maxima's (local maxima's), which have the greatest contribution to a spectrum. Threshold ε is considered adaptive, as it is set under the maximum maxima (global maxima) in the normalized power spectrum of a particular signal. Moreover, the value of a signal should not be defined by multiplying threshold, since only significant maxima's are present:

$$Y(k) = \begin{cases} X(k), & k \in \{PosMax_i\} \vee (N-k) \in \{PosMax_i\} \\ 0, & else \end{cases}, \quad k \in \overline{0, N-1}, \quad i \in \overline{1, CountMax}. \tag{5}$$

Where $Y(k)$ - filtered spectrum. Consequently, signal reconstruction using inverse discrete Fourier transform was performed.

4. EMPIRICAL REALIZATION OF BIOSIGNAL-BASED METHOD

Hybrid biosignal-based filters were realized for 1000 simulations using the experimental results of signal from inner retinal functional output and the probability of the correct analysis was of 0.99 comparing experimental and simulated results.

In figure 2 the filtered signal in time frame is presented, which was obtained using a technique of a threshold filtration of a signal on the basis of discrete Fourier transform and metamaterials spectral analysis.

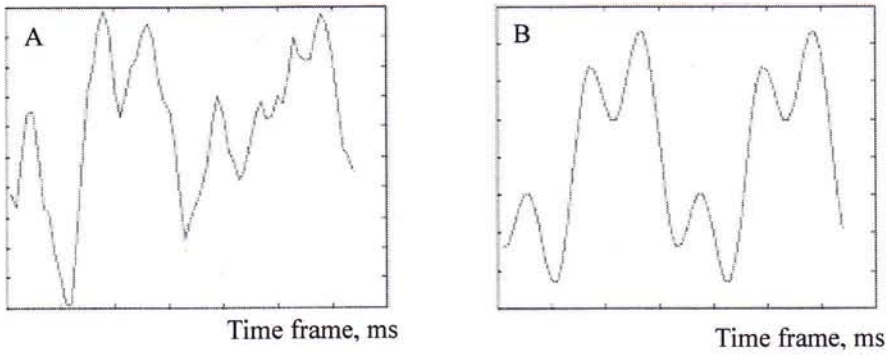


Figure 2. Realization of biosignal-based method (A-source signal, B-filtered signal).

Six maxima were used for particular signal extraction. $PosMaxSource = (6,17,27,38,49,59)$ applied and

distances $\delta_1 = 1$, $\delta_2 = 0$ were calculated. Condition $\delta_1 \leq \varepsilon_1 \wedge \delta_2 \leq \varepsilon_2$ was carried out. Technique includes all significant maxima and the analogue filter based on metamaterials approach for processing of the signal, was utilized.

4. CONCLUSIONS

In conclusion, we present numerical simulations and experimental measurements of the hybrid biosignal-based filters, with particular emphasis on their application for metamaterials-based hardware spectral mode analysis. The technique is applicable for allocation the precise significant maxima of a signal for an investigated object and could be applied, when characteristics of noise and the demanded form of a signal are not known or not clear priori. Thus, the hybrid biosignal-based filters may be effective in reducing the scattering from acoustic objects and might be applied for signals connected to various frequency bands and in different data domains spectral analysis.

REFERENCES

1. Al-Naib, I. A. I., Jansen, C. and M. Koch, "Miniaturized bandpass filter based on metamaterial resonators: a conceptual study," *J. Phys. D: Appl. Phys.*, Vol.41, No 20, 2008.
2. Vinogradov, A.P., Burokur, N., and S. Zouhdi, "Effective parameters of metal-dielectric composites. Influence of eddy currents due to density fluctuations," *Eur. Phys. J. Appl. Phys*, 46, 32604, 2009.
3. Jiusheng, L. and D. Tieying, "Application of metamaterial unit cell in bandpass filter," *Microwave and Optical Technology Letters*, Vol. 49, No 9, 2109 – 2111, 2007.
4. Doyle, M., Chapman, B.L.W., Blackwell, G.., Walsh, E.G., and G..M. Pohost, "Adaptive Fourier threshold filtering: A method to reduce noise and incoherent artifacts in high resolution cardiac images," *Magnetic Resonance in Medicine*, Vol. 31, No 5, 546–550, 1994.
5. Fedorov, E.E., *Models and methods transform speech signals*, Nord-Press, Donetsk, 2006.
6. Timar, A. and M. Rencz, "Design issues of a low frequency low-pass filter for medical applications using CMOS technology," *IEEE Design and Diagnostics of Electronic Circuits and Systems*, 325-328, 2007.

Fabrication and characterization of membranes for extraordinary optical transmission

G. Zacco[1,2,3], T. Ongarello [1,3], D. Garoli [*1,2,3,4], P. Zilio [1,3], M.Massari [1,3], H. Kang [5], M.Tormen [2] and F. Romanato [1,2,3]

1 Physical Department "G.Galilei", University of Padova

2 TASC Natl. Lab. CNR-INFM, Trieste, Italy

3 LANN Laboratory for Nanofabrication of Nanodevices , Corso Stati Uniti 4, Padova, Italy

4 CNR-ICIS Corso Stati Uniti 4, Padova, Italy

5 School of Materials Science and Engineering, Nanyang Technological University, Singapore

garoli@pd.infn.it

Abstract- 1D nano-slits arrays that show extraordinary transmission of light have been fabricated on silicon nitride membranes by means of 30keV electron beam lithography process and gold electroplating. The electrolytic growth method is a simple and economical technique that allows a careful control of the thickness and high fidelity reproducibility of the lithographic pattern. Optical characterization techniques have been used to characterize the transmission spectra both at near field and far field. We discuss the correlation between the far field and near field optical distribution as a function of the polarization of light. Experimental results have been compared with numerical simulation in order to elucidate the different modes of propagation light in the nano-slits.

1. INTRODUCTION

The transmission of light through sub wavelength holes of dielectric materials is governed by diffraction that strongly affects both the total intensity and power angular distribution. The radiation transmittance dramatically changes when sub wavelength holes or linear grids are periodically organized on noble metallic film. In this case an unusual high transmission spectra can be observed. This phenomenon had been reported for the first time in 1998 by Ebbesen et Al. [1] who called it: Extraordinary Optical Transmission (EOT). Several following works [2-4] have clearly shown the crucial role the Surface Plasmon Polaritons (SPP) play in EOT. The transmission of TM polarized light through subwavelength straights slit apertures has been studied by Pang et al. [4]. They have shown that the EOT resonances strongly depends on the geometry of the hole arrays (as length, depth, period and number of slits) and on the propagation of SPP on their patterned surface. Also light polarization plays an important role as shown by Crouse et al. [5] that have reported the case of TE polarized incident light. In this case no extended SPP resonances can be excited and EOT can arise from the presence of cavity modes inside the slits. Several other studies have investigated and have elucidated the microscopic mechanisms of the light propagation [6].

What is not still clear in literature is the correlation between the far field and near field features of the electromagnetic wave propagation. The aim of this paper is to give an example of complete correlation, both experimental and simulation, description, microscopic (at near filed) and macroscopic (transmittance) view of the EOT. We compare simulated and experimental data for both TE and TM polarizations of light illuminating

the simplified and emblematic structure of the 1D periodic metallic grating. We will revise the different propagation modes generating EOT and correlate their presence to features of the transmission spectra. The simulations have been performed by using Finite Elements Method (FEM) [7]. This method allows to point out the role of the different plasmonic resonances in influencing the transmission properties of the grating. Moreover FEM permits a realistic simulation of both near field experimental data, obtained respectively by Scanning Near field optical Microscopy (SNOM) technique, and reflectivity.

In this paper we want also to present our fabrication procedure for the realization of plasmonic nanopatterned 1D arrays. As reported in literature, different techniques have been used [8,9] for patterned devices realization. The most used technique is Focused Ion Beam (FIB) that directly etches the trenches in a noble metallic film. FIB allows a great control of the patterning but it has an extremely low throughput. The other most used technique, Electron Beam Lithography (EBL) [4,6], it is always combined with complex lithographic processes (dry etching, evaporation and liftoff). In this work, EBL is used in combination with electrolytic growth for the fabrication of gold rod arrays on thin Si_3N_4 membranes. Electroplating growth technique allows to obtain high quality structures with good vertical walls regardless of the pattern aspect ratio. Silicon nitride membranes are thin and transparent in the Vis/NIR that perfectly match the requirements for a precise SNOM and transmittance optical characterization.

2. EXPERIMENTAL METHODS

The fabrication of EOT membranes requires few step of process: electron-beam lithography; electrolytic growth, wet and dry etching. A schematic illustration of the process is reported in Fig. 1. A 1mmx1mm large Si_3N_4 membrane has been fabricated starting from a double-polished Si(100) wafer, where a 100 nm thick Si_3N_4 low-stress layer had been previously deposited on both sides. The optical window has been obtained by (dry) etching of on the back side Si_3N_4 film and wet etching (in hot KOH) of the silicon substrate down to the other side Si_3N_4 film. As plating base electrode for the electolytical growth a chromium/gold bilayer (10nm/20nm thick) has been deposited on the nitride layer by e-beam evaporation.

The nanopatterns have been fabricated by Electron Beam Lithography (EBL) technique using a ZEISS 1540XB Cross-Beam equipped with RAITH ELPHY nanolithography system using 30keV of accelerating voltage and a beam probe current of 140pA. A 950 kDa average molecular weight poly(methyl-metacrylate) (PMMA) resist had been spun on the substrate with a thickness of 450 nm. After the spin coating, the resist has been soft baked at 180 °C on a hot plate for 15 min. A dose of 390 $\mu C/cm^2$ has been used during the exposure. In order to maximize the aspect ratio, the whole membrane area has been patterned employing a multi-field writing strategy which avoids uncovered transparent borders. Careful field calibration minimized alignment and stitching errors between fields.

After the exposure, a methyl-isobutyl-ketone (MIBK) solution diluted with isopropyl-alcohol (IPA) (volume ratio: MIBK:IPA=1:3) had been used for the resist development (1 min at room temperature). After the development the resist has been rinsed in pure IPA. Gold electroplating has been realized on the developed substrate. The electrolytic bath is a commercial solution from ?? [ritrovare il nome della ditta]. For an optimal film growth quality the following condition have been used: the solution Ph was 4.35, at a temperature of 36 (°C), with a density of gold salts 9.4 (gr/l). The growth has been carried on at a current density of 1 (mA/cm^2) and a growth rate of 10nm/sec. After growth, the remaining resist has been stripped in hot acetone and the base plating layer on Si_3N_4 (Cr/Au bilayer) has to be removed. A two step etching process has been followed: firstly the Au layer had been removed by Ar dry etching and then the Cr layer has been removed by wet etching

solution based on NaOH and $K_3Fe(CN)_6$ and H_2O.

Following these procedure different types of 1D slits gratings patterns have been realized. In this paper we will focus our analyses on the sample reported in figure 2. The structure has a period of 500 nm with a slit apertures of 250nm. The thickness of the gold walls is 370nm.

3. RESULT AND DISCUSSION

Experimental far field analyses are based on transmission measurements. They have been performed by using a J.A.Woollam Co. variable angle spectroscopic ellipsometer (VASE). The equipment is capable of taking measurements over a wide spectral range from 193nm up to 2200nm and its variable wavelength and polarization angle of incidence light allow flexible measurements. In particular, our measurements have been performed at normal incidence, and the polarization angle has been varied from 0° (tangential component of electric filed perpendicular to the slits axis - TM) to 90° (tangential component of electric filed parallel to slits axis - TE).

In figure 3 transmission spectra for the 1D array of gold slits illustrated in figure 2 is reported. As can be easily observed in fig.3a, for the s-polarization (TE) a resonant peak is present around 500nm while, as illustrated in fig.3b, for the p-polarization (TM), a positive trend in the transmittance spectra is evident starting from 520nm and a peak is present at 1000nm. These resonance peals can be explained by two kinds of plasmonic resonances [5,6,10]. The first one arises from the coupling of the incident EM field with a periodic metal structure and it leads to high near field enhancements and to a strong transmission extinction. The second one is a cavity mode resonance which takes place within the slits and it is responsible for the enhanced transmission. The spectrum behavior trend actually can be explained in terms of multiple scattering of overlapping surface plasmons on the vertical walls of the slits. These two type of resonances inside the slits have been also analyzed in term of electric and magnetic field norm as illustrated in figure 4.

For TM polarization both the two known type of resonances are evident [6]. The SPP resonance is characterized by high EM field enhancement in proximity of the grating (fig.4a). In correspondence of this SPP resonance a minimum of transmittance is usually observed. Cavity mode resonance at 1000nm is responsible for the high optical transmittance and field concentration inside the slits (fig.4b). The resonance peak at 530nm observed with the TE polarization is representative of a type of resonance different from the classic surface plasmon polariton (SPP) one. As referred by Crouse et al. [5], this kind of resonance does not involve SPP excitation directly, but it is related to excitation of cavity modes inside the slits.

Experimental near field analyses have been performed by using Near field Scanning Optical Microscopy (SNOM). SNOM analyses have been performed on the sample in order to collect the spatial intensity profile of the light emitted from the slits. Figure 5a reports the light intensity as function of the direction along the grating (periodicity direction) for our 1D grating. The measurements have been collected by using unpolarized light at a distance of few tens of nanometers from the sample.

As can be seen, two types of peaks are present. The more intense peaks appear to be coherent to the grating's period and correspond to the SPP excited on the top of the grating gold ridges (Fig. 4a). The less intense peaks are present between major peaks. In the near field regime, the small peak corresponds to the cavity modes excited inside the slits, which is related to the excitation of the evanescent waveguide modes (Fig. 4c). This interpretation is further confirmed by a topographic image of the grating (figure 5b). Also in this picture the more intense areas correspond to the gold ridges in perfect correlation with the morphologic AFM image providing a direct vision of the SPP excitation. The less intense area corresponds, on the contrary, to the light

passing directly through the slits. A FEM simulation of the SNOM image has been also performed in figure 6. The experimental results are in fairly good agreement with the FEM simulated data. This result confirms that using unpolarized light both the two the SPP and cavity modes resonances. can be excited at the same time reinforcing the far field EOT.

4. CONCLUSIONS

Gratings allowing EOT effect have been fabricated with EBL process on Si3N4 thin membranes. After the EBL exposure, structures have been grown by a proper gold electroplating process. Wet etching process have also been developed in order to remove the base plating metallic film used as electrode during the electrolytic growth. Numerical simulations and optical characterization techniques allow us to measure transmittance spectra and validate our fabrication results. A EOT transmittance has been measured, but probably the presence of residual base plate affects the efficiency of the structure.

Experimental data show interesting results on TE polarization transmittance spectra. In fact, a resonance peak has been observed. It is not directly related to the SPP excitation, but it is related to cavity modes inside the slits of the structure. This give an experimental confirmation of numerical predictions reported in literature [5]. SNOM data shows two types of peaks. The more intense corresponds directly to the SPP excited on the gold ridges of the grating confirming the active role played by SPP on EOT process. The weaker peak corresponds to light directly scattered inside the slits, which is related to the excitation of the cavity modes inside the slits.

REFERENCES

1. Ebbesen T. W., Lezec H. J., Ghaemi H. F., Thio T., and Wolff P. A., *Nature* **391**, 667 (1998).
2. Genet C. and Ebbesen T. W., *Nature*, **445**, 39 (2007).
3. Busch K., Von Freymann G., Linden S., Mingaleev S. F., Tkeshelashvili L., Wegener M., *Phys. Reports*, **444**, 101 (2007).
4. Pang Y., Genet C., Ebbesen T. W., *Optics Communications*, **280**, 10 (2007).
5. Crouse D., Keshavareddy P., *Opt. Exp.* **15**, 4, pp.1415 (2007).
6. Lalanne P., Hugonin J.P.,, Rodier J.C., Phys. Rev. Lett.,95 , 263902, (2005)14 Liu H., Lalanne P., *Nature* **452**, 728 (2008)
7. Finite Elements Frequency Domain code COMSOL Multiphysics
8. Ghaemi H.F., Tineke Thio, Grupp D.E., Ebbesen T.W., and Lezec H.J.. *Phys. Rev. B*, **58** (11) 6779 (1998).
9. Degiron A., Lezec H., Yamamoto N., and Ebbesen T., *Optics Communications* **239**, 61 (2004).
10. Collin S., Pardo F., Teissier R., and Pelouard J. L., *Phys. Rev. B*, **63**, 033107 (2001).

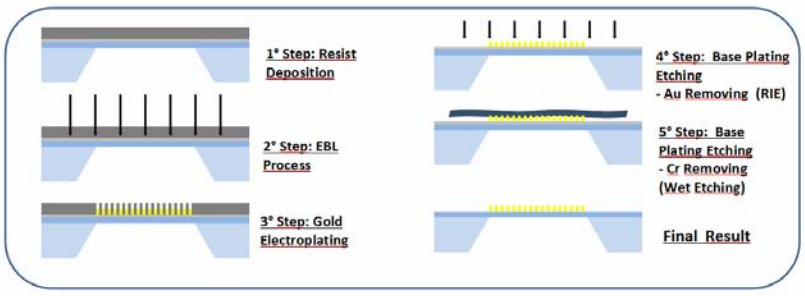


Figure 1. Steps of the nanofabrication process.

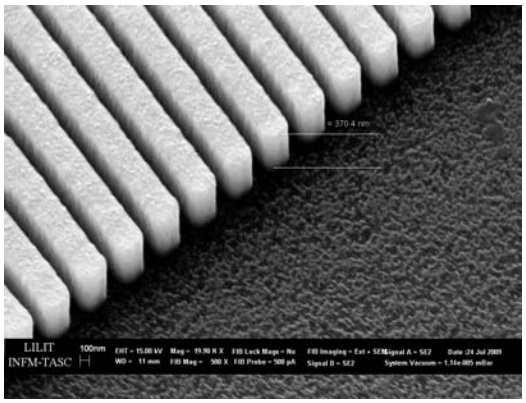


Figure 2. Linear 1D array patterned on silicon nitride membranes.

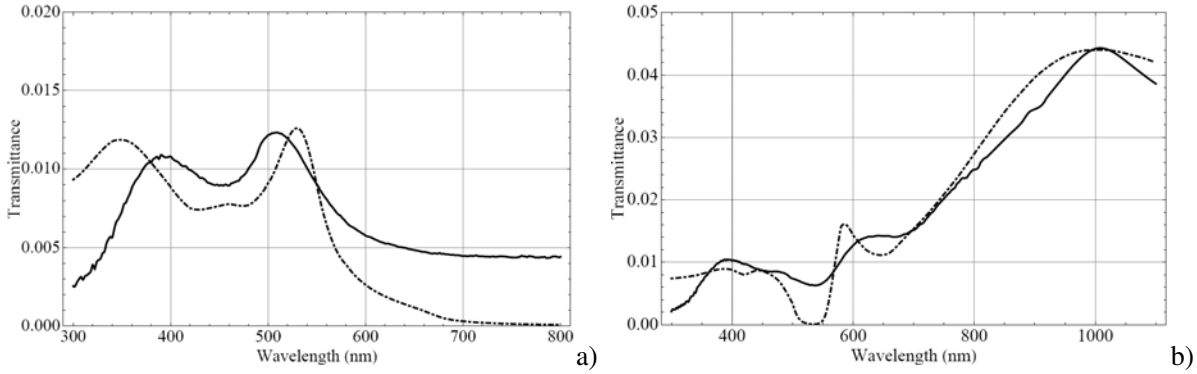


Figure 3. Transmission spectra for 1D array of the gold slits. Dashed line corresponds to FEM simulation data. Continuous line refers to experimental data. Figure a) refers to TE polarization; Figure b) refers to TM polarization

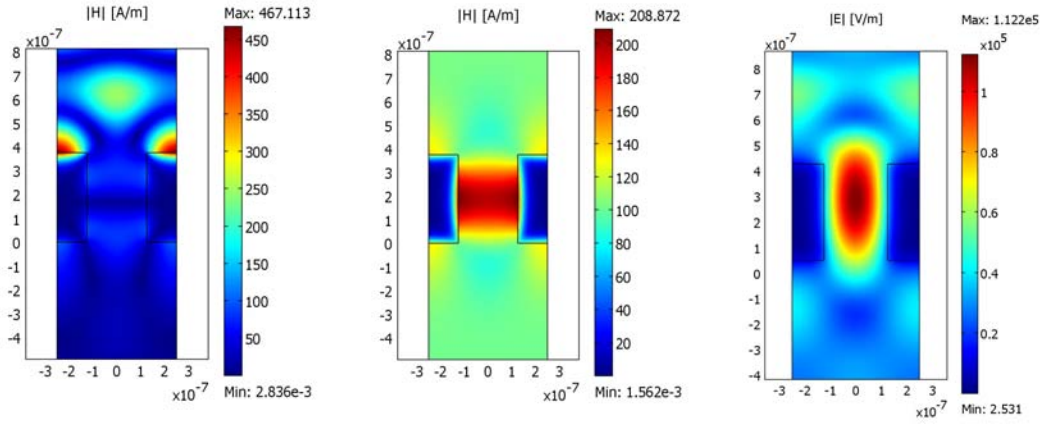


Figure 4. a) TM magnetic field norm at the SPP resonance (corresponding to the wavelength 530nm); b) TM

magnetic field norm at the cavity mode resonance (corresponding to the wavelength 1000nm) c) TE electric field norm at the cavity mode resonance (corresponding to the wavelength 530nm);.

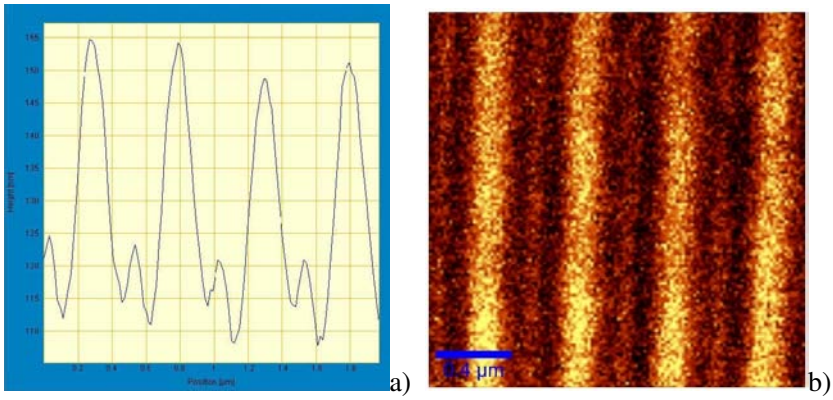


Figure 5. a) SNOM intensity profile of 1D gold slits grating; b) SNOM topographical image of 1D gold slits grating.

The major peaks and the brighter areas corresponds to SPP excitations on the gold ridges of the array while the small peaks and darker areas correspond to the light directly scattered inside the slits.

.

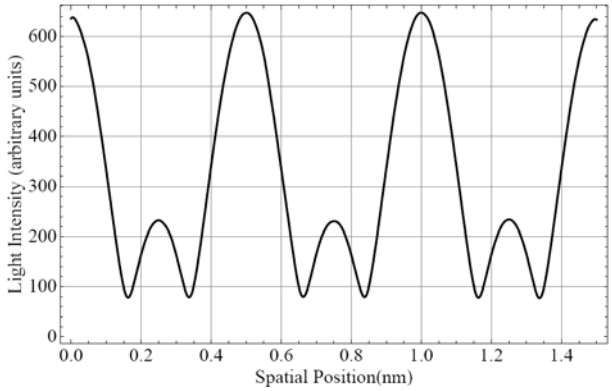


Figure 6. FEM simulation of SNOM light intensity profile.

Microwave Metamaterials With Ferromagnetic Microwires

L. V. Panina[1,2], M. Ipatov[2], V. Zhukova[2], J. Gonzalez[2] and A. Zhukov[2]

[1]School of Comp., Comm. and Electr., Univ. of Plymouth, Drake Circus, PL4 AA, Plymouth, UK

[2]Dpto. de Física de Materiales, Fac. Químicas, UPV/EHU San Sebastián 20009, Spain

lpanina@plymouth.ac.uk

Abstract- This paper discusses a new type of wire media based on amorphous ferromagnetic microwires. The combination of two effects, namely, a strong dispersion of the effective permittivity in metallic wire composites (resonance or plasmonic type) and giant magnetoimpedance effect in wires will result in unusual property that an effective dielectric response may strongly depend on the wire magnetization which can be changed with external stimuli: magnetic field, mechanical stress and temperature.

1. INTRODUCTION

Artificially structured electromagnetic materials (often referred to as metamaterials) can be designed to have specific dispersion properties. In particularly, the effective permittivity of composites with diluted arrays of conducting wires show a plasma or resonance like spectra, producing a highly frequency selective (band-gap or bandpass) propagation regime [1-4]. In thin wires the currents are constrained with the associated resonances determined by the geometrical parameters. Thus, lattices of wires with a diameter of few microns spaced 1 cm apart have a characteristic plasma frequency of about 4 GHz. This differs greatly from natural dielectrics, where the charge oscillation resonances become important only at optical frequencies. The dispersion properties of wire media were used in such applications as beam shaping systems and broadband absorption systems. Recently the wire composites gained much attention as systems with negative real part of the effective permittivity to constitute the materials with left-handed properties [5]. Recently the concept of wire media as actively tunable dielectrics has been put forward, in which the effective permittivity depends on the local magnetic properties of constituent wires [6-9].

Adjustability of electromagnetic properties is important for many applications, especially in communication, antenna engineering, defense and non-destructive testing. This will be highly needed in realization of reconfigurable local network environment, beam steering antennas, and microwave methods of remote sensing and control. Several methods were proposed based on biased ferroelectric, ferrite or magnetic composite substrates and reconfigurable resonant elements implementing active devices or a system of micro actuators. These technologies each have its advantages and limitations such as high power consumption, low operational speed, limited frequency band and high cost. In this paper we discuss the development of metamaterials containing ferromagnetic microwires, exploiting unique magnetic properties of wires to tune the effective electromagnetic parameters in the microwave frequency band. From this perspective, it is possible to tailor the collective response of the wire media by changing the local magnetic properties with external stimuli (magnetic field, current, stress, temperature) without changing the structural parameters.

The underlying physical mechanism is based on the combination of the dispersive properties of the wire media and the magnetoimpedance (MI) effect [10]. The high frequency impedance of a soft magnetic conductor may

experience enormous changes when its static magnetic structure undergoes transformation due to application of a magnetic field, stress or temperature. The nominal ratio of the impedance change, called the MI ratio, reaches several hundred percents at MHz frequencies [11,12] and about 50-100% at GHz frequencies [13,14] in amorphous microwires having circumferential (or helical) anisotropy. The characteristic magnetic fields required to cause this impedance change could be quite small, in the range of 1-5 Oe.

The discussed results involve theoretical modeling based on effective medium, measurements of the impedance in a single wire as a function of the external dc field at microwave frequencies, and free space measurements of reflection/transmission spectra with extracting the effective parameters. We also discuss the feasibility of using the magnetic wire composites for such applications as tunable microwave systems and remote sensing.

2. EFFECTIVE PERMITTIVITY OF MAGNTETIC WIRE COMPOSITES

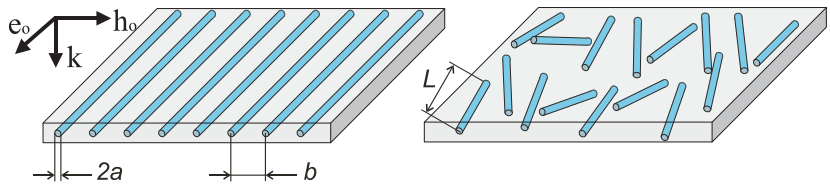


Fig. 1. Sketch of wire composites

We consider two types of wire composites as shown in Fig. 1. The composites containing short pieces of conducting wires are characterized by a resonance type of the effective permittivity as the wires behave as dipole antennas with the resonance at half wave length condition: $f_{res} = c/2l\varepsilon$ where l is the wire length, c is the velocity of light and ε is the permittivity of matrix. Then, ε_{ef} becomes negative in some frequency band past the resonance and the wave propagation is restricted in this frequency range. If the relaxation in the system is large, the dispersion of ε_{ef} broadens and its real part remains positive. In this case, the bandgap will be essentially eliminated. In composites with magnetic wires the relaxation can be controlled by the magnetic properties of wires. This is explained as following. When the composite is irradiated by the electrical field e parallel to the wires, this field also creates a circular magnetic field h within the wire (the wire axis is denoted as z-axis). At the wire surface, the fields e and h are related via the longitudinal component ς_{zz} of the wire impedance tensor:

$$e = \varsigma_{zz} h \tag{1}$$

Equation (1) should be taken as a boundary condition when solving the scattering problem from a conducting wire. In a magnetic wire, the parameter ς_{zz} depends on the circular permeability associated with h. If the interaction between the short wire inclusions is neglected, the average polarization η of a wire and the effective permittivity ε_{ef} of the whole composite take simple analytical forms:

$$\eta = \frac{1}{2\pi \ln(l/a)(\tilde{k}a)^2}\left(\frac{2}{\tilde{k}l}\tan(\tilde{k}l/2) - 1\right) \tag{2}$$

$$\varepsilon_{ef} = \varepsilon + 4\pi\, p\eta\,.$$

Here a is the wire radius and $\tilde{k}$ is the renormalized wave number depending on the surface impedance in the following way:

$$\tilde{k} = k\left(1 + i\frac{\gamma_0}{\ln l/a}\right)^{1/2}, \quad \gamma_0 = \frac{c\varsigma_{zz}}{\omega a} \tag{3}$$

where $k = \omega\sqrt{\varepsilon}/c$ is the wave number of the dielectric matrix. In Eq. (3), the polarization η was derived assuming that the radiation losses can be neglected in comparison with the magnetic and resistive losses, which is reasonable in the case of a moderate skin effect. The renormalization of the wave number in (3) is also essential in the same approximation.

In the case of composites with continuous wires, the dispersion of the effective permittivity corresponds to that for a diluted plasma:

$$\varepsilon_{ef} = 1 - \frac{\omega_p^2}{\omega^2(1+i\gamma)} \tag{4}$$

Different approaches to calculate ε_{ef} give slightly varying results for the plasma frequency ω_p. Customarily, ω_p is written as

$$\omega_P^2 = \frac{2\pi c^2}{b^2 \ln(b/a)} \tag{5}$$

where b is the spacing between the wires. A rigorous approach allowing the determination of ω_p and γ was proposed in [15], which is based on the solution of the Maxwell equations in the elementary cell and the consequent homogenisation procedure to find the averaged electric field and displacement. We extended the method for magnetic wires demonstrating that γ is given by

$$\gamma = \frac{\gamma_0}{\ln(b/a)} \tag{6}$$

Therefore, for both types of magnetic wires composites the relaxation parameter in the effective permittivity spectra depends on the wire impedance. The detailed analysis of the surface impedance in magnetic wires with a uniaxial anisotropy valid for any frequency has been developed in [10]. The calculation of the impedance tensor is based on the solution of the Maxwell equations inside the wire together with the linearized equation of motion for the magnetization vector. In the approximation of a strong skin effect, the wire longitudinal impedance is given by

$$\varsigma_{zz} = (1-i)\frac{\omega\delta}{2c}(\sqrt{\mu}\cos^2\theta + \sin^2\theta) \tag{7}$$

Here μ is the circular permeability with respect to the static magnetization M_0, and θ is the angle between M_0 and the wire axis, δ is the skin depth for $\mu = 1$. Substituting (7) into (3) shows that γ_0 increases as a square root of the permeability. It is also seen that γ_0 depends on the static magnetization angle. However, with increasing the frequency well beyond the frequency of ferromagnetic resonance the permeability tends to be unity and the dependence on θ vanishes. Therefore, we demonstrated that the dispersion properties of permittivity in magnetic wire media depend on the wire internal magnetic structure following the magnetic behavior of the wire impedance

(known as magnetoimpedance (MI) effect).

3. MI IN AMORPHOUS WIRES

Thin amorphous ferromagnetic wires of Co-rich compositions having a negative magnetostriction are very popular for MI applications. In the outer layer of the wire, an internal stress from quenching coupled with the negative magnetostriction results in a circumferential anisotropy and an alternate left and right handed circular domain structure. In this case, the circular magnetization processes determining the MI behaviour are very sensitive to the axial magnetic field. Along with this, special types of anisotropy as a helical one can be established in the outer layer by a corresponding annealing treatment, which is needed to have a stress sensitive MI. Many experimental results on MI utilize amorphous wires of $(Co_{1-x}Fe_x)SiB$ compositions with $x < 0.06$ to decrease the magnetostriction down to -10^{-7} and the characteristic saturation magnetic fields down to few Oe. The wires of the composition $Co_{72.5}Si_{12.5}B_{15}$ with larger magnetostriction of $-3 \cdot 10^{-6}$ are used for stress-impedance (SI) sensors showing the strain-gauge factor of nearly 2000 which is more than ten times larger than that of the semiconductor strain gauge. Currently, there are basically two methods of wire fabrication techniques. The first one utilises in-water-spinning method for which as-cast wires have a diameter of 125 microns. The wires then cold drawn down to 20 - 30 μm, and finally annealed under stress to established a needed anisotropy. The other technique produces amorphous wires in a glass cover by a modified Tailor method (referred to as Talor-Ulitovsky method [16]) which is based on drawing a thin glass capillary with molten metal alloy. The diameter of the metal core is ranging between 2-50 microns. In this case, different temperature expansion coefficients of glass and metal alloy result in a longitudinal tensile stress, which is needed for the circumferential anisotropy. The value of this stress and induced anisotropy depends on the wire composition and ratio of the metal core diameter to the total diameter. This is a simple one-step process allowing a strict control of properties in as-cast state and optimization of the MI characteristics. For a very thin glass layer, the MI ratio reaches 600% for a field of about 1 Oe at a frequency of 10 MHz [11]. The MI behavior for higher frequencies is shown in Fig. 2. With increasing frequency in the GHz range, the MI sensitivity in the low field region decreases but still remains very high, nearly 40% for a field of 500 A/m.

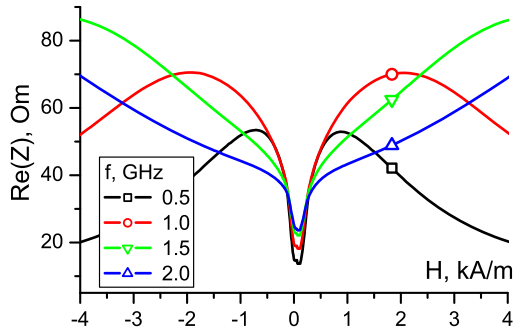


Fig. 2. Field plots for different frequencies of the real part of the impedance in $Co_{66}Fe_{3.5}B_{16}Si_{11}Cr_{3.5}$ amorphous wires with metal core radius of 20 μm and glass thickness of 10 μm.

MI in these wires can be made very sensitive to stresses. At MHz frequencies, the effect of tensile stresses (referred to as SI effect) results in increase in magnetic anisotropy, which shifts the MI peaks to higher fields [12]. However, in

GHz range the tensile stress effect on MI plots becomes very small in wires with the circumferential anisotropy since it does not alter the direction of the DC magnetisation (angle θ in equation (2)). To realise high sensitivity of MI to stresses at high frequencies, anisotropy should be established in near-axial direction. Annealing and consequent cooling under stress can induce such anisotropy in negative magnetostrictive wires.

4. TUNABLE PERMITTIVITY SPECTRA

Combining the dispersion properties of wire media and MI effect it is possible to actively tune the permittivity spectra of arrays of Co-rich microwires by application of a small magnetic field and a stress. The modeling results with the external field as a parameter are shown in Fig. 3. It is seen that in the presence of the field the dispersion region broadens since the losses are increased in high impedance state of the wires.

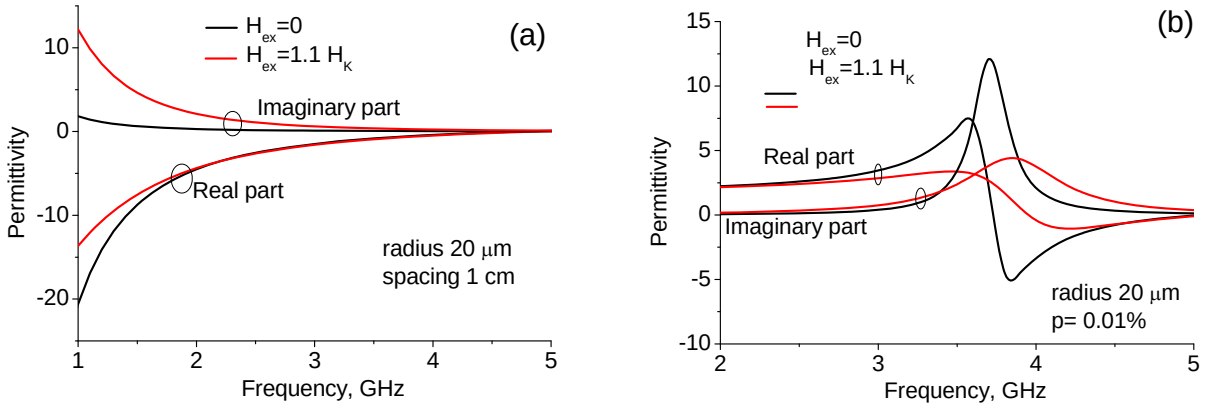


Fig. 3. Effective permittivity spectra in composites depicted in Fig.1 with the external field as a parameter. Modelling is performed for wires with a circumferential anisotropy (anisotropy field H_k=500A/m). The other parameters are: resistivity 130μΩcm, magnetisation 0.05T, wire radius 20 μm. For (a), b=1cm. For (b), l=4cm, p=0.01%.

The microwave properties of wire composites were investigated by free space method requiring large samples. The S-parameters were measured in the frequency range of 0.9-17 GHz in the presence of external magnetic field ranging up to 3000A/m applied along the wires. The magnetic field was generated by means of a plane coil [9] with turns perpendicular to the electrical field in the incident wave. The effective permittivity spectra were deduced from S-parameters with the help of Reflection/Transmission Epsilon Fast Model.

Figure 4 show the permittivity spectra for short-cut wire composites for different values of the external field. In agreement with the theory, the application of the field broadens the spectra since the wire impedance and losses increase. For composites with shorter wires this effect is much less pronounced, since the dispersion range shifts to higher frequencies where the wire permeability is nearly unity. The experimental permittivity spectra of composites with continuous wires are given in Fig. 5. In the case the strong field dependence is also seen for frequencies below and near the plasma frequency. In the presence of the field, the absolute value of the real part of the permittivity is reduced favoring the wave propagation.

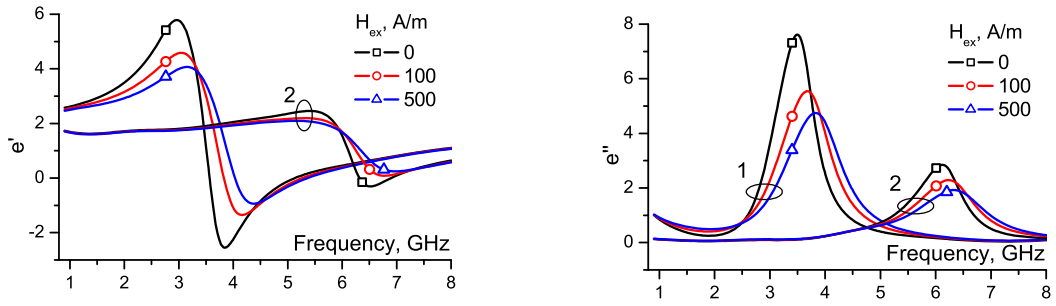


Fig. 4. Real and imaginary parts of ε_{ef} for cut wires composites of length 40 (1) and 20 (2) mm with the field H_{ex} as a parameter. Wires of the composition $Co_{66}Fe_{3.5}B_{16}Si_{11}Cr_{3.5}$ with metal core radius of 20 μm coated with 10 μm glass sheath were glued in paper to form 50x50 cm^2 samples.

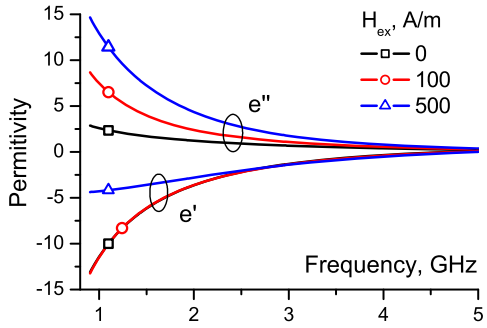


Fig. 5. Real and imaginary parts of ε_{ef} for continuous wires composites (the same wires as in Fig. 4). The spacing b=1cm which was also used as the effective sample thickness.

Concluding, we have demonstrated that the effective permittivity spectra in composites with magnetic wires showing large magnetoimpedance (MI) effect can be actively tuned applying an external magnetic field. Similar effects could be achieved with proper wire systems by applying a stress or changing a temperature. The proposed materials can be used as free space filters for secure wireless systems to obtain the desired band-pass or band-gap result. The other large area of applications is related with sensory materials. The magnetic wire composites may either provide information about the material's properties (stress, strain, temperature) or change the response in the desirable way. The technology of MI-wire structured composites is cost-effective and is suitable for large-scale applications. It could be used for microwave NDT and control in civil engineering.

Acknowledgements. We acknowledge support under projects MAT2007-66798-CO3-01 (MEC), DEVMAGMIWIRTEC (MANUNET-2007-BASQUE-3) under EU ERA-NET programme, Saiotek 08 METAMAT and Saiotek 09 MICMAGN (SPRI). One of the authors, L.P, wishes to thank Ikerbasque Foundation for fellowship. A.Z. wishes to acknowledge support of the Basque Government under Program of Mobility of the Investigating Personnel of the Department of Education, Universities and Investigation for stay in Moscow Technological University (grant MV-2009-2-21)

REFERENCES

1. Brown, J. “Artificial dielectrics,” *Progress in Dielectr.*, Vol. 2, 193–225,1960.
2. Pendry, J. B., Holden, A. J., Robbins, D. J., and Stewart, W. J. “Low frequency plasmons in thin-wire structures,” *J. Phys.:Condens. Matter*, Vol. 10, No. 22, 4785–4809, 1998.
3. Sievenpiper,D. F., Sickmiller, M. E., and Yablonovitch, E. “3D wire mesh photonic crystals,” *Phys. Rev. Lett.*, Vol. 76, 2480–2483,1996.
4. Matitsine, S. M., Hock, K. M., Liu, L. , Gan Y. B., Lagarikov, A.N., and Rozanov, K.N. “Shift of resonance frequency of long conducting fibers embedded in a composite”, J. Appl. Phys., Vol. 94, No 1, 063313-21, 2003.
5. Smith, D. R., Padilla, W. J. , Vier, D. C. , Nemat-Nasser, S. C., and Schultz , S. “ Composite Medium with Simultaneously Negative Permeability and Permittivity”, Phys. Rev. B, VOL., N0 18, 4184-87, 2000.
6. Makhnovskiy, D.P, Panina, L.V “Field Dependent Permittivity of Composite Materials Containing Ferromagnetic Wires”, *J. Appl. Phys* , Vol. 93, pp. 4120-4129, 2003.
7. Reynet, O., Adent, A.-L., Deprot, S., Acher, O. , Latrach, M. “Effect of the magnetic properties of the inclusions on the high-frequency dielectric response of diluted composites”, *Phys. Rev. B*, Vol. 66, 94412-21, 2002.
8. Panina, L. V., Sandacci, S.I, and Makhnovskiy, D.P. “Stress effect on magnetoimpedance in amorphous wires at gigahertz frequencies and application to stress-tunable microwave composite materials”, *J. Appl. Phys*., Vol. 97, 013701-07, 2005.
9. Makhnovskiy, D.P., Panina, L. V., Garcia, C. , Zhukov, A. P. , and Gonzalez J. “Experimental demonstration of tunable scattering spectra at microwave frequencies in composite media containing CoFeCrSiB glass-coated amorphous ferromagnetic wires and comparison with theory”, *Phys. Rev. B*., **74**, 064205-15, 2006.
10. Makhnovskiy, D.P., Panina, L. V., and Mapps, D. J. “Field-dependent surface impedance tensor in amorphous wires with two types of magnetic anisotropy: helical and circumferential,” *Phys. Rev. B*, Vol. 63, 144 424–41, 2001
11. Zhukova, V, Chizhik, A., Zhukov, A., Torcunov, A., Larin, V., and Gonzalez, J. “Optimization of giant magneto-impedance in Co-rich amorphous microwires”, *IEEE Trans. Magn*. Vol. 38, 3090-92, 2002
12. García,C., Zhukov, A., Zhukova,V., Ipatov,M., Blanco, J.M., and Gonzalez, J. "Effect of Tensile Stresses on GMI of Co-rich Amorphous Microwires " , *IEEE Trans Magn*. Vol. 41, 3688-3690, 2005
13. Lofland, S. E., Bhagat, S. M., Domı´nguez, M., Garcı´a-Beneytez, J. M., Guerrero, F., and Va´zquez ,M. “Low-field microwave magnetoimpedance in amorphous microwires”, VOL.85, No 8, 4442-44, 1999
14. Sandacci, S., Makhnovskiy, D.P., Panina, L. V, and. Larin, V. *2* “Valve–like behavior of the magnetoimpedance in the GHz range”, *J. Magn. Magn. Mat*., Vol. *272/276*, 1855-57, 2004.
15. Sarychev, A.K., Shalaev, V.M. “Electromagnetic field fluctuations and optical nonlinearities in metal-dielectric composites”, *Physics Reports*, Vol. 335 275-371 *(see equation 7.67)*, 2000.
16. Larin, V. S., Torcunov, A. V. , Zhukov, A. P., Gonzalez, J. , Vazquez, M., and Panina, L. V. “Preparation and properties of glass-coated microwires,” *J. Magn. Magn. Mater.*, Vol. 249/1–2, 39–45, 2002.

Design and Characterization of a Tunable DNG Metamaterial Superstrate for Small Beam Steering Antennas

H. Griguer[1,2], M. Drissi[2], E. Marzolf[2], H. Lalj[1,2] and F. Riouch[3]
[1]EMSI of Rabat, Morocco
[2]UEB, INSA of Rennes, IETR, France
[3]INPT of Rabat, Morocco
griguer@emsi.ac.ma

Abstract- The design and the characterization of a tunable double negative metamaterial is proposed in order to create a superstrate for beam steering applications in small antennas. The tunable metamaterial is based on an omega shaped unit cell and is investigated and validated by waveguide measurements. An appropriate loading of the metamaterial unit cell, through the use of a varactor diode, enables to vary the medium index of the superstrate in an interesting range. This metamaterial superstrate is then associated to a patch antenna permitting to steer the beam in different directions of the elevation plane.

1. INTRODUCTION

The advance of the wireless telecommunications networks ought heavily to the development of smart antenna systems. For a best quality of service, it is necessary to dynamically steer the radiation of the antennas in privileged directions and to present nulls in all the other directions for interference minimization. For this purpose, phased arrays are a well proven technology; however it doesn't really fit in mobile terminals due to limited space availability. We have proposed in [1] the covering of a primary radiating source by a metamaterial superstrate having a varying index medium, in order to introduce the beam steering control of the antenna. In this paper, we propose to develop the design and the characterization of an actual metamaterial superstrate based on an omega shaped unit cell. The tuning of the metamaterial resonators is obtained by varying the gap impedance of the omega cell by an appropriate loading through a varactor diode. The details of the metamaterial design are presented in the first part of this paper. The geometry is optimized by 3D electromagnetic simulations and the medium index is then characterized by microwave measurements performed under a metallic waveguide technology. In the second part, we propose a particular configuration associating a patch antenna and the tunable metamaterial as a superstrate. The obtained results show an important beam steering capability in accordance with the applied biasing of the metamaterial.

2. TUNABLE METAMATERIAL UNIT CELL DESIGN

The proposed metamaterial is based on a omega shaped unit cell which, was firstly introduced by N. Engheta as a pseudochiral medium [2], and later studied for metamaterial applications [3]. This metamaterial unit cell exhibits a double negative behavior, as the magnetic and the electric resonators operate in the same frequency band. Compared to usual structures such as split ring resonators, omega cells present the advantage to reach a large index medium, thanks essentially to its magnetic and electric contributions.

Fig. 1 shows the omega cell geometry and its dimensions: the magnetic resonator is formed by the metallic split ring and the electric resonator is formed by the metallic split strip. To realize this omega cell, both resonators are printed on a RT/Duroid substrate characterized by ε_r =2.2, tanδ =0.00027 and h=0.8mm. The dimensions of the

unit cell are optimized in order to operate at 10 GHz, where the global size is around $\lambda_0/8$. The omega unit cell is designed and optimized by means of a 3D electromagnetic simulation, respecting the conditions of the homogenization method [4]. The intrinsic parameters of the effective medium (ε_{eff} and μ_{eff}) are computed from the transmission and reflection coefficients. The simulation result presented in Fig. 2 shows for the case of g=0.2mm a double negative metamaterial behavior around 10.3 GHz, with a negative medium index of n_{eff} =-4.

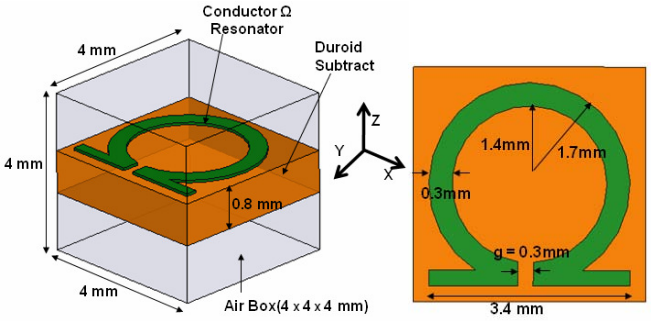


Fig. 1: Geometry of the proposed omega unit cell

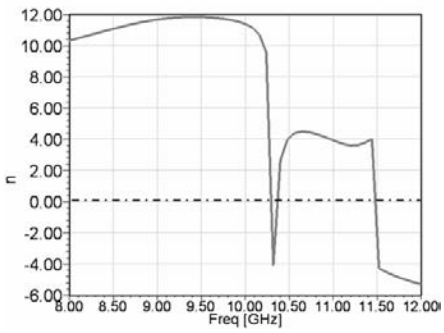


Fig. 2: Simulation result of the effective medium index for the proposed unit cell with a gap of g=0.2mm

The gap width is then varied from 0.2mm to 0.6mm in order to illustrate the sensitivity of the gap impedance on the medium index. Fig. 3 shows the tendency of the effective medium index to increase with the gap width, as much as the working frequency, attaining n_{eff}=-9 for g =0.6mm and f=10.65 GHz. The observable differences in the medium index and in the operating frequency are related to the small frequency shift between electric and magnetic resonances happening in the metamaterial cell during the control of the gap impedance.

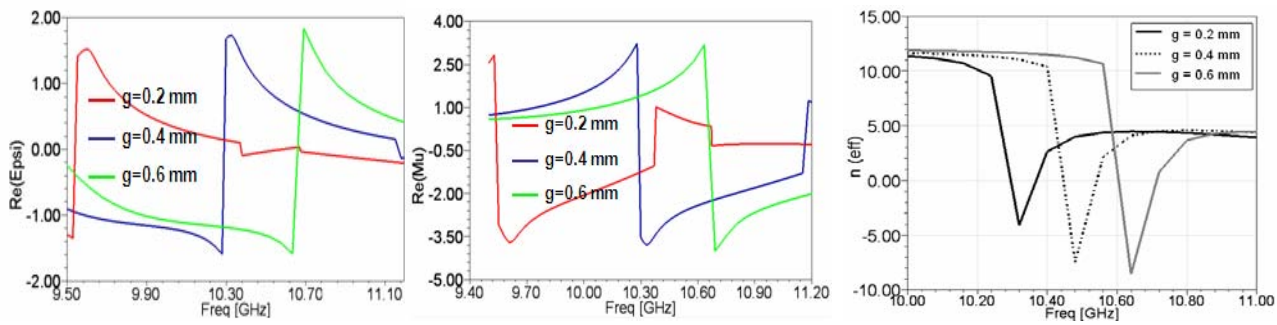


Fig. 3: Variation of the intrinsic properties of the omega unit cell according to the gap width (effective permeability, effective permittivity and effective medium index)

For the validation purpose, the omega unit cell is fabricated with different gap widths and characterized under a metallic waveguide technology based on a non-standard section of 4x4mm^2 for the porting of the test slab [5-7]. Fig. 4 shows the different realizations - unit cell, waveguide measurement setup - and the S parameters highlighting a pass band phenomenon that appears due to an evanescent waveguide mode.

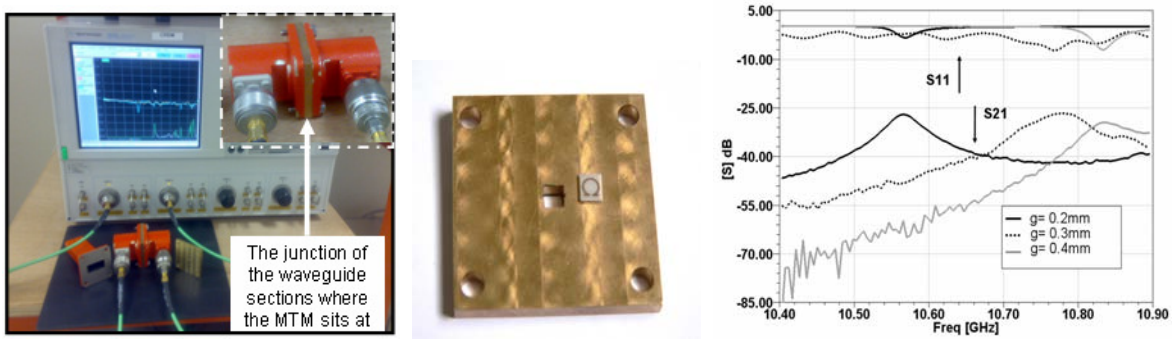


Fig. 4: Waveguide measurement setup, unit cell with the non-standard section and the obtained S parameters

The propagation in the evanescent frequency range of the waveguide is only possible if the medium is left handed, thus confirming the metamaterial effect of the cell. The tuning of the gap width permits also to control the frequency where this metamaterial effect arises. In a second stage of the tuning study, we have loaded the gap of the omega cell by an equivalent complex impedance Z_d corresponding to the varactor diode model (Fig. 5). As such, the obtained near-field cartography demonstrates that the gap is truly the most sensitive position for an appropriate control of the resonating structure through the insertion of the variable load. The simulation results in Fig. 5 present the real part of the effective parameters (μ_{eff}, ε_{eff}) when the loading of different capacity values is applied.

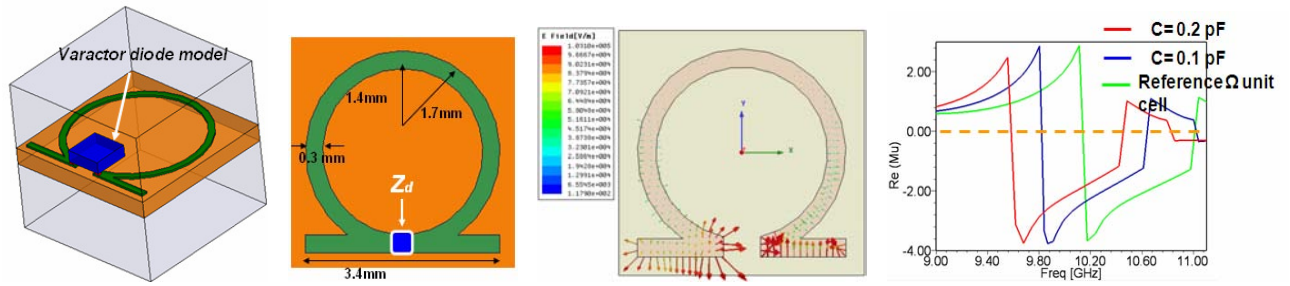


Fig. 5: Omega unit cell loading with a varactor diode and corresponding performances (electric field along the structure and effective permittivity)

By a closer electromagnetic analysis, we find that a satisfactory control could be obtained with a varactor diode having a variation of 0.1-3pF for a voltage biasing range of 1-20V. Fig. 6 shows the intrinsic parameters obtained by the voltage biasing of the chosen varactor diode. At the biasing of 10V, Re(μ_{eff})=-0.3 and Re(ε_{eff})=-1.8.

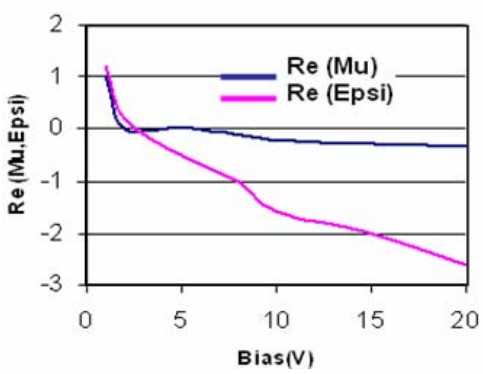


Fig. 6: Intrinsic properties versus the voltage biasing applied to the varactor diode

3. ASSOCIATION OF A PATCH ANTENNA WITH THE METAMATERIAL SUPERSTRATE

Fig. 7 shows a configuration of the proposed tunable metamaterial used as a superstrate covering a patch antenna. The superstrate is formed by 4x4 active cells in the XY-plane and 1 cell along the Z-axis. The dimensions of the patch antenna and of the superstrate (L_X=16mm, L_Y=16mm, L_Z=4mm) were optimized in order to operate around the resonance frequency of the metamaterial cells fr=10GHz. The orientation of the superstrate is chosen in a particular way in order to match the electromagnetic excitation requirements of the unit cells with the near field radiating of the primary source. Fig. 7 shows also the beam steering behavior according to the variation of the capacitive values of the varactor diode. For the case C=0.1pF, the steering angle is around θ_t =-30°. With an other loading of C=3pF, we observe a beam steering around θ_t=+30°. These results prove the feasibility of the beam steering through the tunable metamaterial superstrate added to the simple patch antenna.

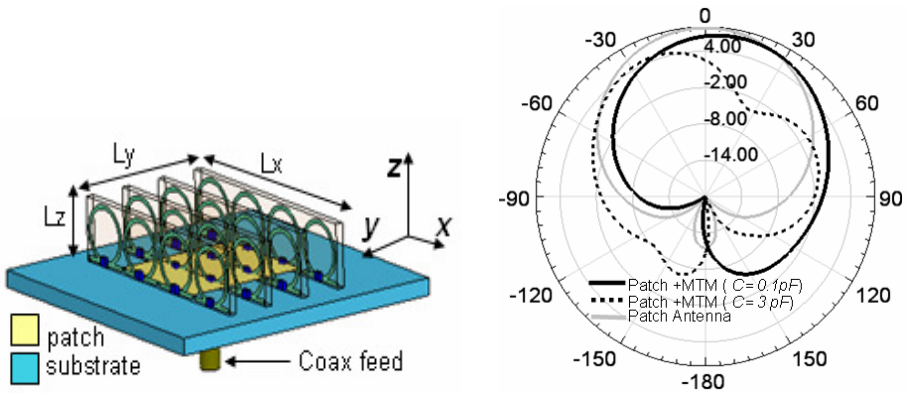


Fig. 7: Association of the metamaterial superstrate with a primary antenna source and corresponding beam variation for different impedance varactor loading

4. CONCLUSION

In this work, the design and the characterization of a tunable metamaterial based on the omega unit cell has been presented. The experimental results of simulations and measurements have confirmed the tunable double negative behavior according to the gap width, the loading impedance and the chosen varactor diode capacitance. An implementation of a simple square patch antenna covered with the proposed tunable metamaterial superstrate has been fabricated and tested. The radiating pattern of this smart antenna can be steered thanks to the tuning of the superstrate over a range of (θt = +/-30°) in the elevation plane.

REFERENCES

1. H. Griguer, E. Marzolf, M. Drissi, H. Lalj and F. Riouch, "Investigation and Design of 3D Metamaterial for the Enhancement of Patch Antenna Radiation", in *Proceedings of the IEEE International Symposium on Antennas and Propagation*, Charleston, USA, June 1-5, 2009.
2. M. M. I. Saadoum and N. Engheta, "A Reciprocal Phase Shifter Using Novel Pseudochiral or Omega Medium", *Microwave and Optical Technology Letters*, Vol. 5, 184–188, April 1992.
3. C. R. Simovski and S. He, "Frequency Range and Explicit Expressions for Negative Permittivity and Permeability for an Isotropic Medium Formed by a Lattice of Perfectly Conducting Omega Particles", *Physics Letters A*, Vol. 311, No. 2-3, 254–263, May 2003.
4. D. R. Smith, D. C. Vier, N. Kroll and S. Schultz, "Determination of Effective Permittivity and Permeability of Metamaterials from Reflection and Transmission Coefficients", *Physical Review B*, Vol. 65, No. 19, April 2002.
5. H. Griguer, E. Marzolf, M. Drissi, H. Lalj and F. Riouch, "Design and Measurement of DNG Metamaterial for Tunable Microwave devices", in *Proceedings of the IEEE Mediterranean Microwave Symposium*, Tangiers, Morocco, November 15-17, 2009.
6. S. Hrabar, J. Bartolic and Z. Sipus, "Waveguide Miniaturization Using Uniaxial Negative Permeability Metamaterial", *IEEE Transactions on Antennas and Propagation*, Vol. 53, No. 1, 110–119, January 2005.
7. J. Carbonell, L. J. Rogla, V. E. Boria, "Equivalent circuit analysis of left handed SRR loaded metamaterial Waveguides", *Journal of the European Microwave Association*, Vol. 2, No. 1, 52–59, March 2006.

Multipole approach in electrodynamics of metamaterials

A. Chipouline, J. Petschulat, A. Tuennermann, T. Pertsch
Institute of Applied Physics, Friedrich-Schiller-Universität Jena, Max Wien Platz 1, 07743, Jena, Germany

C. Menzel, C. Rockstuhl, F. Lederer
Institute of Condensed Matter Theory and Solid State Optics, Friedrich-Schiller-Universität Jena, Max Wien Platz 1, 07743, Jena, Germany

Introduction

Metamaterials are artificial media that allow tailoring the macroscopic properties of light propagation by a careful choice of a microscopic unit cell (called the metaatom) it is made of. By controlling the geometrical and material dispersion of the metaatom, novel effects such as negative refraction [1-3], optical cloaking [4-9], as well as a series of optical analogues to phenomena known from different disciplines in physics could be observed [10-14]. In addition to a bi-axial anisotropic (linear dichroism) material response [1-3, 15-17], research was also recently extended towards the exploration of metaatoms that affect off-diagonal elements of the material tensors (elliptical dichroism) leading to, e.g., optical activity [18-22], bidirectional and asymmetric transmission [23-25] or chirality induced negative refraction [26-28].
However, despite the possibility to rely on rigorous computations for describing the light propagation on the microscopic level of the metaatoms, an enduring problem in metamaterial research is the question on how the effective material tensor looks like for a certain metamaterial.
Here a simple and versatile analytical model describing propagation of electro magnetic waves in metamaterials is suggested. The model has been developed following classical approach of Maxwell equation averaging procedure [29]. This transition from microscopic to macroscopic system of Maxwell equations takes into account all peculiarities of carriers dynamics under the action of resulted electro magnetic field through the introduction of multipole moments which are supposed to be represented as functions of the electro magnetic field. There are two main issues which have to be mentioned in connection with the use of this approach. First, averaging means consideration of sufficiently large number of objects into the volume over the averaging procedure is performed. In case of solid state physics it is easily satisfied down to optical wavelengths of several nanometers (a wavelength is appeared to be a natural scale for the averaging). Second, the charge dynamics is supposed to be expressed as a function of the averaged macroscopic (not microscopic!!!) field in order to get self consistent system of equations for the macroscopic field. From the other side, it is clear, that charge dynamics is stipulated by a local, microscopic field, and the difference between the micro and macro fields has to be somehow taken into account.
Our model is based on the secondary averaging procedure in full analogy with the ordinary one, where the nanoplasmonic inclusions are considered as atoms or molecules (are called usually metaatoms or metamolecules), and consequently the two above mentioned restrictions are to be applied here. The first one (large enough number of metaatoms per averaged volume with typical scale of wavelength) is barely satisfied due to the fact that typical sizes of the plasmonic inclusions are only 3-5 times less than the respective resonance wavelengths. The second one (difference between local and averaged field) has not been taken into account at all, in other words, for charge dynamics we did not distinguish between local and averaged fields. In contrast with the first limitation, the second one can be in principle addressed (through, for example, known Clausius-Mossotti expression), which is one of the possible forthcoming extension of the model. In spite of the mentioned assumptions, the model turns out to be adequate enough, can be used to gain physical understanding of optical phenomena in metamaterials, obey good quantitative correspondence with the results of rigorous numerical methods, and is able to predict new effects (like metamaterial nonlinearity, see below).

The paper consists of the following parts. First, the basic formalism is described; linear properties (dispersion relations and effective parameters) are presented and compared with the results of rigorous numerical calculations. Second, a new type of nonlinearity, specific for certain particular metaatoms, will be analysed based on the results of our model. Third, optical activity phenomena for planar metaatoms will be considered and the possibility to predict resonance properties is shown.

Linear properties of metamaterials

The presence of the metaatoms in a dielectric host is described by adding extra charge and current distributions in Maxwell equations

$$\begin{aligned} &\operatorname{div} D = \rho_{meta} && \operatorname{div} B = 0 \\ &\operatorname{rot} H = \frac{\partial D}{\partial t} + j_{meta} && \operatorname{rot} E = -\frac{\partial B}{\partial t} \end{aligned} \qquad (1)$$

At this stage, the Maxwell equations are not secondary averaged, and are to be considered as a starting point, in analogy with microscopic Maxwell equations in solid state physics before averaging and transformation to macroscopic ones. The difference between H and B here is stipulated by possible magnetic properties of the host material or metal itself (and thus is negligible for sure for the optical frequencies), and the difference between D and E reflects their dielectric properties. After formal averaging (again, with all mentioned in introduction restrictions) the charge density in the first equation and the current density in the second one give rise to the multipole moments according to the common rules

$$\begin{aligned} &\operatorname{div} D = \langle \rho_{meta} \rangle && \operatorname{div} B = 0 && \langle \rho_{meta} \rangle = -\operatorname{div} P \\ &\operatorname{rot} H = \frac{\partial D}{\partial t} + \langle j_{meta} \rangle && \operatorname{rot} E = -\frac{\partial B}{\partial t} && \langle j_{meta} \rangle = \frac{\partial P}{\partial t} + \frac{1}{\mu_0} \operatorname{rot} M \end{aligned} \qquad (2)$$

The notation for E, B, D, and H remain unchanged but are considered already averaged over large enough volume values to be averaged ones, and respective dielectric and magnetic constants, appearing thereafter, are those for the homogenized media. This is the first starting assumption of our model. The second one consists of substitution of rather complicated plasmon dynamics by set of associated auxiliary charge distribution (see Fig. 1), driven by an external electric field.

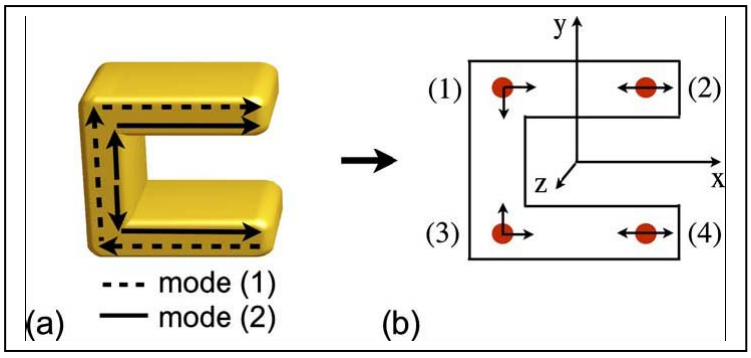


FIG. 1 (a) SRR meta-atom and the intrinsic currents for the fundamental electric (black solid line) and magnetic (black dashed line) mode. (b) The associated auxiliary charge distribution (red points) with predefined degrees of freedom (black arrows).

The associated auxiliary charge dynamics is described by set of coupled harmonic oscillator equations

$$\frac{\partial^2 \vec{r}_i}{\partial t^2} + \gamma_i \frac{\partial \vec{r}_i}{\partial t} + \omega_i^2 \vec{r} + \sum_{l=1}^{N} \sigma_{il} \vec{r}_l = \frac{q}{m} E(\vec{R}) \qquad (3)$$

Here r_k are micro variables which describe the dynamics of *i* - th oscillator with eigen frequency ω_k and damping constant γ_k, σ_{kp} is the coupling coefficient between *i* - th and *l* - th oscillators, $E(\vec{R})$ is the averaged field as a function of the macroscopic coordinates $\vec{R}$, and $\frac{q}{m}$ accounts for effective charge and mass of plasmons. It is worth noting again, that in these equations we use an averaged field (which definitively differs from the local ones), but in the current version of our model no correction to local field has been applied.

With known charge dynamics the dipole, quadruple, and magnetic dipole moments can be calculated straightforwardly, and after substitution into Maxwell equations respective dispersion relations for plane waves can be found [30]. It has to be pointed out, that the quadruple term has to be taken into consideration: due to basic principles [29] it has the same order as a magnetic dipole moment. Appearance of the quadruple moment is responsible for the multipole nonlinearity, a specific effect in metamaterials, considered in the second part.

Below a comparison of wavevectors and dielectric and magnetic constants calculated from analytical model and numerically is presented for Split Ring Resonators (SRR) structure (see Fig. 2). The pictures demonstrate pretty well for such inherently approximative model agreement.

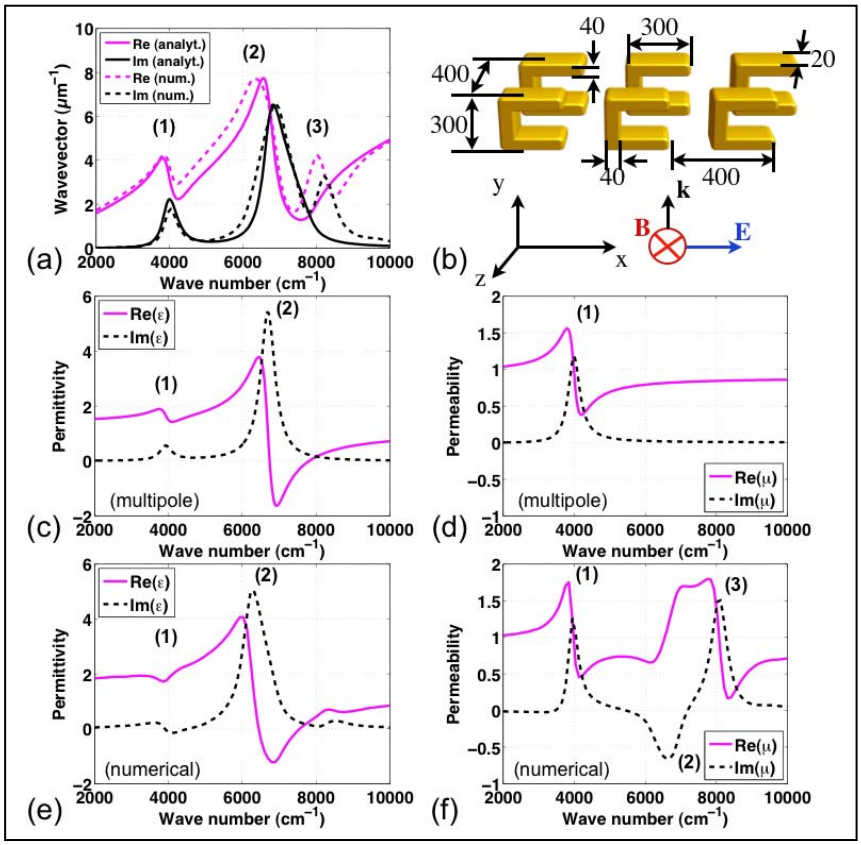


FIG. 2 (a) Comparison of the dispersion relation - numerical model (dashed), analytical model (solid); (b) single metamaterial layer (gold SRR) used for the numerical simulation (dimensions in nm); spectral dependence of (c) effective permittivity and (d) effective permeability from the multipole model; spectral dependence of (e) effective permittivity and (f) effective permeability from the numerical simulations.

The phenomenological constants of plasmon dynamics (eigen frequency, damping constant, and the coupling coefficient) are specific for each metaatom and are supposed to be found experimentally or through comparison with the results of rigorous calculations. This fact seems to reduce the universality of the model, but actually it repeats situation in, for example, solid state physics where all constants are specific for each material as well.

Multipole nonlinearity of metamaterials

The nonlinearity appears in the model through the quadruple moment, which is comprised of multiplication of dynamical variables. In this case the crucial point is the ability to excite oscillation in one direction by an electric field, polarized in some another direction. It is clear, that this does not take place in any structure: for example, cut wires do not provide the required dynamics, while the SRR geometry does. It has to be also noted, that the magnetic moment does not contribute to the nonlinear response; the only way to obtain the nonlinearity is in consideration of contribution of the quadruple moment (let us repeat again, that the quadruple moment has to be taken into consideration as soon as the magnetic dipole moment is considered. It is required by basics of macroscopic Maxwell equations elaboration procedure [29]).
The detailed consideration of the nonlinear response of the metamaterials is given in [31]. Our model predicts second harmonic generation on the level of 10^{-8} to pump signal for the SRR geometry – see Fig 3. The derived coupled equations for fundamental and second harmonics allow us to analyse various parametric effects, including possibility of loss compensation using the multipole nonlinearity.

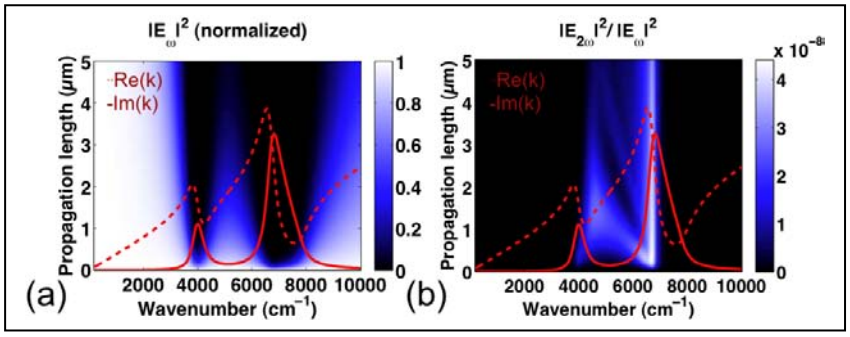


FIG. 3. Evolution of normalized electric field intensity for (a) the Fundamental Frequency and (b) the Second Harmonic as a function of the wave number of the fundamental wave. The red lines indicate the real (dashed) and the imaginary part (solid) of the linear dispersion relation.

Optical activity in metamaterials

The optical activity phenomena, which received a significant interest in contest of metamaterials recently, can be analysed in framework of the model as well. Starting again from the SRR geometry, one can modify the structure in order to get necessarily for optical activity asymmetry, how it is shown in Fig. 4.
The plasmonic dynamics and the electro-magnetic wave propagation are described the same way as before, but here we state the problem a bit differently, namely: is it possible after modification to use the same constants which have been found for another structure? More particular: if we have found the dynamic constants for a SRR, could they be used in order to describe L-structure or S-structure? The presented below data in Fig. 5 answer this question for L-structure.
It is seen that this approach allows us to predict resonance position with rather good accuracy. The resonance dips can be predicted much worse, but the coincidence becomes again better for cross polarized terms, which are actually of interest at the optical activity consideration. The detailed discussion can be found in [32].

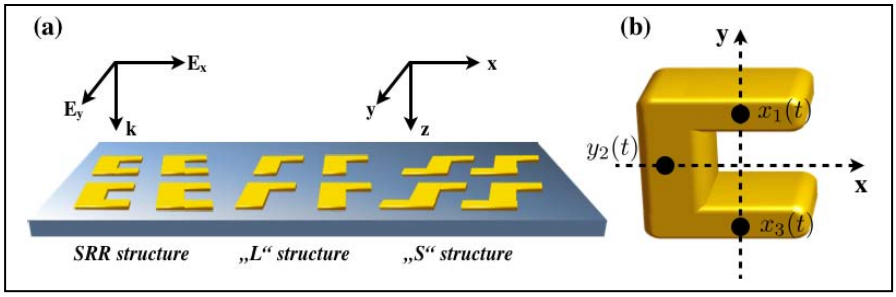


FIG. 4 (a) The original SRR structure (left), the first modification, namely the L – structure (center) and the second modification, the S – structure (right).

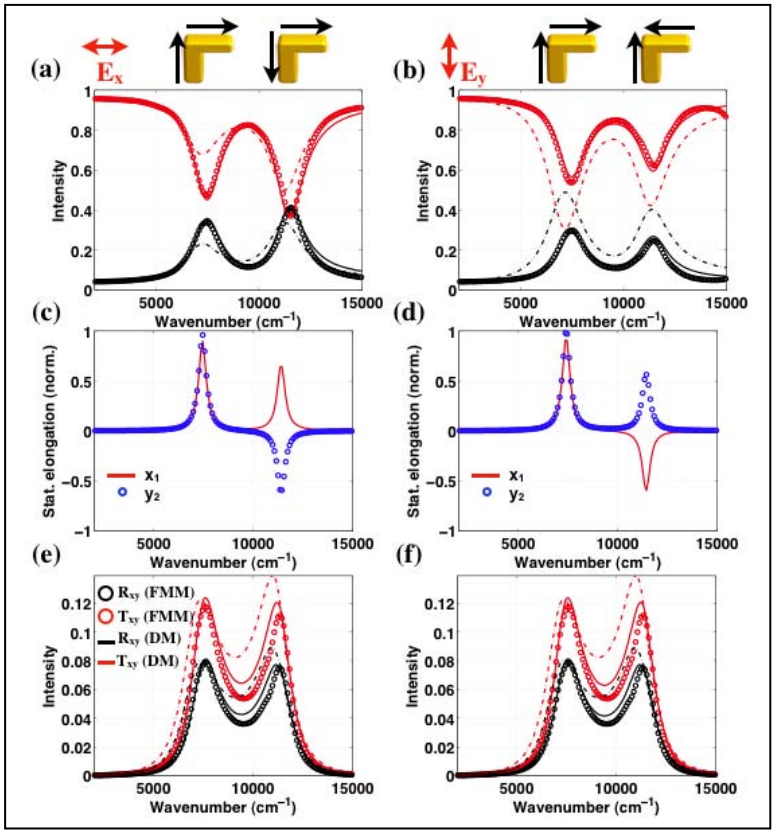


FIG. 5 The far field structure of the L structure for x (a) and for y (b) polarization. Additionally to the numerical data (spheres) and the fitted spectra (solid lines) the predicted spectra incorporating the SRR parameters (dashed-dotted lines) is plotted. (c), (d) In contrast to the SRR both eigenmodes are excited for each polarization direction, simultaneously. The respective numerical cross-polarization contributions (circles) compared with the model predicted (dashed-dotted lines) and the fitted (solid lines) values are shown in (e), (f). Note that both figures are identical as required for such kind of effective media and are only shown for completeness.

Conclusion

In summary, an analytical model, allowing the description of various optical effects in metamaterials in the frame work of secondary averaged Maxwell equations is presented. The model gives excellent agreement with rigorous numerical data for linear dispersion relation, gives a tool to prescribe effective dielectric and magnetic constants to a particular metamaterial, and predicts their specific nonlinear properties. Moreover, the model represents a “building block approach”, where constant being found for one meta structure, can be applied to a series of modified structures and predict their linear optical response (for example, optical activity) with good accuracy.

Acknowledgement

Financial support by the Federal Ministry of Education and Research as well as from the State of Thuringia within the Pro-Excellence program is acknowledged.

References

[1] Yuan, W. Cai, S. Xiao, V. Drachev, and V. Shalaev, Opt. Lett. 32, 1671 (2007)
[2] G. Dolling, M.Wegener, and C. Soukoulis, Opt. Lett. 32, 53 (2007)
[3] J. Valentine, S. Zhang, T. Zentgraf, G. B. E Ulin-Avila, Dentcho A. Genov, and X. Zhang, Nature 455, 376 (2008)
[4] J. Valentine, J. Li, T. Zentgraf, G. Bartal, and X. Zhang, Nature Mat. 8, 568 (2009)
[5] A. Al_u and N. Engheta, Phys. Rev. Lett. 102, 1 (2009)
[6] Y. Lai, J. Ng, H. Chen, D. Han, J. Xiao, Z.-Q. Zhang, and C. T. Chan, Phys. Rev. Lett. 102, 1 (2009)
[7] M. Farhat, S. Guenneau, and S. Enoch, Phys. Rev. Lett. 103, 1 (2009)
[8] Justice, S. Cummer, J. Pendry, and A. Starr, Science 314, 977 (2006)
[9] U. Leonhardt, Science 312, 1777 (2006)
[10] E. E. Narimanov and A. V. Kildishev, Appl. Phys. Lett. 95, 041106 (2009)
[11] S. M. Vukovic, I. V. Shadrivov, and Y. S. Kivshar, Appl. Phys. Lett. 95, 041902 (2009)
[12] D. Ö. Göuney and D. A. Meyer, Phys. Rev. A 79, 1 (2009)
[13] N. Papasimakis, V. Fedotov, and N. Zheludev, Phys. Rev. Lett. 101, 253903 (2008)
[14] N. Liu, L. Langguth, J. K. Thomas Weiss and, M. Fleischhauer, T. Pfau, and H. Giessen, Nature Materials 8, 758 (2009)
[15] C. Helgert, C. Menzel, C. Rockstuhl, E. Pshenay-Severin, E. B. Kley, A. Chipouline, A. T unnermann, F. Lederer, and T. Pertsch, Opt. Lett. 34, 704 (2009)
[16] C. Garcia-Meca, R. Ortuno, F. J. Rodriguez-Fortuno, J. Marti, and A. Martinez, Opt. Lett. 34, 1603 (2009)
[17] M. Thiel, G. von Freymann, S. Linden, and M. Wegener, Opt. Lett. 34, 19 (2009)
[18] B. Bai, Y. Svirko, J. Turunen, and T. Vallius, Phys. Rev. A 76, 023811 (2007)
[19] L. Arnaut, J. Electromagn.Waves Appl. 11, 1459 (1997)
[20] J. A. Reyes and A. Lakhtakia, Opt. Comm. 266, 565 (2006)
[21] S. Prosvirnin and N. Zheludev, J. Opt. A: Pure Appl. Opt. 11, 074002 (2009)
[22] S. Tretyakov, I. Nefedov, A. Shivola, S. Maslovski, and C. Simovski, J. Electromagn. Waves Appl. 17, 695 (2003)
[23] V. Fedotov, P. Mladyonov, S. Prosvirnin, A. V. Rogacheva, Y. Chen, and N. I. Zheludev, Phys. Rev. Lett. 97, 167401 (2006)
[24] V. Fedotov, A. Schwanecke, and N. Zheludev, Nano Lett 7, 1997 (2007)
[25] S. V. Zhukovsky, A. V. Novitsky, and V. M. Galynsky, Opt. Lett. 34, 1988 (2009)
[26] J. Pendry, Science 306, 1353 (2004)
[27] S. Tretyakov, A. Sihvola, and L. Jylhä, Photonics Nanostruct. Fundam. Appl. 3, 107 (2005)
[28] J. Zhou, J. Dong, B. Wang, T. Koschny, M. Kafesaki, and C. M. Soukoulis, Phys. Rev. B 79, 1 (2009)
[29] P. Mazur and B. R. A. Nijboer, “On the statistical mechanics of matter in an electromagnetic field – I. Derivation of the Maxwell Equations from Electron Theory”, Physica XIX, p. 971-986 (1953)
[30] J. Petschulat, C. Menzel, A. Chipouline, C. Rockstuhl, A. Tüunnermann, F. Lederer, and T. Pertsch, Phys. Rev. A 78, 043811 (2008)
[31] J. Petschulat, A. Chipouline, A. Tüunnermann, T. Pertsch, C. Menzel, C. Rockstuhl, F. Lederer, Phys. Rev. A 80, 063828 (2009)
[32] J. Petschulat, A. Chipouline, A. Tüunnermann, T. Pertsch, C. Menzel, C. Rockstuhl, F. Lederer, J. Yang, P. Lalanne, http://arxiv.org/abs/0909.0778

Scattering by a nihility elliptic cylinder

A.-K. Hamid[1*] **and M. I. Hussein**[2]

[1]Department of Electrical & Computer Engineering, University of Sharjah,
P.O. Box 27272, Sharjah, United Arab Emirates

[2] Department of Electrical Engineeringl, United Arab University,
P.O. Box 17555, Al-Ain, United Arab Emirates

[*]corresponding author: akhamid@sharjah.ac.ae

Abstract- The backscattering echo width of a nihility elliptic cylinder illuminated by an incident plane electromagnetic wave is obtained by solving the analogous problem of scattering of the plane wave by a dielectric elliptic cylinder of the same size, and letting its refractive index approaches zero. Numerical results are obtained for the scattered fields of nihility elliptic cylinder to show its effect on the backscattering width.

1. INTRODUCTION

Nihility materials having zero permittivity and permeability have been of interest to many EM researchers, recently. Exact solutions to scattering by nihility objects of canonical shapes such as cylinders and spheres have already been published in the literature [1-2]. Here, we present an analytic solution to the problem of scattering of an incident plane wave from an infinitely long nihility elliptic cylinder, using the method of separation of variables. The problem is formulated by expanding the incident, scattered, and the transmitted electromagnetic fields corresponding to an analogous dielectric elliptic cylinder in terms of appropriate angular and radial Mathieu functions, and a set of expansion coefficients. The incident field expansion coefficients are known, but the scattered and the transmitted field expansion coefficients are unknown. The unknown expansion coefficients are evaluated by imposing the boundary conditions corresponding to the continuity of the tangential electric and magnetic fields at the surface of the dielectric elliptic cylinder.

In this paper, the solution of the electromagnetic wave scattering by a nihility elliptic is obtained by solving the problem of scattering by a dielectric elliptic cylinder and letting the refractive index approaches zero (relative permittivity and relative permeability are approximately null-valued). Nihility is unachievable, but it may be approximately simulated in some narrow frequency range [1-2]. Nnumerical results are presented as normalized echo pattern widths for nihility circular and elliptic cylinders of different sizes, axial ratios and incident angles, for both TM and TE polarizations of the incident wave.

2. FORMULATION OF THE SCATTERING PROBLEM

Consider the case of a linearly polarized electromagnetic plane wave incident on dielectric elliptic cylinder at an angle ϕ_i with respect to the positive x axis, as shown in Figure 1. The dielectric cylinder has permittivity ϵ_1 and permeability μ_1. The semi- major and semi-minor axes of the cylinder are a and b. It is convenient to define the x and y coordinates of the Cartesian coordinate system in terms of u and v coordinates of an elliptical coordinate system also located at the centre of the cylinder in the form of $x = F\cosh u\cos v$ and $y = F\sinh u\sin v$. A

time dependence of $e^{j\omega t}$ is assumed throughout the analysis, but suppressed for convenience. The electric field component of the TM polarized plane wave of amplitude E_0 is given by

$$E_z^i = E_0 e^{jk_0\rho\cos(\varphi-\varphi_i)} \tag{1}$$

where k_0 is the wave number in free space and $j=\sqrt{-1}$. The incident electric field may be expressed in terms of angular and radial Mathieu functions as follows

$$E_z^i = \sum_{m=0}^{\infty} A_{em} R_{em}^{(1)}(c_0,\xi) S_{em}(c_0,\eta) + \sum_{m=1}^{\infty} A_{om} R_{om}^{(1)}(c_0,\xi) S_{om}(c_0,\eta) \tag{2}$$

where $A_{\substack{em\\om}}$ are incident field coefficients [3], $N_{\substack{em\\om}}(c_o)$ are the normalized incident field coefficients [3], $c_0 = k_0 F$, F is the semifocal length of the elliptical cross section, $\xi = \cosh u$, $\eta = \cos v$, S_{em} and S_{om} are the even and odd angular Mathieu functions of order m, respectively, $R_{em}^{(1)}$ and $R_{om}^{(1)}$ are the even and odd radial Mathieu functions of the first kind, and N_{em} and N_{om} are the even and odd normalized functions. The scattered electric field may be expressed in terms of Mathieu functions as follows

$$E_z^s = \sum_{m=0}^{\infty} B_{em} R_{em}^{(4)}(c_0,\xi) S_{em}(c_0,\eta) + \sum_{m=1}^{\infty} B_{om} R_{om}^{(4)}(c_0,\xi) S_{om}(c_0,\eta) \tag{3}$$

where B_{em} and B_{om} are the unknown scattered field expansion coefficients, $R_{em}^{(4)}$ and $R_{om}^{(4)}$ are the even and odd Mathieu functions of the fourth kind. Similarly, the transmitted electric field into the inner dielectric layer may be written as

$$E_z^t = \sum_{m=0}^{\infty} C_{em} R_{em}^{(1)}(c_1,\xi) S_{em}(c_1,\eta) + \sum_{m=1}^{\infty} C_{om} R_{om}^{(1)}(c_1,\xi) S_{om}(c_1,\eta) \tag{4}$$

where $c_1 = k_1 F$, $k_1 = \omega\sqrt{\mu_1\varepsilon_1}$, and C_{em}, C_{om} are the unknown transmitted field expansion coefficients. The magnetic field components inside and outside the elliptic cylinder can be obtained using Maxwell's equation.

The unknown expansion coefficients in equation (5) can be obtained by imposing the boundary conditions at the interface of the cylinder [3]. The TE case can be obtained by using the duality principle of the TM case.

3. NUMERICAL RESULTS

The obtained numerical results are presented as normalized echo pattern widths for nihility circular and elliptic cylinders of different sizes, axial ratios and incident angles, for both TM and TE polarizations of the incident wave. To validate the analysis and the software used for calculating the results, we have computed the normalized echo pattern widths for PEC and nihility elliptic cylinders of axial ratio 1.001 [1], $k_o a = 2.0$ and $\varphi_i = 180^o$, as shown in Fig. 2. The agreement is excellent. Fig. 3 shows the echo width for nihility elliptic cylinder for both TM and TE cases with an incident angle of $\varphi_i = 180^o$. The electrical dimensions of the cylinder are $k_o a = 2.5$, $k_o b_1 = 1.25$. It can be seen that the TM and TE cases for nihility cylinders have equal widths. The nihility cases also have higher echo width values in the backward directions when compared to the PEC cases. Fig. 4 shows a similar case with an incident of $\phi_i = 90^o$.

4. CONCLUSION

Analytical solution of the electromagnetic wave scattering by nihility elliptic cylinder is obtained for TM and TE polarizations. The solution is general where the special case of nihility circular cylinder may be obtained by letting the axial ratios approximately equal to 1.0 while the special case of nihility strip may be obtained by letting the thickness of the cylinder vanishes (letting the minor axis of the inner cylinder approaches zero). It was shown that the echo width for both TM and TE polarizations are equal for circular and elliptic nihility cylinders.

ACKNOWLEDGMNETS

The authors wish to acknowledge the support provided by the United Arab Emirates University and University of Sharjah.

REFERENCES

1. Lakhtakia, A. and J. B. Geddes III, "Scattering by a nihility cylinder," *AEÜ*, Vol. 61, No. 1, 62–65, 2007.
2. Lakhtakia, A., "Scattering by a nihility sphere," *Microwave Opt. Technol. Lett.*, Vol. 48, No. 5, 895-896, 2006.
3. M.I. Hussein and A-K. Hamid, "Electromagnetic scattering by a lossy dielectric elliptic cylinder", J. of electromagnetic waves and applications, vol. 15, no. 11, pp. 1469-1482, 2001.

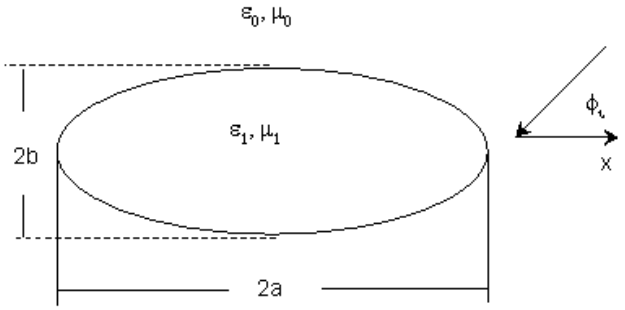


Fig. 1 Geometry of the scattering problem.

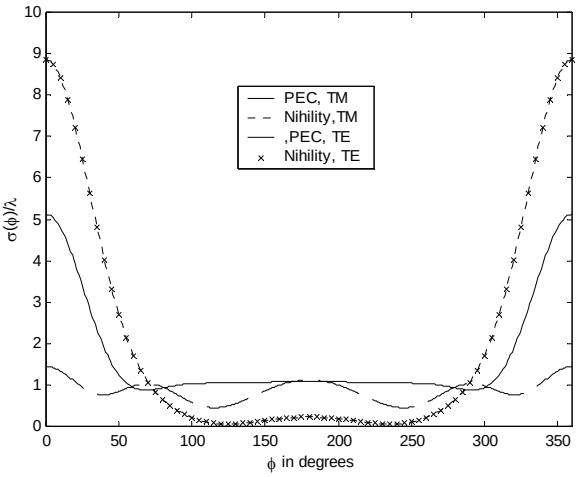


Fig. 2 Echo width against ϕ for nihility circular cylinder with $k_o a = 2.0$, $\varphi_i = 180^o$.

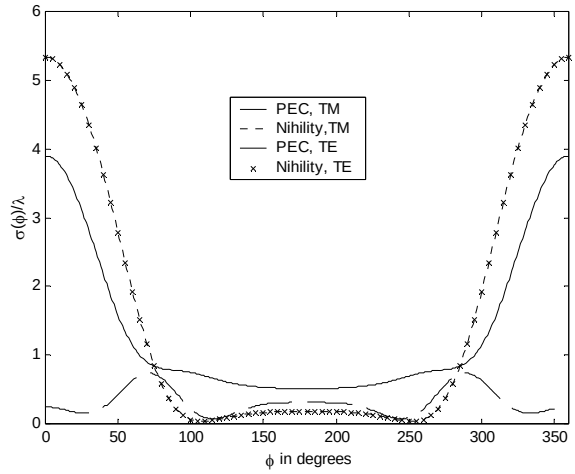


Fig. 3 Echo width against ϕ for nihility elliptic cylinder with $k_o a = 2.50$, $k_o b = 1.25$ and $\varphi_i = 180^o$.

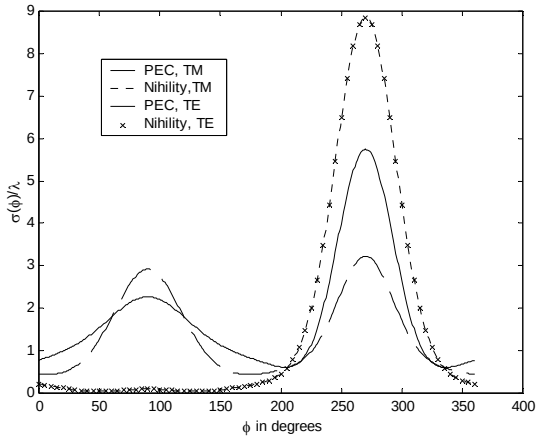


Fig. Echo width against ϕ for nihility elliptic cylinder with $k_o a = 2.50$, $k_o b = 1.25$ and $\varphi_i = 90^o$.

TM Scattering by a Perfect Electromagnetic Conducting Strip

A.-K. Hamid[1*] **and M. I. Hussein**[2]
[1]Department of Electrical & Computer Engineering, University of Sharjah,
P.O. Box 27272, Sharjah, United Arab Emirates
[2] Department of Electrical Engineeringl, United Arab University,
P.O. Box 17555, Al-Ain, United Arab Emirates
[*]corresponding author: akhamid@sharjah.ac.ae

Abstract: Analytic solution to the problem of scattering by an infinitely long perfect electromagnetic conducting (PEMC) strip is obtained using the method of separation of variables. The scattering widths can be enhanced/reduced by choosing appropriate values of PEMC admittance.

1. INTRODUCTION

Recently, there has been a lot of interest in the literature on research related to perfect electromagnetic conducting objects. Exact solutions to scattering by PEMC objects of many canonical shapes such as circular and elliptic cylinders have already been presented [1-2]. In this paper, we present an analytic solution to the problem of scattering of a plane wave from an infinitely long perfect electromagnetic conducting strip (which is another object of canonical shape), using the method of separation of variables. The problem is formulated by expanding the incident as well as the scattered electromagnetic fields in terms of appropriate angular and radial Mathieu functions and a set of expansion coefficients. The incident field expansion coefficients are known, but the scattered field expansion coefficients are to be determined. Imposing boundary conditions at the surface of the strip in terms of the PEMC admittance parameter *M* leads to an analytical determination of the scattered field expansion coefficients in closed form.

The solution to scattering of a plane wave from a PEC strip is obtained from that of the PEMC strip of a corresponding size, in the limit when *M* goes to plus or minus infinity (The final solution has only the even Mathieu functions as the odd Mathieu functions are zero at surface of the strip (ξ = 1), while that for a PMC strip is obtained when *M* = 0 (The final solution has only the odd Mathieu functions as the even Mathieu functions are zero at surface of the strip (ξ = 1). Nnumerical results are presented as normalized echo pattern widths for PEMC strip with different admittance values and incident angles, for TM polarization of the incident.

2. FORMULATION OF THE SCATTERING PROBLEM

Consider the case of a linearly polarized electromagnetic plane wave incident on dielectric elliptic cylinder at an angle ϕ_i with respect to the positive x axis, as shown in Figure 1. The strip has width donated by a . It is convenient to define the *x* and *y* coordinates of the Cartesian coordinate system in terms of *u* and *v* coordinates of an elliptical coordinate system also located at the centre of the cylinder in the form of $x = F\cosh u\cos v$ and $y = F\sinh u\sin v$. A time dependence of $e^{j\omega t}$ is assumed throughout the analysis, but suppressed for convenience. The electric field component of the TM polarized plane wave of amplitude E_0 is given by

$$E_z^i = E_0 e^{jk\rho\cos(\varphi-\varphi_i)} \tag{1}$$

where k is the wave number in free space and $j=\sqrt{-1}$. Let the elliptic cylindrical vector wave functions $\mathbf{N}$ and $\mathbf{M} = k^{-1}(\nabla\times\mathbf{N})$ be defined as

$$\mathbf{N}_{qm}^{(i)}(c,\xi,\eta) = \hat{z}\, R_{qm}^{(i)}(c,\xi) S_{qm}(c,\eta) \tag{2}$$

$$\mathbf{M}_{qm}^{(i)}(c,\xi,\eta) = \frac{1}{kh}\left[\hat{u} R_{qm}^{(i)}(c,\xi) S_{qm}^{'}(c,\eta) - \hat{v} R_{qm}^{(i)'}(c,\xi) S_{qm}(c,\eta)\right] \tag{3}$$

where q=e,o, S_{qm} and $R_{qm}^{(i)}$ are the even and odd angular and radial Mathieu functions of the *ith* kind, both of m order, respectively, $\xi = \cosh u$, $\eta = \cos v$, $c = kF$, $\hat{k}$ denotes a unit vector in the positive k direction, the prime on *S* and *R* denotes their respective derivative with respect to *v* and *u*, and $h = F\sqrt{\xi^2 - \eta^2}$.

The incident electric fields may be expressed in terms of $\mathbf{N}_{qm}^{(1)}$ as

$$\mathbf{E}^i = \sum_{m=0}^{\infty} A_{em}\, \mathbf{N}_{em}^{(1)} + \sum_{m=1}^{\infty} A_{om}\, \mathbf{N}_{om}^{(1)} \tag{4}$$

where the incident field expansion coefficients are given in [2]. Similarly, the incident magnetic fields may be expressed in terms of $\mathbf{M}_{qm}^{(1)}$ as

$$\mathbf{H}^i = \frac{j}{z}\left[\sum_{m=0}^{\infty} A_{em}\, \mathbf{M}_{em}^{(1)} + \sum_{m=1}^{\infty} A_{om}\, \mathbf{M}_{om}^{(1)}\right] \tag{5}$$

where z is the wave impedance of the region surrounding the strip. The scattered electric field has both co-polarized and cross-polarized field components as the strip is made of PEMC material. Thus, the scattered electric field may be expanded in terms of $\mathbf{N}_{qm}^{(4)}$ and $\mathbf{M}_{qm}^{(4)}$ as

$$\mathbf{E}^s = \sum_{m=0}^{\infty}\left[B_{em}\, \mathbf{N}_{em}^{(4)} + C_{em}\, \mathbf{M}_{em}^{(4)}\right] + \sum_{m=1}^{\infty}\left[B_{om}\, \mathbf{N}_{om}^{(4)} + C_{om}\, \mathbf{M}_{om}^{(4)}\right] \tag{6}$$

where B_{em}, C_{em}, B_{om}, C_{om} are the unknown scattered field coefficients. Similarly, the scattered magnetic field may be written as

$$\mathbf{H}^s = \frac{j}{z}\left(\sum_{m=0}^{\infty}\left[B_{em}\, \mathbf{M}_{em}^{(4)} + C_{em}\, \mathbf{N}_{em}^{(4)}\right] + \sum_{m=1}^{\infty}\left[B_{om}\, \mathbf{M}_{om}^{(4)} + C_{om}\, \mathbf{N}_{om}^{(4)}\right]\right) \tag{7}$$

The unknown expansion field coefficients may be determined in closed form by imposing the tangential boundary conditions at the surface of the strip at $\xi = 1$ as

$$H_z^i + H_z^r + H_z^s + M\,(E_z^i + E_z^r + E_z^s) = 0 \tag{8}$$

$$H_v^i + H_v^r + H_v^s + M\,(E_v^i + E_v^r + E_v^s) = 0 \tag{9}$$

Substituting the appropriate equations in (8) and (9) and using the orthogonality property of the angular Mathieu functions, we obtain

$$\frac{j}{z} C_{\substack{em \\ om}} R_{\substack{em \\ om}}^{(4)}(c,1) + M A_{\substack{em \\ om}} R_{\substack{em \\ om}}^{(1)}(c,1) + M B_{\substack{em \\ om}} R_{\substack{em \\ om}}^{(4)}(c,1) = 0 \tag{10}$$

$$\frac{1}{jkhz} A_{\substack{em \\ om}} R_{\substack{em \\ om}}^{(1)'}(c,1) + \frac{1}{jkhz} B_{\substack{em \\ om}} R_{\substack{em \\ om}}^{(4)'}(c,1) - \frac{1}{kh} C_{\substack{em \\ om}} R_{\substack{em \\ om}}^{(4)'}(c,1) = 0 \tag{11}$$

solving for $B_{\substack{em \\ om}}$ and $C_{\substack{em \\ om}}$ from equations (10) and (11), we obtain

$$B_{em} = -\frac{z^2 M^2 R_{em}^{(1)}(c,1)}{(1 + M^2 z^2) R_{em}^{(4)}(c,1)} A_{em} \tag{12}$$

$$B_{om} = -\frac{R_{om}^{(1)'}(c,1)}{(1 + M^2 z^2) R_{om}^{(4)'}(c,1)} A_{om} \tag{13}$$

$$C_{em} = -\frac{jMzR_{em}^{(1)}(c,1)}{(1+M^2z^2)R_{em}^{(4)}(c,1)}A_{em} \tag{14}$$

$$C_{om} = \frac{jMzR_{om}^{(1)'}(c,1)}{(1+M^2z^2)R_{om}^{(4)'}(c,1)}A_{om} \tag{15}$$

3. NUMERICAL RESULTS

Results obtained are presented as normalized bistatic and backscattering widths for PEMC strip of electrical width $ka = 2.0$, several values of the PEMC admittance *M*, expressed in the form of the dimensionless parameter *MZ*, defined by $MZ = \tan\theta$. Accordingly, $\theta = 0^o$ corresponds to a perfect magnetic conducting (PMC) cylinder while $\theta = 90^o$ to a perfect electric conducting (PEC) strip. Fig. 2 shows the normalized backscattering width versus the incident angle for a PEMC strip with electrical width $ka = 2.0$ and θ is varied form 0° to 90° . Figure 3 shows the variation of the normalized bistatic scattering width against the scattering angle for the same dimension considered in Fig. 2, at incident angle of 0^0, and the same values of admittance. Fig. 4 is similar to Fig. 3 but the incident angle is 90^0.

4. CONCLUSION

An analytic solution to the problem of scattering of a plane wave by PEMC strip has been obtained using the method of separation of variables, for the TM case. Results have been presented as normalized bistatic and back-scattering widths for strips with different PEMC admittance values. It was shown that the backscattering width is enhanced or reduced for some specific values of admittance values.

ACKNOWLEDGMNETS

The authors wish to acknowledge the support provided by the United Arab Emirates University and University of Sharjah.

REFERENCES

[1] Ruppin, R.: 'Scattering of electromagnetic radiation by a perfect electromagnetic conductor cylinder', J. Electromag. Waves Appl., 2006, 20, (13), pp. 1853–1860.

[2] Hamid, A-K., and Cooray, F.R.: "Scattering by a Perfect Electromagnetic Conducting Elliptic Cylinder" Progress In Electromagnetic Research, PIER, Vol. 10, 59-67, 2009.

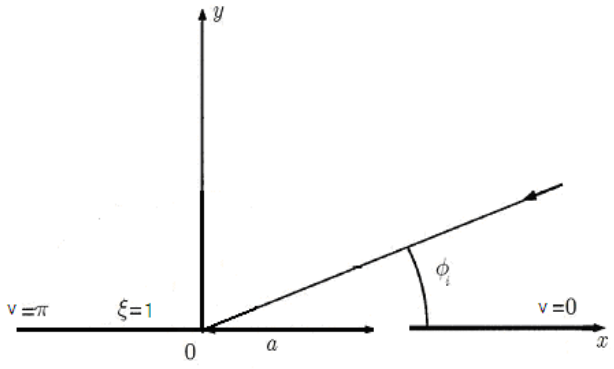


Fig. 1 Geometry of the scattering problem.

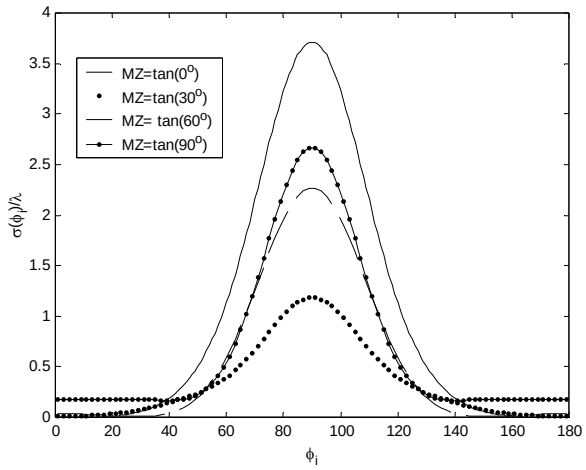


Fig. 2 Normalized backscattering width against incident angle ϕ_i for PEMC strip with $ka = 2.0$.

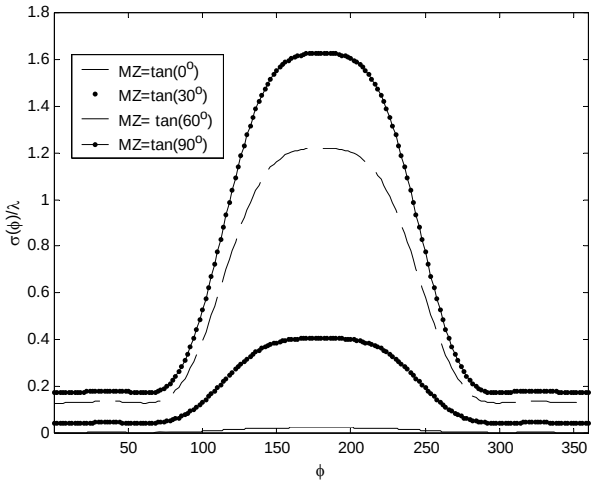


Fig. 3 Normalized bistatic scattering width against ϕ for PEMC strip with $ka = 2.0$ and $\phi_i = 0^o$.

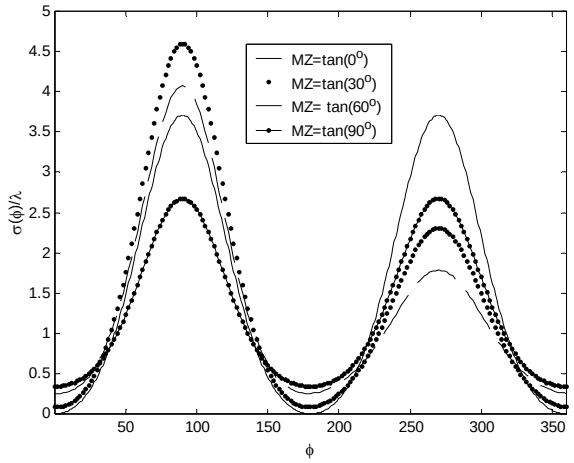


Fig. 4 Normalized bistatic scattering width against ϕ for PEMC strip with $ka = 2.0$ and $\phi_i = 90^o$.

Sensitivity enhancement in optical waveguide sensors using metamaterials

Sofyan A. Taya* **and Mohammed M. Shabat**

Physics Department, Islamic University, Gaza, P.O.Box 108, Gaza Strip, Palestine.

*corresponding author: staya@iugaza.edu.ps

Abstract- We consider a four-layer waveguide structure as an optical waveguide sensor. One of the layers is a metamaterial with negative permittivity and permeability. We show that the sensitivity of the proposed optical waveguide sensor can be dramatically enhanced by using a metamaterial layer between the guiding and the cladding layers. The variation of the sensitivity of the proposed waveguide sensor with different parameters of the waveguide is studied.

1. INTRODUCTION

The non-communication applications of slab waveguides as optical sensors have drawn considerable attention in the past few years [1,2]. The use of slab waveguides as optical sensors offers numerous advantageous features such as small size, ruggedness, potential for realizing various optical functions on a single chip (integration with other optical components), multi-channel sensing etc. In one class of commonly used optical waveguide chemical sensors, an analyte (the material to be detected) is placed in the evanescent field of the waveguide. As a result, changes take place in the absorption or in the phase of the electromagnetic wave propagating in the structure. Measuring this change between the analyte and a reference material is used to determine the change in the effective refractive index N of the waveguide structure. The measured change in the effective refractive index allows one to determine the refractive index of the analyte through the characteristic equation of the optical waveguide structure. Optical waveguide sensors have been used in a wide range of applications such as detection of harmful gases (methane, SO_2), monitoring pollutants and other compounds in water, pH detection, and detection of certain chemicals in blood.

Recently, the concept of double-negative (negative ε and negative μ) materials has achieved remarkable importance due to the exhibition of unusual electromagnetic properties different from the known materials. These phenomena are observed in microwave, millimeter-wave, and optical frequency bands. The materials of double negativity are called metamaterials or Left-Handed Materials (LHMs). The history of these materials begins with the work of Veselago [3], who proposed a medium with simultaneously negative ε and μ and studied the propagation of electromagnetic waves in such a medium. Pendry et al [4] presented the artificial metallic construction of periodic rods which shows negative permittivity and they also presented a structure of split rings which exhibits a negative permittivity [5]. Smith et al [6] constructed a LHM using the combination of periodic rods and split rings and they performed many experiments in the microwave range to point out that the nature of this material is unlike any existing material. The first experimental investigation of negative index of refraction was achieved by Shelby et al in 2001 [7]. The interaction of electromagnetic waves with stratified isotropic LHMs was studied by Kong [8]. The theory of LHMs and their electromagnetic properties, possible future applications, physical remarks, and intuitive justifications are provided by Engheta in 2003 [9]. Chew [10] analyzed the energy conservation property of a LHM and the realistic Sommerfeld problem of a point source over a LHM half space and a LHM slab. In 2006, Sabah et al [11] studied the effects of the structure parameters,

incidence angle, and the frequency on the reflected and transmitted powers for lossless LHM. The electromagnetic wave propagation through frequency-dispersive and lossy double-negative slab embedded between two different semi-infinite media was presented in 2007 [12].

In this work, we show that the sensitivity of the slab waveguide sensors can be dramatically enhanced by inserting a layer of left-handed material between the cladding and the guiding layer.

2. THEORY

We consider a guiding layer with permittivity ε_f, permeability μ_f and thickness d_1 is sandwiched between a semi-infinite substrate with permittivity ε_s and permeability μ_s and a semi-infinite cladding with permittivity ε_c and permeability μ_c. An additional layer of metamaterial with negative permittivity ε_m, negative permeability μ_m and thickness d_2 is inserted between the cladding and the guiding layer. All the materials are assumed to be lossless. We also consider s-polarized (TE) waves in which the electric field $\boldsymbol{E}$ is polarized along the y-axis. It's straightforward to show that the dispersion relation of the structure is given by

$$g_f d_1 = \arctan\left(\frac{g_s m_f}{g_f m_s}\right) + \arctan\left(\frac{g_m m_f}{g_f m_m}\frac{(g_m m_c + g_c m_m) - (g_m m_c - g_c m_m)e^{-2g_m d_2}}{(g_m m_c + g_c m_m) + (g_m m_c - g_c m_m)e^{-2g_m d_2}}\right) + mp, \tag{1}$$

where $g_c = \sqrt{b^2 - e_o e_c m_c w^2}$, $g_m = \sqrt{b^2 - e_o e_m m_m w^2}$, $g_f = \sqrt{e_o e_f m_f w^2 - b^2}$, and $g_s = \sqrt{b^2 - e_o e_s m_s w^2}$. m = 0,1,2,… is the mode order and β is the propagation constant in x-direction.

For the sake of simplicity in the evaluation of the sensitivity, we assume the cladding, the film and the substrate are nonmagnetic materials and the permeability of the metamaterial is given by $\mu_m = n\mu_o$, where n is a negative number. We also assume $g_c = k_o q_c$, $g_m = k_o q_m$, $g_f = k_o q_f$, and $g_s = k_o q_s$, where k_o is the free space wave number, $q_c = \sqrt{N^2 - e_c}$, $q_m = \sqrt{N^2 - n e_m}$, $q_f = \sqrt{e_f - N^2}$, and $q_s = \sqrt{N^2 - e_s}$. To obtain the sensitivity of the proposed sensor in a condensed form, we define three normalized effective indices X_s, X_c, and X_m and three asymmetry parameters a_s, a_c, and a_m as

$$X_s = \frac{q_s}{q_f},\ X_c = \frac{q_c}{q_f},\ X_m = \frac{q_m}{q_f},\ a_s = \frac{e_s}{e_f},\ a_c = \frac{e_c}{e_f} \text{ and } a_m = \frac{e_m}{e_f} \tag{2}$$

In the light of these assumptions, Eq. (1) can be written as

$$k_o q_f d_1 = \arctan(X_s) + \arctan\left(\frac{X_m}{n}\frac{b_1}{b_2}\right) + mp, \tag{3}$$

where $b_1 = (X_m + nX_c) - (X_m - nX_c)e^{-2k_o X_m q_f d_2}$ and $b_2 = (X_m + nX_c) + (X_m - nX_c)e^{-2k_o X_m q_f d_2}$.

In the case of homogenous sensing, the sensitivity is defined as the rate of change of the modal effective index N under an index change of the cover n_c. The sensitivity $S_2 = \partial N / \partial n_c$ of the proposed sensor is calculated by differentiating Eq. (3) with respect to N. After some algebraic manipulations the sensitivity can be written as

$$S_2 = \frac{\sqrt{a_c}\sqrt{1 + X_c^2}X_m[b_2 - b_1 + e^{-f}(b_1 + b_2)]}{X_c\sqrt{a_c + X_c^2}[(A_{mTE} + \frac{1}{X_s})(b_2^2 + \frac{X_m^2 b_1^2}{n^2}) + G_1 + G_2 + \frac{b_1 b_2 C_1}{nX_m}]} \tag{4}$$

where $f = 2k_o X_m q_f d_2$, $G_1 = (b_2 - b_1)(\frac{C_1}{n} + \frac{C_2 X_m}{X_c})$, $G_2 = \frac{e^{-f}(b_1 + b_2)}{n}[\frac{(X_m - nX_c)f}{X_m} - C_1 + \frac{C_2 X_m n}{X_c}]$,

$A_{mTE} = \arctan(X_s) + \arctan(\frac{X_m}{n}\frac{b_1}{b_2}) + mp$, $C_1 = 1 + X_m^2$, and $C_2 = 1 + X_c^2$.

As d_2 approaches zero, i.e., no metamaterial is available, Eq. (4) reduces to

$$S_1 = \frac{\sqrt{a_c}}{X_c\sqrt{a_c + X_c^2}\sqrt{1 + X_c^2}(\arctan(X_s) + \arctan(X_c) + mp + \frac{1}{X_c} + \frac{1}{X_s})} \tag{5}$$

Eq. (5) gives sensitivity of the conventional three-layer waveguide sensor without the left-handed material.
To evaluate the enhancement effect due to the left-handed material, we define the sensitivity enhancement factor F_{en} as $F_{en} = S_2 / S_1$.

3. RESULTS AND DISCUSSION

In the analysis below we will assume the guiding layer to be Si_3N_4 ($\varepsilon_f = 4$), the free space wavelength to have the value 1550nm, and m = 0 which corresponds to the fundamental mode. We will also assume $g_c m_m = -g_m m_c$ which corresponds to the surface polariton conditions at the boundary between the metamaterial and the dielectric cladding [13].

In Fig. 1 the sensitivity of the proposed sensor is shown as a function of the guiding layer thickness d_1. When the guiding layer thickness approaches the cutoff thickness, the effective refractive index approaches the substrate refractive index, the penetration depth of the evanescent field into the substrate medium becomes infinite, and the total power of the mode flows mainly in the substrate. In this case the sensitivity of the sensor approaches zero. For thick waveguides, the sensitivity decreases to zero again because the power of the guided mode flows mainly in the guiding layer itself. The effective refractive index approached the guiding layer refractive index. The figure shows that the sensitivities have their maxima between these two limits at waveguide thickness somewhat higher than the cutoff thickness of the guided mode considered. Moreover, Fig. 1 shows a comparison between the sensitivity of the proposed sensor with the left-handed medium and the sensitivity of conventional three-layer waveguide sensors. As can be seen, the presence of the left-handed material can considerably enhance the sensitivity.
The variation of the sensitivity S_2 with the thickness of the metamaterial is shown in Figs. 2. The sensitivity increases with the increasing of the thickness of the metamaterial. The sensitivity enhancement with the thickness of the metamaterial can be interpreted by surface polariton effects: the evanescent wave generated at the metamaterial-guiding layer interface excites a surface wave at the metamaterial-cladding interface. The fields intensities in both the metamaterial and the cladding keep on building until the boundary conditions of Maxwell equations are satisfied for the whole waveguide structure.
Fig. 3 shows the sensitivity enhancement factor versus the thickness of the left-handed material for different values of μ_m. As can seen, the sensitivity enhancement factor increases with the thickness of the metamaterial due to the generation of the surface polaritons as we discussed above. Also for a given metamaterial thickness, the sensitivity enhancement factor increases as $|m_m|$ increases. To obtain a given sensitivity enhancement factor, a smaller thickness of the metamaterial is required as $|m_m|$ increases.

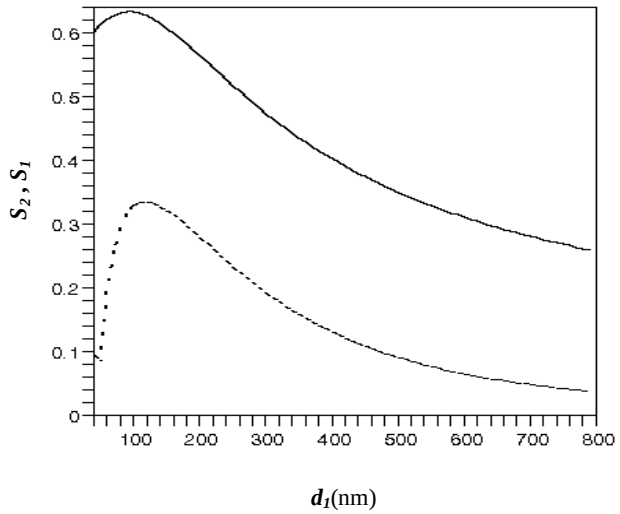


Figure 1. Sensitivity versus the guiding layer thickness d_1 for a_s = 0.62, a_c = 0.6, a_m = -0.5, n = -0.6 and d_2 = 80nm for the proposed sensor with the metamaterial (solid line) and a conventional three-layer waveguide sensor without the metamaterial (dotted line).

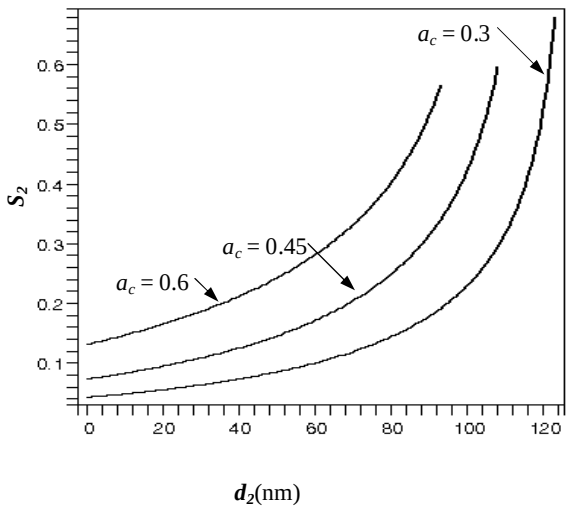


Figure 2. Sensitivity S_2 versus the thickness of the metamaterial d_2 for different values of a_c, a_s = 0.62, a_m = -0.5, and n = -0.6.

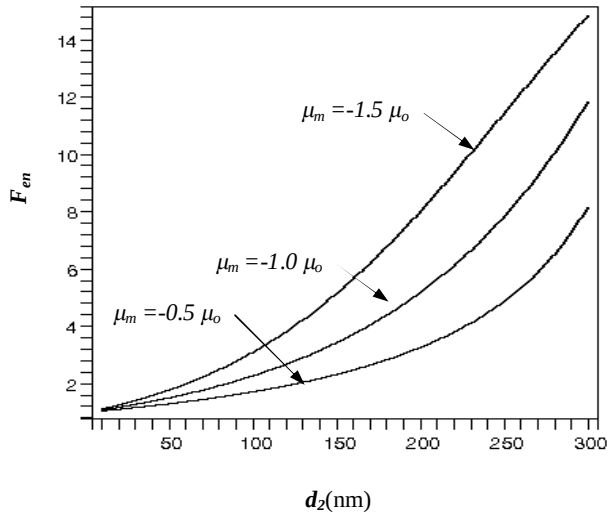


Figure 3. The sensitivity enhancement factor as a function of the thickness of the metamaterial for different values of n, a_c = 0.6, a_s = 0.62, and d_1 = 400nm.

4. CONCLUSION

We have analytically proved that the sensitivity of waveguide optical sensors can be enhanced when there is a layer of left-handed material between the cladding layer and the guiding layer. We believe that metamaterials with simultaneously negative dielectric permittivity and magnetic permeability could be used to improve the performance of waveguide chemical and biochemical sensors.

REFERENCES

1. Taya, S. A., M. M. Shabat, H. Khalil, and D. Jäger, "Theoretical Analysis of TM Nonlinear ymmetrical Waveguide Optical sensors," *Sens and Actuators A.,* Vol. 147, 137-141, 2008.
2. Horvath, R., H. Pederson, and N. Larsen, "Demonstration of reverse symmetry waveguide sensing in aqueous solutions," *App. Phys. Lett.,* Vol. 81, No. 12, 2166-2168, 2002.
3. Veselago, V. "The electrodynamics of substance with simultaneously negative values of ε and μ," *Sov. Phy. Usp.,* Vol. 10, 509-514, 1968.
4. Pendry , J. B., A. J. Holden, W. J. Stewart, and I. Youngs, "Extremely low frequency plasmons in metallic mesostructures," *Phys. Rev. Lett.,* Vol. 76, 4773-4776, 1996.
5. Pendry, J. B., A. J. Holden, W. J. Stewart, and I. Youngs, "Extremely low frequency plasmons in metallic mesostructures," *Phys. Rev. Lett.,* Vol. 76, 4773-4776, 1996.
6. Smith, D. R., W. J. Padilla, D. C. Vier, S. C. Nemat-Nasser, and S. Schults, "Composite medium with simultaneously negative permeability and permittivity," *Phys. Rev. Lett.,* Vol. 84, 4184-4187, 2000.
7. Shelby, R. A., D. R. Smith, and S. Schults, "Experimental verification of a negative index of refraction," *Science,* Vol. 292, 77-79, 2001.
8. Kong, J. A., "Electromagnetic wave interaction with stratified negative isotropic media," *Progress in Electromagnetic research,* Vol. 35, 1-52, 2002.
9. Engheta, N., "Metamaterials with negative permittivity and permeability: background, salient features, and new trends," *IEEE MTT_S Int. Microwave Symp. Digest,* Vol. 1, 187-190, 2003.

10. Chew, W. C., "Some reflections on double negative materials," *Progress in Electromagnetic research*, Vol. 51, 1-26, 2005.
11. Sabah, C., G. Ogucu, and S. Uckun, "Reflected and transmitted powers of electromagnetic wave through a doubl-negative slab," *J. Optoelectronics and Advanced Materials*, Vol. 8, 1925-1930, 2006.
12. Sabah, C., and S. Uckun, "Electromagnetic wave propagation through frequency-dispersive and lossy double-negative slab," *Optoelectronics Rev.*, Vol. 15, No. 3, 133-143, 2007.
13. Ruppin, R., "Surface polaritons of a left-handed medium," *Phys. Lett. A*, Vol. 227, 61-64, 2000.

Electromagnetic response of a slit diffraction grating embedded in a dielectric slab via an equivalent circuit model

R. Rodríguez-Berral[1], **F. Mesa**[1], **and F. Medina**[2]

[1] Dep. of Applied Physics 1, University of Seville, Spain
[2] Dep. of Electronics & Electromagnetism, University of Seville, Spain
rrberral@us.es, mesa@us.es, medina@us.es

Abstract— This paper provides an equivalent circuit model to characterize the electromagnetic transmission properties of an array of slits sandwiched between a pair of dielectric slabs. The presence of the dielectric slabs makes the electromagnetic spectrum much more complex than that without slabs. Fortunately, all the details of the spectrum can be accounted for by adding appropriate lumped and distributed elements to a previous equivalent circuit presented by some of the authors, which was valid for free standing diffraction gratings.

1. INTRODUCTION

Since the experimental observation of extraordinary optical transmission through 2-D periodic arrays of holes in metallic films [1], a lot of effort has been devoted to the analysis of the electromagnetic response of a variety of periodically perforated or structured surfaces. As a particular case, the issue of the transmission properties of slit diffraction gratings (1-D periodic surfaces) has received a renewed attention in the last few years (see [2, 3] and references therein). Among the unexpected characteristics of these gratings we can emphasize (i) extraordinary transmission peaks associated with the periodicity of the structure and (ii) the presence of total transmission bands with some centered/off-centered transmission dips (provided electrically thick screens and compound gratings with more than one slit per period are considered). In the Optics frame, these phenomena were completely accounted for by full dynamic diffraction theories [2]. Although these theories provide some physical insight into the shape of the transmission spectra, they are complex and it can be said that they mostly provide a "numerical" explanation. A simple and easy physical understanding of the problem would be welcome. Fortunately, all the above mentioned phenomena have also been perfectly explained by the simplified equivalent circuit model reported in [4]. The equivalent circuit is composed by a simple network of transmission lines and some appropriate capacitances. When the slit thickness is almost negligible, the only "anomalous" phenomenon that appears is the expected total reflection due to the Wood's anomaly, and this is accounted for by the equivalent circuit model. Nevertheless, if the slitted diffraction grating incorporates the presence of dielectric slabs in the front and/or back sides of the perforated metal screen, the transmission spectrum becomes much more complex. This is due to the appearance of new phenomenology; in particular, new total-reflection and total-transmission effects. In this paper we will present some modifications of our original circuit model [4] that are able to account for all the details of the modified transmission characteristics. More specifically, we add a shunt capacitance-loaded transmission line to account for the excitation of possible high-order modes in the dielectric slab.

2. CIRCUIT MODEL

The general structure under analysis consists of a periodic array of slits on a perfect conducting screen sandwiched between two different dielectric slabs, excited by an impinging TEM wave at normal incident and with the electric field directed perpendicular to the slits. Due to the symmetries of the structure and the orientation of the impinging electric field, we can place perfect electric walls (EW's) at the middle planes between adjacent slits. The original problem is thus reduced to a waveguide discontinuity problem, namely, an iris in a parallel plate waveguide (the plates are any two adjacent EW's) as shown in Fig. 1. Due to the presence of the dielectric slabs in the original problem, the waveguide has different dielectric regions at both sides of the discontinuity. The propagation of the incident, transmitted and reflected TEM waves along the different dielectric regions can be reproduced by transmission line segments with different characteristic impedances.

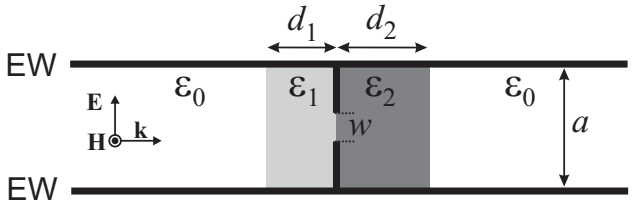


Figure 1: Equivalent waveguide discontinuity problem for normal incidence on a periodic array of slits sandwiched between two dielectric slabs.

In order to model the effect of the discontinuity, an equivalent circuit is introduced between the transmission line segments that represent the dielectric regions. The resulting transmission line model and the equivalent circuit proposed is shown in Fig. 2 and explained next.

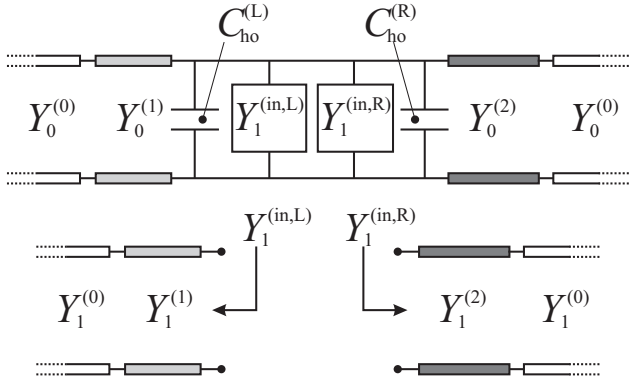


Figure 2: Transmission line and equivalent circuit model for the waveguide problem in Fig. 1.

The characteristic admittance of each transmission line segment that model the propagation of the TEM mode is given by the wave admittance of the corresponding media, namely

$$Y_0^{(i)} = \eta_i^{-1} = \frac{\sqrt{\varepsilon_{ri}}}{\eta_0} \,, \tag{1}$$

where ε_{ri} is the relative permittivity of the medium and η_0 is the free-space wave admittance. The equivalent circuit that models the perforated screen consists of a parallel connection of admittances, each one representing the excitation of high-order modes at one side of the discontinuity (in the problem under consideration, only even-order TM modes are excited). These admittances are proportional to the input admittance to the transmission line that represents the propagation of the corresponding high-order mode. Thus, the admittance associated with the TM_{2n} mode ($n \geq 1$) at the left/right hand side of the discontinuity is given by

$$Y_n^{\mathrm{in,L/R}} = A_n^{\mathrm{L/R}} Y_n^{(1/2)} \frac{Y_n^{(0)} + \mathrm{j} Y_n^{(1/2)} \tan(\beta_n^{(1/2)} d_{1/2})}{Y_n^{(1/2)} + \mathrm{j} Y_n^{(0)} \tan(\beta_n^{(1/2)} d_{1/2})} \,, \tag{2}$$

where $A_n^{\mathrm{L/R}}$ is a coefficient that accounts for the degree of excitation of the TM_{2n} mode, $\beta_n^{(i)}$ is its propagation wavenumber in the i-th dielectric region and the characteristic admittances $Y_n^{(i)}$ are given by the wave admittance of the TM_{2n} mode in the i-th dielectric region, namely,

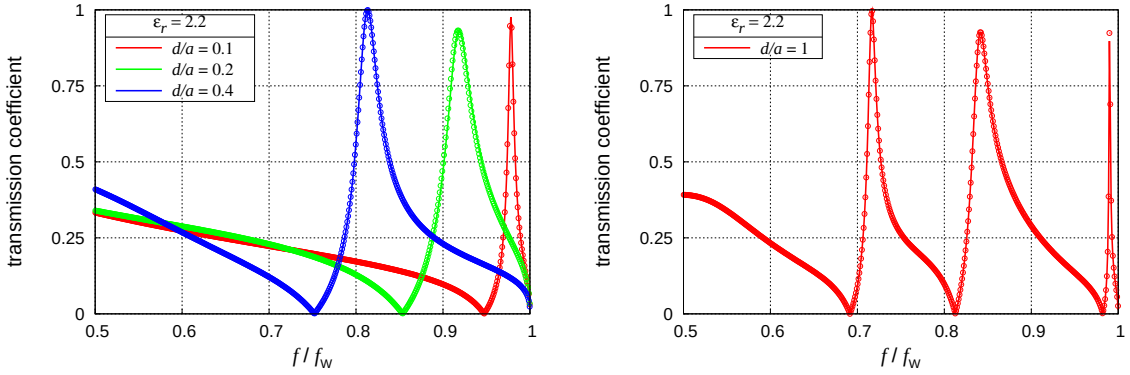
$$Y_n^{(i)} = \frac{1}{\eta_i \sqrt{1 - (f_n^{(i)}/f)^2}} \quad \text{with} \quad f_n^{(i)} = \frac{n}{\sqrt{\varepsilon_{ri}}} \frac{c}{a} \,. \tag{3}$$

In this last equation, $f_n^{(i)}$ is the cutoff frequency of the n-th high-order mode in the i-th dielectric region. The cutoff frequency of the TM_2 (the first high-order mode) in vacuum is $f_1^{(0)} = c/a$, which is commonly referred to as the Wood's anomaly frequency, f_{W}. For high-order modes whose cutoff

frequencies are well above the highest working frequency, it is easy to show that the corresponding input admittance behaves approximately as a linear function of frequency. Therefore, they can be regarded as capacitances. On the contrary, the complete frequency behavior given by Eqs. (2) and (3) must be taken into account for the admittances associated with high-order modes whose cutoff frequencies are below (or not far above) the highest frequency of interest (we will refer to these admittances as "frequency-dependent"). In Fig. 2 it has been assumed for simplicity that only the first high-order mode (at both the left and right hand side of the discontinuity) has to be considered as a frequency-dependent lumped element. The remaining higher-order modes ($n \geq 2$) are represented by the "higher-order capacitances" $C_{\mathrm{ho}}^{\mathrm{L}}$ and $C_{\mathrm{ho}}^{\mathrm{R}}$, which can in turn be grouped together as a global capacitance $C_{\mathrm{ho}} = C_{\mathrm{ho}}^{\mathrm{R}} + C_{\mathrm{ho}}^{\mathrm{L}}$. In general, it is found that a single frequency-dependent admittance at both sides is not enough to obtain accurate quantitative results. The number needed may vary depending on the permittivities and thicknesses of the dielectric slabs, but for practical values it is very rarely higher than three or four. In order to obtain numerical results using our model, we first need to compute the circuit parameters $A_n^{\mathrm{L/R}}$ and C_{ho}. These can be obtained from a few values of the scattering parameters provided by some independent full-wave analysis. For instance, if we are considering two frequency-dependent admittances at the left and one at the right hand side of the discontinuity, we will need four external values of the scattering parameters (at four different frequencies) to compute the four circuit parameters. Finally, it should be pointed out that the validity of the model proposed here is restricted to narrow slits.

3. NUMERICAL RESULTS AND DISCUSSION

In this section we will present some numerical results and interpret them in terms of the proposed circuit model. To make the discussion clearer, we will consider the case in which only one dielectric slab is present. Thus, Fig. 3 shows some numerical results of the transmission coefficient for a periodic array of slits printed on a dielectric substrate. First of all, it should be noted that the



(a) (b)

Figure 3: Transmission coefficient versus frequency for a periodic array of slits printed on a dielectric slab with relative permittivity $\varepsilon_r = 2.2$ for different slab thicknesses. The solid lines correspond to the values obtained with a full-wave numerical code based on the mode matching technique whereas the circles represent the results obtained with our model.

agreement between the results provided by our circuit model (circles) and those obtained with an independent code based on mode matching (solid lines) is excellent in all the cases shown. One feature we can observe in all the spectra shown is that the transmission approaches zero at $f/f_{\mathrm{W}} = 1$ (the usual Wood's anomaly). In the cases shown in Fig. 3(a), there is an additional transmission zero at a lower frequency, and a transmission maximum between both transmission zeros. Both the additional transmission zero and the maximum move to lower frequencies as the dielectric slab becomes thicker. Fig. 3(b) shows that several alternating transmission zeros and maxima appear for even thicker slabs. All these features can be easily explained in terms of our circuit model as follows.

Since only one dielectric slab is present, one of the frequency-dependent admittances in the model is proportional to the wave admittance of the first high-order mode in free-space, $Y_1^{(0)}$. According to Eq. (3), this characteristic admittance diverges at $f = f_{\mathrm{W}}$, thus short-circuiting the

line and causing a total reflection.

The admittance corresponding to the first high-order mode at the dielectric side of the discontinuity will be given by Eq. (2) with $n = 1$. For frequencies slightly above the cutoff frequency of the TM_2 mode in the dielectric region, $f_1^{(1)} = c/(a\sqrt{\varepsilon_r})$, the $Y_1^{(1)}$ wave admittance is real and very large ($Y_1^{(1)} \to \infty$ at $f = f_1^{(1)}$), whereas $Y_1^{(0)}$ is capacitive (imaginary and positive). As a result, both addends in the denominator in Eq. (2) are real and have opposite sign. Taking into account that $Y_1^{(0)} \to \infty$ at $f = f_W$, there is necessarily a frequency value between $f_1^{(1)}$ and f_W at which the denominator in Eq. (2) vanishes. As a result, the admittance in the model becomes infinite and we have an additional transmission zero. At this transmission-zero frequency, the denominator changes its sign so that the admittance becomes inductive. Recalling that the remaining admittances in the equivalent circuit are capacitive and that the frequency-dependent admittance at the free-space side diverges at $f = f_W$, we conclude that there is some intermediate frequency at which the equivalent circuit constitutes a resonant LC tank (open circuit), which explains the transmission maxima observed in the graphs.

Finally, if the dielectric thickness is large enough, the tangents in Eq. (2) can complete several periods in the frequency range from $f_1^{(1)}$ to f_W, thus giving rise to the successive alternating zeros and maxima observed in Fig. 3(b).

4. CONCLUSION

This work has proposed a simple transmission-line and circuit model for the scattering of a normally incident plane wave on a metallic screen perforated with periodic slits and embedded in dielectric slabs. The model provides simple qualitative explanations of the main features of the transmission spectra of such structures, as well as accurate numerical results. These facts make the proposed circuit model a very interesting potential tool for the efficient analysis and/or design of slitted screens with different configurations of dielectric slabs.

ACKNOWLEDGMENT

This work has been supported by the Spanish Ministerio de Educación y Ciencia and European Union FEDER funds (projects # TEC2007-65376 and Consolider Ingenio 2010 CSD2008-00066).

REFERENCES

1. T. W. Ebbesen, H. J. Lezec, H. F. Ghaemi, T. Thio, and P. A. Wolff, "Extraordinary optical transmission through sub-wavelength hole arrays," *Nature*, vol. 391, pp. 667-669, Feb. 1998.
2. D. C. Skigin and R. Depine, "Transmission resonances of metallic compound gratings with subwavelength slits," *Phy. Rev. Lett.*, vol. 95, pp. 217402(1-4), 2005.
3. M. Navarro-Cía, D. C. Skigin, M. Beruete, and M. Sorolla, "Experimental demonstration of phase resonances in metallic compound gratings with subwavelength slits in the millimeter wave regime," *App. Phys. Lett.*, vol. 94, pp. 091107(1-3), March 2009.
4. F. Medina, F. Mesa, and D. C. Skigin, "Extraordinary Transmission Through Arrays of Slits: a Circuit Theory Model," *IEEE Trans. Microw. Theory Tech.*, vol. 58, pp. 105-115, Jan. 2010.

Analysis of a Transmission Line Periodically Loaded with Position-Modulated Loads

E. S. Sakr[1*], **and I. A. Eshrah**[1]

[1]Department of Electronics and Communications Engineering, Cairo University, Egypt
enas_sa2r@hotmail.com

Abstract— The dispersion characteristics of a periodically loaded transmission line is engineered via varying the amplitudes and/or positions of the periodic shunt loads. The band diagram of the periodic structure is obtained using two approaches: the Bloch-Floquet approach and a Green's function-based approach. The effect of both amplitude and position modulation on the band diagram is discussed, to provide a step to bandgap engineering of the structure.

1. INTRODUCTION

Periodic structures have wide applications in microwave and optical engineering due to their frequency selective properties and slow wave effect. The periodically loaded transmission line is a well-known problem that has been investigated in numerous books [1] [2]. Understanding this simple 1-D structure gives an insight that can be extended to 2-D and 3-D structures [3]. Special loading of such lines exhibits negative refractive index and negative group delay, which results in the so-called metamaterial transmission line [4]. The numerical and analytical study of the non-periodic excitation of periodic structures is a much more complicated problem. In [5], a closed-form expression for the Green's function of a periodically loaded transmission line excited by an aperiodic source is derived. In [6], the practical excitation of a shielded microstrip line periodically perturbed by gaps was studied through a numerical implementation of the array scanning method. The analysis of the periodically loaded transmission line with modulated loads is introduced in [7] where the effect of step-amplitude modulation is investigated on the dispersion characteristics. This work studies the effect of load position and amplitude modulation on the band diagram of the structure. The analysis of such structures provides the first step to engineer the bandgap of the structure by proper selection of the modulation function and type.

2. ANALYSIS OF PERIODICALLY LOADED TRANSMISSION LINE WITH MODULATED LOADS

The proposed structure shown in Fig.1 assumes an infinite transmission line loaded with N periodic shunt loads of normalized susceptance b_n and separated by distances p_n, to form a super-cell repeated periodically with a period $p_b = Np_0$, where:

$$b_n = b_0 + \Delta b_n, \tag{1}$$

$$p_n = p_0 + \Delta p_n. \tag{2}$$

The Bloch-Floquet Theorem Approach: By evaluating and multiplying the ABCD matrices of elements within the super-cell [1], considering p_b as the period of the structure, and since the structure is infinitely long, the dispersion relation may be obtained as the solution of the matrix determinant equation [1]:

$$\left| \prod_{n=1}^{N} \begin{bmatrix} (\cos kp_n - \frac{b_n}{2}\sin kp_n) & j(\sin kp_n + \frac{b_n}{2}(\cos kp_n - 1)) \\ j(\sin kp_n + \frac{b_n}{2}(\cos kp_n + 1)) & (\cos kp_n - \frac{b_n}{2}\sin kp_n) \end{bmatrix} - \begin{bmatrix} e^{j\beta p_b} & 0 \\ 0 & e^{j\beta p_b} \end{bmatrix} \right| = 0, \tag{3}$$

where β and k are the propagation constants of the loaded and unloaded line respectively.

The Green's Function Approach: To provide more physical insight of the problem, the derivations in [5] and [7] are used to express the voltage along the line in the form:

$$V(z) = \frac{jkZ_0}{p_b} \sum_{l=-\infty}^{\infty} \bar{g}(z; k_l)\tilde{s_0}(-k_l), \quad k_l = \beta + \frac{2l\pi}{p_b} \tag{4}$$

where $\bar{g}$ and $\tilde{s_0}$ are the Fourier transforms of the one dimensional Green's function and the equivalent source within the reference period respectively and are given by:

$$\bar{g}(z;\alpha) = \int_{-\infty}^{\infty} \frac{e^{-jk|z-z'|}}{2jk} e^{-j\alpha z'} dz' = \frac{e^{-j\alpha z}}{\alpha^2 - k^2} \tag{5}$$

$$\tilde{s_0}(\alpha) = \int_{-\infty}^{\infty} s_0(z) e^{-j\alpha z} dz = \sum_{n=1}^{N} -jb_n Y_0 V(z_n) e^{-j\alpha z_n}, \quad z_n = \sum_{l=1}^{n} p_l. \tag{6}$$

Substituting in (4), we get

$$V(z) = \sum_{n=1}^{N} b_n V(z_n) f(z - z_n; \beta), \tag{7}$$

where

$$f(z;\beta) = \frac{e^{-j\beta(z-\zeta)}}{2} \frac{\sin k(p_b - |\zeta|) + \sin k|\zeta| e^{-j\beta p_b \mathrm{sgn}(\zeta)}}{\cos kp_b - \cos \beta p_b}, \quad \zeta < p_b \tag{8}$$

where $\zeta = \mathrm{mod}(z, p_b)$. Then, substituting in (7) at the load positions within the reference period, we get a linear system of equations

$$\overline{\overline{\Lambda} V} = \overline{0}, \tag{9}$$

where $\Lambda_{mn} = b_n f(z_m - z_n; \beta) - \delta_{mn}$, $V_m = V(z_m)$, and $m, n = 1, 2, \ldots, N$. For non-trivial solution, the determinant of $\overline{\overline{\Lambda}}$ must equal zero. From this condition the dispersion relation and the null space vector $\overline{V}$ are obtained to express the source-free voltage along the line.

3. SPECIAL CASE: TWO STEP-MODULATED LOADS

Taking $N = 2$, i.e. two loads per period, and assuming amplitude modulation only, it is possible to determine the stopband edges that appear when βp_b equals odd multiples of π , since the off-diagonal elements of the matrix $\overline{\overline{\Lambda}}$ vanish. In this case, the stopband edges are the solutions of:

$$(\cos kp_b + 1 - \frac{b_1}{2} \sin kp_b)(\cos kp_b + 1 - \frac{b_2}{2} \sin kp_b) = 0, \quad p_b = 2p_0 \tag{10}$$

that are at: $b_1 \tan kp_0 = 2$ and $b_2 \tan kp_0 = 2$. Consequently, this bandgap disappears when the loads are equal, since the two solutions reduce to one solution. When βp_b equals even multiples of π the equation needs to be solved for k numerically, but in general, for load amplitude modulation, a band edge should appear at $kp_0 = m\pi$, $m = 0, \pm 1, \pm 2, \ldots$ [2].

4. RESULTS AND DISCUSSION

To illustrate the effect of amplitude and position modulation on the band structure, consider a periodic structure with $b_0 = 1$. In Fig.2(a), two amplitude-modulated loads are used with the following parameters: $b_1 = 0.5$, and $b_2 = 2$. While Fig.2(b) represents two position-modulated loads with the following parameters: $\Delta p_1 = 0.25 p_0$, and $\Delta p_2 = 0.75 p_0$.

Fig.3 to Fig.5 illustrate the effect of increasing N and changing the modulation function in both amplitude and position modulated structures.

All figures show that there are N different bandgaps within the range $0 < kp_0 < \pi$. The band diagram in Fig.2(a) shows the creation of a new bandgap, in the region $0 < kp_0 < \pi$, in correspondence with (10), while the second bandgap coincides with the bandgap of the average unmodulated structure, hence this structure realizes a dual band frequency selective structure. It is worth noting that this effect may be generalized to larger values of N, since in Fig.3(a) mini sub-bands are created at $\beta p_b = m\pi$, and grow larger when the differences between the values of the loads'susceptance increase (Fig.4). This means that changing the modulation function controls the bandwidths of the bandgaps. Hence, we can design a multi-band frequency selective structure, in which the main band corresponds to the average unmodulated structure, while the mini sub-bands correspond to the swing of the modulation function. Similar interpretations are noticed for the position modulated structure as in Fig.2(b), Fig.3(b), and Fig.5.

5. CONCLUSION

The dispersion curves of a periodically loaded transmission line with amplitude and position modulated loads are obtained. The selection of modulation type, modulation function and number of loads within the period was proved to change the band structure. The obtained results imply the ability to engineer the bandgap of any periodic structure such as microwave filters, EBG surfaces and frequency selective surfaces for multi-band applications by changing the design of the unit cell of the periodic structure.

REFERENCES

1. Pozar, D. M., *Microwave Engineering*, Wiley, New York, 2005.
2. Collin, R. E., *Foundations for Microwave Engineering*, Wiley, New York, 2001.
3. Boutayeb, H., T. A. Denidni, A. R. Sebak and L. Talbi, "Band structure analysis of crystals with discontinuous metallic wires," *IEEE Microw. Wireless Compon. Lett.*, Vol. 15, No. 7, 484–486, 2005.
4. Siddiqui, O. F., M. Mojahedi and G. V. Eleftheriades, "Periodically loaded transmission line with effective negative refractive index and negative group velocity," *IEEE Trans. Antennas Propag.*, Vol. 51, No. 10, 2619–2625, 2003.
5. Eshrah, I. A. and A. A. Kishk, "A Periodically loaded transmission line excited by an aperiodic source–A Green's function approach," *IEEE Trans. Micro. Theory Tech.*, Vol. 55, No. 6, 1118–1123, 2007.
6. Valerio, G., P. Baccarelli, P. Burghignoli, A. Galli, R. Rodríguez-Berral and F. Mesa, "Analysis of periodic shielded microstrip lines excited by nonperiodic sources through the array scanning method," *Radio Sci.*, Vol. 43, RS1009, doi:10.1029/2007RS003697, 2008.
7. Eshrah, I. A., "Analysis of a transmission line periodically loaded with modulated loads," in *Proc. IEEE AP-S Int. Symp.*, Charleston, SC, USA, June 2009, 1-4.

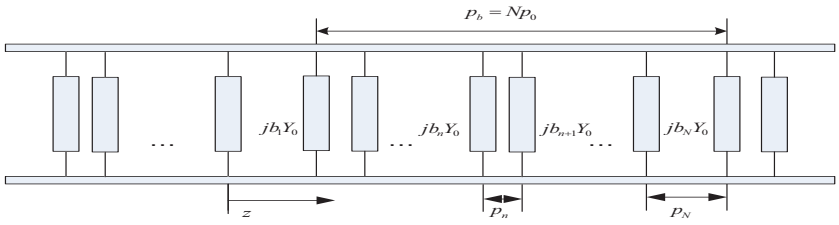
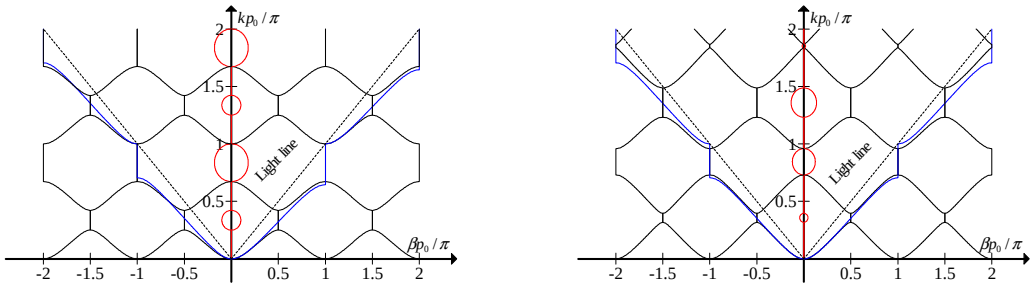


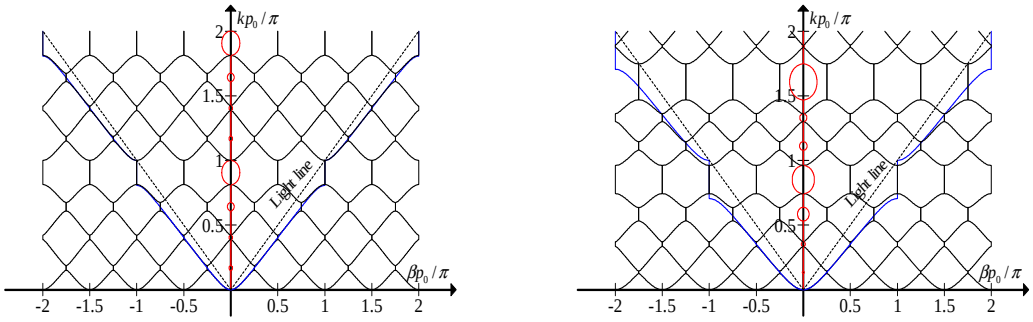
Figure 1: The proposed periodic structure. One period p_b is loaded by N shunt loads of normalized susceptance b_n, p_n is the separation between loads, $p_b = Np_0$ and $p_n = p_0 + \Delta p_n$.



(a) Two-amplitude modulated loads.

(b) Two-position modulated loads.

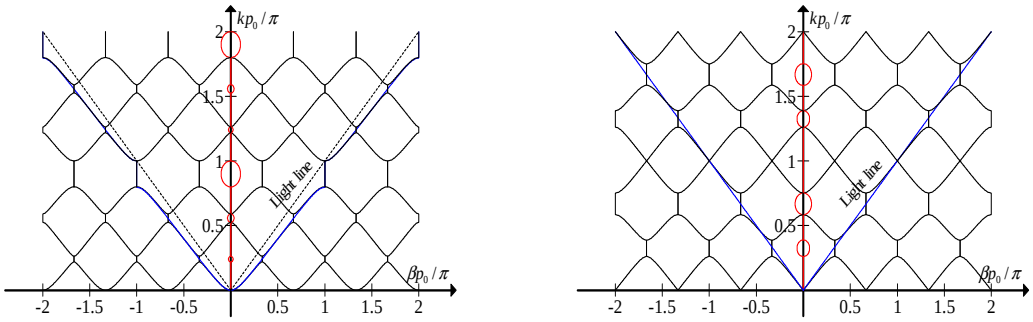
Figure 2: The dispersion diagrams of a transmission line loaded by: (a) two amplitude-modulated loads with $b_1 = 0.5$ and $b_2 = 2$, (b) two position-modulated loads with $\Delta p_1 = 0.25p_0$ and $\Delta p_2 = 0.75p_0$. The black and red lines indicate real and imaginary parts of β respectively. The blue line indicates the average unmodulated structure dispersion curve.



(a) Amplitude-modulated loads with $N = 4$.

(b) Position-modulated loads with $N = 4$.

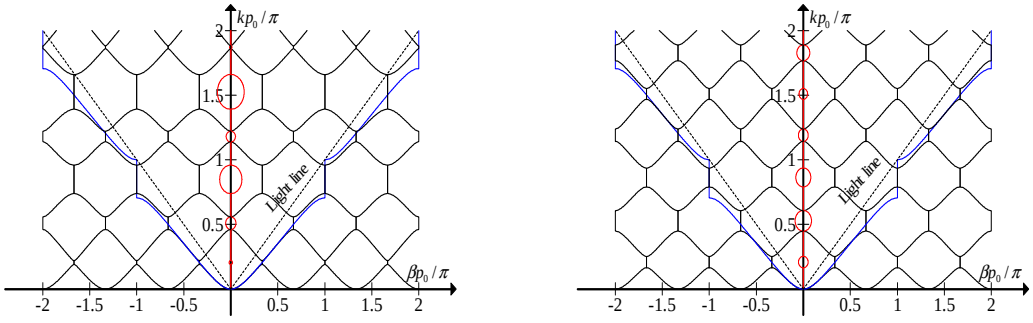
Figure 3: Effect of sampling on amplitude and position modulation case using a ramp function. The black and red lines indicate real and imaginary parts of β respectively. The blue line indicates the average unmodulated structure dispersion curve. In view of Fig.2, N gaps appear within the region $0 < kp_0 < \pi$.



(a) Ramp function and $N = 3$.

(b) Sinusoidal function and $N = 3$.

Figure 4: Effect of modulation function on amplitude modulation case. The black and red lines indicate real and imaginary parts of β respectively. The blue line indicates the average unmodulated structure dispersion curve. In (a) and (b) one gap coincides with the unmodulated average load curve. The mini sub-bands in (b) are wider than those in (a).



(a) Ramp function with $N = 3$.

(b) Sinusoidal function with $N = 3$.

Figure 5: Effect of modulation function on position modulation case. The black and red lines indicate real and imaginary parts of β respectively. The blue line indicates the average unmodulated structure dispersion curve. The figure shows a multi-band frequency selective behavior depending on the modulation function.

Characteristics of multilayer slab waveguide structure with a double negativity material

M. M. Shabat[1*], S. A. Taya[1], and M. M. Abadla[2]
[1] Physics Department, Islamic University, Gaza, P.O.Box 108, Gaza Strip, Palestine
[2] Physics Department, Alaqsa University, Gaza Strip, Palestine
[*]corresponding author: shabat@iugaza.edu.ps

We examine analytically the propagation of TE-polarized waves in a four-layer slab waveguide structure. One of the layers is considered as a Left-handed or metamaterial with simultaneously negative ε and μ. The dispersion relation of such a structure is shown in terms of the normalized thickness and the asymmetry factors. The effect of the doubly negative material parameters on the propagation characteristics has been examined. The variation of the effective index of the structure with different parameters of the layers is studied extensively. A comparison of the structure under consideration with the conventional right handed four-layer waveguide structure is also shown.

Keywords: Left-handed materials, slab waveguide, effective index, penetration depth.

1. Introduction

The process of development of integrated optics devices may comprise four steps. First, the function of the device is defined. Second, the architecture of the structure is determined. Third, a simulation process of the device is implemented. Fourth, the device fabrication and testing are examined. In this article we examine by simulation the properties of a four-layer slab waveguide structure which forms the actual components of active or passive devices.

Much progress has been made in the studies of multilayer optical waveguide due to its high importance as a basic guiding structure in integrated optics. Many applications have been proposed for the four-layer structure such as lens [1], large optical cavity laser [2], thin film taper coupler [3], and thin film waveguide TE-TM mode converters [4].

Recently, the concept of double-negative (negative ε and negative μ) materials has achieved remarkable importance due to the exhibition of unusual electromagnetic properties different from the known materials. These phenomena are observed in microwave, millimeter-wave, and optical frequency bands. The materials of double negativity are called metamaterials or Left-Handed Materials (LHMs). These are hand made structures that can be designed to exhibit specific phenomena not commonly found in nature. The LHM is a composite material in which both the electric permittivity ε and the magnetic permeability μ are simultaneously negative. The history of these materials begins with the work of Veselago [5], who proposed a medium with simultaneously negative ε and μ and studied the propagation of electromagnetic waves in such a medium. He predicted a number of unusual features of waves in LHMs, including negative index of refraction, the reversal of Doppler effect, and Pointing vector is antiparallel to phase velocity. Pendry et al [6] presented

the artificial metallic construction of periodic rods which shows negative permittivity and they also presented a structure of split rings which exhibits a negative permittivity [7]. Smith et al [8] constructed a LHM using the combination of periodic rods and split rings and they performed many experiments in the microwave range to point out that the nature of this material is unlike any existing material. The first experimental investigation of negative index of refraction was achieved by Shelby et al in 2001 [9]. The interaction of electromagnetic waves with stratified isotropic LHMs was investigated by Kong [10]. He investigated the reflection and transmission beams, field solution of guided waves, and linear and dipole antennas in stratified structure of LHMs. The theory of LHMs and their electromagnetic properties, possible future applications, physical remarks, and intuitive justifications are provided by Engheta in 2003 [11]. Chew [12] analyzed the energy conservation property of a LHM and the realistic Sommerfeld problem of a point source over a LHM half space and a LHM slab. In 2006, Sabah et al [13] presented the reflected and transmitted powers due to the interaction of electromagnetic waves with a LHM. They studied the effects of the structure parameters, incidence angle, and the frequency on the reflected and transmitted powers for lossless LHM. The electromagnetic wave propagation through frequency-dispersive and lossy double-negative slab embedded between two different semi-infinite media was presented by Sabah et al [14]. Due to the fabrication technologies, the LHMs are widely used in filters, absorbers, lens, microwave components, and antennas, etc. Furthermore, many researchers continue to study the potential applications of LHMs [15-17].

In this article, we investigate analytically the propagation of electromagnetic waves in a multilayer waveguide structure. A lossless double negative slab is embedded between a semi-infinite substrate and a thin film as a guiding layer. The film is covered with a semi-infinite cladding. After examining the electric and magnetic fields using Helmholtz equation in the four layers, we study the wave penetration depth in the cladding and the substrate. The power in different layers is also derived. The effect of the doubly negative material parameters on the propagation characteristics has been examined. The variation of the effective index of the structure with different parameters of the layers is studied extensively. A comparison of the physical parameters of the proposed structure with that of the conventional right handed four-layer waveguide structure is also shown

2. Characteristic Equation

We consider the waveguide structure shown in Fig. 1. It consists of a guiding layer with permittivity ε_f, permeability μ_f and thickness d_3. The semi-infinite substrate has permittivity ε_s and permeability μ_s and the semi-infinite cladding has permittivity ε_c and permeability μ_c. An additional layer of Left-Handed material with negative permittivity ε_m, negative permeability μ_m and thickness d_2 is inserted between the substrate and the guiding layer. Here we assume all the materials are lossless. We also consider the TE waves in which the electric field $\boldsymbol{E}$ is polarized along the y-axis.

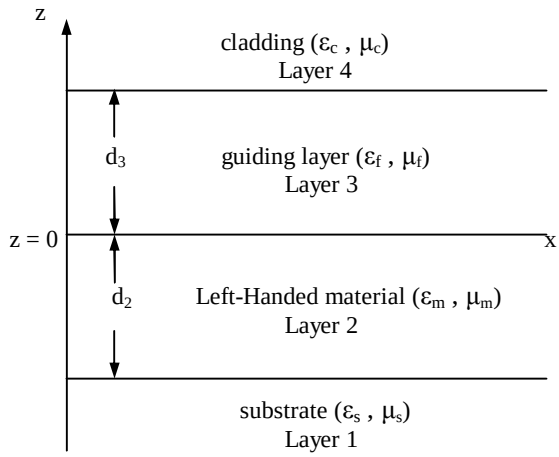


Fig. 1. Four-layer planar waveguide structure with layer 2 being left-handed material.

The solutions to Helmholtz equation for TE modes in the four layers are given by

$$E_{y1}(z) = Ae^{g_s(z+d_2)}, \quad z < -d_2 \ , \tag{1}$$

$$E_{y2}(z) = Be^{-g_m z} + Ge^{g_m z}, \quad -d_2 < z < 0 \tag{2}$$

$$E_{y3}(z) = C\cos(g_f z) + D\sin(g_f z), \quad 0 < z < d_3 \tag{3}$$

$$E_{y4}(z) = Fe^{-g_c(z-d_3)}, \quad z > d_3 \tag{4}$$

where $g_s = k_o\sqrt{N^2 - e_s m_s}$, $g_m = k_o\sqrt{N^2 - e_m m_m}$, $g_f = k_o\sqrt{e_f m_f - N^2}$, $g_c = k_o\sqrt{N^2 - e_c m_c}$, k_o is the free space wave number, N is the modal effective index, and the constants A, B, C, D, F, G represent the amplitudes of the wave in the layers.
It is convenient to express the characteristic equation of the optical waveguide in terms of the normalized parameters. Thus we begin by redefining the familiar normalized parameters commonly used in the three-layer case. We define a normalized thickness for layer 2 and layer 3 as

$$V_2 = k_o d_2\sqrt{e_f m_f - e_s m_s}\ , \ V_3 = k_o d_3\sqrt{e_f m_f - e_s m_s} \tag{5}$$

Layers 1 and 4 have semi-infinite thicknesses and thus need not be normalized. We also define the asymmetry factor a and the normalized index b as

$$a = \frac{e_s m_s - e_c m_c}{e_f m_f - e_s m_s}, \quad b = \frac{N^2 - e_s m_s}{e_f m_f - e_s m_s} \tag{6}$$

In addition, we introduce a new parameter which can be called the guiding ratio [18].

$$g = \frac{e_m m_m - e_s m_s}{e_f m_f - e_s m_s} \tag{7}$$

Matching the tangential components of the ***E*** and ***H*** fields, the characteristic equation of the structure shown in Fig. 1 can be written in terms of the above mentioned parameters as,

$$2V_3\sqrt{1-b} - f_{34} - f_{32} = 2mp \tag{8}$$

where f_{34} and f_{32} are the phase shifts at the boundaries above and below the principal guiding layer and are defined as

$$f_{34} = 2\tan^{-1}\left(\frac{m_f}{m_c}\sqrt{\frac{a+b}{1-b}}\right) \tag{9}$$

$$f_{32} = 2\tan^{-1}\left[\frac{m_f}{m_m}\sqrt{\frac{b-g}{1-b}}\,\frac{s_+ - s_- e^{-2V_2\sqrt{b-g}}}{s_+ + s_- e^{-2V_2\sqrt{b-g}}}\right] \tag{10}$$

where $s_+ = 1 + \frac{m_m}{m_s}\sqrt{\frac{b}{b-g}}$ and $s_- = 1 - \frac{m_m}{m_s}\sqrt{\frac{b}{b-g}}$.

3. Penetration Depth

The effective guide thickness is an important factor in the dispersion of the effective refractive index and in the application of optical sensing. Foreknowing this, we first calculate the effective guide thickness from the ray penetrations at the upper and lower boundaries of the guiding layer. The penetration of the guided wave from the guiding layer into the surrounding media can be written as [19]

$$x_2 = \frac{1}{2k_o N}\left(\frac{\partial f_{32}}{\partial g}\right) \tag{11}$$

$$x_4 = \frac{1}{2k_o N}\left(\frac{\partial f_{34}}{\partial g}\right) \tag{12}$$

where $N = \sqrt{e_f m_f}\sin(g)$ and g is the angle a ray makes with the normal to the boundary as shown in Fig. 2. In terms of the penetrations x_2 and x_4, the effective guide thickness is given by

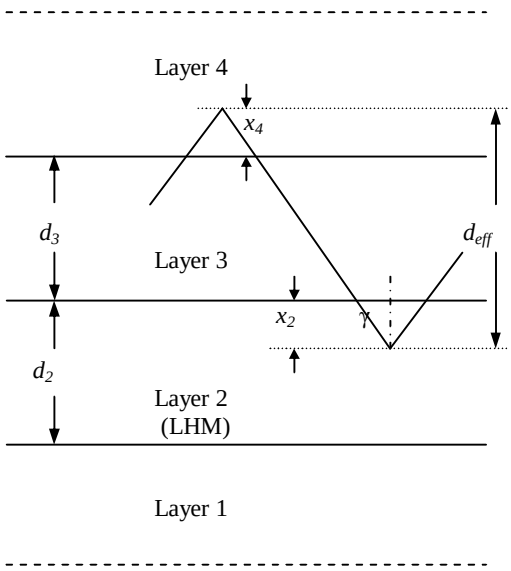


Fig. 2. Ray diagram illustrating the effective guide thickness d_{eff}.

$$d_{eff} = d_3 + x_2 + x_4 \tag{13}$$

and the normalized effective guide thickness can be written as

$$V_3' = k_o d_{eff}\sqrt{e_f m_f - e_s m_s} \tag{14}$$

Calculating the derivatives in Eqs. (11) and (12), we get

$$x_2 = \frac{m_f\sqrt{e_f m_f - N^2}\left(\sqrt{\frac{b-g}{1-b}}q_3 + q_2 s\right)}{m_m k_o N\left(1+\frac{m_f^2}{m_m^2}\frac{(b-g)}{(1-b)}s^2\right)} \tag{15}$$

$$x_4 = \frac{m_f(1+a)}{m_c k_o(1-b)\left(1+\frac{m_f^2}{m_c^2}\frac{(a+b)}{(1-b)}\right)\sqrt{N^2 - e_c m_c}} \tag{16}$$

where $s = \frac{s_1}{s_2}$, $s_1 = s_+ - s_- e^{-2V_2\sqrt{b-g}}$, $s_2 = s_+ + s_- e^{-2V_2\sqrt{b-g}}$,

$$q_2 = \sqrt{\frac{1-b}{b-g}}\,\frac{N(1-g)}{(1-b)^2(e_f m_f - e_s m_s)}, q_3 = \frac{-s_2(q+q_1)-s_1(q_1-q)}{s_2^2},$$

$$q = \frac{m_m}{m_s}\sqrt{\frac{b-g}{b}}\,\frac{N\ g}{(b-g)^2(e_f m_f - e_s m_s)},\quad q_1 = e^{-2V_2\sqrt{b-g}}\left(q - \frac{2V_2 N s_-}{\sqrt{b-g}(e_f m_f - e_s m_s)}\right)$$

4. Power flow through the waveguide layers

In this section we derive the power carried by each layer to fully investigate the four-layer waveguide properties when one of the layers is considered to exhibit a negative index of refraction. The guided wave power per unit length along x-axis is given by

$$P_{total} = \frac{Nk_o}{2wm}\int_{-\infty}^{\infty} E_y^2(z)dz \tag{17}$$

where ω is the angular frequency. Using Eqs. (1)-(4) to calculate the integral given by Eq. (15), we obtain

$$P_1 = \frac{Nk_o A^2 d_3}{4wm_s V_3\sqrt{b}} \tag{18}$$

$$P_2 = \frac{Nk_o d_3}{4wm_m V_3\sqrt{b-g}}\{-B^2(1-e^{2V_2\sqrt{b-g}}) + G^2(1-e^{-2V_2\sqrt{b-g}}) + 4BGV_2\sqrt{b-g} \tag{19}$$

$$P_3 = \frac{Nk_o d_3}{4wm_f V_3\sqrt{1-b}}\{C^2 S_+ + D^2 S_- + CD[1-\cos(2V_3\sqrt{1-b})]\} \tag{20}$$

$$P_4 = \frac{Nk_o F^2 d_3}{4wm_c V_3\sqrt{a+b}} \tag{21}$$

where $S_+ = V_3\sqrt{1-b} + \frac{1}{2}\sin(2V_3\sqrt{1-b})$ and $S_- = V_3\sqrt{1-b} - \frac{1}{2}\sin(2V_3\sqrt{1-b})$

When the continuity requirement is applied to Eqs. (1)-(4) and their derivatives, the following relations between the constants *A*, *B*, *C*, *D*, *F*, *G* are obtained

$$G = \frac{1}{2}Ae^{V_2\sqrt{b-g}}\left(1+\frac{m_m}{m_s}\sqrt{\frac{b}{b-g}}\right) \tag{22}$$

$$B = \frac{1}{2} A e^{-V_2\sqrt{b-g}} \left(1 - \frac{m_m}{m_s}\sqrt{\frac{b}{b-g}}\right) \tag{23}$$

$$C = B + G \tag{24}$$

$$D = \frac{m_f}{m_m}\sqrt{\frac{b-g}{1-b}}(-B + G) \tag{25}$$

$$F = C\cos(V_3\sqrt{1-b}) + D\sin(V_3\sqrt{1-b}) \tag{26}$$

5. Discussion

We have carried out the computations of the effective refractive index as a function of the guiding layer thickness (d_3), the thickness of the LHM layer (d_2) and the penetration depths (x_2 and x_4). In our calculations we suppose the cladding to have the lowest refractive index and the guiding layer to have the highest one, μ_m = -1 and λ = 630nm. Fig. 3 shows the variation of the effective refractive index with d_3. As d_3 approaches the cut-off thickness, the effective index approaches the substrate index n_s since in this limit all the power of the mode propagates in the substrate. The guided mode probes the substrate side only. As d_3 increases the confinement of the guided wave increases and the effective index approaches the guiding layer index n_f. For a given d_3, the effective index increases as n_f increases. Fig. 4 shows a comparison between the conventional four-layer waveguide with all the refractive indices being positive and the structure under consideration (i.e. Layer 2 is a LHM). It is clear that for a given d_3 and n_f, the conventional waveguide has a higher effective index. This behavior can be interpreted as: the evanescent wave generated at the boundary between the guiding layer and the LHM layer excites a surface wave at the boundary between the LHM layer and the substrate [20,21]. This effect enhances the field in the substrate so that the effective index decreases in the structure under consideration when compared with the case of four positive-index layers. The effective index as a function of layer 2 thickness d_2 (thickness of the LHM layer) is shown in Fig. 5. In contrary to its behavior with d_3, the effective index decreases with increasing d_2. Fig. 6 shows that the effective index decreases with increasing the penetration depths x_2 and x_4 and that it is very sensitive to the penetration depth x_4 in the cladding medium. This means that the structure under consideration is an eligible candidate for optical sensing applications.

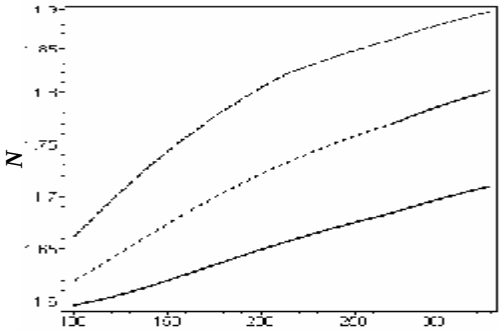


Fig. 3. Effective refractive index versus the guiding layer thickness for n_s = 1.55, n_c = 1.33, n_m = -1.6, d_2 = 100nm, n_f = 1.8 (solid line), n_f = 1.9 (dotted line), and n_f = 2 (dashed line).

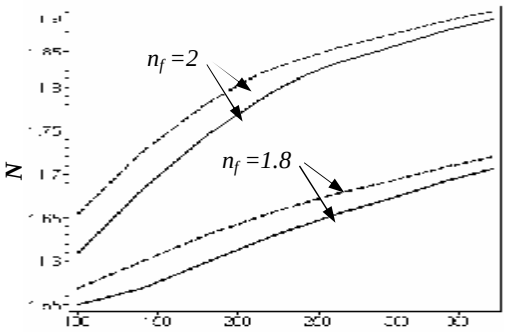


Fig. 4. Effective refractive index versus the guiding layer thickness for n_s = 1.55, n_c = 1.33, n_m = -1.6, d_2 = 100nm, for different values of n_f . The dashed lines represent the case when layer 2 is an ordinary dielectric with positive index and the solid lines represent the case when it is LHM.

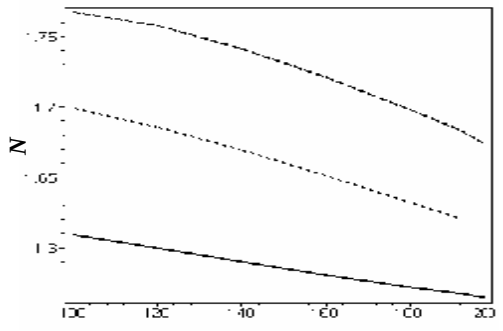


Fig. 5. Effective refractive index versus the thickness of layer 2 for n_s = 1.55, n_c = 1.33, n_m = -1.6, n_f = 2, d_3 = 100nm (solid line), d_3 = 150nm (dotted line), and d_3 = 200nm (dashed line).

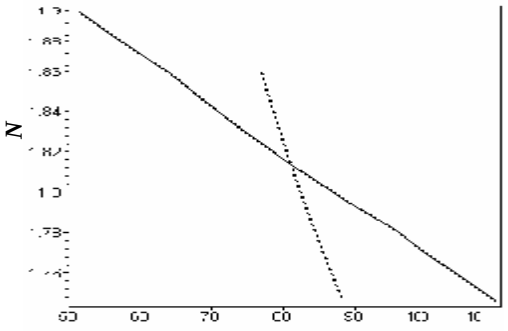


Fig. 6. Effective refractive index versus the penetration depths x_2 (solid line) and x_4 (dotted line) for n_s = 1.55, n_c = 1.33, n_m = -1.65, d_2 = 100nm, n_f = 1.8 and d_3 = 400nm.

The electric field configuration for the proposed structure is shown in Figs 7 and 8. As can be seen as the thickness of the LHM d_2 is increased from 50nm in Fig. 7 to 100nm in Fig. 8, two maxima arise in the field configuration. Thus the guided wave is supported by both of layer 2 and layer 3. Also we notice that the evanescent field strength in the cladding is higher in Fig. 8 (d_3 = 120nm) than that in Fig. 7 (d_3 = 100nm).

The powers P_2 in Layer 2, P_3 in the guiding layer, and P_4 in the cladding as functions of the thickness of the LHM layer (d_2) are shown in Fig. 9. As d_2 increases P_2 of the LHM increases while the power P_4 in the clad decreases. The power P_2 increases on expense of the cladding power. When the LHM layer thickness increases, the power concentrates in that layer because it becomes more bulky and nearly guiding. The powers P_1 in the substrate, P_2 in Layer 2, P_3 in the guiding layer, and P_4

in the cladding as functions of the guiding layer d_3 are shown in Figs. 10-13. For small values of d_3 (near cut-off thickness) most of the power flows in the substrate (P_1), and the powers P_2 and P_3 have minimum values. As d_3 increases, P_1 decreases and both P_2 and P_3 increase due to the guidance of the wave in these two layers. The power P_4 in the cladding has the minimum value among the other powers since the refractive index of this layer has the lowest value. To increase P_4 (power flow in cladding) for some applications such as optical sensing, a reverse asymmetry configuration is suggested. In this configuration, the index of the cladding is taken to be greater than that of the substrate. In this case, the part P_4 of the power increases and the part P_1 of the power decreases. Fig. 14 shows the fraction of total power flowing in the cladding as a function of the guiding layer refractive index n_f for different values of the refractive index of the LHM n_m. This fraction decreases with increasing the guiding layer refractive index due to the increase of the wave confinement in the guiding layer. For a given value of n_f, this fraction can be enhanced by increasing the absolute value of the refractive index of layer 2 (LHM).

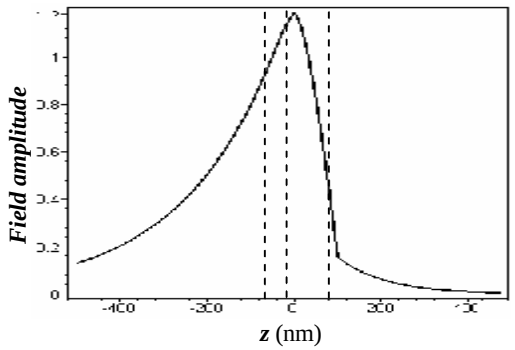


Fig. 7. Electric field configuration for n_s = 1.55, n_c = 1.33, n_m = -1.65n_f = 2, d_2 = 50, and d_3 = 100nm.

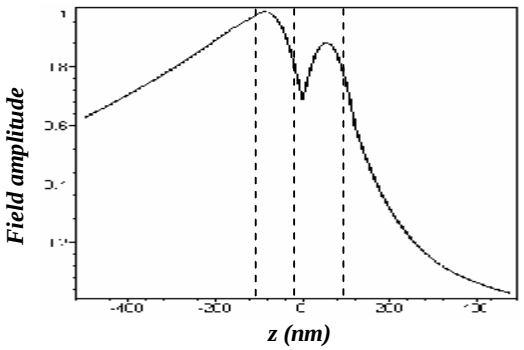


Fig. 8. Electric field configuration for n_s = 1.55, n_c = 1.33, n_m = -1.65, n_f = 2, d_2 = 100nm, and d_3 = 120nm.

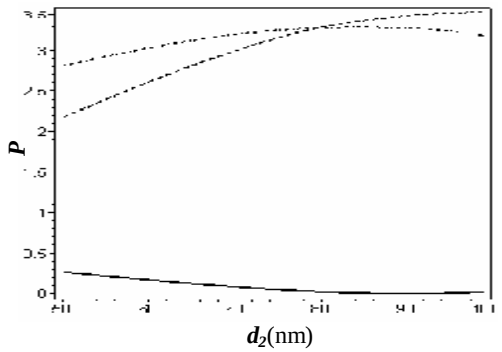


Fig. 9. Powers P_2 (dashed), P_3 (dotted), and P_4 (solid) versus the thickness of layer 2 for n_s = 1.55, n_c = 1.33, n_m = -1.82, n_f = 2, d_3 = 150nm.

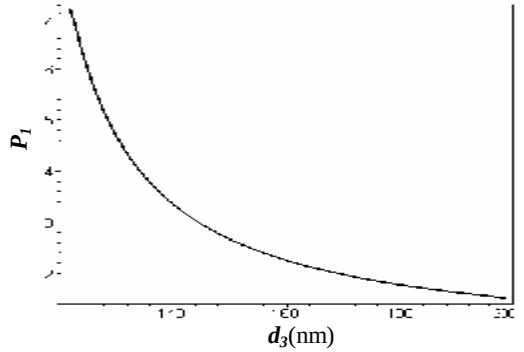


Fig. 10. Power flow in the substrate P_1 as a function of the guiding layer thickness for n_s = 1.55, n_c = 1.33, n_m = -1.82, d_2 = 100nm, and n_f = 2.

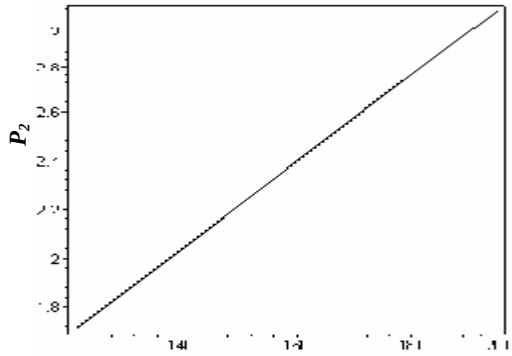


Fig. 11. Power flow in the layer 2 (LHM) P_2 as a function of the guiding layer thickness for n_s = 1.55, n_c = 1.33, n_m = -1.82, n_f = 2, and d_2 = 100nm.

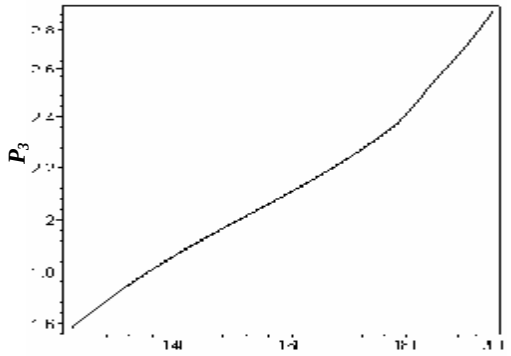


Fig. 12. Power flow in the guiding layer P_3 as a function of the guiding layer thickness for n_s = 1.55, n_c = 1.33, n_m = -1.82, n_f = 2, and d_2 = 100nm.

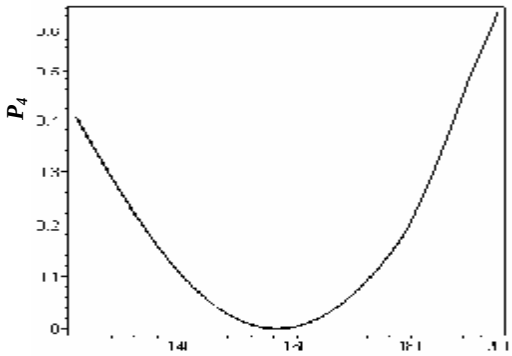


Fig. 13. Power flow in the cladding P_4 as a function of the guiding layer thickness for n_s = 1.55, n_c = 1.33, n_m = -1.82, n_f = 2, and d_2 = 100nm.

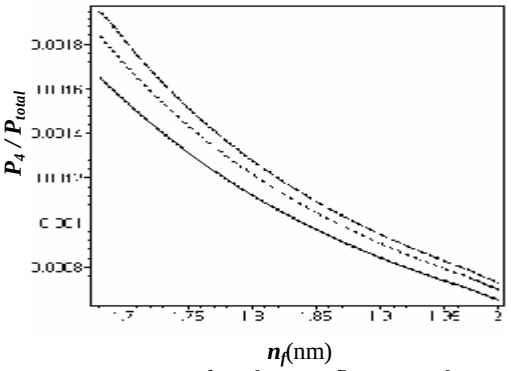


Fig. 14. Fraction of total power flowing in the cladding as a function of the guiding layer refractive index for n_s = 1.55, n_c = 1.33, n_m = -1.55 (solid line), n_m = -1.6 (dotted line), and n_m = -1.65 (dashed line).

6. Conclusion

In conclusion, we have analyzed a four-layer waveguide in which one of the layers is a left-handed material (LHM) of simultaneously negative ε and μ. The behavior of the effective refractive index with different parameters of the structure is studied and analyzed. The electric field configuration in such a structure is shown for different cases. The power flow in through the waveguide structure is also shown. We believe that structures containing LHMs can improve the performance of various slab waveguide devices.

References

[1] Southwell W., *Inhomogeneous optical waveguide lens analysis*, Journal Optics Society of America **67**, 1971, pp. 1004-1009.

[2] Lockwood H., Kressel H., Sommers H., Hawrylo F., *An efficient large optical cavity injection laser*, Applied Physics Letters **17**, 1970, pp. 499-502.

[3] Tien P., Martin R., Smolinsky G., *Formation of light guiding interconnection in an integrated optical circuit by composite tapered-film coupling*, Applied Optics **12**, 1973, pp. 1909-1916.

[4] Shibukawa A., Koba-yashi M., *Optical TE-TM mode conversion in double epitaxial garnet waveguide*, Applied Optics **20**, 1981, pp. 2444-2450.

[5] Veselago V., *The electrodynamics of substance with simultaneously negative values of ε and μ*, Sov. Phy. Usp. **10**, 1968, pp. 509-514.

[6] Pendry J., Holden A., Stewart W., Youngs I., *Extremely low frequency plasmons in metallic mesostructures*, Physical Review Letters **76**, 1996, pp. 4773-4776.

[7] Pendry J., Holden A., Robbins D., Stewart W., *Magnetism from conductors and enhanced nonlinear phenomena*, IEEE Transactions on Microwave Theory and Techniques **47**, 1999, pp. 2075-2084.

[8] Smith D., Padilla W., Vier D., Nemat-Nasser S., Schults S., *Composite medium with simultaneously negative permeability and permittivity*, Physical Review Letters **84**, 2000, pp. 4184-4187.

[9] Shelby R., Smith D., Schults S., *Experimental verification of a negative index of refraction*, Science **292**, 2001, pp. 77-79.

[10] Kong J., *Electromagnetic wave interaction with stratified negative isotropic media*, Progress in Electromagnetic research **35**, 2002, pp. 1-52.

[11] Engheta N., *Metamaterials with negative permittivity and permeability: background, salient features, and new trends*, IEEE MTT_S Int. Microwave Symp. Digest **1**, 2003, pp. 187-190.

[12] Chew W., *Some reflections on double negative materials*, Progress in Electromagnetic research **51**, 2005, pp. 1-26.

[13] Sabah C., Ogucu G., Uckun S., *Reflected and transmitted powers of electromagnetic wave through a doubl-negative slab*, J. Optoelectronics and Advanced Materials **8**, 2006, pp. 1925-1930.

[14] Sabah C., Uckun S., *Electromagnetic wave propagation through frequency-dispersive and lossy double-negative slab*, Optoelectronics Review **15**, 2007, pp. 133-143.

[15] Tretyakov S., *Meta-material with wide-band negative permittivity and permeability*, Microwave and Optical Technology Letters **31**, 2001, pp. 163-165.

[16] Caloz C., Chang C., Itoh T., *Full-wave verification of the fundamental properties of left-handed materials in waveguide configuration*, Journal of Applied Physics **90**, 2001, pp. 5483-5486.

[17] Guven K., Ozbay E., *Near field imaging in microwave regime using double layer split-ring resonator based metamaterials*, Opto-Electron. Review **14**, 2006, pp. 213-216.

[18] Hewak D., Lit J., *Generalized dispersion properties of a four-layer thin-film waveguide*, Applied Optics **26**, 1987, pp. 833-841.

[19] Adams M., *An introduction to optical waveguides*, Wiley, Toronto 1981, p. 17

[20] Ruppin R., *Surface polaritons of a left-handed medium*, Physics Letters A **227**, 2000, pp. 61-64.

[21] Qing D., Chen G., *Enhancement of evanescent waves in waveguides using metamaterials of negative permittivity and permeability*, Applied Physics Letters **21**, 2004, pp. 669-671.

Optical Memory Made of Photonic Crystal Working over the C-Band of ITU

A. Wirth Lima Jr.[1] **and A. S. B. Sombra**[1]
1Federal University of Ceará, Brazil
*corresponding author: awljeng@gmail.com

Abstract - After several decades pushing the technology and the development of the world the electronics is giving space for technologies that use light. We propose and analyze an optical memory embedded in nonlinear photonic crystal (PhC), whose system of writing and reading of data is controlled by an external command signal. This optical memory is based on optical directional couplers connected to a shared waveguide. That device has a small coupling length and can works over the C-Band of ITU (International Telecommunication Union).

1. INTRODUCTION

Electronics can not indefinitely growth. For instance, electronics in modern computers is forced to operate at ever-higher frequencies. Hence, these computers are submitted hardware heating, which is a serious problem. However, the greater problem is the nodes of optical telecommunication networks, due the even higher operational frequencies and bandwidths [1]. We can make the following analogy between Semiconductors and PhCs: "The Semiconductors make the electronics and PhCs enable the integrated optical." We can use nonlinear PhC to work with high efficiency in systems using high frequency and large bandwidth.

The optical memory we are presenting is embedded in a two-dimensional (2D) triangular lattice of air holes with radius rb = 0.31a, where "a" is the lattice constant. The vertical layer of the PhC is formed by a cladding of InP (n = 3.17), a core of InGaAsP (n = 3.35), and a substrate of InP. This structure can be represented accurately by an effective refractive index neff = 3.258.

Therefore, we have analyzed and proposed an optical memory embedded in nonlinear photonic crystal driven by an external command signal.

2. OPTICAL MEMORY DETAILING

Figure 1 shows the structure of the optical memory. Both couplers share one of their W1 waveguide. The optical memory is embedded in a two-dimensional (2D) triangular lattice of air holes.

(Figure 1)

Figure 2 shows the dispersion relation of the couplers, where "u" is the normalized frequency ($u = a/\lambda$; λ is the wavelength) for TE polarized light. The even mode splits into an even-even (e-e) and an even-odd (e-o) mode and the odd mode splits into an odd-even and an odd-odd mode. The area where only the (e-e) and the (e-o) modes are present is called "quasi-single mode region" [2]. Indeed, the modes in the coupler (supermodes) have even and odd symmetries with respect to the plane equidistant from the axis of the waveguides. The inset at the top of the graph sketches the "quasi-single mode region.

(Figure 2)

If we decrease the radius of the air holes between the waveguides (r_c), the difference between the propagations

constants become smaller and the coupling length is reduced. However, the bandwidth is reduced too. Moreover, with the increasing of the outer border air holes (r_e) of the two coupled W_1, the change in the coupling length is not strong, but the bandwidth is not negatively affected.

Figure 2 shows that the bandwidth for the coupler with r_b = 0.31a, r_c = 0.19a and r_e = 0.35a covers the normalized frequencies from u = 0.274 to u = 0.286. As we are interested in working over the C-band of the ITU (from 1530nm to 1565nm) we have adopted a = 0.434nm. Hence, the minimal coupling length regarding the bar state is L_c = 23.436μm for the whole normalized frequencies band [3].

Each directional coupler is driven by an external command signal, along the periodic waveguide between the W_1 waveguides in the coupling region. If the command signal is working in the coupling region the refractive index decreases (due to the non-linear effects), which causes the increase of the coupling coefficient value. The normalized frequency of the command signal is within the PBG, but outside of the C Band of the ITU. This signal is inserted in the coupling region, which acts as a periodic waveguide [4]. If the command signal is working in the coupling region the refractive index decreases (due to the non-linear effects), which causes the increase of the coupling coefficient value. If we consider that the coupler was designed to operate in the bar state, the increase of the coupling coefficient should be sufficient to bring the coupler to work in the cross state. The normalized frequency of the command signal is u = 0.2194. The wave number of this command signal is located very near of the limit of the irreducible Brillouin zone. Therefore, it is within the Photonic Band-Gap (PBG), but outside of the 1530 nm – 1565 nm band of the data signals. The calculation of the necessary power should take into account the increase of the refractive index in the coupling region[5], which depend on the used PhC structure, and on the normalized frequency of the command signal.

$$\Delta n = 3n_2\left|E\right|^2\frac{V_{gcr}}{V_{gcw}} = 3n^2 I\frac{V_{gcr}}{V_{gcw}} = 3\frac{n_2 P}{A_{eff}}\frac{V_{gcr}}{V_{gcw}} \rightarrow P = \frac{(\Delta n)A_{eff}}{3n_2\left(\frac{V_{gcw}}{V_{gcr}}\right)} \quad (1)$$

In equation (1) P is the desired optical power of the command signal, n2 is the non-linear refractive index (Indium Gallium Arsenide Phosphide (InGaAsP) has $n_2 \approx -5.9\text{x}10^{-16}\text{m}^2/\text{W}$ at λ = 1.55 μm [6], E is the electric field, is the optical intensity, A_{eff} is the mode effective area, V_{gcw}, is the command signal group velocity in a conventional axial uniform waveguide, and V_{gcr} is the low group velocity of the command signal in the coupling region (the wave number is located very near of the limit of the irreducible Brillouin zone). The factor of 3 is due the cross-phase modulation, which induces an index change twice as strong as self-phase modulation, and because the longitudinal confinement of the mode is not uniform [7]. Since our coupler was originally designed to works in the bar state, for the coupler with L = nxL_c to change from the bar state to the cross state it is needed:

$$\Delta\beta_{c(n)} = \frac{(2n+1)}{2n}\Delta\beta_d \quad (2)$$

Figure 3 shows the values of the needed differences between the propagation constants of the two supermodes for the coupler working in the bar state ($\Delta\beta_d$) and in the cross state ($\Delta\beta_c$) as well as the value of the increase of $\Delta\beta$ to change the coupler of the bar state to the cross state depending on the length of the coupler (λ = 1.55 nm). (Figure 3)

We can demonstrate, that to bring the coupler from bar state to cross state we need:

$$\Delta n_{(n)} = \frac{\lambda\Delta\beta_d}{4\pi n} \quad (5)$$

As the group velocity of the data signal is approximately ten times larger than the group velocity of the command signal, the transmission rate of the pulses in the transmission line should be calculated assuming that its width has a value ten times higher than its real value.

To obtain the writing of the data signal in the optical memory we need to insert the data signal in the waveguide located at the top of the optical memory, at the same time of the command signal. Hence, the coupler change from the bar state to the cross state and the data signal is trapped in our optical memory. After insertion of the data signal the command signal is removed, so that the coupler reverts back to work in the bar state and the data signal is retained in the coupler.

Plots of the Hz fields of the lowest-order of the TE modes at k very near of the limit of the irreducible Brillouin zone (u = 0.2194), which are travelling within the periodic guide is shown in figure 4(a). We can see that the electrical field is completely confined in the coupling region. Hence, the increasing of the value of the refractive index due the nonlinear effect arises only in the coupling region, where the periodic waveguide is located and this command signal influences the process of switching only by modifying of the refractive index. Figure 4(b) shows the electric field in the coupling region, which is located in the holes and also in approximately 92% of the area of the dielectric in the coupling region. Hence, we can neglect the consequences it causes for the resultant Δn_{eff} in the coupling region.

(Figure 4)

The Q factor is high for defect resonators and increases with increasing cavity length. It will approach infinity in the limit of the infinite cavity length because the photonic crystal waveguide mode below the light line is lossless. Taking into account that the W_1 shared waveguide has great length, we concluded that the losses due to reflections at the ends of this waveguide can be considered negligible. The Q value of the high-Q TE defect mode regarding similar PhC structure is 13,000, corresponding to a time period of 2,000 oscillations [8]. So, to improve the efficiency of our optical memory, we can use a refresh signal which must have the period equal to 2000xT, where T is the temporal width of the data signal pulse.

3. CONCLUSIONS

We have analyzed and proposed an optical memory embedded in a nonlinear photonic crystal, which can acts by an external command signal. This optical memory is formed by two directional optical couplers. Each coupler shares a W_1 waveguide. We can read and write data signal on that optical memory inserting an external command signal within periodic waveguide localized in coupling regions. So, among countless other applications we can replace the optical memory buffers based in Optical Delay Lines (ODLs) working in Wavelength Division Multiplex (WDM) systems and thus greatly improving the efficiency of such systems.

ACKNOWLEDGEMENT

This work was partly sponsored by National Council of Scientific and Technological Development (Conselho Nacional de Desenvolvimento Científico e Tecnológico – CNPq).

REFERENCES

1. Soldjacic, M. and Joannopoulos, J. D., “Enhancement of nonlinear effects using photonic crystals, *“Physics Department, Massachusetts Institute of Technology”*, 211 – 218, 2004.
2. Strasser P., Flückiger, R, Wüest, Robin, R., and Jäckel, H., “InP-based compact photonic crystal directional

coupler with large operation range", "*Optics Express*" 8472, (2007).
3. Sharkawy, A., Shi, S. and Prather, D.W, "Electro-optical switching using coupled photonic crystal waveguides", *Optics Express* 1048, (2002).
4. Luan, P.G and Chang, K.D., Transmission characteristics of finite periodic dielectric waveguides, "*Optical Society of America*", (2006).
5. Beggs, D.M, White, T.P, O'Faolain, L and Krauss, T.F, "Ultracompact and low-power optical switch based on silicon photonic crystals", "*Optics Letters*" Vol. 33 No. 2, (2008).
6. Fushman, I and Vuckovic, J., "Analysis of a quantum nondemolition measurement scheme based on Kerr nonlinearity in photonic crystal waveguides", "*Optics Express*", Vol. 15, No. 9, pp. 5559-5571, (2007).
7. Cuesta-Soto, F, Martinez, A., Garcia, J., Ramos, F., Sanchis, P., Blasco, J. and Marti, J., "All-optical switching structure based on a photonic crystal directional coupler", "*Optics Express*" 161 (2004).

8. Fan S., Winn, J.N, Devenyi, A., Chen, J.C., Meade, R.D and Joannopoulos, J.D., "Guided and defect modes in periodic dielectric waveguides", "*J. Opt. Soc. Am. B*", Vol. 12, No. 7, 1267-1272 (1995).

FIGURE CAPTIONS

Figure 1 Structure of the optical memory.

Figure 2 Dispersion relation of the PhC coupler (even mode and odd mode).

Figure 3 Values of the needed propagation constants.

Figure 4 Plots of the fields of the first band of the TE modes within the periodic guide.

FIGURE 1

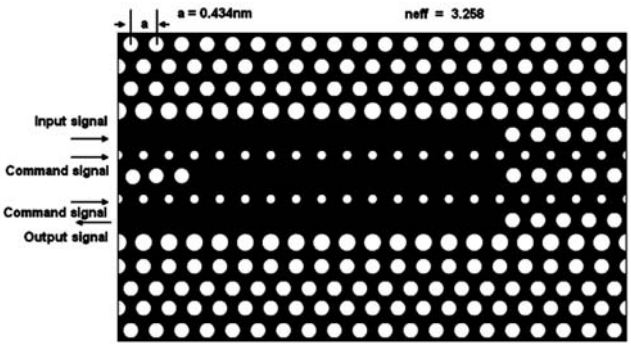


FIGURE 2

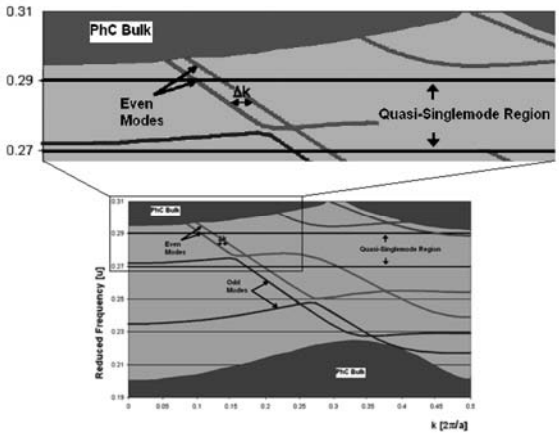


FIGURE 3

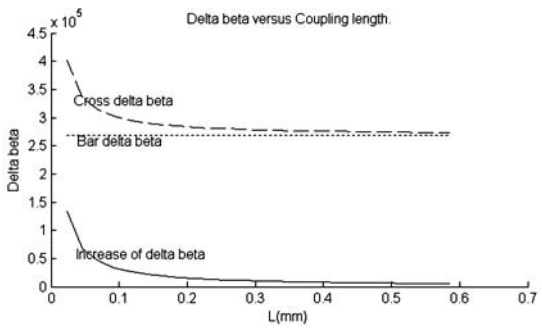
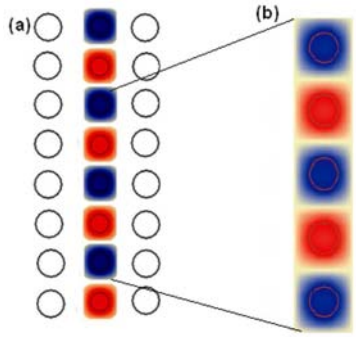


FIGURE 4



Zero-Reflection Metal Slabs: A Mechanism of Light Tunneling in Metamaterials

Guiqiang Du, Haitao Jiang , Zhanshan Wang and Hong Chen[a)]
Pohl Institute of Solid State Physics, Tongji University, Shanghai, 200092, China
[a)]hongchen@tongji.edu.cn

Abstract- Thick metals are nearly opaque due to high reflectance and the huge third-order nonlinear susceptibility of metals is hardly utilized. In the present paper, zero-reflection phenomenon in a thick metal (M) slab covered with one-dimensional dielectric photonic crystals (PC's) (CD)n are studied in heterostructures M(DC)n and sandwiched structures (CD)nM(DC)n. Visible-light tunneling modes can be realized in M(DC)n or (CD)nM(DC)n in which the optical epsilon-negative medium (metal) are paired with the PC that mimics a lossless optical mu-negative medium in the gap region. The transmittance as high as 33% and 38% are observed at wavelength of 589 nm for M=Ag, with thickness d = 60.2 nm in a heterostructure and d = 83.1 nm in a sandwiched structure, respectively. The transmittance is more than 200 times larger than that of a single Ag layer with the same thickness in the later case. Possible applications on metal-based nonlinearity enhancement and optical absorber are also discussed.

1. INTRODUCTION

Metals have big third-order nonlinear susceptibilities that are several orders larger than those of typical dielectrics. However, metals are epsilon-negative (ENG) materials ($\varepsilon < 0, \mu > 0$) in visible regions below plasma frequencies. Therefore, when the thickness is much larger than the skin depth, the metal slabs are opaque since the light is strongly reflected. Because of the very weak field in the thick metal, the nonlinear effect is nearly inaccessible. So, how to couple the light into the metal, or realize zero reflection at the surface of the metal is a very important problem. One-dimensional (1D) metal-dielectric photonic crystals (PCs) composed of the thin metal film and thick dielectrics could be transparent through Bragg resonance [1, 2]. But the enhancement of fields in the metal is very limited since the nodes of the electric fields should be located in the each metal film. On the other hand, the nano-structured metals can couple the light into the metal through the excitation of some kinds of resonance including surface plasmon polaritons [3-5]. But the fabrication of nano-structured metals is complicated. Therefore, it is more fascinating to induce the light into an unstructured thick metal slabs with no reflection and a strong enhancement of the local fields in the metals simultaneously.

In 2003, people found that the electromagnetic (EM) waves can tunnel through a heterostructure consisting of an ENG material and a mu-negative (MNG) material ($\varepsilon > 0$, $\mu < 0$) under the impedance and the phase matching conditions [6]. The EM fields of the tunneling mode are highly localized at the interface of the two kinds of media. Recently, it is found that the all-dielectric PCs may play the role of a optical MNG material in the photonic gap [9-11]. Moreover, a tunneling mode can be realized in a heterostructure composed of a thick metal slab and a truncated all-dielectric PC that mimics a MNG medium [7, 8]. In this paper, we experimentally demonstrate that zero reflection and a strong enhancement of local fields can be realized in the metal slab based on the tunneling mechanism. The paper is organized as follows. In section 2, we analyze the tunneling mechanism of a metal slab paired with a PC in details. In section 3, we discuss some possible applications of zero-reflection metal slabs.

Finally, we conclude in section 4.

2. TUNNELING IN A METAL SLAB PAIRED WITH A PHOTONIC CRYSTAL

In this paper, the all-dielectric PC is denoted by $(DC)^N$ where C and D represent different dielectrics. N is the periodic number. Normal incidence is considered. In the forbidden gap, the Bloch wave vector K of the PCs satisfies the relation $K\Lambda = m\pi + iK_i\Lambda$ [9], where Λ is the thickness of the unit cell and m is integer. Moreover, the wave impedance of the PC can be obtained with $Z = Z_r + iZ_i = Z_0(1+r)/(1-r)$ [10, 11], where Z_0 represents the characteristic impedance of the air and r is the reflection coefficient that can be described with $r = |r| \cdot e^{i\phi}$ in which ϕ represents the reflection phase. When ϕ belongs to $[(2m+1)\pi, (2m+2)\pi]$ and $|r| \approx 1$, $Z_i < 0$. When N is large enough, the wave impedance Z is equivalent of the characteristic impedance and K can be taken as the wave vector of the PC with the total thickness of $N\Lambda$. So $Z_i < 0$ means the PC have the effect of a MNG material.

On the other hand, metals denoted by M are the natural ENG materials below the plasma frequency. The wave vector and characteristic impedance of the metal are $k_M = (\omega/c)\sqrt{\varepsilon_M} = k_{Mr} + ik_{Mi}$ and $\eta_M = 1/\sqrt{\varepsilon_M} = \eta_{Mr} + i\eta_{Mi}$, respectively, where ε_M denotes the permittivity and the permeability of metals is considered to be 1. Firstly, the loss of metals is not considered and $k_M = ik_{Mi}$ and $\eta_M = i\eta_{Mi}$ are obtained. Based on the above analysis, the zero-reflection condition [12] of the heterostructure $M(DC)^N$ at entrance face can be obtained as fllows:

$$\left(Z - \frac{1}{Z}\right)\tan NK\Lambda - \left(\eta_{Mi} + \frac{1}{\eta_{Mi}}\right)\tanh k_{Mi}d_M + i\left(\frac{Z}{\eta_{Mi}} + \frac{\eta_{Mi}}{Z}\right)\tan NK\Lambda \cdot \tanh k_{Mi}d_M = 0 \quad , \tag{1}$$

where d_M is the thickness of the metal slab. In the forbidden gap of the PC, $K = m\pi/\Lambda + iK_i$ and $Z \approx Z_i$ so Eq.(1) can be simplified to

$$NK_i\Lambda = k_{Mi}d_M \ , \ Z_i = -\eta_{Mi} \ . \tag{2}$$

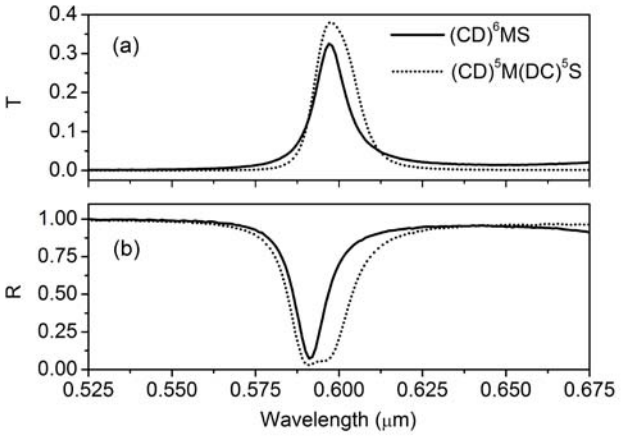
Equations (2) are similar to the zero-reflection condition for the heterostructure composed of ENG and MNG media [6]. At zero reflection, the EM fields are highly localized around the interface of the metal and the PC. Considering the loss of metal, though the wave vector and characteristic impedance of the metal have minor real parts, the zero reflection at the entrance face can still be realized with appropriate parameters.

3. APPLICATIONS OF ZERO-REFLECTION METAL SLABS

3.1 Enhancement of the transmission

Based on the theoretical analysis in section 2, we design the heterostructure $(CD)^NMS$ and the sandwiched structure $(CD)^NM(DC)^NS$, respectively, where S represents the substrate. The samples are fabricated by an ion-assisted-deposition-based 1300 mm diameter box-type coater system (OTFC-1300DBI, Optorun Co., Ltd). The metal M is selected to be silver. The truncated dielectric PC is composed of SiO_2 (C) and TiO_2 (D) whose refractive indices and thicknesses are $n_C = 1.443$, $n_D = 2.327$ [13], $d_C = 89.0nm$ and $d_D = 55.2nm$, respectively. The substrate is BK7 with the refractive index $n_s = 1.51$. We firstly fabricate $(CD)^6MS$ and $(CD)^5M(DC)^5S$. To obtain zero reflectance, the thickness of the silver slabs in the former (latter) structure is 60.2 nm (83.1 nm) at the tunneling wavelength of 589.01 nm (589.14 nm). Due to the limitation of the spectrophotometer, reflection spectra are scanned with the minimal oblique angle 15° for transverse magnetic (TM) waves. The tunneling

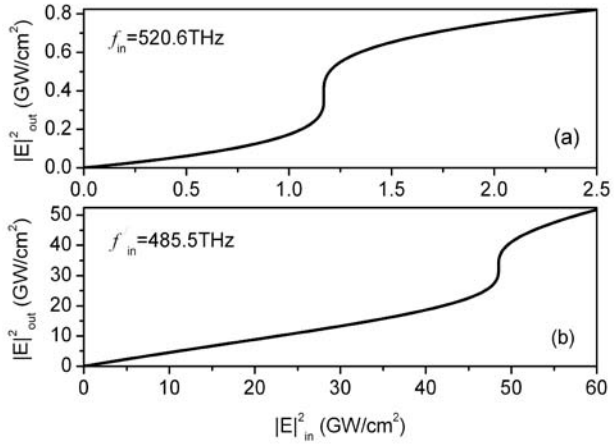
modes appear within the first forbidden gap (from 446.5 nm to 604.9 nm) of the PC. Figures 1 (a) and (b) give the measured transmittance T at normal incidence and reflectance R at 15° of TM waves for $(CD)^6MS$ (denoted by the solid lines) and $(CD)^5M(DC)^5S$ (denoted by the dashed lines), respectively. The measured tunneling wavelength (λ_0) at normal incidence are 597 nm for $(CD)^6MS$ and 598 nm for $(CD)^5M(DC)^5S$. As shown in Fig.1 (b) under 15° of incidence for TM wave, the minimal measured reflectance are 0.0735 for $(CD)^6MS$ and 0.0294 for $(CD)^5M(DC)^5S$, respectively. Though the reflectance at normal incidence cannot be measured, we can deduce that it is less than the measured value under 15° of incidence and near zero. At the wavelength of 597 nm, the maximal measured transmittance T=0.3257 for $(CD)^6MS$ that is nearly 25 times larger than that of a single silver slab with the same thickness. At the wavelength of 598 nm, the maximal measured transmittance T=0.3797 for $(CD)^5M(DC)^5S$ that is about 204 times larger than that of a single silver slab with the same thickness.



Figs. 1 (a) and (b) show the measured T at normal incidence and R at 15° of TM waves for $(CD)^6MS$ (the solid lines) and $(CD)^5M(DC)^5S$ (the dashed lines), respectively.

3.2 Enhancement of the nonlinearity

Since the local fields are strongly enhanced in the metal at the tunneling mode, the nonlinear effect of the metal can be greatly boosted. For comparison, we theoretically study the nonlinear responses [8] of heterostructrue $(CD)^7M$ and a 1D metal-dielectric PC $(CM)^7$ with the same thickness of metal M, respectively, by means of the nonlinear transfer-matrix method [14]. C and D denote SiO_2 and TiO_2, respectively. Their refractive indices are the same to those in Figs. 1 and their thicknesses are $d_C = 85.5$ nm and $d_D = 53.0$ nm, respectively. The metal is selected to be silver and its linear permittivity is described by the Drude model $\varepsilon_M^L = 1.0 - \omega_P^2/(\omega^2 + i\gamma\omega)$ [2], where $\hbar\omega_P$=7.2eV, $\hbar\gamma$=0.05eV and γ denotes the damping. The dielectric function of silver with nonlinearity is $\varepsilon_M^{NL} = \varepsilon_M^L + \varepsilon_0\chi_3|E|^2$, where $|E|^2$ is the intensity of electric field. In the following calculations, we suppose $\chi_3 = 2.4\times10^{-9}$ esu [15]. The thickness of silver is 67.2 nm. The frequency of the tunneling mode is f_C=525 THz. In order to realize the same resonant frequency, the thicknesses of C and M in $(CM)^7$ are 176.96 nm and 9.6 nm, respectively. Figures 2 (a) and (b) show the bistabilities for $(CD)^7M$ and $(CM)^7$, respectively. $|E|^2_{ir}$ ($|E|^2_{ou}$) is the intensity of electric field of incident (output) wave. f_{ir}=520.6 THz and f_{ir}'=485.5 THz are the frequencies of incident wave for $(CD)^7M$ and $(CM)^7$, respectively. The intensities of critical thresholds for the bistabilities at f_{ir} and f_{ir}' are 1.17GW/cm^2 and 48.6GW/cm^2, respectively. This means the intensity of critical threshold in $(CD)^7M$ is reduced by

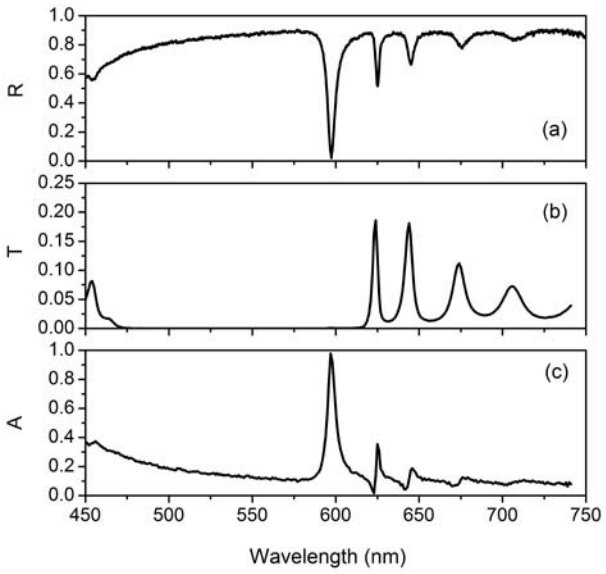


Figs.2 (a) and (b) show the bistabilities for $(CD)^7M$ and $(CM)^7$, respectively.

nearly two orders of magnitude compared to that in $(CM)^7$. The reason is that the average intensity of electric field in the silver slab of $(CD)^7M$ is nearly 6 times of that in the silver slabs of $(CM)^7$. The strong nonlinear effect in the heterostructure with thick metal will play an important role in designing highly efferent optical bistable switching and optical diode, etc.

3.3 Enhancement of absorption

Under tunneling mechanism, the light can also be coupled into the heterostructure and strongly absorbed by the lossy metal. We fabricate a heterostructure $BM(DC)^{21}S$ by electronic beam evaporation, where M denotes the silver. C and D are SiO_2 and TiO_2, respectively. Their refractive indices are $n_C = 1.46$ and $n_D = 2.13$, respectively [13]. Their thicknesses satisfy the formula $n_C d_C = n_D d_D$, where d_I is 62.68 nm. The protection film B is SiO_2 to prevent the silver slab being oxidized in the air and its thickness is 50 nm. The substrate S is K9 and its refractive index is 1.52. The thickness of silver is 57.71 nm. Figures 3 (a), (b) and (c) show the measured reflectance R, measured transmittance T and absorbance A of $BM(DC)^{21}S$, respectively. The absorbance is calculated based on the formula A=1-R-T, where T and R are measured directly by a UV-Vis-Near IR Spectrophotometer (V-570, Jasco Inc). The wavelength of tunneling mode (λ_t) is 597.4 nm. A and R at λ_t are 0.979 and 0.021, respectively. With easy fabrication, this kind of heterostructure with thick metal slab that can perfectly absorb light will play an important role in many applications involving photonic absorption.



Figs. 3 (a), (b) and (c) show the measured R, measured T and A of $BM(DC)^{21}S$, respectively.

4. CONCLUSIONS

In conclusion, zero reflection at the entrance face of the heterostructure or the sandwiched structure with thick metal slab and truncated dielectric PC can be realized under the tunneling mechanism. Since the EM fields can totally enter the structure and are strongly enhanced in the thick metal, the transmittance, the nonlinear effect and the absorption of the thick metal can be greatly boosted. This kind of zero-reflection metal will play an impotent role in many applications.

ACKNOWLEDGEMENT

This research was supported by CNKBRSF (Grant No. 2006CB921701), by CNSF (Grants Nos. 10634050 and 10704055), by the Program for Key Basic Research of the Shanghai Science and Technology Committee (Grant No. 08dj1400301), and by the Scientific Research Foundation for the Returned Overseas Chinese Scholars, State Education Ministry.

REFERENCES

1. Bloemer, M. J. and M. Scalora, "Transmissive properties of Ag/MgF_2 photonic band gaps," *Appl. Phys. Lett.*, Vol. 72, No. 14, 1676-1678, 1998.
2. Scalora, M., M. J. Bloemer, A. S. Pethel, J. P. Dowling, C. M. Bowden, and A. S. Manka, "Transparent, metallo-dielectric one dimensional photonic band gap structures," *J. Appl. Phys.*, Vol. 83, No. 5, 2377-2383, 1998.
3. Teperik, T. V., V. V. Popov, and F. J. Garc□a de Abajo, "Void plasmons and total absorption of light in nanoporous metallic films," *Phys. Rev. B*, Vol. 71, No. 8, 085408(9), 2005.
4. Sun, G. and C. T. Chan, "Frequency-selective absorption characteristics of a metal surface with embedded dielectric microspheres," *Phys. Rev. E*, Vol. 73, No. 3, 036613(5), 2006.
5. Teperik, T. V., F. J. Garc□a De Abajo, A. G. Borisov, M. Abdelsalam, P. N. Bartlett, Y. Sugawara, and J. J. Baumberg, "Omnidirectional absorption in nanostructured metal surfaces," *Nature Photonics*, Vol. 2, 299-301, 2008.
6. Al□, A. and N. Engheta, "Pairing an epsilon-negative slab with a mu-negative slab: resonance, tunneling and transparency," *IEEE Trans. Antennas Propagat.*, Vol. 51, No. 10, 2558-2571, 2003.
7. Guo, J. Y., Y. Sun, Y. W. Zhang, H. Q. Li, H. T. Jiang, and H. Chen, "Experimental investigation of interface states in photonic crystal heterostructures," *Phys. Rev. E*, Vol. 78, No. 2, 026607(6), 2008.
8. Du, G. Q., H. T. Jiang, Z. S. Wang, and H. Chen, "Optical nonlinearity enhancement in heterostructures with thick metallic film and truncated photonic crystals," *Opt. Lett.*, Vol. 34, No. 5, 578-580, 2009.
9. Yariv, A., and P. Yeh, *Optical waves in Crystals*, New York: Wiley, 1984.
10. Biswas, R., Z. Y. Li, and K. M. Ho, "Impedance of photonic crystals and photonic crystal waveguides," Appl. Phys. Lett. Vol. 84, No. 8, 1254-1256, 2004.
11. Lubkowski, G., R. Schuhmann, and T. Weiland, "Extraction of effective metamaterial parameters by parameter fitting of dispersive models," *Microwave Opt. Technol. Lett.*, Vol. 49, No. 2, 285-288, 2007.
12. Busch, K., C. T. Chan, and C. M. Soukoulis, *Photonic Band Gap Materials*, Kluwer, Dordrecht, 1996.
13. Manifacier, J. C., J. Gasiot and J. P. Fillard, "A simple method for the determination of the optical constant n,k and the thickness of a weakly absorbing thin film," *J. Phys. E: Scientific instruments*, Vol. 45, 1002-1004, 1976.
14. He, J. and M. Cada, "Combined distributed feedback and Fabry□Perot structures with a phase-matching layer for optical bistable devices," *Appl. Phys. Lett.*, Vol.61, No.18, 2150-2152, 1992.
15. Ricard, D., Ph. Roussignol, and Chr. Flytzanis, "Surface-mediated enhancement of optical phase conjugation in metal colloids," *Opt. Lett.*, Vol. 10, No.10, 511-513, 1985.

Phonon considerations in the reduction of thermal conductivity in phononic crystals

P. E. HOPKINS,[1,*] L. M. PHINNEY,[1] P. T. RAKICH,[1] R. H. OLSSON III,[1] and I. EL-KADY[1,2]

[1]Sandia National Laboratories, Albuquerque, NM 87185-0346, USA

[2]Electrical and Computer Engineering, University of New Mexico, Albuquerque, NM 87131-0001, USA

*Author to whom correspondence should be addressed: Electronic mail: pehopki@sandia.gov

Abstract – Periodic porous structures offer unique material solutions to thermoelectric applications. With recent interest in phonon band gap engineering, these periodic structures can result in reduction of the phonon thermal conductivity due to coherent destruction of phonon modes characteristic in phononic crystals. In this paper, we numerically study phonon transport in periodic porous silicon phononic crystal structures. We develop a model for the thermal conductivity of phononic crystal that accounts for both coherent and incoherent phonon effects, and show that the phonon thermal conductivity is reduced to less than 4% of the bulk value for Si at room temperature. This has substantial impact on thermoelectric applications, where the efficiency of thermoelectric materials is inversely proportional to the thermal conductivity.

1. INTRODUCTION

Size effects significantly impact phonon thermal transport in micro and nanoscale systems [1]. Thorough understanding of such effects is crucial to the understand of thermal transport in micro- and nanosystems and for continued advancement of nanoscale applications, such as design and development of novel thermoelectric materials [2-5]. In particular, periodic porous structures are known to have strong tunable size effects due to increased surface area [6-8]. While electron thermal size effects have been observed on nanometer length scales in periodic porous structures [9], phonon thermal size effects have been observed on micron length scales [8]. This has substantial impact on phonon transport in phononic crystal structures, which can provide efficient material solutions for thermoelectric applications [10].

In this paper, we numerically study phonon transport in periodic porous silicon phononic crystal structures. In Section 2, we develop a model for the phonon thermal conductivity of bulk Si based on the measured phonon dispersion. We then modify the phonon dispersion to include phononic band gaps from 1 GHz – 500 GHz, 1GHz – 1 THz and from 1 GHz – 4 THz in Section 3, and show that a reduction in thermal conductivity due to these "coherent" band gap effects can arise solely from the modified phonon dispersion due to the phononic band gap. Considering incoherent phonon scattering mechanisms and the porosity of the phononic crystal structure, the predicted thermal conductivity of the Si phononic crystal can decrease to less than 4% of that of bulk Si, as discussed in Section 4. Since the efficiency of thermoelectric materials is evaluated by the Thermoelectric Figure of Merit, Z, which is inversely proportional to the thermal conductivity, κ, phononic crystals show promise as novel thermoelectric solutions.

2. THERMAL CONDUCTIVITY MODEL

To model the thermal conductivity of a Si phononic crystal, we must determine the various phonon scattering times that contribute to the phonon conductivity in Si. For this, we use a procedure to determine the thermal conductivity similar to that outlined by Holland [11, 12]. The thermal conductivity is given by

$$\kappa = \frac{1}{6\pi}\sum_j \int_0^{q_{\max,j}} \frac{\hbar^2 \omega_j^2(q)}{k_B T^2} \frac{\exp\left[\frac{\hbar\omega(q)}{k_B T}\right]}{\left(\exp\left[\frac{\hbar\omega(q)}{k_B T}\right]-1\right)^2} v_j^2(q)\tau_j(q)q^2 dq \tag{1}$$

where $\hbar$ is the reduced Planck's constant, $\omega(q)$ is the phonon dispersion, k_B is the Boltzmann constant, T is the phonon temperature, $v(q) = \partial\omega(q)/\partial q$ is the phonon group velocity, $\tau(q)$ is the scattering time of the phonons, q is the wavevector, and the thermal conductivity, κ is summed over j = 3 modes (one longitudinal and two transverse). To evaluate this expression, we must determine the Si dispersion and scattering times. We use measured Si dispersion data in the (100) direction [13, 14] and fit the data to a 4th degree polynomial for an analytical expression for $\omega(q)$ and $v(q) = \partial\omega(q)/\partial q$ [12]; we assume a doubly degenerate transverse branch. In bulk Si, phonon scattering is dominated by Umklapp scattering, impurity scattering, and boundary scattering. These scattering times are given by [15]

$$\frac{1}{\tau_{Umklapp,j}} = BT\omega_j^2(q)\exp\left[\frac{C}{T}\right] \tag{2}$$

$$\frac{1}{\tau_{impurity,j}} = D\omega_j^4(q) \tag{3}$$

$$\frac{1}{\tau_{boundary,j}} = \frac{v_j(q)}{E} \tag{4}$$

where *B*, *C*, *D*, and *E* are constants determined by fitting Eq. (1) to data. Equations (2) – (4) are related to the phonon scattering time in Eq. (1) via Matthiessen's Rule, so that

$$\frac{1}{\tau_j(q)} = \frac{1}{\tau_{Umklapp,j}} + \frac{1}{\tau_{impurity,j}} + \frac{1}{\tau_{boundary,j}}. \tag{5}$$

Given Eq. (5) with Eq. (1), the thermal conductivity of Si is calculated and the coefficients in Eq. (2) – (4) are iterated to achieve a best fit with measured data on bulk Si [16]. The fit to the data is shown in Fig. 1.

3. COHERENT EFFECTS ON THE PHONONIC CRYSTAL THERMAL CONDUCTIVITY

With all the parameters determined for the case of bulk Si, we now modify the phonon dispersion to imitate reflection or blocking of certain frequencies expected in the phononic crystal. We consider the 3 different cases of modified phonon dispersion: Case a – blocked frequencies from 1 GHz – 500 GHz; Case b – blocked frequencies from 1GHz – 1 THz; and Case c – blocked frequencies from 1 GHz – 4 THz. Figure 2a shows the

calculations of the thermal conductivity of Si using Eq. (1) with these modified dispersion relations over a wide range of temperatures (10 – 1,000 K). Figure 2b shows the fraction of the "bulk" (unmodified dispersion) thermal conductivity for each of the three cases in the temperature regime of interest for thermoelectric devices in most terrestrial microelectronic applications (100 – 500 K). The reduction in thermal conductivity due to blocking certain phonon frequencies is apparent, especially at lower temperatures. At room temperature, significant reduction is realized by blocking longitudinal and transverse modes up to 4 THz.

A useful exercise is to analyze the spectral contribution to the thermal conductivity to evaluate why blocking certain phonon states will cause a reduction in thermal conductivity [17]. The spectral contribution to thermal conductivity is given by [12]

$$\kappa_{\omega,j} = \frac{1}{6\pi}\frac{\hbar^2\omega_j^2(q)}{k_B T^2}\frac{\exp\left[\frac{\hbar\omega_j(q)}{k_B T}\right]}{\left(\exp\left[\frac{\hbar\omega_j(q)}{k_B T}\right]-1\right)^2} v_j(q)\tau_j(q)q^2 . \tag{6}$$

Here the transverse spectral thermal conductivity is multiplied by 2 since we assume doubly degenerate transverse branches. Figure 2c shows the fraction of the total spectral thermal conductivity at 300 K for a bulk Si dispersion and the three cases of dispersion modification (Cases a, b, and c). This fraction is defined as $\kappa_{\omega,j} \Big/ \sum_j \sum_\omega \kappa_{\omega,j}$. In bulk Si, the contribution from the transverse modes is much greater than that from the longitudinal modes below 4 THz. As the phononic bandgap increases, the dominant phonon frequencies participating in transport increase. Blocking up to 4 THz eliminates nearly all of the transverse phonon modes, which explains the large decrease in the thermal conductivity seen in Figs. 2a and b.

4. INCOHERENT EFFECTS ON THE PHONONIC CRYSTAL THERMAL CONDUCTIVITY

We now turn our attention to the effects of incoherent, classical scattering from the geometry of the phononic crystal. Our crystal will have periodic "holes" or large vacancies that are arranged to block the various phonon frequencies. Therefore, further reduction in thermal conductivity will occur from classical boundary scattering along with reducing the amount of bulk material in the crystal (i.e., the porous nature of the phononic crystal). To simulate this, we consider the approach to analyzing a porous nanowire matrix discussed by Hopkins *et al* [9]. In this approach, we introduce an addition boundary scattering mechanism in Eq. (5), given by

$$\frac{1}{\tau_{porescattering,j}} = \frac{v_j(q)}{L} \tag{7}$$

where L is linear distance between scattering sites. Note that this differs from Eq. (4) since L is not a fitting parameter. The thermal conductivity is then calculated by adding Eq. (7) into Eq. (5), and calculating the bulk thermal conductivity via Eq. (1).

Now, let's consider the effects of boundary scattering for the phononic crystals discussed in this work. The scattering sites are the voids in the Si crystals that occur at periodic distances, so mathematically we treat them similar to grain boundaries via Eq. (7) [18, 19]. We estimate the center-to-center spacing of the vacancies in the

phononic crystal as $a = \pi v / f$, where v is the average speed of sound in Si, which we estimate as v = 6,545 m s^{-1} by averaging the zone center phonon velocities of the longitudinal and transverse branches [20], and f is the upper limit of the phononic band gap. Assuming r/a = 0.4, which is a reasonable ratio of the vacancy radius, r, to the center-to-center spacing for a Si phononic crystal with evacuated periodic inclusions [10], the linear distance between the scattering sites (edges of the periodic vacancies) is estimated as $L = a - 2r$. Therefore, the scattering distances for Cases a, b, and c are L = 8.2, 4.1, and 1.0 nm, respectively.

Finally, we consider the thermal conductivity reduction due to physically removing areas of the crystal to create the phononic lattice. This can be modeled as a reduction due to porosity; to calculate the effects of the porosity, we use the effective medium approximation derived by Eucken for a solid with cylindrical pore inclusions given by [21]

$$\frac{\kappa_r}{\kappa_s} = \frac{1-p}{1+\frac{2}{3}p} \tag{8}$$

where κ_s is the thermal conductivity of the corresponding solid assuming no porosity (i.e., Eq. (1) with Eqs. (5) and (7)), κ_r is the resultant thermal conductivity of the porous structures, and p is the porosity. For a square phononic crystalline lattice with r/a = 0.4, we estimate the porosity from geometrical considerations as p = 0.64. This approach of accounting for the thermal conductivity reduction due to porosity has been validated in periodic porous Si films [12].

Using Eq. (8), with Eqs. (7) and (5) in Eq. (1), we calculate the thermal conductivity of a Si phononic crystal accounting for coherent and incoherent effects for the three cases. The resulting thermal conductivity as a function of temperature is shown in Fig. 3a, and the corresponding fraction of the bulk thermal conductivity for each case is shown in Fig. 3b. We have previously studied the spectral conductivity due to incoherent effects, and so omit the analysis here, but refer the reader to our previous work for further analysis of how incoherent scattering reduces the thermal conductivity of bulk Si at different frequencies [12]. The incoherent effects reduce the thermal conductivity of the Si phononic crystals even further, and cause a greater reduction in κ than the coherent effects. However, coherent and incoherent effects together substantially reduce the thermal conductivity of the phononic crystal, leading to reductions in κ to 0.7 – 3.5 % of the bulk value at 300 K. In practice, Case c is extremely difficult to fabricate, however, Cases a and b are more feasible for device engineers. Assuming a thermoelectric module designed from silicon phononic crystals with coherent properties of Case a, the reduction in the phonon thermal conductivity to 3.5% of the bulk value leads to an enhancement in Z by a factor of 28.5, showing that phononic crystals offer a unique material solution to enhancing thermoelectric applications. Note that in this work, we consider a bulk Si dispersion as the basis of our thermal conductivity model. In nanostructured materials, the phonon dispersion will be different than that of bulk [22]; however, this change in dispersion will result in a reduction in the phonon group velocity which would create an even further reduction in the thermal conductivity of the phononic crystal. Therefore, the model developed in this work based on a bulk Si dispersion is considered an upper limit to the thermal conductivity of phononic crystals.

4. CONCLUSIONS

We numerically study phonon transport in silicon phononic crystals. We develop a model for the thermal conductivity of phononic crystal that accounts for both coherent and incoherent phonon effects, and show that the phonon thermal conductivity can be reduced to less than 4% of the bulk value for Si at room temperature. This has substantial impact on thermoelectric applications, as a reduction in thermal conductivity will increase the thermoelectric figure of merit.

ACKNOWLEDGEMENTS

P.E.H. is greatly appreciative for funding by the Harry S. Truman Fellowship through the LDRD Program at Sandia National Laboratories. Sandia is a multiprogram laboratory operated by Sandia Corporation, a Lockheed-Martin Co. for the United States Department of Energy's National Nuclear Security Administration under Contract No. DE-AC04-94A185000.

REFERENCES

[1] Cahill, D. G., Ford, W. K., Goodson, K. E., Mahan, G. D., Majumdar, A., Maris, H. J., Merlin, R., and Phillpot, S. R., 2003, "Nanoscale thermal transport," Journal of Applied Physics, 93, pp. 793-818.

[2] Boukai, A. I., Bunimovich, Y., Tahir-Kheli, J., Yu, J.-K., Goddard, W. A., and Heath, J. R., 2008, "Silicon nanowires as efficient thermoelectric materials," Nature, 451, pp. 168-171.

[3] Chen, G., 1997, "Size and interface effects on thermal conductivity of superlattices and periodic thin-film structures," Journal of Heat Transfer, 119, pp. 220-229.

[4] Dresselhaus, M. S., Dresselhaus, G., Sun, X., Zhang, Z., Cronin, S. B., Koga, T., Ying, J. Y., and Chen, G., 1999, "The promise of low-dimensional thermoelectric materials," Microscale Thermophysical Engineering, 3, pp. 89-100.

[5] Riffat, S., and Ma, X., 2003, "Thermoelectrics: A review of present and potential applications," Applied Thermal Engineering, 23, pp. 913-935.

[6] Benedetto, G., Boarino, L., and Spangnolo, R., 1997, "Evaluation of thermal conductivity of porous silicon layers by a photoacoustic method," Applied Physics A, 64, pp. 155-159.

[7] Bernini, U., Bernini, R., Maddalena, P., Massera, E., and Rucco, P., 2005, "Determination of thermal diffusivity of suspended porous silicon films by thermal lens techniques," Applied Physics A, 81, pp. 399-404.

[8] Song, D., and Chen, G., 2004, "Thermal conductivity of periodic microporous silicon films," Applied Physics Letters, 84, pp. 687-689.

[9] Hopkins, P. E., Norris, P. M., Phinney, L. M., Policastro, S. A., and Kelly, R. G., 2008, "Thermal conductivity in nanoporous gold films during electron-phonon nonequilibrium," Journal of Nanomaterials, 2008, pp. 418050, doi:10.1155/2008/418050.

[10] Olsson III, R. H., and El-Kady, I., 2009, "Microfabricated phononic crystals devices and applications," Measurement Science and Technology, 20, pp. 012002.

[11] Holland, M. G., 1963, "Analysis of lattice thermal conductivity," Physical Review, 132, pp. 2461-2471.

[12] Hopkins, P. E., Rakich, P. T., Olsson III, R. H., El-Kady, I., and Phinney, L. M., 2009, "Origin of reduction in phonon thermal conductivity of microporous solids," Applied Physics Letters, 95, pp. 161902.

[13] Nilsson, G., and Nelin, G., 1972, "Study of the homology between silicon and germanium by

thermal-neutron spectrometry," Physical Review B, 6, pp. 3777-3786.

[14] Brockhouse, B. N., 1959, "Lattice vibrations in silicon and germanium," Physical Review Letters, 2, pp. 256-258.

[15] Chen, G., 2005, *Nanoscale Energy Transport and Conversion: A Parallel Treatment of Electrons, Molecules, Phonons, and Photons*, Oxford University Press, New York.

[16] Ho, C. Y., Powell, R. W., and Liley, P. E., 1972, "Thermal conductivity of the elements," Journal of Physical and Chemical Reference Data, 1, pp. 279-422.

[17] Henry, A. S., and Chen, G., 2008, "Spectral phonon transport properties of silicon based on molecular dynamics simulations and lattice dynamics," Computational and Theoretical Nanoscience, 5, pp. 1-12.

[18] Mcconnell, A. D., and Goodson, K. E., 2005, "Thermal conduction in silicon micro- and nanostructures," Annual Review of Heat Transfer, 14, pp. 129-168.

[19] Mcconnell, A. D., Uma, S., and Goodson, K. E., 2001, "Thermal conductivity of doped polysilicon layers," Journal of Microelectromechanical Systems, 10, pp. 360-369.

[20] Gray, D. E., 1972, *American Institute of Physics Handbook*, McGraw Hill, New York.

[21] Eucken, A., 1932, "Die warmeleitfahigkeit keramischer feuerfester stoffe: Ihre berechnung aus der warmeleitfahigkeit der bestandteile (Thermal conductivity of ceramic refractory materials: calculations from thermal conductivity of constituents)," Forschung auf dem Gebiete des Ingenieurwesens, Ausgabe B, pp. 3/4 VDI Forschungsheft 353.

[22] Mingo, N., 2003, "Calculation of Si nanowire thermal conductivity using complete phonon dispersion relation," Physical Review B, 68, pp. 113308.

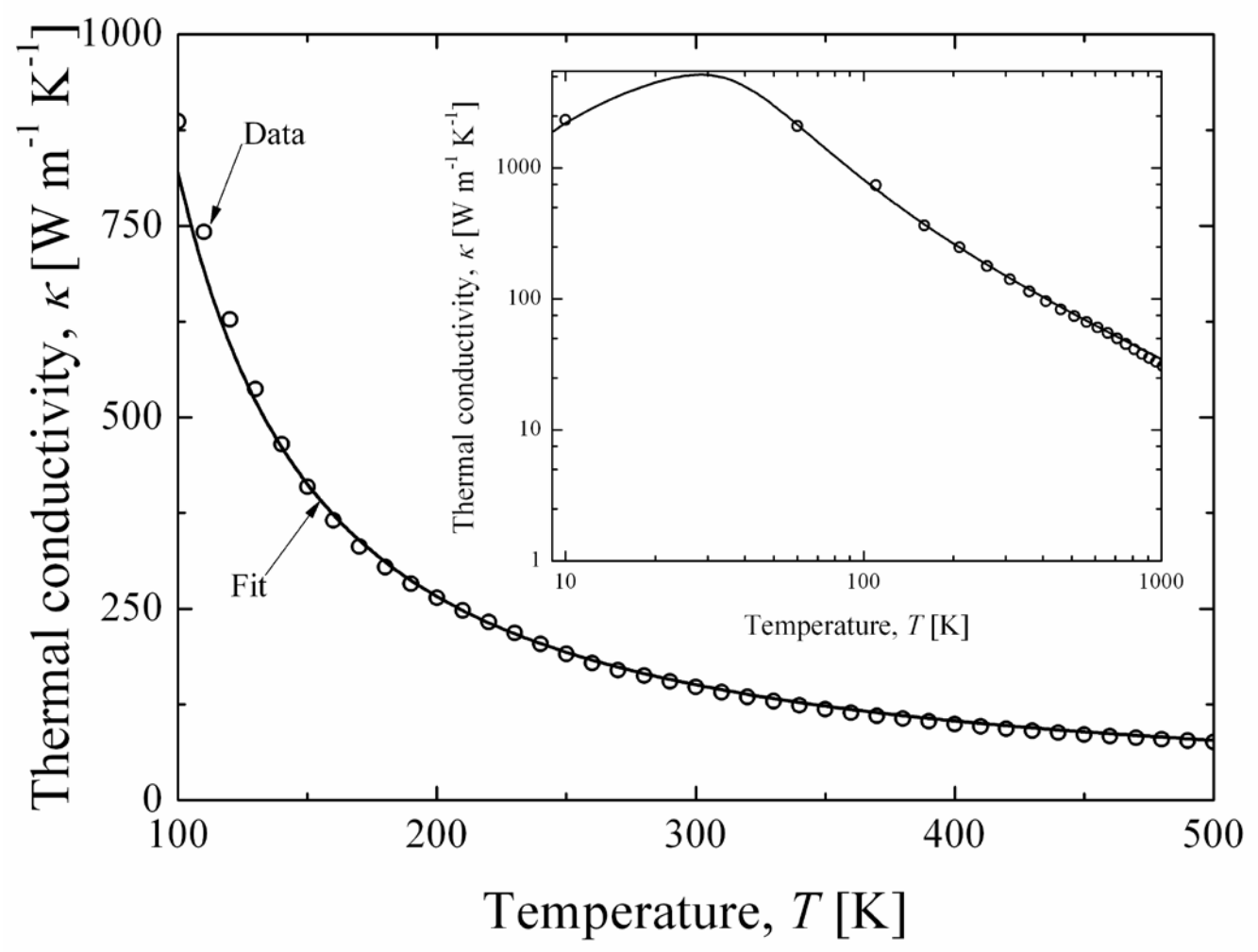


Figure 1. Thermal conductivity model fit to experimental data on single crystalline Si [16]. The best fit coefficients for the various scattering times (Eqs. (2) – (4)) are B = 3.73 x 10-^{19} s K^{-1}, C = 157.3 K, D = 9.32 x 10^{-45} s^3, and E = 2.3 x 10^{-3} m.

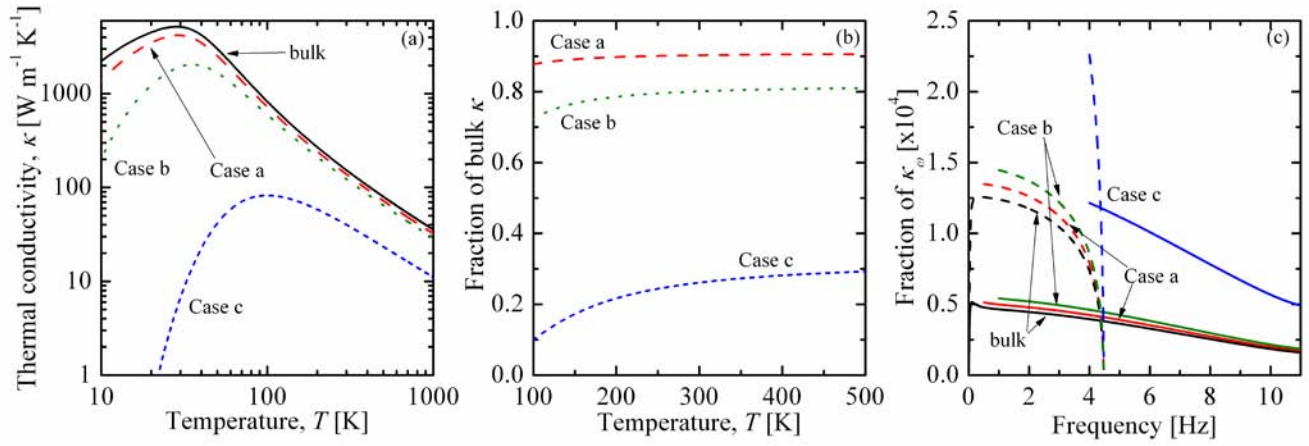


Figure 2. (a) Thermal conductivity of Si assuming an unmodified dispersion relation (bulk), blocked frequencies from 1 GHz – 500 GHz (Case a), blocked frequencies from 1GHz – 1 THz (Case b), and blocked frequencies from 1 GHz – 4 THz (Case c). (b) Fraction of the "bulk" (unmodified dispersion) thermal conductivity for each of the three cases in the temperature regime of interest for thermoelectric devices in most terrestrial microelectronic applications (100 – 500 K). (c) Fraction of the total spectral thermal conductivity at 300 K for a bulk Si dispersion and the three cases of dispersion modification (Cases a, b, and c). The longitudinal modes are represented by the solid lines and the transverse modes by the dashed lines.

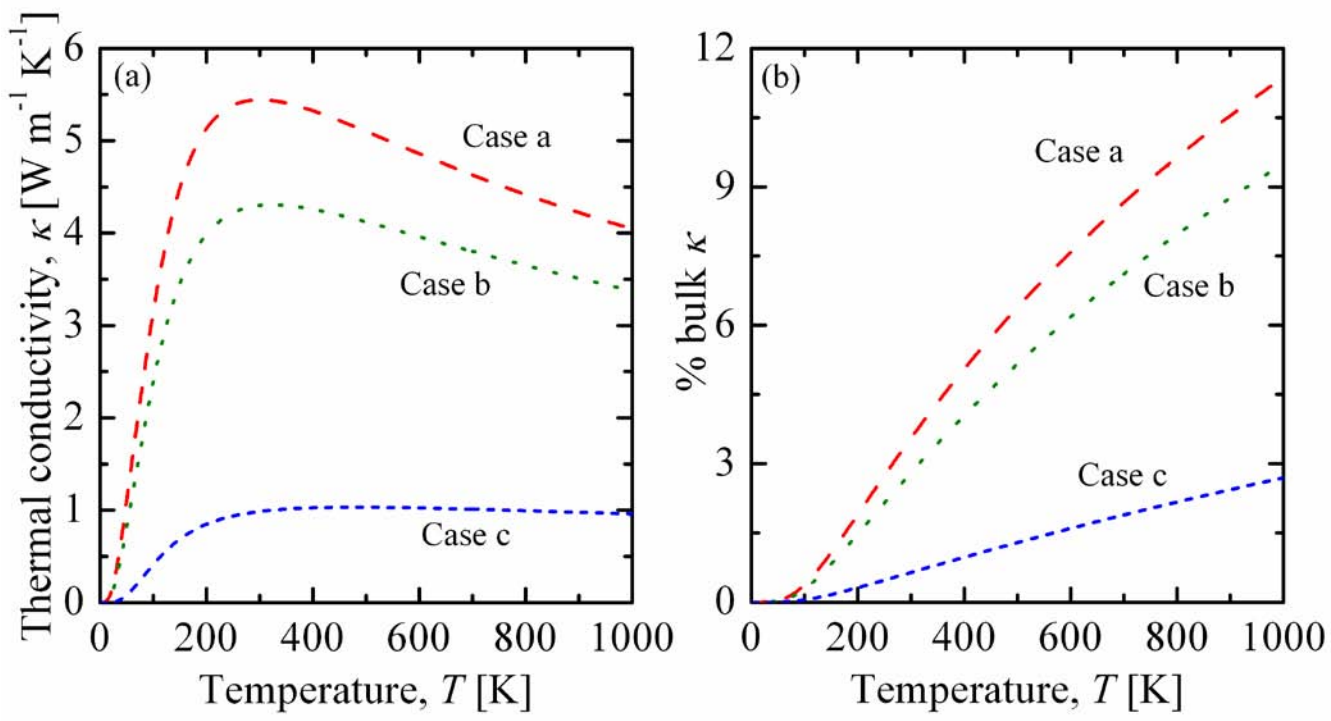


Figure 3. Thermal conductivity of a Si phononic crystal accounting for coherent and incoherent effects for the three modified dispersion cases in Fig. 2: (a) thermal conductivity as a function of temperature; and (b) corresponding fraction of the bulk thermal conductivity.

Acoustic wave propagation in fluid metamaterial with solid inclusions

I. V. Lisenkov, **R. S. Popov and S. A. Nikitov**

Kotel'nikov Institute of Radio-engineering and Electronics of RAS
lisenkov@cplire.ru

Abstract— Propagation of acoustic waves in composite of water with embedded double-layered silicone resin/silver roads are considered. Approximate values of effective dynamical constitutive parameters are obtained. Frequency domains where constitutive parameters are simultaneous negative are found. Localized surface states on the interface between metamaterial and "normal" material are found. Doppler effect in metamaterial is considered. Presence of anomalous modes is shown.

1. INTRODUCTION

Metamaterials attract attention for several decades due to unique properties of wave propagation in them. In pioneering works of Veselago [1] and Pendry [2] electromagnetic waves in media with simultaneous negative ϵ and μ were considered. Since that time, a lot of theoretical and experimental work has been done on this subject [3].

In fact, for acoustic waves metamaterials are possible too. Some proposals and experiments to archive negative effective constitutive parameters for acoustic composites were made in past [4]. The aim of this work is to show that it is possible to construct a metamaterial to exhibit negative constitutive parameters in ultrasonic range and demonstrate that acoustic waves can exhibit exotic behavior, namely presence of localized states at the boundary between metamaterial and "normal" material and anomalous Doppler effect in metamaterial.

2. MATHEMATICAL MODEL

2.1. Effective constitutive parameters

In our work we consider a composite consist of fluid host with rods embedded in it. Rods have cylindrical shape and consist of elastic materials. Acoustic waves propagate in host material (density ρ_0 and bulk modulus B_0) with wave-vector perpendicular to generatixes of the rods. By definition [3], a metamaterial should be quasi-isotropic, so the wavelength is much longer than distance between centers of cylinders(L) and their radii(R). We consider all cylinders identical and placed at random at approximate equal distance between neighbors. Our aim is to compute the dynamical effective constitutive parameters of the metamaterial on given frequency and dispersion of propagating bulk acoustic wave.

In our calculations we are using coherent potential approximation [5] (CPA). This method is widely used to estimate effective parameters of composites and, in particular, metamaterials [4]. In this work we apply this method for fluid/solid composite taking in account longitudinal and shear polarizations in solid inclusions and acoustical dumping.

In order to proceed CPA we surround one inclusion with cylinder of radius L (call it coated inclusion) and say that outside the cylinder there is some effective fluid with constitutive parameters (ρ_e for effective density and B_e for effective bulk modulus) to be estimated. Pressure and radial component of velocity in host material and in effective material can be decomposed by cylindrical harmonics [6]:

$$\begin{aligned} \Psi &= e^{i\omega t}\sum_{n=0}^{\infty} X_n^m J_n(k_m r)e^{in\phi} + Y_n^m H_n(k_m r)e^{in\phi} \\ v_r &= e^{i\omega t}\frac{k_m}{\rho_m}\sum_{n=0}^{\infty} X_n^m J_n'(k_m r)e^{in\phi} + Y_n^m H_n'(kr)e^{in\phi}, \end{aligned} \tag{1}$$

where $J_n()$ and $H_n()$ are Bessel and Hankel functions of the first kind, n-th order, X_n^m, Y_n^m are unknowns and m stands for e in effective media and for 0 in host material.

On the interface between host fluid and effective medium we should satisfy standard boundary conditions of velocity and pressure continuity. Due to cylindrical symmetry, we could satisfy boundary conditions for each cylindrical harmonics independently:

$$\begin{bmatrix} J_n(k_eL) & H_n(k_eL) \\ \frac{k_e}{\rho_e}J_n(k_eL) & \frac{k_e}{\rho_e}H_n(k_eL) \end{bmatrix} \cdot \begin{bmatrix} X_n^e \\ Y_n^e \end{bmatrix} = \begin{bmatrix} J_n(k_0L) & H_n(k_0L) \\ \frac{k_0}{\rho_0}J_n(k_0L) & \frac{k_0}{\rho_0}H_n(k_0L) \end{bmatrix} \cdot \begin{bmatrix} X_n^0 \\ Y_n^0 \end{bmatrix}, \tag{2}$$

where k_e is the wave-number in effective medium, k_0 is the wave-number in host medium and $e^{in\phi}$ and $e^{i\omega t}$ factors are dropped out.

Main CPA condition is absence of scattering on the boundary, which means that there is a perfect matching between coated inclusion and surrounding effective medium. Setting $X_n^e = 1$ and $Y_n^e = 0$ in (2) we obtain the CPA equation:

$$-\frac{k_0}{B_0}J_n'(k_0L)J(k_eL) + \frac{k_e}{B_e}J_n(k_0L)J'(k_eL) = \frac{Y_n}{X_n}\left[\frac{k_0}{B_0}H_n'(k_0L)J(k_eL) - \frac{k_e}{B_e}H_n(k_0L)J'(k_eL)\right] \tag{3}$$

Using the fact that metamaterial should be quasi-isotropic, in other words, phase of wave in host material should not change much in distance between neighbor inclusions ($k_0L \to 0$ and $k_eL \to 0$), we use asymptotic formulas for Bessel and Hankel functions for zero argument limit. In this approximation only zero-th and first orders of Bessel and Hankel functions are significant. After some algebra we obtain approximate formulas for effective constitutive parameters:

$$B_e = \frac{B_0}{1 - S_0}, \quad \rho_e = \rho_0\frac{1 - S_1}{1 + S_1} \tag{4}$$

where:

$$S_n = \frac{D_n}{1 + D_n}\frac{4}{\pi}\frac{1}{k_0^2L^2} \cdot i \tag{5}$$

and $D_n = Y_n/X_n$ — scattering amplitude of the embedded rod in infinite fluid. In our case it is scattering of the wave in fluid on solid cylinder. This problem is was solved past see eg. [7].

It is seen from formulas (4) that dynamical effective constitutive parameters are frequency dependent and in case of resonance in inclusion could change dramatically and even became negative. Thus speed of sound inside the inclusions should be much slower than in host fluid. Also we should note, that bulk modulus depend on monopolar scattering coefficient and effective density is depend on dipole coefficient. This is logical, because monopole mode is uniform compression/expansion of the inclusion and dipole mode is the inclusion shift.

Dynamical effective constitutive parameters are frequency dependent and does not have clear physical meaning by themselves. But their combination, the wave-number, fully describes propagating wave in composite [6]:

$$k(\omega) = \sqrt{1/B_e(\omega)} \cdot \sqrt{\rho_e(\omega)}\omega \tag{6}$$

The phase of the wave-number has clear physical meaning. If phase is tend to zero the wave-vector is pointing the same direction as Poynting vector, phase is about $\pi/2$ means that one of the constitutive parameters are negative and other is not, thus the wave is decaying, finally, phase is about π means that wave-vector and Poynting are pointing in opposite directions and the wave is backward.

2.2. Surface acoustic wave

Along the boundary between two ideal fluids no surface wave is able to propagate, because boundary conditions could not be satisfied. But if one of the materials has one negative constitutive parameter boundary states could be excited [9]. This is direct analogy to surface plasmon-polariton states in plasma with $\epsilon < 0$ [3].

Let us consider a wave travels form a half-space occupied by pure host fluid to a half-space occupied by a fluid with embedded rods in it. The reflection coefficient is [6]:

$$\Gamma = \frac{\rho_e k_e^z - \rho_0 k_0^z}{\rho_e k_e^z + \rho_0 k_0^z}, \tag{7}$$

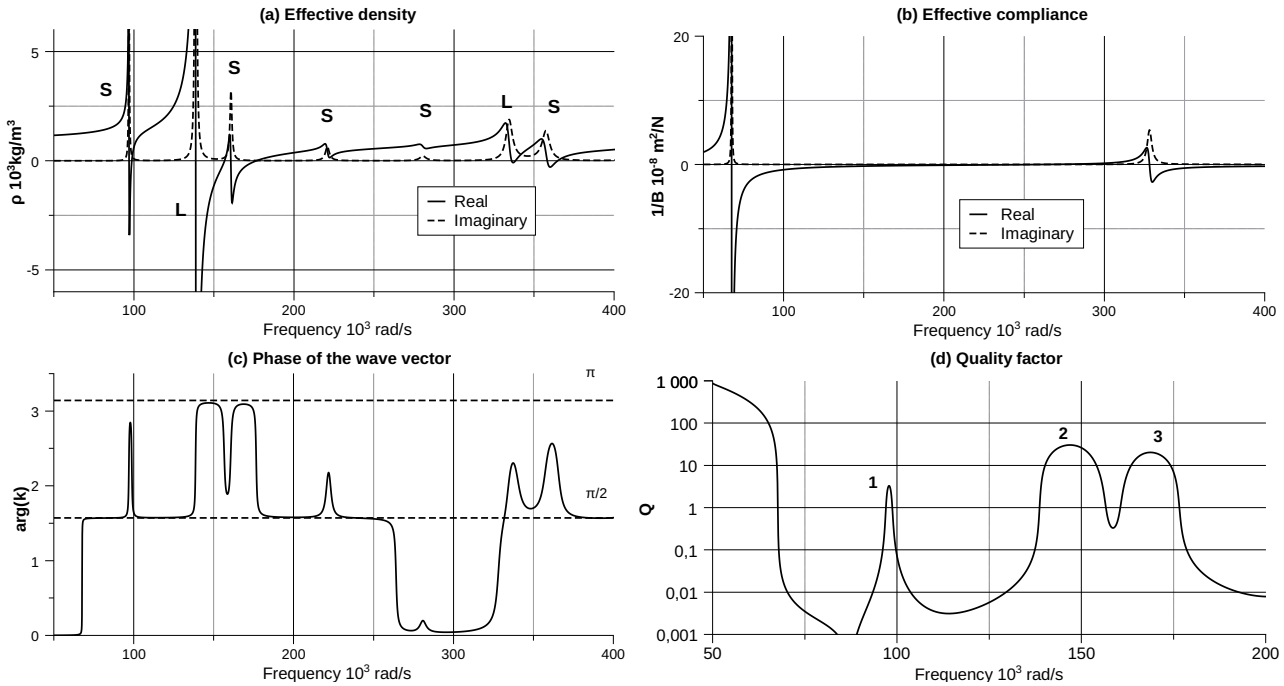


Figure 1: Frequency dependence of effective density (a), compliance (b), phase of wave-number (c) and losses per wavelength (d)

where k_0^z and k_0^z are projections of wave-vector perpendicular to the interface in pure fluid and metamaterial, respectively. Condition for boundary states to present is vanishing of reflection $\Gamma = 0$. Thus one can derive dispersion equation for surface wave:

$$k_s = \sqrt{\frac{(\rho_0\rho_e)(\rho_0 B_e - \rho_e B_0)}{\rho_0^2 - \rho_e^2}}\omega. \tag{8}$$

It will be shown, that boundary states are present only if one of the constitutive parameters is negative.

3. RESULTS

3.1. Bulk wave

In our calculations rods are considered to be two-layered cylinders. Shell of the cylinder is made of soft silicone resin[1] ($\rho = 1.3 \cdot 10^3 kg/m^3$, $c_{11} = 5.2 \cdot 10^7 N/m^2$, $c_{44} = 3.25 \cdot 10^6 N/m^2$, Loss: 600 $dB/m/MHz$), core of the cylinder is made of poly-crystal silver [6] ($\rho = 10.5 \cdot 10^3 kg/m^3$, $c_{11} = 1.397 \cdot 10^{11} N/m^2$, $c_{44} = 2.7 \cdot 10^{10} N/m^2$, Loss: 40 $dB/m/MHz$). Outher raidus of the rod is 3 mm, radius of the core is 0.5 mm, distance between cylinders is taken 5 mm. Host material is water ($\rho = 10^3 kg/m^3$, $B = 2.25 \cdot 10^9 N/m^2$).

In the Figure 1 results of the calculations for bulk wave are presented. On low frequencies effective constitutive parameters tend to be close "classic" values for composites [8]. But at frequencies close to resonances inside the inclusions values of dynamical effective constitutive parameters dramatically change. In Fig. 1(b) two frequencies of monopolar resonances are seen and after the resonances there are two domains where real part of compliance is negative (In this section we use compliance ($1/B$) instead of stiffness to emphasize similarity to electromagnetic case).

In Fig. 1(a) frequency dependence of dynamical effective density is shown. Due to complex shear and longitudinal field structure inside the inclusion, there are two families of resonances associated to shear waves and longitudinal waves (S and L in the figure, respectively). Thus dynamical effective density has lots of frequency domains where real part is negative. Shear components became significant because of inertia of the core.

[1]There are various types of silicone resins, our parameters are approximate

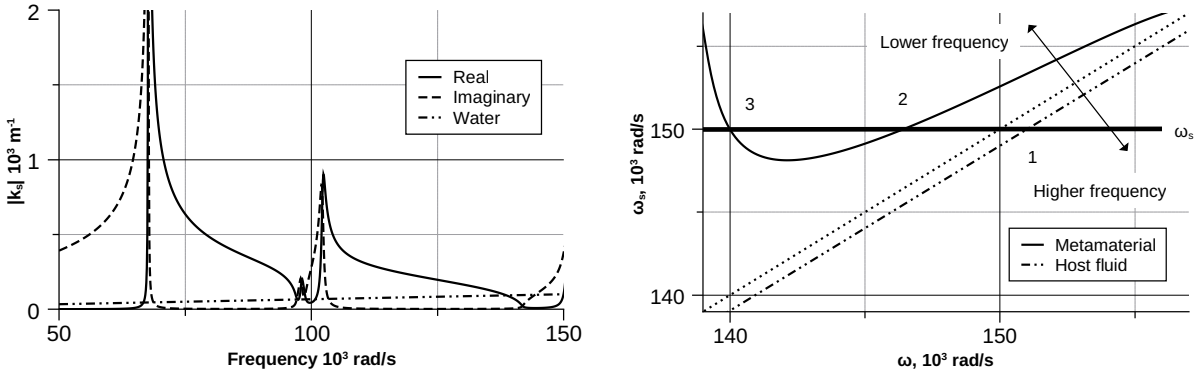


Figure 2: (a) Dispersion of surface acoustic wave at the interface between metamaterial and "normal" material (b) Graphical solution for Doppler equation in metamaterial (solid line) and host fluid (dot-dashed line)

In Fig. 1(c) dependence of the argument of the wave-number is plotted. As it was pointed out the plot shows character of the propagating wave. At the low frequency before any resonance metamaterial exhibits properties of "normal" medium. After the monopolar resonance in the inclusion, real part of $1/B$ become negative and the phase of wave vector is shifted to $\pi/2$. In this domain wave-number is close to be pure imaginary, thus no oscillations could be supported and no wave is able to propagate. In such way a forbidden gap is formed. After dipole resonance effective density become negative and phase is shifted again for another $\pi/2$ and the wave-number become close to negative real. Thus phase velocity of the wave is points backwards and opposite to the Poynting vector, the domain of simultaneously negative constitutive parameters is formed. In Fig. 1(d) acoustic Q-factor is presented. Dependence shows, that in frequency domain where constitutive parameters have simultaneous significant negative parts the wave is still able to propagate in spite of losses in inclusions (regions 1,2 and 3 in the figure).

3.2. Surface acoustic wave

In Figure 2(a) dispersion for surface wave is shown. As it was predicted, wave-number does not have real part at low frequencies, since parameters of metamaterial remain positive, so the wave does not propagate along the interface. But after a resonance (compare to Fig. 1(a)) one of material parameters become negative and surface states appear. Dispersion of bulk acoustic wave in pure fluid is plotted by dot-dashed line. Surface wave is much slower than bulk wave, thus the surface states are bounded to the interface.

3.3. Anomalous Doppler effect

Veselago [1] showed that in media with simultaneous negative ϵ and μ Doppler effect is inversed. Obviously, similar effect is in acoustic metamaterials. Let us consider a source travels inside composite with velocity V and transmitting signal with angular frequency ω_s. Not narrowing generality we can assume that source is approaching directly to receiver. To obtain frequency on the receiver(ω) we should solve the equation:

$$\omega - V \cdot k(\omega) = \omega_s \tag{9}$$

For medium with linear dispersion equation (9) is trivial, but for dispersive medium like metamaterial it is not. Graphical solution for equation (9) is plotted in Fig. 2(b) (We assume that dumping is not very high and take only real part of k in this section).

Angular frequency of source is taken $1.5 \cdot 10^5$ rad/s and speed is 10 m/s. The frequency is chosen in domain where composite has simultaneous negative dynamical effective density and stiffness. For pure host material the result is predictable, intersection 1 shows the root and it is seen that frequency of receiver is up-shifted. In contrast, for composite the equation has two roots (points 2 and 3 on the Figure) and the frequencies are down-shifted. Also we should notice that Doppler shift is depend on frequency and several Doppler modes can occur only in case source frequency is close to resonance, speed of source is high enough and dumping is not very high.

4. CONCLUSIONS

In the paper effective dynamic density and stiffness of composite consisted of water with embedded solid two-layered rods in terms of coherent potential approximation are calculated. It is shown, that there are some frequency domains in which dynamic constitutive parameters are simultaneously negative and propagating wave is backward.

Dispersion of the surface acoustic wave at the interface between metamaterial and "normal" material is calculated, showed that there are frequency domains in which surface states are bounded to the interface.

Doppler effect in composite is considered. It is shown, that in metamaterial Doppler shift is reversed and several modes could be excited.

ACKNOWLEDGMENT

The work is supported by RFBR Grants #08-02-00785-a and #09-02-12433

REFERENCES

1. V. G. Veselago, "The Electrodynamics of Substances with Simultaneously Negative Values of ϵ and μ," *Soviet Physics Uspekhi*, Vol. 10, pp. 509–+, Jan. 1968.
2. Pendry, J. B. and Smith D. R. "Reversing Light: Negative Refraction," *Physics Today* Vol. 37 pp. 3745. 2003
3. C. Caloz and T. Itoh, *Electromagnetic Metamaterials: Transmission Line Theory and Microwave Applications*, Wiley-IEEE Press, Hoboken, New Jersey, 2005
4. J. Li and C. T. Chan, "Double-negative acoustic metamaterial," *Phys. Rev. E*, Vol. 70, no. 5, p. 055602, Nov 2004.
5. P. Sheng, *Introduction to Wave Scattering, Localization and Mesoscopic Phenomena*, Academic Press, New York, 1995.
6. B. A. Auld, *Acoustic Fields and Waves in Solids* vol. 1, John Wiley & Sons, Inc, New York, 1973.
7. Faran Jr., J. J. "Sound Scattering by Solid Cylinders and Spheres, " *J. Acoust. Soc. Am.*, Vol. 23, Issue 4, 1951
8. J. G. Berryman, "Long-wavelength propagation in composite elastic media II. Ellipsoidal inclusions," *Acoustical Society of America Journal*, Vol. 68, pp. 1820–1831, Dec. 1980.
9. M. Ambati, N. Fang, C. Sun, and X. Zhang, "Surface resonant states and superlensing in acoustic metamaterials," *Phys. Rev. B*, Vol. 75, no. 19, p. 195447, 2007.

Band Gap Engineering in Simultaneous Phononic and Photonic Crystal Slabs

B. Djafari Rouhani[1], Y. Pennec[1], E.H. El Boudouti[1,2], J.O. Vasseur[1], Y. El Hassouani[1], C. Li[1], A.Akjouj[1] and D. Bria[1,2]

[1]Institut d'Electronique, de Microélectronique et de Nanotechnologie, UMR CNRS 8520, Université de Lille1 Sciences et Technologies, Cité scientifique, 59652 Villeneuve d'Ascq, France

[2]Laboratoire de Dynamique et d'Optique des Matériaux, Faculté des Sciences, Université d'Oujda, Morocco

Bahram.djafari-rouhani@univ-lille1.fr

Abstract- We discuss the simultaneous existence of phononic and photonic band gaps in two types of phononic crystals slabs, namely periodic arrays of nanoholes in a Si membrane and of Si nanodots on a SiO_2 membrane. In the former geometry, we investigate in detail both the boron nitride lattice and the square lattice with two atoms per unit cell (these include the square, triangular and honeycomb lattices as particular cases). In the latter geometry some preliminary results are reported for a square lattice.

1. INTRODUCTION

Phononic crystals [1-2], constituted by a periodical repetition of inclusions in a matrix background, has received a great deal of attention during the last two decades [3]. Associated with the possibility of absolute band gaps in their band structure, these materials have found several potential applications, in particular in the field of wave guiding and filtering (in relation to the properties of their linear and point defects) as well as in the field of sound isolation. Another issue of interest is based on the refractive properties of these materials for exploring phenomena such as negative refraction, focusing, self-collimation and beam splitting as well as for the realization of metamaterials for controlling the propagation of sound.

The study of slabs of phononic crystals has become a topic of major interest since a few years only. Indeed we and other authors have demonstrated [4-6] that with an appropriate choice of the geometrical and physical parameters these finite thickness structures can also exhibit absolute band gaps. This makes them suitable for similar applications as in the case of 2D phononic crystals with the additional property of confinement in the vertical direction. More recently we have proposed a new type of finite thickness phononic crystal constituted by a periodic array of dots (or beams) on a membrane [7-8]. In this paper we briefly recall some of the results about the phononic band structure in the above systems. Then, we mainly focus on a detailed study of simultaneous phononic and photonic band gaps in these materials. Indeed, many papers have investigated separately the existence of photonic [9-10] and phononic band gaps, but relatively few works have been devoted to simultaneous control of phonons and photons [11-14] and most of the papers are dealing with the case of 2D structures [11-13]. The two following sections are respectively devoted to the geometries of periodic nanoholes in a Si membrane and periodic array of Si nanodots deposited on a SiO_2 membrane. Most of the calculations are performed with the Plane Wave Expansion (PWE) method and the good convergence of the results is also checked in some cases by using the Finite Difference Time Domain (FDTD) and Finite Element (FE) methods.

2. PERIODIC ARRAY OF HOLES IN A SILICON MEMBRANE

In a previous work [4], we demonstrated the existence of absolute phononic band gaps in square and honeycomb lattices of holes in a Si membrane provided the thickness of the slab is about half of the lattice period and the

filling fraction is sufficiently high. Here we consider the more general cases, shown in Figure 1, of the square lattice with two atoms per unit cell and of the boron nitride (BN) lattice (which includes triangular and honeycomb lattices) and investigate both the phononic and photonic band gaps. By considering the lattice period *a* as the unit of length, there are several geometrical parameters involved in the problem, namely the thickness *h* of the slab, the filling fraction *f* and the ration $\alpha = r_1/r_2$ of the radii of the two types of holes in the unit cell. The band structures are calculated for a large variety of these parameters in the useful ranges (*h/a* from 0.4 to 0.7, *f* from 0.3 to 0.7, and α from 0 to 1). The frequencies are given in the dimensionless units $\Omega = \omega a/2\pi c$ where c is the velocity of light in vacuum for electromagnetic waves and the transverse velocity of sound in Si for elastic waves. According to the symmetry of the structure with respect to the middle plane of the slab, the modes can be classified into symmetric (even) and antisymmetric (odd) modes. Let us mention that in the slab geometry, the photonic gaps have to be searched only below the light cone in vacuum; however, these gaps should preferably occur at frequencies Ω below 0.5, otherwise they will be restricted to a very small area of the Brillouin zone and are therefore not very interesting.

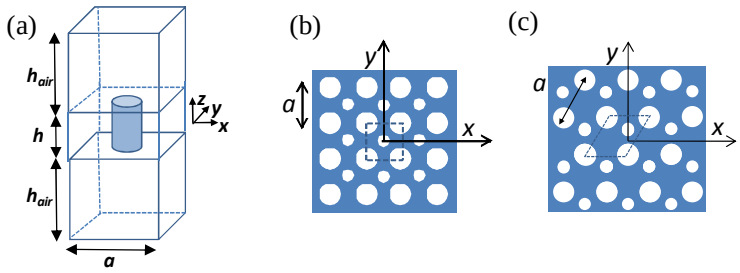


Fig. 1: (a) Representation of the unit cell for the numerical calculations. (b) Square lattice with two atoms per unit cell. (c)Boron Nitride (BN) lattice.

In the square lattice, the trends are the followings. In the phononic side, the limitation comes from the odd modes which only display narrow gaps. Moreover, these gaps occur for high filling fraction ($f > 0.6$, i.e. very close holes) and almost near $\alpha=0$ (simple square) as illustrated in Figure 2a. In the photonic side, absolute band gaps can only exist for $h/a \sim 0.4$ in a very restricted region of the Brillouin zone (near the M point) just below the light cone; so this solution is not very interesting. At lower frequencies, there is in general no overlap between the gaps of both symmetries. The odd gap mainly occurs near $\alpha=0$ whereas other favorable solutions can be found for even modes when the lattice contains two different atoms in the unit cell (see Figures 2b and c).

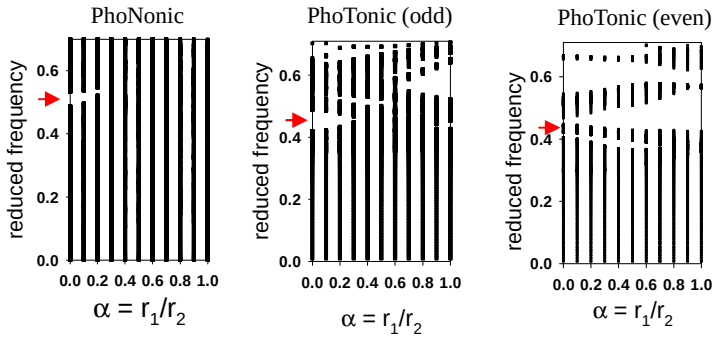


Fig. 2 Phononic and photonic band gaps (white areas) in a square lattice with two atoms per unit cell, with h=0.6a and f=0.65. The odd and even photonic modes are shown separately because they do not overlap. The red arrows represent the domains where there are simultaneous phononic and photonic gaps.

Based on the above discussions, the choice of a crystal can be made by searching a structure that exhibits an absolute phononic band gap though a photonic gap of a given symmetry only. Figure 2 illustrates the evolution of the bang gaps for a thickness h=0.6a of the plate and a filling factor *f*=0.65. The existence of an absolute phononic gap together with a photonic gap of a given symmetry requires $\alpha \leq 0.2$.

In the BN lattice, the following trends are obtained. In the phononic side, the largest gaps are obtained towards the honeycomb lattice (α=1) and then the odd gaps are in general included in the even gaps. However, for *h/a*~0.6 to 0.7, an odd gap can appear for all BN lattices (from α=0 (triangular) to α=1 (honeycomb)) whereas the even gaps remain open towards the honeycomb lattice. In the photonic side, we have found a narrow absolute gap only for a very restricted range of the geometrical parameters as shown in Figure 3 for *h/a*=0.4 and *f*=0.55. Otherwise, one can find separate band gaps of even and odd symmetries. The largest gaps of even (resp. odd) symmetry occur towards the triangular (resp. honeycomb) lattice at frequencies around or below (resp. above) Ω=0.4. Nevertheless, the even modes can also display a narrow gap towards the honeycomb lattice provided the thickness of the slab is relatively small (*h/a*~0.4-0.5) whereas the odd modes can have a narrow gap towards the triangular lattice for large thicknesses (*h/a*~0.6-0.7).

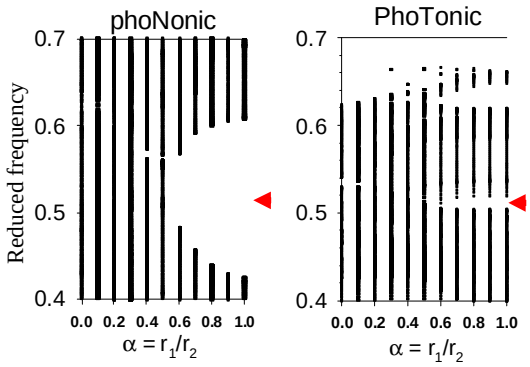


Fig. 3 Absolute phononic and photonic band gaps in a BN lattice with h=0.4a and f=0.55. The frequencies are given in dimensionless units $\Omega=\omega a/2\pi c$

Again, the choice of a crystal can be made by searching a structure that exhibits an absolute phononic band gap though a photonic gap of a given symmetry only. With this limitation, many possibilities exist in the frame of BN lattices as illustrated in Figure 4 for *h/a*=0.6 and *f*=0.45.

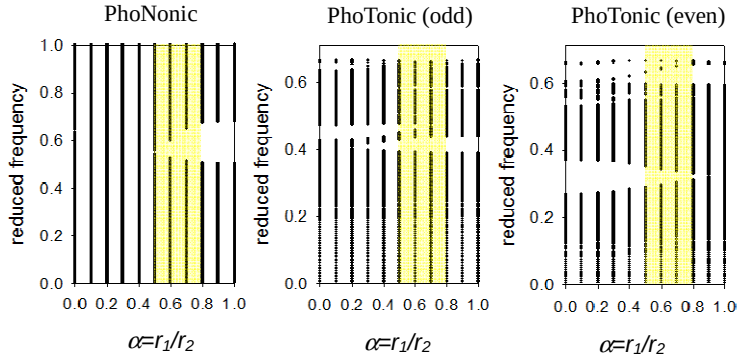


Fig. 4 Phononic and photonic band gaps in a BN lattice with h=0.6a, f=0.45. The odd and even photonic modes are shown separately. The hatched areas represent the domain of α *where there are photonic gaps of both symmetries, although at different frequencies*

More precisely, the following discussion gives the limits of the geometrical parameters for the simultaneous existence of even and odd photonic gaps at two different frequencies. First, the existence of the absolute phononic gap requires a filling factor $f \geq 0.4$ and $\alpha \geq 0.5$. In the photonic side, the thickness of the slab should be taken above $h=0.5a$ in order to keep the gap in the frequency range below $\Omega=0.5$ (otherwise the gap occurs only in a very restricted range of the Brillouin zone close to the light cone). Finally, a sufficiently wide gap of even symmetry requires $\alpha \leq 0.8$.

Table I summarizes the main structures suitable to exhibit an absolute phononic band gap together with photonic band gaps either for both or for only one type of symmetry. Of course, the choice of the lengths for the practical realization of the structure depends on the frequency range of interest for specific applications. For instance, in telecommunication applications, the wavelength of the light is around 1550 nm in vacuum. Referring to the example mentioned in the last row in table I, one obtains the following dimensions of the crystal:

(i) for an even photonic gap, a=491nm, h=295nm, r_1=89nm, r_2=148nm, central phononic frequency= 6.7 GHz;

(ii) for an odd photonic gap, a=637nm, h=382nm, r_1=115nm, r_2=192nm, central phononic frequency= 5.1 GHz.

Array	α	f	r/a	h	PhoNonic band gap	PhoTonic band gap (odd modes)	PhoTonic band gap (even modes)	observations
Square	0	0.7	0.47	0.4a	[0.439, 0.544]	[0.553, 0.658]		Absolute photonic gap in the neighborhood of M
Square	0	0.65	0.45	0.6a	[0.472, 0.534]	[0.410, 0.495]	[0.361, 0.400]	High value of f (holes very close to each other)
Honeycomb	1	0.55	0.418	0.4a	[0.415, 0.617]	[0.502, 0.503]		Small absolute photonic gap
Honeycomb	1	0.6	0.437	0.7a	[0.215, 0.605] [0.616, 0.776]	[0.392, 0.482]	[0.474, 0.508]	High value of f (holes very close to each other)
BN	≥ 0.5 ≤ 0.8	≥ 0.4		$\geq 0.5a$				Most suitable phoxonic crystals
Example	0.6	0.45	$r_1=0.195a$ $r_2=0.32a$	0.6a	[0.521, 0.602]	[0.390, 0.432]	[0.291, 0.343]	

Table 1: Summary of the most suitable phoxonic crystals and the corresponding band gaps frequencies.

3. PERIODIC ARRAY OF DOTS ON A MEMBRANE

In two recent papers [7-8], we studied the phononic band structure and wave guiding in a new type of phononic crystal constituted by a periodic array of dots deposited on a thin homogeneous membrane (Fig.5a). Up to now only the square lattice with one atom per unit cell has been investigated. An illustration corresponding to nanodots of Si on a SiO_2 membrane is shown in Figure 5b with the parameters h/a=0.8, e/a=0.1, and f=0.4 (h and e are respectively the height of the dots and the thickness of the membrane). A new finding of this work was the possibility of a low frequency acoustic gap where the wavelengths in the constituting materials are much larger than the typical lengths in the structure (like in the so-called locally resonant materials). The existence of this gap is closely related to the choice of the geometrical parameters which affect the behavior of the lowest dispersion curves and, in particular, the bending of the first three acoustic branches (actually this gap is almost closed in the example of Fig. 5b). Besides, the band structure contains also one or more higher gaps whose number and width are dependent upon the height of the cylinders. So, in this structure, there is in general not too

much constraint about the existence of phononic absolute band gaps.

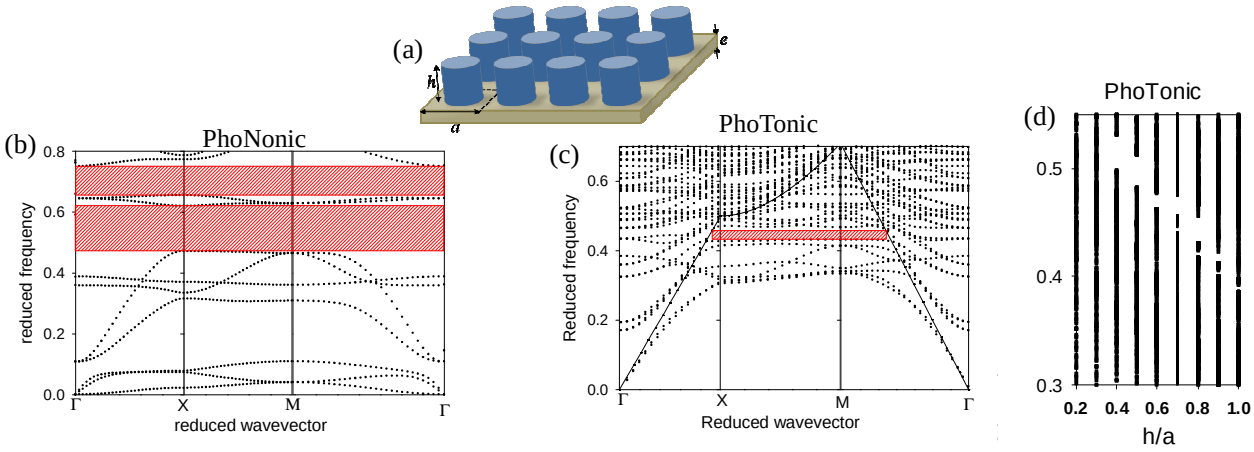


Fig. 5: (a) Schematic of the phononic crystal made up of cylindrical Si dots on a SiO_2 membrane. h, e and f represent respectively the height of the dots, the thickness of the plate and the filling factor. (b) Phononic and (c) photonic dispersions curves calculated for the set of parameters e=0.1a, h=0.8a and f=0.4. (d) Evolution of the photonic band gap as a function of the height of the dots.

We present now some preliminary results about the existence of photonic gaps. Since we have here one more geometrical parameter than in section 2 (namely the height of the dots), we limit ourselves only to the case of a square lattice. In figure 5c, we show that the same structure as before displays an absolute, although relatively narrow, photonic gap. Figure 5d shows the evolution of this gap as a function of the height of the dots for *f*=0.4: the width of the gap increases when decreasing h, but its central frequency increases above 0.5 which means that the gap appears then only in a small region of the Brillouin zone around the M point. Now, by decreasing the filling fraction *f* from 0.4 to 0.3 and then to 0.2, the gap still persists but go to frequencies above 0.5. On the other hand, by increasing *f* to 0.5, the narrow gap closes except when the height of the cylinders is about *h/a*~0.8-0.9. Finally, the photonic gap closes when going to higher filling fraction *f* (up to 0.7in our calculation).

4. CONCLUSIONS

We have shown that BN lattices of holes in a Si membrane can exhibit a complete phononic gap together with either a narrow complete photonic gap or wider photonic gaps of a given symmetry (odd or even) only. Also a structure constituted by a square lattice of dots on a membrane exhibits large complete phononic gaps together with a narrow photonic gap. Other lattices will be investigated in subsequent works as well as the properties of linear and point defects in such phoxonic crystals.

ACKNOWLEDGEMENT

This work is supported in part by the European Commission Seventh Framework programs (FP7) under the FET-Open project TAILPHOX N° 233833.

REFERENCES

1. Kushwaha M.S., Halevi P., Dobrzynski L.and Djafari-Rouhani B. “Acoustic band structure of periodic elastic composites,” *Phys. Rev. Lett.* Vol. 71, 2022-2025, 1993.
2. Sigalas M.M. and Economou E.N. “Band structure of elastic waves in two dimensional systems,” *Solid State*

Commun. Vol. 86, 141, 1993.

3. For a comprehensive list of references on phononic crystals, see the phononic database at http://www.phys.uoa.gr/phononics/phononicDatabase.html.
4. Vasseur J.O., Deymier P.A., Djafari-Rouhani B. and Pennec Y. "Absolute band gaps in two-dimensional phononic crystal plates," *in Proceedings of ASME 2006 International Mechanical Engineering Congress and Exposition (IMECE2006)*, Chicago, USA, November 2006, 125- 133. See also: Vasseur J.O., Deymier P.A., Djafari-Rouhani B., Pennec Y. and Hladky-Hennion A.C. "Absolute forbidden bands and waveguiding in two-dimensional phononic crystal plates," *Phys. Rev. B* Vol. 77, 085415, 2008.
5. Hsu J. C. and Wu T. T., "Efficient formulation for band structure calculations of two-dimensional phononic crystal plates," *Phys. Rev. B* Vol. 74, 144303, 2006.
6. Khelif A., Aoubiza B., Mohammadi S., Adibi A. and Laude V. "Complete band gaps in two-dimensional phononic crystal slab," *Phys. Rev. E* Vol. 74, 046610, 2006.
7. Pennec Y., Djafari-Rouhani B., Larabi H., Vasseur J. O. and Hladky-Hennion A. C. "Low-frequency gaps in a phononic crystal constituted of cylindrical dots deposited on a thin homogeneous plate," *Phys. Rev. B* Vol.78, 104105, 2008.
8. Pennec Y., Djafari-Rouhani B., Larabi H., Akjouj A., Gillet J. N., Vasseur J. O. and Thabet G. "Phonon transport and waveguiding in a phononic crystal made up of cylindrical dots on a thin homogeneous plate," *Phys. Rev. B* Vol.80, 144302, 2008.
9. Johnson S.G., Fan S., Villeneuve P.R., Joannopoulos J.D. and Kolodziejski L.A. "Guided modes in phononic crystal slabs," *Phys. Rev. B* Vol. 60, 5751-5758, 1999.
10. Shi S., Chen C. and Prather D. W. "Plane-wave expansion method for calculating bandstructure of phononic crystal slabs with perfectly matched layers," *J. Opt. Soc. Am.* Vol21, 1769-1775, 2004.
11. Maldovan M. and Thomas E. L. "Simultaneous localization of photons and phonons in two-dimensional periodic structures," *Appl. Phys. Lett*. Vol. 88, 251907, 2006.
12. Maldovan M. and Thomas E. L. "Simultaneous complete elastic and electromagnetic band gaps in periodic structures," *Appl. Phys. B*. Vol. 83, 595-600, 2006.
13. Sadat-Saleh S., Benchabane S., Baida F. I. Bernal M. and Laude V. "Tailoring simultaneous photonic and phononic band gaps,"*J. Appl. Phys.* Vol. 106, 074912, 2009.
14. Mohammadi S., Eftekhar A. A. and Adibi A. "Large simultaneous band gaps for photonic and phononic slabs," OSA/CLEO/QELS 2008.

Acoustic meta-materials in MEMS bar resonators

X. Rottenberg[1], R. Jansen[1], Y. Zhang[2], A. Coosemans[3], G. Delcour[3], K. Herdewyn[3], J. Vanpaemel[3], C. Van Hoof[1,3] and H.A.C. Tilmans[1]

[1] IMEC v.z.w., SSET Unit, Kapeldreef 75, B3001 Leuven, Belgium

[2] Groep-T, Andreas Vesaliusstraat 13, B3000 Leuven, Belgium

[3] K.U.Leuven, ESAT, Kasteelpark Arenberg 10, B3001 Leuven, Belgium

Xavier.Rottenberg@imec.be

Abstract - This paper presents a meta-material-based design method for bar resonators with enhanced characteristics compared to those obtained with the typical bulk material implementation. We take advantage of the required release holes of MEMS processes to modify the local equivalent material properties (ρ, E and ν) of the bar. While the available bulk material is homogeneous, the bar consists of an equivalent non-homogeneous material that can for example be distributed by design in order to shrink the overall resonator size, enhance electromechanical transduction coefficients or reject spurious modes. Our paper compares two extraction methods for the equivalent material properties of a periodically hole-punched material: the steady-state mechanical simulation of a unit cell and its "phase delay" counterpart. We discuss their validity and practical use for the design of bar resonators.

1. INTRODUCTION

MEMS resonators are recognized as key components for future sensing, wireless and communications applications. Among those resonators, Si-based bulk-mode resonators, *e.g.*, disks or bars, have recently gained special interest since they allow reaching high frequencies up to hundreds of MHz, while preserving their very high Q-factor of several thousands, and depicting a high linearity [1][2]. This type of resonators can further be produced through relatively simple processes like SOI (Silicon on Insulator).

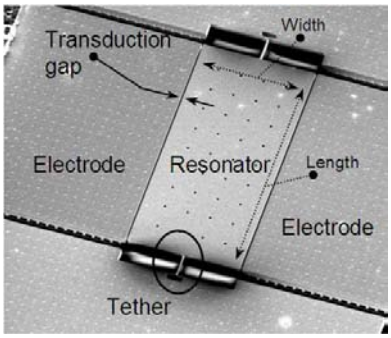


Fig. 1 SEM of a 50x100µm bar resonator [1]

The longitudinal resonance modes for a bulk mode "bar" resonator are in essence analogous to the resonance modes supported by a closed electromagnetic cavity. Resonance occurs when an acoustic wave, trapped in the bulk of a parallelepipedic slab of material, bounces in phase on opposite faces. The frequencies f_{res} of the allowed modes of vibration are given by eq. (1) where v_{sound}, E, ρ, and ν are respectively the acoustic phase velocity, Young's modulus, density and Poisson's ratio of the material constituting the bar with dimensions W (width), L (length) and T (thickness). The mode numbers are represented by l, m and n. Typically, in case of electrostatic transduction, f_{100} is the favored mode of resonance as the thin surface micromachined layers do not lean themselves for a proper out of plane bulk excitation/detection, while the length dimension is used to increase the transduction efficiency.

In a given technology, with fixed material properties, the design freedom is strongly limited. The designer can only change the dimension of the resonant direction of the bar to reach the design goal, *e.g.*, a certain resonant frequency. However, the effective material properties of the material constituting a bar resonator can be designed by adding holes, or macro-pores, to the bulk material [3][5]. These macro-porous materials behave like meta-materials which can be used to

design non-homogeneous bar resonators, thus providing more design freedom.

$$f_{lmn} = \frac{1}{2} v_{sound}(E, \rho, \upsilon) \sqrt{\frac{l^2}{W^2} + \frac{m^2}{L^2} + \frac{n^2}{T^2}} \quad (1)$$

In this paper, we report on the modeling of these equivalent materials. In particular, we present and discuss the extraction of equivalent material properties and their use to design bar resonators with characteristics beyond the possibilities offered by their standard bulk implementation.

2. EQUIVALENT MATERIAL PROPERTIES - QUASI-STATIC EXTRACTION

In this section, we consider the perturbation of the bulk mechanical material properties introduced by the periodic organisation of square holes in a square pattern as shown in Fig. 2. This family of equivalent materials presents equivalent densities ranging from ρ_0, the bulk material density, to zero. To extract equivalent E and ν properties, i.e. E^* and ν^*, we simulate a pull-test in the considered direction of propagation. This test is performed on a unit cell of the effective material on which the effective periodicity of the material is imposed, as shown in Fig. 3 and Fig. 4. Applying a fixed y-displacement on one external face and a symmetry boundary plane on the opposite face, the cell is allowed to relax maintaining its remaining external faces parallel until a minimum of strain energy is reached. In this situation, Young's modulus and Poisson's ratio are respectively defined as the ratio of the force density, *i.e.* stress, to the applied strain and as the ratio of the induced strain in the x-direction to the applied strain in the y-direction.

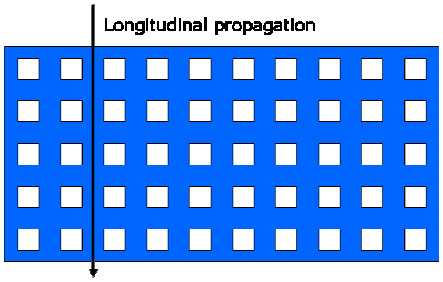


Fig. 2 Square pattern of square holes and parallel propagation

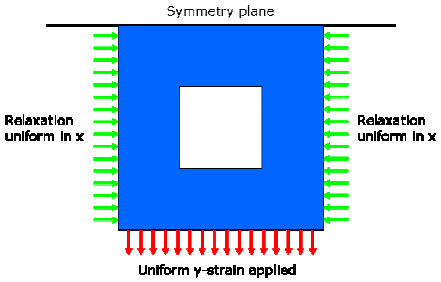


Fig. 3 Pull experiment with relaxation and periodic boundaries

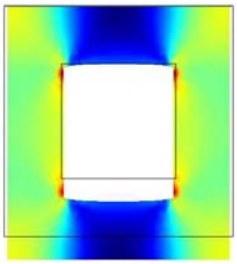


Fig. 4 COMSOL simulation of the stress distribution in the setup from Fig. 3

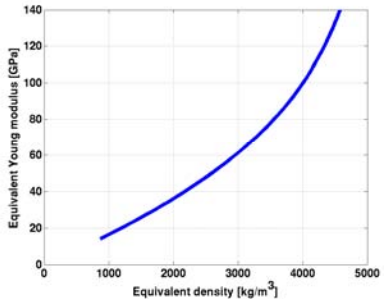


Fig. 5 Extracted E^*

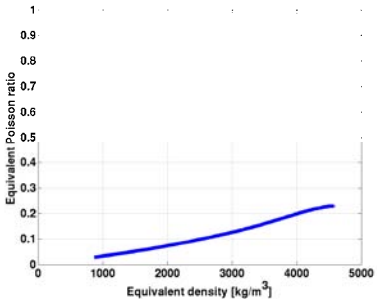


Fig. 6 Extracted ν^*

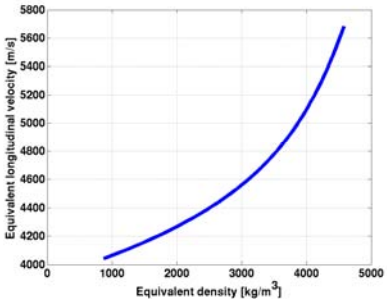


Fig. 7 Computed equivalent v_{long}

Fig. 5, Fig. 6 and Fig. 7 present the material properties extracted for an arbitrary material with ρ_0=4577kg/m³ E_0=140GPa, and ν_0=0.23. The unit cell dimensions are not mentioned as ρ^*, the effective density, is the governing parameter. E^* and ν^* are unequivocal monotonous functions of ρ^*. In the limit with no material, both quantities go naturally to zero as the material looses its strength. The longitudinal acoustic velocity, computed according to eq. (2) for propagation in a 2D-material, also drops. Its dependency on ρ, however, prevents it from going to zero. This defines a limit on the bar resonator miniaturization. Indeed, as v_{long} drops, the width of a bar to reach a fixed resonance frequency drops as expressed by eq. (1).

$$v_{long} = \sqrt{\frac{E}{\rho\left(1-\nu^2\right)}} \tag{2}$$

3. MODEL DISCUSSION

The material description suggested by Fig. 5, Fig. 6 and Fig. 7 has a limited validity. While E^* and ν^* can be extracted as proposed, their interpretation and direct use to describe the propagation of an acoustic wave is questionable. Indeed, eq. (2) is only valid for isotropic 2D-materials, our effective, or meta-, material is not. An analogous extraction performed along a direction 45° inclined through the hole lattice, as shown in Fig. 8, Fig. 9 and Fig. 10, produces different results. Fig. 11 shows that E^*_{45} decreases with decreasing ρ^* faster than in the previous case. More strikingly, ν^* along this 45° direction increases towards 1 as reported in Fig. 12. Both results are due to the hinges developing within the unit cell during its progressive hollowing. The longitudinal acoustic velocity obtained in this case using (2) decreases towards zero before numerical instabilities arise as shown in Fig. 13.

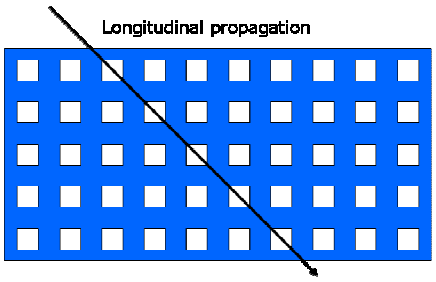


Fig. 8 Square pattern of square holes and 45° propagation

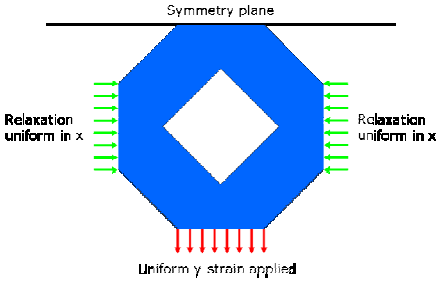


Fig. 9 Pull experiment with relaxation and periodic boundaries

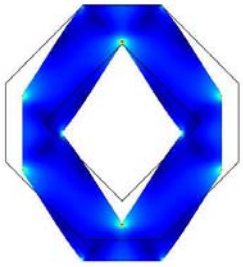


Fig. 10 COMSOL simulation of the stress distribution in the setup from Fig. 9

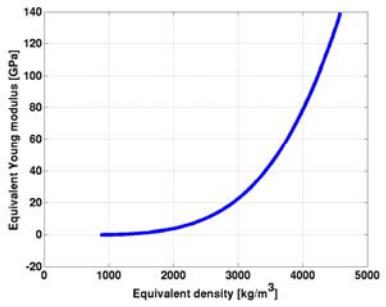


Fig. 11 Extracted E_{45}^*

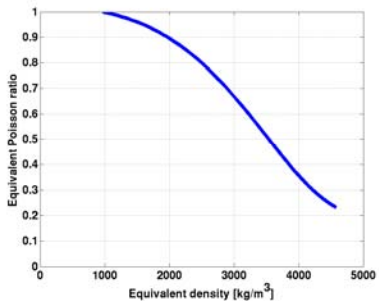


Fig. 12 Extracted ν_{45}^*

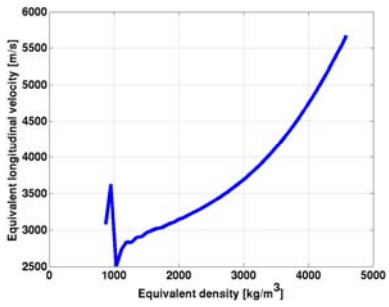


Fig. 13 Computed equivalent v_{long_45}

Further, one can question the validity of the quasi-static approach to derive dynamic characteristics of the envisaged meta-materials. A more natural approach consists in applying the phase delay technique presented in [5] to the unit cell from Fig. 3. However this technique does not give direct access to equivalent material properties, needed to efficiently simulate the materials of our interest, we can use it to derive dispersion diagrams as shown in Fig. 14. Focusing on the linear portions from the two first modes of such graphs at small phase delays, *i.e.* sound lines, the shear and longitudinal velocities can be extracted and compared to their quasi-static counterparts from Fig. 7 and Fig. 13. The longitudinal acoustic velocity from Fig. 7, for propagation parallel with the hole lattice in the meta-material, is in very good agreement with the one presented in Fig. 15. This tends to validate the quasi-static description we proposed for the longitudinal vibration of a bar constituted of a material with periodic square lattice of square holes aligned parallel with the edges of the bar, hence with the propagation of the resonant wave.

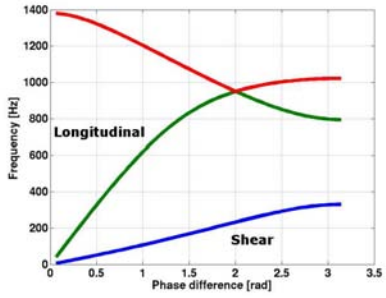


Fig. 14 dispersion diagram for a material with unit cell and hole 1m and 0.8m wide

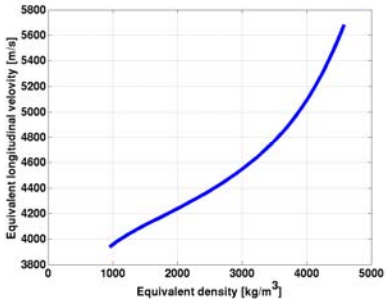


Fig. 15 Extracted equivalent v_{long} longitudinal acoustic velocity

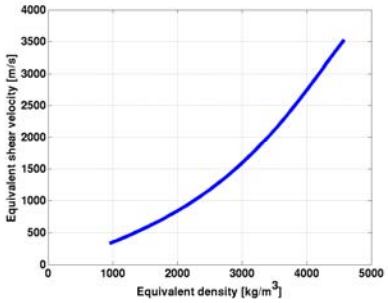


Fig. 16 Extracted equivalent v_{shear} shear acoustic velocity

It is noted that we could have tried and extracted E^* and ν^* from Fig. 15 and Fig. 16, using the definition of the longitudinal velocity (2) and of the shear velocity (3) in 2D-isotropic media [4]. This would result in erroneous results as both waves differ in the components of the tensorial quantities E^* and ν^* they rely on.

$$v_{shear} = \sqrt{\frac{E}{\rho\ 2(1+\nu)}} \tag{3}$$

Note then in Fig. 14 the clipping behaviour of the delay lines for both shear and longitudinal modes. These are introduced by the non-uniformity of the 2D-media and the finite dimension of the unit cell considered. These cut-off frequencies seem to limit the validity of the material representation. However, as the extraction, quasi-static or phase delay-based in the linear regions of Fig. 14, is not unit-size dependent, one can shift these cut-off frequencies to higher values simply by shrinking the unit cell and maintaining the effective density. The unit cell has to be small compared to the characteristic wavelengths, which translates the fact that the cell can not vibrate on itself. Of course, a lower limitation of the unit cell size is imposed by the technology of fabrication.

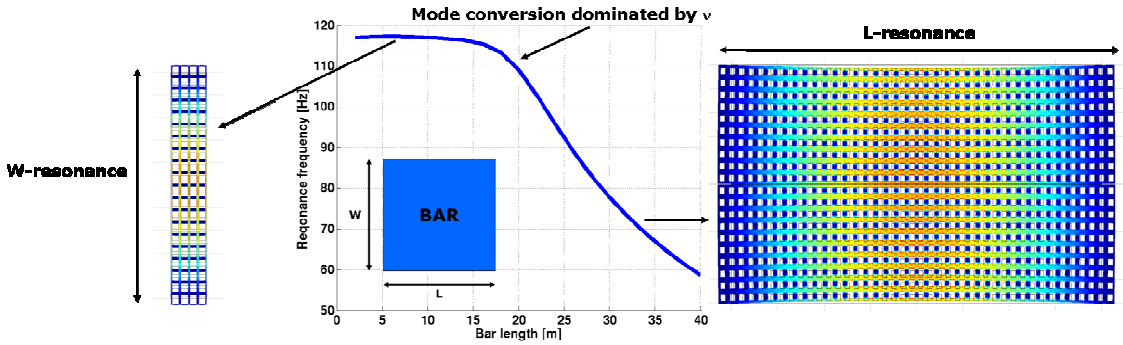


Fig. 17 Evolution of the first longitudinal resonance mode in bar resonators of increasing *L*-dimension, at constant *W*

Finally, to validate our simplified extraction technique, we have implemented a more pragmatic approach. We have simulated the longitudinal resonance frequencies of a family of bar resonators of different dimensions, composed of a periodic repetition of a given unit cell. We have then matched these frequencies with those obtained for bar resonators of equal dimensions constituted of uniform materials of known ρ and unknown E and ν. This final extraction provided Young's moduli and Poisson's ratios in close agreement with those derived in Section 2, which validates at least the practicality of our approach. Note in particular that the introduction of boundary conditions due to the finitude of the actual bars did not lead to a breakdown of our material description. Fig. 17 shows for example the evolution of the first longitudinal resonance in a bar of constant W increasing L. At small L, the f_{100} resonance occurs along the W-dimension, while at large L, the f_{010} resonance is along the L-dimension. The roll-off in the mode conversion region is characteristic of

the effective ν of the material. Therefore, such a curve alone suffices already to fit the E and ν parameters for a given hole-to-unit cell dimension ratio, *i.e.* a given density of the material.

4. APPLICATIONS

The previous sections have presented and discussed the modeling of meta-materials constituted of a square lattice of square holes targeting applications using longitudinal resonance modes. This model has an established sufficient but limited validity. To use this model and design enhanced resonators, we implement polynomial fits of $E^*(\rho^*)$ and $\nu^*(\rho^*)$ in COMSOL to perform efficient simulations of bar resonators, without holes, mimicking holes distributions. Implementing non-uniform density distributions, we allow ourselves to qualitatively experiment with non-uniform holes distributions.

However, the natural implementation of this class of meta-materials, with homogeneous characteristics, is that of shrinking the resonating dimension of the bar. Fig. 18 and Fig. 19 present the first width mode longitudinal resonance of two bar resonators with equal dimensions. While the one consists of the full bulk material, the second one is punched of large periodic holes, i.e. hole-to-unit cell dimension ratio=0.75. Using the same area, the hollow resonator resonates at a frequency 20% lower than its full counterpart, in agreement with Fig. 7. Further, the mode shape of the hollow resonator is flatter as a result of its vanishing Poisson ratio. This, along with the lower stiffness of the resonator, increases the electrostatic transduction efficiency as well as enhances the mode selectivity of the excitation.

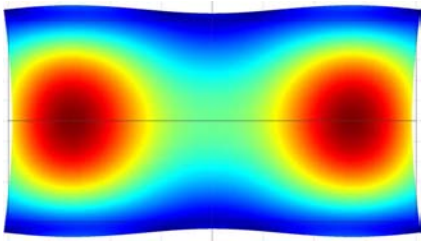


Fig. 18 First width mode of a full bar

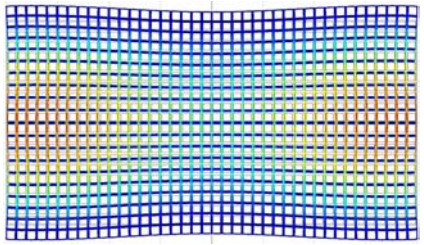


Fig. 19 First width mode of a hollow bar (0.75)

5. CONCLUSIONS

This paper presented and discussed a quasi-static modeling technique for acoustic meta-materials constituted of a square lattice of square holes targeting applications using longitudinal resonance modes. This model has an established sufficient but limited validity. To use this model and design enhanced resonators, we implement polynomial fits of $E^*(\rho^*)$ and $\nu^*(\rho^*)$ in COMSOL to perform efficient simulations of bar resonators, without holes, mimicking holes distributions. Implementing non-uniform density distributions, we allow ourselves to qualitatively experiment with non-uniform holes distributions. Further work is ongoing to extend the description of the material properties to tensors as well as investigate and quantify the Q-factor degradation due to the introduction of internal boundaries.

REFERENCES

[1] S. Stoffels, S. Severi, R. Vanhoof, R.Mertens, R.Puers, A. Witvrouw and H.A.C. Tilmans, “Light sensitive SiGe MEM resonator for detection and frequency tuning applications”, accepted for pres. at MEMS 2010, Hong Kong, 24-28 Jan. ‘10

[2] J. Wang, Z. Ren, and C. T.-C. Nguyen, “1.156-GHz self-aligned vibrating micromechanical disk resonator,” IEEE Trans. Ultrason., Ferroelect., Freq. Contr., vol. 51, no. 12, pp. 1607-1628, Dec. 2004.

[3] Mohammadi, S. and Eftekhar, A.A., “Acoustic Band Gap-Enabled High-Q Micro-Mechanical Resonators,” Transducers’09, 2330–2333.

[4] McSkimin, H. J. “Theoretical Analysis of Modes of Vibration for Isotropic Rectangular Plates Having All Surfaces Free,” The Bell System Technical Journal, Vol. 23, 151-177, 1944.

[5] Langlet, P., AC Hladky-Hennoin and J-N Decarpigny, “Analysis of the propagation of plane acoustic waves in passive periodic materials using the finite element method”, J. Acoust.Soc.Am. Vol. 98, No.5 Pt.1, November 1995.

Optical Properties of HTcSc-Dielectric Photonic Crystals

Arafa H Aly
Department of Physics, Faculty of Sciences,Beni-Suef University, Egypt
arafa16@yahoo.com

Abstract- We have investigated the optical properties of one-dimensional photonic crystals (1DPCs) composed of high temperature superconducting-dielectric (HTcScD) layers. The variance of the intensity and the bandwidth of the transmission and reflection are strongly dependent on the different thicknesses, different temperatures, and different incident angles as well as we obtained the different band gaps dependent on the thickness of layers. Also we have examined the influence of the increased of the number of periods on the transmittance and reflectance spectra as well as on the band gap positions.

1. INTRODUCTION

During the last two decades, huge attention has been concentrated on the theoretical and experimental investigation of photonic crystals (PCs) or photonic band gap materials (PBGs), due to the broad applications of PCs[1-6]. These PCs can be presented as periodic one-, two-, and three dimensional structures, composed of two different materials or more with different refractive indices with the period comparable with the wavelength of the incident electromagnetic wave. The difference in the refractive indices of the PC components leads to the appearance of photonic band gaps in the spectra of normal electromagnetic waves, i.e. forbidden regimes where electromagnetic waves cannot propagate through the photonic structure. The damping of electromagnetic waves in metals tends to deteriorate the performance of the periodic structure. Such loss issue in metals can be remedied by utilization of superconductor instead. In fact, the metallic loss can be greatly reduced and negligibly small when metals are replaced with superconductors [7]. In new experiments, superconducting (SC) metals have been used as components in optical transmission nanomaterials. Researchers found that dielectric losses were substantially reduced in the SC metals relative to analogous structures made out of normal metals. The dielectric losses of such a SC nanomaterial [7] were found to be reduced by a factor of 6 when the SC state was penetrated. Indeed, studies of the optical properties of superconductor metal/ dielectric multilayers are not numerous. It is possible that the results have been used in the design of high reflection mirrors, beam splitters, and bandpass filters [8]. In our work we have investigated the optical properties of 1D HTcScD multilayer and the influence of a dielectric thickness layers on the spectra of the transmittance and reflectance.

2. THEORETICAL TREATMENT

The superconductor is strongly sensitive to temperature and external magnetic fields [9]. We use the two-fluid model to describe the electromagnetic response of a typical superconductor without an additional magnetic field [9]. In the model, the electrons in the superconductor occupy one of two states. We consider the superconductor in the London approximation [10,11], i.e, assuming that the London penetration depth λ_o of the bulk superconductor is much greater than the coherence length ξ ; here $\lambda_o = [m_e c^2/(4\pi n_e \varepsilon^2)]^{1/2} \succ\succ \xi; \xi \sim \hbar v_F \Delta^{-1}; n_e$ is the electron density; m_e and e are the mass and the charge of an electron , respectively; Δ is the superconducting gap; and v_F is the Fermi velocity.

From Gorter–Casimir model we have

$$\varepsilon(\omega) = 1 - \alpha \frac{\omega_p^2}{\omega^2} - (1-\alpha)\frac{\omega_p^2}{\omega(\omega + i\gamma)}, \qquad \omega \prec 2\Delta \qquad [1]$$

$\omega_p = \sqrt{4n_e e^2 / \varepsilon_o m}$ is the plasma frequency, m is the electron effective mass, γ is the phenomenological attenuation coefficient describing the relaxation of normal component, and α is the superconducting component fraction, $\alpha(\beta = 0, T \prec T_c) = 1 - (T/T_c)^4.$ The London penetration depth is $\lambda_L, = \lambda_L(T) = \lambda_o / \sqrt{\alpha}$. When the temperature is above 0.8 times the critical temperature, the London penetration depth increases rapidly and approaches infinity as the temperature is close to Tc [9]. Adjusting the temperature of superconductors can control the refractive indices of superconductors as well as the photonic band structures of PCs composed of superconductors. We consider that a TE wave is incident at an angle θ_1 from the top medium which is taken to be free space with a refractive index, $n_1 = 1$. The index of refraction of the lossless dielectric is given by $n_3 = \sqrt{\varepsilon_{r3}}$, where ε_{r3} is its relative permittivity. For the superconductor, the index of refraction, n_2 , can be described on the basis of the conventional two-fluid model [12-14]. We have designed our system as a periodic superconductor-dielectric multilayer structure with a large number of periods where $d = d_2 + d_3$ is the spatial periodicity, where d_2 is the thickness of the superconducting layer, and d_3 denotes the thickness of the dielectric layer.

3. RESULTS AND DISCUSSION

For numerical simulation, referring our system, HTcSc (YBaCuO) with T_c =92.2K and λ_o =200nm is taken as first layer whereas SiO2 with n_3 =1.46180 and the glass substrate with n_ℓ =1.52083 are taken as the second and final layers, respectively. The thicknesses of the corresponding layers are set to be d_1 =40nm, d_2 =100(Fig.2a), 170nm (Fig.2b), 205nm (Fg.2c) with the number of periods N =20, and operating temperature T =7.7K are adopted for simulation. The refractive index (n_R) together with the extinction coefficient (n_E) of the HTcSC (YBaCuO) with a T_c =92.2K are plotted as a function of the wavelength in Fig. 1.a. It is clearly observed the value of real part of n_R is from 0 0.935 to 0.992 but the value of n_E closed zero. Such material with extremely low index of refraction retains some special features of interests. Fig. 1a

shows the variation wavelength (nm). Optical constants of the HTcSc have been calculated using Essential Macleod. The real part of refractive index of the HTcSc has larger value than the imaginary part. Fig. 1b shows the optical constant of SiO2 versus wavelength has been calculated using Essential Macleod. The real part of refractive index of the SiO2 has larger value than the imaginary part except some electromagnetic waves ranges. The optical properties of HTcScDPCs are very clear in our results fig.2. We studied the transmittance and reflectance spectra with different thickness layers ; d_2 = 100 nm (fig.2a), d_2 =170(fig.2b), and d_2 = 205nm (fig.2c), and we have showed two clear photonic band gaps (fig.2a); the first is between 185 and 208nm and the second is between 349 and 405nm. After that, the thickness of dielectric layers increased to 170 nm, we obtained three band gaps (fig.2b); the first one is formed between 156 and 165nm, the second appeared between 195 and 210nm and the third one is formed between 280 and 307nm. That mean the dielectric thickness is significance parameter in our structure. In fig.2c we obtained four band gaps with d_2 =205nm; the first between 150 and 160nm, the second between 177 and 189nm, the third between 225 and 246, and the fourth obtained between 330 and 358nm. Also, we have examined the influence of the number of periods on our structure as shown in fig.3; we have designed our structure with three different numbers of periods, 20, 40, 60. With these numbers of periods we got the same spectra and the same PBGs positions, there is no influence on the spectra or the PBGs positions with 20 or 40 or 60 periods in our case. The results of HTcSc photonic crystals may be have a potential application in the near future in the optical devices.

4. CONCLUSIONS

By using transfer matrix method and two-fluid model for a superconductor, we have calculated the transmittance and reflectance spectrum for a one dimensional high Tc superconducting–dielectric multi layers. The band structure shows a multiple-PBG structure, not just the first band as shown previously works [15]. Besides the first band gap, we also have investigated the second, third and fourth PBGs as a function of thickness, angle of incidence, and permittivity of dielectric. The number of band gaps increased with the dielectric thickness increased. Furthermore, we have examined the influence of the number of periods; N=20,40,60. With these numbers of periods we got the same spectra and the same PBGs positions, there is no influence on the spectra or the PBGs positions with 20 or 40 or 60 periods in our case. The results of HTcSc photonic crystals may be have a potential application in the near future in the optical devices. Also, theses results make known more basic information for the electromagnetic response of superconductor and it could be of technical use in superconducting electronics.

REFERENCES

1. Jannopoulos *J.* D, Johnson S G, Winn J N and Meade R D; *Photonic Crystals: Molding the Flow of* Light 2nd edn(Princeton, NJ: Princeton University Press),2008
2. Sakoda K,*Optical Properties of Photonic Crystals*, (Berlin: Springer),2005
3. Yablonovitch,E.," Inhibited Spontaneous Emission in Solid-State Physics and Electronics" Phys. Rev. Lett. 58, 2059-2062,1987.
4. John S.," Strong localization of photons in certain disordered dielectric superlattices, Phys. Rev. Lett. 58,

2486–2489,1987.
5. Eldada L., "Advances in telecom and datacom optical components" Opt. Eng., Vol. 40, 1165-1178,2001.
6. Chigrin.D.N. and Sotomayor Torres C.M.," Periodic thin-film interference filters as one-dimensional photonic crystals " Opt. Spectrosc. 91,484-489,2001.
7. Ricci M., Orloff N., and Anlage.S.M., " Superconducting metamaterials", Appl. Phys Lett., 87, 034102-034102-3,2005.
8. Macleod H.A., Thin-Film Optical Filters, 3rd ed. (Institute of Publishing, Bristol 2001), Chap. 7.
9. Tinkham M., Introduction to Superconductivity, 2nd ed. McGraw-Hill, New York, 1996.
10. Pei ,T.-H.,and Huang Y.-H.," A temperature modulation photonic crystal Mach-Cehnder interferometer composed of copper oxide high-temperature superconductor", J.Appl.Phys.,101, 084502-084506,2007.
11. Abrikosov A.A., Fundamentals of the Theory of Metals,North Holland, Amsterdam,1988.
12. Born M., Wofl E., Principles of Optics, Cambridge,London, 1999.
13. Wu C.-J,Chen M.-S., Yang T.-J," Photonic band structure for a superconductor-dielectric superlattice" Physica C 432,133-139,2005.
14. Aly Arafa.H.,Hsu H.-T,Yang T.-J,Wu C.-J, and Hwangbo C.-K;"Extraordinary optical properties of a superconducting periodic multilayer in near-zero-permittivity operation range"- J.Appl.Phys,105, 083917-083917-6,2009.
15. Raymond Ooi C.H.,Yeung T.C, Kam C.H,Lim T.K.," Photonic band gap in a superconductor- dielectric superlattice", Phys.Rev.B 61, 5920-5923,2000.

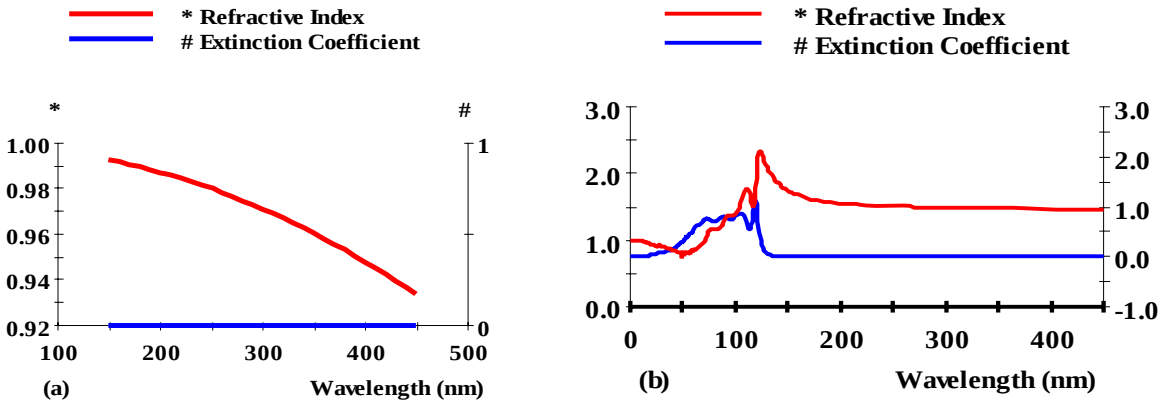


Fig.1.Plot of refractive index, n_R and the extinction coefficient, n_E of a) HTcSc at 92.2 K; and b) The refractive index of SiO2.

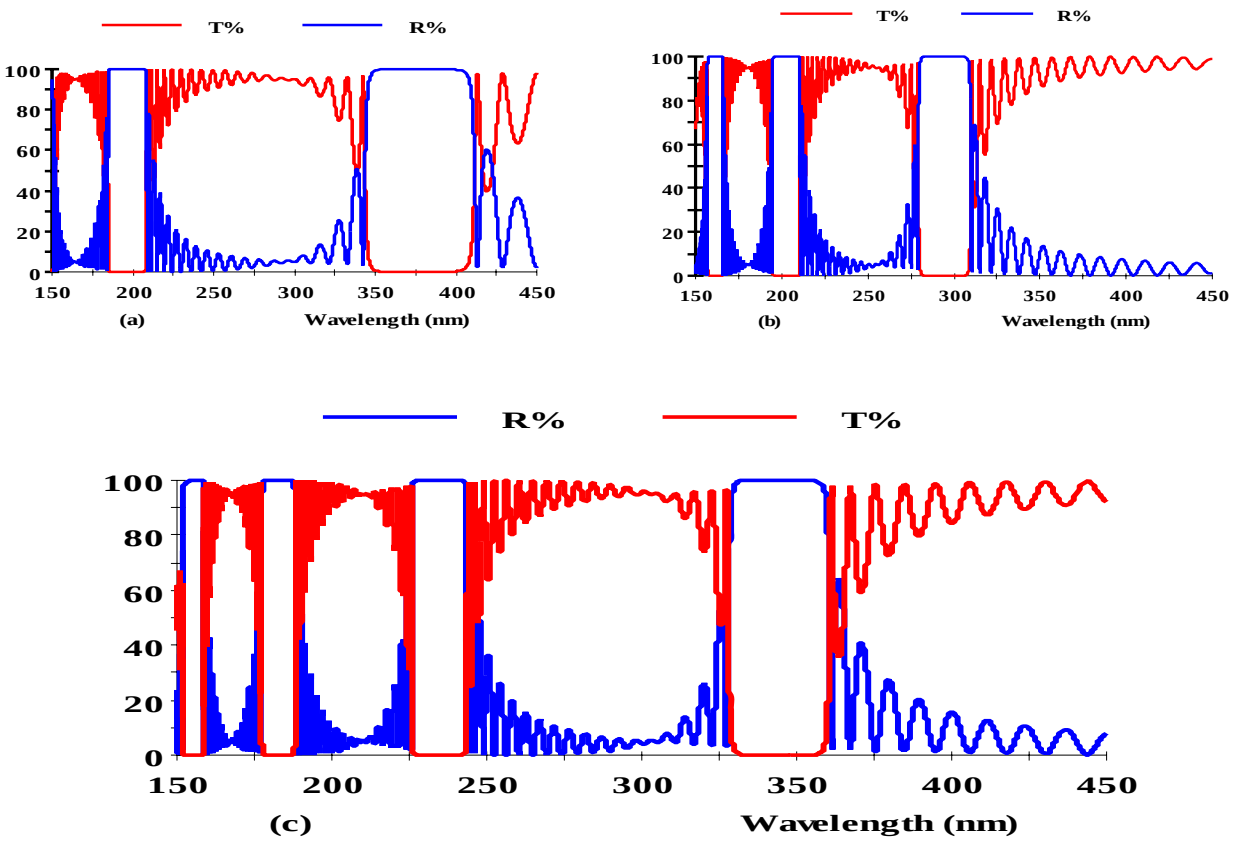


Fig.2. Transmittance (T) and Reflectance (R) spectra; HTcSc/SiO2 multilayer with d_1=40nm,N=20, $\theta = 0^\circ$ and a) d_2=100nm, b) d_2=170nm, and c) d_2=205nm

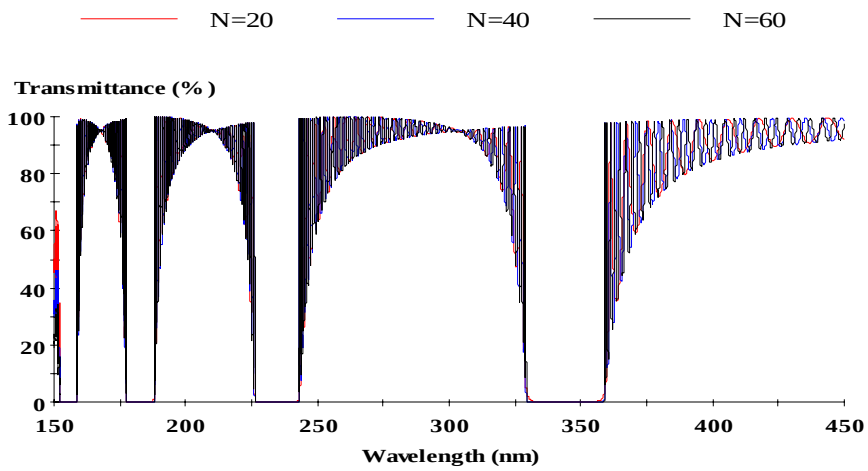


Fig.3. Transmittance (T) spectrum; HTcSc/SiO2 multilayer with d_1=40nm, $\theta = 0^\circ$ and a) d_2=205nm with different N=20,40,60.

Design and fabrication of subwavelength nanogratings based light-emitting diodes

Liang. Zhang[1,2], **Jinghua Teng**[3*], **Soo Jin Chua**[1,2,3], **Eugene. A. Fitzgerald**[1,4]

[1] Advanced Materials for Micro- and Nano-systems Programme, Singapore-MIT Alliance, Singapore 117576

[2] Department of Electrical and Computer Engineering, National University of Singapore, Singapore 117576

[3] Institute of Materials Research and Engineering, A*Star, 3 Research Link, Singapore 117602

[4] Department of Materials Science and Engineering, Massachusetts Institute of Technology, USA 02139

[*]corresponding author: jh-teng@imre.a-star.edu.sg

Abstract- Linearly polarized light from InGaN green light emitting diode grown on (0001) oriented sapphire is demonstrated by using subwavelength metallic nano-gratings. Polarization ratio can reach 7:1 (~88%), the highest ever reported from a single light emitting device. We discuss the design and fabrication of this device in detail.

1. INTRODUCTION

Upon successful commercialization of InGaN based semiconductor optoelectronic devices, light emitting diodes (LEDs) have become universal in illumination and signal applications. Even though the basic characteristics like efficiency and power level will benefit the replacement of the conventional light sources to realize solid-state lighting, Polarized emission from InGaN LEDs are also under research as it is highly desirable for many applications including imaging[1,2] and liquid crystal backlighting.[3,4] Previous efforts have been emphasized on the growth with nonpolar[5-8]or semipolar GaN substrates.[9]In recent years, emphasis has shifted back to (0001) oriented sapphire substrate because of its high efficiency, power, and long lifetime in the market. Different approaches such as using special reflector design[10]and photonic crystals[11] have been investigated recently to get polarized light emission from this most commonly used LED structures.

We have recently reported a method to achieve highly polarized light emission from InGaN LED by using subwavelength metallic nanograting (SMNG)[12]. Here we report more detailed optimization on both design and fabrication process based on this method.

2. DESIGN AND SIMULATION

Figure 1(a) shows the cross-sectional view of the GaN green SWNG LED structure demonstrated in this work. The SMNG is designed on top of the emitting surface of LED. The restricted movement of electrons perpendicular to the SMN attribute to the polarized emission in Ewald-Oseen picture. When the unpolarized emission from QW arrives LED surface, for polarization along SWN, the conduction electrons are coherently driven along SWN with unrestricted movement, the physical response of SWN is exactly the same as the case of thin metal sheet. For polarization perpendicular to SWN, since the period of SWN is much smaller than the incident wavelength, the electron movement is confined similar as in the case of dielectric, the Ewald-Oseen field generated by electrons is no longer sufficiently strong to cancel the incoming field, resulting transmission of this single polarization. Considering the choice of metal for SMNG, we have investigated aluminum, gold and silver, whose refractive index[13] are plotted in

figure 2 (a) (b) and (c) in visible wavelength range. According to this value, the transmission spectrums were calculated using rigorous coupled-wave analysis (RCWA) [14], as shown in figure 2 (d). It is clear that aluminum gives better performance of transmission efficiency in visible range compared with silver and gold. To determine the period of SMNG, we calculated the transmitivity and reflectivity of TE wave, which has its electrical field parallel to the grating and is supposed to be totally reflected when hitting at SMNG, at fixed wavelength of 550nm which is the center wavelength of emission spectrum of our green LED. It can be seen from figure 3 that, the reflectivity of TE wave decrease dramatically when the period goes beyond 200nm, and more importantly, the transmitivity of TE wave, which is supposed to be zero, start to increase thus will decrease the polarization ratio of total emission seriously. From fabrication point of view, the lager period the better, we finally fixed our SMNG period at 150nm. Figure 4 shows the optimization on the grating height and duty cycle, we found that a duty cylce of 0.3 with grating height range from 110nm to 140nm will give a good performance.

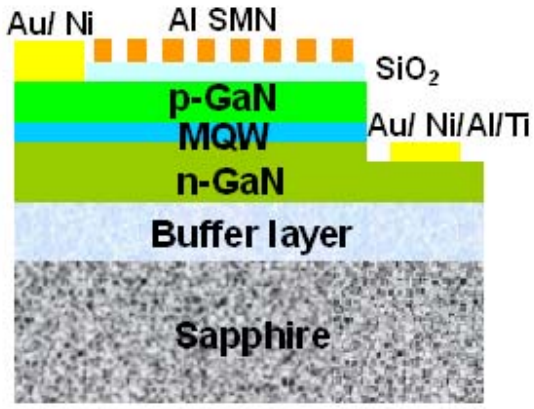
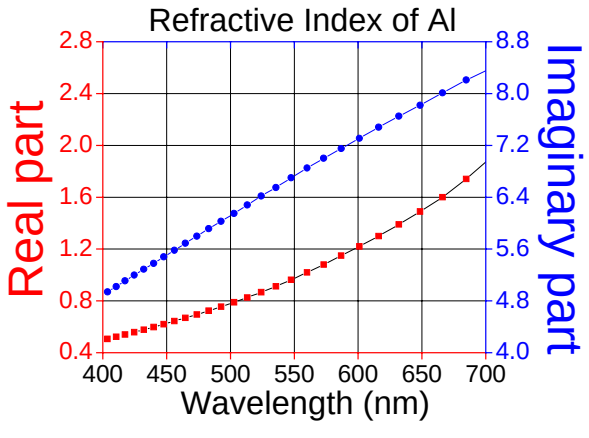
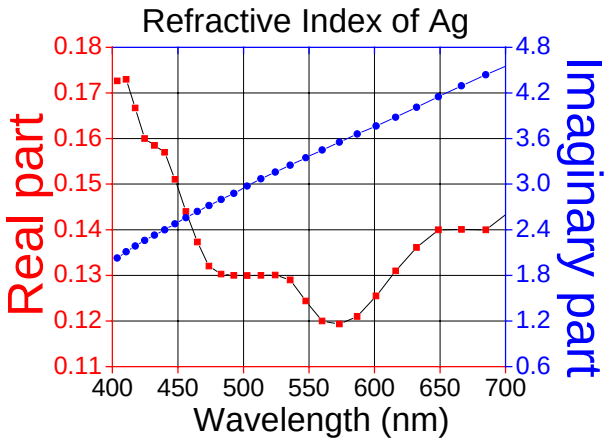


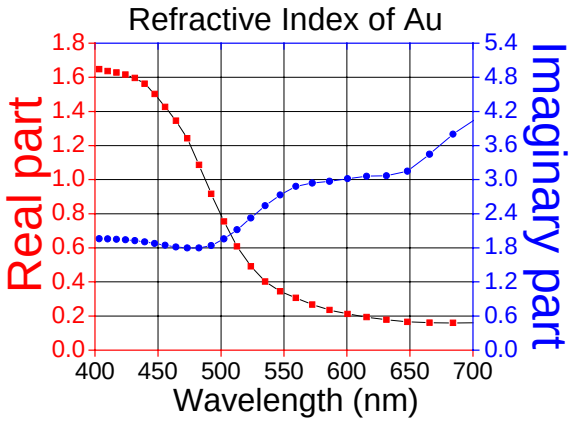
FIG. 1. Schematic of the cross section of the GaN SWN LED.



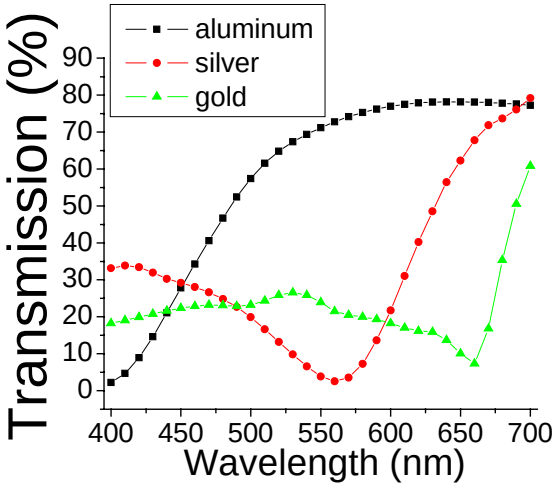
(a)



(b)

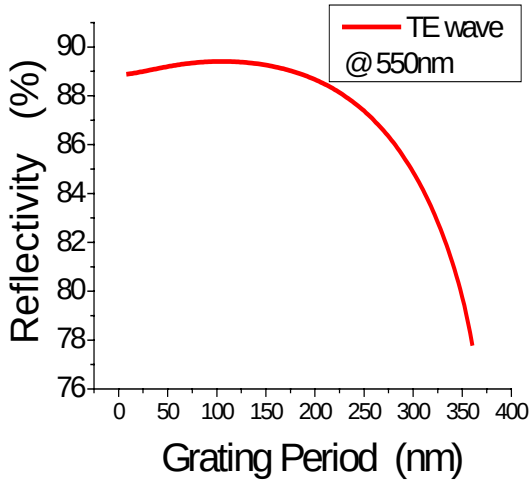


(c)

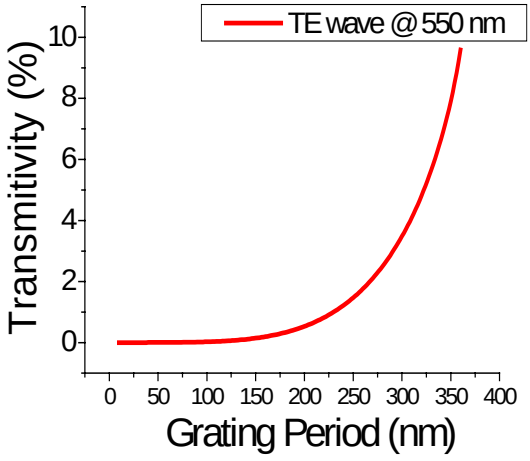


(d)

FIG. 2. (a)-(c) refractive index of aluminum, gold and silver in in visible range. (d) transmission spectrums of aluminum, gold and silver based SMNG.

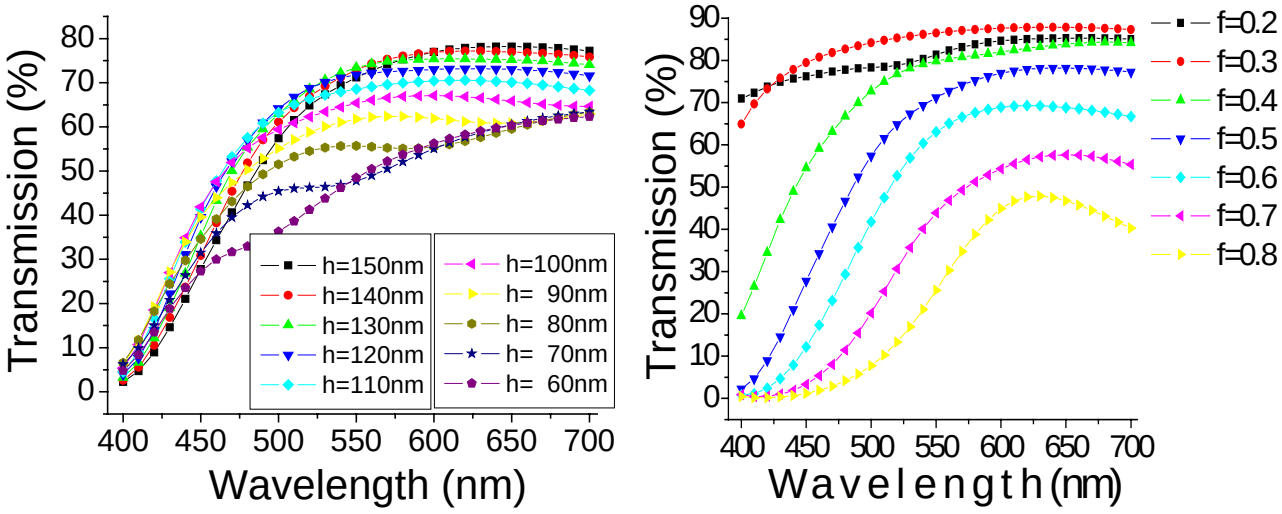


(a)



(b)

FIG. 3. (a) Reflectivity and (b) transmitivity of TE wave at 550nm of aluminum SMNG.



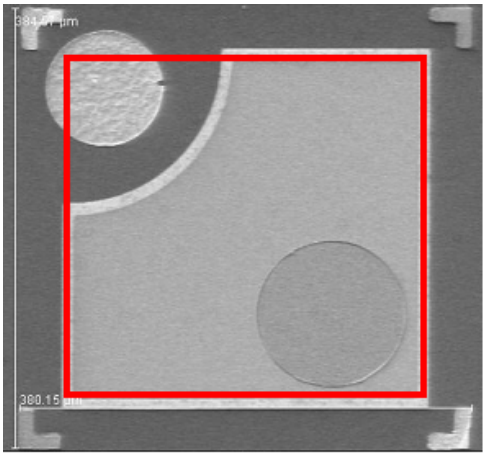
(a) (b)

FIG. 4. Transmitivity of TM wave through aluminum SMNG with different grating height (a) and duty cycle (b)

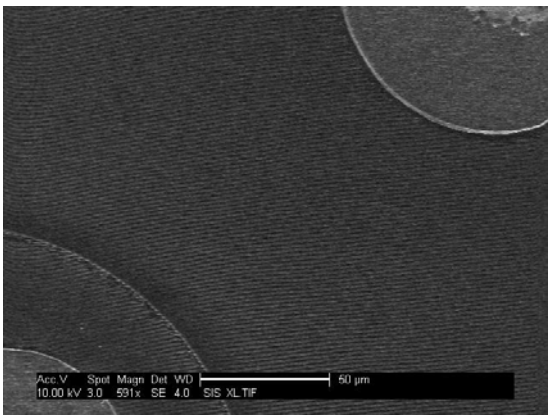
3. FABRICATION

The LED structure is grown on (0001) sapphire substrate by metal organic chemical vapor deposition. The layered structure starting from the top has a ~200 nm thick *p*-GaN layer, four InGaN/GaN quantum wells, ~2000 nm thick *n*-GaN and a ~2000 nm thick *u*-GaN layer. LED mesa structures are defined by standard photolithographic patterning, using AZ5214 photoresist, spinned at 2000rpm for 1sec, 3000rpm for 1sec then 5000rpm for 30sec with all acceleration of 2000rpm/sec, achieve ~1.3um thickness. Parts of the *p*-GaN and MQWs were first etched to expose the *n*-type GaN layer and to form a mesa. ICP etching using BCl3 20sccm and Cl2 10 sccm under pressure 5 mtorr at 6 °C. RIE 200w ICP 500W with an etching rate about 0.3um/min. Second photolithographic patterning was done with alignment to the mesa, then a 10nm/150 nm/10nm/100 nm Ti/Al/Ni/Au metal layer was deposited by electron-beam evaporation followed by lift-off, and then annealed at air ambient at 650 °C to form ohmic contact for *n*-type GaN. By repeating a 3rd alignment photolithography, a 5 nm/5 nm thick Ni/Au metal layer was deposited and annealed at 550°C to form ohmic contact to *p*-type GaN. After a 4th alignment photolithography, ~200nm Au was deposited and form *p*-bond. A thin layer of SiO_2 is deposited by plasma enhanced chemical vapor deposition on top of the Ni/Au *p*-type 5 nm/5 nm ohmic contact layer, then a 5th alignment photolithography is done to open window on top of *p*-bond, on which the deposited SiO_2 was away by immersion into buffered HF solution. Aluminum is then evaporated on top of SiO2 by thermal evaporation with a thin titanium transition layer to enhancing adhesion. ZEP520 resist is mixed with Aniso by 2:1 ratio, then spinned onto sample surface at 3000rpm for 90sec, getting a thickness of ~250nm. Then baked on hotplate at 180°C for 2min to evaporate the solvent. Then a thin layer of carbon particle inside water solvent is spinned on top of resist at 1000rpm for 30sec, then baked on hotplate at 95°C for 2min to evaporating water solvent, to form a conductive coating for accumulated charge during e beam writing, which is especially helpful for non-conductive sapphire substrate here. Electron beam lithography (EBL) is then performed on ELS-7000 e-beam

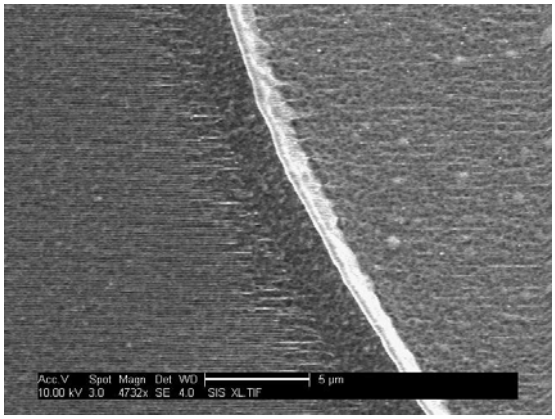
direct write system with 100 kV acceleration voltage to define accurate 150 nm period grating array on ZEP resist. A field of 300um by 300um is used to covers whole writing area indicated by the red square shown in the SEM image figure 5(a). Such a writing strategy gives uniform pattern in large area since no relative movement is needed between gun and stage within one field writing time, thus could avoid any mis-alliment of nanograting pattern which degrade the polarization effect. After writing, the sample is rinsed with DI water to clean the carbon conduction layer, and then immersed into oxylene for 30s developing time. The grating pattern was replicated into the underlying aluminum layer through etching process. Figure 5 (b) shows that the grating pattern is uniform across the emission region of LED surface, while figure 5 (c) shows that the grating pattern is discontinuous around p-pad, leaving a gap where unpolarized emission should come out through the gap.



(a)



(b)



(c)

FIG. 5. SEM image of (a) LED mesa and EBL writing area (b) uniform grating pattern across the emission region of LED surface (c) discontinuous grating pattern around p-pad.

4. CONCLUSIONS

In conclusion, we have discussed in detail on the design and fabrication of subwavelength metallic nano-gratings based InGaN green light emitting diode grown on (0001) oriented sapphire for linearly polarized light emission.

It is a real-world device application of nanophotonics. This method simply requires no special LED design, package, substrate and growth conditions, and is general to be extended to almost any wavelength range light emitter by scaling the dimension of SMN period only, and can be high throughput for commercialization when nanoimprint lithography is used.

REFERENCES

1 R. Oldenbourg, "A new view on polarization microscopy," Nature **381**, 811-812 (1996)

2 S.-S. Lin, K. M. Yemelyanov, E. N. Pugh. Jr., and N. Engheta, "Separation and contrast enhancement of overlapping cast shadow components using polarization," Opt. Express **14**, 7099-7108 (2006)

3 S. H. B. J. Jagt, H. J. Cornelissen, D. J. Broer, and C. W. M. Bastiaansen, "Linearly polarized light-emitting backlight," J. Soc. Inf. Disp. **10**, 107-112 (2002)

4 S. M. P. Blom, H. P. M. Huck, H. J. Cornelissen, and H. Greiner, "Towards a polarized light-emitting backlight: micro-structured anisotropic layers," J. Soc. Inf. Disp. **10**, 209-213 (2002)

5. H. Masui, A. A. Chakrabory, B. A. Haskell, U. K. Mishra, J. S. Speck, S. Nakamura, and S. P. DenBaars, "Polarized light emission from nonpolar InGaN light-emitting diodes grown on a bulk *m*-plane GaN substrate," Jpn. J. Appl. Phys. **44**, L1329-L1332 (2005)

6. N. F. Gardner, J. C. Kim, J. J. Wierer, Y. C. Shen, and M. R. Krames, "Polarization anisotropy in the electroluminescence of *m*-plane InGaN-GaN multiple-quantum-well light-emitting diodes," Appl. Phys. Lett. **86**, 111101 (2005)

7. H. Masui, T. J. Baker, M. Iza, H. Zhong, S. Nakamura, and S. P. DenBaars, "Light-polarization characteristics of electroluminescence from InGaN/GaN light-emitting diodes prepared on (1122)-plane GaN," J. Appl. Phys. **100**, 113109 (2006)

8. T. Koyama, T. Onuma, H. Masui, A. Chakraborty, B. A. Haskell, S. Keller, U. K. Mishra, J. S. Speck, S. Nakamura, S. P. DenBaars, T. Sota, and S. F. Chichibu, "Prospective emission efficiency and in-plane light polarization of nonpolar *m*-plane InxGa1-xN/GaN blue light emitting diodes fabricated on freestanding GaN substrates," Appl. Phys. Lett. **89**, 091906 (2006)

9. R. Sharma, M. Pattison, H. Masui, R. M. Farrell, T. J. Baker, B. A. Haskell, F. Wu, S. P. DenBaars, J. S. Speck, and S. Nakamura, Appl. Phys. Lett. **87**, 231110 (2005)

10. Martin F. Schubert, Sameer Chhajed, Jong Kyu Kim, E. Fred Schubert, and Jaehee Cho "Linearly polarized emission from GaInN lightemitting diodes with polarization-enhancing reflector Opt. Express Vol. 15, No. 18 11213

11. Chun-Feng Lai, Jim-Yong Chi, Hsi-Hsuan Yen, Hao-Chung Kuo, Chia-Hsin Chao, Han-Tsung Hsueh, Jih-Fu Trevor Wang, Chen-Yang Huang, and Wen-Yung Yeh "Polarized light emission from photonic crystal light-emitting diodes" Appl. Phys. Lett. **92**, 243118 (2008)

12. L. Zhang, J. H. Teng, S. J. Chua, E. A. Fitzgerald, "Linearly polarized light emission from InGaN light emitting diode with sub-wavelength metallic nanograting", Applied Physics Letters, 95, 261110, 2009

13. E.D. Palik, *Handbook of Optical Constants of Solids* (Academic, San Diego, CA, 1985)

14 M. G. Moharam and T. K. Gaylord, J. Opt. Soc. Am. A **3**, 1780, 1986.

Influence of the Group-velocity on the Pulse Propagation in 1D Silicon Photonic Crystal Waveguides

N. C. Panoiu
Photonics Group, Department of Electronic and Electrical Engineering, University College London, Torrington Place, London WC1E 7JE, UK

J. F. McMillan and C. W. Wong
Optical Nanostructures Laboratory, Columbia University, New York, New York 10027, USA

Abstract— We present a detailed analysis of the influence of the group-velocity (GV) on the dynamics of optical pulses upon their propagation in one-dimensional photonic crystal waveguides (PhCW). The theoretical model used in our analysis incorporates the linear optical properties of the PhCW (GV dispersion and optical losses), free-carrier (FC) effects (FC dispersion and FC-induced optical losses) and nonlinear optical effects (Kerr nonlinearity and two-photon absorption). Our analysis shows that, unlike the case of uniform waveguides, the GV of the pulse, dispersion coefficients, and the waveguide nonlinear coefficient are periodic functions with respect to the propagation distance. We also demonstrate that linear and nonlinear effects depend on the group-velocity, v_g, as v_g^{-1} and v_g^{-2}, respectively.

1. INTRODUCTION

Silicon photonics represents an emerging fast growing area of research, which is envisioned to revolutionize on-chip and chip-to-chip optical communications systems by developing silicon-based photonic devices manufactured using the well-established CMOS technology [1, 2, 3]. There are several unique properties of silicon that make it an ideal integration medium for functional photonic devices. For example, by using waveguides with a silicon core ($n_{Si} = 3.45$) and a low-index cladding ($n = 1$ for air and $n_{SiO_2} = 1.45$ for silica) one can achieve a very tight optical field confinement and, consequently, enhanced optical power flux. The second key optical property of silicon is an extremely large third-order susceptibility – about 3-4 orders of magnitude larger than that of silica. This large optical nonlinearity, in connection with the strong optical field confinement, leads to further enhancement of the effective optical nonlinearity of silicon-based photonic devices. This enhancement results in achieving strong nonlinear optical effects at low optical power [4], as well as very compact nonlinear optical devices [5, 6, 7]. In addition, for subwavelength waveguides both the linear dispersion coefficients [8, 9], as well as the nonlinear effective coefficient of the waveguide [3], depend chiefly on the geometry of the photonic structure.

One very promising approach to further decrease the size of silicon-based photonic systems is to employ nanostructured devices based on photonic crystals (PhCs). Thus, subwavelength patterning increases the device parameter space and therefore it provides an efficient approach to tailor and optimize the device functionality. For example, by simply tuning the geometrical parameters of PhC waveguides (PhCWs) one can achieve an optical guiding regime in which the group-velocity (GV) of the propagating modes of the waveguide is as small as $10^{-4}c$ [10]. In this slow-light regime nonlinear optical effects, such as Raman interaction [11], third-harmonic generation [12, 13], and superprism effects [14], are dramatically enhanced and therefore the footprint of active devices can be reduced significantly. It is expected that, in addition, these enhanced nonlinear optical effects would strongly affect the dynamics of optical pulses propagating in subwavelength silicon waveguides. In this connection, in this paper we study the influence of the GV on the temporal and spectral characteristics of optical pulses propagating in PhCWs made of silicon.

2. DISPERSION PROPERTIES OF THE PHOTONIC CRYSTAL WAVEGUIDE

To begin with, we consider a PhC slab waveguide with thickness h, made of silicon, perforated by a hexagonal lattice of holes; the lattice constant and hole radius are a and r, respectively. A one-dimensional (1D) waveguide is then obtained by filling one of the rows of holes, which is assumed to be oriented along the ΓK crystal symmetry axis [see Fig. 1(a)]. The coordinate system is chosen

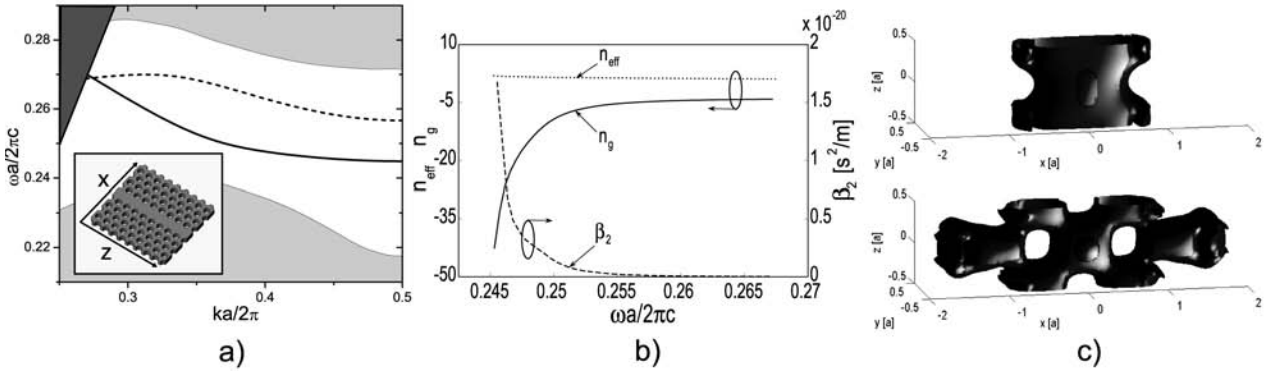


Figure 1: a) Projected band structure of a Si PhC slab waveguide with $h = 0.6a$ and $r = 0.22a$. Solid and dashed curves correspond to the fundamental and second mode, respectively. Dark grey and light grey regions correspond to leaky modes and slab guiding modes, respectively. b) Dependence of n_{eff}, n_g, and β_2 on the normalized frequency, calculated for $a = 412$ nm. c) Isosurface plots of the field intensity of a mode with $\tilde{\omega} = 0.267$ (top panel) and a slow-light mode with $\tilde{\omega} = 0.245$ (bottom panel).

such that the line defect is oriented along the z-axis whereas the y-axis is perpendicular to the plane of the PhC slab. Then, the spatial distribution of the index of refraction is described by the function $n(\mathbf{r})$, where $n(\mathbf{r}) = 1$ and $n(\mathbf{r}) = n_{Si} \equiv n$ for the regions of the holes and outside the slab, and for the silicon regions, respectively.

We have determined the photonic band structure of the 1D PhC waveguide by using a numerical method based on the plane wave expansion algorithm. We have considered a PhCW with $h = 0.6a$ and $r = 0.22a$, and used a super-cell with size of $6\sqrt{3}a \times 4a \times a$ along the x-, y-, and z-axis, respectively. The size of the computational step along the x, y, and z directions was $a\sqrt{3}/40$, $a/20$, and $a/20$, respectively. The results of our numerical simulations, presented in Fig. 1(a), show that the PhCW has two (TE-like) guiding modes located in the full frequency band gap of the PhC slab waveguide. Since the index of refraction $n(\mathbf{r})$ of the 1D PhCW is periodic along the z-axis, the Bloch theorem implies that the mode propagation constant, β, which is oriented along the z-axis, is restricted to the first Brillouin zone, $\beta \in [-\pi/a, \pi/a]$. Note also that the dispersion curves shown in Fig. 1(a) are given in dimensionless units, namely, $\tilde{\omega} = \frac{\omega a}{2\pi c}$ for the normalized frequency and $\tilde{k} = \frac{\beta a}{2\pi}$ for the normalized wave vector.

One important property of the guiding modes of the PhCW, which is illustrated in Fig. 1(c), is that the mode field profile is strongly dependent on the frequency, Therefore, one expects that the mode propagation constant varies strongly with the frequency. The dependence $\beta = \beta(\omega) \equiv \frac{n_{eff}\omega}{c}$, where n_{eff} is the effective index of the mode, allows us to determine a set of dispersion coefficients that characterize the optical pulse dispersion in the waveguide. Specifically, $\beta_1 \equiv \frac{\partial\beta}{\partial\omega} = \frac{1}{v_g}$ defines the GV of the optical pulse, whereas $\beta_2 \equiv \frac{\partial^2\beta}{\partial\omega^2}$ describes the pulse GV dispersion (GVD). The frequency dependence of these dispersion coefficients, calculated for the fundamental mode, is presented in Fig. 1(b). Among other things, this figure shows that near the edge of the first Brillouin zone the group index $n_g = c/v_g$ has large absolute value, one immediate consequence being that β_2 becomes very large in this slow-light regime.

3. MATHEMATICAL MODEL

The theoretical model that describes the pulse propagation in 1D PhCWs, which has been derived in Ref. [15], consists of an equation that governs the evolution of the optical field,

$$i\left[\frac{\partial A}{\partial z} + \frac{\delta(z)}{v_g}\frac{\partial A}{\partial t}\right] - \frac{\beta_2\delta(z)}{2}\frac{\partial^2 A}{\partial t^2} = -\frac{\omega\delta n_{FC}}{nv_g}\kappa(z)A - i\frac{c\alpha_{FC}}{2nv_g}\kappa(z)A - \gamma(z)|A|^2A, \tag{1}$$

coupled with a standard rate equation, which describes the FC dynamics,

$$\frac{\partial N(z,t)}{\partial t} = -\frac{N(z,t)}{\tau_c} + \frac{3\Gamma''(z)}{4\epsilon_0\hbar a^2 v_g^2 A_{nl}(z)}|A(z,t)|^4. \tag{2}$$

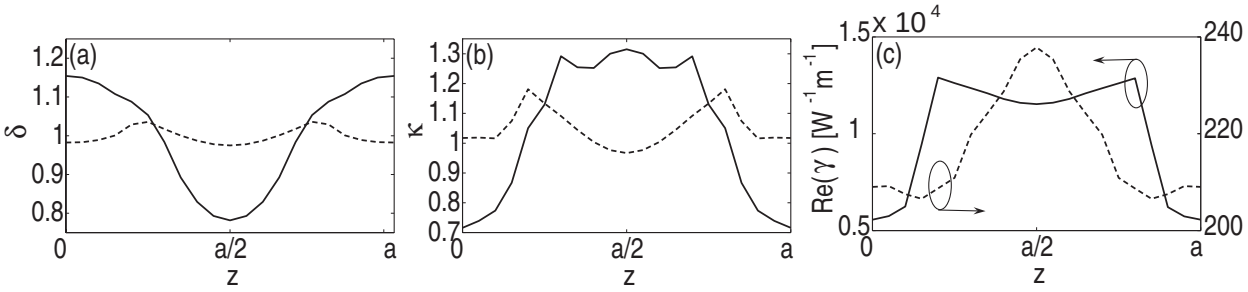


Figure 2: The group-velocity shift δ, the mode overlap parameter κ, and waveguide nonlinear coefficient γ *vs.* distance z, calculated for the fast- and slow-light modes presented in Fig. 1(c). Dashed and solid curves correspond to the fast- and slow-light modes, respectively.

In these equations, $A(z,t)$ is the field amplitude (measured in $\sqrt{\text{W}}$), $N(z,t)$ is the FC density, τ_c is the FC relaxation time, δn_{FC} and α_{FC} are the FC-induced change in the index of refraction and the FC loss coefficient, respectively, and are proportional to the FC density N, A_{nl} is the effective area of the mode, and

$$\gamma(z) = \frac{3\omega\Gamma(z)}{4\epsilon_0 a^2 v_g^2} \tag{3}$$

is the nonlinear coefficient of the waveguide. Furthermore, the averaged third-order susceptibility, Γ, the GV shift, δ, and the mode overlap coefficient, κ, are given by the following expressions:

$$\Gamma(z) = \frac{a^4 \int \mathbf{e}^* \cdot \hat{\chi}^{(3)} \vdots \mathbf{e}\mathbf{e}\mathbf{e}^* dS}{\int_{V_{cell}} n^2(\mathbf{r})|\mathbf{e}|^2 dV}; \quad \delta(z) = \frac{a \int \left[\mu_0|\mathbf{h}|^2 + n^2(\mathbf{r})|\mathbf{e}|^2\right] dS}{\int_{V_{cell}} \left[\mu_0|\mathbf{h}|^2 + n^2(\mathbf{r})|\mathbf{e}|^2\right] dV}; \quad \kappa(z) = \frac{an^2 \int_{S_{nl}} |\mathbf{e}|^2 dS}{\int_{V_{cell}} n^2(\mathbf{r})|\mathbf{e}|^2 dV}, \tag{4}$$

where $\hat{\chi}^{(3)}$ is the third-order susceptibility of bulk silicon and $\mathbf{e}(\mathbf{r})$ and $\mathbf{h}(\mathbf{r})$ are the electric and magnetic field of the waveguide mode, respectively. It should be noted that, as shown in Fig. 2, and unlike the case of uniform waveguides, these physical quantities are periodic functions of the distance z. Figure 2 also shows that this dependence on z is much stronger in the case of the slow-light mode as compared to the case of the fast-light mode, which emphasizes the strong frequency dispersion of these PhCWs.

4. INFLUENCE OF GROUP-VELOCITY ON PULSE DYNAMICS

One important conclusion illustrated by the Eq. (1) and Eq. (2) is that the GV of the optical pulse would have a strong influence on the pulse dynamics, especially at large peak power, P. To be more specific, the linear terms in the Eq. (1) are inverse proportional to v_g, which implies that the FC-induced losses are inverse proportional to v_g, whereas the nonlinear terms in the Eq. (1) and Eq. (2) are inverse proportional to v_g^2. In other words, when compared to the fast-light regime, in the slow-light regime the nonlinear optical effects are enhanced significantly more than the linear ones. This dependence, however, becomes more complicated as the power increases, since in this case the generated FCs increase the linear and nonlinear absorption *via* the FC absorption and two-photon absorption (TPA), respectively. Thus, as can be seen from the Eq. (2), the amount of FCs generated *via* TPA is inverse proportional to v_g^2, and therefore the FC-induced losses become inverse proportional to v_g^3.

In order to illustrate this strong dependence of the pulse dynamics on the GV, we present in Fig. 3 the temporal and spectral profiles of a pulse that propagates in a silicon PhCW, both in the fast-light and the slow-light regimes. In these numerical simulations the spatial integration step was $a/20$ and the relaxation time $\tau_c = 0.5$ ns. In both cases the pulse temporal width $T_0 = 2$ ps and the propagation distance $z = 1000a$ are the same. Among other things, this figure shows that in the fast-light regime the temporal profile of the pulse remains almost unchanged during the propagation, except for a small decrease in amplitude due to the FC losses and TPA. On the other hand, it can be seen that at large optical power the spectrum of the pulse becomes asymmetric and splits in two separate pulses, the latter feature being the signature of the self-phase modulation effect. By contrast, in the slow-light regime both the temporal profiles of the pulse, as well as the pulse spectra, are modified dramatically during the pulse propagation in the waveguide. Specifically, because in

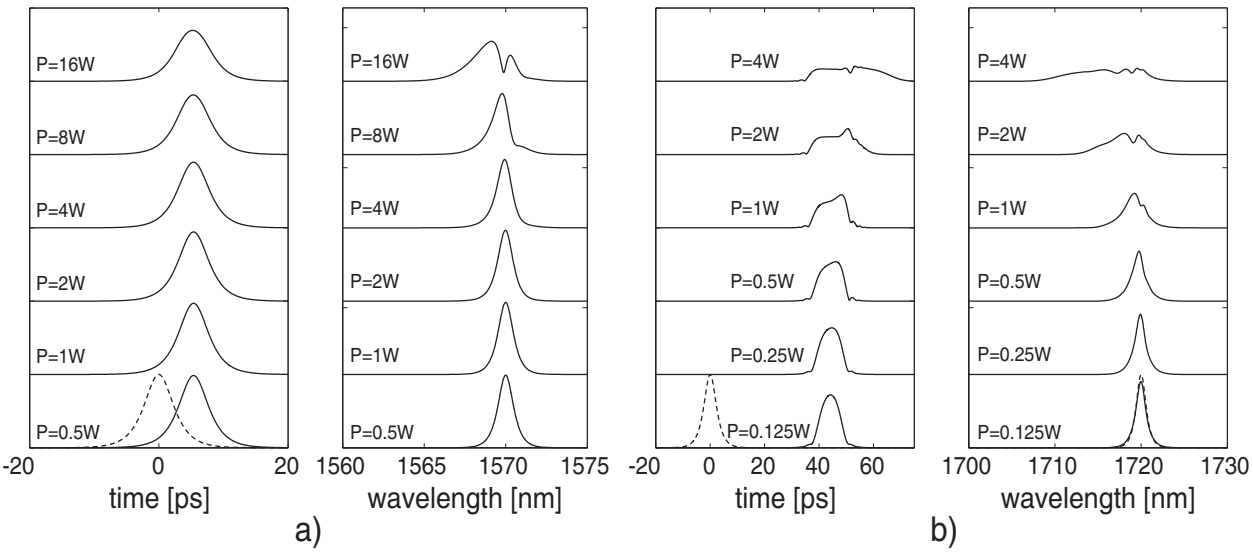


Figure 3: a) The temporal and spectral pulse profiles calculated for several values of power P. For a better illustration, the pulse profiles are displaced vertically by a constant shift. The pulse GV $v_g = c/4.125$, which corresponds to $\tilde{\omega} = 0.267$. The PhCW has $h = 0.6a$ and $r = 0.22a$, with $a = 421$ nm. The pulse width $T_0 = 2$ ps, $\beta_2 = 10$ ps^2/m, and the propagation distance $z = 1000a$. b) The same as in a), but for a slow-light mode with $v_g = c/35$, $\tilde{\omega} = 0.245$, and $\beta_2 = 10^4$ ps^2/m. The dashed curves correspond to the input pulse.

this case β_2 is three orders of magnitude larger than in the fast-light regime, the temporal width of the pulse broadens significantly. Moreover, even at moderate optical power the pulse decay is much stronger in this case, which means that the optical losses due to the generation of FCs and TPA are larger. Note also that in the slow-light regime the spectrum of the pulse develops a series of oscillations, which again is a signature of the phase modulation induced by the FC dispersion and the Kerr effect. Indeed, the nonlinear coefficient γ of the slow-light mode is about two orders of magnitude larger than in the case of the fast mode, and therefore in this case one expects that the pulse is much more strongly influenced by the increased amount of generated FCs and the enhanced nonlinear optical effects.

5. CONCLUSION

In conclusion, we have presented a detailed analysis of the influence of the GV on the pulse propagation in 1D PhCWs made of silicon. In particular, we have included in our analysis linear optical effects induced by the waveguide dispersion and nonlinear optical effects due to the (Kerr) nonlinearity of silicon, and studied their influence on the pulse propagation. We have applied the general theoretical formalism to two particular cases, namely, the propagation of optical pulses in a single mode PhCW in the slow-light and fast-light regimes. One important conclusion of this theoretical analysis is that due to a complex interplay between effects induced by the generation of FCs and nonlinear optical effects, the pulse dynamics in the slow-light and fast-light regimes show markedly different physical characteristics.

ACKNOWLEDGMENT

This work was supported by the UK Engineering and Physical Sciences Research Council (EPSRC), grant no. EP/G030502/1.

REFERENCES

1. G. T. Reed and A. P. Knights, *Silicon Photonics: An Introduction*, John Wiley, 2004.
2. Q. Lin, O. J. Painter, and G. P. Agrawal, "Nonlinear optical phenomena in silicon waveguides: Modeling and applications," *Opt. Express*, Vol. 15, 16604-16644, 2007.
3. R. M. Osgood, N. C. Panoiu, J. I. Dadap, X. Liu, X. Chen, I-W. Hsieh, E. Dulkeith, W. M. J. Green, and Y. A. Vlasov, "Engineering nonlinearities in nanoscale optical systems: physics and applications in dispersion-engineered silicon nanophotonic wires," *Adv. Opt. Photon.*, Vol. 1, 162-235, 2009.

4. E. Dulkeith, Y. A. Vlasov, X. Chen, N. C. Panoiu, and R. M. Osgood, "Self-phase-modulation in submicron silicon-on-insulator photonic wires," *Opt. Express*, Vol. 14, 5524-5534, 2006.
5. R. Claps, D. Dimitropoulos, V. Raghunathan, Y. Han, and B. Jalali, "Observation of stimulated Raman amplification in silicon waveguides," *Opt. Express*, Vol. 11, 1731-1739, 2003.
6. H. Rong, A. Liu, R. Jones, O. Cohen, D. Hak, R. Nicolaescu, A. Fang, and M. Paniccia, "An all-silicon Raman laser," *Nature*, Vol. 433, 292-294, 2005.
7. I-W. Hsieh, X. Chen, J. I. Dadap, N. C. Panoiu, R. M. Osgood, S. J. McNab, and Y. A. Vlasov, "Crossphase modulation-induced spectral and temporal effects on co-propagating femtosecond pulses in silicon photonic wires," *Opt. Express*, Vol. 15, 1135-1146, 2007.
8. X. Chen, N. C. Panoiu, and R. M. Osgood, "Theory of Raman-mediated pulsed amplification in silicon-wire waveguides," *IEEE J. Quantum Electron.*, Vol. 42, 160-170, 2006.
9. A. C. Turner, C. Manolatou, B. S. Schmidt, M. Lipson, M. A. Foster, J. E. Sharping, and A. L. Gaeta, "Tailored anomalous group-velocity dispersion in silicon channel waveguides," *Opt. Express*, Vol. 14, 4357-4362, 2006.
10. M. Soljacic, S. G. Johnson, S. Fan, M. Ibanescu, E. Ippen, and J. D. Joannopoulos, "Photonic-crystal slow-light enhancement of nonlinear phase sensitivity," *J. Opt. Soc. Am. B*, Vol. 19, 2052-2059, 2002.
11. J. F. McMillan, X. Yang, N. C. Panoiu, R. M. Osgood, and C. W. Wong, "Enhanced stimulated Raman scattering in slow-light photonic crystal waveguides," *Opt. Lett.*, Vol. 31, 1235-1237, 2006.
12. M. Bahl, N. C. Panoiu, and R. M. Osgood, "Nonlinear optical effects in a two-dimensional photonic crystal containing one-dimensional Kerr defects," *Phys. Rev. E*, Vol. 67, 056604(1-9), 2003.
13. B. Corcoran, C. Monat, C. Grillet, D. J. Moss, B. J. Eggleton, T. P. White, L. O'Faolain, and T. F. Krauss, "Green light emission in silicon through slow-light enhanced third-harmonic generation in photonic crystal waveguides," *Nature Photon.*, Vol. 3, 206-210, 2009.
14. N. C. Panoiu, M. Bahl, and R. M. Osgood, "Optically tunable superprism effect in nonlinear photonic crystals," *Opt. Lett.*, Vol. 28, 2503-2505, 2003.
15. N. C. Panoiu, J. F. McMillan, and C. W. Wong, "Theoretical analysis of pulse dynamics in silicon photonic crystal wire waveguides," *IEEE J. Sel. Top. Quantum Electron.*, (to be published).

Gold Film-Terminated 3-Dimensional Photonic Crystals

B. Ding[1], M. E. Pemble[1], A. V. Korovin[2], U. Peschel[2], S. G. Romanov[2]
[1] Tyndall National Institute, Prospect Row, Cork, Ireland
[2] Institute of Optics, Information and Photonics, University of Erlangen-Nuremberg,
Günther-Scharowsky-Str.1, 91058 Erlangen, Germany
Sergei.Romanov@mpl.mpg.de

Abstract- A hybrid metal-dielectric photonic crystal – the opal film coated by a gold film has been designed in order to realize optical spectra that emanate from superposition of photonic bandgaps in the opal and extraordinary transmission in the gold films. The photonic crystal provides a spatial template for the gold film profile and modifies the electromagnetic vacuum around the gold layer. The correlation between bands of enhanced transmission and the surface plasmon polariton dispersion suggests the plasmon excitation by photonic crystal eigenmodes.

1. INTRODUCTION

Since invention of photonic crystals (PhCs) the special attention was paid to the control upon their properties by changing the lattice symmetry, refractive index contrast, filling fraction of heavy dielectric and so on. Among these parameters, the boundary of a PhC is responsible for the light coupling to the PhC interior. However, the surface of 3-dimensional (3D) PhCs was not in the focus of interest until recently[1] because truly evanescent waves do not contribute to the PhC optical response.

If the interface is designed to support evanescent waves, the influence of a surface upon PhC properties can be dramatically enhanced. Surface plasmon polaritons (SPP) bounded to the metal-dielectric interface is the prominent example of such excitations. Correspondingly, deposition of a metal film on a 3D PhC template could provide yet another means of tailoring the PhC properties. Such hybrid architecture brings a synergy of photonic band gap (PBG) structure for the electromagnetic (EM) waves and the extraordinary transmission (EOT) through a metal film containing subwavelength-sized holes[2,3].

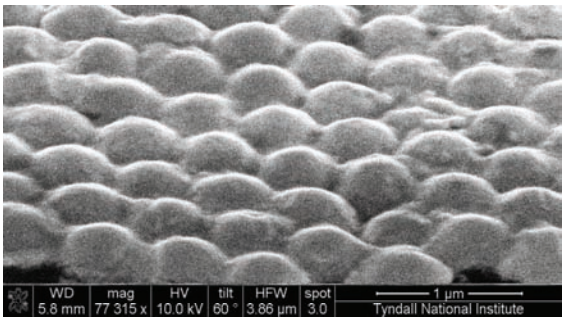
Among many methods of creating metal films with regular arrays of holes or with periodic profiles[4,5] the simplest and cheapest method is that which involves coating of an ordered array of nanospheres by a metal layer[6]. In the case of metal-capped spheres, the EOT phenomenon becomes modified[7,8,9] by underlying 2D PhC slabs[10], in particular, the strong field confinement in the eigenmodes of the 2D PhC slabs enhances the EOT magnitude. As a result, the spectral range of higher transparency appears in the vicinity to the PBG.

In the case of 3D PhCs one can expect that the Au film becomes exposed to the PhC-structured EM vacuum. The crucial question to be asked is how the transmission enhancement will interfere with the PBG transmission suppression. In order to examine this issue, we have deposited a thin gold film on the surface of a thin opal film and compared the optical properties of this structure to those of the bare opal film. A clear correlation between the spectral features of the PBG and EOT confirms their relationship, but the deviation from a simple superposition of these optical effects points to the indirect character of this link.

2. EXPERIMENTAL TECHNIQUE

Opal films were crystallized in a vertically moving meniscus on hydrophilic glass slides, which were lifted up and out of a suspension of poly-methyl methacrylate spheres of 559 nm in diameter as described

elsewhere[11]. Application of acoustic noise agitation of the colloid suspension during the course of film crystallization improved the crystal structure[12]. A nominally 50 nm thick Au film was sputtered on top of the freshly crystallized opal (Fig.1, left).



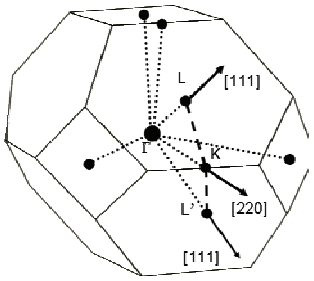


Fig.1. Left panel – SEM image of the opal surface coated by 50nm thick Au film. Right – Brillouin zone of the opal PhC. Numbers indicate Miller indices of crystal plane in the real space that correspond to some characteristic directions in the reciprocal space.

Angle-resolved transmission/reflectance spectra were acquired at different angles of incidence, θ, with respect to the film normal from -40° to 40°. The samples were illuminated by a collimated beam of ~1mm in diameter from a tungsten lamp. The spectra were acquired using s- and p-polarized light, the electrical field of which is oriented either perpendicular or parallel to the plane of light incidence. The control of the azimuthal orientation of this plane allowed the interrogation of the optical properties along the ULK line of the 1st Brillouin zone of the opal PhC (Fig.1, right). A depolariser plate was used to scramble the light polarization before approaching the spectrometer.

In what follows we will denote the diffraction resonances according to the Miller indices of an 3D fcc lattice and 2D hexagonal lattice. The most densely packed (111) planes represent the hexagonal lattice of touching spheres. This plane forms the surface of the opal film. The dispersion of diffraction resonances for different families of opal crystal planes was obtained using the Bragg law approximation and the dispersion of the SPP waves was obtained taking into account the dielectric constant of gold[13].

2. RESULTS AND DISCUSSION

Fig.2a is a map of the transmission spectra of a bare opal film obtained at different incidence angles under p-polarized light. From the Bragg approximation to the dispersion of the (111) diffraction resonance, the sphere diameter D=559 nm and the effective index of refraction n_{eff}=1.38 were obtained. Using these values, the dispersions of the $(\bar{1}11)$, (200), (220), (311) and (222) resonances in the fcc lattice were calculated and, then, they were identified in transmission spectra.

After coating with an Au film, the transmission of the hybrid structure is dramatically reduced from 70% down to 2% at the long wavelength edge of studied spectral interval. However, the transmission then increases as the wavelength decreases and reaches its maximum at 725 nm for the normal incidence of the light ($\theta = 0^o$) (Fig.2, right). With the increase of the angle of incidence the magnitude of the EOT peak decreases rapidly. However, this peak is surrounded by several other transmission peaks of lower intensity, which extend to higher incident angles. The EOT bands then coexist along with the transmission minima associated with PBGs.

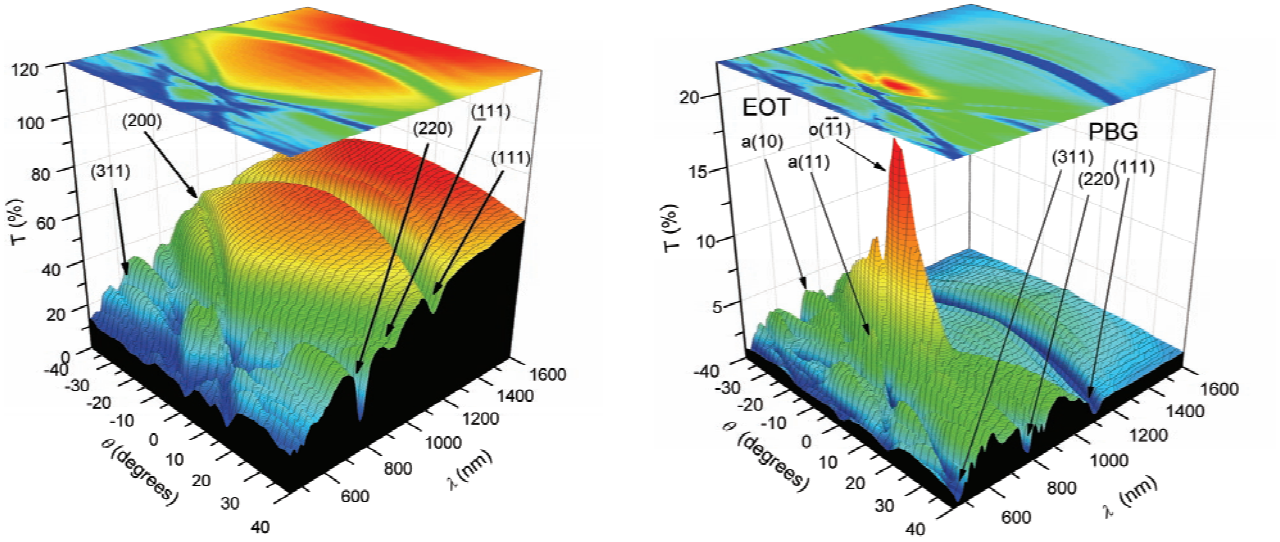


Fig.2. Transmission spectra of the parent opal film (left panel) and Au-coated hybrid PhC (right panel) under illumination with p-polarized light. Arrows indicate the diffraction resonances (left) and superposition of diffraction and EOT bands (right).

It is readily seen that the EOT observed under p-polarized light tightly correlates the SPP resonance dispersions. The EOT maximum at 725 nm corresponds exactly to the node of SPP resonance branches that propagate along the opal-gold film interface. At oblique light incidence the long wavelength edge of the EOT band follows the dispersion of o(11) and $o(\bar{1}\bar{1})$ SPP branches of the hexagonal 2D Au grating at the opal-gold interface. The next set of SPP dispersion curves that belong to the air-gold film interface have their origin in the smaller EOT peak at 605 nm. At oblique light incidence the EOT bands stick to dispersions of the corresponding SPPs, e.g. a(11) and $a(\bar{1}\bar{1})$ bands. Remarkably, that $(\bar{1}11)$ and (200) diffraction minima that would normally appear in the transmission spectrum of the opal lattice are replaced by EOT bands in the Au-opal hybrid.

The transmission pattern contains regions of avoided crossing of SPP modes that leads to a “patchy” map of the enhanced transmission (Fig.2, right). The transmission attenuation inherited from the PBG structure of the underlying opal PhC contributes to the transmission map in p-polarized light only for (111), (220) and (311) resonances. In the short-wavelength range, the transmission pattern of Au-opal hybrid acquires a degree of asymmetry with respect to the change of the incidence angle sign in correspondence to the asymmetry of the PBG structure of the opal substrate (Fig.2, left).

Transformation of reflectance spectra is also dramatically strong. Reflectance of parent opal film is dominated by the (111) diffraction peak in both polarizations (Fig.3). After deposition of the Au film, the reflectance acquired the non-reciprocity with respect to the illumination direction. Being illuminated from the opal side (through a glass substrate), the hybrid reflectance appears as a superposition of the gold film reflectance and the opal diffraction resonances (Fig.4, bottom row). In contrast, if the Au film side is illuminated, no PhC diffraction can be resolved. In this case, the reflectance spectra are dominated by the minimum, related to the energy spent for the SPP excitation (Fig.4, top row). It is this reflectance that provides the background for the spectra in Fig.4, bottom row. Thus, the gold film blocks the p-polarized light that is backdiffracted by a PhC.

The spectra in s-polarized light are less affected by SPP, because this process is mediated by the s-p polarization conversion.

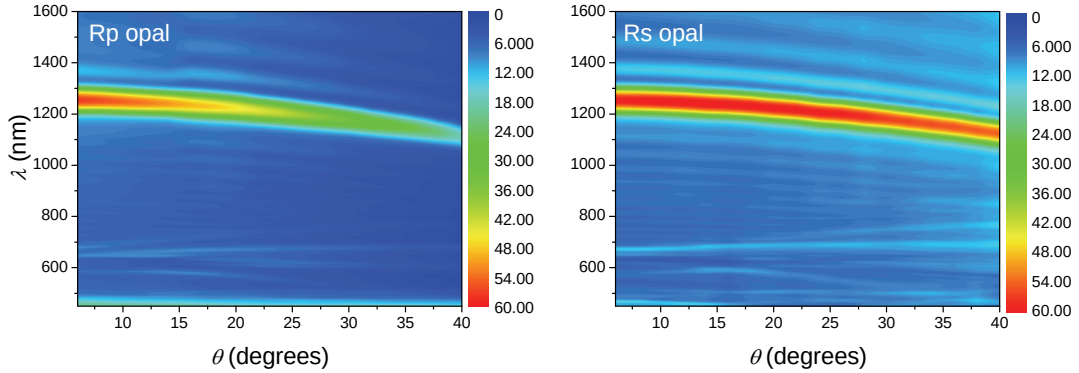


Fig.3. Reflectance spectra of bare opal film under p- (left panel) and s- (right panel) polarized light illumination. Colour coding shows the reflectance magnitude in percents.

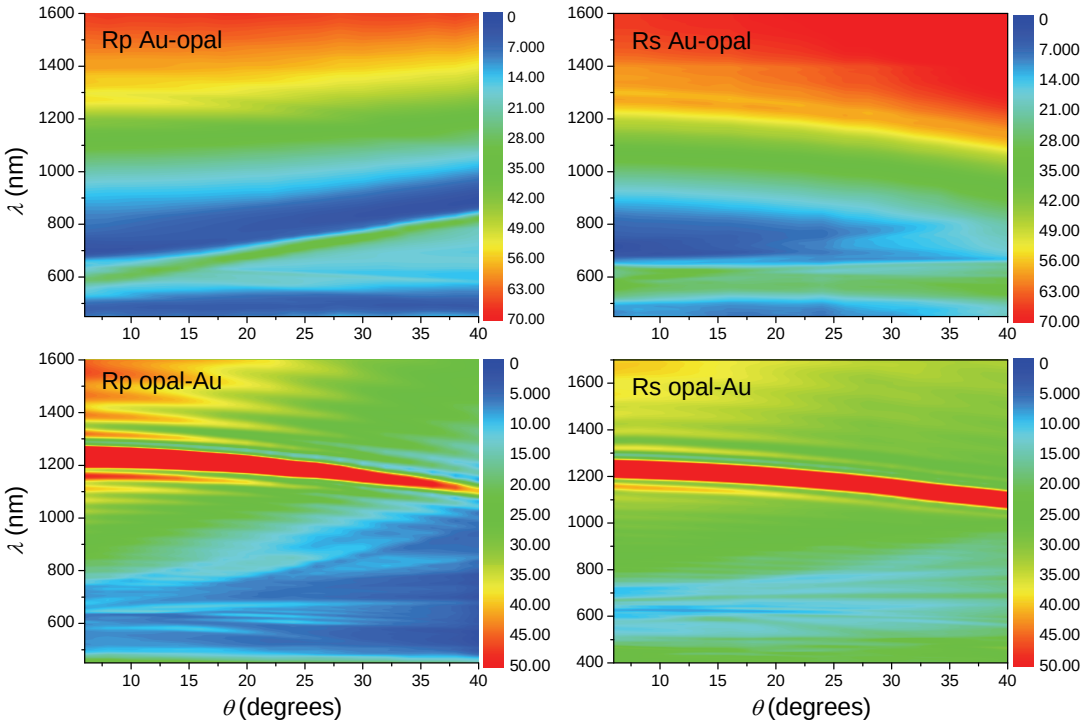


Fig.4. Reflectance spectra of Au-opal hybrid under p- (left column) and s- (right column) polarized light illumination from the Au film (top row) and opal film (bottom row) sides of the hybrid sample. Colour coding shows the reflectance magnitude in percents.

The observed EOT effect resembles that reported for the EOT of Au-coated 2D PhCs slabs consisting of a hexagonally packed monolayer of spheres. Previously, comprehensive numerical studies have demonstrated the direct connection between the EOT peak and the 2D PBG structure, linking not only the position of the EOT

peak and the sphere diameter, but also assuming localization of the EM field in the eigenmodes of the 2D PhC as being the major driving force for induced EOT [10]. Similarly, the excitation of SPP in the metal film by 3D PhC eigenmodes can be linked to diffractive coupling. Moreover, by necessarily matching the periodicities of the opal and the Au film corrugation we ensure the efficiency of SPP excitation.

In the case of the 3D opal-based PhC, the EM field pattern affecting the Au film is much more complex as compared to the 2D case, being composed of 3D eigenmodes. In fact, the SPP is excited not only from the direction of the incident beam, but simultaneously by beams that are diffracted in a 3D lattice. This effect leads to substantial broadening of the EOT spectrum towards longer wavelengths. Certainly, a 3D PhC slab should be thick enough to produce intense beams diffracted by high-index planes in order to achieve such broadening. Moreover, one should take into account the 'crescent-moon' shape of the Au cap formed on each sphere. Thus, the EOT pattern acquires a complex appearance, which is not fully explained by 2D mode dispersion only.

The EOT directional anisotropy naturally follows from the directionality of the opal PBG. The s-p polarization coupling is an efficient process for light propagating along the film normal, leading to near equal intensities of the EOT peaks under both polarizations. But at oblique incidence where the spatial EM field profile excited in a PhC by s- and polarized light becomes essentially different, the polarization anisotropy of the EOT becomes dependent on PBG attenuation that is much stronger under s-polarized light[14].

4. CONCLUSIONS

The spectra of hybrid Au-coated opal films represents a superposition of PBG resonances in a 3D PhC lattice and SPP resonances in the corrugated Au film. The SPP excitation in such hybrids can be achieved by coupling to surface and volume modes of the PhC. We suggest that these new type of hybrid metal-dielectric colloidal crystals can be exploited in order to be able to further engineer the optical response of PhCs.

ACKNOWLEDGEMENTS

This work was supported in part by the DFG Cluster of Excellence "Engineering of Advanced Materials" (Germany), the SFI grants RFP PHY076 and PI 07/IN.1/1787 (Ireland) and COST Action MP0702.

REFERENCES

[1] K. Ishizaki, S.Noda, *Nature* **460**, 367 (2009).

[2] T. W. Ebbesen, H. J. Lezec, H. F. Ghaemi, T. Thio, P. A. Wolff, *Nature*, **391**, 667 (1998).

[3] W. L. Barnes, A. Dereux, T. W. Ebbesen, *Nature*, **424**, 824 (2003).

[4] S.A. Maier, Plasmonics: Fundamentals and Applications, Springer, New York, 2007.

[5] Y.-S. Shon, H. Y. Choi, M. S. Guerrero, C. Kwon, *Plasmonics*, **4**, 1557-1955 (2009).

[6] J. C. Hulteen, R. P. Van Duynea, *J. Vac. Sci. Technol. A* **13**, 1553 (1995).

[7] P.Zhan, Z.Wang, H.Dong, J.Sun, J.Wu, H.-T.Wang, S.Zhu, N.Ming, J Zi, *Adv. Mater*., 18, 1612–1616 (2006).

[8] L. Landström, D. Brodoceanu, K. Piglmayer, D. Bäuerle, *Appl. Phys.*, *A* **84**, 373–377 (2006).

[9] C. Farcau, S. Astilean, *J. Opt. A: Pure Appl. Opt.* **9**, S345–S349 (2007).

[10] L. Landstrom, D. Brodoceanu, D. Bauerle, F. J. Garcia-Vidal, S. G. Rodrigo, L. Martin-Moreno, *Optics Express*, 17, 761 (2009).

[11] M.Müller, R.Zentel, T.Maka, S.G. Romanov, C.M. Sotomayor Torres, *Chem. Materials*, **12**, 2508-2512 (2000).

[12] W. Khunsin, G. Kocher, S.G. Romanov, C.M. Sotomayor Torres, *Adv.Funt.Mat.*,**18**, 2471 (2008).

[13] P. B. Johnson, R. W. Christy, *Phys.Rev.B* **6**, 4370 (1972).

[14] S.G. Romanov, *Phys.Solid State*, **49** 536-546 (2007).

Rectangular Patch Antennas over Electromagnetic Band Gap Structure

Nihal F. F. Areed

Mansoura University, Mansoura, Egypt
nahoolaf@yahoo.com

Abstract- In this paper, I propose a new design of a Defected Structure (DS) for use as an Electromagnetic Band Gap (EBG) configuration for printed antennas and circuit applications. The proposed defected structure embodies a honeycomb lattice of air cylindrical holes. The proposed DS is applied to three different configurations using dielectric substrate (dielectric constant 6 and thickness *1.5 mm*); namely: dielectric substrate backed by defected ground plane, defected dielectric substrate backed by normal substrate and defected dielectric substrate backed by defected ground plane. The simulated values of the transmission coefficient S_{21} for the latest one show two well defined stop bands around 8.5 and 9.5GHz, respectively. The first band has been used to reduce mutual coupling in a microstrip array. On the other hand, the stop band defined around 9.5GHz has been applied to enhance the characteristics of rectangular patch antenna and improve the operational 10dB bandwidth.

1. INTRODUCTION

Electromagnetic Band Gap structures (EBG) are 3-D periodic objects that prevent the propagation of the electromagnetic waves in a specified band of frequency for all angles and for all polarization states [1], [2]. EBG structures have become very popular as well as an active area of research in the antenna communities and microwave printed circuit filters [3], [4]. A good fraction of these developments involves, the ground planes printed with various patterns, slots and cuts [5].

In this paper, I propose a simple design of a Defected Structure (DS) in the form of a honeycomb lattice of air cylindrical holes of equal diameter as a wide band EBG material. The proposed EBG structures have been used to reduce mutual coupling in a microstrip array and to enhance the characteristics of rectangular patch antenna. 3D simulator based on finite difference time domain (FDTD) algorithm [6] was used for our design.

3. RESULTS

First, the 3D simulator based on FDTD code is tested, we present the analysis of transmission line fed rectangular patch antenna [7]. Figure 1.a illustrates the dimensions of the tested antenna. Figure 1.b shows the calculated decibel magnitude of the return loss for rectangular patch antenna [7]. Agreement between the calculated results (resonant frequency and 10-dB bandwidth) of (7.5GHz and 4.3%) with the measured values shown in reference [7] corroborates the validity of our used 3D FDTD simulator.

Next, the proposed DS embodies honeycomb lattice array of air cylindrical holes of 14mm lattice spacing. The proposed DS is applied to three different configurations using dielectric substrate (dielectric constant 6 and thickness *1.5 mm*): (i) Geometry #1, dielectric substrate backed by defected ground plane, (ii) Geometry #2, defected dielectric substrate backed by normal substrate and (iii) Geometry #3, defected dielectric substrate backed by defected ground plane. The schematic diagrams are shown in Fig. 2.a.

The EBG of each configuration is tested by calculating the transmission coefficient (S_{21}) plots for the 2-port network: microstrip transmission line, designed on the dielectric substrate as shown in Fig.2.b. The calculated transmission characteristics of a microstrip line for the three considered DS for different values of hole diameter *d* are shown in Fig. 3. The figure shows that, for the hole diameter *d=6.7mm*, the DS#1 results in a stop band ($S_{21} < -15$dB) over 10-12 GHz, , whereas the DS#2 results in a stop band ($S_{21} < -15$dB) over 8.6-9.5 GHz, and the DS#3 results in a two stop bands ($S_{21} < -15$dB) over 8.3-8.8 GHz and 9.2-11GHz, respectively, The figures prove that, the honeycomb lattice that possesses two atoms per unit cell present a complete band-gap between high order bands.

Next, the EBG over 8.3-8.8 GHz of the geometry#3 is applied to improve the mutual coupling between the elements of a two element rectangular patch array. The schematic diagrams of a two-element rectangular patch array with the proposed DS#3 are shown in Fig.4. Figure 4.d shows the calculated scattering parameter S_{11} and S_{21} which are nearly identical to S_{22} and S_{12}, respectively. The simulation illustrates that the reduction in E-plane coupling between the radiating elements is nearly 3 dB.

Finally, the S parameter calculations for coaxial probe feed rectangular patch antenna over DS#3 with EBG over 9.2-11GHz are presented. The geometry details of the suggested configuration are shown in Fig. 5. Figure 5.d shows the comparable results between normal substrate and proposed EBG substrate shown in Fig.2.b. The calculated values of S_{11} show that the 10dB operational bandwidth is 1.3369GHz or 14.3%. Conventional patch design, without the proposed EBG structure, typically only resonant with less than 5.6% bandwidth.

4. CONCLUSION

Three simply defected structures are designed and simulated theoretically for X-band printed antenna and microstrip circuit applications namely: dielectric substrate backed by defected ground plane, defected dielectric substrate backed by normal ground plane and defected dielectric substrate backed by defected ground plane. The simulated transmission characteristics of a microstrip line etched for the latest one show two well defined stop bands (transmission coefficient below –15dB) over 8.3 to 8.8GHz and 9.2 to 11GHz frequency ranges, respectively. The first band has been used to reduce mutual coupling in a microstrip array. The S_{21} results show that the reduction in E-plane coupling between the radiating elements is nearly 3dB**.** On the other hand, the stop band defined around 9.5GHz has been applied to enhance the characteristics of rectangular patch antenna. The S_{11} values show that the 10dB operational bandwidth is 1.3369GHz or 14.3%. Conventional patch design, without the proposed EBG structure, typically only resonant with less than 5.6% bandwidth.

5. REFRENCES

1. Min Qiu, Computational Methods for The Analysis and Design of Photonic Band Gap Structures, Ph. D., Royal Institute of Technology, Stockholm, 2000.
2. J. M. Lourtioz, H. Benisty V. Berger, J. M. Gerard D. Maystre, and A. Techelonkov, Photonic Crystals Towards Nanoscale Photonic Device, Springer Verlag Berlin Heidelberg, 2005.
3. R. Gonzalo and G. Nagore, "Simulated and measured performance of a patch antenna on a 2-dimensional photonic crystals substrate," *Prog. In Elect. Res.*, *PIER*, vol. 37, pp. 257–269, 2002.
4. F. Yang and Y. Rahmat-Samii, "Microstrip antennas integrated with electromagnetic band-gap (EBG) structures: A low mutual coupling design for array applications," *IEEE Trans. Antennas and Propagat.*, vol. 51, no. 10, pp. 2836-2946, Oct. 2003.
5. D. Sievenpiper, L. Zhang, R. F. J. Broas, N. G. Alexopolus, and E. Yablonovitch, "High-impedance electromagnetic surfaces with a forbidden frequency band," *IEEE Trans. Microwave Theory Technol.*, vol. 47, pp. 2059–2074, Nov. 1999.
6. Taflov and S. C. Hagness, Computational Electrodynamics- The Finite Difference Time Domain Method. 3rd Ed., London: Artech House, Boston, 2005.
7. D. M. Sheen, S. M. Ali, M. D. Abouzahra, and J. A.Kong, "Application of the three-dimensional finite-difference time-domain method to the analysis of planar microstrip circuits," IEEE Trans., Microwave Theory Tech. ,vol. MTT-38, no.7, pp. 849-857, July.1990.

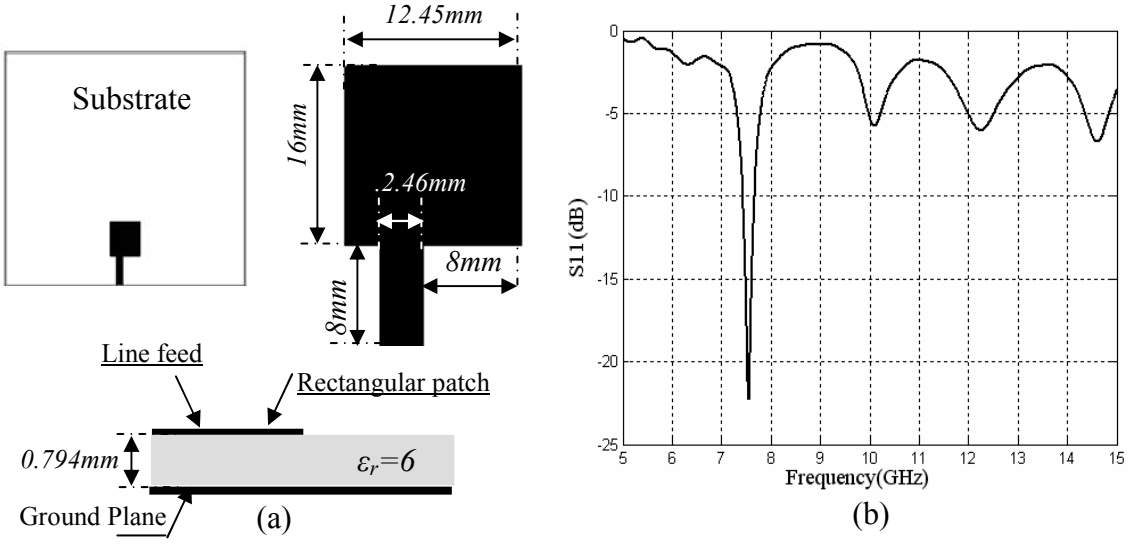


Fig.1: Microstrip line fed rectangular patch antenna, (a) Geometry details [7], (b) Return loss.

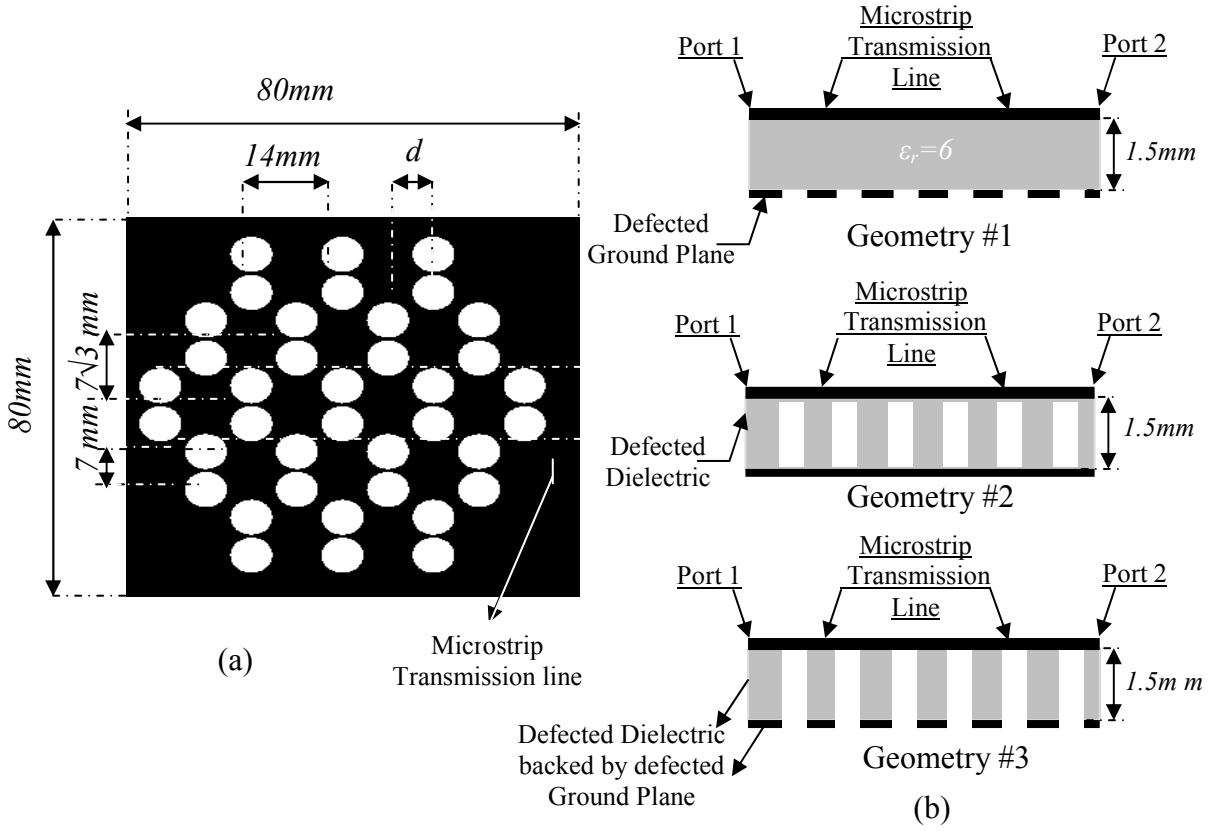


Fig.2: (a) Front view of the honeycomb lattice of air circular holes: (b) Cross sectional view of three defected configurations with microstrip transmission line of width *14mm* etched on the dielectric substrate.

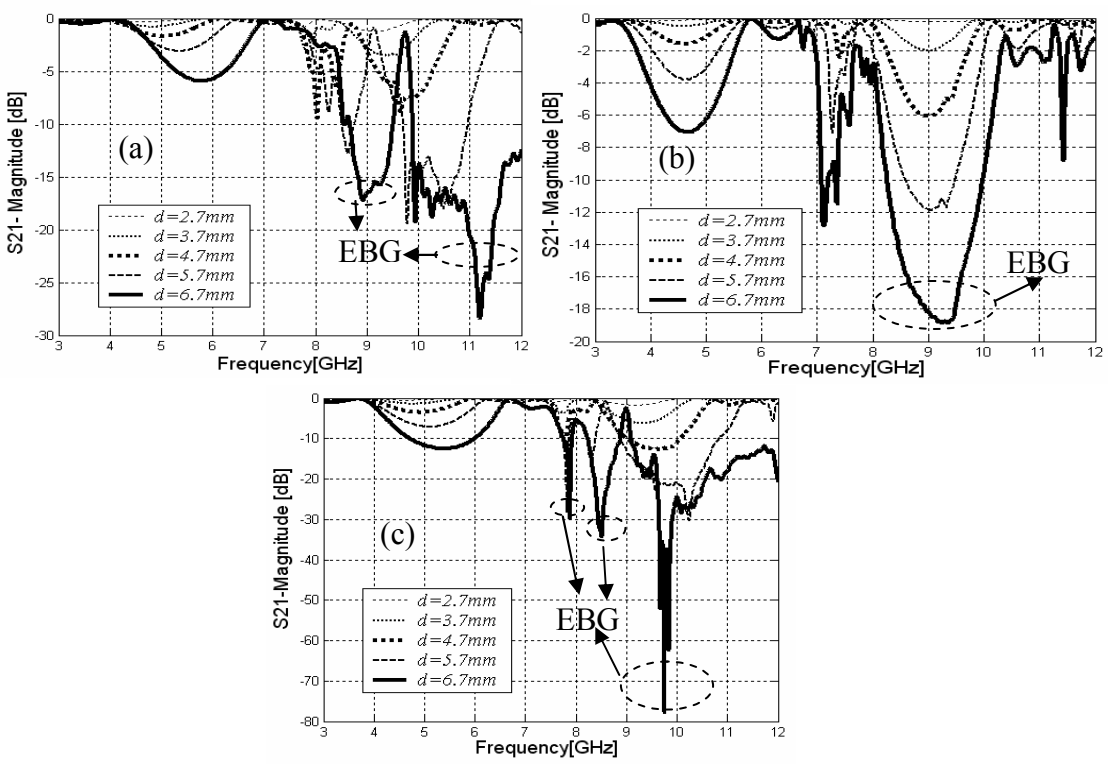


Fig.3: Transmission characteristics plot illustrating a band-gap in a microstrip transmission line: (a) Geometry #1, (b) Geometry #2 and (b) Geometry #3.

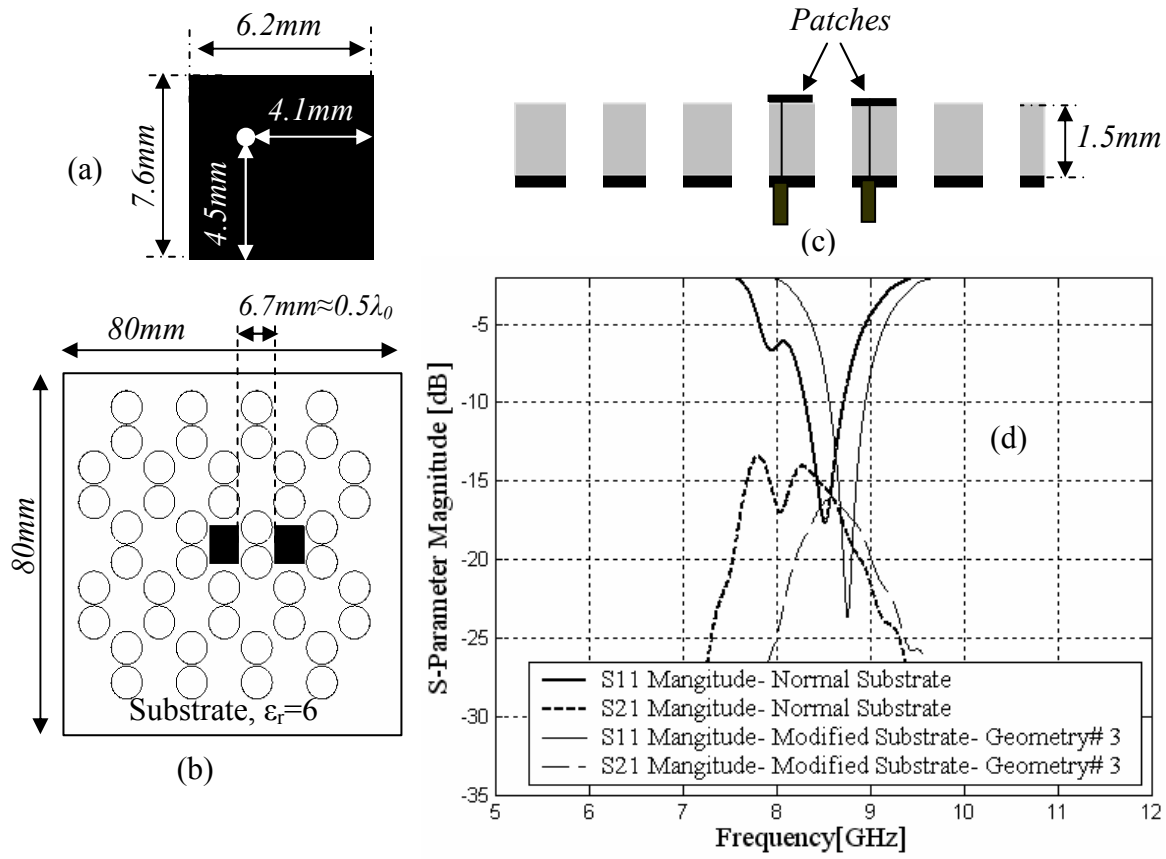


Fig.4: Two element rectangular patch array on a geometry #3, (a) Patch Geometry, (b) Front view, (c) Cross sectional view, (d) S-Parameter.

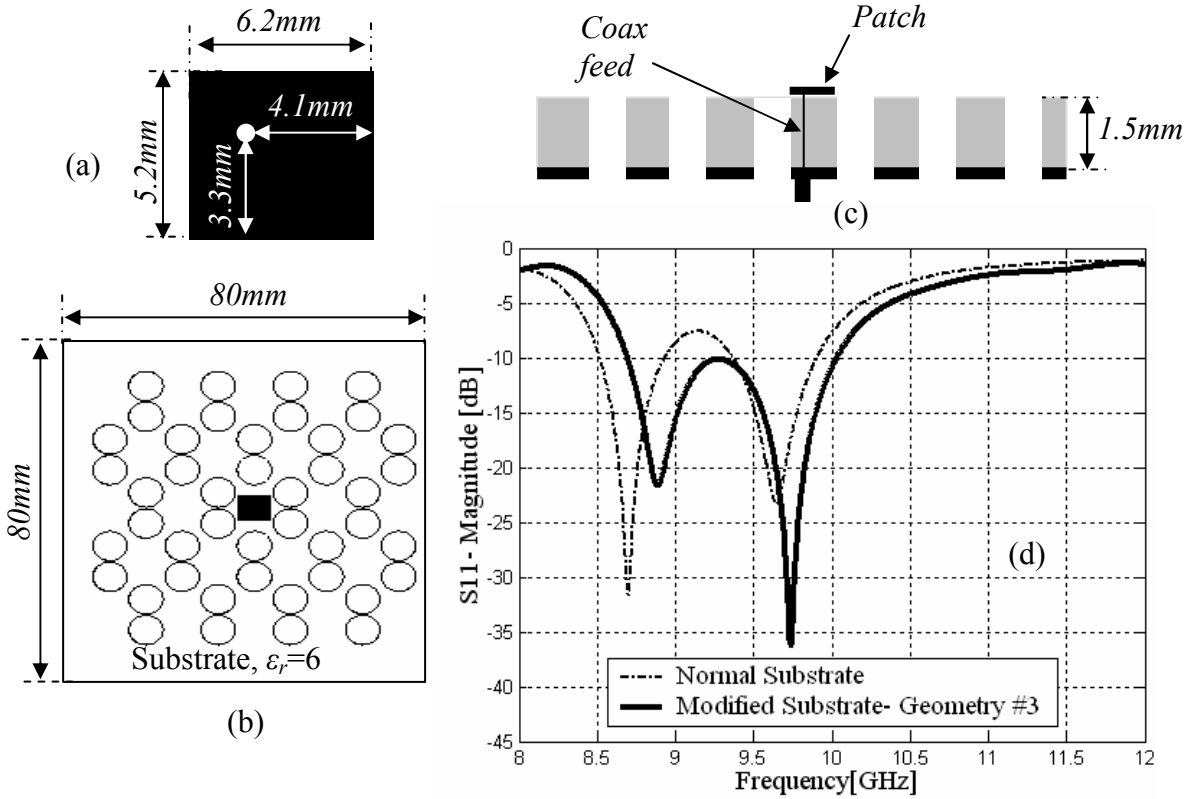


Fig.5: Coaxial probe-fed rectangular patch antenna, (a) Patch Geometry, (b) Front view, (c) Cross sectional view, (d) Return loss.

Palladium sub-wavelength hole arrays for hydrogen sensing

E. Maeda, S. Mikuriya, M. Shuzo, I. Yamada, and J.-J. Delaunay

Department of Mechanical Engineering, School of Engineering, The University of Tokyo, Japan
jean@mech.t.u-tokyo.ac.jp

Abstract— We developed a hydrogen sensor using the extraordinary optical transmission of sub-wavelength hole arrays. The sensor consisted of a palladium thin layer with an array of sub-wavelength holes on a silicon substrate. The main resonance peak of the transmitted spectrum moved toward longer wavelengths when the sensor was exposed to hydrogen. In this study, the dependence of the peak shift with the aspect ratio of the rectangular hole arrays and the thickness of the palladium layer was investigated by simulation. Our simulation results showed that the largest shifts with sharp resonance peaks were obtained for large aspect ratios with a thickness of 100 nm.

1. INTRODUCTION

The extraordinary optical transmission (EOT) phenomenon through the periodic sub-wavelength hole arrays on the metallic layer was discovered by Ebbesen and his co-workers in 1998 [1]. Generally, the zero-order of the transmitted light is diffracted through the sub-wavelength aperture and the magnitude of the far-field transmission is small. In the EOT phenomenon, the light wave passes through the sub-wavelength apertures. It is caused by the coupling between the surface plasmons and the incident wave on the metallic layer. After Ebbesen's discovery, the EOT phenomenon has been applied to fabricating left-handed materials [2] and alternative surface plasmon resonance sensors [3]. In our research, the EOT phenomenon was applied as a new scheme for optical detection of gases.

Sensing H_2 leakage near the lower explosive limit (LEL) is important for preventing H_2 explosion. A leakage of H_2 over 4%, the LEL, in dry air would easily lead to an explosion with an ignition. Potentially, optical H_2 sensors are attractive owing to their safety when they are compared to other electrical measurement sensors, because they do not have connections with electrical components and H_2.

In this study, the EOT phenomenon was applied to an optical H_2 sensing. Pd was used as a material of the sub-wavelength hole arrays since it allows the selective detection of H_2. Through H_2 exposure, a Pd hydride is formed, which is known for its lattice parameter expansion and its dielectric constant variation. Under 2% H_2 concentration, near the LEL, the lattice parameter expands by 3.5% and the dielectric constant decreases by 20%. These effects are expected to affect the transmitted spectra in the EOT phenomenon. We investigated the amplitude of the hole shape and the Pd thickness toward the H_2 sensitivity of the sub-wavelength Pd hole arrays.

2. THEORY OF EXTRAORDINARY OPTICAL TRANSMISSION

The enhanced transmission is due to the coupling of the light wave to the surface plasmons on the metallic layer. The coupling condition is described by the following equation:

$$|\vec{k_{\mathrm{sp}}}| = |\vec{k_{\mathrm{in}}} + i\vec{G_{\mathrm{x}}} + j\vec{G_{\mathrm{y}}}|, \tag{1}$$

where k_{sp} is the surface plasmon wave vector, k_{in} is the incident wave vector, G_{x}, G_{y} are the lattice vectors, and i, j are the integers. Additionally, the propagation length L_{sp} of the surface plasmon is described by the following equation:

$$L_{\mathrm{sp}} = \frac{1}{2\mathrm{Imag}(k_{\mathrm{sp}})}. \tag{2}$$

For the normal incidence on the square arrays, the main resonance peak λ_{sp} is described by the following equation:

$$\lambda_{\mathrm{sp}}(i,j) = \frac{d}{\sqrt{i^2+j^2}}\sqrt{\frac{\epsilon_1\epsilon_2}{\epsilon_1+\epsilon_2}}, \tag{3}$$

where d is the period of the arrays, ϵ_1, ϵ_2 are the dielectric constant of the metal and the dielectric media.

3. HYDROGEN DETECTION SCHEME

Si was used as the substrate for the fabrication, because Si is transparent in the infrared region. For the purpose of coupling the incident wave and the surface plasmons, the propagation length must be large enough to propagate along the whole array. The propagation length of surface plasmons at Pd/Air is long in the infrared wavelength region (Fig. 1).

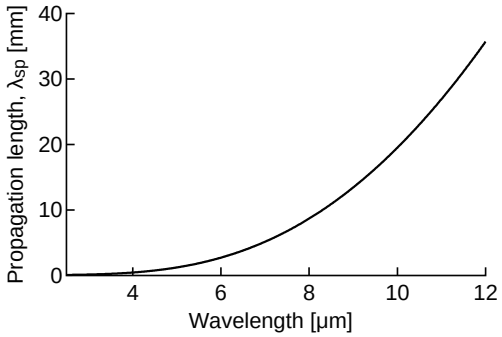


Figure 1: The propagation length L_{sp} of surface plasmon at Pd/Air was calculated by Eq. (2).

First, the square shaped Pd sub-wavelength hole arrays were prepared on Si substrates [4]. The main resonance peak reduced its amplitude by 3.8% when it was exposed to near LEL of (2%). The main reason of the reduction was the formation of Pd hydride which caused the lattice expansion of the Pd layer and the reduction of optical parameters.

Second, the various effects of the Pd hydride toward the transmitted spectrum was investigated [5]. The finite-difference time-domain method was applied to simulate the electromagnetic wave propagation through the metallic Pd hole arrays. It was revealed that the lateral expansion corresponded to a decrease in the hole width and it played a predominant role in the decrease in transmittance.

Finally, we developed an all-optical and room temperature H_2 sensor [6]. The main resonance peak shifts 200 nm toward longer wavelengths when the sensor is exposed to the near LEL of (2%) H_2. The main point of our sensor was the rectangular shaped hole arrays. In 2005, van der Molen and his co-workers found that the main resonance peak moves toward longer wavelengths when the hole aspect ratio is increased [7]. The Pd rectangular shaped holes increase their aspect ratio when exposed to H_2, thus shifting the main resonance peak. We investigated the dependence of the hole aspect ratio, the optical index and the expansion in the Pd sub-wavelength hole arrays on the sensitivity to H_2. The magnitude of the peak shift value was found to have an optimum aspect ratio.

In this study, the dependence of the hole shape and the Pd layer thickness were investigated for detecting H_2 by simulation. The thickness of the metallic layer affects the coupling on the two sides of the metallic layer [8]. The optimum thickness was investigated as well as the aspect ratio.

4. SIMULATION SETUP

The rigorous coupled-wave analysis (RCWA) method was applied to simulate the electromagnetic wave propagation through the periodic sub-wavelength hole arrays. We used DiffractMOD (RSoft Design Group, Ossining, NY, USA) to compute the zero-order transmission spectra. Fig. 2 shows the three-dimensional schematic diagram for the Pd sub-wavelength hole arrays on the Si substrate. A 10-μm-thick Si substrate was used. The thickness of the Pd layer on the Si substrate was changed from 25-nm-to 150-nm. The long side of the rectangular hole was fixed to 800 nm and the short side was changed from 400 nm to 800 nm. The incident wave was polarized along the axis parallel to the short side of the rectangular hole. The zero-order transmission spectra were measured at normal incidence.

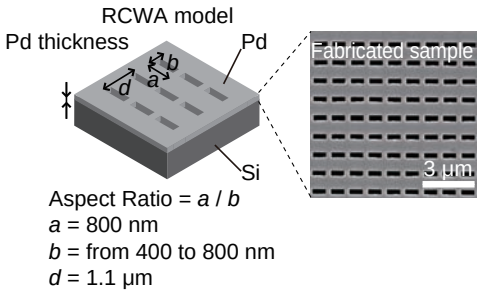


Figure 2: The simulated RCWA model and a scanning electron microscope image of the fabricated sample [6].

5. RESULTS & DISCUSSIONS

First, the representation of the EOT phenomenon using the RCWA method was investigated. The position of $\lambda_{\mathrm{sp}}(1,0)$ and the main resonance peak were in good agreement with the observed positions. Therefore, a correct representation of the effect of the EOT phenomenon was achieved by the RCWA simulation. The simulated and measured spectra in dry air and under 2% H_2 are shown in Fig. 3.

Second, the representation of van der Molen's results using RCWA method was investigated. In dry air, the shift of the main resonance peaks toward longer wavelengths depends on the hole aspect ratio as shown in Fig. 4. Additionally, $\lambda_{\mathrm{sp}}(1,0)$ did not shift with Pd thickness because it depends on the hole period, dielectric constant of Pd and integers.

Finally, we investigated the effect of the Pd layer thickness on the peak shift of the hole arrays. The peak shifts were calculated from simulated zero-order transmission spectra (Fig. 5). Large peak shifts were observed for thin Pd layers. The 25, 50 and 75 nm Pd layers were semi-transparent and the change in their optical index was the dominant effect. Smaller peak shifts were observed for thicker Pd layers in the opaque region. The 100, 125 and 150 nm Pd layers were opaque and the coupling on the two sides of the metallic layer was reduced in strength. The amplitude of the effect of the lattice parameter expansion and the dielectric constant were investigated in Fig. 6. Large peaks shifts toward longer wavelengths were produced by the additive effects of the Pd lateral expansion and the Pd dielectric constant reduction. The vertical expansion of the Pd layer reduced the total shift.

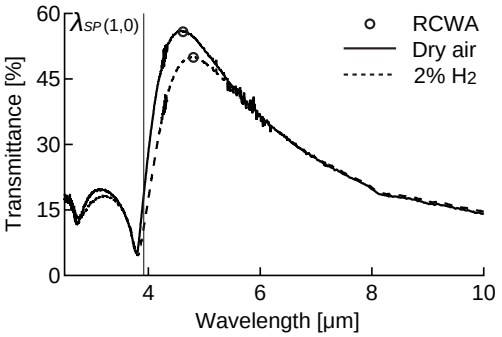


Figure 3: The measured spectra in dry air and 2% H_2, the Pd thickness was 100 nm and the aspect ratio was 1.6 [6]. $\lambda_{\mathrm{sp}}(1,0)$ was calculated by Eq. (3). The main resonance peak position was simulated by the RCWA method.

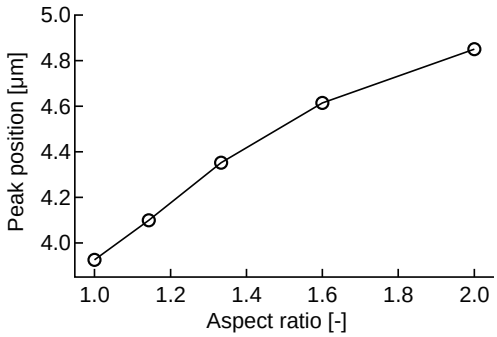


Figure 4: The main resonance peaks were calculated by the RCWA method. The Pd thickness was 100 nm.

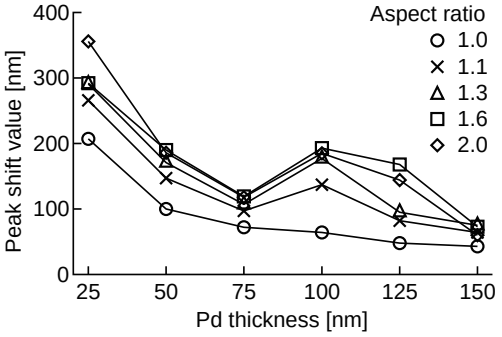


Figure 5: The simulated peak shifts for different Pd thicknesses and different aspect ratios.

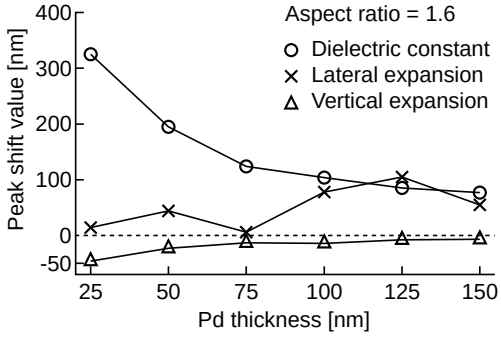


Figure 6: The simulated peak shifts for the separated effects of the change in dielectric constant, the lateral expansion and the vertical expansion.

6. CONCLUSION

In this report, we studied the shift of the main resonance peak of Pd sub-wavelength hole arrays exposed to near LEL H_2. In the EOT phenomenon, the thickness of the metallic layer is one of the parameters that affect the coupling between the two sides of the Pd layer. Our sensor exhibited enhanced peak shift for thin Pd layers. However, for too thin layers, the Pd layers became semi-transparent and the resonance peaks of the hole arrays were too broad to be useful for sensing. The thick opaque Pd layers produced sharp main resonance peaks with smaller shifts than those of the thin semi-transparent Pd layers.

ACKNOWLEDGMENT

E. Maeda was supported through the Global COE Program, "Global Center of Excellence for Mechanical Systems Innovation," by the Ministry of Education, Culture, Sports, Science and Technology.

REFERENCES

1. Ebbesen, T.W., Lesec, H.J., Ghaemi, H.F., Thio, T., and Wolff, P.A.: "Extraordinary optical transmission through sub-wavelength hole arrays," *Nature*, Vol. 391, 667, 1998.
2. Beruete, M., Sorolla, M., and Campillo, I.: "Left-handed extraordinary optical transmission through a photonic crystal of subwavelength hole arrays" *Optics Express*, Vol. 14, 5445, 2006.
3. Williams, S.M., Rodriguez, K.R., Teeters-Kennedy, S., Stafford, A.D., Bishop, S.R., Lincoln, U.K., and Coe J.V.: "Use of the Extraordinary Infrared Transmission of Metallic Subwavelength Arrays To Study the Catalyzed Reaction of Methanol to Formaldehyde on Copper Oxide" *Journal of Physical Chemistry B*, Vol. 108, 11833, 2004.
4. Tusji, R., Endo, K., Shuzo, M., Yamada, I., and Delaunay, J.-J.: "Hydrogen detection with sub-wavelength palladium hole arrays," *Journal of Micro/Nanolithography, MEMS, and MOEMS*, Vol. 8, 021140, 2009.
5. Maeda, E., Endo, K., Mikuriya, S., Shuzo, M., Yamada, I., and Delaunay, J.-J.: "Analysis of hydrogen exposure effects on the transmittance of periodic sub-wavelength palladium hole arrays," in *Proceedings of SPIE*, San Jose, USA, January 2009, 7218C.
6. Maeda, E., Mikuriya, S., Endo, K., Yamada, I., Suda, A., and Delaunay, J.-J.: "Optical hydrogen detection with periodic subwavelength palladium hole arrays," *Applied Physics Letters*, Vol. 95, 133504, 2009.
7. van der Molen, K.L., Klein Koerkamp, K.J., Enoch, S., Segerink, F.B., van Hulst, N.F., and Kuipers, L.: "Role of shape and localized resonances in extraordinary transmission through periodic arrays of subwavelength holes: Experiment and theory," *Physical Review B*, Vol. 72, 045421, 2005.
8. Degiron, A., Lezec, H.J., Barnes, W.L., and Ebbesen, T.W.: "Effects of hole depth on enhanced light transmission through subwavelength hole arrays," *Applied Physics Letters*, Vol. 81, 4327, 2002.

Performance Improvement of Patch-Antenna by Beam Focusing Using Left-Handed Metamaterial Perfect Lens Composed of Complementary Split Ring Resonators

E. K. I. Hamad, and A. A. A. Abdel-Raheem,

Electrical Engineering Dept., Aswan Faculty of Engineering, South Valley University, Aswan 81542, Egypt
e.hamad@ieee.org, adel_amin45@yahoo.com

Abstract— In this paper, the performance of a square microstrip patch antenna is improved using left-handed metamaterial (LHMTM) perfect lens based on complementary split ring resonators (CSRRs). The microstrip patch antenna is fed by a coaxial probe and is integrated with the LHMTM perfect lens, which is placed on the patch. Based on the negative refractive index (NRI) of the LHMTM perfect lens, the radiated electromagnetic beam is focused. As a result, the gain and directivity of the patch antenna as well as the radiation efficiency increase. The optimized radiation properties of the proposed antenna are obtained using a finite-element-method-based 3-D full-wave electromagnetic simulator. A parametric analysis is carried out to design a CSRRs-based LHM perfect lens with NRI in a specific frequency range to be matched with the original patch antenna bandwidth. For validation purpose, a parametric analysis is carried out on an integrated patch antenna with a MTM perfect lens composed of CSRR 2-D periodic structure, which is suspended above the patch through a nylon spacer. The results demonstrate that an enhancement in the gain and directivity by 4 dB, in the radiation efficiency by 11 %, in the return loss by 15 dB, in the bandwidth by 150 % of their original values without MTM lens, while a reduction in the beam area by 26 %.

1. INTRODUCTION

Microstrip patch antennas offer an attractive solution to compact, conformal and low-cost designs of many wireless application systems [1]. It is known that the gain of a single patch antenna is generally low. The gain of patch antennas can be increased by using multiple patches connected to an array or by reducing the surface wave, which can create ripples in the radiation pattern. Several methods have been proposed to reduce the effects of surface waves [2–5]. One approach suggested earlier is the synthesized substrate that lowers the effective dielectric constant of the substrate either under or around the patch [2, 3]. Other approaches are to use parasitic elements [4, 5]. A recent approach is the Left-Handed Metamaterial (LHMTM) layer [6], which is to be located above the patch to congregate the radiated electromagnetic waves from the patch into a point within the MTM layer and radiates them again with a specific beam width based on the value of the Negative Refractive Index (NRI) of the MTM layer. So that, the gain, directivity, and radiation efficiency can be significantly improved [7, 8]. Metamaterials are also called left-handed materials (LHM) in particular, in which the electric field **E**, magnetic field **H**, and the wave vector k form a left-handed system. Since the idea proposed by Victor Veselago in 1968 [9], the availability of such a material is taken up nowadays and extended. The LHM is a combination of split ring resonators (SRRs) and thin wires (TWs). However, metamaterial structure composed of copper grids with square lattice was proposed by Stefan Enoch et al. for directive emission [10]. It was shown that the electromagnetic waves in the media can be gather together in a narrow rectangle area properly. When applied to a monopole antenna, this structure can greatly improve the directivity of the antenna [7].

In this paper, a new design for a patch antenna system is presented, in which a metamaterial structure is introduced as a cover for the antenna to operate as a MTM perfect lens that congregates the electromagnetic waves in a narrow area. The metamaterial structure used is composed of CSRR 2-D periodic structure [11]. The input return loss, radiation pattern, gain, directivity, beam area, and radiation efficiency of such a patch antenna are computed by a 3-D full-wave EM simulator. This paper is organized as follows: First, a theory background for the LHMTM perfect lens is introduced. Then the analysis and design of the patch antenna at different operating frequencies are provided. After that, the proposed square patch antenna that integrated with the LHMTM perfect lens are studied for the validation purpose of the proposed concept of beam focusing using LHMTM perfect lens.

2. THEORY BACKGROUND

Metamaterials perfect lens are firstly proposed by Pendry in 2000 [6], and then it is lately discussed by others [12–15]. The function of the lens is to apply a phase correction to each of the Fourier components so that, at some distance beyond the lens, the fields reassemble to a focus, and an image of the dipole source appears [16]. So, when integrating the LHMTM perfect lens with a patch antenna, beam focusing occurs. As a result, an improvement in the radiation properties of a patch antenna such as gain, directivity, and radiation efficiency would be achieved. The MTM lens operates as follow: The index of refraction (n) is defined as [9]:

$$n = \pm\sqrt{\mu\epsilon} \tag{1}$$

It does not affected by simultaneous change of signs for both permittivity, ϵ and permeability, μ (losses are not taken into account). In left-handed media, the reversed Snell's law is possible, which is given in a more precise form for different media rightness as follow (see Fig. 1):

$$\frac{\sin\alpha}{\sin\beta} = n = \frac{p_2}{p_1}\left|\sqrt{\frac{\epsilon_2\mu_2}{\epsilon_1\mu_1}}\right| \tag{2}$$

Where p_1 and p_2 are the rightness of the first and second media, respectively. While α is the incident angle in the first medium and β is the refracted angle in the second medium. It is obvious from Eq. (2) that the refraction index of two media can be negative if the rightness of the two media are different.

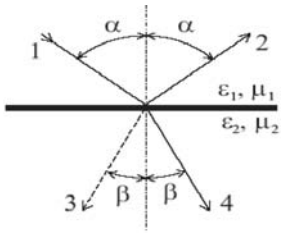


Figure 1: Passage of the ray through the boundary between two media, 1 - incident ray, 2 - reflected ray, 3 - refracted ray, if the second medium is left-handed, 4 - refracted ray in conventional medium.

As it is known, there is no lens can focus objects smaller than the wavelength. However, the perfect lens is in contrast to the conventional lens, the conventional lens is able to focus light only with curved surfaces by virtue of the refractive index contrast. While, the perfect lens will focus the light even when in the form of a parallel-sided slab of material. Such type of lens is depicted in Fig. 2. It is assumed that the refractive index n is -1. In this case the permittivity, ϵ and permeability μ are negative and equal to -1. Through this study, the scattered field from the patch antenna can be focused in a narrow area as illustrated in Figs. 1 and 2, so that a beam focusing occurs. As a result, the radiation properties can be improved .

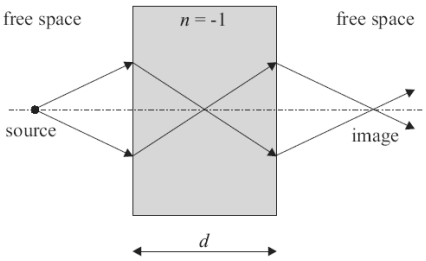


Figure 2: Example of a perfect lens; a negative refractive index medium bends light to a negative angle with the surface normal. It is possible to focus point source to point source again.

3. ANALYSIS AND DESIGN

A square microstrip patch antenna, MTM perfect lens, and patch antenna integrated with the MTM perfect lens are designed and simulated using a 3-D full-wave electromagnetic simulator (HFSS). In

the simulation process, convergence and minimization of numerical errors were obtained by ensuring that the mesh was sufficiently fine. The design procedure is as follow: the patch antenna is designed to operate at an arbitrary chosen frequency. Then, the LHM perfect lens is designed. Finally, the patch antenna is integrated with LHM perfect lens to be simulated and optimized.

3.1. Design of a Square Microstrip Patch Antenna

The microstrip patch antenna that is described here is to perform two tasks. First, is to be integrated later with the LHMTM prefect lens to compose the proposed patch antenna. Secondly, is to be taken as a reference antenna to measure the enhancement percentage in the proposed antenna parameters. The antenna is a square patch antenna with a 15.58×15.58 mm^2 size and is printed on a substrate with a relative permittivity of $\epsilon_r = 3.38$ and a thickness of $h = 0.813$ mm. The patch is fed by a probe with a radius of 0.5 mm. The feed location was optimized to give a good impedance matching. The size of the substrate is 80×80 mm^2. The antenna resonates at 4.75 GHz.

3.2. Design of MTM Perfect Lens

Here a MTM perfect lens unit cell with double negative parameters (DNG) is designed in a frequency range to be matched with the bandwidth of the original patch antenna to achieve an optimal beam focusing when it is integrated with the patch antenna. Using the EM simulator, the effective parameters of a CSRR unit cell have been extracted by using a retrieval method based upon the simulated transmission and reflection coefficients [17], see Figs. 3–b through 3–e. The effective parameters is obtained with a single unit cell using boundary conditions of perfect magnetic walls (PMC) at the back and front (y-direction) and perfect electric walls (PEC) on the left and right sides (x-direction) and wave ports on the top and bottom side planes. The CSRRs are etched on a commercial low loss dielectric substrate (Arlon 250-LX-0193-43-11) with relative dielectric permittivity $\epsilon_r = 2.43$ and height $h = 0.49$ mm, coated with a conductive layer of copper with thickness $t = 35$ μm. The CSRR unit cell is depicted in Fig. 3–a with $r_{ex} = 3.4$ mm and $c = d = 0.4$ mm, which gives a theoretical resonant frequency of 4.75 GHz according to the theories developed in [11], which is matched with the operating frequency of the patch antenna. The transversal periodicity is $a = 8$ mm, which is approximately 1/8 of the free space wave length at resonance, which is used to construct the 2-D MTM periodic structure to employ the MTM perfect lens as will be illustrated in the coming section.

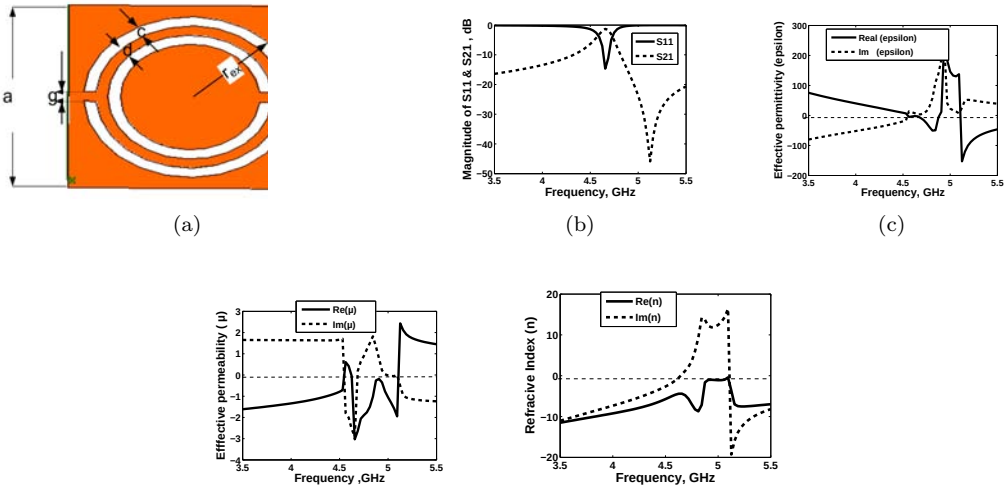
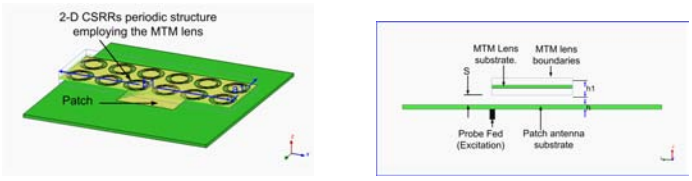


Figure 3: (a) Layout of the CSRR unit cell of $a = 8$ mm, $r_{ex} = 3.4$ mm and $g = c = d = 0.4$ mm, $\epsilon_r = 2.43$ and height $h = 0.49$ mm, (b) S-parameters for a CSRR unit cell, (c) The extracted effective permittivity ϵ, (d) The extracted effective permeability μ, and (e) Effective refractive index (n).

3.3. Integrating the Patch Antenna with the LHM Perfect Lens

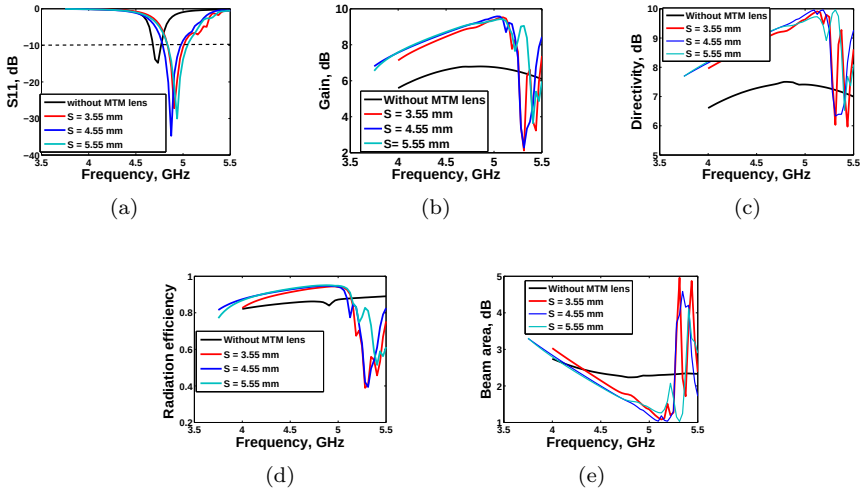
The square microstrip patch antenna designed above here is integrated with the perfect lens to construct a 2-D MTM periodic structure as depicted in Fig. 4. To obtain the optimal radiation

properties; the 2-D MTM periodic structure dimensions (N×M) and the patch-MTM perfect lens separation (S) are justified. The radiation properties are obtained for (2×5) 2-D MTM structure, at different S, as shown in Fig. 5. The results given in Fig. 5 demonstrate that an enhancement by 4 dB in the antenna gain, G and directivity, D. While the radiation efficiency, *Eff.* improved by about 11 % and the return loss, S_{11} by 15 dB. Farther improvement in the antenna bandwidth, BW by 150 % of its original value without MTM lens is observed, also Fig. 6 illustrate the radiation pattern for the co-polarization and cross-polarization. Finally, a reduction in the beam area, BA of 26 % is obtained. The improvement in the BW is due to the band gap caused by the LHMTM structure, since the band gap is much wider than that in the conventional antenna as shown in Fig. 3. The improvement in the radiation efficiency attributables to the reduction in the power accepted by the patch antenna substrate, since there is a part of the fringing fields gathered together toward the direction of the propagation as a result of the beam focusing caused by the MTM lens. However, the impedance matching is obtained by slightly varying the position of the feeder.



(a) (b)

Figure 4: Schematic diagram of the proposed patch antenna, (a) 3-D view and (b) Side view.



(a) (b) (c)

(d) (e)

Figure 5: The radiation properties of the patch antenna with and without MTM perfect lens at different patch-MTM lens separation, at a 2 × 5 MTM periodic structure employing MTM lens (a) Return loss, (b) Gain, (c) Directivity, (d) Radiation efficiency, and (e) Beam area.

4. CONCLUSION

In this paper, the performance of a patch antenna is greatly improved by beam focusing when it is integrated with a 2-D CSRR periodic structure employing a MTM perfect lens. The MTM lens was suspended above the patch antenna through bears, the MTM perfect lens focused the radiated EM waves of the patch antenna in a narrow area. As results, the antenna gain and directivity have been enhanced as well as the return loss, bandwidth, and radiation efficiency. The beam area reduced as well. The optimized radiation properties of the proposed patch antenna have been obtained through the justification of the patch-MTM lens separation and the dimensions of the 2-D MTM periodic structure employing the MTM lens. The results demonstrated that an enhancement in the gain and directivity by 4 dB, in the radiation efficiency by 11 %, in the return loss by 15 dB,



(a) (b)

Figure 6: Radiation patterns for the conventional patch antenna (dashed) and the metamaterial patch antenna (solid). (a) the co-polarization. (b) the cross-polarization.

in the bandwidth by 150 % over their original values without MTM lens, and a reduction in the beam area by 26 %.

REFERENCES

1. Collin, R., *Field Theory of Guided Waves, 2nd Ed.* , New York, IEEE Press, 1991.
2. Gauthier, G. P., Courtay, A., and Rebeiz, G. H., "Microstrip Antennas on Synthesized Low Dielectric-Constant Substrate", *IEEE Trans. Microwave Theory Tech.*, Vol. 45, 1310–1314, Aug. 1997.
3. Colburn, J S., and Rahmat-Sammii, Y., "Patch Antennas on Externally Perforated High Dielectric Constant Substrate", *IEEE Trans. Microwave Theory Tech.*, Vol. 47, 1785–1794, Dec. 1999.
4. Kokotoff, D. M., Waterhouse, R. B., Britcher , C. R., and Aberle, J. T., "Angular Ring Coupled Circular Patch with Enhanced Performance", *Electron Letters.*, Vol. 33, 2000–2001, Nov. 1997.
5. Rojas, R. G., and Lee, W. K., "Surface Wave Control Using Nonperiodic Parasitic Strips in Printed Antennas", *IEE Pros. Microwave Antennas Propag.*, Vol. 148, 25–28, Feb. 2001.
6. Pendry, J. B., "Negative Refraction Makes a Perfect Lens", *Phys. Rev. Lett.*, Vol. 85, No. 18, 3966–3969, Oct. 2000.
7. Fangming , J. B., "A Directive Patch Antenna with a Metamaterial Cover", *APMC2005 Proceedings.*, Vol. 3, Dec. 2005
8. Yahong , L., and Xiaopeng , Z., "Enhanced Patch Antenna Performances Using Dendritic Structure Metamaterials", *Microwave & Optical Tech. Lett.*, Vol. 51, No. 21, 1732–1738, Apr. 2009.
9. Veselago, G., V., "The Electrodynamics of Substances with Simultaneously Negative Values of ϵ and μ", *Soviet Phys. Uspekhi.*, Vol. 10, No. 4, 509-514, Jan.Feb 1968.
10. Enoch, S., Tayeb, G., Sabouroux, P., Guerin, N., Vincent, P., "A Metamaterial for Directive Emission", *Phys. Rev. Lett.*, Vol. 89, No. 21, 213902–1–213902–4, Nov. 2002.
11. Baena, J., D., Bonache, J., Martin, F., Marques, R., Falcone, F.,Lopetegi, T., Laso, M., A., G., Garcia, J.,Gil, I., Flores, M., and Sorolla, M.,"Equivalent Circuit Models for Split Ring Resonators and Complementary Split Ring Resonators Coupled to Planar Transmission Lines", *IEEE Trans. Microwave Theory Tech.*, Vol. 53, 1451–1461, Month 2005.
12. Lagarkov, A., N., and Kissel, V., N., "Near-Perfect Imaging in a Focusing System Based on a Left-Handed-Material Plate", *Physical Review Letters.*, Vol. 92, No. 7, 077401, Feb. 2004.
13. Grbic, A., and Eleftheriades, G., V., "Negative Refraction, Growing Evanescent Waves and Sub-Diffraction Imaging in Loaded Transmission-Line Metamaterials", *IEEE Trans. Microwave Theory & Tech.*, Vol. 51, No. 12, 2297–2305, Dec. 2003.
14. Grbic, A.,and Eleftheriades, G., V.,"Subwavelength Focusing Using a Negative-Refractive-Index Transmission Line Lens", *IEEE Antennas & Wireless Propag. Lett.*, Vol. 2, 186–189, 2003.
15. Alitalo, P., Maslovski, S., and Tretyakov, S., "Design of a Three-Dimensional Isotropic Perfect Lens using LC-Loaded Transmission Lines", *J. Applied Phys.*, Vol. 98, 043106, 2005.
16. Martin, H.,"Application of Metamaterials Perfect Lens", *J. Applied Phys.*, Vol. 70, 016608, July 2004
17. Chen, X., Grzegorczyk, T., M., Wu, B., I., Pacheco, J., Jr., and Kong, J., A., "Robust Method to Retrieve the Constitutive Effective Parameters of Metamaterials", *Physical Review E.*, 2005.

Near-field Subsurface Detection using Metamaterial Inspired Probes

Zhao Ren*[1], Muhammed S. Boybay[1], and Omar M. Ramahi[1]

[1]Department of Electrical and Computer Engineering, University of Waterloo, Canada
z3ren@uwaterloo.ca

Abstract— Recently, it was shown that single negative media can significantly enhance the sensitivity of near-field probes. Inspired by this recent finding, a new near-field probe is proposed for noninvasive subsurface detection. The new probe uses a single split ring resonator (SRR) instead of a periodic arrangement of SRRs for negative material realization. Experimental tests were conducted to detect the presence of cracks on aluminum plates, the presence of small aluminum blocks located behind a layer of ground chicken (lossy medium), and the presence of a small aluminum block submerged in Sodium Chloride solution (lossy medium) with a salinity of 1%. Preliminary results show that the proposed near-field probe enables detection of electrically small targets buried in lossy media.

1. INTRODUCTION

Near-field or Evanescent Microwave Probes (EMPs) are known for their subwavelength resolution and their applications to noninvasive detection and characterization. EMPs have been used on various materials, such as circuit boards [1], semiconductors and biological samples [2, 3]. EMPs also have the ability of sensing subsurface features through poorly conducting or dielectric materials [4]. Due to its nondestructive subsurface sensing ability, EMP is a versatile method for detecting defects buried within materials.

The evanescent fields generated by EMPs are confined to small regions that are much shorter than the wavelength at the operation frequency. Since the spatial frequency of evanescent waves are higher than propagating waves, they can couple to smaller material features compared to the propagating waves. This phenomenon enables high sensitivity and resolution for detection of features much smaller than the Abbé's diffraction limit [1, 2, 3, 4].

The microwave response of a material is a function of local permittivity, conductivity, permeability and geometry. Electrical properties of materials depend on the content, moisture level, carrier concentration etc. [3]. Therefore the microwave response of materials has valuable information about the shape and composition of sample under test. The impedance of an EMP is a function of the evanescent field generated around the tip of the EMP. Since the evanescent fields decay exponentially from the probe tip, these fields are confined to a small volume around the tip. As the sample under test enters the near field region, evanescent fields are perturbed, resulting in a change in the impedance of the probe. If the material has a defect inside, the local microwave properties of the material is different than microwave properties of the regions without any defect. Therefore, any defect or any change in the composition is reflected to a change in the probe impedance.

Waveguide probes, such as open-ended, tapered, slab-loaded or dielectric waveguides, and coaxial line probes, such as open-ended or tapered coaxial lines, have been used for near-field subsurface detection [5, 6]. These types of probes concentrate less evanescent field in the close proximity of the opening. In addition, the waveguide probes are limited by a cutoff frequency therefore are not suitable for low frequency operations. To achieve resolutions in the order of millimeters, an operation frequency at the decades of gigahertz is needed. As a result of the high operation frequency, the penetration depth is restrained to a few millimeters for subsurface detection. Other types of EMPs used in near-field imaging are coaxial line resonator with aperture [7], the center conductor of coaxial line [8, 9], rectangular waveguide with end-plane aperture [10], and microstrip resonators utilizing wire tips or loops [1]. These types of probes provide ultra-high resolution, and are applied to a wide range of materials because of the high concentration of the evanescent field around the tip of EMP. However, they often need sophisticated equipment or labor-intensive sample preparation [11]. For extremely sharp probe tips, applications are only limited to measurements in the laboratory [6].

Recent developments in the metamaterials introduce new methods for designing EMPs. By using the evanescent field amplification property of negative materials, single negative (SNG) superlenses can be used to improve the sensitivity and range of the evanescent field probes [12]. The primary reason for the enhancement in the sensitivity is altering the electric field and magnetic field energies stored in the close proximity of the probe. The numerical and experimental demonstration of the theory was presented in Ref. [12] where the SNG media was realized by using an array of Split Ring Resonators (SRRs). In this work, instead of using an array of SRRs, a new probe composed of a traditional electrically-small loop and a single SRR is used. Compared to the method used in Ref. [12], the new probe can confine evanescent fields to a smaller volume, is more compact and does not need negative medium fabrication.

2. SINGLE SRR PROBE

In the probe design, a simple rectangular loop is used for the excitation of the SRR. The size of the loop is 20 mm × 20 mm and presented in Fig. 1(a). The loop generates an H field which induces a current on the SRR. The loop with SRR placed at the center is shown in Fig. 1(b). The SRR is made of rectangular loops with a size of 10 mm × 10 mm and with a trace width of 1 mm. The size of the SRR corresponds to 1/25 of the wavelength at the resonance frequency. The substrate is Rogers Duroid 4350 with a dielectric constant of 3.48 and a substrate thickness of 0.762 mm. The size of the substrate is 16 mm×16 mm.

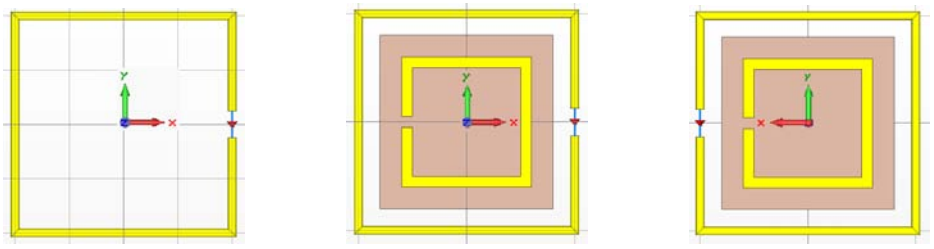


Figure 1: The structure of the probe. (a) Rectangular loop (b) Front view of rectangular loop with SRR, the loop is 0.432 mm away from the center of SRR. (c) Back view of rectangular loop with SRR

In Ref [13], by applying Fourier-transform to the H-field distribution at $z = 1$ mm and by normalizing to free space wavenumber, it was shown that the evanescent field strength is significantly enhanced with the insertion of the SRR. Therefore, more microwave energy is concentrated in the near-field region, which is crucial for an EMP with high sensitivity. More results and detailed explanation can be found in Ref. [13].

3. EXPERIMENT RESULTS

To study the sensing capability of the new probe, three test structures were fabricated. Experiments for detecting cracks on aluminum plates, detecting metallic inclusions in ground chicken and metallic inclusions in saline water were conducted. The sample surface is scanned by the probe while measuring the phase of the reflection coefficient (S_{11}) at a fixed operating frequency. Cracks or inclusions are detected by the change in the reflection phase. The experimental configuration is shown in Fig. 2.

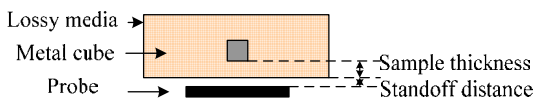


Figure 2: Schematic illustration of experimental setups. The probe is placed underneath, and the metal defect is buried in the test sample.

Fig. 3(a) shows the scanning results of a 5 mm ×15 mm × 15 mm crack on a 24.5 mm × 300 mm × 300 mm aluminum plate at an operation frequency of 1.24 GHz. The aluminum plate is covered by a 6.35 mm acrylic layer. A maximum phase change of 12.5° is achieved at the center location of the crack.

Next, the detection performance of the probe for metallic inclusion buried in lossy media is studied. Fig. 3(b) demonstrates that a phase change of 15.5° in S_{11} can be achieved for a 6.24 mm aluminum cube placed under 2 mm thick ground chicken at an operation frequency of 1.16 GHz. Between the ground chicken surface and the probe, there is a 1 mm air layer and a 1 mm acrylic layer. In addition, saline water is used as a different lossy medium for detection measurements. A phase change of 6.5° in S_{11} is obtained for a 3 mm aluminum cube immersed 1 mm under saline water (approximately 1% salinity) at an operation frequency of 1.23 GHz (see Fig. 3(c)). The probe is separated from the saline water surface by a 1 mm air layer and a 6.35 mm acrylic layer.

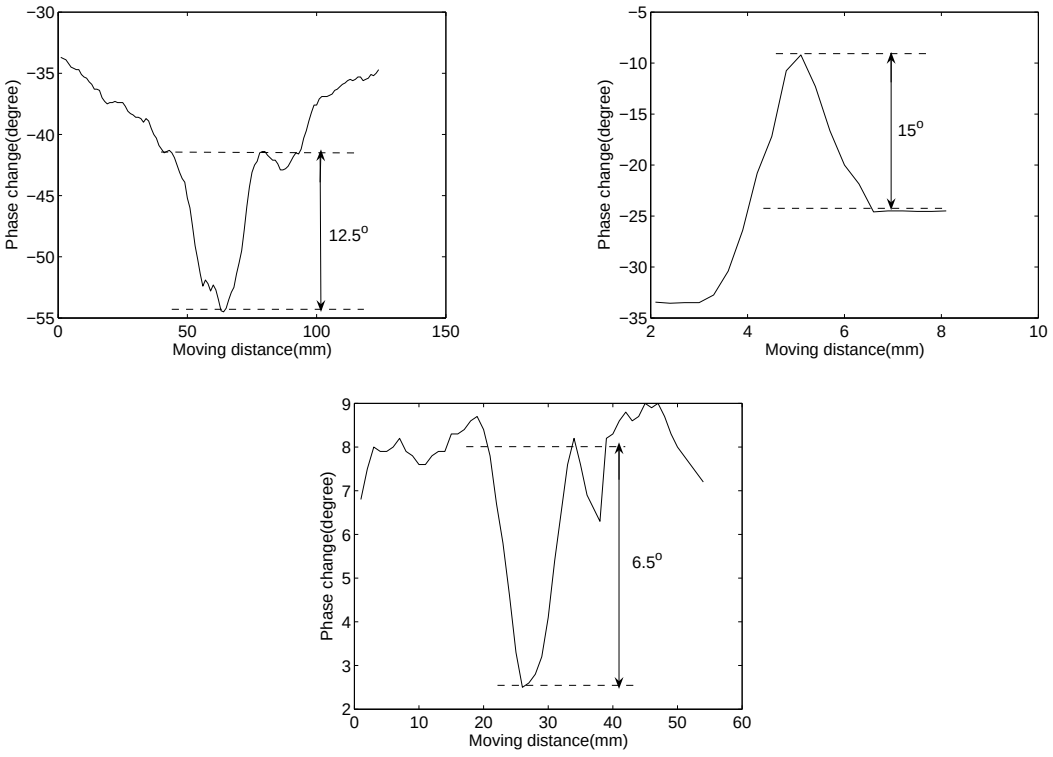


Figure 3: Experimental results (a) A crack on an aluminum plate. (b) An aluminum inclusion buried in ground chicken. (c) An aluminum inclusion merged in saline water.

The relative permittivity of ground chicken is a function of its moisture, operation temperature, and the operation frequency. The relative permittivity at around 1.2 GHz is expected to be 58-18j [14]. The relative permittivity of the saline water is determined by its salinity, operation temperature etc.. In the experiments presented above, the relative permittivity of the saline water is determined by using the theoretical model of saline water presented in Ref. [15] and is equal to 77-25j. Although loss tangents of ground chicken and saline water are high, the new probe successfully senses the inclusions buried in these media. On the other hand, the probe without single SRR cannot detect the inclusions. These results conclude that the insertion of SRR enhances the evanescent field in the close proximity of the probe. As a result, when the new probe is used, a perturbation in the near field region has a more explicit effect on the reflection coefficient and the resonance frequency compared to the probe without SRR.

4. CONCLUSION

In this work, a new structure for EMP design is presented. The probe is a single SRR excited by a simple rectangular loop, which has advantages of inexpensive and easy fabrication. Numerical and experimental results show that the presence of the single SRR enhances the evanescent field concentration in the close proximity of the probe. Therefore the sensitivity of the probe is improved significantly. The experiments in different media show that the new probe can sense the defects buried in media with high electromagnetic loss.

ACKNOWLEDGMENT

This work was supported by Research in Motion and the National Science and Engineering Research Council of Canada under the NSERC/RIM Industrial Research Associate Chair Program.

REFERENCES

1. Tabib-Azar, M., N. S. Shoemaker, and S. Harris, "Non-destructive characterization of materials by evanescent microwaves," *Meas. Sci. Technol.*, Vol. 4, 583–590, 1993.
2. Tabib-Azar, M., J. L. Katz and S. R. LeClair, "Evanescent Microwaves: A Novel Super-Resolution Noncontact Nondestructive Imaging Technique for Biological Applications," *IEEE. Trans. Instrum. Meas*, Vol. 48, No. 6, 1111–1116, 1999.
3. Tabib-Azar, M., P. S. Pathak and G. Ponchak and S. R. LeClair, "Nondestructive superresolution imaging of defects and nonuniformities in metals, semiconductors, dielectrics, composites, and plants using evanescent microwaves," *Rev. Sci. Instrum.*, Vol. 70, No. 6, 2783–2792, 1999.
4. Fitzgerald, W. C., M. N. Davis, J. L. Blackshire, J. F. Maguire and D. B. Mast, "Evanescent Microwave Sensor Scanning for Detection of Sub-Coating Corrosion," *J. Corr. Sci. Eng.*, Vol. 3, Paper No. 15, 2783–2792, 2001.
5. Ghasr, M. T., S. Kharkovsky, R. Zoughi and R. Austin, "Comparison of Near-Field Millimeter-Wave Probes for Detecting Corrosion Precursor Pitting Under Paint," *IEEE. Trans. Instrum. Meas.*, Vol. 54, No. 4, 1497–1504, 2005.
6. Kawata, S., "Near-Field Optics and Surface Plasmon Polaritons," in *Near-Field Optics and Surface Plasmon Polaritons*, S. Kawata ed., Springer-Verlag, Berlin, 2001, 15-27.
7. Wei, T., X. Xiang and P.G. Shultz, "Scanning Tip Microwave Near-Field Microscope," *Appl. Phys. Lett.*, Vol. 68, No. 24, 3506–3508, 1996.
8. Vlahacos, C. P., R. C. Black, S. M. Anlage, A. Amar and F. C. Wellstood, "Near- field scanning microwave microscope with 100 mm resolution," *Appl. Phys. Lett.*, Vol. 69, No. 21, 3272–3274, 1996.
9. Feenstra, B. J., C. P. Vlahacos, A.S. Thanawalla, D.E. Steinhauer, S. K. Dutta and S. M. Anlage, "Near- field scanning microwave microscopy: measuring local microwave properties and electric field distributions," in *IEEE MTT-S Int. Microwave Symp. Dig.*, Baltimore, MD, June 1998, 965-968.
10. Lann, A. F., M. Golosovsky, D. Davidov and A. Frankel, "Mapping the thickness of conducting layers by a mm-wave near-field microscope," in *IEEE MTT-S Int. Microwave Symp. Dig.*, Baltimore, MD, June 1998, 1337-1340.
11. Lee, H. J. and J. G. Yook, "Biosensing using split-ring resonators at microwave regime," *Appl. Phys. Lett.*, Vol. 92, No. 254103, 1–3, 2008.
12. Boybay, M. S. and O. M. Ramahi, "Experimental Verification of Sensitivity Improvement in Near Field Probes using Single Negative Metamaterials," in *IEEE MTT-S Int. Microwave Symp. Dig.*, Boston, MA, June 2009, 1677-1608.
13. Ren, Z., M. S. Boybay and O. M. Ramahi, "Near-field Subsurface detection in lossy media using Single Split Resonator Probe," in *IEEE MTT-s IMWS.*, Cavtat, Croatia, September 2009, 1-3.
14. Kent, M., R. Knöchel, F. Daschner and U. K. Berger, "Composition of foods using microwave dielectric spectra," *Eur. Food Res. Technol.*, No. 201, 359–366, 2001.
15. Klein, L. A., C. T. Swift, "An improved model for the dielectric constant of sea water at microwave frequencies," *IEEE. Trans. Ant. Prop*, Vol. AP-25, No. 1, 104–111, 1977.

Manipulation of near field by means of arrays of wires

P.A. Belov[1,3], **G. Palikaras**[1], **Y. Zhao**[1], **R. Dubrovka** [1], **and C.R. Simovski**[2,3]

[1]Queen Mary University of London, London, UK
[2]Helsinki University of Technology, Espoo, Finland
[3]St. Petersburg State University of Information Technologies, Mechanics and Optics, Russia
pavel.belov@elec.qmul.ac.uk

Abstract— Tapered arrays of metallic wires enable magnification, demagnification and transmission to distances of several wavelengths of near-field distributions with subwavelength resolution. Our experiments demonstrate these capabilities to manipulate the electromagnetic waves at the subwavelength scale in the microwave frequency range.

1. INTRODUCTION

A possibility to transfer electromagnetic field distribution with subwavelength resolution using the canalization regime was proposed in [1]. Later, two experiments were carried out to demonstrate the canalization of TE-polarized (transverse electric field with respect to the slab interface) [2] and TM-polarized (transverse magnetic field) waves [3] at microwave frequencies. The slab used in the former experiment was based on capacitively loaded wires aligned parallel to the slab interfaces, whereas in the latter experiment unloaded wires aligned perpendicular to the slab interfaces were used. The canalization slab considered in [3] utilizes so called wire-medium TEM-modes (transverse electromagnetic modes) [4] to transport the details of the source distribution across the slab. The limitations of subwavelength imaging using such slabs were analytically studied in [5], and experimental results aimed to verify the analytical findings are reported in [6].

Recently, motivated mainly by the limitations in the optical microscopy, there has been a growing interest in structures that are able to *magnify* subwavelength field distributions in the visible range [7-10]. This means that the details of the source distribution are retained while transferring the distribution over a certain distance, and at the same time the distribution is linearly magnified or enlarged. The capability of tapered arrays of wires to transmit, magnify and demagnify images with subwavelength details was demonstrated in [11]. The proposed magnifying slab utilizes the canalization phenomenon, thus, it is capable of magnifying distributions comprising any TM-polarized incident wave (propagating or evanescent) with any transverse component of the wave vector [1].

However, the device proposed in [11] has spherical input and output interfaces which is not convenient for near-field imaging applications. In the paper we show that it is possible to design a similar device but with planar interfaces. In contrast to spherical geometry the device contains wires with slightly different length. This limits imaging performance of the structure producing distortion of the image. The distortion is negligible provided that the maximum difference in between of the lengths of the wires is small, but if the difference is significant then the image appears distorted. This problem can be solved using a dielectric block embedded into the array providing phase compensation operation. Basically, this allows us to make electrical length of all wires the same whereas their physical lengths remain different. Our conclusions are confirmed by extensive numerical simulations using CST Microwave Studio and experiment.

The magnifying lenses are expected to find immediate application in near-field microscopy as near-field to far-field transformers since they allow mapping field distributions with subwavelength details into images with details larger than the wavelength, which can be processed using conventional diffraction-limited imaging techniques. The demagnifying lenses allow creating complex near-field distributions on demand from their enlarged copies created in the far-field. On this route, it may be possible to create extremely compact near-field spots. The tapered wire medium lenses are especially attractive for application in the terahertz range [12]. In the microwave range the tapered wire medium endoscopes can be readily applied for the improvement of magnetic resonance imaging (MRI) systems and mechanical near-field microwave scanners.

2. MAGNIFICATION OF MICROWAVE NEAR-FIELD IMAGES WITH SUBWAVELENGTH RESOLUTION

A photo of the manufactured wire medium lens is depicted in Fig. 1. The lens consists of metallic (copper) wires whose separation is radially enlarged. The wire endings corresponding to the source plane (input interface of the slab) form a planar square (100x100mm square) sector and the wire endings corresponding to the canalized field (image plane - the output interface of the slab) form a corresponding planar sector which is 3 times bigger. The slab is assembled as an array of 21x21 wires, with the lattice period being $a = 5$mm at the input interface. When the operational frequency (for a fixed slab thickness) is tuned to the Fabry-Perot resonance (corresponding to the slab thickness), the source field distortion due to reflections from the input interface is minimized, and the pattern details are transferred across the slab with the help of the wire-medium TEM modes. Note that in theory, the Fabry-Perot resonance condition holds for any (including complex) incidence angle [1]. When the Fabry-Perot resonance condition is met, there is no need to maintain a uniform transmission line characteristic impedance (e.g., by altering the radius of wires), and this would ease significantly a practical implementation of the slab.

The source is a printed copper loop in the shape of a crown, and it is fed by a coaxial cable (50 Ohms). The distance between the planar crown-source and the planar wire end at the input interface of the slab is 3 mm. The source field distribution is scanned over a planar surface that covers the slab input interface, and is located at a distance 2 mm behind the crown-source plane. The canalized field distribution is scanned over a planar surface that covers the slab output interface, and is located at a 10 mm distance behind the output interface. The two scanned regions are in the following referred to as the "source plane" and "image plane," respectively, and they are schematically depicted in Fig. 2.

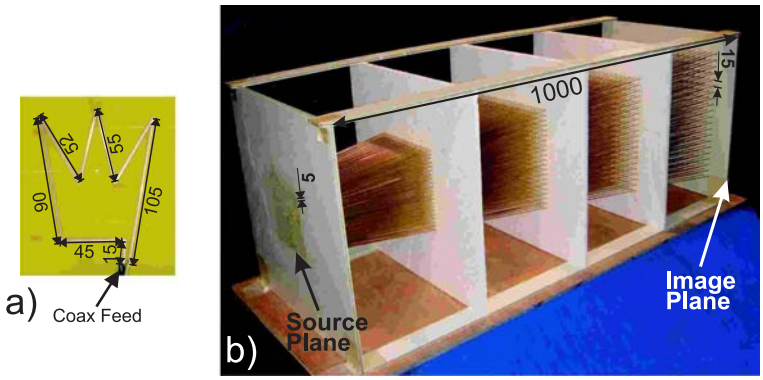


Figure 1: Setup for magnification experiment. a) The crown-shaped near-field source. b) The tapered array of wires. The source and image planes are marked by arrows. All dimensions are in mm.

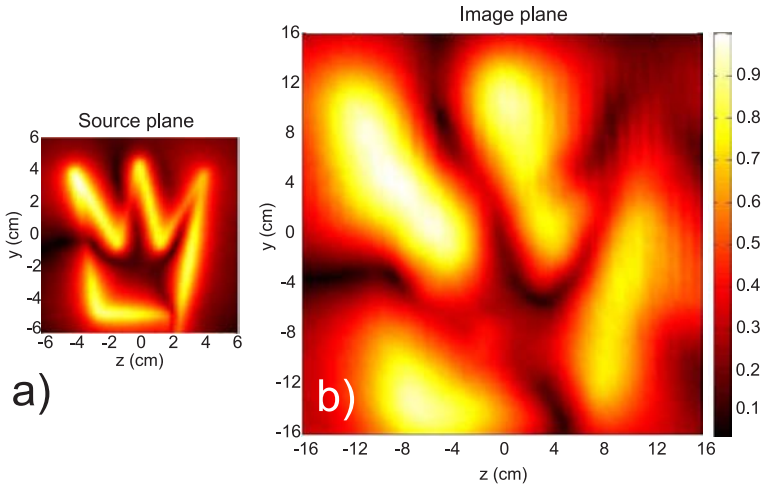


Figure 2: Near-field measurement results of magnification by the tapered array of wires (see Fig. 1). Distributions of electric field amplitude in a) source and b) image planes. The frequency of operation is 1047 MHz

We have performed a series of measurements at several frequencies in the vicinity of 1050 MHz to identify the frequency that corresponds to the Fabry-Perot resonance (the electrical thickness of the slab in this frequency range is roughly 3.5 wavelengths). The results indicate that the realized operational frequency corresponds approximately to 1047 MHz, and at this frequency, the electrical length of the wires is about 3.49. A small deviation from the theoretical Fabry-Perot condition is most likely caused by the radially enlarging characteristic dimension of the slab. At the operational frequency, the source distribution is not affected by reflections, and the details of the distribution are canalized and simultaneously magnified across the slab. The crown shape (radial electric field component) is satisfactorily reproduced at the image plane, and the characteristic size of the pattern is magnified by a factor of 3. Additional experimental results indicate that when the canalized field distribution is scanned very close to the output interface, the radiation of the field from the wire endings is clearly visible. However, when the field is scanned at a distance corresponding to the half of the lattice period at the output interface, this interference vanishes. Measurements performed at frequencies deviating from the predicted Fabry-Perot resonance indicate the following: As the frequency is tuned below the predicted resonance, strong interference is observed upon a very small frequency shift. Such interference is attributed to strong excitation of surface waves [5, 6].

3. COMPENSATION OF DISTORTIONS DUE TO DIFFERENT LENGTHS OF WIRES

The larger is difference between lengths of different wires composing the imaging device the higher distortion the image will experience. This effect is caused by the fact that implementation of the canalization regime requires to have length of all wired to be equal to an integer number of half-wavelengths. The deviation of the length of a particular wire from an optimal value leads to detuning from Fabry-Perot resonance and as result to degradation of imaging performance. Here we speak about actual physical length of the wires since the structure is located in free space. However, the Fabry-Perot resonance requires equality of electrical lengths of the wires. It is possible to keep the physical lengths of the wires to be different from each other but have the electrical lengths equal. For this purpose one may embed a dielectric block (see Fig. 3) into the array.

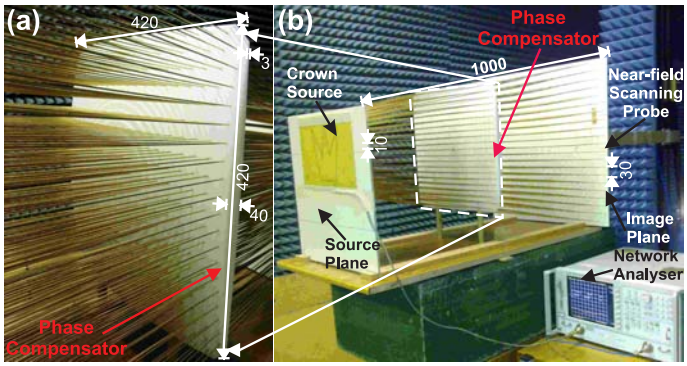


Figure 3: The tapered array of wires with embedded dielectric phase compensator. All dimensions are in mm. The phase concentrator is made of acetal. The largest thickness of compensator (in the center) is 4cm.

The thickness of the block can be different in vicinity of every wire and can be tuned to ensure equal electrical lengths of the wires. For experiment we have chosen a tapered array of wires with 2 times larger periods then in our previous experiment 1. Our numerical simulations revealed that the difference of lengths of wires in this case is so large that no satisfactory subwavelength imaging is possible if the wires are just placed in the free space. We decided to use a dielectric phase compensator (see Fig. 3) in order to eliminate the problem. One of the interfaces of the dielectric phase compensator is flat. The other one was specially cut to ensure uniform electrical length of the wires. The material of the compensator is acetal.

The results of our subwavelength imaging experiments with the tapered array of wires improved with the help of the phase compensator are presented in Fig. 4. In contrast to the case without the phase compensator, the measured setup demonstrated good imaging performance at 465 MHz. At this frequency the wire length is equal to approximately 1.53 wavelength that corresponds to 3rd Fabry-Perot resonance.

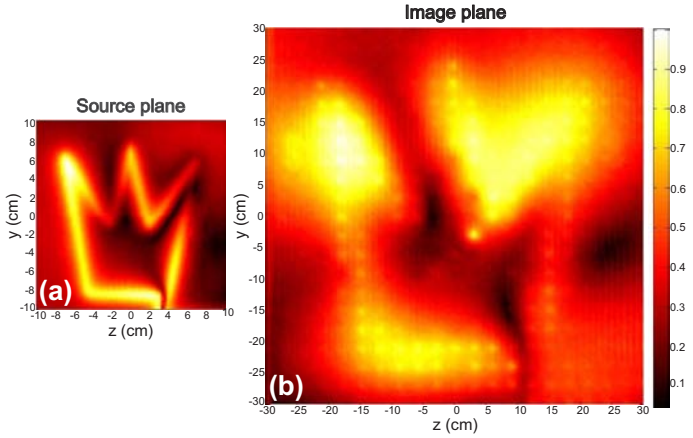


Figure 4: Near-field measurement results of magnification by the tapered array of wires with dielectric phase compensator (see Fig. 3). The near-field amplitude distribution in a) source and b) image planes. The frequency of operation is 465 MHz

4. DEMAGNIFICATION OF MICROWAVE NEAR-FIELD IMAGES WITH SUBWAVELENGTH RESOLUTION

The most interesting application of tapered arrays of wires is magnification of images with subwavelength resolution. This way one can enlarge details which are smaller than wavelength up to sizes which enable their detection using conventional diffraction-limited imaging system. However, the inverse operation is also possible. The tapered arrays are capable of demagnifying electromagnetic field distributions. This enables to obtain very tiny subwavelength distributions with any particular shape required for applications.

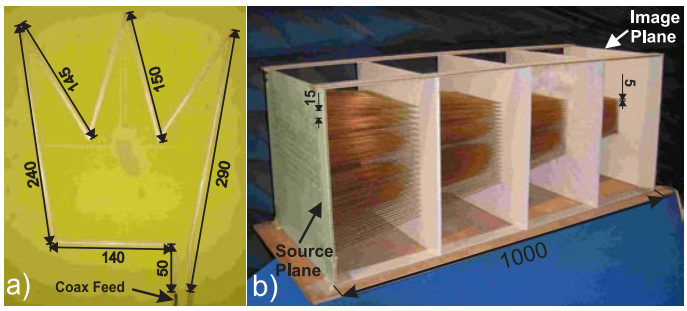


Figure 5: Tapered array of wires used for demagnification experiment. All dimensions are in mm.

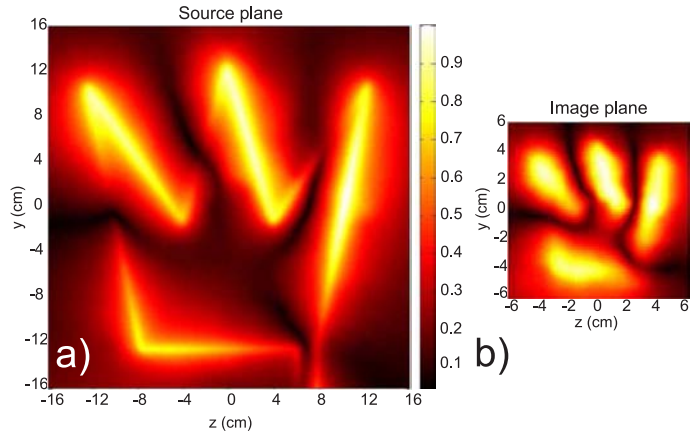


Figure 6: Near-field measurement results of demagnification by the tapered array of wires (see Fig. 5). The Frequency of operation is 455 MHz

In order to demonstrate such a capability of tapered arrays of wires, we rotated the structure used in the magnification setup (Fig. 1) and interchanged source and image planes, see Fig. 5 for details. We used a source in the form of a crown-shaped loop antenna which is approximately 3 times larger than one used in the magnification experiment. The source was placed in front of the larger interface of the slab and an excellent demagnified distribution has been created at the opposite interface. The results of the near-field scan are presented in Fig. 6. The distribution in the image plane reproduces all details of the source and appears to be three times smaller in size.

5. CONCLUSION

We have experimentally demonstrated the possibility of using dense arrays of metallic wires to magnify and transmit images with a deeply sub-wavelength resolution to significant distances in terms of the wavelength at microwave frequencies. In particular, the transmission of an image with a $\lambda/15$ resolution to an electrical distance that is as large as 3λ was experimentally shown. The resolution of the proposed imaging systems is ultimately determined by the granularity of the artificial material, which can be made as small as required by a particular application. We anticipate that such near-field lenses may find applications in near-field microscopy and in medical imaging, starting from MRI systems that operate at low microwave frequencies and completing with a new generation of terahertz and infrared imaging devices. It is important to note that apart from the magnification effect, the proposed slab can be utilized in the opposite way. Electrically large source distributions can be "concentrated" by placing the source at the opposite slab interface. In this case, the source pattern is also canalized through the slab, but the characteristic dimensions of the pattern are scaled down resulting in the demagnification of an image.

ACKNOWLEDGMENT

Pavel Belov acknowledges financial support by EPSRC Advanced Research Fellowship EP/E053025/1.

REFERENCES

1. P. A. Belov, C. R. Simovski, and P. Ikonen, "Canalization of sub-wavelength images by electromagnetic crystals," *Phys. Rev. B.*, vol. 71, p. 193105, 2005.
2. P. Ikonen, P. A. Belov, C. R. Simovski, and S. I. Maslovski, "Experimental demonstration of subwavelength field channeling at microwave frequencies using a capacitively loaded wire medium," *Phys. Rev. B*, vol. 73, p. 073102, 2006.
3. P. A. Belov, Y. Hao, and S. Sudhakaran, "Subwavelength microwave imaging using an array of parallel conducting wires as a lens," *Phys. Rev. B*, vol. 73, p. 033108, 2006.
4. P. Belov, R. Marques, S. Maslovski, I. Nefedov, M. Silverinha, C. Simovski, and S. Tretyakov, "Strong spatial dispersion in wire media in the very large wavelength limit," *Phys. Rev. B*, vol. 67, p. 113103, 2003.
5. P. A. Belov and M. G. Silveirinha, "Resolution of sub-wavelength lenses formed by a wire medium," *Phys. Rev. E*, vol. 73, p. 056607, 2006.
6. P. Belov, Y. Zhao, S. Sudhakaran, A. Alomainy, and Y. Hao, "Experimental study of the sub-wavelength imaging by a wire medium slab," *Appl. Phys. Lett.*, vol. 89, p. 262109, 2006.
7. A. Salandrino and N. Engheta, "Far-field subdiffraction optical microscopy using metamaterial crystals: Theory and simulations," *Phys. Rev. B*, vol. 74, p. 075103, 2006.
8. Z. Jacob, L. V. Alekseyev, and E. Narimanov, "Optical hyperlens: Far-field imaging beyond the diffraction limit," *Optics Express*, vol. 14, pp. 8247–8256, 2006.
9. Z. Liu, H. Lee, Y. Xiong, C. Sun, and X. Zhang, "Far-field optical hyperlens magnifying sub-diffraction-limited objects," *Science*, vol. 315, p. 1686, 2007.
10. I. I. Smolyaninov, Y.-J. Hung, and C. C. Davis, "Magnifying superlens in the visible frequency range," *Science*, vol. 315, pp. 1699–1701, 2007.
11. P. Ikonen, C. Simovski, S. Tretyakov, P. Belov, and Y. Hao, "Magnification of subwavelength field distributions at microwave frequencies using a wire medium slab operating in the canalization regime," *Appl. Phys. Lett.*, vol. 91, p. 104102, 2007.
12. G. Shvets, S. Trendafilov, J. B. Pendry, and A. Sarychev, "Guiding, focusing, and sensing on the subwavelength scale using metallic wire arrays," *Phys. Rev. Lett.*, vol. 99, p. 053903, 2007.

All-dielectric Metamaterials for Patch Antenna Gain Enhancement

R.Alaee[1], and K.Moussakhani[2]
[1]Dept. of Electrical Engineering, Amirkabir University of Technology, Iran
[2]Dept. of Electrical and Computer Engineering, McMaster University, Canada
rasoul.alaee@gmail.com

Abstract- In this paper, all-dielectric sphere metamaterials as a flat lens in front of circular patch antenna have purposed. We have investigated one and two layers dielectric lenses that each layer consists of dielectric spheres with different dimension. The purposed lenses enhanced the gain of circular patch antenna around 7 and 11.4 dB for one-layer and two-layer lenses respectively.

1. INTRODUCTION

Patch antennas have been widely used in modern wireless communication systems due to their attractive properties such as low cost, light weight, low profile, and compatibility with integrated circuits. Low gain, however, is one of the drawbacks of patch antennas. In the past decades, vast efforts have been devoted towards achieving high gain patch antennas.

Metamaterials with unusual electromagnetic properties have received a growing amount of interest in the past few years. These artificial materials are composed of periodic structures and have unusual permittivity and permeability, which are finding numerous microwave and optical applications. One such application is the use of this novel material for gain enhancement of antennas. Inspiring by work of Enoch et al. [1], different works have been done on directive emission of antennas by using different metamaterials structures, and several lenses have been designed. Most of previous works on lens design have used metallic elements. The major drawbacks of metallic structures are their conduction loss and fabrication difficulty [2]. Another approach for realization of metamaterials has been introduced by [3], [4] in which dielectric spheres have been used in constructing of electric and magnetic dipole of metamaterials.

In order to enhance the directivity of circular patch antenna by collimating the electromagnetic energy, we utilized all-dielectric metamaterials in this paper. For this purpose 1-layer and 2-layer dielectric spheres have investigated as a superstrate of circular patch antenna.

2. DESIGN OF THE PATCH ANTENNA SUPERSTRATE BASED ON METAMATERIALS

The geometry of all-dielectric metamaterials is depicted in Figure.1. The parameters as given in the Figure.1 are $\Delta x = 25mm$, $\Delta y = 25mm$ $r = 5mm$ and permittivity of spheres $\varepsilon_r = 40$. This high permittivity embedded inside the host media with permittivity $\varepsilon_h = 2.2$. The all-dielectric spheres create electric and magnetic dipole moments. The dominants modes are TM and TE for electric dipole and magnetic dipole respectively based on Mie series [2]. The simulation results have been obtained by a full wave numerical simulation, CST Microwave Studio.

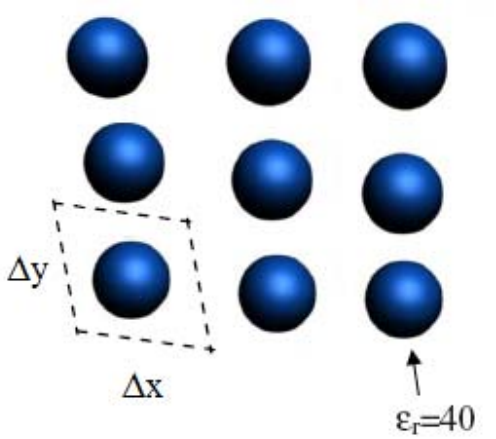


Figure 1: One-layer all-dielectric spheres as a lens

All-dielectric metamaterials as a superstrate of circular patch antenna at operating frequency utilized for gain enhancement. 1-layer and 2-layer dielectric spheres have investigated as a superstrate of circular patch antenna. Figure.2 shows, a nominal circular patch antenna with 2-layers and 1-layer all dielectric lens which consist of nine spheres with permittivity of 40 in each layer. For 1-layer all dielectric lens, the lens is 20mm above the patch antenna. Also, for 2-layer all-dielectric lenses, the lens is 35mm above the patch antenna and the radius of spheres are 4.8mm.

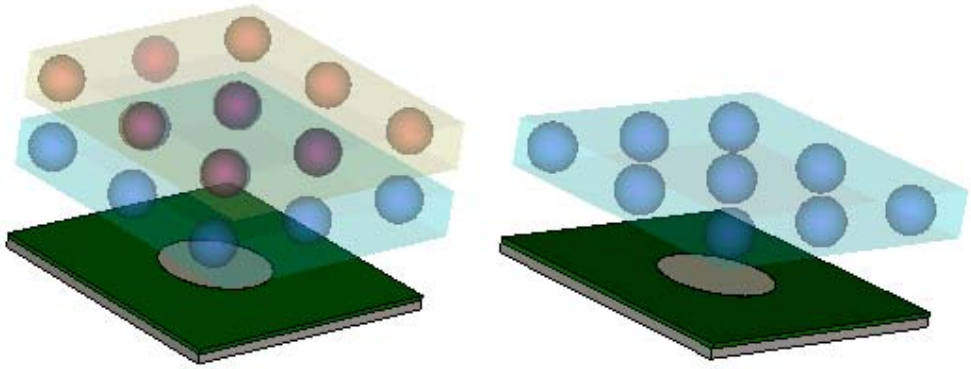


Figure 2: Patch antenna with 2-layers and 1-layer all-dielectric spheres MTMs lens

In Figure.3-(a) radiation pattern of circular pattern without lens has been shown with 4.9dB gain at 4.6GHz. In Figure.3-(b) shows radiation pattern of the patch antenna with one-layer lens with 11.9dB gain. Furthermore, Figure.3-(c) shows 16.3 gain radiation pattern of 2-layer lens with patch antenna. As a result, the directivity of the circular patch antenna was improved around 7 and 11.4 dB for one-layer and two-layer lenses respectively without degrading the radiation efficiency. The gain enhancement of circular patch antenna is related to permittivity of spheres. By increasing the permittivity, the gain will be increased.

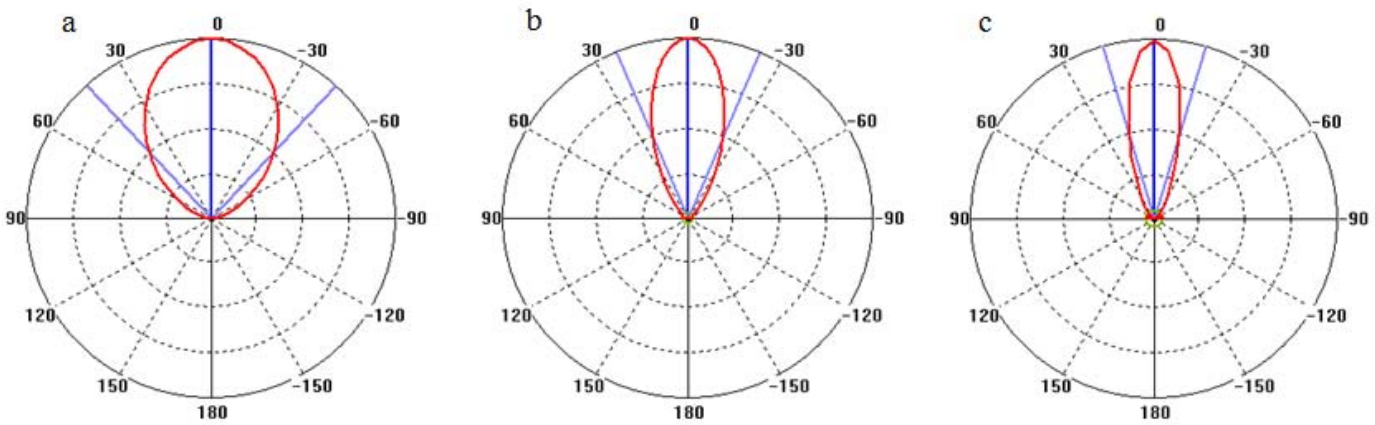


Figure 3: Radiation pattern for patch antenna a) without lens b) with 1-layer lens c) with 2-layers lens

The magnitude of S11 for circular patch antenna with 1-layer and 2-layer all-dielectric lens depicted in Figure.4 and Figure5. The operating frequency of antenna is about 4.6GHz, with 80 MHz bandwidth for 1-layer lens. In comparison to 1-layer lens, the bandwidth of 2-layers lens slightly decreased. However, the gain of 2-layers lens is 4.4dB larger than 1-layer lens. Therefore, tradeoff can be made between high bandwidth and high gain for different applications.

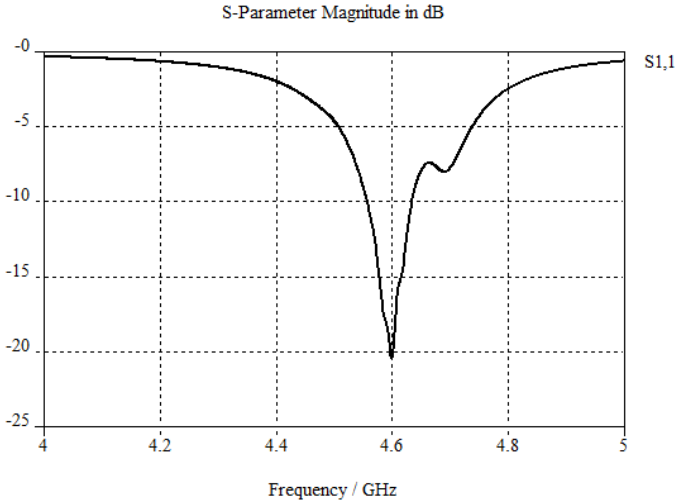


Figure 4: Magnitude of S11 for the circular patch antenna with 1-layer all-dielectric lens

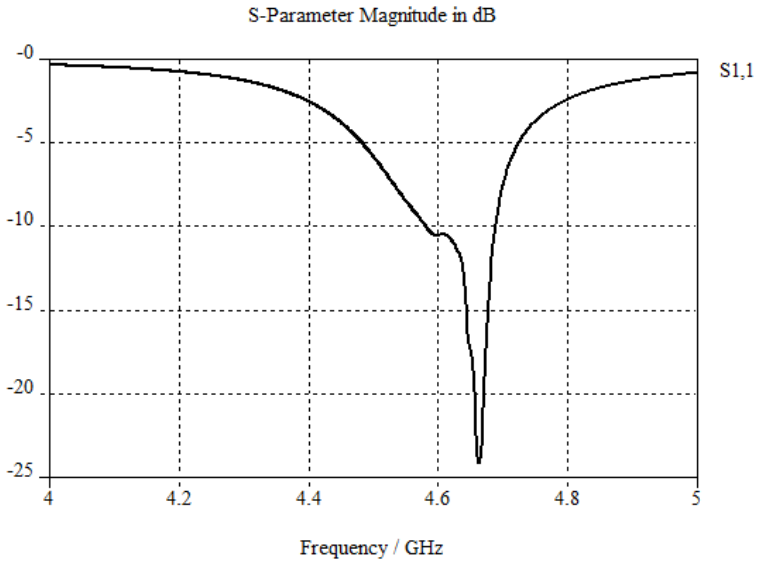


Figure 5: Magnitude of S11 for the circular patch antenna with 2-layers all-dielectric lens

4. CONCLUSIONS

In conclusion, we have designed all-dielectric metamaterials as a superstarte for the circular patch antenna. This lens by collimating the waves from the patch antenna enhanced the gain. The results show the significant improvement on patch antenna gain. Moreover, those high gains have been obtained with simple and low loss lens and also could be easily fabricated. The gains also can be improved slightly by increasing the number of sphere in each layer.

REFERENCES

1. Enoch, S., G.Tayeb, P.Sabouroux, N.Guerin, and P.Vincent, "A metamaterial for directive emission," *Physical review Lett,* Vol. 89, 213902, 2002.
2. Ahmadi, A. and H .Mosallaei "Physical configuration and performance modeling of all-dielectric metamaterials," *Physical review B,* Vol. 77,045104, 2008.
3. Vendik, I.B., O.G.Vendik, and M.S.Gashinova, "Artificial dielectric medium possessing simultaneously negative permittivity and magnetic permeability," *Technical Physics Letters,* Vol. 32, No.5,429-433, 2006.
4. Jylha, L., I.Kolmakov, S.Maslovski, and S.Tertyakov, "Modeling of isotropic backward-wave materials compose of resonant spheres," *Journal of Applied Physics,* Vol. 99,043102, 2006.

Analytical Theory of Effective Global Cloaking Processes: designing the Spherical EM Cloaking Nano-Element

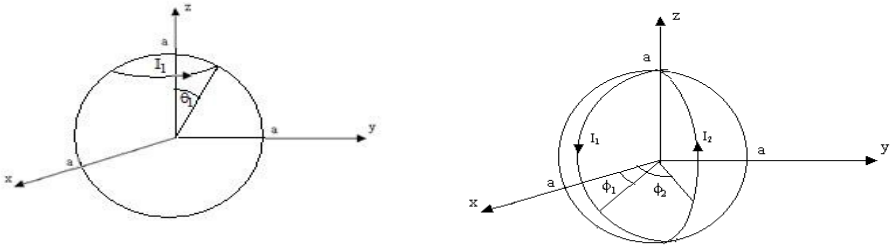
T. Sengor[1]

[1] Yildiz Technical University, Depart. of Electronics and Communication. Engineering, Istanbul 34349, Turkey
sengor@yildiz.edu.tr

Abstract- Properties of non-planar ring sources are studied and possibilities creating structures providing almost global cloaking are given. Co-rings in nanometric dimensions lying on different azimuth and/or equatorial planes are defined as a cloaking nano-element. Several compositions of nano rings on spherical substrates are studied. The necessary conditions for the electromagnetically effective cloaking are generated.

1. INTRODUCTION

The loops are used at meta-material applications, frequently. The using of circular loop combinations on non-planar substrates is offered in this paper to consider in both of artificial material studies and cloaking applications [1]. Two basic combinations are used: i) Parallelly located circular loop lying on latitude circles on a spherical core. We call this element smooth ring ball. ii) Intersecting circular loop lying on meridian circles on a spherical core. We call this element cross ring ball. The circular loop is located on a spherical core having the radius a, that is sufficiently small. The magnitudes of the currents on the circular loops must be sufficiently large. These necessary conditions give a chance to generate TM_θ waves, which we call principal wave. Additionally, using of materials having time independent permittivity and θ-independent permeability brings the property of TE_ϕ waves to the previous TM_θ waves. We call the last TM_θ-TE_ϕ waves secondary wave. The arrangements at the circumstance of the ring balls bring the property of TM_r waves to the waves under the discussion. The last property enforces to bring the behaviour of TE_θ waves to the principal wave; therefore the principal wave gains the property of TEM_θ waves. The last property enforces adding the behaviour of TM_ϕ waves to the principal wave. So the wave under the discussion gains the property of TEM_ϕ waves. After all, the use of suitably built up layers of almost zero epsilon material and/or perfectly conducting material brings the behaviour of TE_r waves to the waves under the discussion. The final wave is gained a propagation characteristic fitting on the propagation characteristics of $TEM_{\theta\phi}$ waves and almost TEM_r waves.



(a) (b)

Figure 1. a) The smooth ring ball: parallelly located loop lying on latitude circle of a spherical core.
b) The cross ring ball: intersecting two semi-loops located on meridian circles of a spherical core.

The above said characteristic gives a way to produce suitable objects with spherical shapes in nanometre scale; those change the RCS of objects and therefore provide us to built structures demonstrating effective electromagnetic cloaking property. We call this structure effective electromagnetic cloaking device.

2. THE COMPONENT CASE

The smooth ring ball and the cross ring ball are illustrated at Figure 1. The current density is given at Table 1 for several ring ball configurations, where the δ is the Dirac's distribution and a is the radius of the spherical substrate. The u is the unit step function.

TABLE 1. The definitions of current densities induced on the several configurations of ring balls on spherical substrate

Cross ring ball	$J_\theta = \frac{1}{a} I_1[\delta(\phi-\phi_1)-\delta(\phi-\phi_1-\pi)]\delta(r-a)[u(\theta)-u(\theta-\pi)]$
A couple of cross ring balls	$J_\theta = \{I_1[\delta(\phi-\phi_1)-\delta(\phi-\phi_1-\pi)]-I_2[\delta(\phi-\phi_2)-\delta(\phi-\phi_2-\pi)]\}\times \times\frac{1}{a}\delta(r-a)[u(\theta)-u(\theta-\pi)]$
Semi- cross ring ball	$J_\theta = \frac{1}{a} I_1\delta(\phi-\phi_1)\delta(r-a)\left[u(\theta)-u(\theta-\pi)\right]$
A couple of semi-cross ring balls	$J_\theta = \frac{1}{a}\{I_1\delta(\phi-\phi_1)-I_2\delta(\phi-\phi_2)\}\delta(r-a)[u(\theta)-u(\theta-\pi)]$
Smooth ring ball	$\vec{J} = \vec{e}_\theta \frac{1}{a} I_1\delta(\theta-\theta_1)\delta(r-a)\left[u(\phi)-u(\phi-2\pi)\right]$
Semi-smooth ring ball	$\vec{J} = \vec{e}_\theta \frac{1}{a} I_1\delta(\theta-\theta_1)[u(\phi)-u(\phi-\pi)]\delta(r-a)$
A couple of smooth ring balls	$\vec{J} = \vec{e}_\theta \frac{1}{a}[I_1\delta(\theta-\theta_1)-I_3\delta(\theta-\theta_2)][u(\phi)-u(\phi-2\pi)]\delta(r-a)$
A couple of semi-smooth ring balls	$\vec{J} = \vec{e}_\theta \frac{1}{a}[I_1\delta(\theta-\theta_1)-I_2\delta(\theta-\theta_2)][u(\phi)-u(\phi-\pi)]\delta(r-a)$
Multiple cross ring balls	$J_\theta = \frac{1}{a}\sum_n I_n[\delta(\phi-\phi_n)-\delta(\phi-\phi_n-\pi)]\delta(r-a)[u(\theta)-u(\theta-\pi)]$

3. THE FORMULATION OF THE PROBLEM

The conditions those are given in section 1 bring the equations below:

$$\sin\theta\frac{\partial E_\phi}{\partial\theta} + \cos\theta\, E_\phi + r\sin\theta\frac{\partial(\mu H_r)}{\partial t} = 0 \tag{1a}$$

$$\sin\theta\frac{\partial H_\phi}{\partial\theta} + \cos\theta\, H_\phi - \sigma r\sin\theta\, E_r - r\sin\theta\frac{\partial(\varepsilon E_r)}{\partial t} = 0 \tag{1b}$$

$$E_\phi - r\frac{\partial(\mu H_\theta)}{\partial t} = 0, \qquad E_\theta - \frac{\partial(E_r)}{\partial\theta} + r\frac{\partial(\mu H_\phi)}{\partial t} = 0 \tag{1c}$$

$$H_\phi + \sigma r E_\theta + r\frac{\partial(\epsilon E_\theta)}{\partial t} = 0, \qquad H_\theta - \frac{\partial(H_r)}{\partial\theta} - \sigma r E_\phi - r\frac{\partial(\epsilon E_\theta)}{\partial t} = 0 \tag{1d}$$

The principal wave TM_θ generates TE_ϕ wave under the condition below:

$$\frac{\partial\mu}{\partial t} = 0, \qquad \frac{\partial\varepsilon}{\partial t} = 0, \qquad \frac{\partial^2\mu}{\partial t\partial\theta} = 0 \tag{2}$$

The conditions (2) provide the generation of secondary wave; i.e., TM_θ-TE_ϕ. The equation (1a) gives $H_r \equiv H_r(r,\phi)$, which gives $E_\theta \equiv 0$ due to the radiation condition for $t\to\infty$ and $\forall r\in[0,\infty)$, when the conditions at (2) are provided. So we get $H_\phi \equiv 0$, from (1d). After substituting these results at (1b) and (1c) we get

$$\frac{\partial(\varepsilon E_r)}{\partial t} = -\sigma E_r \tag{3}$$

therefore the nonzero components of the field are below, only:

$$E_r \equiv E_r(r,\theta,\phi,t), \qquad H_r \equiv H_r(r,\phi) \tag{4}$$

The solution of (3) is below:

$$E_r = \frac{1}{\varepsilon} e^{-(\sigma/\varepsilon)t} e^{C(r,\theta,\phi)} \tag{5}$$

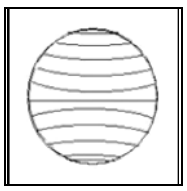
4. THE GLOBAL INVISIBILITY CONDITIONS FOR EM AND/OR OPTICAL CLOAKING

The equations (1a)-(1d) gives

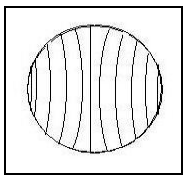
$$H_r = -(1/r)R(r)\frac{\partial F(\phi)}{\partial\phi}\cos(\omega t) \tag{6}$$

However, H_r is time independent due to (4); therefore, the functions R and F should provide the conditions of $R(r)\equiv 0$ and/or $(\partial F/\partial\phi)\equiv 0$. So we get $H_r \equiv 0$. The only non zero component remains as E_r. The solution at (5) gives the conditions below for almost invisibility and global invisibility, respectively:

i) $\sigma >> \varepsilon$, ii) $\sigma \equiv 0$ and/or $\varepsilon\to\infty$.



(a)



(b)

Figure 2. The Spherical EM Cloaking Nano-Elements: cloaking balls.
a) Horizontal cloaking ball: horizontally located loops lying on latitude circles on a spherical core.
b) Vertical cloaking ball: vertically located loops lying on latitude circles on a spherical core.

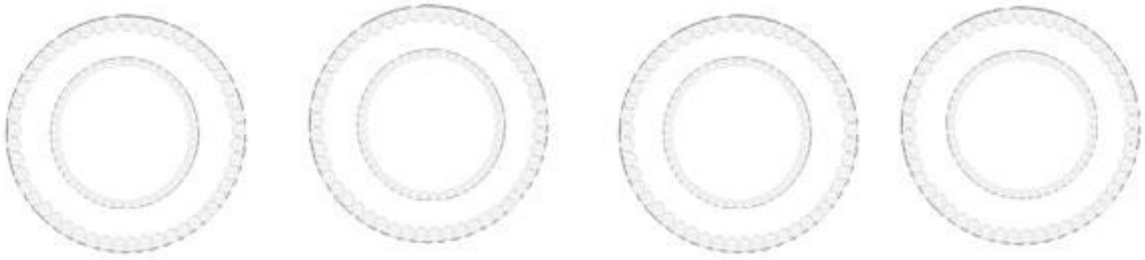
4. THE ALMOST INVISIBILITY BUCKLER DESIGN FOR EM CLOAKING

The suitable configured spherical substrate involving conducting rings (see Figure 2) enforces the scattered field to propagate with a propagation characteristic fitting on the propagation characteristics of $TEM_{\theta\phi}$ waves and almost TEM_r waves if the diameter of the substrate is around 1 nm; therefore the using of the cloaking balls provide a suitable way to built global EM cloaking device for the waves of $f<3\times10^{17}$ Hz. The cloaking balls are collated on a sphere enclosing the object that will be hided (see Figure 3 and 4).



(a) (b)

Figure 3. The EM buckler configurations.
a) Horizontal outer buckler. b) Vertical inner buckler.



(a) (b) (c) (d)

Figure 4. The EM outer-inner buckler configurations.
a) Horizontal outer-Horizontal inner buckler. b) Horizontal outer-Vertical inner buckler.
c) Vertical outer-Vertical inner buckler. d) Vertical outer-Horizontal inner buckler.

If the diameter of cloaking ball is less than 10^{-10} m then realization of the global optical cloaking is possible.

4. CONCLUSIONS

Several compositions of nano-rings on spherical substrates are studied. The necessary conditions for both of the electromagnetically effective cloaking and the optically effective cloaking are generated.

REFERENCES

1. Sengor, T., “Properties of a non-planar metamaterial elements: ring resonators on a spherical substrate,” in *Proceedings of The First International Congress on Advanced Electromagnetic Materials in Microwaves and Optics*, Rome, Italy, 22-26 October 2007.

Disorder in optical metamaterials made of silver nanospirals

G. Guida[1], B. Gallas[2], R. Abdeddaim[3], A. Priou[1], J. Rivory[2], K. Robbie[4]

[1] LEME (EA4416-OMS), Université Paris Ouest, 50 rue de Sèvres, 92410 Ville d'Avray, France

[2] INSP, CNRS, Université Pierre et Marie Curie, 140 rue de Lourmel, 75015 Paris, France

[3] Institut Langevin, LOA – ESPCI CNRS UMR 7587, 10 rue Vauquelin 75005 Paris, France

[4] Department of Physics - Queen's University Kingston, Canada K7L 3N6

bruno.gallas@insp.jussieu.fr

Abstract- We report on a numerical study of the optical properties of silver square nanospirals. The resonant modes of isolated nanospirals presented current distributions similar to those of U-shaped resonators. 'Electric' modes were relatively insensitive to coupling, except for the shortest distance, and to disorder. In contrast, 'magnetic' modes were modified by both coupling and disorder.

1. INTRODUCTION

The tailoring of permittivity and permeability values by arrays of sub-wavelength metallic structures allows for control of the propagation of electromagnetic waves. For instance, coupled split-ring resonators (SRR) associated with thin wires lattice resulted in a negative refractive index at microwave frequencies [1,2]. These results opened up the field of a new class of materials, referred to as metamaterials. Recent realizations presented in the near-infrared and visible were based on simpler structures [3-5]. A limitation to large scale realizations arises from the need of structuring the material at dimensions of the order of one third of the operation wavelength. Consequently, the structures realized so far consisted in 2D arrays of resonators. Recently, we have shown that square nanospirals, which could be realized by Glancing Angle Deposition [6], may have negative permittivity and permeability at optical frequency [7]. However, in such materials it would be difficult to control exactly the position of the nanospirals and disorder would occur which may be detrimental to the optical properties obtained. The influence of different types of disorder on the resonances has been considered in the GHz regime with magnetic field was normal to the plane containing the SRR. The magnetic resonance was strongly affected by perturbations in the shape of the resonators [8-10] or the absence of some resonators [10]. Misalignments and aperiodicity reduced the depth of the stop-band in arrays of SRR [11], although the resonance was rather robust against disorder provided it did not occur along the propagation direction of the electromagnetic wave [11,12]. As a rule of thumb, a variation by 10% in the properties of the resonators eliminated the region of negative permeability although the magnetic resonance was still present. In this work we investigate the influence of aperiodicity on the resonances of square nanospirals in the THz regime.

2. MODELLING

The first three arms of a square nanospiral (Fig. 1(a)) define a structure similar to U-shaped resonators illuminated at oblique incidence [3]. The spirals were defined so that they were wrapped along the z axis with the first arm in the (x,z) plane. The projection of the spiral in the (x,y) plane would be a U of side L ≈ 250 nm (Fig 1(a)). The arms had a circular section with 60 nm diameter. The height of the square spirals was set to 270 nm. The nanospirals were illuminated at normal incidence, i.e. along the z axis with electric field of light polarized along x and y. The optical constants of silver in the arms were obtained using a damped Drude term to describe the free electrons response modified by scattering [13].

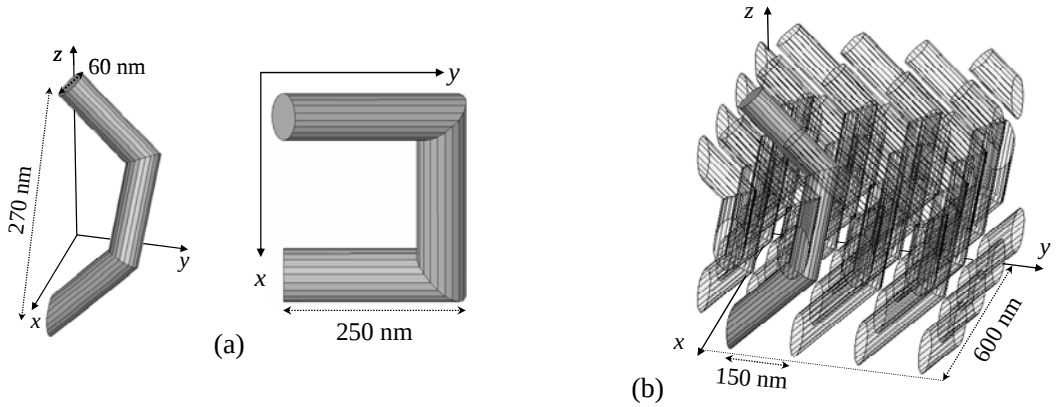


Fig. 1: Geometrical parameters of the spirals. (a) lateral and top view for one nanospiral, (b) lateral view of 16 nanospirals located on a lattice of 150 nm in a box of 600 nm of size along *x* and *y*. One nanospiral has been highlighted in (b) for clarity sake.

We have calculated the optical response of square nanospirals with three arms between 50 THz and 900 THz using HFSS by Ansoft. The values of the absorbance A were obtained as $A = 1 - |S_{11}|^2 - |S_{12}|^2$. The spirals were placed in a unit box with periodic conditions applied along *x* and *y*. We compared the optical properties of one isolated spiral to that of densely packed periodic and aperiodic spirals. The case of isolated spirals was obtained by calculating the S matrix with one spiral every 600 nm resulting in a packing density of silver of approximately 1.3%. The aperiodic case was approximated by calculating the S matrix of 16 nanospirals in a 600x600 nm² box (packing density of 20%) with their positions randomly varied about their initial ones by ±10% at most along *x* and *y* (Fig 1(b)). In this case the absorbance <A> was obtained by averaging R and T over ten realizations to model a sample where the different random realizations would contribute independently, i.e. incoherently, to reflection and transmission. It must be noted that for light polarized along *x* (resp. *y*) transfer of polarization from *x* to *y* (resp. *y* to *x*) were observed, maybe because of the presence of circular dichroïsm [14], which prevented any retrieval of the effective permittivity and permeability of the film containing the nanospirals.

3. RESULTS

Figures 2(a) and 2(b) present the spectral values of A as a function of frequency for the case of the spirals separated by 600 nm for light polarized along *x* and *y*, respectively. A sharp peak was observed at 500 THz which was related to light coupling to a mode diffracted in the sample's plane (Wood's anomaly). Indeed, this frequency corresponds to a wavelength in vacuum of 600 nm. In addition, different absorption bands were observed. For light polarized along *x*, one band was observed near 160 THz and a second one near 420 THz. For light polarized along *y*, a broad band was observed near 350 THz, however it consisted in the superposition of two absorption bands with a principal one near310 THz and a shoulder, distorted by the Wood's anomaly, near 420 THz. Because of the effect of packing density on the position of the effective absorption bands we will identify the origins and actual resonance frequencies of the modes at the maximum of calculated current density in the nanospirals.

Figure 3 presents a top view of the instantaneous current distribution in the case of one isolated spiral in a 600x600 nm² box at the resonances for electric field of light polarized along *x* and *y*. For light polarized along *x* the first resonance was located near 160 THz. It was characterized by current circulating in the whole nanospiral: it may be seen as the dipolar mode of the nanospiral and it is generally associated with a 'magnetic' resonance in U-shaped resonators [3]. The following resonance was located near 380 THz and was associated with excitation of the second arm only ('electric' mode). For light polarized along y, the first resonance was located near 300 THz and was

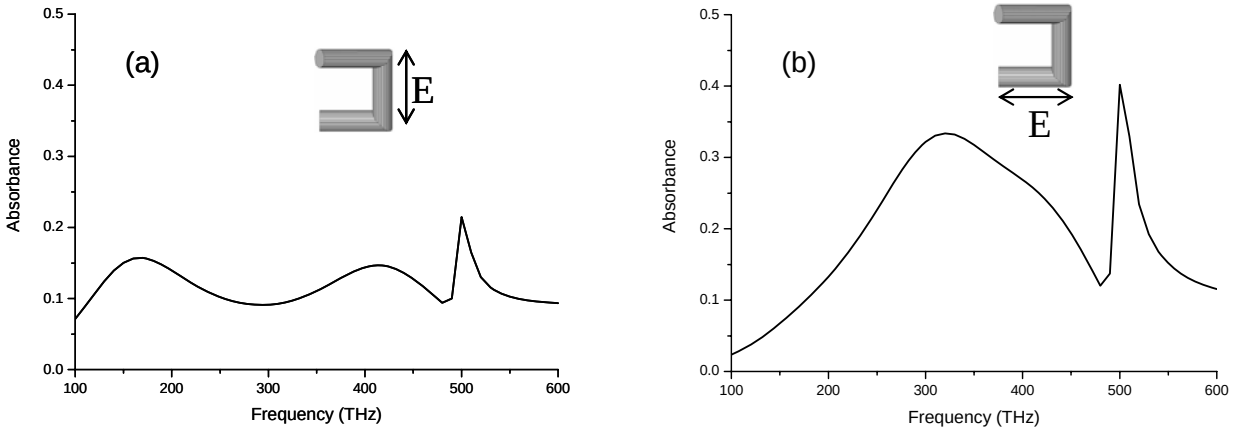


Fig. 2: Absorbance of an isolated nanospiral for (a) incident field E along *x* and (b) incident field E along *y*.

characterized by current flowing in the first and third arms in parallel directions. This resonance should be associated with the second 'electric' mode of the nanospiral with a current node in the middle of the second arm. The second resonance was observed near 510 Thz, associated with the distorted shoulder at high frequency in absorbance. It was characterized by the excitation of the first and third arms but with current flowing in opposite directions. This current configuration is generally associated with a 'magnetic' mode in metamaterials [15].

Figure 4 presents the resonance frequencies of the modes of the nanospirals determined as a function of nanospiral-nanospiral distance ranging from 900 nm to 150 nm. The high frequency resonances could not easily be determined in the case of the 900 nm because the peaks associated with the Wood's anomaly distorted the spectra too much. The 'electric' modes remained approximately at the same frequency whereas the 'magnetic' modes frequency upshifted steadily. The case of nanospirals-nanospirals separation of 150 nm corresponds to separation smaller than the nanospirals dimensions and the first arm of each nanospiral was below the third arm of the adjacent spiral along *x*. For light polarized along *x*, the first mode could no longer be observed in the spectral range investigated. Instead the third mode of the nanospiral was downshifted to 280 THz. A new resonance appeared near 550 THz associated to the excitation of the second arm with a current node in its middle and would correspond to the second resonance mode of the second arm. These two resonances would correspond to 'electric' modes. For light polarized along *y*, the first resonance near 190 THz corresponded to out of phase excitation (i.e. alternating) of the first and third arms with parallel currents. The maximum of current was phase shifted by π/4 with respect to the electric field of light. The

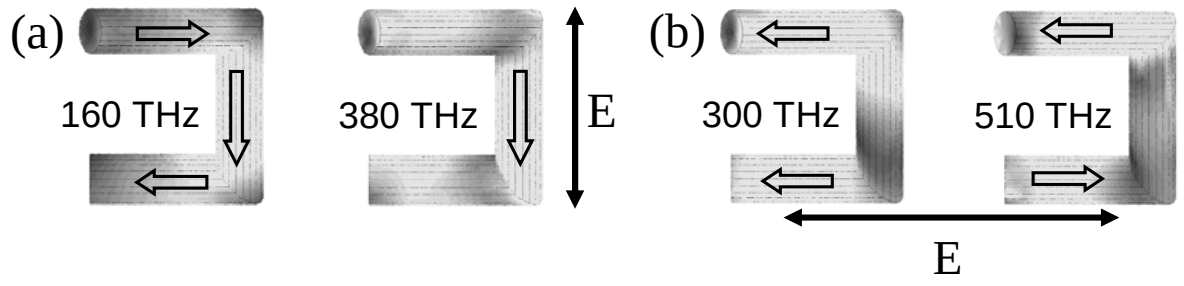


Fig 3: Top view of the instantaneous current distribution in the isolated spiral at the resonances (a) E incident along *x* and (b) E incident along *y*. The arrows indicate the current direction and their size is proportional to current value. In each polarization case the color scale has been multiplied by 1.7 for the high frequency resonance.

‘magnetic’ mode was merely shifted to 700 THz.

Figure 5 compares the absorbance values as a function of frequency of the periodic and aperiodic cases. For light polarized along *x*, two broad absorption bands were observed near 180 THz and 500 THz associated with the resonances described above. Disorder did not change both positions and magnitudes of these absorption bands. For light polarized along *y*, two absorption bands were observed near 290 THz and 680 THz associated with the resonances with parallel and opposite currents in opposite arms, respectively. Whereas the resonance near 290 THz was only slightly modified by aperiodicity, the resonance near 680 THz, associated with the ‘magnetic’ mode was damped in the aperiodic case.

4. DISCUSSION

In the following we will discuss the influence of coupling and disorder on the resonances excited as a function of the polarization of the exciting wave. The calculated current distributions in the arms at the resonances did present the same properties and polarization dependence as the resonance modes of U-shaped resonators [16]. However, the second mode, associated with current flowing in the same direction in opposite arms in U-shaped resonators, was split in ‘electric’ and ‘magnetic’ modes in the square nanospirals. This effect has been observed in asymmetric parallel rods and was attributed to excitation of this mode, otherwise silent, owing to asymmetry [17]. In our case the asymmetry between the first and third arms is intrinsic to the very shape of the nanospirals and this asymmetry would be at the origin of the existence of the two modes even in the case of isolated spirals. Alternatively, we may propose that the component of the magnetic field of light acquired a component normal to the average plane of the nanospirals which may help couple light to ‘magnetic’ modes [3]. By changing the distance between nanospirals and then the periodicity we probed the sensitivity of the different modes to nanospiral-nanospiral coupling. We will separate the discussion between the cases of ‘electric’ and ‘magnetic’ modes.

We have observed in Fig. 4 that the electric resonances were not affected by coupling as long as the separation between nanospirals was larger than the dimensions of the nanospirals. The resonance’s frequency decreased with separation between nanospirals. The second resonance mode of the second arm (*x*-polarized case) observed at 550 THz would have been at much higher frequency for larger nanospiral-nanospiral separation and out of our spectral range. There are some works on the effect of coupling on the dipolar modes of dots or disks in the THz regime. In the

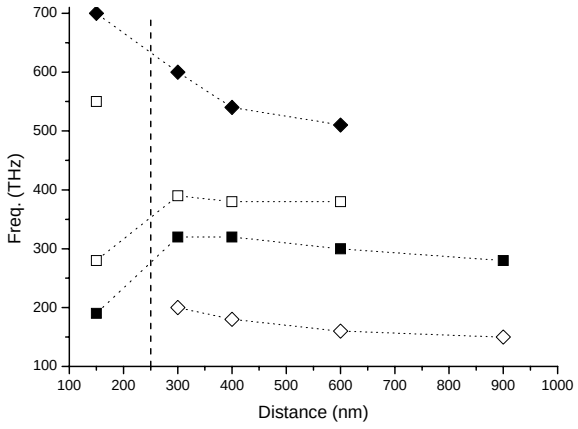


Fig. 4 : Position of the modes observed in the square nanospirals as a function of nanospiral-nanospiral distance for E polarized along *x* (open symbols) and *y* (full symbols). The square symbols correspond to ‘electric’ modes and the diamonds to ‘magnetic’ modes. The vertical dashed line indicates the projected size of the nanospiral in the (*x*,*y*) plane.

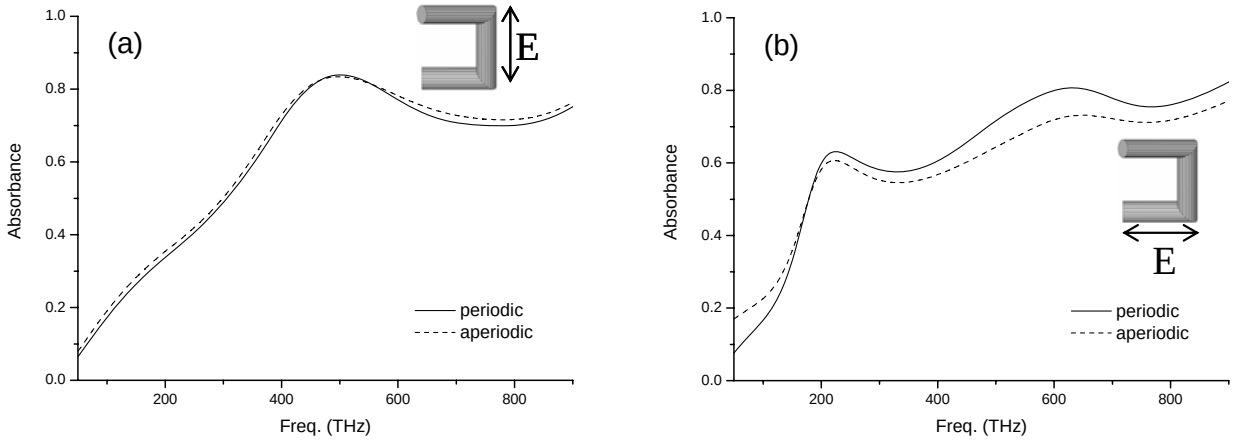


Fig. 5: Absorbance periodic (solid line) and aperiodic (dotted line) arrays of nanospirals for (a) E polarized along *x* and (b) E polarized along *y*.

ordered case, the position of the dipolar modes was not modified by distance between dots or rods as long as the distance between their surfaces was larger than their diameter [18,19,20]. A universal scaling law was proposed based on near-field dipole-dipole interaction which showed that the coupling efficiency decreased exponentially with distance [18]. Consequently, we should not expect coupling to affect strongly the position of the 'electric' resonances in our study as observed in Fig. 4. Figure 5 hints toward a relative insensitivity of the electric modes to disorder. It has been shown that pseudo-aperiodicity could split the dipolar resonance of disks in longitudinal and transverse modes [21,22]. In our case, such splitting would be smeared out by randomness and averaging.

In the case of 'magnetic' modes we observed a steady shift toward high frequencies when the nanospiral-nanospiral distance decreased. It has been shown in SRR that this mode could shift to lower or higher frequencies upon coupling depending on the polarization conditions [23,24]. However, since our polarization conditions differ from those of literature and since the arms of the nanospirals overlapped along *z* in the strong coupling case, comparisons are difficult. The first 'magnetic' mode disappeared from the spectral range investigated here in the strong coupling case. It is possible that if the resonance frequency of this mode continued to shift to higher frequency it was screened by the 'electric' mode. The second 'magnetic' resonance originated from asymmetric arms interacting through Coulomb interaction [17]. This long range interaction could be at the origin of the shift of the resonance frequency even for large nanospiral-nanospiral separation (Fig. 4). In contrast to the 'electric' modes, this 'magnetic' mode was damped in the aperiodic case (Fig. 5) probably because each particular local position originating from disorder induced its own resonance's frequency and, on the average, the absorbance associated with this 'magnetic' mode was broadened and damped. It has also been shown in SRR that 'magnetic' modes were damped by disorder when it was applied in the propagation direction of light [11,12]. We applied disorder perpendicularly to the propagation direction, but owing to the shape of the nanospirals and overlapping of the arms along *z*, disorder in our case may also be seen as partly disorder along the propagation direction. This would explain the damping of the 'magnetic' mode too.

5. CONCLUSIONS

We have investigated the optical properties of periodic and disordered assemblies of silver square nanospirals and compared them to the optical properties of isolated nanospiral. Isolated nanospiral presented resonant modes similar to

those observed in U-shaped resonators. An additional ‘magnetic’ mode was observed, probably associated with the asymmetry of the spirals. The resonance frequency of the ‘electric’ modes remained constant as long as the separation between nanospirals remained larger than the nanospirals’ diameter and decreased for smaller distances. The resonance frequency of the ‘magnetic’ modes increased steadily when the distance between the nanospirals decreased. Positional disorder did not modify the ‘electric’ modes and damped the ‘magnetic’ modes.

REFERENCES

1. J.B. Pendry, A.J. Holden, D.J. Robbins, W.J. Stewart, IEEE Trans. Microwave Theory Tech. **47**, 2075 (1999) ; J. Phys. Cond. Matt. **10**, 4785 (1998)
2. D.R. Smith, W.J. Padilla, D.C. Nemat-Nasser, S. Schulz, Phys. Rev. Lett. **84**, 4184 (2000)
3. C. Enkrich, M. Weneger, S. Linden, S. Burger, L. Zschiedrich, F. Schmidt, J.F. Zhou, Th. Koschny, C.M. Soukoulis, Phys. Rev. Lett. **95**, 203901 (2005)
4. F. Garwe, C. Rockstuhl, C. Etrich, U. Hübner, U. Bauerschäfer, F. Setzpfandt, M. Augustin, T. Pertsch, A. Tünnermann, F. Lederer, Appl. Phys. B **84**, 139 (2006) ; V.M Shalaev, W. Cai, U.K. Chettiar, H.-K. Yuan, A.K. Sarychev, V.P. Drachev, A.V. Kildishev, Opt. Lett. **30**, 3356 (2005)
5. G. Dolling, M. Wegener, C.M. Soukoulis, S. Linden, Opt. Lett. **32**, 53 (2007)
6. K. Robbie, G. Beydaghyan, T. Brown, C. Dean, J. Adams, C. Buzea, Rev. Sci. Inst. **75**, 1089 (2004)
7. R. Abdeddaim, G. Guida, A. Priou, B. Gallas, J. Rivory, Appl. Phys. Lett. **94**, 081907 (2009)
8. A.A. Zharov, I.V. Shadrivov, Y.S. Kivshar, J. Appl. Phys. **97**, 113906 (2005)
9. J. Gollub, T. Hand, S. Sajuyigbe, S. Mendonca, S. Cummer, D.R. Smith, Appl. Phys. Lett. **91**, 162907 (2007)
10. M.V. Gorkunov, A.A. Gredeskul, I.V. Shadrivov, Y.S. Kivshar, Phys. Rev. E **73**, 056605 (2006)
11. K. Aydin, K. Guven, N. Katsarakis, C.M. Soukoulis, E. Ozbay, Opt. Express **12**, 5896 (2004)
12. E. Ozbay, K. Guvan, K. Aydin, J. Opt. A : Pure Appl. Opt. **9**, S301 (2007)
13. H. Wormeester, A.-I. Henry, E.S. Kooija, B. Poelsema, M.-P. Pileni, J. Chem. Phys. **124**, 204713 (2006)
14. J.K. Gansel, M. Thiel, M.S. Rill, M. Decker, K. Bade, V. Saile, G. von Freymann, S. Linden, M. Wegener, Science **325**, 1513 (2009)
15. C. Rockstuhl, T. Zentgraf, E. Pshenay-Severin, J. Petschulat, A. Chipouline, J. Kuhl, T. Pertsch, H. Giessen, F. Lederer, Opt. Express **15**, 8871 (2007)
16. C. Rockstuhl, F. Lederer, C. Etrich, T. Zengraf, J. Kuhl, H. Giessen, Opt. Express **14**, 8827 (2006)
17. A. Christ, O.J.F. Martin, Y. Ekinci, N.A. Gippius, S.G. Tikhodeev, NanoLett **8**, 2171 (2008)
18. P.K. Jain, W. Huang, M.A. El-Sayed, NanoLett. **7**, 2080 (2007) and references therein
19. H.E. Ruda, A. Shika, Appl. Phys. Lett. **90**, 223106 (2007)
20. J.P. Kottmann, O.J.F. Martin, Opt. Express **8**, 655 (2001)
21. C. Forestiere, G. Miano, S.V. Boriskina, L. Dal Negro, Opt. Express **17**, 9648 (2009)
22. L. Dal Negro, N.-N. Feng, A. Gopinath, J. Opt. A: Pure Appl. Opt. **10**, 064013 (2008)
23. P. Gay-Balmaz, O.J.F. Martin, J. Appl. Phys. **92**, 2929 (2002)
24. R.S. Penciu, K. Aydin, M. Kafesaki, Th. Koschny, E. Ozbay, E.N. Economou, C.M. Soukoulis, Opt. Express **16**, 18131 (2008)

Control of near-field radiative heat transfer via surface phonon-polariton coupling in thin films

M. Francoeur[1], M. P. Mengüç[1,2], and R. Vaillon[3]
[1]Department of Mechanical Engineering, University of Kentucky, Lexington, KY 40506-0503, USA
[2]Ozyegin University, Altunizade, Uskudar, 34662 Istanbul, Turkey
[3]Université de Lyon, CNRS, INSA-Lyon, UCBL, CETHIL, UMR5008, F-69621, Villeurbanne, France
Correspondence: pinar.menguc@ozyegin.edu.tr

Abstract- The possibility of controlling near-field radiative heat transfer with the use of silicon carbide thin films supporting surface phonon-polaritons in the infrared spectrum is explored. For this purpose, the local density of electromagnetic states is calculated and analyzed within the nanometric gap formed between two SiC films as well as the radiative heat flux exchanged between the thin layers.

1. INTRODUCTION

Radiative heat transfer between bodies separated by sub-wavelength distances can exceed the values predicted by the Planck blackbody distribution due to tunneling of evanescent waves. Moreover, if the bodies support surface plasmon-polaritons (SPPs) or surface phonon-polaritons (SPhPs), radiant energy exchanges can become quasi-monochromatic.

Near-field effects of thermal radiation can be used to improve the performances of thermophotovoltaic (TPV) power generators, by spacing the radiator and cells by a sub-wavelength vacuum gap. Research on these nanoscale-gap TPV devices has shown that the power output can significantly increase due to radiation tunneling [1]. However, our recent analyzes suggest that nano-TPV systems previously proposed in the literature are likely to suffer from excessive cell heating. One way to circumvent this problem is to design structures emitting thermal radiation selectively in the near-field, a subject that has attracted attention only very recently [2-4].

The near-field thermal spectrum can be tuned by using thin films supporting surface polaritons. In general, SPhPs are more interesting than SPPs for thermal radiation applications, as their resonant frequency is in the infrared. The objective of this work is to analyze near-field radiative heat transfer between two silicon carbide (SiC) thin films supporting SPhPs. This is accomplished by calculating the local density of electromagnetic states (LDOS) within the gap formed between two SiC films and the radiative heat flux exchanged between the two layers.

2. THEORETICAL FORMULATION AND MODELING

Thermal radiation between two parallel films with perfectly smooth surfaces is considered, as shown in Fig. 1. The media are assumed infinite along the ρ-direction and azimuthally symmetric, such that only the variations along the z-direction are accounted for. Both films are in local thermodynamic equilibrium, homogeneous, isotropic, nonmagnetic, and described by a frequency-dependent dielectric function local in space. The SiC layers are separated by a gap of length d_c, and medium 3 is assumed to be non-emitting (i.e., $T_3 = 0$ K).

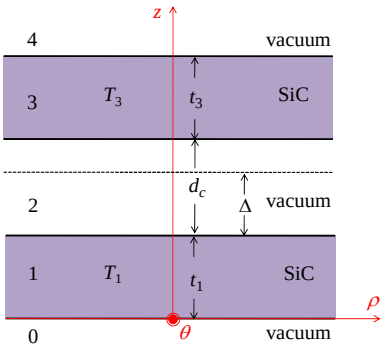


Figure 1. Schematic representation of the geometry considered.

The LDOS and radiative heat flux are derived using the fluctuational electrodynamics formalism, where a stochastic current density vector $\mathbf{J}^r$ is added in the Maxwell equations to account for thermal emission. The LDOS at a distance Δ above the emitting layer 1 (see Fig. 1) is calculated from the energy density at Δ normalized by the mean energy of an electromagnetic state, $\Theta(\omega,T_1)$. For this, only the TM evanescent component of the LDOS is analyzed, as SPhPs exist in TM-polarization for nonmagnetic materials. By applying the fluctuation-dissipation theorem (FDT), relating the ensemble average of $\mathbf{J}^r$ with the local temperature of the emitting medium, the following expression is obtained for the monochromatic LDOS at Δ above film 1 [3]:

$$\rho_{\omega,12}^{evan,TM}(\Delta)=\frac{1}{2\pi^2\omega}\int_{k_v}^{\infty}\frac{k_\rho^3 dk_\rho}{|k_{z2}|}\frac{\mathrm{Im}(R_1^{TM})e^{-2\mathrm{Im}(k_{z2})\Delta}}{\left|1-R_1^{TM}R_3^{TM}e^{2ik_{z2}d_c}\right|^2}\left[\left|1+R_3^{TM}e^{-2\mathrm{Im}(k_{z2})(d_c-\Delta)}\right|^2-2\frac{|k_{z2}|^2}{k_\rho^2}\mathrm{Re}(R_3^{TM})e^{-2\mathrm{Im}(k_{z2})(d_c-\Delta)}\right] \quad (1)$$

In Eq. (1), R_j^{TM} is the reflection coefficient of film j, k_ρ is the wavevector parallel to the surfaces, k_{zj} is the z-component of the wavevector in medium j, and k_v is the magnitude of the wavevector in vacuum. The term $\mathrm{Im}(R_1^{TM})$ in Eq. (1) can be seen as the spectral near-field emittance of film 1, while the term in square brackets accounts for the increase of thermal emission due to the presence of medium 3 [3].

The monochromatic radiative heat flux emitted by medium 1 and absorbed by medium 3 is determined by calculating the z-component of the Poynting vector and by applying the FDT; after a series of algebraic manipulations, the following expression is obtained for the TM evanescent component of the flux [4]:

$$q_{\omega,abs}^{evan}=\frac{\Theta(\omega,T_1)}{\pi^2}\int_{k_v}^{\infty}k_\rho dk_\rho e^{-2\mathrm{Im}(k_{z2})d_c}\frac{\mathrm{Im}(R_1^{TM})\,\mathrm{Im}(R_3^{TM})}{\left|1-R_1^{TM}R_3^{TM}e^{2ik_{z2}d_c}\right|^2} \quad (2)$$

Since $\mathrm{Im}(R_1^{TM})$ can be seen as the near-field spectral emittance of layer 1, $\mathrm{Im}(R_3^{TM})$ can be interpreted as the near-field spectral absorptance of film 3.

3. RESULTS AND DISCUSSION

SPhP dispersion relation for the two film system is determined by solving: $1 - R_1^{TM}R_3^{TM}\exp(2ik_{z2}d_c) = 0$. For the two film system, SPhP interactions within and between the layers split the dispersion relation into four branches, showing anti-symmetric and symmetric resonances for each film and for the whole structure [3]. This splitting of the SPhP dispersion relation in multiple branches can be employed to control near-field thermal emission.

To analyze the impact of SPhP coupling on near-field thermal emission, the LDOS is calculated above layer 1 (thicknesses of 10 nm and 100 nm) in the absence of layer 3 (Fig. 2(a)), and at $\Delta = d_c^-$ (i.e., before crossing the interface 2-3). Calculations are repeated when layer 3 is present; these results are depicted in Fig. 2(b). The dielectric function of SiC is modeled using a damped harmonic oscillator [3,4].

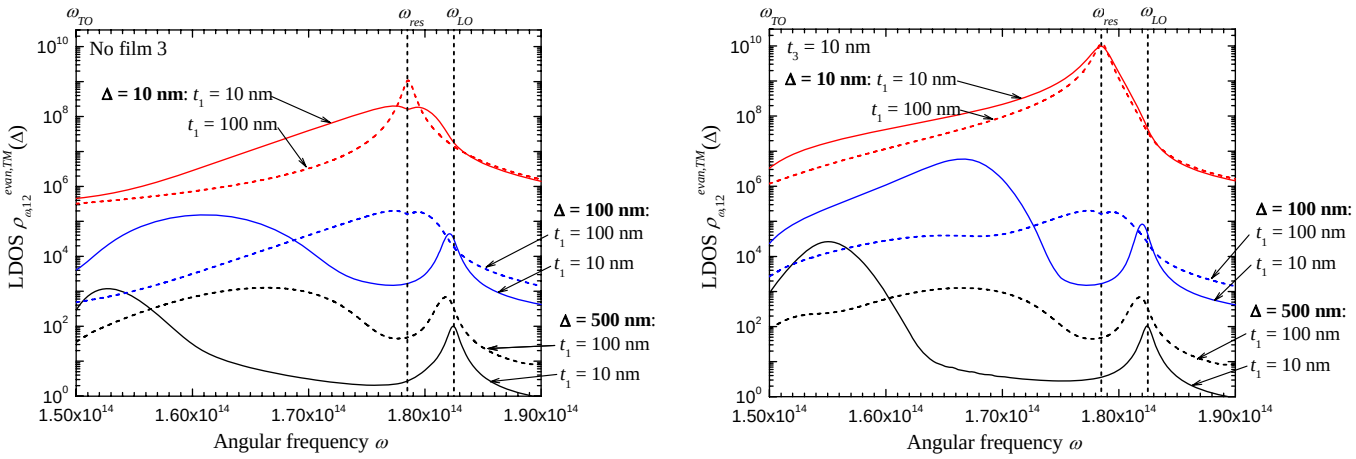


Figure 2. Spectral distribution of TM evanescent component of the LDOS above the emitting layer 1 (t_1 = 10 nm and 100 nm): (a) Δ = 10 nm, 100 nm, and 500 nm (no film 3). (b) $\Delta = d_c^- $ = 10 nm, 100 nm, and 500 nm.

Figure 2(a) shows that the LDOS profile is a function of the ratio t_1/Δ. The single resonance at ω_{res} = 1.786×10^{14} rad/s (resonant frequency of a single SiC-vacuum interface) observed for small t_1/Δ split in anti-symmetric and symmetric modes converging respectively toward ω_{LO} (longitudinal optical phonon frequency) and ω_{TO} (tranverse optical phonon frequency). It can be shown via an asymptotic analysis of SPhP dispersion relation that the splitting of the near-field thermal spectrum in two modes occurs when t_1/Δ is equals or less than unity [3]. When medium 3 is present, the near-field spectrum can significantly increase, and SPhP inter-film coupling also affect the spectral location and coherence of the resonance of the LDOS, albeit slightly.

Spectral distributions of TM evanescent component of the radiative heat flux per unit parallel wavevector k_ρ are depicted in Fig. 3. The thickness of the emitter (the first film) is 10 nm, the vacuum gap d_c is fixed at 100 nm. The thickness of the receiver t_3 takes values of 10 nm, 50 nm, 100 nm, and 500 nm. The results show clearly that near-field radiant energy exchanges are highly dependent on the thickness of the receiver. For t_1 = t_3 = 10 nm, the resonances of thermal emission and absorption are almost the same; the small discrepancies come from inter-film SPhP coupling. As a result, two distinct resonances can be observed on the flux profile [4]. As t_3 increases, SPhP coupling within film 3 decreases, and the resonance of absorption converges toward ω_{res}. This can be clearly seen by comparing the panels (b) to (d) where two branches of high radiative flux merge into ω_{res} as t_3 increases. Also, the high and low frequency resonant branches observed in Fig. 3(a) remains present as t_3 increase, while decreasing in strength. These branches can be interpreted as coming from high near-field thermal emission from layer 1. As t_1 does not vary, the spectral location of these modes is only slightly (in a non-perceptible manner) affected by the variations of t_3. The decrease in strength of these resonant modes is explained by the increasing mismatch between the resonances of emission and absorption at t_3 increases.

To summarize, the LDOS analysis revealed that the design of a near-field thermal spectrum depends not only on the emitter, but also the receiver. The results also showed that the near-field thermal spectrum is highly sensitive to the structure of the device where radiant energy exchanges occur, due to SPhP coupling within and between the layers. Via an asymptotic analysis of SPhP dispersion relation for the two film system, we developed an expression to predict the frequencies at which the radiative heat flux is maximal as a function of the film thicknesses and their distance of separation [4]. We aim to extend this procedure for multiple thin films in order to design highly-efficient nano-TPV energy conversion devices.

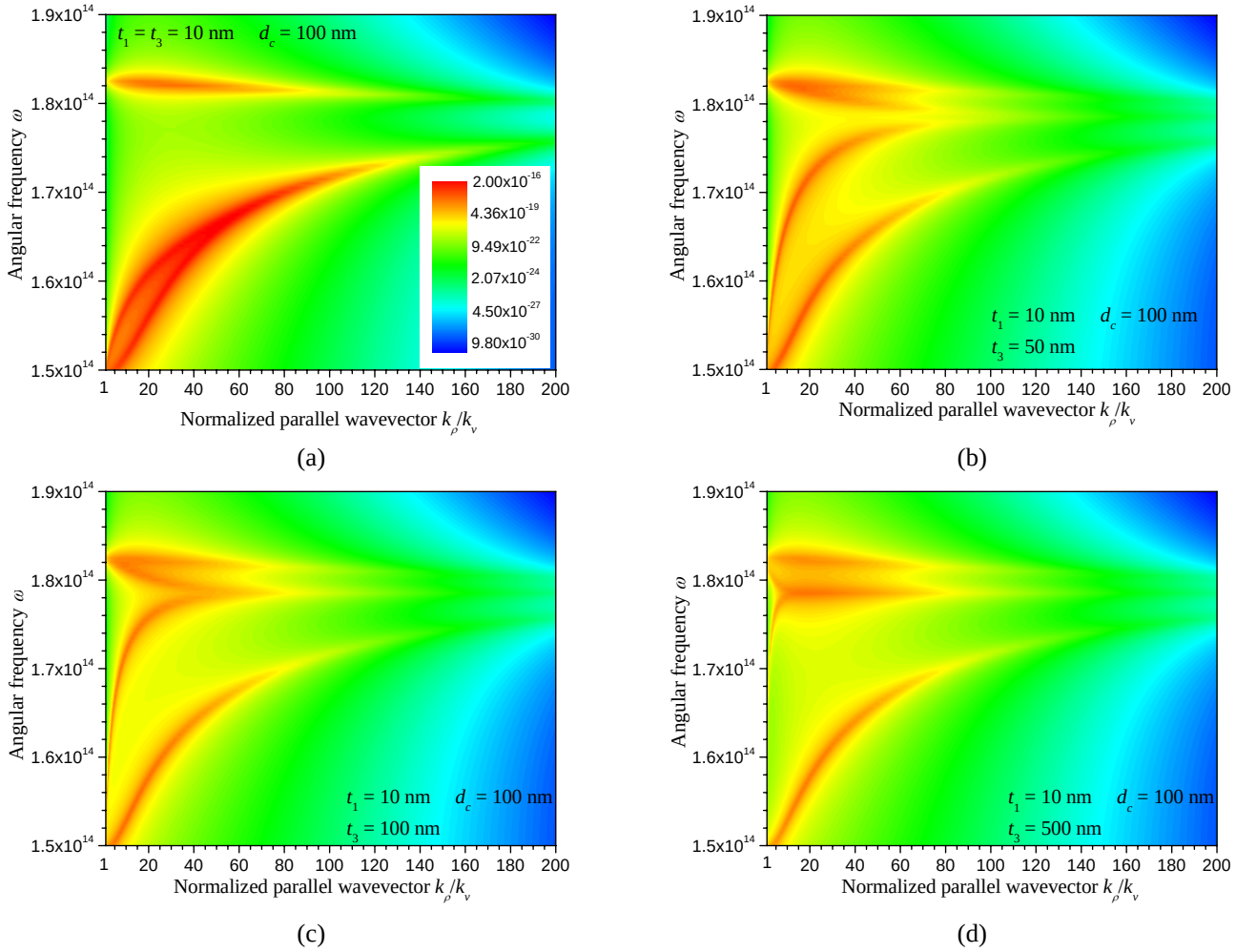


Figure 3. Spectral distribution of TM evanescent component of the radiative heat flux as a function of k_ρ (in log-scale) for t_1 = 10 nm and d_c = 100 nm: (a) t_3 = 10 nm. (b) t_3 = 50 nm. (c) t_3 = 100 nm. (d) t_3 = 500 nm. The scale shown in panel (a) is also valid for panels (b), (c), and (d).

ACKNOWLEDGEMENT

This work is partially sponsored by the Kentucky Science and Engineering Foundation (Grant No: KSEF-1718-RDE-011). Partial support for MPM is received from the FP-7-PEOPLE-IRG-2008 (Grant No: 239382) and a TUBITAK 1001 Grant (No: 109M170) at Ozyegin University, Istanbul.

REFERENCES

1. Park, K., Basu, S., King, W. P. and Zhang, Z. M., "Performance analysis of near-field thermophotovoltaic devices considering absorption distribution," *J. Quant. Spectrosc. Radiat. Transfer*, Vol. 109, 305-316, 2008.
2. Ben-Abdallah, P., Joulain, K., Drevillon, J. and Domingues, G., "Tailoring the local density of states of nonradiative field at the surface of nanolayered materials," *Appl. Phys. Lett.*, Vol. 94, 153117, 2009.
3. Francoeur, M., Mengüç, M.P. and Vaillon, R., "Local density of electromagnetic states within a nanometric gap formed between two thin films supporting surface phonon-polaritons," *J. Appl. Phys.*, in press, 2010.
4. Francoeur, M., Mengüç, M.P. and Vaillon, R., "Spectral tuning of near-field radiative heat flux between two thin silicon carbide films," *J. Phys. D: Appl. Phys.*, accepted, 2010.

The optical characteristics of planar bi-layered metallic prisms

K. Yamaguchi[1, 3], M. Fujii[2], T. Inoue[3], M. Haraguchi[3], T. Okamoto[3] and M. Fukui[3]

[1] Department of Electrical and Electronic Engineering, Toyohashi University of Technology, Japan

[2] Department of Electronics and Mechanics, Toba National College of Maritime Technology, Japan

[3] Department of Optical Science and Technology, The University of Tokushima, Japan

yamaguchi@eee.tut.ac.jp

Abstract A planar bi-layered silver prisms with rounded corner is shown to have a singular optical mode depends of gaps by numerical simulation. Such behavior results from the plasmon resonance in the pairs of nano prisms both the electric and the magnetic components of light.

1. INTRODUCTION

Localized surface plasmon (LSP) of metallic nano particle has recently received much attention [1]. The bi-layered structure that two metal films are formed on the both side a dielectric film (metal / insulator / metal) was expected to have a singular optical mode, and paid attention to achieve a negative refractive index [2, 3]. However, the discussion of the optical mode of bi-layered structure is especially undefined in nano particle. In this research we report the light intensity enhancement depended of gap distances consist from a polymethylmethacrylate (PMMA) film were sandwiched two silver prisms using the finite-difference time-domain method.

2. NUMERICAL METHOD

As shown in Fig. 1(a), a basic calculation structure of a planar bi-layered prism (Ag / PMMA (n_{PMMA}: 1.49) / Ag) with rounded corner was setup on a glass substrate of refractive index of 1.515 in air atmosphere (n_{air}: 1.00). The schematic cross sections represented in Fig. 1(b) and (c) are that of a planar bi-layered prism of x-z plane and y-z plane, respectively.

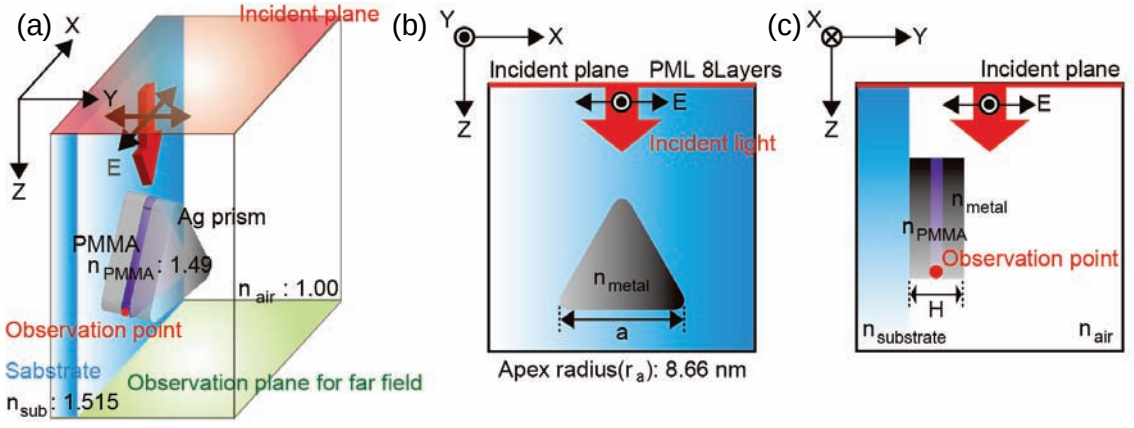


Fig. 1. Configuration for numerical simulation of a planar bi-layered prism (Ag / PMMA / Ag) with rounded corner. (a) Whole structure, FDTD geometry in a cross section of (b) x-z plane and (c) y-z plane. A planar bi-layered prism with side length, a, (as drown in Fig. 1 (b)) and height, H, (as drown in Fig. 1 (c)).

The height, the side length and the angle of prism were 25 nm, 100 nm and 60 degrees, respectively. Furthermore, the apex radius of prism was 8.66 nm. This apex radius of 8.66 nm is derived from the prism with smallest apex radius, in which we fabricate use of the focused ion beam [4]. The film thickness of PMMA was changed from 1 nm to 10 nm. Incident light intensity was 1×10^{-10} W/μm^2, the light polarized in the TE- and TM-polarized (x- and y-direction), parallel to the substrate surface illuminated toward the corner of prism. Then the light intensity enhancement was observed at an observation point (the red dot as shown in Fig. 1(a) and (c)), and the distributions of light intensity were calculated when LSP resonance occurs. The permittivity of the silver was expressed by the combination of the Drude model and Lorentz model.

3. RESULTS AND DISCUSSIONS

Figure 2 exhibits the wavelength dependency of light intensity enhancement effect at observation point from Fig. 1. In the incident light polarized TE-mode, two or three LSP resonance peaks were observed in visible range as shown in Fig. 2(a). Moreover, the wavelength of LSP peak resonances appeared the same wavelength depends on the gap distance. The light intensity enhancement decrease as the gap distance becomes large. By contrast, one LSP peak resonance peak was observed using the light polarized TM-mode. The wavelength of LSP peak resonance shifts red as the gap distance becomes large. The light intensity enhancement was the largest when the gap distance was 5 nm at TM-polarized. In these results, the light intensity enhancement of TM-polarized was 10 times TE-polarized.

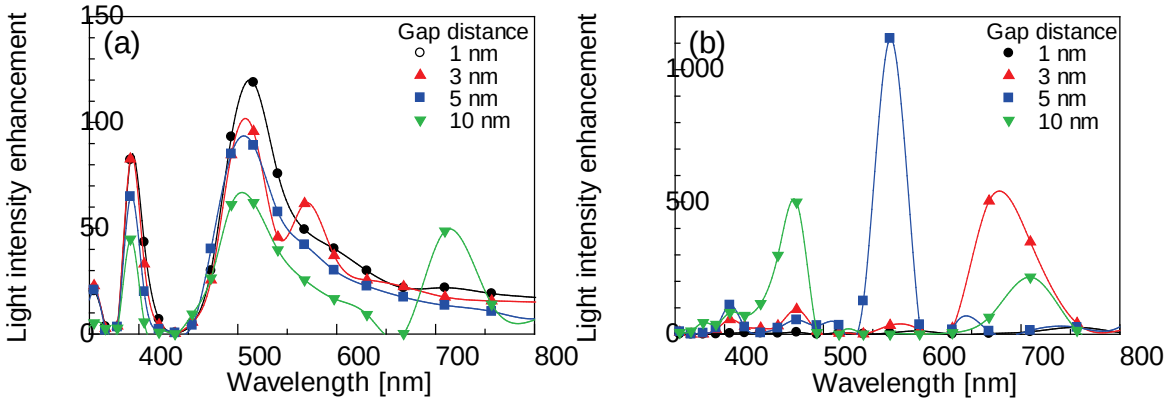


Fig. 2. The gap distance dependency of light intensity enhancement effect versus wavelength at (a) TE- and (b) TM-polarized. The black dot, the red triangle, the blue rectangle and the green triangle show the gap distance of a planar bi-layered prism of 1 nm, 3 nm, 5 nm and 10 nm, respectively.

The distributions of the light intensity enhancement in different gap distances of a planar bi-layered prism at TE-mode are shown in Fig. 3. From Fig. 3, the largest light intensity enhancement at the rounded corners in the air side was shown that 1×10^3 times, whereas about 10^4 times in the substrate side and the dielectric film side. The light intensity enhancement at the rounded corner decrease as the gap distance becomes large. The characteristic of the light intensity enhancement was the same as single nano prism when the gap distance was 1 nm. Therefore the light intensity distribution of the LSP mode resembles a so-called dipole mode [4]. However, the light intensity enhancement separate at the dielectric film as the gap distance becomes large. Namely, the incident light was localized into a large refractive index because of the refractive index difference around.

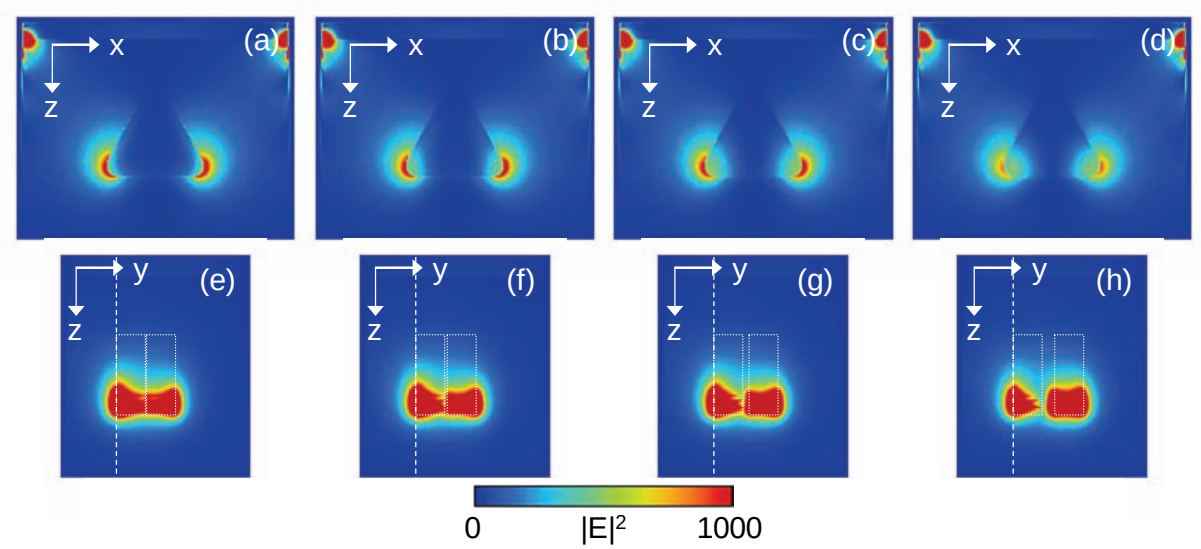


Fig. 3. Snap shots of distribution of light intensity in several nm gaps of a planar bi-layered prism at TE-polarized. (a), (b), (c) and (d) show the gap distance of 1 nm, 3 nm, 5 nm and 10 nm in a cross section of x-z plane, respectively. (e), (f), (g) and (h) show the gap distance of 1 nm, 3 nm, 5 nm and 10 nm in a cross section of y-z plane, respectively.

The distributions of the light intensity enhancement in different gap distances of a planar bi-layered prism at TM-mode are shown in Fig. 4. From Fig. 4, the light intensity enhancement was observed at corner and center in gap layer and shown that 1×10^3 times, whereas about 10^4 times in the dielectric film side. The light intensity enhancement at the dielectric film increase as the gap distance becomes large. The incident light was localized into the surface of the top prism when the gap distance was 1 nm. The light intensity enhancement focused in gap layer as the gap distance becomes large.

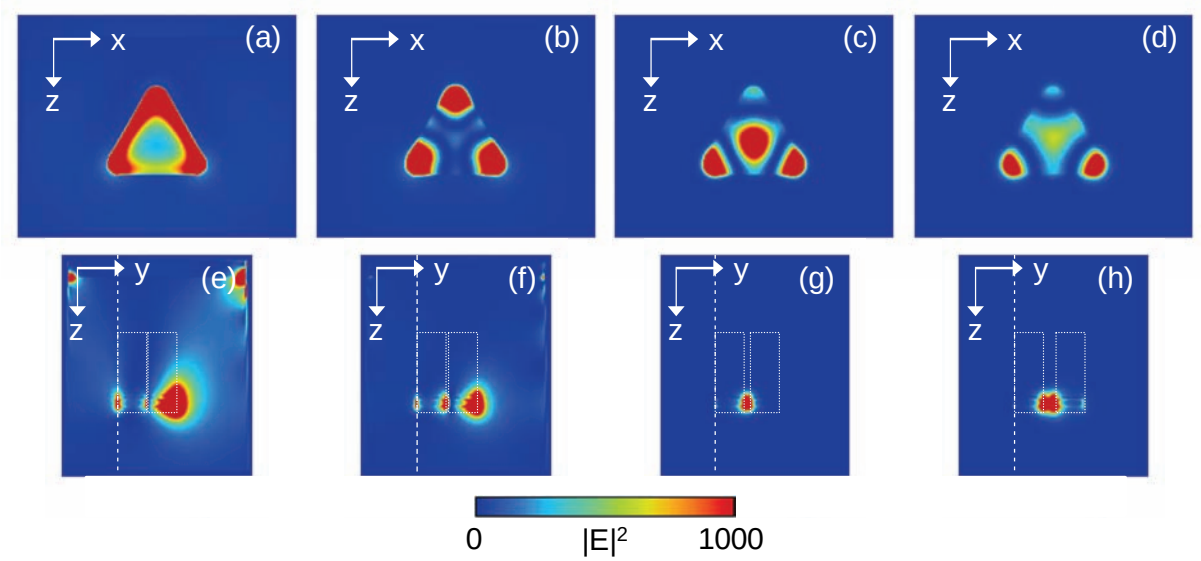


Fig. 4. Snap shots of distribution of light intensity in several nm gaps of a planar bi-layered prism at TM-polarized. (a), (b), (c) and (d) show the gap distance of 1 nm, 3 nm, 5 nm and 10 nm in a cross section of x-z plane, respectively. (e), (f), (g) and (h) show the gap distance of 1 nm, 3 nm, 5 nm and 10 nm in a cross section of y-z plane, respectively.

4. CONCLUSIONS

Figure 5 shows the relationship between the gap distance of a planar bi-layered prism and the characteristics of the light intensity enhancement. The characteristics of light intensity enhancement of the single nano prism and bowties with different gap distance, in which the side length, the apex radius and different gap distances are 100 nm, 8.66 nm, 20 nm and 1 nm, respectively, are shown by the red, blue and green lines, respectively [4, 5]. As a result, when the gap distance of a planar bi-layered prism becomes 5 nm at TM-mode, the light intensity enhancement of a planar bi-layered prism is clarified to be larger than that in single nano prism. Unfortunately, it has been understood that another gap distance and polarization, the light intensity enhancement is smaller than for a single nano prism. Therefore, this structure is not expected as for a large light intensity enhancement. However, we confirmed a very interesting distribution of light intensity in several nm gaps of a planar bi-layered prism at TM-polarized. Finally, we defined the optical mode of bi-layered structure in nano particle.

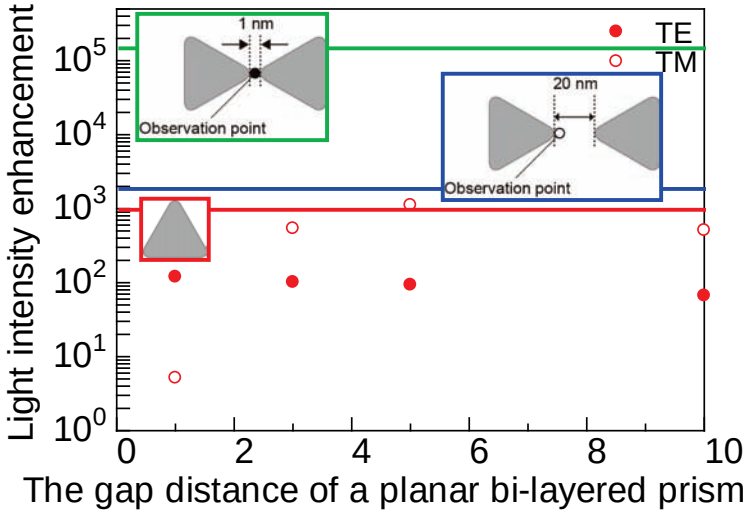


Fig. 5. The characteristics of light intensity enhancement of tripartite relationship (i.e., a planar bi-layered prism as indicated by the red dot and the red circle, single nano prism as indicated by the red line and nano bowtie as indicated by the blue and the green lines). The black dots and the black circles show TE- and TM mode, respectively. The blue and green lines show the difference gap distance of 20 nm and 1 nm, respectively.

REFERENCES

1. Haraguchi, M., T. Okamoto, T. Inoue, M. Nakagaki, H. Koizumi, K. Yamaguchi, C. Lai, M. Fukui, M. Kamano and M. Fujii, "Linear and Nonlinear Optical Phenomena of Metallic Nanoparticles," *IEEE J. Sel. Top. Quantum Electron.*, Vol. 14, No. 6, 1540–1551, 2008.
2. Soukoulis, C. M., S. Linden and M. Wegener, "Negative Refractive Index at Optical Wavelengths," *Science*, Vol. 315, 47–49, 2007.
3. SHALAEV, V. M., "Optical negative-index metamaterials," *Nat. Photonics*, Vol. 1, 41–48, 2007.
4. Yamaguchi, K., T. Inoue, M. Fujii, T. Ogawa, Y. Matsuzaki, T. Okamoto, M. Haraguchi and M. Fukui, "Characteristics of light intensity enhancement of a silver nanoprism with rounded corners," *J. Micros.*, Vol. 229, Pt. 3, 545–550, 2007.
5. Yamaguchi, K., T. Inoue, M. Fujii, M. Haraguchi, T. Okamoto, M. Fukui, S. Seki and S. Tagawa, "Electric Field Enhancement of Nano Gap of Silver Prisms," *Chin. Phys. Lett.*, Vol. 24, No. 10, 2934–2937, 2007.

Investigation of coupling length in a semi-cylindrical surface plasmonic coupler

Pouya Dastmalchi, Nosrat Granpayeh, and Majid Rasouli Disfani
Faculty of Electrical Engineering, K. N. Toosi University of Technology, P.O. Box 16315-1355, Tehran, Iran
Pouya_dastmalchi@ee.kntu.ac.ir

Abstract- We have investigated the performance of a nano-optical directional coupler based on gap plasmon waveguides. The coupler consists of two waveguides having a localized coupled plasmon propagating between two semi-cylindrical surfaces. After introducing a fundamental mode of studied waveguides, effects of the structure parameters on the coupling length are shown. Simulation results of the coupler obtained by the compact-2D finite-difference time-domain (FDTD) method comply with those derived by an analytic method with the aid of the finite-element frequency-domain (FEFD) software package of COMSOL.

1. INTRODUCTION

Achieving high speed and high efficiency information processing is one of the major goals in modern technology. Thus light could be an efficient carrier in optical integrated circuits and devices. In conventional dielectric optical devices, the diffraction of light is the limit of miniaturizing the devices [1]. This means that, these structures could not confine and localize the electromagnetic waves within a region smaller than their wavelength. To overcome this problem these materials have been replaced by metals, and surface plasmons have been used in metallic nanostructures [2-4]. In recent years, different metallic nanostructures, such as metallic gaps [5-6], triangular metal wedges [7], and metal V-grooves [8] have been widely studied and there have been great interests in the novel applications of these structures at optical frequencies. One of the most important devices in optical communications is directional coupler, the plasmonic types of which can be used in integrated structures [9, 10].

Coupling can be investigated from two points of view. From one side, it can be related to the crosstalk and demonstrates how much the plasmonic components can be integrated. On the other side, verifying the coupling between waveguides and investigating the effects of the parameters of the structures on coupling strength can lead to the design of directional couplers to be used in integrated optical circuits.

In this paper, after introducing a fundamental mode of the plasmonic waveguide which is used in our structure, we have demonstrated the effects of important parameters of a novel directional gap plasmon coupler on its coupling length. There are some numerical methods, such as finite-difference time-domain (FDTD) and finite-element method (FEM) that can be used for simulation of these structures to obtain their characteristics. The structures mentioned here have been simulated by compact FDTD method and the results have been confirmed by using an analytic method with the aid of the commercial finite-element frequency-domain (FEFD) software package of COMSOL.

2. Coupler Structure and Analysis Methods

We have investigated a coupler consisting of two slot waveguides, having a localized coupled plasmon propagating between two semi- cylindrical surfaces of radii R. The slot widths are W and the

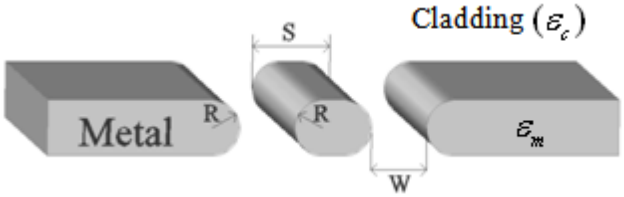


Figure 1. Configuration of the plasmonic coupler under study consisting of two identical slot waveguides of width W separated by a metal strip of width S. The radii of the semi-cylindrical surfaces are R.

separation distance between them is S (figure 1). The permittivities of the metal and cladding are ε_m, ε_c respectively.

For the fundamental mode at the free space wavelength of 632.8 nm, which we are focused on, the symmetric features of electric and magnetic field distributions of the anti-symmetric coupled semi-cylindrical surface plasmons (ACSCSPs) in each of these identical waveguides are similar to those in anti-symmetric coupled wedge plasmons (ACWPs) [11].

The slot waveguides in the coupler (Fig. 1) should be identical and satisfy the mirror symmetry relation:

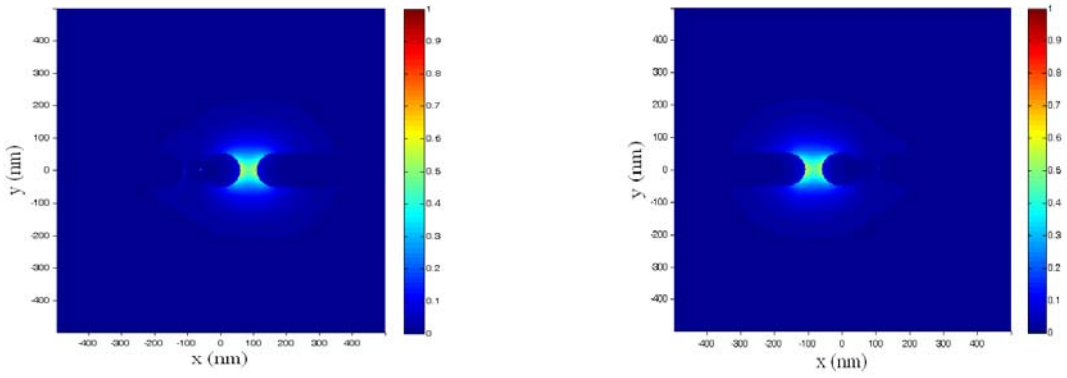
$$\varepsilon_r(x, y) = \varepsilon_r(-x, y) \tag{1}$$

where ε_r is the relative dielectric function. This condition causes that the guided modes in each of the waveguides have the same phase velocities, and leads to the possibility of energy coupling from one of the waveguides to the other. The coupler structure is supposed to be uniform along the propagation direction of z. If the propagation length is not too short and the lightwave has been launched in one of the waveguides, then the coupling length is [12]:

$$L_c = \frac{\pi}{k_s - k_a} \tag{2}$$

where k_s and k_a are the wave numbers of the symmetric and anti-symmetric modes of the coupler.

To simulate the proposed structure performance, two different approaches have been used: 2D-compact finite-difference time-domain (FDTD) algorithm [13], and results of an analytic method with the aid of a commercial finite-element frequency-domain (FEFD) software package (COMSOL). In the FDTD method, for simulating the metal we have modeled the motion of electronic charges using kinetic force equation [14] and substituted the current densities into the three dimensional Maxwell equations. By assuming that the structure is uniform along the z axis we could simplify the 3D problem into a 2D problem. The calculated area is surrounded by first-order Mur's absorbing boundary [15]. For excitation of our structure, a pulse is launched to one of the slot waveguides. The pulse is periodic along the z axis with a preselected period [13]. The input pulse propagates in one slot waveguide and gradually couples to the other one and vice versa. By deriving the temporal period of this coupling by FDTD method, and the phase velocity, which could be calculated by the wave number of the guided mode in the waveguide, the coupling length can be obtained. For example, in figure 2, by FDTD method, the electric field distributions are illustrated, while most of the lightwave is in the right waveguide (figure 2(a)) and after coupling time ($t_c \approx 1.33\times10^{-14}\,s$), the lightwave is coupled to the left one (figure 2(b)). Therefore, by finding this time of coupling, consequently we can calculate the coupling length.



(a) **(b)**

Figure 2. The field distribution, obtained by our compact-2D FDTD, while the lightwave is in the right waveguide **(a)** and while the lightwave is coupled to the left one after coupling time of $t_c \approx 1.335\times10^{-14}\,s$ **(b)**. Structure parameters are: $R = 50$ nm, $W = 50$ nm, $S = 120$ nm.

Also, by determining the wave numbers of symmetric and anti-symmetric modes using commercial finite-element frequency-domain (COMSOL), the coupling length can be calculated from Eq. 2.

3. Coupling Length as a Function of Coupler Parameters

3.1. Effect of separation distance

First, we have considered the dependency of the coupling length to the separation distance of the slot waveguides, S. As shown in figure 3, for the considered fundamental mode for a constant radius, R, increasing width S results in significant increase of the coupling length. The reason is that increasing S leads to reduction of coupling efficiency between two waveguides. The coupling lengths are calculated by FDTD method and equation (2) with the aid of COMSOL software. The difference in the results of the two methods may be returned to the different mesh types of the two methods.

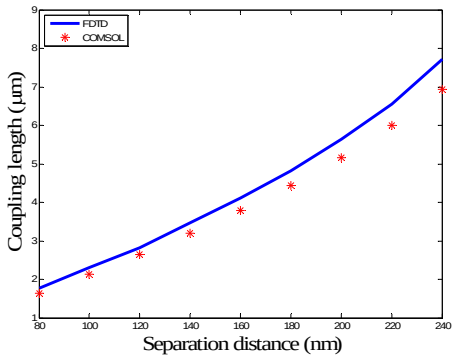


Figure 3. The dependency of the coupling length L_c for the considered coupled mode on the separation S between the waveguides of figure 1, with $\varepsilon_m = -16.2 + 0.52i$ (silver), $\varepsilon_c = 1$, $\lambda = 632.8\,\text{nm}$, $W = 100\,\text{nm}$, and $R = 50\,\text{nm}$. The results obtained by our compact-2D FDTD (solid) are compared with those of determined by equation (2) and COMSOL software (*).

3.2. Effect of radius of semi-cylindrical surfaces

When the radii of the semi-cylindrical surfaces are increased, in fact their sharpness is decreased leading to weaker localization of plasmons, smaller wave number, and higher coupling strength; hence it should result in decreasing the coupling length. But as shown in figure 4, the results are quite the contrary. The reason is that by increasing the radius, the volume occupied by the electric field is increased and the mode stores more energy. As a result, L_c increases with increasing radii because of the larger amount of stored energy which needs longer time to be coupled from one waveguide to the other, even though the coupling strength is increased.

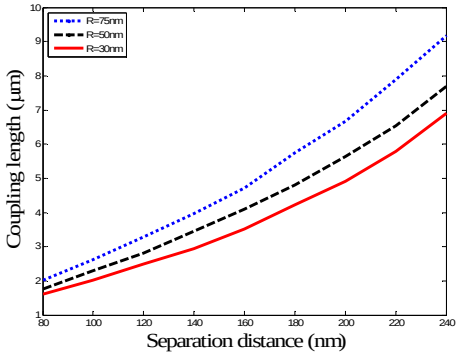


Figure 4. The dependencies of the coupling length L_c for the considered coupled mode on separation S between the waveguides of figure 1, obtained by our compact-2D FDTD for different radii with $\varepsilon_m = -16.2 + 0.52i$ (silver), $\varepsilon_c = 1$, $\lambda = 632.8\,\text{nm}$, $W = 100\,\text{nm}$.

3.3. Effect of waveguide widths

The other parameter which has been considered is the width of the slot waveguides, W, and the dependency of the coupling length on it. By decreasing the width, the wave number and correspondingly the localization of the fields are increased, so the coupling strength decreases. But again to get exact justification, the stored energy in the waveguides must be considered. By reducing W, the field confinement is increased leading to increasing the coupling length and on the other hand reducing the stored energy leading to decreasing the coupling length. As shown in figure 5, there is a specific separation distance in which these two factors frustrate each other and come to equilibrium. Therefore, in this separation distance, W will not be a critical parameter and will not affect significantly the coupling length. This means that when separation distance is less than a specific value, the effect of the amount of energy stored in waveguide is more powerful than the confinement effect. But the effects in larger separation distances are quite the contrary.

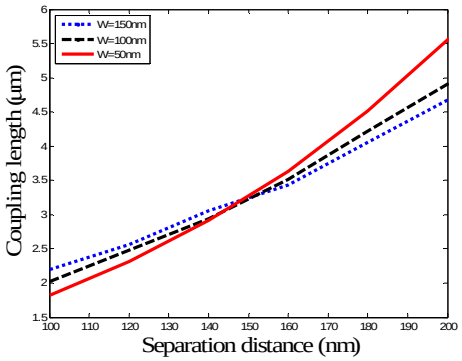


Figure 5. The dependencies of the coupling length L_c for the considered coupled mode on separation S between the waveguides of figure 1, obtained by our compact-2D FDTD, for different waveguide widths. $R = 30\,\text{nm}$ with $\varepsilon_m = -16.2 + 0.52i$ (silver), $\varepsilon_c = 1$, $\lambda = 632.8\,\text{nm}$.

4. CONCLUSIONS

In this paper, we have demonstrated the performance of a coupler based on gap plasmon waveguides. The dependencies of the coupling length on the structure parameters have been shown by the compact-2D-FDTD method and the results have been confirmed by using commercial finite-element frequency-domain (FEFD) software package of COMSOL. These directional couplers can be used in integrated nanophotonics according to their small dimensions and low coupling lengths.

ACKNOWLEDGEMENT

The authors thank Iran Telecommunication Research Center for the financial support of this project.

REFERENCES

1. Brongersma, M. L. and P. G. Kik, *Surface Plasmon Nanophotonics*, Springer, 2007.
2. Maier, S. A., P. G. Kik, H. A. Atwater, S. Meltzer, E. Harel, B. E. Koel and A. A. G. Requicha, "Local detection of electromagnetic energy transport below the diffraction limit in metal nanoparticle Plasmon waveguides," *Nature Mat.*, Vol. 2, 229-232, 2003.
3. Oulton, R. F., G. Bartal, D. F. P. Pile and X. Zhang, "Confinement and propagation characteristics of subwavelength plasmonic modes," *New J. Physics*, Vol. 10, 105018, 1-14, 2008.
4. Zia, R., M. D. Selker, P. B. Catrysse and M. L. Brongersma, "Geometries and materials for subwavelength surface plasmon modes," *J. Opt. Soc. Am. A*, Vol. 21, 2442-2446, 2004.
5. Pile, D. F. P., D. K. Gramotnev, R. F. Oulton and X. Zhang, "On long-range plasmonic modes in metallic gaps," *Opt. Express*, Vol. 15, 13669-13674, 2007.
6. Veronis, G. and S. Fan, "Guided subwavelength plasmonic mode support by a slot in a thin metal film," *Opt. Lett.*, Vol. 30, 3359-3361, 2005.
7. Boltasseva, A., V. S. Volkov, R. B. Nielsen, E. Moreno, S. G. Rodrigo and S. I. Bozhevolnyi, "Triangular metal wedges for subwavelength plasmon-polariton guiding at telecom

wavelengths," *Opt. Express*, Vol. 16, 5252-5260, 2008.
8. Vernon, K. C., D. K. Gramotnev and D. F. P. Pile, "Channel plasmon-polariton modes in V-grooves filled with dielectric," *J. Appl. Phys.*, Vol. 103, 034304, 2008.
9. Gramotnev, D. K., K. C. Vernon and D. F. P. Pile, "Directional coupler using gap Plasmon waveguides," *Appl. Phys. B*, Vol. 93, 99–106, 2008.
10. Hoffman, G. B. and R. M. Reano, "Vertical coupling between gap plasmon waveguides," *Opt. Express*, Vol. 16, 12677-12687, 2008.
11. Pile, D. F., P. D. K. Gramotnev, M. Haraguchi, T. Okamoto and M. Fukui, "Numerical analysis of coupled wedge plasmons in a structure of two metal wedges separated by a gap," *J. Appl. Phys.*, Vol. 100, 013101, 2006.
12. Veronis, G. and S. Fan, "Crosstalk between three-dimensional plasmonic slot waveguides," *Opt. Express*, Vol. 16, 2129-2140, 2008.
13. Pile D. F. P. "Compact-2D FDTD for waveguides including materials with negative dielectric permittivity, magnetic permeability and refractive index," *Appl. Phys. B*, Vol. 81, 607–613, 2005.
14. Christensen, D. and D. Fowers, "Modeling SPR sensors with the finite-difference time-domain method," *Biosens. Bioelectron.*, Vol. 11, 677-684, 1996.
15. Mur, G. "Total-Field Absorbing Boundary Conditions for the Time-Domain Electromagnetic Field Equations," *IEEE Trans. Electromagn. Compat.*, Vol. 40, 100-102, 1998.

Plasmonic Dicke effect

T. V. Shahbazyan, V. N. Pustovit

Department of Physics, Jackson State University
Jackson, MS 39217 USA
tigran.shahbazyan@jsums.edu

Abstract— We study cooperative emission by an ensemble of emitters, such as fluorescing molecules or semiconductor quantum dots, near a metal nanoparticle. The primary mechanism of cooperative emission is resonant energy transfer between emitters and plasmons rather than Dicke radiative coupling between emitters. The emission is dominated by three superradiant states with the same quantum yield as a single emitter, leading to a drastic reduction of ensemble radiated energy down to just thrice of that by a single emitter, the remaining energy being dissipated in the metal through subradiant states. We perform numerical calculations of system eigenstates and find that the plasmonic Dicke effect interactions affect is not impacted by the interactions between emitters or non-radiative losses in the metal.

1. INTRODUCTION

Superradiance of an ensemble of dipoles confined within a limited region in space has been discovered in the pioneering work by Dicke[1, 2] The underlying physical mechanism can be described as follows. Suppose that a large number N of dipoles with frequency ω_0 are confined in a volume with characteristic size L much smaller than the radiation wavelength $\lambda_0 = 2\pi/\omega_0$. Then radiation of an ensemble is a cooperative process in which emission of a photon is accompanied by virtual photon exchange between individual dipoles. This near field radiative coupling between dipoles leads to the formation of new system eigenstates, each comprised of all individual dipoles. The eigenstates with angular momentum $l = 1$ are *superradiant*, i.e., their radiative lifetimes are very short, $\sim \tau/N$, where τ is radiative lifetime of an individual dipole; the remaining states are *subradiant* with much longer decay times, $\sim \tau(\lambda_0/L)^2 \gg \tau$.

Recently, we extended the Dicke effect to plasmonic systems comprised of N dipoles located in the vicinity of a metal nanostructure, e.g., metal nanoparticle (NP), supporting localized surface plasmon (SP) [3]. In such systems, the dominant coupling mechanism between dipoles is *plasmonic* rather than radiative, i.e., it is based on virtual plasmon exchange (see Fig. 1). This plasmonic coupling leads to the formation of collective states, similar to Dicke superradiant states, that dominate photon emission. Furthermore, the metal nanostructure acts as a hub that couples nearby and remote dipoles with about equal strength and hence provides a more efficient hybridization of dipoles than does the radiative coupling. In general, as dipoles orientations in space are non-uniform, there are three superradiant states with total angular momentum $l = 1$, each having radiative decay decay $\sim N\Gamma^r/3$, where Γ^r is radiative decay rate of a *single* dipole near a nanostructure [3].

The principal difference between plasmonic and usual (photonic) Dicke effects stems from non-radiative energy transfer between the dipoles and the nanostructure. Let us first outline its role for the case of a *single* dipole near metal NP. When an excited emitter is located close to metal

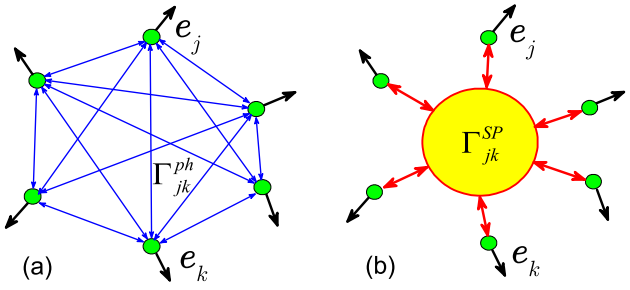


Figure 1: (Color online) Radiative coupling of emitters in free space (a), and plasmonic coupling of emitters near a metal nanoparticle (b).

surface, its energy can be transferred to optically inactive excitations in the metal and eventually dissipated (Ohmic losses). This is described by the *non-radiative decay* rate, $\Gamma^{nr} \propto d^{-3}$, where d is the dipole–surface separation [4]. As a result, the radiation of a coupled dipole-NP system is determined by a competition between non-radiative losses and plasmon enhancement [5]; this competition manifests itself through quantum efficiency as $Q = \Gamma^r/\Gamma$, where $\Gamma = \Gamma^r + \Gamma^{nr}$ is the *full* decay rate. Indeed, the radiated energy of dipole-NP system is $W = (\hbar kc/2)Q$, k and c being wavevector and speed of light, and its distance dependence follows that of Q: with decreasing d, the emission first increases due to plasmon enhancement, and then, at closer distances, it decreases due to suppression of Q by non-radiative losses in the metal. Both enhancement and quenching were observed in recent experiments on fluorescing molecules attached to a metal NP [6, 7, 8, 9, 10], and, not too close to NP surface, the distance dependence of *single-molecule* fluorescence [8, 9] was found in excellent agreement with single dipole-NP models [11].

When radiation takes place from an ensemble of emitters near metal nanostructure, there are *two* distinct types of plasmon-induced coupling mechanisms between the emitters. The first is *plasmon-enhanced radiative coupling*, described by the radiative decay matrix Γ^r_{jk}, where indexes $j, k = 1, \cdots, N$ refer to emitters. This mechanism is a straightforward extension of Dicke radiative coupling that incorporates SP local field into the common radiation field; hence, in similar way, the eigenstates of Γ^r_{jk} are superradiant and subradiant states. In the ideal case of "point sample", i.e., $kL \ll 1$, the subradiant decay rates are negligibly small and Γ^r_{jk} essentially has just three non-zero eigenvalues, corresponding to superradiant decay rates, each scaling with N according to $\sim N\Gamma^r/3$ [3]. The second coupling mechanism is *non-radiative energy transfer* between dipoles via NP plasmons. It can be viewed as plasmon-enhanced Forster transfer whereby a plasmon non-radiatively excited by one dipole transfers its energy to another dipole; this is described by non-radiative decay matrix, Γ^{nr}_{jk}. As a result, the system eigenstates are determined by the *full decay matrix* $\Gamma_{jk} = \Gamma^r_{jk} + \Gamma^{nr}_{jk}$, in contrast to the usual Dicke effect which involves only radiative coupling channel. Not too close to NP surface, the energy transfer takes place primarily via optically active dipole surface plasmon (SP) and therefore no significant mixing superradiant and subradiant states is expected. Therefore, the total radiated energy of the ensemble is just thrice that of the single dipole-NP system, $W_{ens} \simeq 3W$, regardless of the ensemble size. The remaining energy that is trapped in the $N - 3$ subradiant states is dissipated in the metal rather than emitted with a much slower rate.

Here we study the role of interactions in plasmon-mediated cooperative emission, which has several distinctive aspects. First, as the decay matrices contain plasmon pole, the relative strength of dipole-dipole interactions is effectively reduced as compared to that in the absence of NP. Second, there are additional corrections to emitters' frequency due to the fact that NP polarizability is complex, one originating from plasmon-enhanced radiative coupling and another from nonradiative coupling; these corrections, however, remain finite when dipoles approach each other. Therefore, the actual system eigenstates are determined by *both* the interactions and the energy exchange, and their frequencies and decays rates must be found simultaneously. Here we calculate the full spectrum of *interacting* emitters near a metal NP.

Specifically, we consider the common situation when emitters, e.g., fluorescent molecules or quantum dots, are attached to NP surface via flexible linkers. Typically, fluorophores bound to linker molecules have certain orientation of their dipole moments with respect to NP surface and, due to repulsive interactions, their angular positions are ordered rather then random.[7] Therefore, in our numerical simulations below, we assumed that angular positions of emitters coincide with the sites of spherical lattice, such as fullerenes. We find that the structure of system eigenstates reflects the competition between *all* coupling channels. Importantly, the interactions have *no* significant effect on superradiant states, so the cooperative emission remain intact. Specifically, the eigenstate most affected by direct dipole-dipole interactions is subradiant state with the smallest decay rate, while the frequencies of remaining subradiant states are determined by plasmon-mediated interactions, mentioned above.

2. NUMERICAL RESULTS

We consider an ensemble of N molecular dyes attached to an Ag spherical particle with radius $R = 20$ nm via molecular linkers at positions $\mathbf{r}_j$. The system is embedded in aqueous solution with dielectric constant $\epsilon_0 = 1.77$, and two types of dyes with quantum efficiencies $q = 0.3$ and

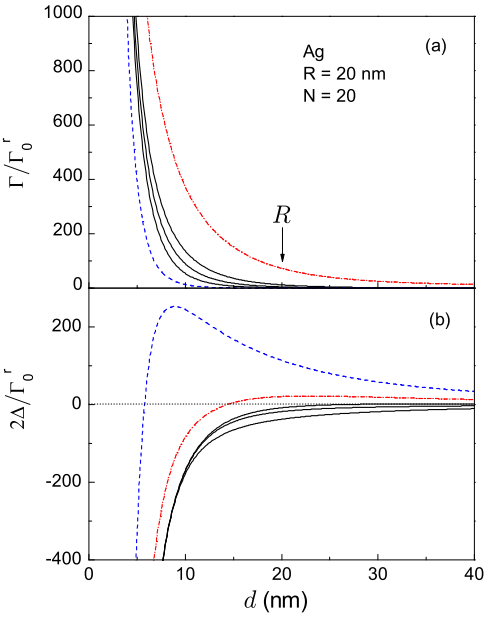


Figure 2: (Color online) Decay rates (a) and energy shifts (b) vs. distance for 20 dipoles in C20 configuration around Ag NP.

$q = 0.95$ are used in the calculations. In our simulations, the dyes with *normal* dipole orientations were located at the sites of symmetrical spherical lattice, specifically, fullerenes with $N = 20$, 32, 60, and 80 sites. The eigenstates are found by numerical diagonalization of self-energy matrix [3], $\Delta_{jk} - \frac{i}{2}\Gamma_{jk}$, with its real (energy shifts) and imaginary (recay rates) parts given by

$$\Delta_{jk} = \Delta^0_{jk} + \Gamma^r_0\alpha''_1\left(\frac{1}{r^3_j} + \frac{1}{r^3_k}\right)\cos\gamma_{jk} - \frac{3\Gamma^r_0}{4k^3}\sum_l \frac{\alpha'_l(l+1)^2}{r^{l+2}_j r^{l+2}_k}P_l(\cos\gamma_{jk}), \quad (1)$$

$$\Gamma_{jk} = \Gamma^r_0\left[1 + 2\alpha'_1\left(\frac{1}{r^3_j} + \frac{1}{r^3_k}\right) + \frac{4|\alpha_1|^2}{r^3_j r^3_k}\right]\cos\gamma_{jk} + \frac{3\Gamma^r_0}{2k^3}\sum_l \frac{\alpha''_l(l+1)^2}{r^{l+2}_j r^{l+2}_k}P_l(\cos\gamma_{jk}), \quad (2)$$

where P_l is Legendre polynomial, γ_{jk} is the angle between positions of dipoles j and k measured from NP center, Γ^r_0 is radiative decay rate of an isolated dipole, Δ^0_{jk} is the pair dipole-dipole interaction, and $\alpha_l(\omega) = \frac{R^{2l+1}[\epsilon(\omega)-\epsilon_0]}{\epsilon(\omega)+(1+1/l)\epsilon_0}$ is metal NP l-pole polarizability, $\epsilon(\omega)$ being metal dielectric function. Calculations were carried at the SP energy of 3.0 eV, the size-dependent Landau damping was incorporated for all plasmon modes, and NP polarizabilities with angular momenta up to $l = 30$ were calculated using the experimental bulk Ag complex dielectric function.

In Fig. 2, we plot distance dependences of complex eigenvalues for C20 configuration. There are five sets of eigenvalues with 3, 4, 4, 7, and 1-fold degeneracies, in descending order of Γ magnitudes. Down to the distance of $d = 5$ nm, the largest decay rates, corresponding to three predominantly superradiant states, are well separated from the rest. The steep rise of Γ at small distances is due to the dominant role of high-l plasmon modes in nonradiative coupling very close to NP surface [see Eqs. (2) and (1)]. The interplay between various coupling mechanisms is especially revealing when comparing the plots for Δ_J and Γ_J (curves for same eigenvalue sets have similar patterns). The superradiant states have the largest decay rate for all d and relatively small mainly *positive* frequency shift for $d \gtrsim R/2$; these states are dominated by *plasmon-enhanced radiative coupling*. The non-degenerate state with large *positive* energy shift and smallest decay rate is dominated by direct nearest-neighbor dipoles interaction; this state is least affected by the presence of NP and does not participate in the emission. The third group of states with mostly *negative* Δ_J and small Γ_J is dominated by *nonradiative plasmon coupling*. Closer to NP surface, the nonradiative coupling becomes dominant due to high-l plasmons and all states develop large decay rates and negative energy shifts.

For larger ensembles, the eigenstates have similar structure, as illustrated in Fig. 3 for C80

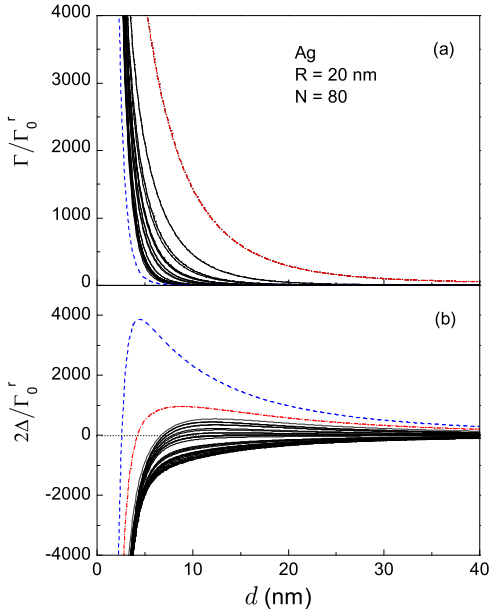


Figure 3: (Color online) Decay rates (a) and energy shifts (b) vs. distance for 80 dipoles in C80 configuration around Ag NP.

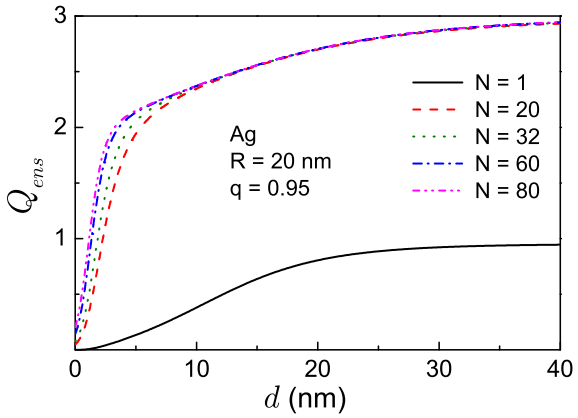


Figure 4: (Color online) Fluorescence quantum efficiency vs. distance for several ensembles of high-yield emitters on spherical lattices around AG NP.

configurations. There are three degenerate superradiant states and a nondegenerate subradiant state with longest lifetime that bears the main effect of dipole-dipole interactions. All the remaining subradiant states decay primarily through nonradiative energy transfer to NP with rates that are substantial only close to metal surface. This stands in sharp contrast to the usual cooperative emission by an ensemble of ideal dipoles, where the energy trapped in subradiant states is eventually radiated, albeit with a much slower rate, resulting in sharp spectral features of emission spectrum. Instead, in plasmonic systems, the trapped energy is dissipated in the NP and only small fraction of total energy leaves the system via superradoant states. Thus, the net effect of plasmonic Dicke effect is to drastically *reduce* the emission as compared to same number of individual dipoles. Remarkably, as the eigenvalues scale *uniformly* with N, the *quantum efficiencies* of superradiant states are nearly independent of the ensemble size, leading to the simple relation $Q_{ens} \simeq 3Q$.

This is illustrated in Fig. 4 which shows *ensemble* quantum efficiencies Q_{ens} for dyes with quantum yield $q = 0.95$. Two regimes can be clearly distinguished in the distance dependence of Q_{ens}: it first rises with the slope proportional to N, and then switches to slower rise after $d \simeq 5$ nm. The linear N-dependence of Q_{ens} indicates the dominant role of high-l plasmons in nonradiative coupling which prevent superradiant and subradiant states from being formed, while for larger distances the plasmon-enhanced radiative coupling is dominant leading to $Q_{ens} \simeq 3Q$ behavior.

3. CONCLUSION

We studied here plasmon-mediated superradiance from an ensemble of dipoles near metal nanoparticle. Our main conclusion is that the plasmonic Dicke effect is a robust phenomenon, more so than the usual photonic Dicke effect because of a more efficient hybridization of individual dipoles via nanoparticle plasmon. We have established that hybridization takes place through two types of plasmon coupling mechanisms, plasmon-enhanced radiative coupling and nonradiative plasmon coupling, the latter having no analogue in the usual Dicke effect.

An obvious application of the plasmon-mediated superradiance is related to fluorescence of a large but uncertain number of molecules linked to a metal nanostructure at some average distances from its surface. For single-molecule case, the modifications of fluorescence intensity with distance was proposed to serve as nanoscopic ruler [12], owing to the excellent agreement of measured distance dependences with single-dipole models [11]. In the case of molecular layer, the ambiguities caused by uncertain molecules number and distribution of their positions relative to the metal surface prevent, in general, determination of system characteristics from fluorescence variations. However, in the cooperative regime, the ambiguity related to molecules number is removed, and the intensity is essentially determined by $Q_{ens} \simeq 3Q$ with *distance-averaged* single-molecule quantum efficiency.

ACKNOWLEDGMENT

This work was supported in part by the NSF under grant Nos. DMR-0906945 and HRD-0833178, and under the EPSCOR Program.

REFERENCES

1. R. H. Dicke, Phys. Rev. **93**, 99 (1954).
2. A. V. Andreev, V. I. Emel'yanov, and Yu. A. Il'inskii, *Cooperative Effects in Optics* (IOP Publishing, 1993).
3. V. N. Pustovit and T. V. Shahbazyan, Phys. Rev. Lett. **102**, 077401 (2009).
4. R. R. Chance, A. Prock, and R. Silbey, Adv. Chem. Phys. **37**, 1 (1978).
5. M. Moskovits, Rev. Mod. Phys. **57**, 783 (1985).
6. E. Dulkeith, A. C. Morteani, T. Niedereichholz, T. A. Klar, J. Feldmann, S. A. Levi, F. C. J. M.. van Veggel, D. N. Reinhoudt, M. Moller, and D. I. Gittins, Phys. Rev. Lett. **89**, 203002 (2002).
7. E. Dulkeith, M. Ringler, T. A. Klar, J. Feldmann, A. M. Javier, and W. J. Parak, Nano Lett. **5**, 585 (2005).
8. P. Anger, P. Bharadwaj, and L. Novotny, Phys. Rev. Lett. **96**, 113002 (2006).
9. S. Kuhn, U. Hakanson, L. Rogobete, and V. Sandoghdar, Phys. Rev. Lett. **97**, 017402 (2006).
10. F. Tam, G. P. Goodrich, B. R. Johnson, and N. J. Halas, Nano Lett. **7**, 496 (2007).
11. J. Gersten and A. Nitzan, J. Chem. Phys. **75**, 1139 (1981).
12. J. Seelig, K. Leslie, A. Renn, S. K1uhn, V. Jacobsen, M. van de Corput, C. Wyman, and V. Sandoghdar, Nano Lett. **7**, 685 (2007).

Low loss surface polaritons and quantum memory in meta-materials

Ali A. Kamli [1,2,3] , Sergey A. Moiseev [4] , and Barry C Sanders [5]

[1] Department of Physics, King Khalid University, Abha;

[2] Department of Physics, University of Jazan , Jazan;

[3] And The National Centre for Mathematics and Physics, KACST, Riyadh, Saudi Arabia.

[4] Kazan Physical-technical Institute of Russian Academy of Sciences, Russia

[5] Institute for Quantum Information Science, University of Calgary, Calgary, Alberta , Canada.

Abstract

Coherent control of light field was a subject of numerous investigations and considerable progress has been achieved in last decades. There are a number of approaches to manipulation of the light field propagation in the media using optical solitons, photonic crystals electromagnetically induced transparency (EIT) , coherent population oscillation , and hole burning. For more extensive reviews the reader is referred to the literature.

EIT is based on the interaction of light with coherent resonant atomic ensembles which provides considerable enhancement of the interaction between the light and atoms. It is quite desirable to increase light–atom interaction in order to achieve high enough optical depth at the resonance atomic transition. This can be performed by increasing the medium size and density of the atoms, but practical applications and device sizes put some limitations on these methods. Another possibility is to increase the atom-photon coupling as it is exploited in the cavity quantum electrodynamics. In this work we propose to control slow surface polariton (SP) fields in meta-materials using EIT technique by exploiting the enhancement of the interaction between the SP modes and three-level atomic media. The aim of our investigation is to find the optimal conditions which can provide an effective quantum control of weak SP fields. Surface polaritons (SP) are electromagnetic excitations at the interface of two media. Strong spatial confinement of

SP leads to a huge enhancement of the electromagnetic field near the media surface, albeit these modes are notoriously lossy. Basic properties of SP field depend on the electrical and magnetic properties of the two media. In ordinary media ($\mu = 1$) only the electric SP modes can exist. Modern technology made it possible to artificially fabricate materials with both $\varepsilon < 0, \mu < 0$ called meta-materials where new types of SP modes can be effectively generated. We show that using a meta-material medium on one side of the structure provides the advantage to reduce SP losses and also to support both transverse electric and magnetic polarized SPs modes whereas in conventional materials only lossy transverse magnetic SPs exist. Here we theoretically study SP modes in meta-materials and discuss how to reduce SP losses. We study the properties of SP-SP-control which are determined by the strong spatial confinement of the SP modes, and their application for slow light control based on EIT. We show that the confinement increases the effective coupling coefficient between SP-modes and three-level atomic media which is then used in SP control. Using SP confinement, we demonstrate the possibility of very slow surface polariton fields with group velocity down to about 500 m/s at EIT conditions. Potential applications of SP fields in nano-photonics and quantum memory are highlighted.

References

1. A.V. Zayats, I. I. Smolyaninov and A.A. Maradudin, Phys. Rep. **408** , 131 (2005);

2. S.A.Maier, *Plasmonics: Fundamentals and Applications*, (Springer Science, New York, 2007).

3. Metamaterials: Physics and Engineering Explorations, edited by N.Engheta, R.W.Ziolkowski, (John Wiley & Sons, Inc. 2006]

4. M. Fleischhauer, A.Imamoglu and J.P. Marangos, Rev. Mod. Phys, 77 633 (2005).

5. P.W.Milonni, *Fast Light, Slow Light and Left-Handed Light* , (IOP, London ,2005) .

Investigated New Embedded Shapes of Electromagnetic Bandgap Structures and Via Effect for Improved Microstrip Patch Antenna Performance

D. N. Elsheakh[(1)], H. A. Elsadek[(1)], E. A. Abdallah[(1)], M. F. Iskander[(2)], and H. Elhenawy[(3)]
(1)Electronics Research Institute, Cairo, Egypt.
(2)Hawaii Center for Advanced Communication, Hawaii, Honolulu, USA.
(3)Faculty of Engineering, Ain Shams University, Cairo, Egypt.
dalia179175@yahoo.com

Abstract:- Three novel shapes of mushroom-like electromagnetic band-gap (EBG) structures are presented in this paper. The three shapes are based on rectangular metal strip with different combinations. The performances of the three-shape structures are studied by using both incident plane wave method and transmission coefficient approach. The effect of height and via location are also studied to achieve multi or wide band gap. These shapes are embedded in microstrip patch antenna substrate. The performance of the MPA is improved as increasing the antenna gain by 5dBi, decreasing the surface current so improving the antenna radiation pattern as well as reducing the antenna size by more than 70% compared to the original size. The new shapes of EBG structures are integrated with MPA as a ground plane, where the conducting ground plane is replaced by a high impedance surface EBG layer. Parametric studies are conducted to maximize their impedance bandwidth and gain. It is found that the antenna bandwidth increased by about four times than original band and its gain is similarly increased. Sample of these antennas are fabricated and tested, to verify the designs.

I. Introduction

In recent years, unique properties of electromagnetic band-gap (EBG) structures have made them applicable in many antenna and microwave applications. Various kinds of EBG structures have been suggested at microwave frequencies for applications in the electromagnetic and antenna community [1, 2]. EBG structures are periodic structures which can suppress the propagation of electromagnetic waves in particular frequency bands. The mushroom-like EBG structure with square patches connected to a dielectric substrate ground by vertical posts or metal-plated via was first developed by Sievenpiper et al in 1999 [1]. The study reveals that: first, the resonant frequency is decreased as via height increased and bandwidth of the bandgap is increased. Second, the resonant frequency is decreased when the position of via is moved from the patch center and the bandwidth of the bandgap is decreased. Curve fitting was used to obtain an approximate equations of the via effect on both bandgap resonance frequency and bandwidth. The new shapes parameters are compared with conventional square EBG mushroom shape.

A unique feature of the proposed structure is the realization of tuned two stop-bands without changing the size of the structure. By adjusting the position of via simultaneously, the frequency of the stop-band can be tuned easily over a wide frequency range and the antenna can be wideband by tuning the via position to produce staggered modes. The metal patch area used in these shapes is less than that used in the conventional square patch at the same periodicity and same resonance of the bandgap. Therefore, the performance of the structure is maximized by occupying the spacing area between patches by embedding another structure with smaller dimension to get another bandgap. Two main interesting features associated with this EBG structures which are suppression of surface waves and increased in-phase refection coefficient bandwidth [3, 4]. Suppression of surface waves results in higher efficiency, smoother radiation pattern, and less back lobe and side lobe levels in antenna applications [5]. On the other hand, these structures are used in design of low profile antennas because the radiating current lies directly adjacent to the ground plane without being shorted. Then embedding these shapes of EBG structure on the MPA substrate improves the performance compared with conventional square shape. As well as integrating these structures as a ground plane of MPA increases the antenna bandwidth and reduces the antenna size.

II. Design the Model of a Unit Cell and Equivalent Circuit

The three new shapes of EBG structures are investigated and compared with conventional square shape of EBG. Both incident plane wave method and suspended microstrip line approach are utilized to investigate the performance of these shapes. Geometries of the four shapes of EBG cell are shown in figure 1. The

EBG structure is designed on a substrate with relative permittivity ε_{r2} = 10.2 and height h_2 = 1.25 mm. The side length of the square patch is L = 5 mm. The center of the pad is connected to the ground plane by a thin metal via with a radius r = 0.25 mm. The dimensions of the three new shapes consist of metal strip with length **L**=5mm and width W =1mm for the fist shape like add sign (**plus shape**), second shape is obtained by rotating the plus sign with 45 degree (**cross shape**) and the final shape is composed of the two previous shapes (**compound shape**). All structures have the same periodicity P=5.5mm and h_2 varies between 0 to 2.45 mm to study its effect. The relative permittivity of the supporting material is ε_{r1} = 10.2 and the width of 50Ω microstrip line is d = 2.1mm. The coupling between the microstrip line and the patch generates a capacitance C_1, the coupling between the embedded EBG and the ground plane creates a capacitance C_2, and the metal via yields an inductance L, C_{offset} is an additional capacitance due to displacement of via hole from the center of the patch. The effect of via can be represented by an additional capacitor due to increasing the area of the patches. C depends on the patch area from the center patch edge and C_{offset} depends on the area from the patch center to via position. variation of the via height effect for the four shapes on bandgap resonance and bandwidth are studied. A curve fitting approach is used to generate an approximate equation for each shape as given in table 1.

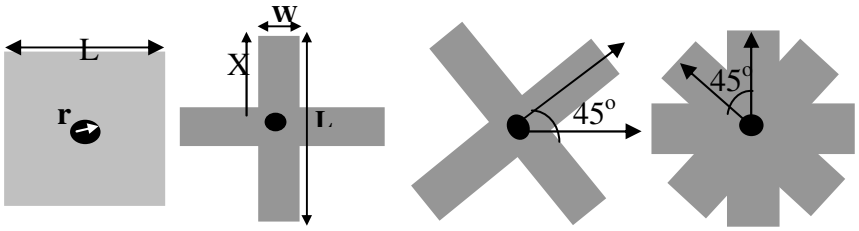


Fig.1: Geometry of the four suspended patches EBG unit, (a) square shape, (b) plus shape, (c) cross shape and (d) compound plus-cross shape

Table 1: The bandwidth and resonance frequency of embedded EBG patches as function of h_2 (mm).

Shapes / Parameters	Square shape	Plus shape	Cross shape	Compound shape
Bandwidth	$\frac{1}{0.94 - 0.211\ h_2}$	$\frac{1}{0.946 - 0.2411\ h_2}$	$\frac{1}{1.386 - 0.416\ h_2}$	$\frac{1}{2.2 - 0.712\ h_2}$
Resonance frequency	$4.13\cos(0.43h_2)$	$4.38\cos(0.44h_2)$	$4.852\cos(0.45h_2$	$5.25\cos(0.477h_2)$

The effect of via position is also studied as given in table 2, where X is the distance between the center of the via hole and the center of the patch. Note that as position of the via is changed, the distance between via and the edge of the metal patch decreases. The distribution of electric field on the patch will change as well. By adjusting the position of the via, the center frequency can vary in a certain range. From above equations, the inductor is nearly fixed and the capacitor increases so resonance frequency decreases as well as bandwidth of the bandgap as given in table 2. It can be noticed that the bandwidth of the new shapes are larger than conventional square shape at the same resonance frequency and the same periodicity. Moreover, metal area used for these three shapes is less than used in square from L^2 to 2WL, 2WL and 4WL, respectively. From this concept we can use two columns with center via followed by two columns with offset via so the bandwidth can be increased to achieve broadband of EBG band gap.

Table 2: The bandwidth and resonance frequency of embedded EBG patches as function of via position X (mm).

Shapes / Parameters	Square shape	Plus shape	Cross shape	Compound shape
Bandwidth	-0.388X+1.5	-0.1657X+1.7	-0.1X+2	-0.286X+2.16
Resonance	-0.88X+7.483	-1.083X+7.433	-0.988X+6.729	-0.86X+6.58

As mentioned earlier when position of the vias is moved off the center of the metal, the bandwidth of the stop-band is decreased as well as decreasing the resonant frequency of the band. So, we use two columns when vias are at the center followed by two columns with offset vias. The four columns units which have the same patches and radius of via are arranged along the *Y*-direction to form a cascaded structure. The reflection angle is also studied by using plane wave incident on a single unit cell for these shapes and compared with conventional square shape, then the effect of via position is studied.

As mention before, the metal patch areas used in these three shapes are smaller than that used in square at same periodicity. So, dual band-gap structures are provided by occupying the space area between these patch cells and printing another patch with different dimension as shown in figure 2. The transmission coefficient response for this structure is shown in figure 3. The two structures are fabricated and their photos are shown in figure 4.

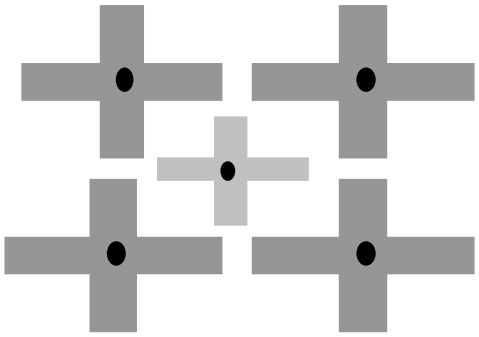


Fig. 2: The geometry of two different shapes together

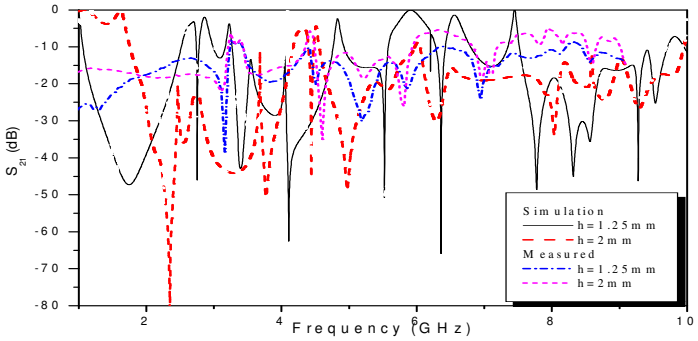
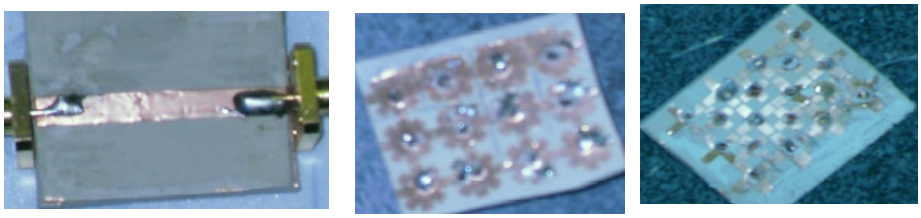


Fig. 3: The transmission response for the structure shown in fig. 2



(a) (b) (c)

Fig. 4: The fabricated structures (a) transmission line, (b) wide band gap structure and (c) dual band gap structure

III. Microstrip Antenna Performance

The MPA is applied at the surface of the structure instead of the transmission line with dimension W_p and L_p equal to 12mm and 11mm, respectively. The substrate dimension W_g xL_g = 30x30mm^2 with height 2.5mm and W_f =2.1mm as shown in figure 5. The antenna resonates without embedded EBG at 3.8GHz. The three new shapes are embedded in the MPA substrate as well as the conventional square shape, then the antennas performances are simulated and the results are given in table 3.

Table 3: The antenna performance with different embedded EBG shapes.

Types / Antenna parameters	Patch without EBG	Patch with embedded square	Patch with embedded plus	Patch with embedded cross	Patch with embedded compound
Frequency (GHz)	3.8	3.4	3	2.9	2.65
Gain (dBi)	2.5	3.5	4.75	5.5	7
Fractional bandwidth	5%	2.9%	3%	3.1%	3.5%

It was found that for an EBG patch antenna operating at the fundamental mode, the embedded EBG patch size is significantly smaller than the size of the radiator patch without EBG. This property is useful for antenna miniaturization. The antenna reflection coefficient is shown in figure 6, without and with embedded EBG. From this figure it is noted that the compound shape reduces the antenna size by 25% at height =1.25mm and by increasing the via height to 2.45mm, the resonance frequency reaches 1.1GHz which indicates 70% size reduction from the original size. In addition to increasing the antenna gain by 4.5dBi than that of the conventional MPA.

Compound EBG as a ground plane is used to increase antenna bandwidth and improve antenna reflection coefficient. The EBG ground plane was built on RTD6010 substrate with dielectric constant 10.2 and thickness 2.5mm, then the radiator of microstrip patch antenna was built on foam substrate with dielectric constant 1.7 and height=2.5mm. The prototype geometry is shown in figure 5. The comparison between reflection coefficient for the antenna with and without EBG is shown in figure 6. Figure 6 shows that the bandwidth is increased by about four times than the original bandwidth with 18 % reduction in antenna size. It gives better reflection coefficient by -10dB than using conventional ground.

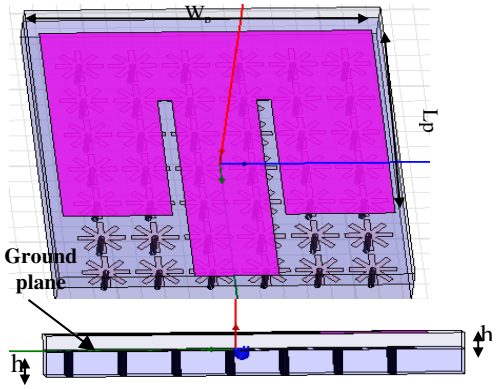


Fig. 5: The antenna geometry with EBG ground plane.

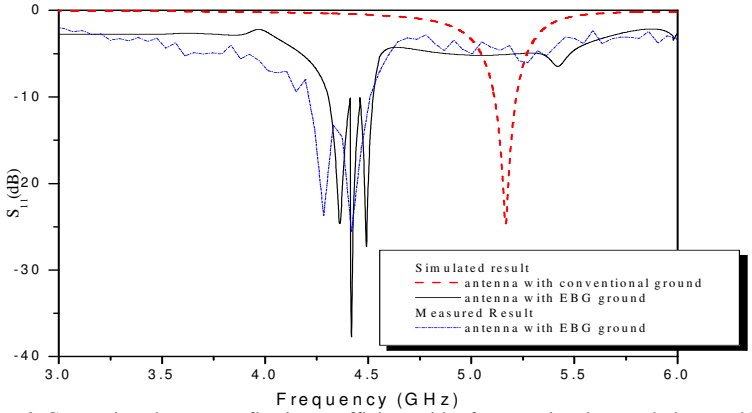


Fig. 6: Comparison between reflection coefficient with of conventional ground plane and EBG

IV. Conclusion

This paper presented three new shapes of unit cell patches used as EBG structure. These shapes give performance better than conventional square EBG. The effect of via height and position were studied and new equations that describe the relation between bandgap resonance and bandwidth with height and position of via were derived. Multi-band and broad-band were achieved by using two ways, first by cascaded two columns with different via positions and second by occupying the space area between unit cells with another type of EBG structures. The compound shape is used as embedded EBG and integrated with microstrip patch antenna. It was found that for an EBG patch antenna operated at the fundamental mode, the patch size is significantly smaller than the size of a conventional microstrip patch. This property is useful for antenna miniaturization. For the MPA with the EEBG substrate, and operating inside its bandgap, antenna area is reduced by 70% compared to original size and increasing the antenna gain by 4.5dBi. Detailed parametric studies were conducted for patch antennas with an embedded EBG substrate. Then the compound EBG shape was integrated as a ground plane of microstrip patch antenna. The patch antenna was designed to work within its bandgap. Bandwidth is increased by about four times than the original bandwidth with 18 % reduction in antenna size. It gives better reflection coefficient by -10dB than that using conventional ground.

V. References

[1] Sievenpiper, D.,L. Zhang ,R. F. J. Broas, N. G. Alexopolous, and E. Yablonovitch, "High impedance electromagnetic surfaces with a forbid-den frequency band," *IEEE Trans. Microwave Theory Tech.*, Vol. 47, PP: 2059–2074, 1999.

[2] Yan, D.-B.,Q. Gao,Y.-Q. Fu, G.-H. Zhang, and N.-C. Yuan, "Novel improvement of broad band AMC structure," *Chinese Journal of Radio Science*, Vol. 20, PP: 586–589, 2005.

[3] Cheng-Chi Yu, Meng-Hsiang Haung and Yao-Tien Chang, " A novel electromagnetic bandgap (EBG) structure for electromagnetic compatibility (EMC) application," Progress In Electromagnetics Research Symposium, China, PP: 581-585, March 2009.

[4] Lee, D. H.,J. H. Kim, J. H. Jang, and W. S. Park, "Dual-frequency dual-polarization antenna of high isolation with embedded mushroom-like EBG cells," *Microwave Opt. Technol. Lett.*, Vol. 49, PP:1764–1768, 2007.

[5] K.-L. Wong, *"Compact and Broadband Microstrip Antennas*", New York: Wiley, 2002.

Dual-band microwave duplexer based on metamaterial concepts

A.Vélez*, G.Sisó, A.Campo, M.Durán-Sindreu, J.Bonache and F. Martín
CIMITEC, Departament d´Enginyeria Electrònica, Universitat Autónoma de Barcelona, Spain
Adolfo.velez@uab.cat

Abstract- In this paper, a dual-band duplexer based on metamaterial inspired resonators is presented. To this end, a complex system, composed of several microwave components based on metamaterial-inspired resonators, such as complementary split ring resonators (CSRRs) and spiral resonators (SRs) has been designed in order to implement this dual-band communication system. CSRRs are used in order to implement hybrid couplers, while SRs are used to implement two identical dual-band band-stop filters. Simulation results show the functionality of this system and the clear size reduction compared to the standard approach.

1. INTRODUCTION

Complementary split ring resonators (CSRRs) have been used for the design of compact filters [1-8] and diplexers [9] since they are electrically small resonant particles. For instance, combined with series gaps in microstrip technology, CSRRs can be applied to the synthesis of artificial lines exhibiting backward (or left handed) wave propagation at low frequencies and forward (or right handed) wave propagation at high frequencies [10], and these composite right/left handed (CRLH) lines have been demonstrated to be useful for the design of dual-band microwave components with arbitrary (within certain margins) operating frequencies. On this basis, CSRR-based CRLH lines have been recently applied to the synthesis of dual-band power splitters [11] and hybrid couplers [12] by the authors. In these implementations, the required characteristic impedance and electrical length of the different transmission line sections of the structures at the two system frequencies are achieved thanks to the controllability of the line impedance and the dispersion diagram of these CSRR-based lines.

In the present paper, the main aim is to demonstrate that a complex dual-band system consisting on a combination of several microwave components implemented by means of CSRR- or SR-based lines, can be achieved. Specifically, we will consider the design of a dual-band microwave diplexer for operation at the mobile GSM bands (0.9GHz and 1.8GHz).

2. DUPLEXER ANALYSIS AND DESIGN

The main idea on the design of a communications duplexer is to implement a system able to transmit and receive under some arbitrarily fixed frequencies. In this case, the chosen frequencies correspond to the GSM bands 0.9 GHz and 1.8 GHz. Both, emission and reception frequencies, named uplink and downlink, are fixed for each GSM band and defined into a closed and narrow frequency band separated by a small interval. The implementation of this system has been typically solved in literature for the mono-band case [13] by means of two conventional branch line hybrid couplers and a band-reject filter. While the hybrids were used to ensure transmission in the limited frequency bands, the filter is needed to ensure rejection at the receiving frequencies. The typical scheme for this standard approximation is depicted in Fig.1.a. As it can be seen from Fig.1.a, on

hybrid A, port (1) represents the TX port while ports (2,3) are connected to identical band-stop filters connected to hybrid B. Port (4) is matched to a 50 Ω load. The filter has to be properly tuned in order to allow all the frequencies into the GSM bands pass to the antenna (port 3 on hybrid B) except those belonging to the RX band that will be received by the antenna (port 3 on hybrid B) and rejected afterwards by the filters to be redirected to the RX port (port 2 on hybrid B).

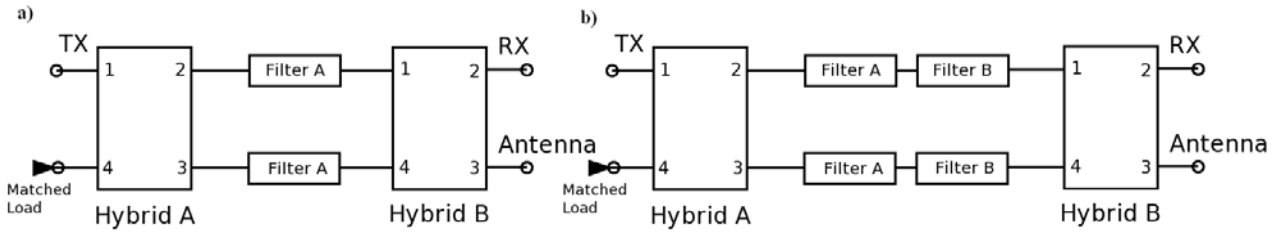


Fig.1 Duplexer scheme for the mono-band case (a) and dual-band case (b)

The proposed dual-band system design consists on a similar approximation to the problem, but in this case extended to two different GSM bands. To that end, a system integrated by two dual-band hybrids and two dual-band band-reject filters cascaded between the hybrids has been designed. The scheme for this approximation is depicted in Fig.1.b. For the hybrid design, the same approximation used by Bonache *et al*. has been implemented [12]. On this metamaterial approach, conventional lines implemented on the conventional configuration [13] have been substituted by composite right-left handed CRLH microstrip 50 Ω and 35 Ω lines loaded with complementary split ring resonators (CSRR). The width and the length of the lines are imposed in order to ensure the proper impedance and phase requirements respectively, as well as the CSRRs dimensions needed to ensure transmission at the required frequencies. Hybrid dimensions are equal to those presented in [12]. This approach constitutes the key point in the present design due to the use of these CRLH lines. The designed hybrid shows a composite response, that is, two transmission bands can be obtained, a LH (first one) and a RH (second one), giving rise to dual band operation. Moreover, this constitutes important size reduction due to the short electrical length of the left handed lines compared to the conventional lines. Thus, it takes advantage of the special characteristics of metamaterials in terms of electrical length allowing the designer to obtain much smaller dimensions than for the conventional mono-band case. The frequency response is depicted in Fig. 2 together with the layout. As it can be seen, these hybrids show good performance in both frequency bands. Nevertheless, the obtained frequency response is narrow, specifically for the first band but not representing this narrow band response a significant restriction parameter, due to the important proximity between TX and RX sub-bands for each GSM band.

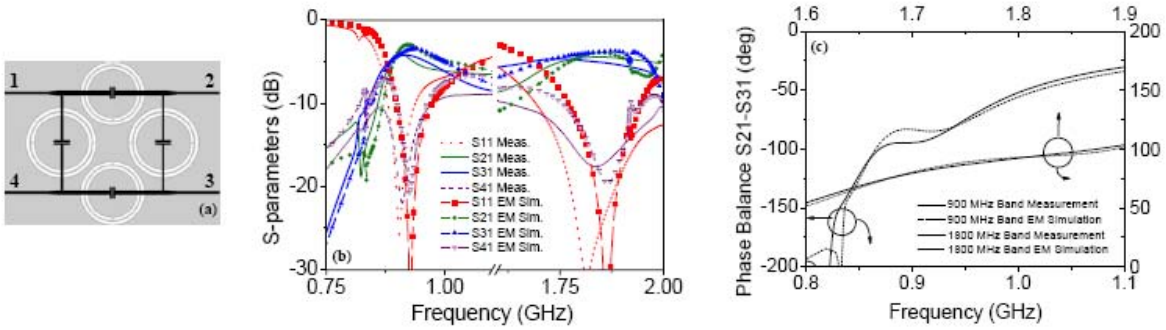


Fig.2 Layout of the hybrid (a), S parameters (b) and phase response (c). The considered substrate is the Rogers RO3010 with thickness h=635µm and dielectric constant ε_r=10.2. Dimensions are r_{CSRR1}=7.4mm (35Ω lines), r_{CSRR2}=7.9mm (50Ω lines), c_{CSRR1}= c_{CSRR2}=0.5mm (width of the rings), d_{CSRR1}= d_{CSRR2}=0.5mm (distance between rings), W_{50}=0.46mm (width of the 50Ω lines) and W_{35}=1.0mm (width of the 35Ω lines). Extracted from [12]

Due to this known proximity between TX and RX regions, and the narrow characteristics of each band imposed by the hybrids, band-reject filters are needed to be very frequency selective in order to ensure proper reception. To this end, spiral resonators (SRs) coupled to the host microstrip lines have been chosen due to its characteristic narrow band response. In order to obtain dual band operation, two different size resonators are implemented, each one tuned at the RX frequency for its correspondent band. Due to the transmission response characteristics of the SRs, only one resonator is enough to achieve the needed rejection level to ensure proper reflection from antenna to RX port. Fig.3.(a,b) show the transmission response for the final implemented filters on each band. The layout for the filters is depicted on Fig.3.c

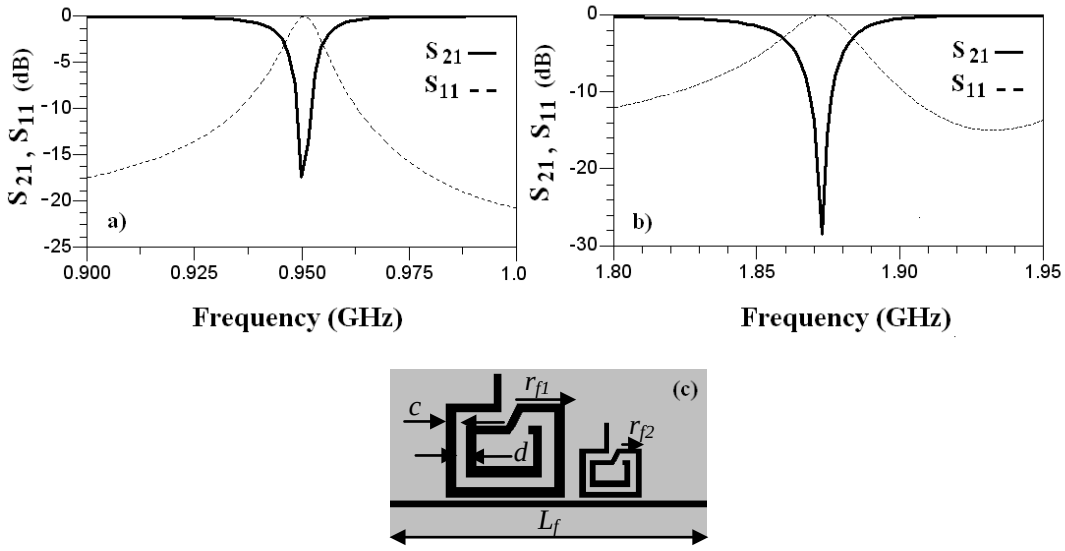


Fig.3. Simulated response for the 0.9 GHz band (a). Simulated response for the 1.8 GHz band (b). Layout of the filters (c), dimensions are: length L_f=21.44mm, r_{f1}=6mm, r_{f2}=3mm, ring width (for the 0.9 GHz band) c=0.5mm, ring loops separations (for the 0.9 GHz band) d=1.1mm, ring width (for the 1.8 GHz band) c=0.5mm, ring loops separations (for the 1.8 GHz band) d=1.1mm. The separation between the line and the rings is 0.15mm.

3. RESULTS

The final layout proposed for the dual-band duplexer is depicted in figure 4. As it can be seen, filters are placed in between both hybrids A and B on a symmetric configuration. Also, they have been allocated in the outside region of the microstrip lines in order to avoid possible coupling and undesirable interactions between lines. The final dimensions of the system are proved to be much smaller than those resulting with the conventional approach [13] for the mono-band case. Total length of the fabricated system is depicted in Fig.4. Simulation results inferred from electromagnetic simulations (*Agilent Momentum*) are depicted in figure 5 and show good performance for the system with a good TX and RX levels for both bands. Also isolation has been successfully achieved (15 dB on 0.9 GHz band, 25 dB on 1.8 GHz band).

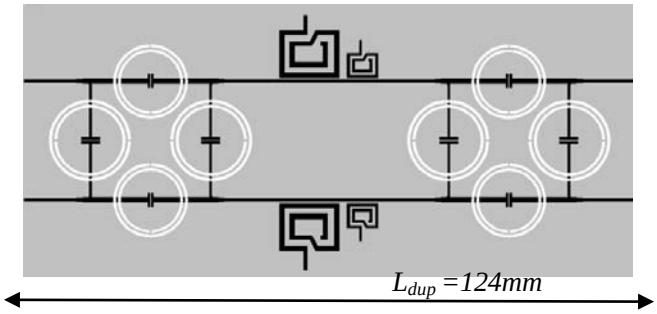


Fig.4 Layout of the hybrid (a).

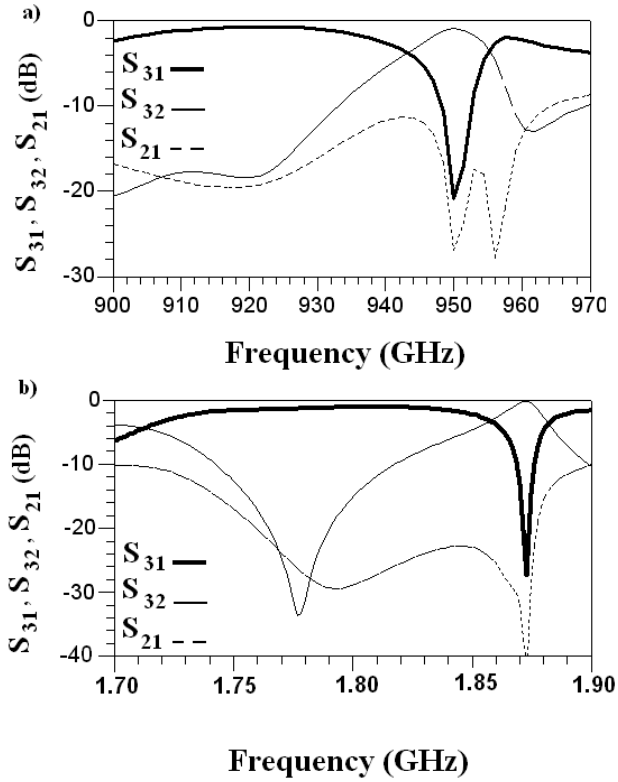


Fig.5. Simulated dual-band duplexer response for the 0.9 GHz band (a). Simulated dual-band duplexer response for the 1.8 GHz band (b).

ACKNOWLEDGEMENT

This work has been supported by MEC (Spain) by project contract TEC2007-68013-C02-02 METAINNOVA. Thanks are also given to Generalitat de Catalunya) for funding CIMITEC and GEMMA (project 2009SGR-421). The authors are in debt with MCI for giving us the CONSOLIDER INGENIO 2010 project EMET CSD2008-00066 F. Martín acknowledges the ICREA Foundation (Generalitat de Catalunya and Fundació Catalana per a la Recerca i la Innovació) and VPE-Parc de Recerca (UAB) for supporting his work.

REFERENCES

1. R. Marqués, F. Martín, M. Sorolla, Metamaterials with negative parameters : theory, design and microwave applications, John Wiley, New Jersey, 2007.
2. J. Bonache, F. Martín, J. García-García, I. Gil, R. Marqués and M. Sorolla, "Ultra wide band pass filtres (UWBPF) based on complementary split rings resonators", Microwave and Optical Technology Letters, vol. 46, pp.283-286, August 2005.
3. J. Bonache, F. Falcone, J.D. Baena, T. Lopetegi, J. García-García, M.A.G. Laso, I. Gil, A. Marcotegui, R. Marqués, F. Martín and M. Sorolla, "Application of complementary split rings resonators to the design of compact narrow band pass structure in microstrip technology", Microwave and Optical Technology Letters, vol. 46, pp. 508-512, September 2005.
4. J. Bonache, I. Gil, J. García-García, F. Martín, "Novel Microstrip Band Pass Filters Based on Complementary Split Rings Resonators", IEEE Transactions on Microwave Theory and Techniques, vol. 54, pp. 265-271, January 2006.
5. P. Mondal, M.K. Mandal, A. Chakrabarty, S. Sanyal, "Compact bandpass filters with wide controllable fractional bandwidth", IEEE Microwave and Wireless Components Letters, vol. 16, pp. 540-542, October 2006.
6. H-W. Wu, Y-K. Su, M-H. Weng, C-Y. Hung, "A compact narrow-band microstrip band pass filter with a complementary split ring resonator". Microwave and Optical Technology Letters, vol. 48, pp. 2103-2106, October 2006.
7. M.K. Mandal, P. Mondal, S. Sanyal, A. Chakrabarty, "Low insertion-loss, sharp-rejection and compact microstrip low-pass filters", IEEE Microwave and Wireless Components Letters, vol. 16, pp. 600-602, Novenber 2006.
8. M. Gil, J. Bonache, J. García-García, J. Martel and F. Martín, "Composite Right/Left Handed (CRLH) Metamaterial Transmission Lines Based on Complementary Split Rings Resonators (CSRRs) and Their Applications to Very Wide Band and Compact Filter Design", IEEE Transactions on Microwave Theory and Techniques, vol. 55, pp. 1296-1304, June 2007.
9. J. Bonache, I. Gil, J. García-García and F. Martín, "Complementary split rings resonator for microstrip diplexer design", Electronics Letters, vol. 41, pp. 810-811, July 2005.
10. M. Gil, J. Bonache, J. Selga, J. García-García, F. Martín, "Broadband resonant type metamaterial transmission lines", IEEE Microwave and Wireless Components Letters, vol. 17, pp. 97-99, February 2007.
11. G. Sisó, J. Bonache and F. Martín, "Dual-Band Y-Junction Power Dividers Implemented Through Artificial Lines Based on Complementary Resonators", IEEE MTT-S International Microwave Symposium, Atlanta (USA), June 2008, pp. 663-666.

12. J. Bonache, G. Sisó, M. Gil, A. Iniesta, J. García-Rincón and F. Martín, “Application of composite right/left handed (CRLH) transmission lines based on complementary split ring resonators (CSRRs) to the design of dual band microwave components”, IEEE Microwave and Wireless Components Letters, vol. 18, pp. 524-526, August 2008.
13. J-S. Hong and M.J. Lancaster, Microstrip filters for RF/microwave applications, John Wiley, New Jersey, 2001.

Design of waveguides with Left-handed materials

Mondher LABIDI, Jamel BELHAD TAHAR, Fethi ChOUBANI
Research Unit Systems of Telecommunications (6'Tel), SUP'COM, Tunisia
E-mail: abidi_mondher@yahoo.fr, belhadj.tahar@supcom.rnu.tn, fethi.choubani@supcom.rnu.tn

Abstract- In this paper, we have presented the interesting properties of the metamaterials. Metamaterials are a new class of ordered composites that exhibit electromagnetic properties that are not readily observed in nature. There is currently considerable interest in the development of metamaterials, with particular emphasis on double-negative (DNG) materials, i.e., artificial materials with simultaneously negative permittivity and permeability. DNG materials are referred to by several names, including left-handed materials (LHM) , and negative index of refraction (NIR) materials. In this paper, we propose an interesting idea which is how to make use of a LHM presenting simultaneously negative values for the permittivity and the permeability. Moreover, we describe a technique that shows the influence of left handed metamaterials on waveguide characteristics.

1. INTRODUCTION

Metamaterials are artificial materials synthesized by embedding specific inclusions, for example, periodic structures, in host media. Some of these materials show the property of either negative permittivity or permeability [1,2]. If both happen at the same time, then the composite exhibits an effective negative index of refraction and is referred to as left-handed metamaterials.

The electric and magnetic properties of materials are determined by two important material parameters, dielectric permittivity, ε and magnetic permeability, μ. Together the permeability and the permittivity, determine the response of the material to the electromagnetic radiation. Generally, ε and μ are both positive in ordinary materials. While ε could be negative in some materials (for instance, ε possesses negative values below the plasma frequency of metals), no natural materials with negative μ are known. However, for certain structures, which are called left-handed materials (LHM), both the effective permittivity, ε_{eff} and permeability, μ_{eff} possesses negative values [3]. In such materials the index of refraction, n, is less than zero, and therefore, phase and group velocity of an electromagnetic wave can propagate in opposite directions such as the direction of propagation is reversed with respect to the direction of energy flow.

This paper encompasses an introduction to the metamaterial which includes the definition of the metamaterial, the early theory to the negative index of refraction, the structure that shows the left-handed properties and the applications for the Left Handed Materials (LHM) in the waveguides. The rest of the paper is organized as follows. In section 2, we introduce the left handed material, the Split Ring Resonator « SRR ». The waveguides design is presented in section 3. Conclusion is drawn in section 4.

2. STUDY OF METAMATERIALS

The idea of metamaterial or negative index of refraction was first proposed theoretically in 1968 by V.G.Veselago. This metamaterial exhibits a negative permittivity and permeability which is also known as left –handed material (LHM). The negative permittivity is easily obtained by an array of metallic wires and was theorized in 1996 [1,2]. JB Pendry also theorized the structure of negative permeability which was established in 1999 with split ring resonator (SRR) structure. The transmission – reflection problem is translated by the inversion method,[1,2] which consists in calculating the effective permittivity ε_{eff} and the effective permeability μ_{eff} from the coefficients of transmission and reflection. These two coefficients are obtained from simulations under the software HFSS:

$$t^{-1} = \left[\cos(nkd) - \frac{i}{2}\left(z + \frac{1}{z}\right)\sin(nkd)\right] e^{ikd} \qquad (1)$$

Where $k = \frac{\omega}{c}$ is the wavenumber of the incident wave, the length d and n is the refraction index. The reflection coefficient is also related to n and z by:

$$\frac{r}{t'} = -\frac{i}{2}\left(z - \frac{1}{z}\right)\sin(nkd) \qquad (2)$$

Eqs. (1) and (2) can be inverted to find n and z as functions of t and r. The permittivity ε and the permeability μ can be easily obtained from the following relations:

$$\varepsilon = \frac{n}{z} \qquad \mu = nz \qquad (3)$$

$$when: \ cos(nkd) = \frac{1}{2t}(1 - r^2 + t^2) \ \text{And:} \ z = \pm\sqrt{\frac{(1+r^2)-t^2}{(1-r^2)-t^2}}$$

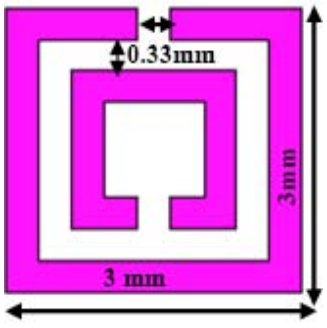


Fig 1. Square SRR design

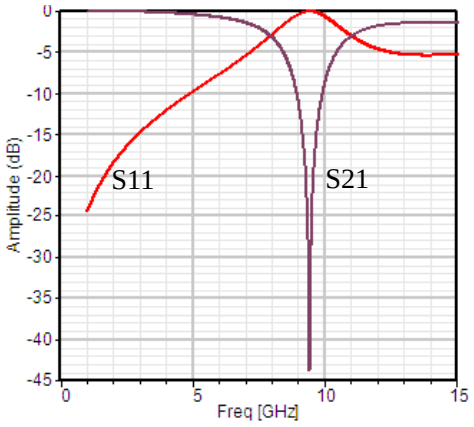


Fig 2. Reflection and transmission coefficient

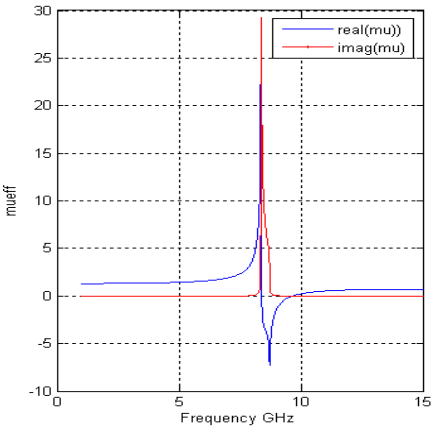


Fig 3. Real and imaginary values of permeability

The various dimensions of the squared SRR for a functioning in band X [8,2 GHz; 12,4 GHz] are given onto the figure 1. Figure 1 shows the square for double-ring SRR, dielectric used is the Rogers R04003 with ε=3.38 and tanδ = 0.0027. Reflection (S11) and transmission (S21) coefficients are given in figure 2, the SRR presents a resonance frequency f_{res}= 9.4 GHz with the transmission in term around -43.7dB. The variations of the real and imaginary parts of the effective permeability are given in figure 3. We can note that the real part of the permeability at the resonance frequency, f_{res} = 8.72 GHz, is negative and takes values varying from 0 to -7.2.

3. STUDY OF WAVEGUIDES

In this paper we focus on waveguides for electromagnetic wave propagation at microwave and radio wave frequencies. A closed guide established can propagate the electromagnetic energy only above of a certain frequency cutoff, f_c [3].

Generally, a waveguide is used to propagate energy on a single mode, and under this condition, it can be described as an environment with a complex constant $(\gamma = \alpha + j\beta)$ distribution and a wave impedance Z. The latter varies with the frequency. In a wave guide without losses, the relative permittivity ε_r, the driven wavelength λ_g, the cutoff free space λ_c, are given by this relation:

$$\gamma = \sqrt{{k_c}^2 - k^2} \tag{4}$$

In this paper, a rectangular waveguide study of width a and height b operating on the mode TE10 (figure 4). The frequency cutoff is:

$$f_c = \frac{c}{2\pi}\sqrt{\left(\frac{m\pi}{a}\right)^2 + \left(\frac{n\pi}{b}\right)^2} \tag{5}$$

This section is devoted to studying the SRR influence on the guided propagation of electromagnetic waves in the X-band [8.2 GHz, 12.4 GHz]. For this, we use rectangular waveguides. In X-band, the cross section of the guide is 22, 86 × 10, 16 mm^2. The cutoff frequency of the guide for the TE_{10} fundamental mode is 6.56 GHz.

In this section, four configurations are considered [4]. These configurations are determined in relation to possible directions of a SRR inside waveguide. Two of the four configurations involve placing the SRR,[5,6] so that the magnetic field H may penetrate through the rings forming the SRR. And among these two configurations, there is one where the electric field E respects the SRR symmetry.

Case1: The field H is parallel to the axis of the rings. Both openings of the SRR are parallel to the short side of the waveguide and therefore the field E does not respect the symmetry of the resonator.

Case 2: The field H is parallel to the axis of the rings. Both openings of the SRR are parallel to the long side of the waveguide and therefore the field E respects the symmetry of the resonator.

Case3: The field H is perpendicular to the axis of the rings. Both openings of the SRR are parallel to the short side of the waveguide and therefore the field E does not respect the symmetry of resonator.

Case4: The field H is perpendicular to the axis of the rings. Both openings of the SRR are parallel to the long side of the waveguide and therefore the field E respects the symmetry of resonator.

The resonant frequency of the SRR in case 1 is 9.59 GHz and the corresponding attenuation is -19.25 dB. In case 2, the resonance occurs at 9.6 GHz and the attenuation is -9.47 dB. The resonance of the case 3 occurs at 9.64 GHz and the attenuation is -15 dB. In case 4, the SRR has no effect on the transmission of waves in the waveguide. Simulation results presented in Figure 5, show a phenomenon of filtering cutoff band as has been demonstrated by P. N.

Katsarakis [5] and Mr. Kafesaki [6]. The authors of [5,6] had placed the RAF in a rectangular waveguide operating in the band [0.75 GHz, 1.12 GHz]. For case 3 and 4, the magnetic field is perpendicular to the axis of the rings and thus does not penetrate through the SRR. Therefore, it does not contribute to the induced currents in the SRR. Thus, we can say that the induced currents are only due to the Electrical field.

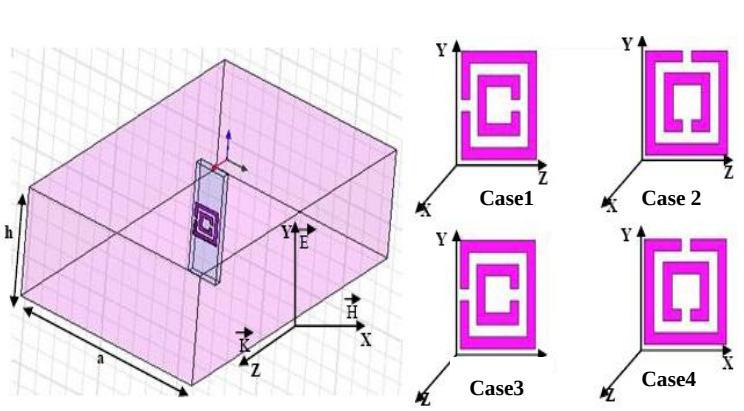


Fig 4. The four SRR configurations into the waveguide

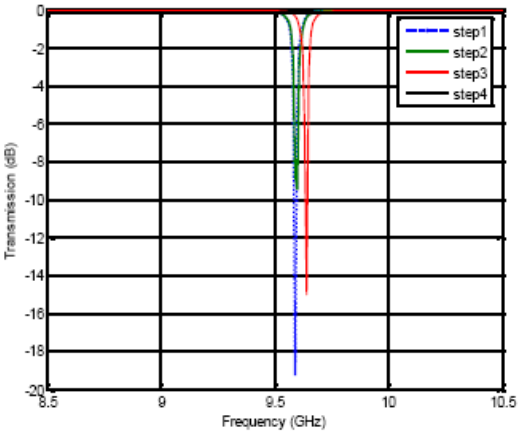


Fig 5 Transmission of the four SRR wave guide configurations

4. CONCLUSIONS

In this paper, the first part is reserved to examine a left hand metamaterial. We have presented the properties of these structures and the main physical effects behind these periodic structures. In the design of the metamaterial, simulation results shows that the structure, the parameters and dimensions of each component play an important role in determining the LHM properties and the frequency in which the negative index lies. The second part is especially devoted to the study of the left handed metamaterials application in the rectangular waveguide environment.

REFERENCES

1. J. B. Pendry, "Negative refraction makes a perfect lens", *Physical Review Letters*, vol. 85, no.18, pp. 3966–3969, October 2000.
2. D. R. Smith and N. Kroll, "Negative refractive index in left-handed materials", *Physical Review Letters*, vol. 85, no. 14, pp. 2933–2936, October 2000.
3. D. R. Smith, D. C. Vier, N. Kroll, and S. Schultz, "Determination of effective permittivity and permeability of metamaterials from reflection and transmission coefficients", *Physical Review B*,vol. 65, no. 19, April 2002.
4. S. N. Burokur, M. Latrach, et S. Toutain. "Miniaturized planar filters using Slot Split Ring Resonators", *4 èmes Journées Franco-Maghrébines des Microondes et leurs applications*, Rabat, Mars 2005.
5. N. Katsarakis, T. Koschny, M. Kafesaki, E. N. Economou, and C. M. Soukoulis, "Electric coupling to the magnetic resonance of split-ring resonators", *Applied Physics Letters*, vol. 84,no. 15, pp. 2943–2945, April 2004.
6. M. Kafesaki, T. Koschny, R. S. Penciu, T. F. Gundogdu, E. N. Economou, and C. M. Soukoulis, "Left-handed metamaterials : detailed numerical studies of the transmission properties", *Journal of Optics A*, vol. 7, pp. 12–22, February 2005.

Automated Design and Sensitivity of CRLH Balanced Structures using Co-Design Approach

R. Siragusa[1], **E. Perret**[1], **H. V. Hoang**[2], **P. Lemaître-Auger**[1], **S. Tedjini**[1], **and C. Caloz**[2]

[1]Laboratoire de Conception et d'Integration des Systèmes (LCIS) / Grenoble Institute of Technology, Valence, France

[2]Poly-Grames Research Center / École Polytechnique de Montreal, Montréal, Québec, Canada

romain.siragusa@lcis.grenoble-inp.fr

Abstract— A fully automated tool for designing CRLH structures using a co-design synthesis computational approach is proposed and demonstrated experimentally. The co-design approach uses a computation tool and an electromagnetic simulation tool to synthesize, simulate and optimize a balanced CRLH transmission line. The sensitivity of long balanced transmission line is shown and controlled by the use of a 3D simulator during the process. A 12 UC CRLH transmission line is finally designed with this approach.

1. INTRODUCTION

The planar microstrip composite right/left-handed (CRLH)transmission lines (TLs), introduced by Caloz et. al. in 2002, has led to many novel microwave circuit components and antennas, such as enhanced broadband coupled-line couplers, multiband devices, zeroth-order resonators, and full-space scanning leaky-wave antenna and reflectors [1, 2]. However, up to now, the design of the CRLH TLs is still based on a tedious manual synthesis approach requiring multiple iterations between fullwave analysis and circuit curve fitting. This design approach can be used when the number of unit cells (UC) of the structure is small but it becomes inappropriate for CRLH TLs with a large number of UCs or integrated active devices such as varactor diodes used in fixed-frequency beamforming or electronic-scanning leaky-wave antennas [3, 4, 5].

In [6], the authors proposed an improved model for the interdigital CRLH UC and a quasi-automated synthesis approach for the design of CRLH TLs. This approach provides an interactive tool to assist designers in quickly obtaining an initial layout of the CRLH UC. In [7], the authors proposed an automated co-design synthesis computational approach for balanced CRLH TLs. The approach does not require the designers' interaction during its automated layout initialization, simulation and optimization. The optimization steps are made with a Genetic Algorithm coupled with a 2.5D ElectroMagnetic (EM) software, Ansoft Designer. The approach has been demonstrated successfully for the design of balanced structures having a number of UCs less than 10.

In this work, we show that a long balanced TL with a large number of UCs are more sensitive than a short TL. For this reason, we propose a second optimization step using a 3D EM simulation software to increase the accuracy of our approach when the number of UCs of CRLH TLs is larger than 10. The advantages of this approach compared to the previous one are illustrated through the realization of a 12 UC balanced CRLH TL.

The paper is organized as follows. Sec. II outlines the CRLH TL theory and the conventional design approach. In Sec. III, the fully automated design approach is presented along with an example of the design of a 12 UC balanced CRLH TL.

2. CRLH BALANCED STRUCTURES AND CONVENTIONAL DESIGN APPROACH

CRLH TLs are artificial, engineered periodic structures realized by repeating a UC of size p along the axis of propagation. Figure 1(a) shows the layout of a planar microstrip CRLH UC structure implemented with series of interdigital capacitors and shunt stub inductors. The equivalent circuit model of the symetric CRLH UC is shown in Fig. 1(b), where the interdigital capacitor and stub inductor are represented by left-handed elements C_L and L_L, respectively. The right-handed capacitor C_R and inductor L_R are inherent parasitic elements of the microstrip TL.

Figure 1(c) shows the dispersion diagram of the balanced CRLH structure. Balanced CRLH structures are often preferred in practical circuit design because they have equal characteristic impedances $Z_0 = Z_R = Z_L$ and do not have a stop band around the transition frequency ω_0. As a result, balanced CRLH structures can be relatively well matched over their operating bandwidth.

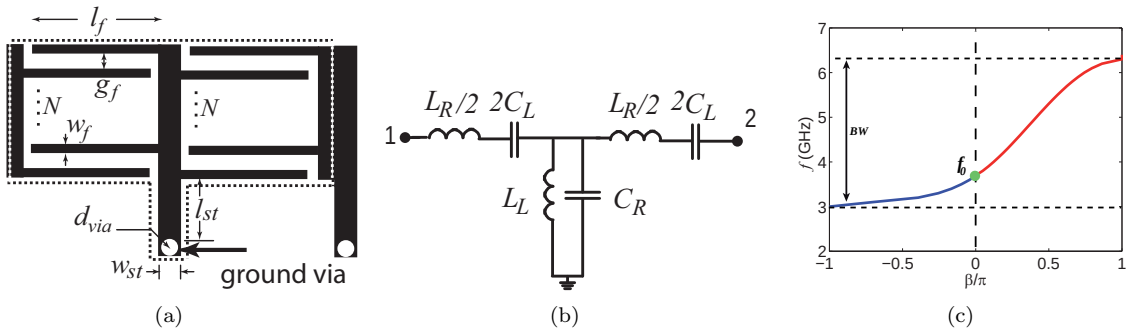


Figure 1: CRLH TL structure. (a) Layout of an interdigital/stub simmetric unit cell. (b) Equivalent circuit model of a symmetric unit cell. (c) Dispersion diagram of a balanced CRLH UC plotted with the following circuit parameters: $C_L = 7$ pF, $L_L = 2$ nH, $C_R = 7$ pF, $L_R = 2$ nH.

However, the equivalent circuit model shown in Fig. 1(b) does not account for the most important and fundamental aspect of this periodic structure which is the mutual coupling between UC elements of a finite size CRLH structure consisting of N UCs. (In practice, the response of a CRLH structure, which was balanced according to circuit design, is often unbalanced.) Because of this mutual coupling, the conventional CRLH manual design approach involves many iterations between circuit and full-wave (FW) simulations before an optimum layout can be obtained; it is often tedious and time consuming.

This manual approach, describe in details in [7], has numerous disadvantages. Firstly, human/machine cost is high as the designers are required to be present at all of the above design steps. This time increases exponentially as the number of UCs increases. Secondly, optimization procedure of a finite size CRLH TL is often performed using curve fitting between design specifications and FW. Finally, the manual approach is empirical, with the final results greatly dependent on designers' experience. The proposed fully-automated approach, which uses a co-design synthesis computation procedure, greatly simplifies the manual design and is presented in the next section.

3. AUTOMATED CO-DESIGN TECHNIQUE USING GENETIC ALGORITHM OPTIMIZATION

3.1. General Overview

The proposed approach is composed of three fully automated steps as shown in Fig. 2. These three steps reduce the total time by working at different design levels: circuit, 2D and 3D simulation. Each level becomes more accurate, however requires longer computational time. For this reason, the optimization steps using 3D simulation cannot be performed directly from the design specifications. The first and second steps are to find a layout as close to the final design as possible. First, the design specifications (ω_0, BW, Z_0), substrate characteristics (ϵ_r, loss tangent, thickness) and fabrication limits (minimum linewidth, spacing, overetching factor, ground via hole size) are specified by the designer before the process begins. Then, the co-design procedure is undertaken with the three steps describe below.

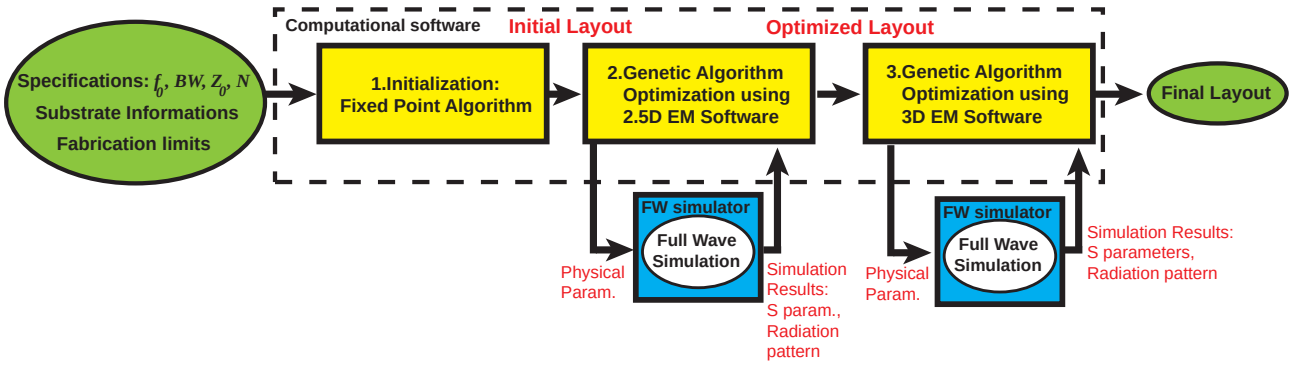


Figure 2: General overview of the procedure for the automated co-design synthesis computational approach.

3.2. Step1: Layout initialization of the single UC

The first step, shown in Fig. 2, produces an initial layout from the design specifications. The interdigital capacitors and short-stub inductor UC model proposed in [6] are solved numerically to find the best fit layout parameters that satisfy the design specifications. It should be noted that no FW simulation is performed and no mutual coupling between UCs is considered at this step.

To demonstrate this approach, we designed a 12 UC TL with the following specifications: transition frequency: $f_0 = 2.45$ GHz, lower cut-off frequency: $f_c = 1$ GHz, characteristic impedance: $Z_0 = 50\Omega$, number of UC: N = 12 and minimum line width: $w_{min} = 0.5$ mm. The substrate is a Rogers Duroid RT5880 with a dielectric permittivity, $\epsilon_r = 2.20$ and a thickness, h = 1.52 mm. The layout parameters of a UC are summarized in Tab. 1. The scattering parameters of the structure are shown in Fig. 4. It can be noticed that the TL seems to be balanced as the return loss ($S_{11} < -10dB$) at f_0. However, the angle of radiation is equal to $-36°$ so the transition frequency is not equal to 2.45 GHz as specified. To obtain the final layout, the second design step is performed to optimize the TL using a GA coupled with a 2.5D simulator.

3.3. Step2: Optimization using GA and 2.5D EM software

A computational program written using Matlab with a built-in GA tool box performs the optimization and FW simulation as follows. First, each layout parameter of a UC is coded and organized in a set of values that represents a solution. This set is called a chromosome. Next, the program initializes the FW simulation software (Ansoft Designer in this case) and sends the chromosome as layout variables to the FW simulator. After the simulation finishes, the results (S-parameters and radiation patterns) are stored and compared with the original design specifications using cost functions. If the values of the cost functions are larger than a specific threshold level, the optimization process continues by selecting another set of chromosomes and send them back to FW simulator. Otherwise, the optimization stops.

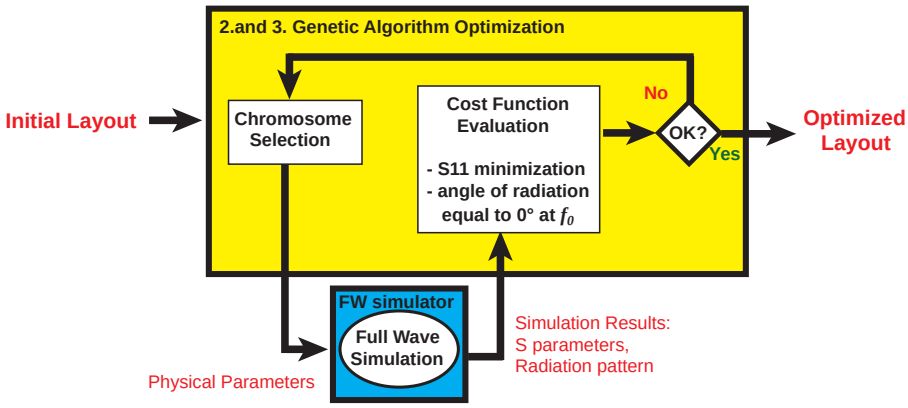
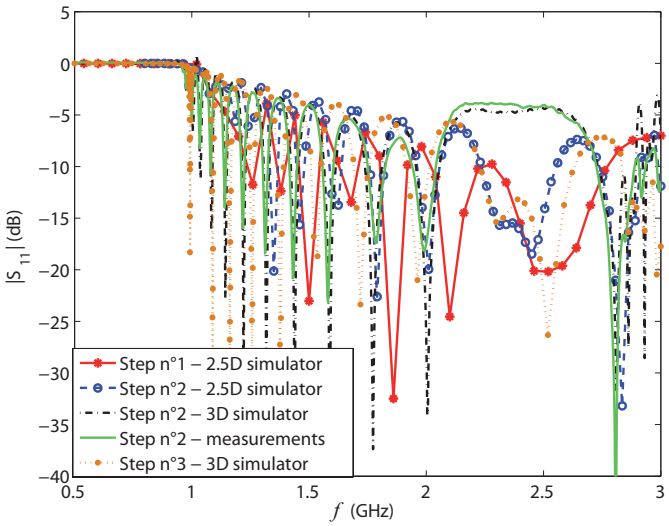


Figure 3: Block diagram of step 2 and 3 of Fig. 2. A genetic algorithm optimization is performed by coupling the computational software with the 2.5D and 3D EM simulation.

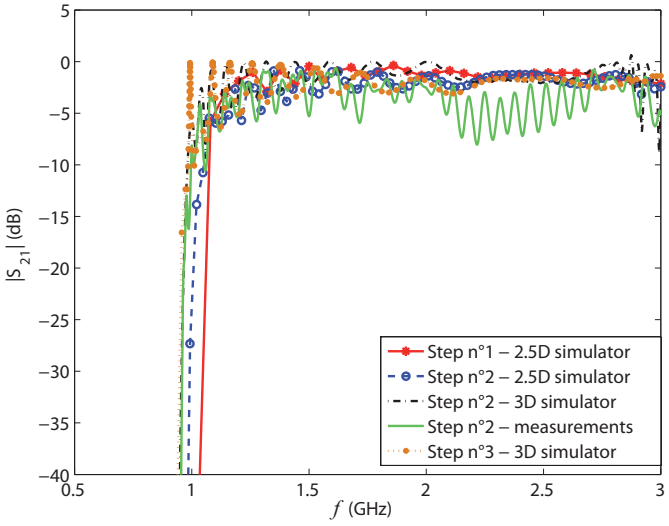
In the above GA optimization process, the choice of appropriate cost-functions is very important as it greatly affects the efficiency of the method. In the proposed co-design, two cost functions are used in the GA optimization. The first one uses the transition frequency f_0 as the optimization criteria. As this frequency also corresponds to the broadside radiation of the CRLH structure, we use this property to accurately compute f_0. The second cost function uses the characteristic impedance and the balanced condition at f_0. As an unbalanced CRLH structure will have a strong mismatch (high S_{11}) at f_0, the second function computes the value of S_{11} at f_0. Doing that, we necessarily obtain a balanced CRLH TL and a good matching over the bandwidth.

As shown in Fig. 4, the CRLH TL of the previous example is clearly balanced in simulation. The S_{11} coefficient is less than -10 dB at f_0. This frequency corresponds to the transition frequency because the angle of radiation is equal to 0°. However, measurement of a fabricated prototype showed a strong mismatch around 2.45 GHz compare to simulation. This effect is not due to a poor meshing because a convergence study was made before the simulations. Figure 4 also shows the simulation of the same parameters performed with CST Microwave Studio. There is a large discrepancy with Ansoft Designer results but a good agreement with the measurement. This problem shows the high sensitivity of the balanced design and the limit of the Method of Moments

for the design of long balanced CRLH TL. This point explains the necessity of a third simulation stage using a 3D EM software to take into account the finite size of the substrate and the mutual coupling effects with higher accuracy.



(a)



(b)

Figure 4: Results of a 12 UC CRLH TL after each step of the design process for $f_0 = 2.45$ GHz, $Z_0 = 50\Omega$ and a Rogers Duroid RT5880 substrate. (a) Return loss S_{11} (b) Insertion loss S_{21}.

3.4. Step3: Optimization using 3D EM software

This last stage is similar to the second step except that the EM simulator is now a 3D software, here CST Microwave Studio. After this last optimization, the final layout is obtained. The parameters are summarized in Tab. 1 and the S-parameters are shown in Fig. 4. It can be seen that the CRLH TL is now balanced at f_0, the angle of radiation is equal to 0° at this frequency, and the results meet the specifications. We noticed that the layout parameters obtained at each stage are very closed to each other, however the behavior of each structure is quite different. It demonstrates the sensitivity of the balanced structure and the importance of the proposed approach compare to the conventional one.

The complete co-design process finishes in 4 days where step 1 takes one minute, step 2 takes 10 hours, and step 3 takes 3.5 days.

Table 1: Layout parameters of the CRLH TL obtained with the automatic approach.

Layout	Step 1	Step 2	Step 3
w_f	0.20 mm	0.19 mm	0.18 mm
g_f	0.20 mm	0.25 mm	0.28 mm
l_f	9.13 mm	10.73 mm	10.0852 mm
w_{st}	0.50 mm	0.58 mm	0.52 mm
l_{st}	4.46 mm	4.64 mm	4.68 mm
N	10	10	10
Id Cap. Input/Output			
w_f	0.20 mm	0.19 mm	0.22 mm
g_f	0.20 mm	0.23 mm	0.27 mm
l_f	9.13 mm	9.17 mm	8.6 mm
N	12	12	12

4. CONCLUSION

An automated design for CRLH structures using co-design synthesis computational approach has been proposed and demonstrated experimentally with a 12 UC CRLH TL. In comparison with the manual approach and the approach presented in [7], the proposed co-design is accurate, has low human/machine cost and fast convergence for a large number of UC. In this work, we showed the sensitivity of long balanced CRLH TL and introduced an additional design step to include a 3D EM optimization which allows the design of long CRLH TL structures with high accuracy.

REFERENCES

1. C. Caloz and T. Itoh, "Application of the transmission line theory of left-handed (LH) materials to the realization of a microstrip LH line," in *Proc. IEEE Antennas Propagat. Soc. Int. Sympo. Dig.*, vol. 2, pp. 412-415, Jun. 2002.
2. C. Caloz and T. Itoh, "Electromagnetic metamaterials: transmission line theory and microwave applications," *New York: Wiley*, 2005.
3. S. Abielmona, H.V. Nguyen, F. Caseres-Miranda, C. Camacho-Peñalosa and C. Caloz, "Real-time digital beam-forming active leaky-wave antenna," in *Proc. IEEE AP-S International Symposium*, Honolulu, pp. 5593-5596, Jun. 2007.
4. F. Caseres-Miranda, C. Camacho-Peñalosa and C. Caloz, "High-gain active composite right/left-handed leaky-wave antenna," *IEEE trans. Antennas Propagat.*, vol. 54, pp. 2292-2300, Aug. 2006.
5. C. Caloz and T. Itoh, "Electronically controlled metamaterial based transmission line as a continuous-scanning leaky-wave antenna," *IEEE MTT-S Int. Microwave Symp. Dig.*, pp. 313-316, 2004.
6. R. Siragusa, H.V. Nguyen, P. Lemaître-Auger, S. Tedjini and C. Caloz, "Modeling and synthesis of the Interdigital/Stub Composite Right/Left Handed Artificial Transmission Line," *Int. Journal of RF and Microwave Computer-Aided Engin.*, vol. 19, no. 5, pp.549-560, Sept. 2009.
7. R. Siragusa, H.V. Nguyen, E. Perret, P. Lemaître-Auger, S. Tedjini and C. Caloz, "Automated Design of CRLH Structures using Co-Design Synthesis Computational Approach," in *Proc. IEEE Asia-Pacific Microw. Conference*, Singapore, Dec. 2009.

Compact cavity resonators using high impedance surfaces

D. Dancila [1,2], X. Rottenberg [1], N. Focant [2], H.A.C. Tilmans [1], W. De Raedt [1] and I. Huynen [2]
[1]IMEC/SSET, Kapeldreef 75, 3001 Leuven, Belgium
[2]UCL/EMIC, Place du Levant 3, 1348 Louvain-la-Neuve, Belgium
dragos.dancila@uclouvain.be

Abstract- This paper presents a miniaturization concept for cavity resonators. The idea is to create a λ/4 long cavity resonator by using a combination of Perfect Electric Conductor (PEC) and Perfect Magnetic Conductor (PMC) boundary conditions. Reducing by half the length and width of a metallic cavity resonator and placing PMC boundary conditions on two adjacent side walls allows the resonance of a λ/4 mode inside the hybrid cavity resonator, at the same frequency as the λ/2 long metallic one. The practical implementation of the PMC boundary condition is realized by using High Impedance Surfaces (HIS). The design of the surfaces is realized at the element level and is implemented on standard microwave substrate. Measurements demonstrate a cavity resonator operating at 4 GHz with half the length and width of a standard metallic cavity resonator, meanwhile its volume is divided by four.

1. INTRODUCTION

Satellite payload transportation cost is around 10.000$/Kg for placement on a geosynchronous transfer orbit [1]. Since the late '60s, the number and applications of satellite communication systems is growing exponentially [2]. The satellite systems extend from traditional fixed telecommunication to mobile, navigation and remote-sensing applications [3]. Microwave components, and in particular waveguide filters, are key elements present in the payload of those satellites [4]. In this context, every reduction of the volume and weight of the satellite payload is very much welcomed. Theoretical developments proposed metamaterials to reduce the size of cavity resonators [5] and waveguides [6]. Another approach demonstrated TEM propagation in a waveguide composed by Artificial Magnetic Conductors (AMC) [7]. Similar to AMC are High Impedance Surfaces (HIS), electromagnetic structures showing a high impedance and in-phase reflection [8]. HIS are used to reduce antennas profiles [9], improve the radiation pattern by suppressing the surface waves [8] and for beam steering [10]. In this paper, we propose to use HIS to reduce by four the volume of cavity resonators. Equivalently keeping all dimensions constant, the cavity with HIS sidewalls resonates at half the frequency of a full metallic one. We measured the resonance of a fabricated hybrid HIS-metallic cavity resonator to be 4 GHz while measured without the HIS to be 8 GHz.

2. COMPACT CAVITY RESONATORS DESIGN

A full metallic cavity resonator is characterized by a field distribution related to the modes of resonance and geometry of the resonator. The boundary conditions at all ends are assimilated to PEC and impose a zero of the electric field. Considering a rectangular metallic cavity of dimensions *d*, *a*, and *b*, along the x, y, and z-axes, see Figure 1 a), filled with a material of permittivity ε_r and permeability μ_r, the resonant frequency is given by [11] :

$$f_{mnl} = \frac{c}{2\sqrt{\mu_r \varepsilon_r}} \sqrt{\left(\frac{m}{a}\right)^2 + \left(\frac{n}{b}\right)^2 + \left(\frac{l}{d}\right)^2} \quad \text{with as lowest resonant frequency :} \quad f_{101} = \frac{c}{2\sqrt{\mu_r \varepsilon_r}} \sqrt{\left(\frac{1}{a}\right)^2 + \left(\frac{1}{d}\right)^2} \tag{1}$$

Instead of using PEC boundary conditions spaced by half a waveguide length, a combination of PEC and PMC

boundary conditions spaced by a quarter waveguide length are used to maintain the same field distribution e.g. maxima and minima (Figure 1b). In this case the resonant frequency is given by:

$$f_{mnl} = \frac{c}{2\sqrt{\mu_r \varepsilon_r}} \sqrt{\left(\frac{m-1/2}{a}\right)^2 + \left(\frac{n\pi}{b}\right)^2 + \left(\frac{l-1/2}{d}\right)^2} \text{ with as lowest resonant frequency: } f_{101} = \frac{c}{2\sqrt{\mu_r \varepsilon_r}} \sqrt{\left(\frac{1}{2a}\right)^2 + \left(\frac{1}{2d}\right)^2} \quad (2)$$

Comparison of equations (1) and (2) shows that the cavity with two PMC sidewalls resonates at half the frequency of a cavity having the same dimensions and all PEC sidewalls. Equivalently, since the TE_{101} field distribution corresponds to a quarter-wavelength instead of a half-wavelength, the volume of the hybrid PEC-PMC design is a quarter of the volume of a standard PEC rectangular design, for a specified resonant frequency, see Figure 1 b).

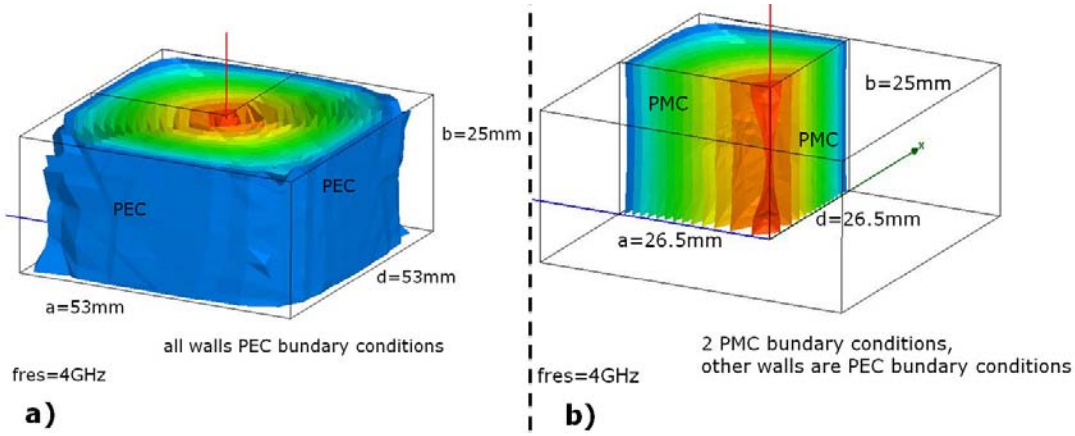


Figure 1: First resonant mode TE_{101} at 4GHz in a full PEC cavity and hybrid PEC-PMC cavity, with respective dimensions a x d x b = 53 x 53 x 25mm and 26.5 x 26.5 x 25mm

3. HIGH IMPEDANCE SURFACE DESIGN

High Impedance Surfaces (HIS) are known to show, around the design frequency, a PMC behavior. While the metallic sheet imposes a phase reversal (180°) for reflected plane waves, HIS imposes no (0°) phase shift while reflecting plane waves. This surface is realized by gathering together metallic patches, see Figure 2. The patches are lying on the microwave substrate and are enclosed by the metallic walls of the cavity. As the surface impedance is determined by the ratio of in plane electric field to magnetic field, at resonance, the in plane electric field is maximum and the in plane magnetic field vanishes, characteristic for AMC surfaces. The behavior of each element is described using lumped parameter circuit model shown in the inset of Figure 2. The value of each capacitor is given by the fringing field capacitance between neighboring metal plates, derived using conformal mapping [8]. The inductance is strongly dependent of the substrate thickness, forming a solenoid of current defined on one side by the metallic patch and on the other side by the walls of the cavity in which the PCB is included. The magnetic energy stored in the inductor is directly proportional to the volume of the solenoid wherein the magnetic field engulfs, generating surface currents flowing around. Values for the capacitance and inductance of a single patch element are presented in [8], with ε_1 and ε_2 the permittivity of dielectric and air, μ the permeability and t substrate's thickness:

$$C = \frac{W(\varepsilon_1 + \varepsilon_2)}{\pi} \cosh^{-1}\left(\frac{slot}{2W + slot}\right) \quad \text{and} \quad L = \mu t \quad (3)$$

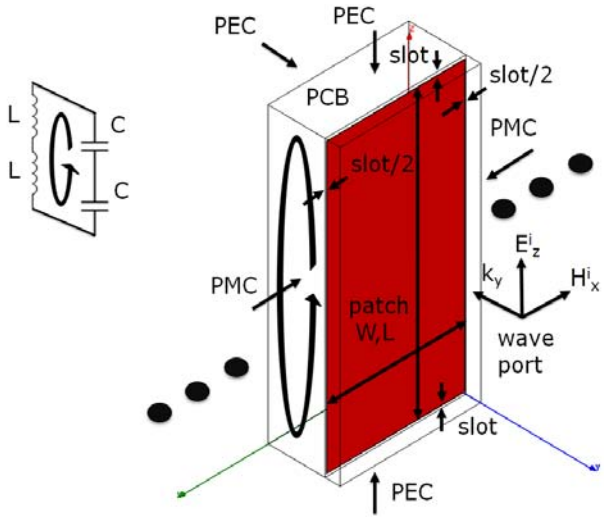


Figure 2: Each element of the HIS surface is composed by a metallic patch lying on the microwave substrate, enclosed by the metallic walls of the cavity. The element is presented in the configuration used to assess its own frequency of resonance, wherein a plane wave directly excites them. Inset of the lumped LC model.

Expressions (3) are adapted to the characteristic geometry presented in Figure 2, where the HIS element is composed by the cavity's walls, the substrate and a metallic patch. The patch is spaced by a slot from the top and bottom of the cavity's walls. A lumped circuit is derived (see inset Figure 2) wherein 2 series inductors and 2 series capacitors are identified as equivalent to equation (3). The frequency of resonance of the full element is given by the following equation:

$$f_{res} = \frac{1}{2\pi\sqrt{2L\frac{C}{2}}} \tag{4}$$

Further FEM simulations were performed using the configurations presented at the Figure 2. The element is enclosed in PEC boundary conditions at the rear, the top and bottom. On both lateral sides PMC boundary conditions are placed at half the slot length, in order to render the periodicity of the HIS. The element is excited by a plane wave with vertical E_z field and horizontal H_x field. The resonant frequency is obtained from HFSS simulations as the frequency where the phase of reflection coefficient vanishes, in Figure 3. A good agreement is observed in Figure 3 between the resonant frequencies calculated for the configuration proposed in Figure 2 using respectively, the lumped element approach of formulas (3-4) (solid black lines) and the full wave simulations with HFSS (dotted red lines).

4. EXPERIMENTAL SETUP AND MEASUREMENTS

A prototype, shown Figure 4, is realized with standard PCB technology (RO4010 substrate from Rogers Co.) with a dielectric permittivity ε_r=10.2, thickness t=0.635mm, tan delta=0.0035 and copper thickness 17µm. It consists of a rectangular metallic patch (W=4.85mm, L=9.8mm) spaced by a slot of 0.1mm from the top and bottom of the cavity walls, as in Figure 2. Figure 5 shows the reflection coefficient measured for two configurations: the empty cavity of Figure 4a), and the same cavity filled with two adjacent HIS walls disposed as in Figure 4b). The influence of the HIS inclusion on the measured frequency of resonance validates the theoretical developments of Section 2: the cavity with two HIS sidewalls (red solid line) resonates in the TE_{101} mode at half the frequency, i.e. 4 GHz, of a cavity of same dimensions and having all metallic walls, i.e. 8 GHz

(black dotted lines). E field maps are shown respectively at 4 GHz and 8 GHz, as insets in the Figure 5. The best intrinsic quality factor, Q_0, measured at 4 GHz in a hybrid cavity with 2 HIS walls, is Q_0=205 meanwhile it is Q_0=710 at 8 GHz for the cavity with all walls metallic. The reduction of Q_0 is due to the implementation of the PMC boundary condition by the HIS made of resonant elements, which used at resonance generate additional dielectric and ohmic losses.

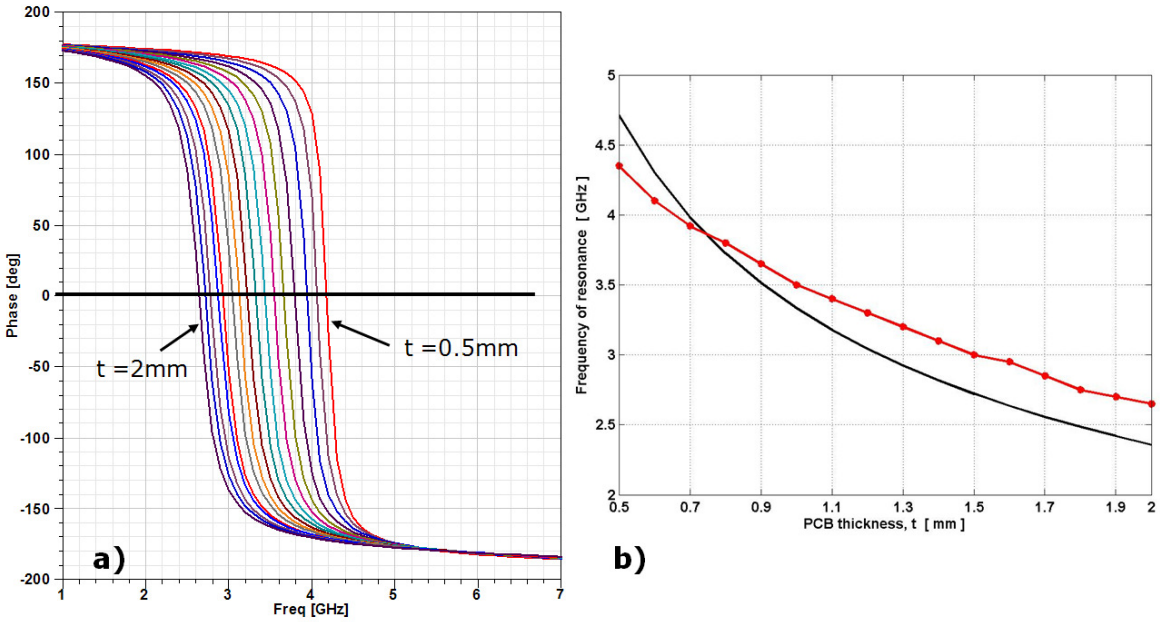


Figure 3: (a) Phase of reflection coefficient S_{11} simulated using HFSS software for the cell described in Figure 2. The phase is computed versus frequency for various thicknesses t of the substrate, varying from 0.5 to 2mm. (b) Continuous black curve use equations (3-4) and dotted red curve are extracted from (a).

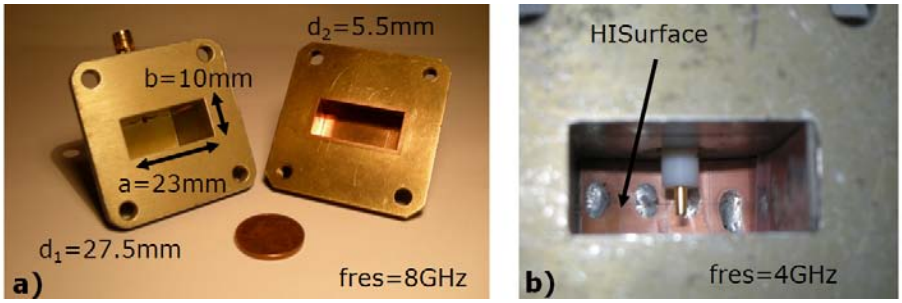


Figure 4: a) Metallic cavity resonator showing a resonance at 8 GHz and b) hybrid metallic-HIS cavity resonator demonstrating a frequency of resonance of 4 GHz, for the same dimensions.

5. CONCLUSIONS

This paper demonstrated a miniaturization concept for cavity resonators using PMC boundary conditions placed at half the length and width of a λ/2 long metallic cavity resonator. The practical implementation of the PMC boundary condition is realized using High Impedance Surfaces (HIS) designed using either a lumped element approach or full-wave simulations. Measurements validate the theoretical predictions i.e. the resonant frequency of a rectangular cavity is shifted from 8 GHz to 4 GHz when two of its sidewalls are covered with the HIS designed for 4 GHz. This demonstrates equivalently that a cavity resonator with HIS operating at 4 GHz has half the length and width of a standard metallic cavity resonator and its volume is divided by four.

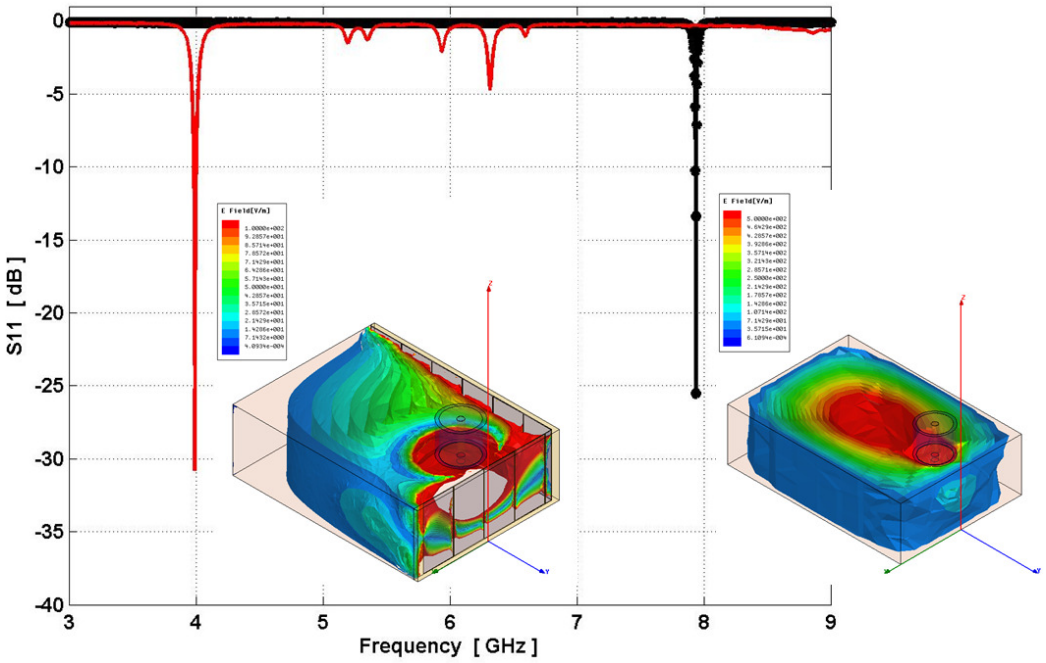


Figure 5: Measured reflection coefficient of rectangular waveguide cavities: with two sidewalls covered by HIS (red) and empty (black dotted line). Inset of the E field maps respectively at 4 GHz and 8 GHz.

ACKNOWLEDGEMENT

Dragos Dancila is supported by a F.R.I.A. Ph.D. fellowship. I. Huynen is Research Director from the F.R.S.-F.N.R.S., Belgium.

REFERENCES

[1] Futron Corporation, "Space transportation costs: trends in price per pound to orbit 1990-2000", White Paper, 2002.

[2] V.E. Boria and B. Gimeno, "Waveguide Filters for Satellites", IEEE microwave magazine, Oct. 2007.

[3] G. Maral and M. Bousquet, "Satellite Communication Systems", 3rd ed. Chichester: Wiley, 1998.

[4] R. Coirault, S. J. Feltham, G. Gatti, G. Guglielmi, and D. Perring, "Overview of microwave components activity at the European Space Agency", IEEE Trans. Microwave Theory Tech., vol. 40, no. 6, pp. 1150–1158, 1992.

[5] N. Engheta, "An idea for thin subwavelength cavity resonators using metamaterials with negative permittivity and permeability", IEEE Antennas and Wireless Propagation Letters, vol. 1, pp. 10-13, 2002.

[6] S. Hrabar, J. Bartolic and Z. Sipius, "Waveguide miniaturization using uniaxial negative permeability metamaterial", Antennas and Wireless Propagation Letters, vol. 53, no.1, pp. 110-119, 2005.

[7] F. R. Yang, K. P. Ma, Y. Qian, and T. Itoh, "A novel TEM waveguide using uniplanar compact photonic-bandgap (UC-PBG) structure", IEEE Trans. Microwave Theory Tech., Vol. 47, No. 11, 2092–2098, 1999.

[8] D. F. Sievenpiper, "High-impedance electromagnetic surfaces", Ph.D. dissertation, Dept. Elect. Eng., Univ. of California, Los Angeles, UCLA, 1999.

[9] R. M. Mateos, "Low-profile antennas based on aperiodic and compact meta-surfaces", Ph.D. dissertation, Ecole Polytechnique, Univ.catholique de Louvain, Louvain-la-Neuve, UCL, 2009.

[10] D. Chicherina, S. Dudorova, M. Sternerb, J. Oberhammerb, and A. V. Räisänena, "Micro-fabricated High-Impedance Surface for millimeter wave beam steering applications", Proc. of 33rd International Conference on Infrared, Millimeter, and Terahertz Waves, Pasadena USA, in press, 2008.

[11] D. M. Pozar, Microwave Engineering, Addison-Wesley, 1990.

Extraction of Capacitive Profiles with a Planar Metamaterial Sensor

M. Puentes[1], **M. Schüßler**[1], **C. Damm**[1], **and R. Jakoby**[1]

[1]Wireless Communications / Microwave Engineering, TU Darmstadt
Merckstr. 25, 64283, Darmstadt, Germany.
puentes@mwt.tu-darmstadt.de

Abstract— The extraction of the capacitive profile along a planar metamaterial sensor is presented. Using broadband techniques, the input impedance in the LH and RH bands can be measured. The capacitance values along the line can be evaluated by applying an extraction method based on the classical network synthesis with a combination between the Cauer canonical forms I and II to obtain the values of the lumped elements in the equivalent circuit. Two prototype sensors have been developed and tested to prove the concept. The areas of application of these types of sensors are transportation of materials in industrial processes where the position of the Material Under Test (MUT) is of interest and can be derived from the changes in the capacitances with a one unit cell resolution.

1. INTRODUCTION

In several industrial processes where transportation of MUT must be performed, the accurate determination of the position and velocity of each object is necessary for an adequate process monitoring and control [1]. A new sensor concept for this purpose has been developed using a Composite Right/Left-Handed (CRLH) metamaterial transmission line [2]. The physical implementation of the line is done in a way that the left-handed capacitances of the unit cells are strongly affected by the ambient. By tracking one or several line resonances, the averaged capacitance change of all unit cells can be measured and the mean permittivity of the MUT on a belt system can be extracted, furthermore by applying dedicated signal processing the mean velocity of the material can be calculated as well. With these type of sensors it is also possible to measure the input impedance in the transmission bands of the CRLH-line resonator and extract its poles and zeros. The location of the altered capacitance can be derived by different techniques, for example, time domain reflectometry where the amount of reflected and transmitted energy is measured. With this information the time the pulse needs to cross one cell can be calculated and therefore the position of the altered capacitance [3]. Another method is based on the resonant perturbation theory where with the frequency shifts of the poles and zeros related to the unloaded resonator the capacity profile along the line can be derived. In this paper a different approach will be presented based on classical network synthesis techniques, particularly a combination between the Cauer canonical forms I and II, where a continued fraction expansion is performed to extract all the elements from the CRLH-line. An overview is shown on Fig. 1. The theory behind the principle of operation of the prototype is presented in section 2. The sensor design is discussed in section 3 and finally the obtained results are described in section 4.

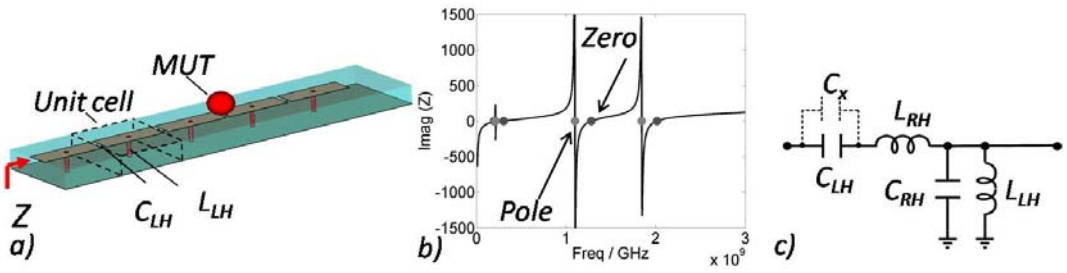


Figure 1: Overview of the extraction process. a) Sensor draft. b) Impedance plot. c) Extracted equivalent circuit for one unit cell.

2. THEORETICAL CONSIDERATIONS

2.1. Metamaterial-Transmission Line Theory

For the accurate determination of the position of a MUT in the vicinity of a sensor, some key design objectives should be considered. The sensing element must be as close as possible to the MUT and the sensitivity must be sufficient. Additionally the frequency must be low but without sacrificing accuracy in pursuance of a cost reduction and to facilitate the needed technology. With this in mind the best suited structure is a Metamaterial transmission line based sensor, where some of the advantages are having the sensing element in the serial branch, operating at a lower frequency and higher sensitivity than a right hand oriented element with the same physical size. Unfortunately, for real applications the development of a pure left-handed line is not possible due to the parasitic effects within the line and the real structure can be approximated to a CRLH-line which will bring additional challenges in the extraction algorithms. The unit cell configurations of a RH-line, a LH-line and a CRLH-line are presented in Fig. 2.

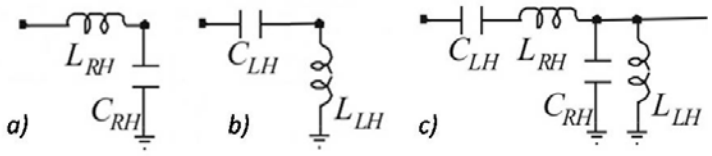


Figure 2: Unit cell configurations. a) RH-line, b) LH-line, c) CRLH-line [2].

2.2. Network Synthesis

In order to calculate the position of an object in the vicinity of a transmission line, different approaches can be used based on broadband techniques where every impedance variation along the line will result in a partial reflection of the signal, this is represented by a change in the C_{LH} denoted on Fig. 1c as a capacitance C_x in parallel with C_{LH}. The first method that was applied to this planar structures was time domain reflectometry [3] and the location of the altered capacitances was determined but not with a one unit cell resolution. As a result a more robust method had to be implemented based on network synthesis.

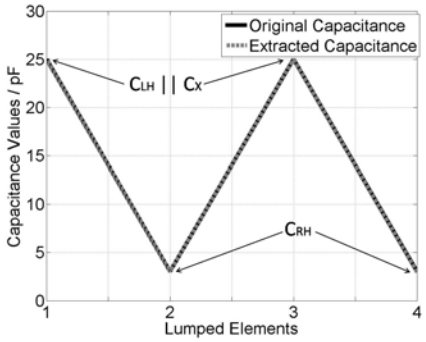


Figure 3: Mixed Cauer canonical form extraction for the capacitances of a CRLH-Line.

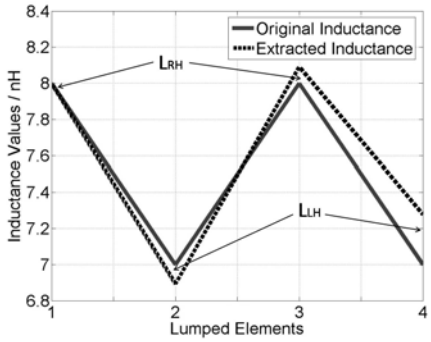


Figure 4: Mixed Cauer canonical form extraction for the inductances of a CRLH-Line.

The principle of position detection using network synthesis can be derived from different methods to construct the equivalent circuit of a structure, from literature the Foster and the Cauer canonical forms are well known [4]. When an ideal LH-line is considered as shown on Fig. 2b, the equivalent circuit can be extracted with the Cauer canonical form II where the impedance transfer function is assumed to have the degree of the numerator $N(s)$ lower than that of the denominator $D(s)$ and must differ by unity. Otherwise, we must consider the admittance $Y(s) = 1/Z(s)$ instead of $Z(s)$. The coefficients of both polynomials must be arranged in ascending power of s and a continued fraction expansion is then performed:

$$Z(s) = \frac{V_{in}}{I_{in}} = \frac{N(s)}{D(s)} = \frac{a_0 + a_2 s^2 + a_4 s^4 + ... + a_k s^k}{b_1 s + b_3 s^3 + b_5 s^5 + ... + b_{k+1} s^{k+1}} = \frac{1}{C_1 s} + \frac{1}{\frac{1}{L_2 s} + \frac{1}{\frac{1}{C_3 s} + \frac{1}{\frac{1}{L_4 s} + \frac{1}{...}}}} \qquad (1)$$

From (2) the values of each inductor and capacitor of the equivalent circuit can be calculated and it is clear that on each step of the continued fraction expansion a pole at the origin is removed. With this method only the calculations for the ideal LH-line can be performed with very high accuracy as shown on Fig. 3 and Fig. 4. Here is presented a comparison between the original values and the extracted values for a structure with two identical unit cells. For the real case where parasitic effects are considered, due to a more complicated structure such as the CRLH-line, a combination between the Cauer canonical form I and II has to be implemented. The Cauer canonical form I has a very similar behavior as the Cauer canonical form II, the differences lie on the following aspects: the equivalent circuit is a RH-line as shown on Fig. 2a, the coefficients of both polynomials must be arranged in descending power of s, the degree of the numerator $N(s)$ must be higher than that of the denominator $D(s)$ and finally on each step of the continued fraction expansion a pole at infinity is removed as presented on the following equation:

$$Z(s) = \frac{N(s)}{D(s)} = \frac{a_k s^k + a_{k-2} s^{k-2} + ... + a_3 s^3 + a_1 s}{b_{k-1} s^{k-1} + b_{k-3} s^{k-3} + ... + b_2 s^2 + b_0} = L_1 s + \cfrac{1}{C_2 s + \cfrac{1}{L_3 s + \cfrac{1}{C_4 s + \cfrac{1}{...}}}} \tag{2}$$

When the two Cauer canonical methods are used in an alternating fashion, it is possible to extract a CRLH equivalent circuit as shown on Fig. 2c. The starting transfer function must be arranged in descending power of s because the first element to be extracted is L_{RH}, this means a Cauer canonical form I is performed and a pole at infinity is removed. Then the polynomials must be flipped and inverted to extract the C_{LH} with the Cauer canonical form II and remove a pole at origin. The third step is to flip again the polynomials and perform a Cauer canonical form I to extract C_{RH}. The last step consists on flipping and inverting one last time the polynomials and a Cauer canonical form II is performed for the extraction of L_{LH}. This procedure completes the extraction of one CRLH unit cell and can be repeated for several unit cells as necessary accordingly to the size of the actual structure. The expanded impedance transfer function will look as follow:

$$Z(s) = L_{RH} s + \frac{1}{C_{LH} s} + \frac{1}{C_{RH} s + \frac{1}{L_{LH} s}} + ... \tag{3}$$

In summary the principle of operation can be explained when considering the sensor element with no MUT in the vicinity, then from the measurement of the reflection coefficient the impedance of the line at a certain frequency can be extracted. From this impedance information the poles and the zeros are found and the transfer function of Z is then constructed. By using a combination between the Cauer canonical form I and II, an equivalent circuit from a CRLH-line can be found with all capacitance and inductance values. After obtaining these reference values, the measurement with MUT in the vicinity of the sensor can be done and the same procedure is performed. For the detection of the position of each object, it is only necessary to compare these values with the ones obtained in the reference measurements. It is important to emphasize that with this approach a one cell resolution can be achieved and then the performance is limited only by the signal to noise ratio.

3. SENSOR DESIGN

The implementation of the left-handed transmission line sensor into a physical layout was carried out with the help of the software package CST Microwave Studio. The major design objectives were the LH-line impedance of 50Ω at a frequency of 10 GHz and maximum spatial resolution for detection of small capacitance changes in a single unit cell. In Fig. 5 and Fig. 6 are presented the model and the results from the static simulations in CST Microwave Studio. The structure is a planar sensor with one unit cell and a variable C_{LH} represented by a change in the size of the gap between the two patches. The structure is inserted in an air box along with a perturber that can adjust its distance to the structure itself and its permittivity value. With these simulations, it could be determined that the maximum distance from the perturber to the sensor, in order to comply with the design objectives, depends mainly on the permittivity of the MUT and the distance between the patches of the sensor that will determine the maximum possible penetration of the field into the MUT and hence the resolution. This is important for the applications where the MUT is not on direct contact with the sensor but located at a defined distance from the sensitive area or when the MUT is immersed in other substances that have a considerable thickness.

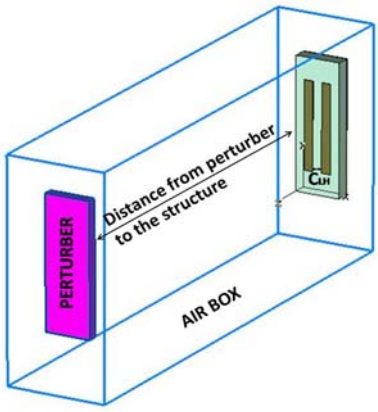


Figure 5: CST model for static simulations.

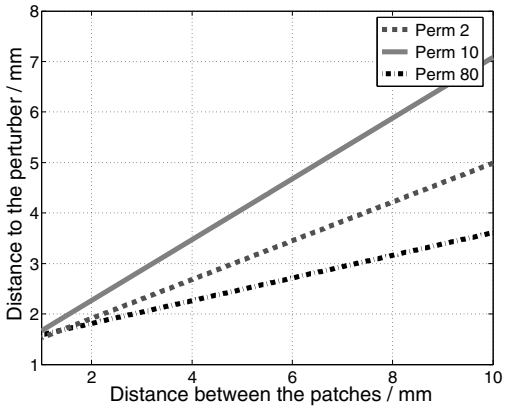


Figure 6: Maximum resolution of the sensor.

For the design of the actual structure the software CST Microwave Studio was again selected for its advantages in modeling planar structures. To prove the concept, two different prototypes where constructed as shown in Fig. 7. They were built on Rogers RT/Duroid 5880 with dielectric constant of $\varepsilon_r = 2.2$, and a thickness of $h = 1.57\,\text{mm}$. The prototype shown on the upper side consists of 2 unit cells and the prototype shown on the bottom has 4 unit cells. The structure is a microstrip design with the ground plane on the bottom side and the inductors are realized by SMD elements going through the center of the patches down to the ground plane. The first patch is soldered to a 3.5 mm SMA connector which is used to connect the sensor element to a Network Analyzer for measurements.

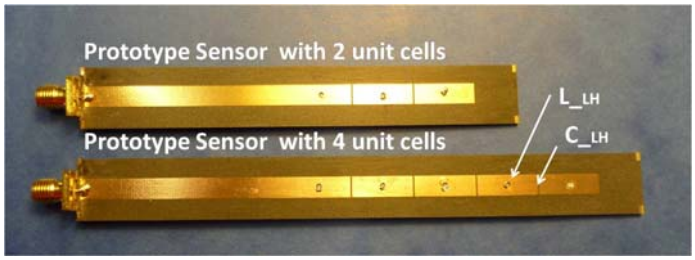


Figure 7: Prototypes of the capacitive sensor.

A TRL calibration kit had to be included in the design process in order to keep the equivalent circuit as an authentic CRLH-line structure and simplify the extraction process. In Fig. 8 the comparison between CST simulations and measurements are shown for the sensor prototype of two unit cells and a good agreement is achieved. In Fig. 9 the imaginary part of the input impedance is depicted where the poles and the zeroes can be clearly identified, as well as the left and right handed bands.

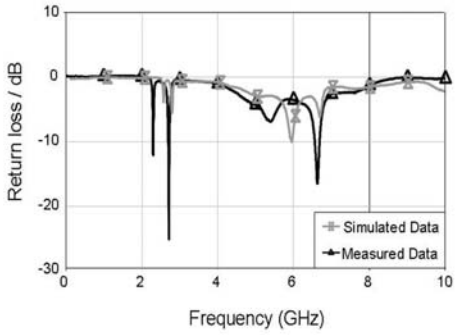


Figure 8: Comparison between simulated and measured results for the prototype sensor.

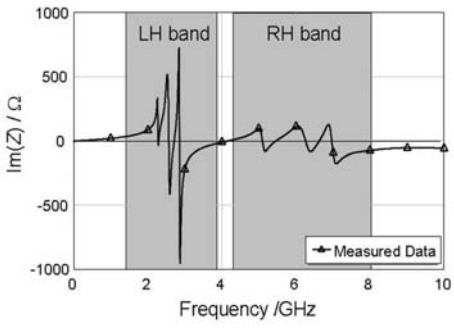


Figure 9: Imaginary part of the impedance.

4. MEASUREMENT RESULTS

In Fig. 10 is presented, for the prototype of two unit cells, a comparison between the unloaded prototype sensor and two different capacitance profiles. The first profile consists of a single per-

turber with permittivity $\varepsilon_r = 2.2$ located in the first unit cell and the second profile includes two perturbers with $\varepsilon_r = 2.2$ located on the first and second unit cell respectively. The relative change of C_x is plotted versus the number of lumped elements in the equivalent circuit. The results for the prototype of four unit cells are presented in Fig. 11. Again the unloaded sensor is compared against two capacitance profiles where perturbers with $\varepsilon_r = 2.2$ and $\varepsilon_r = 10.8$ are located on different unit cells.

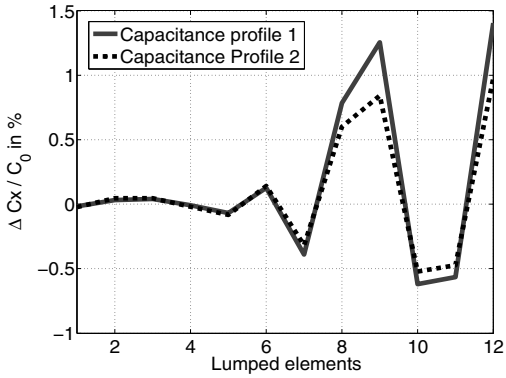


Figure 10: Measurement results from the prototype sensor of two unit cells.

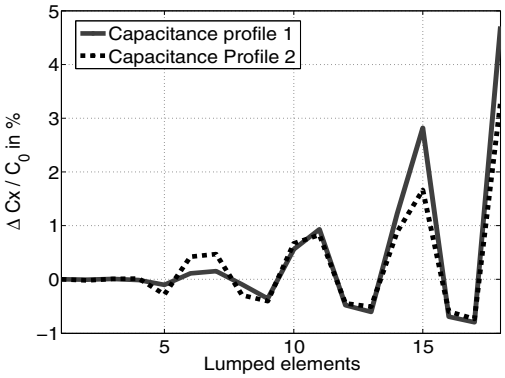


Figure 11: Measurement results from the prototype sensor of four unit cells.

From the measurement results is clear that the capacitive profile based on the relative change of the capacitances can be detected. The extraction is done with a one unit cell resolution even when the changes are small. The technique used is based on the classical network synthesis approach presented in section 2, which is appropriate for a CRLH-line equivalent circuit. Although the accuracy of the extraction is adequate, it is affected by the signal to noise ratio which makes the detection of the poles and zeroes more difficult and hence the development of the exact impedance transfer function. This is the reason for the existence of negative values of up to -0.5% visible on the measurement results graphs, although they all must be above zero accordingly to the theory. Also additional post-processing of the data is necessary to obtain the absolute values of the capacitance profiles. This issue will be considered in future work.

5. CONCLUSION

A new metamaterial planar sensor is presented for the extraction of the capacitive profile using the mixed Cauer canonical form extraction algorithm from classical network synthesis. The theoretical background for this circuit element and for the extraction process is briefly discussed, advantages of the structure in terms of performance and applicability for the specific problem are highlighted and the derivation of its physical layout is explained. Measurements with a prototype sensor have been performed to proof the concept. The network synthesis based on a mixed Cauer canonical form extraction method permits a single cell resolution with adequate accuracy but is very sensitive to any error in the detection of the zeros and the poles and therefore the construction of the impedance transfer function. In further work a more robust technique will be developed by mixing the presented method with the perturbation theory approach.

ACKNOWLEDGMENT

The authors would like to thank the company CST for providing the CST Microwave Studio software package.

REFERENCES

1. Puentes, M., Stelling, B., Schüßler, M., Penirschke, A. and Jakoby, R., "Planar Sensor for Permittivity and Velocity Detection Based on Metamaterial Transmission Line Resonator", *Proceedings of 39th European Microwave Conference 2009*, Rome, Italy, September 2009.
2. Caloz, C. and Itoh, T., *Electromagnetic Metamaterials: Transmission Line Theory and Microwave Applications*, Wiley-IEEE Press, December 2005.
3. Puentes, M., Stelling, B., Schüßler, M., Penirschke, A., Damm, C. and Jakoby, R., "Dual Mode Sensor for Belt Conveyor Systems Based on Planar Metamaterials", *Proceedings of International Conference IEEE Sensors 2009*, Christchurch, New Zealand, October 2009.
4. Ghosh, S.,*Network Theory. Analysis and Synthesis*, Prentice Hall, 2005.

Planar Superstrate for Dual-frequency RHCP-LHCP Array

E. Ugarte-Muñoz[1], F. J. Herraiz-Martínez[1], J. Montero-de-Paz[1], L.E. García-Muñoz[1] and D. Segovia-Vargas[1]

[1]Department of Signal Theory and Communications, Carlos III University of Madrid, Avenida de la Universidad 30, 28911, Leganés, Madrid, Spain.

eugarte@tsc.uc3m.es

Abstract- Patch antennas are low profile, lightweight and most suitable for aerospace and mobile applications. In recent years Fabry-Perot cavities and meta-surfaces have been used as superstrates to improve the radiation performance of planar antennas [1], such as directivity, mutual coupling on array configuration and bandwidth. These structures usually work for a single polarization and frequency band while an increasing number of applications require multi-frequency operation. In this paper a Fabry-Perot cavity that works with dual polarized and dual frequency patch antennas (rectangular patch excited orthogonally) is proposed in order to design high directivity dual-frequency RHCP-LHCP Arrays.

1. INTRODUCTION

As shown in the figure below, a Fabry-Perot cavity is mainly formed by a radiant element between a complete reflecting screen (PEC), and a partially reflecting surface (PRS). In this paper a patch antenna covered with a PRS is used. As it was shown in [3], depending on the reflection coefficient of the PRS $\Gamma=\rho\cdot e^{j\psi}$ and the distance between the PEC and the PRS, d, the directivity of the antenna can be improved in an arbitrary direction α, by a factor of S given by (1).

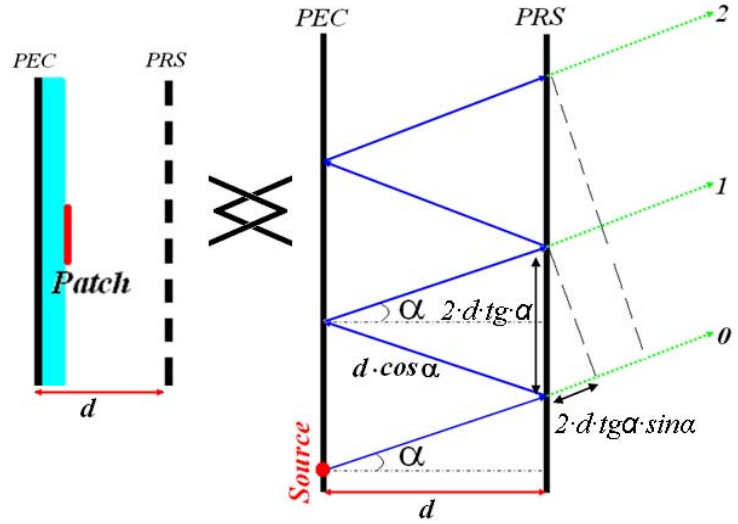


Figure 1. Patch inside a cavity (left) and operation principle (right)

$$S = \frac{1-\rho^2}{1+\rho^2-2\cdot\rho\cdot\cos\left(\psi-\pi-\frac{4\cdot\pi}{\lambda}\cdot d\cdot\cos\alpha\right)} \tag{1}$$

The maximum directivity improvement is given when all the refracted rays (green rays in the figure above) are radiated in phase into the space. If this is taken into account, for a half wavelength cavity (d=λ/2), in the broadside direction (α=0), the maximum directivity is obtainedwhen the reflection coefficient of the PRS is close to the short-circuit condition as we can see in Figure 2.

According to these results the PRS should be designed to present a reflection coefficient Γ close to minus one, in order to obtain the maximum directivity enhancement.

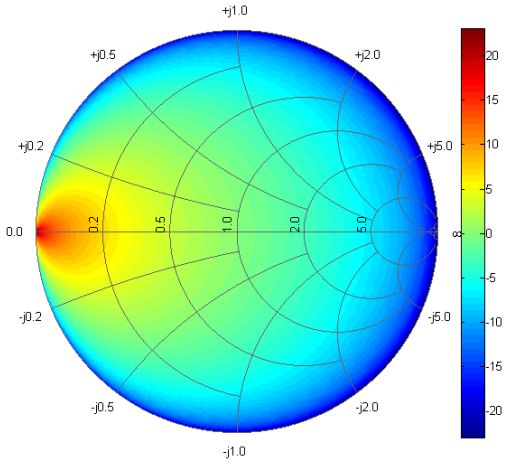


Figure 2. Directivity enhancement (dB) vs PRS reflection coefficient

2. CAVITY FOR LINEARLY POLARIZED ANTENNA

The first cavity studied is the one proposed in [4]. In that paper, a cover for patch antennas formed by a dielectric slab and open rings is proposed as a negative permeability meta-surface. When the open rings are conveniently excited the propagation is inhibited in the sideward radiation due to a negative μ effect, while the propagation in the forward direction is enhanced. In this way, this meta-surface improves the directivity (and the gain) of the planar antenna, but only at one frequency and one linear polarization. The sketch of the PRS is shown in Figure 3. This PRS works for the Y-axis polarization and does not affect the X-axis polarization.

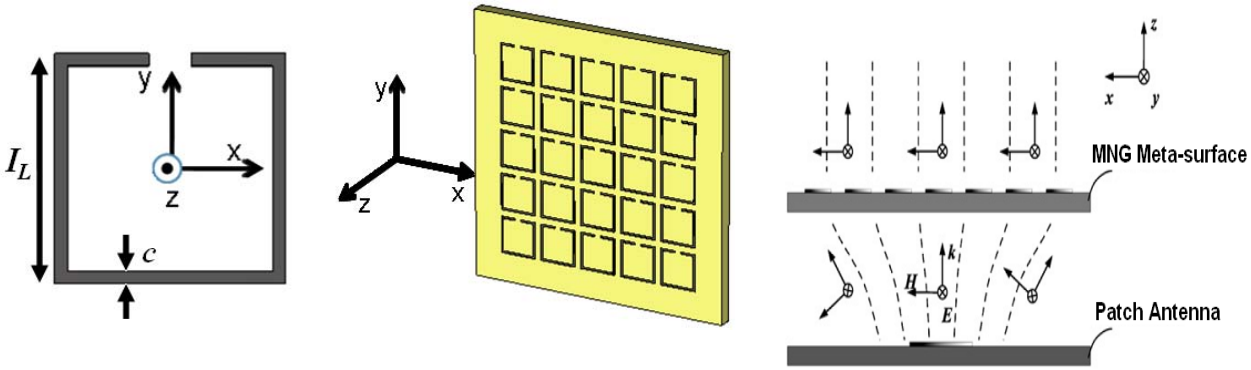


Figure 3. Unit cell of the PRS (left) and sketch of the PRS formed by 5x5 unit cells

As it will be shown, this directivity improvement can also be explained from the Fabry-Perot caviy principle point of view. The reflection coefficient Γ of the PRS can be easily obtained from an EM simulator with very low computational cost. For instance, the reflection coefficient of a PRS with I_L=5.6mm, c=0.3mm and a gap between rings of 1mm, is shown in Figure 4. In this case, the maximum directivity is obtained from (1) at a frequency of 8.35GHz, where $\Gamma = 0.86_{170^o} \cdot$ and is close to the short-circuit.

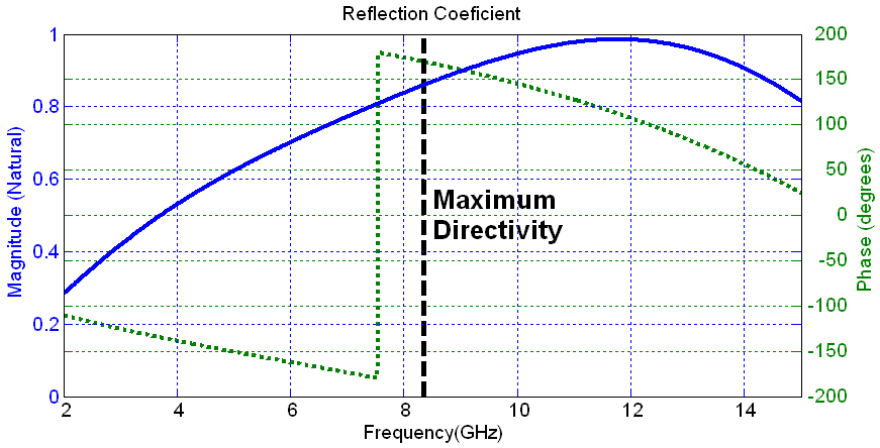


Figure 4. Simulated reflection coefficient of the PRS

A parametric study has been undertaken in order to validate this quasi-analytical model with the full electromagnetic simulations (PRS and patch antenna simulated together). In this study we have analyzed the variation of the frequency of maximum directivity improvement with the variation of the basic parameters of the PRS (I_L, gap, ε_r, and substrate thickness).The results of the parametric study are shown in Figure 5. As it can be observed there is a good agreement between the quasi-analytical model and the full EM simulations for all the cases. It can also be concluded that the basic parameters of this PRS (I_L, gap, ε_r, h) are not very critical and that the critical parameter is the separation between the PRS and the patch antenna.

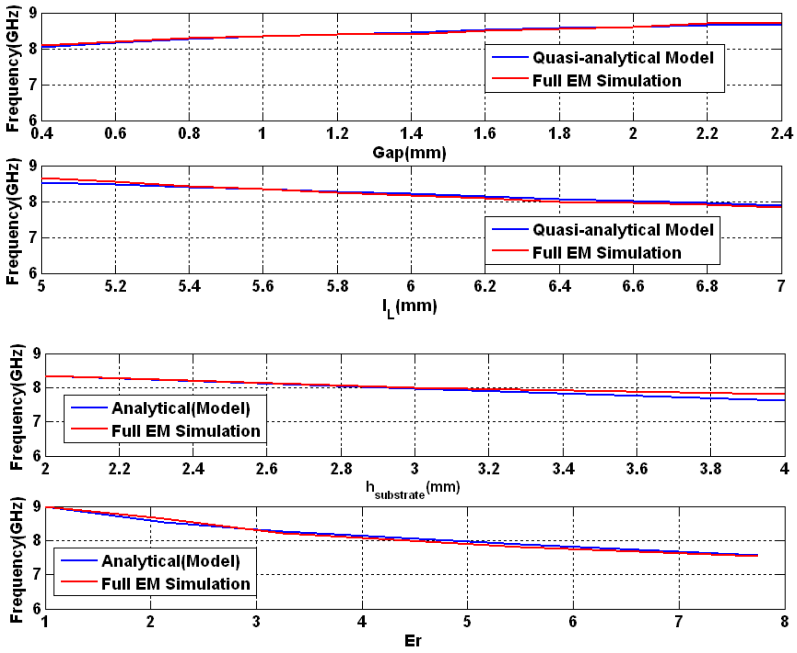


Figure 5. Comparison between the full EM simulation parametric study and the analytical model parametric study

As it can be seen in the figure below, when the PRS is placed conveniently (according to Figure 3 for Y-axis polarization), the open rings behave as a set of wires radiating in phase. In this way, the radiation from the primary source (the patch antenna) spreads over a greater surface, or what is the same, the effective aperture of the antenna increases which results in a directivity enhancement. On the other hand, for the orthogonal polarization (X-axis polarization according to Figure 3) the open rings behave as a set of wires radiating in opposite phase. Then the radiation pattern of the primary source is not dramatically modified by the PRS.

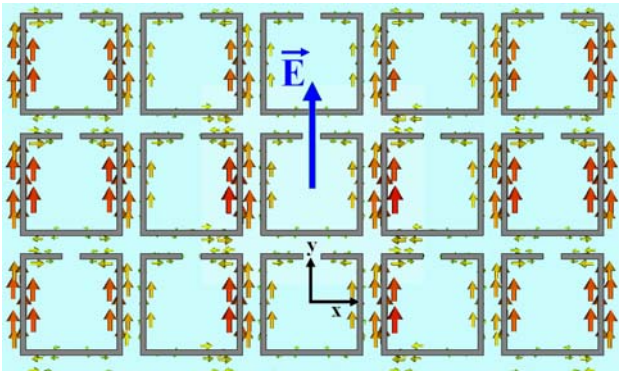


Figure 6. Radiation principle of the cavity (patch antenna with the PRS)

A prototype of this cavity has been manufactured and a gain improvement of 5dB has been measured between the conventional patch, and the patch antenna with the PRS.

3. CAVITIES FOR DUAL-POLARIZED DUAL-FREQUENCY ANTENNAS

A dual-polarized-dual-frequency PRS has to provide a gain improvement for both horizontal and vertical polarization in different frequency bands. In this section we propose two PRS with these characteristics, based on the PRS studied in the previous section.

PRS with concentric rings: The first PRS consists of a 5x5 concentric open-rings (see Figure 7). The larger ones work at the lower frequency (7.5GHz) and is X-polarized, while the smaller ones work at the higher frequency (8.15GHz) and is Y-polarized. With this configuration a gain improvement up to 7dB in both frequency bands can be achieved as it is shown in Figure 7.

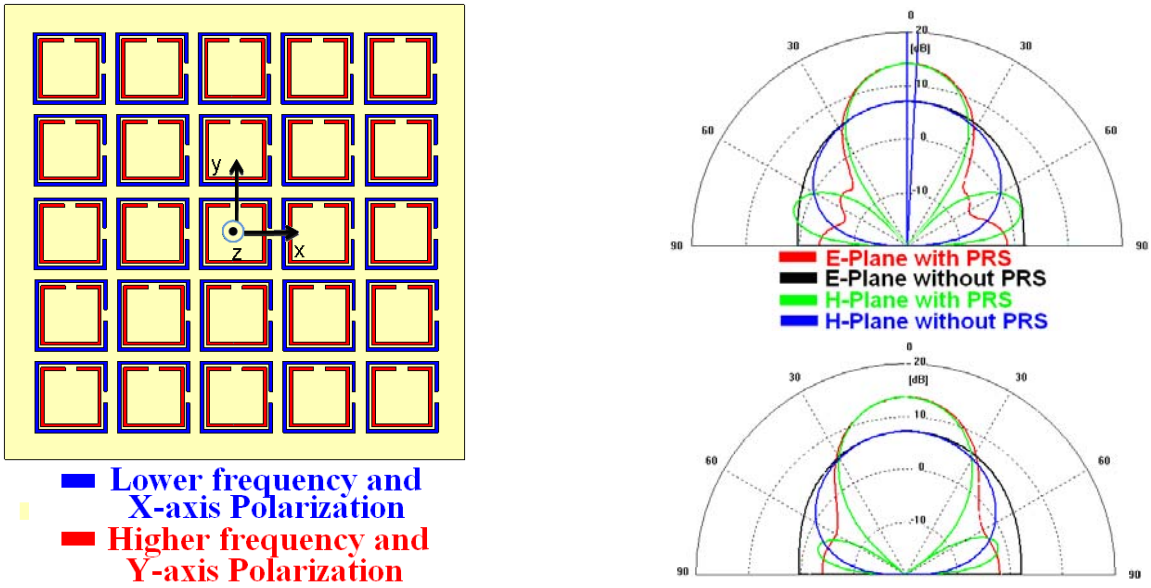


Figure 7. PRS based on concentric rings (left), Simulated radiation pattern, lower frequency (top-right), higher frequency (bottom-right)

PRS with alternated rings: The second PRS proposed is shown in Figure 8. In this case, there are large and small open-rings, being both alternated. This configuration is easier to manufacture (there are not any gap between the rings), and allows the use of closer operation frequencies than in the previous one. Using this kind of PRS, gain improvements up to 8.3dB and 6.5dB have been obtained for the lower and higher frequency band respectively.

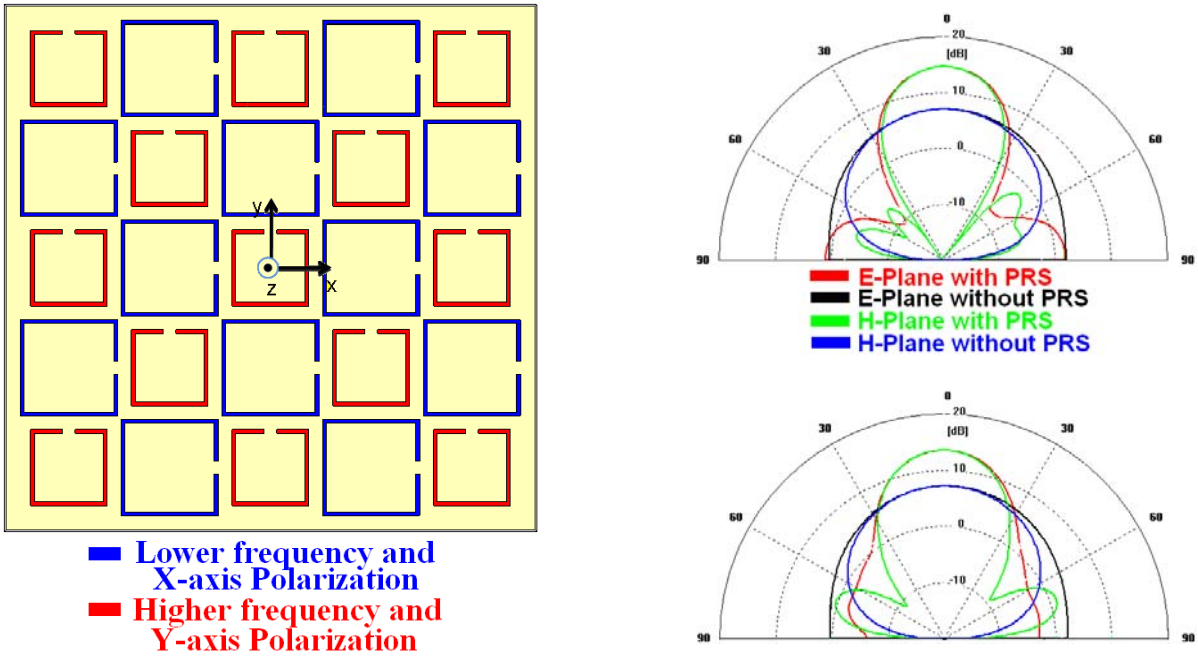


Figure 8. PRS based on alternated rings (left), Simulated radiation pattern, lower frequency (top-right), higher frequency (bottom-right)

4. 2X2 DUAL-FREQUENCY RHCP-LHCP ARRAY

In this section we propose a 2x2 sub-array using the sequential-rotation principle in order to obtain LHCP in the lower frequency band and RHCP in the higher one. The sequential-rotation principle was first proposed in [5], and it describes how to obtain circularly polarized arrays from linearly polarized radiant elements by applying geometrical rotations and feeding phase shifts to the elements, as it is shown in the figure below. In this way, LHCP polarization is obtained in the lower frequency band (Ports 5, 6, 7 and 8), while RHCP is obtained in the higher frequency band (Ports 1, 2, 3 and 4). A rectangular patch orthogonally excited has been chosen as a radiant element. It has also been shown [6] that this technique also improves the axial ratio bandwidth and the purity of the circularly polarization.

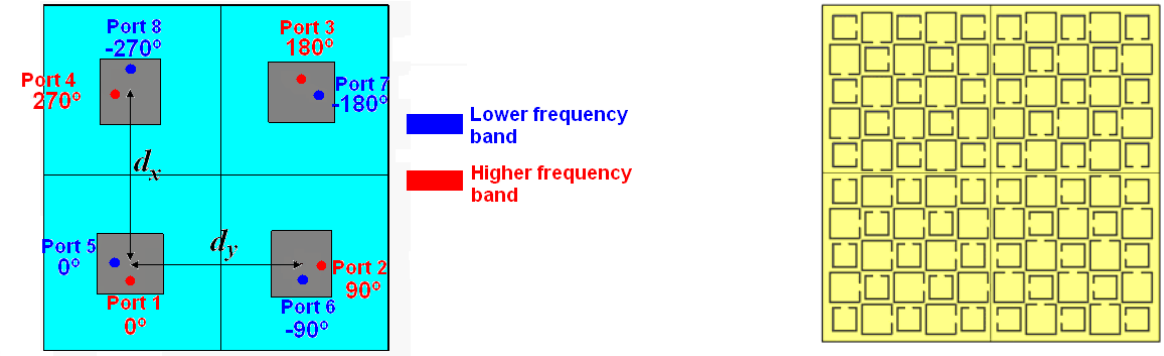


Figure 9. 2x2 RCHP-LHCP sequentially rotated array (left), and the sequentially rotated PRS used (right)

We have chosen the PRS with alternated rings for the 2x2 sub-array design, because it generally provides greater gain improvements and it is easier to manufacture. This sequentially rotated PRS still provides a gain improvement up to 6dB with respect to a 2x2 sub-array with sequential rotation without PRS in both frequency bands in spite of the fact that the physical area of the antenna is not dramatically increased. In this way, the number of elements needed to achieve a fixed gain can be reduced by a factor of four by using the proposed PRS. The radiation patterns of both, the 2x2 array with PRS, and without PRS, are shown in Figure 10.

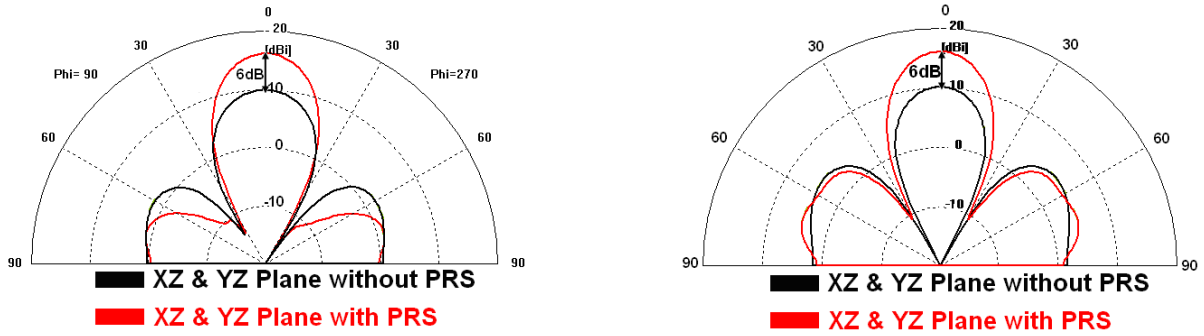


Figure 10. Radiation pattern of the dual-frequency 2x2 sequentially rotated RHCP-LHCP sub-array. Lower frequency band (left) and higher frequency band (right).

5. CONCLUSIONS

In this paper we have studied a partially reflecting surface (PRS) for linearly polarized antennas using a quasi-analytical model. The agreement between the model and the full EM simulation is great. Furthermore, the proposed structure with two PRS for dual-polarized and dual-frequency antennas provide a gain improvements up to 7dB. After that, we have designed a 2x2 dual-frequency RHCP-LHCP sub-array using the sequentially rotation technique. It has been seen that the PRS in array configuration performs in a similar way that with a single radiating element configuration. In such a way, gain improvements up to 6dB have been obtained in both frequency bands. Thus the number of elements (and the antenna size) needed to achieve a fixed gain can be reduced by a factor of four by using these kind of PRSs.

REFERENCES

1. E. Saenz, R. Gonzalo, I. Ederra, J.C. Vardaxoglou and P. de Maagt, "Resonant Meta-surface Superstrate for Single and Multifrequency Dipole Antenna Arrays", *IEEE Transactions on Antennas and Propagation*, Vol. 56, No. 4, April 2008.
2. J.C.Iriarte, I.Ederra, R.Gonzalo, Y.Brand, A.Fourmault, Y.Demers, L.Salgetti-Drioli and P. de Maagt, "EBG Superstrate Array Configuration for the WAAS Space Segment", *IEEE Transactions on Antennas and Propagation*, Vol.57, No.1, January 2009.
3. Giswalt Von Trentini, "Partially Reflecting Sheet Arrays", *IRE Transactions on Antennas and Propagation, October 1956.*
4. Y. H. Liu, X.P. Zhao, "Investigation of anisotropic negative permeability medium cover for patch antenna", *IET Microwave, Antennas and Propagation*, Vol. 2, No. 7, 2008.
5. T. Teshirogi, M. Tanaka, and W. Chujo, "Wideband Circularly polarized array antenna with sequential rotations and phase shifts of elements", *Int. Symp. On Antennas and Propagation.*,ISAP 85, Tokyo, 1985
6. P.S. Hall, J.S. Dahele, J.R. James, "Design principles of sequentially fed, wide bandwidth, circularly polarized microstrip antennas", *IEE Procedings,* Vol. 136, Pt. H, No. 5, October 1989.

Effects of anisotropic disorder in an optical metamaterial

C. Helgert[1], C. Rockstuhl[2], C. Etrich[1], E.-B. Kley[1], A. Tünnermann[1], F. Lederer[2], and T. Pertsch[1]

[1]Institute of Applied Physics, Friedrich-Schiller-Universität, Max-Wien-Platz 1, 07743 Jena, Germany
[2]Institute of Condensed Matter Theory and Solid State Optics, Friedrich-Schiller-Universität, Max-Wien-Platz 1, 07743 Jena, Germany
christianhelgert@uni-jena.de

Abstract— We consider the effect of disorder in one transverse dimension, termed anisotropic disorder, on the optical properties of a metamaterial consisting of cut-wire-pair meta-atoms. The work comprises experimental and numerical studies. The appropriate samples were fabricated and their optical properties quantified in the far-field. For comparison large scale rigorous numerical simulations were performed. We observe excellent agreement between experiment and theory. Based on our results we reveal how the electric dipole interactions between adjacent meta-atoms affect the overall spectral response of the metamaterial. Our main observation is a polarization-sensitive degradation of the symmetric resonance for anisotropic disorder.

1. INTRODUCTION

Artificial electromagnetic metamaterials (MMs) are obtained by assembling sub-wavelength unit cells. These unit cells may be called meta-atoms. Metamaterials represent a mesoscopic material that permits the control of light propagation beyond that in natural media [1]. To ease their fabrication as well as their design, these unit cells are usually arranged on a periodic lattice. Nonetheless, this periodicity often causes undesired propagation characteristics since the MM merely acts as a metallo-dielectric photonic crystal where the respective Bloch mode dispersion relation attains a complex, non-spherical shape. Hence, it is quite a challenge to implement MMs with isotropic or specific anisotropic properties, which are frequently required for a large number of potential MM applications. Lifting the periodicity condition and implementing amorphous meta-atom arrangements [2, 3] is usually regarded as a promising path to achieve isotropic properties. Recent studies to understand the effect of positional disorder on the optical functionality considered single and double split-ring resonators in various spectral domains [4, 5, 6]. However, the emphasis was exclusivley on MM systems where only electric dipoles could be excited under normal incidence illumination. It is imperative to extend those studies towards more complex meta-atoms that support higher order multipoles in order to develop a comprehensive understanding of disordered MMs. Most notably, a respective experimental approach will constitute a quantitative benchmark for multipole electrodynamics applied to MMs [7].

Here we examine metallic double cut-wire pairs (DCWPs), which are promising potential optical negative index MMs [8, 9]. Their spectral response is governed by two plasmonic eigenmodes. They are termed 'symmetric' and 'anti-symmetric', referring to the relative phases of the current that oscillates in both wires upon excitation. The anti-symmetric mode is significant in that it acts as a 'magnetic resonance'. Recently, we reported on the robustness of this mode against isotropic positional disorder [10]. Simultaneously, the symmetric eigenmode suffers from degradation and resonance broadening. To probe for further details of the lack of periodicity, we analyze here how disorder in one transverse direction influences the optical properties of the samples. The motivation for our approach is twofold. Firstly, the nearest-neighbor interactions of adjacent meta-atoms can be discriminated with respect to their electromagnetic eigenmodes and to polarization of the incident field . Secondly, anisotropic disorder constitutes an elegant way to break the symmetry in an arrangement of otherwise geometrically isotropic unit cells. Thus it provides a new degree of freedom for the design of biaxial anisotropic MMs as demanded for imaging applications [11].

2. ISOTROPIC VS. ANISOTROPIC DISORDER

Each fabricated DCWP consists of two 30 nm thick gold layers separated by 45 nm of magnesia. The layers have a square cross section of $180 \times 180\,\mathrm{nm}^2$ (see inset in Fig. 1a). Figure 1a shows a referential DCWP sample with a periodicity of p=512 nm in both lateral directions. Further

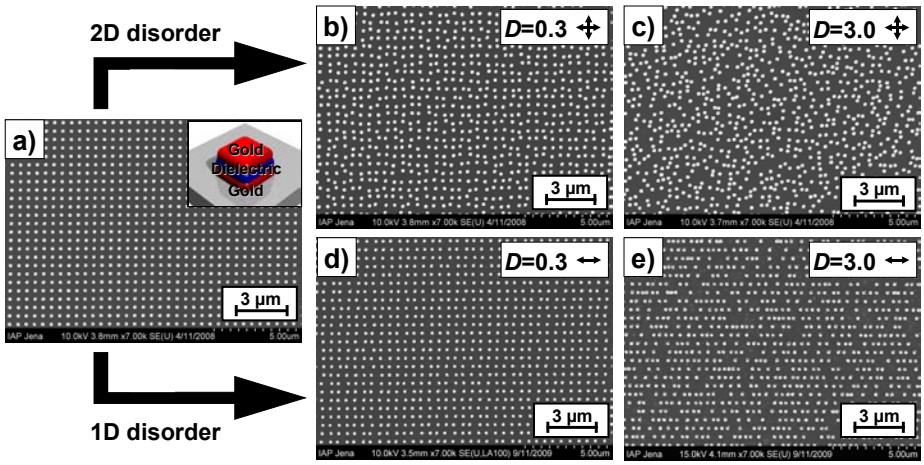


Figure 1: Normal view SEM micrographs of the fabricated MMs associated with different types of positional disorder. a) Periodic cut-wire-pair MM (inset: schematic of a unit cell). 2D (isotropic) disorder with b) $D = 0.3$ and c) $D = 3.0$; 1D (anisotropic) disorder with d) $D = 0.3$ and e) $D = 3.0$.

fabrication details are described elsewhere [10]. We introduce positional disorder to each individual DCWP by adding a random, uniformly distributed displacement $\Delta \in [-D \cdot p/2, D \cdot p/2]$. D is a dimensionless parameter that quantizes the average magnitude of disorder. While $D = 0.0$ corresponds to the periodic case, an increase towards $D = 1.0$ reflects the transition to a partially disordered arrangement of the DCWPs. For values of D (much) larger than unity the short-range as well as the long-range correlations in the spatial positions of the meta-atoms disappear. Although many samples with various values of D were fabricated, we restrict our discussion to the cases of $D = 0.3$ and $D = 3.0$ as they contain already sufficient information. By means of supplementary experiments and simulations we verified that for $D > 3.0$ the conclusions to be drawn are not affected, since the statistical displacement of a DCWP from its regular grid position outnumbers the average size of the meta-atom. The ensembles are then indistinguishable. The only restriction we enforced was a minimum distance between adjacent DCWPs in order to suppress near-field coupling in excess. The disorder in such deterministic samples can be either introduced for both transverse dimensions simultaneously or for a single transverse dimension only. In the first case, 2D (isotropic) disorder can be carried on towards full amorphisation (Fig. 1b and 1c) whereas in the latter case 1D (anisotropic) disorder emerges (Fig. 1d and 1e). Using e-beam lithography as the tool to define the nanopatterns, we are able to precisely control both the dimensionionality and the magnitude of disorder. Consequently, their individual influence on the optical response of the respective MMs can be explored.

3. NEAR-FIELD OPTICAL RESPONSE

To get insight into the underlying physics of heterogeneous nanooptical devices, current numerical techniques offer an equivalent alternative to optical near-field measurements [12]. The local electromagnetic fields of such non-periodic arrangements of strongly scattering entities can be obtained by large scale simulations. Here we used the finite-difference time-domain (FDTD) method [13] to treat $7\,\mu\text{m} \times 7\,\mu\text{m}$ supercells containing 196 metaatoms in various arrangements. Details of the numerical technique are outlined in [14].

Selected results of the simulations are shown in Fig. 2. At first, we focus on the field of the anti-symmetric plasmonic eigenmode at longer wavelengths (λ=1094 nm). The scattered field of this eigenmode is dominated by an electric quadrupole and a magnetic dipole [15]. Intriguingly, the in-plane components of the electric fields vanish for both multipolar contributions in the plane of the DCWPs. Hence, the driving field of each DCWP is exclusively the external illumination. The interaction among neighboring DCWPs is negligible and independent of their actual arrangement. Exemplarily, Fig. 2a shows the case of full isotropic disorder for the anti-symmetric resonance. Note that the field amplitudes are nearly equal for each DCWP independent of its individual position and proximity to its next neighbors. Basically, the anti-symmetric eigenmode is virtually unaffected by disorder regardless of its magnitude or degree of isotropy.

The behavior gets more complex for the symmetric resonance at shorter wavelengths (λ=797 nm).

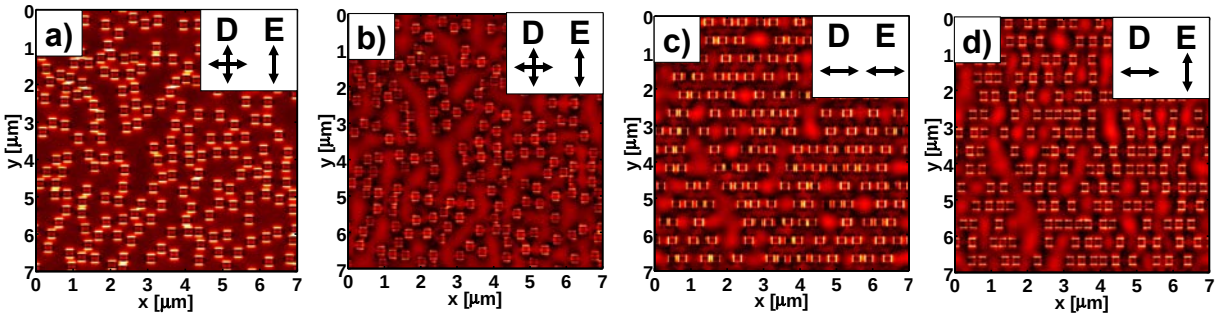


Figure 2: Optical near-fields obtained by supercell FDTD simulations. The figures show the modulus of the electric field 10 nm above the DCWPs for plane wave illumination at normal incidence. a) Isotropic disorder with $D = 3.0$ at the anti-symmetric resonance ($\lambda = 1094$ nm). b) Isotropic disorder with $D = 3.0$ at the symmetric resonance ($\lambda = 797$ nm). Anisotropic disorder with $D = 3.0$ at the symmetric resonance with c) electric field polarized parallel and d) orthogonal to the direction of disorder, respectively.

Here, the positional disorder will perceptibly affect the field distributions since the scattered field corresponds to that of an electric dipole which has a strong in-plane field component. We start our investigation with isotropic disorder (Fig. 2b). Because of the C_4 symmetry of both the DCWPs and the average disorder vector we anticipate a polarization-independent response. The local electric field driving each DCWP is a superposition of the external illumination and the field scattered from all the other DCWPs. The amplitude and phase of this contribution vary strongly from element to element because of the disordered arrangement. This results in a modification of the driving field for each DCWP. Hence the amplitudes of the electric fields decrease with increasing disorder. Furthermore, Fig. 2b shows that the field strength at individual DCWPs varies strongly depending on their very proximity.

The decreasing of the phase correlations between the excited DCWPs can further be analyzed by enforcing anisotropic disorder. In this way the degradation of the dipole-based resonance becomes polarization-dependent. A perceptible difference is anticipated, since the angular distribution of the scattered field for the dipole is also strongly anisotropic. Figures 2c and 2d reveal the two situations where the electric field is polarized either parallel or perpendicular to the disorder vector.

If the electric field is polarized parallel to the disorder vector, the oscillator strength in the excited DCWPs is in general lower and, most notably, homogenous when compared to the periodic arrangement, but may locally even exceed this value. Particularly, if two DCWPs are brought in close proximity along the chains, the arrangement resembles a coupled-antenna configuration where the feed gap between the two antennas sustains an extraordinarily strong field enhancement at resonance [16]. Such bright spots are clearly visible in Fig. 2c. Note that due to the enforced separation distance a spatial overlap of two DCWPs is impossible. However, performing a spatial averaging these extrema are negligible and a rather constant field emerges. This capacitive coupling regime is generally suppressed since a minimum distance among neighboring DCWPs was enforced. Moreover, the coherent interaction among disordered DCWPS for a disorder vector parallel to the polarization in the sense described above is strongly suppressed, since the electric dipole will not scatter light into the direction of its orientation. For this reason it is expected that in the limit of very small DCWPs, this anisotropic disorder is ineffective at first glance. However, this is necessarily an approximation.

If the electric field is perpendicularly polarized to the disorder vector, the picture appears differently. Since the scattered field of the electric dipole is strongest perpendicular to its orientation, the scattered field that adds to the external illumination depends sensitively on disorder. It becomes obvious from Fig. 2d, that the interaction between the DCWPs is stronger since the amplitude of the field above each DCWP is strongly fluctuating.

Based on these considerations we expect the strongest effect on the optical properties of the sample, when compared to the periodic case, to occur for the sample that exhibits an isotropic disorder. The influence of an anisotropic disorder perpendicular to the incident polarization will be slightly weaker. An even further decrease of this influence will be observed for the anisotropic disorder being parallel to the incident polarization. This hypothesis is verified in the study of the far-field optical response.

4. FAR-FIELD OPTICAL RESPONSE

The distinct effects of isotropic and anisotropic disorder in a DCWP MM translate directly into its optical far-field response. To compare experiments to simulations, the complex transmission and reflection spectra can be extracted from the locally resolved simulated amplitudes by imposing a spatial Fourier transform. The zeroth order corresponds to the normal transmission/reflection. These quantities can be experimentally accessed by standard spectroscopy. Here we restrict our investigations to the spectral region containing the symmetric resonance. The persistence of the anti-symmetric mode against positional disorder was already shown [10] and depends neither on the degree of the disorder nor on its isotropic or anisotropic character. Hence we shall focus on the symmetric resonance. Figures 3a and 3b display its degradation in transmission and reflection, if isotropic disorder with $D = 3.0$ is imposed. The main observations are a blue-shift, broadening and damping of the symmetric resonance [17]. The very good qualitative agreement between theory and experiment also asserts that the finite size of our FDTD supercell and its individual implementation of disorder do not influence the general spectral characteristics compared to the fabricated samples. Remaining discrepancies may be likely attributed to imperfections in the fabrication of the samples.

For anisotropic disorder the excitation of the symmetric resonance depends on the polarization of the incident field with respect to the disorder vector. Fully in line with the investigations of the optical near-field, a polarization-sensitive far-field response is revealed. Compared to the isotropic disorder, a smaller resonance degradation is found that is clearly observable in Fig. 3. The degradation remains stronger when the polarization of the electric field is orthogonal to the anisotropic disorder vector. The weakest degradation when compared to the perfect periodic case is found for a polarization vector that is parallel to the disorder vector. These findings are consistent with our interpretation of electric dipole-dipole interactions between neighboring DCWPs in the near-field.

5. CONCLUSIONS

We experimentally and theoretically investigated the effects of isotropic and anisotropic positional disorder of meta-atoms on the spectral properties of the constituting MMs. Based on far-field spectroscopic measurements we reveal that the degradation of the symmetric resonance depends on the dimensionality of disorder. For anisotropic disorder it becomes polarization-sensitive. Sup-

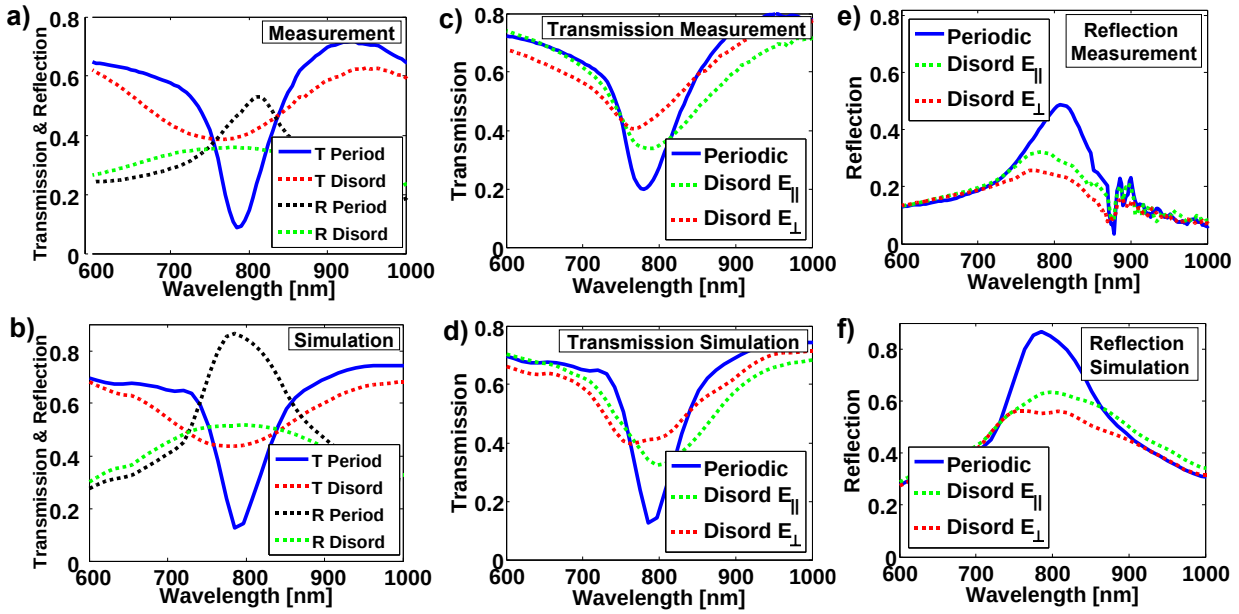


Figure 3: a) Measured and b) simulated transmission and reflection spectra of periodic and isotropically disordered MMs showing the degradation of the symmetric resonance. c) Measured, d) simulated transmission spectra and e) measured, f) simulated reflection spectra of periodic and anisotropically disordered MMs showing the degradation of the symmetric resonance depending on the orientation of the disorder with respect to the polarization state of the illumination.

ported by rigorous large-scale near-field simulations, we may relate our findings to nearest-neighbor interactions of the excited electric dipoles. Anisotropic disorder provides an alternative means of symmetry breaking in an arrangement of geometrically isotropic meta-atoms. Our results constitute a solid benchmark for analytical multipole theories for MMs [7], whose exploration will be subject to future work.

ACKNOWLEDGMENT

We acknowledge financial support by the Federal Ministry of Education and Research (ZIK ultraoptics and Metamat) and the Thuringian State Government (MeMa).

REFERENCES

1. Engheta, N. and R. Ziolkowski, *Metamaterials: Physics and Engineering Explorations*, Wiley-IEEE Press, 2006.
2. Shalkevich, N., A. Shalkevich, L. Si-Ahmed and T. Bürgi, "Reversible formation of gold nanoparticle-surfactant composite assemblies for the preparation of concentrated colloidal solutions," *Phys. Chem. Chem. Phys.*, Vol. 11, 10175-10179, 2009.
3. Pakizeh, T., A. Dmitriev, M. S. Abrishamian, N. Granpayeh and M. Käll, "Structural asymmetry and induced optical magnetism in plasmonic nanosandwiches," *J. Opt. Soc. Am. B*, Vol. 25, No. 4, 659-667, 2008.
4. Aydin, K., K. Guven, N. Katsarakis, C. Soukoulis and E. Ozbay, "Effect of disorder on magnetic resonance band gap of split-ring resonator structures," *Opt. Express*, Vol. 12, No. 24, 5896–5901, 2004.
5. Papasimakis, N., V.A. Fedotov, Y.H. Fu, D.P. Tsai and N.I. Zheludev, "Coherent and incoherent metamaterials and order-disorder transitions," *Phys. Rev. B*, Vol. 80, 041102(R), 2009.
6. Singh, R., X. Lu, J. Gu, Z. Tian and W. Zhang, "Random terahertz metamaterials," *J. Opt.*, Vol. 12, 015101, 2010.
7. Petschulat, J., C. Menzel, A. Chipouline, C. Rockstuhl, A. Tünnermann, F. Lederer and T. Pertsch, "Multipole approach to metamaterials," *Phys. Rev. A*, Vol. 78, 043811, 2008.
8. Dolling, G., C. Enkrich, M. Wegener, F.J. Zhou, C.M. Soukoulis and S. Linden, "Cut-wire pairs and plate pairs as magnetic atoms for optical metamaterials, *Opt. Lett.* , Vol. 30, No. 23, 3198–4000, 2005.
9. Shalaev, V., W. Cai, U. Chettiar, H. Yuan, A. Sarychev, V. Drachev and A. Kildishev, "Negative index of refraction in optical metamaterials," *Opt. Lett.*, Vol. 30, No. 24, 3356–3358, 2005.
10. Helgert, C., C. Rockstuhl, C. Etrich, C. Menzel, E.-B. Kley, A. Tünnermann, F. Lederer and T. Pertsch, "Effective properties of amorphous metamaterials," *Phys. Rev. B*, Vol. 79, 233107, 2009.
11. Paul. T., C. Rockstuhl, C. Menzel, and F. Lederer, "Anomalous refraction, diffraction, and imaging in metamaterials," *Phys. Rev. B*, Vol. 79, 115430, 2009.
12. Zentgraf, T., J. Dorfmüller, C. Rockstuhl, C. Etrich, R. Vogelgesang, K. Kern, T. Pertsch, F. Lederer, and H. Giessen, "Amplitude- and phase-resolved optical near fields of split-ring-resonator-based metamaterials," *Opt. Lett.* , Vol. 33, No. 8, 848–850, 2008.
13. Taflove, A. and S. Hagness, *Computational Electrodynamics: The Finite-Difference Time-Domain Method*, Artech House, Boston, 3rd ed., 2005.
14. Esteban, R., R. Vogelgesang, J. Dorfmüller, A. Dmitriev, C. Rockstuhl, C. Etrich and K. Kern, "Direct Near-Field Optical Imaging of Higher Order Plasmonic Resonances," *Nano Lett.*, Vol. 8, No. 10, 3155–3159, 2008.
15. Cho, D.J., F. Wang, X. Zhang and Y. R. Shen, "Contribution of the electric quadrupole resonance in optical metamaterials," *Phys. Rev. B*, Vol. 78, 121101(R), 2008.
16. Mühlschlegel, P., H. Eisler, O. Martin, B. Hecht and D. Pohl, "Resonant Optical Antennas," *Science*, Vol. 308, 1607–1609, 2005.
17. Zou, S. and G. Schatz, "Narrow plasmonic/photonic extinction and scattering line shapes for one and two dimensional silver nanoparticle arrays," *J. Chem. Phys.*, Vol. 121, No. 24, 12606–12612, 2004.

Theoretical and experimental investigations of easy made fishnet metamaterials at microwave frequencies

Riad Yahiaoui[1, 2], Valérie Vignéras[2], and Patrick Mounaix[1]

1Centre de Physique Moléculaire Optique et Hertzienne, Université Bordeaux 1, UMR 5798, 351 Cours de la libération 33405 Talence Cedex.

2 Laboratoire de l'intégration du matériau au système, UMR 5218, Université Bordeaux1 16 avenue Pey Berland 33607 Pessac

p.mounaix@cpmoh.u-bordeaux1.fr

Abstract- In this work, we demonstrate theoretically and experimentally a left handed behaviour of a planar fishnet type metamaterial in the microwave regime. The fabrication process is very easy, unique and doesn't involve optical lithography. The effective parameters were extracted using the S parameter retrieval method and show a perfect agreement between simulation and experiment. Using finite element method based simulations and W-band (75GHz – 110GHz) experiments, we obtained a negative index of refraction of -4 at 85GHz. The left handed materials discussed here represent a step towards the easy fabrication of metamaterials with a negative refractive index and paves the way for the active manipulation of millimeter wavelengths.

1. INTRODUCTION

Since the pioneering work of V.G.Veselago [1] in 1968 on the general properties of wave propagation in a negative refractive index medium, and the proposed structure of Pendry et al [2], many researchers investigated Left Handed Materials (LHM). Smith et al [3] first demonstrated the feasibility of a left handed metamaterial at microwave frequencies experimentally. This LHM combines a split ring resonator (SRR) array to achieve negative effective permeability and a continued wires array to obtain negative effective permeability. Subsequently many kinds of structures with different shapes were studied and built in order to obtain the desired effective properties of permittivity, permeability and refractive index. Various planar structures were then designed in order to show the LH property in the near infrared and even optical frequency regimes [4-9]. In this paper, we study a fishnet type metamaterial [10-13]. The target W–band, establishes an intermediary zone where it is fairly easy to check physical concepts, because the dimensions of the elementary cells do not raise real technological problems. The fabrication of the structure which requires no optical lithography is both simple and inexpensive.

2. DESIGN AND FABRICATION OF THE METAMATERIAL

The unit cell of the metamaterial is schematically shown in Fig. 1(a). The sample is illuminated by a plane wave at normal incidence with the electric field parallel to the x axis ($\boldsymbol{E} \parallel$ x axis) and the magnetic field parallel to the y axis ($\boldsymbol{H} \parallel$ y axis). The resulting propagation direction is along the z axis ($\boldsymbol{k} \parallel$ z axis). The structure is manufactured using a commercial printed circuit board (PCB) designed for ultra high frequency operation. The PCB is composed of a dielectric interlayer substrate characterised by thickness=100µm, ε_r=2.17, tan(δ)=0.009, coated on both side with copper (thickness=35 µm). The structure is fabricated on a CNC drill by drilling holes (diameter=1.9 mm) through both the metal layers and the dielectric substrate resulting in an array of perfect cylindrical air holes. The unit cell is repeated periodically along the x and y directions with a periodicity of a_x=a_y=2.5 mm. Although this is only slightly smaller than λ, diffraction still cannot occur because the electromagnetic waves do not propagate along x and y directions [14]. We believe that this fast, easy and cheap fabrication process will open the possibility of mass production for applications. Moreover, for higher frequency designs which require smaller, narrower holes or holes of rectangular shape in any material matrix, a laser ablation method using a Yb:KGW 1.03 µm femtosecond laser at Alphanov technological center [15] can be employed. The ultrafast regime offers an enhanced control in sculpting the desired microstructures as the deposition of the laser energy occurs on a much shorter timescale than the heat transport and the electron-phonon coupling resulting in a very low damage regime and a restricted heat affected zone [16-17]. The

measurements were performed in free space using a vector network analyzer and two microwave horn antennas in the W-band.

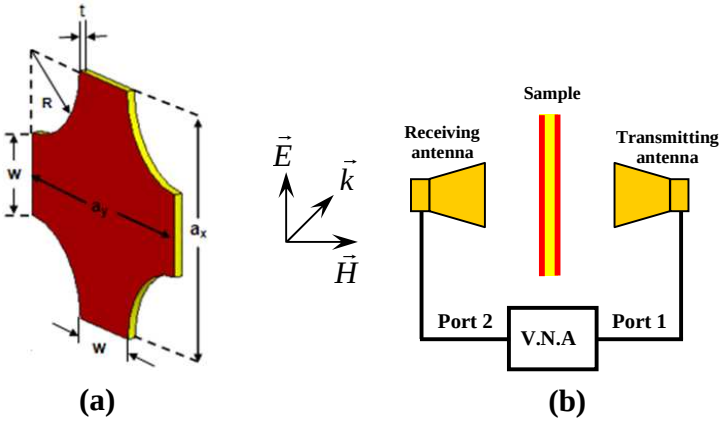


Fig. 1. (a) Schematic view of a fishnet unit cell with geometric dimensions $a_x=a_y=2.5$ mm, R=0.95 mm, w=0.6 mm, t=100 µm. (b) Schematic free space S-parameter measurement setup.

The reflection and transmission measurements are carried out applying an AB Millimetre^{TM} vector network analyzer. In the transmission measurements, the plane incident waves are normal to the sample surface and the transmitted intensity is normalised with respect to the transmitted signal in free space between the two horn antennas. Similarly S_{11} is measured with a directional coupler in the reflection geometry. The normalisation for the reflection is obtained with a sheet of copper as reflecting mirror.

3. SPECTRAL RESPONSE AND EFFECTIVE PARAMETERS

The spectrum of the structure was simulated using commercial electromagnetic simulations software based on the finite element method (HFSS: High Frequency Structure Simulator)[18]. Figures 2(a)-(b) respectively show magnitude and phase of the calculated (solid line) and measured (dashed line) S_{21} and S_{11} parameters of the investigated metamaterial. There is a very good quantitative agreement between simulations and measurements. We observe a transmission band between 85 GHz and 90 GHz (highlighted in fig. 2(a)), which corresponds to the spectral region exhibiting negative refractive index. The minor shift of the measured spectrum towards lower frequencies compared to the simulated one is due to the lack of precision in the fabrication.

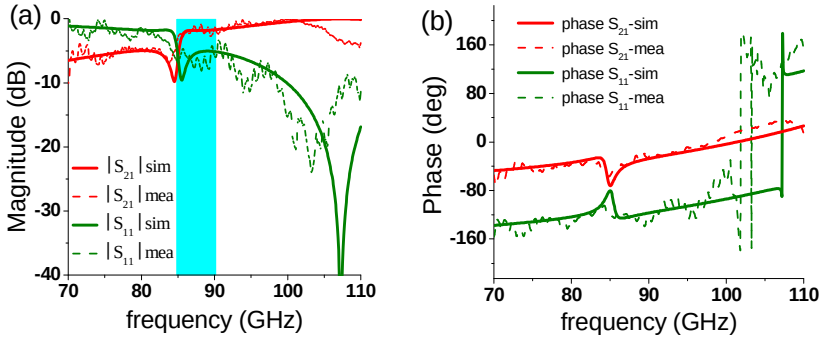


Fig. 2. Simulated (solid lines) and measured (dashed lines) (a) reflexion and transmission magnitude in dB (b) phase in degree for one layer of fishnet metamaterial in the propagation direction.

The effective parameters µ, ε, z and n shown in figures 3(a)-(d) were extracted using the method described in ref.[19], where $\mu=\mu_1+i\mu_2$, $\varepsilon=\varepsilon_1+i\varepsilon_2$, $z=z_1+iz_2$ and $n=n_1+in_2$. The retrieved results indicate that our metamaterial exhibits a negative refractive index within the frequency range from 80 GHz to 90 GHz with a very high level of

-4 stemming from the very low dielectric losses at this frequency. The negative index band includes a single-negative ($\varepsilon_1<0$ and $\mu_1>0$) band from 80 GHz to 85 GHz and the double negative ($\varepsilon_1<0$ and $\mu_1<0$) band from 85 GHz to 90 GHz. As explained by Depine et al [20], although the real part of permeability μ_1 doesn't reach negative values, at the low-frequency side, negative index can be achieved when the condition $\varepsilon_1\mu_1+\varepsilon_2\ \mu_2<0$ is satisfied. The dip in the reflection spectrum in fig. 2(a) around 105 GHz is due to the fact that the sample impedance $z_1=1$ at that frequency, and so no reflection is possible.

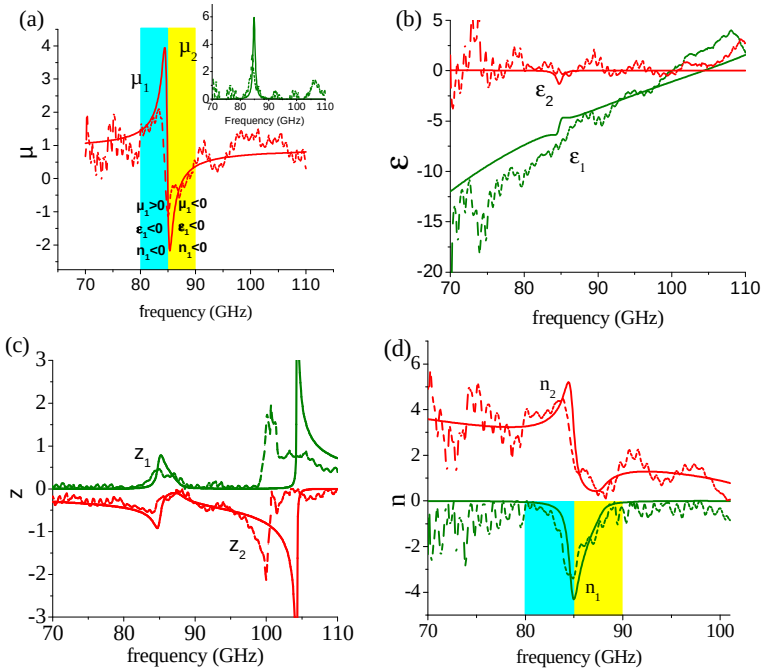


Fig. 3. Measured (dashed lines) and simulated (solid lines) of retrieval parameters. (a) effective permeability, (b) effective permittivity, (c) effective impedance (d) effective refractive index.

We can observe minor differences between the simulation and the experiment because, in the simulation the structure is modelled as a laterally infinite periodic material along the x and y directions. However, the experimental structure has a finite size which may cause diffraction at the edges. Moreover, with other fishnet structures designed for different frequencies 35 GHz, 55 GHz, and 94 GHz also fabricated and measured (but not presented here), we found an effective index at the same level (i.e. ~-4).

4. CONCLUSION

Easily manufactured, the fishnet-structure-type metamaterial presented in this work exhibits a very high negative refractive index value of – 4 at 85GHz. The effective parameters were retrieved from the S parameters measured in the W-band and an excellent agreement between simulation and experiment was demonstrated. Numerical simulations were performed in order to present the magnitude and phase of the transmission and reflection coefficients with the effective material responses. The LH structure exhibits a magnetic resonance confirmed by calculations. The demonstrated principle represents a step towards the easy fabrication of a metamaterials with negative refractive index, which opens a new path for the active manipulation of millimeter wavelengths.

ACKNOWLEDGMENT

This work is financed by the University of Bordeaux 1 within the project "GIS AMA-SAMM". The authors would like to thank P. Kužel and H. Němec for sharing their experience, their advices and discussions about the metamaterial structures. The authors would like to thank M .E. Maillard for the fabrication of the metamaterials sample with the CPMOH mechanics facilities.

REFERENCES

1. V. G. Veselago, "the electrodynamics of substances with simultaneously negative values of ε and μ," Sov. Phys. Usp. 10, 509-514 (1968).
2. J.B Pendry, "Negative refraction makes a perfect lense," Phys. Rev. Lett. 85, 3966 (2000).
3. D. R. Smith, W. J. Padilla, D. C. Vier, S. C. Nemat-Nasser, and S. Schultz, "Composite medium with simultaneously negative permeability and permittivity," Phys. Rev. Lett. 84, 4184 (2000).
4. S. Zhang, W. Fan, N. C. Panoiu, K. J. Malloy, R. M. Osgood, and S. R. J. Bruek, "Experimental demonstration of near-infrared negative-index metamaterials," Phys. Rev. Lett. 95, 137404 (2005).
5. V. M. Shalaev, W. Cai, U. K. Chettiar, H. K. Yuan, A. K. Sarychev, V. P. Drachev, and A. V. Kildishev, "Negative index of refraction in optical metamaterials," Opt. Lett. 30, 3356-3358 (2005).
6. G. Dolling, C. Enkrich, M. Wegener, C. M. Soukoulis, and S. Linden, "Simultaneously negative phase and velocity of light in a metamaterial," Science 312, 892 (2006).
7. G. Dolling, C. Enkrich, M. Wegener, C. M. Soukoulis, and S. Linden, "Low-loss negative-index metamaterial at telecommunication wavelengths," Opt. Lett. 31, 1800-1802 (2006).
8. S. Zhang, W. Fan, N. C. Panoiu, K. J. Malloy, R. M. Osgood, and S. R. J. Brueck, "Optical negative-index bulk metamaterial consisting of 2D perforated metal-dielectric stacks," Opt. Express 14, 6778-6787(2006).
9. K Guven, A. O. Cakmak, M. D. Caliskan, T. F. Gundogdu, M. Kafesaki, C. M. Soukoulis, and E. Ozbay, "Bilayer metamaterial: analysis of left-handed transmission and retrieval of effective medium parameters," J. Opt. A: Pure Appl. Opt. 9, S361-S365 (2007).
10. K.B Alici and E.Ozbay, "Characterization and tilted response of a fishnet metamatrial operating at 100 GHz," J. Phys. D: Appl. Phys. 41, 135011(2008).
11. G,Doliind, M.Wegener, C.M.Soukoulis and S.Linden, "Design-related losses of double-fishnet negative-index photonic metamaterials," Optics Express 15, 11536-11541 (2007).
12. S. Zhang, W. Fan, K. J. Malloy, S.R. Brueck, N. C. Panoiu, and R. M. Osgood, "Near-infrared double negative metamaterial," Optics Express 13, 4922-4930 (2005).
13. M.Kafesaki, I. Tsiapa, N. Katsarakis, Th. Koschny, C. M. Soukoulis, and E. N. Economou, "Left handd metamterials: The fishnet structure and its variations," Phys. Rev. B 75, 235114 (2007).
14. C. Yan, Y. Cui, Q. Wang and S. Zhuo, 'Negative refractive indices of a confined discrete fishnet metamaterial at visible wavelengths," J. Opt. Soc. Am. B 25, 1815-1819 (2008).
15. http://www.alphanov.com
16. H. Němec, H. Němec, P. Kužel, F. Kadlec, C. Kadlec, R. Yahiaoui, and P. Mounaix, "Tunable terahertz metamaterials with negative permeability," *Phys. Rev. B* 79**,** 241108(R) (2009).
17. R. Yahiaoui, H. Němec, P. Kužel, F. Kadlec, C. Kadlec, and P. Mounaix, "Broadband dielectric terahertz metamaterials with negative permeability," *Opt. Lett*. 34, 3541-3543 (2009).
18. High Frequency Structure Simulator, HFSS v11.1, Ansoft Ltd.
19. D. R. Smith, S. Schultz, P. Markos, C. M. Soukoulis, "Determination of effective permittivity and permeability of metamaterials from reflection and transmission coefficients," Phys. Rev. B 65, 195104 (2002).
20. R.A. Depine and A. Lakhtakia, "A new condition to identify isotropic dielectric-magnetic materials displaying negative phase velocity," Microwave Opt. Technol. Lett. 41, 315-316 (2004).

Crystallographic-oriented metal nanowires on semiconductor surface: technology and modeling

N. L. Dmitruk[1], T. R. Barlas[1], A. M. Dmytruk[2,3], A. V. Korovin[1], and V. R. Romanyuk[1]

[1]Institute of Semiconductor Physics, National Academy of Sciences of Ukraine, Kyiv, Ukraine
[2]Center for Interdisciplinary Research, Tohoku University, Sendai, Japan
[3]Institute of Physics, National Academy of Sciences of Ukraine, Kyiv, Ukraine
dmitruk@isp.kiev.ua

Abstract- A simple technique for synthesis of noble metal nanoparticles from corresponding salts on semiconductor substrates has been elaborated. The metal nanowires on the ledges of surface microrelief of quasigrating type were obtained and modeling of their optical properties was carried out.

1. INTRODUCTION

Semiconductor nanowires (nanorods) and nanotubes have an unique physical properties (electronic and phononic), which arise owing to their 1D geometry, large surface to volume ratio, and charge carriers and phonon confinement in two dimensions. Therefore they can be used as nanoelectronic devices (field-effect transistors, inverters, *p-n* junctions, sensors, thermoelectric converters etc.), as optoelectronic devices (photodetectors, light-emitting diodes/lasers, solar cells etc.), and as wires for access to these devices. For last aim and other nanophotonic applications for generation, waveguides, and detection of light on the nanoscale (i.e. with subwavelength dimension) metallic 1D structures are used too.

These applications are based on the geometry-dependent surface plasmon resonance. 1D periodical array of noble metals wires exhibit anomalous optical properties in visible and near-infrared regions due to excitation of localized (surface) plasmons (SP) and surface plasmon polaritons (SPP) and their interaction. SPP are guided modes between a metal and dielectric medium with the negative and positive real part of the electric permittivity, respectively. They compress electromagnetic energy in subwavelength volume beyond the diffraction limit. Therefore the metal 1D array on a semiconductor substrate is especially promising for electronic control of optical devices.

This paper is devoted to self-formation of 1D metal wires on semiconductor substrate, investigation of their morphology and statistical parameters, and modeling of the optical properties in visible spectral region. Technology of 1D metal (Au) array formation on the semiconductor (GaAs, InP) consists in anisotropic etching of the single crystal substrate, and following photoinduced chemical gold deposition from an aqueous gold salt solution on it. Morphology and statistical characteristics of 1D structures formed was characterized by atomic force microscopy (AFM) and scanning electron microscopy (SEM) with X-ray energy dispersive element analysis (EDX).

Modelling of optical properties of 1D metal nanowires array has been fulfilled by two methods: 1) the anisotropic Bruggeman's effective medium approximation (EMA) [1], and 2) the differential formalism using the covariant form of Maxwell's equations in the curvilinear coordinates [2]. Experimentally optical response of array of selforiented metal 1D wires was measured using reflectance spectra.

2. TECHNOLOGY AND MORPHOLOGY

As a substrate for 1D metal array deposition, the single crystals GaAs and InP with (100) orientation were used. The template for metal deposition was prepared by wet chemical anisotropic etching GaAs and InP in constantly stirred multicomponent selective etchants based on the mixture of $HF+H_2SO_4+H_2O_2$ (2:2:1) and concentrated HCl for GaAs and InP, respectively. The mechanism of etching process was studied earlier using kinetic curves [3]. It manifests on the (100) InP surfaces long narrow etch grooves parallel to the ⟨011⟩ direction. The average period increases with process duration (t=1−10 min.).

Using an analyzer Hitachi S-4000, we investigated several GaAs samples with microrelief and flat surfaces (for comparison) to determine the effect of anisotropic etching on the stoichiometry of near-surface layer. The analyzer is an integral "EDS/X-ray microanalysis system" that enables one to obtain concurrently both surface pattern and elemental composition at any point at which an electron beam is focused. Such instrument combines a scanning electron microscope (SEM) and system for analysis of x-rays appearing when a sample is irradiated with electrons. A depth of electron beam penetration depends on the electron energy and compactness of the material studied. In our experiments the penetration depth was about 1 μm.

The obtained surface patterns are presented in Fig.1. (The flat surface is not shown because its topology had no considerable features.)

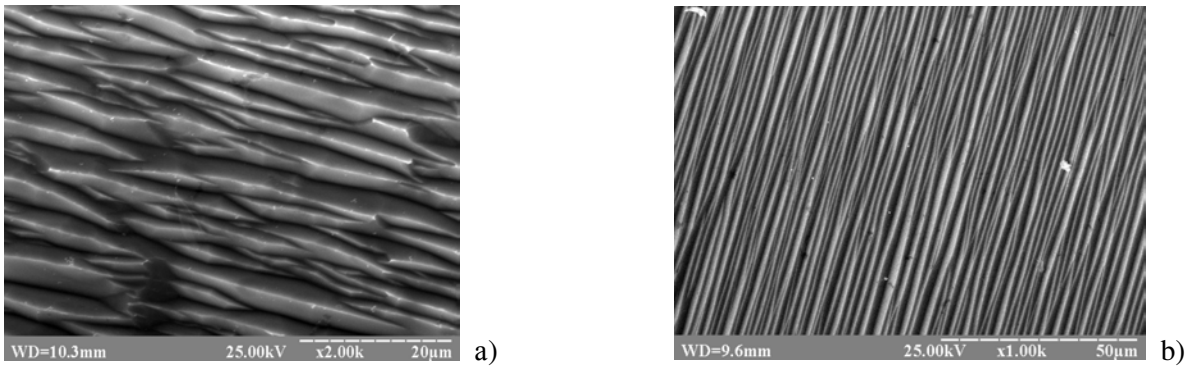


Fig. 1. SEM patterns of quasi-grating GaAs (a) and InP (b) surfaces.

Investigation of large (several mm^2) areas of both flat and microrelief surfaces showed that stoichiometry (Ga:As = 1:1) remains on average. However, if the area analyzed is reduced down to several 0.1 μm^2, then the ratio Ga:As of atomic contents for microrelief surfaces becomes dependent on the surface region and may be both over and below unity. The samples with flat surface demonstrate the same ratio Ga:As = 1:1 on large as well as small scale. Thus the microrelief surfaces, having uniform stoichiometry at large areas, become nonuniform on microscale.

An interrelation between the atomic content ratio Ga:As and relief features can be seen well if one plots the Ga and As concentrations, as well as relief height, as function of the coordinate x. The structures with one-dimensional (1D) or quasi-1D reliefs of quasi-grating-type are more appropriate for such analysis (Fig.2).

To make quantitative estimation of the surface microrelief effect on the atomic contents of components, we calculated the coefficients of correlation between the As and Ga contents and surface microrelief.

The corresponding values are K_{As} = 0.603 and K_{Ga} = 0.542. Since $K_{As} > K_{Ga}$, this is quantitative evidence that the microrelief surfaces are nonuniform on the microscale, and location of As atoms on relief ridges is more probable than that of Ga atoms. The experimental results obtained enable one to conclude that microrelief GaAs surfaces demonstrate increase of As (Ga) concentration on the ridges (in the valleys) of the relief.

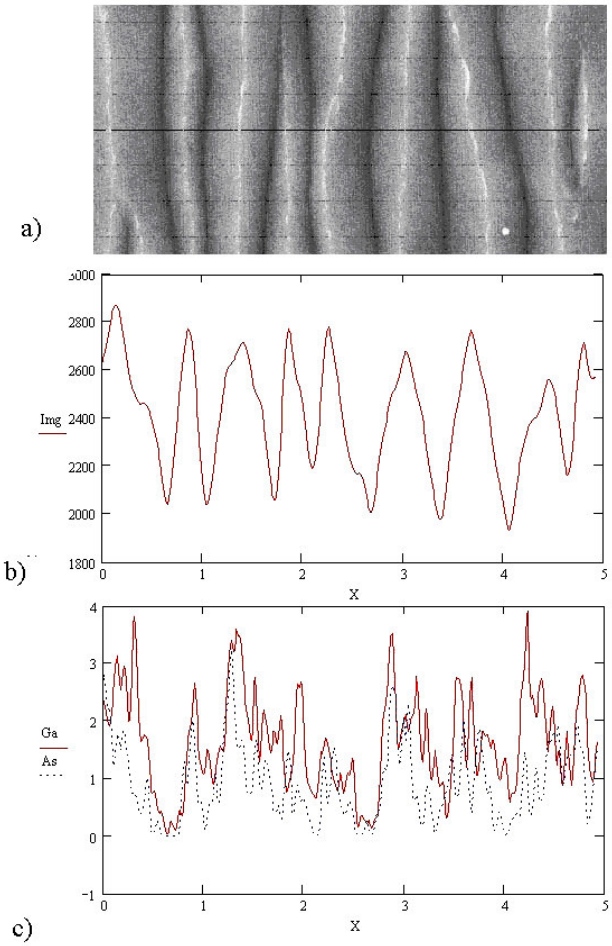


Fig. 2. SEM surface pattern and section lines along which the elemental analysis was performed (a), surface relief along the section line (b) and variation of As and Ga atomic contents with x (in μm) along the section (c).

Such interrelation between contents does not depend on the relief type (and hence on the way of chemical treatment of surface). The different affinity of elements on the tops of relief may be responsible for the selectivity of metal nanoparticles deposition.

Fig. 1b presents the microrelief produced by the anisotropic etching of the InP surface. It appears as a system of practically parallel edges triangular in cross-section. To describe a spontaneously formed microrelief of this kind and to characterize its perfection, the average value of the structural period can be conveniently used. The etching procedure was optimized so as to obtain the minimum possible period (< 1 μm) and maximum length of edges. The edges lengths thus obtained amount to 100 - 200 μm, i.e. they are two orders of magnitude large than the interedge period.

Metal (Au) nanoclusters were grown by the photoinduced chemical deposition from aqueous gold salt $AuCl_3$ [4, 5]. AFM and SEM measurements show that metal nanoclusters are deposited predominantly at the tops of the microrelief. Therefore for the quasi-grating type of microrelief we have got nanoparticle array in the shape of 1D system of near-parallel quasiperiodical metal wires.

It is clear from the comparison of Fig. 1a and b that GaAs and InP radically differ in perfection and periodicity of the corresponding system of nanowires. The wires on GaAs are characterized by a rather wide dispersion of geometrical parameters, with the interwire period ranging from 1 to 10 μm and the wire length from 5 to 30 μm.

Contrary to this, the wire ensembles on the quasi-grating microrelief formed on the InP single-crystal surface demonstrate a stricter periodicity, with the wire length ranging from tens to hundreds of micrometers and practically reaching a macroscopic size.

3. THEORETICAL MODELING

For simulation of optical properties of the 1D metal wires system on microrelief semiconductor surface we used two simplicated models: 1) the effective medium approximation in the Bruggeman's form (see, for example, [6]), then this system is modeled as an anisotropic layer of uniform thickness and composition, with taking into account the roughness of the surface layer the metal nanoparticles shape as a prolate spheroid with the surface parallel long axe x: a>>b=c, and the electron scattering value in the wire parallel and perpendicular directions may be different; 2) according to the differential formalism method [2] the periodic ensembles of 1D absorptive wires is represented as continuous flat metal film with some effective thickness using the covariant form of Maxwell's equations in curvilinear coordinate system.

In the first case, for a system of prolate spheroids oriented along the x, or y, or z direction the corresponding principal tensor components, $\tilde{\varepsilon}_i$, *i*= *x, y, z* can be obtained from the following relation [1]:

$$f\frac{\varepsilon_m-\tilde{\varepsilon}_i}{\tilde{\varepsilon}_i+L_i(\varepsilon_m-\tilde{\varepsilon}_i)}+(1-f)\frac{\varepsilon_s-\tilde{\varepsilon}_i}{\tilde{\varepsilon}_i+\frac{1}{3}(\varepsilon_s-\tilde{\varepsilon}_i)}=0\,, \tag{1}$$

where ε_m and ε_s are the respective permittivities of the metal wires and the effective environment of the spherical shape, *f* is the metal filling factor, L_i is the geometrical depolarizing factor, $\sum_i L_i=1$, $L_i=1/3$ for sphere, and

$$L_x=\frac{1-e^2}{e^2}\left[\frac{1}{2e}\ln\left(\frac{1+e}{1-e}\right)-1\right],\quad e^2=1-(b/a)^2 \text{ for spheroid.} \tag{2}$$

For arbitrary oriented ellipsoids (here – spheroids, this result (1) should be averaged over the orientations [6].

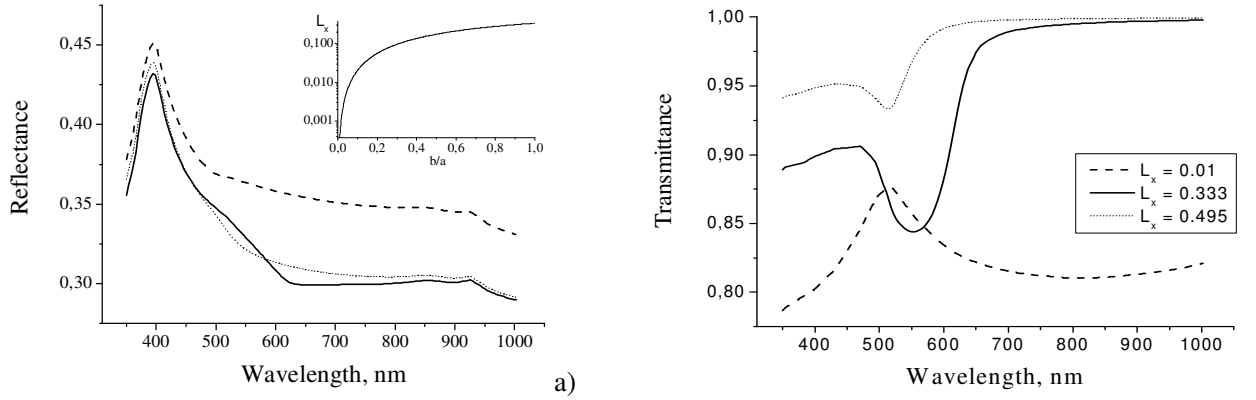


Fig. 3. Calculated near-normal reflectance (on the InP substrate) and transmittance spectra of the s-polarized light in anisotropic Bruggeman approximation (d=25nm, *f*=0.1) simulating an ensemble of prolate gold ellipsoids L_x=0.01 corresponds to the electric vector of the incident light **E** || X axis; L_y=L_z=0.495 corresponds to the **E** || Y axis. The same spectrum is presented for an isotropic film simulating an ensemble of spherical particles (L_x=L_y=L_z=*1/3*).

Fig. 3 demonstrates the calculated near-normal-to-incidence reflectance/transmittance spectra for the light polarizations parallel and perpendicular to the longest ellipsoid axe *x* for the spectral region in which SPP modes in metal 1D wires are excited. It is seen from Fig. 3, the anisotropy effect in the reflectance spectrum is very small and it is much more pronounced in the transmittance spectrum. Therefore, transferring ordered 1D array of metal nanoparticles onto polymer transparent substrate is desirable.

However the Bruggeman's EMA does not take into account the topological peculiarities of 1D wires system. Therefore we theoretically analyzed the SPP excitation in the periodic ensembles of absorptive nanowires. We have performed modeling by a system of the 1D periodic (in the x-direction) nanowires which are infinitely long in the y axis direction. We used covariant form of Maxwell's equations in curvilinear coordinate systems, each of which transforms the non-flat interface into flat one with some effective thickness. Then we applicated the differential formalism for theoretical estimation of the interaction between interfaces on optical properties of non-flat-interfaces multilayer system. For determination of the reflectance/transmittance we use the interface-normal Poynting's vector component $S_\perp$ which is defined in covariant coordinates as follows [5] $S_\perp \equiv \vec{S}\cdot\vec{n} \sim \mathrm{Re}\left(E_1^* H_2 - E_2^* H_1\right)$, where *n* is the normal to interface.

Earlier [5] the periodic 1D array of metal nanowires has been considered for the case of flat surface of substrate. Here for the case of wires localization on the edge tops of microrelief, the system analyzed is represented by four layers: air-conducting film with complicated profiles of interfaces-air-substrate. Spectral reflectance/transmittance dependencies were calculated for p, s-polarized incident light for the Au nanowires periodic ensembles on the GaAs substrate (Fig. 4). The obtained peculiarities correspond to the diffraction orders as follows from the momentum conservation law for SPP excitation: $K_{SPP}=k_x\pm n\cdot 2\pi/l_x$, where K_{SPP} is the SPP wave vector, n is diffraction order, l_x is the period. Peak amplitudes change with both the relief height and the nanowires diameter increase. Effect is especially large for p-polarized light, when excitation of SPP modes takes place.

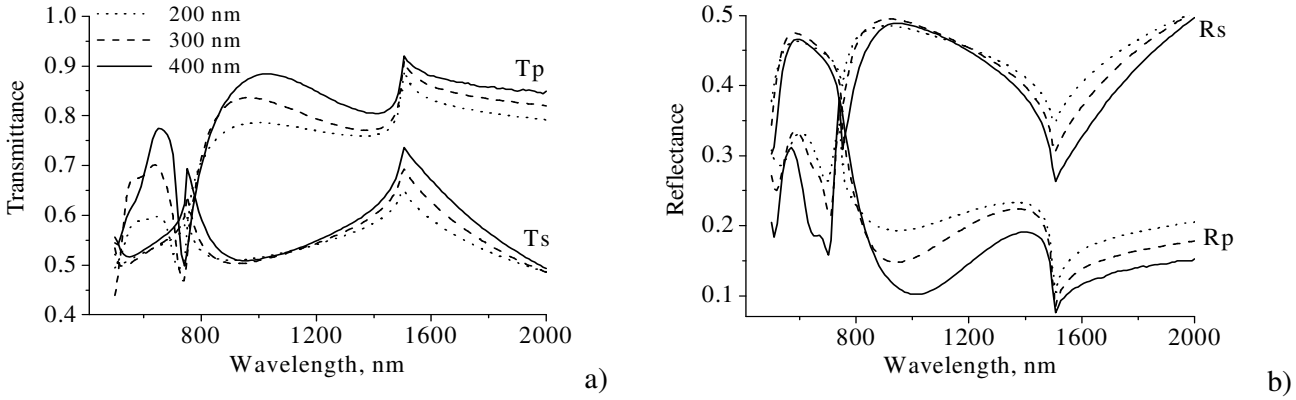


Fig. 4. Calculated transmittance (a) and reflectance (b) spectra for periodic Au wire (d=200 nm) ensembles on the top of GaAs periodical (l_x = 1500 nm) microrelief with different values of depth.

4. CONCLUSIONS

The optical response of array metal wires on the dissipative (semiconductor) substrate is essentially large under conditions of SPP excitation in wires with big diameter in transmittance measurements. Therefore, the development of the technology of ordered metal nanoparticle transferring onto transparent substrates is important. Due to these reasons the comparison of experimental results with theoretical modeling is in progress.

REFERENCES

1. Bohren, K., D. Hufman, *Absorption and Scattering of Light by Small Particles*, John Wiley and Sons Inc, New York, 1986.
2. Korovin, A. V.,"Improved method of light-matter interaction in multilayer corrugated structures," *JOSA A*, Vol. 25, No. 2, 394–399, 2008.
3. Dmitruk, N. L., T. R. Barlas and E. V. Basiuk, "Preparation, morphology and physical properties of microrelief InP surfaces," *Solar Energy Materials and Solar Cells*, Vol. 31, 371–382, 1993.
4. Dmitruk N., T. Barlas, N. Kotova, V. Romanyuk and A. Dmytruk, "Metal 1D Micro(nano) Self-organized Wires on Semiconductor Surface: Preparation, Topology, and Optical Properties", *Materials Science and Engineering C,* Vol. 27, 1141-1144, 2007.
5. Dmitruk N., T. Barlas, A. Dmytruk, A. Korovin and V. Romanyuk, "Synthesis of 1D Regular Arrays of Gold Nanoparticles and Modeling of Their Optical Properties", *J. Nanosci. Nanotechnol.* Vol. 8, No. 2, 564-571, 2008.
6. Dmitruk N. L., A. V. Goncharenko and E. F. Venger, *Optics of Small Particles and Composite Media*, Naukova Dumka, Kyiv, 2009.

n^{th} Order Rose Curve as a Generic Candidate for RF Artificial Magnetic Material

A. Kabiri[1] and **O. M. Ramahi**[1]

[1]Univeristy of Waterloo, Canada
akabiri@maxwell.uwaterloo.ca, oramahi@uwaterloo.ca

Abstract— In recent work, we demonstrated that the permeability and magnetic loss tangent of artificial magnetic material inclusion can be represented simply in terms of the circumference and area of the inclusion. While such representation makes direct use of the inclusions's circuit model, the fact that the magnetic properties can be described in terms of the perimeter and area of the inclusion allows us to design inclusion to achieve specific constraints without the need for intensive full-wave trial and error simulation procedure. Because of such flexibility, here, we propose a new set of generic curves described as n^{th} order rose curves as candidates for AMMs. In fact, the new curves, not only provide significant design flexibility but provide features not present in traditional topologies, most pronouncedly, wider band over which negative permeability is achieved with minimized dispersion.

1. INTRODUCTION

Artificial Magnetic Material (AMM) are artificial structures that provide enhanced positive or negative permeability at radio frequencies [1]. The tremendous interest in such material lies in it being an enabling technology in several key applications, These growing applications are using metamaterial slabs as a probe for the near-field sensing [2], as a substrate or a superstrate for enhancing low-profile antenna performance [3] and as many other applications.

In fact, AMM is a composition of electrically small metallic broken-loop inclusions aligned in planes that are perpendicular to the direction of incident magnetic field. The incident magnetic field induces electric current leading to an enhanced magnetic response within and in the close proximity of the inclusion. The magnetic behavior of the inclusions, therefore, can entirely be described by an RLC circuit-based model. Most circuit model proposed in the literature have addressed the magnetic properties, though indirectly, in terms of the area and perimeter of the inclusions. Those approaches were naturally adopted since the area and perimeter directly affect the inductive and capacitive properties of the inclusions, respectively.

2. BACKGROUND

In an earlier work [4], we showed that the magnetic properties of the AMMs can be expressed simply in terms of physical and geometrical properties of inclusions. The basic geometrical properties of the inclusions are the area and perimeter of the closed loop, and the physical properties of the inclusions consist of the structural and electrical characteristics of the inclusions and the host medium. According to this work, the real effective permeability and the magnetic loss tangent of the artificial medium can be expressed respectively as:

$$\mu_{Re}(\Omega) = 1 + \chi_0(1 + \xi(\Omega))^{-1} \tag{1}$$

$$\tan\delta(\Omega) = -\frac{\mathrm{Im}(\mu(\Omega))}{\mathrm{Re}(\mu(\Omega))} = \chi_0\sqrt{\xi(\Omega)}\,(1 + \chi_0 + \xi(\Omega)))^{-1} \tag{2}$$

where Ω is the normalized resonance frequency with respect to resonant frequency of the inclusions ($\Omega = \frac{\omega}{\omega_0}$). χ_0 is the magnetic susceptibility of a lossless medium and it is given as:

$$\chi_0 = \frac{F\Omega^2}{1 - \Omega^2} \tag{3}$$

and $\xi(\Omega)$ is given by

$$\xi(\Omega) = \alpha^2\frac{\Omega^3}{(1 - \Omega^2)^2} \tag{4}$$

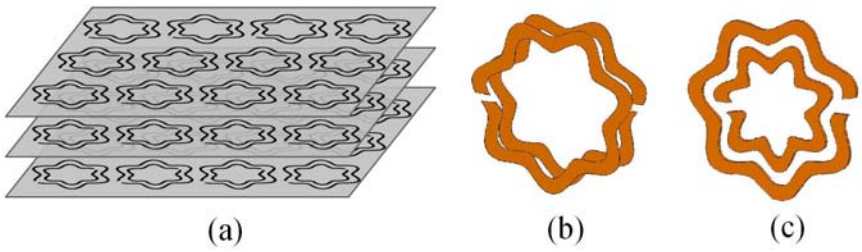


Figure 1: (a) A stack of Rose curve inclusions, (b) A broad-side coupled inclusion designed by 7th order Rose curve. (c) An edge-coupled inclusion designed by 7th order Rose curve.

where $\alpha = \frac{P}{F^2}$. The geometrical factor F and the physical factor P are expressed as:

$$F = \frac{s}{A} \tag{5}$$

$$P = \mathcal{K}(sl)^{\frac{5}{4}} \tag{6}$$

where ω_0 is a frequency in which the inclusion resonates, and $\mathcal{K}$ is a function of structural and electrical properties of the inclusions and host medium.

Inclusions having various geometrical configurations have been proposed in the literature. Each proposed structure has its own advantages and disadvantages in terms of resultant permeability, dispersive characteristics and loss. The main drawback of all proposed designs is that the area and perimeter of the inclusions vary dependently, leading to mutually-related capacitance and inductance of the inclusions. In other words, to produce a specific response, we need to tune the capacitance and inductance of the inclusions independently. The capacitance of the inclusions is tuned by the length of the inclusions's trace, and the inductance of the inclusions are effectively tuned by the area occupied by the interior of the inclusions. However, as the area of the inclusion is set by its perimeter value, the inductance will be determined uncontrollably or vice versa. Consequently, designs are only able to address specific cases, and many other possible designs resulting from any valid combinations of the area and perimeter of inclusions are left untouched.

3. N^{TH} ORDER ROSE CURVE

In this work, we propose a novel inclusion geometry, henceforth referred to as the nth order Rose Curve. The primary feature of these curves is that the perimeter and area can be tuned independently. Accordingly, the introduced curve minimizes the dependency of the capacitive and inductive response of the inclusions. The curve is characterized in polar coordinates by the parametrization

$$R_n(r_0, a) : r(\theta) = r_0 + a\cos(n\theta) \tag{7}$$

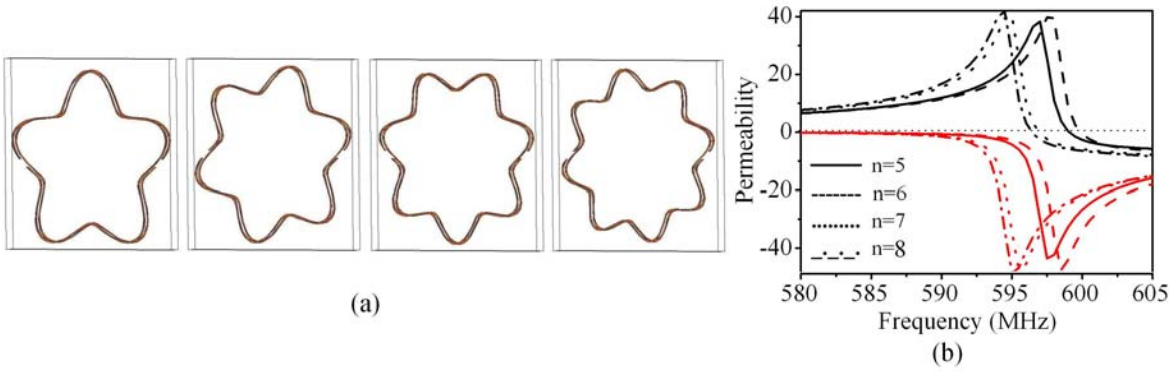


Figure 2: (a) Rose curve inclusions of order 5,6,7 and 8. The area and perimeters of the inclusions are identical, and are equal to half of unit cell area and $\frac{\lambda_0}{8}$, respectively. (b) Numerical analysis of inclusions introduced in (a).

Table 1: Design Data Sheet

Material and Fabrication Constraints	*Design Specifications*
Metal thickness: $t = 35\mu m$	Slab size: $(d_x, d_y, d_z) = (120.0mm, 24.53mm, 120.0mm)$
Host medium: `Duroid 5880` ($\varepsilon_r = 2.2$)	Unit cell size: $(\delta_x, \delta_y, \delta_z) = (20.0mm, 800\mu m, 20.0mm)$
Traces: `Copper`$(\sigma = 59.6\frac{S}{\mu m})$	Operational frequency: $f_{op} = 600MHz$
Trace width: $b = 200\mu m$	Bandwidth: $BW \approx 2MHz$
Trace gap: $g = 800\mu m$	Real effective permeability: $\mu_{op} \pm \delta\mu = 9.00 \pm 5.0\%$
Inclusions arrangement: `Broad-side coupled`	Magnetic Loss Tangent (MLT): $\tan\delta < 0.050$

Table 2: A Set of Candidates for Rose-Curved Inclusions

Order	$r_0(mm)$	$a(mm)$	$MaxDimension(mm)$
7	7.97	1.56	19.06
8	7.98	1.36	18.68
9	7.99	1.21	18.40

where $r(\theta)$ shows the position of the contour in $xz-plane$ and θ is the polar angle over y axis and measured from the x axis. The angle θ sweeps the contour and not the slit on the contour; thus, for a broken inclusion with opening's width of h we have $\theta \in [\frac{h}{2}, 2\pi - \frac{h}{2}]$. r_0 and a are constants and n is an integer representing the order of the curve. Figure (1-a) shows a stack made from single broken loops of the new inclusion, and the typical topology of the new inclusion in a broadside-coupled and edge-coupled schemes are shown in Figure (1-b) and (1-c), respectively.

More precisely, the relations (1) and (2) characterize the effective permeability and MLT in terms of χ_0 and ξ for a specific frequency. From (3) and (4), the physical and geometrical factors adjust χ_0 and ξ. Finally, the physical and geometrical factors are expressed in terms of the area and perimeter of the inclusions. Therefore, as the area and perimeter of the Rose curve are independently tuned by the parameters r_0 and a, the Rose curve can be offered as the generic candidate for AMMs.

Figure (2-a) shows Rose curve of different order but the same area and perimeter, and Figure (2-b) presents the numerical analysis of the magnetic response of AMMs composed with the inclusions in Figure (2-a). The inclusions occupy 50% of the unit cell area and carry the perimeter equals to $\frac{\lambda_0}{8}$, where λ_0 is the resonant wavelength. Although the shapes are different, they provide fairly identical response. The higher order rose curves brings about more coupling and shrinks the largest dimension of the inclusions to fit in the unit cell.

Moreover, a methodology can be defined to tune r_0 and a for realizing an AMM with a desired magnetic specifications. In an earlier work [5], we developed a general methodic approach to design AMMs. Using the proposed procedure and the design specification requested in Table. I, we design Rose curve inclusions whose artificial compositions meet the requirements. Table II summarizes the design parameters. The numerical simulations shows a promising error of less than 1.6% from the desired properties.

Further parametric studies carried out on the effect of area and perimeters on the magnetic response of the same order Rose curves. Figure (3-a) shows the numerical analysis of 7th order Rose curve inclusion with similar surface area equal to the half of the unit cell area and different perimeters. It can be concluded that inclusions with larger perimeter resonates at lower frequencies and provide more miniaturization in certain applications. In addition, Figure (3-b) shows the numerical analysis of 7th order Rose curve inclusion with equal perimeter and different areas. The areas vary from 30% to 70% of the unit cell area.

Note that near the resonance the real part of the effective permeability can be negative if the quality factor of the resonator is enough high. Another attractive feature of the proposed Rose curves is widening the frequency band over which the medium provides negative permeability with minimized dispersion. Figure (3-c) shows that the frequency band is two times widened (widened from normalized frequency 1.2 to 1.4) and also flattened in average over the band. A new coupling scheme between adjacent segments of the rose curve introduces additional capacitance that highly likely introduces a second or multiple resonances in the inclusion, and widen the band over the frequency with negative permeability.

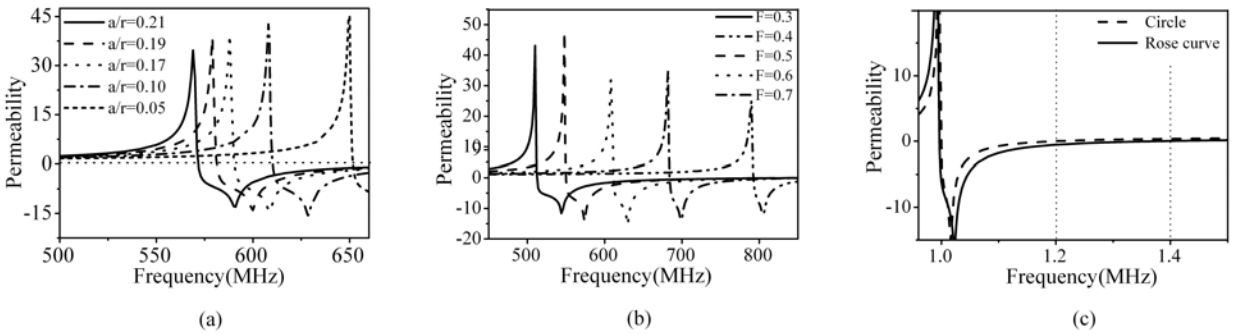


Figure 3: (a) The real permeability of inclusions which occupied half of unit cell area and vary in length. (b) The real permeability of inclusions which encompasses different areas with the same trace length. (c) Analysis of the negative permeability. Higher order Rose curve inclusions provide wider frequency band. For the sake of comparison, the graphs are normalized ro their resonant frequency.

4. CONCLUSION

In this work, we proposed a new inclusion design with a metallic trace called Rose Curve. The proposed contour and the method to characterize them can be considered as a generic topology and design procedure to realize artificial magnetic material meeting specific constraints without extensive and full-wave simulations. Numerical examples has been provided to demonstrate the effectiveness and design efficiency when using the nth order Rose curves to design AMM meeting specific requirements. It has been shown that the new design offers wider frequency band over the negative section of the permeability function

REFERENCES

1. Pendry, J. B., A. J. Holden, D. J. Robbins and W. J. Stewart, "Magnetism from Conductors and Enhanced Nonlinear Phenomena," *IEEE Trans. Microwave Theory Tech.* , Vol. 47, No. 10, 2075–2084, 1999.
2. Boybay, M. S. and O. M. Ramahi, "Near-field probes using double and single negative media," *Phys. Rev. E: Stat. Nonlinear Soft Matter Phys.*, Vol. 79, No. 1, 1-10, 2009.
3. Ikonen, P. K., S. I. Maslovski, C. R. Simovski and S. A. Tretyakov, "On artificial magnetodielectric loading for improving thempedance bandwidth properties of microstrip antennas," *IEEE Trans. Antennas Propag.*, Vol. 54, No. 6, 1654–1662, 2006.
4. Kabiri, A and O. M. Ramahi, "Magnetic loss tangent optimization in design of artificial magnetic slabs," *Proceeding of Antennas and Propagation Society International Symposium*, Boston, USA, July 2008.
5. Kabiri, A and O. M. Ramahi, "A design recipe for artificial magnetic materials," *Proceeding of Antennas and Propagation Society International Symposium*, San Diego, USA, June 2009.

A new model of dispersion for metals leading to a more accurate modeling of plasmonic structures using the FDTD method

A. Vial[1], **T. Laroche**[2], **and M. Dridi**[1]

[1]Institut Charles Delaunay - Université de technologie de Troyes - Laboratoire de Nanotechnologie et d'Instrumentation Optique - 12, rue Marie Curie BP-2060 F-10010 Troyes Cedex, France
[2]Institut FEMTO-ST - CNRS UMR 6174 - Université de Franche-Comté
Département de Physique et de Métrologie des Oscillateurs - 32, avenue de l'Observatoire F-25044 Besançon Cedex, France
alexandre.vial@utt.fr - thierry.laroche@femto-st.fr

Abstract— We present FDTD simulations results obtained using the Drude-Critical points model. This model enables spectroscopic studies of metallic structures over wider wavelength ranges than usually used, and facilitates the study of structures made of several metals.

1. INTRODUCTION

Modeling the optical properties of metamaterials is a crucial step for the tailoring of their features, and the Finite-Difference Time-Domain (FDTD) method is among one the of the most used in the field [1], owing its wide use to the fact that results for a wide range of frequencies may be obtained with a single run of the code [2].

Accuracy of the results strongly depends on the way tabulated permittivities were fitted by means of a combination of analytical laws of dispersion, mainly the Drude and Lorentz models in the case of metals [3, 4, 5, 6, 7]. The difficulty arises from the fact that the number of terms required for a precise description over a wide spectrum may become too large for a FDTD usage, as this number has an influence on the memory requirements of the code.

Recently, a new analytical model called the Critical Point (CP) model was introduced for the description of gold in the 200-1000 nm wavelength range [8, 9]. It was shown that this model could be implemented with only few modifications to existing codes already written to take the Lorentz model into account [10]. Moreover, when used as a correction of the Drude model, it would allow a better description of the permittivity than the Drude-Lorentz model, over a wider range of wavelengths, for several metals [11, 12, 13].

This opens the possibility to perform spectroscopic studies for metallic structures over a wide spectrum without the need of too many additional lorentzian terms, thus keeping the FDTD memory requirements as low as possible. Moreover, it also becomes possible to perform spectroscopic studies of structures made of different metals [14] which were previously described on different range of wavelengths, or to compare the same structure made of different metals over the same wavelength range. These two possibilities will be presented here.

2. REVIEW OF THE DISPERSION MODELS

We briefly review here the main models previously cited.

The Drude model, also known as the free electron gas model, is widely used for the description of metals in the near-infrared, but also in the high wavelength part of the visible spectrum. From a physical point of view, it corresponds to intraband electronic transitions [15], and is expressed as

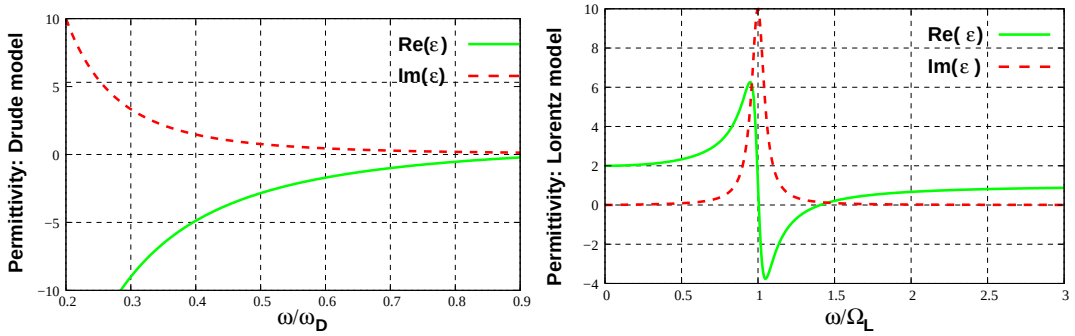
$$\chi_D(\omega) = \epsilon(\omega) - \epsilon_\infty = -\frac{\omega_D^2}{\omega^2 + i\gamma\omega}. \tag{1}$$

It is depicted on Fig. 1(a).

The Lorentz model corresponds to interband electronic transitions, and can be written as

$$\chi_L(\omega) = \epsilon(\omega) - \epsilon_\infty = A\frac{\Omega_L^2}{\Omega_L^2 - \omega^2 - i\Gamma_L\omega}. \tag{2}$$

It is depicted on Fig. 1(b).



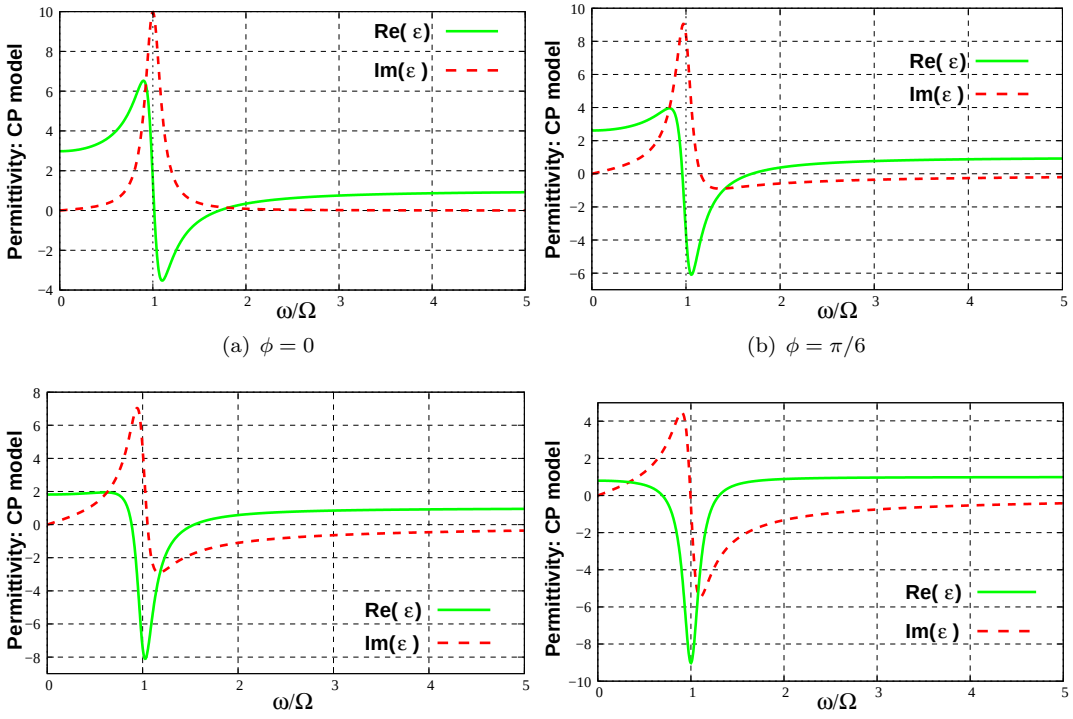
(a) Drude model. $\epsilon_\infty = 1$, $\gamma = 0.1\omega_D$ (b) Lorentz model. $\epsilon_\infty = 1$, $\Gamma_L = 0.1\Omega_L$, $A = 1$.

Figure 1: Drude and Lorentz models. Solid line: real part of the permittivity, dashed line: imaginary part of the permittivity.

The critical points model was recently used in conjunction with the Drude model for the description of the gold permittivity [8], and is defined by

$$\chi_{CP}(\omega) = \epsilon(\omega) - \epsilon_\infty = A\Omega\left(\frac{e^{i\phi}}{\Omega - \omega - i\Gamma} + \frac{e^{-i\phi}}{\Omega + \omega + i\Gamma}\right). \tag{3}$$

Examples of permittivities described by this model are presented on Fig. 2.



(a) $\phi = 0$ (b) $\phi = \pi/6$

(c) $\phi = \pi/3$ (d) $\phi = \pi/2$

Figure 2: Critical points model. Solid line: real part of the permittivity, dashed line: imaginary part of the permittivity. $\epsilon_\infty = 1$, $\Gamma = 0.1\Omega$, $A = 1$, and $\phi = 0$ (a), $\phi = \pi/6$ (b), $\phi = \pi/3$ (c), $\phi = \pi/2$ (d).

Incidentally, there was also an effort toward the unification of the different dispersion models treatment within the FDTD method [16, 17]. It was show that it is possible to describe the Debye, Drude and Lorentz models with the general equation

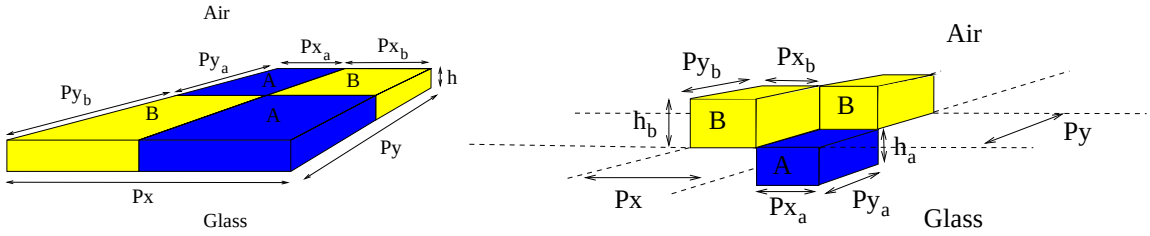
$$\epsilon(\omega) = \epsilon_\infty + \sum_{p=0}^{P}\left(\frac{c_p}{i\omega - a_p} + \frac{c_p^*}{i\omega - a_p^*}\right), \tag{4}$$

with $z*$ the complex-conjugate of z. The CP model naturally finds its place in this framework, with

$$c_p = -iA\Omega e^{i\phi}, \quad (5)$$
$$a_p = \Gamma + i\Omega. \quad (6)$$

3. EXAMPLES OF APPLICATION

In this section, we will study two configurations, described on figure 3.



(a) Configuration 1 (b) Configuration 2

Figure 3: Configurations studied. In configuration 1, both materials A and B lie on a glas substrate. In configuration 2, material A is in the substrate, while material B is on the substrate.

In first set of computations, we have computed extinction spectra for configuration 1, taking material B as air. Material A is respectively chromium, aluminum, gold and silver. Light is incident from the substrate and linearly polrized along the x-axis. Results are depicted on figure 4(a). Two well defined plasmon resonance can be observed for silver and gold. Using the same materials, we computed extinction spectra for configuration 2 (see figure 4(b)). In this case, metals structures are actually embedded in the substrate, resulting to a red-shift of the plasmon resonance wavelgenth previously observed. It should be noted that all these results were achieved for wavelengths between 400 and 1000nm, whereas results for gold, for example, were previously only available for wavelengths above 500nm.

In a second set of computations, we keep configuration 2, but study two metals at the same time. On figure 4(c), material A is silver and material B is gold. On figure 4(d), material A is chromium and material B is gold. In both cases, the periodicity p_y is kept constant while p_x is changed. The main consequence of the increase of p_x is a red-shift of the plasmon resonances, which is actually expected as the incident polarisation is along the x-axis.

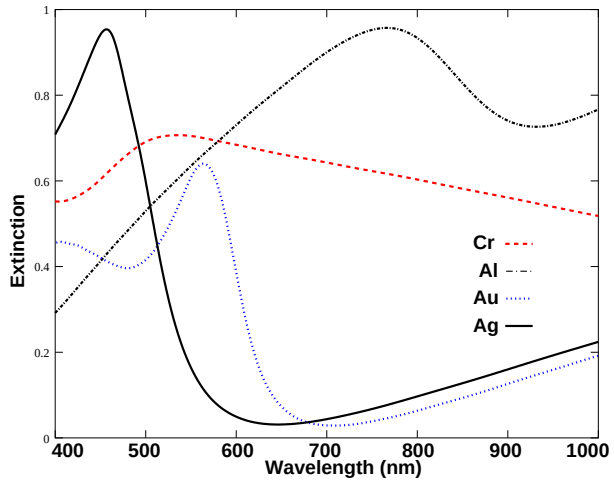
By optimizing the configuration involving silver and gold (figure 4(c)), it seems it should be possible to obtain two resonances close to each other, which would be of great interest for the development of SERS substrate, as the electromagnetic gain is proportional to the product of the electric field value at the incident wavelength and at the Raman wavelength. Other configurations could also be studied, provided they are technologically realistic.

4. CONCLUSION

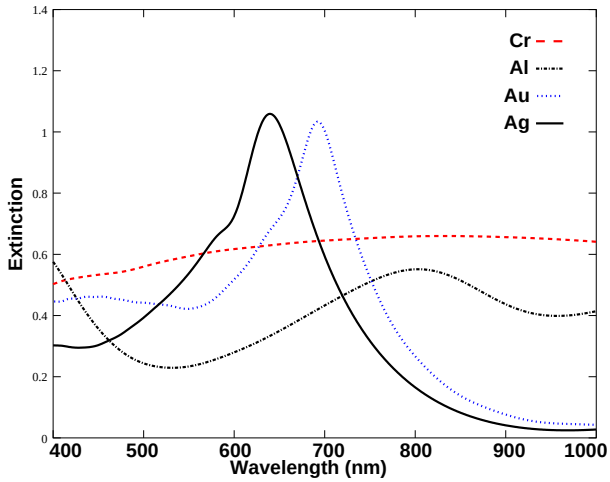
The Drude-Critical points model can be used to describe the interaction of light with metallic features using the FDTD method. It provides enough flexibility so that broader wavelength ranges can be investigated, and facilitates the study of structures made of several metals. This is an important step toward a better modeling of metamaterials and the tailoring of their geometrical features for specific applications.

REFERENCES

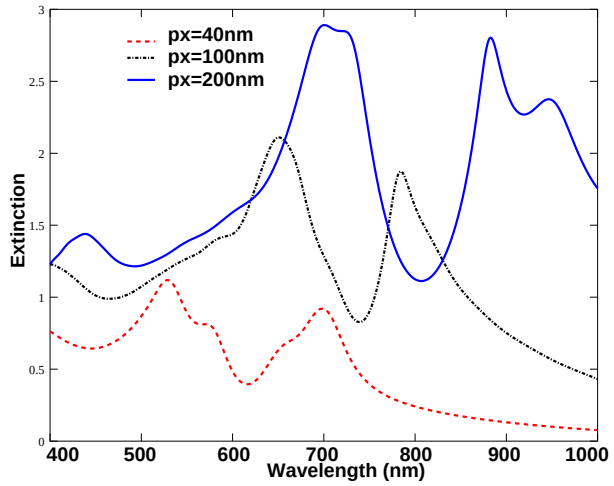
1. Y. Hao and R. Mittra. *FDTD Modeling of Metamaterials: Theory and Applications*. Artech House Publishers, 2008.
2. A. Taflove and S. C. Hagness. *Computational Electrodynamics: The Finite-Difference Time Domain Method*. Artech House, Boston, 2nd edition, 2000.
3. M. C. Beard and C. A. Schmuttenmaer. Using the finite-difference time-domain pulse propagation method to simulate time-resolved thz experiments. *J. Chem. Phys.*, 114(7):2903–2909, 2001.



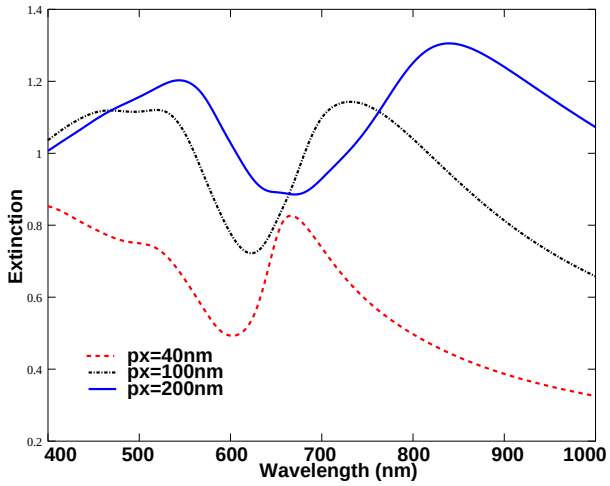
(a) Configuration 1: material A is respectively chromium, aluminum, gold and silver, material B is air



(b) Configuration 2: material A is respectively chromium, aluminum, gold and silver, material B is air



(c) Configuration 2: material A is silver, material B is gold



(d) Configuration 2: material A is chromium, material B is gold

Figure 4: Extinction spectra for different configurations. Exepct when otherwise stated, $p_x = p_y = 100$nm, $h = 50$nm.

4. A. Vial, A.-S. Grimault, D. Macías, D. Barchiesi, and M. Lamy de la Chapelle. Improved analytical fit of gold dispersion: application to the modelling of extinction spectra with the FDTD method. *Phys. Rev. B*, 71(8):085416–085422, 2005.
5. T.-W. Lee and S. K. Gray. Subwavelength light bending by metal slit structures. *Opt. Express*, 13(24):9652–9659, 2005.
6. N. G. Skinner and D. M. Byrne. Finite-difference time-domain analysis of frequency-selective surfaces in the mid-infrared. *Appl. Opt.*, 45(9):1943–1950, 2006.
7. F. Hao and P. Nordlander. Efficient dielectric function for FDTD simulation of the optical properties of silver and gold nanoparticles. *Chem. Phys. Lett.*, 446:115–118, 2007.
8. P. G. Etchegoin, E. C. Le Ru, and M. Meyer. An analytic model for the optical properties of gold. *J. Chem. Phys.*, 125:164705, 2006.
9. P. G. Etchegoin, E. C. Le Ru, and M. Meyer. Erratum: "an analytic model for the optical properties of gold". *J. Chem. Phys.*, 127:189901, 2007.
10. A. Vial. Implementation of the critical points model in the recursive convolution method for dispersive media modeling with the fdtd method. *J. Opt. A: Pure Appl. Opt.*, 9(7):745–748, 2007.
11. A. Vial and T. Laroche. Description of dispersion properties of metals by mean of the critical points model and application to the study of resonant structures using the FDTD method. *J. Phys. D: Appl. Phys.*, 40:7152–7158, 2007.

12. A. Vial and T. Laroche. Comparison of gold and silver dispersion laws suitable for FDTD simulations. *Appl. Phys. B-Lasers Opt.*, 93(1):139–143, 2008.
13. J. Y. Lu and Y. H. Chang. Optical singularities associated with the energy flow of two closely spaced core-shell nanocylinders. *Opt. Express*, 17(22):19451–19458, 2009.
14. Vladimir M. Shalaev, Wenshan Cai, Uday K. Chettiar, Hsiao-Kuan Yuan, Andrey K. Sarychev, Vladimir P. Drachev, and Alexander V. Kildishev. Negative index of refraction in optical metamaterials. *Opt. Lett.*, 30(24):3356–3358, 2005.
15. C.F. Bohren and D.R. Huffman. *Absorption and scattering of light by small particles*. Wiley, 1983.
16. M. Han, R.W. Dutton, and S. Fan. Model dispersive media in finite-difference time-domain method with complex-conjugate pole-residue pairs. *IEEE Microwave Compon. Lett.*, 16(3):119–121, 2006.
17. I. Udagedara, M. Premaratne, I. D. Rukhlenko, H. T. Hattori, and G. P. Agrawal. Unified perfectly matched layer for finite-difference time-domain modelingof dispersive optical materials. *Opt. Express*, 17(23):21179–21190, 2009.

Effective Parameters of Metamaterial Substrate: Analytical and Semi-Analytical Methods

W. Abdouni, A. C. Tarot, A. Sharaiha
IETR, University of Rennes 1, Campus de Beaulieu, 35042 Rennes Cedex, France
tarot@univ-rennes1.fr

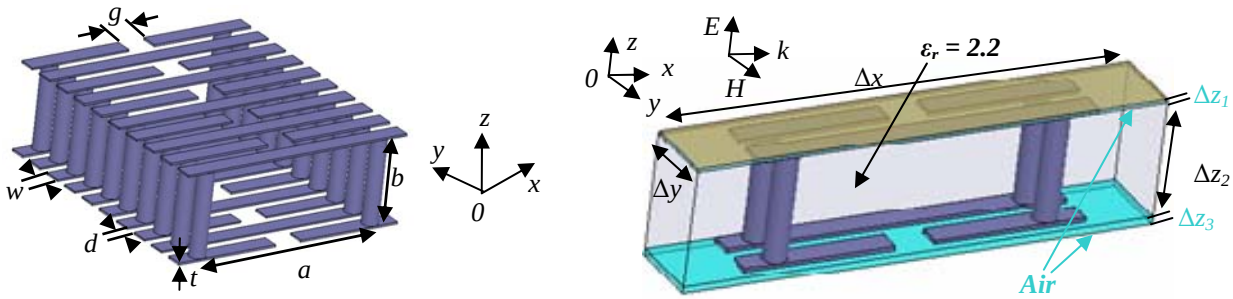
Abstract- The metamaterial substrate is constructed of periodic resonant loop circuits embedded in a low dielectric host medium. These resonant loops modify the effective parameters ε_{eff} and μ_{eff}. A new geometry of metamaterial substrate in 3D is used. An analytical method is developed to extract the effective parameters of metamaterial structure. The results are then compared to the ones obtained with a semi-analytical method (Inversion Method). A good agreement was found.

1. INTRODUCTION

The effective permittivity (ε_{eff}) and permeability (μ_{eff}) are fundamentals quantities in the conception of a material. A semi-analytical method, called the inversion method (IM) [1,2], was used and consists in extracting the effective parameters from the reflection (r) and transmission (t) coefficients obtained from simulation. The HFSS commercial software [3] is used to compute these parameters. Then, an analytical method is developed to retrieve the effective parameters. Finally analytical results are compared to the semi-analytical ones.

2. EFFECTIVE PARAMETERS OF METAMTERIAL SUBASTRATE

A metasolenoid [4] is used as a metamaterial substrate. This one is composed of an array of stacked Split-Ring Resonators (SRR) printed on a dielectric substrate (Figure 1(a)).



(a) (b)

Figure 1: (a) Geometry of the metasolenoid (b) Unit cell of metasolenoid simulated with HFSS

The infinite medium of metasolenoid (Figure 1(a)) can be modelled with HFSS [3] by two split rings in a unit cell (Figure 1(b)) with suitable boundary conditions. The ports are on the right and left sides of the cell.

The dimensions of the unit cell are Δx = 6mm, Δy = 1mm and $\Delta z = \Delta z_1 + \Delta z_2 + \Delta z_3$ = 1.8mm and the permittivity of the host substrate is ε_r = 2.22 (1−j0.0009) and its height is Δz_2 = 1.575mm. Δz_1 and Δz_3 represent the air gaps between the sample and the conducting strips.

A. Inversion method (IM)

A retrieval procedure (inversion method) is used to obtain the effective parameters. This one consists of calculating the effective normalized wave impedance z (normalized to the free-space wave impedance) and the effective refractive index n from the reflection (r) and transmission (t) coefficients obtained from simulation (HFSS Code), by using these formulas [1,2]:

$$z = \pm\sqrt{\frac{(1+r)^2 - t^2 e^{-2jk_0 d}}{(1-r)^2 - t^2 e^{-2jk_0 d}}} \qquad (1)$$

$$n = n' - jn'' = \frac{ar\tan(\mathrm{Im}(Y)/\mathrm{Re}(Y)) \pm m\pi}{k_0 d} - j\frac{\ln|Y|}{k_0 d} \qquad (2)$$

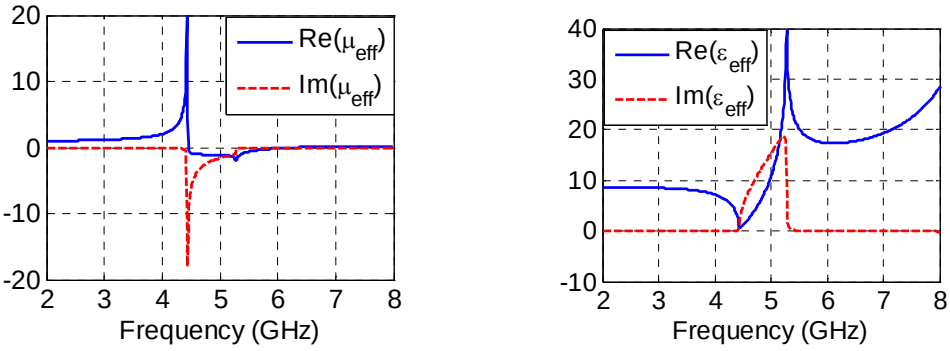
Where d is the thickness of the material, m is an integer ($m \geq 0$), $k_0 = 2\pi/\lambda_0$ is the propagation vector and λ_0 is the free-space wavelength. The intermediary variable Y is defined by:

$$Y = e^{-njkd} = X \pm \sqrt{X^2 - 1} \qquad \text{where} \qquad X = \frac{e^{jk_0 d}}{2t}(1 - r^2 + t^2 e^{-2jk_0 d})$$

The effective parameters (ε_{eff} and μ_{eff}) are then extracted by applying the two well known independent equations:

$$n = \sqrt{\varepsilon_{eff}}\sqrt{\mu_{eff}} \quad \text{and} \quad z = \sqrt{\frac{\mu_{eff}}{\varepsilon_{eff}}} \qquad (3)$$

The unit cell of metamaterial substrate presented previously in Figure 1(b) was simulated by HFSS [3]. We calculate the effective normalized wave impedance z and the effective refractive index n from the reflection (S_{11}) and transmission (S_{21}) coefficients obtained from HFSS simulation. Then effective permeability (μ_{eff}) and permittivity (ε_{eff}) are extracted. These ones are presented in Figure 2.



(a) (b)

Figure 2: Effective (a) permeability and (b) permittivity calculated by the Inversion Method (IM)

B. Analytical method (Anal)

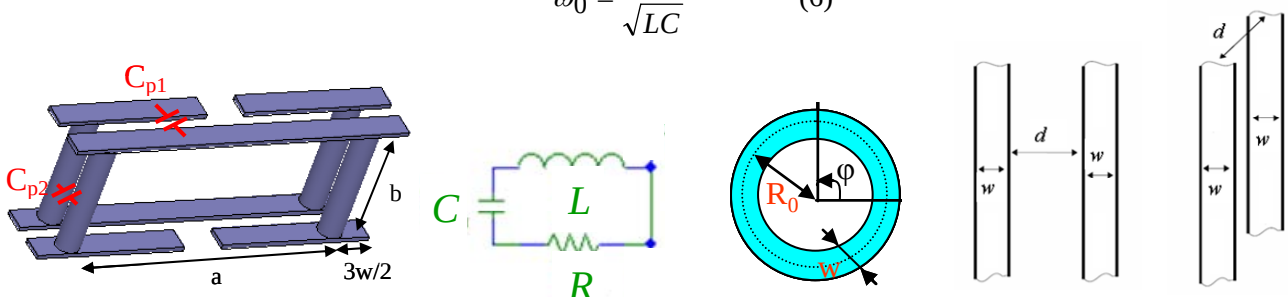
From Pendry et al [5], the effective permeability of the dielectric medium loaded by SRRs (or metasolenoids) follows Lorentz dispersion:

$$\mu_{eff}(\omega) = \mu_r\left(1 + \frac{\omega_p^2 - \omega_0^2}{\omega^2 - \omega_0^2 - j\gamma_m\omega}\right) \qquad (5)$$

Where, μ_r is the relative permeability of the dielectric medium ($\mu_r = 1$), ω_0 is the resonance frequency of the homogeneous medium, ω_p is the resonance plasma frequency and γ_m is the damping coefficient associated to the magnetic losses.

The geometry of SRR is shown in Figure 3(a). It's equivalent circuit is equivalent to the RLC resonance circuit (Figure 3(b)). The resonance frequency of the metamaterial substrate is equivalent to the RLC circuit one's:

$$\omega_0 = \frac{1}{\sqrt{LC}} \qquad (6)$$



(a) (b) (c) (d) (e)

Figure 3: (a) geometry of SRR (b) Equivalent circuit model (c) closed loop
(d) two microstrip lines coupled by their thickness (e) two microstrip lines coupled by their width

The self-inductance L is equivalent to the inductance of a closed loop (Figure 3(c)) with an area equivalent to the SRR shown in Figure 3(a):

$$L = \frac{\mu_0 \pi^3}{4w^2}\int_0^\infty \frac{1}{k^2}[b\beta(kb) - a\beta(ka)]^2\, dk \qquad (7)$$

With $a = R_0 - w/2$, $b = R_0 + w/2$ and the $\beta(x)$ function is defined by $\beta(x) = S_0(x)J_1(x) - S_0(x)J_0(x)$, where S_n and J_n are respectively the Struve and Bessel functions of first kind and n order.

The capacitance C represents the coupling capacitance between the two rings: it is equivalent to two parallel capacitances C_{P1} and C_{P2} (Figure 3(a)). C_{P1} is the capacitance between two coplanar lines coupled by their thickness (Figure 3(d)) and C_{P2}, the capacitance between two microstrip lines coupled by their width (Figure 3(e)).

The capacitance per unit length, C_0^{coplan}, of two coplanar lines coupled by their thickness (Figure 3(d)) is computed using the following relationship [6]:

$$C_0^{coplan} = \frac{\varepsilon K\left(\sqrt{1-\left(\frac{d/2}{w}\right)^2}\right)}{K\left(\frac{d/2}{w}\right)} \qquad (8)$$

Where $K(z)$ is the elliptic integral of first kind:

$$K(z) = \int_0^{\pi/2} \frac{d\varphi}{\sqrt{1 - z^2 \sin^2 \varphi}}$$

The $K(z)$ function is defined for $z^2 < 1$. To take into account the dielectric permittivity ε, we consider that half of the line is in the dielectric and the other half is in the air (Figure 1(b)). The relationship is $\varepsilon = (\varepsilon_r + 1)/2$.

The parallel capacitance C_{p1} is deduced by the capacitance per unit length, C_0^{coplan} multiplied by the effective length: $C_{p1} = C_0^{coplan} L_{eff1}$ where $L_{eff1} = \frac{2a}{\pi}$.

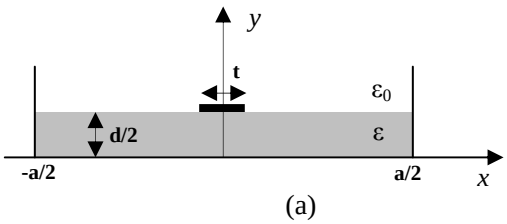
The capacitance per unit length, C_0^{large}, for two microstrip lines coupled by their width (Figure 3(e)) is calculated using existing formulas for the capacitance of a microstrip line on the same substrate but $d/2$ thickness (Figure 4(a)). The capacitance is computed using the resolution of the Laplace equation in the area between the vertical electric walls placed in $-a/2$ and $a/2$ (Figure 4(a)).

The expression of the capacitance per unit length C_0^{large} is:

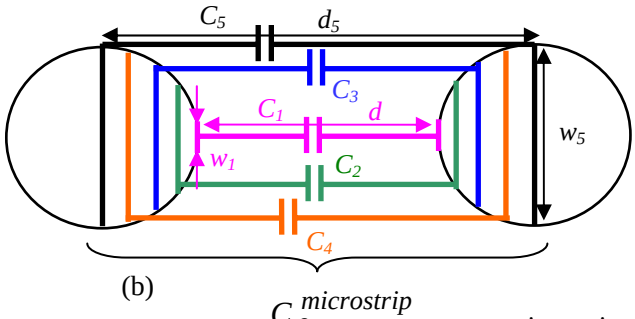
$$C_0^{microstrip} = \left\{ \sum_{n=1(odd)}^{\infty} \frac{4a \sin(n\pi t/2a) \sinh(n\pi d/2a)}{(n\pi)^2 t\varepsilon_0 [\sinh(n\pi d/2a) + \varepsilon \sinh(n\pi d/2a)]} \right\} \qquad (9)$$

For the numerical calculation of $C_0^{microstrip}$, it should be $a >> d$. In the following example, $a = 100d$ is chosen. In our case, the capacitance per unit length is estimated by the average capacitance per unit length (C_1, C_2, ..., C_5). C_i is the capacitance per unit length between two microstrip lines coupled by their width w_i (separated from a distances d_i).

The parallel capacitance C_{p2} is deduced by the capacitance per unit length, $C_0^{microstrip}$ multiplied by the effective length: $C_{p2} = C_0^{microstrip} L_{eff2}$ where $L_{eff2} = \frac{2b}{\pi}$.



(a)



(b)

$C_0^{microstrip}$

Figure 4: (a) Geometry of the microstrip line with vertical electric walls (b) Capacitance per unit length $C_0^{microstrip}$ estimated by the average capacitance per unit length (C_1, C_2, ..., C_5)

The capacitance C is equivalent to the two parallel capacitances C_{P1} and C_{P2} (Figure 3(a)):

$$C = C_{p1} + C_{p2} = C_0^{coplan} L_{eff1} + C_0^{microstrip} L_{eff2} \quad (12)$$

The effective permittivity of the elementary cell (Figure 1(a)) is calculated and shown in Figure 6(a).

The effective permittivity of a dielectric medium with a SRR follows an anti-resonant dispersion given by:

$$\varepsilon_{eff}(\omega) = \varepsilon_{reff}\left(1 + \frac{\omega^2 - \omega_0^2 - j\gamma_e}{8\omega^2 - 9\omega_0^2 - 8j\gamma_e}\right) \quad (15)$$

This equation exhibits the inverse of a Lorentz function. ε_{reff} is the static effective relative permittivity of the medium, ω_0 is the resonance frequency of the system and γ_e is the damping coefficient associated with dielectric losses.

The static relative effective permittivity ε_{reff} of the medium will be determined using the transmission line model of an elementary cell (Figure 1(b)). The presence of air gaps in the elementary cell (Figure 1(b)) requires to use the equivalent model of a transmission line printed on a multilayered medium (Figure 5(a)). The equivalent circuit of the multilayered medium is shown in Figure 5(b).

The equivalent series capacitance (C_L) is composed of three equivalent series capacitance (C_{L1}, C_{L2} and C_{L3}):

$$C_L = \frac{C_{L1}C_{L2}C_{L3}}{C_{L1}C_{L2} + C_{L2}C_{L3} + C_{L1}C_{L3}} \quad (16)$$

Where $C_{L1} = \Delta y / \Delta z_1$ and $C_{L3} = \Delta y / \Delta z_3$ are the series capacitances of the air gaps (ε_r = 1) and $C_{L2} = \varepsilon_r \Delta y / \Delta z_2$ is the series capacitance of the dielectric (ε_r = 2.2).

The equivalent circuit of the elementary cell (Figure 1(b)) is therefore represented in Figure 5(c). In this equivalent transmission line model, we ignored certain parasitic elements for the sake of simplicity. However, these parasitic elements have a significant effect on the equivalent relative permittivity of the medium (ε_{reff}). There exist coupling capacitors (C_1 and C_2) between the SRR and the conductors of transmission line in the equivalent circuit model (Figure 5(d)) [7].

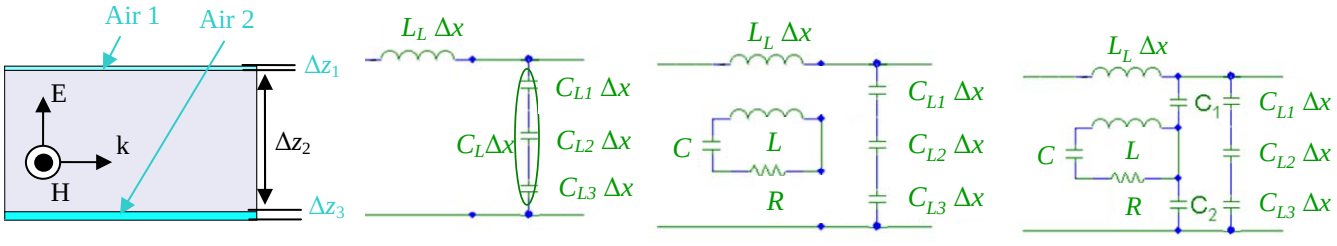
The equivalent circuit model depicted in Figure 5(d) shown that the equivalent capacitance per unit length of the line segment is:

$$C_{eq} = \varepsilon_{reff}\frac{\Delta y}{\Delta z} = C_L + \frac{C_1 C_2}{(C_1 + C_2)\Delta x} \quad (17)$$

Where $C_{1/2} = \dfrac{2(a+3w)w}{\Delta z_{1/2}}$ with neglecting g compared to a.

The relative permittivity of the medium (ε_{reff}) is expressed by the following formula:

$$\varepsilon_{reff} = \left(C_l + \frac{C_1 C_2}{C_1 + C_2}\right)\frac{\Delta z}{\Delta x \Delta y} \quad (18)$$



(a) (b) (c) (d)

Figure 5 : (a) Multilayered transmission line - (b) Equivalent circuit model - (c) Equivalent circuit model of the unit cell (d) Complete equivalent circuit model including the parasitic capacitances (C_1 and C_2) existing between the wires and the transmission line

The effective permittivity of the elementary cell (Figure 1(b)) is computed and shown in Figure 6(b).

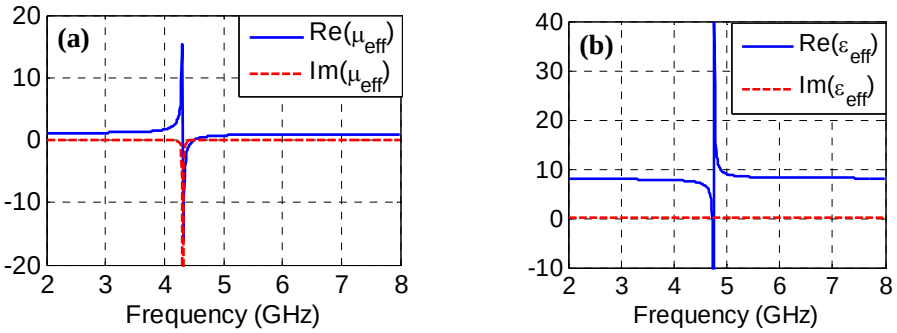


Figure 6 : Effective (a) permeability and (b) permittivity calculated by the analytical method

The analytical results are compared to the semi-analytical ones. The effective permeability and permittivity are found respectively in Figure 7 and Figure 8 : a good agreement is observed between the both results.

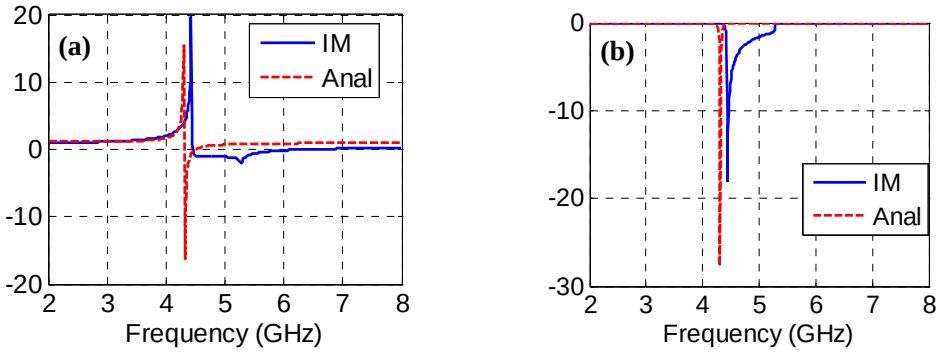


Figure 7 : Analytical and Semi-analytical (a) Real and (b) Imaginary part of effective permeability

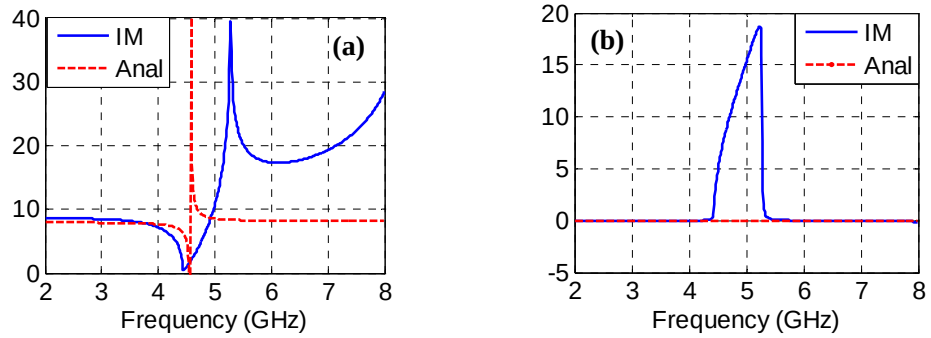


Figure 8 : Analytical and Semi-analytical (a) Real and (b) Imaginary part of effective permittivity

3. CONCLUSION

In this paper, an analytical method was proposed to retrieve the effective parameters of a metamaterial substrate. The computed results were compared to the ones obtained with the inversion method. A good agreement is obtained, except for the imaginary part of the effective permittivity which still equals zero. Netherless, this analytical method provides quickly the results.

REFERENCES

1. W. B. Weir, “Automatic measurement of complex dielectric constant and permeability at microwave frequencies” Proceedings of the IEEE, vol. 62, no. 1, pp. 33-36, Jan. 1974.
2. A. M. Nicolson et G. F. Ross, “Measurement of the intrinsic properties of materials by timedomain techniques” IEEE Trans. Instr. Measurements, vol. 19, no. 4, pp. 377-382, Nov. 1970.
3. HFSS, High Frequency Structure Simulator v 10.1.2, finite element package. Ansoft Corp.
4. Maslovski, S., P. Ikonen, I. Kolmakov, and S. Tretyakov, “Artificial magnetic materials based on the new magnetic particle: metasolenoid,” Progress In Electromagnetics Research, PIER 54, 61-81, 2005.
5. J.B Pendry, A.J. Holden, D.J. Robbins, et W.J. Stewart. “Magnetism from conductors and enhanced nonlinear phenomena”. IEEE Trans. MTT, 47(11) :2075–2084, 1999.
6. R. E. Collin, foundation for microwave engineering, New York : IEEE Press, 2001.
7. H. Mosallaei and K. Sarabandi, “Design and Modeling of Patch Antenna Printed on Magneto-Dielectric Embedded-Circuit Metasubstrate”, IEEE Trans. on Antennas and Propagation, vol. 55, no. 1, January 2007

Rigorous surface polarizability models for oblique incidence on metamaterial mono-layers

A. I. Dimitriadis, D. L. Sounas, N. V. Kantartzis, and T. D. Tsiboukis

Department of Electrical and Computer Engineering
Aristotle University of Thessaloniki, Thessaloniki GR-54124, Greece
tsibukis@auth.gr

Abstract— A method for the characterization of metafilms via a set of electric and magnetic polarizability densities is presented in this paper. This method, derived with the least possible assumptions, can be regarded as a generalization of existing techniques. Numerical simulations of various types of metamaterial cells are conducted to validate the accuracy of the proposed scheme, in comparison with other well-established algorithms.

1. INTRODUCTION

During the last decade there has been a constantly growing interest on the field of metamaterials. Usually comprising of scatterer arrays embedded in a dielectric host medium, metamaterial structures have been proposed for various applications, such as perfect lenses, antennas, substrates, cloaking devices and others, due to their unique electromagnetic properties, normally not encountered in nature [1]. On the other hand, understanding the physical background of metamaterials and modeling them by sets of appropriate effective parameters, remains an open research challenge.

Metafilms of metasurfaces, engineered by arranging electrically small scatterers at a surface, are usually considered as the 2-D equivalent of metamaterials. Recently, it has been proven in [2] that homogenization techniques which apply on bulk metamaterials can lead to the determination of non-unique effective constitutive parameters for a metafilm, since the latter does not have a well-defined thickness as a bulk medium. Hence, accurate and unambiguous modeling of metasurfaces can only be achieved through the calculation of effective polarizability densities [3–6].

In this paper, an algorithm for the calculation of effective polarizability densities is introduced, by improving existing schemes, which can be applied for the oblique incidence of a TE polarized plane wave on a metamaterial mono-layer. To this end, electric and magnetic dipole moments of the constituent particles are efficiently related to the incident field via suitable intra-planar interaction constants and their previously evaluated electric and magnetic polarizabilities. From the above, equivalent polarizability densities can be evaluated for the metasurface. Comparisons between the proposed methodology and other efficient techniques for diverse kinds of electric and magnetic resonators are presented in order to demonstrate the validity of the novel approach.

2. THEORETICAL METHODOLOGY

Consider a periodic mono-layer of discrete particles on the x-y plane with lattice periods a and b along the x and y directions, respectively. Assuming that the dimensions of the particles are small enough compared to the wavelength, such a structure is efficiently modeled by replacing each particle with three electric and three magnetic point-dipoles towards the x,y,z axes, located at its center. Therefore, each scatterer is characterized by electric and magnetic dipole moments p_i and m_i ($i = x, y, z$), related to the local electric $E_i^{\rm loc}$ and magnetic $H_i^{\rm loc}$ fields through the expressions

$$p_i = \epsilon_0 \alpha_E^{ii} E_i^{\rm loc}, \qquad m_i = \alpha_M^{ii} H_i^{\rm loc}. \tag{1}$$

In the above equations, $\alpha_E^{ii}, \alpha_M^{ii}$ are the electric and magnetic polarizabilities of the scatterer, which can be extracted from the S-parameters of a normally incident plane wave, as analyzed in [6]. In the rest of the present paper, we assume that only α_E^{xx} and α_M^{yy} are nonzero, which is a reasonable assumption for the majority of the structures investigated.

Let us now suppose that the aforementioned mono-layer is illuminated by a TE polarized (electric field intensity along the x axis) plane wave propagating on the y-z plane at an angle θ with respect

to the z-axis. The x-directed electric and y-directed magnetic field intensities of this plane wave, which interact with the scatterers of the mono-layer, are given by

$$E_x^{\text{inc}} = E_0 e^{-j(q_y y + q_z z)}, \tag{2}$$

$$H_y^{\text{inc}} = \frac{E_0}{\eta_0} \cos\theta e^{-j(q_y y + q_z z)}, \tag{3}$$

with E_0 the electric field amplitude, $q_y = -k_0 \sin\theta$, $q_z = k_0 \cos\theta$, k_0 the wavenumber and η_0 the wave impedance. Then, according to [6], the local fields for an arbitrary scatterer with dipole moments p_x, m_y are

$$E_x^{\text{loc}} = E_x^{\text{inc}} + \frac{1}{(ab)^{3/2}\epsilon_0} \left(C_0^{xx} p_x + \frac{D_0^{xy}}{c} m_y \right), \tag{4}$$

$$H_y^{\text{loc}} = H_y^{\text{inc}} + \frac{1}{(ab)^{3/2}} \left(c D_0^{yx} p_x + C_0^{yy} m_y \right), \tag{5}$$

where c is the speed of light and $C_0^{xx}, C_0^{yy}, D_0^{xy}, D_0^{yx}$ are the dimensionless interaction constants which specify the contribution of the whole array to the local field of a specific scatterer. Notice that the interaction constants D_0^{xy}, D_0^{yx} between electric and magnetic dipoles are zero since the y-directed magnetic field intensity (x-directed electric field intensity) of a x-oriented electric dipole (y-oriented magnetic dipole) is zero. On the other hand, C_0^{xx} equals to the sum of C_2, C_3 of the appendix of [7] multiplied by $(ab)^{3/2}$, while for the calculation of C_0^{yy} the x-axis should be rotated to the direction of the magnetic dipoles. Combining (1)-(5), it is extracted that

$$p_x = \frac{\epsilon_0 \alpha_E^{xx}}{1 - \alpha_E^{xx} C_0^{xx}/(ab)^{3/2}} E_0 e^{-j q_y y}, \tag{6}$$

$$m_y = \frac{\alpha_M^{yy} \cos\theta}{1 - \alpha_M^{yy} C_0^{yy}/(ab)^{3/2}} \frac{E_0}{\eta_0} e^{-j q_y y}. \tag{7}$$

Having determined p_x, m_y it is possible to extract effective surface polarizability densities α_{ES}^{xx} and α_{MS}^{yy} for the mono-layer. Recall that α_{ES}^{xx} and α_{MS}^{yy} obey to

$$P_{sx} = \epsilon_0 \alpha_{ES}^{xx} E_{sx}, \tag{8}$$

$$M_{sy} = -\alpha_{MS}^{yy} H_{sy}, \tag{9}$$

with $P_{sx} = p_x/(ab)$, $M_{sy} = m_y/(ab)$ the average polarization densities of the mono-layer, $E_{sx} = (E_x\big|_{z=0^+} + E_x\big|_{z=0^-})/2$ and $H_{sy} = (H_y\big|_{z=0^+} + H_y\big|_{z=0^-})/2$. It has to be stressed that (8) are meaningfull if $b < \lambda/2$, with λ the medium wavelength, for which only the zeroth order Floquet mode lies inside the light cone and Bragg scattering mechanisms are absent in the far-field region. From its definition, E_{sx} equals to E_x^{inc} plus the average of the scattered electric field produced by P_{sx}, M_{sy}. Following well known methods of electromagnetic theory, the later can be found as

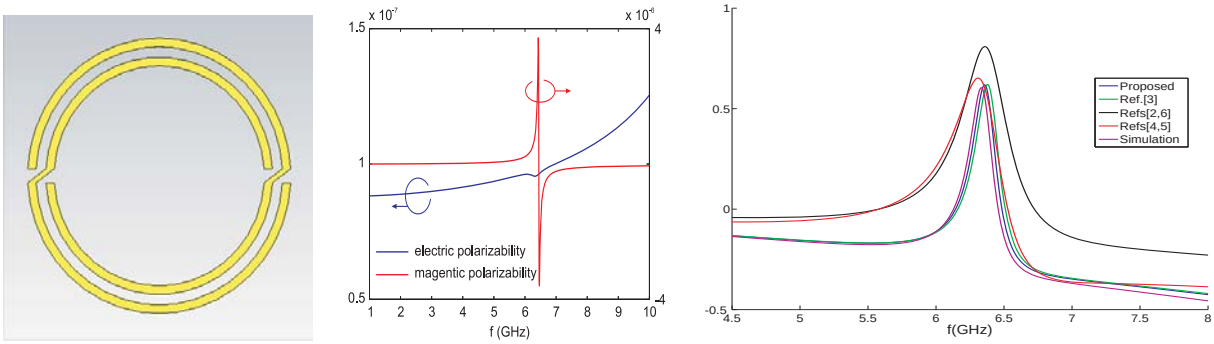
$$E_x^{\text{scat}} = -j k_0 P_{sx}/(2\epsilon_0), \tag{10}$$

thus leading to $E_{sx} = E_0 - j k_0 p_x/(2\epsilon_0 ab)$. Inserting the last expression into (8) and using (6)

$$a_{ES}^{xx} = \frac{a_E^{xx}/(ab)}{1 - a_E^{xx} \left[C_0^{xx}/(ab)^{3/2} + j k_0/(2ab) \right]}. \tag{11}$$

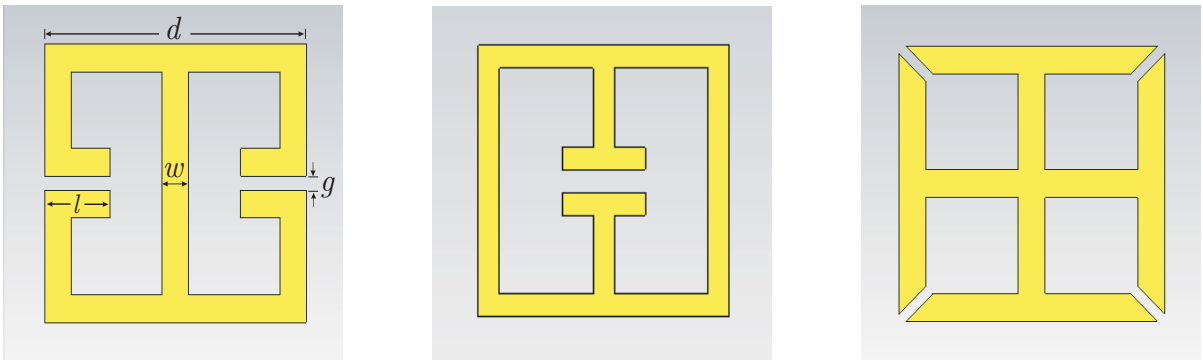
Similarly according to the definition of the equivalent surface magnetization density $M_{sy} = -a_{MS}^{yy} H_x^{\text{loc}}$, an analogous expression for the magnetic polarizability density a_{MS}^{yy} can be reached

$$a_{MS}^{yy} = \frac{a_M^{yy} \cos\theta/(ab)}{1 - a_M^{yy} \left[C_0^{xx}/(ab)^{3/2} + j k_0 \cos\theta/(2ab) \right]}. \tag{12}$$



(a) (b) (c)

Figure 1: An NB-SRR mono-layer: (a) geometry (dimensions from [1]), (b) electric/magnetic polarizabilities, and (c) real part of the reflection coefficient.



(a) (b) (c)

Figure 2: Geometry of several EFCLs: (a) type OE1 (dimensions: $d = 5\,\text{mm}$, $l = 1.25\,\text{mm}$, $g = 0.25\,\text{mm}$, $w = 0.5\,\text{mm}$), (b) type OE2 (dimensions from [10]), and (c) type OE3 (dimensions from [10]).

Equations (11) and (12) are the desired results. To compute polarizability densities, only the scattering parameters for the normal incidence and the geometrical details of the metafilm are required. Then, S-parameters for any oblique θ-angle incidence can be estimated through (see [2])

$$S_{11} = \frac{-j\frac{k_0}{2\cos\theta}\left(a_{ES}^{xx} + a_{MS}^{yy}\cos^2\theta\right)}{1 + \left(\frac{k_0}{2}\right)^2 a_{MS}^{yy} a_{ES}^{xx} + j\frac{k_0}{2\cos\theta}\left(a_{ES}^{xx} - a_{MS}^{yy}\cos^2\theta\right)}, \tag{13}$$

$$S_{21} = \frac{1 - \left(\frac{k_0}{2}\right)^2 a_{MS}^{yy} a_{ES}^{xx}}{1 + \left(\frac{k_0}{2}\right)^2 a_{MS}^{yy} a_{ES}^{xx} + j\frac{k_0}{2\cos\theta}\left(a_{ES}^{xx} - a_{MS}^{yy}\cos^2\theta\right)}. \tag{14}$$

The validity of this approach is verified in the next section.

3. NUMERICAL VERIFICATION AND DISCUSSION

The merits of our method are certified via several comparisons with well-established homogenization techniques [3–6], involving both electric and magnetic resonators, made of a $10\,\mu$m-thick copper medium. Moreover, all simulations are performed through the frequency domain solver of the CST MWS^{TM}package [8]. The first structure, under study, is the non-bianisotropic split ring resonator (NB-SRR) of Fig. 1(a), whose magnetic resonance is presented in Fig. 1(b), depicting the electric and magnetic polarizabilities of the particle. Selecting a 60° plane wave, the real part of the reflection coefficient is shown in Fig. 1(c). As observed, the proposed method – compared to existing ones and simulation results – is proven very accurate and consistent, even in the case of large incidence angles.

Next, the electric-field-coupled resonators (EFCLs) of OE1, OE2, and OE3 type (see Fig. 2), described in [9], are explored. In all cases, a cubic unit cell with a lattice period of $a = 6.75\,\text{mm}$ has been selected. Figures 3(a) and 3(b) display the S_{11}- and S_{21}-parameter for the OE1 type.

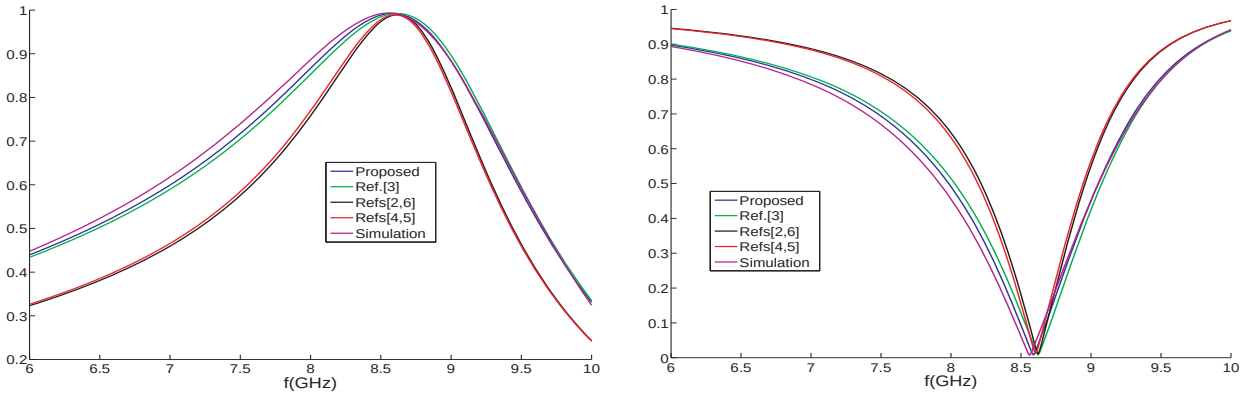


Figure 3: S-parameters for a 45° incidence on the OE1-type EFCL of Fig. 2(a): (a) S_{11} and (b) S_{21}.

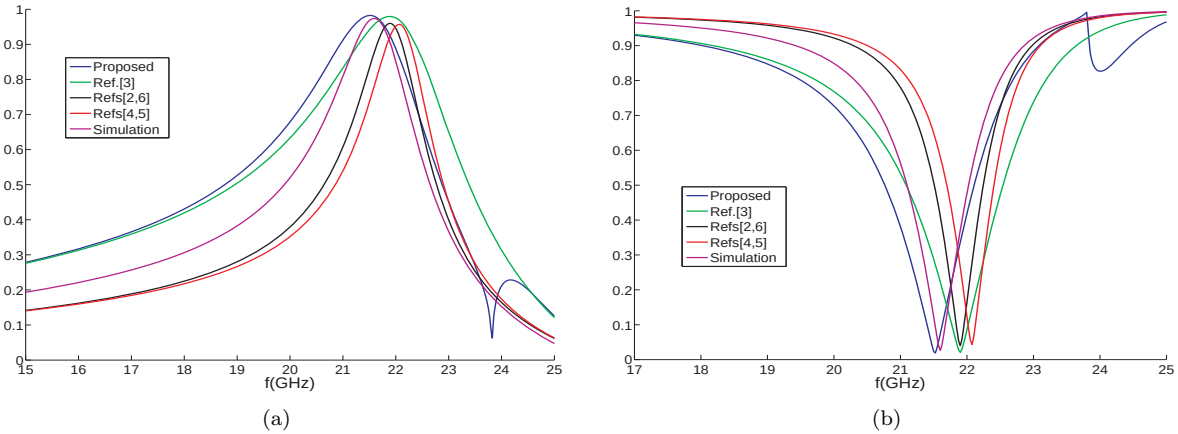


Figure 4: S-parameters for a 60° incidence on the OE2 EFCL of Fig.2(b): a) S_{11} and (b) S_{21}.

Specifically, the techniques of [5] and [6] lead to almost identical results, while that of [3] and the proposed one are, also, very satisfactory. On the contrary for the OE2 inclusion, none of the algorithms can be deemed reliable below the resonance, as illustrated in Fig. 4. In the vicinity of and above the resonance, however, our technique is, again, in good agreement with the simulation outcomes, except for a possible artifact occurring around 24 GHz. Finally, for the S-parameters of the OE3 resonator (Figs 5 and 6) and an incidence of 30°, an interesting phenomenon is observed. Although all methods prove accurate till the frequency of 20 GHz, none of them can actually retrieve the second resonance of the structure around 24.5 GHz. This resonance is possibly due to a quadruple mode and the point-dipole approximation model is unable to predict it.

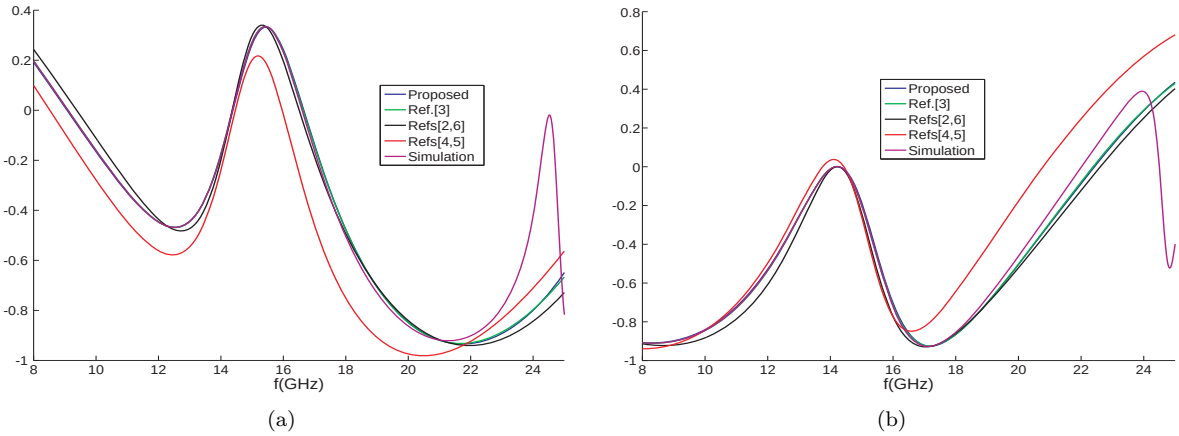
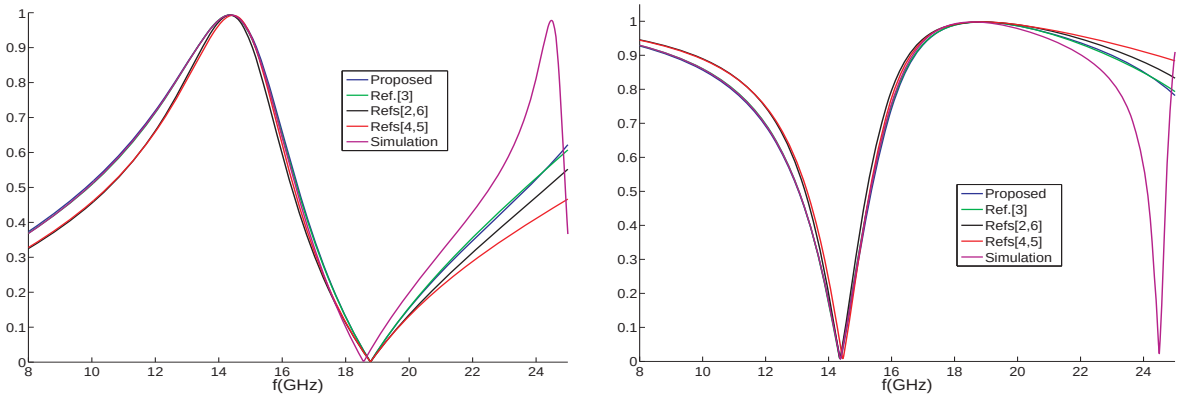


Figure 5: S_{21}-parameter for a 30° incidence on the OE3 EFCL of Fig.2(c): (a) real and (b) imaginary part.



(a) (b)

Figure 6: S-parameters for a 30° incidence on the OE3 EFCL of Fig.2(c): (a) S_{11} and (b) S_{21}.

4. CONCLUSION

In this paper, enhanced formulas for the electric and magnetic polarizability densities of a metafilm were introduced. The corresponding particle polarizabilities are extracted from the scattering parameters of a normally incident plane wave and combined with the appropriate inter-planar interaction coefficients. The resulting model – assuming only the electrically small size of the particles in order for the point-dipole approximation to apply – is employed to predict the scattering parameters for obliquely incident TE polarized waves, thus improving and generalizing existing schemes. Future improvements of the proposed method include its modification to account for higher order modes as well as its application to bianisotropic media, such as the EC-SRR.

REFERENCES

1. Marqués, R., F. Martín and M. Sorolla, *Metamaterials with Negative Parameters: Theory, Design and Microwave Applications*, Wiley-Interscience, New York, 2008.
2. Holloway, C. L., A. Dienstfrey, E. F. Kuester, J. F. O'Hara, A. K. Azad and A. J. Taylor, "A discussion on the interpretation and characterization of metafilms/metasurfaces: The two-dimensional equivalent of metamaterials," *Metamaterials*, Vol. 3, No. 2, 100–112, 2009.
3. Tretyakov, S. A., *Analytical Modeling in Applied Electromagnetics*, Artech House, Boston, 2003.
4. Ziolkowski, R. W., "Design, fabrication, and testing of double negative metamaterials," *IEEE Trans. Antennas Propag.*, Vol. 51, No. 7, 1516–1529, 2003.
5. Smith, D. R., D. C. Vier, T. Koschny and C. M. Soukoulis, "Electromagnetic parameter retrieval from inhomogeneous metamaterials," *Phys. Rev. E*, Vol. 71, No. 3, 036617(1–11), 2005.
6. Scher, D. A. and E. F. Kuester, "Extracting the bulk effective parameters of a metamaterial via the scattering from a single planar array of particles," *Metamaterials*, Vol. 3, No. 1, 44–55, 2009.
7. Belov, P. A. and C. R. Simovski, "Homogenization of electromagnetic crystals formed by uniaxial resonant scatterers," *Phys. Rev. E*, Vol. 72, No. 2, 026615(1–15), 2005.
8. *CST MWS^{TM}: Computer Simulation Technology: Microwave Studio*, 2009. Computer Simulation Technology.
9. Chen, H. T., J. F. O'Hara, A. J. Taylor, R. D. Averitt, C. Highstrete, M. Lee and W. J. Padilla, "Complementary planar terahertz metamaterials," *Opt. Express*, Vol. 11, No. 7, 1127–1130, 2007.
10. Gordon, J. A., C. L. Holloway and A. Dienstfrey, "A physical explanation of angle-independent reflection and transmission properties of metafilms/metasurfaces," *IEEE Antennas Wireless Propag. Lett.*, Vol. 8, 1127–1130, 2009.

Frequency-dependent homogenization of split-ring arrays

M. H. Belyamoun, A. Bossavit and S. Zouhdi
Laboratoire de Génie Electrique de Paris
11 rue Joliot-Curie
91192 Gif-sur-Yvette, France

Abstract- In this paper, we present a novel homogenization method to compute the frequency dependent permeability of a split-ring periodic structure. Instead of meshing the small split of the metallic ring, we introduce a cutting surface through which the magnetic potential has a jump. Thus, we obtain the expected negative permeability of this metamaterial with a minimal cost.

1. INTRODUCTION

Homogenization is the exploitation of translational symmetry of the periodic structure. Therefore, instead of solving the problem over the whole structure, we only study the symmetry cell. This approach implies that the incident wave considers the material as homogeneous, which is the case when the dimensions of the inclusions are considered very small compared to the wavelength.
The unfolding method, presented in [1], is a simple way to compute the equivalent parameters of a periodic structure, even if it is bianisotropic and dispersive. But this homogenization method doesn't apply to metamaterials which contain resonant inclusions, as the split ring resonator. In fact, when the structure's period tends to zero, we loose the frequency dependence of the electromagnetic parameters as the permittivity and permeability.
These limitations have been overcome by a novel homogenization method. Its theoretical basis is presented in [2], we have implemented it and we present the results in this paper.

2. THE CELL PROBLEM

Let's consider an array of split ring resonators immersed in a static field B. Our goal is to compute the effective permeability of such a material.

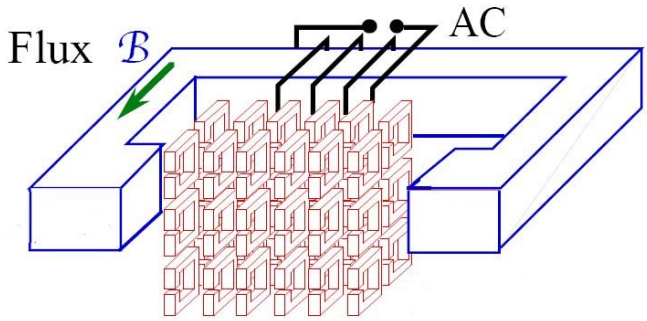


Fig 1: Split-ring array with a period ℓ

The homogenization does apply to full Maxwell equations, but with disappointing results. In fact, the obtained electromagnetic parameters are the static one, with no frequency dependency, and therefore no negative index could be obtained by this method. It has been proven in [2] that a solution to this problem is introducing a second small parameter, which competes with the structure period ℓ. In the case of the split ring resonator, this small parameter would be the slit's width δ. Assuming that:

$$l \prec\prec \lambda$$

$$\delta \prec\prec l$$

We found in [2] the week solution of the problem. And instead of meshing the small slit and the ring "skin", we model the slit by a surface Σ that bears a capacitive layer and by introducing the losses in the weak formulation:

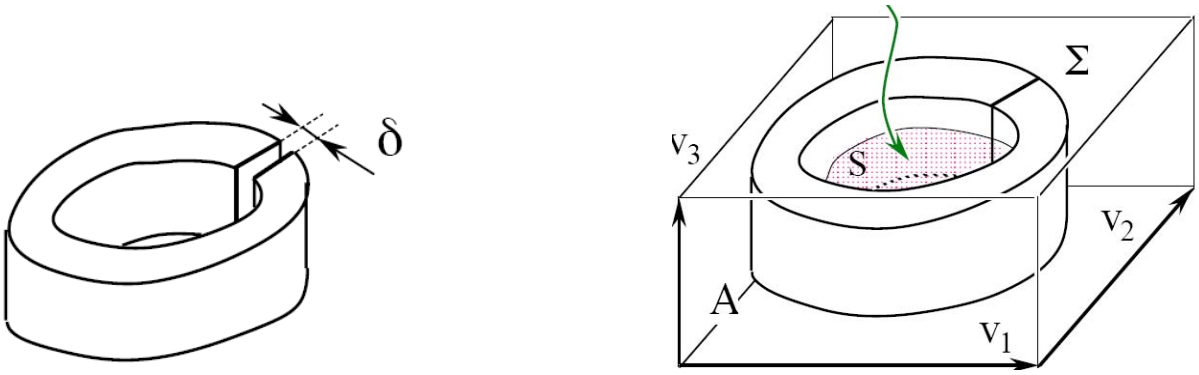


Fig 1: Modeling the slit with a capacitive layer

When this materiel is immersed in a static field B, a current I flows in the ring across the surface Σ. And because rot(h)=0, a multivalued magnetic potential h = grad(φ) exits. We introduce then a cutting surface S through which the magnetic potential φ have a jump [φ] equals to the current I. The main result of [2] is the weak formulation of this electromagnetic problem:

$$\int_A \mu \nabla\varphi \nabla\varphi' dV \quad + \quad \int_{@A} \frac{1-i}{\sigma\omega d} \nabla_S\varphi \nabla_S\varphi' dS \quad - \quad \frac{1}{C\omega^2}[\varphi][\varphi'] \quad = \quad \int_A B\nabla\varphi' dV \qquad \forall \varphi' \in \Phi \tag{1}$$

Once the potential φ found, we can compute the effective permittivity μ_{eff} by using the following formula

$$\frac{V}{\mu_{eff}} B^2 = \int_A \mu \left|\nabla\varphi\right|^2 \quad + \quad \int_{@A} \frac{1-i}{\sigma\omega d} \left|\nabla_S\varphi\right|^2 \quad - \quad \frac{1}{C\omega^2}[\varphi]^2 \tag{2}$$

The complex effective permittivity is defined by considering that the energy of the equivalent homogenized material must by equal to the energy of the studied split-ring array. The imaginary part of the permeability is clearly positive, while the real part becomes negative at the resonance frequency.

3. FINITE ELEMENTS RESOLUTION

First, given the previous model, we have to take into account the periodicity of the unit cell when we mesh it. Therefore, each opposite faces of the unit cell are identically meshed. Also, because the behavior of the resonant ring is described by the cutting surface S and the skin depth d, it becomes unnecessary to mesh inside the ring.

Finally, we know that the potential has a jump thought the surface S. We can model these phenomena by doubling the nodes on the surface S. In fact, for each node N_{s+} of the surface S, we will add to the mesh another node N_{s-} having the same coordinates. Ns- is connected to the tetrahedral elements located “under” the cutting surface S while N_{s+} will be only connected to the tetrahedrons above S.

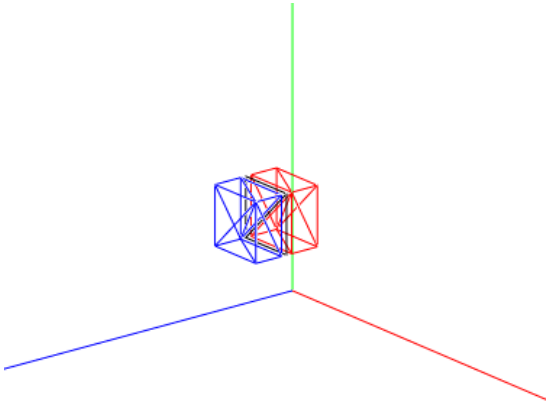


Fig 3: Node doubling on the cutting surface S.

The initial mesh and the geometry are created under COMSOL which allows choosing the dimensions, the orientation and the ring geometry. Then, another program transforms the mesh, by detecting the nodes correspondence between the opposite faces of the unit cell and by doubling the nodes on the cutting surface S.



Fig 4: Periodicity detection

At this point, it is necessary to change the nodes order. In fact, several equations link the potential on the opposite faces of the unit cell and the potentials on the cutting surface. We have for each opposite nodes on the faces of the unit cell:

$$\varphi_{xa} - \varphi_{x0} = C_x$$
$$\varphi_{ya} - \varphi_{y0} = C_y$$
$$\varphi_{za} - \varphi_{z0} = C_z$$

And the following equation links the unknowns on the doubled nodes of the surface S with the current I :

$$\varphi_{s+} - \varphi_{s-} = I$$

Considering these equations, we have to eliminate the unknowns φ_{xa}, φ_{ya}, φ_{za} and φ_{s+}, and then calculate the values of the four unknowns Cx, Cy, Cz and I as well as the value of the potential on the remaining nodes.

4. NUMERICAL RESULTS

Several simulations have been made for different orientations, ring's dimensions, slit's width and conductivity. In this paper, we have chosen a copper ring (σ = 60e6 S/m) immersed in air (μ_r=1). The resonant ring have a slit's width of δ=0.1mm. As we can see on the following results, the resonance is obtained between 9 and 10 Ghz.

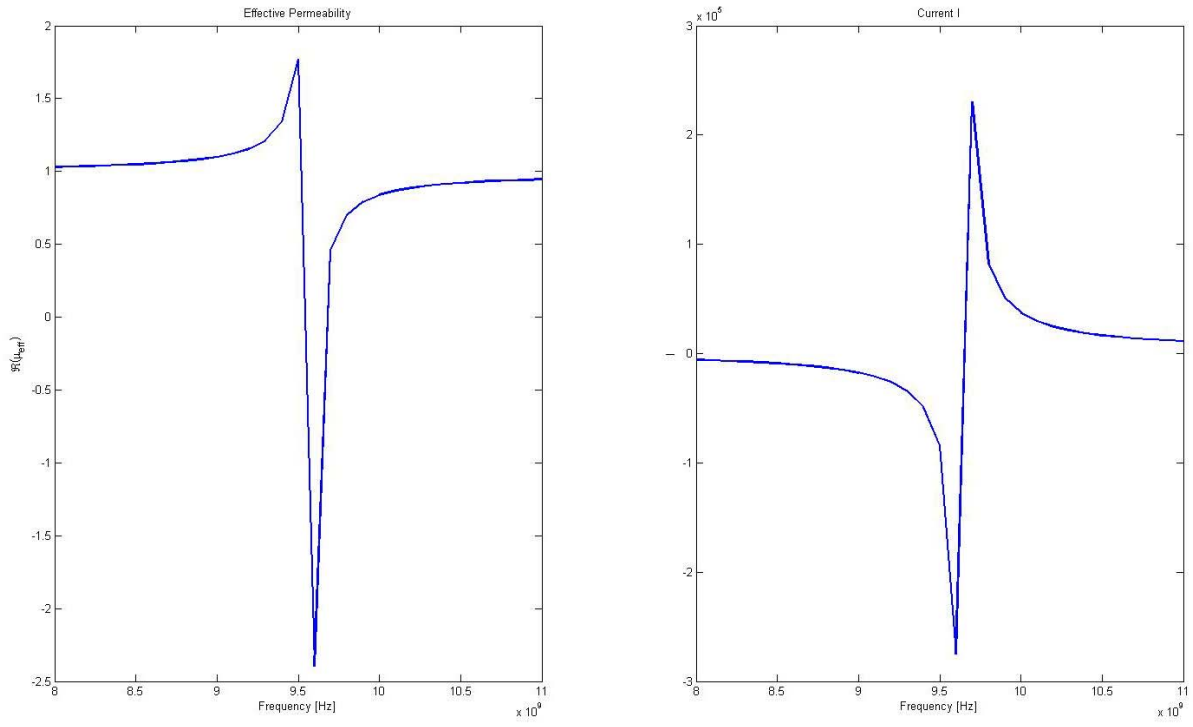


Fig 5: the effective permittivity and the current near the resonance

The current and the relative effective permeability diverge near the resonance if we consider a perfect conductor.

The iso-potentiels have shown that the "jump" through the cutting surface S equals the current. As h=grad(φ) and from the following iso-potentiel, it seems that the major part of the magnetic field flows through the cutting surface S.

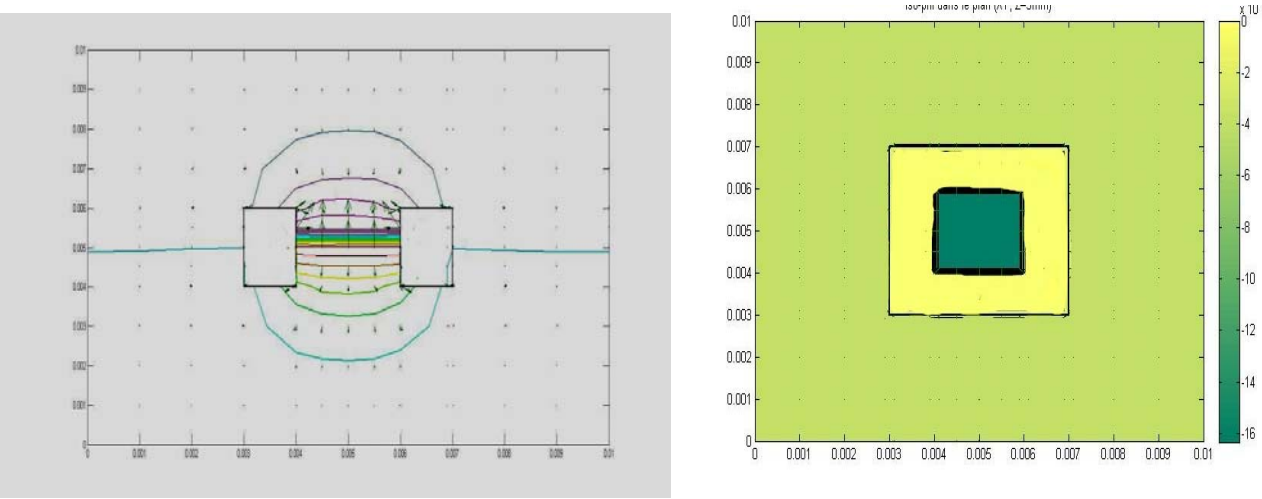


Fig 6: Iso-potentials and the magnetic field orientation in the unit cell

5. CONCLUSIONS

The previous results prove that the attempt to obtain by homogenization a frequency dependent permeability, with a negative real part, has been successful. By its interesting modeling of split-ring arrays, this homogenization technique allows a very fast computation of the complex effective permittivity. Also, given the calculus code structure and effectiveness, evaluating the effects of dimensions change or materials properties on the resonance frequency offers a simple way to optimize the split-ring arrays.

REFERENCES

1. M.H. Belyamoun, S. Zouhdi, “Electromagnetic modeling of bianisotropic Debye materials”, ICEAA’09.

2. A. Bossavit, “Effective, Frequency-Dependent, Permeability of Split-Ring Metamaterials via Homogenization”, IEEE Trans, mag-45, 3, pp. 1276-9, 2008.

Novel magnetic properties of metamaterials LH devices

M. A. Abdalla[1], and Z. Hu[2]
[1]Electronic Engineering Department, MTC, Cairo, Egypt.
[2]MACG, EEE School, University of Manchester, UK.
[1]*maaabdallah@googlemail.com , [2]z.hu@manchester.ac.uk

Abstract-
This paper introduces different varieties of novel left handed metamaterials devices with novel magnetic operation properties. The reported devices have the advantages of their small size, multi frequency band in addition to broadband operation (≈ 60 %) compared to their conventional design. Moreover, these devices are designed to illustrate novel magnetic properties such as their tuning and non reciprocity operation capabilities. Theoretical explanations supported by simulation results of presented devices confirmed the operation of a tunable and nonreciprocal coupler and tunable transformer

1. INTRODUCTION

Electromagnetic Metamaterials (MTMs) were first introduced in 1967 by the Russian physicist Victor Veselago. He named MTMs that illustrate simultaneous negative electric permittivity ε and permeability μ as left-handed metamaterials (LHM) [1]. Thanks to theses negative parameter values, these LH MTMs, are characterized by unconventional electromagnetic propagation parameters. Not until of early of this century where LH MTMs were first experimentally demonstrated by pioneering works of Pendry by using array of split ring resonators (SRRs) with a wire array placed in space [2]. However, such model was not suitable for microwave applications. Therefore, planar LH MTM versions have been proposed for RF/microwave applications in both microstrip and coplanar waveguide (CPW) configurations [3,4]. However, all these examples were suggested using dielectric substrates. Later on, it has been suggested using of ferrite substrates in implementing the LH TLs. Unlike dielectric materials, ferrite medium is nonreciprocal and has a dispersive permeability tensor where the permeability element value can be negative or positive depending on the applied DC magnetic bias. Thus a novel tunable and nonreciprocal LH transmission line can be realized. Examples of these new LH TLs have been introduced using microstrip configuration, and (CPW) configuration [5,6]. LH CPW TL requires smaller DC magnetic bias than microstrip one due to its smaller demagnetization field.

In this paper, we introduce a survey on novel set of microwave devices implemented using ferrite substrate in LH MTMs configurations. These devices were implemented in CPW configuration to have the advantage of its small DC magnetic bias. Thanks to the employed LH configuration, the reported devices demonstrate the advantages of the compact size and the power enhancement. Moreover, these devices can be tunable and nonreciprocal thanks to the magnetic properties of the ferrite. The performance of these devices are explained theoretically and confirmed by both numerical simulations and measurements.

2. THEORY

The ferrite LH TL can be realizable by loading a conventional hosting ferrite TL by a series capacitive load and shunt inductive load, similar to conventional (dielectric) LH TLs. The equivalent circuit of a lossless unit cell of ferrite LH TL of length (d), it is much smaller than the travelling wavelength, can be expressed as a standard

lossless composite right/left handed CRLH unit cell shown in Figure 1. In the equivalent circuit, the parasitic inductance (L_R) and capacitance (C_R) of the hosting ferrite TL while (L_L) and (C_L) are the shunt inductive and series capacitive load, respectively. The dispersion propagation constant (β_{LH}) for all reported LH TLs can be calculated approximately by expressing the hosting ferrite TL parameters in terms of its medium parameters, the ferrite medium permittivity and the equivalent relative ferrite permeability which depends of the DC magnetic bias direction as [5,6].

$$\cos(\beta_{LH}\, d) = 1 - \frac{1}{2}\omega^2 d^2 \left(\mu_o \mu_f - \frac{1}{\omega^2 C_L d}\right)\left(\varepsilon_o \varepsilon_f - \frac{1}{\omega^2 L_L d}\right) \tag{1}$$

In case of ferrite LH CPW TL, the DC magnetic bias direction is horizontal. Thus, it has small demagnetization field. The front view of a horizontally magnetized ferrite CPW TL is shown in Figure 2. As shown, an external DC magnetic field is applied to the ferrite substrate in the direction shown in the figure, inducing an internal magnetic field (H_0) which causes the ferrite substrate to have the saturation magnetization (M_0) in the same direction. For the shown direction of DC magnetic bias, the ferrite has a permeability tensor, [μ], given as

$$[\mu] = \mu_0 \begin{bmatrix} \mu & 0 & -jk \\ 0 & 1 & 0 \\ jk & 0 & \mu \end{bmatrix} \tag{2}$$

where $\mu = \dfrac{\omega_{hm}^2 - \omega^2}{\omega_h^2 - \omega^2}$, $k = \dfrac{\omega\omega_m}{\omega_h^2 - \omega^2}$, $\omega_h = \mu_0 \gamma H_0$, $\omega_m = \mu_0 \gamma M_0$, $\omega_{hm} = \mu_0 \gamma \sqrt{H_0 (H_0 + M_0)}$, γ is the gyromagnetic ratio of the ferrite and μ_0 is the free space permeability. In this case, the effective relative ferrite permeability for horizontal magnetic bias can be expressed as

$$\mu_f = \mu \tag{3}$$

It is shown that the effective permeability has a dispersion nature whose value is negative or positive depending on the applied magnetic field, the ferrite substrate specification and the DC magnetic bias.

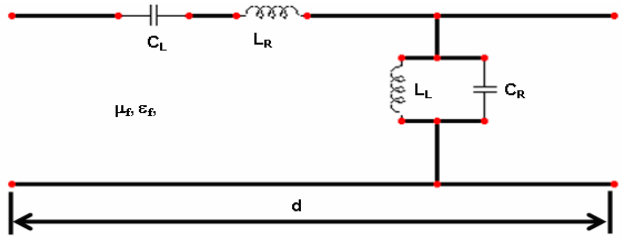


Figure 1 The equivalent circuit model of a ferrite LH TL unit cell.

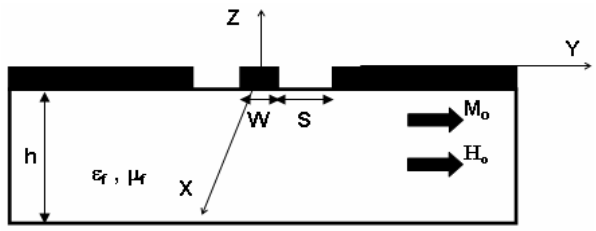


Figure 2 front view of the CPW TL on ferrite substrate horizontally magnetized.

3. TUNABLE COUPLED LINE COUPLER

The backward coupling of a symmetrical LH coupled line coupler (CLC) has been explained using coupled line approach [7] as

$$C = \frac{A(\beta_I - \beta_{LH})\, e^{-j\beta_I l} + B\,(\beta_{II} - \beta_{LH}) e^{-j\beta_{II} l}}{A(\beta_I - \beta_{LH}) + B(\beta_{II} - \beta_{LH})} \tag{4}$$

where A and B are constants, $\beta_{I,II}$ are the coupled propagation constants defined in terms of the propagation constant along the hosting LH TL (β_{LH}) and the backward coupling coefficient between the two hosting coupled lines (C_{BW}) as

$$\beta_{I,II} = \sqrt{\beta_{LH}{}^2 - C_{BW}^2} \tag{5}$$

Since, as seen from (5), $\beta_{I,II}$ may be imaginary at some frequencies, hence, from (4), it can be seen that even 0 dB backward coupling is possible within these frequency bands. Thus, LH CLC can provide much higher coupling, up to 0 dB, with relatively wide line separation over a broad bandwidth and very compact size, especially at lower frequencies compared to a conventional one [2,3]. From ferrite LH TL concepts explained above, it can be claimed that, a ferrite LH CLC has dispersive (β_{LH}) and (C_{BW}) due to the dispersive nature of the ferrite permeability. Consequently, a ferrite LH CLC has a dispersive backward coupling (C) as it can be seen from (4). Detailed explanation about this coupling mechanism is explained in [8].

In our paper, we present a novel dual mode, tunable, and nonreciprocal ferrite LH backward CPW CLC. The proposed coupler was designed using two identical LH TLs over ferrite substrate as shown in Figure 3.An internal horizontal DC magnetic field (H_0) is applied to the ferrite substrate. The coupler's through output and the backward coupling output are located in two separated bands. The first mode was designed to demonstrate a reciprocal backward coupling propagation with almost 0 dB coupling level in the first band. The second band has nonreciprocal through propagation. Moreover, the coupler can be tuned by changing (H_0). The coupler was designed through comparing its equivalent circuit model simulating results to the real structure simulation results obtained using the commercial electromagnetic full wave simulation software ANSOFT- HFSS. The simulated scattering parameters of both the circuit model and the real layout structure using HFSS; for H_0=50,000 Oe, are shown in Figure 4. .This very high DC magnetic bias is selected such that the ferrite is isotropic within the frequency band of interest; so that the equivalent circuit model is valid. The figure shows good agreement between the two simulated results especially for the backward coupling level. The backward coupling level is approximately -1 dB, within the frequency band from 5 GHz to 9 GHz (57 %). Considering the HFSS results, we can conclude within that frequency bandwidth, the coupler has approximately better than -10 dB reflection coefficient, through propagation level below -12 dB, and better than 20 dB forward coupling isolation difference.

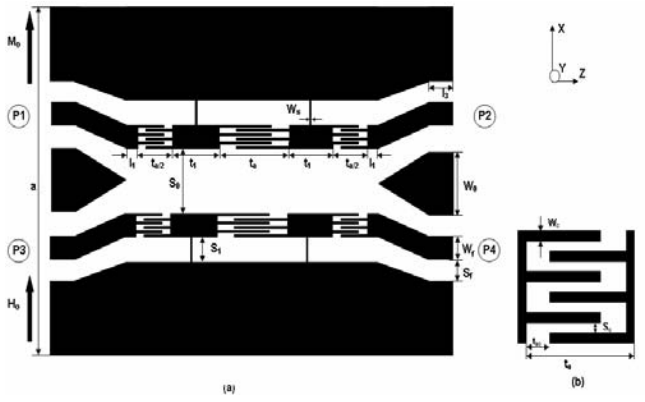


Figure 4 The ferrite LH CPW CLC layout, W_0= 6mm, t_a=2.mm, t_1=1.5mm, S_o=0.5mm, W_f=1.3mm, W_s=0.25 mm(b) The interdigital capacitor geometry S_c=W_c=0.1mm, t_{ac}=0.2 mm.

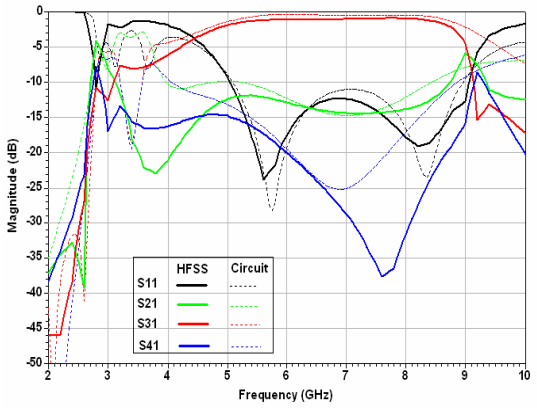


Figure 5 HFSS (for H_0=50,000 Oe) and equivalent circuit simulated scattering parameter magnitudes of the ferrite LH CPW CLC.

By applying lower DC magnetic bias values, the upper cut off frequency of the backward coupling propagation will coincide with the onset of the negative permeability of the hosting CPW ferrite TL. Thus, the coupler can be tunable by changing H_0. This can be confirmed by studying the CLC performance for different values of H_0. For H_0=1750 Oe, the results in Figure 5 (a), illustrates a backward propagation with a very close to 0 dB level over a frequency bandwidth that extends from 3.4 GHz to 5.5 GHz. Then it decreases from approximately -3 dB at 5.7 GHz with a very high slope to reach approximately -10 dB at 6 GHz. Following the backward propagation passband, the coupler has through propagation, no stopband separates them. On contract to the backward coupling performance, the through level increases from approximately -13 dB at 6 GHz up to -5 dB at 6.2 GHz with nonreciprocal propagation with nonreciprocity isolation level that extend up to 35 dB at 6.8 GHz. However, the through propagation level is some how lossy compared to the backward coupling in the first band due to the lossy nature of the ferrite substrate within the negative permeability frequency band. Finally, the coupler has low forward coupling signal (S_{41}) whose isolation level is better than 20 dB over most of the operating bandwidths.
By changing H_0 to 2250 Oe, As illustrated in Figure 5 (b), the 3 dB upper cut off frequency of the backward coupler propagation is increased to approximately 6.5 GHz while the nonreciprocal through propagation exists within the frequency band from 6 GHz to approximately 8 GHz.

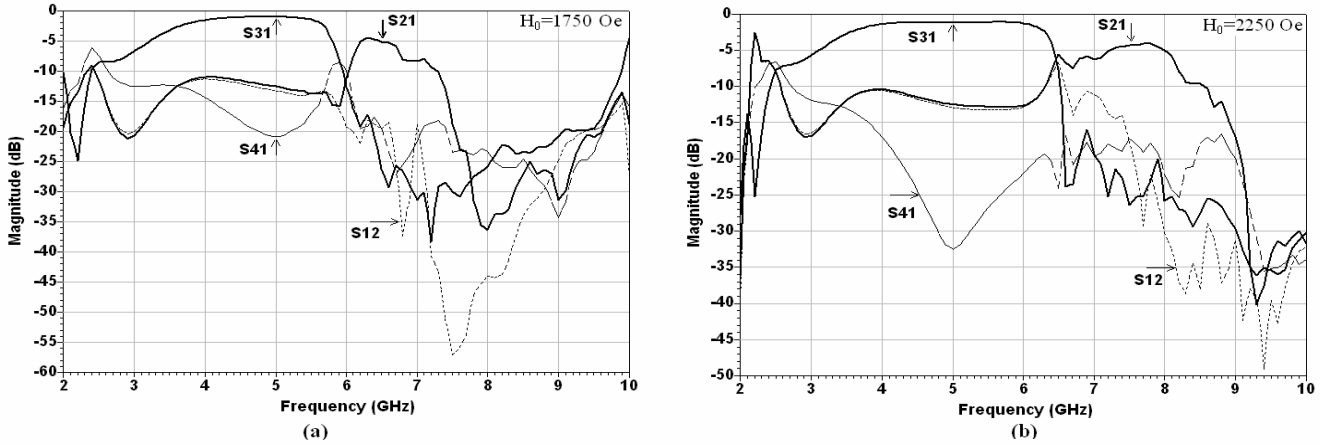


Figure 5 The full wave simulated scattering parameter magnitudes of the dual mode ferrite LH CPW CLC for (a) H_0=1750 Oe and (b) 2250 Oe.

3. TUNABLE WIDE BAND TRANSFMER

A compact quarter wavelength LH transformer can be designed using a CRLH TL. The LH transformer can satisfy arbitrary $\pm 90^0$ phase shift controlled by the CRLH elements. The dispersive ferrite permeability can be utilized to design a wide band tunable ferrite LH transformer. The upper cut off frequency of the transformer was setting by the selection of the applied DC magnetic bias value to be the onset of the lossy propagation within the negative ferrite permeability frequency band. The transformer consists of only a CRLH unit cell formed by series air gap capacitors and a shunt meandered line inductor whose detailed sketch is shown in Figure 6. The simulated scattering parameters of the proposed LH transformer is for H_0= 2000 Oe, 2250 Oe, and 2500 Oe as shown in Figure 7. It is clear that the both of the lower cut off and operating centre frequencies of the transformer are increasing by increasing H_0. On the other hand, the upper cut off frequency is kept constant at 7 GHz. Within the operating bandwidth, the insertion loss is close to 0 dB at its perfect matching, centre, frequency while it increases to no more than 1.5 dB over the rest bandwidth. On the other hand, return loss is close to 20 dB at the perfect matching frequencies while its worst case value, over the whole operating bandwidth is 8 dB, at which the insertion loss is 1.2 dB which still satisfy a reasonable transformer operation

condition. The results confirm that the transformer can match a 25Ω load and a 50Ω line with tunable nature over a wide bandwidth (more than 64%) by changing the applied DC magnetic bias.

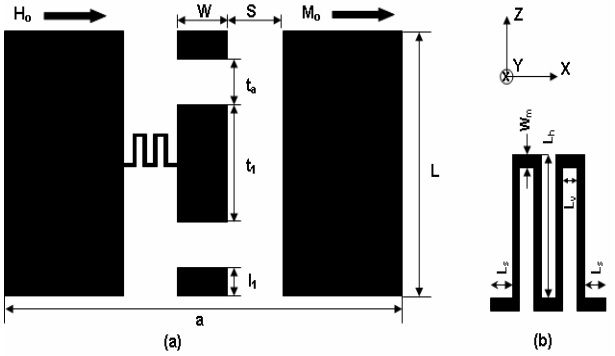


Figure 6 (a) The layout geometry of the ferrite LH CPW transformer a=30 mm, L=1.7mm, W=1.8 mm, l_1=0.5 mm, t_a =0.1 mm, t_1 =0.5 mm (b) The meandered line inductor geometry.

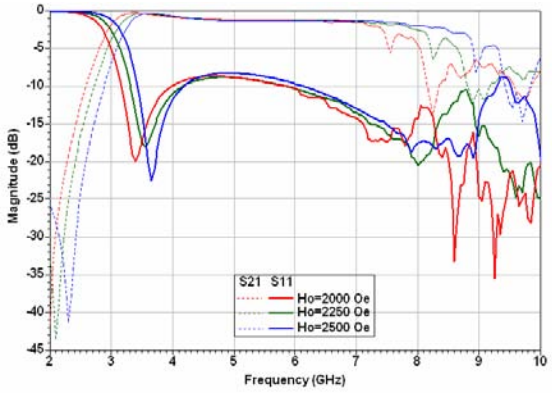


Figure 7 The full wave scattering parameters magnitudes of the wide band ferrite transformer for different H_0 values.

5. CONCLUSIONS

The paper introduces examples of novel microwave LH devices. These devices combine the novel LH properties and the ferrite properties to introduce novel microwave components demonstrating compact size, broadband and novel magnetic properties. First, the basics of ferrite LH TL are reviewed. A dual mode, tunable and nonreciprocal ferrite LH CPW CLC is introduced. The CLC is compact in size and has broad band (up to 57%). Also, a compact and wideband LH tunable transformer (more than 64%) is introduced.

REFERENCES

1. Veselago V. G., "The electrodynamics of substances with simultaneously negative values of ε and μ," *Soviet Physics – Uspekhi* Vol.10, No.4, 509–514, 1968.
2. Smith D. R., W. J. Padilla, D. C. Vier, S. C. Nemat-Nasser and S. Schultz, "Composite medium with simultaneously negative permeability and permittivity," *Phys. Rev. Lett.,* Vol.84, No.18, 4184–4187, 2000.
3. Caloz C., T. Itoh, *Electromagnetic Metamaterials Transmission Line Theory and Microwave Applications.* New Jersey: John Wiley & Sons, 2006.
4. Eleftheriades G. V., K. H. Balmin, *Negative Refractive Metamaterials.* New Jersey: John Wiley & Sons, 2005.
5. Tsutsumi M. and T. Ueda, "Nonreciprocal left-handed microstrip lines using ferrite substrate," in *Proceedings of IEEE MTT-S Int. Microwave Symposium,* Fort Worth, USA, June 2004, 249-252.
6. Abdalla M. and Z. Hu, "On the study of CWP dual band left handed propagation with reciprocal and nonreciprocal characteristics over ferrite substrates," in *Proceedings of IEEE AP-S Int. Symp,* Honolulu, USA, June 2007, 2578-2581.
7. Nguyen H. V. and C. Caloz, "Generalized coupled-mode approach of metamaterial coupled-line couplers: coupling theory, phenomenological explanation, and experimental demonstration," *IEEE Transactions on Microwave Theory and Techniques*, vol. 55, pp. 1029-39, 2007
8. Abdalla M. A. and Z. Hu, "Compact tunable single and dual mode ferrite left-handed coplanar waveguide coupled line couplers,"IET Microwaves, Antennas & Propagation, June 2009 vol.3, Issue 4, p. 695-702.

Broadband filters based on OSRR and OCSRR balanced composite right/left handed transmission lines

Miguel Durán-Sindreu*, Adolfo Vélez, Jordi Bonache and Ferran Martín
GEMMA/CIMITEC Departament d'Enginyeria Electrònica, Universitat Autònoma de Barcelona, BELLATERRA (Barcelona), Spain
*corresponding author: Miguel.DuranSindreu@uab.es

Abstract- In this paper, filters implemented by combining open split ring resonators (OSRRs) and open complementary split ring resonators (OCSRRs) in a composite right/left handed transmission line configuration are pointed out. The relevant aspect of the approach is that it is possible to implement standard responses (Butterworth or Chebyshev) with broad bandwidths. Also, due to the small electrical size of the employed resonators, the filters are very compact.

1. INTRODUCTION

Artificial transmission lines exhibiting backward wave transmission at low frequencies and forward wave propagation at high frequencies have been previously implemented in microstrip [1,2] CPW [3,4], LTCC [5] and MMIC [6] technologies, among others. Such composite right/left handed (CRLH) lines can be fabricated by loading a host line with series capacitances and shunt inductances (in practice implemented by means of lumped or semi-lumped planar components) [1,3,5,6]. Alternatively, CRLH lines can be synthesized by combining split ring resonators (SRRs), originally proposed by Pendry [7], and shunt connected inductors in a host transmission line [4], or by combining complementary split ring resonators (CSRRs) [8] and series capacitances [2,9]. In all the cases, the series reactance and shunt susceptance of the equivalent T- or π-circuit model change from negative to positive values when frequency increases, one particular case being that corresponding to the situation where the series and shunt resonators exhibit the same resonance frequency (balanced case).

In this paper, another implementation of CRLH lines is considered. We make use of a combination of open resonant particles: the open split ring resonators (OSRRs) [10] and the open complementary split ring resonators [11] (OCSRR). Both particles are depicted in Figure 1. As compared to their closed counterparts (SRRs and CSRRs), OSRRs and OCSRRs are electrically smaller by a factor of two, as is justified in [10] and [11]. Thus, it is possible to implement very small components based on these particles.

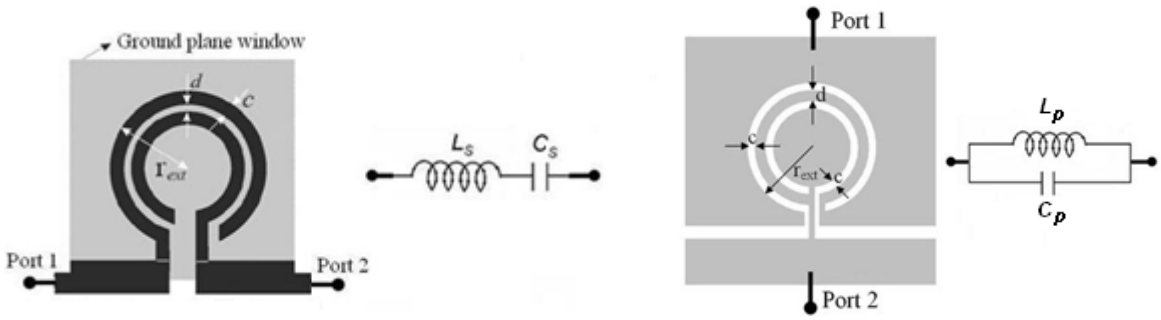


Figure 1: Typical topology and equivalent circuits of a OSRR (a) and OCSRR (b).

2. CRLH LINES BASED ON OSRRs AND OCSRRs

Since the OSRR is an open series resonator, it can be series connected to a host line to implement the series reactance of the canonical T- or π-circuit model of a CRLH line (see Fig. 2). Similarly, the OCSRR can be employed to implement the shunt branch of the canonical circuit model of the CRLH line. This is the key idea behind our approach of CRLH lines based on the combination of OSRRs and OCSRRs. In CPW technology, potential CRLH lines based on a combination of OSRRs and OCSRRs, are depicted in Figure 3. However, an accurate analysis of these structures reveals that they can not be accurately described by the models of Figure 2. The reason is the presence of some parasitics that must be taken into account to properly model the structures. The main deviation from the canonical models of Figure 2 comes from some phase shift introduced by the particles. Although the OSRRs and OCSRRs are electrically small, they provide some phase shift at resonance, and this parasitic effect must be taken into account for an accurate description of the structure. This effect can be modeled by introducing phase shifting lines at both sides of the resonators. Such transmission line sections can be modeled through a series inductance and a shunt capacitance, which can be determined from the analysis of the isolated resonators. Thus, for the OSRR, the inductances of the transmission line sections are series connected to the LC series resonator and the capacitances are shunt connected at both sides forming a π-circuit. For the OCSRR, the capacitances of the phase shifting lines are parallel connected to the LC tank of the OCSRR and the inductances are series connected, thus forming a T-circuit. Thus, the model of the structure is that shown in Figure 4, which can be simplified to the equivalent circuit shown in Figure 5.

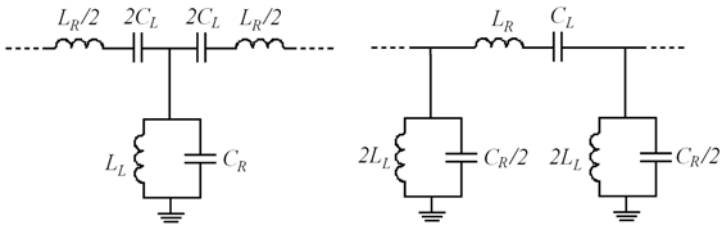


Figure 2: T- and π-circuits describing the unit cell of the canonical CRLH transmission lines

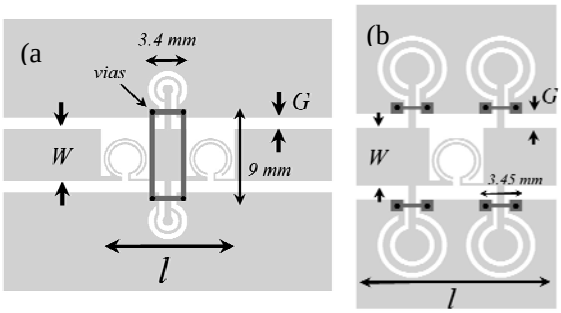


Figure 3: Typical topologies of the unit cell of a CPW CRLH line based on a combination of OSRRs and OCSRRs. (a) Structure with series connected OSRRs in the external stages and a pair of shunt connected OCSRRs in the central stage; (b) Structure with OCSRRs shunt connected in the external stages and a series connected OSRR in the central stage. The structures has been fabricated on the *Rogers RO3010* substrate with thickness h = 1.27 mm and measured dielectric constant ε_r = 11.2. Dimensions are: (a): *l=12.4 mm, W=5mm, G=1.16mm.* For OCSRR: r_{ext}*=1.8mm, c=0.5mm, d=0.3mm*. For OSRR: r_{ext}*=2mm, c=d=0.2mm.* (b): *l=16.13mm, W=5mm, G=1.16mm.* For OCSRR: r_{ext}*=2.8mm, c=0.4mm, d=0.6mm*. For OSRR: r_{ext}*=2mm, c=d=0.2mm.*

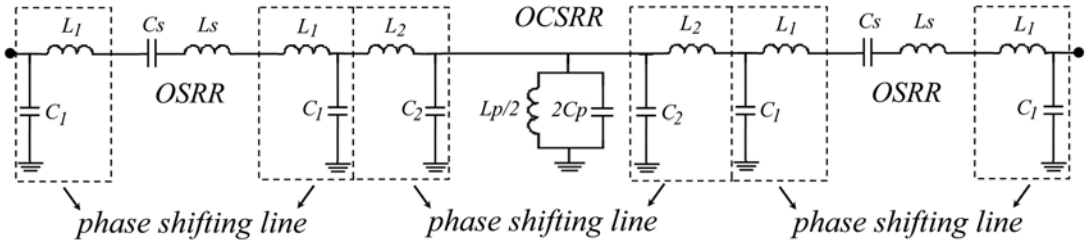


Figure 4: Accurate circuit model for the structure of Fig. 3(a).

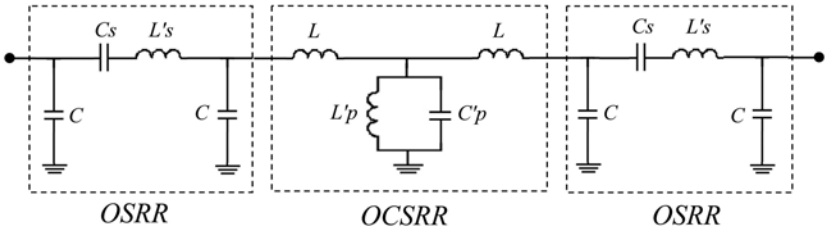


Figure 5: Simplified equivalent circuit of Figure 4, where $L'_s = 2L_1+L_s$, $C'_p = 2(C_p +C)$, $L'_p = L_p/2$.

The simulated and measured characteristics of the structure (un-balanced) of Figure 3(a) are depicted in Figures 6-8. It can be clearly appreciated that the structure is un-balanced, that is, the left handed band and the right handed band are separated by a frequency gap. The agreement between measurement and both electromagnetic and circuit simulation is good. For the circuit simulations, the circuit parameters have been inferred according to the extraction parameter procedure described in [12]. The next step is the implementation of band pass filters based on these structures. Since the model of Figure 5 does not exactly correspond to the canonical model of a band pass filter, it is not possible to implement standard frequency responses. However, it will be shown in the next section that in spite of the parasitics, standard responses can be synthesized to a good approximation.

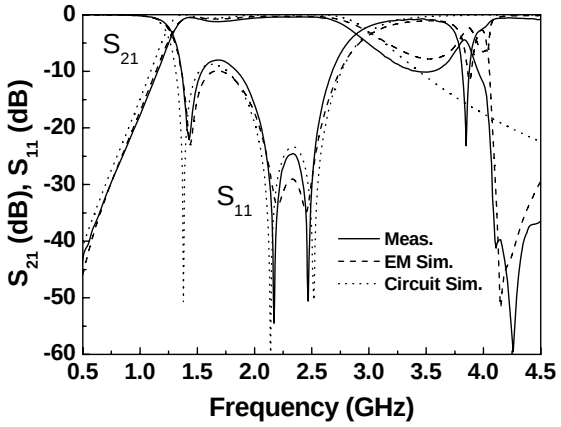


Figure 6: Insertion and return losses corresponding to the structure of Fig. 3(a). The values of the equivalent circuit on reference of Figure 5 are: C = 0.24 pF, L = 0.56 nH, L'_s = 6.76 nH, C_s = 0.95 pF, C'_p = 2.44 pF, L'_p = 2.53 nH.

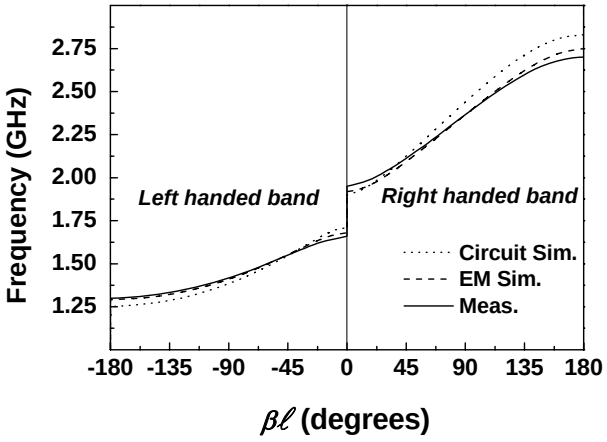


Figure 7: Phase constant for the structure of Fig. 3(a).

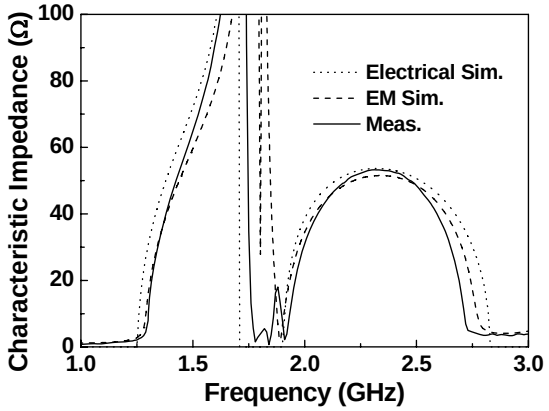


Figure 8: Dependence of the characteristic impedance with frequency for the structure of Fig. 3(a).

3. BROADBAND FILTERS BASED ON OSRRs AND OCSRRs

In this section it is presented an order-3 Chebyshev band pass filter as a proof of concept demonstrator. The filter is designed at f_c = 2.9 GHz with a fractional bandwidth of 35 % and a ripple of 0.02 dB. The design procedure consists on three steps. First of all, we obtain the values of the band pass prototype that fits the specifications. In our case, the values in reference of Figure 2(a) are: C_L = 0.27 pF, L_L = 0.93 nH, C_R = 3.3 pF and L_R = 11.52 nH. Secondly, we design the particles individually to accomplish these values of the equivalent circuit with the help of the parameter extraction method reported in [12]. From this method, we also infer the values of the parasitcs which allows us to tune the equivalent circuit response of the whole filter to fit the requirements of the filter. Thus, the third and final step consist on redesign the particles to meet the specifications.

In Figure 9 it is shown the layout and photograph of the filter using this procedure. In this case, it was used only one central connection between the upper and lower ground plane to avoid any coupling between these vias and the OSRR (that would cause a less accurate prediction of the equivalent circuit values). Moreover, it has been experimentally observed that by reducing the thickness of the substrate, the spurious response is separated from the main pass band. Thus, the filter designed has been implemented on a substrate with thickness h = 0.254 mm, instead of the h = 1.27 mm used in the case of the CRLH transmission line.

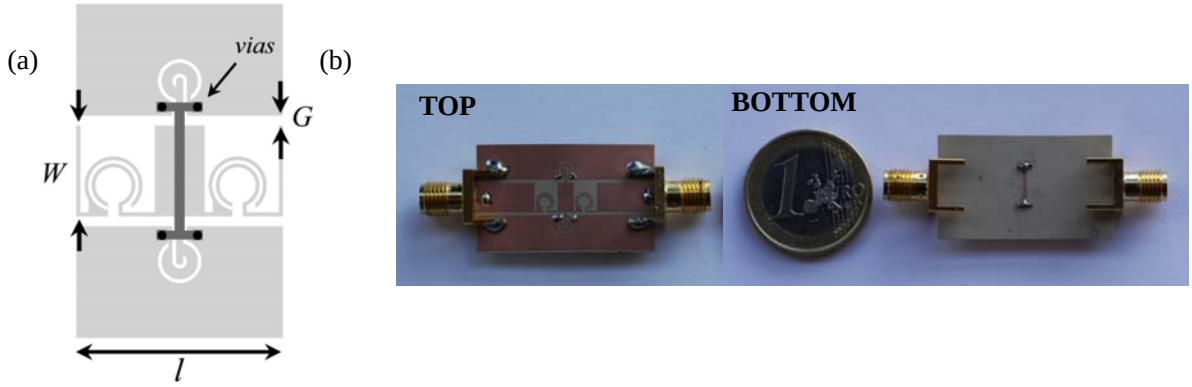


Figure 9: Layout (a) and photograph (b) of the wide-band band-pass filter based on the CRLH transmission line shown in Figure 3 (a). The substrate is the Rogers RO3010 with thickness h = 0.254 mm and dielectric constant ε_r = 11.2. Dimensions are: l = 9 mm, W = 5 mm, G = 0.55 mm. For the OCSRR: r_{ext} =1.2 mm, c = 0.2 mm, d = 0.6 mm. For the OSRR: r_{ext} = 1.6 mm, c = d = 0.2 mm.

In Figure 10 it is shown the electromagnetic and measured response of the filter shown in Figure 9. It is also depicted the circuit simulation of the equivalent circuit taking into account the parasitics and the ideal Chebyshev response. As can be seen, all responses are in good agreement, and the first spurious appears at approximately 2.3f_c.

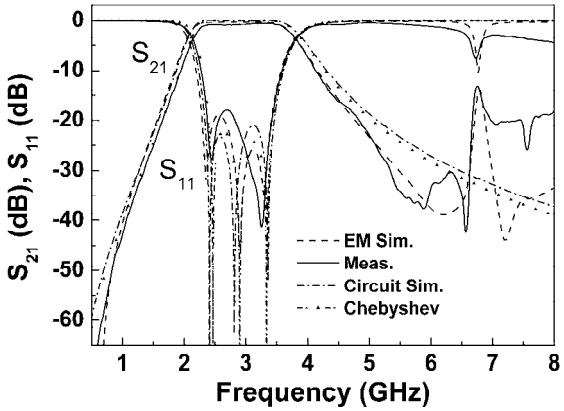


Figure 10: Frequency response of the circuit of Figure 8. The values of the equivalent circuit are: C = 0.19 pF, L = 0.4 nH, C_s = 0.58 pF, L'_s = 5.55 nH, C'_p = 3 pF and L'_p = 0.94 nH.

4. CONCLUSIONS

In this paper it has been demonstrated the possibility to implement composite right left handed transmission lines using the combination of OSRRs and OCSRRs. Moreover, it has been presented the design and fabrication of a wideband band pass filter as proof of concept demonstrator, which validates this approach. The possibility to enhance the bandwidth and selectivity with higher order filters is being investigated by the authors.

ACKNOWLEDGEMENTS

This work has been supported by MEC-Spain (contract TEC2007-68013-C02-02 METAINNOVA), *Generalitat de Catalunya* (project 2009SGR-421) and MCI-Spain (project CONSOLIDER EMET CSD2008-00066).

REFERENCES

1. C. Caloz and T. Itoh, "Novel microwave devices and structures based on the transmission line approach of metamaterials", in *IEEE-MTT Int'l Microwave Symp*, vol. 1 Philadelphia, PA, pp. 195-198, June 2003.
2. F. Falcone, T. Lopetegi, M.A.G. Laso, J.D. Baena, J. Bonache, R. Marqués, F. Martín, M. Sorolla, "Babinet principle applied to the design of metasurfaces and metamaterials", *Phys. Rev. Lett.*, vol. 93, p 197401, November 2004.
3. A. Grbic A. and G.V. Eleftheriades, "Experimental verification of backward wave radiation from a negative refractive index metamaterial", *J. Appl. Phys*. Vol. 92, pp. 5930-5935, November 2002.
4. F. Martín, F. Falcone, J. Bonache, R. Marqués and M. Sorolla, "Split ring resonator based left handed coplanar waveguide", *Appl. Phys. Lett*., vol. 83, pp. 4652-4654, December 2003.
5. I.B. Vendik, D.V. Kholodnyak, I.V. Kolmakova, E.V. Serebryakova, P.V. Kapitanova, "Microwave devices based on transmission lines with positive/negative dispersion", *Microwave and Optical Technology Letters*, vol. 48, pp. 2632-2638, Dec. 2006.
6. J. Perruisseau-Carrier, A.K. Skrivervik, "Composite right/left-handed transmission line metamaterial phase shifters (MPS) in MMIC technology", *IEEE Transactions on Microwave Theory and Techniques*, vol. 54, pp. 1582-1589, June 2006.
7. J.B. Pendry, A.J. Holden, D.J. Robbins and W.J. Stewart, "Magnetism from conductors and enhanced nonlinear phenomena", *IEEE Transactions Microwave Theory Tech.*, vol. 47, pp. 2075-2084, November 1999.
8. F. Falcone, T. Lopetegi, J.D. Baena, R. Marqués, F. Martín and M. Sorolla, "Effective negative-ε stop-band microstrip lines based on complementary split ring resonators", *IEEE Microwave and Wireless Components Letters*, vol. 14, pp. 280-282, June 2004.
9. M. Gil, J. Bonache, J. Selga, J. García-García, F. Martín, "Broadband resonant type metamaterial transmission lines", *IEEE Microwave and Wireless Components Letters*, vol. 17, pp. 97-99, February 2007.
10. J. Martel, R. Marqués, F. Falcone, J.D. Baena, F. Medina, F. Martín and M. Sorolla, "A new LC series element for compact band pass filter design", *IEEE Microwave Wireless Comp. Lett.*, vol. 14, pp. 210-212, May 2004.
11. A. Velez, F. Aznar, J. Bonache, M. C. Velázquez-Ahumada, J. Martel and F. Martín, "Open complementary split ring resonators (OCSRRs) and their Application to Wideband CPW Band Pass Filters", *IEEE Microwave and Wireless Comp. Lett.*, vol. 19, pp. 197-199, April 2009.
12. M. Durán-Sindreu, A. Vélez, F. Aznar, J. Bonache and F. Martín, "Application of Open Split Ring Resonators and Open Complementary Split Ring Resonators to the Synthesis of Artificial Transmission Lines and Microwave Passive Components", *IEEE Trans. Microwave Theory and Techniques*, vol. 57, No. 12, pp. 3395-3403, December 2009.

Increasing the bandwidth of coaxial apertures arrays in radar frequencies

S. Nosal[1*], P. Soudais[2], and J.-J. Greffet[3]

[1]Laboratory for Electromagnetic Waves and Microwave Electronics,
Swiss Federal Institute of Technology, Zürich, Switzerland

[2]Dassault Aviation, Saint-Cloud, France

[3]Laboratoire Charles Fabry, Institut d Optique, Université Paris Sud, CNRS, Palaiseau, France

[*]corresponding author: samuel.nosal@graduates.centraliens.net

Abstract- Arrays of coaxial cavities in a silver slab are an angle-independent frequency selective structure in the optical wavelengths. We show that understanding major resonant effects can achieve a similar structure in the radar frequencies. We use a biperiodic boundary integral method to explain the resonances. We suggest a geometrical evolution of the coaxial cavities that presents an enhanced bandwidth under oblique incidence in TM polarization.

1. INTRODUCTION

A possible use for metamaterials and frequency selective surfaces (FSS) is the conception of radomes (cf. [1]). We are interested in radomes that show specific properties in the X band: similar behavior for both TE and TM polarizations, independence to the angle of incidence and wideband. Obtaining such properties with structures that are light and not too expensive is a challenge.

In the optical frequencies, a structure that meets these requirements well is presented in ref. [2]: an array of square coaxial cavities made in a silver slab. The properties are stable with the angle of incidence and relatively similar for both polarizations. The transposition to radar frequencies is not straightforward. By using our own developed numerical code, based on a boundary element method and described in ref. [3] and [4], we study how the different resonances relate to the bandwidth.

In section 2, we summarize the different resonant phenomena that influence the bandwidth. In section 3, we show that simple physical laws can be derived and explained with the help of the developed numerical code to describe the behavior of the array of coaxial cavities. Finally, in section 4, we suggest an evolutive profile of the coaxial cavities that creates an interesting transmitting behavior: nearly 100% on a 7% bandwidth in TM polarization under oblique incidence.

2. IDENTIFYING THE RESONANCES

In ref [2], an array of square coaxial cavities in a slab of silver is presented. At optical wavelengths, silver is not a perfectly conducting metal: the skin depth is not negligible and virtually enlarges the cavity (cf. ref. [5]). This results in a wide transmission band, but the transmission is not total. The transposition to the radar frequencies is not straightforward as perfect metals (Perfect Electrical Conductors, PEC) modify the resonant phenomena that create the band pass behavior: the transmission coefficient reaches 100% but the transmission band is much narrower (cf. [3], chap. 7), due to the absence of losses. The resonances must be correctly understood in order to choose the best geometrical parameters. In this paper, we study cylindrical coaxial cavities instead of square ones, as shown on Figure 1.

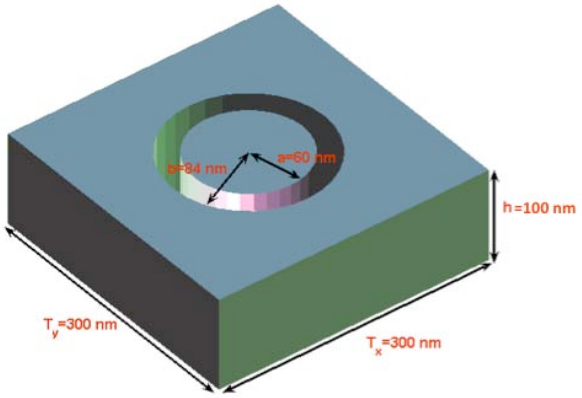


Figure 1: Unit cell of the array of cylindrical coaxial cavities for the optical wavelengths.

In ref. [6], the coaxial waveguide modes are used to describe the fields in the cavities, in a mode-matching method of moments. But the cavities are of finite height and the coaxial waveguide modes (see e.g. [7]) can not very accurately describe the fields in the cavities. Nevertheless, the different involved resonances that explain the transmission peaks (cf. ref. [2] and [5]) are the Fabry-Pérot-like resonances due to coaxial waveguide modes. They can be identified by plotting the fields in the cavities or the (equivalent) currents on the interfaces of the model. Two of these resonances are of primary interest, as they appear at the lowest frequencies:

- Fabry-Pérot-like resonance of order 1, due to the TEM mode.
- Fabry-Pérot-like resonance of order 0, due to the TE11 mode, at the cutoff of the TE11 mode.

The grating resonances (Wood's anomalies) are usually to be avoided as we don't want high-order Floquet modes.

3. INFLUENCES OF GEOMETRICAL PARAMETERS

The coaxial waveguide modes that are involved in the resonances are affected by the finite height of the structure. Thus the analytical formulas for the cutoff frequencies and morphology of the modes are not accurate anymore. Here, we focus on the influence of the height of the structure. We set all the parameters as follows:

- Lattice constants: T_x=T_y=8 mm
- Inner and outer radii: R_{int}=2.13 mm and R_{ext}=2.7 mm
- Cavities filled with PTFE with refraction index n=1.58 without losses
- Oblique incidence at 44° (k_x=0.7) and 64° (k_x=0.9) for frequencies from 8 GHz to 24 GHz, under TE (H) and TM (V) polarizations.

The height of the structure is successively taken to 1mm, 2.5 mm, 5 mm and 10 mm. We calculate the bandwidth as a function of the height h. The variations can be explained by invoking the quality factor, *Q*, which is the inverse of the bandwidth, and it can also be defined as the ratio of the energy stored w_{cav} in the cavity by the losses P_{rad}/ω (cf. [8]):

$$Q = \frac{f_{res}}{\Delta f} = \frac{\mathrm{w}_{\mathrm{cav}}}{P_{cav}/\omega} \qquad (1)$$

Under the assumption that the electromagnetic energy per unit of volume $\mathcal{E}$ is uniform in the cavity of volume *V*, then we have $\mathrm{w}_{\mathrm{cav}} = \mathcal{E}V$. Likewise, as the only possible losses are radiative losses on the apertures of the cavities, it is reasonable to expect that P_{cav}/ω is proportional to the surface of the apertures: $P_{cav}/\omega = \mathcal{P}\mathcal{S}$.

Thus, the quality factor is directly proportional to the height of the structure :

$$Q = \frac{\mathcal{E}}{\mathcal{P}} h \qquad (2)$$

Figure 2 shows how the approximation is relevant for both polarizations and all the angles of incidence. The value of $\frac{\mathcal{E}}{\mathcal{P}}$ is different for each case. It is possible to adopt the same point of view to explain the modification of the resonance frequency, appearing at the cutoff of the TE11 mode (cf. [3]). The accuracy of the law becomes bad when the height tends to 0, when the waveguide vanishes.

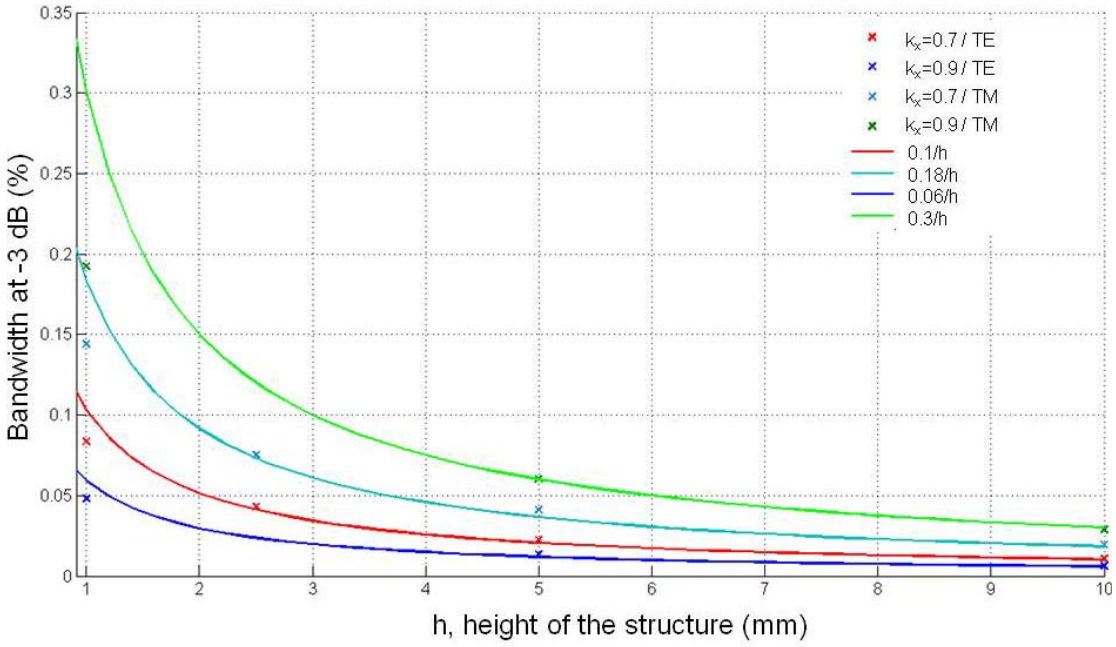


Figure 2: Influence of the height of the structure on the bandwidth.

Other simple physical laws can be derived for different parameters and help choose the best parameters that achieve the desired bandwidth. The main drawback of this approach is that enlarging the bandwidth also increases the transmission efficiency of the filter out of the passing band, which should be near 0. A modification of the shape of the structure can be then explored to improve the transmission response.

4. SUGGESTION OF AN EVOLUTIVE PROFILE OF THE CAVITIES

From the last paragraph, we can deduce that arrays of cavities with a large aperture (R_{ext}-$R_{int} \rightarrow T_x/2$) are less selective than arrays of cavities with a small aperture (R_{ext}-$R_{int} \rightarrow 0$). We wondered if the analogy could be made with stacks of FSS, where it is advised to place the most selective ones in the centre of the stack and the least selective ones on each side of the stack. The array of coaxial cavities can then be considered as a continuous version of a stack of FSS: increasing its selectivity in the center would mean reducing the aperture (R_{ext}-R_{int}) in the center of the cavity, as shown on Figure 3, where the geometrical parameters are given. The evolutive profile consists in arcs of circle in any vertical planes of symmetry of the cavity, which is filled with PTFE (n=1.58). The calculations are done in a extended X band, from 8 GHz to 15 GHz, under normal and oblique incidences (44° and 64°), for both TE and TM polarizations.

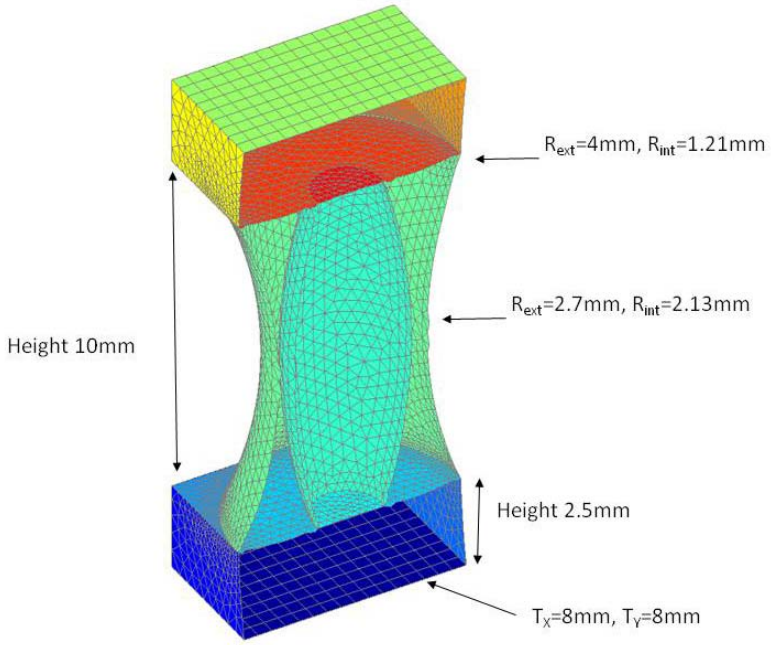


Figure 3: Geometrical parameters of the coaxial cavity with an evolutive profile.

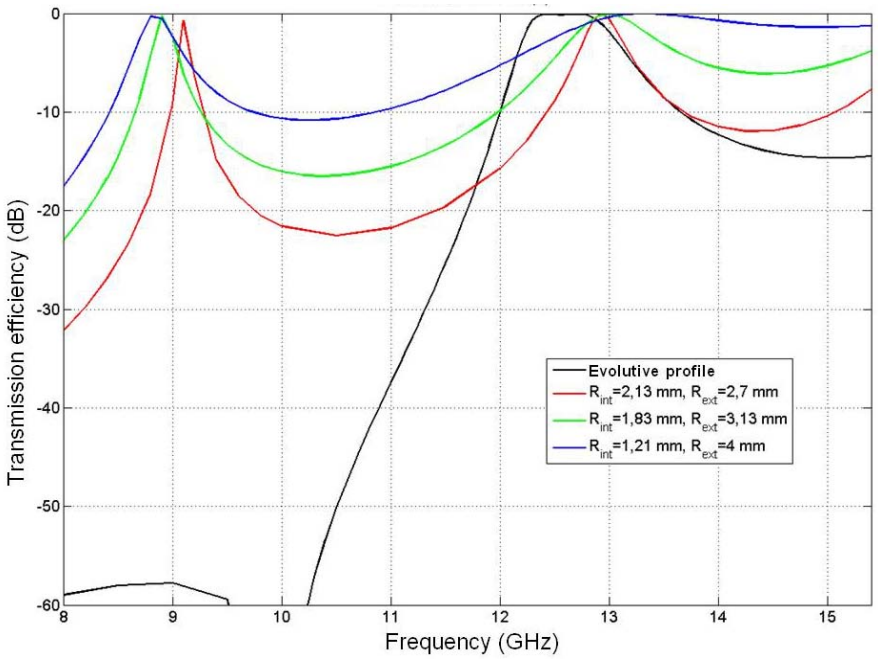


Figure 4: Transmission response of the array of evolutive coaxial cavities in TM polarization under oblique incidence (k_x=0.9), compared to the responses of arrays of straight coaxial cavities with the narrowest, median and the largest apertures.

The modification of the structure does not affect much the transmission responses under normal incidence or TE polarization (results not shown here, but in [3] and [4]). The changes are significant and interesting under oblique incidence in the TM polarization, as seen on Figure 4: there is nearly total transmission for almost 0.6 GHz and very low transmission out of the passing band.

Contrary to what we thought, it does not behave as a continuous variant of a stack of FSS, but the transmission response is due to a coupling between the resonances listed in paragraph 2, due to the modes TEM and TE11.

5. CONCLUSIONS

One of the purposes of this work was to show that our numerical code (included in Dassault Aviation's *Spectre* code) could be used to describe and study physical problems.

The array of coaxial cavities with an evolutive profile show a nearly 100% transmission efficiency on an about 7% bandwidth in the TM polarization under oblique incidence (64°). We have shown that the influence of the thickness of the film can be qualitatively explained. The large broadening of the transmission peak has been attributed to the coupling between two different coaxial cylinder modes. The structure could be improved by using optimization tools to find the best parameters. Moreover, a further study of the coupling between the modes should allow to clarify if the modes are in a strong coupling regime.

ACKNOWLEDGEMENT

This work was supported by the DGA (National Armament Directorate, French Ministry of Defense), through S. Nosal's PhD scholarship. Contact: Dr. Philippe Masclet.

REFERENCES

[1] Poulsen, S., *Stealth radomes*, PhD dissertation, Department of Electroscience, University of Lund, Sweden, 2006.

[2] Van Labeke, D. *et al.*, "An angle-independent Frequency Selective Surface in the optical range," *Optics Express*, Vol. 14, No. 25, 2006.

[3] Nosal, S., *Modélisation électromagnétique de structures périodiques et matériaux artificiels, Application à la conception d'un radôme passe-bande*, PhD dissertation, Laboratoire EM2C, École Centrale Paris, France, 2009. Available online: http://theses.abes.fr/2009ECAP0030

[4] Nosal, S., Soudais, P. and Greffet, J.-J., "Integral Equation Modeling of doubly periodic structures with an efficient PMCHWT formulation", submitted, *IEEE Trans. Ant. Prop.*, 2009.

[5] Baida, F., Belkhir, A. and Van Labeke, D., "Subwavelength metallic coaxial waveguides in the optical range: Role of the plasmonic modes", *Physical Review B*, Vol. 74, 2006.

[6] Roberts, A. and McPhedran, R., "Bandpass Grids with Annular Apertures", *IEEE Trans. Ant. Prop.*, Vol. 36, No. 5, 1988.

[7] Marcuvitz, N., *Waveguide Handbook*, IET, London, 3rd edition, 2009

[8] Stealin, D. H., Morgenthaler, A. W. and Kong, J. A., *Electromagnetic Waves*, chapter 8: Resonators, pp 336-401, Prentice Hall, 1994.

Wideband FSS for Electromagnetic Architecture in buildings

B. Sanz-Izquierdo, J.-B. Robertson, E. A. Parker and J.C. Batchelor

School of Engineering and Digital Arts, University of Kent, Canterbury CT2 7NT, UK

b.sanz@kent.ac.uk, jr244@kent.ac.uk, e.a.parker@kent.ac.uk, j.c.batchelor@kent.ac.uk

Abstract- Interweaving the elements of a frequency selective surface (FSS) is a technique that allows wideband frequency filtering as well as size reduction. FSS structures using this method are well suited to wireless indoor applications where the operating bands are spread over a wide spectrum. Interwoven square loop slots FSS have been designed, fabricated and measured. The FSS structure to be presented offers transparency at the emergency services band at around 400 MHz and suppresses most of the mobile and wireless bands up to 3GHz. The size of the unit cell developed is around 3% of the corresponding wavelength, significantly smaller than a half wavelength resonant dipole.

1. INTRODUCTION

Activity in the UHF band, dubbed the "sweet-spot" by OFCOM, has significantly increased in recent years and portable radio devices that make use of the GSM, 3G, WIMAX or Wi-Fi bands, such as cell phones and laptops, are prevalent in most environments, potentially leading to significant radio interference, spectrum overcrowding and signal security issues. As a result, there is an increased interest in solutions that would allow for the management of such signals in buildings, among those, the incorporation of Frequency Selective Surfaces in walls, windows and doors [1, 2].

This solution, however, comes with some challenges: the signals of interest have wavelengths that are comparable to the size of structures such was windows and doors and, for safety reasons, it is important that buildings be as transparent as possible in the bands used by emergency services (in Europe, such radio systems use the TETRA band, at a wavelength of approximately 75cm), requiring non-trivial frequency selectivity goals. In light of these two constraints, designing elements that are both versatile and of small footprint is of significant interest. Works on fractal and convoluted elements have shown that they may be of some use to fulfill such goals and that their versatility can be further improved by way of interweaving techniques [3, 4].

In this paper, we consider the modification of a simple loop element by way of convolution and interweaving to obtain a wideband stop effect with only a band pass at TETRA frequencies.

2. SQUARE LOOP SLOTS

Recently, we have investigated the performance of small FSS arrays inserted in a partition wall separating two office type rooms [5]. The array sizes were 3 x 3, i.e. 9 elements located on a square lattice, 2 x 2, and also just a single element. Square loops in slot form were chosen for their dual polarised property and for simplicity. To improve the roll-off between the transmission and reflection band, and more specifically to create a pass band for the TETRA band, two identical layers have been cascaded, to produce a double layer FSS with a minimal number of elements.

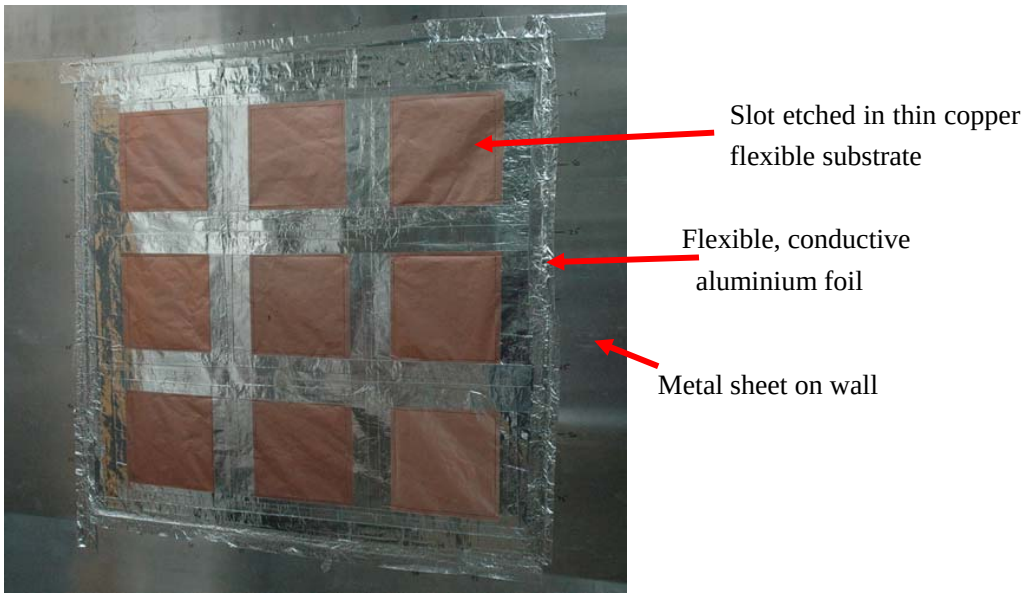


Figure 1 Fabricated 3x3 square slot array as it was mounted on the wall

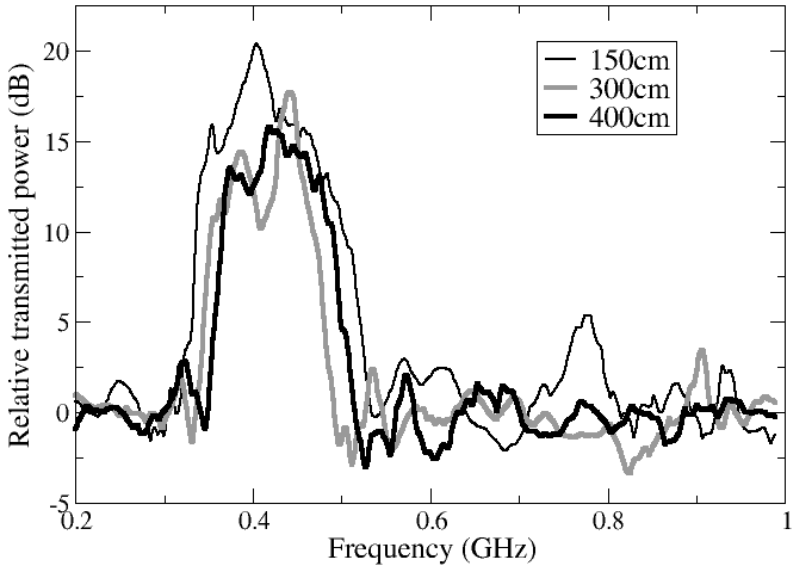


Figure 2 Measured transmission response at receiver distances of 1.5, 3.0 and 4.0m

The dimensions of the square loop slot elements were: square side length D = 19.7 mm, slot width w = 1.0mm, periodicity p = 30cm and separation between the two layers S = 100 mm. A 3x3 slot array was fabricated and measured. The slots were etched into copper foil on a polyester substrate. The FSS was applied to a cement brick wall approximately 4m high and 5m wide, separating two rooms. Metal sheets contiguous with the array foil extended the shield by a metre on all four sides, but beyond that, the wall was unshielded. The transmitted

power measured at distances of 1.5, 3 and 4m from the wall is shown in Figure 2. The signal source was placed 1.5 metres from the centre of the FSS. There is a clear pass band about 100MHz wide at the -3dB points, and 150MHz wide between the -10dB points, elsewhere there is an isolation varying from about 15dB to 20dB with strong ripple generated by scattering via other propagation paths.

3. INTERWOVEN SQUARE LOOP SLOTS AND POSSIBLE APPLICATIONS

The square loop slots seen in the previous section are simple and dual polarized, but the footprint of the elements is significant and their large size and resulting periodicity not practical for all uses, and do not ensure angular stability. A convoluted version of this element, improving upon compactness and stability, has been developed and is illustrated in Figure 3b, together with the original structure in Figure 3a. Each arm has eight stubs on each side. The length of the cross employed was l = 19 mm, the element periodicity p = 20 mm, the width of the slot in the simulations was w = 0.22 mm, the width of the stubs was c = 0.56mm, and their periodicity was 2c.

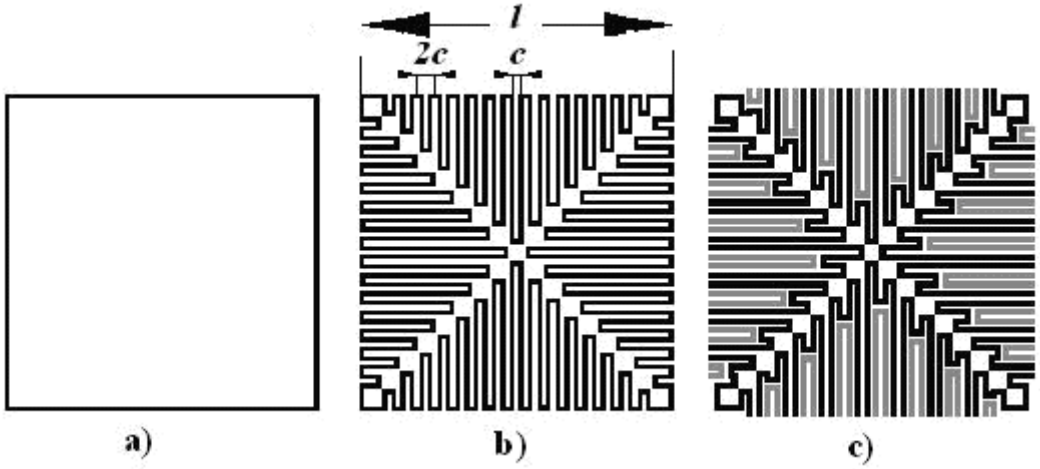


Figure 3 Square loop (a), its convoluted equivalent (b) and its interwoven equivalent (c)

The transmission response of a convoluted loop in Fig.3a had a first resonant frequency at 1GHz and a second at about 2.75GHz, as seen in Figure 4. In the simulations, the -10dB widths were 68% and 11% respectively. The insertion losses were just below 2dB at the lower band and around 5dB at the higher one. The corresponding figure of merit is $\lambda_1/p = 15$ and the efficiency of the loop $L/\lambda_1 = 2.1$. A real advantage of this structure is that adjacent elements can be interwoven, to modify the transmission response, as described in [3]: The unit cell of a convoluted square loop structure can be interwoven with its neighboring unit cell as shown in Figure 3c. Essentially, half of the cycle has been extended beyond the unit cell while the other half has been shortened to allow for the extended cycle from the adjacent cell. An array structure with dimensions (l = 19 mm, p = 20mm, c = 1.12mm and w = 0.22mm) similar to the equivalent convoluted square loop slot configuration represented in Figure 3b was fabricated and measured. The transmission response had peaks near 550MHz and 2050 MHz. In the simulations, the -10dB widths were 126% and 6% respectively. The measured insertion loss at the low band was about 1.8dB, but greater than 10dB at the narrow 2 GHz band pass. Again, the transmission response simulated for plane wave illumination predicted well the behavior of the FSS. There was a 45% reduction in the lower resonant frequency with respect to the original convoluted square loop, while the bandwidth increased

by a factor of 1.8.

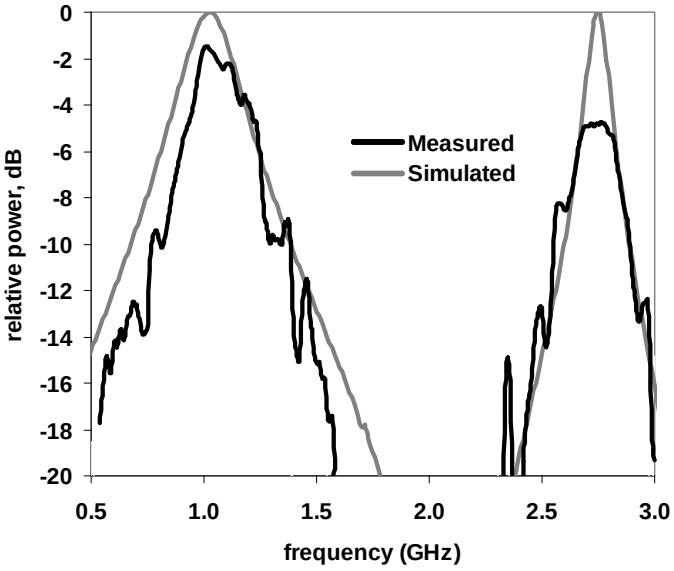


Figure 4 Transmission response of convoluted square loop (Fig. 4b)

The dimensions of the interwoven element were scaled by a factor of 1.35 to encompass the 400 MHz emergency band employed for emergency services in Europe, while attenuating the higher section of the radio spectrum. The fractional frequency range across the various forms of mobile communications is very wide, for example there is a 10 to 1 wavelength range between TETRA (400MHz) and WLAN (2.45GHz). As a result, wideband performance is important for FSS designs at mobile frequencies. As pointed out in [6], in the built environment relatively small interference attenuation can result in significant improvements in the system outage probability. A 15dB increase in the carrier-to-interference ratio can reduce the outage probability by a factor of almost 30, and with an inverse square law approximation, just 10 dB reduces the cell separation required for frequency reuse by a factor of 3.

Figure 5 shows the wideband simulated and measured transmission responses. In the simulation, there is a transmission peak at around 400 MHz with -10dB bandwidth extending from nearly 200MHz to 700MHz. It is followed by two very narrow band resonant modes, at 1.5GHz and 2.1GHz, where the *measured* insertion losses are 10 dB and 18dB respectively. Simulations using CST Microwave Studio^{TM} showed very acceptable angular stability. Between normal incidence, TE45^0 and TM45^0 there was no appreciable drift at 400MHz, although the two narrow pass bands drift in frequency between 1.4GHz and 1.55GHz, and from 2.1GHz to 2.3 GHz, consistent with [7].

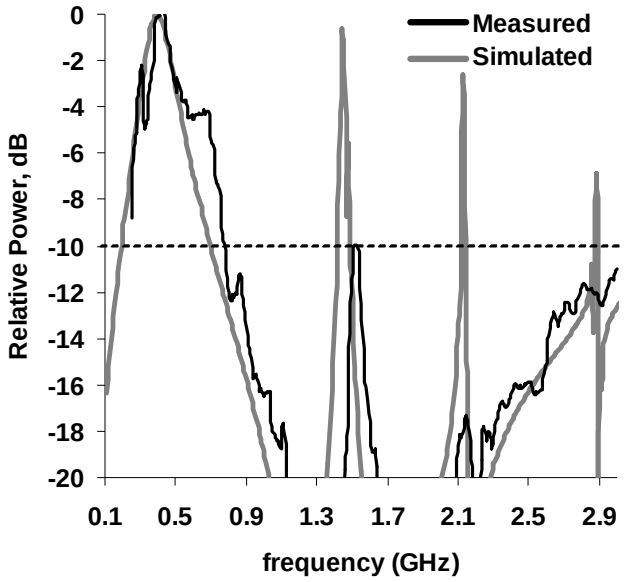


Figure 5 Transmission response of the interwoven element FSS (see Figure 3c), scaled by a factor of 1.35.

4. CONCLUSIONS

The dual-polarized designs presented here are based on convoluted loops. The geometry of the convoluted square loop provides a further degree of flexibility in wideband design, enabling adjacent elements to be interwoven. Here, interweaving decreased the resonant frequency by over 50% and increased the -10dB pass band width by over 60%. An FSS specifically designed for mobile communications in the built environment attenuates the mobile and wireless bands between 700MHz and 3GHz while passing the general mobile radio systems (GMRS) in the USA, and the personal mobile radio systems (PMR446) and the emergency services TETRA band in Europe.

ACKNOWLEDGEMENTS

This work was funded by the UK Engineering and Physical Sciences Research Council and by the National Policing Improvement Agency.

REFERENCES

1. Philippakis, M., Martel, C., Kemp D., Allan, R., Clift M., Massey, S., Appleton, S., Damerell, W., Burton, C., and Parker, E.A., “Application of FSS structures to selective control the propagation of signals into and out of buildings”, OFCOM Report AY4464A, 2003.

2. Hook, M., Ward, K.D. and Mias, C., “Project to demonstrate the ability of Frequency Selective Surface Structures to enhanced the spectral efficiency of radio systems when used within buildings”, OFCOM Report AY4462A, 2003.

3. Huang, F., Batchelor, J.C. and Parker, E.A., “Interwoven Convoluted Element Frequency Selective Surfaces with Wide Bandwidths”, *IEE Electronics Letters*, Vol. 42, pp. 788-790, 14 July 2006.

4. Sanz-Izquierdo, B., Parker, E. A., Robertson, J.-B. and Batchelor, J. C., “Singly and dual polarized convoluted frequency selective structures”, *IEEE Transactions on Antennas and Propagation*, to be published.

5. Parker, E.A., Robertson, J.-B., Sanz-Izquierdo, B. and Batchelor, J.C., “Minimal Size FSS for Long Wavelength Operation”, *IET Electronic Letters*, Vol. 44, No. 6, pp. 394-395, March 2008.
6. Wong, A. H., Neve, M, J. and Sowerby, K. W., “Performance analysis for indoor wireless systems employing directional antennas in the presence of external interference”, *Proceedings IEEE AP-S International Symposium*, 2005, 1A, Washington, D.C., USA, pp. 799–802.
7. Callaghan, P. and Parker, E. A., “Loss- bandwidth product for frequency selective surfaces”, *Electronic Letters*, 1992, 28 (4), p. 365.

Wideband QAMC reflector's antenna for low profile applications

M. Grelier[1,2*], M. Jousset[2], S. Mallégol[2], A. C. Lepage[1], X. Begaud[1] and J.M. LeMener[2]
[1]Institut TELECOM, TELECOM ParisTech - LTCI CNRS UMR 5141,
46 rue Barrault 75634 Paris Cedex 13, France
[2]Thales Systèmes Aéroportés, 10 avenue de la 1ere DFL 29238 Brest Cedex 3, France
[*]corresponding author: grelier@ieee.org

Abstract- A wideband reflector's antenna based on quasi artificial magnetic conductor is proposed. To validate the design, an Archimedean spiral has been backed to this new reflector. In comparison to classical solution using absorbent material, the prototype presents a very low thickness of λ/15 at the lowest operating frequency and an improved gain over a 2.4:1 bandwidth. The whole methodology to design this reflector can be applied to other wideband antenna.

1. INTRODUCTION

The current trend for civilian as well as military applications needs low cost, compact and wideband antenna designs. It's a real challenge to gather all these requirements. Planar spiral antennas are widely used to fulfill the aforementioned specifications. An Archimedean spiral antenna located in free space radiates a circularly polarized bi-directional beam. In most applications, this bi-directional beam must be transformed into a unidirectional beam. A classical solution consists in backing a cavity filled by an electromagnetic (EM) absorber behind the radiating element. Thus the lossy cavity suppresses the backward radiation and preserves the inherent wideband properties. However, the antenna is bulky and loses one half of the radiated power [1].

Another approach consists in taking advantage of the backward radiation by reflecting it in-phase with the forward radiation thanks to an artificial magnetic conductor (AMC) [2]. Such periodic surfaces enabling the radiating element to be closely placed to the ground plane without deterioration of the antenna performances. These surfaces have already demonstrated their abilities as reflector to improve antenna performances [3]. Nevertheless their properties occur within a narrow frequency bandwidth.

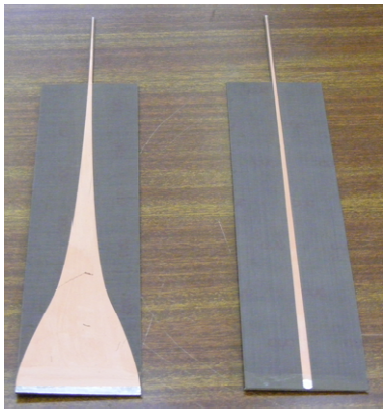
In this work, we present an antenna reflector based on AMC theory call QAMC reflector. Unlike traditional periodic AMC structures, only a few numbers of elementary cells are used. We propose to compare its performances with the classical solution based on absorber by using an Archimedean spiral as radiating element.

2. ARCHIMEDEAN SPIRAL

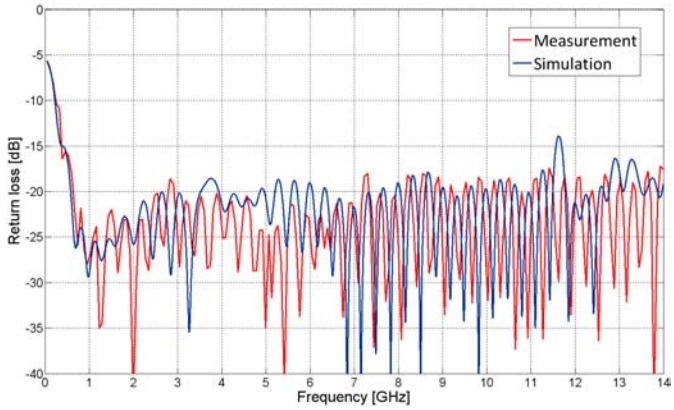
A two-wire Archimedean spiral antenna is designed to achieve wideband properties [4]. The active area in free space of such a spiral is defined as $D=\lambda_0/\pi$ where D is the diameter and λ_0 the wavelength in free space. The inner diameter and the outer diameter are respectively D_{in}=6.3mm and D_{out}=300mm which theoretically define the highest and the lowest frequencies f_{high}=15GHz and f_{low}=0.3GHz. The spiral arms are spaced at a distance equal to the arm width to produce a self-complementary structure and thus maintain broadband characteristics. The width of the spiral arms is w_{arm}=1.25mm. The spiral is printed on a RT5880 substrate with a thickness h_{sub}=1.575mm and the relative dielectric constant ε_r=2.2.

The antenna is fed at the center of the spiral through a broadband tapered balun. It's required to transform the impedance Z_{spi}=160Ω presented by the balanced line of the spiral to the unbalanced line of the coaxial connector

where Z_{sma}=50Ω. Fig. 1(a) shows the photograph of the face-up and face-down of this printed circuit whose dimensions are 300mm × 60mm. In this study we focus on the reduction of the antenna's height without considering the feeding network. Simulation and measurement of the return loss is given by Fig. 1(b) when the balun is loaded by a CMS resistor R=160Ω. Simulations have been performed with CST Microwave Studio based on the finite integrals method [5]. We notice a good agreement and a good impedance matching through a 0.3-14GHz bandwidth.



(a)

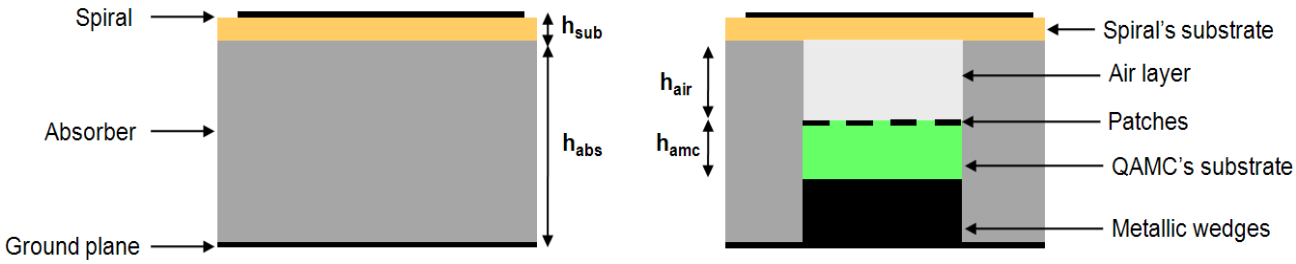


(b)

Fig.1: (a) Photograph of the two sides of the balun (b) Return loss of the loaded balun

3. CONFIGURATIONS AND REALISATION

Fig. 2 displays the side view of two studied structures. The previous Archimedean spiral (AS) is placed above a lossy cavity completely filled by an EM absorber. An Emerson & Cuming type AN-79 Ecosorb is employed as absorbing material with a height h_{abs}=55.26mm. This configuration, referred to as AS_{ref}, will be used as the reference to evaluate the benefits provided by the proposed structure.



(a) (b)

Fig.2: Configurations of the antenna: (a) AS_{ref}: with the lossy cavity, (b) AS_{QAMC}: with the QAMC reflector

Then, the spiral is backed with the QAMC reflector, referred to as AS_{QAMC}. Metallic wedges allow us to adjust and place the QAMC surface close to the spiral using the same antenna support. At low frequency, in order not to short-circuited the spiral by the ground plane proximity, the QAMC reflector diameter is reduced to D_{amc}=100.8mm and absorber is put all around it. Moreover an air layer, h_{air}=4mm≈λ_0/28 at 2.7GHz and ε_r=1, is inserted between the top of the AMC substrate side and the bottom of the spiral substrate to avoid a strong coupling between patches and spiral.

The geometry of the QAMC reflector is shown in Fig. 3. The length of each square patch is w=17.35mm and the gap between the adjacent patches is g=2.65mm. The reflection phase method is used to identify the frequency band in which the AMC behavior occurs [6]. The unit cell is surrounded with periodic boundary conditions to model an infinite array. The principle consists in illuminating it by an incident plane wave. The dimensions have been chosen to obtain a zero-phase reflection around 2.7GHz (Fig. 4).

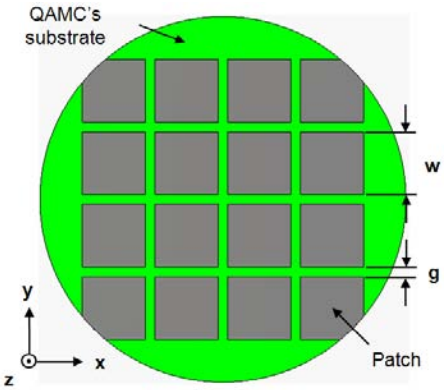


Fig.3: QAMC top view

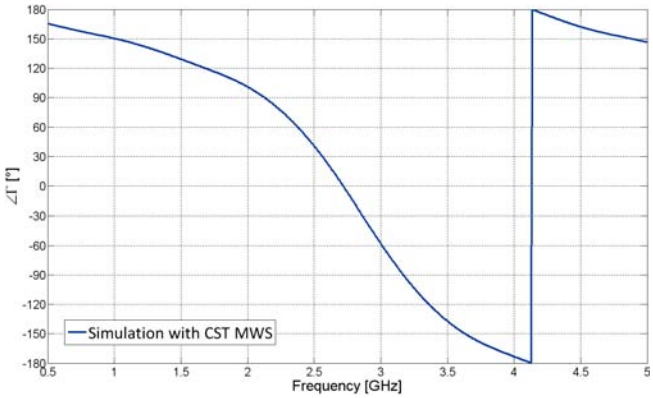
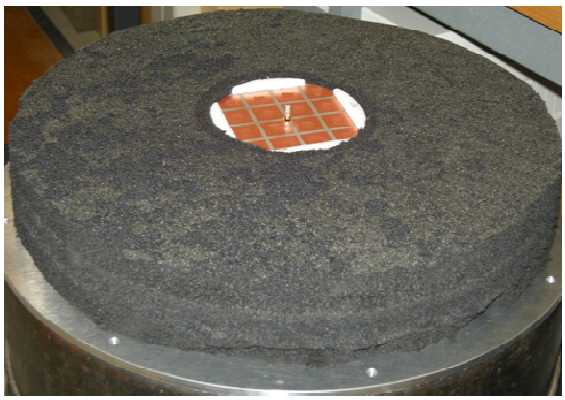


Fig.4: Reflection phase diagram

It's composed of a planar array of only 4x4 square metal patches without vias printed on a grounded CuClad 250 dielectric slab. The parameters of the QAMC's substrate are its thickness h_{amc}=6.26mm and the relative dielectric constant ε_r=2.5. Fig. 5 shows the photographs of the realized antenna. Most authors use AMC reflector whose surface area is larger than the radiating element. Contrary to this commonly configuration, we are in the opposite case since we have $D_{out} \approx 3.D_{amc}$ and the total number of cells is reduced. The proposed structure is not periodic but quasi-periodic. As mentioned in [7], few studies deal with the required periodicity to realize a low profile antenna whereas one of the most noteworthy features of an AMC structure is its periodicity.



(a)



(b)

Fig.5: (a) The QAMC reflector inserted inside an absorber ring, (b) The whole antenna

3. RESULTS AND DISCUSSION

We analyze the characteristics of the two antenna configurations presented above. Simulations results for the AS_{QAMC} case are also presented. Fig. 6 indicates that the antenna exhibits a good impedance matching with a return loss less than -10dB from 0.5GHz to 5GHz.

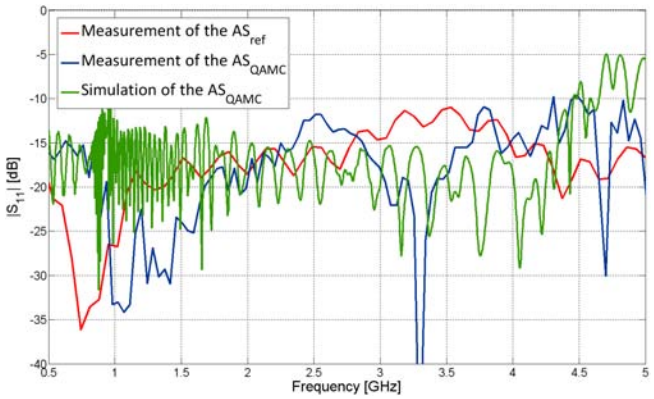


Fig.6: Return loss versus frequency

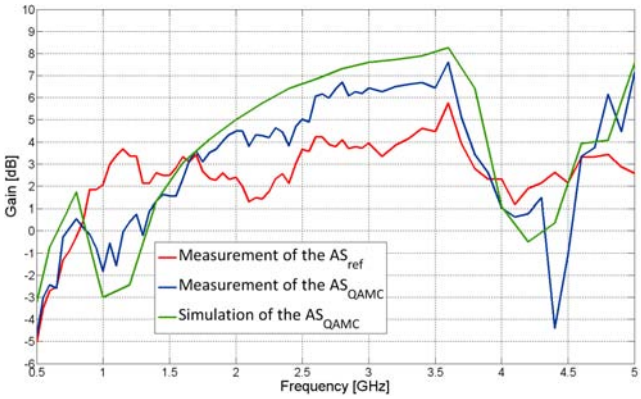


Fig.7: Broadside gain (RHCP) versus frequency

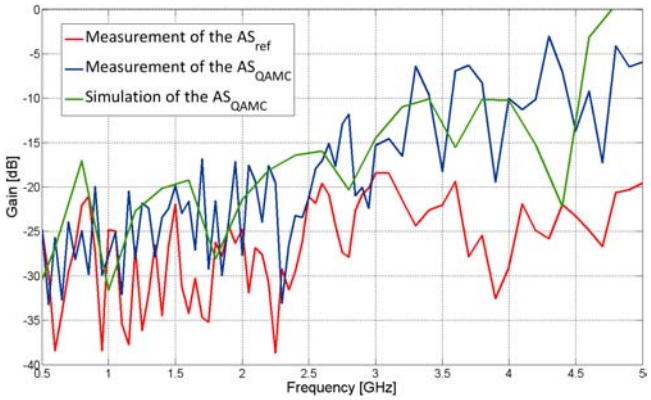


Fig.8: Broadside gain (LHCP) versus frequency

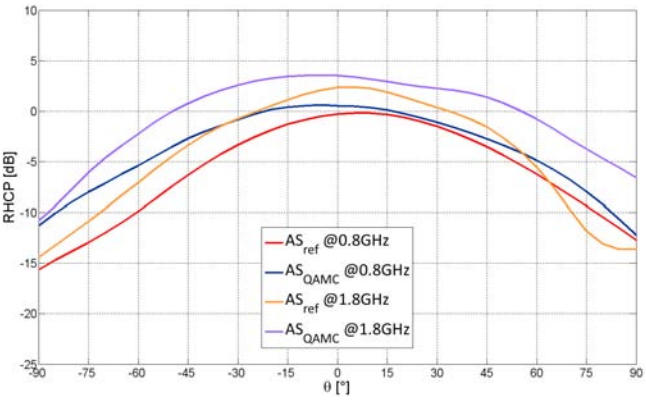


Fig.9: Radiation patterns at 0.8GHz and 1.2GHz

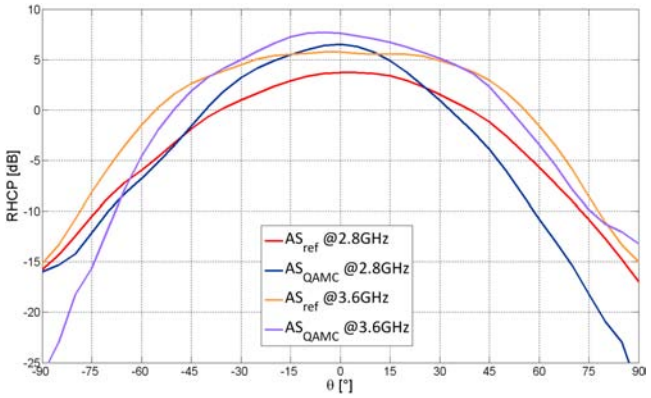


Fig.10: Radiation patterns at 2.8GHz and 3.6GHz

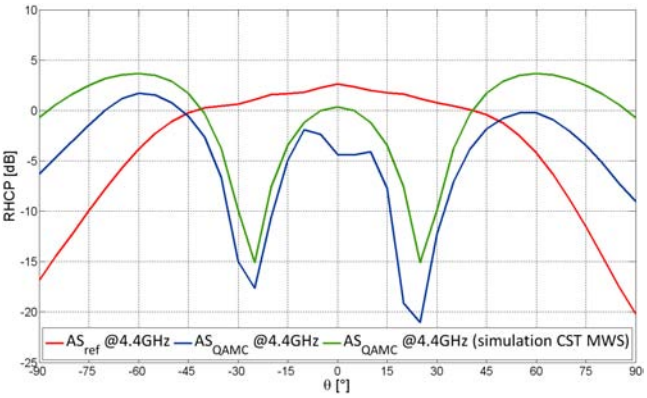


Fig.11: Radiation patterns at 4.4GHz

The broadside gains for both co-polar and cross-polar components are respectively displayed on Fig. 7 and Fig. 8. We particularly observe the effect of the QAMC reflector in Fig. 7. We adopt the following criterion: the QAMC band is defined as the frequency band where the antenna gain with AS_{QAMC} is greater than AS_{ref}. This band occurs from 1.65GHz until 3.9GHz which represents a 2.4:1 bandwidth. In this band, we notice that AS_{ref} and

AS_{QAMC} curves follow the same behaviour with a 2dB offset in average. The manufactured antenna with AS_{QAMC} has an attractive thickness of only 11.835mm which is equal to $\lambda_{low}/15$ where λ_{low} is the free space wavelength at the lowest frequency. In comparison, the AS_{ref} presents at the same frequency a total thickness of $\lambda_{low}/3.2$.
Fig. 8 brings us information about the axial ratio. We note that from 0.5GHz to 3.2GHz the cross-polar gain of the AS_{QAMC} is comparable to those realized by the AS_{ref}. All these graphs also highlight a good agreement between measurements and simulations for the AS_{QAMC} case.
We can draw a parallel between these observations and those of Fig. 4. The middle of the QAMC band is centered near the zero phase-shift frequency 2.7GHz. Moreover, if we consider the co-polar and cross-polar gains, a useful frequency band appears between 1.65GHz and 3.2GHz. This frequency band corresponds to a reflection phase in the range $0 \pm 120°$ which is wider than those commonly used of $0 \pm 90°$ [2].
Several Right Handed Circularly Polarized (RHCP) radiation patterns of the AS_{ref} and AS_{QAMC} are plotted in Figs. 9, 10 and 11. They represent the cut for phi=0° for different frequencies The radiation patterns of AS_{QAMC} are stable and smooth excepted at 4.4GHz

4. CONCLUSIONS

In this communication a reflector based on AMC theory is investigated by measurements and simulations. We show that periodicity and vias are not necessary to achieve wideband and low profile properties. The antenna with the proposed structure presents attractive features. The overall height has been reduced to $\lambda_{low}/15$ at 1.65GHz and the gain has been increased in a 2.4:1 bandwidth in relation to the reference case. Good impedance matching is obtained over a 10:1 bandwidth. Furthermore realization is entirely planar for easy fabrication which implies a low cost process. The same design procedure can be employed with other wideband radiating element. A new prototype with fewer number cells will be realized to yield additional information about the required periodicity.

REFERENCES

1. Wang, J. J. H. and V. K. Tripp, "Design of multioctave spiral-mode microstrip antenna, " *IEEE Trans. on Antennas and Propagation.*, Vol. 39, No. 3, 332-335, 1991.
2. Sievenpiper, D., L. Zhang, R. F. J. Broas, N. G. Alexopolous and E. Yablonovitch, "High impedance electromagnetic surfaces with a forbidden frequency band," *IEEE Trans. on Microwave Theory and Techniques*, Vol. 47, No. 11, 2059–2074, 1999.
3. Kildal, P. S., A. A. Kishk and S. Maci, "Special issue on artificial magnetic conductors, soft/hard surfaces, and other complex surfaces," *IEEE Trans. on Antennas and Propagation.*, Vol. 53, No. 1, 2–7, 2005.
4. Kaiser, J. A, "The Archimedean two-wire spiral antenna," *IEEE Trans. on Antennas and Propagation.*, Vol. 8, No. 3, 312–323, 1960.
5. CST MICROWAVE STUDIO®, User Manual Version 2009, Sep. 2008, CST AG, Darmstadt, Germany, www.cst.com.
6. Yang, F. and Y. Rahmat-Samii, "*Reflection phase characterizations of the EBG ground plane for low profile wire antenna applications*," IEEE Trans. on Antennas and Propagation., Vol. 51, No. 10, 2691-2703, 2003.
7. Higaki, M., K. Inoue, S. Obayashi, S. Sekine, H. Shoki and T. Morooka, "Small artificial structure for low profile antenna by analogy with EBG structure," in *Proceedings of iWAT2008*, Chiba, Japan, 127–130, 2008.

Eigenmode and Array-Scanning Approaches for the Analysis of Wideband Metamaterials

N. A. Ozdemir[1], X. Radu[1], R.Mateos[1] and C. Craeye[1]
[1]Université catholique de Louvain, Place du Levant, 2, 1348 Louvain-la-Neuve, Belgium
nilufer.ozdemir@uclouvain.be

Abstract- This paper focuses on the eigenmode and array scanning approaches for the numerical analysis of wideband metamaterials with the help of the Method of Moments. The aforementioned approaches are exploited for three different applications: design of a ground plane, which behaves as a magnetic conductor that supports leaky waves, wire-medium metamaterial that ensures collimation of images as part a of magnetic resonance imaging system and extension of the wire-medium metamaterial to optical frequencies.

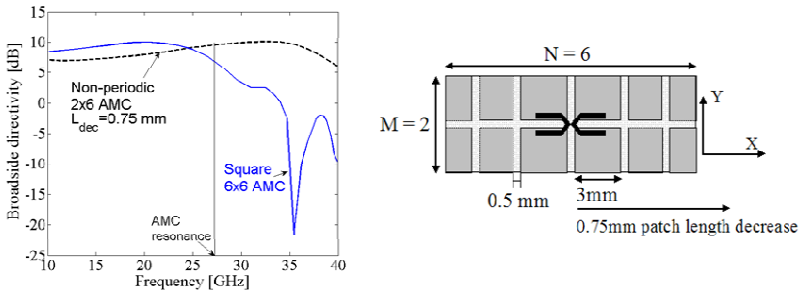
1. INTRODUCTION

Metamaterials are –often periodically- structured materials that exhibit extraordinary behavior within some frequency ranges. The extraordinary behavior is very often due to resonant particles, which often create very strong fields within a narrow bandwidth when confined to small volumes with respect to wavelength. The strong fields can lead to efficiency problems when the constitutive parameters are not perfectly lossless, while bandwidth limitations may narrow the range of applications. A possible route to overcome these limitations is to distribute the resonances over large domains by coupling the resonant particles with each other or to lengthen the domains over which resonance occurs. In this paper, we will present three applications of wide-band metamaterials with a special focus on the numerical analysis with the help of Method of Moments (MoM).

In Section 2, we analyze eigenmodes for complex phase shifts which may be necessary to design surfaces to realize wide-band, low-profile antennas. For example, the ground plane located directly below the antenna behaves as a surface that supports leaky waves as exploited for the antenna in Figure 1.a [1]. In Section 3, we study the isofrequency curves of a wire-medium (WM) metamaterial that ensures the collimation of images [2] as part of a magnetic resonance imaging (MRI) system as shown in [3] through experimental results. Based on these isofrequency curves, we distinguish the frequencies at which eigenmodes appear and reach a conclusion on the exploitable frequency bands [4]-[5]. In Section 4, we study the WM metamaterial in the optical frequency range where metals may have negative permittivity and can also be substantially penetrable. This leads to different phenomena [6] which may find applications in sub-wavelength optical imaging [7]. When periodic structures are excited by non-periodic sources, one may apply the Array Scanning Method (ASM), which replaces the non-periodic problem with an integral superposition of periodic problems. The integration is performed over the phase shifts between adjacent elements of the structure from 0 to 2π and requires the numerical solution of periodic sub-problems by the MoM [8]-[9]. With the help of the Array Scanning Method (ASM), we produce the Point Spread Function of a doubly periodic, nanorod array with complex permittivity (with negative real part) excited by an electrical point source to investigate collimation effects. Finally, conclusions are drawn in Section 5.

2. AMC-LEAKY WAVE SURFACE: EIGENMODE ANALYSIS

In [1], we observed that the radiation patterns of a double-dipole antenna placed above a periodic artificial magnetic conductor (AMC), consisting of a back-grounded array of patches, split at broadside near and beyond the AMC resonant frequency, which limits the useful bandwidth of the design. Figure 1.a provides the broadside directivity for a double-dipole antenna placed above both a 6x6 periodic AMC and a rectangular non-periodic structure like the one shown in Figure 1.b. We can clearly see the directivity improvement obtained with the non-periodic surface, especially at frequencies beyond the AMC resonance.



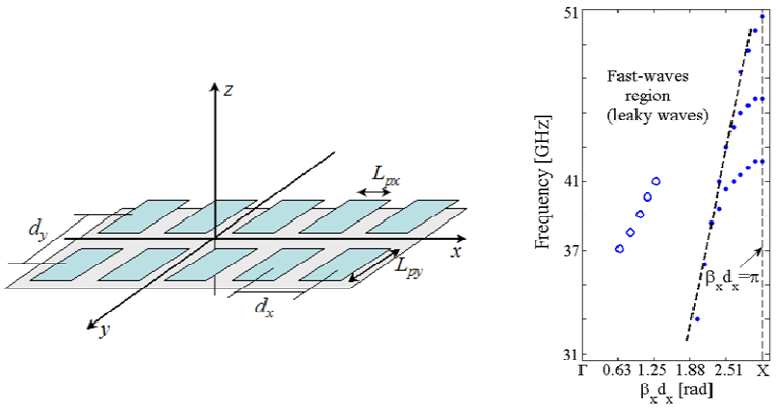
(a) **(b)**

Figure 1. (a) Broadside directivity for a double-dipole antenna placed above both a 6x6 periodic AMC and a rectangular non-periodic structure; (b) A wideband antenna over an AMC/leaky wave surface.

The ground plane located below the double-dipole antenna in Figure 1.b behaves as a magnetic conductor and as a leaky wave structure at the same time. The patches just below the antenna provide the magnetic conductor behavior, and the patches that decrease gradually away from the center transform the surface into a leaky-wave surface. We have performed an eigenmode analysis of the surface described in Figure 2(a) with the help of a Method of Moments (MoM) approach. An extension of it has been developed to search for the leaky modes traveling along the surface. The patches are L_{px}=2.25 mm x L_{py}=3 mm, they are separated by a 0.5 mm gap and at 1 mm height from the backing ground plane. Figure 2.b contains the dispersion diagram in the ΓX path of the Brillouin zone [10]. It is important to notice the presence of leaky modes that radiate near broadside (closer to the Γ point) instead of near-grazing angles (as is the case for a rectangular surface with square patches). The radiation of these leaky waves will contribute to the directivity of an antenna employing such surfaces. This means that the gradually-decreasing patches of the non-periodic design in Figure 1(b) create a surface that supports leaky waves that contribute constructively to the broadside radiation of the whole design, helping to recover the broadside directivity.

3. WIRE-MEDIUM METAMATERIAL FOR MRI: EIGENMODE ANALYSIS

We have recently developed a wire-medium (WM) metamaterial that ensures the collimation of MRI images, which opens new prospects in MRI to realize more reliable devices devoted to medical imaging. The WM has a very wide bandwidth disrupted by some frequencies at which transferred images are uncollimated. We propose to analyze this anomalous behavior with the help MoM which employs doubly periodic Green's function. In this aim, we compute the magnetic field transferred through a WM with the help of the Array Scanning Method (ASM) [8]-[9]. The geometrical configuration employed is presented in Figure 3.b, the unit cell consists of 2x2 wires, the the source employed is a small dipole, on the other side the magnetic field is observed with the help of



(a) **(b)**

Figure 2. The dispersion diagram in the ΓX path of the Brillouin zone (b) obtained from the eigenmode analysis of the structure in (a), L_{px}=2.25 mm x L_{py}=3 mm.

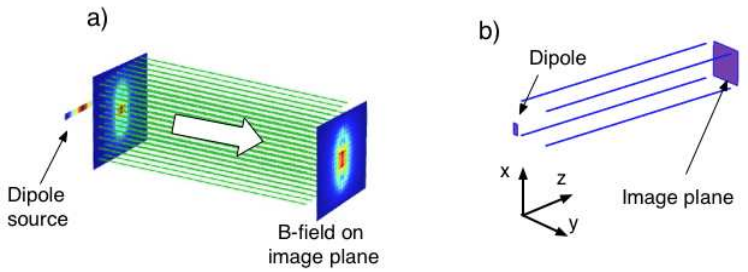


Figure 3. (a) Principle of the wire medium, (b) Unit cell used for the infinite array analysis.

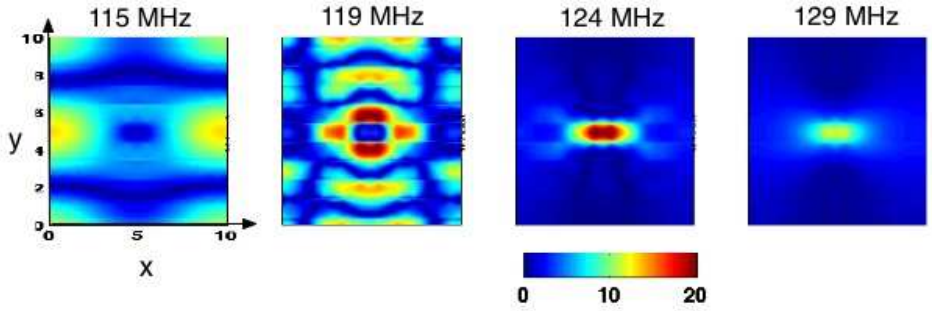


Figure 4. Component of the magnetic field along x, in the XY plane, obtained with a 5x5 ASM and within a unit cell comprising 2x2 strips. Arbitrary units.

testing functions on the image plane. Figure 4 shows the magnetic field transferred for different operational frequencies by using the ASM, involving 5x5 unit cells. It can be seen that for certain frequencies, the magnetic field is uncollimated while for the other frequencies the field is neatly collimated.

This behavior may be explained by the existence of eigenmodes that may appear for frequencies below which the length of the structure is half a wavelength (in our case 123MHz) [4]-[5]. More precisely, the eigenmodes can be identified by determining for which inter-elements phase shifts along x and y directions, Ψ_x and Ψ_y, respectively, and for which frequencies the determinant of the MoM matrix is zero (or below a given threshold). Isofrequency curves are given in Figure 5 for frequencies from 115 MHz to 123 MHz, which lie in the zone where the anomalous behavior appears. We can see that for frequencies below 123 MHz the determinant of the impedance matrix tends toward for certain (Ψ_x ,Ψ_y), illustrated by the dark lines in the first two plots. This

means that an eigenwave for these phase shifts may propagate transversally in the wire medium (XY plane) and perturb the transmission along the z direction. In MRI, this range of frequencies must be avoided in order to preserve a realiable field transfer.

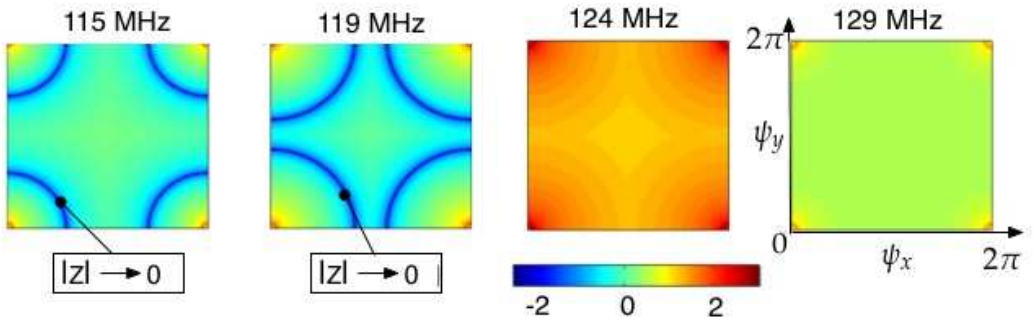


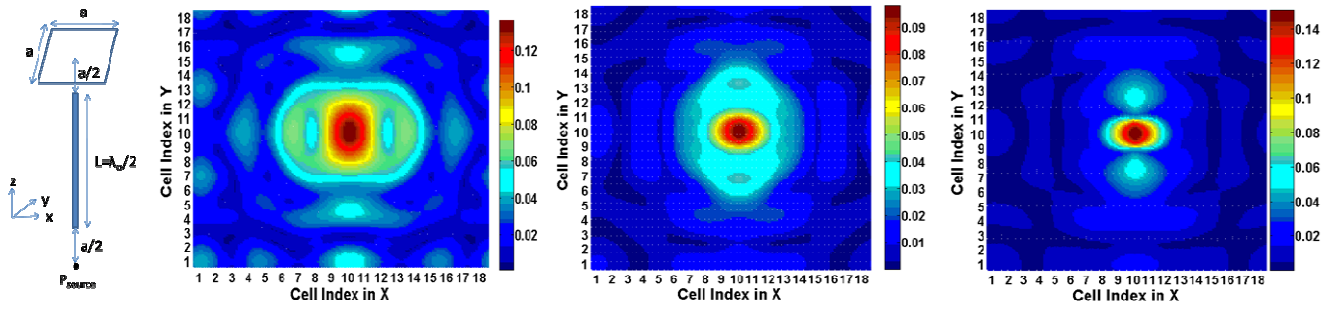
Figure 5. Iso-frequency curves for various frequencies (normalized) computed with the MoM. The plotted quantity is the determinant of the MoM impedance matrix. Dark blue lines correspond to the lowest values and indicate eigenmodes.

4. WIRE-MEDIUM METAMATERIAL AT OPTICAL FREQUENCIES: ARRAY SCANNING APPROACH

In this section, we exploit the ASM to compute the scattered electric field from a doubly periodic infinite array of nanorods with complex permittivity excited by a single point source in the optical frequency range. The unit cell of the infinite array of nanorods with size $a=\lambda_o/5$ is shown in Figure 6.a where the wavelength at the frequency of operation is λ_o=400 nm. The rod has length $L=\lambda_o/2$ and circular cross section with diameter $D=\lambda_o/40$.The source excitation is simulated by a single rooftop basis function on a rectangle centered at the source point, which is located at (0,0,-a/2), with an $\hat{x}$-directed electric current density of unit amplitude. The scattered field is tested on an infinite plane which extends in x and y directions placed at a distance of a/2 from the infinite array. The unit cell of the observation plane, which extends in x and y directions consists of 8x8 rooftop basis functions in x and y directions. First, the infinite array solution is obtained for inter-element phase shifts $\Psi_{x,p}=p(2\pi/N)$, $\Psi_{y,q}=q(2\pi/N)$, for M=N=18 where p=0,1,…,(M-1), q=0,1,…,(N-1). Next, we superimpose the infinite-array solutions in the ASM to obtain the scattered electric field for an excitation source located every M cells along x and every N cells along y [8]-[9]:

$$E_{sca}^{m,n} = \frac{1}{MN}\sum_{p=0}^{M-1}\sum_{q=0}^{N-1} E_{sca}^{\infty}\left(\psi_{x,p}\psi_{y,q}\right)e^{-jqy}e^{-jpx} \quad . \tag{1}$$

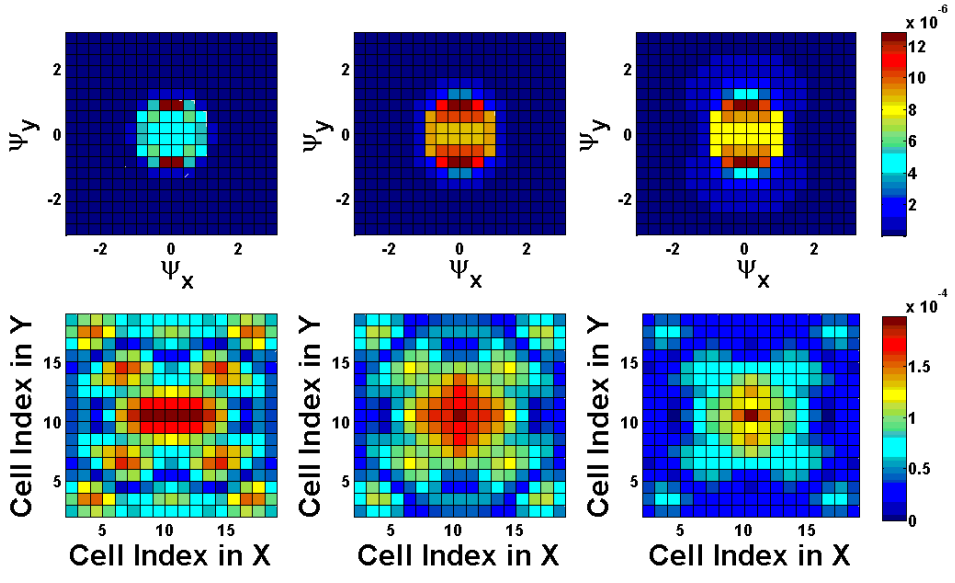
We observe the x component of the scattered electric field on a portion of the observation plane, which includes 18x18 unit squares shown in Figure 6.a. Figures 6.b, 6.c and 6.d show the field distributions for the periodic nanorod arrays with dielectric constant ε_r-=-10-j10; -10-j100; -10-j1000, respectively. Hence the skin depth of the structures considered for Figures 6.b, 6.c and 6.d is approximately 0.225 λ_o, 0.071 λ_o, 0.022 λ_o, respectively, which correspond to 9 D, 3.15 D and 0.88 D where D is the diameter of the nanorod. With increasing conductivity, the diameter of the nanorod gets closer and becomes comparable with the skin depth. Thus the scattered field distribution becomes more focused at the center of the observation plane where the source is located. In Figure 6.b, the 3 dB width of the field distribution covers almost 3 unit cells along x direction, while it covers almost 2.5 and 2 unit cells in Figures 6.c and Figures 6.d, respectively



(a) **(b)** **(c)** **(d)**

Figure 6. Electric field distribution in x direction for a doubly periodic array of nanorods in (a) with dielectric constant (b) ε_r-=-10-j10, (c) ε_r-=-10-j100; (d) ε_r-=-10-j1000.

Here, we investigate the y component of the total magnetic field tested at the midpoint between nanorods both in the spectral and spatial domains. The upper plots in Figure 7 show the magnitude of the field obtained for 18x18 uniformly distributed (Ψ_x ,Ψ_y) pairs in [-π,π) range. The lower plots correspond to the total field distribution in the spatial domain where the observation plane includes 18x18 unit cells. Three pairs of plots are given for dielectric constants ε_r-=-10-j10, -10-j100, -10-j1000 in the respective order. As the skin depth becomes comparable to the diameter of the rod, the field distribution becomes more focused around the testing point as we have observed before. In the spectral domain, this corresponds to the singular behavior of the field around the boundary of the visible space which leads to oscillations at the free space wavelength as the conductivity decreases.



(a) **(b)** **(c)**

Figure 7. Magnetic field observed along y direction at the midpoint between nanorods in the spectral (lower plots) and spatial (upper plots) domains for dielectric constant (a) ε_r-=-10-j10, (b) ε_r-=-10-j100, (c) ε_r-=-10-j1000.

5. CONCLUSIONS

Eigenmode analysis and ASM have been exploited to analyze and design wideband metamaterials using MoM. Both approaches rely on scanning periodic problems over the whole reciprocal space (both in visible and

invisible region). Eigenmode analysis has been employed to search for the leaky modes traveling along the ground plane below an antenna which contribute constructively to the broadside radiation of the whole design, hence providing wider bandwidth. Eigenmode analysis has also been found to be useful to study image transfer through a wire-medium metamaterial as a part of an MRI system. It is shown that for certain frequencies and inter-element phase shifts eigenwaves may propagate transversally in the wire medium (XY plane) and perturb the transmission along the wire medium Finally, the ASM has been used to analyze the distribution of fields from a doubly periodic nanorod array with complex permittivity excited by a single source at optical frequencies. The field distribution points to a focusing effect as the skin dept becomes comparable to the diameter of the rod.

ACKNOWLEDGEMENT

This study has been partially funded by EC under the Metachem Project.

REFERENCES

1. Mateos, C. Craeye, G. Toso, High-gain wideband low-profile antenna, *Special Issue on Metamaterials of Microwaves Optical and Technology Letters*, vol. 48, pp. 2615-2619, Dec. 2006.
2. P. Belov, Y. Hao, and S. Sudhakaran, “Sub-wavelength microwave imaging using an array of parallel conducting wires as a lens,” *Physical Review B*, 73(033108), 2006.
3. X. Radu, D. Garray, C. Craeye, “Toward a wire medium endoscope for MRI imaging,” *Metamaterials*, vol. 3, pp. 90-99, Oct. 2009.
4. P. Belov and M.G. Silveirinha, “Resolution of subwavelength transmission devices formed by a wire medium,” *Phys. Rev. E*, vol.73:056607, May 2006.
5. X. Radu, A. Lapeyronnie, and C. Craeye. Numerical and experimental analysis of a wire medium collimator for magnetic resonance imaging, *Electromagnetics*, vol.28, no. 7, pp. 431 – 543, September 2008.
6. S. Zhang, W. Fan, K. J. Malloy, et al., “Demonstration of metal-dielectric negative-index metamaterials with improved performance at optical frequencies,” *J. Opt. Soc. Am. B*, vol. 23, pp. 434-438, March 2006.
7. S. Kawata, A. Ono, P. Verma, “Sub-wavelength color imaging with a metallic nanolens,” *Nature Photonics*, vol. 2, pp. 438-442, 2008.
8. B. A. Munk and G. A. Burrel, “Plane-wave expansion for arrays of arbitrarily oriented piecewise linear elements and its application in determining the impedance of a single linear antenna in a lossy-half space,” *IEEE Trans. Antennas Propag.*, vol. 27, pp. 331-343, 1979.
9. F. Capolino, D. R. Jackson, D. R. Wilton, L. B. Felsen, “Comparison of methods for calculating the field excited by a dipole near a 2-D periodic material,” *IEEE Trans. Antennas Propag.*, vol. 55, no. 6, pp. 1644-1655, June 2007.
10. S. Enoch, G. Tayeb, B. Gralak, “The richness of the dispersion relation of electromagnetic bandgap materials,” 2659- 2666, vol. 51, no. 10, October 2003.

Substrateless micrometric metal mesh for mid-infrared plasmonic sensors

F. Mattioli[1], M. Ortolani[1], S. Lupi[2], O. Limaj[2] and R. Leoni[1]

[1]CNR-Istituto di Fotonica e Nanotecnologie, via Cineto Romano 42, 00156 Rome (Italy)

[2]CNR-INFM Coherentia and Dipartimento di Fisica, Università di Roma "La Sapienza", Piazzale Aldo Moro 2, 00185 Roma (Italy)

francesco.mattioli@ifn.cnr.it

Abstract- We report on the fabrication and optical properties of thin metal films periodically patterned with square hole arrays of 2 micron pitch, which behave as substrateless plasmonic devices at mid-infrared frequencies. Large (3x3 mm^2) meshes were fabricated by metallizing a patterned silicon nitride membrane. The mid-infrared spectra display resonant absorption lines with a Q-factor up to 22 in both transmission and reflection, due to the interaction of the radiation with surface plasmon modes on both faces of the film, allowed by substrate removal. The devices can be used to fabricate surface plasmon-based chemical sensors employing mid-infrared radiation.

1. INTRODUCTION

The frequency-dependent optical properties of thin metal films can be tailored by patterning them at sub-wavelength periods, to produce photonic devices in the infrared (IR) range and beyond[1]. Patterned metal films-on-substrates (mostly square lattices) have been also fabricated to study resonant surface plasmons (SP)[1-5] or metamaterial properties[6-8]. For the wavelength range λ = 2-10 μm (mid-IR), which is of high interest for spectroscopy as it comprises the fingerprints of biomolecules and gases, lithographic techniques are employed to pattern evaporated thin metal films with structures of few-micron periods and sub-micron precision (polarizers[9], filters, waveguides[10]). More recently, mid-IR spectroscopic sensor applications based on surface plasmons (SPs) are being considered: for example, a mid-IR SP-sensor based on a non-patterned metal film on a prism substrate plus a quantum cascade laser (QCL) has been proposed[11], exploiting the great sensitivity of the resonant SP optical properties to the refractive index of a dielectric medium deposited at the film surface. However, resonant SP modes are strongly affected by the presence of the substrate on one side of the thin metal film, as the symmetry between the two faces of the film is broken[3]. As a consequence, the interaction between SPs on the two faces is not resonant any more so that the resonance Q-factor and the sensing capability are strongly reduced[12-14]. Indeed, in the far-IR range, properly designed substrateless metal meshes with pitch of 76 μm have been used to obtain narrow SP resonances[15], whose frequency position shifts as a function of the amount of material deposited on the mesh. The frequency shift can be measured in simple transmission geometry with a blackbody source and a compact spectrometer. In the mid-IR a blackbody source emits more power than in the THz range and both uncooled QCLs and sensitive detectors are available to realize a compact spectrometer. In this framework, it is important to develop a technique to fabricate truly substrateless thin metal films for metamaterials and other advanced IR-photonic devices, and in particular micrometric-pitch substrateless metal meshes for SP-based sensing applications.

In this paper, we present a technique to fabricate meshes made of evaporated thin metal films, behaving as

substrateless devices from the optical point of view. By using electron beam lithography (EBL), we could fabricate large area (3x3 mm^2) metal meshes with lattice period g = 2.00 μm and sharp square holes of side g/2 (see inset of Fig. 3). We then used Fourier-transform spectroscopy (FT-IR) to measure the spectrum of resonant SP modes in the mid-IR. We will show that the substrate removal allows the resonant coupling of SPs on both faces of the film, so that they display symmetry along the direction orthogonal to the mesh plane. In particular, we studied antisymmetric resonant SP modes (a-modes) at non-normal incidence with high Q-factor. The a-modes display simultaneous charge displacement of opposite sign on the two surfaces of the metal film and were previously observed at far-IR/THz frequencies on free-standing metal meshes with periods of hundreds to tens of micrometers[13-15]. In this paper we show that, due to both a Q-factor up to 22 and a featureless wavelength-dependent background, the a-modes are especially suitable for metal mesh sensor applications in the mid-IR.

2. SAMPLE FABRICATION AND EXPERIMENTAL SET-UP

The mesh fabrication process starts with a <100> silicon wafer covered on both sides with a low-stress, 1 μm thick silicon nitride (SiN) layer. On the front side of the wafer we used EBL followed by dry Reactive Ion Etching (RIE) to obtain the desired pattern on the SiN layer together with alignment markers. A double-side optical mask aligner and a second RIE step are used to obtain clear windows, aligned with the front pattern, on the back SiN layer. A KOH solution (23% in deionized water at 80 °C) is used to etch the Si wafer underneath each pattern and hence obtain a free-standing SiN mesh. 150 nm of Al are then evaporated on SiN to produce the metal mesh. The main advantage of this technique over standard metal film-on-membrane[4, 6] is that the metal film needs not to be patterned. As a reference for the optical properties, we fabricated the same mesh pattern on a second double-side polished Si wafer.

The mid-IR transmittance and reflectance were measured in an evacuated FT-IR interferometer (Bruker IFS66v). The radiation was linearly polarized along one side of the squares. The sample was positioned in the focus of an f/4 parabolic (ellipsoidal) mirror and the transmitted (reflected) beam was collected by a twin mirror. Only the radiation transmitted at an angle close to the incidence angle was then focused into a HgCdTe mid-IR detector.

3. EXPERIMENTAL DATA

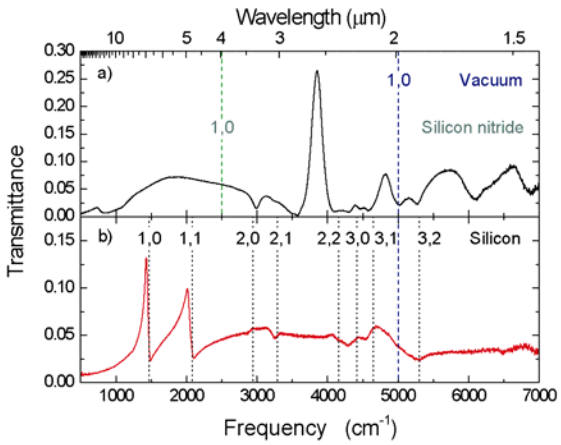


FIG. 1 (color online) Mid-IR transmittance at normal incidence of (a) the substrateless metal mesh compared to (b) the same mesh fabricated on a silicon substrate. Dashed lines mark the position of Wood's anomalies calculated with Eq. (1) (see text) for silicon, vacuum and silicon nitride .

Fig. 1 shows the normal-incidence transmittance of two identical meshes, one fabricated on a Si substrate (Fig. 1b) and the other fabricated with our substrateless technique (Fig. 1a). Both spectra display extraordinary transmission peaks related to the excitation of SPs[2-5, 7] and several dips related to energy loss into modes diffracted at grazing angle (Wood's anomalies[16]). Apparently, the number and the frequency position of peaks/dips strongly depend on the presence of the substrate. The frequency of Wood's anomalies (narrow dips) for a square lattice is given by:

$$\omega(i,j) = \frac{\sqrt{i^2 + j^2}}{g\ \varepsilon^{1/2}} \qquad (1)$$

where $\varepsilon^{1/2}$ is the refractive index of the material in which the diffracted beam propagates and (i, j) are integer values defining the two-dimensional diffraction order. In Fig. 1, dashed lines indicate the calculated frequency for the first eight diffraction orders in Si (ε = 11.6), the first order in vacuum (ε = 1) and in SiN (ε = 4.0). We observe that at least the first four orders diffracted in Si and the first order diffracted in vacuum perfectly match the frequencies measured in the mesh-on-Si spectra, as observed before on similar samples[3-5]. Concerning the substrateless mesh, there is a broad step corresponding to the (1,0) order in vacuum. However all the other features do not correspond to orders diffracted in vacuum, nor into a SiN substrate. Since the SiN membrane is patterned by holes, it plays no role in the propagation of mid-IR radiation. We can therefore conclude that our mesh is indeed substrateless as far as optical properties are concerned. Note that, at odds with the mesh-on-Si, the substrateless mesh displays a smooth, featureless transmittance in the 3.5 - 10 μm wavelength range, i.e. in the molecular fingerprint region.

Extraordinary transmission peaks have been interpreted as coherent re-emission of excited SP modes with wavevectors matching the lattice periodicity. The peak frequencies are calculated from a free SP dispersion unperturbed by the presence of holes, for each of the two faces of the metal film:

$$\varpi(i,j) = \frac{\sqrt{i^2 + j^2}}{g} \sqrt{\frac{\varepsilon + \varepsilon_M}{\varepsilon\ \varepsilon_M}} \qquad (2)$$

where ε_M is the dielectric constant of the metal, which is negative and much larger than unity at mid-IR frequencies. As a result, the peaks appear at frequencies slightly lower than the Wood's anomalies[3]. Peaks at 4700 cm^{-1} in both Fig. 1a and 1b, and at 1430 and 2010 cm^{-1} in Fig 1b are in good agreement with Eq. 2 if we set ε = 1 (11.6) for the metal-vacuum interface (metal-Si interface) respectively. Features above 5000 cm^{-1} can be instead attributed to diffraction effects.

Surprisingly enough, the main peak of the substrateless mesh spectrum at ϖ = 3850 cm^{-1} remains out of this assignment. Once again we can exclude an effect of the SiN membrane, as the nearest frequencies calculated from Eq. 2 are $\varpi_{SiN}(1,1)$= 3530 cm^{-1} and $\varpi_{SiN}(2,0)$= 4920 cm^{-1}. We must then conclude that the unperturbed SP dispersion (Eq. 2) does not hold for the substrateless mesh in the mid-IR. Full electromagnetic treatment of SPs in a periodic lattice, developed for far-IR metal meshes[14], including a coupling of SPs between the metallic film

faces and a periodic perturbation term due to the presence of holes (Bloch's theorem), leads to two main consequences: i) a gap opens at the plasmonic Brillouin zone edge and two symmetric (s-) mode frequencies exist at normal incidence producing the two peaks at 3850 and 4820 cm^{-1} in Fig. 1a; ii) the degeneracy between s- and a-modes is removed and the s- and a-modes appear at different frequencies. Therefore, the a-modes can be easily isolated in the substrateless metal mesh.

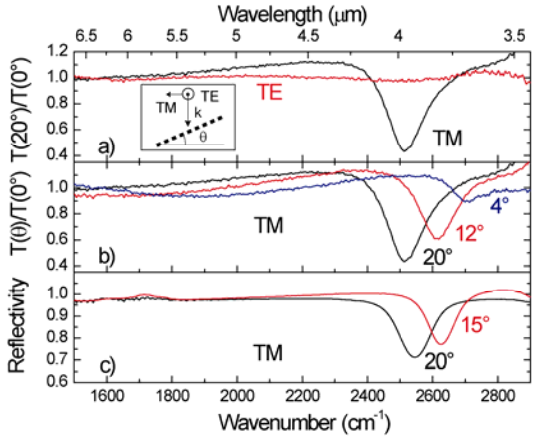


FIG. 2 (color online) (a) Ratio of transmittance at oblique and normal incidence for in-plane (TM) and out-of-plane (TE) polarized radiation in the case of substrateless mesh (the measurement geometry is indicated in the inset). In the TM spectra, the dip close to $\lambda = 2g$ indicates resonant absorption by surface plasmons guided on the mesh (leaky mode). Frequency shift as a function of incidence angle in the TM polarization, due to leaky mode dispersion, for both transmittance (b) and reflectivity data (c).

For radiation impinging at an angle θ and polarization parallel to the incidence plane (TM-polarization), the radiation has a field component orthogonal to the mesh plane. In the TM polarization, the dipole moment of *a*-modes can be directly excited, as it is also orthogonal to the mesh plane (leaky mode, directly coupled to the radiation). This condition is satisfied by measuring the transmittance $T(\theta)$ of the substrateless mesh at an angle θ with respect to the beam direction. Indeed the *a*-mode, not visible at normal incidence, clearly appears around 2500 cm^{-1}, as shown by the transmittance ratio $T(\theta)/T(0°)$ in Fig. 2a. The dip becomes sharper and shifts to lower frequency for increasing $|\theta|$, while an overshoot appears due to a Fano interference between the directly transmitted beam and radiation re-emitted by the excited leaky modes. This trend has been confirmed by the reflectivity R as observed in Fig. 2c. The *Q*-factor of the resonance is ~ 22, much higher than that of extraordinary transmission peaks (Q-factor of ~ 6). This is due to the flat dispersion close to the Brillouin zone edge[14] caused by coupling between the SPs of the two faces of the metal film. The substrate removal provides then a resonant absorption with a remarkable *Q*-factor and far from other resonances, with a certain degree of mechanical tunability, which is an ideal building block for sensor design[11].

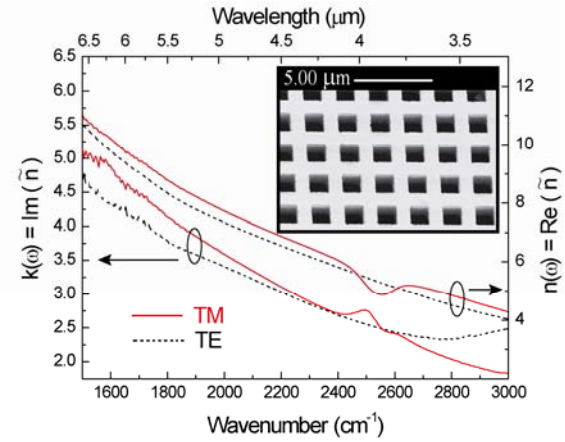


FIG. 3 (color online) Extinction coefficient (left axis) and refractive index (right axis) computed from the data at θ= 20° in Fig. 2. A sharp peak (dip) is observable in k (n) for the TM polarization only (solid line). Inset- Scanning Electron Micrographs of the substrateless grid that covers a 3x3 mm^2 area. The sharp corners of the square geometry are due to the EBL technique employed. A Si frame sustains a patterned SiN membrane on top of which an Al layer is deposited.

In order to prove the coupling of the mid-IR radiation with surface plasmons we have calculated the effective refractive index of the mesh. On this aim the mesh has been considered, i.e. a sub-wavelength patterned system which behaves as a homogeneous medium with respect to an incident beam. The complex phase of both the transmission and reflection coefficients was obtained from their absolute values by means of the Kramers-Kronig transformations, neglecting multiple reflections inside the mesh, as allowed by the fact that R~1 and T~0 around 2500 cm^{-1}. Using the formulas provided in Ref. [17], we computed the effective refractive index n and extinction coefficient k for both TE and TM polarization which are displayed in Fig. 3 for θ = 20°. For the TE polarization no significant feature is observable neither in n nor in k, and their values are comparable to that of bulk Al. On the contrary, for the TM polarization n shows a dip and k a peak at approximately 2500 cm^{-1}. The peak in k is a clear indication of energy absorption by the plasmonic a-mode. Energy-absorbing SP modes produce local field enhancement in a region within few wavelengths from the surface[2], resulting in a strong interaction between SPs and a dielectric medium in contact with the metal. This implies a modification of the s- and a- mode dispersion, and hence of their resonant frequency [14].

The observable shift of the a-mode frequency can be used as a sensing mechanism of a small amount of any substance deposited on the mesh, a robust method if compared to the direct measure of very weak absorbance signals. This results in a sensitivity only limited by the resolving power of the spectrometer. Moreover, at odds with conventional plasmonic approaches involving non-patterned films[11], the sensing capability does not necessarily require resonant absorption of the target substance at mid-IR frequency, as the resonance is provided by the mesh structure. These ideas have been already applied in the THz range as reported in Ref. 15, where small variations in the average refractive index of the dielectric medium could be revealed by a free-standing metal mesh. With the present micrometric mesh, the same kind of sensor could be built in the more accessible mid-IR range.

4. CONCLUSIONS

In conclusion, we fabricated and optically characterized substrateless sub-wavelength metal structures with periods in the few-micron range. We performed full spectroscopic analysis of SP modes in the mid-IR. Due to substrate removal, resonant absorption was obtained at design frequencies with a Q-factor up to 22 in a broad mid-infrared frequency window with high transmittance and free of other spectral features. The technique here presented can be used to fabricate mid-infrared sensors and metamaterials.

ACKNOWLEDGEMENT

We thank M. G. Castellano, S. Selci and A. Dilellis for discussions. One of us (F.M.) acknowledge the support of the of the SERENA /BepiColombo ASI/INAF contract I/090/06/0.

REFERENCES

[1] W. L. Barnes, A. Dereux and T. W. Ebbesen, Nature 424, 824 (2003)

[2] F. J. Garcia de Abajo, Rev. Mod. Phys. 79, 1267 (2007).

[3] H. F. Ghaemi, Tineke Thio, D. E. Grupp, T. W. Ebbesen, H. J. Lezec, Phys. Rev. B, 58, 6779 (1998).

[4] D. E. Grupp, H. J. Lezec, T. W. Ebbesen, K. M. Pellerin and Tineke Thio, Appl. Phys. Lett. 77, 1569 (2000).

[5] W. L. Barnes, W. A. Murray, J. Dintinger, E. Devaux, and T. W. Ebbesen, Phys. Rev. Lett. 92, 107401 (2004)

[6] Z. Haoa, M. C. Martin, B. Harteneck, S. Cabrini and E. H. Anderson, Appl Phys. Lett. 91, 253119 (2007)

[7] G. Dolling, M. Weg, A. Schädle, S. Burger and S. Linden, Appl. Phys. Lett. 89, 231118 (2006).

[8] S. Zhang, W. Fan, N. C. Panoiu, K. J. Malloy, R. M. Osgood, and S. R. J. Brueck, Phys. Rev. Lett. 95, 137404 (2005)

[9] J. P. Auton, Appl. Optics 6, 1023 (1967).

[10] R. Colombelli, K. Srinivasan, M. Troccoli, O. Painter, C. F. Gmachl, D. M. Tennant, A. M. Sergent, D. L. Sivco, A. Y. Cho, and F. Capasso, Science 302, 1374 (2003).

[11] S. Herminjard, L. Sirigu, H. P. Herzig, E. Studemann, A. Crottini, J. Pellaux, T. Gresch, M. Fischer and J. Faist, Opt. Expr. 17 No. 1, 293 (2009).

[12] S. Zhang, W. Fan, B. K. Minhas, A. Frauenglass, K. J. Malloy, and S. R. J. Brueck, Phys. Rev. Lett. 94, 037402 (2005)

[13] T. Ganz, M. Brehm, H. G. von Ribbeck, D. W. van der Weide and F. Keilmann, New Journal of Physics 10, 123007 (2008).

[14] R. Ulrich, “Modes of propagation on an open periodic waveguide for the far-infrared”, from Optical and Acoustical Microelectronics, ed. By Jerome Fox, Microwave Research Inst. Symp. Ser. Vol. 23, Polytechnic Press, New York (1974).

[15] H. Yoshida, Y. Ogawa, Y. Kawai, S. Hayashi, A. Hayashi, C. Otani, E. Kato, F. Miyamaru and K. Kawase, Appl. Phys. Lett. 91, 253901 (2007).

[16] R. W. Wood, Philos. Mag. 4, 396 (1902); R. W. Wood, Phys. Rev. 48, 928 (1935).

[17] X. Chen, T. M. Grzegorczyk, Bae-Ian Wu, J. Pacheco Jr., and J. Au Kong, Phys. Rev. E 70, 016608 (2004).

Comparison of the Sensitivity of Plasmonic Peaks in Hole and Slit Arrays with the Surrounding Media

J. W. Menezes[1,2], L. F. Avila[2], E. S. Braga[1] and L. Cescato[2*]

[1]Faculdade de Engenharia Elétrica e Computação, DEMIC, Campinas-SP, Brazil
[2]Instituto de Física "Gleb Wataghin", DFMC, UNICAMP, Campinas-SP, Brazil
[*]corresponding author: cescato@ifi.unicamp.br

Abstract- In this paper we compare the sensitivity of the plasmonic peak position deviation with the surrounding media for two types of plasmonic structures: arrays of holes and arrays of slits in Au films. Both types of array were fabricated using interference lithography with period of 700 nm and Au thickness of 150 nm. The plasmonic peak measurements were performed at normal incidence using a spectrophotometer. The results show that the array of slits present a higher sensitivity with the surrounding media than the array of holes. Theoretical simulations of the slit arrays agree very well with the experimental results confirming the better sensitivity of the slit arrays.

1. INTRODUCTION

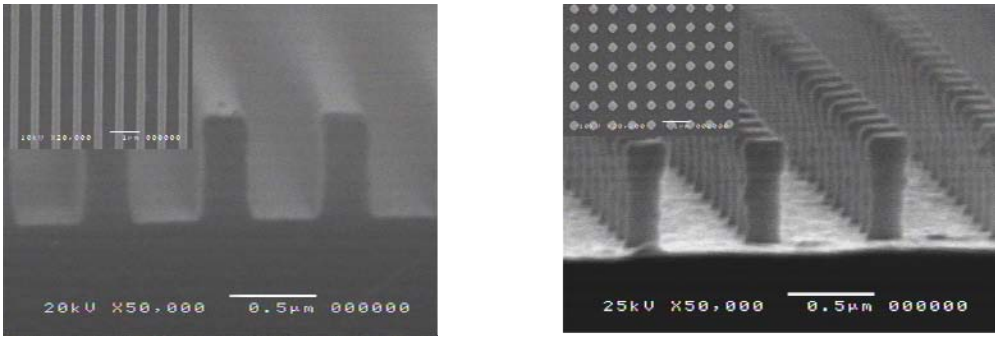
Thin metallic periodic structures exhibit a transmission enhanced at certain wavelengths whose values depend on the relative permittivity of the metal and of the surrounding medium. These peaks occur when the incident light matches the Momentum Conservation Condition[1] and Surface Plasmon (SP) modes are excited in the dielectric-metal interfaces[1]. The SP modes at the first dielectric-metal interface couples with the SP modes at the metal-dielectric interface generating an enhancement in the transmitted light[1]. For an array of slits there are two possible mechanisms to explain such extraordinary transmission peaks[2]: the SPR that occurs only for thin film metallic arrays of slits and the waveguide resonance (FP) that couples the incident light through the slit. Anyway, for array of slits or holes, the position of the extraordinary transmission peaks (of SPR or FP) depends on the surrounding media. Thus both types of structures can be potentially used as refractive index sensor of the surrounding media.

In this paper we compare the sensitivity of both types of structures by fabricating these two types of arrays: holes and slits and by measuring the extraordinary transmittance peaks as a function of the wavelength, for different surrounding media.

2. EXPERIMENTAL

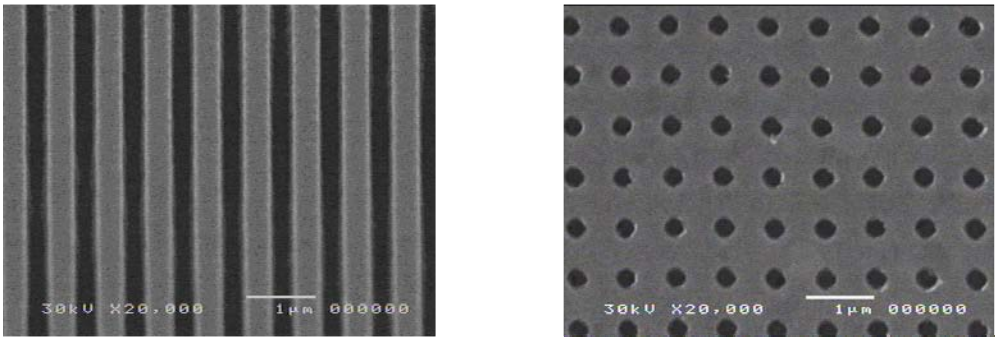
For the fabrication of the both types of metallic structures, high aspect ratio photoresist (1D and 2D) structures were recorded on glass substrates by interference lithography[3], followed by the thermal deposition of Au, and further lift-off of the photoresist template using acetone followed by ultrasound. Figures 1a and 1b show the Scanning Electron Microscope photographs of the one-dimensional and of the two-dimensional photoresist templates recorded in the positive photoresist SC 1827 on glass substrates, respectively. Figure 2 show the corresponding arrays recorded by lift-off in Au films with 150 nm of thickness. In both cases the period of the array was 700 nm. For the slits the width of the Au bars were about 400 nm while for holes, their diameters were

about 250 nm. The transmission spectra were measured using a Perkin Elmer λ-9 spectrophotometer.



(a) (b)

Figure 1. Scanning Electron Microscope (SEM) cross section photographs of the photoresist templates on glass substrates for recording an array of slits (a) and of holes (b). The insets show the corresponding top view of the templates.



(a) (b)

Figure 2. SEM top view photographs of the resulting arrays of slits (a) and holes (b) respectively.

3. EXPERIMENTAL RESULTS

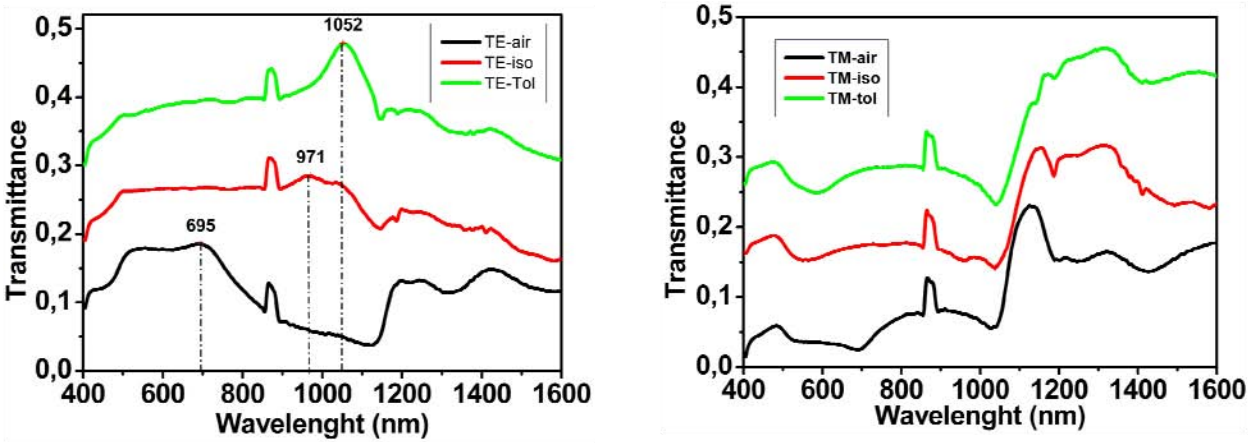
The transmission spectra of the array of slits and of the array of holes are shown in Figure 3 and 4 respectively. Figure 3 shows the transmission spectra for the two orthogonal incident polarization of the light: TE and TM, TE corresponding to the incident light with the electrical field parallel to the slits (Figure 3a) while TM corresponds to the incident electrical field perpendicular to the slits (Figure 3b). Each color curve corresponds to the sample immersed in a different surrounding media: air, isopropyl alcohol and toluene. The refractive indexes of such liquid are approximately equal to 1, 1.38 and 1.49, respectively. Note that for the TE polarization in air we can observe roughly a double peak that red shifts when the refractive index of the surrounding media increases. For the higher refractive index (toluene) we observe only a single peak at 1050 nm.

Figure 4 shows the transmission spectra through the array of holes immersed in the same three surrounding media (air, isopropyl alcohol and toluene). Note that in this case we observe only a single well-defined plasmonic peak that red shifts when the refractive index of the surrounding media increases.

4. THEORETICAL RESULTS

Figure 5 shows the theoretical spectra for the slit array in the same three different surrounding media, for the incident light TE (a) and TM (b) linearly polarized. The spectra were calculated using the software G–Solver[4]. There is a good general accordance between the theoretical and experimental spectra for both TE and TM

polarizations. For the case of TE incidence, note the presence of a double peak for the array of slits immersed in air and isopropyl alcohol. When the refractive index of the surrounding media approaches the refractive index of the substrate (as is the case of the toluene n=1.49), both peaks degenerate to a single peak. Note also that the peak at λ= 1050 nm does not change with the surrounding media while the first peak does change.



(a) (b)

Figure 3. Transmission spectra, at normal incidence, through the array of slits for the incident light linearly polarized at TE (a) and TM (b) respectively, for three surrounding media: air, isopropyl alcohol and toluene. The kink observed around 865 nm corresponds to the change of detector in the spectrophotometer.

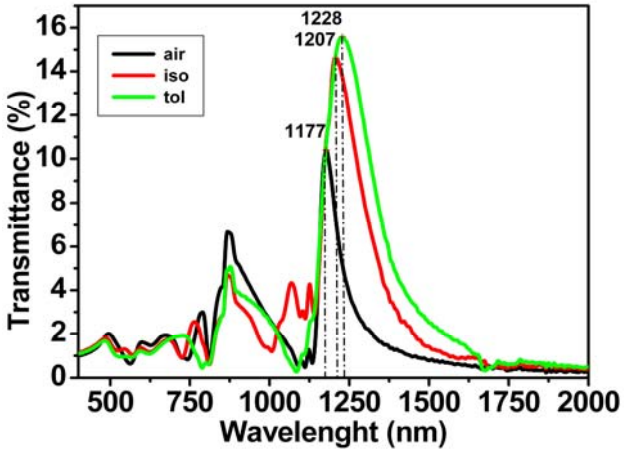
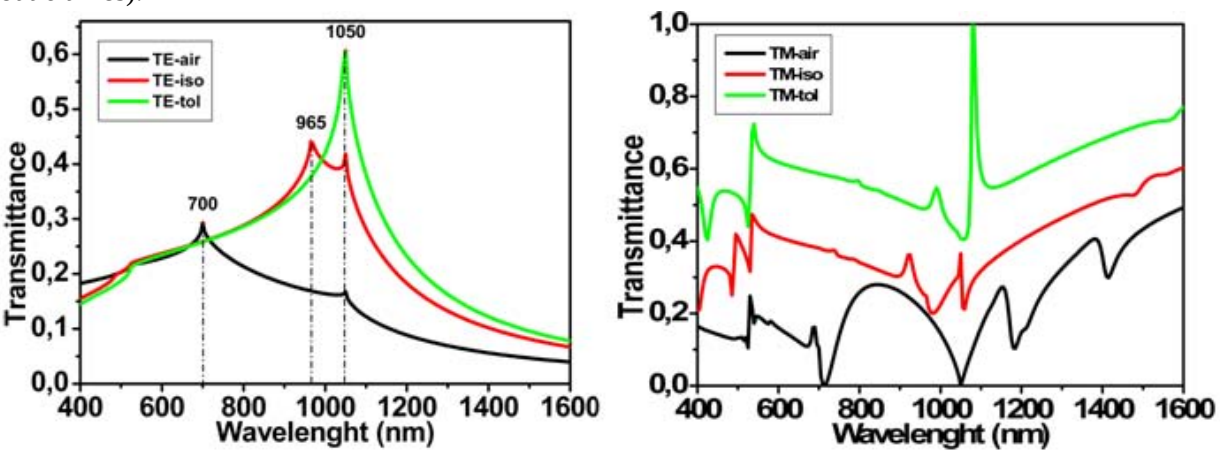


Figure 4. Transmission spectra through the array of holes immersed in air, isopropyl alcohol and toluene.

This occurs because the peak at λ= 1050 nm corresponds to the SPR at the Au-glass substrate interface while the first peak corresponds to the surrounding media-Au interface. By comparing this theoretical TE curve (Figure 5a) of the slits with the experimental curve in Figure 3a, we can observe a good accordance in the position of the peaks (marked with a doted vertical line). Even in the case of air (black curve in Figure 3a), it is possible to observe from the data a small peak at λ= 1050 nm that corresponds to the Au-glass interface. The positions of the SPR peaks (corresponding to the interface surrounding media-Au), for the slit array, are shown in Table I for comparison. The Table I also resumes the positions of the SPR peaks for the experimental measurements of the SPR peaks for the array of holes. In the last column of the same Table I it is shown the corresponding shift of the peak position (Δλ), divided by the variation of the refractive index of the surrounding media (Δn). By comparing

$\Delta\lambda/\Delta n$ we observe a much higher sensitivity of the SPR peak position with the refractive index of the surrounding media for the case of the array of slits (under TE incidence) in comparison with the array of holes (about 6 times).



(a) (b)

Figure 5. Theoretical transmission spectra of an array of slits for TE (a) and TM (b) incident polarization, with the sample immersed in air, isopropyl alcohol and toluene.

Table I – SPR peak position

Array	Curve	thickness	Polarization	Peak: λ_{air}	Peak: λ_{Iso}	Peak: λ_{Tol}	$\Delta\lambda$/RIU
slits	Experimental	150nm	TE	695 nm	971 nm	1052 nm	730 ± 3 nm
slits	Theoretical	150nm	TE	700 nm	965 nm	1050 nm	730 ± 30 nm
holes	Experimental	150nm	unpolarized	1177 nm	1207 nm	1228 nm	120 ± 40 nm

5. CONCLUSIONS

Although the experimental SPR peaks corresponding to the array of holes (Figure 4) were better defined than the SPR peaks associated with the array of slits (Figure 3), the sensitivity of the wavelength peak position with the surrounding media is much higher for the array of slits.

ACKNOWLEDGEMENTS

We acknowledge the financial support of CNPq (Conselho Nacional de Pesquisa), FAPESP (Fundação de Amparo à Pesquisa do Estado de São Paulo) and CAPES (Coordenação de Aperfeiçoamento de Pessoal de Nível Superior).

REFERENCES

1. Ghaemi, H. F., Thio, T., Grupp, D. E., Ebbesen, T. W. and Lezec, H. J. “Surface Plasmons enhcance optical tranmission through subwavelenght holes”, *Physical Review B*, Vol. 58, N_0. 11, 6779-6781, 1998.
2. Porto, J. A., Garcia-Vidal, F. J., Pendry, J. B. “Transmission Resonances on Metallic Gratings with Very Narrow Slits”, *Physical Review Letters*, Vol. 83, N_0. 14, 2845-2848, 1999.
3. Quiñonez F., J. W. Menezes, L. Cescato, et al “Band gap of hexagonal 2D photonic crystal with elliptical holes recorded by interference lithography”, *Optics Express*, 14 (11) 4873-4879 (2006).
4. Program “GRATING SOLVER”, http://www.gsolver.com

Electromagnetic waves refraction on the interface of transparent with absorptive right or left-handed media

N. L. Dmitruk[1], **and A. V. Korovin**[1,2]

[1]Institute for Physics of Semiconductors, National Academy of Sciences of Ukraine, 41 prospect Nauki, 03028 Kiev, Ukraine

[2]Institute of Optics, Information and Photonics, University of Erlangen-Nuremberg, 91058 Erlangen, Germany

Korovin@isp.kiev.ua

Abstract— The expressions for the time averaged Pointing's vector in absorptive left-handed medium based on the classical vector Maxwell's equations for a continuum have been obtained. It was found that in the case of incline incidence with mixed polarization the additional perpendicular to incidence plane component of Poynting's vector is appeared for negative effective refraction. This addition of the in-plane component leads to non-coincidence of refraction and incidence plane.

1. INTRODUCTION

It is well known that introduction of the complex refraction index $\tilde{n} = n + i \cdot \chi$ for absorptive medium, and corresponding complex permittivity $\varepsilon = \varepsilon' + i \cdot \varepsilon''$, leads to some problems for physical interpretation of the refraction of light on the interface between absorptive and transparent media [1, 2]. For example, the group velocity $v_{\rm gr} = \partial\omega/\partial k$ [3] with the complex wave vector $\tilde{k}$ becomes complex too. But the group velocity should be a real one. The condition of real v_{gr}: $v_{gr} = \partial\omega/\partial {\rm Re}\tilde{k}$ or $v_{\rm gr} = |\partial\omega/\partial\tilde{k}|$ leads to non-physical result with the light velocity in vacuum,$v_{\rm gr} > c$. Moreover, for absorptive medium the material optical constants n, χ loss their simple physical sense, and the real and imaginary parts of the permittivity, $\varepsilon' = n^2 - \chi^2$, $\varepsilon'' = 2n\chi$, become more preferable. The same may be attributed to complex permeability $\tilde{\mu}$.

Therefore for many physical phenomena and their practical applications the conception of time-averaged Poynting's vector, which determines the direction of energy propagation of electromagnetic waves, is more preferable. Usage of the time-averaged Poynting's vector for the classical Maxwell equations allows also immediately to ensure the implementation of the energy conservation law at light refraction. Moreover, its value determines the wave intensity, i.e. allows estimate the experimental examination of peculiarities of the refraction/reflection on the interface of transparent and absorptive media. All problems are enhanced when both real parts of permittivity and permeability become negative in the Veselago medium or the left-handed medium (LHM) or metamaterial [4]. Really, using the Poynting's vector for the right absorptive/transparent media interface in [2], the non-coincidence of the incidence and refraction planes has been predicted for mixed polarization of incident beam.

In this paper the expressions for the refraction laws in absorptive right-handed medium (RHM) and LHM on the interface with transparent one have been obtained using only the $\tilde{\varepsilon}$, $\tilde{\mu}$ values of both signs, and the Poynting's vector. The solution of the vector Maxwell's equations in stationary regime can be found in the form of plane transverse wave's superposition, and the eigen modes dispersion has been obtained for s- and p-polarized light, correspondingly. Then, the time-averaged Pointing's vector is determined for both media, and for absorptive medium it has three non-zero components. In simulation we used the effective permeability in Lorentz form and permittivity in Drude form. The mapping of calculated transmittance and in-plane Pointing's vector for mixed s/p-polarization has been obtained. In the case of mixed polarization of incident light, the non-coincidence of the incidence plane and the refraction one is predicted too. These effects are especially high for negative permittivity/permeability.

2. THEORY

The light dispersion in the nth medium is determined from solution of Maxwell's equations in stationary regime (factor $e^{-i\omega t}$ is omitted) and can be written in ω/c units

$$K_n^2 = k^2 + \left(k_n^{\perp}\right)^2 = \varepsilon_n \mu_n, \tag{1}$$

where k and $k_n^{\perp}$ are the in-plane and transverse components of wave vector and amplitude of the wave vector $\mathbf{K}$, ε_n and μ_n are nth medium permittivity and permeability, and the transverse wave vector component are defined as follows

$$K_n = k_n^{\perp}(0), \quad k_n^{\perp}(k) = \sigma\sqrt{\varepsilon_n\mu_n - k^2}. \tag{2}$$

The sign $\sigma = \pm 1$ is determined from condition of positive imaginary part of wave vector that corresponds to wave propagation with component along z-axis (perpendicular to interface), it means that the sign of square root is chosen from positive imaginary part requirement. The eigen modes depend on $\mathbf{k}$ and sign σ, and take the form $\mathbf{K}_n^{\sigma}(\mathbf{k}) = \mathbf{k} + \sigma k_n^{\perp}(k)\hat{\mathbf{z}}$.

The solution of the Maxwell's equations in the form of plane transverse waves for one-interface (z=0) system can be written as follows

$$\mathbf{E}(\mathbf{R}) = e^{i\mathbf{k}_i\cdot\mathbf{r}} \begin{cases} \left(s_i\mathbf{s} + p_i\mathbf{p}_1^{(+)}\right) e^{ik_1^{\perp}(k_i)z} + \left(s_r\mathbf{s} + p_r\mathbf{p}_1^{(-)}\right) e^{-ik_1^{\perp}(k_i)z}, & z < 0 \\ \left(s_t\mathbf{s} + p_t\mathbf{p}_2^{(+)}\right) e^{ik_2^{\perp}(k_i)z}, & z \geq 0 \end{cases}, \tag{3}$$

$$\mathbf{H}(\mathbf{R}) = e^{i\mathbf{k}_i\cdot\mathbf{r}} \begin{cases} \frac{K_1}{\mu_1}\left[\left(s_i\mathbf{p}_1^{(+)} - p_i\mathbf{s}\right) e^{ik_1^{\perp}(k_i)z} + \left(s_r\mathbf{p}_1^{(-)} - p_r\mathbf{s}\right) e^{-ik_1^{\perp}(k_i)z}\right], & z < 0 \\ \frac{K_2}{\mu_2}\left(s_t\mathbf{p}_2^{(+)} - p_t\mathbf{s}\right) e^{ik_2^{\perp}(k_i)z}, & z \geq 0 \end{cases}, \tag{4}$$

where the orthogonal to $\mathbf{K}_n^{\sigma}(\mathbf{k}_i)$ unit vector can be chosen in the form describing s- and p- polarization

$$\mathbf{s} = \frac{\hat{\mathbf{z}} \times \mathbf{K}_n^{\sigma}(\mathbf{k}_i)}{|\hat{\mathbf{z}} \times \mathbf{K}_n^{\sigma}(\mathbf{k}_i)|} = \frac{\hat{\mathbf{z}} \times \mathbf{k}_i}{k_i}, \quad \mathbf{p}_n^{\sigma} = \frac{\mathbf{K}_n^{\sigma}(\mathbf{k}_i)}{K_n} \times \mathbf{s} = \frac{1}{K_n}\left(k_i\hat{\mathbf{z}} - \sigma k_n^{\perp}(k_i)\frac{\mathbf{k}_i}{k_i}\right), \tag{5}$$

where $\mathbf{k}_i$ is the in-plane component of incident wave vector, s_i and p_i are the polarization amplitudes of incident wave (these amplitudes can be normalized by condition $s_i^2 + p_i^2 = 1$), s_r, p_r and s_t, p_t are the polarization amplitudes of reflected and transmitted waves respectively.

For flat interface with normal in the z-direction, boundary conditions take the following form

$$\hat{\mathbf{z}} \times (\mathbf{E}_n(z_n) - \mathbf{E}_{n+1}(z_n)) = 0, \quad \hat{\mathbf{z}} \times (\mathbf{H}_n(z_n) - \mathbf{H}_{n+1}(z_n)) = 0, \tag{6}$$

where z_n is the nth interface position. So, the unknown polarization amplitudes in Eqs. (3) and (4) have the Fresnel's formulas type and can be written as follows

$$\begin{pmatrix} s_r \\ s_t \end{pmatrix} = \frac{1}{\mu_2 k_1^{\perp}(k_i) + \mu_1 k_2^{\perp}(k_i)} \begin{pmatrix} \mu_2 k_1^{\perp}(k_i) - \mu_1 k_2^{\perp}(k_i) \\ 2\mu_2 k_1^{\perp}(k_i) \end{pmatrix} s_i, \tag{7}$$

$$\begin{pmatrix} p_r \\ p_t \end{pmatrix} = \frac{1}{\varepsilon_2 k_1^{\perp}(k_i) + \varepsilon_1 k_2^{\perp}(k_i)} \begin{pmatrix} \varepsilon_2 k_1^{\perp}(k_i) - \varepsilon_1 k_2^{\perp}(k_i) \\ 2\frac{K_1 K_2}{\mu_1} k_1^{\perp}(k_i) \end{pmatrix} p_i. \tag{8}$$

The dispersion of electric modes (in the case of p-polarized light) can be determined from condition of zero denominator in Eqs. (7): $\varepsilon_2\sqrt{\varepsilon_1\mu_1 - k_e^2} + \varepsilon_1\sqrt{\varepsilon_2\mu_2 - k_e^2} = 0$, and the physical solution has the following form

$$k_e^2 = \varepsilon_1\varepsilon_2\frac{\varepsilon_1\mu_2 - \varepsilon_2\mu_1}{\varepsilon_1^2 - \varepsilon_2^2}. \tag{9}$$

Analogically for magnetic modes dispersion (s-polarized light) from condition $\mu_2\sqrt{\varepsilon_1\mu_1 - k_m^2} + \mu_1\sqrt{\varepsilon_2\mu_2 - k_m^2} = 0$ we have obtained:

$$k_m^2 = \mu_1\mu_2\frac{\mu_1\varepsilon_2 - \mu_2\varepsilon_1}{\mu_1^2 - \mu_2^2}. \tag{10}$$

Similar dispersions was obtained in [5] only for non-dissipative media.

The averaging over the high frequency time Poynting's vector ($\mathbf{S} = (c^2/4\pi\omega)\mathrm{Re}\,(\mathbf{E}_n(\mathbf{K})^* \times \mathbf{H}_n(\mathbf{K}))$) is rewritten as

a) for $z < 0$

$$\mathbf{S}_1 = \frac{c^2}{4\pi\omega}\frac{1}{\mu_1}\left(\left(1+|s_r|^2+|p_r|^2+2\mathrm{Re}\{s_i s_r + p_i p_r\}\right)\mathbf{k}_i + \left(1-|s_r|^2-|p_r|^2\right)k_1^{\perp}\hat{\mathbf{z}}\right). \tag{11}$$

b) for $z \geq 0$

$$\mathbf{S}_2 = \frac{c^2}{4\pi\omega}\left[\left(|s_t|^2\mathrm{Re}\frac{1}{\mu_2} + |p_t|^2\mathrm{Re}\frac{1}{\mu_2}\frac{K_2}{K_2^*}\right)\mathbf{k}_i + 2k_i\mathrm{Im}\frac{p_t^* s_t}{\mu_2 K_2^*}\mathrm{Im}k_2^{\perp}\mathbf{s} + \left(|s_t|^2\mathrm{Re}\frac{k_2^{\perp}}{\mu_2} + |p_t|^2\mathrm{Re}\frac{k_2^{\perp *}}{\mu_2}\frac{K_2}{K_2^*}\right)\hat{\mathbf{z}}\right]. \tag{12}$$

In Eqs. (11)-(12) the dependency on k_i in $k_n^{\perp}(k_i)$ is omitted for simplicity sake. As we can see in the second (absorptive) medium the Eq. (12) has three non-zero components in contrary to the first non-absorptive one (11).

Substituting Eqs. (7)-(8) into Poynting's vector definition Eqs. (11)-(12) we finally obtain the following expressions

$$\mathbf{S}_1 = \frac{c^2}{4\pi\omega}\left[\left(1+\left|\frac{\mu_2 k_1^{\perp}-\mu_1 k_2^{\perp}}{\mu_2 k_1^{\perp}+\mu_1 k_2^{\perp}}s_i\right|^2 + \left|\frac{\varepsilon_2 k_1^{\perp}-\varepsilon_1 k_2^{\perp}}{\varepsilon_2 k_1^{\perp}+\varepsilon_1 k_2^{\perp}}p_i\right|^2 + 2s_i p_i\mathrm{Re}\left\{\frac{\mu_2 k_1^{\perp}-\mu_1 k_2^{\perp}}{\mu_2 k_1^{\perp}+\mu_1 k_2^{\perp}}+\frac{\varepsilon_2 k_1^{\perp}-\varepsilon_1 k_2^{\perp}}{\varepsilon_2 k_1^{\perp}+\varepsilon_1 k_2^{\perp}}\right\}\right)\mathbf{k}_i + \left(1-\left|\frac{\mu_2 k_1^{\perp}(k_i)-\mu_1 k_2^{\perp}(k_i)}{\mu_2 k_1^{\perp}(k_i)+\mu_1 k_2^{\perp}(k_i)}s_i\right|^2 - \left|\frac{\varepsilon_2 k_1^{\perp}-\varepsilon_1 k_2^{\perp}}{\varepsilon_2 k_1^{\perp}+\varepsilon_1 k_2^{\perp}}p_i\right|^2\right)k_1^{\perp}\hat{\mathbf{z}}\right], \tag{13}$$

$$\mathbf{S}_2 = \frac{c^2}{4\pi\omega}4(k_1^{\perp})^2\left[\left(\frac{s_i^2\mathrm{Re}\{\mu_2\}}{\left|\mu_2 k_1^{\perp}+\mu_1 k_2^{\perp}\right|^2} + \frac{\frac{\varepsilon_1}{\mu_1}p_i^2\mathrm{Re}\{\varepsilon_2\}}{\left|\varepsilon_2 k_1^{\perp}+\varepsilon_1 k_2^{\perp}\right|^2}\right)\mathbf{k}_i + 2k_i s_i\sqrt{\frac{\varepsilon_1}{\mu_1}}p_i\mathrm{Im}\left\{\frac{1}{\varepsilon_2^* k_1^{\perp}+\varepsilon_1 k_2^{\perp *}}\frac{1}{\mu_2 k_1^{\perp}+\mu_1 k_2^{\perp}}\right\}\mathrm{Im}k_2^{\perp}\mathbf{s} + \left(\frac{s_i^2\mathrm{Re}\left\{\mu_2^* k_2^{\perp}\right\}}{\left|\mu_2 k_1^{\perp}+\mu_1 k_2^{\perp}\right|^2} + \frac{\frac{\varepsilon_1}{\mu_1}p_i^2\mathrm{Re}\left\{\varepsilon_2^* k_2^{\perp}\right\}}{\left|\varepsilon_2 k_1^{\perp}+\varepsilon_1 k_2^{\perp}\right|^2}\right)\hat{\mathbf{z}}\right]. \tag{14}$$

The angle of refraction as angle between the Poynting's vector and normal to the interface can be obtained in the following way

$$\cos\phi_d = \frac{\mathbf{S}_2\cdot\mathbf{n}}{|\mathbf{S}_2|} = \frac{(s_i^2\mathrm{Re}\left\{\mu_2^* k_2^{\perp}\right\})\left|\mu_2 k_1^{\perp}+\mu_1 k_2^{\perp}\right|^{-2} + (\varepsilon_1/\mu_1)p_i^2\mathrm{Re}\left\{\varepsilon_2^* k_2^{\perp}\right\}\left|\varepsilon_2 k_1^{\perp}+\varepsilon_1 k_2^{\perp}\right|^{-2}}{(4\pi\omega/c^2)|\mathbf{S}_2|}. \tag{15}$$

Also we can define the refraction angles in the form of angle between incidence and refraction planes as follows

$$\tan\theta_d = \frac{\mathbf{S}_2\cdot[\hat{\mathbf{z}}\times\mathbf{k}_i]}{\mathbf{S}_2\cdot\mathbf{k}_i} = \frac{2s_i\sqrt{\varepsilon_1/\mu_1}p_i\mathrm{Im}\left\{(\varepsilon_2^* k_1^{\perp}+\varepsilon_1 k_2^{\perp *})^{-1}(\mu_2 k_1^{\perp}+\mu_1 k_2^{\perp})^{-1}\right\}\mathrm{Im}k_2^{\perp}}{s_i^2\mathrm{Re}\{\mu_2\}\left|\mu_2 k_1^{\perp}+\mu_1 k_2^{\perp}\right|^{-2} + (\varepsilon_1/\mu_1)p_i^2\mathrm{Re}\{\varepsilon_2\}\left|\varepsilon_2 k_1^{\perp}+\varepsilon_1 k_2^{\perp}\right|^{-2}} \tag{16}$$

or in the form of angle between the refracted beam direction and the incidence plane

$$\sin\psi_d = \frac{\mathbf{S}_2\cdot\mathbf{s}}{|\mathbf{S}_2|} = \frac{2\kappa_i s_i\sqrt{\varepsilon_1/\mu_1}p_i\mathrm{Im}\left\{(\varepsilon_2^* k_1^{\perp}+\varepsilon_1 k_2^{\perp *})^{-1}(\mu_2 k_1^{\perp}+\mu_1 k_2^{\perp})^{-1}\right\}\mathrm{Im}k_2^{\perp}}{(4\pi\omega/c^2)|\mathbf{S}_2|}. \tag{17}$$

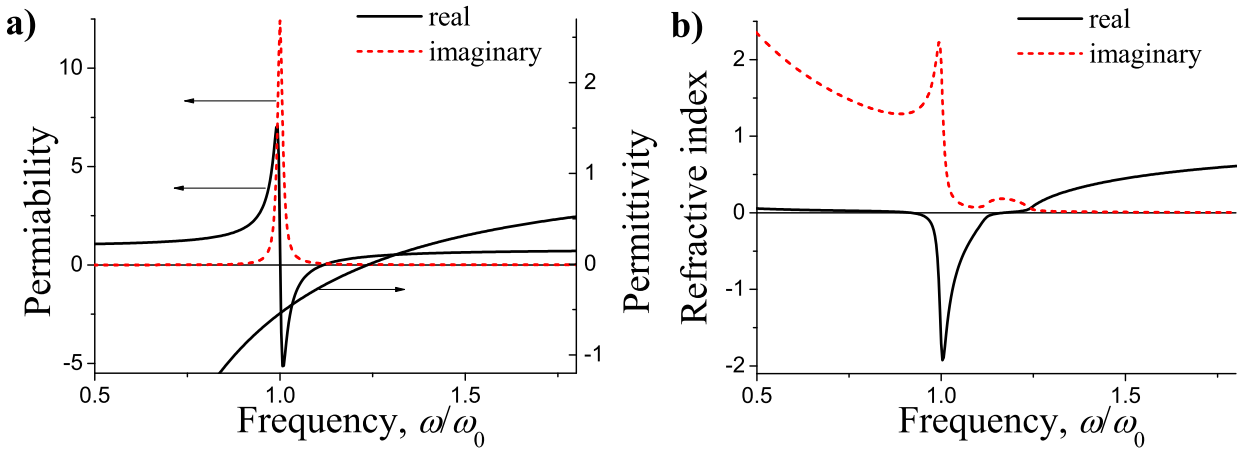


Figure 1: Spectra of effective permeability and permittivity (imaginary part is not shown because it is close to zero) (**a**) and effective refractive index $\sqrt{\mu_{\text{eff}}(\omega)\varepsilon_{\text{eff}}(\omega)}$ (**b**).

3. NUMERICAL RESULTS

In simulation we use effective permeability in Lorentz form and permittivity in Drude form that are taken from [6]

$$\mu_{\text{eff}}(\omega) = 1 - \frac{F\omega^2}{\omega^2 - \omega_0^2 + i\Gamma\omega}, \quad \varepsilon_{\text{eff}}(\omega) = 1 - \frac{\omega_p^2}{\omega^2 + i\Gamma_p\omega}, \tag{18}$$

where F=0.2, ω_0 = 148.9 THz, Γ = 2.4 THz, ω_p = 185 THz, Γ_p = 3 THz. The permittivity and permeability corresponding to Eqs. (18) are presented in Fig. 1**a**. Using data from Fig. 1**a** the effective refractive index for left handed medium is presented in Fig. 1**b**.

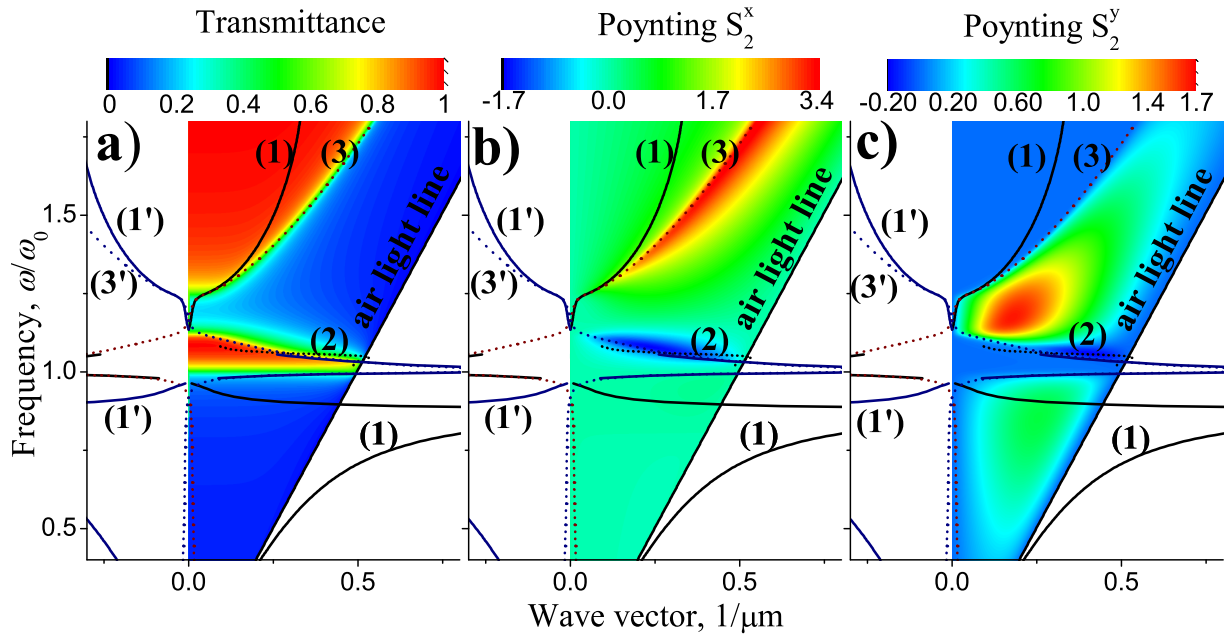


Figure 2: Transmittance (**a**) and in-plane Poynting's (**b, c**) vector versus frequency and incident wave vector at fixed polarization angle 45 deg. By numbers are denoted: (1) electric modes, k_e; (1') $-k_e$; (2) magnetic modes, k_m; (3) bulk polariton in metamaterial, k_{meta}; (3') $-k_{\text{meta}}$.

The calculated transmittance (**a**) and in-plane Poynting's vector (**b**, **c**) for mixed s/p-polarization of incident light (polarization angle is equal to 45 deg.) versus incident frequency and wave vector are presented in Fig. 2 as color mapping. The transmittance is defined from normal component of

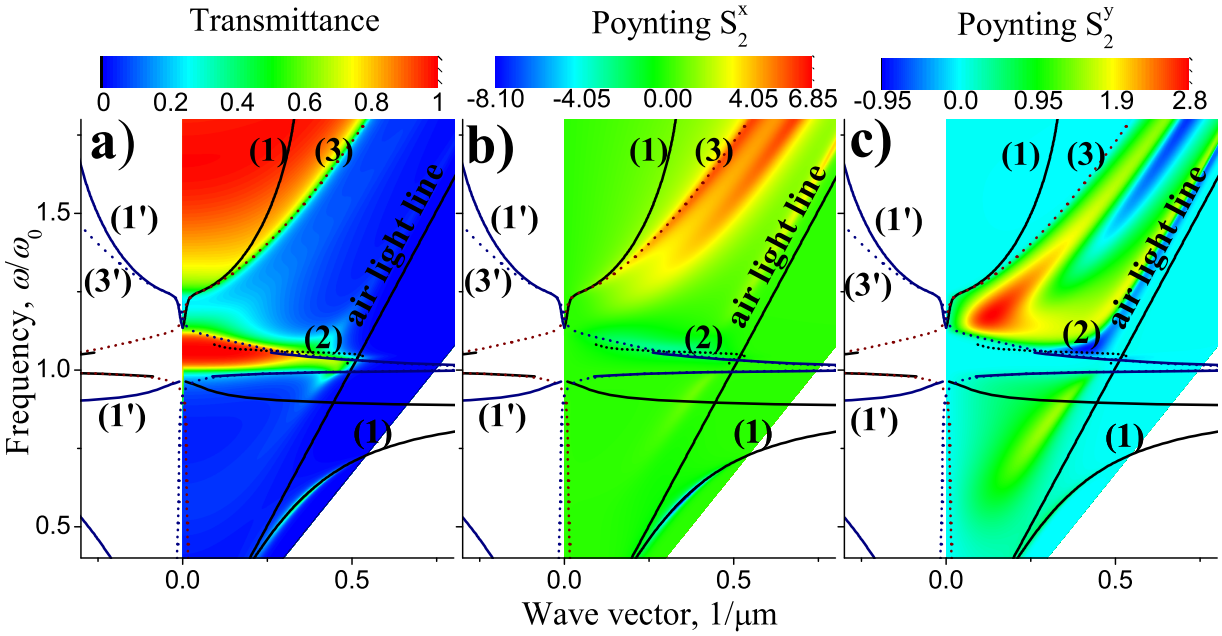


Figure 3: Transmittance (**a**) and in-plane Poynting's (**b, c**) vector versus frequency and incident wave vector at fixed polarization angle 45 deg. for the case of high-refractive index prism. Numerical notations are same as in Fig. 2

Poynting's vector as follows: $T = S_{2z}/k_1^{\perp}$. The magnetic and electric dispersion curves and light line in air and metamaterial are added in Fig. 2 as well as.

Analogous to Fig. 2 dependencies of the transmittance and in-plane Poynting's vector components are presented in Fig. 3 for the case of high-refractive index prism presence that allows reaching resonant condition for light-matter interaction (i.e. surface polariton waves excitation). As it can see from Fig. 2 and 3 the maximum transmittance is lain in the left region from the light line in metamaterial that corresponds to radiative waves in metamaterial. Also in the region around ω_0 there are waves with negative propagation direction contrary to light incidence (S_{2x} takes negative value, see Fig. 2**b** and **c**). Note that such negative propagation direction is also appeared in the case of surface wave (non-resonant excitation in Fig. 2 (see [2] also) and resonant excitation in Fig. 3). In the region of evanescent waves (right region from the light line in metamaterial) the non-zero component of S_{2y} is appeared that lead to the rotation refraction plane contrary to incidence plane if such planes will be determined by Poynting's vector.

4. CONCLUSIONS

Thus, the optics of refraction/reflection on the interface with metamaterial, in the sense of Poynting's vector behavior, is analogous to one for interface with strong dissipative medium under mixed polarization of incident light.

The quantitative differences are caused by the excitation of surface plasmons resonant or non-resonant manner.

REFERENCES

1. Born, M. and E. Wolf, *Principles of Optics*, Pergamon, New York, 1964.
2. Dmitruk, N. L. and A. V. Korovin, "Peculiarities of Electromagnetic Wave Refraction on the Surface of Absorbing Media," *Ukrainian Journal of Physics*, Vol. 49, 858–865, 2004.
3. Elson, J. H., H. E. Benett and J. M. Benett, *Applied Optics and Optics Engineering, Vol.VII: Scattering From Optical Surfaces*, Academic Press, 1979.
4. Veselago, V.G. "The electrodynamics of substances with simultaneously negative values of ε and μ.," *Sov. Phys. Uspekhi* Vol. 10, 509-514, 1968.
5. Panoiu, N.-C. and R. M. Osgood, "Numerical investigation of negative refractive index metamaterials at infrared and optical frequencies," *Opt. Commun.*, Vol. 233, 331-337, 2003.
6. Ruppin, R. "Surface polaritons of a left-handed medium," *Physics Letters A*, Vol. 277, 61–64, 2000.

Nonlinear-optical metamirror

A. K. Popov[1], **S. A. Myslivets**[2,3]

[1]University of Wisconsin-Stevens Point, USA, apopov@uwsp.edu
[2]Institute of Physics of the Russian Academy of Sciences, Siberian Branch, Russian Federation
[3] Siberian Federal University, Russian Federation

Abstract— The possibility of creation of highly efficient frequency-tunable nonlinear-optical micromirror and all-optical data processing microchip is shown, which utilize backwardness of electromagnetic waves in negative-index metamaterials.

1. INTRODUCTION

Metamaterials can exhibit exotic optical properties, such as negative refraction, which have no counterpart in natural media. This can be used to develop a wide variety of devices with enhanced and uncommon operational functionalities. Metamaterials are also expected to play a key role in the development of all-optical data processing chips. Unlike natural materials, the energy flow and the phase velocity are counter-directed in negative-index (NI) metamaterials (NIMs), which determines their extraordinary nonlinear-optical (NLO) propagation properties. Usually, negative refraction index exists only within a certain frequency band, whereas the sample remains positive-index (PI) outside it. Unparalleled features of second-harmonic generation (SHG) and optical parametric amplification (OPA) of NI signal in double-domain NIM slabs were revealed in [1-6], which are in a striking contrast with SHG and OPA in natural, PI materials. Strong absorption, which is inherent to metal-dielectric nanocomposites that exhibit NI property, impose severe limitations on many potential applications of NIMs. Herein, a different process of difference-frequency generation of backward NI wave in a strongly absorbing NIM slab by two incident co-propagating PI waves is explored and shown to be essentially different from earlier investigated process of OPA. Extraordinary properties of nonlinear-optical reflectivity are investigated and proposed for the implementation as a NLO micromirror and an all-optically controlled microchip.

2. COUPLING SCHEME AND BASIC EQUATIONS

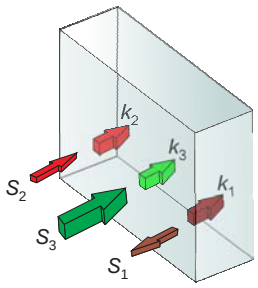


Figure 1: Coupling geometry for the proposed negative-index nonlinear-optical mirror: $\mathbf{S}_2$ – positive-index incident wave, $\mathbf{S}_3$ – positive-index control field, $\mathbf{S}_1$ – negative-index reflected signal. $\mathbf{S}_1$, $\mathbf{k}_1$ and ω_1 are energy flux, wave-vector and frequency for the backward-wave signal; $\mathbf{S}_2$, $\mathbf{k}_2$ and ω_2 – for the ordinary idler; $\mathbf{S}_3$, $\mathbf{k}_3$ and ω_3 – for the ordinary control fields.

Assuming electrical permittivity ϵ, magnetic permeability μ, and the magnitude of wave-vector $k^2 = n^2(\omega/c)^2$ are real numbers, it is easy to show that the direction of the wave-vector $\mathbf{k}$ with respect to the energy flow (Poynting vector) depends on the signs of ϵ and μ:

$$\mathbf{S}(\mathbf{r},t) = \frac{c}{4\pi}[\mathbf{E}\times\mathbf{H}] = \frac{c^2\mathbf{k}}{4\pi\omega\epsilon}H^2 = \frac{c^2\mathbf{k}}{4\pi\omega\mu}E^2. \quad (1)$$

For $\epsilon_i < 0$ and $\mu_i < 0$, vectors **S** and **k** become contra-directed and refraction index – negative, $n = -\sqrt{\mu\epsilon}$. This is in contrast to the electrodynamics of ordinary media and opens opportunities for many revolutionary breakthroughs in photonics. Unparallel properties of nonlinear-optical generation of backward wave explored here is a new example of that. Figure 1 depicts a slab of thickness L, strong control field E_3 at ω_3 and incident wave E_2 at ω_2, both are assumed as PI. Generated difference-frequency wave E_1 at $\omega_1 = \omega_3 - \omega_2$ is NI and, therefore, backward wave. All three waves experience strong dissipation described by absorption indices $\alpha_{1,2,3}$. The slowly-varying effective amplitudes of the waves, $a_{e,m,j}$, (j=$\{1,2,3\}$) and nonlinear coupling parameters, $g_{e,m}$, for the electric and magnetic types of quadratic nonlinearity [7] can be conveniently introduced as

$$a_{ej} = \sqrt{|\epsilon_j/k_j|}E_j, g_e = \sqrt{|k_1k_2/\epsilon_1\epsilon_2|}2\pi\chi^{(2)}_{ej}E_3; \quad a_{mj} = \sqrt{|\mu_j/k_j|}H_j, g_m = \sqrt{|k_1k_2/\mu_1\mu_2|}2\pi\chi^{(2)}_{mj}H_3.$$

The quantities $|a_j|^2$ are proportional to the photon numbers in the energy fluxes. Equations for the amplitudes a_j are identical for the both types of the nonlinearities:

$$da_1/dz = -ga_2^* \exp(i\Delta kz) + (\alpha_1/2)a_1, \quad (2)$$

$$da_2/dz = ga_1^* \exp(i\Delta kz) - (\alpha_2/2)a_2, \quad (3)$$

$$da_3/dz = -(\alpha_3/2)a_3. \quad (4)$$

Here, $\Delta k = k_3 - k_2 - k_1$. The equations account for absorption of all three coupled fields, whereas the depletion of the control fields due to the conversion process is neglected compared to absorption. Three fundamental differences in Eqs. (2) and (3) distinguish them from their counterpart in ordinary, PI materials. First, the signs with g in Eq. (2) is opposite to that in Eq. (3) because $\epsilon_1 < 0$ and $\mu_1 < 0$. Second, the opposite sign appears with α_1 because the energy flow $\mathbf{S_1}$ is against the z-axis. Third, the boundary conditions for the incident and generated waves are defined at the opposite side of the sample ($z = 0$ and $z = L$) because the energy flows $\mathbf{S_1}$ and $\mathbf{S_2}$ are counter-directed. Consequently, the sign on the right side of Eq. (2) is opposite to that in Eq. (3). As will be shown below, this leads to dramatic changes in the solutions to the equations and in the general behavior of the generated wave. At $a_{1L} = 0$, $a_2(z = 0) = a_{20}$, the slab serves as an NLO mirror, which reflects a wave at ω_1 . For the case of spatially homogeneous control field ($\alpha_3 = 0$) and real nonlinear susceptibility, an analytical solution to the Eqs. (2)-(3) can be found, and then the reflectivity, $r_1 = |a_1(0)/a_{20}^*|^2$, is given by the equation

$$r_1 = \left| \frac{(g/R)\sin RL}{\cos RL + (s/R)\sin RL} \right|^2, \quad (5)$$

where $R = \sqrt{g^2 - s^2}$, $s = [(\alpha_1 + \alpha_2)/4][-i\Delta k/2]$. It is seen that the reflectivity presents a *set of "geometrical" resonances*. For example, at $s = 0$, reflectivity $r_{10} = tan^2(gL)$ and tends to infinity at $gL \to \pi/2$, which indicates *mirrorless self-oscillations*. Basically, the reflected wave has a differen frequency, and the reflectivity may significantly exceed 100%. In the case of strong absorption of all three wave, only numerical solution can be found. The results of such numerical simulations, which demonstrate the properties of such mirror, are presented below. A transmission properties for the incident wave, $T_2 = |a_2(L)/a_{20}|^2$, is also numerically investigated.

3. PROPERTIES OF NONLINEAR-OPTICAL REFLECTIVITY AND TRANSMITTANCE

Figure 2 displays the resonances in reflectivity which may exceed the self-oscillation threshold. It is seen that the transmission minima depend on the ratio of absorption rates, which is in stark contrast with the reflectivity minima which remain robust. Alternatively, Fig. 3 shows that phase mismatch causes decrease of the reflectivity maxima and increase the minima. Reflectivity becomes relatively robust against phase mismatch with increase of intensity of the control field. It drops dramatically in the range of small phase mismatch and then remains relatively robust at the lower level within the range of greater phase mismatch, as seen in Figs. 4 and 5. Figures 6 and 7 show that the outlined properties of the NLO mirror are determined by the interplay of several processes which have a strong effect on the NLO coupling of contrapropagating waves and, consequently, on their distribution inside the slab. Ultimately, the simulations show the possibility to tailor and switch the reflectivity of such a mirror over the wide range by changing intensity of the control field.

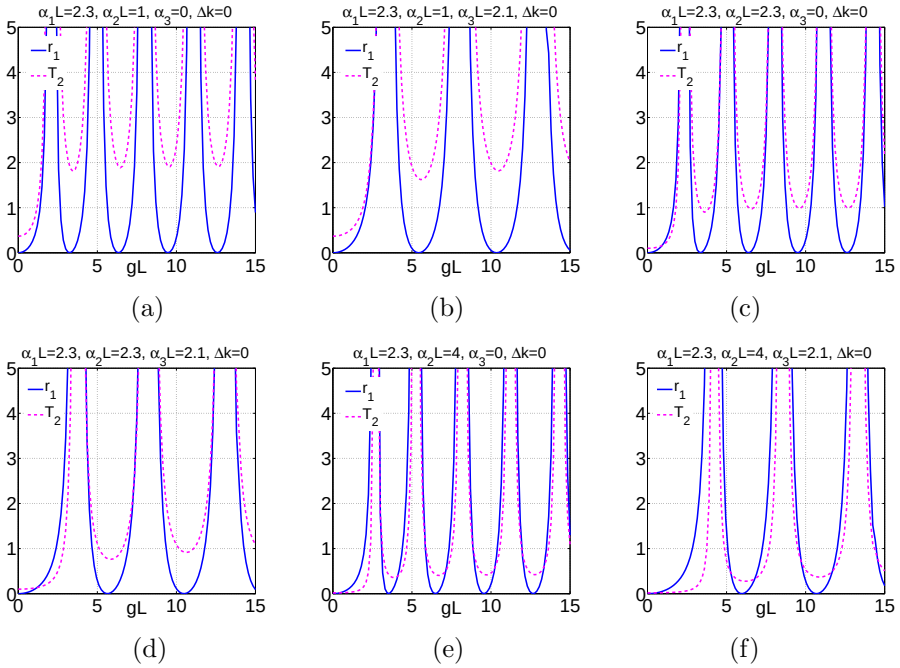


Figure 2: Effect of absorption on reflectivity and transmittance of the NLO mirror. Here, reflectivity can be switched from zero to magnitudes exceeding 100%.

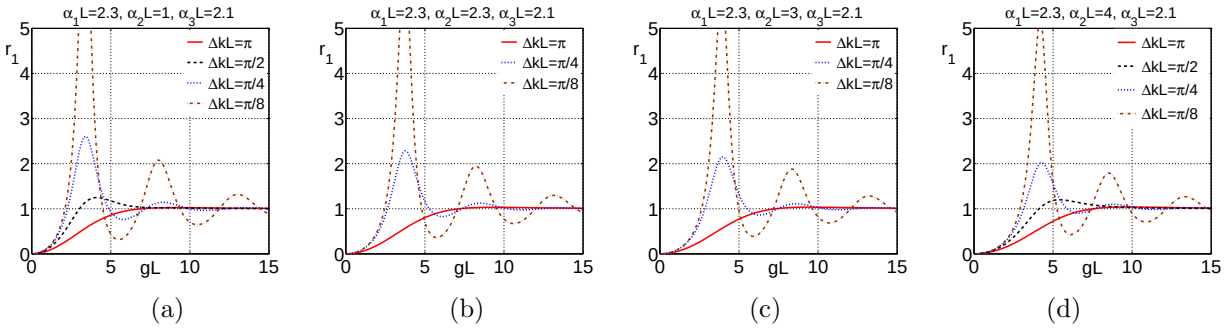


Figure 3: Effect of of absorption on the reflectivity and transmittance of the NLO mirror at different phase mismatches.

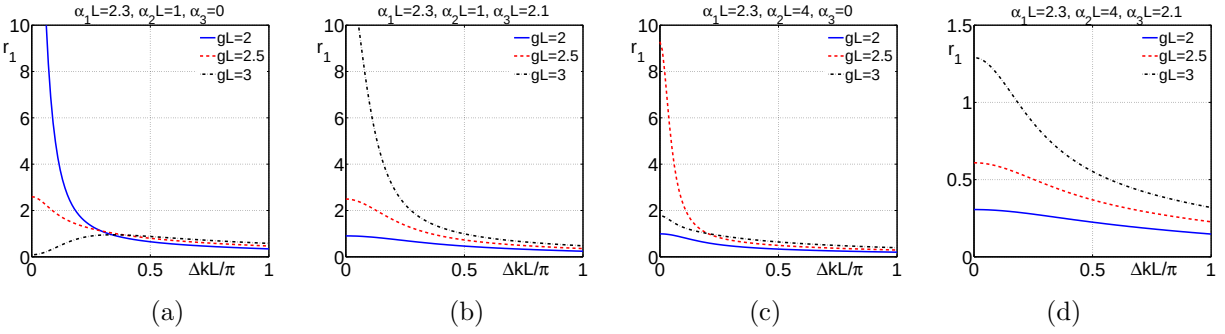


Figure 4: Effect of phase mismatch on the reflectivity and transmittance of the NLO mirror at different absorption and intensity of the control field.

On a fundamental level, the NLO response of nanostructured metamaterials is not completely understood or characterized. Nevertheless, it is well established that local-field enhanced nonlinearities can be attributed to plasmonic nanostructures. The feasibility of crafting NIMs with strong NLO responses in the optical wavelength range has been experimentally demonstrated in [7]. Only

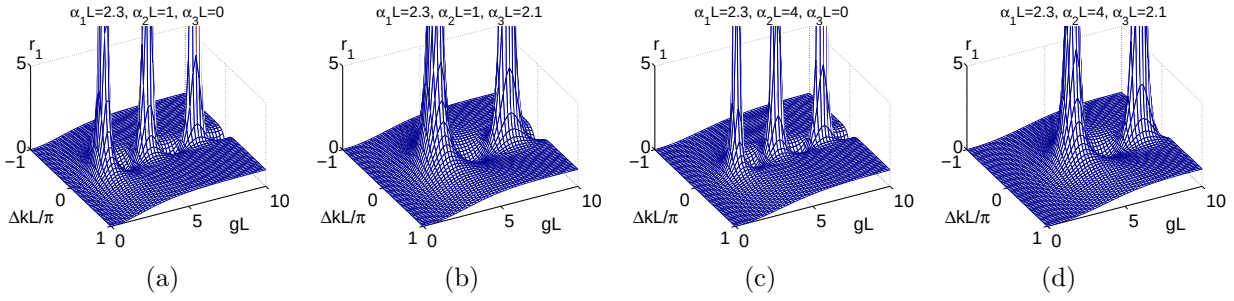


Figure 5: Reflectivity vs. intensity of the control field and phase mismatch for different absorption indices for the coupled waves.

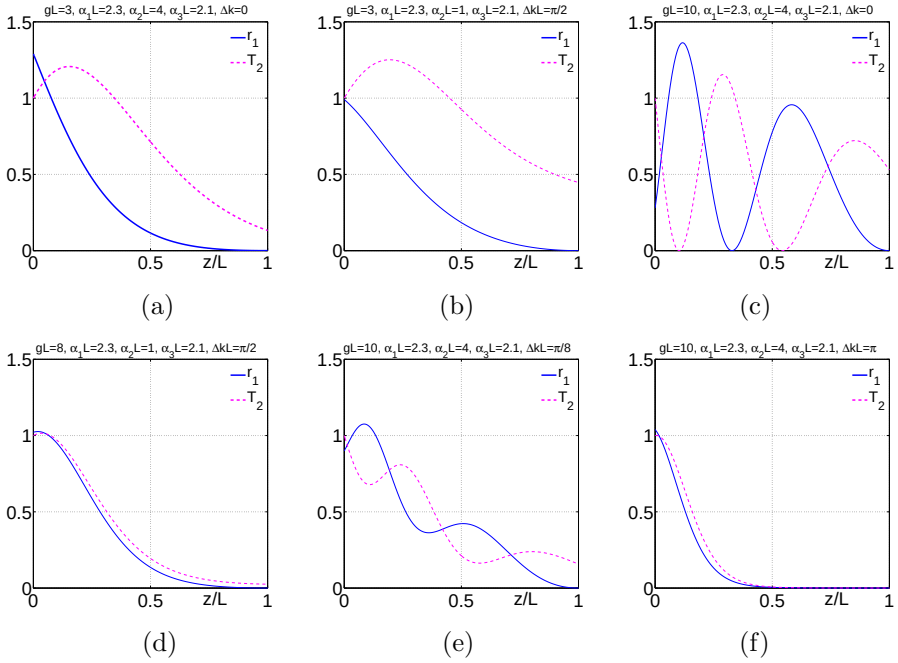


Figure 6: Intensity distribution for the ordinary and backward waves inside the slab for different absorption index, phase mismatch and intensity of the control field.

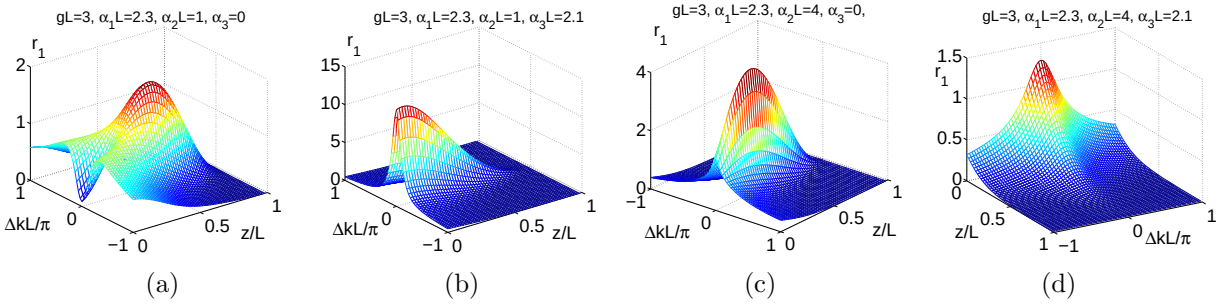


Figure 7: Dependence of distribution of generated backward wave inside the slab on phase mismatch.

rough estimations can be made regarding $\chi^{(2)}$ attributed to metal-dielectric nanostructures. Assuming $\chi^{(2)} \sim 10^{-6}$ ESU ($\sim 10^3$ pm/V), which is on the order of that for $CdGeAs_2$ crystals, and a control field of $I \sim 100$ kW focused on a spot of $D \sim 50$ μm in diameter, one can estimate that the typical required value of the parameter $gL \sim 1$ can be achieved for a slab thickness in the *microscopic* range of $L \sim 1\mu$m, which is comparable with that of the multilayer NIM samples fabricated to date [8-11].

4. CONCLUSION

In conclusion, the possibility and extraordinary properties of coherent NLO propagation process of a three-wave difference-frequency generation of a backward electromagnetic wave in strongly absorptive negative-index metamaterials are demonstrated by the means of numerical experiments. It is shown that the properties of such process are essentially different from the earlier studied optical parametric amplification in NIMs. The majority of NIMs realized to date consist of metal-dielectric nanostructures, meta-atoms, that have highly controllable magnetic and dielectric responses. The challenge, however, is that these structures are strongly lossy which constitute a major hurdle on the way to practical realization of unique applications of these structures in optics. Therefore, developing efficient loss-compensating techniques is of paramount importance. This is the key problems in determining numerous revolutionary applications of such a novel class of electromagnetic metamaterials. It is shown here that the compensation of such losses, all-optical tailoring of transparency and reflectivity of a NIM slab and even generation of counterpropagating flows of entangled photons are possible through coherent nonlinear-optical energy transfer from the ordinary control wave to the backward electromagnetic wave. The backwardness of traveling electromagnetic waves is intrinsic to negative-index metamaterials. The unique features of the proposed ultra-miniature nonlinear-optical mirror and microchip are revealed, such as the strongly resonant behavior with respect to the material thickness, nonlinear susceptibility and the intensity of the control field. Since nonlinear susceptibility and absorption is frequency dependent, among the possible applications of the proposed technique are a novel class of the miniature frequency-tunable narrow-band filters, mirrors, switchers, amplifiers, all-optical data processing microchips and cavity-free microscopic optical parametric oscillators.

ACKNOWLEDGMENT

This work was supported by the U. S. Army Research Laboratory and by the U. S. Army Research Office under Grant number W911NF-0710261 and by the Siberian Division of the Russian Academy of Sciences under Integration Project no 5.

REFERENCES

1. Agranovich, V. M., Y. R. Shen, R. H. Baughman and A. A. Zakhidov, "Linear and nonlinear wave propagation in negative refraction metamaterials," *Phys. Rev. B*, Vol. 69, No. 16, 165112(7), 2004.
2. Shadrivov, I. V., A. A. Zharov and Y. S. Kivshar, "Second-harmonic generation in nonlinear left-handed metamaterials," *J. Opt. Soc. Am. B*, Vol. 23, No. 3, 529–534, 2006.
3. Popov, A. K., V. V. Slabko and V. M. Shalaev, "Second harmonic generation in left-handed metamaterials," *Laser Phys. Lett.*, Vol. 3, No. 6, 293–296, 2006.
4. Scalora, M., G. D'Aguanno, M. Bloemer, M. Centini, D. de Ceglia, N. Mattiucci and Y. S. Kivshar, "Dynamics of short pulses and phase matched second harmonic generation in negative index materials," *Opt. Express*, Vol. 14, No. 11, 4746–4756, 2006.
5. Popov, A. K. and V. M. Shalaev, "Compensating losses in negative-index metamaterials by optical parametric amplification," *Opt. Lett.*, Vol. 31, 2169–2171, 2006.
6. Popov, A. K. and S. A. Myslivets, "Transformable broad-band transparency and amplification in negative-index films," *Appl. Phys. Lett.*, Vol. 93, No. 19, 191117(3), 2008.
7. M. W. Klein, M. Wegener, N. Feth, and S. Linden, "Experiments on second- and third-harmonic generation from magnetic metamaterials," *Opt. Express,* Vol. 15, 5238-5247 (2007); erratum:*ibid*, Vol. 16, 8055 (2008).
8. Soukoulis, C. M. and M. Kafesaki, "Weakly and strongly coupled optical metamaterials," *Invited talk at Nanometa 2009, 2nd European Topical Meeting on Nanophotonics and Metamaterials*, Seefeld, Tirol, Austria, 2009.
9. Katsarakis, N., G. Konstantinidis, A. Kostopoulos, R. S. Penciu, T. F. Gundogdu, M. Kafesaki, E. N. Economou, Th. Koschny, and C. M. Soukoulis, "Magnetic response of split-ring resonators in the far-infrared frequency regime," *Opt. Lett.* Vol. 30, 1348–1350, 2005.
10. Zhang, X., "Optical Bulk Metamaterials," *Plenary talk at Nanometa 2009, 2nd European Topical Meeting on Nanophotonics and Metamaterials*, Seefeld, Tirol, Austria, 2009.
11. Valentine, J., S. Zhang, T. Zentgraf, E. Ulin-Avila, D. A. Genov, G. Bartal and X. Zhang, "Three-dimensional optical metamaterial with a negative refractive index," *Nature*, Vol. 455, 376–378, 2008.

Enhanced broadband optical transmission in metallized woodpiles

R. Malureanu[1], **A. Alabastri**[1,2], **W. Cheng**[3], **R. Kiyan**[3], **B. Chichkov**[3], **A. Andryieuski**[1] **and A. Lavrinenko**[1]

[1]DTU Fotonik, Technical University of Denmark, Denmark
[2]Dipartimento di Fisica, Politecnico di Milano, Italy
[3]Laser Zentrum Hannover, Germany
rmal@fotonik.dtu.dk

Abstract— We present an optimized isotropic metal deposition technique used for coating three-dimensional polymer structures with a 50nm smooth silver layer. The technology allows fast isotropic coating of complex 3D dielectric structures with thin silver layers. Transmission measurements of 3D metallized woodpiles reveal a new phenomenon of enhanced optical transmission in broadband range (up to 300 nm) in the near IR.

1. INTRODUCTION

Deposition of thin, smooth metal layers on three-dimensional structures is one of the challenges within thin film deposition field. Such structures can prove to be extremely useful in a number of research fields and applications ranging from Raman spectroscopy[1] to metamaterials[2, 3], from electronics[4] to medicine[5].

In this work we will concentrate on the metal deposition aiming at metamaterials fabrication. After the first successes[6], the metamaterials research field has gained a huge momentum due to advances in theory, modelling and fabrication. One natural trend is toward increasing the operating frequency from microwaves to the IR and visible regime. A number of new designs and fabrication approaches emerged thus allowing metamaterials based devices in the IR and close to visible regime.[7, 8, 9] However, such tendency brought also challenges in the fabrication procedures due to the decrease in unit cell sizes and enhanced claims for needed resolution and accuracy.

Another trend is to expand the designs to truly 3D ones that can give bulk and eventually isotropic response within the frequency range of interest. Within this trend, several approaches were made. A layer by layer approach for fabrication of 3D metamaterials in IR has been demonstrated recently.[9]

An alternative approach is fabrication of a 3D polymer skeleton structure with further metallization of its surface. The two-photon polymerization technique (2PP)[10] is proven to be very flexible and efficient technology for fabrication of 3D polymer layouts including structures for photonic applications.[11] Still, even if various designs of 3D metamaterials were theoretically proposed,[12, 13] their manufacturability is hampered by the difficulty of controlled metal deposition on 3D structures with complex topology.

To the best of our knowledge, there are two main methods for depositing metals on a 3D dielectric structure. The first one is based on chemical vapor deposition (CVD), and the second is the "electroless" deposition technique. The CVD method shows great promise for depositing metals on the desired three-dimensional structure[14] however, the parameter space for such technique is large thus the optimizing procedure claims exhaustive efforts due to the existence of multiple local minima. The electroless deposition technique provides much more reduced parameter space, thus easier optimization of the former technique, and the lack of volatile poisonous products in the deposition process.

2. FABRICATION

Aiming for the potential applications of devices in the optical range, we decided to obtain thin and smooth metallic layers by optimizing the recipe known as Tollen's test or the silver mirror reaction.[15]

Optimization steps in the above mentioned technique were made within the first rounds of tests on simple planar samples. Eventually we obtained uniform silver layers with thicknesses down to $30nm$ (Figure 1a). The layer thickness is directly proportional on the immersion time. Using the

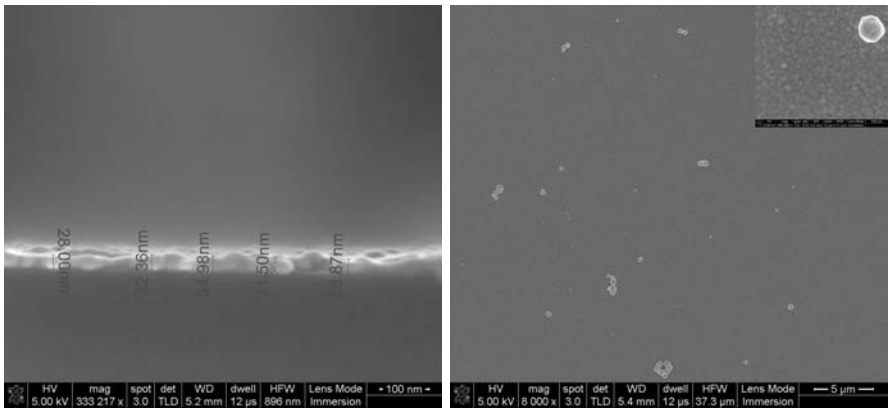


Figure 1: a) Ultrathin uniform silver layer deposited by the electroless technique on the silica substrate. Numbers show the thickness of the silver coating; b) Top view of the sample showing high deposition uniformity over a large area. Some single Ag nanocrystals deposited on top of the layer are visible. In the inset, a zoom-in of the surface is shown.

presented recipe, thicknesses of up to $200nm$ were achieved (not shown) simply by increasing the immersion time. Silver layers, thinner than $30nm$, are not completely formed, exhibiting random clusters formation. We think that this effect is due to the mechanism of the silver seeds growth in the solution. It can be inhibited making possible to deposit thinner silver layers. In figure 1b we present a top-view showing high uniformity in the layer formation. The substrate is uniformly covered, but a few silver nanoparticles can be observed on top of its surface. These Ag nanocrystals are formed in the solution and then they are deposited in the ready form on sample's surface. Still, such nanocrystals formation is minimal and does not restrain the overall deposition process. In the inset of figure 1b one can see a zoom-in of the deposited layer where the polycrystalline growth of the silver is noticeable. Our samples were up to $1 \times 1cm$ in sizes, and no pronounced difference in layer properties was noticeable over such extended surface. So it validates that such technique has no limitations by the depositing area and can be applied to samples of, in principle, whatever dimensions.

For optimizing the deposition parameters we employed a quantitative criteria of the average roughness calculated on a sample portion, where there are no Ag nanocrystals. The roughness analysis was performed by measuring the peak-to-peak difference and then using such value for scaling the scanning electron microscopy image to real coordinates. For safety reasons, the peak-to-peak height was considered in the worst case scenario, when the measuring errors are summed up. While the nanocrystals can reach dimensions of up to $100nm$, the average roughness in the "clean" areas is in the order of $1nm$ and the roughness mean square value (RMS) is about $1.5nm$, what is comparable with the RMS for evaporated films. For a more accurate estimation, the atomic force microscope technique will be employed.

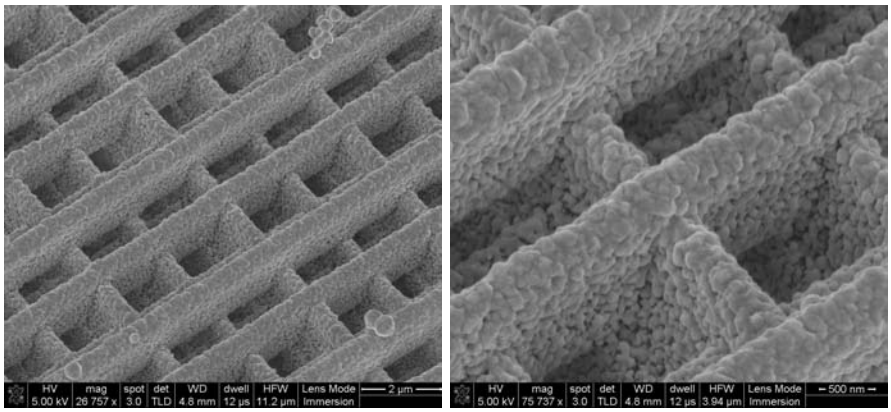


Figure 2: a) A 3D woodpile structure covered by silver after electroless deposition. Silver is deposited also all over the bulk structure and on structure's sidewalls.; b) Zoom in of the 3D structure showing the deposition took place also inside the woodpile.

Following the process optimization on a flat surface we deposited a silver layer on a 3D pattern.

As a sample for thorough checking of deposition on complex 3D structures we chose 2PP polymer woodpile structures.[16] This way we were able to check both the Ag deposition on structure's sidewalls as well as in the bulk volume inside it. The woodpiles are $50 \times 50\mu m$ and have a height of about $16\mu m$ corresponding to 8 periods (32 single layers) of the lattice. Sizes of the bars are $500 \times 500nm$. Such woodpiles possess a face centred tetragonal lattice. We immersed them into the depositing bath and removed after 5 minutes thus obtaining an approximate 50nm layer thickness. The results of silver deposition are presented in figure 2a. The Ag layer is deposited not only on the top of the structure but also on its sidewalls. There is still particle formation in the solution followed by their adhesion to the deposited layer, but it can be further minimized. A zoom-in of the 3D covered structure (Figure 2b) shows the presence of silver layer inside the bulk structure as well. The layer quality when depositing on a 3D structure is different from the one on a plane silica surface. We believe that this dissimilarity is mainly due to the modified surface chemistry of the silica-like polymer used in the 2PP fabrication of the 3D samples.

One should note that the reaction is diffusion driven. Due to this aspect, the silver layer quality is monotonously decreasing from the top to the bottom of the structure (Figure 3a). Nevertheless, the deposition took place everywhere covering the woodpile with a uniform silver coating in one 5-minutes approach only. With further optimization and decreasing of the reaction speed the degradation of coating in depth can be minimized.

The surface pre-treatment is an important part of the process[15]. To prove its significance we tried silver deposition without pre-treatment. As it can be seen from figure 3b in its absence, the silver layer is not adhering to the silica. In the same time this non-adhesion shows that, if needed, the silver can be selectively deposited on a structure by deliberate pre-treatment of the surface.

The obtained results are easily reproduced on various samples of different dimensions as long as the deposition conditions are the same.

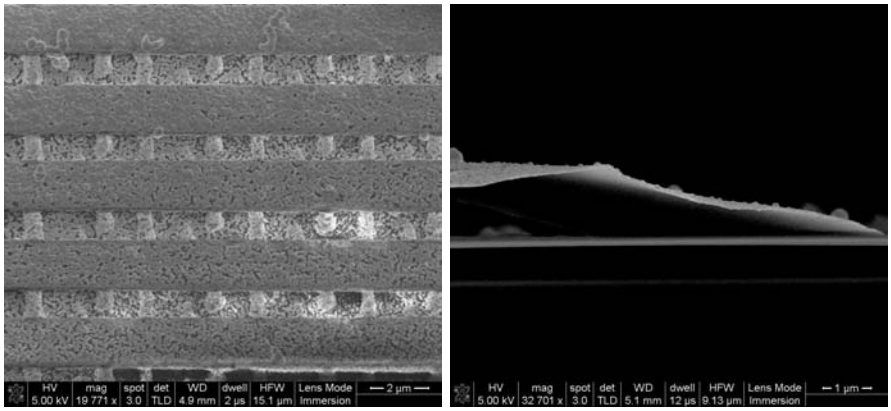


Figure 3: a) Sidewall SEM image of the woodpile. As can be seen, the deposition takes place all through the depth of the woodpile crystal. Here 5 periods in the vertical direction are presented.; b) An example of weak adhesion of the silver layer to the untreated silica surface. It illustrates the importance of pre-treatment for a good adhesion.

3. OPTICAL CHARACTERIZATION

The first measures were performed on the non-covered woodpile structures. We tested transmission of several woodpiles located in different parts of the wafer. The typical spectrum (Figure 4) shows transmission dips around 1100 nm and 1400 nm, which are repeatedly appearing in transmission through randomly chosen woodpile crystals. These dips are interpreted as high-order Bragg reflection peaks (or stop zones) occurred in a polymer woodpile structure as a 3D photonic crystal.[17]

After coating with metal, the signal level just in the central part of the structure dropped to the noise level thus showing a huge decrease in transmission. This decrement of transmission was anticipated due to the substantial number of the woodpile periods completely covered with silver. Meanwhile it confirms implicitly the complete silver deposition inside the bulk woodpile.

In order to obtain a measurable signal, we moved the incident beam toward the border of the woodpile. In this configuration the transmitted signal is increasing while moving from the center ($y = 60nm$) to the borders of the structure ($y = 20nm$ *and* $100nm$) for then to decrease rapidly when moving away from the structure (Figure 5a). After further investigation, we reached

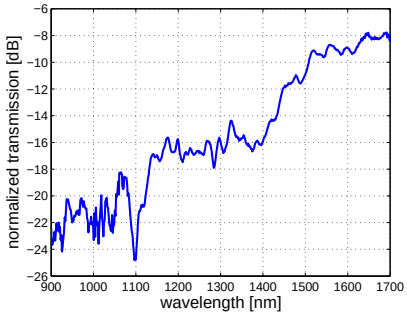


Figure 4: The obtained spectra of a polymer woodpile. The two dips at 1100 and 1400nm are identified as Bragg reflection peaks of the woodpile structure.

the conclusion that such behavior is due to the deposition characteristics. Since the reaction is diffusion driven, the sample presents a depleted region at the interface between the woodpile and the substrate. Owing to this depleted region, the transmission increases at the woodpile's border thus explaining the overall transmission spectra shape.

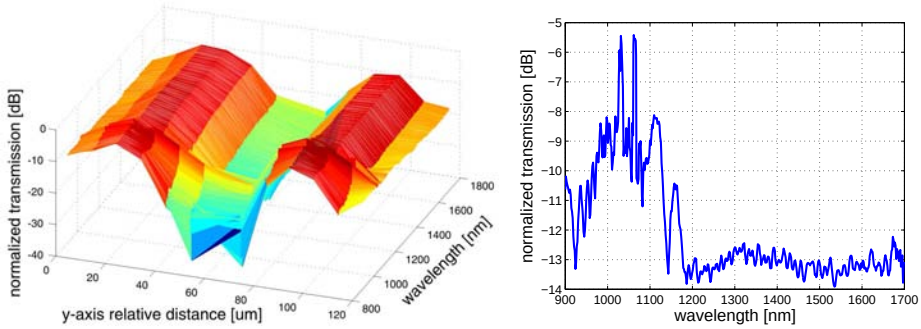


Figure 5: a) The spectra obtained while scanning the sample in the y-axis. The two symmetrical transmission peaks are clearly visible at structure's edges ($y = 20nm\ and\ 100nm$); b) The spectrum at the border of silver-covered woodpile structure. As it can be seen, a wide transmission peak centers at 1050nm is present and overimposed on several other narrow ones.

A typical transmission spectrum on the border of the structure is represented in figure 5b. As it can be seen there is a broad peak in the 900-1100nm range with a pronounced level of transmitted signal, which cannot be assigned to the metallized photonic crystal behavior. We attributed this peak to the coupling of light to surface plasmon polariton (SPP) modes existing on the sidewalls of the woodpiles. SPPs modes transmit energy to the bottom of the structure signal and couple back to the optical modes, so that the signal is detected by the collecting fibre. Unfortunately, any interpretation at 1100 and 1400 nm in concern to the woodpile structure Bragg peaks is impossible. This pronounced feature of broad band with enhanced transmission is not endemic for one particular woodpile crystal, but is statistically supported by observation of 8 woodpile structures in different parts of the array.

4. CONCLUSION

One of the main bottlenecks in advancing the fabrication of metamaterials is due to the difficulty of realizing isotropic, cost effective 3D deposition of metals on a desired structure. By using a combination of electroless deposition and 2PP techniques we believe that a viable solution for fabricating 3D bulk metamaterials can be found. In this work we present an optimized method for depositing silver on silica and silica-like substrates.

Such technique is not limited to the metamaterials field but it can be used for other research areas as well where depositing of metals are required. We think that the technique reported here bears a great potential in many aspects of metal deposition in nanophysics.

The characterization of the polymer woodpile structures was performed both topologically and optically. The optical characterization shows huge behavioral difference with respect to the uncoated polymer structure. Such behavior is probably due both to the decrease in transmission spectra and to the existence of propagating surface plasmon polaritons on the sidewalls of the

structure. The broad enhanced transmission band is an interesting effect that should be explained by further simulation and analysis of the finite metallized woodpile structures.

ACKNOWLEDGMENT

R. Malureanu, A. Andryieuski, A. Lavrinenko acknowledge partial financial support from NIMbus project funded by the Danish Research Council for Technology and Production Science. W. Cheng, R. Kiyan, B. Chichkov acknowledge the financial support of the Cluster of Excellence QUEST.

REFERENCES

1. Campion, A. and P. Kambhampati, "Surface-enhanced Raman scattering," *Chem. Soc. Rev.*, Vol. 27, 241 – 250, 1998.
2. Shalaev, V. M., "Transforming light ," *Science*, Vol. 322, 384 – 386, 2008.
3. Schurig, D., J.J. Mock, B.J. Justice, S.A. Cummer, J.B. Pendry, A.F. Starr and D.R. Smith, "Metamaterial Electromagnetic Cloak at Microwave Frequencies," *Science* Vol. 341, 977 – 980, 2006.
4. Scheibel, T., R. Parthasarathy, G. Sawicki, X.-M. Lin, H. Jaeger and S.L. Lindquist, "Conducting nanowires built by controlled self-assembly of amyloid fibers and selective metal deposition," *PNAS* Vol. 100, 4527 – 4532, 2003.
5. Lal, S., S.E. Clare and N.J. Halas, "Nanoshell-Enabled Photothermal Cancer Therapy: Impending Clinical Impact," *Acc. Chem Res.*, Vol. 41, 1842 – 1851, 2008.
6. Shelby, R. A., D.R. Smith, S.C. Nemat-Nasser and S. Schultz, "Microwave transmission through a two-dimensional, isotropic, left-handed metamaterial," *Appl. Phys. Lett.*, Vol. 78, 489 – 491, 2001.
7. Enkrich, C., M. Wegener, S. Linden, S. Burger, L. Zschiedrich, F. Schmidt, J.F. Zhou, Th. Koschny and C.M. Soukoulis, "Magnetic Metamaterials at Telecommunication and Visible Frequencies," *Phys. Rev. Lett.*, Vol. 95, 203901, 2005.
8. Valentine, J., S. Zhang, T. Zentgraf, E. Ulin-Avila, D.A. Genov, G. Bartal and X. Zhang, "Three-dimensional optical metamaterial with a negative refractive index", *Nature*, Vol. 455, 376 – 379, 2008.
9. Liu, N., H. Guo, L. Fu, S. Kaiser, H. Schweizer and H. Giessen, "Three-dimensional photonic metamaterials at optical frequencies ," *Nature Materials*, Vol. 7, 31 – 37, 2008.
10. Maruo, S., O. Nakamura and S. Kawata, "Three-dimensional microfabrication with two-photon-absorbed photopolymerization", *Opt. Lett.*, Vol. 22, 132 – 134, 1997.
11. Serbin, J., A. Ovsianikov and B. Chichkov, "Fabrication of woodpile structures by two-photon polymerization and investigation of their optical properties," *Opt. Exp.*, Vol. 12, 5221 – 5228, 2004.
12. Alú, A. and N. Engheta, "The quest for magnetic plasmons at optical frequencies," *Opt. Exp.* Vol. 17, 5723 – 5730, 2009.
13. Andryieuski, A., R. Malureanu and A. Lavrinenko, "Nested structures approach in designing an isotropic negative-index material for infrared", *JEOS - Rapid Publications*, Vol. 4, 09003, 2009.
14. Rill, M. S., C. Plet, M. Thiel, I. Staude, G. Von Freymann, S. Linden and M. Wegener, "Photonic metamaterials by direct laser writing and silver chemical vapour deposition," *Nature Materials*, Vol. 7, 543 – 546, 2008.
15. Furness, R. W., *The practice of plating on plastics* Teddington press, Surrey, U.K. 1968
16. Lin, S. Y., J.G. Fleming, D.L. Hetherington, B.K. Smith, R. Biswas, K.M. Ho, M.M. Sigalas, W. Zubrzycki, S.R. Kurtz and J. Bur, "A three-dimensional photonic crystal operating at infrared wavelengths," *Nature*, Vol. 394, 251 – 253, 1998.
17. Deubel, M., M. Wegener, S. Linden and G. von Freymann, "Angle-resolved transmission spectroscopy of three-dimensional photonic crystals fabricated by direct laser writing," *Appl. Phys. Lett.*, Vol. 87, 221104, 2005.

Omega-shaped Stereometamaterials

R.Alaee[1], and K.Moussakhani[2]
[1]Dept. of Electrical Engineering, Amirkabir University of Technology, Iran
[2]Dept. of Electrical and Computer Engineering, McMaster University, Canada
rasoul.alaee@gmail.com

Abstract- Inspiring by concept of stereochemistry, stereometamaterials have been introduced recently. In this paper, omega-shaped stereometamaterials have been investigated. The transmittances of different twisted angles have been obtained. In order to understanding the polarization control of stereometamaterials, the phase difference of one layer stereo-omega dimer metamaterials has been analyzed.

1. INTRODUCTION

Metamaterials are artificially structures that have a negative index of refraction and due to these properties, they have recently attracted worldwide research interest in optics, physics, engineering, chemistry, and material science. In 1968, Veselago found many of fundamental reversed electromagnetic properties of metamaterials such as Snell's law, Cerenkov radiation and Doppler effect. The first metamaterials demonstrated in microwave frequencies was a combination of Split Ring Resonator (SRR) and thin metallic wires [2]. Inspiring by work of Smith *et al.* [2], many variations of Negative Index Metamaterials (NIMs) with different structures have been investigated theoretically and experimentally in microwave and optical frequency ranges. The electromagnetic properties of metamaterials are determined by changing the size, geometry and the shape of resonators. Omega-shaped metamaterials are of special interest due to their interesting electromagnetic properties [4]. These artificial metamaterials were firstly proposed by Engheta [3] and have bianisotropic characteristics and also named as pseudochiral media.

In analogy to stereoisomers in chemistry, stereometamaterials concept has been introduced recently [1]. This concept is related to spatial arrangements of elements of metamaterials. Stereometamaterials could have many applications such as optical polarization control. In [1] a set of stereometamaterials in which unit cell consists of two stacked split-ring resonator (SRRs) with various twist angles theoretically and experimentally has been studied. Twisting the orientation of layers in a U-shaped metamaterial provides a novel way of tailoring their optical properties.

Inspired by work of Liu et al. for SRRs stereometamaterials and due to special optical characteristics of omega shaped metamaterials, optical properties of omega-shaped stereometamaterials have been investigated in this paper. We studied a set of stereometamaterials, each having unit cell consisting of two identical omega-shaped metamaterial or two identical atoms. These atoms have different optical properties by altering twist angles. Moreover, we have studied the phase difference of the two components of transmitted wave for the 90^0 twisted omega dimer for the one of stereo-omega dimer MTMs which can be the helpful in construction of polarization control element.

2. OMEGA-SHAPED STEREOMETAMATERIALS DESIGN AND SIMULATION

The geometry of omega-shaped stereometamaterials is depicted in Figure.1. The parameters as given in the

Figure.1 are R=110 nm, w=50 nm, H=200 nm and periods in x, and y direction is 600nm. Each unit cell consists of two spatially separated omega-shaped metamaterials. In order to understanding the resonance behavior and coupling mechanisms, different twisted angles of omega-shaped metamaterials are presented. The twisted angle of two omega-shaped metamaterials is φ. Optical properties of the twisted metamaterials have been obtained by simulation of one cell with PEC and PMC boundaries which perpendicular respectively on incident E and H fields to model on layer infinite structure in x and y direction. The magnitudes of transmittance of one cell stereometamaterials for the different twisted angles obtained by a full wave simulation, time domain simulation software (CST),. In the simulation, the gold is described by Drude model with plasma frequency $\omega_p = 1.3 \times 10^{16} s^{-1}$ and scattering frequency $\omega_c = 4.08 \times 10^{13} s^{-1}$.

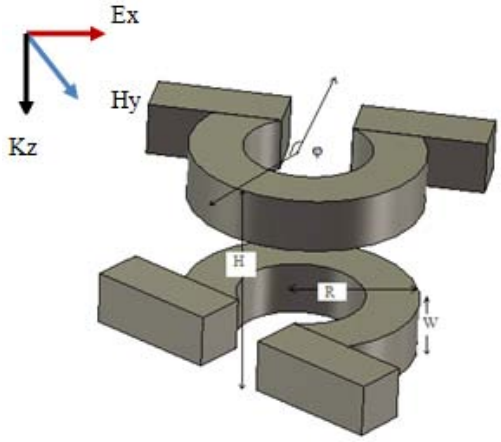


Figure 1: Geometry of omega-shaped stereometamaterials

In Figure.2, Figure.3 and Figure.4 transmittances for O^0, 90^0,and $18O^0$ twisted angles of omega-shaped stereometamaterials have been depicted respectively. For each twisted angle, there are two observable resonances(ω^- and ω^+). The incident field induced current along the two omega-shaped therefore we have magnetic dipole moments in each omega-shaped constituent. As shown in Figure.2, the magnetic dipoles excited in the two omega-shaped are aligned anti-parallel and parallel at resonance ω_0^- and ω_0^+ respectively. For 90^0, and $18O^0$ twisted angles, the magnetic dipole in the two omega-shaped are aligned parallel anti-parallel at resonance $\omega^-$and ω^+ respectively.

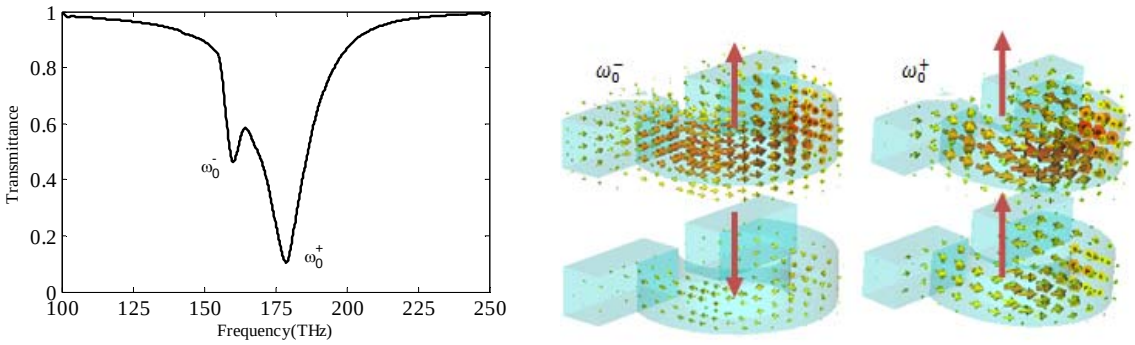


Figure 2: Transmittance of omega-shaped stereometamaterials at O^0 and also current distributions. The red arrows represent direction of magnetic dipoles for resonance frequencies (ω_0^- and ω_0^+).

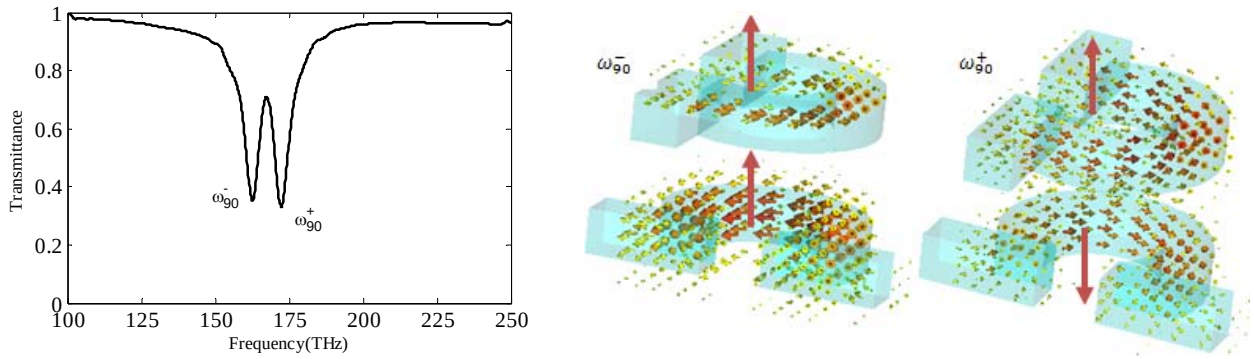


Figure 3: Transmittance of omega-shaped stereometamaterials at 90^0 twisted angle. The red arrows represent direction of magnetic dipoles for resonance frequencies ($\boldsymbol{\omega_{90}^{-}}$ and ω_{90}^{+}).

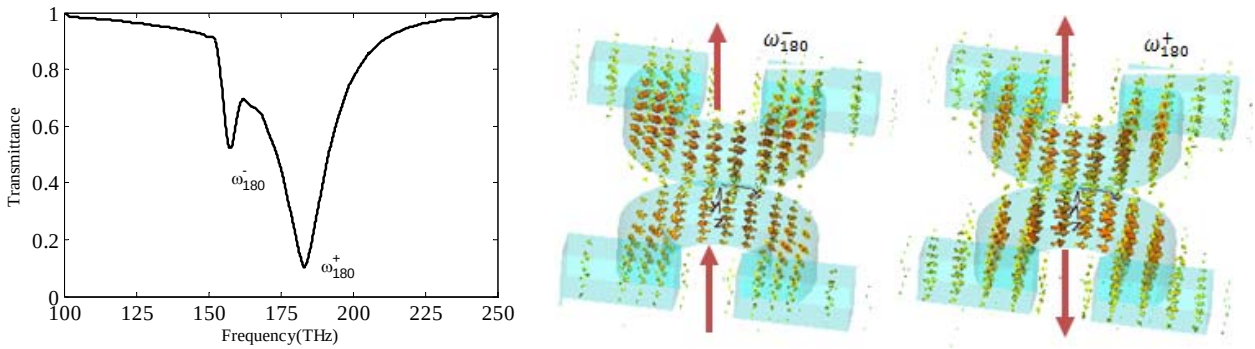


Figure 4: Transmittance of omega-shaped stereometamaterials at 180^0 twisted angle. The red arrows represent direction of magnetic dipoles for resonance frequencies (ω_{180}^{-} and ω_{180}^{+}).

Twisting dispersion of stereo-omega stereometamaterials is shown in Fiqure.5. By increasing the twisting angle, the higher frequency decrease and lower frequency increase and crossing is occurred approximately at 65^0. There is slightly difference between the twisting dispersion of U-shaped and omega-shaped stereometamaterials. In the U-shaped stereometamaterials in [1], the avoiding crossing is observed, whereas in omega-shaped we have crossing point. The avoiding crossing in U-shaped stereometamaterials is happened due to higher-order electric multipolar interactions [1].

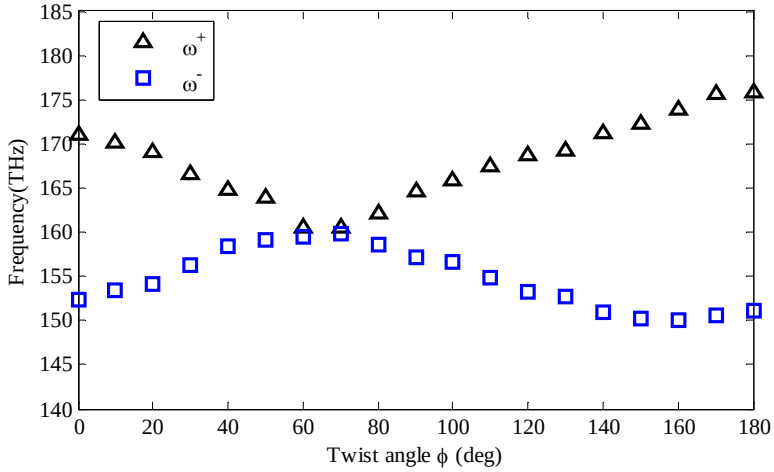


Figure 5: Twisting dispersion of stereo-omega dimer metamaterials

Fiqure.6 shows the phase difference of transmitted wave $\Delta\phi = \phi_y - \phi_x$ for the two opposite propagation directions ($k(z)$ and $k(-z)$)) for one layer of the twisted omega-shaped metamaterials. The phase difference of transmitted wave depends on direction of propagation. By increasing the number of layers of this twisted metamaterials, we can control the polarization of transmitted wave. Therefore, the polarization of transmitted wave is tunable by using appropriate layers of omega-shaped stereometamaterials.

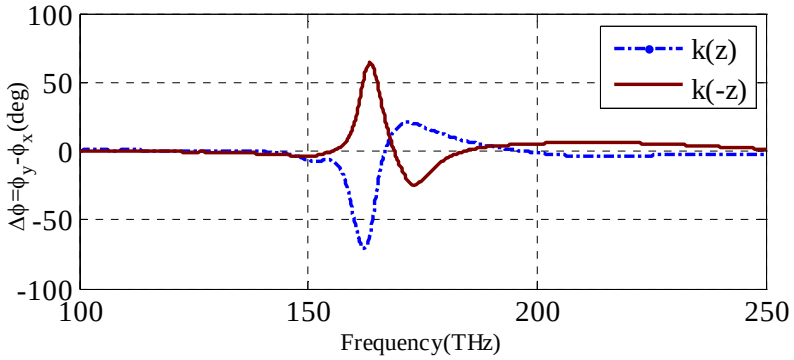


Figure 6: The phase difference of the two components for the twisted omega shaped metamaterials

4. CONCLUSIONS

Stereometamaterials present a novel method for tailoring the electromagnetic properties of metamaterials. For this reason, we have studied the novel optical properties of omega-shaped stereometamaterials. The transmission characteristics of stereometamaterials are reported in different twist angles. Omega-shaped stereometamaterials have two frequency resonances that are considered for different angles. One of the obvious applications of these twisted metamaterials is optical polarization control, by using different layers of twisted metamaterials to have appropriate phase shift. With two or three layers of this twisted metamaterials, we can create polarization rotation devices. It will also be remarkable to study optical properties of complex stereometamaterials.

REFERENCES

1. Liu.N, H.Liu, S.Zhu, H.Giessen, “Stereometamaterials,” *Nature Photonics*, Vol. 3, 157-162, 2009.
2. Smith.D. R., W.J.Padilla, D.C.Vier, S.C.Nemat-Nasser, and S.Schultz, “Composite medium with simultaneously negative permeability and permittivity,” Phys. Rev. Lett. 84, 4184–4187, 2000.
3. Saadoum.M.M.I, N.Engheta, “A reciprocal phase shifter using novel pseudochiral or omega medium,” *Microw.Opt.Technol.Lett.5*, 184, 1992.
4. Tretyakov.S.A, C.A.Simovski, M.Hudlicka, “Bianisotropic route to the realization and matching of backward-wave metamaterial slab,” Phys.Rev. B, 75, 153104, 2007.

Thin-film polarizer made of heterogeneous medium with uniformly oriented silver nanoparticles

S. G. Moiseev
V.A. Kotelnikov Institute of Radio Engineering and Electronics of Russian Academy of Sciences, Ulyanovsk Branch, Russia
Ulyanovsk State Technical University, Russia
serg-moiseev@yandex.ru

Abstract- The optical properties of a composite medium comprised of a transparent host and uniformly oriented prolate silver nanoparticles are investigated theoretically. The results demonstrate that it is possible to fabricate a thin-film polarizer with high performance in transmission and reflection in the visible region of light.

1. INTRODUCTION

The promising candidates for a design of structures with extraordinary optical properties are plasmonic materials [1-4]. Collective electronic excitations called plasmons lead to strong absorption of light in such artificial media. For practical applications, it is important that the absorption of the composite medium incorporating metallic nanoparticles can be controlled by careful selection of geometric parameters of nanoparticles. By selecting distributions of the form of metallic nanoparticles, it is possible to achieve absorption of electromagnetic radiation in specified spectral regions of visible or near IR radiation [5]. An additional effective way of the plasmon resonance control is by spatial arrangement of metal-dielectric nanocomposites, for example, forming the multilayer systems consisting of metallic nanoparticles separated by dielectric layers [6]. It is assumed that such composite materials with controlled absorption of light can be used as cut-of filters and high-absorbing coatings.

In this paper, we explore the possibility of realizing thin-film plasmonic polarizer in the visible region. In our design, the high polarization contrast of composite layer is obtained by using uniformly oriented silver nanoparticles of ellipsoidal shape. The paper is organized as follows. In section 2, the appropriate aspect ratio of silver nanoparticles is determined. In section 3, parameters of metal-dielectric composite layer required to get high polarization contrast, are calculated on the basis of the well known theory of dielectric function of a heterogeneous medium. The applicability of the effective medium model for describing the optical properties of the composite layer is verified using full-wave finite-element simulations.

2. PLASMON RESONANCES IN SILVER NANOPARTICLES

Let V be the particle volume; ε_p be the particle dielectric constant; ε_h be the dielectric constant of a surrounding host medium. In the case of a spheroid and an applied electric field oriented along a spheroid axis, the static polarizability of nanoparticle is

$$\alpha = \frac{V}{4\pi} \frac{\varepsilon_p - \varepsilon_h}{L(\varepsilon_p - \varepsilon_h) + \varepsilon_h}, \tag{1}$$

where L is the geometrical factor (factor of depolarization) that accounts for the shape of a particle [7]. In the long-wavelength limit, factor L is a real value, that depends only on the ratio ξ of the length of polar semi-axis a and equatorial semi-axis b of spheroid, $\xi = a/b$.

As follows from Eq. (1), the plasmon resonance frequency depends on the form of the particle. If a transparent dielectric is used as surrounding host medium, the resonance wavelength λ_{res} of metal spheroid can be estimated by using simple algebraic equation

$$\mathrm{Re}\left[\varepsilon_p(\lambda)\right] + \frac{1-L}{L}\varepsilon_h(\lambda) = 0. \qquad (2)$$

In the case of spheroidal ($\xi \neq 1$) silver nanoparticle, Eq. (2) has two roots corresponding to two polarizations of the electromagnetic field. One root tends to longer wavelengths due to the absorption of light polarized parallel to the long axis of the spheroid (the case of *parallel polarized light*). The other root shifts to shorter wavelengths due to the absorption of light polarized parallel to the short axis of the spheroid (the case of *perpendicular polarized light*). The more different shapes of nanoparticles from the spherical ones, the more is difference in the resonance wavelengths corresponding to two polarizations of the electromagnetic field.

The shape of nanoparticles can be selected so as to observe only one plasmon resonance in the visible region of light. According to Fig. 1, this condition complies with $\xi < 0.85$ or $\xi > 1.5$. In this paper, we consider the case of prolate particles of aspect ratio $\xi = 3$. In this case, the plasmon resonance in the visible region corresponds to the field component polarized parallel to the polar semi-axis of the spheroid.

It should be noted that throughout this communication, size-dependence of the dielectric function ε_p of small silver nanoparticles is taken into account in terms of the model of limitation of the electron mean free path [8].

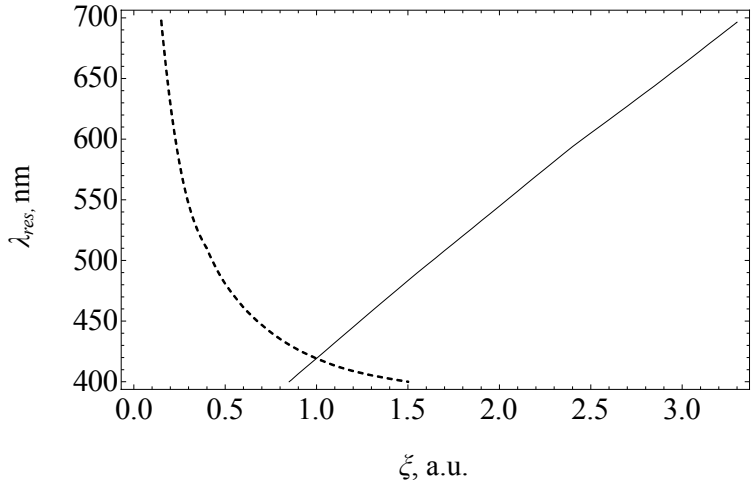


Figure 1: Dependence of the plasmon resonance wavelength λ_{res} of a silver spheroid on the aspect ratio ξ obtained from Eq. (2) for parallel (*solid curve*) and perpendicular (*dashed curve*) polarized light. Dielectric function of the matrix ε_h= 2.25.

3. COMPOSITE LAYER WITH NEEDLE-LIKE SILVER INCLUSIONS

Let us assume that a layer of the composite material with uniformly oriented prolate silver spheroids has been deposited on surface of transparent medium. Let light be incident normally on this layer from vacuum. To

provide maximum optical anisotropy, nanoparticles have to be oriented parallel to the plane interface between media.

For modeling the effective optical characteristics of composite medium with uniformly oriented silver spheroids we shall use a well-known analytical formula of the Maxwell–Garnett approach for the dielectric function ε of mixture

$$\frac{\varepsilon - \varepsilon_h}{L(\varepsilon - \varepsilon_h) + \varepsilon_h} = \eta \frac{\varepsilon_p - \varepsilon_h}{L(\varepsilon_p - \varepsilon_h) + \varepsilon_h}, \qquad (3)$$

where η is the volume concentration of nanoparticles (*filling factor*). Then, the intensity reflection coefficient R and the intensity transmission coefficient T of plane-parallel plate with silver inclusions can be determined from the well-known Airy equation [9]. Using the relation (3) and Airy equation, the reflectance and transmittance can be calculated for arbitrary values of filling factor η and layer thickness h. Results of calculation show that for 600 nm < λ < 650 nm, values of $\eta \sim 0.1$ and $h \approx 100 - 150$ nm are optimal from the point of view of the posed problem.

Indeed, as one can see from Fig. 2a, for $\eta = 0.1$ and $h = 130$ nm composite layer exhibits high polarization contrast. For radiation of the region from 570 nm to 680 nm, this layer absorbs the parallel polarized light, and for the perpendicular polarized light the layer is transparent. From the practical point of view it is interesting that high reflectance corresponds with low transmittance and vice versa. It follows from Fig. 2a that the reflectance and transmittance of this layer possess the values either more than 0.7 or less than 0.1. So, such polarizer can also be used as a polarizing beam splitter with high performance in transmission and reflection.

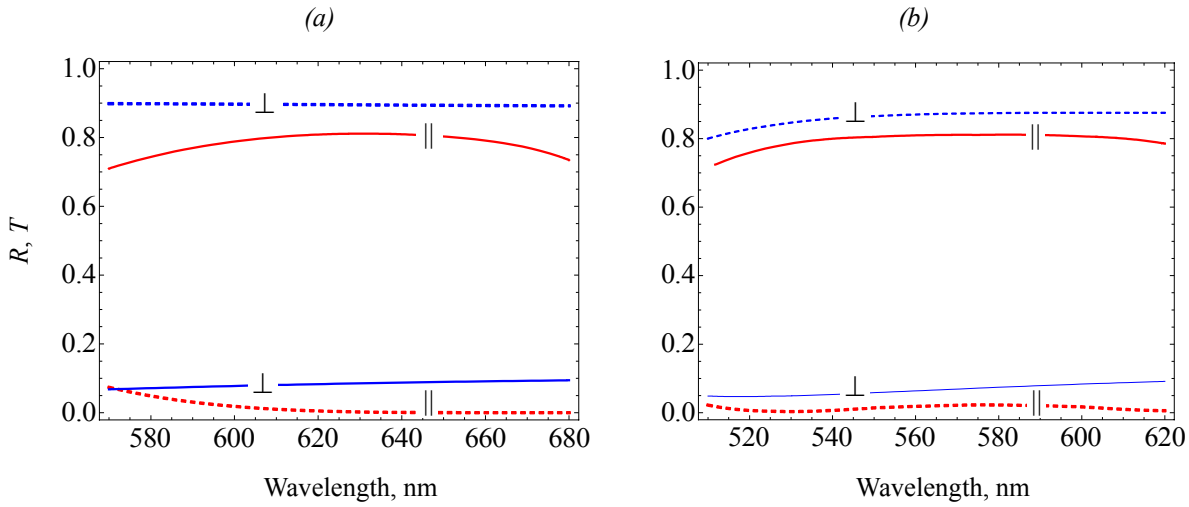


Figure 2: Reflectance (*solid curves*) and transmittance (*dashed curves*) of parallel (||, *red curves*) and perpendicular (⊥, *blue curves*) polarized light of composite layer with uniformly oriented prolate silver spheroids on glass substrate. *Left plot (a)* shows the results of calculation according to electrostatic theory, and *right plot (b)* shows the results of simulation based on the finite elements method. The computational parameters are $\eta = 0.1$, $\xi = 3$, $\varepsilon_s = \varepsilon_h = 2.25$, $h = 130$ nm.

It was shown in [10,11] that *(i)* for moderate volume fraction of inclusions $\eta < 1/3$, Maxwell–Garnett model can be productively used for estimation of the parameters of the metal-dielectric nanocomposites, and *(ii)* during strong electrodynamical interaction of metal inclusions with the field of external light wave, the results obtained in the electrostatic approximation require refinement. In present work, we use three-dimensional full-wave simulations with the commercial finite-element solver COMSOL MULTIPHYSICS [12] to verify the applicability of the electrostatic approximation for describing the optical properties of thin composite layer. The results of exact electrodynamic calculations are shown in Fig. 2b.

Contrasting parts (*a*) and (*b*) of Fig. 2, the following conclusion can be made. The error that appears as a result of using the electrostatic approximation under conditions of plasmon resonance excitation leads to shift and insignificant distortion of curve corresponding to the parallel polarized light. However, the transmission and reflection coefficients calculated by two methods behave identically. Thus, the Maxwell–Garnett approach can be useful in developing of principally new materials with unique optical properties for polarizers, optical filters etc.

4. CONCLUSIONS

Polarization-dependent spectral reflectance and transmittance of composite layer comprised of a transparent host and uniformly oriented prolate silver nanoparticles are investigated theoretically. An analysis based on the Maxwell-Garnett theory and results of three-dimensional full-wave simulations shows that it is possible to fabricate an ultra-thin polarizing structure with high performance in transmission and reflection. Note that currently developed physical and chemical techniques for preparation of metal-dielectric composites allow controlling of the shape of nanoparticles [13-15]. By selecting the proper shape of the nanoparticles or choosing matrices with different refractive indexes it is possible to achieve the polarization contrast at specified spectral regions.

It should be noted that we considered in this paper the normal incidence of an electromagnetic wave on the layer. Generally speaking, the optical properties of the composite layer also depend on the angle of incidence. A separate study will be devoted to an analysis of this problem, as well as to developing of an adequate theory of the optical response of thin composite layers.

ACKNOWLEDGEMENT

The work was supported by the Federal Education Agency (Rosobrazovanie) through project contract # P1423 within the framework of the Federal Target Program ‘Science, Academic and Teaching Staff of Innovative Russia for 2009-2013’.

REFERENCES

1. Oraevskii, A. N., I. E. Protsenko, “High refractive index and other optical properties of heterogeneous media,” *JETP Lett*., Vol. 72, No 9, 445-448, 2000.
2. Zayats, A. V. and I. I. Smolyaninov, “Near-field photonics: surface plasmon polaritons and localized surface plasmons,” *J. Opt. A: Pure Appl. Opt.*, Vol. 5, S16-S50, 2003.
3. Sukhov, S. V., “Nanocomposite material with the unit refractive index,” *Quantum Electron.*, Vol. 35, 741-744, 2005.
4. Kravets, V. G., F. Schedin, and A. N. Grigorenko, “Plasmonic blackbody: Almost complete absorption of

light in nanostructured metallic coatings," *Phys. Rev. B*, Vol. 78, 205405-10, 2008.
5. Protsenko, I. E., O. A. Zaimidoroga, V. N. Samoilov, "Heterogeneous medium as a filter of electromagnetic radiation," *J. Opt. A: Pure Appl. Opt.*, Vol. 9, 363-368, 2007.
6. Kachan, S., O. Stenzel, A. Ponyavina, "High-absorbing gradient multilayer coatings with silver nanoparticles," *Appl. Phys. B*, Vol. 84, 281-287, 2006.
7. Bohren, C. F., D. R. Huffman, *Absorption and Scattering of Light by Small Particles*, Wiley, New York, 1998.
8. Kreibig, U., M. Vollmer, *Optical Properties of Metal Clusters*, Springer, Berlin, 1995.
9. Born, M., E. Wolf, *Principles of Optics*, Cambridge U. Press, 2002.
10. Moiseev, S. G., "Active Maxwell–Garnett composite with the unit refractive index," *Physica B*, 2010, doi:10.1016/j.physb.2010.01.045.
11. Moiseev, S. G., E. A. Pashinina, S. V. Sukhov, "On the problems of transparency of metal-dielectric composite media with dissipative and amplifying components," *Quantum Electron.*, Vol. 37, 446-452, 2007.
12. COMSOL Multiphysics, </http://www.comsol.com/products/multiphysics/>.
13. Wang, Debao, Caixia Song, Zhengshui Hu and Xiaodong Zhou, "Synthesis of silver nanoparticles with flake-like shapes," Materials Letters, Vol. 59, 1760-1763, 2005.
14. Hofmeister, H., W.-G. Drost and A. Berger, "Oriented prolate silver particles in glass – characteristics of novel dichroic polarizers," *Nanostructured Materials*, Vol. 12, 207-210, 1999.
15. Zhang, Wanzhong, Xueliang Qiao, Jianguo Chen and Qingyuan Chen, "Self-assembly and controlled synthesis of silver nanoparticles in SDS quaternary microemulsion," *Materials Letters*, Vol. 62, 1689-1692, 2008.

Effects of Acoustic Band Gap on Stimulated Brillouin Scattering in Microstructured Optical Fiber

Xinzhi Sheng[1,2*], Di Wu[3], Jian Wang[1,2], Yin Wang[3], and Chenying Bao[3]

[1]Key Laboratory of Luminescence and Optical Information, Ministry of Education, PR China

[2]Institute of Optical Information Science and Technology, School of Science, Beijing Jiaotong University, Beijing 100044, PR China

[3]Department of Physics, School of Science, Beijing Jiaotong University, Beijing 100044, PR China

[*]corresponding author: xzhsheng@bjtu.edu.cn

Abstract- We study numerically effects of acoustic band gap on SBS in MOFs by using plane wave expansion method. For the typical kind of MOFs with hexagonally arrayed circular air holes, the band gap of acoustic wave of XY mode appears only when the air holes' filling rate is greater than a threshold value, and the upper and lower boundary values of the band gap decrease with the increasing of the air holes' filling rate. Numerical results show that the Stokes pulse advancement can be achieved in the gain saturation regime.

There is a great deal of recent interest in slow light, where the group velocity of a pulse is much less than the speed of light in vacuum[1-3]. Controllable slow light can be used in applications such as optical buffering, variable true time delay and optical information processing[4-5]. Unlike Electromagnetically induced transparency and coherent population oscillations, an amplifying resonance via stimulated Brillouin scattering (SBS) can be created at any wavelength. The use of microstructured optical fibers (MOFs) as the medium for SBS may offer additional advantages such as acoustic band gap (ABG) waveguide due to the profound effects of their periodic or quasiperiodic structure on wave propagation, and a low pump-power requirement due to long interaction lengths and small mode areas[6-7].

In this paper, we analyze effects of ABG on SBS in MOFs both analytically and numerically. The spatiotemporal evolution of stimulated SBS in MOFs' periodic or quasiperiodic structure and some aspects of the influence that nonlinear and kinetic effects have on the evolution of SBS were studied. A 2-dimensional analytical model based on a fluid description of MOFs was developed initially.

Various types of wave functions have been seen, including extended state, self-similar state with a power-law decay and confined state. It was found that the threshold intensity of the absolute instability and the steady-state spatial growth rate of the convective instability are both independent of the scattering angle. However, the saturation time of the convective instability exhibits a strong inverse dependence on the

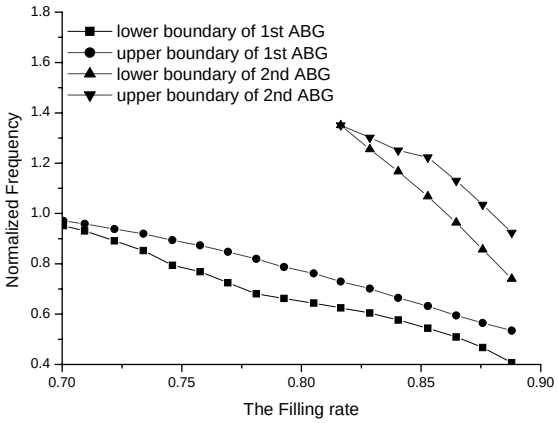


Fig.1 Representations of the boundary values of the lowest and second lowest acoustic band gaps vs the air filling rate

scattering angle. For the typical kind of MOFs with hexagonally arrayed circular air holes, ABG of XY mode appears only when the air holes' filling rate is greater than a certain threshold value, and the upper and lower boundary values of ABG decrease with the increasing of the air holes' filling rate as shown in Fig.1.

Due to the structure of the acoustic wave equation, the engineering of acoustic band gaps is much more efficient than that of photonic band gaps. For elastic waves, a large absolute band gap can be enhanced or created by inserting air inclusions in a two-component elastic phononic crystal or quasicrystal with small density contrast and filling fraction. The positions of the insertion are chosen to suppress the shear potential energy of the acoustic branches and lower their frequencies. The long-range order has been proved important for the formation of gaps at low frequencies. Large full gaps are found owing to its high symmetry. However, the gap structure evolves with the sample size. A gap can be enhanced or created by altering the microstructure according to the field-energy distributions of the Bloch states at the band edges as well as their derivatives.

We also study time delay and pulse broadening of the Stokes pulse in the small-signal and saturation regimes. Numerical results show that pulse advancement can be achieved in the gain saturation regime, which compliments the recent experimental demonstration of slow light in an optical fiber. The SBS reflectivity is shown to depend sensitively on the frequency mismatch between the light wave used to seed the instability and the incident laser. In order to assess the effects that the finite size of the laser beam has on SBS, wide and narrow laser-beam geometries were considered. It was found that the evolution of SBS was characterized by three parameters: the spatial growth rate in the direction of the Stokes wave, the spatial damping rate of the ion-acoustic wave in the direction of the Stokes wave and the normalized width of the interaction region. SBS can be saturated by the damping or the lateral convection of the ion-acoustic wave, both of which limit the growth of the ion- acoustic wave (directly) and the Stokes wave (indirectly). When the laser intensity is strong enough, simulations differ substantially. It was shown that among various saturation mechanisms such as pump depletion, wavebreaking and generation of ion-acoustic wave harmonics, ion-trapping is the mechanism responsible for the observed differences. A good agreement was obtained for weak laser intensities.

Acknowledgements This work was supported by National Natural Science Foundation of China through Grant No.60672004. Jian Wang, Yin Wang and Chenying Bao were also supported by Nationzal High Technology Research and Development Program through Grant No. 2007AA01Z270.

References

[1] D.J.Gauther, A.L.Gaeta, and R.W.Boyd, "Slow Light From Basics to Futures Aspects," *Photonics Spectra*, pp.44-50, March 2006.

[2] S.E.Harris, J.E.Field, and A. Imamoglu, "Nonlinear Optical Processes Using Electromagnetically Induced Transparency," *Phys. Rev. Lett.*, vol.64, no.10, pp.1107-1110, March 1990.

[3] M.M.Kash *et al*, "Ultraslow Group Velocity and Enhanced Nonlinear Optical Effects in a Coherently Driven Hot Atomic Gas," *Phys. Rev. Lett.*, vol.82, no.26, pp.5229-5232, June 1999.

[4] C.J.Chang-Hasnian, P.-C.Ku, J.Kim, and S.-L.Chuang, "Variable Optical Buffer Using Slow Light in Semiconductor Nanostructures," *Proc. IEEE Photon. Technol. Lett.*, vol.91, pp.1884-1897, 2003.

[5] M.G.Herraez, K.Y.Song, and L.Thevenaz, "Arbitrary-Bandwidth Brilloun Slow Light in Optical Fibers," *Opt. Exp.*, vol.14, no.4, pp.1395-1400, Feb. 2006.

[6] Y.Okawachi *et al*, "Tunable All-Optical Delays via Brilloun Slow Light in an Optical Fiber," Phys. Rev. Lett., vol.94, 2005, 153902.

[7] H.Gersen *et al*., "Real-Space Observation of Ultraslow Light in Photonic Crystal Waveguides," *Phys.Rev.Lett.*, vol.94, no.7, pp.073903-1-073903-4, 2005.

Active coated nano-particles: impact of plasmonic material choice

S. Arslanagic[1*], and R. W. Ziolkowski[2]

[1] Department of Electrical Engineering, Electromagnetic Systems,
Technical University of Denmark, Build. 348, Ørsteds Plads, DK-2800 Kgs. Lyngby, Denmark

[2] Department of Electrical and Computer Engineering, University of Arizona,
1230 E. Speedway Blvd., Tucson, AZ 85721-0104, USA

[*]corresponding author: sar@elektro.dtu.dk

Abstract – The near- and far-field properties of a number of active coated spherical nano-particles excited by an electric Hertzian dipole at optical frequencies are investigated. Their enhanced, as well as reduced, radiation effects are demonstrated and compared.

1. Introduction

Along with numerous studies in the optical frequency regime, current metamaterial-engineering research has demonstrated that including plasmonic materials to achieve a negative permittivity in the spherical shell of a coated nano-particle (CNP) can lead to novel optical properties, such as resonant scattering and transparency, that may be useful for sensor technologies, see *e.g.*, [1] and the works referenced therein. Applications of the corresponding active CNPs, i.e., CNPs with gain included in or near them, have also been considered, such as a version of optical cloaking [2], [3], and the electromagnetic responses of fluorescent molecules in the presence of electrically small particles [4]. While the actual excitations of the active molecules in the above cases were plane waves, an electric Hertzian dipole excitation of a number of active CNPs, all consisting of a silica nano-core impregnated with gain material covered with a plasmonic nano-shell of silver, was investigated in [5], [6], where interesting resonance and transparency effects were reported. The present work reports the extension of these studies to the cases where the involved CNPs utilize different plasmonic materials, such as silver, gold, and copper; and compares their ability to provide the resonant, but also the non-radiating/transparent states. Throughout this work, the time factor $\exp(j\omega t)$, with ω being the angular frequency and t being the time, is assumed and suppressed.

2. Theory

The CNP consisting of a sphere (region 1) of radius r_1, layered by a concentric spherical shell (region 2) of outer radius r_2, is immersed in free space (region 3), with the permittivity, ε_0, permeability, μ_0, and wave number, $k_0 = \omega\sqrt{\varepsilon_0\mu_0} = 2\pi/\lambda$, where λ is the wavelength, see figure 1. It is illuminated by an arbitrarily located and oriented electric Hertizan dipole (EHD) having the dipole moment $\vec{p}_s = \hat{p}_s p_s$ with the orientation $\hat{p}_s$ and complex amplitude p_s [Am]. Regions 1 and 2 are composed of simple (isotropic, homogeneous, and linear), lossy materials with permittivities, permeabilities, and wave numbers given by: $\varepsilon_i = \varepsilon_i' - j\varepsilon_i''$, $\mu_i = \mu_i' - j\mu_i''$, and $k_i = \omega\sqrt{\varepsilon_i\mu_i}$, i=1 and 2, where the branch of the square root will be discussed below. The spherical coordinate system (r,θ,φ), and the Cartesian coordinate system (x,y,z) are introduced such that the origin coincides with the common centers of the spheres. The coordinates of the observation point and the EHD are (r,θ,φ) and (r_s,θ_s,φ_s), respectively.

As to the details of the analytical solution, we refer to [6] and its ref. [23]. Only, its main points are

summarized here. The field due to the EHD is given as an expansion of transverse magnetic (TM) and transverse electric (TE) spherical waves with the known expansion coefficients $a_{nm}^{(c)}$ (TM coefficients), and $b_{nm}^{(c)}$, (TE coefficients), where the constant c depends on the region where the field is determined. Similarly, the unknown fields due to the CNP in the three regions are expanded in terms of TM and TE spherical waves, and involve the unknown TM and TE expansion coefficients $A_{i,nm}$ and $B_{i,nm}$, respectively, where $i = 1,...,4$. Specifically, $A_{1,nm}$ and $B_{1,nm}$ are the expansion coefficients of the field in region 1, $A_{i,nm}$ and $B_{i,nm}$, with $i = 2$ and 3, are those of the field in region 2, and $A_{4,nm}$ and $B_{4,nm}$ are the coefficients of the field in region 3. These coefficients depend on the EHD location, and are easily obtained by enforcing the boundary conditions on the two spherical interfaces, $r = r_1$ and $r = r_2$.

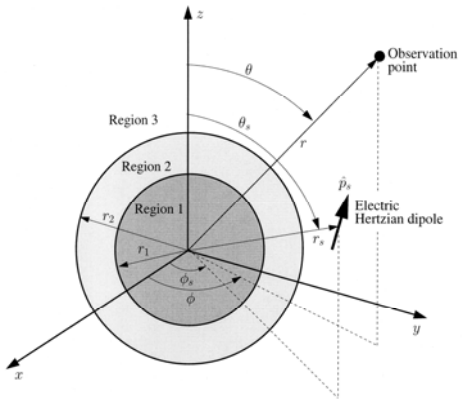


Figure 1: The configuration.

In order to report and compare the resonance phenomena in our active CNPs, the normalized radiation resistance (NRR), which is the radiation resistance of the EHD radiating in the presence of the CNP normalized by the radiation resistance of the EHD radiating in free space, is examined. In mathematical terms, the NRR reads

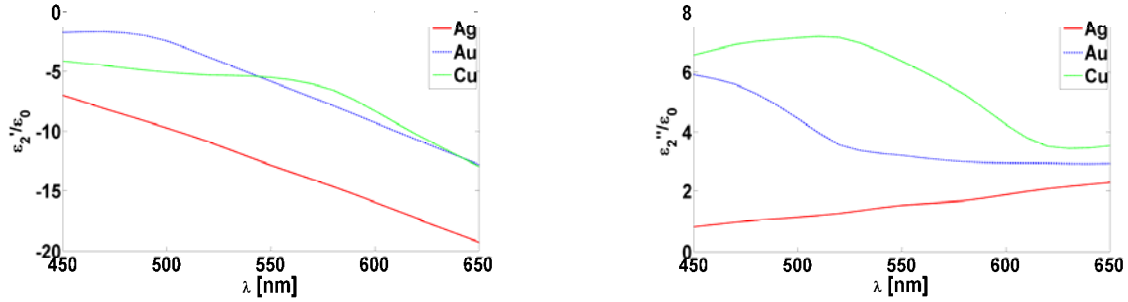
$$NRR = \frac{24\pi^2}{\omega^2 \mu_0 (p_s k_0)^2} \sum_{n=1}^{N_{\max}} \sum_{m=-n}^{n} \frac{n(n+1)}{2n+1} \frac{(n+|m|)!}{(n-|m|)!} \cdot \left(\frac{1}{\varepsilon_0} |\alpha_{nm}|^2 + \frac{1}{\mu_0} |\beta_{nm}|^2 \right), \quad (1)$$

where $\alpha_{nm} = a_{nm}^{(4)} + A_{4,nm}$, $\beta_{nm} = b_{nm}^{(4)} + B_{4,nm}$ if the EHD is located in region 3, and $\alpha_{nm} = A_{4,nm}$, $\beta_{nm} = B_{4,nm}$ if the EHD is located in either region 1 or 2, while $a_{nm}^{(4)}$ and $b_{nm}^{(4)}$ are the TM and TE expansion coefficients, respectively, of the EHD field for $r > r_s$, cf. [6]. Furthermore, the symbol n is the mode number, while $N_{\max}$ is the truncation limit in a practical implementation of the exact infinite summation and is chosen to ensure the convergence of the expansion in (1).

3. Results and Discussions

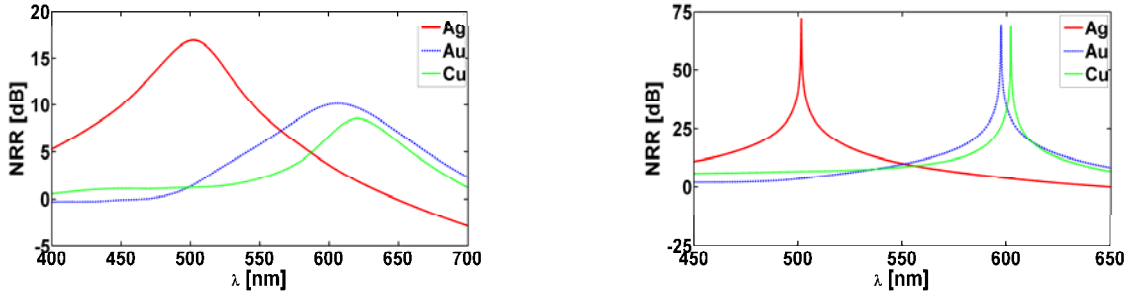
The present work considers three different CNPs. In all cases, region 1 is a silica (SiO_2) nano-core for which the permittivity is modeled by a contribution from the refractive index of silica in the frequency range of interest, $n = \sqrt{2.05}$, and one from the canonical gain model $\varepsilon_1 = (n^2 - \kappa^2 - 2jn\kappa)\varepsilon_0$, where the parameter κ determines the nature of the nano-core: it is lossless (and passive) for $\kappa = 0$, lossy and passive for $\kappa > 0$, and active for $\kappa < 0$, in which case κ is referred to as the optical gain constant. As to the nano-shell (region 2), three different plasmonic materials are considered: silver (Ag), gold (Au), and copper (Cu); their permittivity is denoted by ε_2. The corresponding CNPs are then referred to as the Ag-, Au-, and Cu-based CNPs. The radius of the SiO_2 nano-core is set to $r_1 = 24$ nm, while the outer radius of the nano-shell is set to $r_1 = 30$ nm, resulting in a 6 nm thick nano-shell. Due to the nano-scale dimensions of the CNPs, the size dependence of the Ag, Au, and Cu permittivities must be taken into account. In this regard, empirically determined bulk values of the respective permittivities at optical wavelengths have been used [1], and their real and the negative of the imaginary parts are shown in figures 2(a) and (b) for 6nm thick Ag, Au, and Cu nano-shells. All three nano-shells are rather lossy with the Au one being lossier than the Ag one, and with the Cu one being the lossiest. The real part of each of

these nano-shells attains negative values in the observed wavelength range. Throughout the numerical investigations here, the EHD is taken to be z-oriented and located on the positive x-axis with the coordinates ($r_s, \theta_s = 90^o, \phi_s = 0^o$), and its magnitude is set to $p_s = 5 \cdot 10^{-9}$ Am .



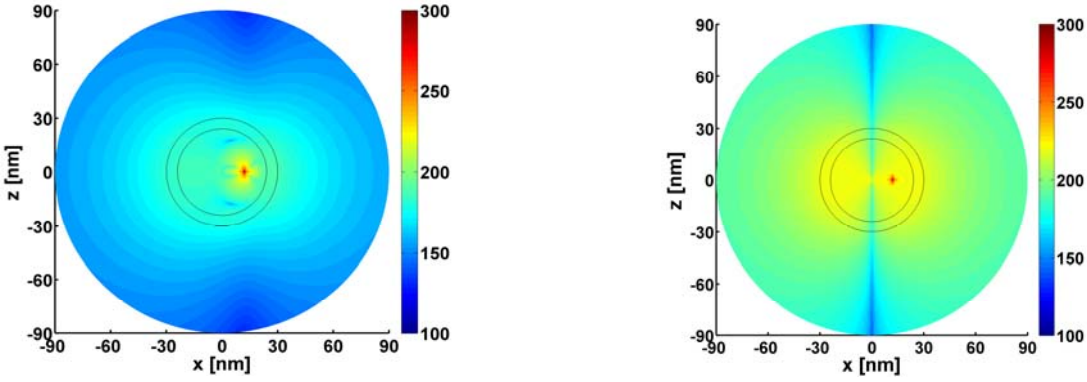
(a) (b)

Figure 2: The real, ε_2', (a) and the negative of the imaginary, ε_2'', (b) parts of the permittivity of the 6 nm thick Ag, Au, and Cu nano-shells normalized to the free-space permittivity.



(a) (b)

Figure 3: The NRR as a function of the wavelength, λ, of the lossless (a) and super-resonant (b) Ag-, Au-, and Cu-based CNPs. In all cases, the EHD is located inside the SiO_2 nano-core at $r_s = 12$ nm.



(a) (b)

Figure 4: The θ-component of the electric field of the lossless (a) and the super-resonant (b) Au-based CNP. In both cases, the EHD is located inside the SiO_2 nano-core at $r_s = 12$ nm.

Figure 3 shows the NRR as a function of the wavelength, λ, for the three CNPs with (a) $\kappa = 0$ and (b) $\kappa = -0.251$, $\kappa = -0.541$, and $\kappa = -0.747$, respectively, for the Ag-, Au-, and Cu-based CNPs. The latter values of κ are those which lead to the largest NRR values (around 72 dB for the Ag-based CNP, 69.5 dB for the Au-based CNP, and 69 dB for the Cu-based CNP). These correspond to a super-resonant state where the NRR values are significantly increased and the intrinsic plasmonic losses are vastly overcome, relative to the case of the corresponding lossless and passive CNPs in Figure 3(a). While the peak levels of the NRR in figure 3(b) are comparable, the wavelength at which they occur is different. It equals 501.5 nm for the Ag-based CNP, 597.3nm for the Au-based CNP, and 602nm for the Cu-based CNP. Moreover, the magnitude of κ needed for the super-resonance to occur is largest for the Cu-based CNP. This is expected as it is the lossiest of the three cases, *cf.*, figure 2(b).

The super-resonances observed in figure 3(b) are due to a strong excitation of the dipole mode in the respective CNPs. This is demonstrated in figure 4(b) which shows the spatial distribution of the quantity $20\log_{10}|E_{t,\theta}|$, where $E_{t,\theta}$ is the θ-component of the total electric field normalized by 1 V/m, for the Au-based CNP with $\kappa = -0.541$ and $\lambda = 597.3$ nm. Similar results were found for the other two CNPs, and are thus not included here. In contrast, the field is only weakly dipolar for $\kappa = 0$ in figure 4(a), and the Ag-based CNP is therefore only very weakly resonant, this being in line with the results of figure 3(a).

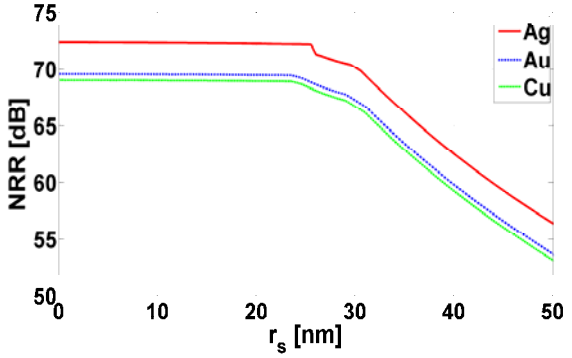
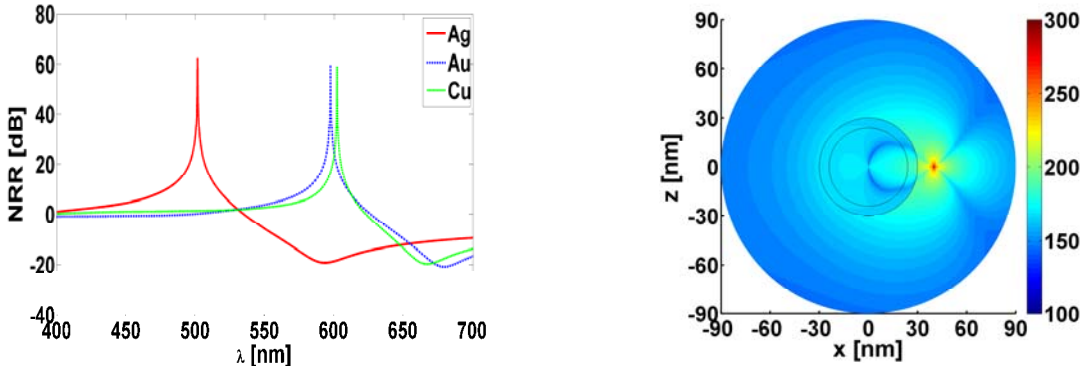


Figure 5. The NRR as function of the EHD location, r_s, of the thee super-resonant CNPs.

It is important to note that the super-resonant behavior for the three CNPs shown above is not restricted to the EHD location being inside the respective nano-cores. Figure 5 shows the NRR as a function of the EHD location, r_s, for the three super-resonant CNPs. Clearly, the NRR is very large and constant for the EHD locations inside the CNPs, whereas it begins to decrease as the EHD moves away from the CNPs. We note again that it is largest for the lowest loss Ag-based CNP. However, provided that the distance between the EHD and the respective CNP is not too large, large values of the NRR will still result, thus enabling one to overcome the plasmonic material losses.

Apart from the super-resonant phenomenon observed in all cases for the indicated values of κ, additional interesting results are found when the EHD is located outside the CNPs. In particular, we refer to figure 6(a), which shows the NRR for the three super-resonant CNPs as a function of the wavelength, λ, when the EHD is at $r_s = 40$ nm. A significant dip is observed in the NRR at $\lambda = 593.2$ nm for the Ag-based CNP, $\lambda = 679.2$ nm for the Au-based CNP, and $\lambda = 666.9$ nm for the Cu-based CNP. As elucidated in detail in [6] for the Ag-based CNP, these dips can be related to quasi non-radiating, i.e., quasi-transparent or quasi-cloaking, states. Thus, the same Ag-, Au-, and Cu-based CNP can provide enhanced, as well as reduced, radiation properties. This effect, of course, is attained for a specific CNP at a different wavelength and EHD location. The quasi non-radiating state is further illustrated with the θ-component of the electric field, see Figure 6(b), for the Au-based CNP for $\lambda = 679.2$ nm, $\kappa = -0.541$, and the EHD being located at $r_s = 40$ nm. Similar field results are obtained for the other two CNP cases.



(a) (b)

Figure 6: The NRR as a function of the wavelength, λ, for the three super-resonant CNPs when the EHD is outside the CNPs at $r_s = 40$ nm (a), and the θ-component of the electric field of the Au-based super-resonant CNP for λ=679.2 nm and the EHD located at $r_s = 40$ nm (b).

4. Summary and conclusions

Comparisons of the super-resonant states for silver, gold and copper coated active silica core CNPs were given. It was demonstrated that larger gain values are required for the larger loss metals to achieve the super-resonant state. It was also shown that the super-resonant state did not depend on the EHD location until it was outside of the CNP. It was further demonstrated that non-radiating states are possible for the active CNPs when the EHD is located in their exterior at a specific distance from the CNP and is driven at a specific frequency.

Acknowledgements

This work is supported in part by the Danish Research Council for Technology and Production Sciences within the TopAnt project and by DARPA Contract number HR0011-05-C-0068.

REFERENCES

1. Gordon, A. A. and R. W. Ziolkowski, "Investigating functionalized active coated nano-particles for use in nano-sensing applications," *Opt. Express*, Vol. 15, 12562-12582, 2007.
2. Alexopoulos N. G. and N. K. Uzungolu, "Electromangetic scattering from active objects: invisible scatters," *Appl. Opt.*, Vol. 17, 235-239, 1978.
3. Kerker M., "Electromagnetic scattering from active objects," *Appl. Opt.*, Vol. 17, 3337-3339, 1978.
4. Chew H. W., McNulty P. J., and M. Kerker, "Model for a Raman and fluorescent scattering by molecules embedded in small particles," *Phys. Rev. A*, Vol. 13, 396-404, 1976.
5. Arslanagic, S. and R. W. Ziolkowski, "Active coated nano-particles driven by an electric Hertzian dipole," URSI Radio Science Meeting, Paper B1-6, Boulder, Colorado, USA, January 2009.
6. Arslanagic, S. and R. W. Ziolkowski, "Active coated nano-particle excited by an arbitrarily located electric Hertzian dipole - resonance and transparency effects," to appear in *J. Opt. A: Pure and Appl. Opt., 2010.*

New surface plasmon polariton photodetectors based on diffraction gratings with anticorrelated relief

S. V. Mamykin[1], M. L. Dmitruk[1], M. V. Sosnova[1], A. V. Korovin[1] and V. I. Mynko[1]
[1]Institute of Semiconductor Physics of NAS of Ukraine, 41, Prospect Nauki , Kyiv, 03028, Ukraine
mamykin@isp.kiev.ua

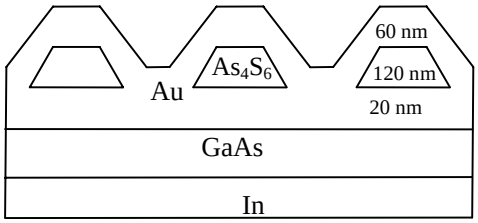
Abstract- Surface plasmon polariton photodetectors based on the gratings with antocorrelated relief have been proposed for the first time. Spectral dependence of light reflectance as well as photocurrent shows peculiarities connected with excitation of surface plasmon polaritons. The technology of grating formation allows to avoid the etching of semiconductor substrate. This simplified the manufacturing process significantly and makes it more compatible with microelectronic technological processing.

1. INTRODUCTION

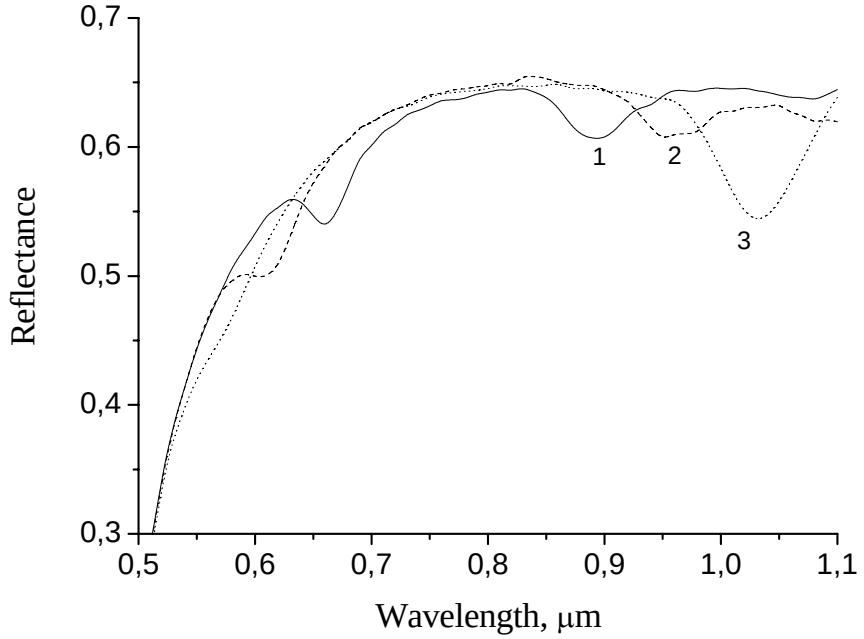
Surface plasmon polariton (SPP) photodetectors usually based on the Schottky barrier like Au/GaAs with periodically corrugated interface [1,2]. It requires the formation of the surface relief of diffraction grating type before the deposition of Au plasmon carrying and barrier forming film. This step complicates the technology of manufacturing of multisensors and sometimes makes it impossible thus significantly obstruct the wide application of this kind of photodetectors or sensors. In this work new method for diffraction grating formation are suggested. This method allows to produce periodically corrugated thin metal films with transmittance strongly depends on the mutual correlation of two metal film interfaces with air and semiconductor. This could be the final stage of manufacturing of this type photodetector when all elements and circuits on the chip (like CCD matrix) are already formed.

2. SAMPLE PREPARATION

The procedure of sample preparation consists in vacuum deposition of thin Au film (20 nm) as a first step. Then film of chalcogenide semiconductor As_4S_6 with 120 nm thickness has been deposited as second layer. This film is photosensitive and changes its physical and chemical properties [3] due to exposition to laser holographic image of diffraction grating. So, chemical etching of As_4S_6 film forms the mask of grating type (1465 nm period). Then part of Au film was removed chemically by iodine based etchant through the opens in As_4S_6 mask. And finally, additional Au film with 60 nm thickness has been deposited forming the structure shown on fig.1 a. As it seen from the cross section, the active plasmon carrying layer consists of gold film with inclusion of periodically placed As_4S_6 nanowires which as a result forms anticorrelated periodic relief. The bottom Ohmic contact made by deposition of Indium. The top Au film forms Schottky barrier contact, so the exposition to the light generates photocurrent in this structure.



a)



b)

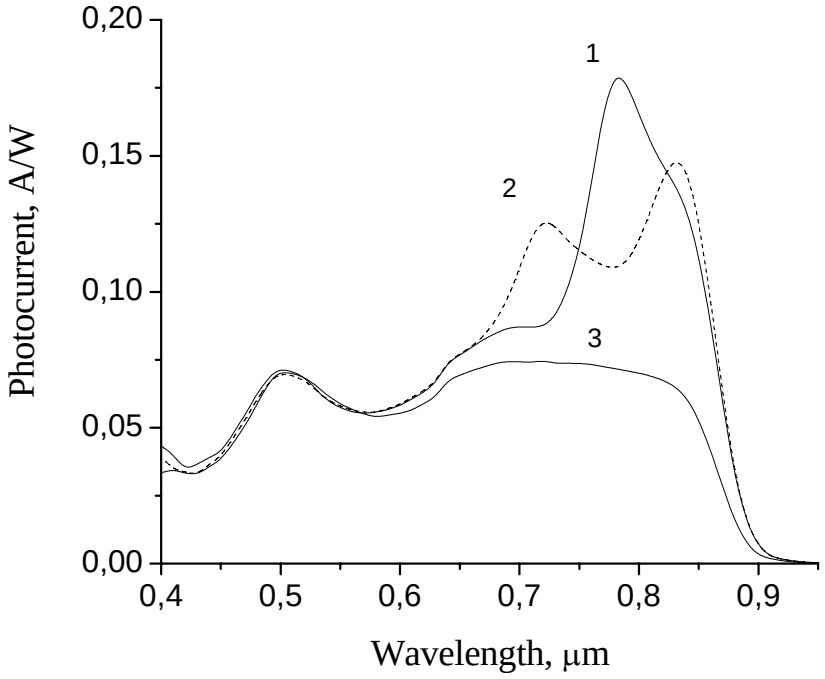
Figure 1. a) Cross section of prepared surface barrier structure.
b) Spectra of light reflectance at different angle of incidence, degs: 1) 10; 2) 15; 3) 20.

3. RESULTS AND DISCUSSIONS

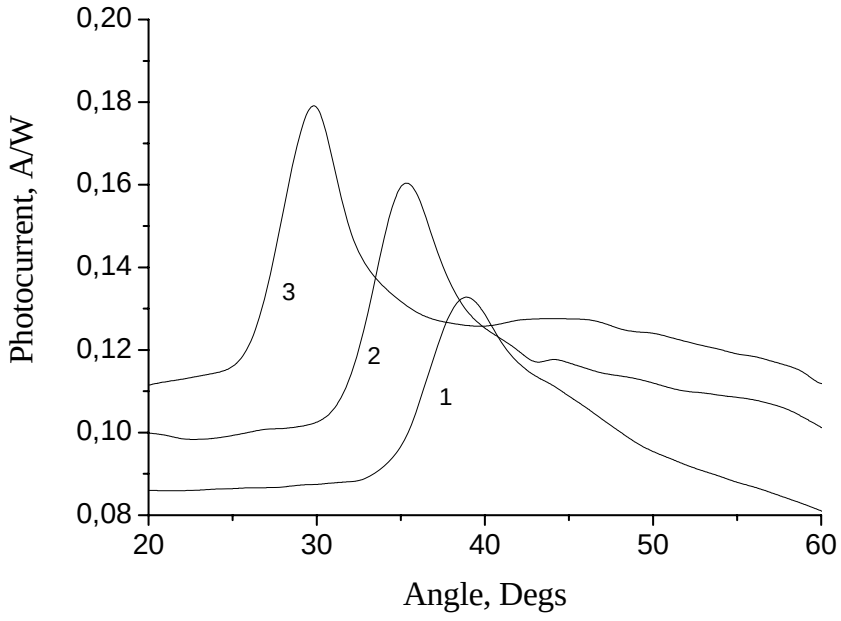
Spectral dependence of reflectance of p-polarized light at different angle of incidence (fig.1 b) shows few minima corresponding to excitation of surface plasmon polariton waves. Their position depends on grating period and corresponds to the condition of the wave vectors matching:

$$K_{spp} = m\frac{2\pi}{a} + \frac{2\pi}{\lambda}\sin(\Theta) \qquad (1)$$

where K_{spp} is the wave vector of the SPP, m is the integer $m=\pm1,2...$



a)



b)

Figure 2. a) Spectral dependence of the photocurrent measured at the angle of light incidence 0 degrees (1,3) for p- (1,2) and s- (3) polarized light.

b) Angular dependence of the photocurrent measured for p-polarized light with wavelength, μm: 1) 0.65; 2) 0.7; 3) 0.8.

Spectral dependence of photocurrent of the structures (fig.2 a) measured at different angle of light incidence shows maximum around 0.8 μm (curves 1 for p-polarized light and normal light incidence) which corresponds to excitation of SPP. This maximum split on two at 0.72 μm and 0.83 μm for the 5 degrees angle of incidence (curve 2). There are not any maxima for s-polarization of the light (curve 3). This behavior of the photocurrent is evidence of SPP excitation. The same resonant photocurrent features are observed on the angle dependencies at different wavelengths of incident light (fig.2 b). The photocurrent maximum position depends on wavelength and defined by relation (1). Besides, due to enhancement of light transmittance into semiconductor absorber layer of surface barrier structure for anticorrelated relief, the photocurrent value and the sensor sensitivity will be increased [4].

4. CONCLUSIONS

In conclusion we can say that surface plasmon polariton photodetectors based on the gratings with anticorrelated relief have been proposed for the first time. Spectral dependence of light reflectance as well as photocurrent reveals peculiarities connected with excitation of surface plasmon polaritons. The technology of grating formation allows to avoid the etching of semiconductor substrate. This simplified the manufacturing process significantly and makes it more compatible with microelectronic technological processing.

REFERENCES

1. Dmitruk, N. L., Mayeva, O. I., Mamykin, S. V., Mamontova, I. B. and Yastrubchak, O. B., Contribution of structure and morphology of design constituents to performance improvement of multilayer polaritonic photodetector, *Sensors*, Vol. 3, No. 10, 480-490, 2003.
2. N.L. Dmitruk, O.I. Mayeva and M.V. Sosnova, *Encyclopedia of Sensors 8*, 2006.
3. Indutnyi, I. Z., Romanenko, P. F., Stronski, A. V., Kostioukevitch, S. A., Shepeljavi, P. E. and Minko, V. I., Chalcogenide inorganic resists as holographic recording media, in *Proceedings of SPIE - The International Society for Optical Engineering*, Vol. 3486, 1997, 82-87.
4. Dmitruk, N. L. and Korovin, A. V., High light transmission through thin absorptive corrugated films, *Optics Letters*, Vol. 33, No. 9, 893-895, 2008.

Tuning the Polarization States of Optical Spots at the Nanoscale on the Poincaré Sphere using a Plasmonic Nanoantenna

E. Öğüt and **K. Şendur**

Sabancı University, Turkey
sendur@sabanciuniv.edu

Abstract— It is shown that the polarization states of optical spots at the nanoscale can be manipulated to various points on the Poincaré sphere using a plasmonic nanoantenna. Linearly, circularly, and elliptically polarized near-field optical spots at the nanoscale are achieved with various polarization states on the Poincaré sphere using a plasmonic nanoantenna. A novel plasmonic nanoantenna is illuminated with diffraction-limited linearly polarized light. It is demonstrated that the plasmonic resonances of perpendicular and longitudinal components of the nanoantenna and the angle of incident polarization can be tuned to obtain optical spots beyond the diffraction limit with a desired polarization and handedness.

1. INTRODUCTION

Polarized electromagnetic radiation has led to interesting technical applications and significant advancements at both optical [1, 2, 3, 4] and microwave frequencies [5]. With advances in nanotechnology, electromagnetic radiation beyond the diffraction limit with a particular polarization is an emerging need for plasmonic nano-applications. Among these applications, all-optical magnetic recording [6, 7] is a novel application which requires circular polarization. In the literature, it has been demonstrated that the magnetization can be reversed in a reproducible manner using a circularly polarized optical beam without an externally applied magnetic field [6, 7]. To advance the areal density of hard disk drives beyond 1 Tbit/in.^{2} using such a scheme, a sub-100 nm circularly polarized optical spot beyond the diffraction limit is required.

Recently, there has been growing interest in obtaining optical spots with various polarizations beyond the diffraction limit. Ohdaira et al. [8] obtained local circular polarization by superposing two cross propagating evanescent waves. Lindfors et al. [9] illuminated an optical lens with unpolarized light, and obtained fully polarized light in rings on the focal planes. It has been recently demonstrated that the polarization of diffraction limited incident beams can be manipulated using nanoparticle based antenna geometries [10, 11, 12, 13] and nanorod arrays [14]. Elliptically and circularly polarized near-field radiation can also be achieved through subwavelength apertures by utilizing a circular hole surrounded by elliptical gratings [15] and L-shaped hole arrays [16].

It is well known that the polarization of an optical beam can be represented by the phase difference and amplitude ratio of the electric field components. Any polarization state on the Poincaré sphere can therefore be achieved by properly tuning the amplitude ratio and phase difference of the beam. In this study, we have achieved this tuning process at the nanoscale by using a plasmonic nanoantenna. A plasmonic nanoantenna is illuminated with diffraction-limited linearly polarized radiation. Plasmonic resonances of perpendicular and longitudital components of the nanoantenna are adjusted to obtain optical spots at the nanoscale with linear, circular, and elliptical polarizations. We have shown that the nanoscale optical spots with different polarizations can be achieved on the Poincaré sphere by tuning two parameters: (a) the horizontal or vertical antenna length and (b) the polarization angle of the incident linearly polarized beam.

2. OPTICAL SPOTS AT THE NANOSCALE WITH LINEAR POLARIZATION STATES

Polarization state of an optical beam can be represented by the amplitude-ratio and phase-difference between field components of the beam. The Stokes parameters and the Poincaré sphere representation [17] are alternative, yet more rigorous ways to characterize the polarization states. These representations are widely used in the literature to describe the polarization state of diffraction-limited electromagnetic radiation. In this study, these representations are utilized to characterize polarization state of optical spots beyond the diffraction limit obtained from a plasmonic nanoantenna. The Stokes parameters that correspond to a specific polarization state are then utilized

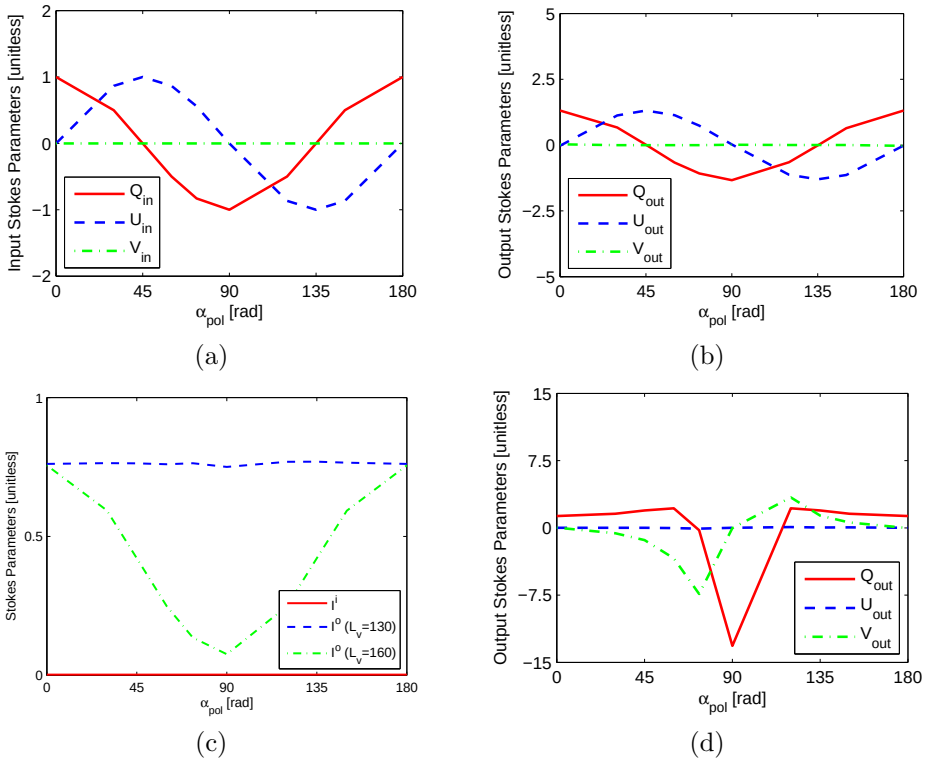


Figure 1: Effect of α_{pol} on (a) the Stokes parameters of the incident linearly polarized radiation (Q^{inc}, U^{inc}, V^{inc}), (b) the Stokes parameters of the output radiation from the nanoantenna for $L_v = 130$ nm, (c) I^{inc}, I^{out} for $L_v = 130$ nm , and I^{out} for $L_v = 160$ nm, and (d) the Stokes parameters of the output radiation from the nanoantenna for $L_v = 160$ nm.

to construct a Poincaré sphere that visually describes the polarization state and intensity of the optical spot. The handedness of the optical spot is determined by its location on the upper or lower half of the Poincaré sphere.

A cross-dipole plasmonic nanoantenna [11, 12, 13] is investigated to convert diffraction limited linearly polarized light into an optical spot with linear, circular or elliptical polarization beyond the diffraction limit. In this study, the thickness of each antenna particle is $T = 20$ nm and the width is $W = 10$ nm. Antennas with various horizontal and vertical lengths are investigated. The operating wavelength is selected as $\lambda = 1100$ nm, which corresponds to the resonance wavelength of the cross-dipole geometry. The dielectric constants of gold at $\lambda = 1100$ nm is chosen as ϵ_{gold} = -58.8971+i4.61164 [18].

To characterize the polarization states of near-field radiation from the nanoantenna, the Stokes parameters 20 nm below the gap center of the antenna are used. The Stokes parameters are given as [17]

$$I^{out} = (1/\eta)[(e_h^{out})^2 + (e_v^{out})^2] \tag{1}$$

$$Q_N^{out} = (1/\eta)[(e_h^{out})^2 - (e_v^{out})^2]/I^{out} \tag{2}$$

$$U_N^{out} = (2/\eta)e_h^{out}e_v^{out}cos\psi^{out}/I^{out} \tag{3}$$

$$V_N^{out} = (2/\eta)e_h^{out}e_v^{out}sin\psi^{out}/I^{out} \tag{4}$$

where the subscript $_N$ represents the normalized Stokes parameters projected onto a Poincaré sphere with unit intensity. The superscript $_{out}$ represents the Stokes parameters of the near-field radiation from the nanoantenna, whereas, superscript $_{in}$ represents the Stokes parameters of the input diffraction limited optical beam. e_h^{out} and e_v^{out} are the field amplitudes within the optical spot and ψ^{out} is the phase difference between field components.

First, we obtain optical spots at the nanoscale with linear polarizations at various points on the equator of a Poincaré sphere. For this purpose, we utilized a symmetric cross-dipole nanoantenna with $L_h = L_v = 130$ nm, where L_h and L_v represent the length of horizontal and vertical particles [12]. The nanoantenna is illuminated with a diffraction limited linearly polarized radiation

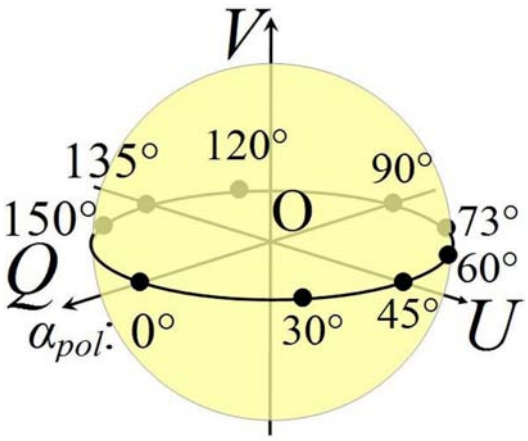


Figure 2: A unit Poincaré sphere with certain polarization states illustrated as points on its surface. Q, U, and V are the Stokes parameters, and α_{pol} is the angle of incident linear polarization.

with a polarization angle α_{pol} varying between 0° and 180°. Fig. 1(a) shows the Stokes parameters of the diffraction-limited incident beam as a function of incident polarization angle α_{pol}. The location of the polarization states of the incident beam on the Poincaré sphere are depicted in Fig. 2. Fig. 1(b) illustrates Stokes parameters of the near-field radiation as a function of α_{pol} for a symmetric nanoantenna with $L_h = L_v = 130$ nm. The result suggests that optical spots with linear polarization are obtained at the output via the nanoantenna.

In Fig. 1(c), I^{inc} is 0.002 for α_{pol} between 0° and 180°. In Fig. 1(c) $I^{out}(L_h = 130)$ shows an increased value of around 0.76, which highlights the enhanced output radiation due to plasmonic resonance of the nanoantenna. The remaining three Stokes parameters of the incident and output radiations, Q^{inc} and Q_N^{out}, U^{inc} and U_N^{out}, and V^{inc} and V_N^{out} behave similarly, as seen in Fig. 1(a) and 1(b). The reason for the similar behavior is due to two reasons:

(i) Since the antenna components have equal lengths, the phase difference between the field components is kept the same without a change at the opposite space of the antenna. We observed that the $\psi^{out} = \psi^{inc}$ at all angles $\alpha_{pol} = 0° - 180°$. This means that $V^{out} = 0$ at all the incident linear polarizations for a symmetric cross-dipole. $V^{out} = 0$ ensures that the polarization states that are obtained from the antenna are located on the same coordinate of the Poincaré sphere for a linearly polarized diffraction-limited illumination. In other words, the output polarization state lies on the equator of the Poincaré sphere, as shown in Figure 2, depending on the angle of incident linear polarization α_{pol}.

(ii) Cross-dipole antenna produces both field components, e_h^{out} and e_v^{out}, within the optical spot. Both e_h^{out} and e_v^{out} are enhanced with the same amount by the horizontal and vertical antenna components, since the antenna is symmetric. For this reason, the polarization angle of the diffraction-limited incident linear polarization is equal to the polarization angle of the linearly polarized optical spot produced by the antenna.

3. OPTICAL SPOTS AT THE NANOSCALE WITH CIRCULAR AND ELLIPTICAL POLARIZATION STATES

A cross-dipole plasmonic nanoantenna is investigated to convert diffraction-limited linearly polarized radiation into circularly and elliptically polarized near-field localized radiation beyond the diffraction limit. The plasmonic resonances of the perpendicular and longitudinal components of the nanoantenna and the angle of incident polarization are tuned to obtain circular and elliptical polarization states from a linearly polarized illumination.

An asymmetric antenna with $L_h = 130$ nm and $L_v = 160$ nm is investigated. In Fig. 1(c), as α_{pol} varies between 0° – 180°, I^{out} varies between 0.08 and 0.76, since e_h^{inc} and e_v^{inc} result in different enhancements for various angles on the horizontal and vertical components of the antenna. For instance, at $\alpha_{pol} = 0°$, e_h^{inc} is supported merely by the horizontal component, and at 90°, e_v^{inc} is supported merely by the vertical component. At $\alpha_{pol} = 0°$ the horizontal antenna particle is in resonant with e_h^{inc}. At 90°, however, the vertical particle is slightly out of resonant with e_v^{inc} because L_v is greater than L_h. Therefore, the plasmonic enhancement at $\alpha_{pol} = 0°$ is larger than the plasmonic enhancement at $\alpha_{pol} = 90°$. As a result, $I^{out} = 0.08$ at $\alpha_{pol} = 90°$, and $I^{out} = 0.76$

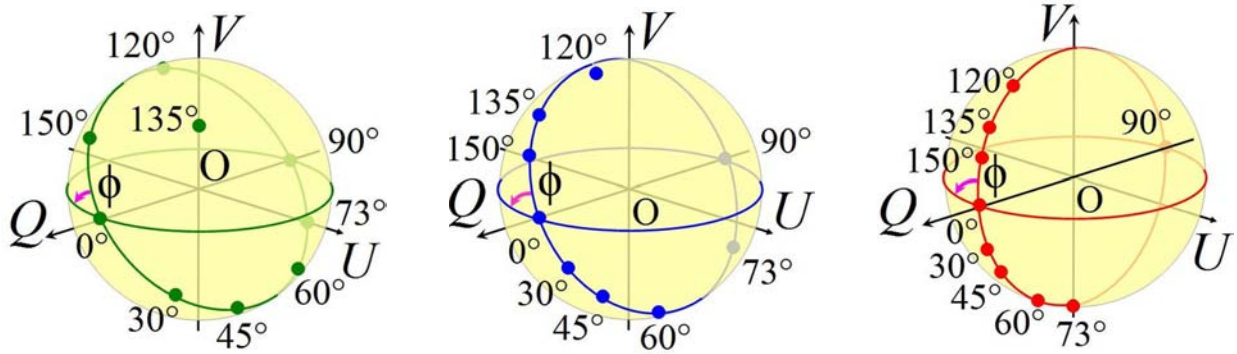


Figure 3: Unit Poincaré spheres with certain polarization states illustrated as points on their surfaces. ϕ illustrates the angular distance from different cut-planes passing through spheres onto the equator of the spheres.

at $\alpha_{pol} = 0°$.

In Fig. 3(a), (b), and (c) various polarization states from an asymmetric antenna geometry are presented for L_v = 140 nm, 150 nm, and 160 nm, respectively. A linearly polarized diffraction-limited radiation is incident upon the antenna at $\alpha_{pol} = 0°$, 30°, 45°, 60°, 73°, 90°, 120°, 135°, and 150°. At L_v = 140 nm and L_v = 150 nm, linear, right-hand, and left-hand elliptical polarization states are obtained on the surface of the Poincaré spheres, as depicted with solid points in Fig. 3(a) and (b). These states exist on the intersection curve between a Poincaré sphere and a cut-plane that passes through the sphere, and which makes an angle ϕ with the equator of the sphere, as illustrated in Fig. 3. If a linear polarization is incident on the antenna with L_v = 130 nm, then $\phi = 0°$ as shown in Fig. 2. When L_v = 160 nm this cut-plane is perpendicular to the equator, as demonstrated in Fig. 3(c). As a result, there exist both linear and elliptical polarization states, as well as at $\alpha_{pol} = 73°$, a left-hand circular polarization state on the surface of the Poincaré sphere. An important consequence of the result in Fig 3 is the following. If L_v is increased from 130 nm to 160 nm when the nanoantenna is illuminated with a linearly polarized diffraction-limited radiation with α_{pol} from 0° to 180°, then the whole surface of the Poincaré sphere can in principle be obtained at the output optical spot at the nanoscale.

4. CONCLUSION

In summary, optical spots with linear, circular, and elliptic polarizations were achieved via symmetric and asymmetric cross-dipole nanoantennas. It was demonstrated that a cross-dipole nanoantenna can convert diffraction-limited linearly polarized light into linearly, circularly, or elliptically polarized optical spots beyond the diffraction limit. It was shown that the nanoscale optical spots with different polarizations can be achieved on the Poincaré sphere by tuning two parameters: (a) the horizontal or vertical antenna length and(b) the polarization angle of the incident linearly polarized beam.

ACKNOWLEDGMENT

This work is supported by TUBITAK under project number 108T482 and by Marie Curie International Reintegration Grant (MIRG-CT-2007-203690). Kursat Sendur acknowledges partial support from the Turkish Academy of Sciences.

REFERENCES

1. Kikkawa, J. M. and D. D. Awschalom, "All-optical magnetic resonance in semiconductors," *Science*, Vol. 287, 1064–1076, 2000.
2. Neale, S., M. Macdonald, K. Dholakia and T. F. Krauss, "All-optical control of microfluidic components using form birefringence," *Nature*, Vol. 4, 530–533, 2005.
3. Hassey, R., E. J. Swain, N. I. Hammer, D. Venkataraman and M. D. Barnes, "Probing the chiroptical response of a single molecule," *Science*, Vol. 314, 1437–1439, 2006.
4. Peng, X., N. Komatsu, S. Bhattacharya, T. Shimawaki, S. Aonuma, T. Kimura and A. Osuka, "Optically active single-walled carbon nanotubes," *Nature*, Vol. 2, 361–365, 2007.
5. Volakis, J. M., *Antenna Engineering Handbook*, McGraw-Hill Professional, 2007.

6. Stanciu, C. D., F. Hansteen, A. V. Kimel, A. Kirilyuk, A. Tsukamoto and A. Itoh, "All-Optical Magnetic Recording with Circularly Polarized Light," *Phys. Rev. Lett.*, Vol. 99, No. 047601, 2007.
7. Vahaplar, K., A. M. Kalashnikova, A. V. Kimel, T. Shimawaki, D. Hinzke, U. Nowak, R. Chantrell, A. Tsukamoto, A. Itoh, A. Kirilyuk and Th. Rasing, "Ultrafast path for optical magnetization reversal via a strongly nonequilibrium state," *Phys. Rev. Lett.*, Vol. 94, No. 117201, 2009.
8. Ohdaira, Y., T. Inoue, H. Hori and K. Kitahara, "Local circular polarization observed in surface vortices of optical near-fields," *Opt. Express*, Vol. 16, 2915–2921, 2008.
9. Lindfors, K., A. Priimagi, T. Setälä, A. Shevchenko, A. T. Friberg and M. Kaivola,"Local polarization of tightly focused unpolarized light," *Nat. Photon.*, Vol. 1, 228–231, 2007.
10. Shegai, T., Z. Li, T. Dadosh, Z. Zhang, H. Xu and G. Haran, "Managing light polarization via plasmon-molecule interactions within an asymmetric metal nanoparticle trimer," *Proc. Natl. Acad. Sci.*, Vol. 105, 16448–16453, 2008.
11. Biagioni, P., J. S. Huang, L. Duò, M. Finazzi and B. Hecht, "Cross Resonant Optical Antenna," *Phys. Rev. Lett.*, Vol. 102, No. 256801, 2009.
12. Ogut, E., G. Kiziltas and K. Sendur, "Circularly-polarized localized near-field radiation at the nanoscale," *Appl. Phys. B*, Published online November 14, 2009, DOI 10.1007/s00340-009-3817-0.
13. Biagioni, P., M. Savoini, J. S. Huang, L. Duò, M. Finazzi and B. Hecht, "Near-field polarization shaping by a near-resonant plasmonic cross antenna," *Phys. Rev. B*, Vol. 80, No. 153409, 2009.
14. Kullock, R., "Polarization conversion through collective surface plasmons in metallic nanorod arrays," *Opt. Express*, Vol. 16, 21671–21681, 2008.
15. Drezet, A., C. Genet and T. Ebbesen, "Miniature Plasmonic Wave Plates," *Phys. Rev. Lett.*, Vol. 101, No. 043902, 2008.
16. Li, T., H. Liu, S. M. Wang, X. G. Yin, F. M. Wang, S. N. Zu and X. Zhang, "Manipulating optical rotation in extraordinary transmission by hybrid plasmonic excitations," *Appl. Phys. Lett.*, Vol. 93, No. 021110, 2008.
17. Kong, J. E., *Electromagnetic Wave Theory*, John Wiley and Sons, Inc., 1986.
18. Palik, E. D., *Handbook of Optical Constants of Solids*, Academic Press, 1998.

Photorealistic depictions of spherical gradient-index metamaterials-based objects

A. J. Danner[1]
[1]National University of Singapore, Singapore
adanner@nus.edu.sg

Abstract- Visually stunning photorealistic images and animations of metamaterials-based devices in action can be created and rendered in real time with a technique that will be described in detail. Such rendering is useful in assessing the ultimate device performance that may be achievable even with imperfect metamaterials.

1. INTRODUCTION

With the advent of transformation optics and metamaterials, objects previously thought impossible to fabricate because of the need for extremely small or large values of the index of refraction have come within practical reach. Recently, an Eaton lens was constructed in the microwave regime for the first time with use of transformation optics to remove the singularity at the origin (where ordinarily the index of refraction would approach infinity) [1]. Being able to visually depict the behavior of devices such as the Eaton Lens, Maxwell's Fisheye (recently proven to allow perfect imaging without negative refraction [2]), or invisibility cloaks [3] is useful not only pedagogically, but also to substantiate the utility of a certain design. For example, if an imperfect invisibility cloak were someday designed, it would be useful to see how it would look in a real-life setting in order to assess its usefulness.

Recently there have been a few reports of achieving photorealistic images of metamaterials-based objects. In 2006, Dolling et al. used the free software POV-Ray to create photorealistic images of glasses of "negative-index" water, and POV-Ray should be useful in depicting any situation involving objects consisting of isotropic, uniform indices of refraction [4]. In 2009, Halimeh et al. depicted the performance of a carpet cloak [5], both ideal and non-ideal. In early 2010, I showed how an invisible sphere can be transformed into a polarization-dependent object with correct ray trajectories for only one polarization but with considerably relaxed materials properties, and then described an overview of the process used to produce a photorealistic image [6]. In this report, the same process is described in great detail, but while using existing free software. It is hoped that this will enable others to produce photorealistic images of future devices designed with use of transformation optics, metamaterials, or with transmutation of singularities.

2. PREPARING THE BACKGROUND

To create a natural-looking background and avoid parallax errors, an outdoor setting should be selected where there are no nearby objects. With a camera mounted on a tripod, 90-100 pictures can be taken in all directions with overlapping features and then stitched together automatically using the free software Autostitch [7]. Figure 1 shows a resulting panorama from this process, this time of the Chinese Garden in Singapore.



Figure 1. A stitched panorama of the Chinese Garden in Singapore

The second step in the process is to split the background into a cubemap, which is essentially a 6-sided polygon that, if placed at the center, the view would be the same as in the original scene. There are a number of free software packages that can convert a panorama into a cubemap. The six faces of the cubemap are shown in Figure 2. (After the six .jpg files are extracted, they can be saved in a .des-formatted file which is a standard cubemap format.) The reason that a cubemap is preferred to a spherical-coordinate map, for example, is because at a later stage, texture lookup can be done faster on 2D objects.



Figure 2. The six faces forming the cubemap for the background.

3. PREPARING THE METAMATERIALS-BASED OBJECT

To achieve real-time rendering, the above cubemap can be used in any software supporting OpenGL or DirectX. For this example, AMD's free RenderMonkey, which is useful for DirectX code debugging, has integrated pixel and vertex shader development environments. A pixel shader can be developed with customized behavior based on the ray trajectories desired in the metamaterials-based object, and ref. [8] is a useful text for learning the necessary skillset.

Figure 3(a) shows an object with a spherically gradient refractive index profile created in Mathematica. With all rays emanating from a certain point in the left part of the figure, this point can be thought of as the camera in RenderMonkey, with the distance between the camera and the sphere in Mathematica equal to the distance in RenderMonkey. Different rays have different angles of incidence with the sphere's surface, and each ray has a different corresponding exit angle after its path through the sphere is complete. A set of data pairs in the form of angle of incidence vs. angle of ultimate refraction can be assembled and an empirical interpolating function can be created for use in the pixel shader to relate the two. The pixel shader is called by the renderer each time a ray from the camera intersects the surface of the object, as is passed vectors representing the normal vector of the surface and the incident ray. The object placed in the environment is a sphere. The shader language used (High Level Shading Language) allows overlapping images, so in cases of multiple ray paths (birefringence) or surface reflection, there would simply be more than one interpolating function, with the ultimate color of the pixel seen at the surface of the sphere (where the shader is invoked) determined by a weighted average of the background pixels pointed to by the exit angles. For Figure 3(a), the formula relating the output ray vector to the input ray vector has a complicated dependence on the input ray vectors. (It corresponeds to the polarization-dependent invisible sphere described in ref. [6]). For Figure 3(b), an Eaton Lens, however, the relationship is simple. Regardless of the position of the camera, each ray simply turns around. The output ray vector is the inverse of the input ray vector at any point. The pixel shader is very simple. It simply looks up the appropriate pixel from the cubemap texture using this vector. (This can be done in a single line of code in the shading language.)

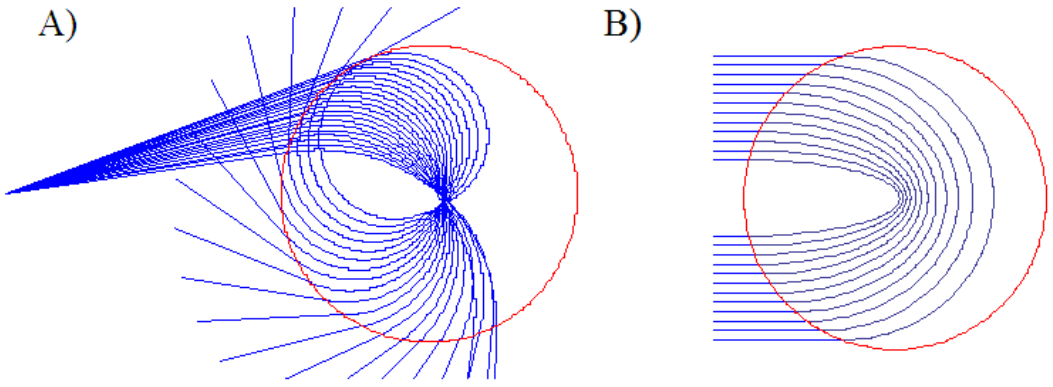


Figure 3. (a) A device with a complicated exit ray vs. incident ray relationship, (b) A device with a very simple exit ray vs. incident ray relationship.

The Eaton lens produces inverted images, because a camera looking towards the top of the Eaton lens will have its ray vector reversed, which then points back past the camera towards the bottom portion of the background (the cubemap behind the camera and sphere). The pixel shader has no knowledge of processes inside the sphere.

It only computes the exit ray direction given the input ray direction at the sphere's surface. That calculation can be done very quickly and fast, real-time animations can be produced with this method, and numerous software packages can create such animations. A shader developed as described above is in a relatively standard format and can be imported into a variety of graphics software packages for use. Figure 4 shows the background and an Eaton lens created with the process described and captured directly from RenderMonkey. The camera is infinitely small, so the picture-taker is not visible. By comparison with Figure 2, it has correct behavior.



Figure 4. Finished rendering of Eaton lens in action

4. CONCLUSIONS

Although the Eaton lens is so simple that this process could have been carried out with a simple copy-and-paste operation to make a realistic image, the process described here is much more powerful and can handle spherically-symmetric refractive index profiles of arbitrary complexity, yielding animations and images that serve both to educate and inspire. The process can be used to render such objects as invisible spheres, invisibility cloaks, the Eaton Lens, Maxwell's Fisheye, and any spherical optical transformations of those structures.

ACKNOWLEDGEMENTS

Photography by T. Ngo and a grant from the Singapore Ministry of Education/National University of Singapore R263000414112/133 are acknowledged.

REFERENCES

1. Ma, Y. G., C. K. Ong, T. Tyc, and U. Leonhardt, "An omnidirectional retroreflector based on the transmutation of dielectric singularities," *Nature Materials*, Vol. 8, 639-642, 2009.
2. Leonhardt, U. "Perfect imaging without negative refraction," *New J. Phys.*, vol. 11, 093040, 2009.
3. Pendry, J. B., D. Schurig, and D. R. Smith, "Controlling electromagnetic fields," *Science*, vol. 312, 1780 –1782, 2006.
4. Dolling, G., M. Wegener, S. Linden, and C. Hormann, "Photorealistic images of objects in effective negative-index materials," *Opt. Express,* vol. 14, 1842-1849, 2006.
5. Halimeh, J. C., T. Ergin, J. Mueller, N. Stenger, and M. Wegener, "Photorealistic images of carpet cloaks," *Opt. Express*, vol. 17, 19328-19336, 2009.
6. Danner, A., "Visualizing invisibility: Metamaterials-based optical devices in natural environments," *Opt.*

Express, in press, 2010.

7. Brown, M. and D. Lowe, "Automatic panoramic image stitching using invariant features," *International J. of Computer Vision*, vol. 74, 59-73, 2007.
8. St-Laurent, S., *Shaders for Game Programmers and Artists*, Thomson, Boston, 2004.

Threshold-free Cerenkov radiation in metallic metamaterials

Jin-Kyu So[1], Jong-Hyo Won[1], Seung-Ho Bak[1], Kyu-Ha Jang[1], D. S. Kim[2], Gun-Sik Park[1*], and F. J. Garcia-Vidal[3]

[1]Center for THz-Bio Application Systems, Department of Physics and Astronomy, Seoul National University, Seoul 151-747, Korea

[2]Center for Subwavelength Optics, Department of Physics and Astronomy, Seoul National University, Seoul 151-747, Korea

[3]Departamento de Fisica Teorica de la Materia Condensada, Universidad Autonoma de Madrid, E-28049 Madrid, Spain

gunsik@snu.ac.kr

Abstract- We report on the excitation of Cerenkov radiation with no energy threshold in metallic metamaterials, one-dimensional arrays of subwavelength cut-through slits. The considered metamaterial supports Cerenkov wakes via transition radiation at each slit opening, which is analogous to its effective anisotropic dielectric medium.

1. INTRODUCTION

Recent introduction of the concept, metamaterial, has been providing breakthroughs to previously unsolved problems mainly in optical sciences. One of those breakthroughs is the geometrically controlled index of refraction from perfect conducting metal slits [1,2]. Here, we note its potential as a medium for the generation of Cerenkov radiation in free-electron-lasers (FELs) and wakefield accelerators where choosing appropriate dielectric material is limited by dielectric breakdown [3] and thermal issues [4]. We show that this metallic metamaterial can serve as a medium which support threshold-free Cerenkov radiation.

2. CERENKOV RADIATION IN METALLIC METAMATERIALS

We considered a metamaterial structure with its effective index of refraction, $\overline{n} = 4$, which is close to the indices of dielectric materials such as Sapphire and GaAs which are commonly used in compact FELs [4]. For comparison, both the isotropic and anisotropic effective dielectric media were modeled using the following parameters, $\overline{n} = d/a = 4$ for the isotropic medium and $\overline{\varepsilon}_x = d/a = 4, \overline{\varepsilon}_z = \infty, \overline{\mu}_y = a/d = 0.25$ for the anisotropic medium. A particle-in-cell (PIC) code, MAGIC, and finite-difference time-domain (FDTD) code, CST studio suite, were used to model the interaction between these media and a bunch of moving electrons with various energies.

The energy of the electron bunch was varied to verify the well-known dependence of Cerenkov radiation on particle's velocity such as the angle of radiation cone and the velocity threshold found in normal isotropic dielectric medium. Since the energy threshold for an isotropic dielectric medium with n = 4 is 16.8 keV, the energy of the electron bunch was varied below and above this value. The resulting angles of radiation cones for the metamaterial and its corresponding effective dielectric media were measured by taking the contour plots of z-component of magnetic field, *Hz*. As expected, for the effective isotropic medium with $\overline{n} = d/a = 4$, the threshold energy was identified as 16.8 keV below which is shaded in gray as shown in Fig. 1 (a). Fig. 1 (b) and

Fig. 1 (c) show typical contour plots for metal slits and isotropic dielectric medium at 20 keV, where the radiation angles are simulated to be 14.8° and 24.6°, respectively.

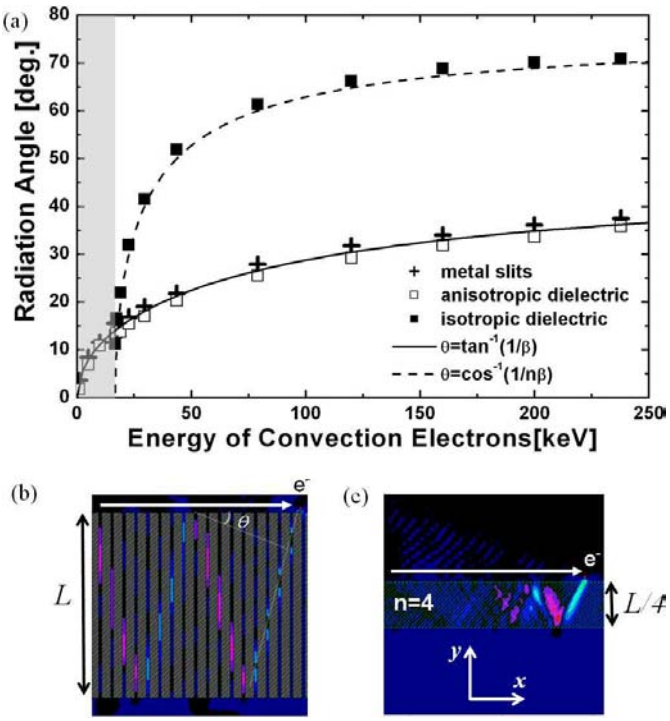


Figure 1. (a) Simulated radiation angles for metal slits structure, effective anisotropic dielectric medium, and effective isotropic dielectric medium are compared at various beam energies. Contour plots of the Hz field distributions are shown for (b) metal slits and (c) its effective isotropic dielectric medium.

3. ENERGY DEPENDENCE OF RADIATION PATTERN

The radiation pattern from the metal slits is similar to that of the ordinary Cerenkov radiation in normal isotropic dielectric slab but its exact dependence on electron's energy does not follow the one for normal isotropic dielectric medium, $\cos\theta = \frac{1}{n(\omega)\beta}$ (dashed line) where θ is the angle formed by the particle velocity $\vec{v}$ and the wave vector of the Cerenkov radiation and $n(\omega)$ is the index of refraction at the considered frequency, ω. Rather, since the propagation of radiated field only occurs in the vertical direction inside each slit with the velocity of light, c, while the electron bunch pass above the structure with the velocity of βc, the radiation angles in metal slits follow those from the relation, $\tan\theta = \frac{c}{v_{beam}} = \frac{1}{\beta}$, as shown in Fig. 2 (a) (solid line) together with those from an effective anisotropic medium as shown in Fig. 2 (a) (hollow square). As a result, in contrast to the isotropic dielectric case where velocity threshold is given as $\beta > 1/n$, no velocity threshold was

found in metal slits and its effective anisotropic dielectric medium. These peculiar characteristics can also be deduced from the well-known kinematic relation for Cerenkov radiation in anisotropic dielectric medium, $\cos\theta_0 = \frac{1}{n_j\left(\omega, \vec{k}/k\right)\beta}$ where $n_j\left(\omega, \vec{k}/k\right)$ denotes the refractive index for ordinary- and extraordinary-waves. This kinematic relation becomes $\tan\theta_0 = \beta$ for extraordinary-waves in the considered effective anisotropic medium.

4. CONCLUSIONS

We showed that metallic metamaterials support Cerenkov wakes when a bunch of electrons moves close to it. The resulting radiation pattern showed equivalence to its effective anisotropic counterpart, which results in no energy threshold for the generation. We expect that such capability of the metallic metamaterial can provide breakthroughs to applications based on Cerenkov radiation by alleviating the limitations of ordinary dielectric materials such as low index of refraction, dielectric breakdown, and thermal issues.

ACKNOWLEDGEMENT

This work was supported by National Research Foundation of Korea Grant funded by the Korean Goverment(grant code: 2009-0083512)

REFERENCES

1. Shen, J. T., P. B. Catrysse, and S. Fan, "Mechanism for Designing Metallic Metamaterials with a High Index of Refraction", Phys. Rev. Lett., Vol. 94, 197401, 2005.
2. Shin, J., J. T. Shen, P. B. Catrysse, and S. Fan, "Cut-Through Metal Slit Array as an Anisotropic Metamaterial Film", IEEE J. Sel. Top. Quant. 12, 1116 (2006).
3. Thompson, M. C., H. Badakov, A. M. Cook, J. B. Rosenzweig, R. Tikhoplav, G. Travish, I. Blumenfeld, M. J. Hogan, R. Ischebeck, N. Kirby, R. Siemann, D. Walz, P. Muggli, A. Scott, and R. B. Yoder, "Breakdown Limits on Gigavolt-per-Meter Electron-Beam-Driven Wakefields in Dielectric Structures", Phys. Rev. Lett.100, 214801 (2008).
4. Owens, I. J. and J. H. Brownell, "", J. Appl. Phys. 97, 104915 (2005).

Monolithic excitation and manipulation of surface plasmon polaritons on a vertical cavity surface emitting laser

J.-M. Lamy*, J. Justice, G. Lévêque and B. Corbett
Tyndall National Institute, Ireland
*corresponding author: jeanmichel.lamy@tyndall.ie

Abstract- We report the manipulation of surface plasmon polaritons (SPPs) on a thin Au layer integrated on top of the mirror of a vertical-cavity surface-emitting laser (VCSEL). Gratings etched into the Au layer to different depths are used to couple the light into and out of the film, and to bend the trajectory of the SPP. The result paves the way to compact integrated plasmonic devices.

1. INTRODUCTION

The use of metal films to confine electromagnetic waves as SPPs continues to receive considerable attention [1]. They have a wide range of applications such as biosensing [2], chip-to-chip optical interconnects applications [3] and more recently for data storage [4]. However, the SPPs are excited using a separate light source which compromises the compactness of the system [2, 4]. We previously demonstrated that SPPs can be directly excited on the top surface of a metallised single mode Vertical Cavity Surface Emitting Laser (VCSEL) [5]. In this paper, we have designed the VCSEL with a customized planar gold surface to permit the propagation and manipulation of the SPPs.

2. DEVICE STRUCTURE AND FABRICATION

The structure of the 850-nm VCSELs used consisted of a bottom n-doped Distributed Bragg Reflector (DBR) made of 35.5 pairs of graded index $Al_{0.12}Ga_{0.88}As$–$Al_{0.9}Ga_{0.1}As$. The active region had three 6-nm-thick GaAs quantum wells. The top p-doped DBR had 22 pairs of graded index $Al_{0.12}Ga_{0.88}As$–$Al_{0.9}Ga_{0.1}As$ layers. An $Al_{0.98}Ga_{0.02}$ As layer replaced an $Al_{0.9}Ga_{0.1}As$ layer in the top mirror close to the optical cavity for the selective oxidation process. Mesas with 57 μm diameter and an arm (see figure 2) were lithographically patterned and dry etched to the cavity region. The selective oxidation formed current confinement apertures of 4 μm diameter in the mesas whereas the narrower "arm" section is completely oxidized to prevent current flow and recombination in this SPP propagation region. This was followed by SiO_2 passivation.

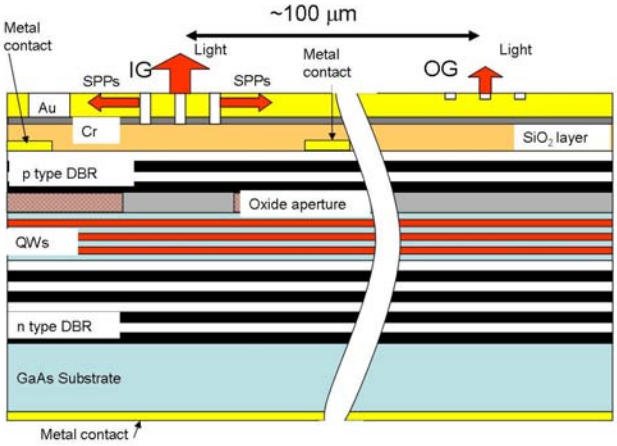


Figure 1 Schematic cross section of the plasmonic VCSEL.

After opening the SiO_2 layer on top of the mesa and "arm", a p-type metal (Ti–Pt–Au) ohmic contact was deposited and a n-type (Au–Ge–Ni) ohmic contact was evaporated on the substrate. The Au-Cr-SiO_2 trilayer was then deposited on the top of the mesas using a lift-off process. The half-wave thickness of the oxide layer ensured that the antinode of the electric field inside the device occurred at the top of the SiO layer. The Cr layer is use as adhesive layer for the Au, which is 200nm thick to get the best efficiency in term of coupling and propagation length. The gratings designed for 850 nm were milled in the Au and Cr layers using a focused ion beam (FIB) system FEI FIB200DE. This apparatus used Ga+ ions accelerated to 30 keV with a pixel dwell time of 1 s and a pixel overlap of 50% to mill patterns. Milling current was 50 pA and the process was carried out at a magnification of 65 000. The excitation grating was placed centrally on the mesa to be aligned with the VCSEL emission from the underlying oxide aperture. The excitation incoupling grating (IG) was milled through the entire layer of Au and Cr to get the maximum of the electric field to launch the SPPs. The SPPs are allowed to propagate along the gold layer. A shallow extraction grating (OG) of 30 nm depth is used to out couple the SPPs to air. On the figure 2 a) is shown the device with a straight arm and on the figure 2 b) is shown the device with a 90° bend arm.

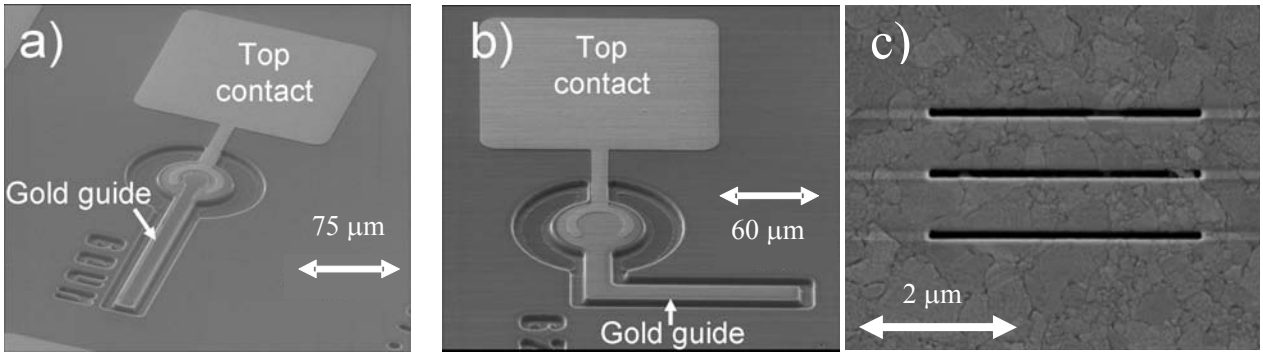


Figure 2 a) Device with a straight gold guide of 180 µm long and 10 µm wide. **b)** Device with a 90° bent gold guide of 10 µm wide and a first part of 70 µm long and a second part of 120 µm long. **c)** Excitation grating

The figure 2 c) shows the excitation grating composed of 3 slits just touching the SiO_2.

3. MEASURE OF THE PROPAGATION LENGTH OF THE SPPs

The devices are characterized in far field by using a CCD camera. In order to determine the propagation length of the SPPs we have used two different methods. The first method consists in milling a first extraction grating at the end of the guide, measure the intensity and then milling another extraction grating closer to the excitation grating and measure again the intensity. The results are plotted on the figure 3. An exponential fit gives a SPP propagation length (P_l) in intensity of about 39 µm. Despite the fact that the SPPs are strongly polarized along the 0° direction which corresponds to the direction of the guide, we see a small contribution from the 90° direction. The explanation is that the guide is very wide, hence the SPPs can propagate with a small angle compared to the guide direction, which creates this unexpected contribution to the scattered light.

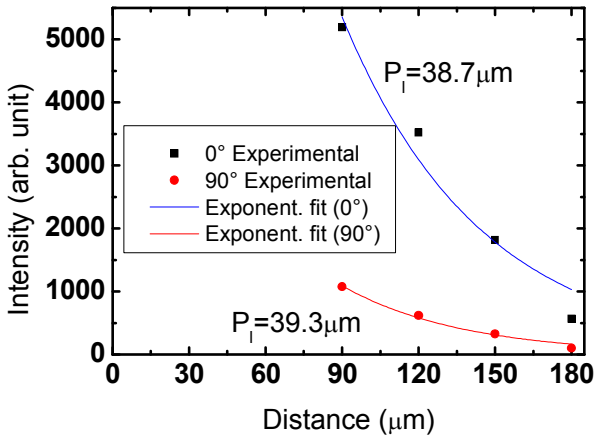


Figure 3 Intensity from the different gratings for the two orthogonal directions of polarization

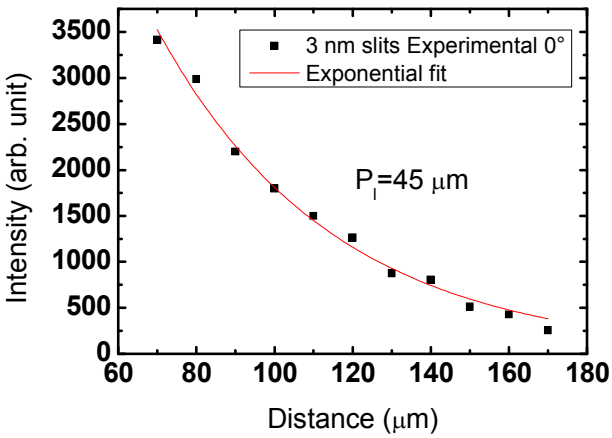


Figure 4 Intensity from the eleven slits spaced by 10 μm, with the first slit placed at 70 μm from the excitation grating.

The second method consists in milling a shallow single slit every 10 μm with a depth of 15 nm, in order to extract only a small amount of light. Then we measured the intensity coming from etch slit, the results are plotted on the figure 4. In this configuration we get a propagation length of 45 μm.

These two methods give a propagation length close to the theoretical estimation of 60 μm for a 200 nm layer of gold with a perfectly smooth surface.

4. MANIPULATION OF THE SPPs

We have also demonstrated the propagation of the SPPs along a 90° bent guide using a shallow etched Bragg mirror. The Bragg mirror is designed to have a period corresponding to λ in the direction of propagation of the SPPs and is composed of 3 slits. It is placed in the corner to change the direction of propagation of the SPPs (figure 5).

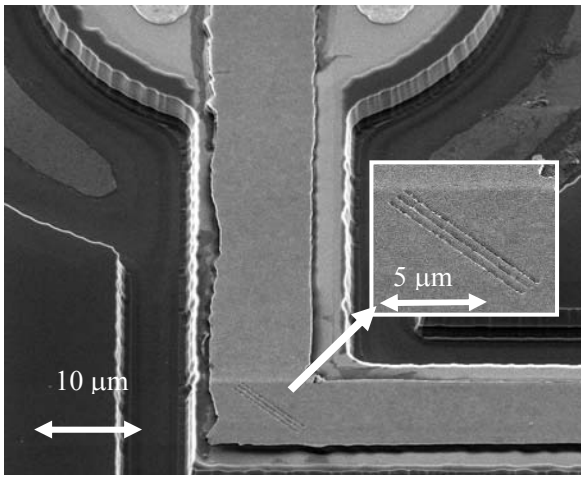


Figure 5 Image of the 90° bent arm with a Bragg mirror. In inset is shown a zoom of the Bragg mirror.

The figures 6 and 7 show respectively the intensity of light we get from the extraction grating placed after the corner with and without the Bragg mirror. Without the Bragg mirror only noise from the VCSEL is measured even with no attenuation filter, whereas a strong bright spot is observed at the location of the extraction grating

with the Bragg mirror present at the corner. This demonstrates the efficiency of the Bragg mirror to control the propagation of the SPPs.

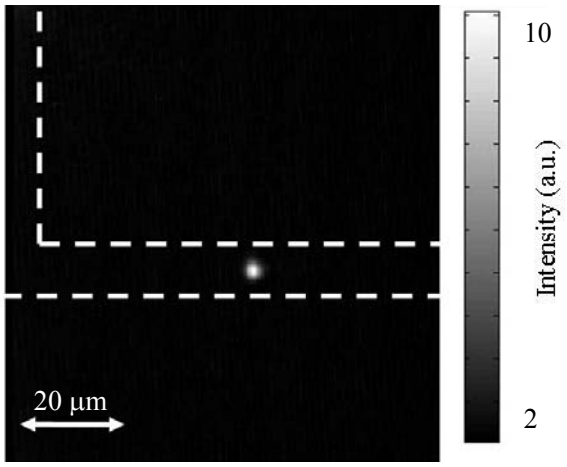


Figure 6 Image with a 30dB attenuation filter of the extraction grating, with a Bragg mirror. The dashed lines represent the gold guide.

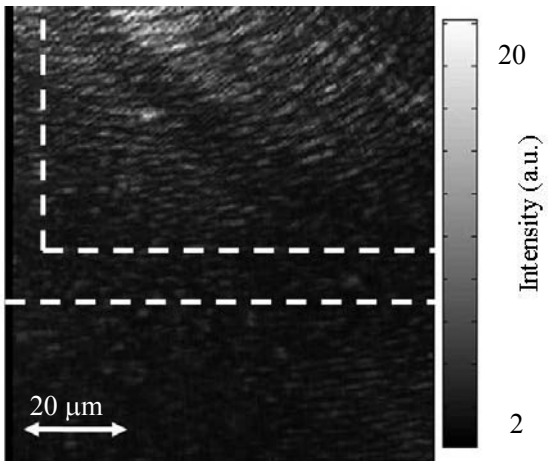


Figure 7 Image without any attenuation filter of the extraction grating, without a Bragg mirror. The dashed lines represent the gold guide.

5. CONCLUSION

We have demonstrated the excitation of SPPs on a gold layer deposited on top of a VCSEL by using a grating. These SPPs show a good propagation length and we demonstrated the possibility to change their trajectory by using a Bragg mirror. Plasmonics is an emerging platform for high sensitivity sensors and will enable applications such as label-free detection of proteins and process control in pharmaceutical industries. The direct integration of laser sources with the plasmonic sensing structures will result in a compact, mass producible low cost sensor platform.

ACKNOWLEDGMENT, this work is supported by Marie Curie Project MTKD-CT-2006- 029570.

REFERENCES

1. W. L. Barnes, A. Dereux, and T. W. Ebbesen, "Surface plasmon subwavelength optics," *Nature*, vol. 424, pp. 824–830, Aug. 2003
2. Homola J., S. S. Yee, and G. Gauglitz, "Surface plasmon resonance sensors: Review," *Sens. Act. B, Chem.*, vol. 54, 3–15, 1999.
3. Kim J.T., J.J. Ju1, S. Park, M.-S. Kim, S.K. Park, and M.-H. Lee, "Chip-to-chip optical interconnect using gold long-range surface plasmon polariton waveguides", *Optics Express*, Vol. 16, No. 17, 13133-13138, 2008.
4. Challener W. A., Chubing Peng, A. V. Itagi, D. Karns, Wei Peng, Yingguo Peng, XiaoMin Yang, Xiaobin Zhu, N. J. Gokemeijer, Y.-T. Hsia, G. Ju, Robert E. Rottmayer, Michael A. Seigler and E. C. Gage, "Heat-assisted magnetic recording by a near-field transducer with efficient optical energy transfer", *Nature Photonics*, vol.3, 220-224, 2009.
5. Porta, P. A., J. Justice, G. Lévêque, and B. Corbett, "Vertical-Cavity Surface-Emitting Lasers With Integrated Excitation of Surface Plasmon polariton Modes," *IEEE Photon. Technol. Lett.*, Vol. 21, No. 4, 222–223, 2009.

Tunable THz metamaterials based on an array of paraelectric $SrTiO_3$ rods

R. Yahiaoui[1], H. Němec[2], P. Kužel[2], F. Kadlec[2], C. Kadlec[2] and P. Mounaix[1]
[1] Centre de Physique Moléculaire Optique et Hertzienne, UMR CNRS 5798, Université Bordeaux I, 351 Cours de la Libération, 33405 Talence cedex, France
[2] Institute of Physics, Academy of Sciences, Na Slovance 2, 182 21 Prague 8, Czech Republic
Corresponding authors: kuzelp@fzu.cz, p.mounaix@cpmoh.u-bordeaux1.fr

Abstract- This work presents theoretical and experimental investigations of a tunable metamaterial which exhibits negative permeability in the THz frequency range. The tunability is obtained by temperature changes, and the sample consists of an array of high-permittivity $SrTiO_3$ (STO) rods micromachined by a femtosecond laser. Structures exhibiting a negative permeability on multiple frequency bands are also investigated and a proper choice of the dimensions of the pattern allows us to achieve a substantial broadening of the frequency band with negative μ.

1. INTRODUCTION

During the last decade, the concept of metamaterials has been conceived and a variety of metamaterial structure was extensively investigated. Most of the works are inspired by of the structures proposed initially by Pendry [1] and deal with metamaterials based on a dielectric substrate with subwavelength metallic patterns. Another approach focusing on the Mie resonances of dielectric particles [2, 3] leads to a different class of metamaterials. In this work, we propose firstly the description and the numerical study of a tunable metamaterial based on the modulation of the permittivity by temperature and so the frequency resonance targeted in the THz wavelength. We also present an extension of this structure, which simultaneously exhibits several magnetic resonances in sub mm range. Finally we will study the impact of the geometry on the frequency broadening band where μ<0. Our investigated metamaterials may offer a possibility to bridge the gap between the microwave and optical frequencies .

2. RESPONSE OF THE METAMATERIAL

Our sample, as shown in fig.1 (a) consists of a high permittivity dielectric material ($SrTiO_3$) with a thickness e = 52μm which was micromachined by a femtosecond laser to obtain a series of bars (width a=42.5μm)[notation must be coherent with what follows: you must change the notation in Fig. 1] separated by air gaps g=32.5μm. Fig.1 (b) shows a scanning electron microscopy image of the structure. The sample is illuminated by plane wave at normal incidence, with the magnetic field parallel to the x axis (H ∥ x axis) and the electric field parallel to the y axis (E ∥ y axis). The resulting propagation direction is along the z axis (***k*** ∥ z axis). Fig2. (a) and (b) show the theoretical and experimental magnitude and phase of the transmittance which are obtained using the transfer matrix method and time-domain terahertz spectroscopy respectively.

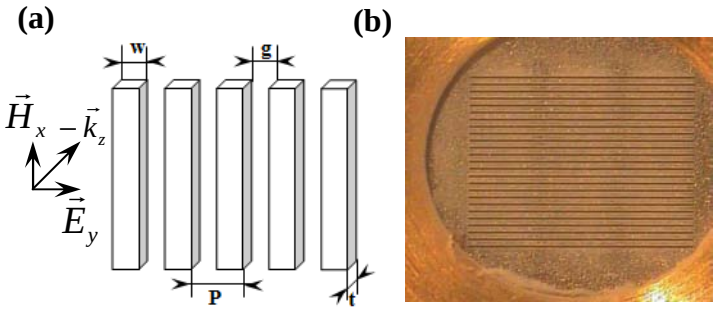


Fig. 1. (a) schematic view of the structure, (b) scanning electron microscopy image of our metamaterial.

The response has been tuned from 0.2 THz to 0.28 THz by changing the temperature from 180K to 324K. Under the given polarisation of magnetic and electric field, magnetic resonances are observed which induce negative values of the effective permeability. Fig. 2 (c) shows a good agreement between the experimental and the calculated response of the magneticproperty. The effective permittivity and permeability are retrieved by applying an extraction procedure described in ref. [4]. For a better

understanding of the physical processes involved within the structure, we use an electromagnetic software simulator HFSS based on the finite element method to calculate the electric and magnetic field distribution within the rods (fig. 2. (d)). The calculation was done for the first resonant mode ~0.28THz at 324K. The wave front of an incident plane wave is subject to a strong distortion close to the metamaterial in order to satisfy simultaneously the continuity and discontinuity conditions of tangential and normal electric-field components at the STO-air interfaces, respectively [5]. The electric field, which develops inside an STO bar, is predominantly tangential close to the surface of the bar. This leads to the creation of displacive eddy currents within the bar cross section, which enhance the magnetic field inside STO along the bar. The resonant behaviour is then expected at specific frequencies.

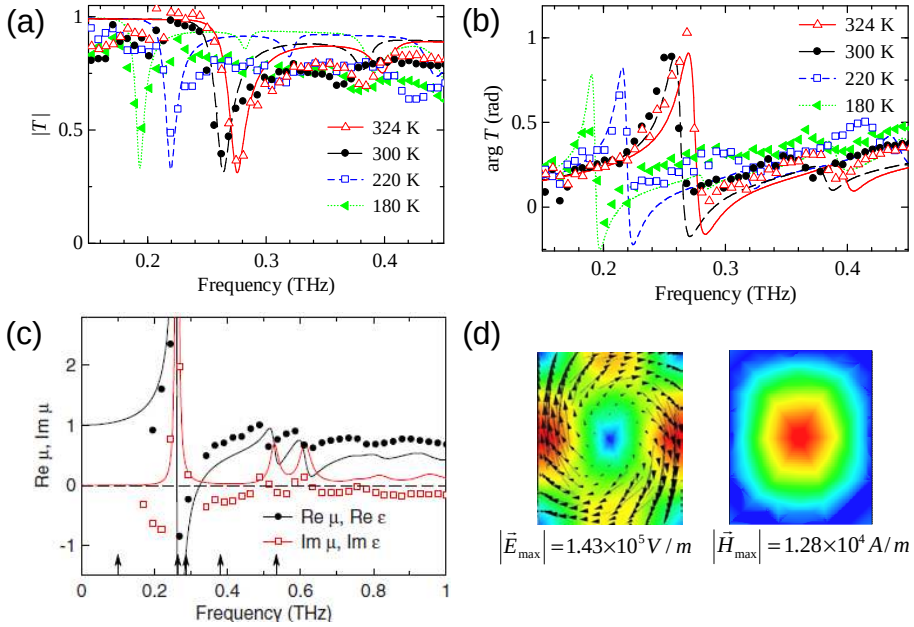


Fig. 2. (a) theoretical and experimental transmission spectrum, (b) theoretical and experimental transmission phase, (c) theoretical and experimental magnetic response at room temperature, (d) electric and magnetic field distribution at the lowest-frequency Mie resonance.

In order to asses the impact of the air-gap *g* and the lateral dimension *w* on the position of the modes of resonance of the metamaterial, we respectively varied *g* within 10–40 µm and *w* within 50–150 µm, while the dimensions of the rods were fixed in such cases. Fig. 3(a) and 3(b) show the result of this parametric study which confirms that *g* has no influence on the position of the magnetic modes, however the resonance frequency presents a hyperbolic decrease as a function of the lateral dimension *w*.

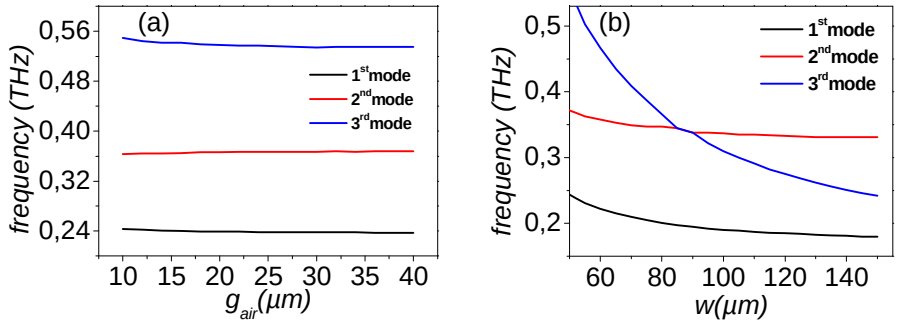


Fig. 3 (a) resonant frequencies as a function of the air gap *g*. (b) resonant frequencies as a function of *w*

3. A MULTIPLE FREQUENCY BANDS METAMATERIAL

A series of works concerning metamaterials which operate at multiple frequency bands have been undertaken at microwave frequencies [6], in terahertz regime [7-8] and even at optical frequencies [9]. In this section, in order to extend the negative permeability region of our metamaterial to several frequency bands, we designed a structure with a set of rods with various widths. Figure 4 (a) shows the unit cell of

the designed metamaterial, which consists of rods with three different widths a, b, and c, respectively, separated by the same air-gap *g*, the thickness *t* of the rods remains constant; we consider an infinite array of such rods in *y* and *z* directions (Fig. 4a). According to fig. 4(b) where $\mu=\mu_1+i\mu_2$, we note that the effective permeability μ is a superposition of the responses of each individual rod, the highlighted zones correspond to the negative permeability regions. The calculated distributions of the magnetic field for the resonance frequencies 0.24THz, 0.334THz and 0.458THz, respectively as illustrated in fig. 4(a) show clearly that the mutual cross couplings are negligible [5]

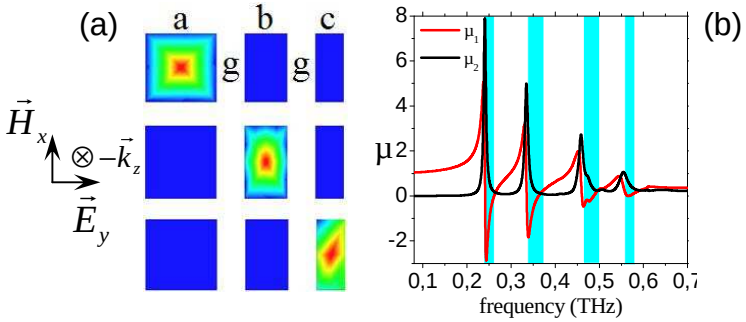


Fig. 4 (a) sections of a unit cell of the MM with the spatial distribution of the resonant magnetic field at 0.24THz, 0.334THz and 0.458THz with the geometrical dimensions: *a*=50μm, *b*=30μm, *c*=20μm, *g*=20μm, (b) calculated spectra of effective μ for the corresponding structure.

4. BROADBAND NEGATIVE PERMEABILITY METAMATERIAL

A broadband planar and non-planar negative refractive index metamaterial based on traditional split ring resonators and wires are reported by Wongkasem et al [10]. In this section, we propose to design an STO based metamaterial which exhibits a much-broader negative permeability band. The investigated metamaterial consists of a single type of rods with a width *a* (varied from 50μm to 200μm in our study), while *g*=30μm and *e*=20μm are kept constant. A broadening of the range with negative μ is achieved with a high aspect ratio (*a*>>*e*). The polarization of the electromagnetic wave is the same as those described in previous sections. The amplitude transmittance and the real part of effective permeability for each value of *a* are depicted in fig. 5(b) and 5(b).

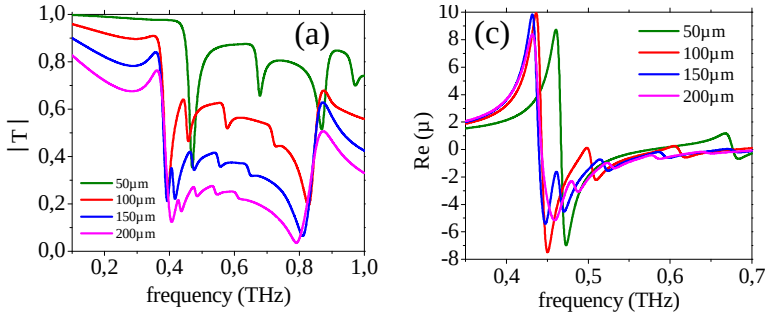


Fig. 5 (a) Calculated amplitude transmittance for several widths *a* of STO rods (*g*=30μm, *e*=20μm, tan δ=2.5%), (b) the corresponding effective permeability.

We note that the position of the first Mie resonance does not shift significantly upon the change of *a*. In fact, it is mainly imposed by the thickness *e* of the metamaterial for *a*>100 μm. By contrast, upon increasing *a*, the distance between the first and higher order resonances is reduced, and the resonances overlap for *a*>>*e* [see Fig. 5(a)]. This leads to a broadening of the region of negative μ [Fig. 5(b)]. For example, the retrieved effective μ for *a*=50 μm is negative within 480–600 GHz, but for higher rod widths this range is much broader; namely for *a*=200 μm it spans over 250 GHz, corresponding to nearly 50% of the central frequency value. Figures 6(a) and 6(b) show the real and imaginary part of the effective permeability, respectively, for *a*=200 μm for different values of tanδ from 0.1% to 5%. According to fig. 6(a), we note that the frequency band of negative permeability becomes increasingly wide, only if the dielectric losses reach a sufficiently high level (tan δ>1%). Upon the increase of tanδ, the amplitude of real part of μ decreases more and more, and a similar behaviour in observed for the

imaginary part of μ (see fig. 6(b)). Further analysis reveals a compromise between a high negative μ limited by the value of tanδ and a large bandwidth where μ is negative. Finally, we propose an optimal geometric dimensions of the structure a=200 μm *g*=30μm, *e*=20μm, which leads to a negative permeability within a frequency band from 430 to 680 GHz.

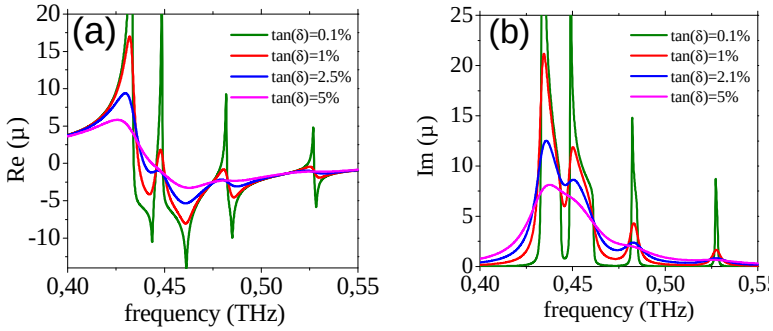


Fig. 6 (a) real part of μ, (b) Imaginary part of μ for *a*=200 μm and tanδ from 0.1% to 5%.

5. CONCLUSION

A high dielectric permittivity metamaterial presented in this work exhibits a negative effective permeability which was tuned by temperature. An alternative structure with negative permeability over than three frequency bands has been investigated. Finally, a smart choice of the lateral dimensions of the metamaterial can lead to a negative permeability over a wide frequency range.

ACKNOWLEDGEMENT

This work was initiated at the University of Bordeaux1 under the project "GIS AMA-SAMM". Financial support from the Ministry of Education of the Czech Republic (project LC-512) and of the Grant Agency of ASCR (project A100100907) is acknowledged.

REFERENCE

1. B. Pendry, A. J. Holden, D. J. Robbins, and W. J. Stewart, "Magnetism from Conductors and Enhanced Nonlinear Phenomena," *IEEE Trans. Microwave Theory Tech*. **47**, 2075 (1999).
2. K. C. Huang, M. L. Povinelli, and J. D. Joannopoulos, "Negative effective permeability in polaritonic photonic crystals," *Appl. Phys. Let*. **85**, 543(2004).
3. Qian Zhao, Lei Kang, B. Du, H. Zhao, Q. Xie, X. Huang, B. Li, J. Zhou, and L. Li, "Experimental Demonstration of Isotropic Negative Permeability in a Three-Dimensional Dielectric Composite," *Phys. Rev. Lett*. **101**, 027402 (2008).
4. H. Němec, P. Kužel, F. Kadlec, C. Kadlec, R. Yahiaoui, and P. Mounaix, "Tunable terahertz metamaterials with negative permeability," *Phys. Rev. B* **79,** 241108(R) (2009).
5. R. Yahiaoui, H. Němec, P. Kužel, F. Kadlec, C. Kadlec, and P. Mounaix, "Broadband dielectric terahertz metamaterials with negative permeability," *Opt. Lett*. **34**, 3541 (2009).
6. H. Chen, L. Ran, J. Huangfu, X. Zhang, K. Chen, T. M. Grzegorczyk and J. A. Kong, "Metamaterial exhibiting left-handed properties over multiple frequency bands," *J. Appl. Phys*. **96**, 5338 (2004).
7. Y. Yuan, C. Bingham, T. Tyler, S. Palit, T. H. Hand, W. J. Padilla, N. M. Jokerst, and S. A. Cummer, "A dual-resonant terahertz metamaterial based on single-particle electric-field-coupled resonators," *Appl. Phys. Lett*. **93**, 191110 (2008).
8. Y. Yuan, C. Bingham, T. Tyler, S. Palit, T. H. Hand, W. J. Padilla, D. R. Smith, N. M. Jokerst, and S. A. Cummer, "Dual-band planar electric metamaterial in the terahertz regime," *Optics Express* **16**, 9746 (2008).
9. N. Shen, M. Kafesaki, T. Koschny, L. Zhang, E. N. Economou, and C.M. Soukoulis, "Broadband blue shift tunable metamaterials and dual-band switches," *Phys. Rev. B* **79**, 161102(R) (2009)
10. N. Wongkasem, A. Akyurtlu, J. Li, A. Tibolt, Z. Kang, and W. D. Goodhue, "Novel broadband terahertz negative refractive index metamaterials: analysis and experiment," *Progress In Electromagnetics Research*, PIER **64**, 205, (2006).

Localized Radiative Energy Transfer from a Plasmonic Bow-Tie Nanoantenna to a Magnetic Thin Film Stack

K. Sendur[1], **A. Kosar**[1], **and M. P. Menguc**[2,3]

[1]Sabanci University, Orhanli-Tuzla, 34956, Istanbul, Turkey
[2]Ozyegin University, Uskudar, 34662 Istanbul, Turkey
[3]University of Kentucky, Lexington, KY 40506, USA
sendur@sabanciuniv.edu

Abstract—

Localized radiative energy transfer from a near-field emitter to a magnetic thin film structure is investigated. A magnetic thin film stack is placed in the near-field of the plasmonic nanoantenna to utilize the evanescent mode coupling between the nanoantenna and magnetic thin film stack. A bow-tie nano-optical antenna is excited with a tightly focused beam of light to improve near-field radiative energy transfer from the antenna to the magnetic thin film structure. A tightly focused incident optical beam with a wide angular spectrum is formulated using Richards-Wolf vector field equations. Radiative energy transfer is investigated using a frequency domain 3-D finite element method solution of Maxwell's equations. Localized radiative energy transfer between the near-field emitter and the magnetic thin film structure is quantified for a given optical laser power at various distances between the near-field emitter and magnetic thin film.

1. INTRODUCTION

Emerging nano-scale plasmonic applications, such as heat-assisted magnetic recording (HAMR), require localized radiative energy transfer that can be achieved using intense optical spots beyond the diffraction limit [1, 2, 3]. When objects are separated by less than a subwavelength scale, the radiative energy transfer between the surfaces can be several orders higher than predicted by Planck's blackbody radiation. The drastic improvement of the radiative energy transfer has potential applications in emerging technologies including heat-assisted magnetic recording [1, 2, 3], thermophotovoltaic energy devices [4, 5], and optically-assisted nanomanufacturing [6, 7].

Recently, there has been increasing research on the radiative energy exchange between object separated by less than a subwavelength scale. In recent studies, Francoeur et al. [8, 9] and Shen et al. [10] demonstrated that the surface phonon polaritons improve the radiative energy transfer between two surfaces at small gaps. Rousseau et al. [11] investigated an experimental setup that can measure the conductance when the objects are separated by varying the distances between 30 nm and 2.5 μm. The experimental data by Rousseau et al. [11] confirms the theoretical results that the near-field radiative energy transfer can be substantially improved at the nanoscale. These studies have demonstrated the potential for engineering near-field emitters for potential applications. Additionally, it has been shown that the radiative energy transfer can be tuned via multiple thin films supporting surface plasmon polaritons [12, 13, 14, 15]. Laser-induced radiative energy transfer involving a scanning probe microscope tip has also been investigated in the literature [16, 17].

An optical nano-antenna can be utilized as a near-field emitter for radiative energy transfer to an object placed in the close vicinity. Antennas have been an efficient means to couple incident electromagnetic energy with small scale electronic devices. A similar coupling mechanism is applicable at optical frequencies between nano-antennas operating at optical frequencies and objects with feature dimensions below the diffraction limit [18, 19, 20, 21, 22, 23]. At optical frequencies, a nanoscale metallic antenna can be utilized to couple an incident optical beam to length scales much smaller than the diffraction limit.

In this study, the radiative energy transfer from a gold bow-tie nano-antenna to a magnetic thin film layer is investigated. A tightly focused beam of light with a wide angular spectrum illuminates the near-field emitter. In Section 2, the formulation for the focused beam model based on Richards-Wolf vector field theory and details of the numerical calculations are presented. In Section 3, the radiative energy transfer between the near-field emitter and the magnetic thin film structure is studied. Localized radiative energy transfer between the emitter and the thin film structure is quantified for a given optical laser power at various distances between them. Concluding remarks appear in Section 4.

2. THEORY

For enhanced localized radiative energy transfer to a magnetic thin-film stack, a bow-tie antenna is used in this study. A bow-tie antenna in the vicinity of the magnetic thin-film structure is illustrated in Fig. 1. An oblique view of the problem geometry is illustrated in Fig. 1(a). Details of the magnetic thin-film stack and some physical parameters regarding the antenna geometry that will be investigated in this study are shown in Fig. 1(b). The bow-tie antenna consists of two triangular gold particles that are separated with a distance of G as shown in Fig. 1. The physical separation between the antenna and the magnetic thin film is D.

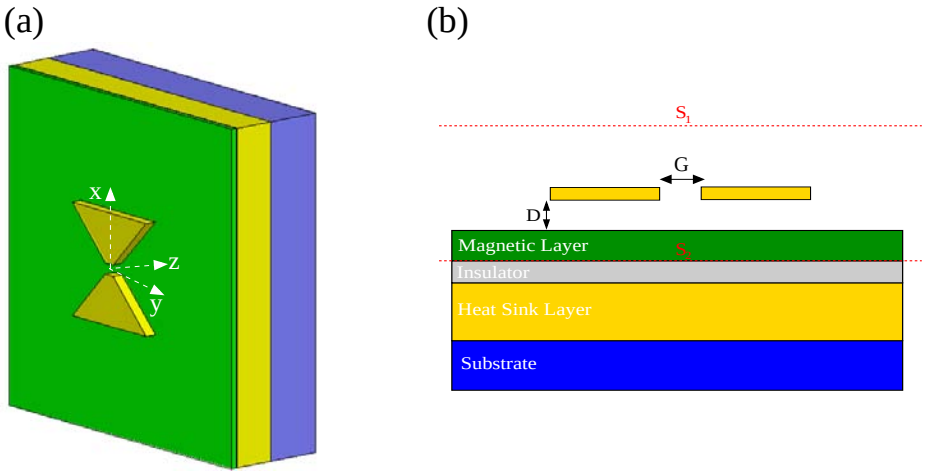


Figure 1: (a) An oblique view of the problem geometry involving a bow-tie antenna and a magnetic thin-film stack. (b) A cross section shows the details of the magnetic thin-film and the antenna's geometry.

The nano-antenna in this study is excited using a focused beam of light from an optical lens. The propagating direction of the incident beam is in the $\hat{z}$-direction. To model the incident focused beam, we used the Richards-Wolf theory [24, 25]. A tightly focused beam of light has a wide angular spectrum. The Richards-Wolf theory [24, 25] provides an accurate representation of an incident beam near the focus of an aplanatic lens. Using the Richards-Wolf vector field representation [24, 25] the total electric field in the vicinity of the focus is given as

$$\mathbf{E}(\mathbf{r}_p) = -\frac{i}{\lambda}\int_0^{\alpha} d\theta \sin\theta \int_0^{2\pi} d\phi\ \mathbf{a}(\theta,\phi)\exp(-i\mathbf{k}\cdot\mathbf{r}_p) \tag{1}$$

where α is the half angle of the beam, $\mathbf{r}_p$ is the observation point

$$\mathbf{r}_p = x_p\hat{x} + y_p\hat{y} + z_p\hat{z} = r_p\cos\phi_p\hat{x} + r_p\sin\phi_p\hat{y} + z_p\hat{z} \tag{2}$$

and

$$\mathbf{k} = \frac{2\pi}{\lambda}(\sin\theta\cos\phi\hat{x} + \sin\theta\sin\phi\hat{y} - \cos\theta\hat{z}). \tag{3}$$

In Eqs. (2) and (3) λ is the wavelength, $r_p = \sqrt{x_p^2 + y_p^2}$, and $\phi_p = \arctan(y_p/x_p)$. In Eq. (1), $\mathbf{a}(\theta,\phi)$ is the weighting vector, which is given as

$$\mathbf{a}(\theta,\phi) = \begin{bmatrix} \cos\theta\cos^2\phi + \sin^2\phi \\ \cos\theta\cos\phi\sin\phi - \cos\phi\sin\phi \\ \sin\theta\cos\phi \end{bmatrix}\sqrt{\cos\theta}, \tag{4}$$

The power of the incident beam propagating in the $\hat{z}$ direction is given by the Poynting's vector

$$P_z = \mathrm{Re}\left[\int\int_{S_1}\left(\frac{1}{2}\mathbf{E}^{\mathbf{i}}(\mathbf{r})\times\mathbf{H}^{\mathbf{i}*}(\mathbf{r})\right)\cdot\hat{n}_1 dS\right] \tag{5}$$

where $\mathbf{E}^{\mathbf{i}}(\mathbf{r})$ is the incident electric field given by Eq. (1) and the $\mathbf{H}^{\mathbf{i}}(\mathbf{r})$ is obtained using Maxwell's equation. The integration surface S_1, shown in Fig. 1(b), is perpendicular to the direction of propagation.

The incident electric field, given by Eq. (1), represents the optical beam generated by the lens system in the absence of the nano-antenna and magnetic thin film stack. Once the incident electric field interacts with the antenna and the magnetic thin film stack, scattered fields $\mathbf{E}^s(\mathbf{r})$ are generated. The total electric field $\mathbf{E}^t(\mathbf{r})$ is composed of two components

$$\mathbf{E}^t(\mathbf{r}) = \mathbf{E}^i(\mathbf{r}) + \mathbf{E}^s(\mathbf{r}) \tag{6}$$

where $\mathbf{E}^t(\mathbf{r})$, $\mathbf{E}^i(\mathbf{r})$, and $\mathbf{E}^s(\mathbf{r})$ are the total, incident, and scattered electric field components, respectively. In this study, to obtain the scattered field, $\mathbf{E}^s(\mathbf{r})$, we used a 3-D finite element method (FEM) based full-wave solution of Maxwells equations. To represent the scattering geometries accurately, tetrahedral elements are used to discretize the computational domain. Radiation boundary conditions are used in FEM simulations. On the tetrahedral elements, edge basis functions and second-order interpolation functions are used to expand the functions. Adaptive mesh refinement is used to improve the coarse solution regions with high field intensities and large field gradients. Adaptive mesh refinement helps to obtain accurate results for different types of geometries. Once the scattered field is solved via the FEM, the total field can be obtained using Eq. (6).

Conversion of the field quantities into power quantities is achieved by applying the Poyntings theorem [27, 28] to the geometry given in Fig 1. The dissipated power within the sample due to the near-field electromagnetic radiation can be obtained by utilizing Poynting's theorem [27, 28]

$$\begin{aligned}\int\int\int_{V_M} \sigma|\mathbf{E}(\mathbf{r})|^2 dV = \int\int_{S_1} \left(\frac{1}{2}\mathbf{E}(\mathbf{r}) \times \mathbf{H}^*(\mathbf{r})\right) \cdot \hat{n}_1 dS - \int\int_{S_2} \left(\frac{1}{2}\mathbf{E}(\mathbf{r}) \times \mathbf{H}^*(\mathbf{r})\right) \cdot \hat{n}_2 dS \\ - \int\int\int_{V_A} \sigma|\mathbf{E}(\mathbf{r})|^2 dV - 2iw \int\int\int_{V} \left(\frac{1}{4}\epsilon|\mathbf{E}(\mathbf{r})|^2 + \frac{1}{4}\mu|\mathbf{H}(\mathbf{r})|^2\right) dV\end{aligned} \tag{7}$$

where V_M represents the magnetic layer, V_A represents the antenna particles, and S_1 and S_2 are the surfaces perpendicular to the direction of propagation shown in Fig. 1. The term on the left-hand side of the equation represents the optical power dissipated over the magnetic film. The first and second terms on the right hand side of the equation represents the optical power entering and exiting the structures from surfaces S_1 and S_2, respectively. The third term represents the optical power dissipated over antenna particles and the last term represents the complex reactive energy stored in the volume between S_1 and S_2. Eq. (7) along with Eq. (1) and Eq. (6) will be utilized to obtain the optical dissipated power profiles over the magnetic film.

3. RESULTS

In this study, the power of the incident optical beam on the antenna is taken as $P_z = 100$ mW and the operating wavelength is 700 nm. The half-beam angle α is selected as 60°, which corresponds to a numerical aperture of about 0.86. The intensity distribution of the incident optical beam onto the nanoantenna is illustrated in Fig. 2(a) for an input power of 100 mW. The optical beam shown in Fig. 2(a) is linearly polarized in the $\hat{x}$ direction. The direction of the polarization of the incident radiation and the orientation of the antenna geometry play an important role in the radiative energy transfer process. If the incident polarization is along the long-axis of the antenna as shown in Fig. 1, then the incident electromagnetic radiation creates induced currents along this axis in the antenna. These induced currents are the source of charge accumulation at the ends of the antenna. The charges created across the gap separating the metallic parts of the antenna have opposite polarity. The oscillation of the charges with opposite polarity is the source of localized radiative energy transfer to the magnetic thin film stack.

The thickness of the gold antenna is selected as 20 nm and the antenna particles are separated by 20 nm. The magnetic thin film stack is composed of a 10 nm magnetic layer, 2 nm insulator layer, 100 nm heat-sink layer deposited over a substrate. The dielectric constants of metals at different wavelength are obtained from Palik [26]. The dissipated optical power density profile in the magnetic recording medium is given in Fig. 2(b) when the antenna is placed 10 nm away from the magnetic thin film stack. The results indicate that a strong localized radiative energy transfer is obtained between the antenna and magnetic thin film.

An important parameter in the radiative energy transfer from the antenna to the magnetic thin film stack is the distance between the antenna and magnetic thin film. In Fig. 3, localized radiative

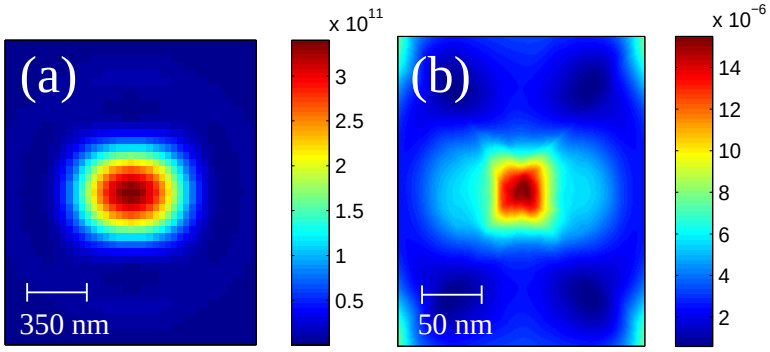


Figure 2: (a) Intensity distribution [V^2/m^2] of the incident optical beam onto the nanoantenna. (b) Dissipated optical power density profile [mW/nm^3] in the cobalt magnetic recording medium.

energy transfer between the near-field emitter and the magnetic thin film structure is quantified at various distances between the near-field emitter and magnetic thin film. The results show the sharp drop in the radiative energy transfer from the antenna to the magnetic thin film. The gold bow-tie nano-antenna primarily utilizes evanescent waves to couple optical energy to the magnetic thin film stack. As the distance is increased from 4 nm to 15 nm, the dissipated power density reduces from 2.4×10^{-5}mW/nm^3 to 1.3×10^{-5}mW/nm^3. It is obvious that the evanescent component of the electromagnetic field is particularly important in large radiative energy transfer from the nanoantenna.

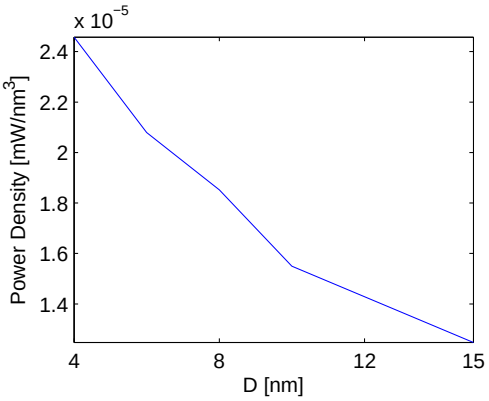


Figure 3: Dissipated optical power density [mW/nm^3] in the cobalt magnetic recording medium as a function of distance from the nanoantenna.

4. CONCLUSION

Radiative energy transfer from a nanoscale bow-tie optical antenna to a magnetic thin film stack was investigated. The dissipated optical power density profile in the magnetic thin film stack shows a strong localized radiative energy transfer from the nanoantenna. Localized radiative energy transfer between the near-field emitter and the magnetic thin film structure was quantified for a given optical laser power at various distances between the near-field emitter and magnetic thin film.

ACKNOWLEDGMENT

This work is supported by TUBITAK under project number 108T482 and by Marie Curie International Reintegration Grant (IRG) to Kursat Sendur (MIRG-CT-2007-203690) and to M. Pinar Menguc (NF-RAD (239382) through FP7-PEOPLE-IRG-2008). Kursat Sendur acknowledges partial support from the Turkish Academy of Sciences.

REFERENCES

1. Challener, W. A., C. Peng, A. V. Itagi, D. Karns, W. Peng, Y. Peng, X. Yang, X. Zhu, N. J. Gokemeijer, Y.-T. Hsia, G. Ju, R. E. Rottmayer, M. A. Seigler, and E. C. Gage, "Heat-assisted

magnetic recording by a near-field transducer with efficient optical energy transfer," *Nature Photon.*, Vol. 3, 220–224, 2009.
2. McDaniel, T., W. Challener, and K. Sendur, "Issues in heat assisted perpendicular recording," *IEEE Trans. Mag.*, Vol. 39, 1972–1979, 2003.
3. Sendur, K., C. Peng, and W. Challener, "Near-field radiation from a ridge waveguide transducer in the vicinity of a solid immersion lens," *Phys. Rev. Lett.*, Vol. 94, 043901, 2005.
4. Narayanaswamy, A. and G. Chen, "Surface modes for near field thermophotovoltaics," *Appl. Phys. Lett.*, Vol. 82, 3544–3546, 2003.
5. DiMatteo, R. S., P. Greiff, S. L. Finberg, K. Young-Waithe, H. K. H. Choy, M. M. Masaki, and C. G. Fonstad, "Enhanced photogeneration of carriers in a semiconductor via coupling across a nonisothermal nanoscale vacuum gap," *Appl. Phys. Lett.*, Vol. 79, 1894, 2001.
6. Lu, Y.-F., B. Hu, Z.-H. Mai, W.-J. Wang, W.-K. Chim, and T.-C. Chong, "Laser-Scanning Probe Microscope Based Nanoprocessing of Electronics Materials," *Jpn. J. Appl. Phys.*, Vol. 40, 4395–4398, 2001.
7. Chimmalgi, A., C. P. Grigoropoulos, and K. Komvopoulos, "Surface nanostructuring by nano-/femtosecond laser-assisted scanning force microscopy," *J. Appl. Phys.*, Vol. 97, 104319, 2005.
8. Francoeur, M. and M. P. Menguc, "Role of the fluctuational electrodynamics theory in near-field radiative heat transfer," *J. Quant. Spectrosc. Radiat. Transfer*, Vol. 109, 280–293, 2008.
9. Francoeur, M., M. P. Menguc, and R. Vaillon, "Near-field radiative heat transfer enhancement ia surface phonon-polaritons coupling in thin films," *Appl. Phys. Lett.*, Vol. 93, 043109, 2008.
10. Shen, S., A. Narayanaswamy, and G. Chen, "Surface phonon polaritons mediated energy transfer between nanoscale gaps," *Nano Lett.*, Vol. 9, 2909–2913, 2009.
11. Rousseau, E., A. Siria, G. Jourdan, S. Volz, F. Comin, J. Chevrier, and J.-J. Greffet, "Radiative heat transfer at the nanoscale," *Nature Photon.*, Vol. 3, 514–517, 2009.
12. Ben-Abdallah, P., K. Joulain, J. Drevillon, and G. Domingues, "Tailoring the local density of states of nonradiative field at the surface of nanolayered materials," *Appl. Phys. Lett.*, Vol. 94, 153117, 2009.
13. Francoeur, M., M. P. Menguc, and R. Vaillon, "Solution of near-field thermal radiation in one-dimensional layered media using dyadic Greens functions and the scattering matrix method," *J. Quant. Spectrosc. Radiat. Transfer*, Vol 110, 2002–2018, 2009.
14. Francoeur, M., M. P. Menguc, and R. Vaillon, "Near-field radiative heat exchanges between two thin films supporting surface phonon-polaritons," *J. Appl. Phys.* (in press) 2010.
15. Francoeur, M., M. P. Menguc, and R. Vaillon, "Local density of electromagnetic states within a nanometric gap formed between two thin films supporting surface phonon-polaritons," *J. Phys. D Appl. Phys.* (in press) 2010.
16. Hawes, E. A., J. T. Hastings, C. Crofcheck, and M. P. Menguc, "Spatial Selective Melting and Evaporation of Nanosized Gold Particles," *Opt. Lett.*, Vol. 33, 1383-1385, 2008.
17. Downes, A., D. Salter, and A. Elfick, "Heating effects in tip-enhanced optical microscopy," *Opt. Express*, Vol. 14, 5216–5222, 2006.
18. Grober, R. D., R. J. Schoelkopf, and D. E. Prober, "Optical antenna: Towards a unit efficiency near-field optical probe," *Appl. Phys. Lett.*, Vol. 70, 1354-1356, 1997.
19. Sendur, K. and W. Challener, "Near-field radiation of bow-tie antennas and apertures at optical frequencies," *J. Microsc.*, Vol. 210, 279-283, 2003.
20. Novotny, L., "Effective Wavelength Scaling for Optical Antennas," *Phys. Rev. Lett.*, Vol. 98, 266802, 2007.
21. Crozier, K. B., A. Sundaramurthy, G. S. Kino, and C. F. Quate, "Optical antennas: Resonators for local field enhancement," *J. Appl. Phys.*, Vol. 94, No. , 4632–4642, 2003.
22. Muhlschlegel, P., H.-J. Eisler, O. J. F. Martin, B. Hecht, and D. W. Pohl, "Resonant Optical Antennas," *Science*, Vol. 308, 1607-1609, 2005.
23. Sendur, K. and E. Baran, "Near-field optical power transmission of dipole nano-antennas," *Appl. Phys. B*, Vol. 96, 325-335, 2009.
24. Wolf, E., "Electromagnetic diffraction in optical systems I. An integral representation of the image field," *Proc. Roy. Soc. London Ser. A*, Vol. 253, 349–357, 1959.
25. Richards, B. and E. Wolf, "Electromagnetic diffraction in optical systems II. Structure of the image field in an aplanatic system," *Proc. Roy. Soc. London Ser. A*, Vol. 253, 358–379, 1959.
26. Palik, E. D., *Handbook of optical constants of solids*, Academic Press, San Diego, 1998.
27. Balanis, C. A., *Advanced Engineering Electromagnetics*, Wiley, New York, 1989.
28. Cheng, D. K., *Field and Wave Electromagnetics*, Addison-Wesley, New York, 1983.

Analytical Formulation of the Radiation Field of Printed Antennas in the Presence of Artificial Magnetic Superstrates

Hussein Attia, Leila Yousefi, Omar Siddiqui and Omar M. Ramahi*
Electrical and Computer Engineering Department,
University of waterloo, Waterloo, Ontario, N2L3G1, Canada
*Corresponding author: oramahi@ece.uwaterloo.ca

Abstract- In this paper, the cavity model of a microstrip patch antenna in conjunction with the reciprocity theorem is used to develop a fast analytical solution for the radiation field of a microstrip patch antenna loaded with a novel artificial magnetic superstrate and to investigate the effect of the engineered superstrate layer on the gain and radiation pattern of the printed patch antenna.

1. INTRODUCTION

Using numerical methods to analyze periodic structures (metamaterials) is an expensive computational task which requires huge computer resources [1]. Therefore; in these problems, numerical methods cannot be used in the design, and optimization process which needs several iterations, and should be used only to validate the final design. In this paper the cavity model of a microstrip patch antenna [2] and the reciprocity theorem are used to develop an analytical solution for the radiation field of a microstrip patch antenna loaded with a novel artificial magnetic superstrate. To investigate the accuracy of the proposed analytical solution, the analytical results for the antenna loaded with the superstrate have been compared with numerical results obtained from the full-wave electromagnetic simulation tool CST "Computer Simulation Technology" for a specific example. In this example, the antenna is designed to operate at 2.2GHz at which the artificial magnetic superstrate has an effective permeability of 15. The modified split ring resonator (MSRR) inclusions are used in the design of the artificial magnetic superstrate [3]. Strong agreement between the analytical and numerical results is achieved.

2. Analytical Formulation for the Antenna's Gain

In this section, the reciprocity theorem and the cavity model [2] of a microstrip patch antenna are used to analyze the radiation properties of a microstrip patch antenna covered with an artificial magnetic material (metamaterial) acting as a superstrate to enhance the gain and efficiency of the antenna. The patch antenna is printed on a grounded substrate of thickness h having relative permeability and permittivity of μ_1, ε_1. At distance d from the substrate is the superstrate layer of thickness B having relative permeability and permittivity of μ_2, ε_2. On top of the superstrate is free space, with total permeability and permittivity of μ_o, ε_o (see Fig. 1).

According to the reciprocity theorem [4], we need to construct two problems. In the first problem, the original radiating patch at $z=h$ is replaced by two magnetic sources M_1 and M_2 (using the cavity model [2]) radiating a far electric field of $E_{1,2}$ at the observation point of $P_{(r,\theta,\emptyset)}$, and in the second problem we will have a fictitious far dipole (reciprocity source) of J_2 at the same observation point having its far magnetic field $\overrightarrow{H_2}$ at the original patch location at $z = h$. The general integral form of the reciprocity theorem is reduced to:

$$\iiint_V \left[\overrightarrow{M_{1,2}} . \overrightarrow{H_2}\right] dV = - \iiint_V \left[\overrightarrow{J_2} . \overrightarrow{E_{1,2}}\right] dV \quad (1)$$

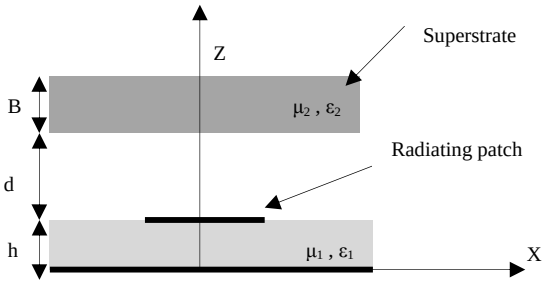


Fig. 1. Microstrip patch antenna covered by a superstrate

The reciprocity source is assumed to have a value of $\overrightarrow{J_2} = \delta(\vec{r} - \overrightarrow{r_p})\hat{u}$ where:

$\hat{u} = \hat{\theta}$ ($\hat{\emptyset}$) for TM (TE) incident wave.

The volume bounded by the microstrip patch and the ground plane can be modeled as a cavity resonator assuming the four walls of this volume to be ideal open circuit (magnetic walls). The mode of concern here is the dominant transverse magnetic mode (TM_{10}) which presumes a zero value of H_z but a non-zero value of E_z. By using the expression of E_z under ideal magnetic walls boundary condition, one can formulate the equivalent magnetic current in the cavity's apertures as $-\vec{n} \times \vec{E}$. The resultant magnetic currents will be y directed. Hence, equation (1) reduces to:

$$\overrightarrow{E_{1,2}}(\overrightarrow{r_p}).\hat{u} = -\iiint_V [\overrightarrow{M_{1,2}} . \overrightarrow{H_2}]\, dV \tag{2}$$

It is clear from (2) that the $\overrightarrow{H_2}$ field is determined at the original patch antenna location due to the reciprocity source at $P(r, \theta, \emptyset)$ in either the $\hat{\theta}$ or $\hat{\emptyset}$ direction, when this dipole source is far from the origin. By reciprocity, this $\overrightarrow{H_2}$ is proportional to the required radiated field $\overrightarrow{E_{1,2}}(\overrightarrow{r_p})$ due to the original patch antenna at $z = h$. The $\overrightarrow{H_2}$ field near the superimposed structure due to this reciprocity source is basically a plane wave, and therefore can be found by modeling each layer as a transmission line (see Fig. 2) having a characteristic impedance and propagation constant which depends on the incident angle of θ [4].

$$n_1^2 = \mu_1 \varepsilon_1 \ , \quad n_2^2 = \mu_2 \varepsilon_2 \ , \quad \eta_o = \sqrt{\frac{\mu_o}{\varepsilon_o}} \ , \quad K_o = \omega \sqrt{\mu_o \varepsilon_o} \tag{3}$$

$$n_1(\theta) = n_1 \cos(\theta_{t2}) = \sqrt{n_1^2 - \sin^2(\theta)} \quad , \quad n_2(\theta) = n_2 \cos(\theta_{t1}) = \sqrt{n_2^2 - \sin^2(\theta)} \tag{4}$$

$$\beta_o = K_{zo} = K_o \cos(\theta) \ , \quad \beta_1 = K_{z1} = K_o\, n_1(\theta) \ , \quad \beta_2 = K_{z2} = K_o\, n_2(\theta) \tag{5}$$

For TE wave or perpendicular polarization:

$$Z_{CO} = \eta_o \sec(\theta) \ , \quad Z_{C1} = \frac{\eta_o\, \mu_1}{n_1(\theta)} \ , \quad Z_{C2} = \frac{\eta_o\, \mu_2}{n_2(\theta)} \tag{6}$$

For TM wave or parallel polarization:

$$Z_{CO} = \eta_o \cos(\theta) \qquad Z_{C1} = \frac{\eta_o\, n_1(\theta)}{\varepsilon_1} \qquad Z_{C2} = \frac{\eta_o\, n_2(\theta)}{\varepsilon_2} \tag{7}$$

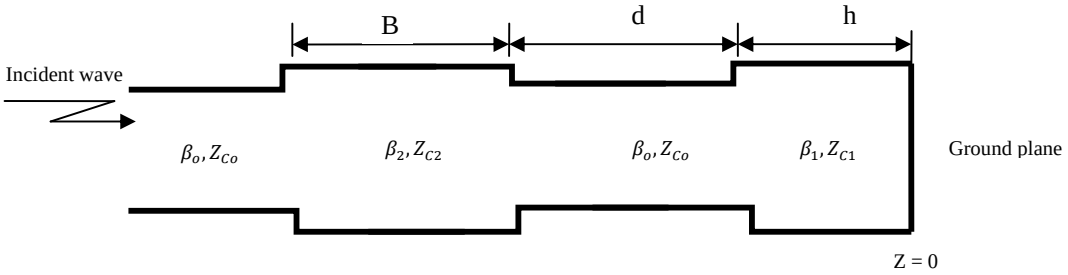


Fig. 2. Transmission line equivalent model of the structure of Fig. 1.

The electric field of the patch antenna is calculated at the desired frequency using (2), and integrated as follows to calculate the antenna gain:

$$Gain\ (\theta,\Phi) = \frac{4\pi * cos^2(X)\ sin^2(Y)/Y^2(\ sin^2(\Phi)\ cos^2(\theta)|F(\theta)|^2 + cos^2(\Phi)\ |G(\theta)|^2\ )}{\int_0^{2\pi}\int_0^{\frac{\pi}{2}}\ cos^2(X)\ sin^2(Y)/Y^2(\ sin^2(\Phi)\ cos^2(\theta)|F(\theta)|^2 + cos^2(\Phi)\ |G(\theta)|^2\ )\ \ sin\ (\theta)\ d\theta\ d\Phi} \quad (8)$$

$$Y\ =\ \frac{K_o\,W}{2} sin(\theta) sin(\Phi\ )\ ,\qquad X\ =\ \frac{K_o\,L}{2} sin(\theta) cos(\Phi\ )$$

Where *W* and *L* are the patch dimensions.

3. Artificial Magnetic Structure as A Superstrate for Planar Antennas

Here we use the method explained in the previous section, to analyze an antenna loaded with an artificial magnetic superstrate (See Fig. 3). The patch antenna used here has dimensions of 36 mm x 36 mm, and is printed on a substrate of Rogers RO4350 having a relative permittivity of 3.48, and a thickness of 0.762 mm. This antenna is designed to operate at the frequency band of 2190-2210 MHz (UMTS) at which the magnetic superstrate has an effective permeability of about 15 (real part) and a magnetic loss tangent of 0.11 (see Fig. 4). For more details about the structure of the artificial magnetic superstrate, and its dimensions, please refer to our previous work in [3].

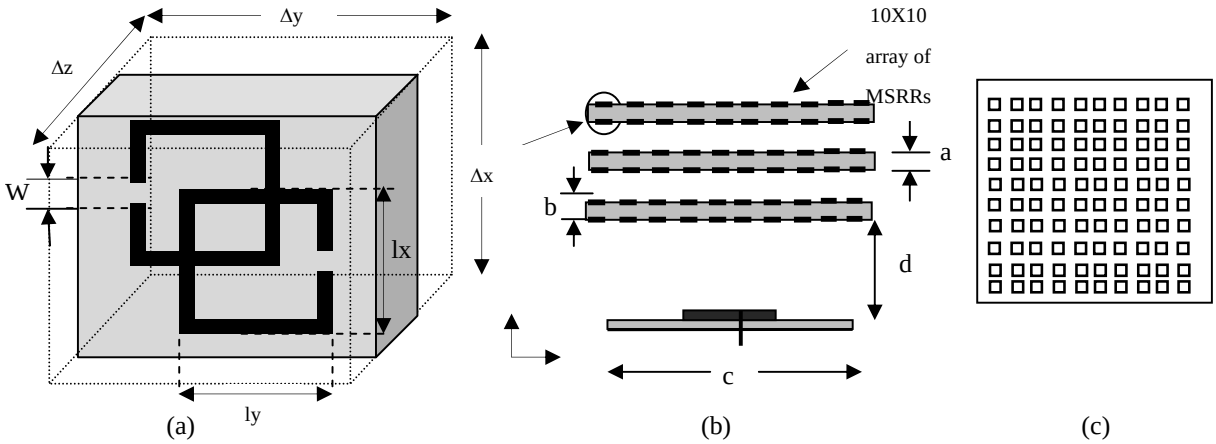


Fig. 3. Geometry of a patch antenna covered by an engineered magnetic superstrate. (a) MSRR unit cell. (b) Side view. (c) Top view. (a = 0.762 mm, b = 2mm, c = 85 mm and d= 12 mm)

Since the MSRRs are aligned in the XY plane, the resultant effective enhanced permeability is provided only in the z direction. Any incident magnetic field in the *x* or *y* direction will not couple to the MSRR inclusion resulting in a permeability equal to that of free-space in those directions. Hence, the engineered material composed of the MSRR inclusions will experience the anisotropic permeability tensor of

$$\bar{\bar{\mu}} = \mu_o \begin{bmatrix} 1 & 0 & 0 \\ 0 & 1 & 0 \\ 0 & 0 & \mu_{r_eff} \end{bmatrix} \tag{9}$$

The analytically calculated effective relative permeability is shown in Fig. 4 (Refer to [3] for formulas used in this calculation). Inter-cell capacitors are formed in the gap regions between the metallic inclusions (unit cells) due to the incident *x*-directed electric field. Therefore, an effective *x* and *y*-directed permittivity is provided by the stored electrical energy in those inter-cell capacitors. In case of a *z*-directed electric field, the metamaterials superstrate will experience an effective permittivity equal to that of its host dielectric as the electric field would be perpendicular to the plane of the unit cell. Therefore, the artificial magnetic material composed of the MSRRs inclusions will experience anisotropic electric permittivity of

$$\bar{\bar{\varepsilon}} = \varepsilon_o \begin{bmatrix} \varepsilon_{r_eff} & 0 & 0 \\ 0 & \varepsilon_{r_eff} & 0 \\ 0 & 0 & \varepsilon_{r_diel} \end{bmatrix} \tag{10}$$

For the formula of ε_{r_eff}, please refer to [3]. According to the above formulas, the effective relative permittivity of the designed structure in the x, and y directions would be equal to 5.62.

Substituting the value of permittivity, and permeability from (9), (10) in the equations presented in section 2, the electric field of the patch antenna is calculated at different frequencies and integrated to calculate the antenna gain using (8).

Fig. 5 shows a comparison between the analytical and numerical results. A strong agreement is observed between both methods. This agreement verifies the accuracy of the proposed analytical model.

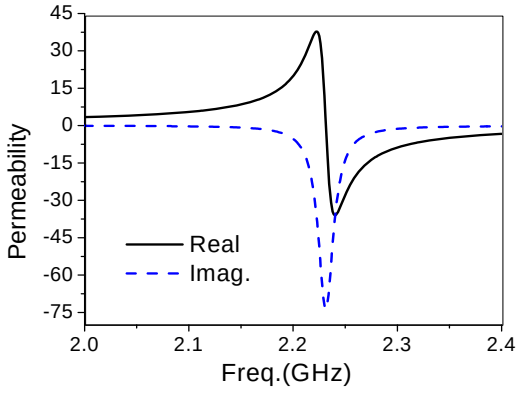
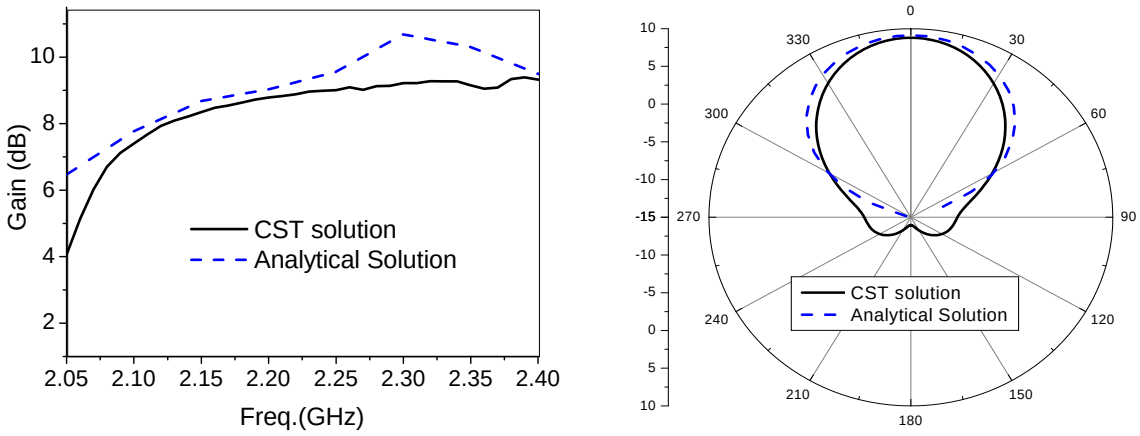


Fig. 4. Analytically calculated relative permeability of the MSRR inclusions.



(a) (b)

Fig. 5. (a) The gain of the microstrip antenna covered with the artificial magnetic superstrate calculated using CST and the analytical solution. (b) The radiation pattern (*E*-plane, *Ø*=0) at 2.2 GHz of the patch antenna covered with the engineered magnetic superstrate.

4. CONCLUSIONS

A fast accurate analytical technique has been presented for the problem of a microstrip patch antenna covered with an artificial magnetic superstrate. The analytical solution is based on the cavity model of a microstrip patch antenna and the reciprocity theorem. A good agreement has been found between this analytical solution and the results obtained from the commercial electromagnetic software CST.

ACKNOWLEDGEMENT

This work has been supported by RIM, *Research In Motion* and the Ministry of Higher Education, Egypt.

REFERENCES

[1] Lee, Y. J., J. Yeo, R. Mittra, and W. S. Park, "Application of Electromagnetic Bandgap (EBG) Superstrates With Controllable Defects for a Class of Patch Antennas as Spatial Angular Filters," *IEEE Trans. Antennas Propag.*, Vol. 53, No. 1, 224-235, 2005.

[2] Carver, K. and J. Mink, "Microstrip antenna technology," *IEEE Trans. Antennas Propag.*, Vol. 29, No. 1, 2-24, 1981.

[3] Attia, H., L. Yousefi, M. M. Bait-Suwailam, M. S. Boybay, O. M. Ramahi, "Enhanced-Gain Microstrip Antenna Using Engineered Magnetic Superstrates," *IEEE Antennas and Wireless Propagation Letters*, Vol. 8, 1198 - 1201, 2009.

[4] Jackson, D. R. and N. G. Alexopoulos, "Gain Enhancement Methods for Printed Circuit Antennas," *IEEE Trans. Antennas Propagation*, Vol. 33, No. 9, 976-987, 1985.



META'10

Edited by
Saïd Zouhdi | LGEP-SUPELEC